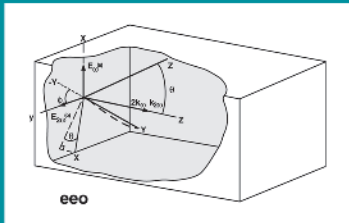


Handbook of Nonlinear Optics

Second Edition, Revised and Expanded



Richard L. Sutherland

Handbook of Nonlinear Optics

Second Edition, Revised and Expanded

Richard L. Sutherland

*Science Applications International Corporation
Dayton, Ohio, U.S.A.*

with contributions by

Daniel G. McLean

*Science Applications International Corporation
Dayton, Ohio, U.S.A.*

Sean Kirkpatrick

*Air Force Research Laboratory
Wright Patterson Air Force Base, Ohio, U.S.A.*



MARCEL DEKKER, INC.

NEW YORK • BASEL

Library of Congress Cataloging-in-Publication Data

A catalog record for this book is available from the Library of Congress

ISBN: 0-8247-4243-5

This book is printed on acid-free paper

Headquarters

Marcel Dekker, Inc
270 Madison Avenue, New York, NY 10016
tel 212-696-9000, fax 212-685-4540

Eastern Hemisphere Distribution

Marcel Dekker AG
Hutgasse 4, Postfach 812, CH-4001 Basel, Switzerland
tel 41-61-260-6300 fax 41-61-260-6333

World Wide Web

<http://www.dekker.com>

The publisher offers discounts on this book when ordered in bulk quantities. For more information, write to Special Sales/Professional Marketing at the headquarters address above

Copyright © 2003 by Marcel Dekker, Inc. All Rights Reserved.

Neither this book nor any part may be reproduced or transmitted in any form or by any means, electronic or mechanical, including photocopying, microfilming, and recording, or by any information storage and retrieval system, without permission in writing from the publisher

Current printing (last digit)
10 9 8 7 6 5 4 3 2 1

PRINTED IN THE UNITED STATES OF AMERICA

OPTICAL ENGINEERING

Founding Editor

Brian J. Thompson

*University of Rochester
Rochester, New York*

Editorial Board

Toshimitsu Asakura
Hokkai-Gakuen University
Sapporo, Hokkaido, Japan

Chris Dainty
Imperial College of Science,
Technology, and Medicine
London, England

Mark Kuzyk
Washington State University
Pullman, Washington

Edmond J. Murphy
JDS/Uniphase
Bloomfield, Connecticut

Joseph Shamir
Technion-Israel Institute
of Technology
Hafai, Israel

Nicholas F. Borrelli
Corning, Inc.
Corning, New York

Bahram Javidi
University of Connecticut
Storrs, Connecticut

Hiroshi Murata
The Furukawa Electric Co , Ltd.
Yokohama, Japan

Dennis R. Pape
Photonic Systems Inc.
Melbourne, Florida

David S. Weiss
Heidelberg Digital L.L.C.
Rochester, New York

1. Electron and Ion Microscopy and Microanalysis: Principles and Applications, *Lawrence E. Murr*
2. Acousto-Optic Signal Processing: Theory and Implementation, *edited by Norman J. Berg and John N. Lee*
3. Electro-Optic and Acousto-Optic Scanning and Deflection, *Milton Gottlieb, Clive L. M. Ireland, and John Martin Ley*
4. Single-Mode Fiber Optics: Principles and Applications, *Luc B. Jeunhomme*
5. Pulse Code Formats for Fiber Optical Data Communication: Basic Principles and Applications, *David J. Morris*
6. Optical Materials: An Introduction to Selection and Application, *Solomon Musikant*
7. Infrared Methods for Gaseous Measurements: Theory and Practice, *edited by Joda Wormhoudt*
8. Laser Beam Scanning: Opto-Mechanical Devices, Systems, and Data Storage Optics, *edited by Gerald F. Marshall*
9. Opto-Mechanical Systems Design, *Paul R. Yoder, Jr.*
10. Optical Fiber Splices and Connectors: Theory and Methods, *Calvin M. Miller with Stephen C. Mettler and Ian A. White*
11. Laser Spectroscopy and Its Applications, *edited by Leon J. Radziemski, Richard W. Solarz, and Jeffrey A. Paisner*
12. Infrared Optoelectronics: Devices and Applications, *William Nunley and J. Scott Bechtel*
13. Integrated Optical Circuits and Components: Design and Applications, *edited by Lynn D. Hutcheson*
14. Handbook of Molecular Lasers, *edited by Peter K. Cheo*
15. Handbook of Optical Fibers and Cables, *Hiroshi Murata*
16. Acousto-Optics, *Adrian Korpel*
17. Procedures in Applied Optics, *John Strong*
18. Handbook of Solid-State Lasers, *edited by Peter K. Cheo*
19. Optical Computing: Digital and Symbolic, *edited by Raymond Arrathoon*
20. Laser Applications in Physical Chemistry, *edited by D. K. Evans*
21. Laser-Induced Plasmas and Applications, *edited by Leon J. Radziemski and David A. Cremers*
22. Infrared Technology Fundamentals, *Irving J. Spiro and Monroe Schlessinger*
23. Single-Mode Fiber Optics: Principles and Applications, Second Edition, Revised and Expanded, *Luc B. Jeunhomme*
24. Image Analysis Applications, *edited by Rangachar Kasturi and Mohan M. Trivedi*
25. Photoconductivity: Art, Science, and Technology, *N. V. Joshi*
26. Principles of Optical Circuit Engineering, *Mark A. Mentzer*
27. Lens Design, *Milton Laikin*
28. Optical Components, Systems, and Measurement Techniques, *Rajpal S. Sirohi and M. P. Kothiyal*
29. Electron and Ion Microscopy and Microanalysis: Principles and Applications, Second Edition, Revised and Expanded, *Lawrence E. Murr*

-
- 30. Handbook of Infrared Optical Materials, *edited by Paul Kloczek*
 - 31. Optical Scanning, *edited by Gerald F. Marshall*
 - 32. Polymers for Lightwave and Integrated Optics: Technology and Applications, *edited by Lawrence A. Hornak*
 - 33. Electro-Optical Displays, *edited by Mohammad A. Karim*
 - 34. Mathematical Morphology in Image Processing, *edited by Edward R. Dougherty*
 - 35. Opto-Mechanical Systems Design: Second Edition, Revised and Expanded, *Paul R. Yoder, Jr.*
 - 36. Polarized Light: Fundamentals and Applications, *Edward Collett*
 - 37. Rare Earth Doped Fiber Lasers and Amplifiers, *edited by Michel J. F. Digonnet*
 - 38. Speckle Metrology, *edited by Rajpal S. Sirohi*
 - 39. Organic Photoreceptors for Imaging Systems, *Paul M. Borsenberger and David S. Weiss*
 - 40. Photonic Switching and Interconnects, *edited by Abdellatif Marrakchi*
 - 41. Design and Fabrication of Acousto-Optic Devices, *edited by Akis P. Goutzoulis and Dennis R. Pape*
 - 42. Digital Image Processing Methods, *edited by Edward R. Dougherty*
 - 43. Visual Science and Engineering: Models and Applications, *edited by D. H. Kelly*
 - 44. Handbook of Lens Design, *Daniel Malacara and Zacarias Malacara*
 - 45. Photonic Devices and Systems, *edited by Robert G. Hunsperger*
 - 46. Infrared Technology Fundamentals: Second Edition, Revised and Expanded, *edited by Monroe Schlessinger*
 - 47. Spatial Light Modulator Technology: Materials, Devices, and Applications, *edited by Uzi Efron*
 - 48. Lens Design: Second Edition, Revised and Expanded, *Milton Laikin*
 - 49. Thin Films for Optical Systems, *edited by François R. Flory*
 - 50. Tunable Laser Applications, *edited by F. J. Duarte*
 - 51. Acousto-Optic Signal Processing: Theory and Implementation, Second Edition, *edited by Norman J. Berg and John M. Pellegrino*
 - 52. Handbook of Nonlinear Optics, *Richard L. Sutherland*
 - 53. Handbook of Optical Fibers and Cables: Second Edition, *Hiroshi Murata*
 - 54. Optical Storage and Retrieval, Memory, Neural Networks, and Fractals, *edited by Francis T. S. Yu and Suganda Jutamulia*
 - 55. Devices for Optoelectronics, *Wallace B. Leigh*
 - 56. Practical Design and Production of Optical Thin Films, *Ronald R. Willey*
 - 57. Acousto-Optics: Second Edition, *Adrian Korpel*
 - 58. Diffraction Gratings and Applications, *Erwin G. Loewen and Evgeny Popov*
 - 59. Organic Photoreceptors for Xerography, *Paul M. Borsenberger and David S. Weiss*
 - 60. Characterization Techniques and Tabulations for Organic Nonlinear Optical Materials, *edited by Mark Kuzyk and Carl Dirk*

61. Interferogram Analysis for Optical Testing, *Daniel Malacara, Manuel Servín, and Zacarias Malacara*
62. Computational Modeling of Vision: The Role of Combination, *William R. Uttal, Ramakrishna Kakarala, Sriram Dayanand, Thomas Shepherd, Jagadeesh Kalki, Charles F. Lunsford, Jr., and Ning Liu*
63. Microoptics Technology: Fabrication and Applications of Lens Arrays and Devices, *Nicholas F. Borrelli*
64. Visual Information Representation, Communication, and Image Processing, *Chang Wen Chen and Ya-Qin Zhang*
65. Optical Methods of Measurement: Wholefield Techniques, *Rajpal S. Sirohi and Fook Siong Chau*
66. Integrated Optical Circuits and Components: Design and Applications, *edited by Edmond J. Murphy*
67. Adaptive Optics Engineering Handbook, *edited by Robert K. Tyson*
68. Entropy and Information Optics, *Francis T. S. Yu*
69. Computational Methods for Electromagnetic and Optical Systems, *John M. Jarem and Partha P. Banerjee*
70. Laser Beam Shaping: Theory and Techniques, *edited by Fred M. Dickey and Scott C. Holswade*
71. Rare-Earth-Doped Fiber Lasers and Amplifiers: Second Edition, Revised and Expanded, *edited by Michel J. F. Digonnet*
72. Lens Design: Third Edition, Revised and Expanded, *Milton Laikin*
73. Handbook of Optical Engineering, *edited by Daniel Malacara and Brian J. Thompson*
74. Handbook of Imaging Materials, *edited by Arthur S. Diamond and David S. Weiss*
75. Handbook of Image Quality: Characterization and Prediction, *Brian W. Keelan*
76. Fiber Optic Sensors, *edited by Francis T. S. Yu and Shizhuo Yin*
77. Optical Switching/Networking and Computing for Multimedia Systems, *edited by Mohsen Guizani and Abdella Battou*
78. Image Recognition and Classification: Algorithms, Systems, and Applications, *edited by Bahram Javidi*
79. Practical Design and Production of Optical Thin Films: Second Edition, Revised and Expanded, *Ronald R. Willey*
80. Ultrafast Lasers: Technology and Applications, *edited by Martin E. Fermann, Almantas Galvanauskas, and Gregg Sucha*
81. Light Propagation in Periodic Media: Differential Theory and Design, *Michel Nevière and Evgeny Popov*
82. Handbook of Nonlinear Optics, Second Edition, Revised and Expanded, *Richard L. Sutherland*

Additional Volumes in Preparation

Optical Remote Sensing: Science and Technology, *Walter Egan*

Preface to Second Edition

The science of optics, the branch of physics that deals with the properties and phenomena of visible and invisible light, has generated a wealth of knowledge that makes its use pervasive in other physical sciences, biology, medicine, forensics, agriculture, art, industry, and the military. This has spawned a technology called photonics, a name based on the quantum of energy in the electromagnetic field, the photon. The domain of photonics extends from energy generation to detection to communications and information processing, and includes all means of generating and harnessing light for useful purposes.

Both the science and technology aspects of optics have and continue to be vastly influenced by the field of nonlinear optics. It is a discipline that has enhanced our understanding of fundamental light–matter interactions as well as provided the means for accomplishing a variety of engineering tasks. The purpose of this book is to provide a balanced treatment of second- and third-order nonlinear optics, covering areas useful to the practicing scientist and engineer. The intent is to serve as a ready source of information useful to those researchers performing characterization of nonlinear materials, using the methods of nonlinear optics in scientific studies, and exploiting nonlinear optical phenomena in photonics.

This edition of the *Handbook of Nonlinear Optics* has been updated and new material has been added. It is evident from a perusal of the scientific literature that advances in nonlinear optics continue at a rapid pace. For example, frequency conversion in new bulk and quasi-phase-matched materials as well as the development of new optical parametric oscillators are areas in which progress is continuing. Ultrafast optics and the sub-picosecond domain of optical characterization offer interesting and challenging avenues for probing the properties of materials and developing new applications. Furthermore, new techniques are continually being developed to measure and modify the properties of materials for diverse applications such as optical limiting, nonlinear fluorescent imaging, and two-photon photopolymerization.

As in the previous edition, selection of topics for inclusion was based on a certain bias for what has been important to me as a general practitioner of nonlinear optics. In this regard, I have chosen to add work done in my group that is relevant primarily to the characterization and application of nonlinear materials. However, in the interest of properly setting the stage for the bulk of the book, and because it so often seems to be a point of confusion for beginners, I have expanded the first chapter, which deals with elements of nonlinear optical theory. Chapter 2, "Frequency Doubling and Mixing," and Chapter 3, "Optical Parametric Generation, Amplification, and Oscillation," so important in the generation of light for other nonlinear optics applications, have been expanded and updated primarily to include new results reported in the literature. Chapters 6 ("Nonlinear Index of Refraction"), 7 ("Characterization of Nonlinear Refractive Index Materials"), 9 ("Nonlinear Absorption"), and 10 ("Experimental Techniques in Nonlinear Absorption") all incorporate new material. Several of the chapters tabulating materials data (Chapters 5, 8, and 13) have also been updated. Chapter 13 replaces Chapter 11 in the previous edition. Two new chapters (Chapter 11, "Ultrafast Characterization Techniques," and Chapter 12, "Laser Flash Photolysis") have been added, covering important topics in the expanding characterization requirements of nonlinear materials. Finally, Chapter 17, "Electro-Optic Effects," has been added because the effect plays such a central role in several devices used in optics, as well as in the photorefractive effect, and because it is arguably a nonlinear effect, depending as it does on the interaction of two or more electric fields.

This second edition also afforded the opportunity to correct errors and misprints that occurred in the first edition. My gratitude goes to those who have graciously pointed these out to me.

As always, I am indebted to several people who have been of great help in preparing this work. Not the least of these is my family, which has stood beside me with patience and support. I would also like to thank my employer, SAIC, and the U.S. Air Force Research Lab (AFRL/MLPJ) for their encouragement of this project. Finally, I acknowledge my colleagues for their helpful advice and criticism, especially Sean Kirkpatrick and Daniel G. McLean, who authored Chapters 11 and 12, respectively, and Suresh Chandra, who contributed to Chapter 3.

Richard L. Sutherland

Preface to the First Edition

Shortly after the demonstration of the first laser in 1960, Peter Frankin and coworkers ushered in nonlinear optics (NLO) with the observation of second harmonic generation in a quartz crystal. Since then, NLO has burgeoned into a mature field of science and engineering. The scope of this discipline includes all phenomena in which the optical parameters of materials are changed with irradiation by light. Generally, this requires high optical intensities, which is the main reason that NLO matured in parallel with laser technology. Judging by the growth and continued good health of publications and international conferences on the subject, NLO appears to have a strong future in areas of photonics devices and scientific investigations.

The impact of NLO on science and technology has been twofold. First, it has enhanced our understanding of fundamental light-matter interactions. Second, it has been a driving force in the rejuvenation of optical technology for several areas of science and engineering. NLO has matured in the sense of being a well-developed and systematic theory as well as providing applications for a variety of engineering tasks. Second and third order phenomena and devices are now at a stage of understanding and development such that a coherent description and summary of these areas forming the core of the subject are now possible and desirable.

The rapid development of the subject has created the need for a handbook that summarizes technical details concerning core areas impacting several engineering and scientific endeavors. The general practitioner of NLO requires information in at least four critical areas: (1) mathematical formulas applicable to a variety of experimental and design situations, (2) examples of ways NLO is applied to specific technical problems, (3) a survey of device and materials data for comparison purposes and numerical evaluation of formulas, and (4) in-depth descriptions of methods required for characterizing new materials. When seeking this information, novice and expert alike are often

bewildered by a lack of continuity in style notation, content, and physical units contained in the literature. Textbooks tend to develop the subject in depth, with an emphasis on pedagogical style and with considerable mathematical detail. This inherently limits the scope of the material covered. Useful results are scattered throughout the text, usually without any helpful summary of important and useful formulas. Moreover, discussions of applications and experimental methods as well as materials and device data, are often sparse. When seeking information, what a practicing scientist or engineer (or student) needs is often more than a cursory treatment of a subject, but not one lost in mathematical detail.

While a few handbooks and treatises on NLO exist, some of these are dated and some lack continuity in style, nomenclature, and use of physical units, primarily because of multiple authorship. Some are rich in materials data but are lacking in the other four areas I describe above. Finally, some treat a limited scope of phenomena, such as only second order effects or a single application area. What is needed is a balanced treatment of both second and third order NLO covering areas useful to the practicing scientist and engineer.

The purpose of this book is to fulfill this need by providing a ready source of information to applied scientists, engineers, students, and others interested in the applications of NLO. Important formulas, experimental methods, and materials data are summarized in the form of a handy reference to several aspects of the field. The scope of the book includes experimental applications and a discussion of devices.

This book is an outgrowth of my years as a general practitioner of NLO. As the leader of an optical characterization group for optical limiting applications, I have been involved in the tasks of conceptualizing devices based on NLO, searching for materials to transform the concepts to practice, characterizing the nonlinear properties of materials, and testing prototypes. Also, on occasion I have had the opportunity to teach a graduate-level course in NLO. The material for this book was gathered from my lecture notes, on-the-job experience, and specific research directed toward this work. It is my intention that the contents should largely fulfill the needs of those researchers performing characterization of nonlinear materials, using NLO methods in scientific studies and exploiting NLO phenomena in photonic devices.

The richness and vitality of NLO dictate against a fully comprehensive treatment at any given point in time, simply not everything can be covered. I admit to a certain bias, and the material given here is largely what has been of importance to me as a general practitioner of NLO. Therefore, this work concentrates on what I consider the core of the subject, including second order phenomena involving frequency conversion, and the third order phenomena of

nonlinear phase modulation, nonlinear absorption, and nonlinear scattering. The book treats technologically significant phenomena and presents a summary of important formulas useful in the understanding and application of NLO. Succinct physical interpretations of the mathematics are also given, with an emphasis on conceptual understanding. Experimental methods for characterizing nonlinear parameters are described for both second and third order materials. A discussion of well-accepted as well as novel, less well-known methods is included. Finally, technical data on selected materials are also summarized.

Differences in notation in the literature can often lead to confusion. Therefore, I feel it imperative to clarify some of the mathematical notation that I strive to use consistently in the book. First, an optical wave propagating in space and time is a real quantity and is represented by a real mathematical expression. The simplest sinusoidal wave has the form

$$\mathbf{E}^{(\sim)}(\mathbf{r}, t) = A' \cos(\mathbf{k} \cdot \mathbf{r} - \omega t)$$

In NLO, the product of two or more waves appears in many formulas, and it is thus convenient to give this expression in complex exponential form:

$$\mathbf{E}^{(\sim)}(\mathbf{r}, t) = \frac{1}{2} A' \exp[i(\mathbf{k} \cdot \mathbf{r} - \omega t)] + \text{complex conjugate} \quad (1)$$

Note that the addition of the complex conjugate (c.c.) keeps the quantity real. It is evident from this expression that the product of several waves will involve 1/2 raised to some power. It is common to avoid this by suppressing the factor of 1/2 and rewriting the equation as

$$\mathbf{E}^{(\sim)}(\mathbf{r}, t) = A \exp[i(\mathbf{k} \cdot \mathbf{r} - \omega t)] + \text{c.c.} \quad (2)$$

where $A = (1/2)A'$. The mathematical form given in Eq. (2) is used for optical waves throughout this book. This is important to note because the use of the other complex form of the field would lead to a different numerical prefactor in the definition of optical intensity, the key parameter connecting theory to measurements.

Another important note is the definition of scalars, vectors, and tensors. Both vectors and tensors are presented as bold symbols, such as \mathbf{E} . Whether the symbol represents a vector or a tensor should be obvious from the context. Scalar quantities are represented by nonbold symbols.

Both SI and cgs (esu) systems of units are used as much as possible throughout the book. The system of units used in formulas is also often a source of much confusion in NLO. Therefore, care has been taken to present formulas in

both sets of units as much as possible, the units of measure in both systems are given for key physical parameters, and conversion formulas between the two systems are summarized.

Chapter 1 introduces elements of NLO theory. It is useful to study this chapter to acquaint oneself with the notation used throughout this book as well as to become familiar with the underlying principles of the subject. Chapters 2 and 3 deal with second order NLO phenomena. These include frequency conversion and optical parametric phenomena. Topics covered range from the operation of ideal devices to realistic optical beams interacting in nonideal materials. Various aspects such as phase matching in uniaxial and biaxial crystals, effective nonlinear coefficients, temporal effects, tuning, bandwidth, and the effects of absorption and diffraction are discussed. The materials characterization techniques for second order NLO coefficients is the subject of Chapter 4. This is followed in Chapter 5 by a tabulation of second order NLO parameters for several selected materials.

The remainder of the book is devoted to third order NLO. Chapters 6 and 9 discuss nonlinear refraction and nonlinear absorption, respectively. A summary of different physical mechanisms contributing to these phenomena is given. Detailed discussions of important applications are included. Experimental techniques for characterizing the respective nonlinearities in materials form the subjects of Chapter 7 and 10. Materials data are tabulated for a variety of gases, liquids, solutions, and solids in Chapters 8 and 11. Nonlinear scattering (stimulated Raman and stimulated Brillouin scattering) is treated in Chapters 12 and 13. Brief descriptions of the utilization of these phenomena for frequency conversion and optical beam control are given. Finally, materials data relating to these phenomena are presented in Chapter 14.

In compiling the information for this book, I have felt like the proverbial discoverer standing on the shoulders of giants. I am much indebted to the countless number of researchers who have paved the way for the rest of us and gave the time to so adequately document their results with great detail and insight. It would be impossible to thank them all by name. I would, however, like to acknowledge a few with whom I have had the pleasure of interacting through workshops or on site visits at Wright Patterson Air Force Base. To Elsa Garmire, Tony Garito, Hyatt Gibbs, Art Smirl, M. J. Soileau, George Stegeman, and Eric Van Stryland I give thanks for insightful discussions. In addition, I would like to thank my colleagues at SAIC, particularly Dan McLean, Bob Epling, Paul Fleitz, and Lalgudi Natarajan, for their contributions to this work. My thanks also to the staff of Marcel Dekker, Inc., for inviting me to write this book and encouraging its completion, as well as to both SAIC and U.S. Air Force Wright Lab (WL/MLPJ) for their encouragement of this project. Finally, my greatest debt

of gratitude is to my wife, Marcine, and my daughters, Kari and Kendra, for their patience, understanding, and unwavering support to me in the sometimes seemingly endless task of completing this book.

Richard L. Sutherland

Contents

<i>Preface to the Second Edition</i>	<i>iii</i>
<i>Preface to the First Edition</i>	<i>v</i>
1. Elements of the Theory of Nonlinear Optics	1
2. Frequency Doubling and Mixing	33
3. Optical Parametric Generation, Amplification, and Oscillation	121
4. Characterization of Second Order Nonlinear Optical Materials	241
5. Properties of Selected Second Order Nonlinear Optical Materials	295
6. Nonlinear Index of Refraction	337
7. Characterization of Nonlinear Refractive Index Materials	433
8. Optical Properties of Selected Third Order Nonlinear Optical Materials	499
9. Nonlinear Absorption	579
10. Experimental Techniques in Nonlinear Absorption	627
11. Ultrafast Characterization Techniques <i>Sean Kirkpatrick</i>	673
12. Laser Flash Photolysis <i>Daniel G. McLean</i>	725

13	Nonlinear Absorption Properties of Selected Materials	767
14	Stimulated Raman Scattering	793
15	Stimulated Brillouin Scattering	813
16	Properties of Selected Stimulated Light-Scattering Materials	835
17.	Electro-Optic Effects	843
	<i>Index</i>	947

1

Elements of the Theory of Nonlinear Optics

Optics is an important part of everyday life. Light seems to flow or propagate through empty space, as well as through material objects, and provides us with visual information about our world. The familiar effects of reflection, refraction, diffraction, absorption, and scattering explain a wide variety of visual experiences common to us, from the focusing of light by a simple lens to the colors seen in a rainbow. Remarkably, these can be explained by assigning a small set of optical parameters to materials. Under the ordinary experiences of everyday life, these parameters are constant, independent of the intensity of light that permits observation of the optical phenomena. This is the realm of what is called linear optics.

The invention of the laser gave rise to the study of optics at high intensities, leading to new phenomena not seen with ordinary light such as the generation of new colors from monochromatic light in a transparent crystal, or the self-focusing of an optical beam in a homogeneous liquid. At the intensities used to generate these types of effects, the usual optical parameters of materials cannot be considered constant but become functions of the light intensity. The science of optics in this regime is called nonlinear optics.

The theory of nonlinear optics builds on the well-understood theory of linear optics, particularly that part known as the interaction of light and matter. Ordinary matter consists of a collection of positively charged cores (of atoms or molecules) and surrounding negatively charged electrons. Light interacts primarily with matter via the valence electrons in the outer shells of electron orbitals. The fundamental parameter in this light-matter interaction theory is

the electronic polarization of the material induced by light. Extending the definition of this parameter to the nonlinear regime allows the description of a rich variety of optical phenomena at high intensity.

This chapter presents a brief overview of the theory of nonlinear optics. Formulas are given which generally apply to a number of phenomena discussed in later chapters. For a more pedagogical treatment, consult the references given at the end of this chapter.

I. ELECTROMAGNETIC BASIS OF OPTICS

A. The Optical Electric Field

Light is an electromagnetic wave. It consists of electric and magnetic fields, $\mathbf{E}^{(\sim)}$ and $\mathbf{H}^{(\sim)}$, respectively. The superscripted tilde (\sim) implies that the fields are rapidly varying in time, and the fields are real quantities. For most of optics, the optical wave may be characterized by defining its electric field. (The magnetic field is related to the electric field through Maxwell's equations from electromagnetic theory [1].)

Nonlinear optics is performed with lasers, which have a highly directional nature. Therefore, it is common to assume that the electric field is a wave propagating primarily in one direction in space. Allowance may be made for a finite amount of beam spreading, or diffraction. This primary direction of propagation is usually taken to be along the z -axis. (For noncollinear propagation of multiple beams, the primary change of the beams with distance is taken to be along a single axis, again usually the z -axis.) Hence, the general form of the electric field wave is given by

$$\mathbf{E}^{(\sim)}(\mathbf{r}, t) = \hat{\mathbf{e}} A(\mathbf{r}, t) \exp[i(kz - \omega t)] + \text{c.c.} \quad (1)$$

In this equation, k is the wave vector of propagation and ω is the circular frequency of the rapidly oscillating wave. The wave amplitude $A(\mathbf{r}, t)$ may have a space- and time-dependence, which is slowly varying compared to the rapidly varying parts (space and time) of the oscillating wave. This amplitude is, in general, complex and includes the possibility of phase accumulation in addition to that contained in the exponent of Eq. (1). The polarization of the wave (i.e., direction of the electric field vector) is given by the unit vector $\hat{\mathbf{e}}$. When this vector is real, the wave is said to be plane polarized. A complex unit vector implies that the wave is elliptically polarized. A special case of this is circular polarization. For most of the cases in this book, plane polarized light waves will be assumed unless otherwise specified. Finally, the notation "c.c." implies complex conjugate. It is included in the definition of Eq. (1) since the field $\mathbf{E}^{(\sim)}$ is a real quantity.

For a large number of problems in linear and nonlinear optics, the field can be assumed to be of infinite extent and constant in amplitude and phase in a plane transverse to the direction of propagation. Thus, the complex field amplitude becomes a function of z and t only: $A(z, t)$. Such a wave is called an infinite plane wave, or sometimes just a plane wave. Certainly this is only an approximation since real laser beams have a finite transverse extent and vary spatially along the transverse direction.

A common form of a finite beam is the TEM₀₀ mode of a circular Gaussian beam. The field of this type of wave has the following form.

$$\mathbf{E}^{(-)}(\mathbf{r}, t) = \hat{\mathbf{e}} A(z, t) \frac{w_0}{w(z)} \exp \left\{ i \left[\frac{kr^2}{2q(z)} + kz - \tan^{-1} \left(\frac{z}{z_R} \right) - \omega t \right] \right\} + \text{c.c.} \quad (2)$$

This beam has azimuthal symmetry and its form is illustrated in Fig. 1. Note that the beam has a Gaussian cross section with a variable radius $w(z)$, which is defined as the half-width of the Gaussian curve at the point r (the radial coordinate), where the curve is at 1/e of its maximum value, as shown in Fig. 1b. The radius has a minimum, defined by w_0 , at the plane $z = 0$, and $w(z)$ is given by

$$w(z) = w_0 \left[1 + \left(\frac{z}{z_R} \right)^2 \right]^{1/2} \quad (3)$$

The diameter of the beam at $z = 0$ is $2w_0$ and is called the beam waist.

The surface of constant phase for a Gaussian beam is curved. At the beam waist the phase has an infinite radius of curvature, and hence mimics a plane wave. For large distances away from the waist, the radius of curvature is $\sim z$. The quantity $q(z)$ is called a complex radius of curvature and is given by

$$q(z) = z - iz_R \quad (4)$$

Finally, the quantity z_R is called the Rayleigh range and is defined by

$$z_R = \frac{n\pi w_0^2}{\lambda} \quad (5)$$

where n is the index of refraction of the medium, and λ is the optical wavelength in free space. The Rayleigh range corresponds to the distance from the waist at which the beam radius increases by a factor of $\sqrt{2}$. The distance between the points $\pm z_R$ about the waist is called the confocal parameter b of the beam ($b = 2z_R$). These parameters are also defined schematically in Fig. 1a.

B. Electric Polarization in a Dielectric Medium

When an electric field is applied to a dielectric medium (of neutral electric charge), a separation of bound charges is induced as illustrated in Fig. 2. This

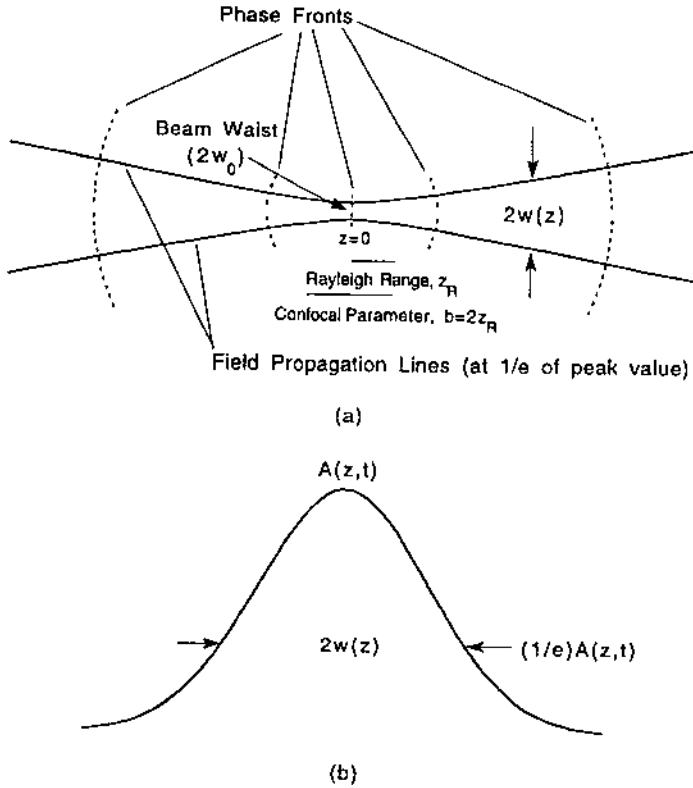


Figure 1 Schematic illustration of a TEM_{00} Gaussian beam. (a) Beam propagation profile; (b) beam cross section.

separation of charge results in a collection of induced dipole moments $\mu^{(\sim)}$, which, as designated, may be rapidly oscillating if induced by a rapidly varying applied field. The electric polarization is defined as the net average dipole moment per unit volume and is given by

$$\mathbf{P}^{(\sim)} = N\langle \mu^{(\sim)} \rangle \quad (6)$$

where N is the number of microscopic dipoles per unit volume, and the angular brackets indicate an ensemble average over all of the dipoles in the medium. In what follows, any permanent dipoles within the medium will be ignored since they will not be oscillating at optical frequencies and hence will not radiate electromagnetic waves.

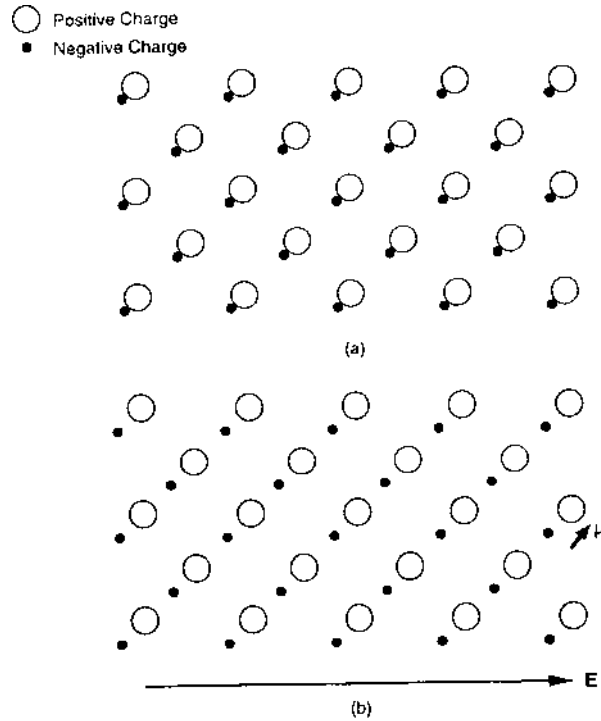


Figure 2 Illustration of the response of a dielectric medium to an applied electric field.
(a) Without field applied; (b) field applied.

By the principle of causality, $\mathbf{P}^{(\sim)}$ must be a function of the applied field $\mathbf{E}^{(\sim)}$. To an excellent approximation, at the low intensity levels of natural light sources, the relation of the polarization to the applied field is linear. This is the regime of linear optics. The most general form of the electric polarization for a homogeneous medium is given by

$$\mathbf{P}_L^{(\sim)}(\mathbf{r}, t) = \begin{cases} \epsilon_0 \int_{-\infty}^{\infty} \int_{-\infty}^{\infty} \chi^{(1)}(\mathbf{r} - \mathbf{r}', t - t') \cdot \mathbf{E}^{(\sim)}(\mathbf{r}', t') d\mathbf{r}' dt' & (\text{SI}) \\ \int_{-\infty}^{\infty} \int_{-\infty}^{\infty} \chi^{(1)}(\mathbf{r} - \mathbf{r}', t - t') \cdot \mathbf{E}^{(\sim)}(\mathbf{r}', t') d\mathbf{r}' dt' & (\text{cgs}) \end{cases} \quad (7)$$

where the subscript L signifies a linear polarization, $\epsilon_0 = 8.85 \times 10^{-12}$ farad/meter is the electric permittivity of free space, and $\chi^{(1)}(\mathbf{r} - \mathbf{r}', t - t')$ is the linear dielectric response tensor. The functional form of $\chi^{(1)}$ reflects the principles of space and time invariance [6]. In other words,

the polarization response of a medium does not depend on when (in an absolute sense) the driving field is applied, but only on the time since it was applied. Consequently, $\chi^{(1)}(\mathbf{r} - \mathbf{r}', t - t')$ must be defined in such a way that it vanishes when $t - t' < 0$ to preserve causality. Similarly, the polarization response in a homogeneous medium does not depend on the absolute position in space of the applied field, but only on the distance away from this position. A nonzero value of $\chi^{(1)}(\mathbf{r} - \mathbf{r}', t - t')$ for $\mathbf{r} \neq \mathbf{r}'$ is called a nonlocal response. If there is no response except within a small neighborhood where $\mathbf{r} \approx \mathbf{r}'$, then the response is called local. This is equivalent to saying that the linear dielectric response tensor has a δ -function spatial dependence. For the vast majority of problems in nonlinear optics, the media of interest produce approximately a local response. Consequently, we will ignore the spatial dependence of $\chi^{(1)}$ in what follows.

The form of the linear dielectric response tensor allows a simpler relation to be made between the Fourier transforms of the linear polarization and the applied field,

$$\mathbf{P}_L(\omega) = \begin{cases} \epsilon_0 \chi^{(1)}(\omega) \cdot \mathbf{E}(\omega) & (\text{SI}) \\ \chi^{(1)}(\omega) \cdot \mathbf{E}(\omega) & (\text{cgs}) \end{cases} \quad (8)$$

where $\chi^{(1)}(\omega)$, the linear susceptibility tensor, is the Fourier transform of the linear dielectric response tensor. The tensor relation in Eq. (8) can also be written as

$$P_{L,i}(\omega) = \begin{cases} \epsilon_0 \sum_j \chi_{ij}^{(1)}(\omega) E_j(\omega) & (\text{SI}) \\ \sum_j \chi_{ij}^{(1)}(\omega) E_j(\omega) & (\text{cgs}) \end{cases} \quad (9)$$

where the subscript i signifies the i th cartesian coordinate ($i = x, y, z$), and the sum is over $j = x, y, z$. The tensor $\chi^{(1)}(\omega)$ thus has nine components. In an isotropic medium, there is only one independent, nonzero component, and the susceptibility is written as a scalar quantity, $\chi^{(1)}(\omega)$.

C. Wave Equation

For the majority of situations considered in nonlinear optics, and for every case treated in this book, it can be assumed that there is no macroscopic magnetization in the dielectric medium (no microscopic magnetic dipoles). The medium is also electrically neutral and nonconducting so that no free charge or current density exists. Under these conditions, the wave equation describing the propagation of

the vector electric field wave is given by

$$\nabla \times \nabla \times \mathbf{E}^{(\sim)} + \frac{1}{c^2} \frac{\partial^2 \mathbf{E}^{(\sim)}}{\partial t^2} = -\frac{K}{c^2} \frac{\partial^2 \mathbf{P}^{(\sim)}}{\partial t^2} \quad (10)$$

where $c = 3 \times 10^8$ m/s (3×10^{10} cm/s) is the speed of light in a vacuum, and K is a constant depending on the system of units used, with

$$K = \begin{cases} (\epsilon_0)^{-1} & \text{(SI)} \\ 4\pi & \text{(cgs)} \end{cases} \quad (11)$$

When the intensity of the light is sufficiently high (e.g., from a laser), a small additional polarization will appear, so that the total polarization can be written as

$$\mathbf{P}^{(\sim)} = \mathbf{P}_L^{(\sim)} + \mathbf{P}_{NL}^{(\sim)} \quad (12)$$

where $\mathbf{P}_{NL}^{(\sim)}$ is a nonlinear function of the applied field. Substituting this expression into Eq. (10), the wave equation becomes

$$\nabla \times \nabla \times \mathbf{E}^{(\sim)} + \frac{1}{c^2} \frac{\partial^2 \mathbf{E}^{(\sim)}}{\partial t^2} + \frac{K}{c^2} \frac{\partial^2 \mathbf{P}_L^{(\sim)}}{\partial t^2} = -\frac{K}{c^2} \frac{\partial^2 \mathbf{P}_{NL}^{(\sim)}}{\partial t^2} \quad (13)$$

When the nonlinear polarization is negligible, the left-hand side of Eq. (13) will be recognized as the homogeneous wave equation for linear optics. This is generally given in terms of the Fourier transform of the electric field by

$$\nabla \times \nabla \times \mathbf{E}(\mathbf{r}, \omega) + \frac{\omega^2}{c^2} \boldsymbol{\kappa}(\omega) \cdot \mathbf{E}(\mathbf{r}, \omega) = 0 \quad (14)$$

where $\boldsymbol{\kappa}$ is the linear dielectric tensor $\boldsymbol{\epsilon}$ (cgs) or $\boldsymbol{\epsilon}/\epsilon_0$ (SI), with

$$\boldsymbol{\epsilon}_{ij}(\omega) = \begin{cases} \epsilon_0 \left(\delta_{ij} + \chi_{ij}^{(1)}(\omega) \right) & \text{(SI)} \\ \delta_{ij} + 4\pi \chi_{ij}^{(1)}(\omega) & \text{(cgs)} \end{cases} \quad (15)$$

with

$$\delta_{ij} = \begin{cases} 1 & (i = j) \\ 0 & (i \neq j) \end{cases} \quad (16)$$

We see then that the nonlinear polarization acts as a source term for an inhomogeneous wave equation. For most situations in nonlinear optics, the total electric field can be considered to be a superposition of quasi-monochromatic

waves (e.g., laser beams). The total field is then written as

$$\mathbf{E}^{(\sim)}(\mathbf{r}, t) = \sum_{\mu} \hat{e}_{\mu} A_{\mu}(\mathbf{r}, t) \exp[i(\mathbf{k}_{\mu} \cdot \mathbf{r} - \omega_{\mu} t)] + \text{c.c.} \quad (17)$$

where the sum is over m waves with frequencies ω_{μ} and wave vectors \mathbf{k}_{μ} . $A_{\mu}(\mathbf{r}, t)$ is a slowly varying amplitude in space and time (compared to the rapidly oscillating part of the wave). If it is sufficiently slowly varying, the μ th component is a monochromatic wave. However, if its time duration is sufficiently short (an ultrashort pulse) such that it cannot be described as a pure monochromatic wave, then the μ th component represents a quasi-monochromatic wave with carrier frequency ω_{μ} .

For the typical case when the nonlinear polarization represents a small perturbation to the total polarization, it can also be written as

$$\mathbf{P}_{\text{NL}}^{(\sim)}(\mathbf{r}, t) = \sum_{\mu} \mathbf{P}_{\text{NL}, \mu}(\mathbf{r}, t) \exp(-i\omega_{\mu} t) + \text{c.c.} \quad (18)$$

where $\mathbf{P}_{\text{NL}, \mu}(\mathbf{r}, t)$ is a slowly varying (compared to the rapidly oscillating part of the wave) complex polarization amplitude. Then by the linearity of the wave equation, each frequency component (Fourier component) of the total field also satisfies Eq. (13), with the corresponding frequency component of the nonlinear polarization appearing on the right-hand side of the equation. Thus, there will be m inhomogeneous wave equations describing the interaction. Also, the dielectric constant in each wave equation is evaluated at the frequency ω_{μ} .

This is the most general form of the wave equation. Under usual conditions, the left-hand side can be simplified, for an excellent approximation in homogeneous media,

$$\nabla \times \nabla \times \mathbf{E}^{(\sim)} \approx -\nabla^2 \mathbf{E}^{(\sim)} \quad (19)$$

where ∇^2 is the Laplacian operator. For most of the nonlinear phenomena considered in this book, this approximation will be used.

II. LINEAR OPTICS

In the linear optics regime, the nonlinear part of the polarization may be neglected (i.e., set equal to zero). The wave equation, Eq. (13), then becomes a homogeneous differential equation. Its solutions are given in the form of Eq. (1). The simplest waves to consider are plane waves in an isotropic medium.

A. Isotropic Media

In an isotropic medium the approximation given in Eq. (19) is exact for a plane wave and the susceptibility is a scalar quantity. The latter will be a complex function of frequency, in general, and can be written as

$$\chi^{(1)} = \chi_R^{(1)} + i\chi_I^{(1)} \quad (20)$$

where the subscripts R and I signify real and imaginary parts, respectively. The dielectric constant is also complex, and

$$\sqrt{\frac{\epsilon(\omega)}{\epsilon_0}} = n(\omega) + i \frac{\alpha(\omega)}{4\pi} \quad (21)$$

in SI units. For cgs units, the expression is identical with the exception that $\epsilon_0 \rightarrow 1$. In Eq. (21) $n(\omega)$ is the index of refraction given by

$$n(\omega) = \begin{cases} \sqrt{1 + \chi_R^{(1)}(\omega)} & \text{(SI)} \\ \sqrt{1 + 4\pi\chi_R^{(1)}(\omega)} & \text{(cgs)} \end{cases} \quad (22)$$

where $\alpha(\omega)$ is the intensity absorption coefficient, with

$$\alpha(\omega) = \begin{cases} \frac{\omega\chi_I^{(1)}(\omega)}{n(\omega)c} & \text{(SI)} \\ \frac{4\pi\omega\chi_I^{(1)}}{n(\omega)c} & \text{(cgs)} \end{cases} \quad (23)$$

Absorption properties of materials are often described in terms of the absorption cross section σ , which is related to the absorption coefficient by $\alpha = \sigma N$, where N is the number of absorbing molecules per unit volume. For solutions, the molecular density is often given as a concentration in mole/liter, with the molar extinction coefficient ϵ_M being analogous to the cross section. The relationship between the two is given by

$$\sigma = \frac{2.3 \times 10^3 \epsilon_M}{N_A} \quad (24)$$

where σ is expressed in cm^2 , ϵ_M is expressed in liter/mole-cm, and N_A is Avagadro's number.

When the medium is conducting, such as a semiconductor or an ionic solution, the conductivity σ_c of the medium will contribute to the absorption

coefficient. In this case, Eq. (23) may be generalized to include conductivity by

$$\alpha(\omega) = \begin{cases} \frac{\omega[\chi_I^{(1)}(\omega) + \sigma_c/\epsilon_0\omega]}{n(\omega)c} & \text{(SI)} \\ \frac{4\pi\omega[\chi_I^{(1)}(\omega) + \sigma_c/\omega]}{n(\omega)c} & \text{(cgs)} \end{cases} \quad (25)$$

The plane wave solution to the wave equation then has the form

$$\mathbf{E}^{(\sim)}(z, t) = \hat{e}A_0 \exp\left(-\frac{\alpha z}{2}\right) \exp[i(kz - \omega t)] + \text{c.c.} \quad (26)$$

where A_0 is the amplitude of the wave at $z = 0$, and the wave vector obeys a dispersion relation given by

$$k(\omega) = n(\omega) \frac{\omega}{c} \quad (27)$$

The wave thus travels with a phase velocity $v_p = c/n$. In isotropic media, the electric field vector is always perpendicular to the wave vector, and the phase velocity of the wave is independent of the direction of propagation.

A homogeneous, isotropic medium will also support the propagation of an ultrashort optical pulse. An ultrashort pulse is only quasi-monochromatic and hence is composed of several frequencies clustered about some center frequency, which can also be considered the carrier frequency of the wave. When the frequency spread of the pulse is such that dispersion of the refractive index cannot be ignored, the concept of a unique phase velocity is meaningless. What does have meaning is the velocity of the pulse itself (i.e., the group of superimposed monochromatic waves comprising the pulse). This is characterized by the group velocity, defined by

$$v_g = \left(\frac{dk}{d\omega} \right)^{-1}_{\omega_c} \quad (28)$$

where ω_c is the carrier frequency. When dispersion cannot be ignored, the wave will no longer have the simple form of Eq. (26) since dispersion will cause the pulse amplitude to decrease and spread as the pulse propagates. The group velocity itself may also exhibit dispersion, which is characterized by the group velocity dispersion coefficient k_2 , defined by

$$k_2 = \left(\frac{d^2 k}{d\omega^2} \right)_{\omega_c} \quad (29)$$

Since detectors cannot respond to the rapidly varying optical frequency, the quantity measured experimentally is the time-averaged field flux, where

the average is over several optical cycles. The quantity of interest then is the optical intensity (or irradiance), which is related to the field amplitude by

$$I(z, t) = \begin{cases} 2\epsilon_0 nc|A(z, t)|^2 & (\text{SI}) \\ \frac{nc}{2\pi}|A(z, t)|^2 & (\text{cgs}) \end{cases} \quad (30)$$

In a cw laser beam of finite cross-sectional area, the optical power is typically measured, and is related to the intensity by

$$\mathcal{P} = \int_A I dA \quad (31)$$

where the integral is over the area of the beam, and A is not to be confused with the complex field amplitude. For a TEM₀₀ Gaussian beam, the relationship at the beam waist is

$$\mathcal{P} = \frac{\pi w_0^2}{2} I_0 \quad (32)$$

where I_0 is the peak, on-axis intensity of the Gaussian beam.

Another microscopic material parameter of interest is the molecular polarizability $\alpha^{(1)}$, defined by

$$\langle \mu(\omega) \rangle = \alpha^{(1)}(\omega) \cdot \mathbf{E}_{\text{local}}(\omega) \quad (33)$$

where $\mathbf{E}_{\text{local}}$ is the local electric field (at the molecule), which is a superposition of the applied field \mathbf{E} and the net field due to surrounding dipoles. An analytical expression for the local field can be obtained for isotropic and cubic media. The relationship between the susceptibility and the polarizability for these media is then given by

$$\chi^{(1)} = \begin{cases} \left(\frac{n^2+2}{3}\right) N \alpha^{(1)} / \epsilon_0 & (\text{SI}) \\ \left(\frac{n^2+2}{3}\right) N \alpha^{(1)} & (\text{cgs}) \end{cases} \quad (34)$$

The quantity $f(\omega) = [n^2(\omega) + 2]/3$ is called the local field factor.

B. The Laws of Linear Optics for Isotropic Media

Maxwell's equations and the form of the electromagnetic waves may also be used to derive the laws of optics at an interface between two dielectric media [1]. The geometry of the interface and the incident, reflected, and transmitted waves are shown in Fig. 3. The laws of linear optics for two homogeneous, isotropic media are given below.

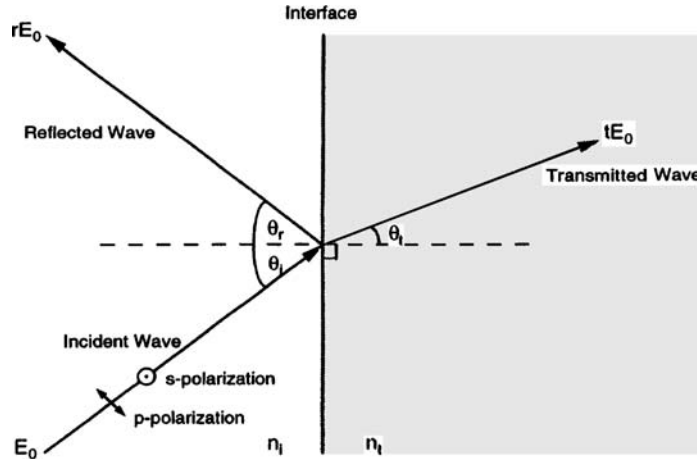


Figure 3 Illustration of propagating electromagnetic fields at an interface between two different isotropic dielectric media.

Law of reflection:

$$\theta_r = \theta_i \quad (35)$$

where θ_i is called the angle of incidence and θ_r the angle of reflection, and both are measured with respect to the normal of the interface. Thus, the wave reflected from the interface will leave at the same angle the incident wave impinges on the interface.

Law of refraction (Snell's Law):

$$n_i \sin \theta_i = n_t \sin \theta_t \quad (36)$$

where subscript i quantities refer to those in the medium where the wave is incident on the interface, and t refers to the medium of the transmitted wave. Since $n_i \neq n_t$, the transmitted ray direction is bent on crossing the interface. The direction of the bend is toward the normal to the interface if $n_i < n_t$ and away from the normal if $n_i > n_t$.

Reflection and transmission coefficients (Fresnel's formulas). The amount of electromagnetic energy reflected and transmitted at an interface can be determined by Fresnel's formulas for the reflection and transmission coefficients. These will depend on the polarization of the incident wave. The polarization vector is specified with respect to the plane of incidence. This is the plane that contains the incident, reflected, and transmitted rays, as shown in Fig. 3. Light polarized normal to the plane of incidence is referred to as *s*-polarization, while light polarized in the plane of incidence is referred to as *p*-polarization. The ratio of the reflected to

incident field amplitudes is given by r , while t corresponds to the ratio of the transmitted to incident field amplitudes. Fresnel's formulas are

$$r_s = \frac{n_i \cos \theta_i - n_t \cos \theta_t}{n_i \cos \theta_i + n_t \cos \theta_t} \quad (37)$$

$$t_s = \frac{2n_i \cos \theta_i}{n_i \cos \theta_i + n_t \cos \theta_t} \quad (38)$$

$$r_p = \frac{n_i \cos \theta_t - n_t \cos \theta_i}{n_i \cos \theta_t + n_t \cos \theta_i} \quad (39)$$

$$t_p = \frac{2n_i \cos \theta_i}{n_i \cos \theta_t + n_t \cos \theta_i} \quad (40)$$

Measurable quantities are the reflectance and transmittance of the interface. These are defined as the ratios of the time-averaged reflected and transmitted power, respectively, to the incident power. For both s - and p -polarization, these quantities are related to the Fresnel coefficients by

$$R_{s,p} = |r_{s,p}|^2 \quad (41)$$

$$T_{s,p} = \frac{n_t \cos \theta_t}{n_i \cos \theta_i} |t_{s,p}|^2 \quad (42)$$

where R and T are the reflectance and transmittance, respectively.

C. Guided Waves

The form of the electromagnetic wave is somewhat different in the confined geometry of waveguides compared to free space. The combined effects of total internal reflection and wave interference limit the number of allowed directions and frequencies of propagating waves.

Waveguides may be considered one-dimensional (1-D) or two-dimensional (2-D), depending on their geometry. An example of a 1-D waveguide is an asymmetric slab waveguide, consisting of a thin film deposited on a dielectric slab. The opposite side of the film is usually air. Examples of 2-D waveguides are rectangular channel waveguides (a rectangular channel embedded in a dielectric slab) and an optical fiber. The latter consists of a cylindrical core surrounded by a cylindrical cladding of lower refractive index. The cross section of the core can be circular or elliptical.

It is customary to take the z -axis to coincide with the waveguide axis. The form of the electric field wave is given by

$$E_{v,i}(r, t) = A_{v,i}(z, t)a_{v,i}(x, y)\exp[i(\beta z - \omega t)] + \text{c.c.} \quad (43)$$

where i is a cartesian coordinate, and the subscript v designates the mode number. The propagation constant β takes on a discrete set of allowed values depending on frequency and waveguide geometry. The normalized quantity $a_{v,i}(x, y)$ is the modal distribution across the cross section of the waveguide. For slab waveguides it is a function only of the coordinate normal to the film plane. $A_{v,i}$ is a normalization function that is proportional to $(\mathcal{P}_v)^{1/2}$, where \mathcal{P}_v is the power in the v th mode. In Eq. (43), this quantity is written as a slowly varying function of space and time to generalize the result to the case in which the field may be a pulse, and the optical power may be changing with propagation.

The exact form of the modal distribution can be quite complicated in situations of practical interest. Other sources should be consulted for a complete description of these [2,3], as well as the eigenvalue equations that determine the allowed values of the propagation constant β . For the purposes of this book, the function $A_{v,i}(z, t)$ will serve as the complex amplitude of interest in computing the interaction of waves in nonlinear optics.

D. Energy Theorem

As alluded to above, energy is stored in the electromagnetic field and can be used to perform work on free electric charges or bound electric charges (i.e., dipoles). Calling u_{em} the energy per unit volume (energy density) stored in the electromagnetic field in some volume V in space, the energy theorem for a dielectric medium (no magnetization and no free currents) states

$$-\frac{\partial}{\partial t} \int_V u_{em} dV = \int_S I \cos \theta dS + \int_V \langle \mathbf{E}^{(\sim)} \cdot \frac{\partial \mathbf{P}^{(\sim)}}{\partial t} \rangle dV \quad (44)$$

where $\cos \theta dS$ is the elemental surface area normal to the direction of energy flow, and the angle brackets imply a time average over an optical cycle. The second term on the right-hand side Eq. (44) gives the rate at which work is done by the electric field on the medium through the dipole moment per unit volume (i.e., the polarization) and becomes the integral of $2\text{Re}(i_\omega \mathbf{E} \cdot \mathbf{P}^*)$ when the time average is performed. If this term is zero, the energy theorem is just a continuity equation. It then states that the average rate of electromagnetic energy lost from a volume V is equal to the net power flowing through the surface S bounding the volume. When the work term is not zero, some of the energy lost is transferred to the medium via the polarization.

Obviously, if the work term is purely imaginary, then no work is done by the field. This is the case in linear optics when the susceptibility is purely real, i.e., the dielectric constant is real. In other words, the field and the polarization are in phase (the time-derivative of the polarization and the electric field are then $\pi/2$ radians out of phase). In this case (pure refractive case), the phase of the field will be modified in passage through the dielectric, but the amplitude remains constant. When the phase difference $\Delta\varphi$ ($\Delta\varphi = \varphi_{pol} - \varphi_{field}$) between the polarization and field is such that $0 < \Delta\varphi < \pi$, then the field does work on the polarization, and the field amplitude decreases. The net power flowing out of the surface of the volume V is thus reduced. In linear optics this is due to the dielectric constant being complex, and the field is reduced due to absorption, which dissipates energy in the form of heat or other radiation. For $-\pi < \Delta\varphi < 0$, the field would do negative work on the polarization. This means that the medium, through the polarization, does work on the field, and the field amplitude grows or is amplified, and the power flowing out through the surface increases. This can only occur if energy is pumped into the medium from some other source, and corresponds in linear optics to the dielectric constant having a negative imaginary part. This field amplification occurs quite frequently in nonlinear optics even though the susceptibility may be purely real.

E. Anisotropic Media

Wave propagation in anisotropic dielectric media is a somewhat more complicated affair. Generally, the electric field vector is not perpendicular to the wave vector (direction of propagation). However, the displacement vector $\mathbf{D}^{(\sim)}$, defined by

$$\mathbf{D}^{(\sim)} = \begin{cases} \epsilon_0 \mathbf{E}^{(\sim)} + \mathbf{P}^{(\sim)} & (\text{SI}) \\ \mathbf{E}^{(\sim)} + 4\pi \mathbf{P}^{(\sim)} & (\text{cgs}) \end{cases} \quad (45)$$

is orthogonal to the wave vector \mathbf{k} . In any anisotropic medium, two independent orthogonally polarized $\mathbf{D}^{(\sim)}$ -waves can propagate with different phase velocities. The problem in the optics of anisotropic media is to find the polarization of these modes and their corresponding phase velocities.

It can be shown that the linear dielectric constant is a symmetric tensor ($\epsilon_{ij} = \epsilon_{ji}$) [1]. By the laws of linear algebra, an orthogonal coordinate system can be found in which this tensor is diagonal [$\epsilon_{ij} = \epsilon_{ii}\delta_{ij}$, where δ_{ij} is given in Eq. (16)]. The axes of this system are called the principal axes, and the corresponding diagonal elements of the dielectric tensor are called the principal dielectric constants of the medium. These are designated ϵ_{XX} , ϵ_{YY} , and ϵ_{ZZ} , where upper case symbols are used to signify the principal axes. Similarly principal refractive indices are found: $n_{ii} = (\epsilon_{ii}/\epsilon_0)^{1/2}$. For the cgs system of units, ϵ_0 is

replaced by 1. Often, these principal quantities are written with a single rather than a double subscript. The phase velocity for a wave polarized along the i th principal axis is $v_{pi} = c/n_i$.

If the dielectric tensor elements are complex, then the principal refractive indices are related to the real part of the square root given above. The imaginary part of the square root is related to principal absorption coefficients α_i analogous to the scalar quantity given by Eq. (25). This polarization-dependent, propagation direction-dependent absorption is called pleochromism [1].

In general, $n_X \neq n_Y \neq n_Z$. Such a medium is called biaxial for reasons discussed below. A great simplification occurs when two of the principal indices are equal, for example, $n_X = n_Y \neq n_Z$. This type of medium is called uniaxial. There is a single axis of symmetry, taken to be the Z-axis, which is called the optic axis. When light propagates along this axis, its phase velocity is independent of polarization. The following designation is made: $n_X = n_Y = n^o$ and $n_Z = n^e$, where the “ o ” stands for ordinary and the “ e ” for extraordinary waves.

Uniaxial media are said to be birefringent and exhibit double refraction [1]. The birefringence of the medium is given by $\Delta n = n^e - n^o$. When $\Delta n > 0$ ($\Delta n < 0$), the medium is said to be a positive (negative) uniaxial medium. Many useful transparent crystals in nonlinear optics have a very small birefringence ($\Delta n \ll 1$). In these types of materials, $\mathbf{E}^{(\sim)}$ and $\mathbf{D}^{(\sim)}$ are nearly parallel and can be treated as such for most practical situations.

One of the independent propagation modes in uniaxial media has its polarization orthogonal to the optic axis and thus has phase velocity given by $v_p = c/n^o$. This is called the ordinary wave. The extraordinary wave will have a component of its polarization along the optic axis, and its phase velocity will be $v_p = c/n^e(\theta)$, where θ is the direction of propagation of the extraordinary wave with respect to the optic axis, and

$$\frac{1}{[n^e(\theta)]^2} = \frac{\cos^2\theta}{(n^o)^2} + \frac{\sin^2\theta}{(n^e)^2} \quad (46)$$

General methods for determining the orthogonal polarizations of the $\mathbf{D}^{(\sim)}$ -waves and the corresponding phase velocities for any uniaxial crystal by use of the so-called optical indicatrix or index ellipsoid are found in several textbooks [1,4,5].

The general form of the index ellipsoid for anisotropic media is given by

$$\frac{X^2}{n_X^2} + \frac{Y^2}{n_Y^2} + \frac{Z^2}{n_Z^2} = 1 \quad (47)$$

It is important to note that the index ellipsoid is not a real object that exists in space; it is a useful mathematical construct. However, its axes do correspond to the principal axes of the medium, and thus are useful for visualizing the directions

of propagation and polarization. When $n_X = n_Y$, Eq. (46) is recovered for propagation at some angle θ with respect to the Z -axis (optic axis).

Let $A = X$ or Z and $C = Z$ or X . Then the convention for a general anisotropic medium is to take $n_A < n_Y < n_C$. The index ellipsoid is thus a prolate spheroid along Z ($A = X, C = Z$) or an oblate spheroid along Z ($A = Z, C = X$). The intersection of the AY -plane with the ellipsoid yields an ellipse with semi-major axis n_Y . Conversely, the intersection of the YC -plane with the ellipsoid yields an ellipse where n_Y is the semi-minor axis. It follows that there is some angle with respect to the C -axis where the intersection of a plane containing the Y -axis through the origin of the ellipsoid will yield a circle of radius n_Y . A wave propagating normal to this plane will have a phase velocity that is independent of polarization. Hence, this direction is called an optic axis of the medium. The points where the plane intersects the ellipsoid in the AC -plane will satisfy the equations $A^2 + C^2 = n_Y^2$ and $(A/n_A)^2 + (C/n_C)^2 = 1$. The angle Ω , that the normal to this plane (i.e., the optic axis), makes with the C -axis is then given by

$$\sin \Omega = \frac{n_C}{n_Y} \left(\frac{n_Y^2 - n_A^2}{n_C^2 - n_A^2} \right)^{1/2} \quad (48)$$

Since the equations are quadratic, there will be two values (\pm) of A and C that satisfy the equations. Hence, there are two optic axes symmetrically situated at an angle Ω about the C -axis in the AC -plane. Such a medium is thus called biaxial.

Propagation in the principal planes of a biaxial medium is similar, but not identical to propagation in a uniaxial medium. Consider propagation in the XY - or YZ -plane. Let $J = X$ or Z and $\psi = \phi$ or θ , respectively. Then an equation like Eq. (46) applies to determine the extraordinary index, with

$$\frac{1}{[n^e(\psi)]^2} = \frac{\cos^2 \psi}{n_Y^2} + \frac{\sin^2 \psi}{n_J^2} \quad (49)$$

Again employing the convention $n_A < n_Y < n_Z$, where $A = X$ or Z and $C = Z$ or X , propagation in the AY -plane leads to $n_A \leq n^e \leq n_Y < n_C = n^o$. This is similar to propagation in a negative uniaxial medium since $n^e < n^o$, however, it is not identical since there is no angle of propagation for which $n^e = n^o$. For propagation in the YC -plane, $n^o = n_A < n_Y \leq n^e \leq n_Z$. Hence, this is similar to propagation in a positive uniaxial medium since $n^e > n^o$. Again, however, there is no angle corresponding to $n^e = n^o$. Finally, it should be noted that for light propagating in the AC -plane, the situation is similar to propagation in a negative uniaxial medium if the angle of propagation with respect to the C -axis is less than Ω . For angles greater than Ω , it is similar to a positive uniaxial medium. The reason for this is that, in the former case, as the angle of propagation approaches the optic axis, the extraordinary refractive index decreases toward n_Y . In the latter case, the extraordinary index increases toward n_Y .

For light propagating in a general direction in a biaxial medium, the phase velocities of the two allowed modes of propagation are determined by solving the Fresnel equation [1,4,5]

$$\frac{\sin^2\theta \cos^2\phi}{n^{-2} - n_X^{-2}} + \frac{\sin^2\theta \sin^2\phi}{n^{-2} - n_Y^{-2}} + \frac{\cos^2\theta}{n^{-2} - n_Z^{-2}} = 0 \quad (50)$$

where θ and ϕ are the spherical angles describing the direction of propagation with respect to the principal axes. Generally, this equation must be solved numerically for the two independent values of the refractive index. The use of this equation is discussed in greater detail in Chapter 2.

In anisotropic media, the direction of wave propagation \mathbf{k} does not coincide with the direction of energy or Poynting vector propagation \mathbf{S} . The wave vector is $\mathbf{k} \perp \mathbf{D}^{(\sim)}, \mathbf{H}^{(\sim)}$ while the Poynting vector is $\mathbf{S} \perp \mathbf{E}^{(\sim)}, \mathbf{H}^{(\sim)}$. The angle α between \mathbf{k} and \mathbf{S} , which is also the angle between $\mathbf{E}^{(\sim)}$ and $\mathbf{D}^{(\sim)}$, is given by

$$\tan \alpha = \frac{[(\epsilon_x - \epsilon_y)^2 E_x^2 E_y^2 + (\epsilon_x - \epsilon_z)^2 E_x^2 E_z^2 + (\epsilon_y - \epsilon_z)^2 E_y^2 E_z^2]^{1/2}}{\epsilon_x E_x^2 + \epsilon_y E_y^2 + \epsilon_z E_z^2} \quad (51)$$

III. NONLINEAR OPTICS

In the nonlinear optics regime, the nonlinear part of the polarization can no longer be ignored. Note by Eq. (13) that the nonlinear polarization serves as a source for the generation of new waves, and the wave equation becomes an inhomogeneous differential equation. Hence, an expression for $\mathbf{P}_{NL}^{(\sim)}$ is required. For most of the applications of nonlinear optics, this quantity can be expressed as a power series expansion in the applied fields.

A. Nonlinear Susceptibilities

It is assumed that the nonlinear polarization can be written as [6–8]

$$\mathbf{P}_{NL}^{(\sim)} = \mathbf{P}^{(\sim)(2)} + \mathbf{P}^{(\sim)(3)} + \dots \quad (52)$$

where

$$\mathbf{P}^{(\sim)(2)}(\mathbf{r}, t) = \epsilon_0 \int_{-\infty}^{\infty} \int_{-\infty}^{\infty} \chi^{(2)}(t - t', t - t'') : \mathbf{E}^{(\sim)}(\mathbf{r}, t') \mathbf{E}^{(\sim)}(\mathbf{r}, t'') dt' dt'' \quad (53)$$

$$\begin{aligned} \mathbf{P}^{(\sim)(3)}(\mathbf{r}, t) = & \epsilon_0 \int_{-\infty}^{\infty} \int_{-\infty}^{\infty} \int_{-\infty}^{\infty} \chi^{(3)}(t - t', t - t'', t - t''') : \mathbf{E}^{(\sim)}(\mathbf{r}, t') \\ & \times \mathbf{E}^{(\sim)}(\mathbf{r}, t'') \mathbf{E}^{(\sim)}(\mathbf{r}, t''') dt' dt'' dt''' \end{aligned} \quad (54)$$

These expressions are given in SI units; for cgs units, $\epsilon_0 \rightarrow 1$. It is important to note that the field in the equations above is the *total* applied field, which can be a superposition of many fields of different frequencies. $\chi^{(n)}$ is called the *n*th order dielectric response, and is a tensor of rank $n + 1$. Note that, as earlier for the linear dielectric response, it is assumed that the response is local and hence the spatial dependence of $\chi^{(n)}$ is suppressed.

If the applied field is a superposition of monochromatic or quasi-monochromatic waves, then it is possible to write expressions analogous to Eq. (8) or Eq. (9) in terms of the Fourier transforms of the nonlinear polarization, fields, and the dielectric response tensor, providing that the frequency dependence of the Fourier transform of $\chi^{(n)}$ is slowly varying in the region of each Fourier component of the applied field. When the *total* field is expanded in terms of its Fourier components (e.g., its various laser frequencies), then the nonlinear polarization will consist of several terms oscillating at various combination frequencies. For example, if the *total* field consists of two waves oscillating at frequencies ω_1 and ω_2 , the second-order nonlinear polarization will have components oscillating at $2\omega_1$, $2\omega_2$, $\omega_1 + \omega_2$, $\omega_1 - \omega_2$, and dc terms at zero frequency. Similarly, with three fields oscillating at frequencies ω_1 , ω_2 , and ω_3 , the third-order polarization will oscillate at $3\omega_1$, $3\omega_2$, $3\omega_3$, $\omega_1 + \omega_2 + \omega_3$, $\omega_1 + \omega_2 - \omega_3$, etc.

It is common to write the Fourier components of the nonlinear polarization in the following way. Consider a second-order polarization oscillating at ω_3 due to the presence of fields oscillating at frequencies ω_1 and ω_2 , with $\omega_3 = \omega_1 + \omega_2$. Then the *i*th cartesian component of the complex polarization amplitude is expressed as

$$P_i^{(2)}(\omega_3) = \epsilon_0 D^{(2)} \sum_{jk} \chi_{ijk}^{(2)}(-\omega_3; \omega_1, \omega_2) E_j(\omega_1) E_k(\omega_2) \quad (55)$$

with

$$D^{(2)} = \begin{cases} 1 & \text{for indistinguishable fields} \\ 2 & \text{for distinguishable fields} \end{cases} \quad (56)$$

where $\chi_{ijk}^{(2)}(-\omega_3; \omega_1, \omega_2)$ is the second-order (complex) susceptibility and the Fourier transform of $\chi^{(2)}(t)$. The form of Eq. (55) allows for the possibility that the frequencies ω_1 and ω_2 are equal, or equal in magnitude and opposite in sign. In this case, there may actually be only one field present, and the degeneracy factor $D^{(2)}$ takes this into account. It should be noted, however, that the determination of the degeneracy factor is whether the fields are physically distinguishable or not. Two fields of the same frequency will be physically distinguishable if they travel in different directions, for example. Also, the negative frequency part of the real field is considered to be distinguishable from the positive frequency part (i.e., they have different frequencies). For negative frequencies, it is important to note that $E(-\omega) = E^*(\omega)$ since the rapidly varying field is a real mathematical quantity. Thus, for example, if $\omega_1 = \omega$ and $\omega_2 = -\omega$, then the second-order polarization would be written as

$$P_i^{(2)}(0) = 2\epsilon_0 \sum_{jk} \chi_{ijk}^{(2)}(0; \omega, -\omega) E_j(\omega) E_k^*(\omega) \quad (57)$$

This polarization drives the phenomenon known as optical rectification, wherein an intense optical wave creates a dc polarization in a nonlinear medium. It is important to remember that in these equations, the field amplitude still contains the rapidly varying spatial part, i.e., $E(\mathbf{r}) = A(\mathbf{r})\exp(i\mathbf{k} \cdot \mathbf{r})$.

This notation is easily extended to higher orders. When three frequencies $\omega_1, \omega_2, \omega_3$ are present, the third-order polarization at $\omega_4 = \omega_1 + \omega_2 + \omega_3$ is given by

$$P_i^{(3)}(\omega_4) = \epsilon_0 D^{(3)} \sum_{jkl} \chi_{ijkl}^{(3)}(-\omega_4; \omega_1, \omega_2, \omega_3) E_j(\omega_1) E_k(\omega_2) E_l(\omega_3) \quad (58)$$

where the degeneracy factor in this case becomes

$$D^{(3)} = \begin{cases} 1 & \text{all fields indistinguishable} \\ 3 & \text{two fields indistinguishable} \\ 6 & \text{all fields distinguishable} \end{cases} \quad (59)$$

This form of the third-order polarization allows for various combination frequencies even when only two fields are present, such as $\omega_1 + 2\omega_2$, or $2\omega_1 - \omega_2$, etc. The degeneracy factor is just due to the number of different ways in which the products of the field Fourier components appear in the expansion of

the *total* field to some power. For example, there is only one way that the product for the frequency $3\omega_1$ appears: $E(\omega_1)E(\omega_1)E(\omega_1)$. However, there are three different ways that the product for the frequency $2\omega_1 - \omega_2$ appears: $E(\omega_1)E(\omega_1)E^*(\omega_2)$, $E(\omega_1)E^*(\omega_2)E(\omega_1)$, and $E^*(\omega_2)E(\omega_1)E(\omega_1)$. The degeneracy factor is thus related to the coefficients of Pascal's triangle from algebra. (The use of a degeneracy factor in these equations also relies on an intrinsic symmetry of the susceptibility tensor, which is discussed below.)

The equations above are written in SI units. To obtain the form in cgs units let ϵ_0 go to 1. Also, it is important to note that the n th order susceptibility is frequency dependent and complex, in general. The reason for writing the frequency dependence as shown in the equations above is for the purpose of expressing symmetry relations of the susceptibility tensor. This is further described below.

B. Symmetry Relations of the Nonlinear Susceptibility

The first symmetry apparent from the form of Eqs. (55) and (58) is due to the fact that it makes no difference physically in which order the product of the field amplitudes is given. Thus, an interchange in the order of the product $E_j(\omega_1)E_k(\omega_2)$ [i.e., $E_j(\omega_1)E_k(\omega_2) \leftrightarrow E_k(\omega_2)E_j(\omega_1)$] will not affect the value or sign of the i th component of the nonlinear polarization. The nonlinear susceptibility should reflect this symmetry. But, note that in the above interchange, both frequencies and subscripts for the cartesian coordinates are interchanged simultaneously. This is important since, for example, exchanging the product $E_x(\omega_1)E_y(\omega_2)$ with the product $E_x(\omega_2)E_y(\omega_1)$ could change the nonlinear polarization, especially, for example, if the two fields are orthogonally polarized. Thus, the symmetry property is expressed as (for third-order susceptibilities)

$$\begin{aligned}\chi_{ijkl}^{(3)}(-\omega_4; \omega_1, \omega_2, \omega_3) &= \chi_{iklj}^{(3)}(-\omega_4; \omega_2, \omega_1, \omega_3) \\ &= \chi_{ilkj}^{(3)}(-\omega_4; \omega_3, \omega_2, \omega_1) = \text{etc.}\end{aligned}\tag{60}$$

In other words, if any of the subscripts $\{jkl\}$ are permuted, then the susceptibility will remain unchanged as long as the corresponding set of subscripts $\{123\}$ are also permuted. This holds even if any of the frequencies are negative. Note that this does not hold for the subscript pair $(i,4)$. The same relation holds for second order and can be generalized to any order. This is called intrinsic permutation symmetry and is the underlying reason why the nonlinear polarization can be written compactly in terms of a degeneracy factor as in Eqs. (55) and (58).

At this point it is important to note another notation that is used in second-order nonlinear optics. Often the susceptibility is represented as the so-called

d -coefficient, where \mathbf{d} is a tensor given by

$$d_{ijk} = \frac{1}{2} \chi_{ijk}^{(2)} \quad (61)$$

Furthermore, the intrinsic permutation symmetry is used to contact the last two subscripts and is written $d_{ijk} \rightarrow d_{il}$. The subscripts are then written as numbers instead of letters using the scheme

$i : x \quad 1$	$jk : xx \quad 1$	
$y \quad 2$	$yy \quad 2$	
$z \quad 3$	$zz \quad 3$	
	$yz = zy \quad 4$	
	$xz = zx \quad 5$	
	$xy = yx \quad 6$	

(62)

For example, $d_{xyz} = d_{zyx} = d_{14}$ and $d_{zxz} = d_{31}$, etc. The utility of this notation is that d -coefficients can be expressed as elements of a 3×6 matrix rather than a $3 \times 3 \times 3$ tensor. To use these coefficients in the nonlinear polarization of Eq. (55), just make the substitution $\chi_{ijk}^{(2)} \rightarrow 2d_{il}$.

Another form of the permutation symmetry can be shown when the nonlinear susceptibility is calculated quantum mechanically. This is usually done using the density matrix method and expressions can be found in textbooks [6,7]. It can be shown generally, for example in third order, that

$$\chi_{ijkl}^{(3)}(-\omega_4; \omega_1, \omega_2, \omega_3) = \chi_{jikl}^{(3)*}(-\omega_1; \omega_4, -\omega_2, -\omega_3) = \text{etc.} \quad (63)$$

First, it is noted that when the complex conjugate of the susceptibility is taken, it just changes the sign of all of the frequencies. This is a consequence of the fact that the rapidly varying nonlinear polarization is a real mathematical quantity. Then, for *any* permutation of the cartesian subscripts, the new susceptibility thus obtained is equal to the original susceptibility if the corresponding frequency subscripts are also permuted, if all of the frequencies are changed by multiplying by -1 , and if the complex conjugate of susceptibility is taken. This important result states that the susceptibilities for different physical processes are simply related. For example, Eq. (63) relates the susceptibilities for the third-order processes of sum-frequency generation ($\omega_4 = \omega_1 + \omega_2 + \omega_3$) and difference-frequency generation ($\omega_1 = \omega_4 - \omega_2 - \omega_3$). The relations in Eq. (63) hold for any permutation and are generalized to all orders. Thus, for example, in second

order

$$\chi_{ijk}^{(2)}(-\omega_3; \omega_1, \omega_2) = \chi_{kji}^{(2)*}(-\omega_2; -\omega_1, \omega_3) = \text{etc.} \quad (64)$$

The above expressions hold generally when the susceptibilities are complex. This is especially important when any single frequency or any combination frequency is near a natural resonance frequency of the material. However, it is often the case in many applications that all frequencies and combination frequencies are far from any material resonance. Then the susceptibilities can be treated as real quantities, and any susceptibility is thus equal to its complex conjugate. In this case, Eq. (63) may be written as

$$\begin{aligned} \chi_{ijkl}^{(3)}(-\omega_4; \omega_1, \omega_2, \omega_3) &= \chi_{jikl}^{(3)}(-\omega_1; \omega_4, -\omega_2, -\omega_3) \\ &= \chi_{kjil}^{(3)}(-\omega_2; -\omega_1, \omega_4, -\omega_3) = \text{etc.} \end{aligned} \quad (65)$$

Thus, under the condition that the susceptibilities are real (all frequencies far from any resonance), the susceptibilities are unchanged for the simultaneous permutation of subscripts from the cartesian set $\{ijkl\}$ and the corresponding subscripts from the frequency set $\{4123\}$, with the stipulation that the frequencies carry the proper sign. Note: The first frequency in the argument, that is, the *generated* frequency, carries a negative sign. The signs on the other frequencies must be such that the algebraic sum of all frequencies is zero. For example, $-\omega_4 + \omega_3 + \omega_2 + \omega_1 = 0$ implies that $-\omega_2 - \omega_1 + \omega_4 - \omega_3 = 0$. This is called full permutation symmetry. This symmetry generalizes to all orders.

Another symmetry follows when the susceptibilities exhibit negligible dispersion over the entire frequency range of interest. Thus, in addition to all frequencies being far from any material resonance, this symmetry requires that there be no resonance between any of the frequencies. This would *not* be the case if, for example, $\omega_2 > \omega_1$ and for some frequency between ω_1 and ω_2 an absorption line exists in the material. When dispersion can be ignored, the frequencies can be freely permuted without permuting the corresponding cartesian subscripts, and vice versa, and the susceptibility will remain unchanged. This is known as Kleinman symmetry.

Nonlinear susceptibilities also reflect the structural symmetry of the material. This is important since in many cases this greatly reduces the number of nonzero, independent tensor components needed to describe the medium. One immediate consequence of this is that for all materials that possess a center of inversion symmetry (e.g., isotropic liquids and crystals of symmetry class 432), all elements of all even-order susceptibility tensors are identically equal to zero. Thus, no even-order nonlinear processes are possible in these types of materials. (This is strictly true only when the susceptibility is derived using the electric dipole approximation in the perturbation Hamiltonian. For example, in an atomic

vapor a second order process may occur when a transition matrix element between two equal parity states, which is forbidden in the electric dipole approximation, is nonzero due to an electric quadrupole allowed transition. Such a transition however, is generally very weak.)

Other simplifications of the susceptibility tensors can be derived based on specific symmetry properties of material, such as rotation axis and mirror plane symmetries. The forms of the d -matrix for crystals of several different symmetry classes are given in Table 1. Note that in many cases the elements are zero or equal to ± 1 times other elements. The form of the matrix when Kleinman symmetry is valid is also given.

The specific form of third order susceptibilities may also be given for each symmetry class. These are shown in Table 2, which gives each symmetry class, the number of nonzero elements, and the relation between nonzero elements. For the lowest symmetry (triclinic), all 81 (3^4) elements are nonzero and independent. In all of the higher order symmetry classes several elements are equal to zero. For classes higher in symmetry than monoclinic and orthorhombic, the number of independent elements is less than the number of nonzero elements, with the isotropic class having the smallest number (3) of independent elements.

C. Coupled-Wave Propagation

The optical waves are coupled through the nonlinear polarization, and the nonlinear polarization acts as a source term in the wave equation for each monochromatic, or quasi-monochromatic, wave. As stated earlier, because of the linearity of the wave equation, each frequency component of the field satisfies the wave equation independently, with the source term being the Fourier component of the nonlinear polarization corresponding to the frequency of that optical field.

In this section, the form of the coupled-wave equations is considered when the waves propagate in an isotropic medium or along one of the principal axes in an anisotropic medium. When the birefringence of an uniaxial medium is small, quite often true in applications, the forms of these equations will be the same to a good approximation for propagation along any axis in a uniaxial medium.

Consider the interaction of $m + 1$ waves through an m th order nonlinear polarization. The frequency of the $(m + 1)$ th wave is given by

$$\omega_{m+1} = \sum_{\mu=1}^m \omega_{\mu} \quad (66)$$

where the set $\{\omega_{\mu}\}$ may contain both positive and negative frequencies. For any wave amplitude, $A(-\omega) = A^*(\omega)$, and for any wave vector, $\mathbf{k}(-\omega) = -\mathbf{k}(\omega)$. The wave amplitudes are assumed to vary primarily along the z -axis.

Table 1 Form of the d -Matrix for Different Symmetry Classes

Symmetry class	General conditions	Kleinman symmetry
<i>Biaxial crystals</i>		
1	$\begin{pmatrix} d_{11} & d_{12} & d_{13} & d_{14} & d_{15} & d_{16} \\ d_{21} & d_{22} & d_{23} & d_{24} & d_{25} & d_{26} \\ d_{31} & d_{32} & d_{33} & d_{34} & d_{35} & d_{36} \end{pmatrix}$	$\begin{pmatrix} d_{11} & d_{12} & d_{13} & d_{14} & d_{15} & d_{16} \\ d_{16} & d_{22} & d_{23} & d_{24} & d_{14} & d_{12} \\ d_{15} & d_{24} & d_{33} & d_{23} & d_{13} & d_{14} \end{pmatrix}$
2	$\begin{pmatrix} 0 & 0 & 0 & d_{14} & 0 & d_{16} \\ d_{21} & d_{22} & d_{23} & 0 & d_{25} & 0 \\ 0 & 0 & 0 & d_{34} & 0 & d_{36} \end{pmatrix}$	$\begin{pmatrix} 0 & 0 & 0 & d_{14} & 0 & d_{16} \\ d_{16} & d_{22} & d_{23} & 0 & d_{14} & 0 \\ 0 & 0 & 0 & d_{23} & 0 & d_{14} \end{pmatrix}$
m	$\begin{pmatrix} d_{11} & d_{12} & d_{13} & 0 & d_{15} & 0 \\ 0 & 0 & 0 & d_{24} & 0 & d_{26} \\ d_{31} & d_{32} & d_{33} & 0 & d_{35} & 0 \end{pmatrix}$	$\begin{pmatrix} d_{11} & d_{12} & d_{13} & 0 & d_{15} & 0 \\ 0 & 0 & 0 & d_{24} & 0 & d_{12} \\ d_{15} & d_{24} & d_{33} & 0 & d_{13} & 0 \end{pmatrix}$
222	$\begin{pmatrix} 0 & 0 & 0 & d_{14} & 0 & 0 \\ 0 & 0 & 0 & 0 & d_{25} & 0 \\ 0 & 0 & 0 & 0 & 0 & d_{36} \end{pmatrix}$	$\begin{pmatrix} 0 & 0 & 0 & d_{14} & 0 & 0 \\ 0 & 0 & 0 & 0 & d_{14} & 0 \\ 0 & 0 & 0 & 0 & 0 & d_{14} \end{pmatrix}$
$mm2$	$\begin{pmatrix} 0 & 0 & 0 & 0 & d_{15} & 0 \\ 0 & 0 & 0 & d_{24} & 0 & 0 \\ d_{31} & d_{32} & d_{33} & 0 & 0 & 0 \end{pmatrix}$	$\begin{pmatrix} 0 & 0 & 0 & 0 & d_{15} & 0 \\ 0 & 0 & 0 & d_{24} & 0 & 0 \\ d_{15} & d_{24} & d_{33} & 0 & 0 & 0 \end{pmatrix}$
<i>Uniaxial crystals</i>		
3	$\begin{pmatrix} d_{11} & -d_{11} & 0 & d_{14} & d_{15} & -d_{22} \\ -d_{22} & d_{22} & 0 & d_{15} & -d_{14} & -d_{11} \\ d_{31} & d_{31} & d_{33} & 0 & 0 & 0 \end{pmatrix}$	$\begin{pmatrix} d_{11} & -d_{11} & 0 & 0 & d_{15} & -d_{22} \\ -d_{22} & d_{22} & 0 & d_{15} & 0 & -d_{11} \\ d_{15} & d_{15} & d_{33} & 0 & 0 & 0 \end{pmatrix}$
$3m$	$\begin{pmatrix} 0 & 0 & 0 & 0 & d_{15} & -d_{22} \\ -d_{22} & d_{22} & 0 & d_{15} & 0 & 0 \\ d_{31} & d_{31} & d_{33} & 0 & 0 & 0 \end{pmatrix}$	$\begin{pmatrix} 0 & 0 & 0 & 0 & d_{15} & -d_{22} \\ -d_{22} & d_{22} & 0 & d_{15} & 0 & 0 \\ d_{15} & d_{15} & d_{33} & 0 & 0 & 0 \end{pmatrix}$
$\bar{6}$	$\begin{pmatrix} d_{11} & -d_{11} & 0 & 0 & 0 & -d_{22} \\ -d_{22} & d_{22} & 0 & 0 & 0 & -d_{11} \\ 0 & 0 & 0 & 0 & 0 & 0 \end{pmatrix}$	$\begin{pmatrix} d_{11} & -d_{11} & 0 & 0 & 0 & -d_{22} \\ -d_{22} & d_{22} & 0 & 0 & 0 & -d_{11} \\ 0 & 0 & 0 & 0 & 0 & 0 \end{pmatrix}$

(continued)

Table 1 Continued

Symmetry class	General conditions	Kleinman symmetry
$\bar{6}m2$	$\begin{pmatrix} 0 & 0 & 0 & 0 & 0 & -d_{22} \\ -d_{22} & d_{22} & 0 & 0 & 0 & 0 \\ 0 & 0 & 0 & 0 & 0 & 0 \end{pmatrix}$	$\begin{pmatrix} 0 & 0 & 0 & 0 & 0 & -d_{22} \\ -d_{22} & d_{22} & 0 & 0 & 0 & 0 \\ 0 & 0 & 0 & 0 & 0 & 0 \end{pmatrix}$
6,4	$\begin{pmatrix} 0 & 0 & 0 & d_{14} & d_{15} & 0 \\ 0 & 0 & 0 & d_{15} & -d_{14} & 0 \\ d_{31} & d_{31} & d_{33} & 0 & 0 & 0 \end{pmatrix}$	$\begin{pmatrix} 0 & 0 & 0 & 0 & d_{15} & 0 \\ 0 & 0 & 0 & d_{15} & 0 & 0 \\ d_{15} & d_{15} & d_{33} & 0 & 0 & 0 \end{pmatrix}$
6mm, 4mm	$\begin{pmatrix} 0 & 0 & 0 & 0 & d_{15} & 0 \\ 0 & 0 & 0 & d_{15} & 0 & 0 \\ d_{31} & d_{31} & d_{33} & 0 & 0 & 0 \end{pmatrix}$	$\begin{pmatrix} 0 & 0 & 0 & 0 & d_{15} & 0 \\ 0 & 0 & 0 & d_{15} & 0 & 0 \\ d_{15} & d_{15} & d_{33} & 0 & 0 & 0 \end{pmatrix}$
622,422	$\begin{pmatrix} 0 & 0 & 0 & d_{14} & 0 & 0 \\ 0 & 0 & 0 & 0 & -d_{14} & 0 \\ 0 & 0 & 0 & 0 & 0 & 0 \end{pmatrix}$	$\begin{pmatrix} 0 & 0 & 0 & 0 & 0 & 0 \\ 0 & 0 & 0 & 0 & 0 & 0 \\ 0 & 0 & 0 & 0 & 0 & 0 \end{pmatrix}$
$\bar{4}$	$\begin{pmatrix} 0 & 0 & 0 & d_{14} & d_{15} & 0 \\ 0 & 0 & 0 & -d_{15} & d_{14} & 0 \\ d_{31} & -d_{31} & 0 & 0 & 0 & d_{36} \end{pmatrix}$	$\begin{pmatrix} 0 & 0 & 0 & d_{14} & d_{15} & 0 \\ 0 & 0 & 0 & -d_{15} & d_{14} & 0 \\ d_{15} & -d_{15} & 0 & 0 & 0 & d_{14} \end{pmatrix}$
32	$\begin{pmatrix} d_{11} & -d_{11} & 0 & d_{14} & 0 & 0 \\ 0 & 0 & 0 & 0 & -d_{14} & -d_{11} \\ 0 & 0 & 0 & 0 & 0 & 0 \end{pmatrix}$	$\begin{pmatrix} d_{11} & -d_{11} & 0 & d_{14} & 0 & 0 \\ 0 & 0 & 0 & 0 & -d_{14} & -d_{11} \\ 0 & 0 & 0 & 0 & 0 & 0 \end{pmatrix}$
$\bar{4}2m$	$\begin{pmatrix} 0 & 0 & 0 & d_{14} & 0 & 0 \\ 0 & 0 & 0 & 0 & d_{14} & 0 \\ 0 & 0 & 0 & 0 & 0 & d_{36} \end{pmatrix}$	$\begin{pmatrix} 0 & 0 & 0 & d_{14} & 0 & 0 \\ 0 & 0 & 0 & 0 & d_{14} & 0 \\ 0 & 0 & 0 & 0 & 0 & d_{14} \end{pmatrix}$
<i>Isotropic crystals</i>		
$\bar{4}3m, 23$	$\begin{pmatrix} 0 & 0 & 0 & d_{14} & 0 & 0 \\ 0 & 0 & 0 & 0 & d_{14} & 0 \\ 0 & 0 & 0 & 0 & 0 & d_{14} \end{pmatrix}$	$\begin{pmatrix} 0 & 0 & 0 & d_{14} & 0 & 0 \\ 0 & 0 & 0 & 0 & d_{14} & 0 \\ 0 & 0 & 0 & 0 & 0 & d_{14} \end{pmatrix}$
432	$\begin{pmatrix} 0 & 0 & 0 & 0 & 0 & 0 \\ 0 & 0 & 0 & 0 & 0 & 0 \\ 0 & 0 & 0 & 0 & 0 & 0 \end{pmatrix}$	$\begin{pmatrix} 0 & 0 & 0 & 0 & 0 & 0 \\ 0 & 0 & 0 & 0 & 0 & 0 \\ 0 & 0 & 0 & 0 & 0 & 0 \end{pmatrix}$

Table 2 Form of the Third Order Susceptibility for Different Symmetry Classes

Symmetry class	Nonzero elements	Form
Triclinic 1, $\bar{1}$	81	$\chi_{ijkl}^{(3)}(i = x, y, z; j = x, y, z; k = x, y, z; l = x, y, z)$
Monoclinic 2, m, 2/m	41	$\chi_{iiii}^{(3)}(i = x, y, z)$ $\chi_{ijij}^{(3)}, \chi_{ijji}^{(3)}, \chi_{ijji}^{(3)}(i = x, j = y, z; i = y, j = x, z; i = z, j = x, y)$ $\chi_{ijij}^{(3)}, \chi_{yyij}^{(3)}, \chi_{iyij}^{(3)}, \chi_{yiyj}^{(3)}, \chi_{yijj}^{(3)}(i = x, j = z; i = z, j = x)$ $\chi_{iiij}^{(3)}, \chi_{ijij}^{(3)}, \chi_{ijji}^{(3)}, \chi_{jiji}^{(3)}(i = x, j = z; i = z, j = x)$
Orthorhombic 2mm, 222, mmm	21	$\chi_{iiii}^{(3)}(i = x, y, z)$ $\chi_{ijij}^{(3)}, \chi_{ijji}^{(3)}, \chi_{ijji}^{(3)}(i = x, j = y, z; i = y, j = x, z; i = z, j = x, y)$
Tetragonal 4, $\bar{4}$, 4/m	41	$\chi_{xxxx}^{(3)} = \chi_{yyyy}^{(3)}, \chi_{zzzz}^{(3)}$ $\chi_{xxyy}^{(3)} = \chi_{yyxx}^{(3)}, \chi_{xyxy}^{(3)} = \chi_{yxxy}^{(3)}, \chi_{xyyx}^{(3)} = \chi_{yxyx}^{(3)}$ $\chi_{xxyy}^{(3)} = -\chi_{yyxx}^{(3)}, \chi_{xyxy}^{(3)} = -\chi_{yxyx}^{(3)}, \chi_{xyyx}^{(3)} = -\chi_{xyxy}^{(3)}$ $\chi_{xxxx}^{(3)} = -\chi_{yyyy}^{(3)}, \chi_{xxxx}^{(3)} = \chi_{yyzz}^{(3)}, \chi_{zzxx}^{(3)} = \chi_{zzyy}^{(3)}, \chi_{zzxx}^{(3)} = \chi_{zyzy}^{(3)}$ $\chi_{xxxx}^{(3)} = \chi_{yyzz}^{(3)}, \chi_{zzxx}^{(3)} = \chi_{zzyy}^{(3)}, \chi_{zzxx}^{(3)} = \chi_{zyyz}^{(3)}$ $\chi_{xyzz}^{(3)} = -\chi_{yxzx}^{(3)}, \chi_{xyzz}^{(3)} = -\chi_{zyyx}^{(3)}, \chi_{xyzz}^{(3)} = -\chi_{zyxz}^{(3)}$ $\chi_{xyzz}^{(3)} = -\chi_{zyzx}^{(3)}, \chi_{xyzz}^{(3)} = -\chi_{zyxz}^{(3)}, \chi_{xyzz}^{(3)} = -\chi_{zyzy}^{(3)}$
Tetragonal 422, 4mm, $\bar{4}2m$, 4/mm	21	$\chi_{xxxx}^{(3)} = \chi_{yyyy}^{(3)}, \chi_{zzzz}^{(3)}$ $\chi_{xxyy}^{(3)} = \chi_{yyxx}^{(3)}, \chi_{xyxy}^{(3)} = \chi_{yxxy}^{(3)}, \chi_{xyyx}^{(3)} = \chi_{yxyx}^{(3)}$ $\chi_{xxxx}^{(3)} = \chi_{yyzz}^{(3)}, \chi_{zzxx}^{(3)} = \chi_{zzyy}^{(3)}, \chi_{zzxx}^{(3)} = \chi_{zyyz}^{(3)}$ $\chi_{zzxx}^{(3)} = \chi_{yzyz}^{(3)}, \chi_{zzxx}^{(3)} = \chi_{zyyz}^{(3)}, \chi_{zzxx}^{(3)} = \chi_{zyyz}^{(3)}$
Trigonal 3, $\bar{3}$	73	$\chi_{xxxx}^{(3)} = \chi_{yyyy}^{(3)}, \chi_{zzzz}^{(3)}$ $\chi_{xxxx}^{(3)} = \chi_{xyyy}^{(3)} + \chi_{xyyy}^{(3)} + \chi_{xyxy}^{(3)}$ $\chi_{xxyy}^{(3)} = \chi_{yyxx}^{(3)}, \chi_{xyxy}^{(3)} = \chi_{yxxy}^{(3)}, \chi_{xyxy}^{(3)} = \chi_{yxyx}^{(3)}$ $\chi_{xxyy}^{(3)} = \chi_{yzyz}^{(3)}, \chi_{zzxx}^{(3)} = \chi_{zzyy}^{(3)}, \chi_{zzxx}^{(3)} = \chi_{zyzy}^{(3)}$ $\chi_{zzxx}^{(3)} = \chi_{yzyz}^{(3)}, \chi_{zzxx}^{(3)} = \chi_{zzyy}^{(3)}, \chi_{zzxx}^{(3)} = \chi_{zyzy}^{(3)}$ $\chi_{zzxx}^{(3)} = \chi_{zyyz}^{(3)}, \chi_{zzxx}^{(3)} = \chi_{zyyz}^{(3)}$ $\chi_{xyzz}^{(3)} = -\chi_{yxzx}^{(3)}, \chi_{xyzz}^{(3)} = -\chi_{zyyx}^{(3)}, \chi_{xyzz}^{(3)} = -\chi_{zyxz}^{(3)}$ $\chi_{xyzz}^{(3)} = -\chi_{zyzx}^{(3)}, \chi_{xyzz}^{(3)} = -\chi_{zyxz}^{(3)}, \chi_{xyzz}^{(3)} = -\chi_{zyzy}^{(3)}$ $\chi_{xyzz}^{(3)} = -\chi_{zzyz}^{(3)}, \chi_{xyzz}^{(3)} = -\chi_{zyyz}^{(3)}$ $\chi_{xxyy}^{(3)} = -\chi_{yyxx}^{(3)} = \chi_{yyxy}^{(3)} + \chi_{yxyy}^{(3)} + \chi_{xyyy}^{(3)}$ $\chi_{xxyy}^{(3)} = -\chi_{yyxy}^{(3)}, \chi_{xxyy}^{(3)} = -\chi_{yxyy}^{(3)}, \chi_{xxyy}^{(3)} = -\chi_{yxyx}^{(3)}$ $\chi_{xxyy}^{(3)} = -\chi_{yxyx}^{(3)} = -\chi_{xyxy}^{(3)}$ $\chi_{xxyz}^{(3)} = -\chi_{yyyz}^{(3)} = -\chi_{yxyz}^{(3)} = -\chi_{yzyx}^{(3)}$ $\chi_{xxyz}^{(3)} = -\chi_{zyzy}^{(3)} = -\chi_{zyxz}^{(3)} = -\chi_{zyyx}^{(3)}$ $\chi_{zxxx}^{(3)} = -\chi_{zzyy}^{(3)} = -\chi_{zyxy}^{(3)} = -\chi_{zyyx}^{(3)}$

(continued)

Table 2 Continued

Symmetry class	Nonzero elements	Form
Trigonal 32, $3m, \bar{3}m$	37	$\chi_{yyy}^{(3)} = -\chi_{yxx}^{(3)} = -\chi_{xyx}^{(3)} = -\chi_{xxy}^{(3)}$, $\chi_{yyz}^{(3)} = -\chi_{yzx}^{(3)} = -\chi_{yzx}^{(3)} = -\chi_{xz}^{(3)}$ $\chi_{zyy}^{(3)} = -\chi_{zxx}^{(3)} = -\chi_{izyx}^{(3)} = -\chi_{izxy}^{(3)}$, $\chi_{zyy}^{(3)} = -\chi_{zxx}^{(3)} = -\chi_{zxyx}^{(3)} = -\chi_{zxx}^{(3)}$
Hexagonal 6, $\bar{6}, 6/m$	41	$\chi_{xxxx}^{(3)} = \chi_{yyyy}^{(3)} \cdot \chi_{zzzz}^{(3)}$ $\chi_{xxxx}^{(3)} = \chi_{xxyy}^{(3)} + \chi_{xyyy}^{(3)} + \chi_{xyxy}^{(3)}$ $\chi_{xxyy}^{(3)} = \chi_{yxxx}^{(3)} \cdot \chi_{xyyx}^{(3)} = \chi_{xyxy}^{(3)} \cdot \chi_{xyxy}^{(3)} = \chi_{yxyx}^{(3)}$ $\chi_{xzzz}^{(3)} = \chi_{yzxz}^{(3)} \cdot \chi_{zzxx}^{(3)} = \chi_{zzyy}^{(3)}, \chi_{zzxx}^{(3)} = \chi_{yzzy}^{(3)} \cdot \chi_{zuxz}^{(3)} = \chi_{zyyz}^{(3)}$ $\chi_{zzxx}^{(3)} = -\chi_{yyz}^{(3)} = -\chi_{yxyz}^{(3)} = -\chi_{yyz}^{(3)}$, $\chi_{xizx}^{(3)} = -\chi_{xyz}^{(3)} = -\chi_{yzy}^{(3)} = -\chi_{yzyx}^{(3)}$ $\chi_{izxx}^{(3)} = -\chi_{izyy}^{(3)} = -\chi_{zyx}^{(3)} = -\chi_{zyx}^{(3)}$, $\chi_{zxxz}^{(3)} = -\chi_{zyy}^{(3)} = -\chi_{zyy}^{(3)} = -\chi_{zyyx}^{(3)}$, $\chi_{zizx}^{(3)} = \chi_{yzyz}^{(3)} \cdot \chi_{zizx}^{(3)} = \chi_{zyzy}^{(3)}$
Hexagonal 622, $6mm, \bar{6}m2, 6/mmm$	21	$\chi_{xxxx}^{(3)} = \chi_{yyyy}^{(3)} \cdot \chi_{zzzz}^{(3)}$ $\chi_{xxxx}^{(3)} = \chi_{xxyy}^{(3)} + \chi_{xyyy}^{(3)} + \chi_{xyxy}^{(3)}$ $\chi_{xxyy}^{(3)} = \chi_{yxxx}^{(3)} \cdot \chi_{xyyx}^{(3)} = \chi_{xyxy}^{(3)} \cdot \chi_{xyxy}^{(3)} = \chi_{yxyx}^{(3)}$ $\chi_{xzzz}^{(3)} = \chi_{yzxz}^{(3)} \cdot \chi_{zzxx}^{(3)} = \chi_{zzyy}^{(3)}, \chi_{zzxx}^{(3)} = \chi_{yzzy}^{(3)} \cdot \chi_{zuxz}^{(3)} = \chi_{zyyz}^{(3)}$, $\chi_{zzxx}^{(3)} = \chi_{yzyz}^{(3)} \cdot \chi_{zizx}^{(3)} = \chi_{zyzy}^{(3)}$ $\chi_{xxyy}^{(3)} = -\chi_{yyyx}^{(3)} = \chi_{yxyy}^{(3)} + \chi_{yxyy}^{(3)} + \chi_{xyyy}^{(3)}$ $\chi_{xxyy}^{(3)} = -\chi_{yyxy}^{(3)} \cdot \chi_{xyxx}^{(3)} = -\chi_{yxyy}^{(3)} \cdot \chi_{xyyy}^{(3)} = -\chi_{yxyx}^{(3)}$
Cubic 23, $m\bar{3}$	21	$\chi_{xxxx}^{(3)} = \chi_{yyyy}^{(3)} = \chi_{zzzz}^{(3)}$ $\chi_{xxyy}^{(3)} = \chi_{yzzz}^{(3)} = \chi_{zzzx}^{(3)}$ $\chi_{yyxx}^{(3)} = \chi_{zzyy}^{(3)} = \chi_{xizx}^{(3)}$ $\chi_{xyxy}^{(3)} = \chi_{yzyz}^{(3)} = \chi_{zizx}^{(3)}$ $\chi_{yxyx}^{(3)} = \chi_{zyzy}^{(3)} = \chi_{iziz}^{(3)}$

(continued)

Table 2 Continued

Symmetry class	Nonzero elements	Form
Cubic 432, $m3m$, $\bar{4}3m$	21	$\chi_{xxxx}^{(3)} = \chi_{yyyy}^{(3)} = \chi_{zzzz}^{(3)}$ $\chi_{xyxy}^{(3)} = \chi_{yxyx}^{(3)} = \chi_{xzxz}^{(3)}$ $\chi_{xxyx}^{(3)} = \chi_{yxyy}^{(3)} = \chi_{xzxx}^{(3)} = \chi_{zzxx}^{(3)} = \chi_{yyzz}^{(3)} = \chi_{zzyy}^{(3)}$ $\chi_{xyyx}^{(3)} = \chi_{yxyx}^{(3)} = \chi_{xzxz}^{(3)} = \chi_{zzxz}^{(3)} = \chi_{yzyz}^{(3)} = \chi_{zyzy}^{(3)}$ $\chi_{xyyx}^{(3)} = \chi_{yxyx}^{(3)} = \chi_{xzxx}^{(3)} = \chi_{zzxx}^{(3)} = \chi_{yzzy}^{(3)} = \chi_{zyyz}^{(3)}$
Isotropic	21	$\chi_{xxxx}^{(3)} = \chi_{yyyy}^{(3)} = \chi_{zzzz}^{(3)}$ $\chi_{xxxx}^{(3)} = \chi_{xyxy}^{(3)} + \chi_{yxyx}^{(3)} + \chi_{xxyx}^{(3)}$ $\chi_{xyxy}^{(3)} = \chi_{yxyx}^{(3)} = \chi_{xzxz}^{(3)} = \chi_{zzxx}^{(3)} = \chi_{yyzz}^{(3)} = \chi_{zzyy}^{(3)}$ $\chi_{xxyx}^{(3)} = \chi_{yxyx}^{(3)} = \chi_{xzxz}^{(3)} = \chi_{zzxz}^{(3)} = \chi_{yzyz}^{(3)} = \chi_{zyzy}^{(3)}$ $\chi_{xyyx}^{(3)} = \chi_{yxyy}^{(3)} = \chi_{xzxx}^{(3)} = \chi_{zzxx}^{(3)} = \chi_{yzzy}^{(3)} = \chi_{zyyz}^{(3)}$

For practically every problem in nonlinear optics, the slowly varying amplitude approximation may be used [6–8]. This assumes that the magnitude and phase of the wave amplitude vary slowly in space and time over an optical wavelength and period, respectively. For any wave amplitude this implies that

$$\left| \frac{\partial^2 A}{\partial z^2} \right| \ll \left| k \frac{\partial A}{\partial z} \right| \quad (67)$$

$$\left| \frac{\partial^2 A}{\partial t^2} \right| \ll \left| \omega \frac{\partial A}{\partial t} \right| \quad (68)$$

and for the complex amplitude of the Fourier component of the nonlinear polarization,

$$\left| \frac{\partial^2 \mathbf{P}^{(m)}}{\partial t^2} \right| \ll \left| \omega \frac{\partial \mathbf{P}^{(m)}}{\partial t} \right| \ll |\omega^2 \mathbf{P}^{(m)}| \quad (69)$$

In all of the wave equations given below, the following definitions apply

$$\chi_{eff}^{(m)} = \hat{e}_{m+1} \cdot \boldsymbol{\chi}^{(m)}(-\omega_{m+1}; \omega_1, \omega_2, \dots, \omega_m) \cdot \hat{e}_1 \hat{e}_2 \cdots \hat{e}_m \quad (70)$$

where \hat{e}_μ is a unit vector pointing in the direction in space of the polarization of the μ th field,

$$\Delta k = \left[\sum_{\mu=1}^m \mathbf{k}_\mu - \mathbf{k}_{m+1} \right] \cdot \hat{\mathbf{z}} \quad (71)$$

$$K' = \begin{cases} 1 & (\text{SI}) \\ 4\pi & (\text{cgs}) \end{cases} \quad (72)$$

and the frequency-dependent index of refraction and absorption coefficient, respectively, are

$$n_{m+1} = n(\omega_{m+1}) \quad (73)$$

$$\alpha_{m+1} = \alpha(\omega_{m+1}) \quad (74)$$

The following equations are the form of the wave equation for A_{m+1} encountered under various situations. The terms quasi-cw, short pulse, and ultrashort pulse have the following meanings. Quasi-cw may refer to a true cw wave or to a pulse with a full-width at half-maximum (t_{FWHM}) such that the physical length of the medium is small compared to the distance ct_{FWHM}/n . A short pulse will have a width such that the physical length of the medium is comparable to or larger than ct_{FWHM}/n . An ultrashort pulse is only quasi-monochromatic, and hence is composed of several frequencies clustered about some carrier frequency. When the frequency spread of the pulse is such that dispersion in the refractive index cannot be ignored, the concept of a unique phase velocity is meaningless. The pulse is then treated as a superposition of monochromatic waves clustered about the carrier frequency, which move as a group with group velocity $v_g = (dk/d\omega)^{-1}$. This term is encountered when the physical length of the medium is comparable to or larger than the distance $v_g t_{\text{FWHM}}$.

The wave equation is thus give by

1. *Infinite plane waves, no absorption, quasi-cw, propagation primarily along +z.*

$$\frac{dA_{m+1}}{dz} = i \frac{K' \omega_{m+1}}{2n_{m+1} c} D^{(m)} \chi_{\text{eff}}^{(m)} \prod_{\mu=1}^m A_\mu \exp(i\Delta kz) \quad (75)$$

2. *Infinite plane waves, absorption, quasi-cw, propagation primarily along +z.*

$$\frac{dA_{m+1}}{dz} + \frac{\alpha_{m+1}}{2} A_{m+1} = i \frac{K' \omega_{m+1}}{2n_{m+1} c} D^{(m)} \chi_{\text{eff}}^{(m)} \prod_{\mu=1}^m A_\mu \exp(i\Delta kz) \quad (76)$$

3. *Infinite plane waves, absorption, quasi-cw, propagation primarily along $-z$.*

$$\frac{dA_{m+1}}{dz} - \frac{\alpha_{m+1}}{2} A_{m+1} = i \frac{K' \omega_{m+1}}{2n_{m+1}c} D^{(m)} \chi_{eff}^{(m)} \prod_{\mu=1}^m A_{\mu} \exp(i\Delta kz) \quad (77)$$

$$\Delta k = \left(\sum_{\mu=1}^m \mathbf{k}_{\mu} + \mathbf{k}_{m+1} \right) \cdot \hat{\mathbf{z}} \quad (78)$$

4. *Finite beams, no absorption, quasi-cw, propagation primarily along $+z$.*

$$\nabla_t^2 + 2ik_{m+1} \frac{\partial A_{m+1}}{\partial z} = - \frac{K' \omega_{m+1}^2}{c^2} D^{(m)} \chi_{eff}^{(m)} \prod_{\mu=1}^m A_{\mu} \exp(i\Delta kz) \quad (79)$$

$$\nabla_t^2 = \begin{cases} \frac{\partial^2}{\partial x^2} + \frac{\partial^2}{\partial y^2} & \text{rectangular coordinates} \\ \frac{1}{r} \frac{\partial}{\partial r} \left(r \frac{\partial}{\partial r} \right) + \frac{1}{r^2} \frac{\partial^2}{\partial \phi^2} & \text{cylindrical coordinates} \end{cases} \quad (80)$$

5. *Infinite plane waves, no absorption, short pulse, propagation primarily along $+z$.*

$$\frac{\partial A_{m+1}}{\partial z} + \frac{n_{m+1}}{c} \frac{\partial A_{m+1}}{\partial t} = i \frac{K' \omega_{m+1}}{2n_{m+1}c} D^{(m)} \chi_{eff}^{(m)} \prod_{\mu=1}^m A_{\mu} \exp(i\Delta kz) \quad (81)$$

6. *Infinite plane waves, no absorption, ultrashort pulse, propagation primarily along $+z$.*

$$\frac{\partial A_{m+1}}{\partial z} + \frac{1}{v_g} \frac{\partial A_{m+1}}{\partial t} = i \frac{K' \omega_{m+1}}{2n_{m+1}c} D^{(m)} \chi_{eff}^{(m)} \prod_{\mu=1}^m A_{\mu} \exp(i\Delta kz) \quad (82)$$

Note: In this equation ω_{m+1} is the carrier frequency of the pulse, and n_{m+1} is the refractive index at the carrier frequency. When group velocity dispersion is important, then the term $(ik_2/2)(\partial^2 A_{m+1}/\partial t^2)$ must be added to the left-hand side of Eq. (82), where k_2 is the group velocity dispersion coefficient given by Eq. (29).

Consider now Eq. (75) which is encountered often for transparent dielectric media. Each wave present in the medium will satisfy a wave equation of this form, and there will be $m + 1$ coupled equations. Some general relations are obtained when the nonlinear susceptibilities are real and thus full permutation symmetry applies. The coupled amplitude equations can be converted into coupled intensity equations by multiplying through by A_{μ}^* , for each wave $\mu = 1 \dots m + 1$, and

adding the complex conjugate of the resulting expression. Then it may be shown that

$$\frac{d}{dz} \sum_{\mu=1}^{m+1} I_{\mu} = 0 \quad (83)$$

This is merely a statement of the conservation of energy within the medium, since there is no linear absorption and the nonlinear susceptibilities are real. Thus, energy can flow between the waves, but remains in the form of electromagnetic energy. This type of interaction is called a parametric process. Also, for each frequency ω_{μ} ($\mu = 1 \dots m$),

$$\frac{d}{dz} \left(\frac{I_{m+1}}{\omega_{m+1}} \pm \frac{I_{\mu}}{\omega_{\mu}} \right) = 0 \quad (84)$$

where the sign corresponds to the sign on the frequency ω_{μ} in the argument of the susceptibility. The quantity (I/ω) is proportional to the photon flux in the field. Thus, Eq. (84) states that in a parametric process where a number of frequencies sum together algebraically to create a new frequency, for each photon created at ω_{m+1} , a photon at ω_{μ} is destroyed (+frequency) or created (-frequency). For example, consider the second order processes of sum-frequency ($\omega_3 = \omega_1 + \omega_2$) and difference-frequency ($\omega_2 = \omega_3 - \omega_1$) generation. For the former process, each photon at ω_3 created results in the annihilation of photons at ω_1 and ω_2 . In the latter process, for each photon at ω_2 created, a photon at ω_3 is annihilated and a photon at ω_1 is created. Equation (84) is known as the Manley–Rowe relation.

REFERENCES

1. M. Born and E. Wolfe, *Principles of Optics*, 5th ed., Pergamon Press, New York, 1975.
2. D. Marcuse, *Theory of Dielectric Optical Waveguides*, Academic Press, New York, 1991.
3. G. P. Agrawal, *Nonlinear Fiber Optics*, Academic Press, New York, 1989.
4. A. Yariv, *Quantum Electronics*, 3rd ed., John Wiley, New York, 1989.
5. A. Yariv and P. Yeh, *Optical Waves in Crystals*, John Wiley, New York, 1984.
6. R. W. Boyd, *Nonlinear Optics*, Academic Press, New York, 1992.
7. Y. R. Shen, *The Principles of Nonlinear Optics*, John Wiley, New York, 1984.
8. P. N. Butcher and D. Cotter, *The Elements of Nonlinear Optics*, Cambridge Univ. Press, New York, 1990.

2

Frequency Doubling and Mixing

The demonstration of optical second harmonic generation by the irradiation of a quartz crystal with a ruby laser [1] marked the opening of the field of nonlinear optics. Since then this process, part of what is known as second order nonlinear optics, has become the subject of the most advanced device technology development in the field.

This chapter and the next cover the primary processes utilized in second order nonlinear optical wave interactions. The special topics of optical parametric amplification and oscillation are reserved for the next chapter. The electrooptic effect is not discussed here. It will be touched upon in Chapter 6 in conjunction with the photorefractive effect and discussed more extensively in Chapter 17.

Specific topics addressed in this chapter are second harmonic generation (SHG) and two types of frequency mixing: sum-frequency generation (SFG) and difference-frequency generation (DFG). Second harmonic generation is described schematically in Fig. 1a. A single pump wave, the fundamental at frequency ω , is incident on a nonlinear medium and generates a wave at the second harmonic frequency 2ω . Figure 1b illustrates sum-frequency generation. Two pump waves at frequencies ω_{p1} and ω_{p2} incident on a nonlinear medium combine to generate a wave at the sum frequency $\omega_s = \omega_{p1} + \omega_{p2}$. Difference-frequency generation, shown in Fig. 1c, is similar to sum-frequency generation, except that the two pump waves combine to produce a wave at the difference frequency $\omega_d = \omega_{p1} - \omega_{p2}$. The latter process is the same as that involved in optical parametric amplification and oscillation. These phenomena, discussed in Chapter 3, will be differentiated from those described here by calling pump wave 2, which is also generated in the difference-frequency process, the signal wave; pump wave 1 will just be called the pump; and the difference-frequency wave will be called the idler wave.

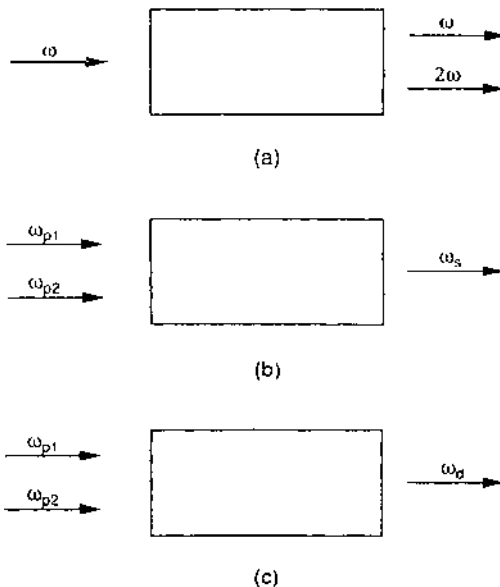


Figure 1 Schematic illustrations of the frequency conversion processes treated in this chapter. (a) Second harmonic generation (SHG). (b) Sum-frequency generation (SFG). (c) Difference-frequency generation (DFG).

The technological significance of the processes described in this chapter is primarily in the area of generating coherent radiation at new frequencies that are not usually available with lasers. Combining different lasers with several different materials and nonlinear processes, tunable coherent radiation from the ultraviolet through the visible and near-infrared to the far-infrared has been generated for spectroscopy, nonlinear optics, remote sensing, optical radar, and various other applications. Currently, intensive research efforts are under way with second harmonic generation materials to be used in conjunction with semiconductor lasers to generate short wavelength radiation for high-density optical data storage. In addition, the processes of frequency doubling and wave mixing have become useful as nonlinear optical probes of the structure and functions of surfaces, and as probes of molecular order in the liquid state.

This chapter presents the many formulas used in describing the processes of frequency doubling and mixing. First, the nonlinear polarization sources that generate the new frequencies are described. Coupled-wave equations for the various frequency conversion processes are also given. Formulas giving the efficiency of the optical power generated at the desired frequency are presented in various orders of approximation, including ideal infinite plane waves in ideal

media, then including the effects of real optical beams in real media. The important topic of phase matching for efficient generation of new frequencies is treated in a separate section, including formulas useful in the different techniques of phase matching. The nonlinear coefficients d_{eff} are discussed and formulas given for different crystal classes. Finally, some formulas for new waves generated by frequency doubling and mixing by reflection at surfaces are given in the last section.

I. SECOND ORDER OPTICAL WAVE INTERACTIONS

Frequency conversion in optics can be understood as the modulation of the refractive index by an electric field at a given optical frequency, or frequencies, through a second order nonlinearity. The modulated index then produces sidebands of the optical frequency, yielding harmonics and sum and difference frequencies.

These types of processes are well known in the linear electrooptic or Pockels effect where the sidebands are at frequencies much smaller than the frequency of the optical wave (i.e., dc to microwave frequency). This effect is described in terms of the change in the optical indicatrix of the nonlinear crystal due to the application of an external low frequency or dc electric field. The Pockels coefficient is directly proportional to the second order nonlinear optical susceptibility.

In optics, it is more convenient to describe frequency conversion optical interactions by the nonlinear polarization than by the nonlinear refractive index. (Modulation of the refractive index by optical waves via a third order nonlinearity is the subject of later chapters; see Chapters 6–8.) The polarization field in a dielectric is the dipole moment per unit volume of the material. The incident optical waves induce a phased array of dipoles that then radiate waves coherently at new frequencies. Since the interacting fields are traveling waves, this is an extended, not a point, interaction. Thus the relative phase of the interacting waves is an important issue. In the following, important elements of the theory of second order interactions are described with definitions of key terms. This will be of help in applying the formulas (given later) to specific applications.

A. Optical Waves

For most interactions of interest, the electric field of the optical wave plays the most important role. As described in Chapter 1, the optical field, a real quantity, is described in complex notation as

$$\mathbf{E}^{(\sim)}(\mathbf{r}, t) = \mathbf{E}(\mathbf{r}, t) \exp(-i\omega t) + \text{c.c.} \quad (1)$$

where the superscripted tilde indicates that the field has a rapidly varying time dependence, and c.c. stands for complex conjugate. The slowly varying time dependence is contained within the complex field amplitude $\mathbf{E}(\mathbf{r}, t)$, which also has a spatial (\mathbf{r}) dependence. The rapidly varying spatial dependence is further factored out as

$$\mathbf{E}(\mathbf{r}, t) = \hat{\epsilon} A(\mathbf{r}, t) \exp(i\mathbf{k} \cdot \mathbf{r}) \quad (2)$$

where $\hat{\epsilon}$ is a unit vector pointing in the direction of the electric field (i.e., the wave polarization direction), \mathbf{k} is the wave vector pointing in the direction of wave propagation, and $A(\mathbf{r}, t)$ is the slowly varying (in both space and time) complex field amplitude. Computations are performed using $A(\mathbf{r}, t)$. This field amplitude takes various limiting forms depending on the nature of the problem.

Short, quasi-monochromatic pulses. Nonlinear optics is done with lasers that in most practical cases can be considered to be monochromatic. However, for extremely short laser pulses (typically < 1 ns), it is often necessary to consider the pulse as composed of a band of frequencies clustered about a center frequency ω_0 . In this case,

$$A(\mathbf{r}, t) = A_{\omega_0}(\mathbf{r}, t) \quad (3)$$

where the subscript indicates that the field is quasi-monochromatic with center frequency ω_0 .

Monochromatic, quasi-cw. For pulse widths typically > 1 ns, the waves can be considered essentially monochromatic. Since the electronic or ionic response of the medium is typically faster than the pulse rise time (except near resonances), these pulses can be treated as quasi-cw. Formulas including optical power or intensity can then be understood to apply for average or instantaneous values. In these cases, for a monochromatic wave of frequency ω_α ,

$$A(\mathbf{r}, t) = A_{\omega_\alpha}(\mathbf{r}) = A_\alpha(\mathbf{r}) \quad (4)$$

where the subscript α labels the frequency (e.g., $\alpha = d$ for difference frequency).

No radial dependence, propagation primarily along z . The waves are typically in the form of optical beams. The convention is to choose the direction of propagation along the z -axis. In the case of noncollinear propagation of waves, all waves are assumed to have a component of their wave vectors along z . Real optical beams have a radial profile and diffract (i.e., their wave vectors have small radial components). For most laser beams of interest, the direction of propagation can still be considered primarily along z , and to a first order of approximation the radial dependence of the field amplitude can be ignored. Thus

$$A(\mathbf{r}, t) = A(z, t) \quad (5)$$

This designation essentially assumes that the interacting waves are infinite place

waves. For a proper description of the wave interactions, the radial dependence cannot be completely ignored. This will be dealt with in an *ad hoc* fashion later.

B. Wave Equations

For the purposes of presenting the formulas pertaining to frequency conversion processes, the starting point will be to treat ideal infinite plane waves in ideal media. Corrections for nonideal conditions will be added later. Thus the formulas to follow later in Sections II–V allow estimates of appropriate quantities in varying degrees of approximation.

Since the waves are monochromatic, the wave equation for the total field can be decomposed into Fourier components, resulting in separate wave equations for each frequency component of the field. In addition, the following conditions will apply.

Cubic media, propagation along a principal axis of the crystal, or low birefringence. If any or all of these assumptions are made, then approximations that apply are

$$\chi^{(1)} \rightarrow \chi^{(1)} \quad (6)$$

$$\hat{e} \cdot \mathbf{k} \approx 0 \quad (7)$$

$$\cos \rho \approx 1 \quad (8)$$

$$\nabla \times \nabla \times \mathbf{E} \approx -\nabla^2 \mathbf{E} \quad (9)$$

These imply that the linear dielectric susceptibility is treated as a scalar quantity, the waves are approximately transverse, and the angle ρ between the wave vector and the Poynting vector is small. For real optical beams, this walk-off angle will be important and will be dealt with later. The approximation in Eq. (9) will not be allowed when boundary effects are included.

No radial dependence. For infinite plane waves propagating along the z -axis,

$$\nabla^2 \rightarrow \frac{d^2}{dz^2} \quad (10)$$

Again, radial dependence will be important for real optical beams and will be included later.

Quasi-cw. For quasi-cw waves,

$$\frac{\partial^2}{\partial t^2} \rightarrow -\omega^2 \quad (11)$$

The case of short, quasi-monochromatic pulses will be considered specifically in Section IV.

Slowly varying amplitude approximation. If the variation of the field amplitudes is small within the distance of one wavelength (as is usually the case), then

$$\frac{d^2\mathbf{E}}{dz^2} \rightarrow \hat{\mathbf{e}} \left(-k^2 A + 2ik \frac{dA}{dz} \right) \exp(ikz) \quad (12)$$

As Shen [2] has pointed out, this assumption also implies that backward generated waves can be ignored. This will not be the case when boundary effects are included.

No losses. Losses such as linear absorption and scattering and nonlinear absorption (e.g., two-photon absorption) are ignored. The effects of linear absorption will be added later. Two-photon absorption can be important but is generally best treated in an *ad hoc* fashion. It can be quite detrimental to efficient frequency conversion. Both linear and nonlinear absorption can lead to thermal effects. The temperature dependence of wave interactions is taken up in Section III.

C. Nonlinear Polarization

For second order processes, the nonlinear polarization, which was introduced in Chapter 1, is truncated after the first term, i.e.,

$$\mathbf{P}_{NL} = \mathbf{P}^{(2)} \quad (13)$$

The form of the nonlinear polarization for each of the frequency conversion processes is given below.

SHG.

$$P_{2\omega}^{(2)} = 2\epsilon_0 d_{eff} A_\omega^2 \exp(i\Delta kz) \quad (14)$$

$$P_\omega^{(2)} = 4\epsilon_0 d_{eff} A_{2\omega} A_\omega^* \exp(-i\Delta kz) \quad (15)$$

$$\Delta k = (2\mathbf{k}_\omega - \mathbf{k}_{2\omega}) \cdot \hat{\mathbf{z}} \quad (16)$$

$$d_{eff} = \hat{\mathbf{e}}_{2\omega} \cdot \mathbf{d} \cdot \hat{\mathbf{e}}_\omega \hat{\mathbf{e}}_\omega \quad (17)$$

SFG.

$$P_s^{(2)} = 4\epsilon_0 d_{\text{eff}} A_{p1} A_{p2} \exp(i\Delta kz) \quad (18)$$

$$P_{p1}^{(2)} = 4\epsilon_0 d_{\text{eff}} A_s A_{p2}^* \exp(-i\Delta kz) \quad (19)$$

$$P_{p2}^{(2)} = 4\epsilon_0 d_{\text{eff}} A_s A_{p1}^* \exp(-i\Delta kz) \quad (20)$$

$$\Delta k = (\mathbf{k}_{p1} + \mathbf{k}_{p2} - \mathbf{k}_s) \cdot \hat{z} \quad (21)$$

$$d_{\text{eff}} = \hat{e}_s \cdot \mathbf{d} \cdot \hat{e}_{p1} \hat{e}_{p2} \quad (22)$$

DFG.

$$P_d^{(2)} = 4\epsilon_0 d_{\text{eff}} A_{p1} A_{p2}^* \exp(i\Delta kz) \quad (23)$$

$$P_{p1}^{(2)} = 4\epsilon_0 d_{\text{eff}} A_d A_{p2} \exp(-i\Delta kz) \quad (24)$$

$$P_{p2}^{(2)} = 4\epsilon_0 d_{\text{eff}} A_d^* A_{p1} \exp(i\Delta kz) \quad (25)$$

$$\Delta k = (\mathbf{k}_{p1} - \mathbf{k}_{p2} - \mathbf{k}_d) \cdot \hat{z} \quad (26)$$

$$d_{\text{eff}} = \hat{e}_d \cdot \mathbf{d} \cdot \hat{e}_{p1} \hat{e}_{p2}^* \quad (27)$$

The above equations are in SI units with $\epsilon_0 = 8.85 \times 10^{-12}$ F/m. The form of the equations in cgs units would be the same, but with ϵ_0 set equal to 1. The nonlinear polarization serves as a source term in the wave equations to generate the new waves, and Δk represents the phase velocity mismatch between the driving polarization and the generated optical wave.

The nonlinear coefficient has been contracted from a tensor to a scalar quantity, which is convenient for applying the formulas that follow. The polarization of the various optical waves is designated by the unit vector \hat{e}_α , where the subscript α is the appropriate descriptor for the wave. Because of permutation symmetry, described in Chapter 1, the nonlinear coefficients for each polarization source are equal for a given frequency conversion process. Thus a single d_{eff} determines the strength of the nonlinearity for any particular problem.

It is important to recognize that, in general, d_{eff} is a sum of terms obtained through the contraction process and must be determined for each particular problem based on the polarizations of the interacting optical waves and the geometry of the nonlinear crystal. Also, the components of the tensor \mathbf{d} are normally given in terms of the principal axes of the crystal and hence must be converted to the laboratory coordinate system used for describing the propagation

of the optical waves. As a simple example, consider Fig. 2, which illustrates SHG with the pump wave polarized along y and the second harmonic wave polarized along x . The lowercase letters will always represent the laboratory coordinate system, and the uppercase letters will always represent the principal axes of the crystal. In this situation, it is obvious that $d_{\text{eff}} = d_{xyy}$. However, in general $d_{xyy} \neq d_{XYY}$ but is a linear combination of all of the tensor components in the principal axes system and depends on the angles θ and ϕ as well. For most crystals, many of these components are zero or related to other components. Formulas for d_{eff} for the various crystal classes and for various optical wave polarizations are given in Section III.

D. Intensities of the Generated Optical Waves

The generated waves are coupled through the nonlinear polarization. The coupled-wave equations are given below. The form of these equations, for a given process, is identical in both SI and cgs units within a constant K , where

$$K = \begin{cases} 1 & (\text{SI}) \\ 4\pi & (\text{cgs}) \end{cases} \quad (28)$$

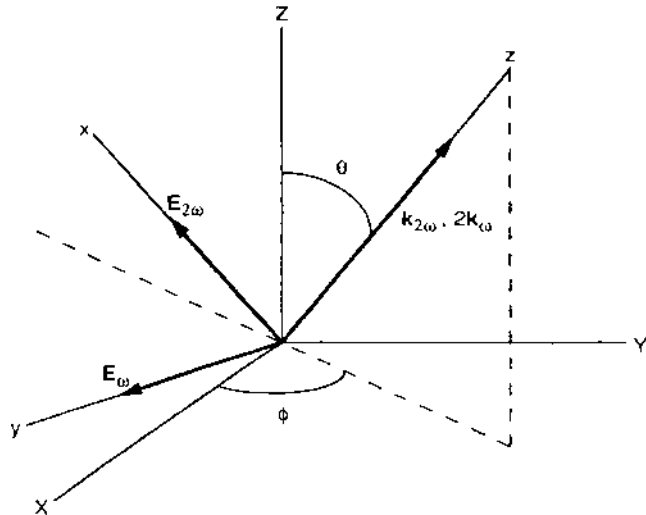


Figure 2 Example of SHG geometry in laboratory coordinate system (x, y, z) and crystal coordinate system (X, Y, Z).

SHG.

$$\frac{dA_{2\omega}}{dz} = iK \frac{2\omega}{n_{2\omega}c} d_{\text{eff}} A_\omega^2 \exp(i\Delta kz) \quad (29)$$

$$\frac{dA_\omega}{dz} = iK \frac{2\omega}{n_\omega c} d_{\text{eff}} A_\omega^* A_{2\omega} \exp(-i\Delta kz) \quad (30)$$

SFG.

$$\frac{dA_s}{dz} = iK \frac{2\omega_s}{n_s c} d_{\text{eff}} A_{p1} A_{p2} \exp(i\Delta kz) \quad (31)$$

$$\frac{dA_{p1}}{dz} = iK \frac{2\omega_{p1}}{n_{p1} c} d_{\text{eff}} A_s A_{p2}^* \exp(-i\Delta kz) \quad (32)$$

$$\frac{dA_{p2}}{dz} = iK \frac{2\omega_{p2}}{n_{p2} c} d_{\text{eff}} A_s A_{p1}^* \exp(-i\Delta kz) \quad (33)$$

DFG.

$$\frac{dA_d}{dz} = iK \frac{2\omega_d}{n_d c} d_{\text{eff}} A_{p1} A_{p2}^* \exp(i\Delta kz) \quad (34)$$

$$\frac{dA_{p1}}{dz} = iK \frac{2\omega_{p1}}{n_{p1} c} d_{\text{eff}} A_d A_{p2} \exp(-i\Delta kz) \quad (35)$$

$$\frac{dA_{p2}}{dz} = iK \frac{2\omega_{p2}}{n_{p2} c} d_{\text{eff}} A_d A_{p1}^* \exp(i\Delta kz) \quad (36)$$

These equations were first solved by Armstrong et al. [3]. In general, both the modulus and phase of the complex field amplitudes are computed. However, to compute the output intensities of the generated waves, only the modulus is used. The intensity of a wave at some position z is given by

$$I_\alpha = 2\epsilon_0 n_\alpha c |A_\alpha|^2 \quad (37)$$

in SI units, and

$$I_\alpha = \frac{n_\alpha c}{2\pi} |A_\alpha|^2 \quad (38)$$

in cgs units. The optical power of a given wave is computed from

$$\mathcal{P} = \int_A I dA \quad (39)$$

where the integration is over the area A of the beam. The area A is not to be confused with the complex field amplitudes.

E. Units and Conversions

Both SI and cgs units of physical quantities are included, since formulas in both of these systems of units are common in the literature. Caution should be exercised to avoid mixing units in a given equation, since this will lead to numerical errors. SI units are convenient for experiments, since these are the units of measure in the laboratory. However, cgs units are often used in theoretical developments.

The correct units of physical quantities in SI and cgs systems are given in Table 1. Formulas for converting cgs units to SI units are included in Table 2.

II. IDEAL PLANE WAVES IN IDEAL MEDIA

The conditions of the problem are illustrated in Fig. 3. All waves are assumed to propagate collinearly along the z -axis. The pump wave intensities are specified at the input of the nonlinear medium at $z = 0$. The output intensities of all waves are then determined at the end of the nonlinear medium at $z = L$. Boundary effects

Table 1 Units of Important Physical Parameters Used in Frequency Conversion Formulas

Parameter	SI units	cgs units
Second order polarization	$[P^{(2)}] = \text{C/m}^2$	$[P^{(2)}] = \text{sC/cm}^2 = \text{dyn}^{1/2}/\text{cm}$ $= (\text{erg/cm}^3)^{1/2}$
Electric field	$[E] = \text{V/m}$	$[E] = \text{sV/cm} = (\text{erg/cm}^3)^{1/2}$
Second order susceptibility	$[d] = \text{m/V}$	$[d] = \text{cm}^2/\text{sC} = \text{cm/dyn}^{1/2}$ $= (\text{cm}^3/\text{erg})^{1/2} = \text{esu}$
Vacuum permittivity	$[\epsilon_0] = \text{F/m} = \text{C/V}\cdot\text{m}$	—
Distance, length	$[z] = [r] = [L] = \text{m}$	$[z] = [r] = [L] = \text{cm}$
Speed of light	$[c] = \text{m/s}$	$[c] = \text{cm/s}$
Wavelength	$[\lambda] = \text{m}$	$[\lambda] = \text{cm}$
Wave vector	$[k] = \text{m}^{-1}$	$[k] = \text{cm}^{-1}$
Absorption coefficient	$[\alpha] = \text{m}^{-1}$	$[\alpha] = \text{cm}^{-1}$
Intensity	$[I] = \text{W/m}^2$	$[I] = \text{erg/s/cm}^2$
Power	$[\mathcal{P}] = \text{W}$	$[\mathcal{P}] = \text{erg/s}$

Table 2 Conversion Formulas

$P^{(2)}$	(SI) = $\frac{1}{3} \times 10^{-5} P^{(2)}$	(cgs)
E	(SI) = $3 \times 10^4 E$	(cgs)
d	(SI) = $(4\pi/3) \times 10^{-4} d$	(cgs)
L	(SI) = $10^{-2} L$	(cgs)
c	(SI) = $10^{-2} c$	(cgs)
λ	(SI) = $10^{-2} \lambda$	(cgs)
k	(SI) = $10^2 k$	(cgs)
α	(SI) = $10^2 \alpha$	(cgs)
I	(SI) = $10^{-3} I$	(cgs)
\mathcal{P}	(SI) = $10^{-7} \mathcal{P}$	(cgs)

are ignored. When there are two pump waves, it will be understood that $I_{p1} \geq I_{p2}$, and conversion efficiencies will be in terms of the smaller pump power.

A. Negligible Pump Depletion

As a first order of approximation, it is assumed that in the frequency conversion process there is negligible depletion of the pump beam(s) power. This means that the conversion efficiency is weak, and the pump power is approximately constant.

Formulas giving the efficiency for SHG, SFG, and DFG are given in Table 3. The $\text{sinc}^2 x = (\sin^2 x)/x^2$ dependence in these formulas describes

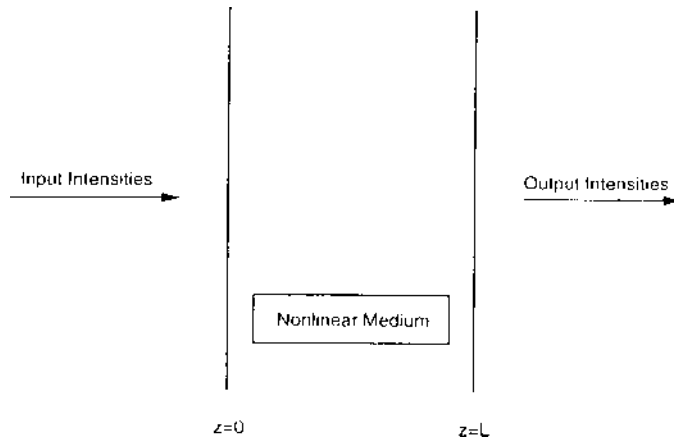


Figure 3 The setup of the problem for calculating frequency conversion efficiencies in a nonlinear medium.

Table 3 Conversion Efficiency Formulas in the Infinite Plane Wave, Nondepleted Pump Approximation

SHG ($2\omega = \omega + \omega$)	$\eta_{2\omega} = \frac{\mathcal{P}_{2\omega}}{\mathcal{P}_\omega} = \eta_{2\omega}^0 \frac{\sin^2(\Delta kL/2)}{(\Delta kL/2)^2}$		
	$\eta_{2\omega}^0 = \frac{8\pi^2 d_{\text{eff}}^2 L^2 I_\omega}{\epsilon_0 n_\omega^2 n_{2\omega} c \lambda_\omega^2} \quad (\text{SI}) \quad \eta_{2\omega}^0 = \frac{512\pi^5 d_{\text{eff}}^2 L^2 I_\omega}{n_\omega^2 n_{2\omega} c \lambda_\omega^2} \quad (\text{cgs})$		
SFG ($\omega_s = \omega_{p1} + \omega_{p2}$)	$\eta_s = \frac{\mathcal{P}_s}{\mathcal{P}_{p2}} = \eta_s^0 \frac{\sin^2(\Delta kL/2)}{(\Delta kL/2)^2}$		
	$\eta_s^0 = \frac{8\pi^2 d_{\text{eff}}^2 L^2 I_{p1}}{\epsilon_0 n_{p1} n_{p2} n_s c \lambda_s^2} \quad (\text{SI}) \quad \eta_s^0 = \frac{512\pi^5 d_{\text{eff}}^2 L^2 I_{p1}}{n_{p1} n_{p2} n_s c \lambda_s^2} \quad (\text{cgs})$		
DFG ($\omega_d = \omega_{p1} - \omega_{p2}$)	$\eta_d = \frac{\mathcal{P}_d}{\mathcal{P}_{p2}} = \eta_d^0 \frac{\sin^2(\Delta kL/2)}{(\Delta kL/2)^2}$		
	$\eta_d^0 = \frac{8\pi^2 d_{\text{eff}}^2 L^2 I_{p1}}{\epsilon_0 n_{p1} n_{p2} n_d c \lambda_d^2} \quad (\text{SI}) \quad \eta_d^0 = \frac{512\pi^5 d_{\text{eff}}^2 L^2 I_{p1}}{n_{p1} n_{p2} n_d c \lambda_d^2} \quad (\text{cgs})$		

the effects of unequal phase velocities of the interacting waves. A plot of this function is shown in Fig. 4. For $\Delta kL \neq 0$, the efficiency of the process is severely reduced. The phase matching bandwidth, defined by the points where the function is reduced to $\frac{1}{2}$, is

$$\Delta k_{BW} = 2.784/L \quad (40)$$

The distance over which this function goes to zero is defined as the coherence length and is given by

$$L_c = \frac{\pi}{|\Delta k|} \quad (41)$$

The coherence length is the distance over which the desired frequency of radiation is generated. The physical interpretation of this by the energy theorem for optical waves is illustrated in Fig. 5. This figure shows a snapshot in time of the time derivative of the driving nonlinear polarization, which has a nearly constant amplitude, the generated optical field, and the work done by the field on the induced dipoles, all through the length of the medium. At the front of the medium, the former two quantities are π radians out of phase. This is the optimum phase relation for negative work to be done (i.e., extraction of energy from the pump

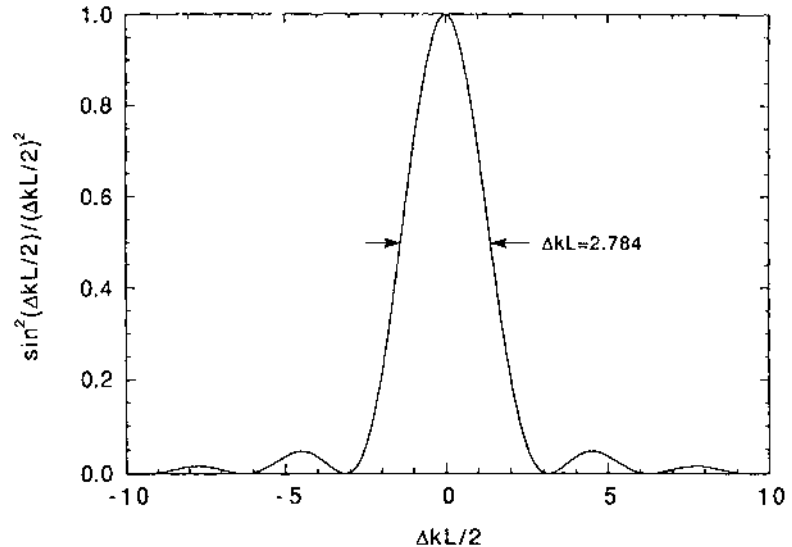


Figure 4 Plot of the sinc^2 function, which describes the effects of phase mismatch in frequency conversion processes.

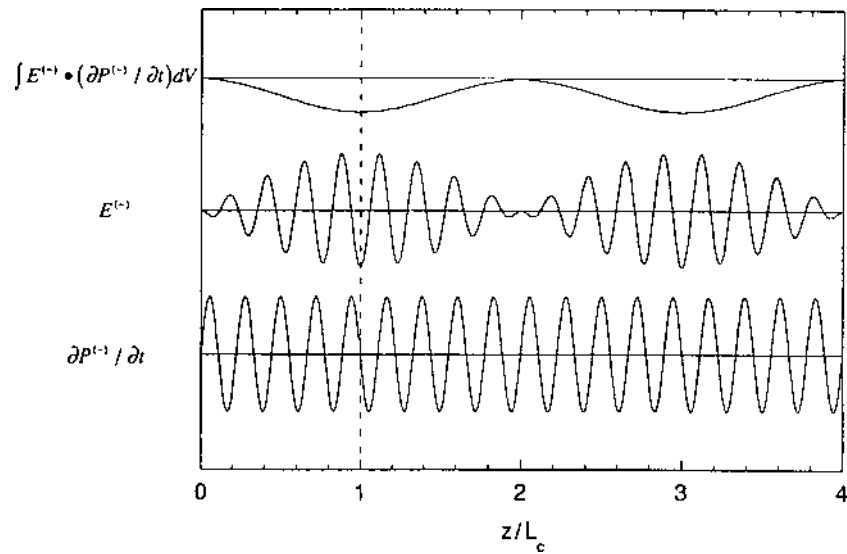


Figure 5 Illustration of optical field generation and work done by the field on the microscopic dipoles in a nonlinear medium as a function of distance in nonphase matched frequency conversion processes.

wave, through the nonlinearity of the medium, and transfer of that energy to the new frequency). Due to the unequal phase velocities, however, this phase relation slips as the waves propagate through the medium, causing the energy transfer to become less efficient. After a distance equal to L_c , the phase has shifted by $\pi/2$. This phase relation leads to no (time averaged) net work done. Beyond L_c the phase has shifted to less than $\pi/2$. This is the region where positive work will be done by the field on the induced dipoles, causing energy to flow from the desired frequency wave back to the pump wave(s). Thus as the waves propagate through the medium, energy flows back and forth between the waves every coherence length.

The severity of this phase mismatch is illustrated in Fig. 6, where the efficiency normalized to its peak value is plotted as a function of z for various values of ΔkL . For example, for a crystal length of 1 cm, $\Delta kL = 5$ implies that $\Delta k = 5 \text{ cm}^{-1}$. A typical optical wave may have $k \sim 15,000 \text{ cm}^{-1}$. Thus a phase velocity mismatch of only $\Delta k/k \sim 3 \times 10^{-4}$ is enough to reduce the efficiency by a factor of about 20 from its maximum value of η^0 .

For perfect phase matching ($\Delta k = 0$), the efficiency takes the maximum value given by the formulas in Table 3. It can be seen that $\eta^0 \propto L^2$, $\eta^0 \propto$ pump intensity, and $\eta^0 \propto d_{\text{eff}}^2/n^3$. In the latter expression, the refractive indices of all the interacting waves are assumed to be approximately equal to their mean value n .

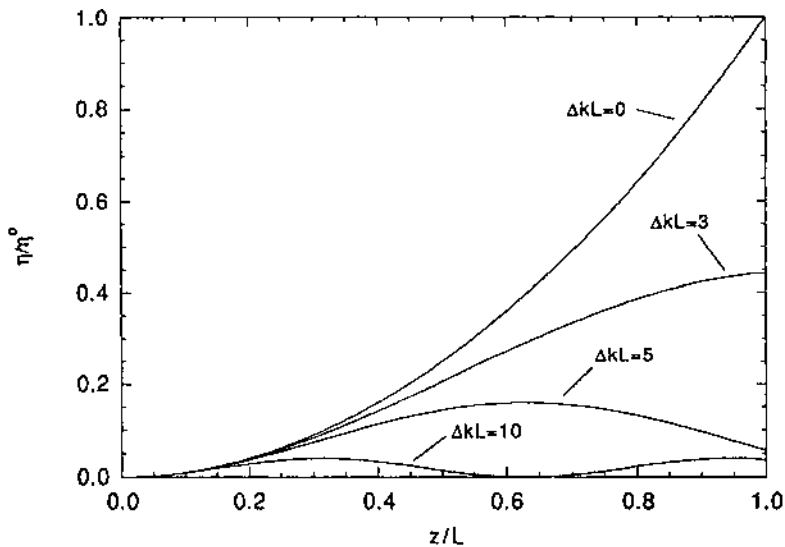


Figure 6 Normalized conversion efficiency as a function of position in a nonlinear medium for various values of phase mismatch for SHG, SFG, and DFG.

B. Pump Depletion

Perfect phase matching. With perfect phase matching, the conversion efficiency can become appreciable, and it is no longer possible to ignore the depletion of the pump beam(s). To present the formulas including pump depletion, it is convenient to define a length scale L_{NL} characteristic of the nonlinear interaction. For example, with perfectly phase matched SHG, L_{NL} is the length of nonlinear crystal that would produce a conversion efficiency of approximately 58%. The stronger the nonlinearity, the shorter L_{NL} will be.

Formulas for conversion efficiencies in SHG, SFG, and DFG under the conditions of perfect phase matching and pump depletion are given in Table 4. Formulas for L_{NL} for each process are also given in both SI and cgs units. It can be seen that L_{NL} is inversely proportional to the pump intensity and inversely proportional to $(d_{\text{eff}}^2/n^3)^{1/2}$.

SHG efficiency exhibits a hyperbolic tangent-squared dependence on L/L_{NL} . The behavior of the fundamental and second harmonic intensities in this regime is illustrated in Fig. 7. It can be seen that as the fundamental intensity is depleted, it asymptotically approaches zero, while the SHG efficiency approaches one. The reason for this behavior is that the fundamental intensity drives the nonlinear polarization producing the second harmonic. As the fundamental is depleted, it becomes less effective in driving the nonlinearity.

Table 4 Frequency Conversion Efficiency Formulas in the Infinite Plane Wave Approximation, Including Pump Depletion

SHG	$\eta_{2\omega} = \tanh^2(L/L_{\text{NL}})$			
	$L_{\text{NL}} = \frac{1}{4\pi d_{\text{eff}}} \sqrt{\frac{2\epsilon_0 n_\omega^2 n_{2\omega} c \lambda_\omega^2}{I_\omega(0)}}$	(SI)	$L_{\text{NL}} = \frac{1}{16\pi^2 d_{\text{eff}}} \sqrt{\frac{n_\omega^2 n_{2\omega} c \lambda_\omega^2}{2\pi I_\omega(0)}}$	(cgs)
SFG	$\eta_s = \frac{\lambda_{p2}}{\lambda_s} \text{sn}^2[(L/L_{\text{NL}}), \gamma]$	$\gamma^2 = \frac{\lambda_{p2} \mathcal{P}_{p2}(0)}{\lambda_{p1} \mathcal{P}_{p1}(0)}$		
	$L_{\text{NL}} = \frac{1}{4\pi d_{\text{eff}}} \sqrt{\frac{2\epsilon_0 n_{p1} n_{p2} n_s c \lambda_{p2} \lambda_s}{I_{p1}(0)}}$	(SI)	$L_{\text{NL}} = \frac{1}{16\pi^2 d_{\text{eff}}} \sqrt{\frac{n_{p1} n_{p2} n_s c \lambda_{p2} \lambda_s}{2\pi I_{p1}(0)}}$	(cgs)
DFG	$\eta_d = -\frac{\lambda_{p2}}{\lambda_d} \text{sn}^2[i(L/L_{\text{NL}}), iy]$	$\gamma^2 = \frac{\lambda_{p2} \mathcal{P}_{p2}(0)}{\lambda_{p1} \mathcal{P}_{p1}(0)}$		
	$L_{\text{NL}} = \frac{1}{4\pi d_{\text{eff}}} \sqrt{\frac{2\epsilon_0 n_{p1} n_{p2} n_d c \lambda_{p2} \lambda_d}{I_{p1}(0)}}$	(SI)	$L_{\text{NL}} = \frac{1}{16\pi^2 d_{\text{eff}}} \sqrt{\frac{n_{p1} n_{p2} n_d c \lambda_{p2} \lambda_d}{2\pi I_{p1}(0)}}$	(cgs)

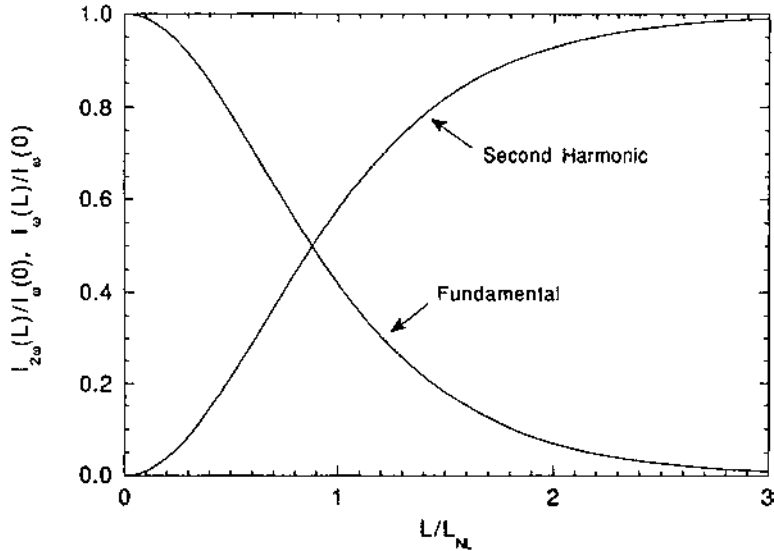


Figure 7 Second harmonic and fundamental intensities as functions of crystal length and nonlinear interaction length for phase matched SHG including pump depletion.

The SFG efficiency is given in terms of the Jacobi elliptic sine function. This function depends on the parameter γ , known as the modulus, as well as L/L_{NL} . The function $\text{sn}(u, \gamma)$ is periodic in u with a period of $2K(\gamma)$, where $K(\gamma)$ is the complete elliptic integral of the first kind, and depends on the modulus γ . The period varies from 2π to ∞ as γ varies from 0 to 1. Although these functions are not as familiar as the trigonometric and hyperbolic functions, tabulated values can be found in the literature [4], and software packages are available to compute them [5,6].

Figure 8 illustrates these properties of the Jacobi elliptic sine function and the behavior of the SFG conversion efficiency. For $\gamma < 0.1$, $\text{sn}(u, \gamma) \approx \sin(u)$ while as $\gamma \rightarrow 1$, $\text{sn}(u, \gamma) \rightarrow \tanh(u)$. Notice that for $\gamma < 1$, the conversion efficiency oscillates periodically with increasing pump intensity (i.e., pump 1). This occurs because the efficiency reaches a maximum when the pump 2 power is completely depleted. Complete depletion of the pump 2 wave is possible in this case since the stronger pump 1 wave is still driving the nonlinear polarization. After the pump 2 power is depleted, there is a phase shift of π radians between the sum-frequency field and the nonlinear polarization. Thus positive work is done by the sum-frequency field on the induced dipoles, and energy is extracted from this wave and flows back to the pump waves.

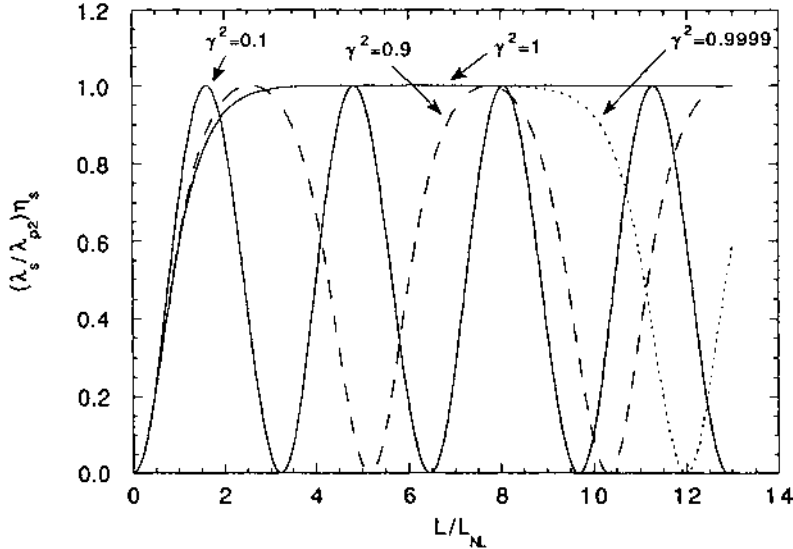


Figure 8 Sum-frequency conversion efficiency as a function of crystal length and nonlinear interaction length with several values of the modulus for phase matched SFG including pump depletion.

The case of $\gamma = 1$ looks like the SHG case. Note that since $\lambda\mathcal{P}$ is proportional to the photon flux, this case corresponds to equal photon flux in both pump beams. Since one sum-frequency photon is created for the destruction of a photon in each pump wave, both pump waves will be depleted asymptotically to zero in this case, just as in the SHG case. The maximum sum-frequency power will be $(\lambda_{p2}/\lambda_s)\mathcal{P}_{p2}(0)$, i.e., the maximum sum-frequency photon flux is the photon flux originally in pump wave 2. Formulas for the limiting cases in SFG when $\gamma = 1$ and $\gamma \ll 1$ are given in Table 5.

Table 5 Limiting Forms of SFG Efficiency Formulas in the Infinite Plane Wave Approximation, Including Pump Depletion

SFG ($\gamma \ll 1$)	$\eta_s = \frac{\lambda_{p2}}{\lambda_s} \sin^2 \frac{L}{L_{NL}}$
SFG ($\gamma = 1$)	$\eta_s = \frac{\lambda_{p2}}{\lambda_s} \tanh^2 \frac{L}{L_{NL}}$ $L_{NL} = \frac{1}{4\pi d_{eff}} \sqrt{\frac{2\epsilon_0 n_{p1} n_{p2} n_s c \lambda_{p2} \lambda_s}{I_{p1}(0)}}$ (SI) $L_{NL} = \frac{1}{16\pi^2 d_{eff}} \sqrt{\frac{n_{p1} n_{p2} n_s c \lambda_{p2} \lambda_s}{2\pi I_{p1}(0)}}$ (cgs)

With pump-depleted DFG, the situation is somewhat different than with SFG. As can be seen in Table 4, the argument and modulus of the Jacobi elliptic function are both imaginary in this case. Two situations of interest again are $\gamma \ll 1$ and $\gamma = 1$. Results for the former, corresponding to one strong pump wave and one weak pump wave, are illustrated in Fig. 9, which shows the behavior of the intensities of the difference-frequency and pump 2 waves. As above, for $\gamma \ll 1$ the Jacobi elliptic sine function reduces to a circular sine function. However, since the argument is imaginary, the sine becomes a hyperbolic sine. Hence, the difference-frequency wave experiences exponential gain. Notice that, in contrast to the SFG case, pump 2 also experiences exponential gain instead of depletion. The situation is somewhat different when $\gamma = 1$, but again both the difference-frequency and pump 2 waves experience growth at the expense of the pump 1 wave, as illustrated in Fig. 10. Here, when pump 1 is completely depleted, there is again a phase reversal that allows positive work to be done by the difference-frequency field, and energy flows back into the pump 1 wave. Physically, since one pump 1 photon must be destroyed to create a difference-frequency photon in the DFG process, a pump 2 photon is also created to conserve energy. This is why the pump 2 wave experiences gain. This process will be further explored in the next chapter. Formulas for these limiting cases of DFG are given in Table 6.

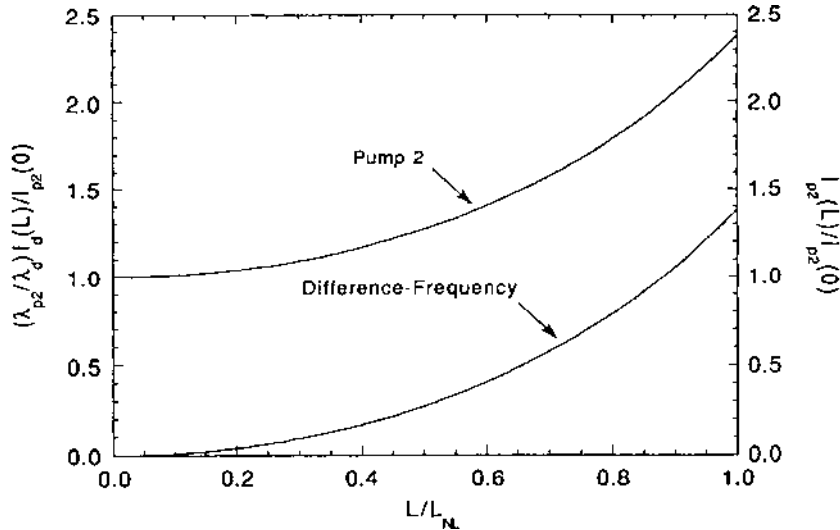


Figure 9 Phase matched difference-frequency and pump 2 intensities as functions of crystal length and nonlinear interaction length for the condition $\lambda_{p2} \mathcal{P}_{p2}(0) \ll \lambda_{p1} \mathcal{P}_{p1}(0)$.

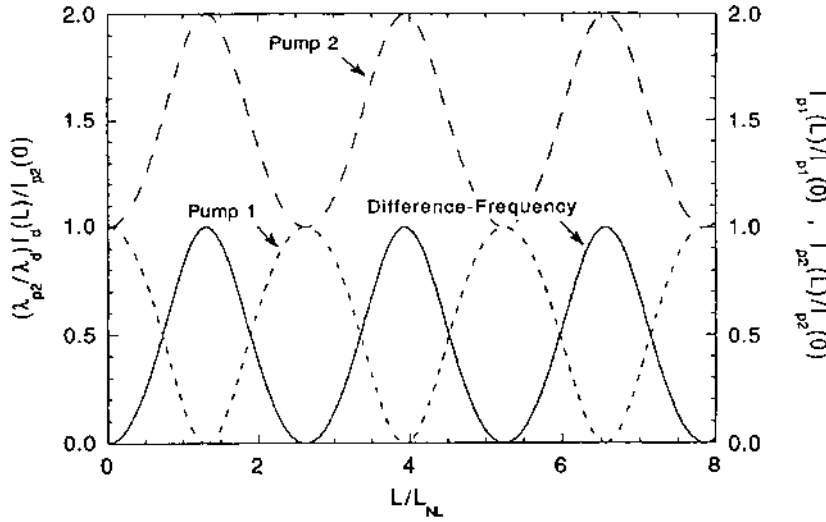


Figure 10 Phase matched difference-frequency, pump 1, and pump 2 intensities as functions of crystal length and nonlinear interaction length for the condition $\lambda_{p2}\mathcal{P}_{p2} = \lambda_{p1}\mathcal{P}_{p1}$.

Effects of phase mismatch. When perfect phase matching cannot be achieved, the amount of phase mismatch will set a limit on the length of crystal over which efficient frequency conversion can take place, at least for ideal materials. Formulas for determining the conversion efficiency that include the effects of both pump depletion and phase mismatch are given in Table 7. For SFG and DFG, the results are given in terms of γ_0 , which is the value of the modulus when $\Delta kL = 0$.

Table 6 Limiting Forms of the DFG Efficiency in the Infinite Plane Wave Approximation, Including Pump Depletion

DFG ($\gamma \ll 1$)	$\eta_d = \frac{\lambda_{p2}}{\lambda_d} \sinh^2 \frac{L}{L_{NL}}$
DFG ($\gamma = 1$)	$\eta_d = \frac{\lambda_{p2}}{\lambda_d} \frac{\operatorname{sn}^2[\sqrt{2}(L/L_{NL}), 1/\sqrt{2}]}{2 - \operatorname{sn}^2[\sqrt{2}(L/L_{NL}), 1/\sqrt{2}]}$
	$L_{NL} = \frac{1}{4\pi d_{\text{eff}}} \sqrt{\frac{2\epsilon_0 n_{p1} n_{p2} n_d c \lambda_{p2} \lambda_d}{I_{p1}(0)}} \quad (\text{SI}) \quad L_{NL} = \frac{1}{16\pi^2 d_{\text{eff}}} \sqrt{\frac{n_{p1} n_{p2} n_d c \lambda_{p2} \lambda_d}{2\pi I_{p1}(0)}} \quad (\text{cgs})$

Table 7 Frequency Conversion Efficiency Formulas in the Infinite Plane Wave Approximation, Including Pump Depletion and the Effects of Phase Matching

SHG	$\eta_{2\omega} = \gamma \operatorname{sn}^2 \left\{ [\sqrt{1 + (\Delta kL/4)^2 (L_{NL}/L)^2} + (\Delta kL/4)(L_{NL}/L)](L/L_{NL}), \gamma \right\}$
SFG	$\eta_s = \frac{\lambda_{p2}}{\lambda_s} \frac{(1 + \gamma_0^{-2})}{2} p_- \operatorname{sn}^2 \left[\sqrt{\frac{1}{2}(1 + \gamma_0^2)} p_+(L/L_{NL}), \gamma \right]$ $\gamma^2 = \frac{p_-}{p_+} \quad \gamma_0^2 = \frac{\lambda_{p2} \mathcal{P}_{p2}(0)}{\lambda_{p1} \mathcal{P}_{p1}(0)}$ $p_{\pm} = 1 + \frac{(\Delta kL/2)^2 (L_{NL}/L)^2}{1 + \gamma_0^2} \pm \sqrt{\left[1 + \frac{(\Delta kL/2)^2 (L_{NL}/L)^2}{1 + \gamma_0^2} \right]^2 - \left(\frac{2\gamma_0}{1 + \gamma_0^2} \right)^2}$
DFG	$\eta_d = -\frac{\lambda_{p2}}{\lambda_d} \frac{(1 - \gamma_0^{-2})}{2} p_- \operatorname{sn}^2 \left[i \sqrt{\frac{1}{2}(1 - \gamma_0^2)} p_+(L/L_{NL}), i\gamma \right]$ $\gamma^2 = -\frac{p_-}{p_+} \quad \gamma_0^2 = \frac{\lambda_{p2} \mathcal{P}_{p2}(0)}{\lambda_{p1} \mathcal{P}_{p1}(0)}$ $p_{\pm} = 1 - \frac{(\Delta kL/2)^2 (L_{NL}/L)^2}{1 - \gamma_0^2} \pm \sqrt{\left[1 - \frac{(\Delta kL/2)^2 (L_{NL}/L)^2}{1 - \gamma_0^2} \right]^2 + \left(\frac{2\gamma_0}{1 - \gamma_0^2} \right)^2}$
$(\gamma \ll 1)$	$\eta_d = \frac{\lambda_{p2}}{\lambda_d} \frac{1}{1 - (\Delta kL/2)^2 (L_{NL}/L)^2} \sinh^2 \left[\sqrt{1 - (\Delta kL/2)^2 (L_{NL}/L)^2} \quad (L/L_{NL}) \right]$

Figures 11–13 illustrate the effects of phase mismatch on SHG, SFG, and DFG, respectively. In all cases, a severe mismatch in phase velocities produces an oscillatory behavior in the intensity of the desired frequency and reduces the maximum conversion efficiency achievable. In Fig. 13, only the $\gamma_0 \ll 1$ limiting case is shown. For larger values of γ_0 , the situation is qualitatively similar to those shown in Fig. 12 for SFG. For the case shown in Fig. 13, where $L = L_{NL}$, there is a transition from a regime of gain when $\Delta kL < 2$ to a regime of oscillation when $\Delta kL > 2$. The transition will occur at a correspondingly different value of ΔkL when $L \neq L_{NL}$. These conditions apply approximately when $\gamma_0 \ll 1$. The approximate formula for this case is also given in Table 7.

Effects of nonzero inputs and input phase. In all of the cases described above, the desired frequency wave had a zero input to the nonlinear medium. Under this condition, the relative phase of the interacting waves is a constant of the motion, provided phase matching has been achieved, i.e., this phase does not change as the waves propagate. For completeness, the case of arbitrary inputs and arbitrary phase have been considered [3]. Generally, if the relative phase of the desired wave and the driving nonlinear polarization at the input ($z = 0$) is not $\pm \pi/2$, then the relative phase is not a constant of the motion, and power will flow back and forth between the pump(s) and the desired signal in an oscillatory

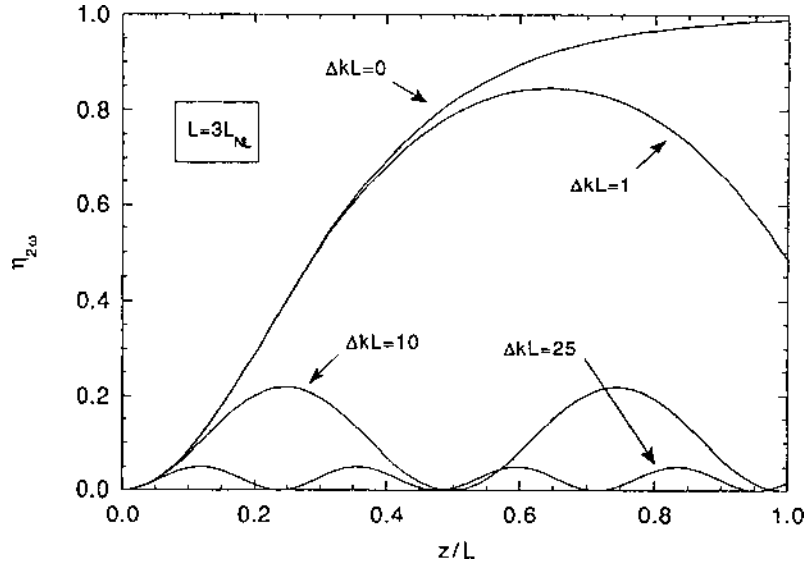


Figure 11 Second harmonic conversion efficiency as a function of position in a nonlinear medium including pump depletion and the effects of phase mismatch.

fashion as the waves propagate. The period of oscillation will depend on the relative strengths of the wave intensities at the input.

An interesting special case is that of SHG when the input relative phase between the second harmonic and fundamental waves is $\pm\pi/2$. If the input phase is $-\pi/2$, then the power flow is one way from the fundamental to the second harmonic in an asymptotic manner as discussed earlier. When the input phase is $+\pi/2$, the power flow is first from the second harmonic to the fundamental. When the second harmonic becomes zero, the power flow reverses and flows to the second harmonic asymptotically.

III. PHASE MATCHING TECHNIQUES

It is clear from Section II that phase matching is necessary for efficient frequency conversion. Four basic phase matching techniques will be reviewed:

- Angle phase matching (scalar and vector)
- Temperature phase matching
- Quasi-phase matching
- Čerenkov phase matching.

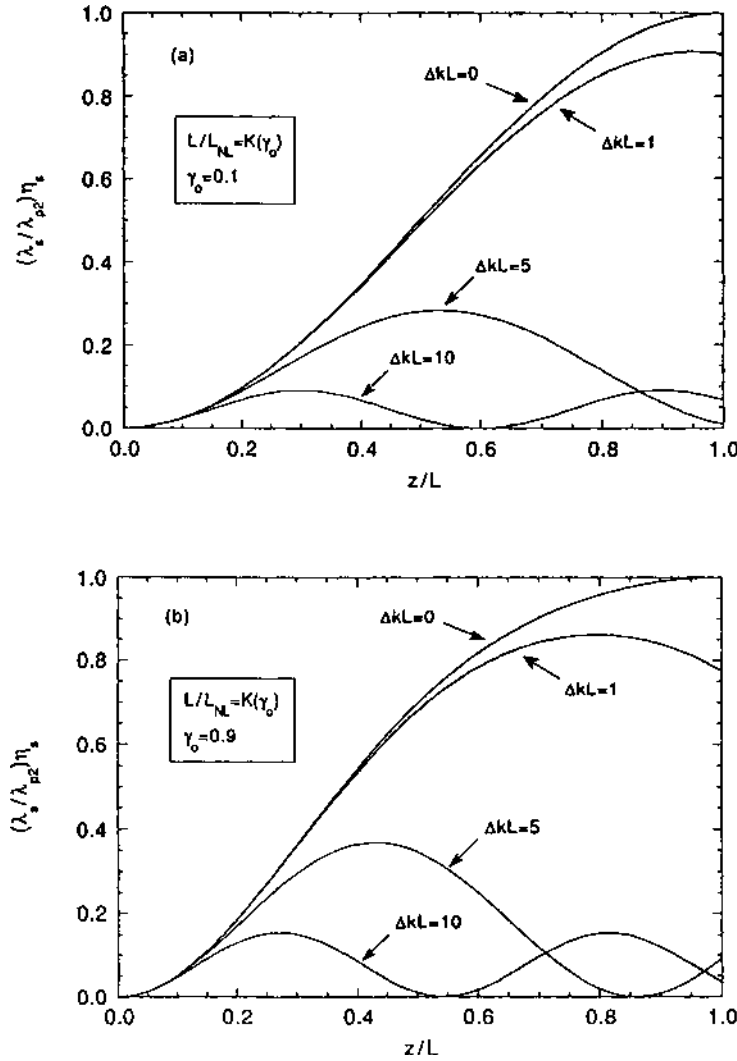


Figure 12 Sum-frequency conversion efficiency as a function of position in a nonlinear medium including pump depletion and the effects of phase mismatch. (a) $\gamma_0 = 0.1$. (b) $\gamma_0 = 0.9$.

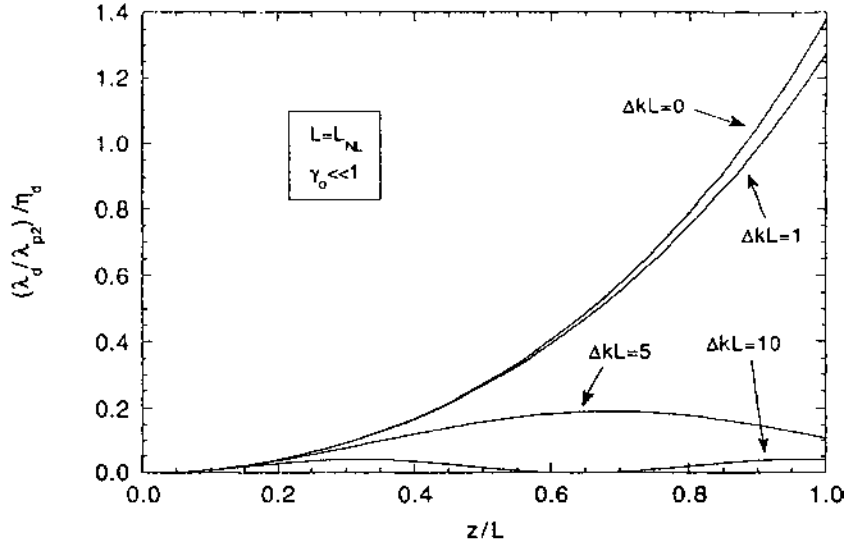


Figure 13 Difference-frequency conversion efficiency as a function of position in a nonlinear medium including pump depletion and the effects of phase mismatch for the condition $\lambda_{p2}\mathcal{P}_{p2}(0) \ll \lambda_{p1}\mathcal{P}_{p1}(0)$.

A. Scalar Angle Phase Matching (Collinear Propagation)

There are two kinds of angle phase matching: scalar and vector. Scalar refers to the situation where all of the interacting waves are propagating collinearly. This is a very common situation and is the type of interaction that the formulas given in Section II describe. Vector implies that the waves do not propagate collinearly. Different conditions apply in the two cases. The case of vector angle phase matching will be briefly discussed in the next subsection.

Phase matching means matching the phase velocities of the desired wave and its driving nonlinear polarization wave. These conditions are summarized here for the various frequency conversion processes.

SHG.

$$\mathbf{k}_\omega + \mathbf{k}'_\omega = \mathbf{k}_{2\omega} \quad (42)$$

SFG.

$$\mathbf{k}_{p1} + \mathbf{k}_{p2} = \mathbf{k}_s \quad (43)$$

DFG.

$$\mathbf{k}_{p1} - \mathbf{k}_{p2} = \mathbf{k}_d \quad (44)$$

For collinear propagation, these reduce to
SHG.

$$n_{2\omega} - n_\omega = 0 \quad (45)$$

SFG.

$$\omega_{p1}(n_s - n_{p1}) + \omega_{p2}(n_s - n_{p2}) = 0 \quad (46)$$

DFG.

$$\omega_{p1}(n_{p1} - n_d) - \omega_{p2}(n_{p2} - n_d) = 0 \quad (47)$$

For normally dispersive materials, i.e., where the index of refraction increases with frequency, these conditions cannot generally be satisfied since $2\omega > \omega$, $\omega_s > \omega_{p1}, \omega_{p2}$, and $\omega_{p1} > \omega_{p2} > \omega_d$ for the three respective processes. However, special conditions do exist in birefringent media where it is possible to satisfy these equations.

In anisotropic materials there are two normal modes of propagation for each frequency. These waves are orthogonally polarized and travel at different phase velocities. In uniaxial crystals, for example, one of these waves, called the ordinary wave, sees a constant index of refraction independent of its direction of propagation. This is called the ordinary index n^o . The second wave, the extraordinary wave, sees a refractive index $n^e(\theta)$ which is dependent on its direction of propagation. The angle θ describes the direction of propagation relative to one of the principal axes of the medium. The limits of the extraordinary index are n^o for $\theta = 0$ and n^e for $\theta = 90^\circ$. Since the nonlinear susceptibility is a tensor and can couple waves of orthogonal polarization, it is possible to mix ordinary and extraordinary waves in an anisotropic medium and achieve the phase matching conditions given above. For example, in a crystal for which $n^e < n^o$, it is possible to achieve phase matching for SHG by finding an angle of propagation θ_{pm} for which $n_{2\omega}^o = n_{2\omega}^e(\theta_{pm})$. This situation is illustrated graphically in Fig. 14.

There are two types of angle phase matching. Type I refers to the situation where the two pump waves have the same polarization. In type II phase matching, the two pump waves have orthogonal polarizations. For SHG, usually there is only one pump, and in type I phase matching it is either ordinary or extraordinary. In type II SHG, the pump is polarized so that one of its orthogonal components is ordinary and the other is extraordinary. The various cases for SHG are shown in Fig. 15.

The cutout of the crystal shows the polarization and propagation of the waves relative to the laboratory axes (x, y, z) and to the crystal's principal axes

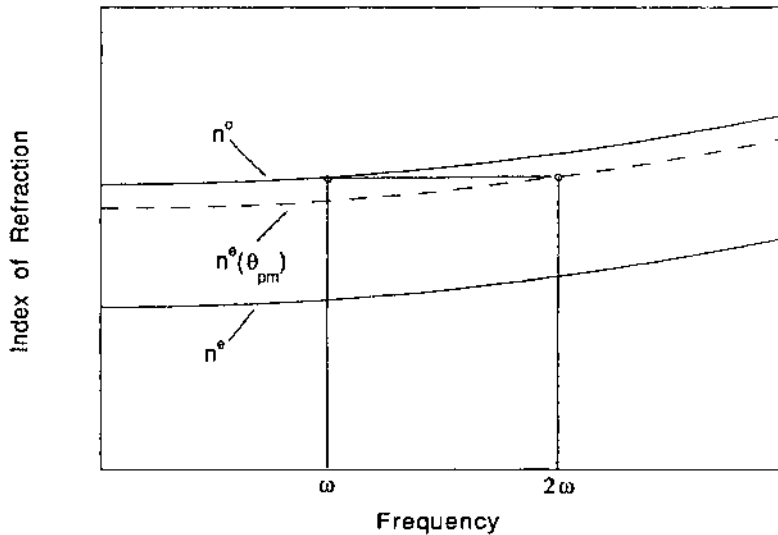


Figure 14 Illustration of the method of matching refractive indices of the fundamental and second harmonic waves in a negative uniaxial crystal.

(X, Y, Z). A common designation is given for the various cases in terms of the types of waves used for the pump(s) and the type of wave generated. For type I phase matching, these are

Extraordinary, extraordinary; ordinary (eeo)
Ordinary, ordinary; extraordinary (ooe)

The designations in type II phase matching are

Extraordinary, ordinary; extraordinary (eo)
Extraordinary, ordinary; ordinary (eo)
Ordinary, extraordinary; extraordinary (oe)
Ordinary, extraordinary; ordinary (oe)

Figure 15 can also be interpreted for SFG and DFG. For type I phase matching, the two pump waves would be parallel, with the resultant field vector pointing along x (eeo) or along y (ooe). With type II phase matching, the pump waves would correspond to the orthogonal field vectors of the resultant pump field vector. The four possibilities are extraordinary pump 1 and ordinary pump 2 (eo or eo) and ordinary pump 1 and extraordinary pump 2 (oe or oe).

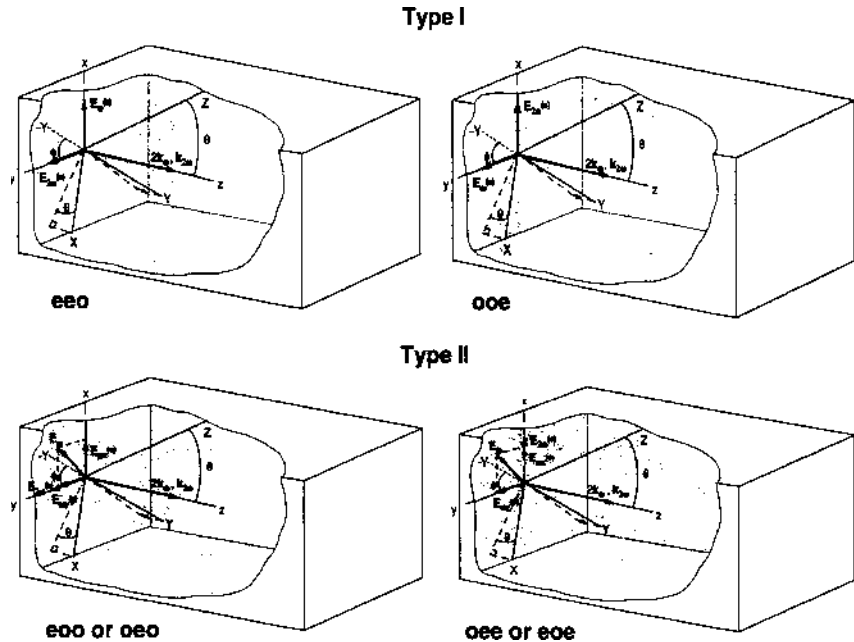


Figure 15 Schematic illustrations of the wave polarization and direction of wave propagation for SHG in types I and II phase matching processes.

Phase matching angles for uniaxial crystals. In uniaxial crystals, there is a single axis of symmetry, commonly designated the Z-axis, which coincides with the principal optic axis. Thus the principal refractive indices are $n_X = n_Y = n^o$ and $n_z = n^e$. When $n^o < n^e$, the crystal is called a positive uniaxial crystal. It is called a negative uniaxial crystal when $n^o > n^e$. For propagation at an angle θ with respect to the Z-axis, the extraordinary wave has an index given by

$$\frac{1}{[n^e(\theta)]^2} = \frac{\cos^2\theta}{[n^o]^2} + \frac{\sin^2\theta}{[n^e]^2} \quad (48)$$

Equation (48) is used in conjunction with Eqs. (45–47) above to solve for the phase matching angles for the various polarization combinations in the type I and type II processes.

The results for the phase matching angles θ_{pm} for the processes SHG, SFG, and DFG are given in Tables 8–10, respectively. Formulas are summarized for both type I and type II phase matching in positive and negative uniaxial crystals.

Table 8 Angle Phase Matching Formulas for SHG in Uniaxial Crystals

Type I	
ooe	$\sin^2 \theta_{\text{pm}} = \frac{(n_{2\omega}^e)^2}{(n_\omega^o)^2} \left[\frac{(n_{2\omega}^o)^2 - (n_\omega^o)^2}{(n_{2\omega}^o)^2 - (n_{2\omega}^e)^2} \right]$
eo0	$\sin^2 \theta_{\text{pm}} = \frac{(n_\omega^e)^2}{(n_{2\omega}^o)^2} \left[\frac{(n_{2\omega}^o)^2 - (n_\omega^o)^2}{(n_{2\omega}^e)^2 - (n_\omega^o)^2} \right]$
Type II	
oe0 or eoe	$\frac{n_{2\omega}^o}{\sqrt{1 + \left[\frac{(n_{2\omega}^o)^2}{(n_{2\omega}^e)^2} - 1 \right] \sin^2 \theta_{\text{pm}}}} - \frac{\frac{1}{2} n_\omega^o}{\sqrt{1 + \left[\frac{(n_\omega^o)^2}{(n_\omega^e)^2} - 1 \right] \sin^2 \theta_{\text{pm}}}} = \frac{1}{2} n_\omega^o$
eo0 or oeo	$\sin^2 \theta_{\text{pm}} = \frac{4n_{2\omega}^o (n_\omega^e)^2 (n_{2\omega}^o - n_\omega^o)}{(2n_{2\omega}^o - n_\omega^o)^2 [(n_\omega^e)^2 - (n_\omega^o)^2]}$

Table 9 Angle Phase Matching Formulas for SFG in Uniaxial Crystals

Type I	
ooe	$\sin^2 \theta_{\text{pm}} = \frac{(n_s^e)^2}{[(\lambda_s/\lambda_{p1})n_{p1}^o + (\lambda_s/\lambda_{p2})n_{p2}^o]^2} \left(\frac{(n_s^o)^2 - [(\lambda_s/\lambda_{p1})n_{p1}^o + (\lambda_s/\lambda_{p2})n_{p2}^o]^2}{(n_s^o)^2 - (n_s^e)^2} \right)$
eo0	$\frac{(\lambda_s/\lambda_{p1})n_{p1}^o}{\sqrt{1 + \left[\frac{(n_{p1}^o)^2}{(n_{p1}^e)^2} - 1 \right] \sin^2 \theta_{\text{pm}}}} + \frac{(\lambda_s/\lambda_{p2})n_{p2}^o}{\sqrt{1 + \left[\frac{(n_{p2}^o)^2}{(n_{p2}^e)^2} - 1 \right] \sin^2 \theta_{\text{pm}}}} = n_s^o$
Type II	
oe0	$\frac{n_s^o}{\sqrt{1 + \left[\frac{(n_s^o)^2}{(n_s^e)^2} - 1 \right] \sin^2 \theta_{\text{pm}}}} - \frac{(\lambda_s/\lambda_{p2})n_{p2}^o}{\sqrt{1 + \left[\frac{(n_{p2}^o)^2}{(n_{p2}^e)^2} - 1 \right] \sin^2 \theta_{\text{pm}}}} = (\lambda_s/\lambda_{p1})n_{p1}^o$
eoe	$\frac{n_s^o}{\sqrt{1 + \left[\frac{(n_s^o)^2}{(n_s^e)^2} - 1 \right] \sin^2 \theta_{\text{pm}}}} - \frac{(\lambda_s/\lambda_{p1})n_{p1}^o}{\sqrt{1 + \left[\frac{(n_{p1}^o)^2}{(n_{p1}^e)^2} - 1 \right] \sin^2 \theta_{\text{pm}}}} = (\lambda_s/\lambda_{p2})n_{p2}^o$
eo0	$\sin^2 \theta_{\text{pm}} = \frac{(n_{p1}^e)^2}{(n_{p1}^e)^2 - (n_{p1}^o)^2} \frac{[n_s^o - (\lambda_s/\lambda_{p2})n_{p2}^o]^2 - (\lambda_s/\lambda_{p1})^2 (n_{p1}^o)^2}{[n_s^o - (\lambda_s/\lambda_{p2})n_{p2}^o]^2}$
oe0	$\sin^2 \theta_{\text{pm}} = \frac{(n_{p2}^e)^2}{(n_{p2}^e)^2 - (n_{p2}^o)^2} \frac{[n_s^o - (\lambda_s/\lambda_{p1})n_{p1}^o]^2 - (\lambda_s/\lambda_{p2})^2 (n_{p2}^o)^2}{[n_s^o - (\lambda_s/\lambda_{p1})n_{p1}^o]^2}$

Table 10 Angle Phase Matching Formulas for DFG in Uniaxial Crystals

Type I	
ooe	$\sin^2 \theta_{\text{pm}} = \frac{(n_d^e)^2}{(n_d^e)^2 - (n_d^o)^2} \frac{[n_{p1}^o - (\lambda_{p1}/\lambda_{p2})n_{p2}^o]^2 - (\lambda_{p1}/\lambda_d)^2(n_d^o)^2}{[n_{p1}^o - (\lambda_{p1}/\lambda_{p2})n_{p2}^o]^2}$
eoo	$\sqrt{\frac{n_{p1}^o}{1 + \left[\frac{(n_{p1}^o)^2}{(n_{p1}^e)^2} - 1\right] \sin^2 \theta_{\text{pm}}}} - \sqrt{\frac{(\lambda_{p1}/\lambda_{p2})n_{p2}^o}{1 + \left[\frac{(n_{p2}^o)^2}{(n_{p2}^e)^2} - 1\right] \sin^2 \theta_{\text{pm}}}} = (\lambda_{p1}/\lambda_d)n_d^o$
Type II	
oee	$\sqrt{\frac{(\lambda_{p1}/\lambda_d)n_d^o}{1 + \left[\frac{(n_d^o)^2}{(n_d^e)^2} - 1\right] \sin^2 \theta_{\text{pm}}}} + \sqrt{\frac{(\lambda_{p1}/\lambda_{p2})n_{p2}^o}{1 + \left[\frac{(n_{p2}^o)^2}{(n_{p2}^e)^2} - 1\right] \sin^2 \theta_{\text{pm}}}} = n_{p1}^o$
eo e	$\sqrt{\frac{n_{p1}^o}{1 + \left[\frac{(n_{p1}^o)^2}{(n_{p1}^e)^2} - 1\right] \sin^2 \theta_{\text{pm}}}} - \sqrt{\frac{(\lambda_{p1}/\lambda_d)n_d^o}{1 + \left[\frac{(n_d^o)^2}{(n_d^e)^2} - 1\right] \sin^2 \theta_{\text{pm}}}} = (\lambda_{p1}/\lambda_{p2})n_{p2}^o$
eoo	$\sin^2 \theta_{\text{pm}} = \frac{(n_{p1}^e)^2}{[(\lambda_{p1}/\lambda_d)n_d^o + (\lambda_{p1}/\lambda_{p2})n_{p2}^o]^2} \times \left(\frac{(n_{p1}^o)^2 - [(\lambda_{p1}/\lambda_d)n_d^o + (\lambda_{p1}/\lambda_{p2})n_{p2}^o]^2}{(n_{p1}^o)^2 - (n_{p1}^e)^2} \right)$
oeo	$\sin^2 \theta_{\text{pm}} = \frac{(n_{p2}^e)^2}{(n_{p2}^o)^2 - (n_{p2}^e)^2} \frac{[n_{p1}^o - (\lambda_{p1}/\lambda_d)n_d^o]^2 - (\lambda_{p1}/\lambda_{p2})^2(n_{p2}^o)^2}{[n_{p1}^o - (\lambda_{p1}/\lambda_d)n_d^o]^2}$

It is noted that for some cases, analytical results for θ_{pm} cannot be obtained. In these situations, the phase matching angle must be calculated numerically. This is very straightforward using available software packages.

A simple example is given using the *root* function of Mathcad®.* Type II SHG is potassium dihydrogen phosphate (KDP), a negative uniaxial crystal, is considered. The fundamental wavelength is 800 nm and the second harmonic wavelength is 400 nm, for which $n_{\omega}^o = 1.501924$, $n_{\omega}^e = 1.463708$, $n_{2\omega}^o = 1.524481$, and $n_{2\omega}^e = 1.480244$ [7]. The computation takes only a few seconds, and the computed angle, 70.204° , is accurate to $< 0.1\%$.

*Mathcad is a registered trademark of MathSoft, Inc., Cambridge, MA.

Nikogosyan and Gurzadyan [8] have shown that for crystals with small birefringence (i.e., $|n^e - n^o| \ll 1$), approximations can be made in the cases discussed above that amount to no more than a 0.1–0.2° error in the computed phase matching angles. These approximations are given in Tables 11–13 for SHG, SFG, and DFG, respectively.

A special case arises if the phase matching angle turns out to be 90°. This is possible in some materials at a particular temperature (see temperature phase matching below). This situation is referred to as noncritical phase matching (NCPM). The case of $\theta_{pm} \neq 90^\circ$ is called critical phase matching (CPM). Noncritical phase matching is advantageous for two reasons. First, it is less sensitive to beam divergence, which lowers the conversion efficiency (see angle bandwidths below). Second, the walk-off angle for this case is zero (see Section IV), which places less constraint on the beam size and the length of the nonlinear crystal. These aspects are discussed in greater detail later.

Phase matching angles in biaxial crystals. In biaxial crystals, there are two optic axes which lie in the XZ plane. For $n_X < n_Y < n_Z$, the optic axes make an angle Ω with respect to the Z-axis, given by

$$\sin \Omega = \frac{n_Z}{n_Y} \left(\frac{n_Y^2 - n_X^2}{n_Z^2 - n_X^2} \right)^{1/2} \quad (49)$$

and are situated symmetrically about the Z-axis. This is illustrated in Fig. 16. For light propagating along the optic axes, the refractive index is independent of polarization. When $n_X > n_Y > n_Z$, the optic axes are at angles Ω' symmetrically about Z, with

$$\cos \Omega' = \frac{n_X}{n_Y} \left(\frac{n_Y^2 - n_Z^2}{n_X^2 - n_Z^2} \right)^{1/2} \quad (50)$$

In this case Ω is replaced by Ω' in Fig. 16. (Note: These definitions are consistent with the general discussion in Chapter 1 where the angle Ω was defined with respect to the principal axis corresponding to the maximum principal index. The angle Ω' is thus the complement of Ω .)

Table 11 Approximate Angle Phase Matching Formula for Type II (oeo or eoe) SHG in Uniaxial Crystals

Type II	
oeo or eoe	$\sin^2 \theta_{pm} \approx \frac{(n_{2\omega}^o)^2 - (n_\omega^o)^2}{(n_\omega^o)^2 \left[\frac{(n_{2\omega}^o)^2}{(n_\omega^e)^2} - 1 \right] - (n_{2\omega}^o)^2 \left[\frac{4(n_\omega^o)^2}{(n_\omega^o + n_\omega^e)^2} - 1 \right]}$

Table 12 Approximate Angle Phase Matching Formulas for SFG in Uniaxial Crystals

Type I	
eeo	$\sin^2 \theta_{\text{pm}} = \left\{ 1 - \left[\frac{(n_{p1}^o/\lambda_{p1}) + (n_{p2}^o/\lambda_{p2})}{(n_s^o/\lambda_s)} \right]^2 \right\} \left\{ 1 - \left[\frac{(n_{p1}^o/\lambda_{p1}) + (n_{p2}^o/\lambda_{p2})}{(n_{p1}^e/\lambda_{p1}) + (n_{p2}^e/\lambda_{p2})} \right]^2 \right\}^{-1}$
Type II	
oeo or eoe	$\begin{aligned} \sin^2 \theta_{\text{pm}} = & \left\{ 1 - \left[\frac{(n_{p1}^o/\lambda_{p1}) + (n_{p2}^o/\lambda_{p2})}{(n_s^o/\lambda_s)} \right]^2 \right\} \times \left\{ 1 - [(n_{p1}^o/\lambda_{p1}) + (n_{p2}^o/\lambda_{p2})]^2 \right. \\ & \times \left. \left[\frac{1}{(n_s^o/\lambda_s)^2} - \frac{1}{(n_s^e/\lambda_s)^2} + \frac{1}{[(n_{p1}^o/\lambda_{p1}) + (n_{p2}^o/\lambda_{p2})]^2} \right] \right\}^{-1} \end{aligned}$

The general case of propagation at an angle θ with respect to the Z -axis and an azimuthal angle ϕ with respect to the X -axis, as illustrated in Fig. 16, is desired for phase matching. The refractive indices of the two allowed modes of propagation are determined by solving the Fresnel equation

$$\frac{\sin^2 \theta \cos^2 \phi}{(n)^{-2} - (n_x)^{-2}} + \frac{\sin^2 \theta \sin^2 \phi}{(n)^{-2} - (n_y)^{-2}} + \frac{\cos^2 \theta}{(n)^{-2} - (n_z)^{-2}} = 0 \quad (51)$$

This equation is used in conjunction with Eqs. (45–47) to compute the phase matching angles for type I and II processes.

To understand phase matching in biaxial crystals, it is instructive to drop back and look at uniaxial crystals again in light of the solutions to Eq. (51). The two independent solutions to Eq. (51) for each frequency describe two surfaces in space: a sphere, corresponding to the ordinary index, and a prolate or oblate

Table 13 Approximate Angle Phase Matching Formulas for DFG in Uniaxial Crystals

Type I	
eeo	$\begin{aligned} \sin^2 \theta_{\text{pm}} = & \left\{ 1 - \left[\frac{(n_d^o/\lambda_d) + (n_{p2}^o/\lambda_{p2})}{(n_{p1}^o/\lambda_{p1})} \right]^2 \right\} \left\{ 1 - [(n_d^o/\lambda_d) + (n_{p2}^o/\lambda_{p2})]^2 \right. \\ & \times \left. \left[\frac{1}{(n_{p1}^o/\lambda_{p1})^2} - \frac{1}{(n_{p1}^e/\lambda_{p1})^2} + \frac{1}{[(n_d^o/\lambda_d) + (n_{p2}^o/\lambda_{p2})]^2} \right] \right\}^{-1} \end{aligned}$
Type II	
oeo or eoe	$\sin^2 \theta_{\text{pm}} = \left\{ 1 - \left[\frac{(n_d^o/\lambda_d) + (n_{p2}^o/\lambda_{p2})}{(n_{p1}^o/\lambda_{p1})} \right]^2 \right\} \left\{ 1 - \left[\frac{(n_d^o/\lambda_d) + (n_{p2}^o/\lambda_{p2})}{(n_d^e/\lambda_d) + (n_{p2}^e/\lambda_{p2})} \right]^2 \right\}^{-1}$

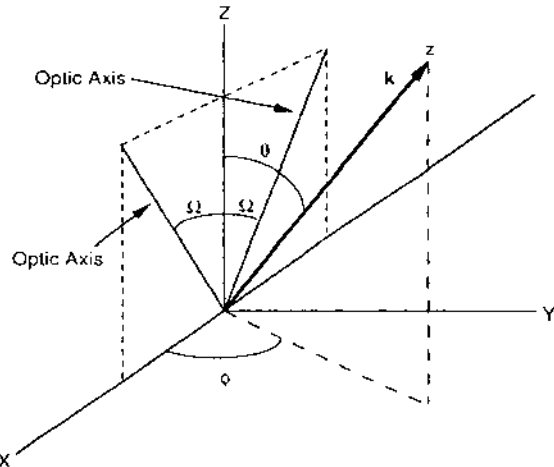


Figure 16 Schematic of wave propagation in the crystal coordinate system for a biaxial crystal.

ellipsoid of revolution, corresponding to the extraordinary index. Consider, for example, the case of SHG in a negative uniaxial crystal. For type I phase matching (ooe), $n_\omega^o = n_{2\omega}^e(\theta_{pm})$, the phase matching angle is given by the locus of points where the index ellipsoid for the second harmonic intersects with the index sphere of the fundamental. In type II phase matching (eo e), $\frac{1}{2}[n_\omega^e(\theta) + n_\omega^o]$ describes a third surface. The phase matching angle in this case, determined by $\frac{1}{2}[n_\omega^e(\theta_{pm}) + n_\omega^o] = n_{2\omega}^e(\theta_{pm})$, is given by the locus of points where this third surface intersects with the index ellipsoid of the second harmonic. These two curves, illustrated in Fig. 17, are circular cones symmetric about the optic (Z) axis. Another way to view this is by the stereographic projection of these cones on the XZ plane, one quadrant of which is shown in Fig. 18. The Y-axis points out of the paper. The solid curve and dashed curve are for type I and type II phase matching, respectively.

In a biaxial crystal, the two independent solutions of Eq. (51) correspond to the refractive indices of two orthogonal modes of propagation in a particular direction (θ, ϕ). Generally, the designations of ordinary and extraordinary do not apply, except for propagation in the principal planes. However, it is still possible to define type I phase matching as parallel pump polarizations, and type II phase matching as orthogonal pump polarizations. The solutions to the Fresnel equation for each frequency are also described by index surfaces, although these are more complex than those for uniaxial crystals. The phase matching directions for SHG are again determined by the intersection of the type I and type II surfaces at

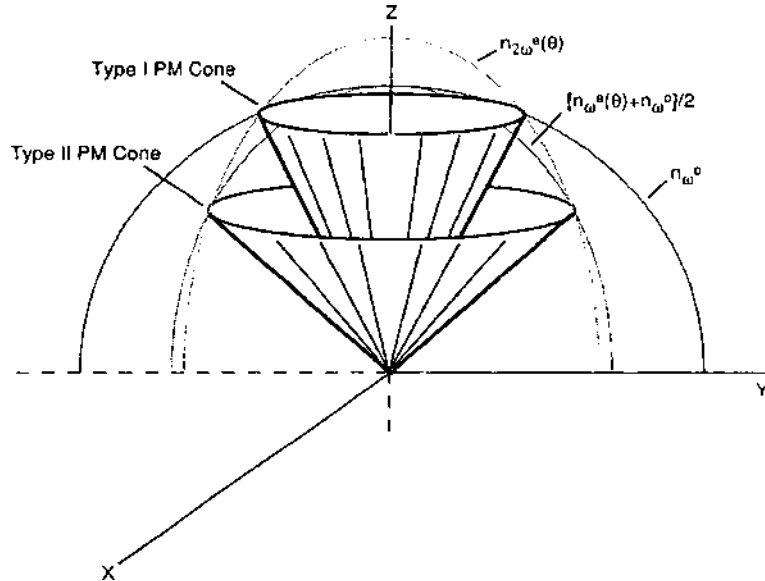


Figure 17 Types I and II phase matching cones for SHG in a uniaxial crystal.

frequencies ω and 2ω . The loci of points are also cones in this case, although not generally circular.

In the general case, the locus of angles $\phi(\theta)$ for type I and II phase matching cannot be given analytically and must be obtained numerically. Hobden [9] has

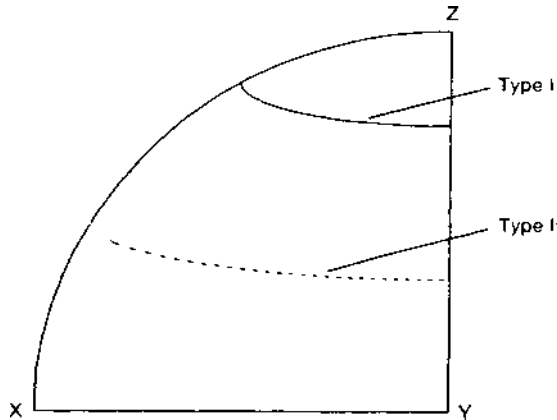


Figure 18 Stereographic projection of the loci of phase matching points for the cones in Fig. 17. The solid and dashed curves are for types I and II phase matching, respectively.

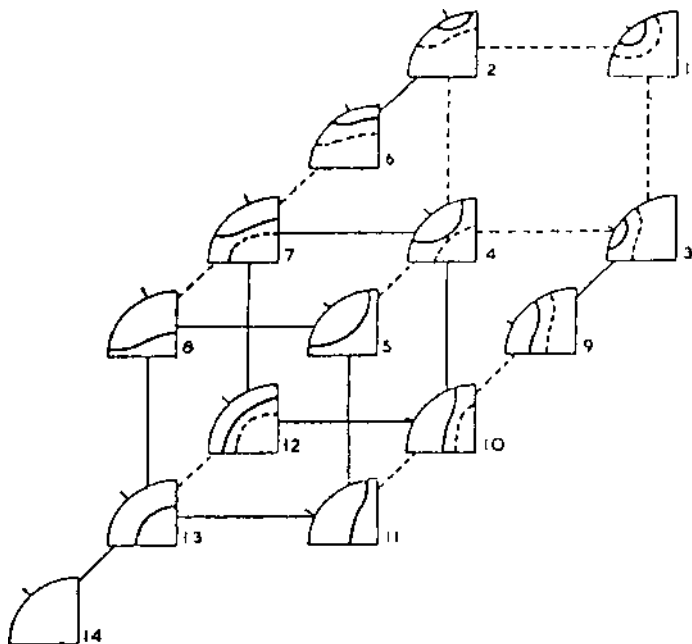


Figure 19 Several classes of stereographic projections of the loci of phase matching points for SHG in biaxial crystals. The solid and dashed curves are for types I and II phase matching, respectively. The straight lines connect different classes where noncritical phase matching occurs. The solid and dashed lines are for types I and II phase matching, respectively. (From Ref. 9.)

computed the general behavior of these processes for optically well-behaved crystals (i.e., those whose principal axes do not change with frequency and whose dispersions are normal, small, and approximately equal between the fundamental and harmonic frequencies), but for otherwise general relations between the principal refractive indices. He has conveniently tabulated the results into 14 classes. The stereographic projections of the phase matching loci for these 14 classes are shown in Fig. 19. The refractive index conditions for these loci are given in Table 14. The solid and dashed curves refer again to type I and II processes, respectively. The lines drawn between quadrants represent transitions from one CPM situation to another wherein NCPM occurs. These occur only along the X-, Y-, or Z-axis. The solid lines represent type I NCPM, while the dashed lines are for type II NCPM. The refractive index conditions and wave polarizations for NCPM are given in Table 15.

Table 14 Refractive Index Conditions for the Loci of Phase Matching Points Shown in Fig. 19

1	$n_{2o,X} < \frac{1}{2}(n_{o,X} + n_{o,Y}); n_{2o,Y} < \frac{1}{2}(n_{o,Y} + n_{o,Z})$	
2	$n_{2o,X} > \frac{1}{2}(n_{o,X} + n_{o,Y}); n_{2o,Y} < \frac{1}{2}(n_{o,Y} + n_{o,Z})$	
3	$n_{2o,X} < \frac{1}{2}(n_{o,X} + n_{o,Y}); n_{2o,Y} > \frac{1}{2}(n_{o,Y} + n_{o,Z})$	$n_{2o,Z} > n_{o,Z} > n_{2o,Y} > n_{o,Y} > n_{2o,X} > n_{o,X}$
4	$n_{2o,X} > \frac{1}{2}(n_{o,X} + n_{o,Y}); n_{2o,Y} > \frac{1}{2}(n_{o,Y} + n_{o,Z})$	
5	$n_{2o,X} > \frac{1}{2}(n_{o,X} + n_{o,Z})$	
6	$n_{2o,X} < \frac{1}{2}(n_{o,X} + n_{o,Z}); n_{2o,Y} < \frac{1}{2}(n_{o,Y} + n_{o,Z})$	
7	$n_{2o,X} < \frac{1}{2}(n_{o,X} + n_{o,Z}); n_{2o,Y} > \frac{1}{2}(n_{o,Y} + n_{o,Z})$	$n_{2o,Z} > n_{o,Z} > n_{2o,Y} > n_{o,Y} > n_{o,X}$
8	$n_{2o,X} > \frac{1}{2}(n_{o,X} + n_{o,Z}); n_{2o,Y} > \frac{1}{2}(n_{o,Y} + n_{o,Z})$	
9	$n_{2o,X} < \frac{1}{2}(n_{o,X} + n_{o,Y})$	
10	$n_{2o,X} > \frac{1}{2}(n_{o,X} + n_{o,Y}); n_{2o,X} < \frac{1}{2}(n_{o,X} + n_{o,Z})$	$n_{2o,Z} > n_{2o,Y} > n_{o,Z} > n_{o,Y} > n_{2o,X} > n_{o,X}$
11	$n_{2o,X} > \frac{1}{2}(n_{o,X} + n_{o,Z})$	
12	$n_{2o,X} < \frac{1}{2}(n_{o,X} + n_{o,Z})$	$n_{2o,Z} > n_{2o,Y} > n_{o,Z} > n_{2o,X} > n_{o,Y} > n_{o,X}$
13	$n_{2o,X} > \frac{1}{2}(n_{o,X} + n_{o,Z})$	
14		$n_{2o,Z} > n_{2o,Y} > n_{2o,X} > n_{o,Z} > n_{o,Y} > n_{o,X}$

Source: Adapted from Ref. 9.

Table 15 Refractive Index Conditions and Polarizations for Noncritical Phase Matching in Biaxial Crystals

Phase matching type (prop. axis)	Index conditions	Fundamental polarization	Harmonic polarization
Type I (X)	$n_{2\omega,X} > n_{\omega,Y}; n_{2\omega,Y} = n_{\omega,Z}$	Z	Y
Type I (X)	$n_{2\omega,X} < n_{\omega,Y}; n_{2\omega,Y} = n_{\omega,Z}$	Z	Y
Type I (Y)	$n_{2\omega,X} = n_{\omega,Z}$	Z	X
Type I (Z)	$n_{2\omega,Y} < n_{\omega,Z}; n_{2\omega,X} = n_{\omega,Y}$	Y	X
Type I (Z)	$n_{2\omega,Y} > n_{\omega,Z}; n_{2\omega,X} = n_{\omega,Y}$	Y	X
Type II (X)	$n_{2\omega,X} > \frac{1}{2}(n_{\omega,X} + n_{\omega,Y});$ $n_{2\omega,Y} = \frac{1}{2}(n_{\omega,Y} + n_{\omega,Z})$	Y, Z	Y
Type II (X)	$n_{2\omega,X} < \frac{1}{2}(n_{\omega,X} + n_{\omega,Y});$ $n_{2\omega,Y} = \frac{1}{2}(n_{\omega,Y} + n_{\omega,Z})$	Y, Z	Y
Type II (Y)	$n_{2\omega,X} = \frac{1}{2}(n_{\omega,X} + n_{\omega,Z})$	X, Z	X
Type II (Z)	$n_{2\omega,Y} < \frac{1}{2}(n_{\omega,Y} + n_{\omega,Z});$ $n_{2\omega,X} = \frac{1}{2}(n_{\omega,X} + n_{\omega,Y})$	X, Y	X
Type II (Z)	$n_{2\omega,Y} > \frac{1}{2}(n_{\omega,Y} + n_{\omega,Z});$ $n_{2\omega,X} = \frac{1}{2}(n_{\omega,X} + n_{\omega,Y})$	X, Y	X

Source: Adapted from Ref. 9.

Stepenov et al. [10] have generalized these results for the SFG and DFG processes. They have defined 30 distinct classes for type I and II phase matching. See Ref. 10 for details.

When propagation is confined to the principal planes of the crystal, Eq. (51) is simplified, and analytical expressions can be obtained for the phase matching angles. The formulas are given in Tables 16 and 17. Table 18 gives the appropriate designations for SHG, SFG, and DFG. The various polarization combinations for type I and II processes and propagation in the XY , YZ , and XZ planes are given.

d_{eff} for types I and II phase matching. With the direction of propagation and polarizations of the interacting waves defined relative to the laboratory axes (x, y, z) and the crystal principal axes (X, Y, Z), it is possible to obtain d_{eff} to be used in the formulas presented in Section II for the various crystal classes. The geometry is defined in Fig. 16 in terms of the usual spherical angles θ and ϕ . The laboratory axes are obtained from the crystal axes by the following transformation, described in Fig. 20. First, perform a clockwise rotation of $\phi + 180^\circ$, as viewed toward $+Z$, about the Z -axis. Second, perform a counterclockwise rotation of θ , as viewed toward $+y$, about the new y -axis. It is important to keep this sense of rotation in mind when examining the formulas

Table 16 Formulas for Calculating the Phase Matching Angles for Light Propagating in the Principal Planes of Biaxial Crystals

Plane		Formula	Notation
XY	ooe	$\tan^2 \phi_{pm} = \frac{1-U}{W-1}$	$A = \frac{n_{a,Z}}{\lambda_a}, B = \frac{n_{b,Z}}{\lambda_b}, C = \frac{n_{c,Y}}{\lambda_c}, F = \frac{n_{c,X}}{\lambda_c}$
	eoe	$\tan^2 \phi_{pm} \simeq \frac{1-U}{W-R}$	$A = \frac{n_{a,Y}}{\lambda_a}, B = \frac{n_{b,Z}}{\lambda_b}, C = \frac{n_{c,Y}}{\lambda_c}, D = \frac{n_{e,X}}{\lambda_a}, F = \frac{n_{c,X}}{\lambda_c}$
	oeo	$\tan^2 \phi_{pm} \simeq \frac{1-U}{W-Q}$	$A = \frac{n_{a,Z}}{\lambda_a}, B = \frac{n_{b,Y}}{\lambda_b}, C = \frac{n_{c,Y}}{\lambda_c}, E = \frac{n_{b,X}}{\lambda_b}, F = \frac{n_{c,X}}{\lambda_c}$
YZ	eeo	$\tan^2 \theta_{pm} \simeq \frac{1-U}{U-S}$	$A = \frac{n_{a,Y}}{\lambda_a}, B = \frac{n_{b,Y}}{\lambda_b}, C = \frac{n_{c,X}}{\lambda_c}, D = \frac{n_{a,Z}}{\lambda_a}, E = \frac{n_{b,Z}}{\lambda_b}$
	oeo	$\tan^2 \theta_{pm} = \frac{1-V}{V-Y}$	$A = \frac{n_{a,X}}{\lambda_a}, B = \frac{n_{b,Y}}{\lambda_b}, C = \frac{n_{c,X}}{\lambda_c}, E = \frac{n_{b,Z}}{\lambda_b}$
	eoo	$\tan^2 \theta_{pm} = \frac{1-T}{T-Z}$	$A = \frac{n_{a,Y}}{\lambda_a}, B = \frac{n_{b,X}}{\lambda_b}, C = \frac{n_{c,X}}{\lambda_c}, D = \frac{n_{a,Z}}{\lambda_a}$
XZ $\theta < \Omega$	ooe	$\tan^2 \theta_{pm} = \frac{1-U}{W-1}$	$A = \frac{n_{a,Y}}{\lambda_a}, B = \frac{n_{b,Y}}{\lambda_b}, C = \frac{n_{c,X}}{\lambda_c}, F = \frac{n_{c,Z}}{\lambda_c}$
	eoe	$\tan^2 \theta_{pm} \simeq \frac{1-U}{W-R}$	$A = \frac{n_{a,X}}{\lambda_a}, B = \frac{n_{b,Y}}{\lambda_b}, C = \frac{n_{c,X}}{\lambda_c}, D = \frac{n_{a,Z}}{\lambda_a}, F = \frac{n_{c,Z}}{\lambda_c}$
	oeo	$\tan^2 \theta_{pm} \simeq \frac{1-U}{W-Q}$	$A = \frac{n_{a,Y}}{\lambda_a}, B = \frac{n_{b,X}}{\lambda_b}, C = \frac{n_{c,X}}{\lambda_c}, E = \frac{n_{b,Z}}{\lambda_b}, F = \frac{n_{c,Z}}{\lambda_c}$
XZ $\theta > \Omega$	eeo	$\tan^2 \theta_{pm} \simeq \frac{1-U}{U-S}$	$A = \frac{n_{a,X}}{\lambda_a}, B = \frac{n_{b,X}}{\lambda_b}, C = \frac{n_{c,Y}}{\lambda_c}, D = \frac{n_{a,Z}}{\lambda_a}, E = \frac{n_{b,Z}}{\lambda_b}$
	oeo	$\tan^2 \theta_{pm} = \frac{1-V}{V-Y}$	$A = \frac{n_{a,Y}}{\lambda_a}, B = \frac{n_{b,X}}{\lambda_b}, C = \frac{n_{c,Y}}{\lambda_c}, E = \frac{n_{b,Z}}{\lambda_b}$
	eoo	$\tan^2 \theta_{pm} = \frac{1-T}{T-Z}$	$A = \frac{n_{a,X}}{\lambda_a}, B = \frac{n_{a,Y}}{\lambda_a}, C = \frac{n_{c,Y}}{\lambda_c}, D = \frac{n_{a,Z}}{\lambda_a}$
$U = \frac{(A+B)^2}{C^2} \quad W = \frac{(A+B)^2}{F^2} \quad R = \frac{(A+B)^2}{(D+B)^2}$ $Q = \frac{(A+B)^2}{(A+E)^2} \quad S = \frac{(A+B)^2}{(D+E)^2} \quad V = \frac{B^2}{(C-A)^2}$ $Y = \left(\frac{B}{E}\right)^2 \quad T = \frac{A^2}{(C-B)^2} \quad Z = \left(\frac{A}{D}\right)^2$			

Source: Adapted from Ref. 13.

that follow for d_{eff} . Other transformations are possible [11], and the corresponding formulas for d_{eff} will differ.

As mentioned earlier, the components of the second order nonlinear susceptibility are normally given in terms of the crystal axes, whereas it is convenient to describe the nonlinear polarization in terms of the laboratory axes. Therefore the susceptibility tensor must be transformed from the crystal system to the laboratory system. When this is done, the i th component of the nonlinear polarization for any second order process, where $i = x, y, z$, is

Table 17 Formulas for Calculating the Phase Matching Angles for Light Propagating in the Principal Planes of Biaxial Crystals ($n_X > n_Y > n_Z$)

Plane		Formula	Notation
XY	eeo	$\tan^2 \phi_{pm} \approx \frac{1-U}{U-S}$	$A = \frac{n_{a,Y}}{\lambda_a}, B = \frac{n_{b,Y}}{\lambda_b}, C = \frac{n_{c,Z}}{\lambda_c}, D = \frac{n_{a,X}}{\lambda_a}, E = \frac{n_{b,X}}{\lambda_b}$
	oeo	$\tan^2 \phi_{pm} = \frac{1-V}{V-Y}$	$A = \frac{n_{a,Z}}{\lambda_a}, B = \frac{n_{b,Y}}{\lambda_b}, C = \frac{n_{c,Z}}{\lambda_c}, E = \frac{n_{b,X}}{\lambda_b}$
	eoo	$\tan^2 \phi_{pm} = \frac{1-T}{T-Z}$	$A = \frac{n_{a,Y}}{\lambda_a}, B = \frac{n_{b,Z}}{\lambda_b}, C = \frac{n_{c,Z}}{\lambda_c}, D = \frac{n_{a,X}}{\lambda_a}$
YZ	ooe	$\tan^2 \theta_{pm} = \frac{1-U}{W-1}$	$A = \frac{n_{a,X}}{\lambda_a}, B = \frac{n_{b,X}}{\lambda_b}, C = \frac{n_{c,Y}}{\lambda_c}, F = \frac{n_{c,Z}}{\lambda_c}$
	eoe	$\tan^2 \theta_{pm} \approx \frac{1-U}{W-R}$	$A = \frac{n_{a,Y}}{\lambda_a}, B = \frac{n_{b,X}}{\lambda_b}, C = \frac{n_{c,Y}}{\lambda_c}, D = \frac{n_{a,Z}}{\lambda_a}, F = \frac{n_{c,Z}}{\lambda_c}$
	oee	$\tan^2 \theta_{pm} \approx \frac{1-U}{W-Q}$	$A = \frac{n_{a,X}}{\lambda_a}, B = \frac{n_{b,Y}}{\lambda_b}, C = \frac{n_{c,Y}}{\lambda_c}, E = \frac{n_{b,Z}}{\lambda_b}, F = \frac{n_{c,Z}}{\lambda_c}$
XZ $\theta < \Omega'$	eeo	$\tan^2 \theta_{pm} \approx \frac{1-U}{U-S}$	$A = \frac{n_{a,X}}{\lambda_a}, B = \frac{n_{b,X}}{\lambda_b}, C = \frac{n_{c,Y}}{\lambda_c}, D = \frac{n_{a,Z}}{\lambda_a}, E = \frac{n_{b,Z}}{\lambda_b}$
	oeo	$\tan^2 \theta_{pm} = \frac{1-V}{V-Y}$	$A = \frac{n_{a,Y}}{\lambda_a}, B = \frac{n_{b,X}}{\lambda_b}, C = \frac{n_{c,Y}}{\lambda_c}, E = \frac{n_{b,Z}}{\lambda_b}$
	eoo	$\tan^2 \theta_{pm} = \frac{1-T}{T-Z}$	$A = \frac{n_{a,X}}{\lambda_a}, B = \frac{n_{b,Y}}{\lambda_b}, C = \frac{n_{c,Y}}{\lambda_c}, D = \frac{n_{a,X}}{\lambda_a}$
XZ $\theta > \Omega'$	ooe	$\tan^2 \theta_{pm} = \frac{1-U}{W-1}$	$A = \frac{n_{a,Y}}{\lambda_a}, B = \frac{n_{b,Y}}{\lambda_b}, C = \frac{n_{c,X}}{\lambda_c}, F = \frac{n_{c,Z}}{\lambda_c}$
	eoe	$\tan^2 \theta_{pm} \approx \frac{1-U}{W-R}$	$A = \frac{n_{a,X}}{\lambda_a}, B = \frac{n_{b,Y}}{\lambda_b}, C = \frac{n_{c,X}}{\lambda_c}, D = \frac{n_{a,Z}}{\lambda_a}, F = \frac{n_{c,Z}}{\lambda_c}$
	oee	$\tan^2 \theta_{pm} \approx \frac{1-U}{W-Q}$	$A = \frac{n_{a,Y}}{\lambda_a}, B = \frac{n_{b,X}}{\lambda_b}, C = \frac{n_{c,X}}{\lambda_c}, E = \frac{n_{b,Z}}{\lambda_b}, F = \frac{n_{c,Z}}{\lambda_c}$
$U = \frac{(A+B)^2}{C^2}$ $W = \frac{(A+B)^2}{F^2}$ $R = \frac{(A+B)^2}{(D+B)^2}$ $Q = \frac{(A+B)^2}{(A+E)^2}$ $S = \frac{(A+B)^2}{(D+E)^2}$ $V = \frac{B^2}{(C-A)^2}$ $Y = \left(\frac{B}{E}\right)^2$ $T = \frac{A^2}{(C-B)^2}$ $Z = \left(\frac{A}{D}\right)^2$			

Source: Adapted from Ref. 13.

given by

$$P_i^{(2)} = 2De_0 \sum_{j,k=x}^z \sum_{I,J,K=X}^Z (\hat{i} \cdot \hat{I})(\hat{j} \cdot \hat{J})(\hat{k} \cdot \hat{K}) d_{IJK} E_j E_k \quad (52)$$

where D is the degeneracy factor for the process (see Chapter 1), and the sums

Table 18 Notation Used with Table 16. Formulas for Calculating Phase Matching Angles for the Three Frequency Conversion Processes^a

SHG	$a = \omega$	$b = \omega$	$c = 2\omega$
SFG	$a = p_1$	$b = p_2$	$c = s$
DFG	$a = d$	$b = p_2$	$c = p_1$

^aFor DFG, the following polarization designations change: ooe \rightarrow eoo, oee \rightarrow eco, eeo \rightarrow oee, eoo \rightarrow ooe.

are over x, y, z and X, Y, Z . The direction cosines in terms of the spherical angles θ, ϕ are

$$\begin{aligned}\hat{x} \cdot \hat{X} &= -\cos \theta \cos \phi & \hat{x} \cdot \hat{Y} &= -\cos \theta \sin \phi & \hat{x} \cdot \hat{Z} &= \sin \theta \\ \hat{y} \cdot \hat{X} &= \sin \phi & \hat{y} \cdot \hat{Y} &= -\cos \phi & \hat{y} \cdot \hat{Z} &= 0 \\ \hat{z} \cdot \hat{X} &= \sin \theta \cos \phi & \hat{z} \cdot \hat{Y} &= \sin \theta \sin \phi & \hat{z} \cdot \hat{Z} &= \cos \theta\end{aligned}\quad (53)$$

The phase matching type sets the values of i, j, k for the polarizations of the various interacting waves. The effective value of the d -coefficient can then be computed from the direction cosines and the nonzero values of the nonlinear susceptibility tensor for each crystal class, as given in Chapter 1.

Consider first uniaxial crystals. For these crystals, ordinary waves are polarized along the y -axis, and extraordinary waves are polarized along the x -axis, as illustrated in Fig. 15. The z -axis is the direction of propagation. At the phase matching condition, set $\theta = \theta_{pm}$. The corresponding formulas for d_{eff} for

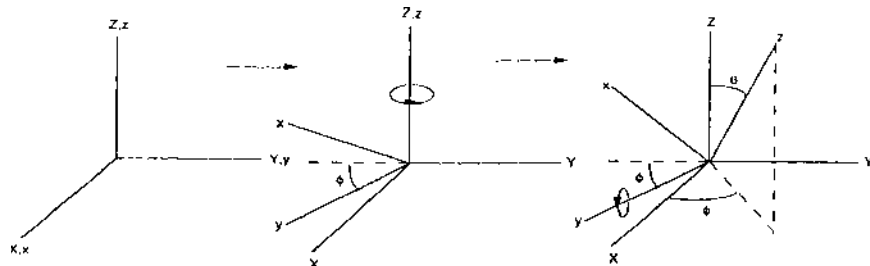


Figure 20 Rotations defining the relation of the laboratory coordinate system to the crystal coordinate system. This system is used in the calculation of d_{eff} .

Table 19 Formulas for d_{eff} in Uniaxial Crystals for the Different Types of Angle Phase Matching

Crystal class	Type I (ooe)	Type II (oeo or eoo)
4, 6	$d_{31} \sin\theta$	$d_{15} \sin\theta$
422, 622	0	0
4 mm, 6 mm	$d_{31} \sin\theta$	$d_{15} \sin\theta$
$\bar{6}m2$	$-d_{22} \cos\theta \sin 3\phi$	$-d_{22} \cos\theta \sin 3\phi$
3 m	$d_{31} \sin\theta - d_{22} \cos\theta \sin 3\phi$	$d_{15} \sin\theta - d_{22} \cos\theta \sin 3\phi$
6	$(d_{11} \cos 3\phi - d_{22} \sin 3\phi) \cos\theta$	$(d_{11} \cos 3\phi - d_{22} \sin 3\phi) \cos\theta$
3	$(d_{11} \cos 3\phi - d_{22} \sin 3\phi) \cos\theta + d_{31} \sin\theta$	$(d_{11} \cos 3\phi - d_{22} \sin 3\phi) \cos\theta + d_{15} \sin\theta$
32	$d_{11} \cos\theta \cos 3\phi$	$d_{11} \cos\theta \cos 3\phi$
$\bar{4}$	$-(d_{31} \cos 2\phi + d_{36} \sin 2\phi) \sin\theta$	$-(d_{14} \sin 2\phi + d_{15} \cos 2\phi) \sin\theta$
$\bar{4}2m$	$-d_{36} \sin\theta \sin 2\phi$	$-d_{14} \sin\theta \sin 2\phi$
	Type I (eeo)	Type II (oeo or oee)
4, 6	$-d_{14} \sin 2\theta$	$d_{14} \sin\theta \cos\theta$
422, 622	$-d_{14} \sin 2\theta$	$d_{14} \sin\theta \cos\theta$
4 mm, 6 mm	0	0
$\bar{6}m2$	$d_{22} \cos^2\theta \cos 3\phi$	$d_{22} \cos^2\theta \cos 3\phi$
3 m	$d_{22} \cos^2\theta \cos 3\phi$	$d_{22} \cos^2\theta \cos 3\phi$
6	$(d_{11} \sin 3\phi + d_{22} \cos 3\phi) \cos^2\theta$	$(d_{11} \sin 3\phi + d_{22} \cos 3\phi) \cos^2\theta$
3	$(d_{11} \sin 3\phi + d_{22} \cos 3\phi) \cos^2\theta - d_{14} \sin 2\theta$	$(d_{11} \sin 3\phi + d_{22} \cos 3\phi) \cos^2\theta + d_{14} \sin\theta \cos\theta$
32	$d_{11} \cos^2\theta \sin 3\phi - d_{14} \sin 2\theta$	$d_{11} \cos^2\theta \sin 3\phi + \frac{1}{2} d_{14} \sin 2\theta$
$\bar{4}$	$(d_{14} \cos 2\phi - d_{15} \sin 2\phi) \sin 2\theta$	$\frac{1}{2} [(d_{14} + d_{36}) \cos 2\phi - (d_{15} + d_{31}) \sin 2\phi] \sin 2\theta$
$\bar{4}2m$	$d_{14} \sin 2\theta \cos 2\phi$	$\frac{1}{2} (d_{14} + d_{36}) \sin 2\theta \cos 2\phi$

Source: Adapted from Ref. 12. [John Wiley & Sons, Inc., Copyright © 1973, reprinted by permission.]

positive and negative uniaxial crystals for both type I and type II phase matching and the various polarization combinations are given in Table 19.

The formulas given in Table 19 are completely general for the various uniaxial crystal classes. When Kleinman symmetry prevails, which is quite often the case, the formulas are somewhat simpler. Kleinman symmetry will generally hold when there are no absorption bands in the vicinity of the interacting frequencies or in between the interacting frequencies. As discussed in Chapter 1, Kleinman symmetry implies that any permutation of the frequency arguments of the nonlinear susceptibility, *leaving the cartesian subscripts fixed*, leaves the tensor unchanged. Under this condition, it is irrelevant, from the standpoint of

Table 20 Formulas for d_{eff} in Uniaxial Crystals for the Different Types of Angle Phase Matching when Kleinman Symmetry Holds

Crystal class	ooe, oeo, eoo	eeo, eoe, oee
4, 6	$d_{15} \sin\theta$	0
422, 622	0	0
4mm, 6mm	$d_{15} \sin\theta$	0
$\bar{6}m2$	$-d_{22} \cos\theta \sin 3\phi$	$d_{22} \cos^2\theta \cos 3\phi$
$3m$	$d_{15} \sin\theta - d_{22} \cos\theta \sin 3\phi$	$d_{22} \cos^2\theta \cos 3\phi$
6	$(d_{11} \cos 3\phi - d_{22} \sin 3\phi) \cos\theta$	$(d_{11} \sin 3\phi + d_{22} \cos 3\phi) \cos^2\theta$
3	$(d_{11} \cos 3\phi - d_{22} \sin 3\phi) \cos\theta + d_{31} \sin\theta$	$(d_{11} \sin 3\phi + d_{22} \cos 3\phi) \cos^2\theta$
32	$d_{11} \cos\theta \cos 3\phi$	$d_{11} \cos^2\theta \sin 3\phi$
$\bar{4}$	$-(d_{14} \sin 2\phi + d_{15} \cos 2\phi) \sin\theta$	$(d_{14} \cos 2\phi - d_{15} \sin 2\phi) \sin 2\theta$
$\bar{4}2m$	$-d_{14} \sin\theta \sin 2\phi$	$d_{14} \sin 2\theta \cos 2\phi$

Source: Adapted from Ref. 12. [John Wiley & Sons, Inc., Copyright © 1973, reprinted by permission.]

d_{eff} , which waves are ordinary and which are extraordinary. The results for d_{eff} under Kleinman symmetry are given in Table 20.

In biaxial crystals, the situation is more complex. Nikogosyan and Gurzadyan [13] and Ito et al. [14] have worked out specific cases for class 222 and $mm2$ crystals. Results are shown in Table 21, corrected as discussed in Ref. 13, and the geometry is illustrated in Fig. 21. These apply to several common situations in a number biaxial crystals [13]. Dmitriev and Nikogosyan [50] have developed the more general cases of d_{eff} for $mm2$ crystals. These expressions are rather complex and will not be given here. Dmitriev et al. [15, 51] tabulate these results and also give expressions for d_{eff} for several crystal classes when propagation is confined to the principal planes of the crystal.

Angle bandwidths. For small deviations $\Delta\theta = \theta - \theta_{\text{pm}}$ about the phase matching direction, the efficiency of the frequency conversion process will decrease in a manner illustrated in Fig. 4. The phase velocity mismatch due to an angular deviation $\Delta\theta$ can be computed by expanding Δk in a Taylor series:

$$\begin{aligned} \Delta k(\theta - \theta_{\text{pm}}) &\simeq \frac{\partial(\Delta k)}{\partial\theta}\Big|_{\theta=\theta_{\text{pm}}} \Delta\theta + \frac{1}{2} \frac{\partial^2(\Delta k)}{\partial\theta^2}\Big|_{\theta=\theta_{\text{pm}}} (\Delta\theta)^2 \\ &\equiv \gamma_{\text{CPM}} \Delta\theta + \gamma_{\text{NCPM}} (\Delta\theta)^2 \end{aligned} \quad (54)$$

where CPM stands for critically phase matched and NCPM stands for noncritically phase matched. Since $\gamma_{\text{CPM}}(\theta_{\text{pm}} = 90^\circ) = 0$, the second term in Eq. (54) is included for the noncritically phase matched case. For critical phase matching, only the first term is retained.

Table 21 Formulas for d_{eff} in Biaxial Crystals for the Different Types of Angle Phase Matching

Crystal class	Type I	Type II
222	$d_{36}[\sin 2\theta \cos 2\phi \cos \delta$ $\times (3 \sin^2 \delta - 1) + \sin \theta \sin 2\phi \sin \delta$ $\times (3 \cos^2 \theta \cos^2 \delta + 3 \cos^2 \delta - 1)]$ $(d_{32} - d_{31})(3 \sin^2 \delta - 1) \sin \theta \cos \theta \sin 2\phi \cos \delta$ $+ 3(d_{31} \cos^2 \phi + d_{32} \sin^2 \phi)$ $\times \sin \theta \cos^2 \theta \sin \delta \cos^2 \delta$ $+ (d_{31} \sin^2 \phi + d_{32} \cos^2 \phi)$ $\times \sin \theta \sin \delta (3 \sin^2 \delta - 2)$ $+ d_{33} \sin^3 \theta \sin \delta \cos^2 \delta$	$d_{36}[\sin 2\theta \cos 2\phi \sin \delta$ $\times (3 \cos^2 \delta - 1) - \sin \theta \sin 2\phi \cos \delta$ $\times (3 \cos^2 \theta \sin^2 \delta + 3 \sin^2 \delta - 1)]$ $(d_{32} - d_{31})(3 \cos^2 \delta - 1)$ $\times \sin \theta \cos \theta \sin 2\phi \sin \delta$ $- 3(d_{31} \cos^2 \phi + d_{32} \sin^2 \phi)$ $\times \sin \theta \cos^2 \theta \sin^2 \delta \cos \delta$ $- (d_{31} \sin^2 \phi + d_{32} \cos^2 \phi)$ $\times \sin \theta \cos \delta (3 \cos^2 \delta - 2)$ $- d_{33} \sin^3 \theta \sin^2 \delta \cos \delta$
mm2	$\cot 2\delta = (\cot^2 \Omega \sin^2 \theta - \cos^2 \theta \cos^2 \phi + \sin^2 \phi) / \cos \theta \sin 2\phi$	

Source: Adapted from Ref. 14. [© 1974 IEEE.]

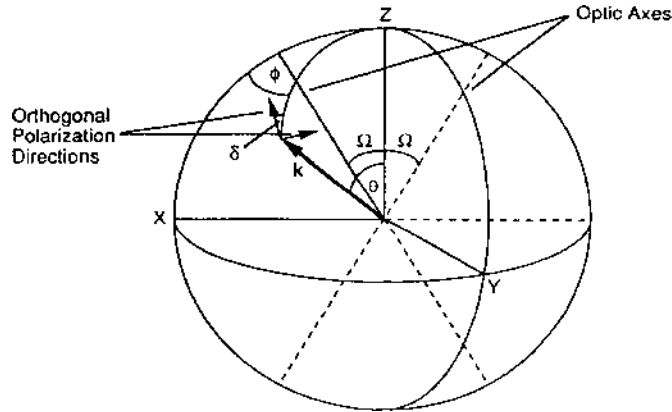


Figure 21 Definitions of angles for propagation in a biaxial crystal used in the formulas given in Table 21. (Adapted from Ref. 14. © 1974 IEEE.)

Substituting for the phase matching bandwidth from Eq. (40), Eq. (54) is used to compute the angle bandwidth. The results for SHG, SFG, and DFG are given in Tables 22 through 27 for both CPM and NCPM conditions.

B. Vector Angle Phase Matching (Noncollinear Propagation)

The vector phase matching conditions were given in Eqs. (42–44). They are illustrated schematically for SHG in Fig. 22 for type I (ooe and eeo) and type II

Table 22 Angle Bandwidths for Types I and II Critically Phase Matched SHG

		$\Delta\theta_{BW} = 2.784/\gamma_{CPM}L $
Type I	ooe	$\gamma_{CPM} = \frac{2\pi}{\lambda_\omega} (n_\omega^o)^3 \left[\frac{(n_{2\omega}^o)^2 - (n_\omega^e)^2}{(n_{2\omega}^o)^2 (n_\omega^e)^2} \right] \sin 2\theta_{pm}$
	eeo	$\gamma_{CPM} = \frac{2\pi}{\lambda_\omega} (n_\omega^e)^3 \left[\frac{(n_\omega^e)^2 - (n_\omega^o)^2}{(n_\omega^e)^2 (n_\omega^o)^2} \right] \sin 2\theta_{pm}$
Type II	ooo	$\gamma_{CPM} = \frac{\pi}{\lambda_\omega} (2n_{2\omega}^o - n_\omega^o)^3 \left[\frac{(n_\omega^e)^2 - (n_\omega^o)^2}{(n_\omega^e)^2 (n_\omega^o)^2} \right] \sin 2\theta_{pm}$
	eoe	$\gamma_{CPM} = \frac{\pi}{\lambda_\omega} \left\{ [n_\omega^e(\theta_{pm})]^3 \left[\frac{(n_\omega^e)^2 - (n_\omega^o)^2}{(n_\omega^e)^2 (n_\omega^o)^2} \right] - 2[n_{2\omega}^e(\theta_{pm})]^3 \left[\frac{(n_{2\omega}^e)^2 - (n_{2\omega}^o)^2}{(n_{2\omega}^e)^2 (n_{2\omega}^o)^2} \right] \right\} \sin 2\theta_{pm}$

Table 23 Angle Bandwidths for Types I and II Critically Phase Matched SFG

		$\Delta\theta_{BW} = 2.784/\gamma_{CPM}L $
Type I		
ooe		$\gamma_{CPM} = \frac{\pi}{\lambda_s} [n_s^e(\theta_{pm})]^3 \left[\frac{(n_s^o)^2 - (n_s^e)^2}{(n_s^o)^2(n_s^e)^2} \right] \sin 2\theta_{pm}$
eo		$\gamma_{CPM} = \pi \left\{ \frac{[n_{p1}^e(\theta_{pm})]^3}{\lambda_{p1}} \left[\frac{(n_{p1}^e)^2 - (n_{p1}^o)^2}{(n_{p1}^e)^2(n_{p1}^o)^2} \right] + \frac{[n_{p2}^e(\theta_{pm})]^3}{\lambda_{p2}} \left[\frac{(n_{p2}^e)^2 - (n_{p2}^o)^2}{(n_{p2}^e)^2(n_{p2}^o)^2} \right] \right\} \sin 2\theta_{pm}$
Type II		
ooo		$\gamma_{CPM} = \frac{\pi}{\lambda_{p2}} [n_{p2}^e(\theta_{pm})]^3 \left[\frac{(n_{p2}^e)^2 - (n_{p2}^o)^2}{(n_{p2}^e)^2(n_{p2}^o)^2} \right] \sin 2\theta_{pm}$
eoo		$\gamma_{CPM} = \frac{\pi}{\lambda_{p1}} [n_{p1}^e(\theta_{pm})]^3 \left[\frac{(n_{p1}^e)^2 - (n_{p1}^o)^2}{(n_{p1}^e)^2(n_{p1}^o)^2} \right] \sin 2\theta_{pm}$
oeo		$\gamma_{CPM} = \pi \left\{ \frac{[n_{p2}^e(\theta_{pm})]^3}{\lambda_{p2}} \left[\frac{(n_{p2}^e)^2 - (n_{p2}^o)^2}{(n_{p2}^e)^2(n_{p2}^o)^2} \right] - \frac{[n_s^e(\theta_{pm})]^3}{\lambda_s} \left[\frac{(n_s^e)^2 - (n_s^o)^2}{(n_s^e)^2(n_s^o)^2} \right] \right\} \sin 2\theta_{pm}$
eoe		$\gamma_{CPM} = \pi \left\{ \frac{[n_{p1}^e(\theta_{pm})]^3}{\lambda_{p1}} \left[\frac{(n_{p1}^e)^2 - (n_{p1}^o)^2}{(n_{p1}^e)^2(n_{p1}^o)^2} \right] - \frac{[n_s^e(\theta_{pm})]^3}{\lambda_s} \left[\frac{(n_s^e)^2 - (n_s^o)^2}{(n_s^e)^2(n_s^o)^2} \right] \right\} \sin 2\theta_{pm}$

Table 24 Angle Bandwidths for Types I and II Critically Phase Matched DFG

		$\Delta\theta_{BW} = 2.784/\gamma_{CPM}L $
Type I		
ooo		$\gamma_{CPM} = \frac{\pi}{\lambda_d} [n_d^e(\theta_{pm})]^3 \left[\frac{(n_d^o)^2 - (n_d^e)^2}{(n_d^o)^2(n_d^e)^2} \right] \sin 2\theta_{pm}$
eoo		$\gamma_{CPM} = \pi \left\{ \frac{[n_{p1}^e(\theta_{pm})]^3}{\lambda_{p1}} \left[\frac{(n_{p1}^e)^2 - (n_{p1}^o)^2}{(n_{p1}^e)^2(n_{p1}^o)^2} \right] - \frac{[n_{p2}^e(\theta_{pm})]^3}{\lambda_{p2}} \left[\frac{(n_{p2}^e)^2 - (n_{p2}^o)^2}{(n_{p2}^e)^2(n_{p2}^o)^2} \right] \right\} \sin 2\theta_{pm}$
Type II		
ooo		$\gamma_{CPM} = \frac{\pi}{\lambda_{p2}} [n_{p2}^e(\theta_{pm})]^3 \left[\frac{(n_{p2}^e)^2 - (n_{p2}^o)^2}{(n_{p2}^e)^2(n_{p2}^o)^2} \right] \sin 2\theta_{pm}$
eoo		$\gamma_{CPM} = \frac{\pi}{\lambda_{p1}} [n_{p1}^e(\theta_{pm})]^3 \left[\frac{(n_{p1}^e)^2 - (n_{p1}^o)^2}{(n_{p1}^e)^2(n_{p1}^o)^2} \right] \sin 2\theta_{pm}$
oeo		$\gamma_{CPM} = \pi \left\{ \frac{[n_{p2}^e(\theta_{pm})]^3}{\lambda_{p2}} \left[\frac{(n_{p2}^e)^2 - (n_{p2}^o)^2}{(n_{p2}^e)^2(n_{p2}^o)^2} \right] + \frac{[n_d^e(\theta_{pm})]^3}{\lambda_d} \left[\frac{(n_d^e)^2 - (n_d^o)^2}{(n_d^e)^2(n_d^o)^2} \right] \right\} \sin 2\theta_{pm}$
eoe		$\gamma_{CPM} = \pi \left\{ \frac{[n_d^e(\theta_{pm})]^3}{\lambda_d} \left[\frac{(n_d^e)^2 - (n_d^o)^2}{(n_d^e)^2(n_d^o)^2} \right] - \frac{[n_{p1}^e(\theta_{pm})]^3}{\lambda_{p1}} \left[\frac{(n_{p1}^e)^2 - (n_{p1}^o)^2}{(n_{p1}^e)^2(n_{p1}^o)^2} \right] \right\} \sin 2\theta_{pm}$

Table 25 Angle Bandwidths for Types I and II Noncritically Phase Matched SHG

$\Delta\theta_{BW} = 2.784/\gamma_{NCPM}L ^{1/2}$		
Type I		
ooe	$\gamma_{NCPM} = \frac{2\pi}{\lambda_\omega} n_{2\omega}^e \left[\frac{(n_{2\omega}^e)^2}{(n_{2\omega}^o)^2} - 1 \right]$	
eo _e	$\gamma_{NCPM} = \frac{2\pi}{\lambda_\omega} n_\omega^e \left[1 - \frac{(n_\omega^e)^2}{(n_\omega^o)^2} \right]$	
Type II		
oeo	$\gamma_{NCPM} = \frac{\pi}{\lambda_\omega} n_\omega^e \left[1 - \frac{(n_\omega^e)^2}{(n_\omega^o)^2} \right]$	
eo _o	$\gamma_{NCPM} = \frac{\pi}{\lambda_\omega} \left\{ n_\omega^e \left[1 - \frac{(n_\omega^e)^2}{(n_\omega^o)^2} \right] - 2n_{2\omega}^e \left[1 - \frac{(n_{2\omega}^e)^2}{(n_{2\omega}^o)^2} \right] \right\}$	

Table 26 Angle Bandwidths for Types I and II Noncritically Phase Matched SFG

$\Delta\theta_{BW} = 2.784/\gamma_{NCPM}L ^{1/2}$		
Type I		
ooe	$\gamma_{NCPM} = \frac{\pi}{\lambda_s} n_s^e \left[\frac{(n_s^e)^2}{(n_s^o)^2} - 1 \right]$	
eo _e	$\gamma_{NCPM} = \pi \left\{ \frac{n_{p1}^e}{\lambda_{p1}} \left[1 - \frac{(n_{p1}^e)^2}{(n_{p1}^o)^2} \right] + \frac{n_{p2}^e}{\lambda_{p2}} \left[1 - \frac{(n_{p2}^e)^2}{(n_{p2}^o)^2} \right] \right\}$	
Type II		
oeo	$\gamma_{NCPM} = \frac{\pi}{\lambda_{p2}} n_{p2}^e \left[1 - \frac{(n_{p2}^e)^2}{(n_{p2}^o)^2} \right]$	
eo _o	$\gamma_{NCPM} = \frac{\pi}{\lambda_{p1}} n_{p1}^e \left[1 - \frac{(n_{p1}^e)^2}{(n_{p1}^o)^2} \right]$	
oe _e	$\gamma_{NCPM} = \pi \left\{ \frac{n_{p2}^e}{\lambda_{p2}} \left[1 - \frac{(n_{p2}^e)^2}{(n_{p2}^o)^2} \right] - \frac{n_s^e}{\lambda_s} \left[1 - \frac{(n_s^e)^2}{(n_s^o)^2} \right] \right\}$	
eo _o	$\gamma_{NCPM} = \pi \left\{ \frac{n_{p1}^e}{\lambda_{p1}} \left[1 - \frac{(n_{p1}^e)^2}{(n_{p1}^o)^2} \right] - \frac{n_s^e}{\lambda_s} \left[1 - \frac{(n_s^e)^2}{(n_s^o)^2} \right] \right\}$	

Table 27 Angle Bandwidths for Types I and II Noncritically Phase Matched DFG

		$\Delta\theta_{BW} = 2.784/\gamma_{NCPM}L ^{1/2}$
Type I		
ooe		$\gamma_{NCPM} = \frac{\pi}{\lambda_d} n_d^e \left[\frac{(n_d^e)^2}{(n_d^o)^2} - 1 \right]$
eoo		$\gamma_{NCPM} = \pi \left\{ \frac{n_{p1}^e}{\lambda_{p1}} \left[1 - \frac{(n_{p1}^e)^2}{(n_{p1}^o)^2} \right] - \frac{n_{p2}^e}{\lambda_{p2}} \left[1 - \frac{(n_{p2}^e)^2}{(n_{p2}^o)^2} \right] \right\}$
Type II		
oeo		$\gamma_{NCPM} = \frac{\pi}{\lambda_{p2}} n_{p2}^e \left[1 - \frac{(n_{p2}^e)^2}{(n_{p2}^o)^2} \right]$
eoo		$\gamma_{NCPM} = \frac{\pi}{\lambda_{p1}} n_{p1}^e \left[1 - \frac{(n_{p1}^e)^2}{(n_{p1}^o)^2} \right]$
oee		$\gamma_{NCPM} = \pi \left\{ \frac{n_{p2}^e}{\lambda_{p2}} \left[1 - \frac{(n_{p2}^e)^2}{(n_{p2}^o)^2} \right] + \frac{n_d^e}{\lambda_d} \left[1 - \frac{(n_d^e)^2}{(n_d^o)^2} \right] \right\}$
eoee		$\gamma_{NCPM} = \pi \left\{ \frac{n_d^e}{\lambda_d} \left[1 - \frac{(n_d^e)^2}{(n_d^o)^2} \right] - \frac{n_{p1}^e}{\lambda_{p1}} \left[1 - \frac{(n_{p1}^e)^2}{(n_{p1}^o)^2} \right] \right\}$

(oee or eoe, and oeo or eoo) processes. The cases for SFG and DFG will be analogous.

Consider, for example, the ooe case. The circle in Fig. 22 is the locus of points given by the collinear sum $\mathbf{k}_\omega + \mathbf{k}'_\omega$ projected onto the XZ or YZ plane, for the two ordinary pump waves. Similarly, the ellipse is the locus of points given by $\mathbf{k}_{2\omega}(\theta)$ for the extraordinary second harmonic. The points of intersection of these surfaces give the directions of collinear phase matching for this type of process. It can be seen that when the collinear sum of the pump wave vectors is longer than $\mathbf{k}_{2\omega}(\theta)$, vector phase matching is possible by orienting the two pump wave vectors at an angle Θ . This occurs for a range of directions of second harmonic wave propagation given by $\theta_{pm} \leq \theta \leq 180^\circ - \theta_{pm}$. For all other directions of propagation, phase matching is not possible by either vector or scalar phase matching. Similar statements apply to the other types of processes shown in Fig. 22.

In general, the angle Θ between the two pump wave vectors that gives vector phase matching for a given second harmonic wave vector direction θ is determined by

$$\cos\Theta = \frac{k_{2\omega}^2 - k_\omega^2 - k'^2_\omega}{2k_\omega k'_\omega} \quad (55)$$

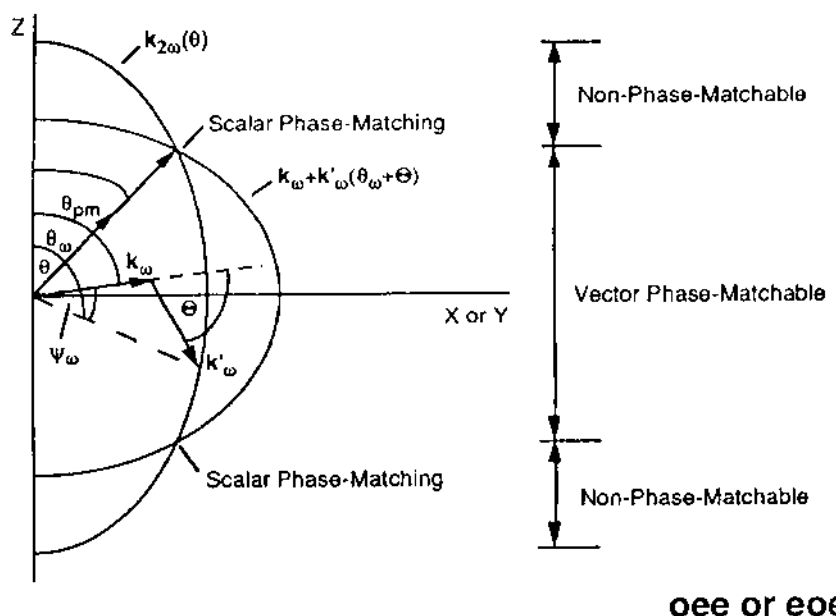
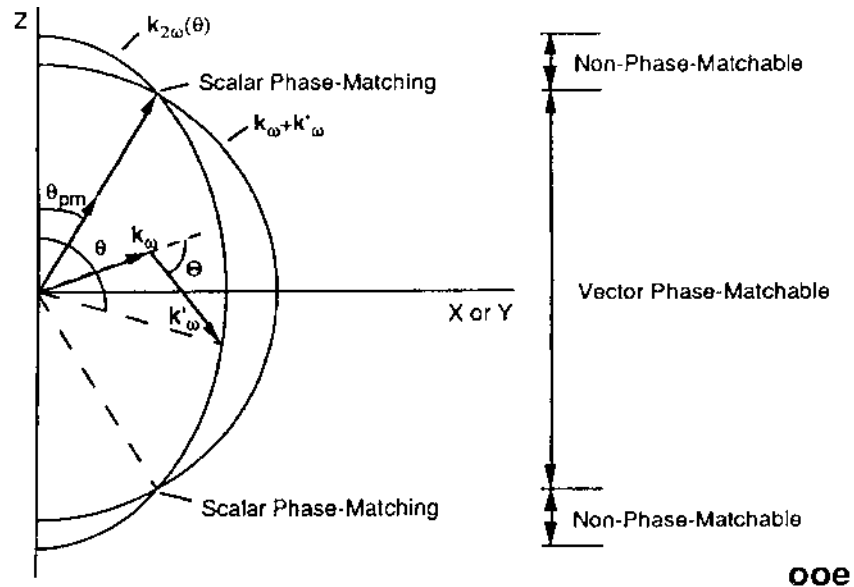


Figure 22 Illustrations of vector phase matching for SHG using various type I and II processes in uniaxial crystals.

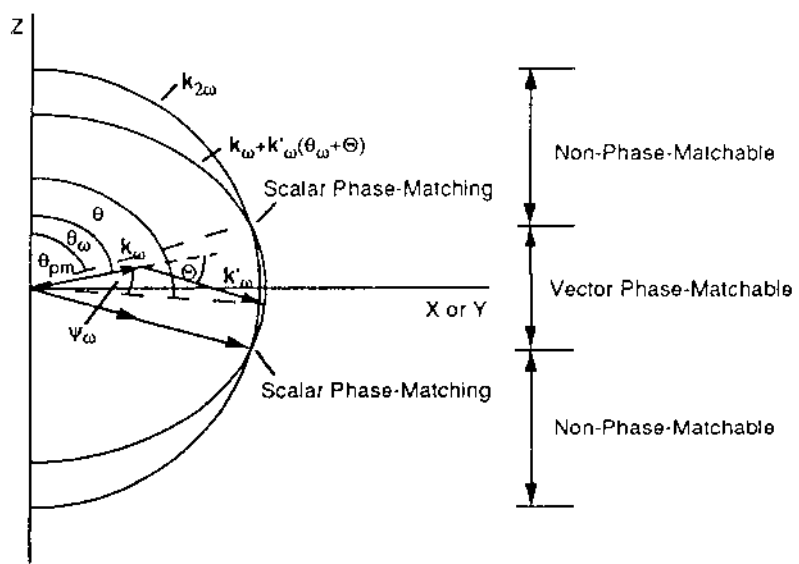
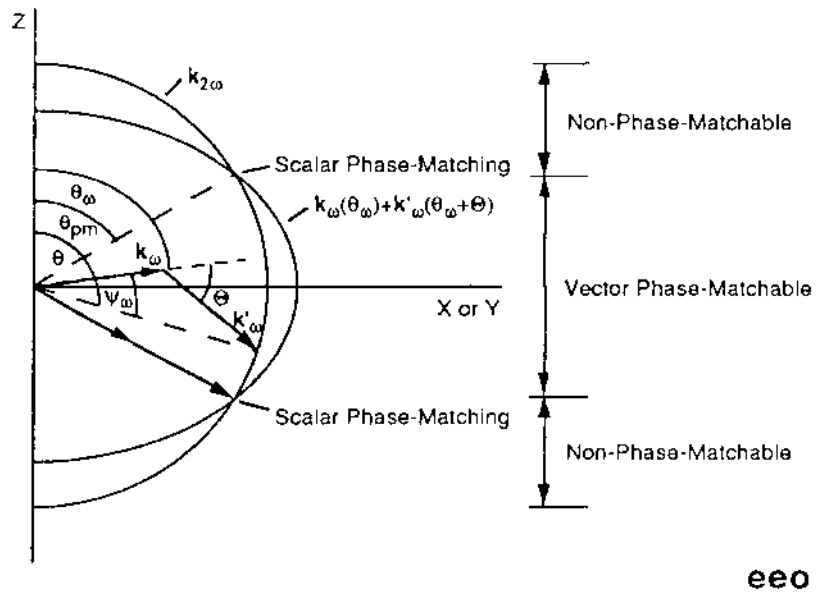
**oeo or eoo****Figure 22** Continued.

Table 28 Angle Formulas for Vector Phase Matching in SHG

Type I	
ooe	$\cos\Theta = \frac{2[n_{2\omega}^e(\theta)]^2 - (n_\omega^o)^2}{(n_\omega^o)^2}$
eoo	$\cos\Theta = \frac{4(n_{2\omega}^o)^2 - [n_\omega^e(\theta - \psi_\omega)]^2 - [n_\omega^e(\theta - \psi_\omega + \Theta)]^2}{2n_\omega^e(\theta - \psi_\omega)n_\omega^e(\theta - \psi_\omega + \Theta)}$
	$\cos\psi_\omega = \frac{4(n_{2\omega}^o)^2 + [n_\omega^e(\theta - \psi_\omega)]^2 - [n_\omega^e(\theta - \psi_\omega + \Theta)]^2}{2n_{2\omega}^o n_\omega^e(\theta - \psi_\omega)}$
Type II	
ooo	$\cos\Theta = \frac{4(n_{2\omega}^o)^2 - (n_\omega^o)^2 - [n_\omega^e(\theta - \psi_\omega + \Theta)]^2}{2n_\omega^o n_\omega^e(\theta - \psi_\omega + \Theta)}$
	$\cos\psi_\omega = \frac{4(n_{2\omega}^o)^2 + (n_\omega^o)^2 - [n_\omega^e(\theta - \psi_\omega + \Theta)]^2}{2n_{2\omega}^o n_\omega^o}$
eoo	$\cos\Theta = \frac{4(n_{2\omega}^o)^2 - [n_\omega^e(\theta - \psi_\omega)]^2 - (n_\omega^o)^2}{2n_\omega^e(\theta - \psi_\omega)n_\omega^o}$
	$\cos\psi_\omega = \frac{4(n_{2\omega}^o)^2 + [n_\omega^e(\theta - \psi_\omega)]^2 - (n_\omega^o)^2}{2n_{2\omega}^o n_\omega^e(\theta - \psi_\omega)}$
oeo	$\cos\Theta = \frac{4[n_{2\omega}^e(\theta)]^2 - (n_\omega^o)^2 - [n_\omega^e(\theta - \psi_\omega + \Theta)]^2}{2n_\omega^o n_\omega^e(\theta - \psi_\omega + \Theta)}$
	$\cos\psi_\omega = \frac{4[n_{2\omega}^e(\theta)]^2 + (n_\omega^o)^2 - [n_\omega^e(\theta - \psi_\omega + \Theta)]^2}{2n_{2\omega}^e(\theta)n_\omega^o}$
eoe	$\cos\Theta = \frac{4[n_{2\omega}^e(\theta)]^2 - [n_\omega^e(\theta - \psi_\omega)]^2 - (n_\omega^o)^2}{2n_\omega^e(\theta - \psi_\omega)n_\omega^o}$
	$\cos\psi_\omega = \frac{4[n_{2\omega}^e(\theta)]^2 + [n_\omega^e(\theta - \psi_\omega)]^2 - (n_\omega^o)^2}{2n_\omega^e(\theta)n_\omega^e(\theta - \psi_\omega)}$

The specific formulas for SHG for type I and II processes are given in Table 28. The ooe case is particularly simple, but the remaining cases must be solved numerically. The extraordinary index as a function of angle is given by Eq. (48). The construction of formulas for vector phase matching in SFG and DFG will follow in an analogous fashion.

C. Temperature Phase Matching

The refractive index is a function of temperature. As mentioned earlier in Section A, noncritical phase matching can be achieved in some materials by adjusting the temperature. The general conditions for collinear NCPM are

SHG.

$$n_{2\omega}(T_{\text{pm}}) = \frac{1}{2}[n_\omega(T_{\text{pm}}) + n'_\omega(T_{\text{pm}})] \quad (56)$$

where, in general, n and n' are different, such as ordinary and extraordinary.

SFG.

$$\omega_s n_s(T_{\text{pm}}) = \omega_{p1} n_{p1}(T_{\text{pm}}) + \omega_{p2} n_{p2}(T_{\text{pm}}) \quad (57)$$

DFG.

$$\omega_d n_d(T_{\text{pm}}) = \omega_{p1} n_{p1}(T_{\text{pm}}) - \omega_{p2} n_{p2}(T_{\text{pm}}) \quad (58)$$

where again the indices can be ordinary or extraordinary depending on the type of process.

The phase matching temperature is found by expanding these equations in a Taylor series about the ambient temperature T_0 . The results for SHG, SFG, and DFG are given in Tables 29 through 31. Refractive index data as functions of wavelength and temperature are required to compute the numerical value of T_{pm} for any specific situation.

Temperature bandwidths. Deviations of the temperature from the phase matching condition ($\Delta T = T - T_{\text{pm}}$) will cause the efficiency of the frequency conversion process to decrease in a manner illustrated by Fig. 4. To determine the temperature bandwidth, the phase velocity mismatch is expanded in a Taylor series about the phase matching temperature:

$$\Delta k(T) \simeq \left. \frac{\partial(\Delta k)}{\partial T} \right|_{T=T_{\text{pm}}} \Delta T \equiv \gamma_T \Delta T \quad (59)$$

Table 29 Formulas for Temperature Phase Matched SHG

Type I

ooe	$T_{\text{pm}} = T_0 + \frac{n_{2\omega}^e - n_\omega^o}{[(\partial n_\omega^o / \partial T) - (\partial n_{2\omega}^e / \partial T)]_{T=T_0}}$
eco	$T_{\text{pm}} = T_0 + \frac{n_{2\omega}^o - n_\omega^e}{[(\partial n_\omega^e / \partial T) - (\partial n_{2\omega}^o / \partial T)]_{T=T_0}}$

Type II

ooo	$T_{\text{pm}} = T_0 + \frac{2n_{2\omega}^o - n_\omega^o - n_\omega^e}{[(\partial n_\omega^o / \partial T) + (\partial n_{2\omega}^e / \partial T) - 2(\partial n_{2\omega}^o / \partial T)]_{T=T_0}}$
eoø	$T_{\text{pm}} = T_0 + \frac{2n_{2\omega}^e - n_\omega^e - n_\omega^o}{[(\partial n_\omega^e / \partial T) + (\partial n_{2\omega}^o / \partial T) - 2(\partial n_{2\omega}^e / \partial T)]_{T=T_0}}$

Table 30 Formulas for Temperature Phase Matched SFG

Type I	
ooo	$T_{pm} = T_0 + \frac{(n_s^e/\lambda_s) - (n_{p1}^o/\lambda_{p1}) - (n_{p2}^o/\lambda_{p2})}{[\lambda_{p1}^{-1}(\partial n_{p1}^o/\partial T) + \lambda_{p2}^{-1}(\partial n_{p2}^o/\partial T) - \lambda_s^{-1}(\partial n_s^e/\partial T)]_{T=T_0}}$
eoo	$T_{pm} = T_0 + \frac{(n_s^o/\lambda_s) - (n_{p1}^e/\lambda_{p1}) - (n_{p2}^e/\lambda_{p2})}{[\lambda_{p1}^{-1}(\partial n_{p1}^e/\partial T) + \lambda_{p2}^{-1}(\partial n_{p2}^e/\partial T) - \lambda_s^{-1}(\partial n_s^o/\partial T)]_{T=T_0}}$
Type II	
ooo	$T_{pm} = T_0 + \frac{(n_s^o/\lambda_s) - (n_{p1}^o/\lambda_{p1}) - (n_{p2}^e/\lambda_{p2})}{[\lambda_{p1}^{-1}(\partial n_{p1}^o/\partial T) + \lambda_{p2}^{-1}(\partial n_{p2}^e/\partial T) - \lambda_s^{-1}(\partial n_s^o/\partial T)]_{T=T_0}}$
eoo	$T_{pm} = T_0 + \frac{(n_s^o/\lambda_s) - (n_{p1}^e/\lambda_{p1}) - (n_{p2}^o/\lambda_{p2})}{[\lambda_{p1}^{-1}(\partial n_{p1}^e/\partial T) + \lambda_{p2}^{-1}(\partial n_{p2}^o/\partial T) - \lambda_s^{-1}(\partial n_s^o/\partial T)]_{T=T_0}}$
oee	$T_{pm} = T_0 + \frac{(n_s^e/\lambda_s) - (n_{p1}^o/\lambda_{p1}) - (n_{p2}^e/\lambda_{p2})}{[\lambda_{p1}^{-1}(\partial n_{p1}^o/\partial T) + \lambda_{p2}^{-1}(\partial n_{p2}^e/\partial T) - \lambda_s^{-1}(\partial n_s^e/\partial T)]_{T=T_0}}$
eoe	$T_{pm} = T_0 + \frac{(n_s^e/\lambda_s) - (n_{p1}^e/\lambda_{p1}) - (n_{p2}^o/\lambda_{p2})}{[\lambda_{p1}^{-1}(\partial n_{p1}^e/\partial T) + \lambda_{p2}^{-1}(\partial n_{p2}^o/\partial T) - \lambda_s^{-1}(\partial n_s^e/\partial T)]_{T=T_0}}$

Table 31 Formulas for Temperature Phase Matched DFG

Type I	
ooo	$T_{pm} = T_0 + \frac{(n_{p1}^o/\lambda_{p1}) - (n_d^e/\lambda_d) - (n_{p2}^o/\lambda_{p2})}{[\lambda_d^{-1}(\partial n_d^e/\partial T) + \lambda_{p2}^{-1}(\partial n_{p2}^o/\partial T) - \lambda_{p1}^{-1}(\partial n_{p1}^o/\partial T)]_{T=T_0}}$
eoo	$T_{pm} = T_0 + \frac{(n_{p1}^e/\lambda_{p1}) - (n_d^o/\lambda_d) - (n_{p2}^e/\lambda_{p2})}{[\lambda_d^{-1}(\partial n_d^o/\partial T) + \lambda_{p2}^{-1}(\partial n_{p2}^e/\partial T) - \lambda_{p1}^{-1}(\partial n_{p1}^e/\partial T)]_{T=T_0}}$
Type II	
ooo	$T_{pm} = T_0 + \frac{(n_{p1}^o/\lambda_{p1}) - (n_d^o/\lambda_d) - (n_{p2}^e/\lambda_{p2})}{[\lambda_d^{-1}(\partial n_d^o/\partial T) + \lambda_{p2}^{-1}(\partial n_{p2}^e/\partial T) - \lambda_{p1}^{-1}(\partial n_{p1}^o/\partial T)]_{T=T_0}}$
eoo	$T_{pm} = T_0 + \frac{(n_{p1}^e/\lambda_{p1}) - (n_d^o/\lambda_d) - (n_{p2}^o/\lambda_{p2})}{[\lambda_d^{-1}(\partial n_d^o/\partial T) + \lambda_{p2}^{-1}(\partial n_{p2}^o/\partial T) - \lambda_{p1}^{-1}(\partial n_{p1}^e/\partial T)]_{T=T_0}}$
oee	$T_{pm} = T_0 + \frac{(n_{p1}^o/\lambda_{p1}) - (n_d^e/\lambda_d) - (n_{p2}^e/\lambda_{p2})}{[\lambda_d^{-1}(\partial n_d^e/\partial T) + \lambda_{p2}^{-1}(\partial n_{p2}^e/\partial T) - \lambda_{p1}^{-1}(\partial n_{p1}^o/\partial T)]_{T=T_0}}$
eoe	$T_{pm} = T_0 + \frac{(n_{p1}^e/\lambda_{p1}) - (n_d^e/\lambda_d) - (n_{p2}^o/\lambda_{p2})}{[\lambda_d^{-1}(\partial n_d^e/\partial T) + \lambda_{p2}^{-1}(\partial n_{p2}^o/\partial T) - \lambda_{p1}^{-1}(\partial n_{p1}^e/\partial T)]_{T=T_0}}$

Substituting the phase matching bandwidth from Eq. (40) into Eq. (59), the temperature bandwidth is found. Results are shown in Tables 32 through 34 for the various processes.

D. Quasi-Phase Matching

Angle phase matching in birefringent crystals has been the most common form of phase matching for frequency conversion. However, it has some disadvantages. For example, as seen above, some angles of propagation are not possible. Also, the use of cubic crystals is not possible, even though they have large nonlinear coefficients in some cases, because they are optically isotropic in the linear regime. In general, it would be desirable to isolate and use one of the diagonal terms of the nonlinear susceptibility since they are generally larger. However, this is not possible in angle phase matching, and the d_{eff} is generally smaller than these diagonal terms. To overcome these limitations, some other form of phase matching must be utilized.

Consider the problem of phase velocity mismatch discussed in Section II and illustrated in Fig. 5. In any frequency conversion process, when the desired frequency field input is zero, the phase of the nonlinearly generated field relative to the driving nonlinear polarization will adjust to maximize its initial growth.

As seen in Section II, this phase is $-\pi/2$, and the phase difference between the field and the time derivative of the nonlinear polarization is π radians. By the energy theorem (Chapter 1), this situation maximizes the negative work done by

Table 32 Temperature Bandwidths for Types I and II
Noncritically Phase Matched SHG

		$\Delta T_{\text{BW}} = 2.784/\gamma_T L $
Type I		
ooe		$\gamma_T = \frac{4\pi}{\lambda_\omega} \left[\frac{\partial n_\omega^o}{\partial T} - \frac{\partial n_{2\omega}^e}{\partial T} \right]_{T=T_{\text{pm}}}$
eoo		$\gamma_T = \frac{4\pi}{\lambda_\omega} \left[\frac{\partial n_\omega^e}{\partial T} - \frac{\partial n_{2\omega}^o}{\partial T} \right]_{T=T_{\text{pm}}}$
Type II		
oeo		$\gamma_T = \frac{2\pi}{\lambda_\omega} \left[\frac{\partial n_\omega^o}{\partial T} + \frac{\partial n_\omega^e}{\partial T} - 2 \frac{\partial n_{2\omega}^o}{\partial T} \right]_{T=T_{\text{pm}}}$
eoo		$\gamma_T = \frac{2\pi}{\lambda_\omega} \left[\frac{\partial n_\omega^e}{\partial T} + \frac{\partial n_\omega^o}{\partial T} - 2 \frac{\partial n_{2\omega}^e}{\partial T} \right]_{T=T_{\text{pm}}}$
oee		
eoe		

Table 33 Temperature Bandwidths for Types I and II
Noncritically Phase Matched SFG

		$\Delta T_{BW} = 2.784/\gamma_T L $
Type I		
oee	$\gamma_T = 2\pi \left[\frac{1}{\lambda_{p1}} \frac{\partial n_{p1}^o}{\partial T} + \frac{1}{\lambda_{p2}} \frac{\partial n_{p2}^o}{\partial T} - \frac{1}{\lambda_s} \frac{\partial n_s^e}{\partial T} \right]_{T=T_{pm}}$	
eoo	$\gamma_T = 2\pi \left[\frac{1}{\lambda_{p1}} \frac{\partial n_{p1}^e}{\partial T} + \frac{1}{\lambda_{p2}} \frac{\partial n_{p2}^e}{\partial T} - \frac{1}{\lambda_s} \frac{\partial n_s^o}{\partial T} \right]_{T=T_{pm}}$	
Type II		
oeo	$\gamma_T = 2\pi \left[\frac{1}{\lambda_{p1}} \frac{\partial n_{p1}^o}{\partial T} + \frac{1}{\lambda_{p2}} \frac{\partial n_{p2}^e}{\partial T} - \frac{1}{\lambda_s} \frac{\partial n_s^o}{\partial T} \right]_{T=T_{pm}}$	
eoo	$\gamma_T = 2\pi \left[\frac{1}{\lambda_{p1}} \frac{\partial n_{p1}^e}{\partial T} + \frac{1}{\lambda_{p2}} \frac{\partial n_{p2}^o}{\partial T} - \frac{1}{\lambda_s} \frac{\partial n_s^o}{\partial T} \right]_{T=T_{pm}}$	
oee	$\gamma_T = 2\pi \left[\frac{1}{\lambda_{p1}} \frac{\partial n_{p1}^o}{\partial T} + \frac{1}{\lambda_{p2}} \frac{\partial n_{p2}^e}{\partial T} - \frac{1}{\lambda_s} \frac{\partial n_s^e}{\partial T} \right]_{T=T_{pm}}$	
eoe	$\gamma_T = 2\pi \left[\frac{1}{\lambda_{p1}} \frac{\partial n_{p1}^e}{\partial T} + \frac{1}{\lambda_{p2}} \frac{\partial n_{p2}^o}{\partial T} - \frac{1}{\lambda_s} \frac{\partial n_s^e}{\partial T} \right]_{T=T_{pm}}$	

Table 34 Temperature Bandwidths for Types I and II
Noncritically Phase-Matched DFG

		$\Delta T_{BW} = 2.784/\gamma_T L $
Type I		
oee	$\gamma_T = 2\pi \left[\frac{1}{\lambda_d} \frac{\partial n_d^e}{\partial T} + \frac{1}{\lambda_{p2}} \frac{\partial n_{p2}^o}{\partial T} - \frac{1}{\lambda_{p1}} \frac{\partial n_{p1}^o}{\partial T} \right]_{T=T_{pm}}$	
eoo	$\gamma_T = 2\pi \left[\frac{1}{\lambda_d} \frac{\partial n_d^o}{\partial T} + \frac{1}{\lambda_{p2}} \frac{\partial n_{p2}^e}{\partial T} - \frac{1}{\lambda_{p1}} \frac{\partial n_{p1}^e}{\partial T} \right]_{T=T_{pm}}$	
Type II		
oeo	$\gamma_T = 2\pi \left[\frac{1}{\lambda_d} \frac{\partial n_d^o}{\partial T} + \frac{1}{\lambda_{p2}} \frac{\partial n_{p2}^e}{\partial T} - \frac{1}{\lambda_{p1}} \frac{\partial n_{p1}^o}{\partial T} \right]_{T=T_{pm}}$	
eoo	$\gamma_T = 2\pi \left[\frac{1}{\lambda_d} \frac{\partial n_d^e}{\partial T} + \frac{1}{\lambda_{p2}} \frac{\partial n_{p2}^o}{\partial T} - \frac{1}{\lambda_{p1}} \frac{\partial n_{p1}^o}{\partial T} \right]_{T=T_{pm}}$	
oee	$\gamma_T = 2\pi \left[\frac{1}{\lambda_d} \frac{\partial n_d^e}{\partial T} + \frac{1}{\lambda_{p2}} \frac{\partial n_{p2}^e}{\partial T} - \frac{1}{\lambda_{p1}} \frac{\partial n_{p1}^o}{\partial T} \right]_{T=T_{pm}}$	
eoe	$\gamma_T = 2\pi \left[\frac{1}{\lambda_d} \frac{\partial n_d^e}{\partial T} + \frac{1}{\lambda_{p2}} \frac{\partial n_{p2}^o}{\partial T} - \frac{1}{\lambda_{p1}} \frac{\partial n_{p1}^e}{\partial T} \right]_{T=T_{pm}}$	

the field, thereby extracting energy from the pump field(s). However, because of the phase mismatch, this relative phase slips by $\pi/2$ in the first coherence length of the material, and the energy flow from the pump(s) to the desired field is less effective. After the first coherence length, the phase has slipped by $>\pi/2$ into a regime where positive work is done by the field. Thus energy is lost from the signal and flows back to the pumps(s). If the phase of the nonlinear polarization were adjusted appropriately after each coherence length, it would be possible to sustain the growth of the desired field. Although the growth of the field would be monotonic, it would not grow as fast as in the case of perfect phase matching. Such a condition is thus called quasi-phase matching (QPM).

Armstrong et al. [3] were the first to suggest ways to achieve QPM. The most common technique is illustrated in Fig. 23. Here the nonlinear crystal is divided into segments each a coherence length long. Each segment is then rotated relative to its neighbors by 180° about the axis of propagation. Because of the lack of inversion symmetry, this has the effect of changing the sign of all of the components of the nonlinear susceptibility tensor. Hence the nonlinear polarization wave is shifted by π radians each coherence length. The way in which this achieves QPM is described below.

McMullen [16] was the first to analyze this type of phase matching for a stack of plates in the nondepleted pump regime. Consider SHG as an example.

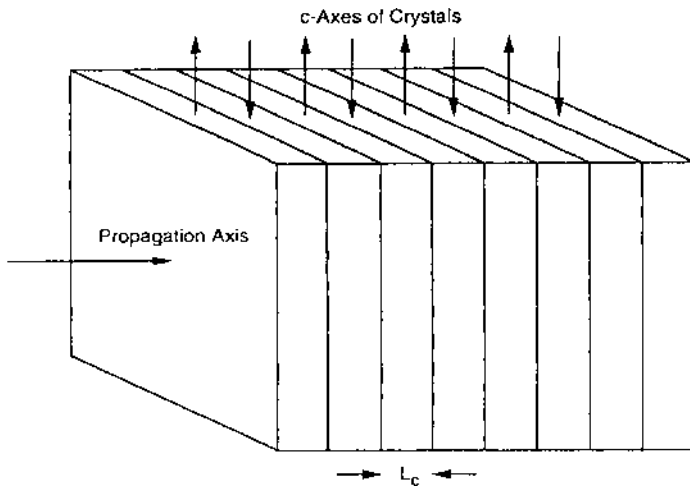


Figure 23 Schematic of a quasi-phase matching technique using a stack of uniaxial crystals of alternating c -axis direction.

For the n th slab in the stack,

$$d_{n,\text{eff}} = (-1)^{n-1} d_{\text{eff}} \quad (60)$$

where d_{eff} is the effective nonlinear coefficient of the first slab for the particular polarizations of the interacting fields and the direction of propagation relative to the crystal principal axes. The complex field amplitude in the n th slab (for the nondepleted pump regime) is given by

$$\begin{aligned} A_{2\omega,n}(z) &= \frac{-8\pi K d_{\text{eff}} A_\omega^2}{n_{2\omega} \lambda_\omega \Delta k} \\ &\times \left\{ (n-1) - i^n \exp\left(i \frac{\Delta kz}{2}\right) \sin\left[\frac{\Delta kz}{2} + (n-1)\frac{\pi}{2}\right] \right\} \end{aligned} \quad (61)$$

where K is given by Eq. (28) for SI and cgs units.

The following should be noted. At the input to the first slab, the second harmonic field is zero and the initial phase relative to the nonlinear polarization is $-\pi/2$. Thus, as discussed above, the amplitude of the second harmonic field begins to grow, and the relative phase slips by $\pi/2$ within the first coherence length. At the end of the first slab, then, the field is in phase with the driving polarization. Because of the π phase shift of the nonlinear polarization at each slab, the input conditions at each of the remaining slabs is different from those of the first slab. Here, the input second harmonic field is nonzero and the initial relative phase is π radians. Under these conditions the phase will slip by π within the distance of a coherence length. The result of this is that the proper phase relation is retained between the field and the time derivative of the nonlinear polarization so that negative work is always done by the field. This is illustrated in Fig. 24, which can be contrasted with Fig. 5. It can be seen that the dot product of the field with the time derivative of the nonlinear polarization always has a negative value. Thus energy is continuously extracted from the pump, and the second harmonic field grows monotonically.

The coherence length for frequency conversion processes is sometimes only a few micrometers. This has inhibited the development of QPM in the past for visible and ultraviolet wavelengths. However, it is possible to use any odd multiple of coherence length for each slab. The effective nonlinear coefficient d_m for the QPM interaction is then related to the effective nonlinear coefficient for a conventional interaction by the component at spatial frequency Δk of the Fourier expansion of a square wave, i.e.,

$$d_m = \begin{cases} (2/m\pi)d_{\text{eff}} & \text{for } m \text{ odd} \\ 0 & \text{for } m \text{ even} \end{cases} \quad (62)$$

The coefficient m is referred to as the order of the QPM. The growth of the second

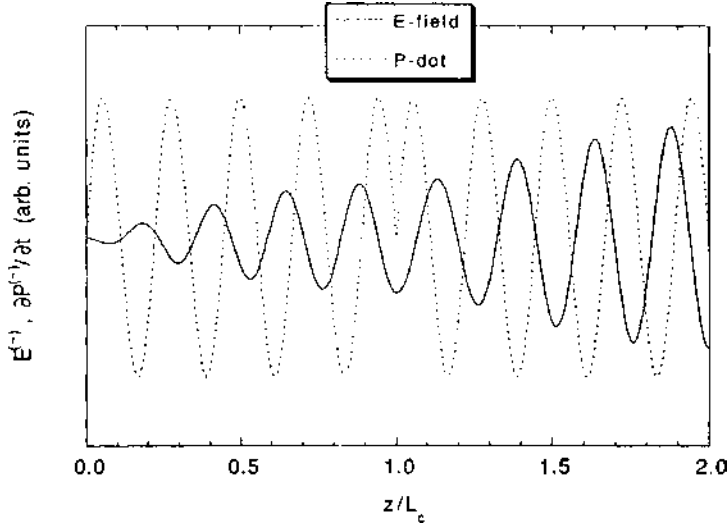


Figure 24 Illustration of the phase relation between the generated optical field and the time derivative of the driving nonlinear polarization for SHG in a quasi-phase matched medium.

harmonic intensity for perfect phase matching and first and third order QPM is illustrated in Fig. 25.

It is clear that QPM is less efficient than perfect phase matching, but this is often compensated by the fact that larger nonlinear coefficients can be accessed. For example, for LiNbO₃ in a noncritical phase matched situation, $d_{\text{eff}} = d_{31}$. With QPM, one can access d_{33} , which is approximately six times larger than d_{31} . Thus first order QPM is $(d_{33}/d_{31})^2(2/\pi)^2 \approx 15$ times more efficient than conventional noncritical phase matching in LiNbO₃. First order interactions are desirable for higher efficiency, but higher order QPM is sometimes used for ease of fabrication.

Formulas for frequency conversion efficiencies are given in Table 35 for m th order QPM in a stack of N plates in the nondepleted pump approximation. Szilagyi et al. [17] have extended the analysis of McMullen to include the effects of transmission coefficients and slab thickness (departure from L_c) on the conversion efficiencies. They also considered techniques to reduce Fresnel reflection losses from the plates by the application of antireflection coatings, by optically contacting the plates, and by placing the plates at the Brewster angle.

Rustagi et al. [18] have generalized the analysis of a stack of plates to include the effects of pump depletion. The important physical parameter in their

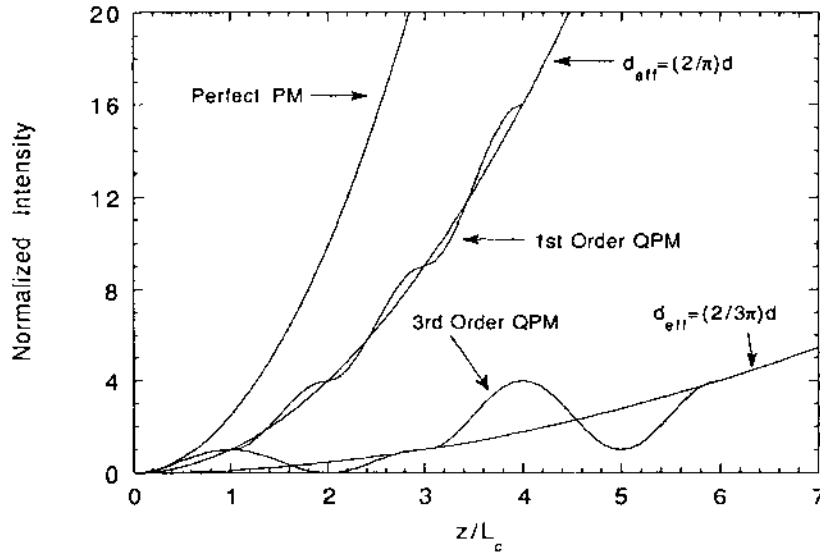


Figure 25 Normalized SHG intensity as a function of position in perfectly phase matched, first order quasi-phase matched, and third order quasi-phase matched nonlinear media.

analysis is a scaled dimensionless wave vector mismatch Δ_s , which is proportional to Δk and inversely proportional to the pump intensity. Rustagi et al. determined that in an ideal stack of plates a relative phase change of π radians on propagation through each plate is required for proper QPM. Note that this is the same requirement determined in the nondepleted pump regime. However,

Table 35 Frequency Conversion Efficiencies in the Infinite Plane Wave, Nondepleted Pump Approximation for m th order Quasi-Phase Matched Interactions in a Stack of N Plates

	SI	cgs
SHG	$\eta_{2\omega} = \frac{8\pi^2(2/m\pi)^2 d_{\text{eff}}^2 (NL_c)^2 I_\omega}{\epsilon_0 n_\omega^2 n_{2\omega} c \lambda_\omega^2}$	$\eta_{2\omega} = \frac{512\pi^5(2/m\pi)^2 d_{\text{eff}}^2 (NL_c)^2 I_\omega}{n_\omega^2 n_{2\omega} c \lambda_\omega^2}$
SFG	$\eta_s = \frac{8\pi^2(2/m\pi)^2 d_{\text{eff}}^2 (NL_c)^2 I_{p1}}{\epsilon_0 n_{p1} n_{p2} n_s c \lambda_s^2}$	$\eta_s = \frac{512\pi^5(2/m\pi)^2 d_{\text{eff}}^2 (NL_c)^2 I_{p1}}{n_{p1} n_{p2} n_s c \lambda_s^2}$
DFG	$\eta_d = \frac{8\pi^2(2/m\pi)^2 d_{\text{eff}}^2 (NL_c)^2 I_{p1}}{\epsilon_0 n_{p1} n_{p2} n_d c \lambda_d^2}$	$\eta_d = \frac{512\pi^5(2/m\pi)^2 d_{\text{eff}}^2 (NL_c)^2 I_{p1}}{n_{p1} n_{p2} n_d c \lambda_d^2}$

the required length of each plate is slightly different. The QPM length requirement for the n th plate is

$$L_n = \frac{2K(\gamma_n)}{|\Delta k|} \quad (63)$$

where $K(\gamma_n)$ is the complete elliptic integral of the first kind, and γ_n is the modulus, determined by the input second harmonic field to the n th plate. For low intensities where $\Delta s \gg 1$, the most common experimental situation, $\gamma_n \approx 2/|\Delta s|$, which yields $K(\gamma_n) \approx \pi/2$. Then from Eq. (63), $L_n \approx \pi/|\Delta k| = L_c$.

Rustagi et al. showed that in the low-intensity regime the formula for second harmonic efficiency with pump depletion is given by the same formula in the conventional case, shown in Table 4 discussed in Section II, but with d_{eff} replaced by $(2/\pi)d_{\text{eff}}$. This is similar to the result in the nondepleted pump case and first order QPM. This approximation is very good for $|\Delta s| \geq 100$.

By contrast, the formulas for SFG and DFG in this same intensity regime are identical to the formulas in the conventional case, given in Section II, but with d_{eff} replaced by $(2/\pi)\cos\Delta\varphi_i d_{\text{eff}}$, where $\Delta\varphi_i$ is the input phase of the field amplitude, for the sum- or difference-frequency, relative to the nonlinear polarization at each plate. For three waves incident on a conventionally phase matched crystal, the most efficient energy transfer to the desired wave occurs when $\Delta\varphi_i = -\pi/2$. In the QPM case, the condition for efficient energy transfer is $\Delta\varphi_i = 0$ or π .

More recently, research on QPM has centered around waveguide technology. Advances in III-V diode laser technology have resulted in commercially available near-infrared diode lasers with single-mode output powers exceeding 100 mW. Materials issues related to developing similar diode lasers in the visible and mid-IR have not been resolved. Hence nonlinear optical devices for frequency conversion with diode lasers have been of considerable interest. With the relatively low output powers of diode lasers, waveguide confinement is necessary for high intensity to achieve useful amounts of frequency-converted radiation. A material such as LiNbO₃ is attractive because of its reasonably large nonlinear coefficients, its high transparency in the desired wavelength region, its well-developed role in waveguide technologies, and its commercial availability. However, its usefulness is limited by its small birefringence, which is too small for SHG of blue light. It is also too large for the noncritically phase matched DFG of mid-IR radiation. Therefore QPM is being investigated for using these types of materials to achieve efficient frequency conversion in waveguide configurations.

Most of the work in waveguide QPM has been for SHG in a planar waveguide geometry and can be described in the nondepleted pump approximation. The conversion efficiency is commonly given in terms of

a normalized efficiency by [19]

$$\eta = \frac{\mathcal{P}_{2\omega}}{\mathcal{P}_\omega} = \eta_{\text{norm}} \mathcal{P}_\omega L^2 \quad (64)$$

where L is the length of the waveguide or the interaction region of the device, and η_{norm} contains information on the nonlinear coefficient, the overlap of the fundamental and second harmonic waveguide modal fields, and the effects of QPM. Explicit formulas for the conversion efficiency in QPM SHG in planar waveguides are given in Table 36. In these formulas y is the depth coordinate of the waveguide, while $a_\omega(y)$ and $a_{2\omega}(y)$ are the normalized modal field distributions. The indices n_ω and $n_{2\omega}$ are the corresponding modal indices of the waveguide. For channel waveguides, an additional integral in the width dimension would have to be added.

Various techniques have been used to fabricate QPM waveguides, but they all generally involve a periodic poling of the waveguide material, either a ferroelectric inorganic material like LiNbO₃ or a nonlinear polymer. This periodic poling produces the alternating sign reversed domains required for QPM. A discussion of these techniques is outside the scope of this book. Details can be found in the cited references (see Table 38).

Fabrication errors producing deviations from the ideal domain period Λ lead to phase error accumulations between the interacting fields, which degrades the conversion efficiency. Fejer [19] has analyzed the effects of small random errors and determined that the efficiency is reduced by 50% when the rms deviation $\delta\Lambda$ in the domain period is

$$\frac{\delta\Lambda}{\Lambda} = \frac{1}{\pi} \sqrt{\frac{L_c}{L}} \quad (65)$$

Table 36 Conversion Efficiency Formulas for SHG in m th Order Quasi-Phase Matched Interactions in Waveguides

$\eta_{2\omega} = \frac{\mathcal{P}_{2\omega}}{\mathcal{P}_\omega} = \eta_{\text{norm}} \mathcal{P}_\omega L^2$	
$\eta_{\text{norm}} = \frac{8\pi^2(2/m\pi)^2 d_{\text{eff}}^2}{\epsilon_0 n_\omega^2 n_{2\omega} c \lambda_\omega^2} \left \int_{-\infty}^{\infty} a_{2\omega}^*(y) a_\omega^2(y) dy \right ^2$	(SI)
$\eta_{\text{norm}} = \frac{512\pi^5(2/m\pi)^2 d_{\text{eff}}^2}{n_\omega^2 n_{2\omega} c \lambda_\omega^2} \left \int_{-\infty}^{\infty} a_{2\omega}^*(y) a_\omega^2(y) dy \right ^2$	(cgs)

For a fixed deviation $\Delta\Lambda$, a 50% reduction in efficiency occurs when

$$\frac{\Delta\Lambda}{\Lambda} = \left(\frac{2.78}{\pi}\right) \frac{L_c}{L} \quad (66)$$

Fejer et al. [19] also describe the changes to the formula for the normalized efficiency in the general nonideal case when the sign reversals in the nonlinear susceptibility are aperiodic.

Some experimental results of QPM frequency conversion are given in Table 37 for a stack of plates, and in Table 38 for waveguides and periodically poled crystals. Quoted efficiencies are either absolute or normalized (i.e., per W-cm² for waveguides or per W-cm for tight focusing in crystals, see Section IV C and Table 40).

E. Čerenkov Phase Matching

This type of phase matching has also been considered for efficient SHG in waveguides. The basic concept is illustrated in Fig. 26. In this type of phase matching, the fundamental wave is a waveguide mode, while the second harmonic is a radiation mode, i.e., it propagates out into the cladding or substrate of the waveguide at some angle θ . The angle is determined by the condition that the phase velocity of the fundamental guided mode is matched to the phase velocity of the second harmonic radiation mode.

The phase matching condition can be understood intuitively from Fig. 26. The guided nonlinear polarization wave generates a radiated second harmonic wave at point A. At some later time it generates another wave at point B. If the two second harmonic radiation waves are to be in phase, then AC \perp BC. The distances AB and AC are just the distances $V_\omega t$ and $v_{2\omega}t$ traveled by the guided polarization wave and the second harmonic radiation wave in time t , respectively, where V_ω and $v_{2\omega}$ are the respective phase velocities of the fundamental and second harmonic. From the geometry of the figure,

$$V_\omega \cos\theta = v_\omega \quad (67)$$

It can be seen that this is possible when the velocity of the polarization wave in the waveguide is greater than the velocity of the wave it radiates into the substrate or cladding. This is analogous to the phenomenon of Čerenkov radiation, in which a particle emitting electromagnetic radiation travels in a medium at a speed greater than the speed of light in that medium, hence the name given to the phase matching condition in Eq. (67). The angle of the phase matched radiated second harmonic is called the Čerenkov angle, and the phase matching condition, from

Table 37 Experimental Conversion Efficiencies for Quasi-Phase Matched Frequency Conversion in a Stack of Plates

Material	Number of plates	Plate thickness	Order	Process	Pump laser	Pump intensity	Conversion efficiency	Ref.
GaAs	5	308 μm	3	SHG	CO_2 10.6 μm	5 MW/cm ²	$(3 \pm 2) \times 10^{-5}$	[17]
CdTe	5	890 μm	5	SHG	CO_2 10.6 μm	—	$(4.4 \pm 2.0) \times 10^{-5}$ /MW/cm ²	[20]
GaAs	12	$97 \pm 5 \mu\text{m}$	1	SHG	CO_2 10.6 μm	19 MW/cm ²	0.020	[21]
GaAs	19	$97 \pm 5 \mu\text{m}$	1	SHG	CO_2 9.15 μm	20 MW/cm ²	0.027	[21]
LiNbO ₃	6	200 μm	—	SHG	Nd:YAG 1.064 μm	~ 1 MW/cm ²	2×10^{-5}	[22]
GaAs	24	252 μm	3	DFG	Er:Cr:YSGG-pumped ZnGeP ₂ OPG	410 MW/cm ²	0.007	[61]
GaAs	53	106 μm	1	SHG	$6.74 \mu\text{m}$ & $4.79 \mu\text{m}$	20 MW/cm ²	0.24	[62]
GaAs	27	106.2 μm	1	SHG	CO_2 10.6 μm	8.2 MW/cm ²	0.02	[63]

Table 38 Experimental Conversion Efficiencies for Quasi-Phase Matched Frequency Conversion in Waveguides and Periodically Poled Crystals

Material	Process	Period (μm)	Length (mm)	Order	Pump laser	Pump power	Conv. Eff.	Ref.	
LiNbO ₃	SHG	6.3–6.7	7	1	Nd:YAG	800 mW	$10^{-3}/\text{W}\cdot\text{cm}^2$	[23]	
LiNbO ₃	SHG	2.7–3.3	3.3	1	Ti:Al ₂ O ₃	2.5 mW	0.7/W	[24]	
LiNbO ₃	SHG	7.9	1.5	1	Ti:Al ₂ O ₃	880 nm	0.4/W·cm ²	[25]	
LiNbO ₃	SHG	18	0.5	3	Nd:YAG	1 mW	0.05/W·cm ²	[19]	
LiNbO ₃	SHG	6.5–7.8	10	3	Dye	1064 nm	0.94 μW	[19]	
LiNbO ₃	SHG	2.7	1.8	1	Dye	820 nm	83 mW	8.0×10^{-5}	[26]
KTiOPO ₄	SHG	4	5	1	Ti:Al ₂ O ₃	80 mW	$0.8 \pm 0.2/\text{W}\cdot\text{cm}^2$	[27]	
LiNbO ₃	SHG	2.8	3	1	Ti:Al ₂ O ₃	850.5 nm	196 mW	6.0/W·cm ²	[28]
LiTaO ₃	SHG	3.6	9	1	Ti:Al ₂ O ₃	851.7 nm	145 mW	$0.86/\text{W}\cdot\text{cm}^2$	[29]
LiNbO ₃	DFG	14.75	42	—	Ti:Al ₂ O ₃	866 nm	90 mW	500%/W	[52]
KTiOPO ₄	SHG	9.01	8.5	1	Ti:Al ₂ O ₃	775.2 nm	$9 \times 10^{-4}/\text{W}\cdot\text{cm}$	[53]	
						797.6 nm		(continued)	

Table 38 Continued

Material	Process	Period (μm)	Length (mm)	Order	Pump laser	Pump power	Conv. Eff.	Ref.
KTiOPO ₄	SHG	14.20–15.45	0.630	—	RbTiOAsO ₄ OPO	—	1.5% avg	[54]
RbTiOPO ₄	SHG	6.63	9	1	Ti:Al ₂ O ₃ 984 nm	228 mW	2.1×10^{-3}	[55]
LiNbO ₃	SHG	29.2/11.0*	48/7	1	Nd:YAG 1064 nm	11.8 W	21%	[56]
KNbO ₃	SHG	30	5	1	Diode 926 nm	1.9 W	2×10^{-3}	[57]
LiNbO ₃	SHG	18.05	16	1	Er-doped fiber 1536 nm	1.4 kW	83%	[58]
KTiOAsO ₄	DFG	39.2	10	1	Nd:YAG 1064 nm	117.2 mW	9.1×10^{-5} /W·cm	[59]
DANS	SHG	~0.15	—	—	Diode 1519.6 nm Nd:YAG 1064 nm	17.4 mW 32 W	6×10^{-3} /W·cm	[60]

* Two stages.

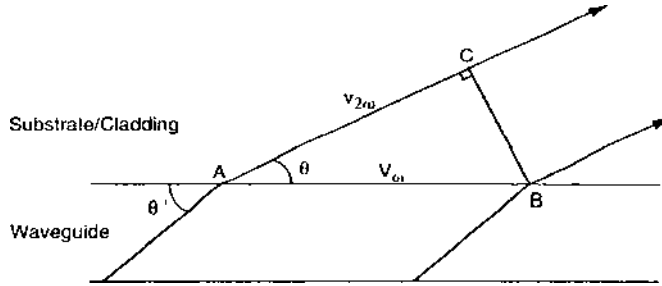


Figure 26 Schematic illustration of Čerenkov phase matching for SHG in a waveguide. (Adapted from Ref. 30.)

Eq. (67), is normally written as

$$\cos\theta = \frac{N_\omega}{n_{2\omega}} \quad (68)$$

N_ω is the modal effective index for the fundamental, and $n_{2\omega}$ is the index of the substrate or cladding for the second harmonic.

Chikuma and Umegaki [30] have presented the theory for SHG with Čerenkov phase matching in crystal-cored fibers and channel waveguides, while Li et al. [31] have treated the case of planar waveguides. The formulas for conversion efficiency are somewhat complex and will not be presented here. By symmetry, the far-field pattern of the second harmonic radiation for a fiber is an annulus centered on the fiber axis. The far-field patterns for other geometries are not as readily realized and must be computed numerically.

IV. REAL OPTICAL BEAMS IN REAL MEDIA

A. Absorption

Linear absorption can be very detrimental to frequency conversion processes. Formulas for conversion efficiencies including the effects of absorption in the nondepleted pump approximation, that is nondepleted by the nonlinear process, are given in Table 39. Generally, these formulas are adequate because linear absorption places severe limits on the conversion efficiency.

The general behavior of the formulas can be illustrated by SHG. Usually, $\alpha_\omega \ll 1$. Generally, one cannot entirely eliminate the absorption of the fundamental, although at very low absorption it is often masked by scattering. For practical purposes, though, it is possible to set $\alpha_\omega = 0$, but the second harmonic may be near an absorption band of the material. The effects of

Table 39 Conversion Efficiency Formulas for SHG, SFG, and DFG in the Infinite Plane Wave, Nondepleted Pump Approximation, Including the Effects of Linear Absorption

SHG	$\eta_{2\omega} = \eta_{2\omega}^0 \exp[-(\alpha_\omega + \alpha_{2\omega}/2)L] \frac{\sin^2(\Delta kL/2) + \sinh^2[(\alpha_\omega - \alpha_{2\omega}/2)L/2]}{(\Delta kL/2)^2 + [(\alpha_\omega - \alpha_{2\omega}/2)L/2]^2}$
	$\eta_{2\omega}^0 = \frac{8\pi^2 d_{\text{eff}}^2 L^2 I_\omega}{\epsilon_0 n_\omega^2 n_{2\omega} c \lambda_\omega^2} \quad (\text{SI}) \quad \eta_{2\omega}^0 = \frac{512\pi^5 d_{\text{eff}}^2 L^2 I_\omega}{n_\omega^2 n_{2\omega} c \lambda_\omega^2} \quad (\text{cgs})$
SFG	$\eta_s = \eta_s^0 \exp[-(\alpha_{p1} + \alpha_{p2} + \alpha_s)L/2] \frac{\sin^2(\Delta kL/2) + \sinh^2[(\alpha_{p1} + \alpha_{p2} - \alpha_s)L/4]}{(\Delta kL/2)^2 + [(\alpha_{p1} + \alpha_{p2} - \alpha_s)L/4]^2}$
	$\eta_s^0 = \frac{8\pi^2 d_{\text{eff}}^2 L^2 I_{p1}}{\epsilon_0 n_{p1} n_{p2} n_s c \lambda_s^2} \quad (\text{SI}) \quad \eta_s^0 = \frac{512\pi^5 d_{\text{eff}}^2 L^2 I_{p1}}{n_{p1} n_{p2} n_s c \lambda_s^2} \quad (\text{cgs})$
DFG	$\eta_d = \eta_d^0 \exp[-(\alpha_{p1} + \alpha_{p2} + \alpha_d)L/2] \frac{\sin^2(\Delta kL/2) + \sinh^2[(\alpha_{p1} + \alpha_{p2} - \alpha_d)L/4]}{(\Delta kL/2)^2 + [(\alpha_{p1} + \alpha_{p2} - \alpha_d)L/4]^2}$
	$\eta_d^0 = \frac{8\pi^2 d_{\text{eff}}^2 L^2 I_{p1}}{\epsilon_0 n_{p1} n_{p2} n_d c \lambda_d^2} \quad (\text{SI}) \quad \eta_d^0 = \frac{512\pi^5 d_{\text{eff}}^2 L^2 I_{p1}}{n_{p1} n_{p2} n_d c \lambda_d^2} \quad (\text{cgs})$

absorption on the SHG phase matching curve are shown in Figs. 27 and 28. Absorption is obviously detrimental to the conversion efficiency. At values of $\alpha_{2\omega}L \geq 5$, the phase matching curve changes shape from sinc^2 to a Lorentzian. The SFG and DFG processes exhibit similar behavior.

Absorption has another detrimental effect in heating the material. As seen previously, the refractive indices, and therefore Δk , are functions of temperature. Thus absorption can produce a drift in the phase matching conditions and a reduction in conversion efficiency. The change in Δk with temperature is given by the Taylor series expansion in Section III.

B. Beam Divergence

All of the results for conversion efficiency given previously apply to the interaction of infinite plane waves. These approximations are good when the size of the interacting beams is large compared to a typical wavelength, or when the nonlinear medium is short compared to the diffraction length of the beam. However, beam size is important, since conversion efficiencies are intensity dependent, and an increase in intensity often requires a reduction in beam size. As a beam gets smaller, its divergence (i.e., diffraction) cannot be ignored.

A diverging (or converging) beam can be thought of as a superposition of plane waves traveling in slightly different directions. For angle phase matching,

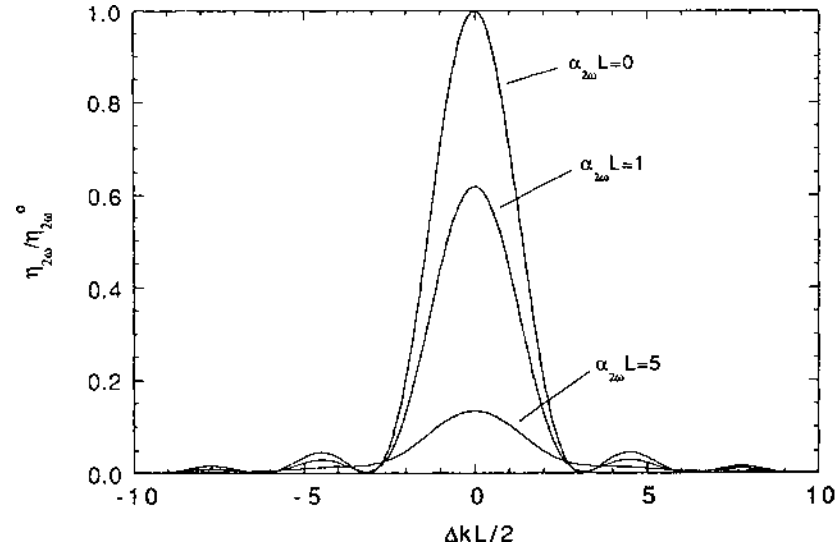


Figure 27 Normalized SHG frequency conversion efficiency as a function of phase mismatch, including the effects of absorption at the second harmonic frequency.

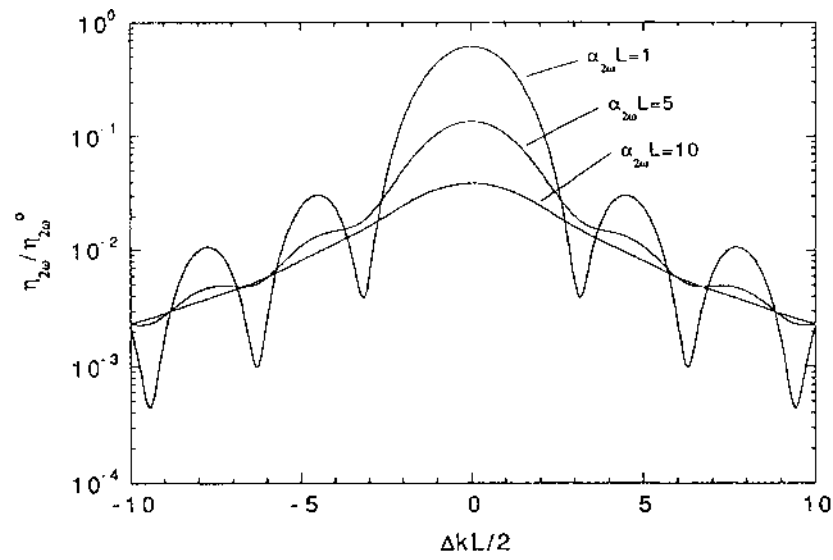


Figure 28 Normalized SHG frequency conversion efficiency (on a log scale) as a function of phase mismatch, including the effects of absorption at the second harmonic frequency.

the direction of propagation is critical. Thus beam divergence defeats perfect angle phase matching. The effect becomes important when the beam divergence angle θ_d is comparable to the angular bandwidth (i.e., $\theta_d \sim \theta_{BW}$), as given in Section III. To compute the effect on phase matching for a given divergence angle, the Taylor series expansion for $\Delta k(\theta)$ in Section III can be used, substituting $\theta_d/2$ for $\Delta\theta$.

C. Birefringence and Beam Focusing

In birefringent media, the direction of wave propagation (i.e., wave vector direction) for an extraordinary wave is not generally the same as the direction of energy (i.e., beam) propagation. Thus for both type I and type II processes, the ordinary and extraordinary beams of finite size will not completely overlap over the full length of the nonlinear medium. The effect is illustrated in Fig. 29. The extraordinary beam is seen to “walk off” the axis of the ordinary beam. The angle ρ is called the walk-off angle and for uniaxial crystals is given by

$$\tan \rho = \frac{[n^e(\theta)]^2}{2} \left[\frac{1}{(n^e)^2} - \frac{1}{(n^o)^2} \right] \sin 2\theta \quad (69)$$

for propagation at an angle θ with respect to the optic axis. Typically, ρ is of the order of a few degrees for $\theta = 45^\circ$. For noncritical phase matching ($\theta = 90^\circ$), the walk-off effect is completely negligible ($\rho = 0$) except for finite beam divergence (see NCPM angle bandwidths in Section III).

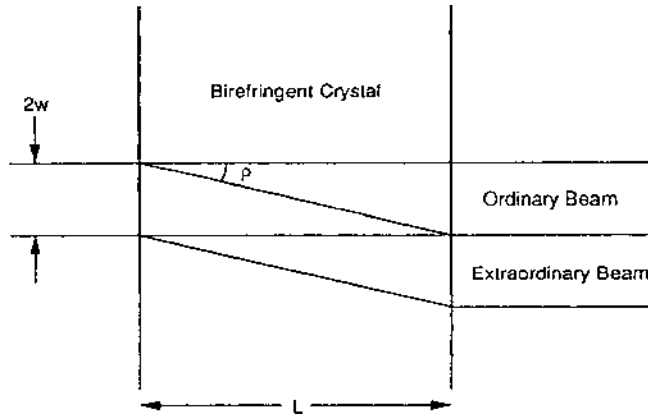


Figure 29 Schematic illustration of the walk-off effect of ordinary and extraordinary beams due to double refraction in birefringent crystals.

For beams of constant radii w , ordinary and extraordinary beams become physically separated in a distance $L_\rho = 2w/\tan\rho \approx 2w/\rho$. For a beam diameter of 1 mm and $\rho = 2^\circ$, this distance is approximately 3 cm. Beams that do not physically overlap cannot interact. Therefore the walk-off effect is a serious detriment to conversion efficiency.

As mentioned earlier, decreasing the beam size (i.e., focusing the beam) is often used to enhance the conversion efficiency due to a concomitant increase in intensity. However, focusing carries penalties due to the effects described above. The converging and diverging parts of the beam(s) result in a departure from perfect phase matching. Also the walk-off effect is more critical as the beam diameter becomes smaller. In addition, focusing limits the interaction length since a tighter focus results in a smaller length over which the beam intensity is maximized.

Clearly, there are trade-offs to consider when focusing the pump beam(s) to optimize the conversion efficiency. Boyd and Kleinman [32] have treated the case of nondepleted SHG in negative uniaxial crystals, including the effects of focusing, walk-off (double refraction), and absorption. Two critical parameters they have defined are the focusing parameter $\xi = L/b$, where b is the confocal parameter of a TEM₀₀ Gaussian beam (see Chapter 1), and the double refraction parameter $B = \rho(k_o L)^{1/2}/2$. Boyd and Kleinman's approach is to solve the wave equation in the infinite plane wave approximation for a slab of material with infinitesimal thickness. Corrections are given to the pump wave for an exponential dependence on absorption, and a transverse Gaussian amplitude profile (cylindrical beam symmetry is assumed). They then integrate over all sources (i.e., all infinitesimal slabs) in the material to obtain the field amplitude outside the material. The beam is propagated to the far field where the intensity is determined. The second harmonic power is found by then integrating over the beam area. The result is given in Table 40.

It can be seen that the infinite plane wave result is modified by a function $h(\sigma, \beta, \kappa, \xi, \mu)$,

$$\begin{aligned}\sigma &= \frac{b\Delta k}{2} \\ \beta &= \frac{\rho\sqrt{k_o b}}{2} \\ \kappa &= \left(\frac{2\alpha_\omega - \alpha_{2\omega}}{2}\right)\frac{b}{2} \\ \xi &= \frac{L}{b} \\ \mu &= \frac{(L - 2f)}{L}\end{aligned}\tag{70}$$

Table 40 Conversion Efficiency Formulas for SHG, SFG, and DFG in the Nondepleted Pump Approximation, Including the Effects of Linear Absorption, Double Refraction, and Focusing

	$\eta_{2\omega} = \eta_{2\omega}^0 \exp[-(\alpha_\omega + \alpha_{2\omega}/2)L] h(\sigma, \beta, \kappa, \xi, \mu)$
SHG	$\eta_{2\omega}^0 = \frac{16\pi^2 d_{\text{eff}}^2 L \mathcal{P}_\omega}{\epsilon_0 n_\omega n_{2\omega} c \lambda_\omega^3}$ (SI) $\eta_{2\omega}^0 = \frac{1024\pi^5 d_{\text{eff}}^2 L \mathcal{P}_\omega}{n_\omega n_{2\omega} c \lambda_\omega^3}$ (cgs)
	$\eta_s = \eta_s^0 \exp[-(\alpha_{p1} + \alpha_{p2} + \alpha_s)L/2][(1 - \zeta^2)(1 - \gamma^2)/(1 + \gamma\zeta)] h(\sigma, \beta, \kappa, \xi, \mu)$
SFG	$\eta_s^0 = \frac{8\pi^2 d_{\text{eff}}^2 L \mathcal{P}_{p1}}{\epsilon_0 n_{p1} n_s c \lambda_s^3}$ (SI) $\eta_s^0 = \frac{1024\pi^5 d_{\text{eff}}^2 L \mathcal{P}_{p1}}{n_{p1} n_s c \lambda_s^3}$ (cgs)
	$\eta_d = \eta_d^0 \exp[-(\alpha_{p1} + \alpha_{p2} + \alpha_d)L/2] h(\sigma, \beta, \kappa'', \xi, \mu)$
DFG	$\eta_d^0 = \frac{16\pi^2 d_{\text{eff}}^2 L \mathcal{P}_{p1}}{\epsilon_0 n_{p1} n_d c \lambda_{p2} \lambda_d^2}$ (SI) $\eta_d^0 = \frac{1024\pi^5 d_{\text{eff}}^2 L \mathcal{P}_{p1}}{n_{p1} n_d c \lambda_{p2} \lambda_d^2}$ (cgs)
	$\kappa'' = \frac{1}{2}\alpha''b$ $\alpha'' = \frac{1}{2}(\alpha_{p1} + \alpha_{p2} - \alpha_d)$

with f being the focal position of the fundamental beam in the crystal. All other parameters have been defined previously. All of these parameters are optimizable. Absorption has already been considered. To determine the effects of focusing and double refraction, consider absorption to be negligible ($\kappa = 0$). Then the optimum focal position is in the center of the crystal, and $\mu = 0$ (i.e., $f = L/2$).

For convenience, Boyd and Kleinman revised the double refraction parameter in this case and defined

$$B = \beta \sqrt{\xi} \quad (71)$$

For a given B and ξ , the phase matching parameter was then optimized to give $\sigma_m(B, \xi)$. This yields the function

$$h_m(B, \xi) \equiv h(\sigma_m, B, \xi) = h(\sigma_m, \beta \sqrt{\xi}, 0, \xi, 0) \quad (72)$$

A plot of this function for various values of B is given in Fig. 30.

Clearly, the optimum conditions are given by $B = 0$, i.e., no walk-off, which is achieved in noncritical phase matching. One would expect under these conditions that the optimum crystal length would be $\sim b$ (i.e., the distance over which the focused beam has a minimum, nearly constant area). The actual optimum length determined by numerical calculations is seen by Fig. 30 to be

approximately $2.84b$. As B increases, the optimum crystal length decreases due to the walk-off effect. From Fig. 30, the optimum crystal length has decreased to $1.39b$ for $B = 16$. The optimum conversion efficiency has also decreased by more than an order of magnitude.

It turns out that the optimum σ_m when focusing is used corresponds to $\Delta k > 0$ for all values of ξ . The reason for this is illustrated in Fig. 31. When $\Delta k > 0$ along the beam axis, there are other portions of the beam where diverging (or converging) rays make $\Delta k = 0$. This is not possible when $\Delta k < 0$ along the axis.

Boyd and Kleinman have defined two characteristic lengths for SHG in the nondepleted pump approximation with no absorption, but where focusing and double refraction are included. These are the aperture length

$$L_a = \frac{\sqrt{\pi}w_0}{\rho} \quad (73)$$

and the effective length of focus

$$L_f = \frac{\pi b}{2} \quad (74)$$

where w_0 is the radius of the fundamental beam at focus. The formula for the second harmonic power has the following limiting forms depending on

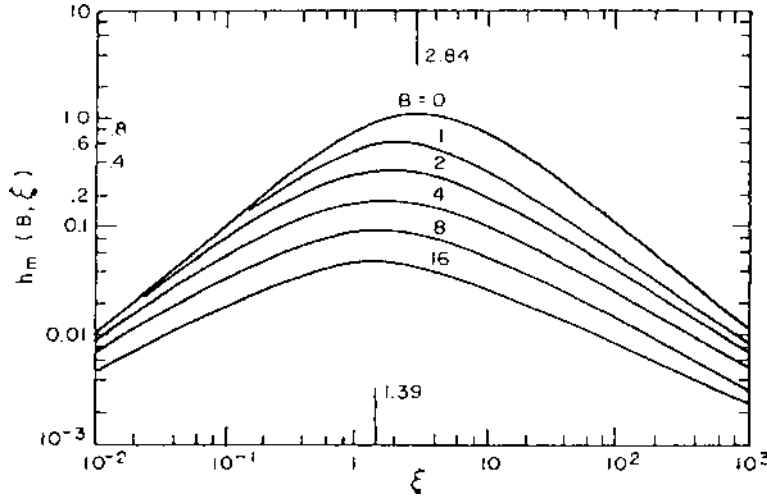


Figure 30 Plot of $h_m(B, \xi)$ as a function of the focusing parameter ξ for various values of the double refraction parameter B . (From Ref. 32.)

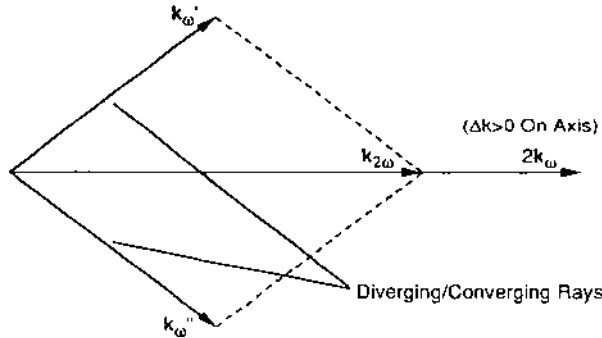


Figure 31 Schematic illustration of phase matching with diverging or converging rays in focused SHG when $\Delta k > 0$ on the axis of beam propagation.

the relation of the crystal size and these two characteristic lengths:

$$\mathcal{P}_{2\omega} = \frac{K \mathcal{P}_\omega^2}{w_0^2} \begin{cases} L^2 & L_a, L_f \gg L \\ LL_a & L_f \gg L \gg L_a \\ L_f L_a & L \gg L_f \gg L_a \\ 4L_f^2 & L \gg L_a \gg L_f \\ 4.75L_f^2 & L_a \gg L \gg L_f \end{cases} \quad (75)$$

where

$$K = \begin{cases} \frac{8\pi d_{\text{eff}}^2}{\epsilon_0 c n_\omega^2 n_{2\omega} \lambda_\omega^2} & (\text{SI}) \\ \frac{512\pi^4 d_{\text{eff}}^2}{c n_\omega^2 n_{2\omega} \lambda_\omega^2} & (\text{cgs}) \end{cases} \quad (76)$$

Clearly, when the crystal length exceeds these two characteristic lengths, the conversion efficiency is limited by L_f and L_a . When absorption is included, another characteristic length to consider is $(\alpha_\omega)^{-1}$ or $(\alpha_{2\omega})^{-1}$ in comparison with L_f and L_a .

The case of SFG is similar to SHG. Boyd and Kleinman considered the case where the two pump beams propagate collinearly with the same focal position

and confocal parameter b_0 . The following definitions apply:

$$\omega_{p1} + \omega_{p2} \equiv 2\omega_0$$

$$n_{p1} + n_{p2} \equiv 2n_0$$

$$\omega_{p1} \equiv \omega_0(1 - \gamma), \quad \omega_{p2} \equiv \omega_0(1 + \gamma)$$

$$n_{p1} \equiv n_0(1 - \zeta), \quad n_{p2} \equiv n_0(1 + \zeta) \quad (77)$$

$$k_0 = \frac{n_0 \omega_0}{c}$$

$$\Delta k = k_{p1} + k_{p2} - k_s$$

$$\alpha \equiv \frac{1}{2}(\alpha_{p1} + \alpha_{p2} - \alpha_s), \quad \alpha' \equiv \frac{1}{2}(\alpha_{p1} + \alpha_{p2} + \alpha_s)$$

The sum-frequency efficiency is given in Table 40. Definitions of other parameters are the same as given previously. For no absorption and an optimized phase matching parameter σ_m , the plots in Fig. 30 and the discussion above concerning SHG apply equally to SFG.

The case of DFG is nontrivial. However, under certain conditions that would apply, for example, to the case of up-conversion from the IR to the visible, an approximate form for the DFG efficiency formula may be obtained that is similar to that of SHG and SFG. The following conditions must be met: $\omega_{p2} \ll \omega_{p1}, \omega_d$; $w_{p20}^2 \gg w_{p10}^2, w_{d0}^2$; $\pi w_{p20}^2 / \rho^2 \gg b_0^2$. In other words, the pump 2 frequency is small, the spot size of the pump 2 beam is large, and its confocal parameter is large compared to the respective value for the pump 1 beam. Then the difference-frequency efficiency is given in Table 40. Notice that certain parameters are modified. The discussions concerning SHG now apply in this DFG case as well.

Boyd and Kleinman have generalized their results to apply to the case of unequal confocal parameters and to positive uniaxial crystals. See Ref. 32 for the details.

One last detail must be considered when applying optimal focusing, and that is laser induced damage to the crystal [2]. Different materials have different threshold intensities (or fluences) at which damage will occur. The threshold is generally statistical, and a safety margin should be considered. Also, the threshold for surface damage is lower than that for the bulk material. Thus the laser spot size at the surface should be determined with this in mind. The surface damage threshold is usually determined by the presence of microscopic pores, cracks, and inclusions that tend to lower the threshold due to an enhanced local

electric field. The bulk damage threshold may also be lowered due to the phenomenon of self-focusing (see Chapter 6).

D. Group Velocity Mismatch

For laser pulses of widths < 1 ns, the quasi-cw approximation begins to break down, and pulse propagation effects must be considered. In general, the interacting pulses will travel with different group velocities (see Chapter 1), and over a certain distance they will no longer physically overlap. This decreases the nonlinear polarization and hence reduces the conversion efficiency.

To determine the effects of group velocity mismatch, the time dependent coupled wave equations for pulses traveling with group velocity $v_{ga} = (\partial k_\alpha / \partial \omega_\alpha)^{-1}$ need to be solved in the slowly varying amplitude approximation (see Chapter 1). The general solution is nontrivial. Akhmanov et al. [33] have discussed the solution for SHG. Taking the incident fundamental wave at $z = 0$ to be a pulse with amplitude given by

$$A_\omega(0, t) = \frac{A_\omega^0}{1 + (t/\tau)^2} \quad (78)$$

where τ is the pulse width, the result for the output second harmonic pulse at $z = L$ is given in Table 41.

Several parameters are defined in the table, but two of physical interest are L_v , the distance over which the fundamental and second harmonic pulses clearly separate, and τ_{cr} , the critical time over which the two pulses interact significantly through the nonlinear polarization. L_{NL} was defined earlier in Section II. Note that $\tau/\tau_{cr} = L_v/L_{NL}$. This ratio, for a given crystal length L , determines the significance of the group velocity mismatch.

Plots of normalized conversion efficiency as a function of retarded time are given in Fig. 32. For these plots, $L = L_v$ was chosen, and results for three

Table 41 Complex Field Amplitude for SHG in the Short Pulse Regime, Including Pump Depletion

$A_{2\omega}(L, t) = A_\omega^0 \frac{\tau_{cr}}{\tau} \left\{ \frac{(L/L_v) \cosh\xi + [f - \tilde{\eta}(\tilde{\eta} - L/L_v)/f] \sinh\xi}{\cosh\xi + (\tilde{\eta}/f) \sinh\xi} \right\} [1 + (\tilde{\eta} - L/L_v)^2]^{-1}$
$\tau_{cr} = \left \frac{v_{g\omega} - v_{g2\omega}}{v_{g\omega} v_{g2\omega}} \right L_{NL} \quad L_v = \left \frac{v_{g\omega} v_{g2\omega}}{v_{g\omega} - v_{g2\omega}} \right \tau$
$\xi = \sqrt{(\tau/\tau_{cr})^2 - 1} [\tan^{-1} \tilde{\eta} - \tan^{-1} (\tilde{\eta} - L/L_v)]$
$f = \sqrt{(\tau/\tau_{cr})^2 - 1} \quad \tilde{\eta} = (t - L/v_{g\omega})/\tau$

difference values of L_v/L_{NL} are given. Note that when $L_v \gg L_{NL}$ (i.e., when significant frequency conversion takes place over a distance small compared to the pulse walk-off distance, the conversion efficiency reaches its maximum value, similar to the quasi-cw case). The amplitude of the second harmonic pulse then reduces to an expression analogous to that of the quasi-cw case [2]:

$$A_{2\omega}(L, t) \rightarrow \frac{A_\omega^0}{1 + \tilde{\eta}^2} \tanh \left[\frac{L/L_{NL}}{(1 + \tilde{\eta})^2} \right] \quad (79)$$

However, as $L_v \rightarrow L_{NL}$ the conversion efficiency is severely reduced due to pulse walk-off.

When $L_v \leq L_{NL}$, group velocity mismatch must be considered when estimating the conversion efficiency. Recall from Chapter 1 that

$$v_{g\alpha} = c \left[n_\alpha + \omega_\alpha \left(\frac{\partial n}{\partial \omega} \right)_{\omega=\omega_\alpha} \right]^{-1} \quad (80)$$

Thus the dispersion of the material must be known in order to calculate the effects of group velocity mismatch. Clearly, the effect is more severe at higher frequencies approaching absorption bands (e.g., doubling visible pulses into the UV region). For example, consider a 1 ps pulse propagating in KDP. At 1064 nm $L_v = 3$ cm, while $L_v = 0.3$ cm at 532 nm [2].

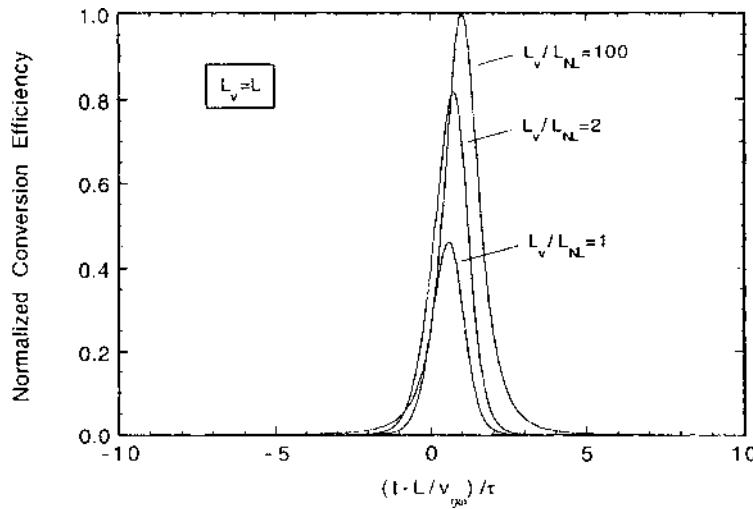


Figure 32 Normalized SHG conversion efficiency as a function of retarded time for various values of the ratio of pulse separation length (L_v) to nonlinear interaction length (L_{NL}) in the short pulse regime.

For pulse widths ≤ 1 ps, the effects of dispersive pulse spreading must also be considered. Pulse spreading occurs because the different frequencies comprising the quasi-monochromatic pulse travel at different phase velocities. This reduces the peak power of the fundamental pulse, reducing the conversion efficiency. The relevant length scale is

$$L_{\text{dis}} = 2\tau^2 \left[\left(\frac{\partial^2 k}{\partial \omega^2} \right)_{\omega=\omega_0} \right]^{-1} \quad (81)$$

where ω_0 is the center frequency of the fundamental pulse. When $L > L_{\text{dis}}$, the effects of dispersive pulse spreading become significant. In general, the full time dependent wave equations then need to be solved numerically to estimate the conversion efficiency.

E. Diffraction Effects

Although diffraction was considered earlier in Sections B and C, it was done within the context of the paraxial approximation of Gaussian beam optics. These approximations are good when the laser spot size is a few to several wavelengths in diameter. However, in far-IR DFG it is possible to generate wavelengths $\lambda_d \sim w_0$, where w_0 is the radius of the pump beams. This can lead to severe diffraction effects that are not accounted for in the paraxial theory.

The wave equation cannot be solved in the usual manner. A general approach is the Green's function solution of the nonlinear inhomogeneous wave equation [2,12]. Boundary effects are neglected (e.g., by assuming the nonlinear crystal to be immersed in a linear index matching medium). The result for the field amplitude in the far-field approximation is

$$\mathbf{E}_d(\mathbf{r}) = K \left(\frac{\omega_d}{c} \right)^2 \int_V d^3 r' (1 - \hat{u}\hat{u}) \cdot \mathbf{P}_d^{(2)}(\mathbf{r}') \times \frac{\exp(i k_d |\mathbf{r} - \mathbf{r}'|)}{|\mathbf{r} - \mathbf{r}'|} \quad (82)$$

where \mathbf{r} is the far-field point, $\hat{u} = \mathbf{r}/|\mathbf{r}|$, the integration is over the interaction volume of the electromagnetic fields, and

$$K = \begin{cases} (4\pi\epsilon_0)^{-1} & \text{(SI)} \\ 1 & \text{(cgs)} \end{cases} \quad (83)$$

An order of magnitude estimate of the far-field intensity can be made by assuming the pump fields to be constant in the crystal within a cylinder of radius w_0 and zero elsewhere. Then the integration in Eq. (82) can be performed, with

the result

$$|\mathbf{E}_d(\mathbf{r})|^2 = \left\{ \begin{array}{ll} \epsilon_0^2 & (\text{SI}) \\ 1 & (\text{cgs}) \end{array} \right\} K^2 \left(\frac{\omega_d}{c} \right)^4 (4d_{\text{eff}})^2 |A_{p1}|^2 |A_{p2}|^2 L^2 \times \frac{(\pi w_0^2)^2}{r^2} \left(\frac{\sin \alpha}{\alpha} \right)^2 \left[\frac{2J_1(\beta)}{\beta} \right]^2 \quad (84)$$

where

$$\alpha = \frac{k_d L}{2} \left(1 + \frac{\Delta k}{k_d} - \cos \theta \right) \quad (85)$$

$$\Delta k = k_{p1} - k_{p2} - k_d \quad (86)$$

$$\beta = k_d w_0 \sin \theta \quad (87)$$

J_1 is the first order Bessel function of the first kind, and θ is the diffraction angle defined in Fig. 33. The far-IR difference-frequency power at the detector is then determined by

$$\mathcal{P}_d = \left\{ \begin{array}{ll} 2\epsilon_0 n_d c & (\text{SI}) \\ \frac{n_d c}{2\pi} & (\text{cgs}) \end{array} \right\} \times \int_0^{\theta_{\max}} |\mathbf{E}_d(\mathbf{r})|^2 2\pi r^2 \sin \theta d\theta \quad (88)$$

where θ_{\max} is the half-angle subtended by the detector at the nonlinear source.

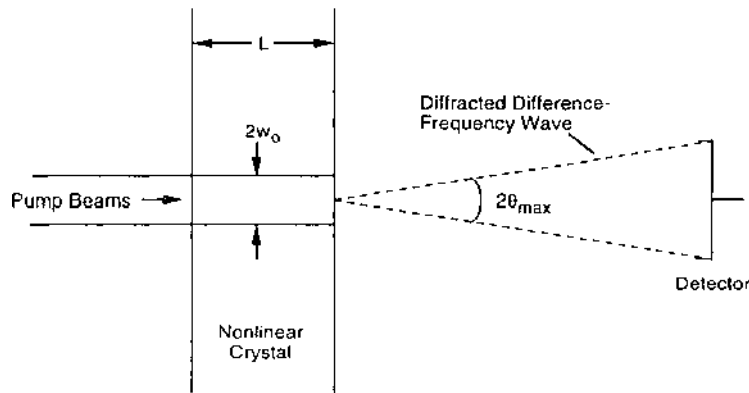


Figure 33 Schematic illustration of the diffracted difference-frequency beam for far-IR DFG in a nonlinear crystal. (Adapted from Ref. 2. John Wiley & Sons, Inc., Copyright © 1984, reprinted by permission.)

The α dependence in Eq. (84) gives the phase matching behavior of the output intensity, while the Bessel function term describes the usual diffraction pattern from a circular aperture. The ω^4 dependence is expected from long wavelength dipole radiation theory. This dependence drastically reduces the efficiency of far-IR production by DFG. Nevertheless, with intense laser pumps, the difference-frequency radiation can still be far more powerful than a blackbody source.

The index matching assumption stated above is rather simplistic. Actually, the refractive index in the far-IR can be quite large, and one must generally account for Fabry–Perot factors (multiple internal reflections) within the crystal [2].

The long wavelengths in the far-IR make the phase matching less angle sensitive, and phase matching is approximately satisfied over a fairly broad output cone. This cone can be substantially broadened outside the crystal through refraction at the boundary. Finally, absorption of far-IR radiation by the nonlinear crystal tends to weaken the far-IR generated by DFG. For more information, see the references given in Shen [2].

F. Incoherent Inputs

Up to this point all of the interactions described have been between coherent waves. It should be noted that in frequency mixing processes using quasi-cw pulses, frequency components comprising the pulses can beat together to generate new frequencies as well as optically rectified (i.e., $\omega = 0$) pulses. This is possible in the case of DFG with picosecond pulses.

It is also possible for one of the input fields in a frequency conversion process to be a cw incoherent field. Such an instance is found in the process of image up-conversion from the IR to the visible. An incoherent IR image field is mixed with a laser field to generate the image in the visible. The incoherent IR field has a spread in both temporal frequency ω and spatial frequency k .

The mathematical approach to analyzing this situation is to decompose the IR field into its spatial and temporal frequency Fourier components, assuming a spread in frequencies $\Delta\omega$ and Δk . However, the IR is assumed to be imaged at infinity so that Δk is small. Assume that the pump laser is a collimated, single mode TEM₀₀ beam. The pump interacts with each frequency component of the IR image independently to generate visible frequencies by SFG. As illustrated in Fig. 34, each IR wave vector interacts with the pump wave vector and produces phase matching at some angle, with

$$\frac{\sin\theta'}{\sin\theta} \approx \frac{\theta'}{\theta} = \frac{k_s}{k_{\text{IR}}} \quad (89)$$

where the angles are defined in the figure. Each sum-frequency wave so generated

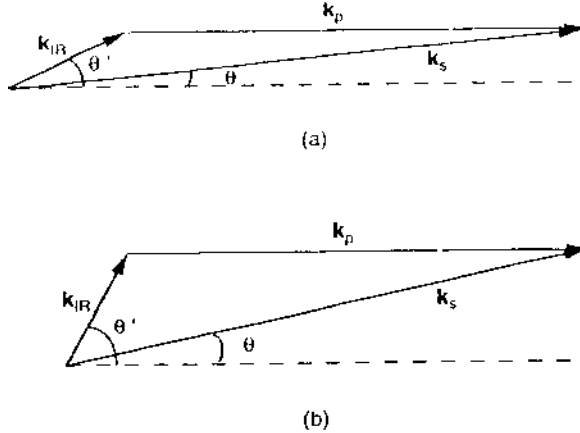


Figure 34 Illustration of phase matching in up-conversion of an incoherent IR image to a visible image by SFG using a monochromatic collimated visible laser beam. (a) and (b) illustrate phase matching for two different IR wave vectors which, with several others, comprise the incoherent IR field.

is then summed (integrated) to obtain the net output wave amplitude [12]:

$$\begin{aligned} A_s &= \int A_s(\theta, \phi, \omega_s) \exp[i(\mathbf{k}_s \cdot \mathbf{r} - \omega_s t)] d\theta d\phi d\omega_s \\ &\propto A_p \int A_{IR}(\theta', \phi', \omega_{IR}) \exp[i(\mathbf{k}_p + \mathbf{k}_{IR}) \cdot \mathbf{r} \\ &\quad - (\omega_p + \omega_{IR})t] d\theta' d\phi' d\omega_{IR} \end{aligned} \quad (90)$$

where $\omega_s = \omega_p + \omega_{IR}$, $\theta = (k_{IR}/k_s)\theta'$, and $\phi = \phi'$. Thus the image is transferred to the visible region by the nonlinear process, but is demagnified. Any departure of the pump wave from a perfect plane wave will lead to image distortion.

V. FREQUENCY CONVERSION BY REFLECTION

In the previous sections boundary effects at the surfaces of the nonlinear medium were ignored, since the emphasis was on the generation of radiation at new frequencies in the bulk of the material. The optical power generated in the bulk is normally orders of magnitude larger than that generated at the surfaces. However, this is not true when the medium possesses inversion symmetry, since then the nonlinear polarization in the bulk is zero. Although the power generated at

the surfaces is weak, it turns out to be a useful tool for probing the structure and composition of a surface or the interface between two different materials. Boundary effects are also of concern when applying experimental techniques to measure the nonlinear susceptibility (see Chapter 4). This section deals with some of the important formulas concerning frequency conversion at the boundaries of materials.

A. Nonlinear Optics Laws of Reflection and Refraction

By way of example, SHG at the surface of a cubic medium is treated first. Figure 35 gives the geometry of the interaction, including definitions of angles and the laboratory coordinate system. Since the medium is cubic, only one refracted fundamental wave is considered. The theory can be extended to crystals of lower symmetry [34]. The unprimed parameters refer to those in the medium from which the fundamental wave is incident on the crystal, and the primed parameters are those in the nonlinear medium. Reflection at the back surface of the crystal is not considered, since only the interaction at the front surface is of

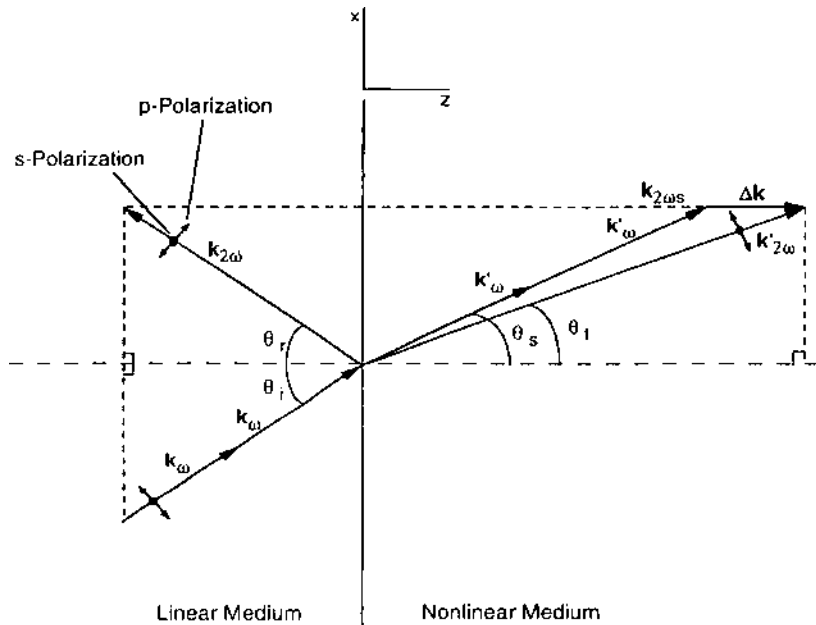


Figure 35 Schematic of the wave vectors for SHG at the boundary between a linear medium and a nonlinear medium illustrating the boundary conditions that lead to the nonlinear Snell's law.

interest here. The subscript s refers to the nonlinear polarization source, and $\mathbf{k}_{2\omega} = 2\mathbf{k}'_{\omega}$.

The laws of electrodynamics require that the tangential components of an electric field be continuous across a boundary. From Fig. 35, this means that the x -components of the wave vectors at the two frequencies on either side of the front surface are equal. This leads directly to the nonlinear form of Snell's law, and corresponding formulas are given in Table 42. Notice that θ_s is the angle of refraction of the fundamental wave. Thus for a given angle of incidence of the fundamental, the directions of propagation for the nonlinear polarization source wave and the generated second harmonic wave in the nonlinear medium are determined. These waves do not in general travel in the same direction.

The nonlinear polarization source will also radiate a reflected second harmonic wave. In a vacuum, $n_{2\omega} = n_{\omega}$ and the reflected second harmonic will then propagate collinearly with the reflected fundamental. This is approximately true if the medium of incidence is air.

Bloembergen and Pershan [35] were the first to calculate the form of the second harmonic reflected and transmitted wave amplitudes. The usual slowly varying amplitude approximation cannot be used in this situation, and for nonnormal incidence the polarization of the fundamental wave must be specified. The form of the reflected harmonic wave is different for polarization in the plane of incidence and perpendicular to the plane of incidence.

The wave equation in the form

$$\nabla \times \nabla \times \mathbf{E}^{(\sim)} + \left(\frac{n_{\alpha}}{c} \right)^2 \frac{\partial^2 \mathbf{E}^{(\sim)}}{\partial t^2} = - \frac{1}{\epsilon_0 c^2} \frac{\partial^2 \mathbf{P}_{NL}^{(\sim)}}{\partial t^2} \quad (91)$$

(in SI units) for the second harmonic field is solved assuming that the nonlinear polarization amplitude is constant (nondepleted pump approximation). The most general solution consists of the sum of a solution to the homogeneous wave equation, where the nonlinear source term is zero, and a particular solution of the inhomogeneous wave equation. These are the so-called "free" and "bound" waves, respectively. The bound wave solution is further simplified using Gauss' law $\nabla \cdot \mathbf{D}^{(\sim)} = 0$, which applies when there are no free charges in the medium ($\mathbf{D}^{(\sim)}$ is the displacement field at the second harmonic frequency).

The solutions for the transmitted and reflected second harmonic complex wave amplitudes are given in Table 43. These apply for a given angle of

Table 42 Nonlinear Snell's Law for SHG

$n_{\omega} \sin \theta_i = n'_{\omega} \sin \theta_s$	$n'_{\omega} \sin \theta_s = n'_{2\omega} \sin \theta_t$
$n_{2\omega} \sin \theta_r = n'_{\omega} \sin \theta_s$	$n_{2\omega} \sin \theta_r = n_{\omega} \sin \theta_i$
$\theta_r = \theta_i$ in a vacuum	

Table 43 Complex Electric Field Amplitudes for SHG at a Boundary

Nonlinear source polarization \perp plane of incidence
<p><i>Reflected wave</i></p> $\mathbf{E}_{2\omega r}^{(s)} = \hat{y}K \left(\frac{n'_{2\omega} \cos\theta_i - n'_\omega \cos\theta_s}{n'_{2\omega} \cos\theta_i + n_{2\omega} \cos\theta} \right) \frac{P_{2\omega}^{(2)}}{(n'_\omega)^2 - (n'_{2\omega})^2} \exp(i\mathbf{k}_{2\omega} \cdot \mathbf{r})$ <p><i>Transmitted wave</i></p> $\mathbf{E}_{2\omega t}^{(s)} = \hat{y}K \frac{P_{2\omega}^{(2)}}{(n'_\omega)^2 - (n'_{2\omega})^2} \left(-\frac{n_{2\omega} \cos\theta_i + n'_\omega \cos\theta_s}{n'_{2\omega} \cos\theta_i + n_{2\omega} \cos\theta_i} + \exp(i\Delta\mathbf{k} \cdot \mathbf{r}) \right) \exp(i\mathbf{k}'_{2\omega} \cdot \mathbf{r})$
Nonlinear source polarization \parallel plane of incidence
<p><i>Reflected wave</i></p> $\mathbf{E}_{2\omega r}^{(p)} = -K(\hat{x} \cos\theta_i + \hat{z} \sin\theta_i)$ $\times \frac{P_{2\omega}^{(2)}}{(n'_\omega)^2 - (n'_{2\omega})^2} \left[\frac{n'_{2\omega}}{n_{2\omega}} \beta + \frac{n'_\omega}{n_{2\omega}} (p_x \cos\theta_s - p_z \sin\theta_s) \right] \exp(i\mathbf{k}_{2\omega} \cdot \mathbf{r})$ <p><i>Transmitted wave</i></p> $\mathbf{E}_{2\omega t}^{(p)} = K \frac{P_{2\omega}^{(2)}}{(n'_\omega)^2 - (n'_{2\omega})^2} [-\beta \hat{e}_t + \hat{e}_s \exp(i\Delta\mathbf{k} \cdot \mathbf{r})] \exp(i\mathbf{k}'_{2\omega} \cdot \mathbf{r})$
$K = \begin{cases} \epsilon_0^{-1} & (\text{SI}) \\ 4\pi & (\text{cgs}) \end{cases}$ $\beta = \frac{n_{2\omega} \left[p_x - \left(\frac{n'_\omega}{n'_{2\omega}} \right)^2 \sin\theta_s (p_x \sin\theta_s + p_z \cos\theta_s) \right] + n'_\omega \cos\theta_i (p_x \cos\theta_s - p_z \sin\theta_s)}{n_{2\omega} \cos\theta_i + n'_{2\omega} \cos\theta_i}$ $p_x = \hat{x} \cdot \hat{p}, \quad p_z = \hat{z} \cdot \hat{p}$ <p>\hat{p} = unit vector along direction of $\mathbf{P}_{2\omega}^{(2)}$ \hat{e}_t = unit vector along direction of $\mathbf{E}_{2\omega t}^{(p)}$ (freewave) \hat{e}_s = unit vector along direction of $\mathbf{E}_{2\omega s}^{(p)}$ (bound wave)</p> $\hat{e}_s = \hat{p} - \frac{\mathbf{k}'_{2\omega s} (\mathbf{k}'_{2\omega s} \cdot \hat{p})}{(k'_{2\omega s})^2}$

incidence of the fundamental wave and for the nonlinear polarization source parallel or perpendicular to the plane of incidence. The various angles used in these formulas can be computed in terms of the angle of incidence by the nonlinear Snell's law.

The nonlinear polarization source will in general depend on the properties of the surface and bulk, and it may be necessary to include higher order nonlinear terms in the bulk if the medium is centrosymmetric.

Physically, the reflected second harmonic can be understood as the field radiated back into the incident medium by a coherent array of nonlinear oscillating dipoles in a slab $\sim \lambda/2\pi$ thick near the surface of the nonlinear medium. Further details of the transmitted wave will be given in Chapter 4, where characterization of the second order nonlinear susceptibility using the Maker fringe technique is discussed.

The nonlinear form of Snell's law can easily be generalized to the case of frequency mixing. The wave vector diagram shown in Fig. 35 is modified to include pump waves at different frequencies. These waves can also travel in different directions. The nonlinear polarization source wave vector and reflected and transmitted signal wave vectors would be analogous to those of SHG shown in the figure. The formulas for the nonlinear Snell's law in the frequency mixing case are given in Table 44.

Bloembergen and Pershan give the reflected *p*-polarized field amplitude generated by SFG, when the nonlinear polarization source is parallel to the plane of incidence, in terms of the angle α between this source vector and its direction of propagation \mathbf{k}_s :

$$A_{\text{SFG}(p\text{-polarized}),r} \propto \sin(\alpha + \theta_t + \theta_s) \quad (92)$$

Thus there is no reflected wave when $\theta_t = 180^\circ - \theta_s - \alpha$. This defines the nonlinear Brewster angle, determined in the medium of incidence through the nonlinear Snell's law. This implies that the nonlinear polarization source vector is oscillating in a direction such that it cannot radiate a reflected wave in the direction θ_r .

B. Surface Nonlinear Optics

The techniques of SHG and SFG by reflection have been developed as measurement probes of surfaces and interfaces. Many of the tools for surface

Table 44 Nonlinear Snell's Law for Frequency Mixing

$\frac{n_a}{\lambda_a} \sin \theta_{ai} + \frac{n_b}{\lambda_b} \sin \theta_{bi} = \left(\frac{n'_a}{\lambda_a} + \frac{n'_b}{\lambda_b} \right) \sin \theta_{cs}$	$\left(\frac{n'_a}{\lambda_a} + \frac{n'_b}{\lambda_b} \right) \sin \theta_{cs} = \frac{n'_a}{\lambda_a} \sin \theta_{at} + \frac{n'_b}{\lambda_b} \sin \theta_{bt}$
$\frac{n_c}{\lambda_c} \sin \theta_{cr} = \left(\frac{n'_a}{\lambda_a} + \frac{n'_b}{\lambda_b} \right) \sin \theta_{cs}$	$\frac{n_c}{\lambda_c} \sin \theta_{cr} = \frac{n_a}{\lambda_a} \sin \theta_{ai} + \frac{n_b}{\lambda_b} \sin \theta_{bi}$
SFG: $a = p1, b = p2, c = s$	DFG: $a = p1, b = p2, c = d$

analysis have limitations. For example, electron scattering and diffraction, photoemission, Auger spectrometry, and mass spectrometry must be performed in a vacuum. Surface SHG and SFG can be performed at atmospheric pressure under ambient conditions. Thus even liquid–air, liquid–solid, and liquid–liquid interfaces can be probed.

SHG by reflection is particularly useful as a surface probe when the bulk materials are centrosymmetric and hence do not allow SHG (in the electric dipole approximation). At an interface, the inversion symmetry is broken, allowing SHG. Thus SHG by reflection is highly surface specific.

Surface SHG has several attractive features. It is a highly directional optical probe, since it is excited by a coherent laser source. Therefore it is suitable for nondestructive, *in situ* remote sensing studies and can be used for real-time surface monitoring in extreme environments. With ultrashort laser pulses, it has the potential for *in situ* probing of fast surface dynamics and chemical reactions with subpicosecond time resolution. Because the laser excitation of a surface can be performed with high spatial and spectral resolution, surface SHG also allows *in situ* mapping of molecular arrangement and composition of surface molecular monolayers.

Since it is the reflected optical power, and not the reflected field amplitude, that is measured experimentally, a theoretical expression for this quantity is desired. Bloembergen and Pershan [35] were the first to consider this theoretically. They calculated the reflected second harmonic wave generated in multiple reflections in a nonlinear slab. Surface effects were then modeled by taking the limit of a thin slab of thickness small compared to a wavelength. Heinz [36] and later Mizarahi and Sipe [37] developed simplified formulas using phenomenological models in which the surface is treated as an infinitesimally thin dipole sheet. Mizarahi and Sipe considered four separate experimental geometries, including two of interest to SHG by reflection: one in which light is incident on the surface from the air (or vacuum), and one in which the light is incident from the substrate. The form of the equation for the reflected second harmonic power is the same for either case and is given in Table 45.

The reflected second harmonic power is angle and polarization dependent and is given in terms of a surface nonlinear susceptibility. The effective susceptibility is a contraction of the second order surface susceptibility tensor. It is a function of the angle of incidence as well as Fresnel transmission and reflection coefficients and the input and output polarizations. In general, measurements of the reflected second harmonic power as a function of incident fundamental angle and input/output polarization will yield information about the surface susceptibility tensor and hence the properties of the surface.

Table 45 Formulas for Reflected Second Harmonic Power from a Surface Due to a Fundamental Wave Incident From a Vacuum

$\frac{\mathcal{P}_{2\omega r}}{\mathcal{P}_{\omega i}} = \frac{2\pi^2}{\epsilon_0 c \lambda_{\omega}^2} I_{\omega i} \sec^2 \theta_i \mathbf{e}_{2\omega} \cdot \chi_s^{(2)} : \mathbf{e}_{\omega} \mathbf{e}_{\omega} ^2$	(SI)
$\frac{\mathcal{P}_{2\omega r}}{\mathcal{P}_{\omega i}} = \frac{128\pi^5}{c \lambda_{\omega}^2} I_{\omega i} \sec^2 \theta_i \mathbf{e}_{2\omega} \cdot \chi_s^{(2)} : \mathbf{e}_{\omega} \mathbf{e}_{\omega} ^2$	(cgs)
<hr/>	
$\mathbf{e}_{\omega} = (\hat{y} t_{\omega}^s \hat{y} + \hat{p}_- t_{\omega}^p \hat{p}_{0-}) \cdot \hat{e}_i$	
$\mathbf{e}_{2\omega} = [\hat{y}(1 + r_{2\omega}^s) \hat{y} + \hat{P}_{0+}(\hat{P}_{0+} + r_{2\omega}^p \hat{P}_{0-})] \cdot \hat{e}_r$	
$t_{\omega}^s = \frac{2\cos\theta_i}{\cos\theta_i + n_{\omega}\cos\theta_t}$	$t_{\omega}^p = \frac{2n_{\omega}\cos\theta_i}{n_{\omega}\cos\theta_i + \cos\theta_t}$
$r_{2\omega}^s = \frac{\cos\theta_i - n_{2\omega}\cos\theta_t}{\cos\theta_i + n_{2\omega}\cos\theta_t}$	$r_{2\omega}^p = \frac{n_{2\omega}\cos\theta_i - \cos\theta_t}{n_{2\omega}\cos\theta_i + \cos\theta_t}$
$\hat{p}_- = \hat{z}\sin\theta_t - \hat{x}\cos\theta_t$	$\hat{p}_{0-} = \hat{z}\sin\theta_i - \hat{x}\cos\theta_i$
$\hat{P}_{0+} = \hat{z}\sin\theta_i + \hat{x}\cos\theta_i$	$\hat{P}_{0-} = \hat{z}\sin\theta_i - \hat{x}\cos\theta_i$
\hat{e}_i = unit polarization vector of incident fundamental wave	
\hat{e}_r = unit polarization vector of reflected second harmonic wave	

xz is the plane of incidence, and y is perpendicular to the plane of incidence.

For example, the surface susceptibility for a monolayer, or partial monolayer, of rod-shaped molecules adsorbed on a surface is given by [38]

$$(\chi_s^{(2)})_{zzz} = N_s \beta_{zzz} \langle \cos^3 \theta_a \rangle \quad (93)$$

$$(\chi_s^{(2)})_{zxx} = (\chi_s^{(2)})_{zyy} = \frac{1}{2} N_s \beta_{zzz} \langle \sin^2 \theta_a \cos \theta_a \rangle$$

where N_s is the surface density of molecules (number per unit area), θ_a is the anchoring angle on the surface (with respect to the surface normal), and angular brackets denote an orientational average. The dominant component of the molecular hyperpolarizability tensor (see Chapter 4) is β_{zzz} , where the Z-axis is along the long axis of the molecule (molecular coordinates).

When the fundamental or second harmonic frequency is close to an energy transition of the molecule, the detected signal can be particularly strong due to a resonant enhancement of the hyperpolarizability tensor. Thus with a tunable laser, surface spectroscopy studies of electronic transitions in the visible can be performed.

To study adsorbed molecules selectively, however, infrared vibrational spectra are more useful. Since an appropriate photomultiplier tube for measuring

the weak IR signal is unavailable, the technique of up-conversion using SFG can be used. One of the incident laser frequencies is in the visible, and the other is from a tunable IR laser. The reflected sum-frequency signal is thus in the visible and readily detectable with a photomultiplier tube. The formula for the detected power will be the SFG analog of that given in Table 45.

Several examples of nonlinear optical probes in surface science can be cited. For SHG, some are the study of oxygen adsorbed on a polycrystalline silver surface [39], vicinal steps on clean aluminum surfaces [40], dynamical screening of free electrons at the surface of a rubidium film on silver [41], determination of the pK_a of *p*-hexadecyl aniline at an air–water interface [42], and the determination of surface adsorbate geometries for a system of rhodamine *B* absorbed on quartz [43].

Some examples of the use of surface SFG include the study of IR spectra from CO adsorbed on Ni(100) [44], thiol adsorbed on polycrystalline gold from solution [45], real-time growth of a polyamic acid film by chemical vapor deposition [45], hydrogen adsorbed on diamond C(111) [45], methanol reactions on Ni(100) [46], carbon monoxide and cyanide adsorbed on a platinum electrode [47], a silver–aqueous electrolyte interface [48], and hydrogen adsorbed on Si(111) [49].

Shen [38] gives several examples of surface nonlinear optical studies of metal surfaces, semiconductor surfaces, liquid–solid interfaces, electrochemistry, gas–liquid interfaces, biological systems, and surface monolayer microscopy.

REFERENCES

1. P. A. Franken, A. E. Hill, C. W. Peters, and G. Weinreich, Generation of optical harmonics, *Phys. Rev. Lett.* 7:118 (1961).
2. Y. R. Shen, *The Principles of Nonlinear Optics*, John Wiley, New York, 1984.
3. J. A. Armstrong, N. Bloembergen, J. Ducuing, and P. S. Pershan, Interactions between light waves in a nonlinear dielectric, *Phys. Rev.* 127:1918 (1962).
4. P. F. Byrd and M. D. Friedman, *Handbook of Elliptic Integrals for Engineers and Scientists*, Springer-Verlag, New York, 1971.
5. W. H. Press, B. P. Flannery, S. A. Teukolsky, and W. T. Vetterling, *Numerical Recipes*, Cambridge Univ. Press, New York, 1986.
6. *Mathcad® 3.1* (Numerical Methods Applications Pack), MathSoft, Inc., Cambridge, Mass., 1992.
7. A. Yariv, *Quantum Electronics*, 3rd ed., John Wiley, New York, 1989, p. 395.
8. D. N. Nikogosyan and G. G. Gurzadyan, New formulas for the calculation of phase-matching angles, *Sov. J. Quantum Electron.* 16:1663 (1986).
9. M. V. Hobden, Phase-matched second harmonic generation in biaxial crystals, *J. Appl. Phys.* 38:4365 (1967).

10. D. Yu. Stepanov, V. D. Shigorin, and G. P. Shipulo, Phase-matching directions in optical mixing in biaxial crystals having quadratic susceptibility, *Sov. J. Quantum Electron.* 14:1315 (1984).
11. S. K. Kurtz, Measurement of nonlinear optical susceptibilities, *Quantum Electronics*, Vol I, Part A (H. Rabin and C. L. Tang, eds), Academic Press, New York, 1975, p. 243.
12. F. Zernike and J. E. Midwinter, *Applied Nonlinear Optics*, John Wiley, New York, 1973.
13. D. N. Nikogosyan and G. G. Gurzadyan, Crystals for nonlinear optics, *Sov. J. Quantum Electron.* 17:970 (1987).
14. H. Ito, H. Naito, and H. Inaba, New phase-matchable nonlinear optical crystals of the formate family, *IEEE J. Quantum Electron.* QE-10:247 (1974).
15. V. G. Dmitriev, G. G. Gurzadyan, and D. N. Nikogosyan, *Handbook of Nonlinear Optical Crystals*, Springer-Verlag, New York, 1991, p. 24.
16. J. D. McMullen, Optical parametric interactions in isotropic materials using a phase-corrected stack of nonlinear dielectric plates, *J. Appl. Phys.* 46:3076 (1975).
17. A. Szilagyi, A. Hordvik, and H. Schlossberg, A quasi-phase-matching technique for efficient optical mixing and frequency doubling, *J. Appl. Phys.* 47:2025 (1976).
18. K. C. Rustagi, S. C. Mehenale, and S. Meenakshi, Optical frequency conversion in quasi-phase-matched stacks of nonlinear crystals, *IEEE J. Quantum Electron.* QE-18:1029 (1982).
19. M. M. Fejer, G. A. Magel, and E. J. Lim, Quasi-phase-matched interactions in lithium niobate, *Proceedings of SPIE*, Vol 1148, 1989, pp. 213–224.
20. M. S. Piltch, C. D. Cantrell, and R. C. Sze, Infrared second harmonic generation in nonbirefringent cadmium telluride, *J. Appl. Phys.* 47:3514 (1976).
21. D. E. Thompson, J. D. McMullen, and D. B. Anderson, Second harmonic generation in GaAs “stack of plates” using high power CO₂ laser radiation, *Appl. Phys. Lett.* 29:113 (1976).
22. M. Okada, K. Takizawa, and S. Ieiri, Second harmonic generation by periodic laminar structure of nonlinear optical crystal, *Opt. Comm.* 18:331 (1976).
23. J. Webjörn, F. Laurell, and G. Arvidsson, Fabrication of periodically domain-inverted channel waveguides in lithium niobate for second harmonic generation, *J. Lightwave Tech.* 7:1597 (1989).
24. M. Fujimura, K. Kintaka, T. Suhara, and H. Nishihara, Blue light generation in LiNbO₃ waveguide SHG device with first-order domain-inverted grating formed by EB scanning, *Electron. Lett.* 28:1868 (1992).
25. H. Ito, C. Takyu, and H. Inaba, Fabrication of periodic domain grating in LiNbO₃ by electron beam writing for applications of nonlinear optical processes, *Electron. Lett.* 27:1221 (1991).
26. G. A. Magel, M. M. Fejer, and R. L. Buyer, Quasi-phase-matched second harmonic generation of blue light in periodically poled LiNbO₃, *Appl. Phys. Lett.* 56:108 (1990).
27. C. J. van der Poel, J. D. Bierlein, and J. B. Brown, Efficient type I blue second harmonic generation in periodically segmented KTiOPO₄ waveguides, *Appl. Phys. Lett.* 57:2074 (1990).

28. M. Yamada, N. Nada, M. Saitoh, and K. Watanabe, First-order quasi-phase-matched LiNbO₃ waveguide periodically poled by applying an external field for efficient blue second harmonic generation, *Appl. Phys. Lett.* 62:435 (1993).
29. K. Mizuuchi and K. Yamamoto, Highly efficient quasi-phase-matched second harmonic generation using a first-order periodically domain-inverted LiTaO₃ waveguide, *Appl. Phys. Lett.* 60:1283 (1992).
30. K. Chikuma and S. Umegaki, Characteristics of optical second harmonic generation due to Čerenkov-radiation-type phase-matching, *J. Opt. Soc. Am. B*7:768 (1990).
31. M. J. Li, M. de Micheli, Q. He, and D. B. Ostrowsky, Čerenkov configuration second harmonic generation in proton-exchanged lithium niobate guides, *IEEE J. Quantum Electron.* QE-26:1384 (1990).
32. G. D. Boyd and D. A. Kleinman, Parametric interactions of focused gaussian light beams, *J. Appl. Phys.* 39:3597 (1968).
33. S. A. Akhmanov, A. S. Chirkin, K. N. Drabovich, A. I. Kovrigin, R. V. Khokhov, and A. P. Sukhorukov, Nonstationary nonlinear optical effects and ultrashort light pulse formation, *IEEE J. Quantum Electron.* QE-4:598 (1968).
34. P. Pavlides and D. Pugh, General theory of maker fringes in crystals of low symmetry, *J. Phys.: Condensed Matter* 3:967 (1991).
35. N. Bloembergen and P. S. Pershan, Light waves at the boundary of nonlinear media, *Phys. Rev.* 128:606 (1962).
36. T. F. Heinz, Ph. D. dissertation, University of California, Berkeley, Ca, 1982.
37. V. Mizarhi, and J. E. Sipe, Phenomenological treatment of surface second harmonic generation, *J. Opt. Soc. Am. B*5:660 (1988).
38. Y. R. Shen, Surface properties probed by second harmonic and sum-frequency generation, *Nature* 337:519 (1989).
39. L. Le, L. Yanghua, Y. Gongda, W. Wencheng, and Z. Zhiming, Optical second harmonic Generation study of oxygen adsorption on a polycrystalline Ag surface, *Phys. Rev. B* 40:10,100 (1989).
40. S. Janz, D. S. Bottomley, and H. M. van Driel, Influence of steps on second harmonic generation from vicinal metal surfaces, *Phys. Rev. Lett.* 66:1201 (1991).
41. K. J. Song, D. Heskett, H. L. Dai, A. Liebsch, and E. W. Plummer, Dynamical screening at a metal surface probed by second harmonic generation, *Phys. Rev. Lett.* 61:1380 (1988).
42. X. Zhao, S. Subrahmanyam, and K. B. Eisenthal, Determination of pK_a at the air/water interface by second harmonic generation, *Chem. Phys. Lett.* 171:558 (1990).
43. E. S. Peterson and C. B. Harris, A new technique for the determination of surface adsorbate geometries utilizing second harmonic generation and absorption band shifts, *J. Chem. Phys.* 91:2683 (1989).
44. J. Mirogliotta, R. S. Polizotti, P. Rabinowitz, S. D. Cameron, and R. B. Hall, Infrared-visible sum-frequency generation spectra of CO on Ni(100), *Appl. Phys.* A51:221 (1990).
45. M. Buck, Organic chemistry at interfaces studied by optical second harmonic and IR-vis sum-frequency generation, *Appl. Phys.* A55:395 (1992).

46. J. Mirogliotta, R. S. Polizotti, P. Rabinowitz, S. D. Cameron, and R. B. Hall, Infrared-visible sum-frequency generation study of methanol adsorption and reaction on Ni(100), *Chem. Phys.* 143:123 (1990).
47. P. Guyot-Sionnest and A. Tadjeddine, Spectroscopic investigations of adsorbates at the metal–electrolyte interface using sum-frequency generation, *Chem. Phys. Lett.* 172:341 (1990).
48. H. M. Rojhantab and G. L. Richmond, Characterization of the silver/aqueous electrolyte interface by optical second harmonic generation and differential capacitance, *J. Phys. Chem.* 93:3269 (1989).
49. P. Guyot-Sionnest, P. Dumas, and Y. J. Chabal, Lifetime of an adsorbate–substrate vibration by sum-frequency generation: H on Si(111), *J. Electron. Spectr. and Related Phenom.* 54/55:27 (1990).
50. V. G. Dmitriev and D. N. Nikogosyan, Effective nonlinearity coefficients for three-wave interactions in biaxial crystals of *mm2* point group symmetry, *Opt. Comm.* 95:173 (1993).
51. V. G. Dmitriev, G. G. Gurzadyan, and D. N. Nikogosyan, *Handbook of Nonlinear Optical Crystals*, 2nd ed., Springer-Verlag, New York, 1997, pp. 28–33.
52. M. H. Chou, K. R. Parameswaran, and M. M. Fejer, Multiple-channel wavelength conversion by use of engineered quasi-phase-matching structures in LiNbO₃ waveguides, *Opt. Lett.* 24:1157 (1999).
53. S. Wang, V. Pasiskevicius, J. Hellström, and F. Laurell, First-order type II quasi-phase-matched UV generation in periodically poled KTP, *Opt. Lett.* 24:978 (1999).
54. P. Loza-Alvarez, D. T. Reid, P. Faller, M. Ebrahimzadeh, and W. Sibbett, Simultaneous second-harmonic generation and femtosecond-pulse compression in aperiodically poled KTiOPO₄ with a RbTiOAsO₄-based optical parametric oscillator, *J. Opt. Soc. Am. B* 16:1553 (1999).
55. W. R. Bosenberg, J. I. Alexander, L. E. Myers, and R. W. Wallace, 2.5-W, continuous-wave, 629-nm solid-state laser source, *Opt. Lett.* 23:207 (1998).
56. J.-P. Meyn, M. E. Klein, D. Woll, R. Wallenstein, and D. Rytz, Periodically poled potassium niobate for second-harmonic generation at 463 nm, *Opt. Lett.* 24:1154 (1999).
57. H. Karlsson, F. Laurell, and L. K. Cheng, Periodic poling of RbTiOPO₄ for quasi-phase-matched blue light generation, *Appl. Phys. Lett.* 74:1519 (1999).
58. D. Taverner, P. Britton, P. G. R. Smith, D. J. Richardson, G. W. Ross, and D. C. Hanna, Highly efficient second-harmonic and sum-frequency generation of nanosecond pulses in a cascaded erbium-doped fiber:periodically poled lithium niobate source, *Opt. Lett.* 23:162 (1998).
59. K. Fradkin-Kashi, A. Arie, P. Urenski, and G. Rosenman, Mid-infrared difference-frequency generation in periodically poled KTiOAsO₄ and application to gas sensing, *Opt. Lett.* 25:743 (2000).
60. A. Otomo, G. I. Stegeman, M. C. Flipse, M. B. J. Diemeer, W. H. G. Horsthuis, and G. R. Möhlmann, Nonlinear contrawave mixing devices in poled-polymer waveguides, *J. Opt. Soc. Am. B* 15:759 (1998).

61. D. Zheng, L. A. Gordon, Y. S. Wu, R. S. Feigelson, M. M. Fejer, R. L. Byer, and K. L. Vodopyanov, 16- μm infrared generation by difference-frequency mixing in diffusion-bonded-stacked GaAs, *Opt. Lett.* 23:1010 (1998).
62. E. Lallier, M. Brevignon, and J. Lehoux, Efficient second-harmonic generation of a CO₂ laser with a quasi-phase-matched GaAs crystal, *Opt. Lett.* 23:1511 (1998).
63. L. Becouarn, E. Lallier, M. Brevignon, and J. Lehoux, Cascaded second-harmonic and sum-frequency generation of a CO₂ laser by use of a single quasi-phase-matched GaAs crystal, *Opt. Lett.* 23:1508 (1998).

3

Optical Parametric Generation, Amplification, and Oscillation

Several areas of research, such as spectroscopy, semiconductor analysis, photochemistry, and remote sensing, have need of a tunable coherent source of high-power or high-energy radiation. Rugged solid state devices are desired to replace tunable dye lasers to avoid, among other things, the handling of toxic materials and requisite changing of dyes due to their continual photodegradation. In addition, a wider tuning range, especially into the near- and far-infrared, is needed.

For three decades, the development of nonlinear optical parametric devices has held the promise of providing these qualities. In 1965, Giordmaine and Miller [1] built and demonstrated the first tunable optical parametric oscillator. After this pioneering effort, the 1960s witnessed rapid progress in the field. Chromatix introduced a commercial product early in the research and development cycle [2], but it did not remain on the market. The pace of the research slowed as new and better nonlinear materials came under development. Recently, with improvements in materials and laser pump sources, new commercial products have emerged, such as a high-energy nanosecond pulse source tunable from 400 to 2000 nm (Spectra-Physics MOPO-700 series) [3], a femtosecond pulse source tunable across the 1.3 to 1.5 μm telecommunications window (Spectra-Physics Opal) [4], and a device tunable further into the mid-IR, from 1.4–4.6 μm (Continuum Mirage 3000) [5].

As these devices find their way into new research and applications markets, new devices are continually under development. In addition, optical parametric generation is continuing to be exploited in fundamental research areas.

Parametric devices have been used to generate a nonclassical form of radiaton called squeezed light. Optical parametric generation has also been a key element in studying some fundamental properties of quantum mechanics, such as the observation of correlated quantum states.

In this chapter, the major formulas relating to the performance of optical parametric devices are summarized. Spontaneous parametric fluorescence, a quantum mechanical phenomenon key to the operation of optical parametric amplifiers and oscillators, is described first. Parametric gain is introduced and is used in the description of the optical parametric amplifier (OPA). Finally, the bulk of the chapter will be devoted to a discussion of the optical parametric oscillator (OPO). This includes formulas relating to threshold pump power or energy, optical power conversion efficiency, stability, and tuning.

I. PARAMETRIC FLUORESCENCE

Optical parametric generation (OPG) is illustrated schematically in Fig. 1. A photon of frequency ω_p is incident on a nonlinear medium and spontaneously splits into two lower-frequency (and hence lower-energy) photons. These are called the signal photon of frequency ω_s and the idler photon of frequency ω_i . To conserve energy, $\omega_p = \omega_s + \omega_i$. This phenomenon is somewhat analogous to spontaneous Raman or Brillouin scattering with the exceptions that both particles created in the scattering are photons and not, for example, phonons, and that no real material excitation is involved. The material rather acts as a catalyst, generating the new photons through the nonlinear polarization. Optical parametric generation is

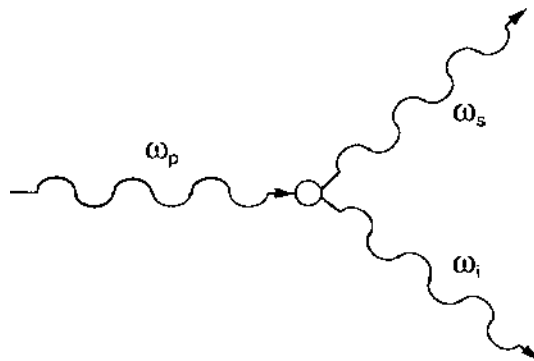


Figure 1 Spontaneous parametric fluorescence in which a pump photon of energy $\hbar\omega_p$ splits into two photons of energy $\hbar\omega_s$ (signal) and $\hbar\omega_i$ (idler).

a strictly quantum mechanical effect that was first predicted and studied by Louisell et al. [6].

Theoretically, parametric fluorescence is treated semiclassically [7,8]. The pump photons are associated with a strong laser field, which has a high photon number and can thus be treated as an approximately constant classical field. A quantized field approach is used for the signal and idler fields, which interact via a perturbation Hamiltonian, based on the second order susceptibility $\chi^{(2)}$, and includes the pump field. The average photon numbers for the signal and idler fields are then computed using first order perturbation theory.

The time dependent perturbation results for the average photon numbers are given in Table 1. It can be seen from these equations that the pump field drives the generation of signal and idler photons through the nonlinear polarization, and the number of signal and idler photons grows in time. An equivalent result exhibiting a spatial rather temporal dependence can be obtained by making the substitution $t \rightarrow (n_s n_i)^{1/2} z/c$.

Note that when there are no input signal or idler photons (i.e., $\langle n_s(0) \rangle = \langle n_i(0) \rangle = 0$), these photons are still generated due to the unity factors in the equations of Table 1. These are the spontaneous emission terms. These new packets of energy can be interpreted as being generated by the negative work performed by zero-point vacuum fluctuations of the signal and idler fields interacting with the nonlinear polarization. Effectively, these quantum fluctuations are equivalent to the presence of $\frac{1}{2}$ photon in both the signal and the idler modes at $t = 0$, or one photon in either mode.

The zero-point fluctuations, interacting with the pump field, produce a nonlinear polarization that attempts to radiate at all frequencies in all directions. The only restriction is that energy be conserved. However, the growth of optical radiation is favored by those frequencies and directions that approximately satisfy the phase matching condition introduced in Chapter 2 (i.e., $\Delta k \approx 0$).

Table 1 Formulas for Calculating Numbers of Signal and Idler Photons Produced in Parametric Fluorescence

Average signal photon number
$\langle n_s(t) \rangle = \langle n_s(0) \rangle \cosh^2(\frac{1}{2} G_0 t) + (1 + \langle n_i(0) \rangle) \sinh^2(\frac{1}{2} G_0 t)$
Average idler photon number
$\langle n_i(t) \rangle = \langle n_i(0) \rangle \cosh^2(\frac{1}{2} G_0 t) + (1 + \langle n_s(0) \rangle) \sinh^2(\frac{1}{2} G_0 t)$
Gain coefficient
$G_0 = 8\pi d_{\text{eff}} \sqrt{\frac{cI_p(0)}{2\epsilon_0 n_p n_s^2 n_i^2 \lambda_s \lambda_i}} \frac{\sin(\Delta k L/2)}{(\Delta k L/2)}$ (SI)
$G_0 = 32\pi^2 d_{\text{eff}} \sqrt{\frac{2\pi c I_p(0)}{n_p n_s^2 n_i^2 \lambda_s \lambda_i}} \frac{\sin(\Delta k L/2)}{(\Delta k L/2)}$ (cgs)

Modes that nearly satisfy this condition are amplified (stimulated emission) as shown by the equations in Table 1. The form of these equations is identical to those given in Chapter 2 for difference-frequency generation under the condition of equal photon fluxes for the pump 2 and difference-frequency waves. Thus, optical parametric generation is formally equivalent to DFG.

Two important experimental parameters in parametric fluorescence are the radiated signal power and bandwidth. Although conservation of energy permits any signal frequency from 0 to ω_p that could be radiated in any direction, the signal will peak at that frequency and direction that yields the best phase matching. The phase matching diagram is given in Fig. 2.

There are a finite number of blackbody modes in the vicinity of a particular frequency ω_{i0} that act as effective inputs for generating the signal power. One idler photon in each of these modes collectively comprises the incremental input idler intensity. The pump wave then mixes with all possible idler modes to generate the signal modes. A sum over all signal modes yields the net signal power generated [7–9].

A finite phase mismatch in the parametric fluorescence process is due to two sources: (1) a finite input bandwidth of frequencies $\Delta\omega = -(\omega_i - \omega_{i0}) = \omega_s - \omega_{s0}$, where the subscript 0 refers to that frequency for which there is perfect phase matching; (2) an angular spread in signal and idler wave vectors as shown in Fig. 2. The phase mismatch is given by

$$\Delta k = a\phi^2 - b\Delta\omega \quad (1)$$

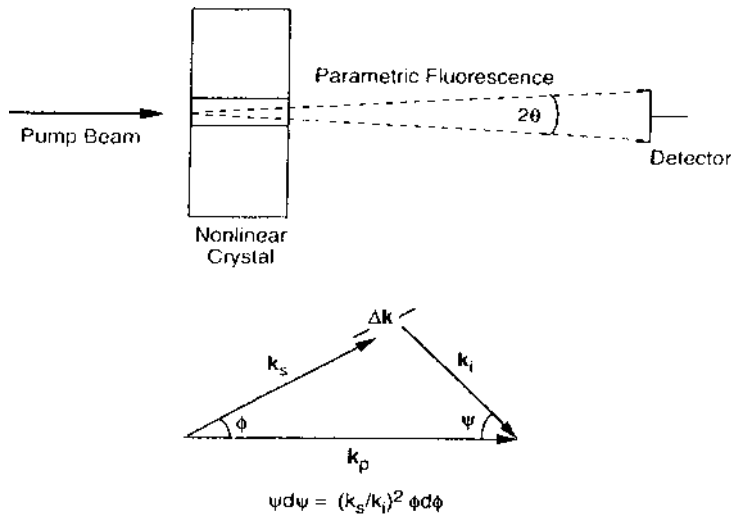


Figure 2 Optical parametric generation and signal power collection geometry.

where

$$a = \frac{k_s k_p}{2k_i} \quad (2)$$

and

$$b = \left(\frac{dk_s}{d\omega_s} \right)_{\omega_s=\omega_{s0}} - \left(\frac{dk_i}{d\omega_i} \right)_{\omega_i=\omega_{i0}} \quad (3)$$

The physical quantity of interest is the net signal power collected by the detector, which subtends an angle 2θ at the nonlinear crystal as shown in Fig. 2. (Instead of a detector, the geometry also applies to the aperture of a second nonlinear crystal serving as an OPA. See Sections II and VI.A below.) The results are given in Table 2. The net signal power is dependent on the pump power and the nonlinear coefficient d_{eff} , which was described in Chapter 2. The integrand contains the effects of the parametric gain coefficient g (see Section II below) and the phase mismatch.

For small gain, $(gL)^2 \ll (aL\Phi^2 - bL\Delta\omega)^2/4$, and therefore $\sinh \rightarrow \sin$. The spectral power distribution ($d\mathcal{P}_s/d\omega_s$) under this condition is also given in Table 2. Plots of this distribution are given in Fig. 3 (see [10] for experimental data). The fixed parameter in these plots is $\Phi = aL\theta^2$. To understand the meaning of this number, consider the case near degeneracy (i.e., $\omega_s = \omega_i = \omega_p/2$). Then from Eq. (2), $a \sim k_s$. Taking typical values of $k_s \sim 10,000 \text{ cm}^{-1}$ and $L \sim 1 \text{ cm}$, the values of Φ in Fig. 3 would correspond to $\theta \sim 10\text{--}50 \text{ mr}$ (i.e., $<0.1^\circ$ to $\sim 0.3^\circ$). For the parameter Δ , taking $b \sim 0.1/c$ and $L \sim 1 \text{ cm}$, $\Delta \sim \Delta\sigma$, where σ is the frequency in wave numbers (cm^{-1}). Therefore the abscissas of these plots can be read as approximately the frequency spread in cm^{-1} .

It can be seen that for small angles (e.g., $\Phi = 1$) the spectral distribution is peaked around the frequency corresponding to perfect phase matching along the pump beam axis and has the typical sinc^2 dependence with a bandwidth independent of angle, as shown in Table 2. For larger angles, this distribution grows and spreads, since more power is collected by the detector. As shown in Table 2, the bandwidth grows as θ^2 . For $\omega_s > \omega_i$, normal dispersion requires that $b > 0$. Therefore as θ increases, ω_s must increase for optimum phase matching, as illustrated in Fig. 2. If $\omega_s < \omega_i$, the opposite would be true.

For small gain, the integral over frequency can be performed [7–9]. The result, given in Table 2, shows that the signal power grows linearly with pump power and crystal length, and quadratically with collection angle.

The bandwidth, discussed above, is typically defined by the condition where the phase matching sinc^2 curve first crosses zero at $\Delta kL = 2\pi$ (see Fig. 3 in Chapter 2). Note that the bandwidth in Chapter 2 for frequency conversion processes was defined in terms of the full width at half maximum (FWHM) of

Table 2 Formulas Relating to the Total Signal Power Generated by Parametric Fluorescence and Collected by a Detector Subtending an Angle 2θ at the Nonlinear Crystal

Signal power collected in angle 2θ			
$\mathcal{P}_s = \beta \mathcal{P}_p L^2 \int_{-\infty}^{\infty} d\omega_s \int_0^\theta \frac{\sinh^2(\sqrt{g^2 - (a\phi^2 - b\Delta\omega)^2/4L})}{[g^2 - (a\phi^2 - b\Delta\omega)^2/4]L^2} \phi d\phi$			
$\beta = \frac{\hbar\omega_i\omega_s^4 n_s d_{\text{eff}}^2}{2\pi^2 \epsilon_0 n_i n_p c^5}$	(SI)	$\beta = \frac{8\pi\hbar\omega_i\omega_s^4 n_s d_{\text{eff}}^2}{n_i n_p c^5}$	(cgs)
$g^2 = \frac{2\omega_s \omega_i d_{\text{eff}}^2 I_p}{\epsilon_0 n_p n_s n_i c^3}$	(SI)	$g^2 = \frac{128\pi^3 \omega_s \omega_i d_{\text{eff}}^2 I_p}{n_p n_s n_i c^3}$	(cgs)
Signal power spectral distribution for small gain ($g^2 \ll (a\phi^2 - b\Delta\omega)^2/4$)			
$\frac{d\mathcal{P}_s}{d\omega_s} = \beta \mathcal{P}_p L^2 \int_0^\theta \frac{\sin^2[(aL\phi^2 - bL\Delta\omega)/2]}{[(aL\phi^2 - bL\Delta\omega)/2]^2} \phi d\phi$			
Small gain ($g^2 \ll (a\phi^2 - b\Delta\omega)^2/4$)			
Signal power			
$\mathcal{P}_s = \frac{\pi\beta L \mathcal{P}_p}{ b } \theta^2$			
Bandwidth			
$\Delta\omega_s = \frac{\pi}{ b L}$		small θ	
$\Delta\omega_s = \frac{a\theta^2}{ b }$		$\theta > \sqrt{2\pi/aL}$	
High gain ($g^2 \gg a\phi^2$)			
Signal power			
$\mathcal{P}_s = \text{numerical integration of formula above}$			
Bandwidth			
$\Delta\omega_s = \frac{2}{ b } \sqrt{\frac{2g}{L} \ln 2}$			

the sinc^2 curve. The reader should be aware that bandwidths are defined either way in other texts). For small gain and small angles, the bandwidth is angle independent, but it grows quadratically with collection angle for $\theta > (2\pi/aL)^{1/2}$.

For large gain ($g^2 \gg a\phi^2$), the integral must be solved numerically to determine the signal power. The bandwidth in this case is seen to be gain dependent [7]. Note that materials with low dispersion, such that the reciprocal group velocities of the signal and idler waves are nearly equal (i.e., b is small), will have large bandwidths. The bandwidth does not actually diverge, even at the degeneracy point, since higher-order group velocity dispersion terms come into play to limit the bandwidth (see Section III.C below).

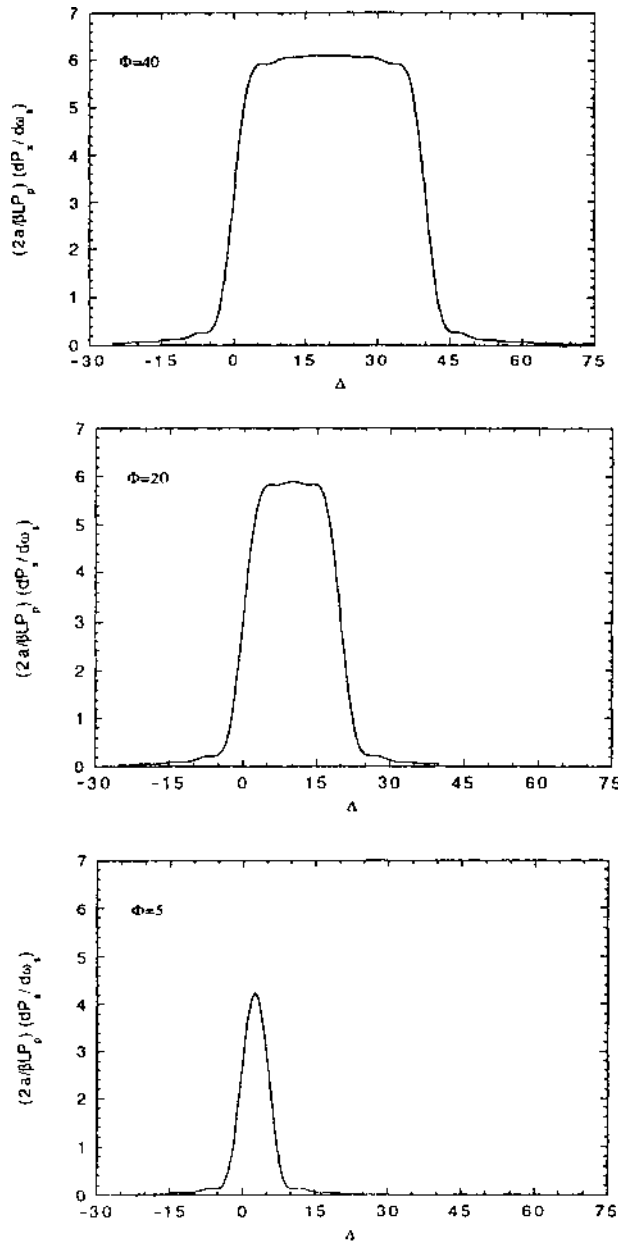


Figure 3 Normalized signal spectral power distribution as a function of normalized frequency shift Δ from the on-pump-axis perfectly phase matched frequency for several normalized detector collection angles Φ .

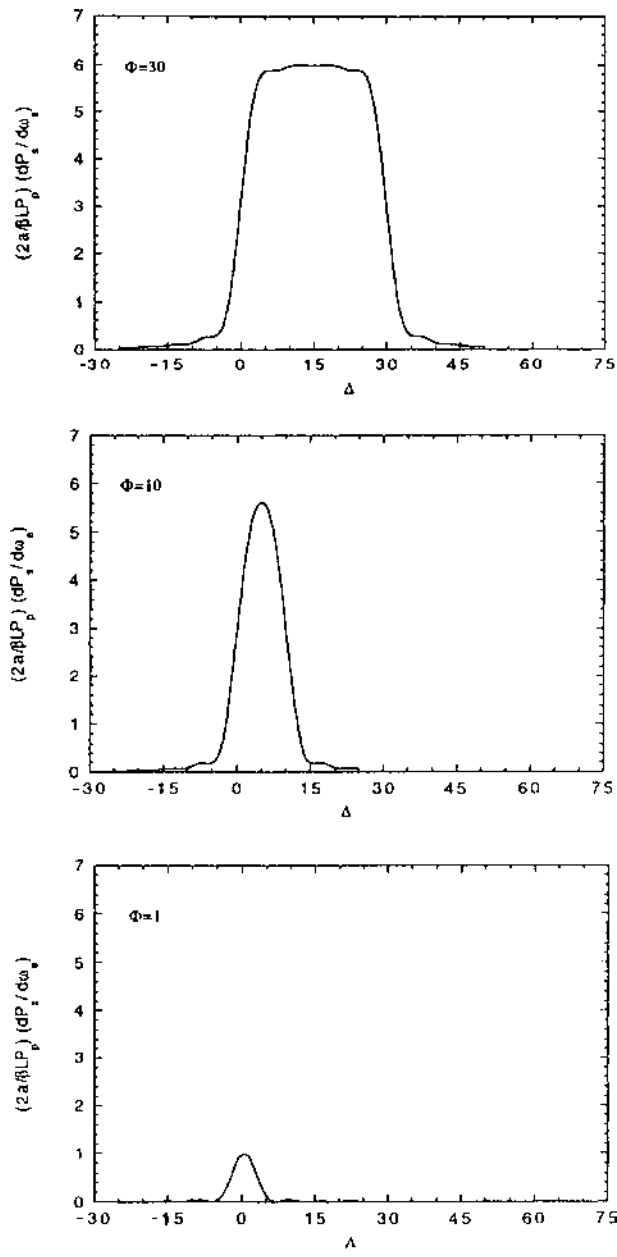


Figure 3 Continued.

II. PARAMETRIC AMPLIFICATION

The physical situation associated with an OPA is that of a pump wave and a signal wave incident on a nonlinear medium. Through the DFG process, the signal wave is amplified, and the idler wave is generated at the difference frequency. This process was described in Chapter 2. Since the one-pass gain through the nonlinear crystal is modest, the process can be described in the nondepleted pump approximation.

The result for the idler wave was given in Table 6 of Chapter 2. Table 3 of the present chapter gives the result for the signal power at the output of the crystal. The parametric gain G is defined through

$$\frac{\mathcal{P}_s(L)}{\mathcal{P}_s(0)} = 1 + G \quad (4)$$

where the expression for G is given in Table 3. The important parameter determining the maximum parametric gain is the gain coefficient g . It can be seen that the gain coefficient is related to the characteristic nonlinear length scale introduced in Chapter 2, i.e., $g = (L_{NL})^{-1}$.

For small gain, the usual case, G is given by $(gL)^2$ multiplied by the sinc² phase matching curve. For perfect phase matching, $G \approx (gL)^2$. Formulas for the gain coefficient g are given in Table 4. Three general conditions are discussed: (1) infinite plane waves; (2) near-field focused Gaussian beams; and (3) optimized tightly focused Gaussian beams, including the effects of double refraction.

Table 3 Formulas for the Signal Power Gain in an OPA

$\frac{\mathcal{P}_s(L)}{\mathcal{P}_s(0)} = 1 + (gL)^2 \frac{\sinh^2(\sqrt{(gL)^2 - (\Delta k L/2)^2})}{(gL)^2 - (\Delta k L/2)^2}$			
$\equiv 1 + G$			
$g = 4\pi d_{\text{eff}} \sqrt{\frac{I_p(0)}{2\epsilon_0 n_p n_s n_i c \lambda_s \lambda_i}}$	(SI)	$g = 16\pi^2 d_{\text{eff}} \sqrt{\frac{2\pi I_p(0)}{n_p n_s n_i c \lambda_s \lambda_i}}$	(cgs)
Small gain ($\Delta k/2 \gg g$)			
$G \approx (gL)^2 \frac{\sin^2(\Delta k L/2)}{(\Delta k L/2)^2}$			
Small gain ($\Delta k = 0$)			
$G \approx (gL)^2$			

Table 4 Formulas for Calculating the Small Signal Parametric Gain

Plane waves ($A = \text{beam area}$)
$(gL)^2 = \frac{16\pi^2 d_{\text{eff}}^2 L^2}{\epsilon_0 n_0^2 c \lambda_0^2} \mathcal{P}_p (1 - \delta^2) \frac{1}{2n_p A} \quad (\text{SI})$
$(gL)^2 = \frac{1024\pi^5 d_{\text{eff}}^2 L^2}{n_0^2 c \lambda_0^2} \mathcal{P}_p (1 - \delta^2) \frac{1}{2n_p A} \quad (\text{cgs})$
Near-field Gaussian beams
$(gL)^2 = \frac{16\pi^2 d_{\text{eff}}^2 L^2}{\epsilon_0 n_0^2 c \lambda_0^2} \mathcal{P}_p (1 - \delta^2) \frac{4M^2}{\pi n_p} \quad (\text{SI})$
$(gL)^2 = \frac{1024\pi^5 d_{\text{eff}}^2 L^2}{n_0^2 c \lambda_0^2} \mathcal{P}_p (1 - \delta^2) \frac{4M^2}{\pi n_p} \quad (\text{cgs})$
$M = \frac{w_s w_i w_p}{w_s^2 w_i^2 + w_s^2 w_p^2 + w_i^2 w_p^2}$
$M_{\max}^2 = \frac{1}{4(w_s^2 + w_i^2)} \text{ for } \frac{1}{w_p^2} = \frac{1}{w_s^2} + \frac{1}{w_i^2}$
Optimized confocal near-field Gaussian beams
$(gL)^2 = \frac{16\pi^2 d_{\text{eff}}^2 L^2}{\epsilon_0 n_0^2 c \lambda_0^2} \mathcal{P}_p (1 - \delta^2) \frac{1}{\lambda_0 L} \quad (\text{SI})$
$(gL)^2 = \frac{1024\pi^5 d_{\text{eff}}^2 L^2}{n_0^2 c \lambda_0^2} \mathcal{P}_p (1 - \delta^2) \frac{1}{\lambda_0 L} \quad (\text{cgs})$
Optimized confocal tightly focused Gaussian beams (including double refraction)
$(gL)^2 = \frac{16\pi^2 d_{\text{eff}}^2 L^2}{\epsilon_0 n_0^2 c \lambda_0^2} \mathcal{P}_p (1 - \delta^2) \frac{\bar{h}_m(B, \xi)}{\lambda_0 L} \quad (\text{SI})$
$(gL)^2 = \frac{1024\pi^5 d_{\text{eff}}^2 L^2}{n_0^2 c \lambda_0^2} \mathcal{P}_p (1 - \delta^2) \frac{\bar{h}_m(B, \xi)}{\lambda_0 L} \quad (\text{cgs})$
$\bar{h}_m(B, \xi)$ given in Fig. 4
$\lambda_0 = 2\lambda_p \quad \lambda_s = \frac{2\lambda_p}{1 + \delta} \quad \lambda_i = \frac{2\lambda_p}{1 - \delta}$
$n_0 \simeq n_s \simeq n_i$
$0 \leq \delta \leq 1$

A. Infinite Plane Waves

When the sizes of the interacting beams are large compared to the crystal length and aperture length of the crystal (see Chapter 2), the infinite plane wave approximation can be used. Note that the dependence of the parametric gain in the low gain limit is the same as that for frequency conversion efficiency, i.e., the gain is proportional to d_{eff}^2/n^3 , L^2 , and I_p .

The gain coefficient is given in terms of a degeneracy factor δ defined through

$$\begin{aligned}\omega_s &= \frac{1}{2}\omega_p(1 + \delta) \\ \omega_i &= \frac{1}{2}\omega_p(1 - \delta)\end{aligned}\quad (5)$$

The limits of δ are 0 and 1, with $\delta = 0$ corresponding to the degenerate point. The gain coefficient is maximum at the degenerate point. The degenerate wavelength is defined as $\lambda_0 = 2\lambda_p$, and n_0 is the refractive index at degeneracy, with $n_0 \simeq n_s \simeq n_i$. Although the gain is maximized at the degenerate point, the bandwidth increases dramatically there also (See Section III.C). The price for operating off degeneracy is that the small signal gain decreases as $1 - \delta^2$.

B. Focused Gaussian Beams (Near-Field)

To increase the parametric gain, the beams are often focused. Optical parametric amplification in the near field with no double refraction is considered in this section. This approximation is valid when the crystal thickness is less than or on the order of the confocal parameters of the interacting beams, and the aperture length is large, or NCPM conditions are imposed.

When the interacting beams have a Gaussian radial dependence, they are generally not optimally overlapped. This is because the nonlinear driving polarization beam is smaller than the beams that generate it. For example, the polarization source at the signal frequency would be proportional to

$$\exp\left(\frac{-2r^2}{w_p^2}\right)\exp\left(\frac{-2r^2}{w_i^2}\right) = \exp[-2r^2(w_p^{-2} + w_i^{-2})] = \exp\left(\frac{-2r^2}{w_s'^2}\right) \quad (6)$$

where w_p and w_i are the $1/e^2$ radii of the pump and idler beams, respectively. In general $w_s' \neq w_s$, the $1/e^2$ radius of the signal beam. Since the beams are not optimally overlapped, this produces a reduction in the gain coefficient from the plane wave value. The key factor is the near field gain reduction parameter M^2 given in Table 4 [9].

For fixed values of the signal and idler radii, M^2 is maximized for a pump radius given by

$$\frac{1}{w_p^2} = \frac{1}{w_s^2} + \frac{1}{w_i^2} \quad (7)$$

The maximum value of M is given in the table.

Although the formula for the gain displays a dependence on L^2 , the intensity will only be large over a distance on the order of the confocal parameter. Setting L equal to the common confocal parameter of the signal and idler beams, it follows that $w_s^2 = \lambda_s L / 2\pi n_s$ and $w_i^2 = \lambda_i L / 2\pi n_i$. Since $w^2 \propto \lambda$ and $\lambda_p^{-1} = \lambda_s^{-1} + \lambda_i^{-1}$, if the signal and idler beams are confocally focused, then by Eq. (7) the pump beam will be confocally focused as well. Under these conditions, the optimized near field confocal gain is given in Table 4. Note that the gain is proportional to L in this case and not to L^2 .

C. Arbitrarily Tightly Focused Gaussian Beams with Double Refraction

The analysis of Boyd and Kleinman [11] concerning frequency mixing with tightly focused beams was discussed in Chapter 2. Here their results for optical parametric gain are given. The formula given in (present) Table 4 is for an optimized confocal geometry in which each beam has a common confocal parameter. Note that the gain is the same as in the near-field analysis of Section II.B multiplied by a gain reduction factor $\bar{h}_m(B, \xi)$. The double refraction parameter B and the focusing parameter ξ were defined in Chapter 2. Plots of $\bar{h}_m(B, \xi)$ are shown in (present) Fig. 4.

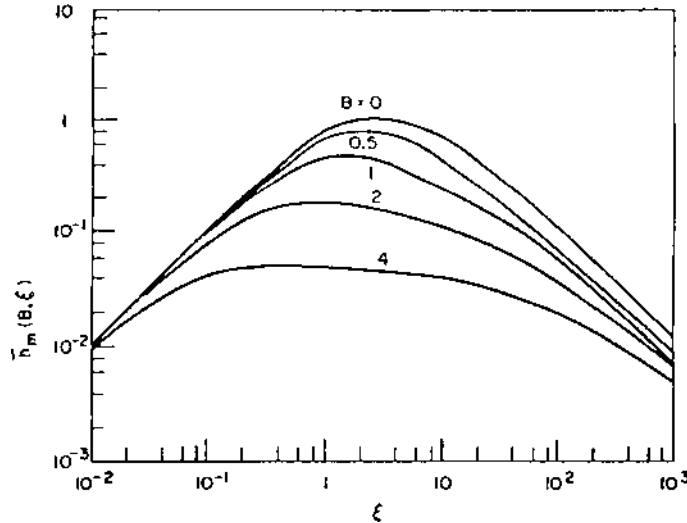


Figure 4 Parametric gain reduction factor as a function of focusing parameter ξ and double refraction parameter B for optimally tightly focused Gaussian beams. (From Ref. 11.)

As in the case of frequency conversion efficiencies discussed in Chapter 2, the confocal parametric gain is maximized when $B = 0$ (i.e., no double refraction, 90° phase matching). For $B \geq 4$, the maximum value of $\bar{h}_m(B, \xi)$ is nearly independent of ξ over a wide range. Within the range $2/B^2 < \xi < B^2/4$,

$$\bar{h}_m(B, \xi) \rightarrow \frac{\pi}{4B^2} \quad (8)$$

to within 10%. Since the optimized confocal gain is proportional to L , and $B^2 \propto L$, the gain is nearly independent of crystal length for large walk-off angles. When L is of the order of the confocal parameter, the $B \sim \rho/\theta_d$, where ρ is the walk-off angle due to double refraction (see Chapter 2), and θ_d is the far-field diffraction angle. Thus under the conditions operative for Eq. (8), the gain reduction factor is approximately $(\pi/4)(\theta_d/\rho)^2$. When the beam radii are larger than $(2)^{1/2}\rho L$, the gain reduction due to walk-off is <15%. It can be made negligible with wider beams [12].

III. PARAMETRIC OSCILLATORS

The gain of an OPA is modest even for high pump intensities. The net gain can be increased by providing positive feedback of the signal. A convenient way of achieving this is to place the nonlinear crystal in a two-mirror resonator. When the optical parametric gain of the resonator exceeds its optical loss, oscillation occurs. Such a device is called an optical parametric oscillator (OPO). Above the threshold for oscillation, the signal and idler waves grow dramatically. The output of such a device is coherent radiation like that of a laser.

The signal and idler frequencies will adjust by phase matching to maximize the gain so that these frequencies will achieve the lowest threshold and be selectively amplified. Hence the output of an OPO is wavelength tunable. Tuning can be achieved by angle or temperature control of the phase matching. The Pockels or linear electrooptical effect can sometimes be used to fine-tune the output. The bandwidth of the output will be controlled by the gain bandwidth of the crystal. Line narrowing and control is also possible with the introduction of dispersive elements such as étalons or gratings into the resonator cavity.

There are two main types of OPO: the doubly resonant oscillator (DRO) and the singly resonant oscillator (SRO). Both of these are discussed below. OPOs can also be classified as cw (or quasi-cw), pulsed, or mode-locked. The former is treated first in Section III.A (DROs) and III.B (SROs). Pulsed OPOs are discussed in Section IV, while synchronously pumped (mode-locked) OPOs are discussed in Section V. The important characteristics of OPOs to be described include oscillation thresholds, conversion efficiency and output power, stability, rise time, tuning, and bandwidth.

A. Doubly Resonant Parametric Oscillators

The simplest DRO consists of a nonlinear crystal inserted in a two-mirror cavity as shown in Fig. 5. The mirrors have low reflectance (near zero) at the pump frequency and high reflectances at the signal and idler frequencies. Both signal and idler frequencies are resonant with the cavity, hence the name of the oscillator. Variations of this simple cavity consist of the double-pass DRO (DPDRO) and the doubly resonant ring oscillator (DRRO), both also illustrated in Fig. 5. In the DPDRO, the back mirror has a high reflectance at the pump

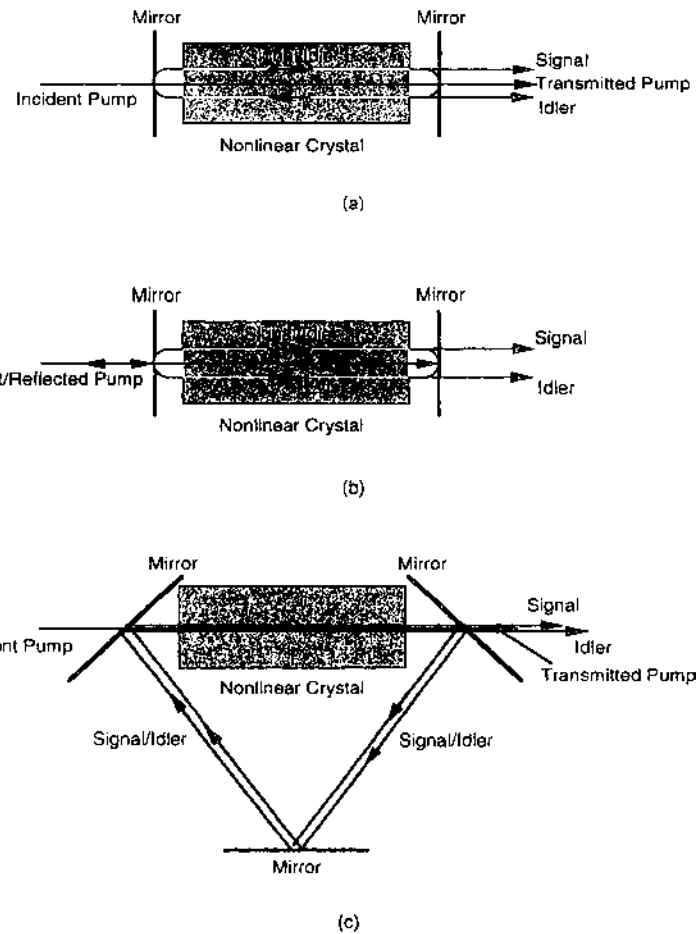


Figure 5 Doubly resonant oscillator (DRO) geometries. (a) Simple two-mirror DRO. (b) Double-pass DRO (DPDRO). (c) Doubly resonant right oscillator (DRRO).

frequency as well, so that the pump makes a double pass through the oscillator to increase the gain. In the DRRO, the pump again passes straight through, but the signal and idler waves travel only in one direction through the nonlinear crystal. The purposes of these special oscillator configurations are described below.

Threshold. In an OPO, unlike a laser, the signal and idler waves are only amplified when traveling in the same direction as the pump wave. Waves propagating counter to the pump wave are not phase matched for DFG. The steady-state threshold gain is determined under self-consistent conditions where the signal-pass parametric gain equals the round-trip electric field loss. In this way the fields replicate themselves on each round-trip [8].

The minimum threshold gain results when the signal and idler frequencies are both resonant and phase matching is achieved ($\Delta k = 0$). The self-consistent analysis described above leads to the following condition on the small signal gain (gL):

$$\cosh(gL)_{\text{th}} = \frac{1 + R_s \exp(-\alpha_s L) R_i \exp(-\alpha_i L)}{R_s \exp(-\alpha_s L) + R_i \exp(-\alpha_i L)} \quad (9)$$

where R_s and R_i are the mirror reflectances (assume the same for both cavity mirrors) at the signal and idler frequencies, respectively, while α_s and α_i are the intensity absorption coefficients for the signal and idler waves. (They may also include any scattering losses as well as Fresnel reflection losses since the absorption is usually very small.) The subscript th signifies that the gain coefficient is that at threshold. Generally, the reflectances are close to 1 and the other losses are low as well. In the low-loss regime, Eq. (9) can be written as

$$(gL)_{\text{th}}^2 \simeq [1 - R_s \exp(-\alpha_s L)][1 - R_i \exp(-\alpha_i L)] \quad (10)$$

Using the formulas in Table 4 along with Eq. (10), the threshold pump power can be computed. The results are shown in Table 5 under the various approximations considered in Section II.

The threshold gain can be lowered using the DPDRO. In this device, gain is achieved on both the forward pass and the backward pass of the signal and idler fields. The following result for the threshold gain has been derived by Bjokholm et al. [13]:

$$(gL)_{\text{th}}^2 \text{sinc}^2(\Delta k L / 2) = \frac{[1 - R_s \exp(-\alpha_s L)][1 - R_i \exp(-\alpha_i L)]}{1 + R_p + 2\sqrt{R_p} \cos(\Delta\varphi + \Delta k L)} \quad (11)$$

where

$$\Delta\varphi = \Delta(\varphi_p - \varphi_s - \varphi_i) \quad (12)$$

is the net phase change of the optical fields upon reflection at the back mirror, and R_p is the reflectance of the back mirror at the pump frequency. Ideally, for $R_p \sim 1$

Table 5 Formulas for the Steady-State Threshold Pump Power for Doubly Resonant Optical Parametric Oscillators

Plane waves	
$\mathcal{P}_{p,\text{th}} = \{\text{beam area}\} \times \frac{\epsilon_0 n_s^2 n_p c \lambda_p^2}{2\pi^2 d_{\text{eff}}^2 L^2 (1 - \delta^2)} (1 - R_s e^{-\alpha_s L}) (1 - R_i e^{-\alpha_i L})$	(SI)
$\mathcal{P}_{p,\text{th}} = \{\text{beam area}\} \times \frac{n_s^2 n_p c \lambda_p^2}{128\pi^5 d_{\text{eff}}^2 L^2 (1 - \delta^2)} (1 - R_s e^{-\alpha_s L}) (1 - R_i e^{-\alpha_i L})$	(cgs)
Near-field Gaussian beams	
$\mathcal{P}_{p,\text{th}} = \frac{\epsilon_0 n_s^2 n_p c \lambda_p^2}{16\pi d_{\text{eff}}^2 L^2 (1 - \delta^2) M^2} (1 - R_s e^{-\alpha_s L}) (1 - R_i e^{-\alpha_i L})$	(SI)
$\mathcal{P}_{p,\text{th}} = \frac{n_s^2 n_p c \lambda_p^2}{1024\pi^4 d_{\text{eff}}^2 L^2 (1 - \delta^2) M^2} (1 - R_s e^{-\alpha_s L}) (1 - R_i e^{-\alpha_i L})$	(cgs)
Optimized confocal near-field Gaussian beams	
$\mathcal{P}_{p,\text{th}} = \frac{\epsilon_0 n_s^2 c \lambda_p^3}{2\pi^2 d_{\text{eff}}^2 L (1 - \delta^2)} (1 - R_s e^{-\alpha_s L}) (1 - R_i e^{-\alpha_i L})$	(SI)
$\mathcal{P}_{p,\text{th}} = \frac{n_s^2 c \lambda_p^3}{128\pi^5 d_{\text{eff}}^2 L (1 - \delta^2)} (1 - R_s e^{-\alpha_s L}) (1 - R_i e^{-\alpha_i L})$	(cgs)
Optimized confocal tightly focused Gaussian beams (including double refraction)	
$\mathcal{P}_{p,\text{th}} = \frac{\epsilon_0 n_s^2 c \lambda_p^3}{2\pi^2 d_{\text{eff}}^2 L (1 - \delta^2) \bar{h}_m(B, \xi)} (1 - R_s e^{-\alpha_s L}) (1 - R_i e^{-\alpha_i L})$	(SI)
$\mathcal{P}_{p,\text{th}} = \frac{n_s^2 c \lambda_p^3}{128\pi^5 d_{\text{eff}}^2 L (1 - \delta^2) \bar{h}_m(B, \xi)} (1 - R_s e^{-\alpha_s L}) (1 - R_i e^{-\alpha_i L})$	(cgs)

and $\Delta\varphi = \Delta k = 0$, the threshold gain for the DPDRO is lower than that of the DRO by a factor of approximately 4.

The equations given above hold true when the pump is single mode (one frequency). Often though, the pump beam from a high-power laser will contain many modes. Not all of the power of the beam will then pump specific signal and idler modes. However, Harris [14] has shown that if the idler longitudinal mode spacing is equal to that of the pump laser, then all of the pump modes may act in unison to produce gain at a single signal frequency mode. Although the pump modes are randomly phased, the idler modes develop compensating phases to maximize the gain [15]. The problem of multiple pump modes hampered the early development of pulsed OPOs. The more recent development of single longitudinal mode lasers by seed injection have alleviated this problem.

Conversion efficiency and output power (plane waves). When steady-state oscillation has been achieved in the OPO, the gain is clamped at the threshold

value. The signal and idler waves are nearly constant across the cavity, while the pump field is strongly depleted [7]. Under these conditions, the overall conversion efficiency defined by

$$\eta = \frac{\mathcal{P}_s + \mathcal{P}_i}{\mathcal{P}_p(0)} \quad (13)$$

can be computed. The results for the DRO are given in Table 6 in terms of the parameter N_{DRO} , which is the number of times the input pump power exceeds the threshold pump power for the DRO. For the DRO, the maximum value of the efficiency is 50% when $N_{DRO} = 4$.

Expressions for the output signal and idler powers are also given in Table 6. Note that the transmitted pump power is clamped at the threshold value. This is a result of the plane wave analysis and was first proposed by Siegman [16] as a means of achieving an optical power limiter. The excess pump power is channeled into the generated signal and idler powers, and into a “reflected” pump wave. The reflected pump power is actually due to a sum-frequency wave generated by the backward traveling signal and idler waves in the resonator cavity. The distribution of the optical power in the various frequencies as a function of input pump power above threshold is shown in Fig. 6a.

The reflected pump wave of the DRO robs energy from the signal and idler waves. In the DRRO, this reflected wave is avoided, since the signal and idler waves travel only in one direction through the nonlinear crystal. The conversion efficiency and output powers for the DRRO are given in Table 7. Note that the maximum efficiency now is 100% when $N_{DRRO} = 4$.

Results for the DPDRO are shown in Table 8. For $R_p \sim 1$ and proper adjustments of the phase (i.e., $\Delta\varphi = \Delta k = 0$), the maximum efficiency is again 100% at $N_{DPDRO} = 4$. Thus the DPDRO has the advantage over the DRO of

Table 6 DRO Efficiency and Output Power Formulas for Plane Waves

Conversion efficiency
$\eta = \frac{2}{N_{DRO}}(\sqrt{N_{DRO}} - 1) \quad N_{DRO} = \frac{(\mathcal{P}_p)_{in}}{\mathcal{P}_{p,th}}$
Output power
$\mathcal{P}_s = 2 \frac{\lambda_p}{\lambda_c} \mathcal{P}_{p,th} (\sqrt{N_{DRO}} - 1)$
$\mathcal{P}_i = 2 \frac{\lambda_p}{\lambda_i} \mathcal{P}_{p,th} (\sqrt{N_{DRO}} - 1)$
$(\mathcal{P}_p)_{out} = \mathcal{P}_{p,th}$
“Reflected” pump power
$(\mathcal{P}_p)_{reflected} = \mathcal{P}_{p,th} (\sqrt{N_{DRO}} - 1)^2$

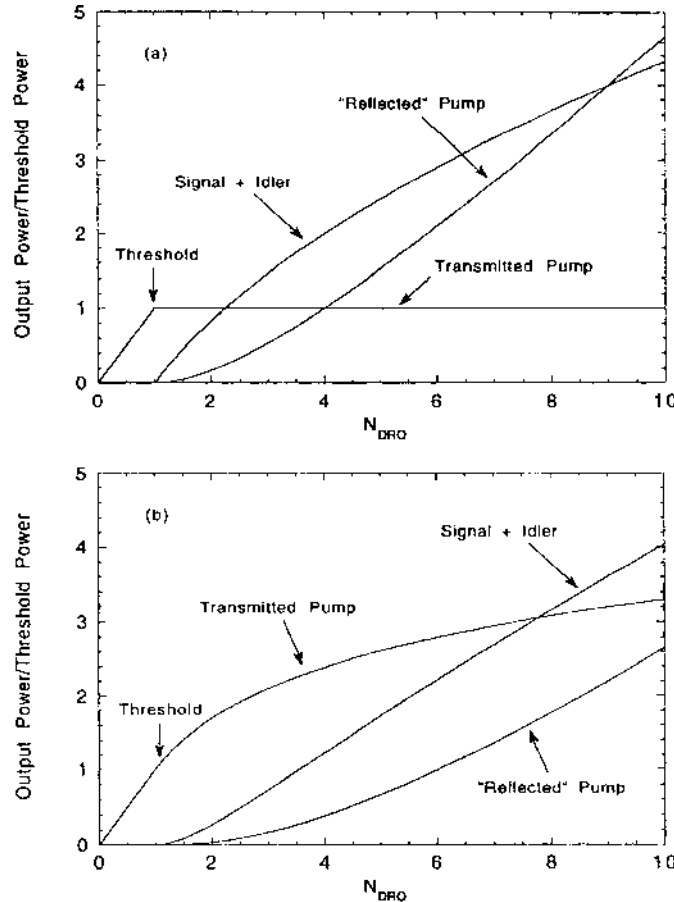


Figure 6 Output powers for the DRO normalized to the DRO threshold power as functions of the number of times the pump power exceeds threshold. (a) Plane wave approximation. (b) Gaussian beams.

increased efficiency with a reduced threshold. The disadvantage is the dependence of the efficiency and threshold on $\Delta\varphi$ and Δk .

Conversion efficiency and output power (Gaussian beams). The results given above are modified for real optical beams with radial intensity dependence. Bjorkholm [17] has treated this case for a “nearly plane wave” pump beam. The meaning of this phrase is that the spatial intensity variation over the beam cross-section is slow enough that the generated signal and idler beams can effectively be divided into independent beamlets of nearly uniform intensity and planar phase over the interaction length of the beams. A uniform plane wave

Table 7 DRRO Efficiency and Output Power Formulas for Plane Waves

Conversion efficiency
$\eta = \frac{4}{N_{\text{DRO}}} (\sqrt{N_{\text{DRO}}} - 1) \quad N_{\text{DRO}} = \frac{(\mathcal{P}_p)_{\text{in}}}{(\mathcal{P}_{p,\text{th}})}$
Output power
$\mathcal{P}_s = 4 \frac{\lambda_p}{\lambda_s} \mathcal{P}_{p,\text{th}} (\sqrt{N_{\text{DRO}}} - 1)$
$\mathcal{P}_i = 4 \frac{\lambda_p}{\lambda_i} \mathcal{P}_{p,\text{th}} (\sqrt{N_{\text{DRO}}} - 1)$
$(\mathcal{P}_p)_{\text{out}} = (\mathcal{P}_p)_{\text{in}} \left[1 - \frac{4}{N_{\text{DRO}}} (\sqrt{N_{\text{DRO}}} - 1) \right]$
“Reflected” pump power
$(\mathcal{P}_p)_{\text{reflected}} = 0$

analysis is applied to each beamlet. These solutions are then summed over the nonuniform pump beam to obtain the net signal and idler powers.

The pump beam is taken to have a Gaussian radial distribution

$$I_p(r) + I_p(0) \exp\left(\frac{-2r^2}{w_p^2}\right) \quad (14)$$

where w_p is the radius of the pump beam waist. This beam is divided into a collection of beamlets of dimension Δ . The condition that the beamlets be independent and of uniform intensity and phase places the following restrictions on the dimension Δ [17]:

- $\Delta \ll w_p$.
- Δ is large enough that diffractive mixing of pump, idler, and signal beamlets is negligible.
- Δ is large enough that double refraction effects on the beamlets are negligible.

Table 8 DPDRO Efficiency and Output Power Formulas for Plane Waves

Conversion efficiency
$\eta = \frac{1 + R_p + 2\sqrt{R_p} \cos(\Delta\varphi + \Delta kL)}{1 + \sqrt{R_p} \cos(\Delta\varphi + \Delta kL)} \frac{2}{N_{\text{DPDRO}}} (\sqrt{N_{\text{DPDRO}}} - 1) \quad N_{\text{DPDRO}} = \frac{(\mathcal{P}_p)_{\text{in}}}{(\mathcal{P}_{p,\text{th}})_{\text{DPDRO}}}$
Output power
$\mathcal{P}_s = \frac{\lambda_p}{\lambda_s} (\mathcal{P}_p)_{\text{in}} \eta$
$\mathcal{P}_i = \frac{\lambda_p}{\lambda_i} (\mathcal{P}_p)_{\text{in}} \eta$
$(\mathcal{P}_p)_{\text{out}} = 0$
“Reflected” pump power
$(\mathcal{P}_p)_{\text{reflected}} \approx (\mathcal{P}_p)_{\text{in}} (1 - \eta)$

Table 9 DRO Efficiency and Output Power
Formulas for Gaussian Beams

Conversion efficiency
$\eta = \frac{4}{N_{\text{DRO}}} (\sqrt{N_{\text{DRO}}} - \ln \sqrt{N_{\text{DRO}}} - 1) \quad N_{\text{DRO}} = \frac{(\mathcal{P}_p)_{\text{in}}}{\mathcal{P}_{p,\text{th}}}$
Output power
$\mathcal{P}_s = 4 \frac{\lambda_p}{\lambda_s} \mathcal{P}_{p,\text{th}} (\sqrt{N_{\text{DRO}}} - \ln \sqrt{N_{\text{DRO}}} - 1)$
$\mathcal{P}_i = 4 \frac{\lambda_p}{\lambda_i} \mathcal{P}_{p,\text{th}} (\sqrt{N_{\text{DRO}}} - \ln \sqrt{N_{\text{DRO}}} - 1)$
$(\mathcal{P}_p)_{\text{out}} = \mathcal{P}_{p,\text{th}} (1 + \ln N_{\text{DRO}})$
“Reflected” pump power
$(\mathcal{P}_p)_{\text{reflected}} = \mathcal{P}_{p,\text{th}} (N_{\text{DRO}} - 4\sqrt{N_{\text{DRO}}} + \ln N_{\text{DRO}} + 3)$

Although these are rather severe restrictions, the results of the analysis show generally good agreement with experiments [17].

The results for conversion efficiency and output power for a DRO with Gaussian beams are given in Table 9. Note that in contrast with the plane wave results, the maximum efficiency now is only 41% for $N_{\text{DRO}} = 12.5$. Also note that although there is still a reflected wave, the transmitted pump power is no longer clamped at the threshold value but increases logarithmically with N_{DRO} . This is a more gradual power limiting than that of the plane wave case. The distribution of output powers in the various frequencies is shown in Fig. 6b.

Results for the DRRO case with Gaussian beams are given in Table 10. The maximum conversion efficiency is now approximately 78% at $N_{\text{DRRO}} = 12.5$. 100% efficiency is not possible, since the pump power in the wings of the Gaussian is too weak to produce any nonlinear frequency conversion. Comparisons of the conversion efficiencies for plane waves and Gaussian beams are given in Fig. 7 for both the DRO and the DRRO.

Table 10 DRRO Efficiency and Output Power Formulas
for Gaussian Beams

Conversion efficiency
$\eta = \frac{8}{N_{\text{DRO}}} (\sqrt{N_{\text{DRO}}} - \ln \sqrt{N_{\text{DRO}}} - 1) \quad N_{\text{DRO}} = \frac{(\mathcal{P}_p)_{\text{in}}}{\mathcal{P}_{p,\text{th}}}$
Output power
$\mathcal{P}_s = 8 \frac{\lambda_p}{\lambda_s} \mathcal{P}_{p,\text{th}} (\sqrt{N_{\text{DRO}}} - \ln \sqrt{N_{\text{DRO}}} - 1)$
$\mathcal{P}_i = 8 \frac{\lambda_p}{\lambda_i} \mathcal{P}_{p,\text{th}} (\sqrt{N_{\text{DRO}}} - \ln \sqrt{N_{\text{DRO}}} - 1)$
$(\mathcal{P}_p)_{\text{out}} = (\mathcal{P}_p)_{\text{in}} \left[1 - \frac{8}{N_{\text{DRO}}} (\sqrt{N_{\text{DRO}}} - 1) + \frac{4}{N_{\text{DRO}}} \ln N_{\text{DRO}} \right]$
“Reflected” pump power
$(\mathcal{P}_p)_{\text{reflected}} = 0$

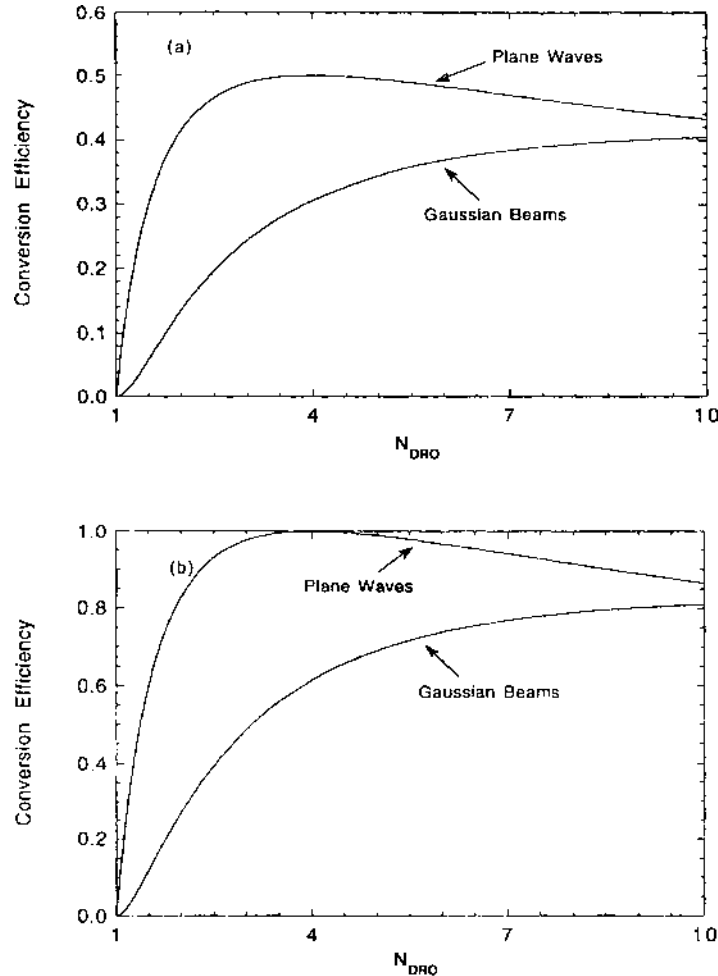


Figure 7 DRO conversion efficiencies. (a) Plane wave and Gaussian beam results for a simple DRO. (b) Plane wave and Gaussian beam results for a DRRO.

Stability. Small changes in cavity length caused by temperature fluctuations or acoustic vibrations will cause a shift in the resonant frequencies of the cavity. However, oscillating modes of the OPO must sum to ω_p to conserve energy. Since modes oscillating at particular values of ω_s and ω_i will shift in the same direction as the cavity length varies, they cannot sum to ω_p . However, there exist other cavity modes that may (see Fig. 8). Thus when the cavity length fluctuates, new modes that are far removed from the original ones may suddenly

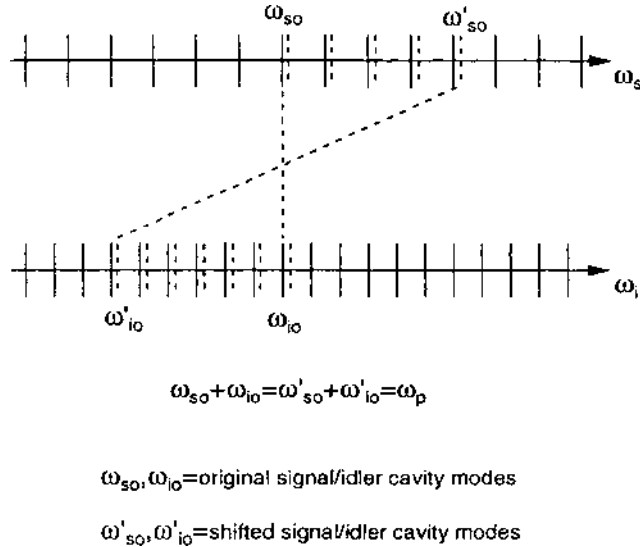


Figure 8 DRO signal and idler cavity modes, illustrating instability in output frequency as cavity modes fluctuate (i.e., shift).

experience the maximum gain, and the OPO will oscillate on these modes. The output will experience a relatively large change in frequency and possibly output power.

In general, the shift $\Delta\omega = \omega'_s - \omega_s$ in the output signal frequency (which is the negative of the shift in the idler frequency) is given by

$$\Delta\omega = \frac{n_i}{n_i - n_s} \omega_p \frac{\Delta l}{l} \quad (15)$$

where l is the cavity length. Typically, $|n_i - n_s|/n_i \sim 10^{-2} - 10^{-1}$. Therefore, for $\Delta l/l \sim 10^{-7}$ the cavity mode shifts only by $10^{-7} \times \omega_s$, but the output frequency shifts by $(10^{-6} - 10^{-5}) \times \omega_p$. This is a relatively large shift. The result is that the output of the DRO is relatively unstable with respect to small cavity fluctuations. This instability is overcome by going to a singly resonant oscillator.

B. Singly Resonant Parametric Oscillator

The simplest SRO, as illustrated in Fig. 9, has two cavity mirrors with high reflectance at the single frequency only. Variations of the simple SRO include a double-pass SRO (DPSRO) where the pump experiences a double pass, or where

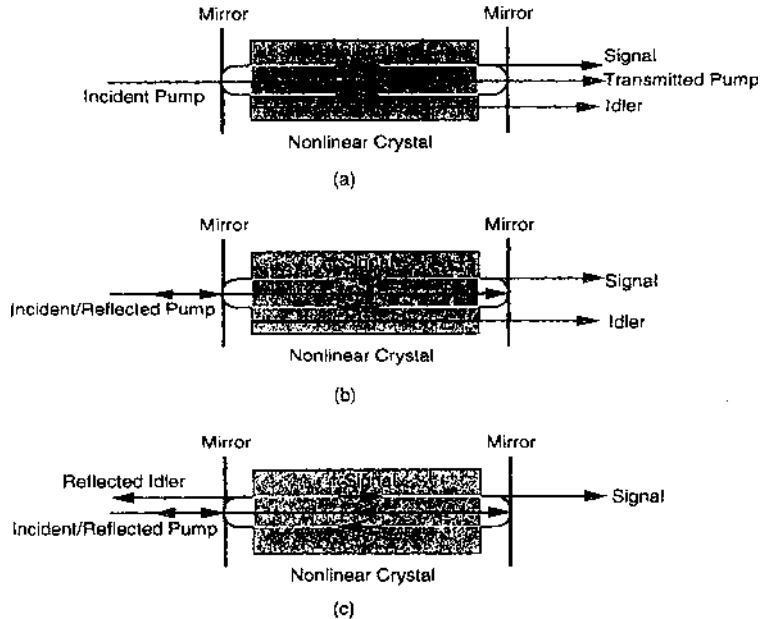


Figure 9 Singly resonant oscillator (SRO) geometries. (a) Simple two-mirror SRO. (b) Double-pass SRO (DPSRO)—pump only. (c) DPSRO-pump and idler.

both the pump and the idler are passed twice through the nonlinear crystal. These are also shown in Fig. 9.

In the SRO, only the signal frequency is resonant, so as the cavity resonant modes fluctuate, ω_i is free to change continuously to accommodate conservation of energy. Hence there are no large jumps in output frequencies, and the SRO is relatively stable against cavity fluctuations.

Threshold. The steady-state threshold gain of the SRO is calculated in the same manner as was done for the DRO. The result in the low-loss regime is

$$(gL)_{\text{th}}^2 \simeq 2[1 - R_s \exp(-\alpha_s L)] \quad (16)$$

This threshold gain is larger than the threshold gain of the DRO by a factor of $2/[1 - R_i \exp(-\alpha_i L)]$. For example, if the net idler round-trip loss for the DRO is 2%, then the SRO threshold gain is larger by a factor of 100. Thus the price of stability bought by the SRO is an increase in threshold pump power by a factor of ~ 100 . This is generally not a problem for pulsed OPOs but is more difficult for cw OPOs. Expressions for the threshold pump power in the various cases are given in Table 11.

Table 11 Formulas for the Steady-State Threshold Pump Power for Singly Resonant Optical Parametric Oscillators

Plane waves	
$\mathcal{P}_{p,\text{th}} = \{\text{beam area}\} \times \frac{\epsilon_0 n_s^2 n_p c \lambda_p^2}{\pi^2 d_{\text{eff}}^2 L^2 (1 - \delta^2)} (1 - R_s e^{-\alpha_s L})$	(SI)
$\mathcal{P}_{p,\text{th}} = \{\text{beam area}\} \times \frac{n_s^2 n_p c \lambda_p^2}{64 \pi^5 d_{\text{eff}}^2 L^2 (1 - \delta^2)} (1 - R_s e^{-\alpha_s L})$	(cgs)
Near-field Gaussian beams	
$\mathcal{P}_{p,\text{th}} = \frac{\epsilon_0 n_s^2 n_p c \lambda_p^2}{8 \pi d_{\text{eff}}^2 L^2 (1 - \delta^2) M^2} (1 - R_s e^{-\alpha_s L})$	(SI)
$\mathcal{P}_{p,\text{th}} = \frac{n_s^2 n_p c \lambda_p^2}{512 \pi^4 d_{\text{eff}}^2 L^2 (1 - \delta^2) M^2} (1 - R_s e^{-\alpha_s L})$	(cgs)
Optimized confocal near-field Gaussian beams	
$\mathcal{P}_{p,\text{th}} = \frac{\epsilon_0 n_s^2 c \lambda_p^3}{\pi^2 d_{\text{eff}}^2 L (1 - \delta^2)} (1 - R_s e^{-\alpha_s L})$	(SI)
$\mathcal{P}_{p,\text{th}} = \frac{n_s^2 c \lambda_p^3}{64 \pi^5 d_{\text{eff}}^2 L (1 - \delta^2)} (1 - R_s e^{-\alpha_s L})$	(cgs)
Optimized confocal tightly focused Gaussian beams (including double refraction)	
$\mathcal{P}_{p,\text{th}} = \frac{\epsilon_0 n_s^2 c \lambda_p^3}{\pi^2 d_{\text{eff}}^2 L (1 - \delta^2) \bar{h}_m(B, \xi)} (1 - R_s e^{-\alpha_s L})$	(SI)
$\mathcal{P}_{p,\text{th}} = \frac{n_s^2 c \lambda_p^3}{64 \pi^5 d_{\text{eff}}^2 L (1 - \delta^2) \bar{h}_m(B, \xi)} (1 - R_s e^{-\alpha_s L})$	(cgs)

For the DPSRO with only the pump beam reflected at the back cavity mirror [13],

$$(gL)_{\text{th}}^2 \approx \frac{2[1 - R_s \exp(-\alpha_s L)]}{1 + R_p} \quad (17)$$

When $R_p \sim 1$, a threshold gain reduction of approximately 2 is achieved.

Harris [18] has treated the case of the DPSRO when both the pump and the idler experience a double pass through the nonlinear crystal. The gain in this case depends on the relative phase shifts of these waves and the signal wave upon reflection at the mirror. When $\Delta k = 0$ and the net phase shift upon reflection is zero, the round-trip gain is $4(gL)^2$. For a phase shift upon reflection of $\Delta(\varphi_p - \varphi_s - \varphi_i) = \pi/2$, the gain on the first pass is exactly cancelled on the return pass. Harris has shown, however, that this is not the case when $\Delta k \neq 0$. When $|2\Delta k L| \leq 2\pi$, the net round-trip gain has a maximum value of $1.6 (gL)^2$.

Table 12 SRO Efficiency and Output Power
Formulas for Plane Waves

Conversion efficiency		
$\eta = \sin^2 \Gamma$	$\frac{\sin^2 \Gamma}{\Gamma^2} = \frac{1}{N_{SRO}}$	$N_{SRO} = \frac{(\mathcal{P}_p)_{in}}{(\mathcal{P}_{p,th})}$
Output power		
$\mathcal{P}_s \approx \frac{\lambda_p}{\lambda_s} \left(\frac{1 - R_s}{1 - R_s + \alpha_s L} \right) \eta (\mathcal{P}_p)_{in}$		
$\mathcal{P}_i = \frac{\lambda_p}{\lambda_i} \eta (\mathcal{P}_p)_{in}$		
$(\mathcal{P}_p)_{out} = (1 - \eta) (\mathcal{P}_p)_{in}$		
“Reflected” pump power		
$(\mathcal{P}_p)_{reflected} = 0$		

Conversion efficiency and output power (plane waves). In the SRO, the signal field is approximately constant over the cavity under steady-state conditions, but both the pump and the idler fields may vary [7]. The computed conversion efficiency and output power under these conditions, assuming the fields are infinite plane waves, are given in Table 12 in terms of the parameter N_{SRO} , which is the number of times the input pump power exceeds the SRO threshold pump power.

In this case, when $N_{SRO} = 4$ the conversion efficiency is approximately 90%. The conversion efficiency reaches a maximum of 100% for $N_{SRO} = (\pi/2)^2$. There is no power limiting for the transmitted pump in this case, and there is no reflected pump wave.

Table 13 gives the conversion efficiency and output power of the DPSRO under the condition of only the pump wave experiencing a double pass. For this

Table 13 DPSRO Efficiency and Output Power Formulas for Plane Waves

Conversion efficiency		
$\eta = \sin^2 \Gamma$	$\frac{\sin^2 \Gamma}{\Gamma^2} = \frac{2}{1 + R_p \cos \Gamma} \frac{1}{N_{DPSRO}}$	$N_{DPSRO} = \frac{(\mathcal{P}_p)_{in}}{(\mathcal{P}_{p,th})_{DPSRO}}$
Output power		
$\mathcal{P}_s \approx \frac{\lambda_p}{\lambda_s} \left(\frac{1 - R_s}{1 - R_s + \alpha_s L} \right) \eta (\mathcal{P}_p)_{in}$		
$\mathcal{P}_i = \frac{\lambda_p}{\lambda_i} \eta (\mathcal{P}_p)_{in}$		
$(\mathcal{P}_p)_{out} = 0$		
“Reflected” pump power		
$(\mathcal{P}_p)_{reflected} = (\mathcal{P}_p)_{in} - (\mathcal{P}_s + \mathcal{P}_i)$		

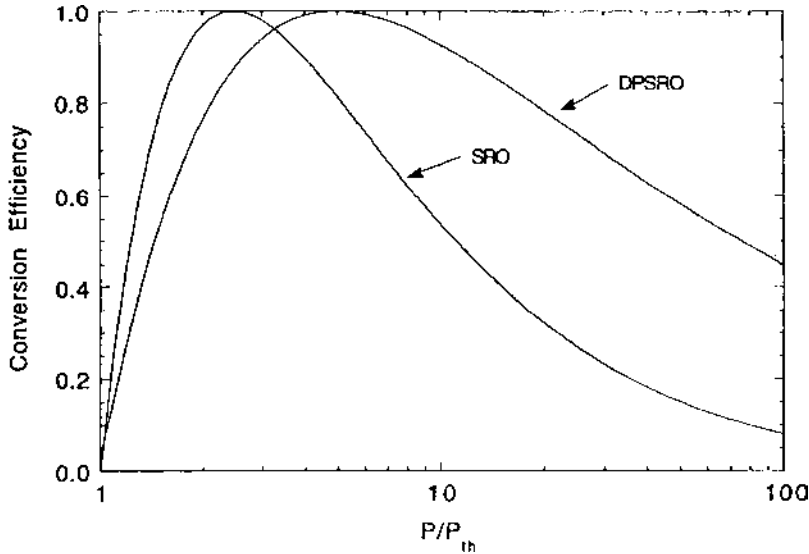


Figure 10 Conversion efficiency as a function of the number of times the pump power exceeds threshold for the SRO and DPSRO (pump only).

case a maximum conversion efficiency of $>90\%$ is obtained over a rather broad range of $2.5 \leq N_{DPSRO} \leq 8.5$. Plots of the SRO and DPSRO efficiencies are given in Fig. 10.

Conversion efficiency and output power (Gaussian beams). The analysis proceeds analogously to the DRO case [17]. The results for the SRO are given in Table 14. The integral must be numerically evaluated. Plots of the efficiency for the SRO in the plane wave and Gaussian beam approximations are shown in Fig. 11. Note again that it is impossible to achieve 100% conversion efficiency when Gaussian beams are used.

C. Tuning and Bandwidth

The output frequencies of the OPO are determined by conservation of energy ($\omega_s + \omega_i = \omega_p$) and momentum ($\mathbf{k}_s + \mathbf{k}_i = \mathbf{k}_p$). For collinear propagation of all three waves, these conditions imply

$$\omega_p[n(\omega_p) - n(\omega_p - \omega_s)] = \omega_s[n(\omega_s) - n(\omega_p - \omega_s)] \quad (18)$$

This relationship dictates the value of ω_s given ω_p and the dispersion of the refractive index of the nonlinear crystal. Tuning is thus achieved by controlling the refractive index. The two principal methods used are angle tuning (critically phase matched, CPM) and temperature tuning (noncritically phase matched, NCPM).

Table 14 SRO Efficiency and Output Power Formulas for Gaussian Beams

Conversion efficiency		
$\eta = 1 - \left[\frac{1}{N_{\text{SRO}}} + \int_0^{\ln N_{\text{SRO}}} e^{-x} \cos^2 \Gamma(x) dx \right]$	$\frac{\sin^2 \Gamma(x)}{\Gamma^2(x)} = \frac{e^x}{N_{\text{SRO}}}$	$N_{\text{SRO}} = \frac{(\mathcal{P}_p)_{\text{in}}}{\mathcal{P}_{p,\text{th}}}$
Output power		
$\mathcal{P}_s = \frac{\lambda_p}{\lambda_s} \left(\frac{1 - R_s}{1 - R_s + \alpha_s L} \right) \eta (\mathcal{P}_p)_{\text{in}}$ $\mathcal{P}_i = \frac{\lambda_p}{\lambda_i} \eta (\mathcal{P}_p)_{\text{in}}$ $(\mathcal{P}_p)_{\text{out}} = (\mathcal{P}_p)_{\text{in}} (1 - \eta)$		
“Reflected” pump power		
$(\mathcal{P}_p)_{\text{reflected}} = 0$		

Another method that is seeing increased use is injection seeding, which controls not only the output frequency of the OPO but also its line width.

Angle tuning. Consider a uniaxial crystal with its *c*-axis set at an angle θ with respect to the direction of the pump wave in a collinear OPO geometry. The wavelength λ_s selected will depend on θ and the pump frequency through

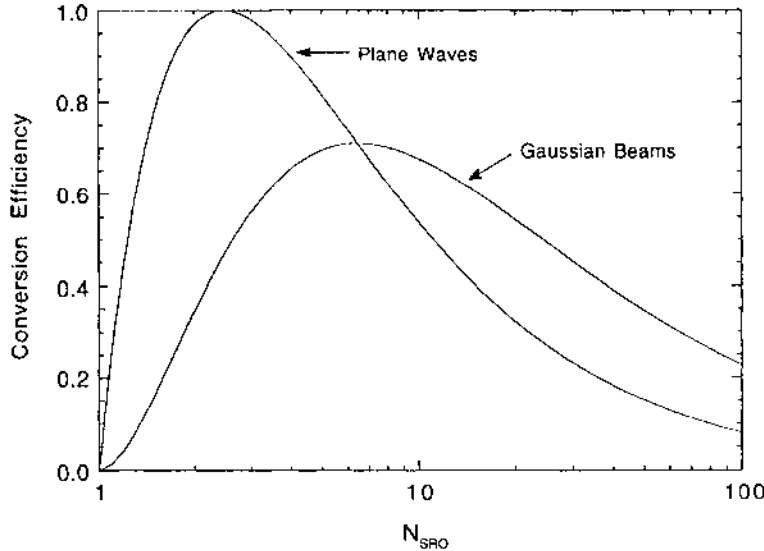


Figure 11 Conversion efficiency as a function of the number of times the pump power exceeds threshold for the SRO, comparing plane wave the Gaussian beam results.

Table 15 Formulas for Calculating Angle Tuning Curves^a

Type I	
ooe	$\lambda_s^{-1}n^o(\lambda_s) + (\lambda_p^{-1} - \lambda_s^{-1})n^o(\lambda_i) = \lambda_p^{-1}n^e(\theta, \lambda_p)$
eo _e	$\lambda_s^{-1}n^e(\theta, \lambda_s) + (\lambda_p^{-1} - \lambda_s^{-1})n^e(\theta, \lambda_i) = \lambda_p^{-1}n^o(\lambda_p)$
Type II	
oe _e	$\lambda_s^{-1}n^o(\lambda_s) + (\lambda_p^{-1} - \lambda_s^{-1})n^e(\theta, \lambda_i) = \lambda_p^{-1}n^e(\theta, \lambda_p)$
eo _e	$\lambda_s^{-1}n^e(\theta, \lambda_s) + (\lambda_p^{-1} - \lambda_s^{-1})n^o(\lambda_i) = \lambda_p^{-1}n^e(\theta, \lambda_p)$
oe _o	$\lambda_s^{-1}n^o(\lambda_s) + (\lambda_p^{-1} - \lambda_s^{-1})n^e(\theta, \lambda_i) = \lambda_p^{-1}n^o(\lambda_p)$
eo _o	$\lambda_s^{-1}n^e(\theta, \lambda_s) + (\lambda_p^{-1} - \lambda_s^{-1})n^o(\lambda_i) = \lambda_p^{-1}n^o(\lambda_p)$

$n(\lambda)$ = index of refraction as a function of wavelength

$$\lambda_i = \frac{\lambda_s \lambda_p}{\lambda_s - \lambda_p}$$

$$\frac{1}{[n^e(\theta, \lambda)]^2} = \frac{\cos^2 \theta}{[n^o(\lambda)]^2} + \frac{\sin^2 \theta}{[n^e(\lambda)]^2}$$

^a In this case, type I refers to generated signal and idler having parallel polarizations, while type II implies orthogonal polarizations.

the phase matching conditions. These conditions are given in Table 15 for the various type I and type II frequency mixing processes in uniaxial crystals.

To obtain accurate tuning curves from these equations, the refractive index as a function of frequency or wavelength should be known to an accuracy of

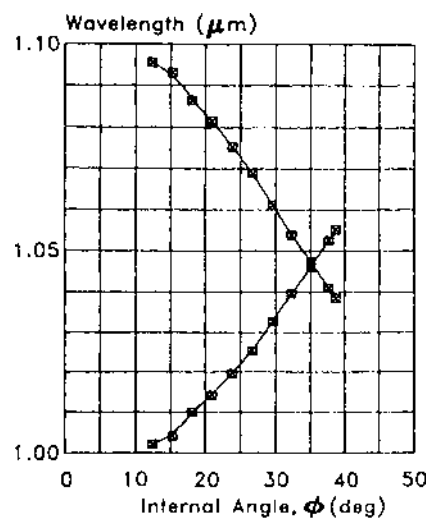


Figure 12 Angle tuning curves for type II cut ($\theta = 90^\circ$, $\phi = 26^\circ$) KTP pumped at 523.5 nm. (From Ref. 19.)

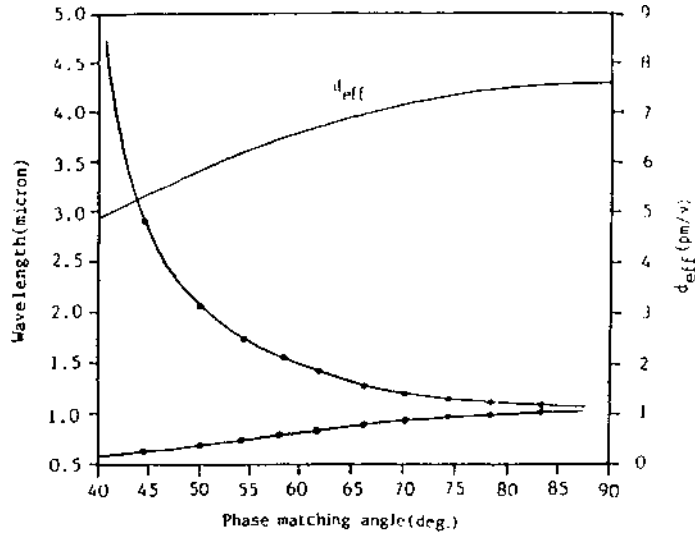


Figure 13 Angle tuning curves for type II cut ($\theta = 67^\circ$) KTP in the XZ plane pumped at 532 nm. (From Ref. 20.)

0.01–0.1%. Normally, given the pump frequency and angle of propagation with respect to the c -axis, a Sellmeier equation for the refractive index dispersion is used to make these computations. The expression for the extraordinary index of refraction as a function of θ is given by Eq. (48) of Chapter 2. Examples from the literature of angle tuning curves for different materials and pump frequencies are shown in (present) Figs. 12 through 26.

Tuning rates ($\Delta\omega$ vs. $\Delta\theta$) can be found by expanding the phase matching equations in a Taylor series. For most of the tuning curve, only first order terms are kept, so that $\Delta\omega$ depends linearly on $\Delta\theta$. However, near the degeneracy point in the curve, the rate begins to diverge for type I phase matching. It is then necessary to include second order terms in the Taylor series expansion for type I processes. Angular tuning rates for the various type I and II processes are given in Table 16. Expressions that are valid near the degeneracy point in type I processes are given in Table 17. To obtain the rate of wavelength change, make the substitution $\Delta\lambda = -(\lambda^2/c)(\Delta\omega/2\pi)$.

Temperature tuning. Consider collinear propagation of the waves in a uniaxial crystal (held at some temperature T) at $\theta = 90^\circ$ with respect to the c -axis (NCPM). The conditions for phase matching in type I and type II processes are listed in Table 18. To compute the tuning curves, the refractive index as a function of temperature as well as wavelength or frequency must be known. Again, through the use of appropriate Sellmeier equations, these computations can be made. Examples of temperature tuning curves are shown in Figs. 27 through 36.

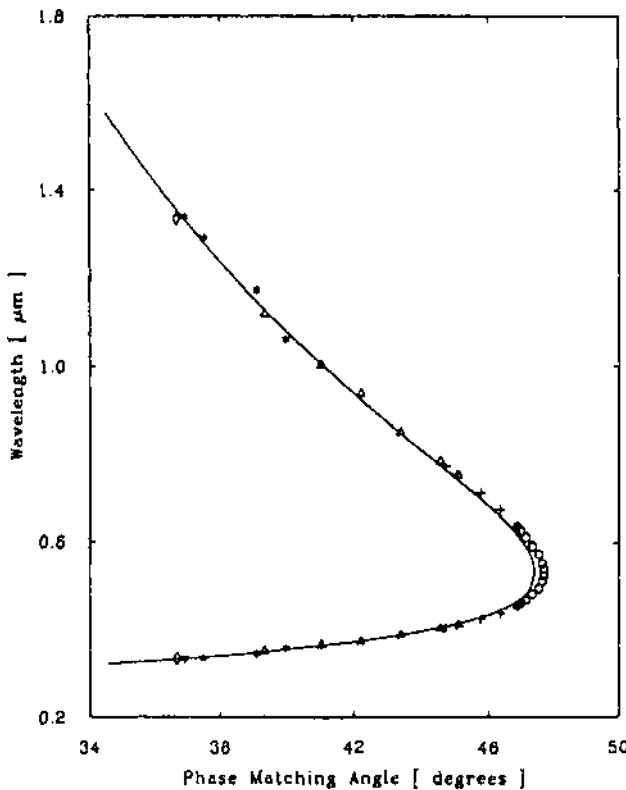


Figure 14 Angle tuning curves for type I cut ($\theta = 39.1^\circ$) BBO pumped at 266 nm. (From Ref. 21.)

Tuning rates ($\Delta\omega$ vs. ΔT) are again obtained by a Taylor series expansion of the phase matching conditions. Tuning rate expressions are given in Table 19. Table 20 lists expressions valid near the degeneracy point for type I processes. To obtain the wavelength changes, make the substitution $\Delta\lambda = -(\lambda^2/c)(\Delta\omega/2\pi)$.

Bandwidth. The gain bandwidth of an OPO is normally defined through the relation $\Delta kL = 2\pi$. Expanding the wave vector phase matching condition as a function of frequency in a Taylor series and setting the result equal to $2\pi/L$ will yield the bandwidth $|\delta\omega|$. Near the degeneracy point, it is necessary to retain terms to second order in the Taylor series expansion for type I processes. Expressions for the gain bandwidth are shown in Table 21. Equivalent expressions in terms of wave numbers or wavelength can be found from

$$|\delta\sigma(\text{cm}^{-1})| = \frac{|\delta\omega|}{2\pi c(\text{cm/s})} \quad (4.19)$$

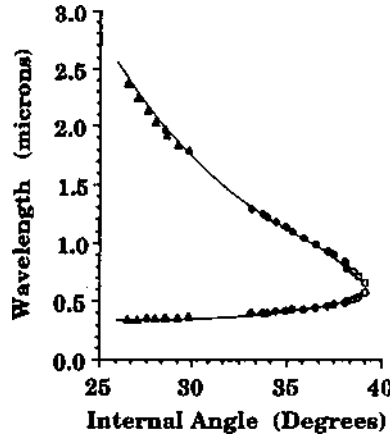


Figure 15 Angle tuning curves for type I cut ($\theta = 32^\circ$) BBO pumped at 308 nm. (From Ref. 22.)

and

$$|\delta\lambda| = \left(\frac{\lambda^2}{c}\right) \frac{|\delta\omega|}{2\pi} \quad (4.20)$$

The detailed spectral characteristics of an OPO will depend on the longitudinal mode structure of the pump laser and the mode spacing ($c/2l$) of

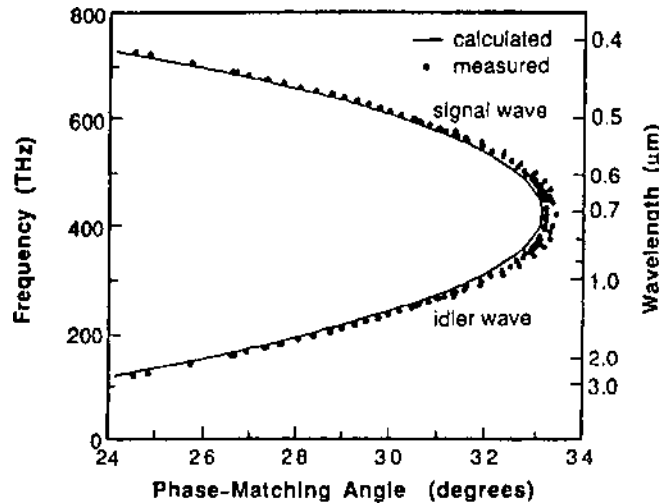


Figure 16 Angle tuning curves for BBO cut at 25° and pumped at 355 nm. (From Ref. 23.)

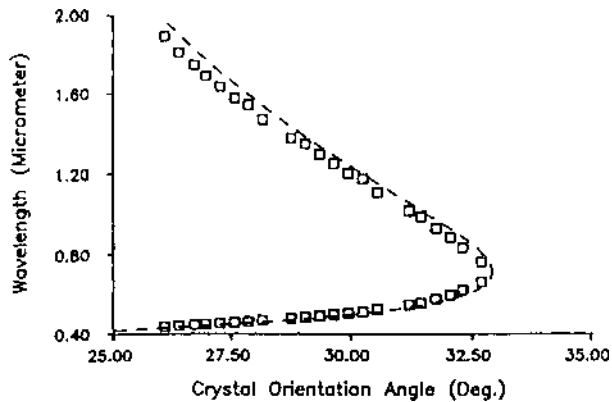


Figure 17 Angle tuning curves for type I cut (31°) BBO pumped at 355 nm. (From Ref. 24.)

the signal and idler cavity modes. A DRO can exhibit clusters of modes spaced a few mode intervals apart within the gain bandwidth profile. In an SRO the idler frequency adjusts freely to optimize the gain and avoid this clustering effect. It is still possible, however, to have several modes oscillating over the gain bandwidth. Étalons, birefringent filters, and gratings have been employed to select a single cavity mode for preferential gain and thus narrow the line width of the output. Current techniques also include injection seeding from a narrow line

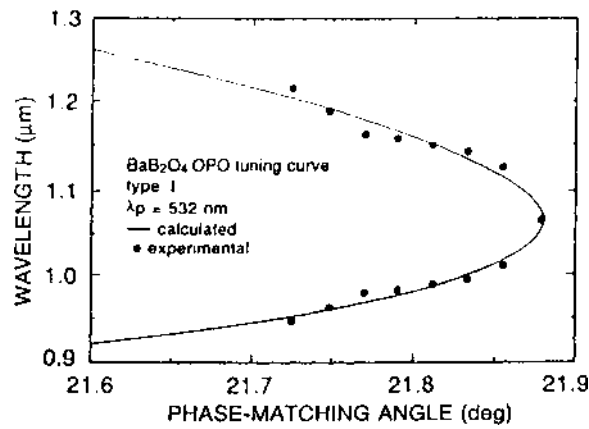


Figure 18 Angle tuning curves for type I cut BBO pumped at 532 nm. (From Ref. 25.)

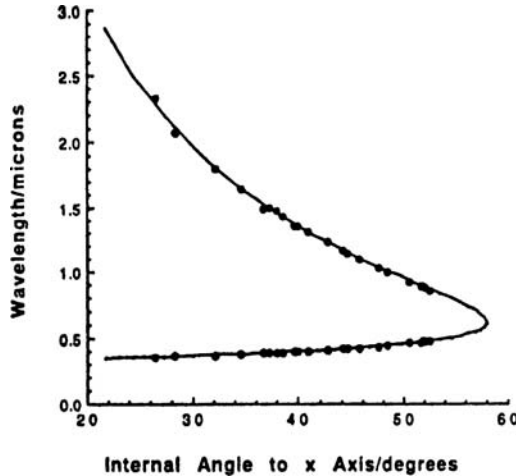


Figure 19 Angle tuning curves for type I cut ($\theta = 40^\circ$) LBO pumped at 308 nm. (From Ref. 26.)

low-energy single-mode oscillator. This could come from another tunable laser or from another OPO operated just above threshold. The injected signal controls the output frequency and line width of the high power OPO. This is sometimes called a master oscillator/power oscillator system.

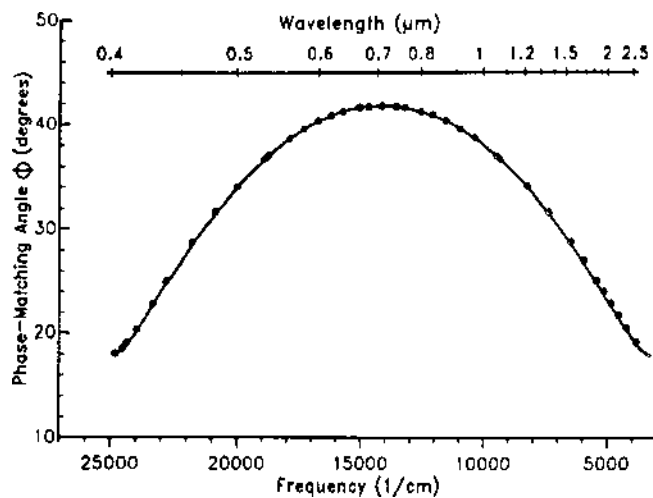


Figure 20 Angle tuning curves for type I cut ($\theta = 90^\circ$, $\phi = 24.5^\circ$) LBO pumped at 255 nm. (From Ref. 27.)

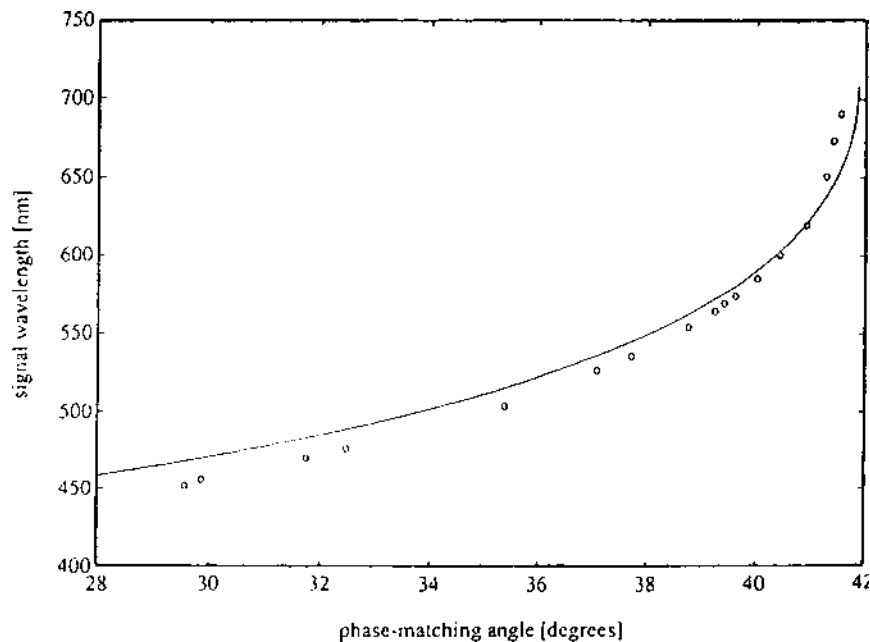


Figure 21 Angle tuning curves for type I cut ($\theta = 90^\circ$, $\phi = 39^\circ$) LBO pumped at 355 nm. (From Ref. 28.)

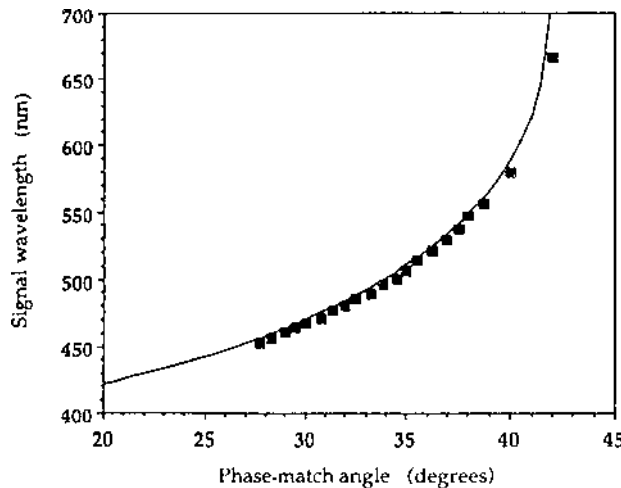


Figure 22 Angle tuning curves for type I cut ($\theta = 25^\circ$ and $\theta = 40^\circ$) LBO crystals pumped at 355 nm. (From Ref. 29.)

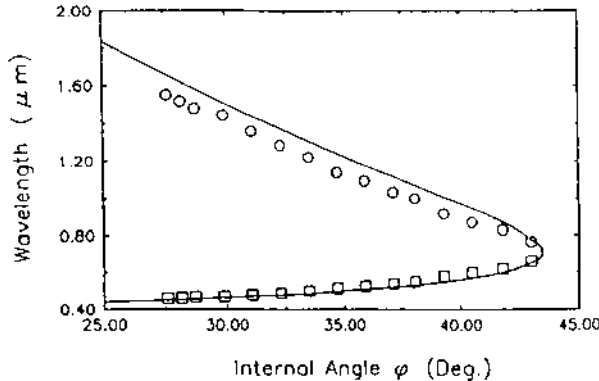


Figure 23 Angle tuning curves for type I cut LBO pumped at 355 nm. (From Ref. 24.)

IV. PULSED OPOS

These systems are typically pumped by Q-switched lasers and produce nanosecond scale pulses at low repetition rates ($\sim 1\text{--}50\text{ Hz}$). The mainly different parameters to consider for pulsed OPOs are rise time and threshold. The two are related, since the pump power incident on the OPO over a finite rise time will require a specific amount of accumulated energy to turn the OPO “on.” These parameters are discussed in the paragraphs below.

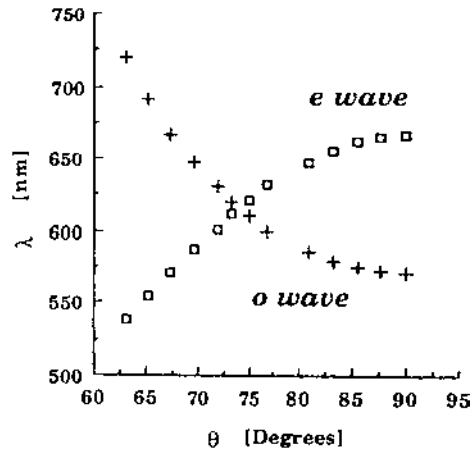


Figure 24 Angle tuning curves for type II cut urea pumped at 308 nm. (From Ref. 30.)

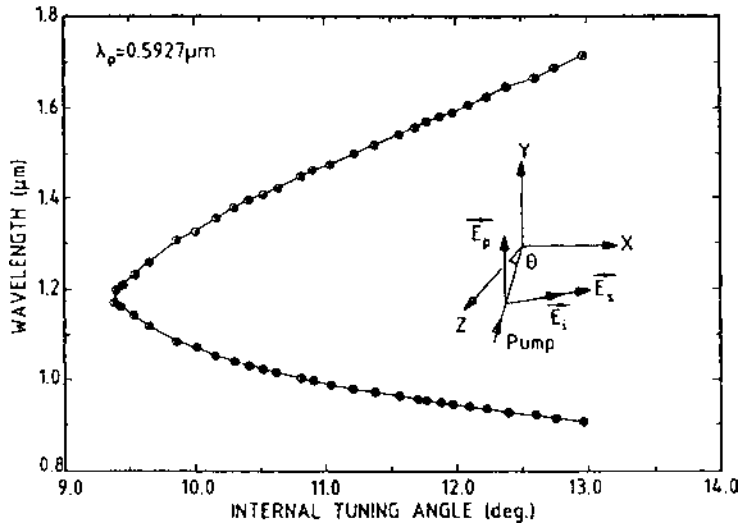


Figure 25 Angle tuning curves for type I cut *N*-(4-nitrophenyl)-*L*-prolinol (NPP) in the XZ plane pumped at 592.7 nm. (From Ref. 31.)

A. Rise Time

Siegman [16] was the first to consider the rise time of a degenerate OPO. Operationally the rise time is the time required to amplify the quantum noise (i.e., spontaneous parametric fluorescence) to a steady-state signal power of the order of the pump power. As discussed earlier, exponential growth of the signal wave can only occur when the net one-way gain exceeds the round-trip loss. In other words, the instantaneous pump power must exceed the steady-state threshold pump power.

Since the one-way gain is modest, many round-trips are required to reach the steady-state regime. After many passes, the signal power will be of the order of the pump power, and pump depletion will then become evident. Until such a condition is reached, the pump power can be treated as a constant. Table 22 gives expressions for the rise time of a DRO and an SRO for the two cases of a step input pulse and a Gaussian-shaped input pulse.

Step input DRO with equal signal and idler losses. Notice that the rise time is given in terms of the usual cavity decay time of a Fabry–Perot resonator, i.e.,

$$\tau_{\text{cav}} = \frac{l/c}{1 - R_s \exp(-\alpha_s L)} \quad (21)$$

where l is the length of the cavity, and L is the length of the nonlinear crystal.

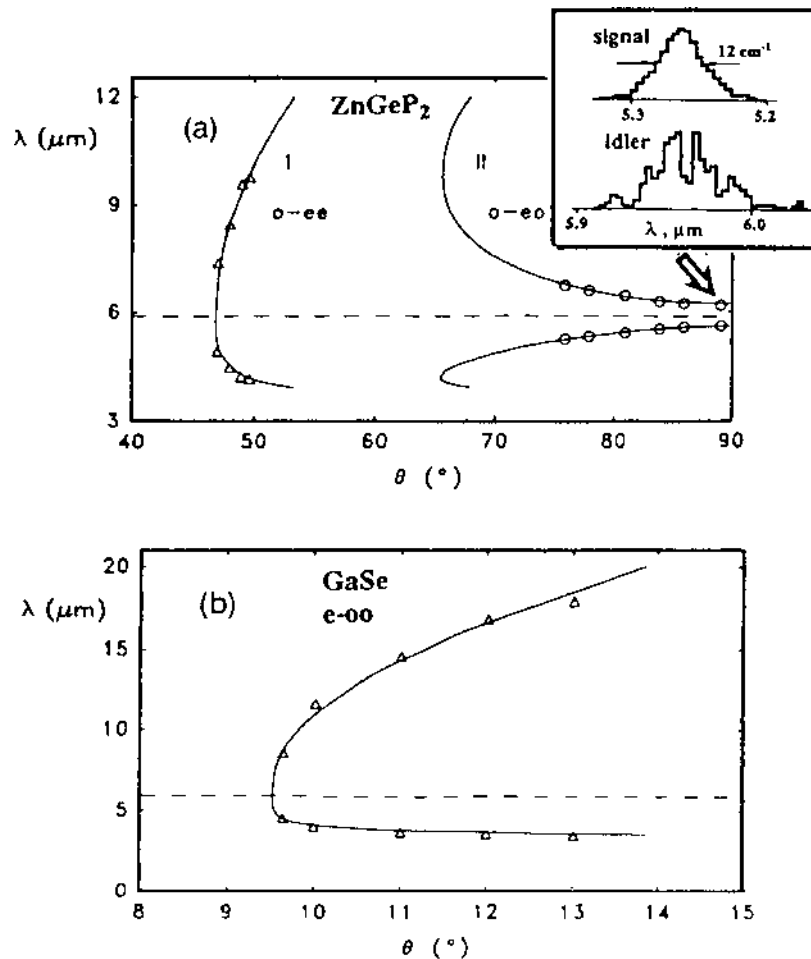


Figure 26 Angle tuning curves for (a) types I and II ZnGeP₂ and (b) type I GaSe pumped at 2900 nm. The inset shows the spectral characteristics of OPG for type II ($\theta = 84^\circ$) ZnGeP₂ pumped at 2790 nm. (From Ref. 32.)

Eq. (21) defines the rate that optical energy “leaks” out of a lossy cavity. Thus the rise time of the OPO must be of the order of this value.

Note that the rise time depends on the amount of gain needed to amplify the signal to the steady state, but only logarithmically through the factor $\ln[\mathcal{P}_s(\text{ss})/\mathcal{P}(0)]$, where $\mathcal{P}_s(\text{ss})$ is the value of the signal power at steady state, and $\mathcal{P}_s(0)$ is the signal power at $t = 0$, equivalent to one photon in the signal channel. This logarithmic dependence indicates that the rise time is not critically

Table 16 Formulas for Calculating Angular Tuning Rates^a

Type I	
ooe	$\Delta\omega = \frac{-\frac{1}{2}\omega_p[n_p^e(\theta)]^3[(n_p^e)^{-2} - (n_p^o)^{-2}]\sin 2\theta}{n_s^o - n_i^o + \omega_s(\partial n^o/\partial\omega)_{\omega_s} - \omega_i(\partial n^o/\partial\omega)_{\omega_i}} \Delta\theta$
e eo	$\Delta\omega = \frac{\frac{1}{2}\{\omega_s[n_s^e(\theta)]^3[(n_s^e)^{-2} - (n_s^o)^{-2}] + \omega_i[n_i^e(\theta)]^3[(n_i^e)^{-2} - (n_i^o)^{-2}]\}\sin 2\theta}{n_s^e(\theta) - n_i^e(\theta) + \omega_s[\partial n^e(\theta)/\partial\omega]_{\omega_s} - \omega_i[\partial n^e(\theta)/\partial\omega]_{\omega_i}} \Delta\theta$
Type II	
ooe	$\Delta\omega = \frac{-\frac{1}{2}\{\omega_p[n_p^e(\theta)]^3[(n_p^e)^{-2} - (n_p^o)^{-2}] - \omega_i[n_i^e(\theta)]^3[(n_i^e)^{-2} - (n_i^o)^{-2}]\}\sin 2\theta}{n_s^o - n_i^e(\theta) + \omega_s(\partial n^o/\partial\omega)_{\omega_s} - \omega_i[\partial n^e(\theta)/\partial\omega]_{\omega_i}} \Delta\theta$
e oe	$\Delta\omega = \frac{-\frac{1}{2}\{\omega_p[n_p^e(\theta)]^3[(n_p^e)^{-2} - (n_p^o)^{-2}] - \omega_s[n_s^e(\theta)]^3[(n_s^e)^{-2} - (n_s^o)^{-2}]\}\sin 2\theta}{n_s^e(\theta) - n_i^o + \omega_s[\partial n^e(\theta)/\partial\omega]_{\omega_s} - \omega_i(\partial n^o/\partial\omega)_{\omega_i}} \Delta\theta$
oeo	$\Delta\omega = \frac{\frac{1}{2}\omega_i[n_i^e(\theta)]^3[(n_i^e)^{-2} - (n_i^o)^{-2}]\sin 2\theta}{n_s^o - n_i^e(\theta) + \omega_s(\partial n^o/\partial\omega)_{\omega_s} - \omega_i(\partial n^e(\theta)/\partial\omega)_{\omega_i}} \Delta\theta$
e oo	$\Delta\omega = \frac{\frac{1}{2}\omega_s[n_s^e(\theta)]^3[(n_s^e)^{-2} - (n_s^o)^{-2}]\sin 2\theta}{n_s^e(\theta) - n_i^o + \omega_s[\partial n^e(\theta)/\partial\omega]_{\omega_s} - \omega_i(\partial n^o/\partial\omega)_{\omega_i}} \Delta\theta$
$\frac{\partial n^e(\theta)}{\partial\omega} = [n^e(\theta)]^3 \left[\frac{\cos^2\theta \partial n^o}{(n^o)^3 \partial\omega} + \frac{\sin^2\theta \partial n^e}{(n^e)^3 \partial\omega} \right]$	
$\Delta\lambda = -\left(\frac{\lambda^2}{c}\right) \frac{\Delta\omega}{2\pi}$	

^a See footnote in Table 15, (p. 148).

dependent on the ratio $\mathcal{P}_s(ss)/\mathcal{P}(0)$. This is reflective of the explosive nature of the exponential signal growth. A value of 10^8 is typical to assume for this ratio, although a variance of two orders of magnitude will not affect the outcome significantly.

From the expression in Table 22, it appears that τ_R will be smaller for larger cavity losses. Note, however, that since $\mathcal{P}_{p,\text{th}} \propto [1 - R_s \exp(-\alpha_s L)]^2$, the rise

Table 17 Formulas for Calculating Angular Tuning Rates for Type I Processes Near Degeneracy^a

ooe	$\Delta\omega = \left\{ \frac{ \omega_p[n_p^e(\theta)]^3[(n_p^e)^{-2} - (n_p^o)^{-2}]\sin 2\theta }{4(\partial n^o/\partial\omega)_{\omega_p/2} + \omega_p(\partial^2 n^o/\partial\omega^2)_{\omega_p/2}} \right\}^{1/2} (\Delta\theta)^{1/2}$
e eo	$\Delta\omega = \left\{ \frac{ \omega_p[n^e(\theta, \omega_p/2)]^3[(n^e(\omega_p/2))^{-2} - (n^o(\omega_p/2))^{-2}]\sin 2\theta }{4[\partial n^e(\theta)/\partial\omega]_{\omega_p/2} + \omega_p[\partial^2 n^e(\theta)/\partial\omega^2]_{\omega_p/2}} \right\}^{1/2} (\Delta\theta)^{1/2}$
$\Delta\lambda = -\left(\frac{\lambda^2}{c}\right) \frac{\Delta\omega}{2\pi}$	

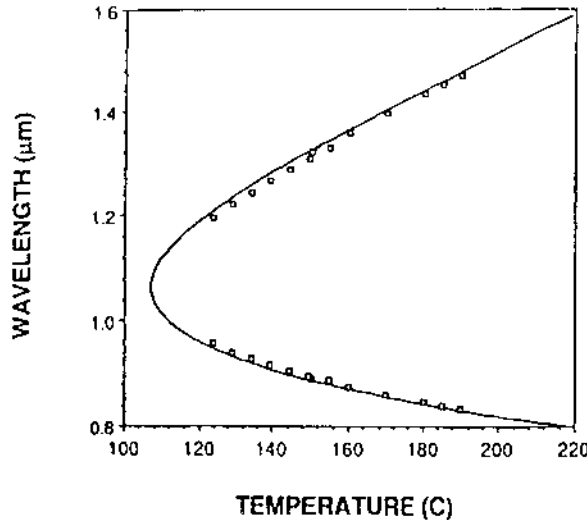
^a See footnote in Table 15.

Table 18 Formulas for Calculating Temperature Tuning Curves^a

Type I	
ooe	$\lambda_s^{-1}n^o(T, \lambda_s) + (\lambda_p^{-1} - \lambda_s^{-1})n^o(T, \lambda_i) = \lambda_p^{-1}n^e(T, \lambda_p)$
eo _e	$\lambda_s^{-1}n^e(T, \lambda_s) + (\lambda_p^{-1} - \lambda_s^{-1})n^e(T, \lambda_i) = \lambda_p^{-1}n^o(T, \lambda_p)$
<hr/>	
Type II	
ooe	$\lambda_s^{-1}n^o(T, \lambda_s) + (\lambda_p^{-1} - \lambda_s^{-1})n^e(T, \lambda_i) = \lambda_p^{-1}n^e(T, \lambda_p)$
eo _e	$\lambda_s^{-1}n^e(T, \lambda_s) + (\lambda_p^{-1} - \lambda_s^{-1})n^o(T, \lambda_i) = \lambda_p^{-1}n^e(T, \lambda_p)$
oe _o	$\lambda_s^{-1}n^o(T, \lambda_s) + (\lambda_p^{-1} - \lambda_s^{-1})n^e(T, \lambda_i) = \lambda_p^{-1}n^o(T, \lambda_p)$
eo _o	$\lambda_s^{-1}n^e(T, \lambda_s) + (\lambda_p^{-1} - \lambda_s^{-1})n^o(T, \lambda_i) = \lambda_p^{-1}n^o(T, \lambda_p)$
<hr/>	
<i>n</i> (<i>T</i> , <i>λ</i>) = index of refraction as a function of temperature and wavelength	
$\lambda_i = \frac{\lambda_s \lambda_p}{\lambda_s - \lambda_p}$	

^a See footnote in Table 15.

time will actually be longer for larger cavity losses. In this case larger loss means that longer times are required to build up the signal to steady state because of "leakage" of energy out of the cavity. For $P_p \gg P_{p,\text{th}}$, τ_R will be independent of the cavity losses.

**Figure 27** Temperature tuning curves for MgO:LiNbO₃ pumped at 532 nm. (From Ref. 33.)

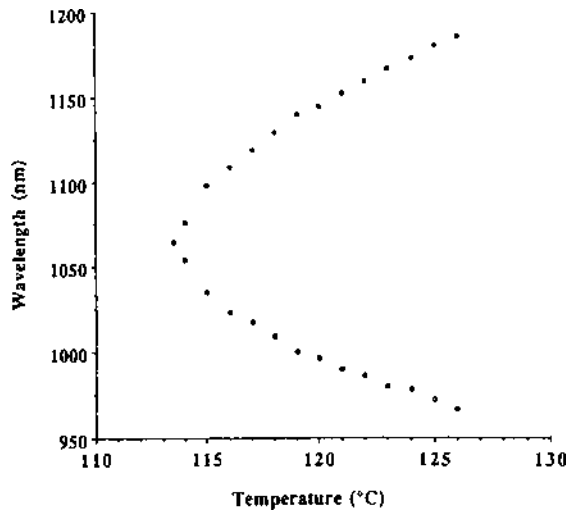


Figure 28 Temperature tuning curves for LiNbO₃ pumped at 532 nm. (From Ref. 34.)

Byer [43] has given an approximate expression of the rise time near degeneracy for a DRO, shown in Table 22, when the input pulse has a Gaussian shape. The primary result is that $(N_{\text{DRO}})^{1/2}$ is replaced by approximately $0.88(N_{\text{DRO}})^{1/2}$, as long as $\tau_R < \tau_p$, where τ_p is the full width at half maximum

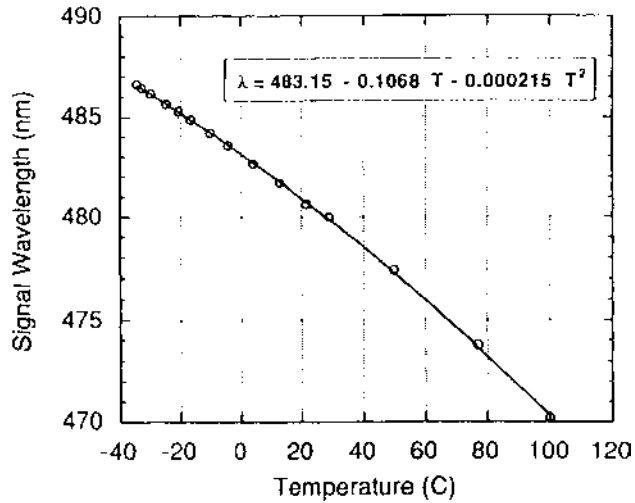


Figure 29 Temperature tuning curves for LBO pumped at 355 nm. (From Ref. 35.)

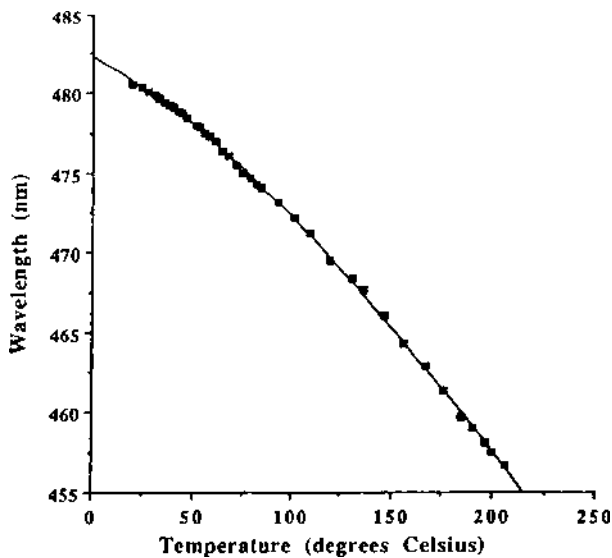


Figure 30 Temperature tuning curves for type II LBO pumped at 355 nm. (From Ref. 36.)

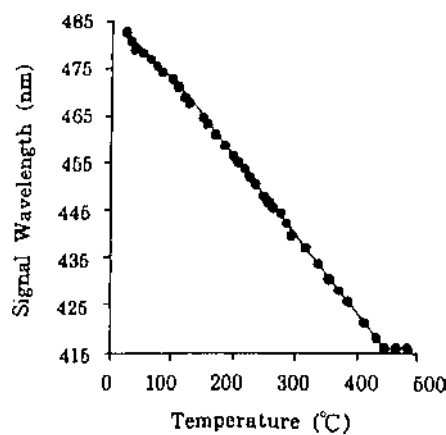


Figure 31 Temperature tuning curves for type II LBO pumped at 355 nm. (From Ref. 37.)

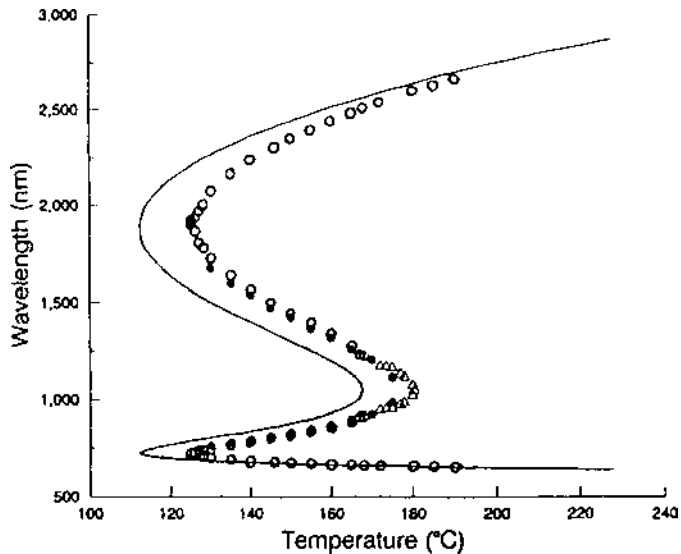


Figure 32 Temperature tuning curves for type I cut LBO in the XY plane pumped at 523.5 nm. The curves show a retracting behavior for LBO in which four distinct wavelengths (two signal and two idler) can be simultaneously obtained at one temperature. (From Ref. 38.)

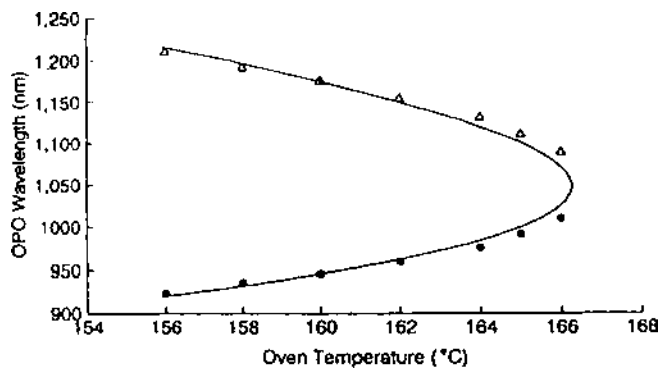


Figure 33 Temperature tuning curves for type I LBO pumped at 523.5 nm. (From Ref. 39.)

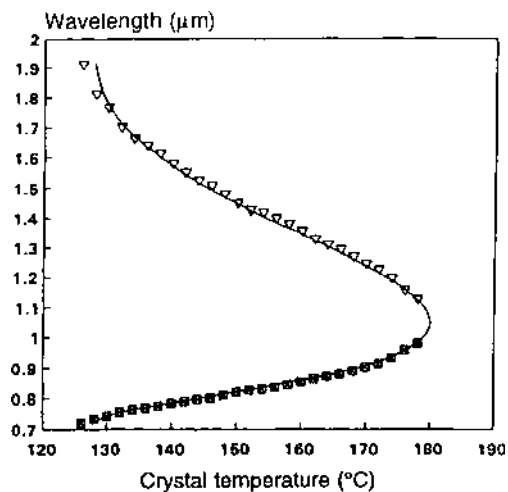


Figure 34 Temperature tuning curves for LBO pumped at 523.5 nm. (From Ref. 40.)

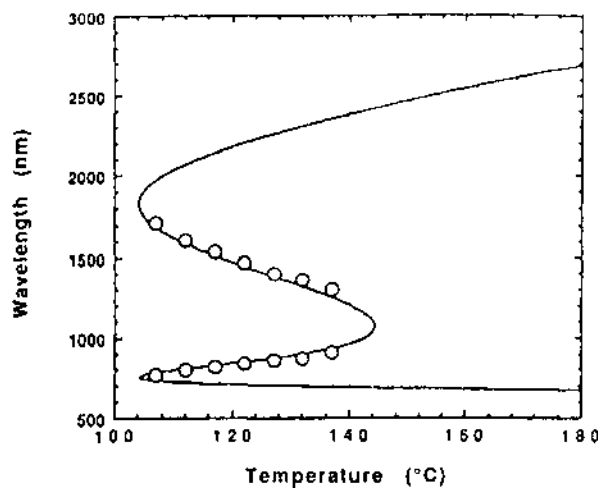


Figure 35 Temperature tuning curves for type I LBO pumped at 532 nm. (From Ref. 41.)

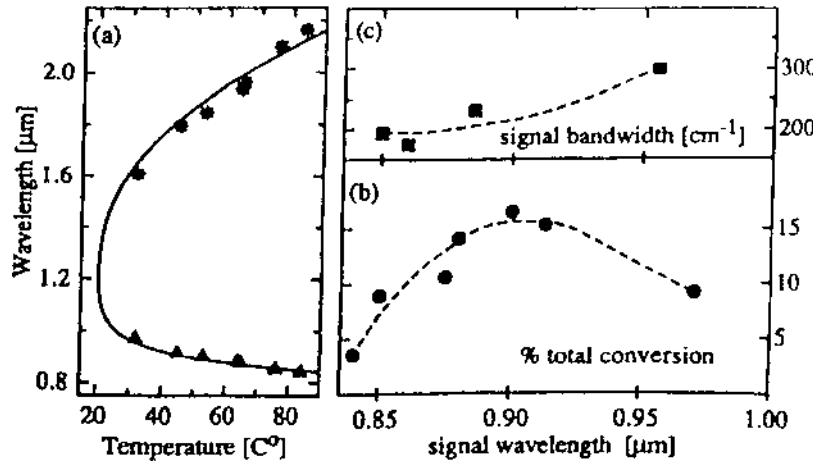


Figure 36 (a) Temperature tuning curves, (b) conversion efficiency, and (c) signal bandwidth for LBO pumped at 605 nm. (From Ref. 42.)

Table 19 Formulas for Calculating Temperature Tuning Rates^a

Type I

$$\begin{aligned} \text{oee} \quad \Delta\omega &= \left[\frac{\omega_p(\partial n_p^e / \partial T)_{T_o} - \omega_s(\partial n_s^o / \partial T)_{T_o} - \omega_i(\partial n_i^o / \partial T)_{T_o}}{n_s^o - n_i^o + \omega_s(\partial n^o / \partial \omega)_{\omega_s, T_o} - \omega_i(\partial n^o / \partial \omega)_{\omega_i, T_o}} \right] \Delta T \\ \text{eo} \quad \Delta\omega &= \left[\frac{\omega_p(\partial n_p^o / \partial T)_{T_o} - \omega_s(\partial n_s^o / \partial T)_{T_o} - \omega_i(\partial n_i^e / \partial T)_{T_o}}{n_s^e - n_i^e + \omega_s(\partial n^e / \partial \omega)_{\omega_s, T_o} - \omega_i(\partial n^e / \partial \omega)_{\omega_i, T_o}} \right] \Delta T \end{aligned}$$

Type II

$$\begin{aligned} \text{oee} \quad \Delta\omega &= \left[\frac{\omega_p(\partial n_p^e / \partial T)_{T_o} - \omega_s(\partial n_s^o / \partial T)_{T_o} - \omega_i(\partial n_i^e / \partial T)_{T_o}}{n_s^o - n_i^e + \omega_s(\partial n^o / \partial \omega)_{\omega_s, T_o} - \omega_i(\partial n^e / \partial \omega)_{\omega_i, T_o}} \right] \Delta T \\ \text{eo} \quad \Delta\omega &= \left[\frac{\omega_p(\partial n_p^e / \partial T)_{T_o} - \omega_s(\partial n_s^e / \partial T)_{T_o} - \omega_i(\partial n_i^o / \partial T)_{T_o}}{n_s^e - n_i^o + \omega_s(\partial n^e / \partial \omega)_{\omega_s, T_o} - \omega_i(\partial n^o / \partial \omega)_{\omega_i, T_o}} \right] \Delta T \\ \text{oeo} \quad \Delta\omega &= \left[\frac{\omega_p(\partial n_p^o / \partial T)_{T_o} - \omega_s(\partial n_s^o / \partial T)_{T_o} - \omega_i(\partial n_i^e / \partial T)_{T_o}}{n_s^o - n_i^e + \omega_s(\partial n^o / \partial \omega)_{\omega_s, T_o} - \omega_i(\partial n^e / \partial \omega)_{\omega_i, T_o}} \right] \Delta T \\ \text{eo} \quad \Delta\omega &= \left[\frac{\omega_p(\partial n_p^o / \partial T)_{T_o} - \omega_s(\partial n_s^e / \partial T)_{T_o} - \omega_i(\partial n_i^o / \partial T)_{T_o}}{n_s^e - n_i^o + \omega_s(\partial n^e / \partial \omega)_{\omega_s, T_o} - \omega_i(\partial n^o / \partial \omega)_{\omega_i, T_o}} \right] \Delta T \end{aligned}$$

$$\Delta\lambda = - \left(\frac{\lambda^2}{c} \right) \frac{\Delta\omega}{2\pi}$$

^a See footnote in Table 15.

Table 20 Formulas for Calculating Temperature Tuning Rates for Type I Processes Near Degeneracy^a

ooe	$\Delta\omega = \left\{ \frac{2\omega_p (\partial n^e / \partial T)_{\omega_{p,T_0}} - (\partial n^o / \partial T)_{\omega_{p/2,T_0}} }{4(\partial n^o / \partial \omega)_{\omega_{p/2,T_0}} + \omega_p (\partial^2 n^o / \partial \omega^2)_{\omega_{p/2,T_0}}} \right\}^{1/2} (\Delta T)^{1/2}$
eoo	$\Delta\omega = \left\{ \frac{2\omega_p (\partial n^o / \partial T)_{\omega_{p,T_0}} - (\partial n^e / \partial T)_{\omega_{p/2,T_0}} }{4(\partial n^e / \partial \omega)_{\omega_{p/2,T_0}} + \omega_p (\partial^2 n^e / \partial \omega^2)_{\omega_{p/2,T_0}}} \right\}^{1/2} (\Delta T)^{1/2}$
	$\Delta\lambda = -\left(\frac{\lambda^2}{c}\right) \frac{\Delta\omega}{2\pi}$

^a See footnote in Table 15.**Table 21** Formulas for Calculating Gain Bandwidths^a

Type I	
ooe	$ \delta\omega = \frac{2\pi c/L}{ n_s^o - n_i^o + \omega_s(\partial n^o / \partial \omega)_{\omega_s} - \omega_i(\partial n^o / \partial \omega)_{\omega_i} }$
eoo	$ \delta\omega = \frac{2\pi c/L}{ n_s^e(\theta) - n_i^e(\theta) + \omega_s[\partial n^e(\theta) / \partial \omega]_{\omega_s} - \omega_i[\partial n^e(\theta) / \partial \omega]_{\omega_i} }$
Type II	
oeo	$ \delta\omega = \frac{2\pi c/L}{ n_s^o - n_i^e(\theta) + \omega_s(\partial n^o / \partial \omega)_{\omega_s} - \omega_i[\partial n^e(\theta) / \partial \omega]_{\omega_i} }$
eo	$ \delta\omega = \frac{2\pi c/L}{ n_s^e(\theta) - n_i^o + \omega_s[\partial n^e(\theta) / \partial \omega]_{\omega_s} - \omega_i(\partial n^o / \partial \omega)_{\omega_i} }$
Type I (near degen.)	
ooe	$ \delta\omega = \left[\frac{4\pi c/L}{4(\partial n^o / \partial \omega)_{\omega_{p/2}} + \omega_p (\partial^2 n^o / \partial \omega^2)_{\omega_{p/2}}} \right]^{1/2}$
eoo	$ \delta\omega = \left[\frac{4\pi c/L}{4[\partial n^e(\theta) / \partial \omega]_{\omega_{p/2}} + \omega_p [\partial^2 n^e(\theta) / \partial \omega^2]_{\omega_{p/2}}} \right]^{1/2}$
	$ \delta\sigma(cm^{-1}) = \frac{ \delta\omega }{2\pi c(cm/s)}$
	$\delta\lambda = \left(\frac{\lambda^2}{c}\right) \frac{ \delta\omega }{2\pi}$

^a In this case, type I refers to generated signal and idler having parallel polarizations, while type II implies orthogonal polarizations.

Table 22 Formulas for Calculating the Rise Time of Pulsed OPOs

Step input pulse DRO (at degeneracy)	$\tau_R \approx \frac{l/c}{(1 - R_s e^{-\alpha_s L})(\sqrt{N_{DRO}} - 1)} \ln \left[\frac{\mathcal{P}_s(ss)}{\mathcal{P}_s(0)} \right]$
SRO	$\tau_R \approx \frac{l/c}{(1 - R_s e^{-\alpha_s L})(N_{SRO} - 1)} \ln \left[\frac{\mathcal{P}_s(ss)}{\mathcal{P}_s(0)} \right]$
Gaussian input pulse DRO (at degeneracy)	$\tau_R \approx \frac{l/c}{(1 - R_s e^{-\alpha_s L})(0.88 \sqrt{N_{DRO}} - 1)} \ln \left[\frac{\mathcal{P}_s(ss)}{\mathcal{P}_s(0)} \right]$ (see also Figs. 39 and 40)
SRO	(see Figs. 37 and 38)

(FWHM) of the pump pulse. It will be remembered that N_{DRO} is the number of times that the incident (peak) pump power exceeds the steady-state DRO threshold pump power.

Step input SRO. For the SRO, the following simple change is made: $(N_{DRO})^{1/2} - 1 \rightarrow N_{SRO} - 1$. Now, since $\mathcal{P}_{p,th} \propto [1 - R_s \exp(-\alpha_s L)]$, statements made above for the DRO apply equally well to the SRO. Again, for $\mathcal{P}_p \gg \mathcal{P}_{p,th}$, the rise time will be independent of cavity losses.

Gaussian input pulse SRO. Pearson et al. [44] have analyzed in detail the rise time of OPOs with Gaussian input pulses. For the SRO, τ_R is again defined operationally by

$$\mathcal{P}_s(\tau_R) = \mathcal{P}_s(0) \frac{r}{a} \quad (22)$$

where $a = 1 - R_s \exp(-\alpha_s L)$ is the cavity loss and r is a number of the order of the amplification factor needed to reach threshold. As before, the explosive nature of the signal growth makes τ_R relatively insensitive to the exact value of r (a change in r by two orders of magnitude changes τ_R by only 10%).

Pearson et al. computed a value for Eq. (22) by solving the time dependent coupled wave equations for the signal and idler waves in the nondepleted pump approximation. The final result must be found numerically. Again, the rise time depends on the amount by which the peak pump power exceeds the steady-state threshold. Pearson et al. performed their calculations in terms of a normalized pump ratio $N_0 = N_{SRO}(100a)$, where a is the cavity loss in %.

The rise time of an SRO as a function of cavity loss for given pump pulse width, normalized pump power ratio, and cavity length L' is shown in Fig. 37. Figure 38 shows τ_R vs. L' for given pump pulse width, pump power ratio, and a cavity loss of 1%. In all of these plots, a value of $r = 10^8$ was assumed.

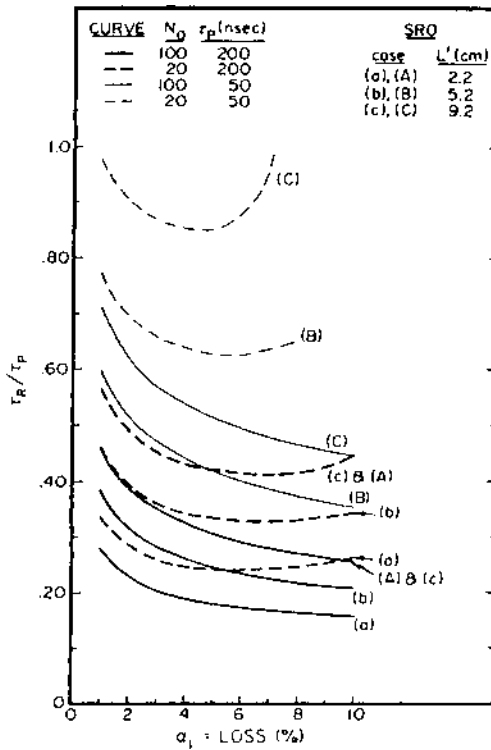


Figure 37 Rise time of a Gaussian-shaped pulse pumped SRO as a function of cavity loss for various pump ratios and cavity lengths. Heavy curves, 200 ns pump pulse. Light curves, 50 ns pump pulse. (From Ref. 44 © IEEE 1972.)

Gaussian input pulse DRO. The DRO treated by Pearson et al. has equal signal and idler losses. The operational definition for τ_R in this case is

$$\mathcal{P}_s(\tau_R) = \mathcal{P}_s(0) \frac{r}{a^2} \quad (23)$$

and τ_R is a function of the normalized pump power ratio for the DRO, $N_0 = N_{DRO}(100a)^2$. The rise time as a function of cavity loss given τ_p , N_0 , and L' is shown in Fig. 39. In Figure 40, τ_R vs. L' is plotted for given τ_p , N_0 , and $a = 1\%$. Again, a value of $r = 10^8$ was assumed in the calculations. The dashed curves in these figures are computed from the formula for the step pulse input given in Table 22.

Figures 37 and 39 show that increasing cavity losses may actually decrease the rise time even though larger loss means larger steady-state threshold. As Pearson et al. have pointed out, this is due to the nature of the Gaussian pulse,

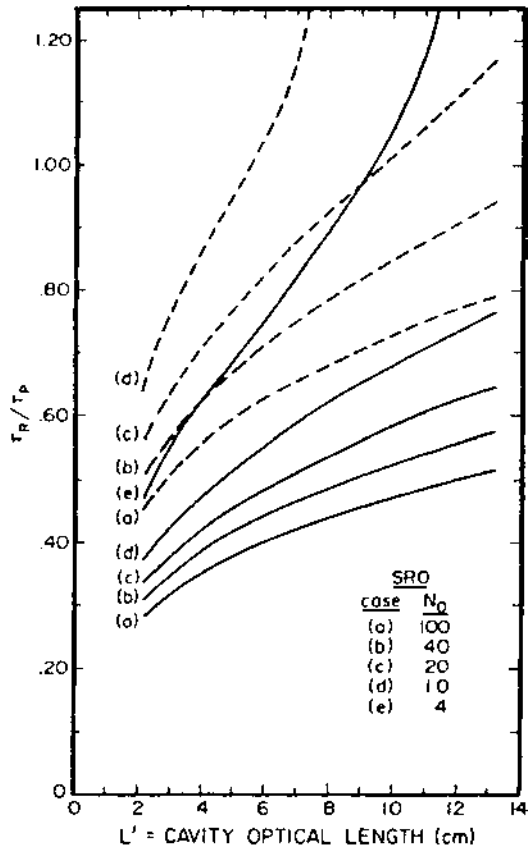


Figure 38 Rise time of a Gaussian-shaped pulse pumped SRO as a function of cavity length for various pump ratios. Cavity loss, 1% Heavy curves, 200 ns pump pulse. Light curves, 50 ns pump pulse. (From Ref. 44 © IEEE 1972.)

which is illustrated in Fig. 41. For $(t/\tau)^2 > \frac{1}{2}$, where $\tau^2 = \tau_p^2/2 \ln(2)$ is the square of the $1/e^2$ half-width of the pump pulse, the slope of the Gaussian increases in magnitude as $(t/\tau)^2$ decreases. The rate of growth of the signal power is proportional to the amount by which the instantaneous pump power exceeds threshold, and the signal power will grow rapidly when this ratio grows rapidly. When the cavity loss is low, the threshold pump level occurs further out in the tail of the Gaussian where the pump ratio changes slowly. Thus the rise time can be longer for smaller losses. Pearson et al. have shown, however, that the amount of time by which the rise time precedes the peak of the pulse increases

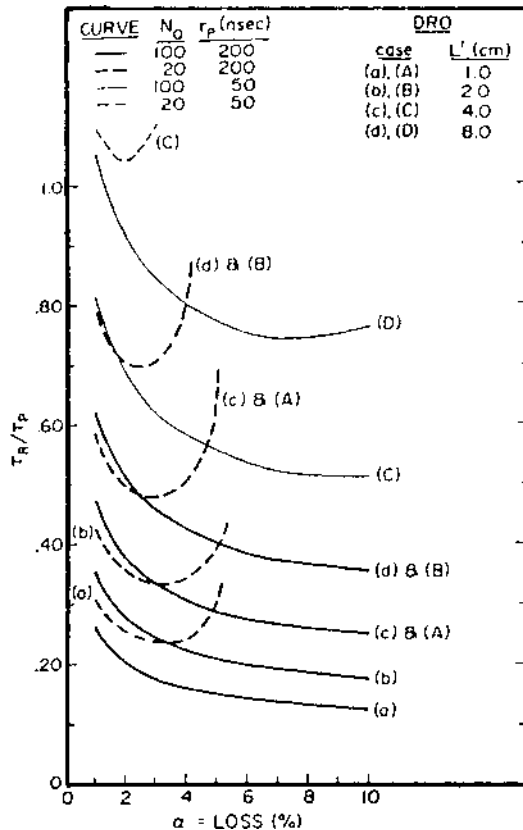


Figure 39 Rise time of a Gaussian-shaped pulse pumped DRO as a function of cavity loss for various pump ratios and cavity lengths. Heavy curves, 200 ns pump pulse. Light curves, 50 ns pump pulse. (From Ref. 44 © IEEE 1972.)

monotonically with increasing cavity losses. This reflects the fact that for larger cavity losses, the pump power is above threshold for a shorter total time.

A critical result of the finite rise time of the OPO is the minimum peak pump power required to reach oscillation. This value N_{\min} as a function of cavity length is shown in Fig. 42 for various values of the pulse width and cavity loss. The values for Gaussian-shaped input pulses are compared to the step input results. It can be seen that as small as possible cavity lengths are desired to decrease the oscillation pumping conditions.

The quantity N_{\min} is the factor by which the pulse threshold is increased due to the finite DRO rise time. Once a steady-state threshold is calculated and a cavity length chosen, the threshold peak pump power is found by multiplying

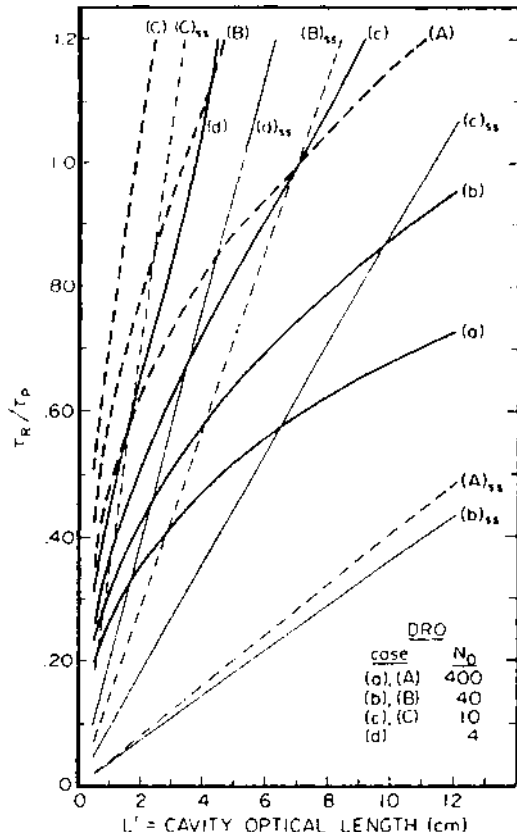


Figure 40 Rise time of a Gaussian-shaped pulse pumped DRO as a function of cavity length for various pump ratios. Cavity loss, 1% Heavy curves, 200 ns pump pulse. Light curves, 50 ns pump pulse. (From Ref. 44 © IEEE 1972.)

the steady-state threshold by N_{\min} . The pulsed DRO threshold is thus defined by the minimum peak pump power for which the oscillator will turn on rather than by the pump power for which the net parametric gain for the signal and idler waves exceeds the cavity loss.

B. Threshold

A finite rise time indicates that a certain minimum energy must accumulate before an OPO turns on. Therefore the threshold can be measured in terms of energy or fluence. Simple expressions for fluence thresholds of the DRO and

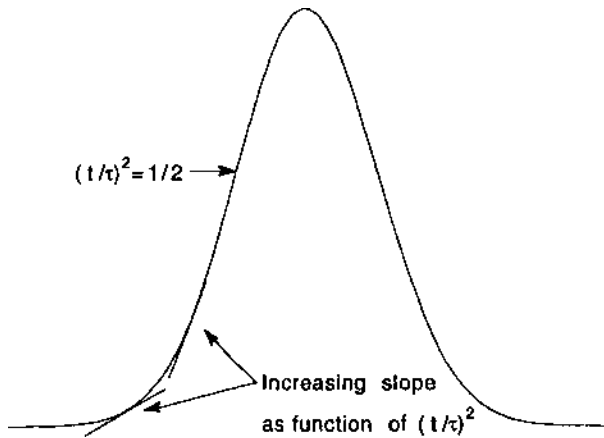


Figure 41 Gaussian-shaped temporal pulse illustrating an increasing slope as a function of decreasing $(t/\tau)^2$ for $(t/\tau)^2 > \frac{1}{2}$.

SRO, assuming step pulse inputs, can be found by multiplying the peak pump intensity by the rise time [43]. These expressions are found in Table 23.

From the results of Pearson et al. [44] (see Fig. 42), the threshold energy \mathcal{E}_{th} can be found by integrating N_{\min} up to the rise time τ_R . Thus

$$\mathcal{E}_{\text{th}} = \int_{-\infty}^{\tau_R} N_{\min} \mathcal{P}_{p,\text{th}} \exp \left[-\frac{2(t - \tau_T)^2}{\tau^2} \right] dt \quad (24)$$

where τ_T is the time corresponding to the peak of the pulse, and $N_{\min} = \mathcal{P}_p(\tau_T)/\mathcal{P}_{p,\text{th}}$.

Brosnan and Byer [45] have analyzed the threshold conditions of an SRO pumped by a Gaussian pulse, including the effects of spatial mode overlap and beam walk-off. They considered the duration of time over which multiple passes amplify the signal power to the steady state from quantum noise. This establishes a condition on the peak of the time dependent parametric gain. They then computed the effective width of the time dependent gain profile for which the net gain exceeds loss (so that a net amplification occurs on each resonator pass) and set this time equal to 2τ , where again τ is the $1/e^2$ half-width of the Gaussian pulse. Integrating over the pump intensity, the threshold fluence is found. This formula is given in Table 23.

Note that although the threshold fluence of the SRO is larger than that of the DRO, the rise time of the SRO may be smaller at high pump power. This implies that a DRO may reach threshold and oscillate as an SRO before the DRO threshold is achieved under certain conditions. For stability reasons, the SRO is

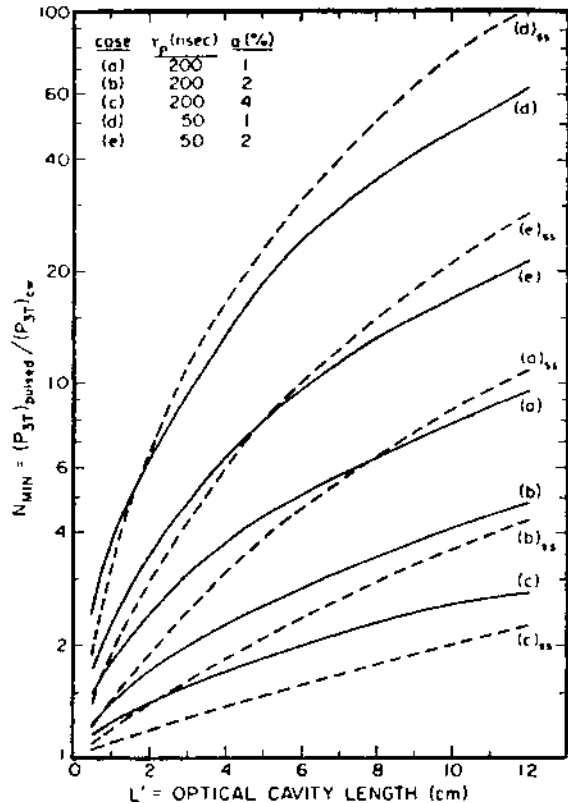


Figure 42 Minimum pump ratio required for oscillation for a Gaussian-shaped pump pulse as a function of cavity length for various pulse widths and cavity losses. Dashed curves correspond to a step input pulse. (From Ref. 44 © IEEE 1972.)

more common than the DRO in the pulse regime since adequate pump power for threshold is readily available.

V. SYNCHRONOUSLY PUMPED OPOs

Many applications require the use of ultrashort pulses. Mode-locked lasers have been heavily employed in such instances, but the wavelength coverage has been limited, especially in the near and mid-IR. A natural extension to fill these needs has been the development of synchronously pumped OPOs. The short pulses have been derived from the mode-locked laser pump, and the properties of the OPO

Table 23 Formulas for Calculating the Threshold Fluence of Pulsed OPOs

Step input pulse	
DRO (at degeneracy)	$F_{p,\text{th}} \approx \frac{(l/c)I_{p,\text{peak}}}{(1 - R_s e^{-\alpha_s L})(\sqrt{N_{\text{DRO}}} - 1)} \ln \left[\frac{\mathcal{P}_s(ss)}{\mathcal{P}_s(0)} \right]$
SRO	$F_{p,\text{th}} \approx \frac{(l/c)I_{p,\text{peak}}}{(1 - R_s e^{-\alpha_s L})(N_{\text{SRO}} - 1)} \ln \left[\frac{\mathcal{P}_s(ss)}{\mathcal{P}_s(0)} \right]$
Gaussian input pulse (including effects of spatial mode overlap and beam walk-off)	
SRO	$F_{p,\text{th}} = \frac{2.25\tau}{\kappa g_s \bar{L}^2} \left\{ \frac{l}{2\tau c} \ln \left[\frac{\mathcal{P}_s(ss)}{\mathcal{P}_s(0)} \right] + \alpha_s L + \ln \frac{2}{\sqrt{R_s}} \right\}$
	$\kappa = \frac{2\pi^2 d_{\text{eff}}^2 (1 - \delta^2)}{\epsilon_0 n_s^2 n_p \lambda_p^2 c} \quad (\text{SI})$
	$g_s = \frac{w_p^2}{w_p^2 + w_s^2}$
	$\bar{L} = L_w \text{erf} \left(\frac{\sqrt{\pi} L}{2 L_w} \right)$
	$L_w = \frac{\sqrt{\pi} w_p}{2} \rho \sqrt{\frac{w_p^2 + w_s^2}{w_p^2 + \frac{1}{2} w_s^2}}$
	$\tau = 1/e^2$ pulse half-width
	$\rho = \text{walk-off angle}$

provide the wide tunability. Synchronous pumping implies that the round-trip time of a pulse in the OPO cavity equals the interpulse time of the pump laser. In this way, the nonlinear crystal is pumped at the appropriate time when the signal pulse to be amplified arrives.

There are two types of mode-locked laser used as a pump source: Q-switched mode-locked, and cw mode-locked. In the first type, the laser is Q-switched to boost the peak power, and the result is a nanosecond scale pulse envelope containing several mode-locked pulses with widths in the picosecond or femtosecond regime. The cw mode-locked laser produces a continuous stream of picosecond or femtosecond pulses which generally have lower peak powers than those of a Q-switched mode-locked laser.

The parameters discussed above for cw and pulsed OPOs are also appropriate for the synchronously pumped OPOs. In particular, thresholds, gain bandwidths, and tuning parameters are calculated in the same way. Rise times and fluence thresholds, discussed in Section III, apply equally well to the Q-switched mode-locked case, since the pulse envelope of the pump has a finite rise time. Rise time is not an issue for cw mode-locked OPOs because the system is in a steady state for periods long compared to the turn-on time of the device.

New parameters of importance for these devices include time synchronization between the pump and the OPO signal pulses, and pulse walk-off and pulse group velocity delay between signal and pump. These arise because of the short time scale of the pulses. Also, the short duration of the pulses results in a finite spectral bandwidth. These spectral properties can be modified by the spectral dispersion and bandwidth of the cavity.

Systems employed for ultrafast spectroscopy are required to have truly repetitive pulses for improved signal-to-noise ratio. The cw mode-locked OPOs with very high pulse repetition rates are well matched to this application. Cheung and Liu [46] have presented a model of these cw systems based on the theory governing actively or passively mode-locked lasers.

The model developed by Chung and Liu treats a cw synchronously pumped, singly resonant OPO. They derived the following differential equation describing the temporal behavior of the signal field amplitude of repetitive pulses in the steady-state regime of the synchronously pumped OPO:

$$\left[G(t) - \Gamma - S(t) + \frac{\pi^2}{3(\Delta\omega_n)^2} a I_p(t) \frac{d^2}{dt^2} + \frac{1}{(\Delta\omega_c)^2} \frac{d^2}{dt^2} - i \frac{D_s L}{\omega_s c} \frac{d^2}{dt^2} - \delta T_n(t) \frac{d}{dt} - 2\delta T_{sp} \frac{d}{dt} + \delta T \frac{d}{dt} \right] A_{\omega_{so}}(t) = 0 \quad (25)$$

In this expression, $G(t)$ is the time dependent gain. Since in the steady state the gain per pass is small, this term is given by an expansion of the exact expression, related to the Jacobi elliptic function, keeping terms quadratic in the pump intensity:

$$G(t) = a I_p(t) + \frac{2}{3} a^2 I_p^2(t) \quad (27)$$

The term $S(t)$ is another term of this expansion and represents gain saturation due to pump depletion:

$$S(t) = \frac{2a^2 \omega_p}{3\omega_s} I_p(t) I_s(t) \quad (28)$$

The static distributed linear loss is given by the term Γ :

$$\Gamma = \alpha_s l - \ln \sqrt{R_{s1} R_{s2}} \simeq 1 - \sqrt{R_{s1} R_{s2}} \exp(-\alpha_s l) \quad (29)$$

for $\alpha_s l \ll 1$ and $R_{s1} \sim R_{s2} \sim 1$, where l is the cavity length and α_s is the effective cavity loss coefficient, which includes all absorption, scattering, and Fresnel reflection losses. R_{s1} and R_{s2} are the mirror reflectances at the signal frequency for the front and back mirrors. The nonlinear parametric coefficient a is

related to the loss term and the steady-state threshold pump intensity by

$$I_{p,\text{th}} = \frac{\Gamma}{a} \quad (30)$$

The fourth term of Eq. (25) represents the gain reduction due to the finite phase mismatch of the frequency components comprising the ultrashort pulse, and is related to the gain bandwidth of the crystal $\Delta\omega_n$. (The subscript n signifies the nondegenerate bandwidth.) The fifth term describes the effect of the finite cavity bandwidth determined by the cavity finesse and any frequency dispersing elements present. The last second order time derivative term represents the effects on the pulse due to group velocity dispersion, and $D_s = \omega_s c(d^2k/d\omega^2)|_{\omega_s}$ is the dimensionless dispersion constant.

The three first order derivative terms describe phase shifts. The first is intensity dependent, derived again from an expansion of the exact Jacobi elliptic function, and is present when a finite phase mismatch is present. It is also given in terms of the gain bandwidth:

$$\delta T_n(t) = \frac{2\pi}{3\Delta\omega_n} a I_p(t) \left\{ 1 - \frac{2}{5} \left[2a I_p(t) + \frac{\omega_p}{\omega_s} a I_s(t) \right] \right\} + \frac{2}{3} a I_p(t) \delta T_{sp} \quad (31)$$

The second phase shift term is due to the pulse walk-off time δT_{sp} , which is given by the difference of the reciprocal group velocities of the two pulses. Finally, the last term is due to cavity detuning, where the cavity detuning time δT is defined as the difference between the repetition period of the pump pulses and the round-trip time of the signal pulses.

Cheung and Liu solved Eq. (25) by the numerical finite difference method. They took the pump intensity to have a Gaussian temporal profile, and ignored the group velocity dispersion term since this is normally zeroed out experimentally using a set of prisms.

Detuning time. Cheung and Liu defined an effective cavity detuning time as $\delta T_{\text{eff}} = \delta T - 2\delta T_{sp}$. This is a static number determined by the cavity length and linear dispersion properties of the nonlinear crystal. To present the calculations, δT_{eff} was normalized to the full width at half maximum (FWHM) of the Gaussian-shaped pump pulse. (All normalized quantities are designated in the following figures with a caret: $\hat{\cdot}$.) The numerical calculations were performed on 2048 equally spaced time points from $-5 \times \text{FWHM}$ to $+5 \times \text{FWHM}$. In the results presented below, the following parameters were used: $\Delta\omega_n \times \text{FWHM} = 25$, $\Delta\omega_c \times \text{FWHM} = 5000$, $\omega_s/\omega_p = 0.4$, $R_{s1} = 1$, and $1 - R_{s2} = 0.03$.

The output signal pulses are asymmetric in time, even for $\delta T_{\text{eff}} = 0$. This is due to the nonlinear dephasing term $\delta T_n(t)$. A finite phase mismatch, present because of the finite frequency spread of an ultrashort pulse, will produce opposite excursions of the net phase difference between the interacting waves

about the optimum value of $-\pi/2$ during the rising and falling parts of the pump pulse. The net effect is that the leading edge of the signal pulse is favored for amplification.

The effect of the cavity detuning on the signal efficiency is shown in Fig. 43. In these plots, the peak pump intensity is normalized to a^{-1} . In the notation of Cheung and Liu, “3” corresponds to the pump frequency ($I_{p0} \rightarrow I_{30}$), and “L” is the cavity loss ($\Gamma \rightarrow L$), not to be confused with the notation of L as the nonlinear crystal length in this book. The notation for the normalized peak pump intensity as some number times loss can be read directly as the pump intensity equaling that number times the steady-state pump threshold (e.g., $aI_{30} = 4L \rightarrow I_{p0} = 4I_{p,th}$).

The cavity detuning can have some obvious dramatic effects on the signal efficiency. The curves in Fig. 43 do not peak at $\delta T_{eff} = 0$. This is due to the nonlinear dephasing term $\delta T_n(t)$. However, because δT_{eff} is a constant, its effect can be minimized by active tuning of the cavity length. This fine tuning is normally performed by mounting one of the cavity mirrors on a piezoelectric transducer.

Gain bandwidth. The gain bandwidth is normalized to $(FWHM)^{-1}$. Other parameters are as specified above, and the effective cavity detuning parameter was chosen to compensate for the intensity dependent phase shift produced by the term proportional to $\delta T_n(t)$.

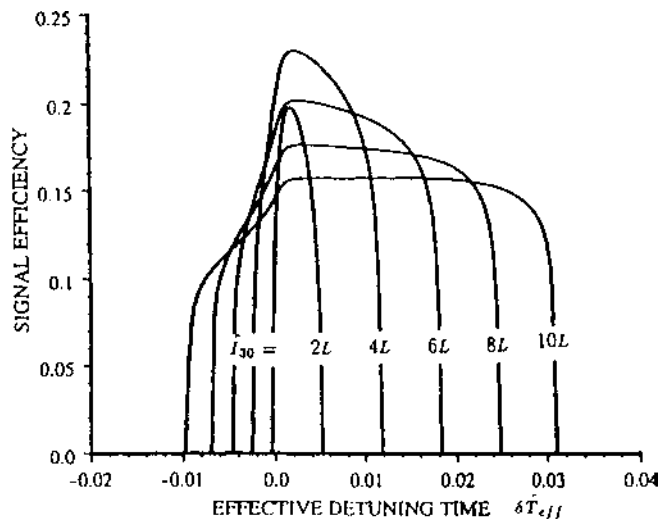


Figure 43 Signal efficiency as a function of the normalized effective cavity dephasing time for various normalized pump intensities (number of times above steady-state threshold) in a cw synchronously pumped singly resonant OPO. (From Ref. 46.)

The primary effect of a finite $\Delta\omega_n$ is a coupling of energy from near the peak of the pulse to its wings. The signal pulse width is narrower at larger values of $\Delta\omega_n$. At lower values of $\Delta\omega_n$, because the bandwidth cannot accommodate all of the frequencies comprising the pulse, appreciable energy is coupled from the pulse peak to the tails. This results in an increased signal pulse width.

Figure 44 shows that the net effect on signal efficiency is a high efficiency at intermediate bandwidths but low efficiency at small bandwidths. The peak of the efficiency curves in Fig. 44 may not be the best operating point since the pulses are not the shortest there.

Cavity bandwidth. The cavity bandwidth $\Delta\omega_c$ is also normalized to $(\text{FWHM})^{-1}$. It produces results similar to those due to $\Delta\omega_n$, but it affects the signal pulses symmetrically in time. This is because intracavity dispersive elements (e.g., étalons) modulate the cavity loss symmetrically in the frequency domain.

Pump intensity. As shown in Fig. 45, the signal efficiency is a maximum for the peak pump intensity near the steady-state threshold, for small positive cavity detuning. The calculations are accurate up to $aI_{30} \sim 10L$ (Cheung and Liu's notation, i.e., $I_{p0} \sim 10I_{p,\text{th}}$ in the notation of this book). The signal output increases with increasing pump intensity, but at the expense of a decreasing efficiency and an increasing signal pulse width. For good efficiency and narrow pulse width, it appears that the best operation of the OPO is near its threshold.

Conclusions. Cheung and Liu draw some conclusions from their model relating to OPO design. The OPO design includes choices of output coupler

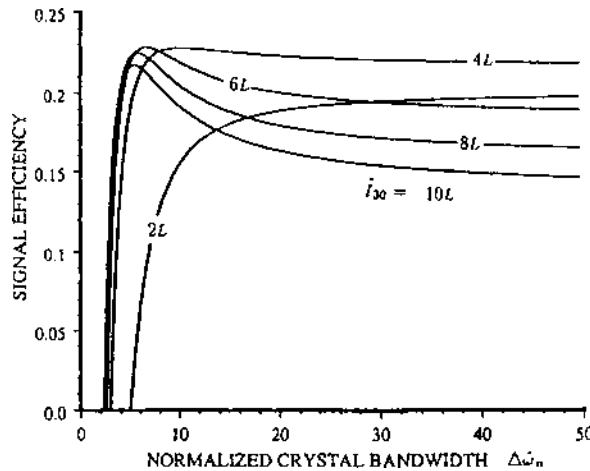


Figure 44 Signal efficiency as a function of the normalized nonlinear crystal gain bandwidth for various normalized pump intensities (number of time above steady-state threshold) in a cw synchronously pumped singly resonant OPO. (From Ref. 46.)

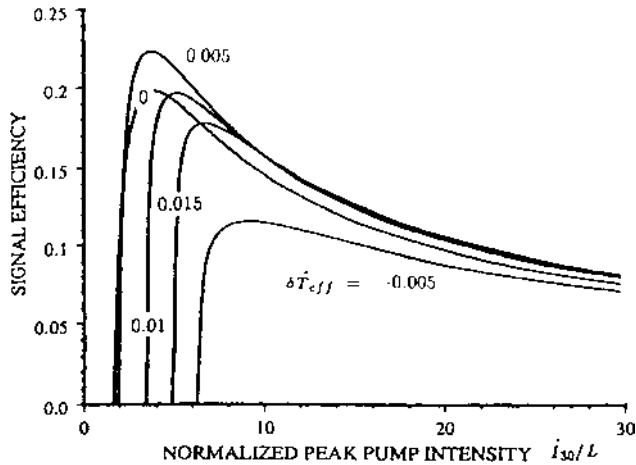


Figure 45 Signal efficiency as a function of the normalized pump intensity ratio (number of times above steady-state threshold) for various normalized cavity dephasing times in a cw synchronously pumped singly resonant OPO. (From Ref. 46.)

transmission, length and type of nonlinear crystal, and pump intensity. For good efficiency and narrow pulses, the OPO should be designed to operate with a peak pump intensity approximately two times the steady-state threshold value. For a given pump laser and nonlinear crystal, the choice of the output mirror transmission will set this parameter. An advantage of working near threshold is that the effect of pulse walk-off can almost be perfectly compensated by fine tuning the OPO cavity length. The choice of nonlinear crystal requires a trade-off in the *crystal length L*. The desire for a large nonlinear parameter $a (\propto L^2)$ for low threshold must be traded against the desire for a large gain bandwidth $\Delta\omega_n (\propto L^{-1})$ for narrow pulses to optimize the design.

VI. A BRIEF SURVEY OF DEVICES

With the improvements in pump sources and nonlinear crystals, several new parametric devices have been reported in the past few years. This section presents a brief survey of devices that have appeared in the literature since 1988. These serve as illustrations of the principles and techniques of parametric devices, but no attempt has been made to give a complete survey of the literature. Devices reported prior to 1988 have been adequately described by other authors [7,47].

A. OPGs and OPAs

For some applications, parametric superfluorescence and amplification are useful even without the advantages given by oscillation. These devices are simpler to align, and can still provide a stable, tunable output. They also serve well as experimental devices for the eventual development of OPOs using new nonlinear crystals.

A picosecond visible/near IR OPG/OPA system [27] is shown in Fig. 46. The system is pumped by 18 ps pulses at 355 nm obtained by frequency doubling the output of an actively and passively mode-locked Nd:YAG laser, then mixing the fundamental and second harmonic in a second LiB₃O₅(LBO) crystal. The UV pump beam is split off using a dichroic mirror and passes through a zoom telescope to adjust its intensity before pumping the LBO crystal of the OPG. This crystal generates a spectral continuum of signal and idler power that propagates to the second LBO crystal. The second crystal is separated from the first crystal by 50 cm to limit the solid angle of light collected and amplified. The signal and idler pulses are thus spectrally narrowed and amplified to the millijoule level. The residual pump energy is separated from the output by a dichroic mirror and filter. The output properties of this OPG/OPA system are given in Table 24.

A visible picosecond OPG/OPA system [37] is illustrated in Fig. 47. This system uses an LBO crystal for the OPG portion and a β -BaB₂O₄(BBO) crystal for the OPA stage. The pump beam at 355 nm is generated by a Nd:YAG mode-locked laser. The beam has a nearly Gaussian shape with 5 mm diameter and 0.7 mr divergence. A portion of the beam split off from the main beam by mirror M1 (1 mJ) is focused with a 1 m focal length quartz lens into the LBO crystal, which was placed 10 cm in front of the focal point. The crystal is polished but uncoated and X, Y, Z cut ($3 \times 3 \times 10$ mm³) for type I NCPM ($\theta = \phi = 0^\circ$).

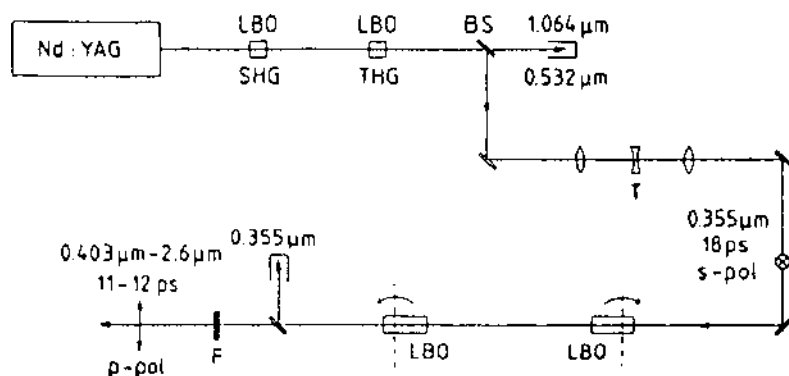


Figure 46 Schematic diagram of an LBO based OPG/OPA system. (From Ref. 27.)

Table 24 OPG/OPA Systems

Pump laser	Nonlinear crystal	Output energy/ power	Conversion efficiency (%)	Tuning range	Line width	Pulse width	Ref.
M-L Nd:YAG 3rd harm. (355 nm) $\tau = 18 \text{ ps}$ 4.3 mJ/pulse	LiB_3O_5 (LBO)	$\sim 1 \text{ mJ}$	28	403–2580 nm cm^{-1}	$\sim 20\text{--}1000$ cm^{-1}	11–12 ps	[27]
M-L Nd:YAG 3rd harm. (355 nm) $\tau = 30 \text{ ps}, 10 \text{ Hz}$ 4.8 mJ/pulse	LiB_3O_5 (LBO) $\beta\text{-BaB}_2\text{O}_4$ (BBO)	1.57 mJ 52 MW, peak	32.7	416–482 nm	0.15 nm	$\sim 30 \text{ ps}$	[37]
M-L Nd:YAG 3rd harm. (355 nm) $\tau = 35 \text{ ps}$ 10 Hz	$\beta\text{-BaB}_2\text{O}_4$ (BBO)	$\sim 1 \text{ mJ}$	30	400–2000 nm 600–2500 nm	$\sim 0.2 \text{ nm}$	—	[24]
M-L Er ³⁺ :YAG (2940 nm) M-L Er ³⁺ :Cr ³⁺ :YSGG (2790 nm) $\tau = 100 \text{ ps}, 1\text{--}2 \text{ Hz}$ 2–4 mJ/pulse	ZnGeP ₂ (oee) ZnGeP ₂ (oeo)	— —	3 17.6	4–10 μm 5.2–6.7 μm	30–540 cm^{-1} 12 cm^{-1}	— —	[32]
Dye (605 nm) $\tau = 190 \text{ fs}$	GaSe (eoo)	—	1	3.5–18 μm	10–850 cm^{-1}	—	[42]
	LiB_3O_5 (LBO)	3–4.5 mJ	10–15	850–970 nm 1.6–2.1 μm	—	—	

30 $\mu\text{J}/\text{pulse}$	LiInS ₂ (800 nm) $\tau = 200 \text{ fs}, 1 \text{ kHz}$ 200 $\mu\text{J}/\text{pulse}$ (20-nJ white-light seed)	—	—	4.8–9.0 μm	—	365– 460 fs	[61]
M-L Ti:sapphire 2nd harm. (387.5 nm) $\tau = 130 \text{ fs}, 1 \text{ kHz}$ 56 $\mu\text{J}/\text{pulse}$ (white-light seed)	$\beta\text{-BaB}_2\text{O}_4$ (BBO) eff	2.5–7.0 μJ	15–35 (quantum eff)	865–1600 nm	~10–20 THz	20–50 fs	[62]
Cr:forsterite regen amp (1250 nm) $\tau = 175 \text{ fs}, 1 \text{ kHz}$ 63 $\mu\text{J}/\text{pulse}$; and 2nd harm (625 nm) 8 $\mu\text{J}/\text{pulse}$ (2-stage OPA)	HgGa ₂ S ₄ (type II) HgGa ₂ S ₄ (type I) AgGaS ₂	0.2–1.1 μJ 0.1–0.8 μJ 0.2–0.5 μJ	11	5–9 μm	0.570 μm	180– 240 fs	[63]
M-L Ti:sapphire (800 nm) $\tau = 100 \text{ fs}, 1 \text{ kHz}$ 600 $\mu\text{J}/\text{pulse}$	MgO:LiNbO ₃ (MLN)	—	—	5–9 μm 5–8 μm	—	—	(continued)

Table 24 Continued

Pump laser	Nonlinear crystal	Output energy/ power	Conversion efficiency (%)	Tuning range	Line width	Pulse width	Ref.
(Nd:YVO ₄ , 8-μJ, 1064-nm seed) (InGaAs, > 1 W, 1064 nm seed)		> 10 μJ	40	3.1–3.9 μm		<200 fs	
		5 μJ	11	3.5 μm		130 fs	
Ho:Tm:Er:YLF (2.06 μm) $\tau = 50$ ns ~ 35 mJ/pulse (HeNe, 3-mW, 3.39-μm seed)	ZnGeP ₂	~30 mW	—	3.39 μm	—	—	[65]
NIR OPG (1.15–2.54 μm) $\tau = 120$ –140 fs 10–40 μJ/pulse	ZnGeP ₂	—	2.5	2.5–10 μm	~0.25–0.30 μm	75–200 fs	[66]
M-L Ti:sapphire 2nd harm. (395 nm) $\tau = 150$ fs, 1 kHz 130 μJ/pulse (white-light seed)	β -BaB ₂ O ₄ (BBO)	5 μJ	—	550–700 nm 900–1300 nm	98 nm 203 nm	6.2 fs 8.4 fs	[67]
M-L Ti:sapphire	β -BaB ₂ O ₄	2 μJ	20	White	180 THz	7.2 fs	[68]

2nd harm. (390 nm) $\tau = 180 \text{ fs}, 1 \text{ kHz}$ 10 $\mu\text{J}/\text{pulse}$ (white-light seed)	(BBO)	—	—	—	—	—	—	$< 20 \text{ fs}$
M-L Ti:sapphire 2nd harm. (395 nm) $\tau = 150 \text{ fs}, 1 \text{ kHz}$ 100 $\mu\text{J}/\text{pulse}$ (white-light seed)	$\beta\text{-BaB}_2\text{O}_4$ (BBO)	2–3 μJ	—	550–690 nm	2000 cm^{-1}	—	—	[69]
Nd:YAG (1064 nm) $\tau = 15 \text{ ns}, 10 \text{ Hz}$ $< 45 \text{ mJ}/\text{pulse}$ (Yb fiber, $< 300 \text{-mW},$ 1074-nm seed)	MgO:LiNbO ₃ (MLN)	900 pJ $> 100 \text{ mW, peak}$	—	$\lambda_s = 190 \mu\text{m}$ (1.6 THz)	$< 200 \text{ MHz}$	3.4 ns	—	[70]
$\sim 2\text{--}4 \text{ mJ}$				$\lambda_i = 1.070 \mu\text{m}$				
Nd:YAG (1064 nm) $\tau = 15 \text{ ns}, 10 \text{ Hz}$ $< 35 \text{ mJ}/\text{pulse}$ (Diode laser, 50-mW, 1066–1074-nm seed)	MgO:LiNbO ₃ (MLN)	1.3 mJ $> 200 \text{ mW, peak}$	—	125–430 μm (0.7– 2.4 THz)	$< 100 \text{ MHz}$	4 ns	—	[71]

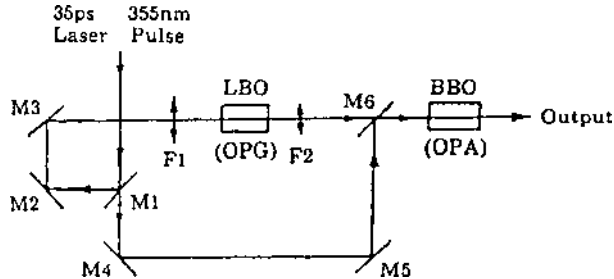


Figure 47 Schematic diagram of an LBO/BBO based OPG/OPA system. (From Ref. 37.)

The crystal was placed in a precision temperature controlled heater with a thermocouple feedback system controlling temperature within 0.5%. The CPM type I BBO crystal ($10 \times 8 \times 12 \text{ mm}^3$) was cut at 28° . Approximately $350 \mu\text{J}$ of signal is injected into the OPA crystal after an adjustment of beam diameter to 5 mm with a 0.25 m focal length lens. This beam is combined collinearly with the 3.8 mJ pump beam at mirror M6. The output properties of this system are also summarized in Table 24.

Another picosecond visible/near-IR system [24] employing BBO crystals is shown in Fig. 48. The third harmonic of an active-passive mode-locked Nd:YAG laser is generated by SHG and SFG using two BBO crystals. The *p*-polarized 355 nm beam of 35 ps pulses at 10 Hz is then split into two parts. One pumps a double-pass OPG/OPA stage, and the other, after an appropriate time delay, pumps a second OPA stage. The BBO crystals were cut at an internal angle of 31° between the surface normal and the optic axis for type I phase matching. The polished end faces were uncoated. Approximately 25–30% of the pump energy, controlled by a half-wave plate/polarizer combination, enters the OPG/OPA stage and generates a broad-band superfluorescence in the first BBO crystal. The second BBO crystal is situated about 20 cm from the first to collect the middle portion of the OPG beam. This crystal serves as a preamplifier as well as a spatial and spectral filter. Angle tuning of the two crystals is employed to select the signal frequency. Tilting the two crystals in opposite directions minimizes the pump and signal beam walk-off. A dichroic mirror separates the signal and residual pump, which are then fed back through the crystals for further amplification. The signal mirror can be replaced by a grating for further frequency and line width control. Finally, the amplified signal is sent through the single OPA stage for an amplification of about 10. The BBO crystals and grating for this system were mounted on rotation stages driven by computer-controlled stepper motors for synchronous rotation and frequency control. Output properties of this system are given in Table 24.

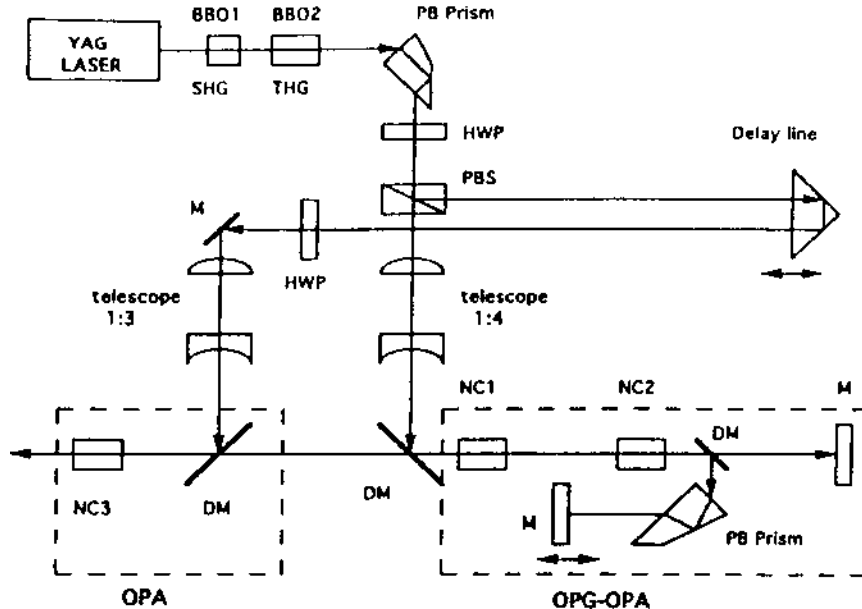


Figure 48 Schematic diagram of a BBO based OPG/OPA system. Mirror M in dashed box at right replaceable with a grating. NCs = nonlinear crystals; DMs = dichroic mirrors; PB = Pellin-Broca prism, HWP = half-wave plate. (From Ref. 24.)

Figure 49 illustrates an IR OPG [32] utilizing ZnGeP₂ or GaSe nonlinear crystals. Pump lasers used with this system include actively mode-locked Er³⁺:YAG (2.94 μm) and Er³⁺:Cr³⁺:YSGG (2.79 μm) lasers. 100 ps pulses extracted from the laser cavity are further amplified to produce pulses in the millijoule level at 1–2 Hz. The high intensity pump beam (>1 GW/cm²) was focused into the nonlinear crystals using CaF₂ lenses. For type I phase matched ZnGeP₂, a 0.25 m focal length lens was used, while for type II phase matching, a 4 × telescope consisting of 10 and 2.5 cm focal length lenses was employed. In the case of GaSe, a 30 cm focal length spherical lens and a 4 cm focal length cylindrical lens combination was used. This focused the pump radiation mostly perpendicular to the (*k*, *z*) plane to avoid significant beam walk-off. The crystal parameters were as follows: type I ZnGeP₂ ($\theta = 47^\circ$, $\phi = 0^\circ$, 12 mm length), type II ZnGeP₂ ($\theta = 84^\circ$, $\phi = 31^\circ$, 42 mm length), type I GaSe ($\theta = 0^\circ$, $\phi = 90^\circ$, 12 mm length). Specific output properties of this OPG are again summarized in Table 24.

A femtosecond visible/near-IR OPG/OPA [42] is illustrated in Fig. 50. The 605 nm, 190 fs pump pulses were generated by a dye laser/amplifier system. The pump beam is split at the beam splitter, with 22% of its energy entering the OPG seeder section, which consisted of two 15 mm long NCPM LBO crystals.

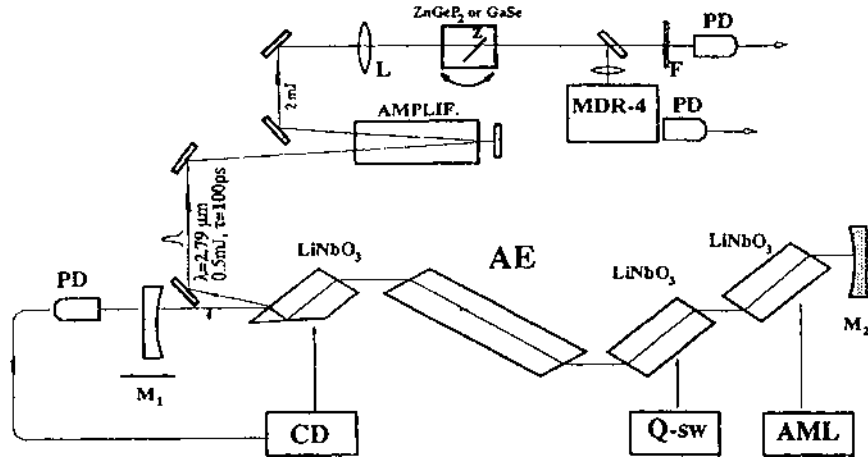


Figure 49 Schematic diagram of a ZnGeP₂/GaSe based OPG system, AE = active laser element, AMPLIF = laser amplifier, AML = active mode-locker, CD = cavity dumper, PD = photodiodes, F = InAs filter, MDR-4 = monochromator. (From Ref. 32.)

The uncoated crystals are surrounded by a metal block embedded with a resistor driven by a constant current generator to heat the crystals. The pump beam in the seeder section is collimated to a spot diameter of approximately 300–350 μm on the first crystal. The generated signal beam was collimated before injection into the OPA section, which consisted of another 15 mm uncoated NCPM LBO crystal. All beams propagated along the crystal X -axis. The pump beam was polarized along the Y -axis, and the signal and idler beams were polarized along the Z -axis (X, Y , and Z denote the principal axes of the crystal with $n_Z > n_Y > n_X$). The output of this system is given in Table 24.

Since the latter half of the 1990s there has been a trend toward production of femtosecond pulses tunable in the near- and mid-infrared. Several systems have been based on a mode-locked Ti:sapphire pump, although a few other pump

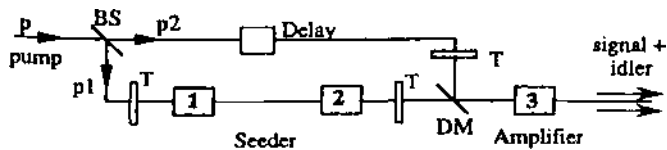


Figure 50 Schematic diagram of an LBO based OPG/OPA system. BS = beam splitter, Ts = telescopes, Boxes 1,2,3 = 15 mm long LBO crystals, DM = dichroic mirror. (From Ref. 42.)

sources have appeared in the literature such as Cr:forsterite and Ho:Tm:Er:YLF systems. Examples of these are given in Table 24. There has also been great interest recently in the development of tunable pulsed terahertz sources. Two examples of these systems, using MgO:LiNbO₃ as the nonlinear medium, are included in Table 24.

B. Continuous Wave OPOs

Most OPOs reported in the literature are pumped by pulsed or mode-locked lasers. However, improvements in pump sources, such as diode pumped solid state lasers with excellent spatial and single longitudinal mode control, and new nonlinear materials have allowed highly efficient cw OPOs with narrow line widths.

A doubly resonant cw OPO [34] is illustrated in Fig. 51. The OPO is monolithic and formed by polishing surfaces of 16 mm radius of curvature onto each end of a $3 \times 3 \times 15$ mm MgO:LiNbO₃ crystal. The long axis of the crystal was parallel to the crystal X-axis. One end of the polished crystal was coated with a highly reflecting coating at 1064 nm, while the other (output) end was coated for 99.5% reflection at 1064 nm. The highly reflecting and output ends of the OPO had approximately 74% transmission at the pump wavelength, which was 532 nm obtained from a single frequency source shown in the figure. The monolithic ring resonator of MgO:LiNbO₃ produces the 532 nm pump beam when pumped by the fundamental of a single frequency Nd:YAG laser. The green output is then mode

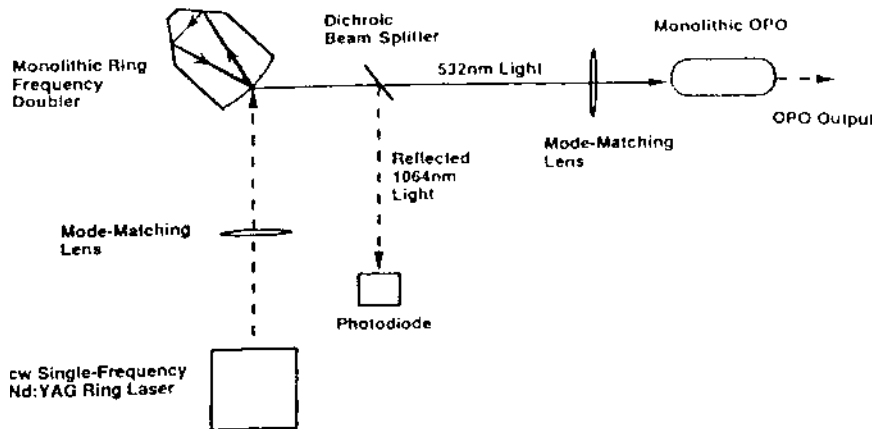


Figure 51 Schematic diagram of a monolithic MgO:LiNbO₃ based doubly resonant cw OPO system. (From Ref. 34.)

matched to the monolithic OPO by a focusing lens. Details of the output characteristics of this OPO are summarized in Table 25.

The singly resonant OPO [48] of Fig. 52 is pumped by a single frequency injection locked Nd:YAG laser producing a TEM_{00} mode with a 20 kHz line width. This output is resonantly doubled to 532 nm in an external enhancement cavity containing a 6 mm long LBO crystal. Potassium titanyl phosphate (KTP) is used in the OPO cavity because of its large nonlinearity, low absorption at the signal and idler frequencies, large temperature-acceptance bandwidth, and high laser damage threshold. The 10 mm long KTP crystal was oriented for propagation along a crystallographic axis ($\theta = 90^\circ$, $\phi = 0^\circ$) with type II NCPM. The 532 nm pump beam propagates along the crystal X -axis with polarization along Y . Signal and idler waves are polarized along the Y - and Z -axes, respectively. The KTP crystal resides at the intracavity focus of a three-mirror standing wave resonator. The resonator consists of two 5 cm radius of curvature mirrors (M_1 , M_2) and one flat mirror (M_3). M_2 is mounted on a piezoelectric transducer for fine adjustment of the cavity length. The incident angle on M_1 is set at 3° to reduce astigmatism. All mirrors are highly reflecting (> 99.9%) over the range of 970 nm to 1160 nm. The KTP crystal has dual-band antireflection coatings centered at 1090 and 532 nm. A Brewster angle LiNbO_3 prism is situated in the long leg of the cavity to spatially separate and dump the idler wave so that the cavity is truly singly resonant. A highly reflecting 25 cm radius of curvature mirror reflects the residual pump beam back through the crystal to lower the threshold. This mirror is mounted on a piezoelectric transducer to adjust the net phase for maximum gain and minimum threshold (see Section III.A and III.B for a discussion of a double-pass OPO). Salient features of this OPO are given in Table 25.

Since the latter half of the 1990s there have been additional new sources used as pumps for cw OPOs, such as Nd:YVO₄, Ti:sapphire, and GaAlAs diode systems. Examples of these are given in Table 25.

C. Pulsed OPOs

This class of OPOs generally operates in the nanosecond pulse regime. Several of these devices have been reported in the literature since the late 1960s. A few examples dating from 1988 forward are cited here. Salient features of all the examples discussed are summarized in Table 26.

One of the early pulsed OPOs employing a BBO crystal [23] is shown in Fig. 53. The OPO is pumped by 355 nm, 6 ns pulses at a 30 Hz repetition rate. The beam, generated as the third harmonic from a seed-injected, Q-switched Nd:YAG laser, was spatially filtered to a Gaussian shape and prismatically separated from the fundamental and second harmonic before entering the OPO. The OPO cavity consisted of two flat mirrors separated by 3 cm and contained a single BBO

Table 25 Continuous Wave OPO Systems

Pump laser	Nonlinear crystal	Output power	Conversion efficiency (%)	Tuning range	Line width	Ref.
Nd:YAG 2nd harm. (532 nm) 3.2 W	KTiOPO ₄ (KTP)	36 mW (signal) 1.07 W (idler)	34.6	$\lambda_s = 1090 \text{ nm}$ $\lambda_i = 1005 \text{ nm}$	—	[48]
Nd:YAG 2nd harm. (532 nm) 300 mW	MgO:LiNbO ₃	104 mW	38.3	966–1185 nm	—	[34]
Nd:YVO ₄ 2nd harm. (532 nm) 220 mW	KTiOPO ₄ (KTP)	10 mW	—	1.7 GHz	<300 kHz	[72]
GaAlAs MOPA (845 nm) 500 mW	AgGaS ₂	2–3 mW	2	$\lambda_s = 1267 \text{ nm}$ $\lambda_i = 2535 \text{ nm}$	—	[73]
Ti:sapphire (800 nm) (Ar-ion pump, 14 W)	KTiOAsO ₄ (KTA)	1.46 W	85	1.11–1.20 μm 2.44–2.86 μm	—	[74]
Nd:YVO ₄ 2nd harm. (532 nm) 1.2 W	MgO:LiNbO ₃	10 mW	~10	788–1640 nm	—	[75]

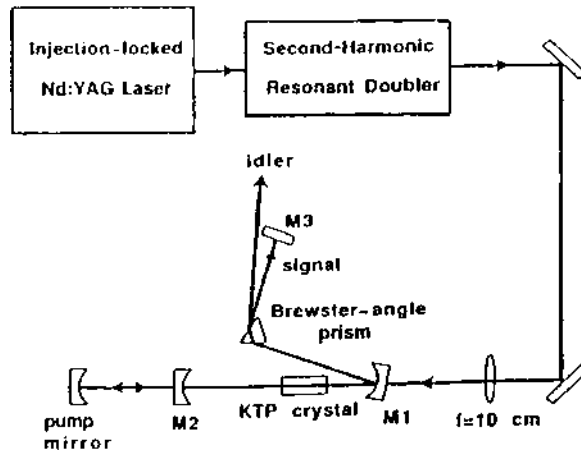


Figure 52 Schematic diagram of a KTP based singly resonant cw OPO system. (From Ref. 48.)

crystal. The reflectance of the mirrors for the signal wavelength was 98% for the input mirror and 80% for the output mirror. The input and output couplers had a transmission of $\geq 80\%$ at the pump and idler wavelengths. Three sets of mirrors were used to cover the entire tuning range. Two separate BBO crystals were used. Each was $6 \times 6 \times 10 \text{ mm}^3$ in dimensions. One was cut at 25° while the other was cut at 35° to allow angle tuning over the entire wavelength range.

A monolithic singly resonant OPO fabricated by specially polishing the ends of a MgO:LiNbO_3 crystal [33] is shown in Fig. 54. The ends of the 2.5 cm long crystal were polished to 20 mm radii of curvature. One end was coated with a high reflectivity dielectric multilayer centered at 900 nm, while a 90% reflectivity coating at 900 nm was deposited on the other end to serve as the output coupler. In addition, a flat total internal reflection surface was polished to within 0.25 mm of the mirror axis. Thus the crystal could serve as a standing-wave resonator or an off-axis ring resonator, as shown in the figure. As illustrated in Fig. 55, the pump beam from a monolithic Nd:YAG nonplanar ring oscillator was amplified by several passes through a Nd:YAG slab before being frequency doubled by a temperature controlled MgO:LiNbO_3 crystal. The acoustooptic modulator selected the pulse width. 500 ns pulses were frequency doubled to 532 nm, and this radiation was focused into the OPO to a beam waist of 37 μm . The oven heated the OPO crystal to its phase matching temperature of 107°C. The output signal and residual pump waves were then separated by a dichroic mirror.

An OPO with tunable output available in the UV portion of the spectrum [21] is shown in Fig. 56. This OPO was pumped with the fourth harmonic of

Table 26 Pulsed OPO Systems

Pump laser	Nonlinear crystal	Output energy/power	Conversion efficiency (%)	Tuning range	Line width	Pulse width	Ref.
Q-Sw. Nd:YAG 3rd harm., 355 nm $\tau = 6$ ns, 30 Hz 30 mJ/pulse	β -BaB ₂ O ₄ (BBO)	4.7 mJ 140 mW, avg.	24	412–250 nm	< 3 GHz	2.5 ns	[23]
Nd:YAG (amplified monolithic nonplanar ring oscillator) 2nd harm., 532 nm $\tau = 500$ ns, 3 Hz 140 W, peak	MgO:LiNbO ₃ monolithic	—	35	834–958 nm 1.2–1.47 μ m	~ 0.7 cm ⁻¹	< 500 ns	[33]
Q-Sw. Nd:YAG 4th harm., 266 nm $\tau = 9$ ns	β -BaB ₂ O ₄ (BBO)	—	—	330–1370 nm	—	—	[21]
Q-Sw. Nd:YAG 3rd harm., 355 nm $\tau = 9$ ns	β -BaB ₂ O ₄ (BBO)	7 mJ	50	420–2300 nm	0.03 nm	—	[49]
Injection-seeded urea XeCl, 308 nm $\tau = 10$ ns, 1 Hz 25 mJ/pulse	—	3.8 mJ	37	537–720 nm	—	4–6 ns	[30]
Q-Sw. Nd:YAG 2nd harm., 532 nm $\tau = 12$ ns 25 mJ/pulse	β -BaB ₂ O ₄ (BBO)	1 mJ 80 kW, peak	10	940–1220 nm	—	—	[25]
Injection-seeded	β -BaB ₂ O ₄ (BBO)	~2 mJ	> 10	354–2370 nm	~ 1.5 –10.5 nm	4–12 ns	[22]

(continued)

Table 26 Continued

Pump laser	Nonlinear crystal	Output energy/power	Conversion efficiency (%)	Tuning range	Line width	Pulse width	Ref.
XeCl, 308 nm $\tau = 10\text{ ns}, 1\text{ Hz}$ 25 mJ/pulse							
Q-Sw. Nd:YAG 1064 nm $\tau = 15\text{ ns}, 540\text{ Hz}$ 22 mJ/pulse cw Color Center (seed) (1500 nm) 20 mW	LiNbO ₃	3 mJ	> 10	1500 nm (locked)	120 MHz	9.5 ns	[50]
Q-Sw. Nd:YAG 1064 nm 10 Hz 150 mJ/pulse	LiNbO ₃	> 4 mJ	7.6–9.9	2.5–4.0 μm	$\leq 0.2\text{ cm}^{-1}$	—	[51]
Q-Sw. Nd:YLF 2nd harm., 523 nm $\tau = 16\text{ ns}$ 300 $\mu\text{J}/\text{pulse}$	LiB ₃ O ₅ (LBO)	6 μJ	45 (internal)	924–1208 nm	—	$\sim 12\text{ ns}$	[39]
Q-Sw. Nd:YAG 2nd harm., 532 nm $\tau = 6\text{ ns}, 10\text{ Hz}$	KTiOPO ₄ (KTP)	3 mJ	12	700–900 nm 1.3–2.2 μm	0.02 cm^{-1}	$\sim 3.5\text{ ns}$	[52]
Q-Sw. Nd:YAG	KTiOPO ₄ (KTP)	21.4 W	~ 35	2153 nm (signal)	$\sim 6\text{ nm}$	—	[76]

1079 nm 6.22 kHz 62 W			2166 nm (idler)		
Q-Sw. Nd:YAG 1064 nm $\tau = 9.6\text{ ns}, 10\text{ Hz}$ 4.5 mJ/pulse	KTiOPO ₄ (KTP)	27.5 μJ	$\sim 6, 11 \pm 4$ (slope)	1570–1647 nm (signal) $> 3000\text{ nm}$ (idler)	$\sim 3\text{ nm}$ —
Q-Sw. Nd:YVO ₄ 1064 nm $\tau = 8.5\text{ ns}, 5\text{ kHz}$ 5 μJ /pulse	KTiOPO ₄ (KTP)	0.4 μJ	$\sim 8\%$	1535 nm (signal) 3.47 μm (idler)	7.5 ns
Q-Sw. Nd:YAG 1064 nm $\tau = 17.5–22.5\text{ ns},$ 100 Hz 100–130 W	KTiOAsO ₄ (KTP)	$\sim 30–35\text{ W}$	~ 32	$1534.7 \pm 0.6\text{ nm}$ (signal)	—
Q-Sw. Nd:YAG 1064 nm $\tau = 16\text{ ns},$ 10Hz 60 mJ/pulse cw Yt-doped fiber (seed)	LiNbO ₃	6.3 mJ (idler, unseeded)	$\sim 11–13$ (idler)	1068–1075 nm (idler, unseeded)	200 MHz (signal) 8 ns (idler)
1070 nm, 90 mW			7.2 mJ (idler, seeded)	194 μm (signal)	[80]
			0.23 nJ (signal, unseeded)		
			0.14 nJ (signal, seeded)		
Q-Sw. Nd:YAG 3rd harm., 355 nm	β -BaB ₂ O ₄ (BBO)	$\sim 1\text{ mJ}$ (signal)	$\sim 500–680\text{ nm}$	$< 300\text{ MHz}$ (DRO)	—
					[81]
					(continued)

Table 26 Continued

Pump laser	Nonlinear crystal	Output energy/power	Conversion efficiency (%)	Tuning range	Line width	Pulse width	Ref.
$\tau = 20\text{ ns}, 12.5\text{ Hz}$ 50 mJ/pulse							
Q-Sw. Nd:YAG 2nd harm., 532 nm $\tau = 5\text{ ns}, 10\text{ Hz}$ 12 mJ/pulse	$\beta\text{-BaB}_2\text{O}_4$ (BBO)	37.6 mJ (signal)	5.3	745–890 nm (signal) 1.32–1.86 μm (idler)	145 nm (signal) 540 nm (idler)	—	[82]
Q-Sw. Er,Cr:Tm:YSGG 2.93 μm	ZnGeP ₂ (ZGP)	1.2 mJ (signal)	12.8–14.7 (idler)	3.9–12.4 μm (type I) 4–10 μm (type II)	6.5 cm^{-1} (type I) 1.5 cm^{-1} (type II)	—	[83]
$\tau = 100\text{--}110\text{ ns},$ 10 Hz 10 mJ/pulse LiNbO ₃ OPO	ZnGeP ₂ (ZGP)	0.5 mJ (idler)	4	3.4–10.5 μm (idler, gap in 4.7–5.6 μm region)	38 cm^{-1} ($\sim 0.1\text{ cm}^{-1}$ with intracavity grating and etalon)	—	[84]
2.55 μm (idler) $\tau = 12\text{ ns}$ 12 mJ/pulse							

Nd:YAG, 1064-nm pump $\tau = 15\text{ ns}$, 90 mJ/pulse	ZnGeP ₂ (ZGP)	4.2 W, avg (signal) 2.1 W, avg (idler)	$53 \text{ (signal) } (85, \text{ slope})$ $37 \text{ (idler) } (44, \text{ slope})$	$\lambda_s = 3.8 \mu\text{m}$ $\lambda_i = 4.65 \mu\text{m}$	170 nm (signal) 260 nm (idler)	26 ns	[85]
Tm:YLF-pumped Ho:YAG $2.09 \mu\text{m}$							
$\tau < 29 \text{ ns}$, 10 kHz 0.95 mJ/pulse, 33 kW peak							
Q-Sw. Nd:YAG 1064 nm $\tau = 12\text{--}100 \text{ ns}$, 10 Hz	AgGaS ₂ (AGS)	372 μJ (idler)	3.1–4.9	$3.9\text{--}11.3 \mu\text{m}$ (idler) 1.17–1.46 μm (sig- nal)	$\sim 1 \text{ cm}^{-1}$ (idler)	—	[86]
40 mJ/pulse							
BBO OPO 565–590 nm $\tau = 5 \text{ ns}$, 4.5 mJ/pulse 7-ns, 355-nm Nd:YAG pump	2A5NPDP	300 μJ (idler)	3–4.5 (idler) 8 (total)	1300–1500 nm (idler) 1000 nm (signal)	3.5 nm (idler) 2 nm (signal)	$\sim 1\text{--}2 \text{ ns}$	[87]

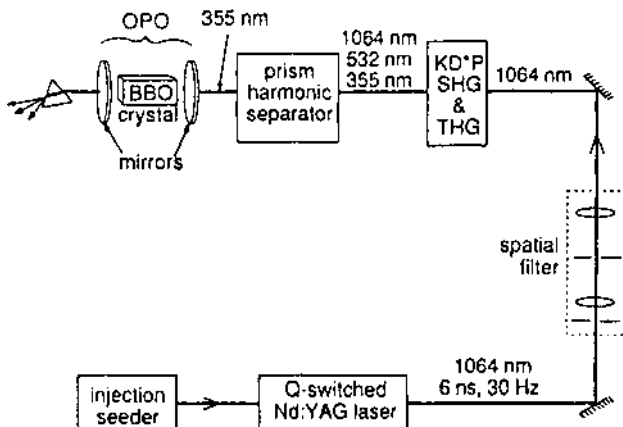


Figure 53 Schematic diagram of a 355 nm pumped BBO based pulsed OPO system. (From Ref. 23.)

a Q-switched Nd:YAG laser. This beam had a diameter of 1.6 mm, a pulse duration of 9 ns, and a wavelength of 266 nm. The type I BBO crystal was cut at 39.1° with a $12 \times 6 \text{ mm}^2$ aperture and a 20.5 mm interaction length. The 55 mm long cavity, corresponding to a 75 mm optical length, consisted of two flat highly reflecting mirrors for the signal wavelengths, and two 45° incident highly reflecting (>98% at 266 nm) pump beam steering mirrors. These mirrors transmit at all wavelengths of interest longer than 300 nm and obviate the need for the OPO mirrors to be transparent at the pump wavelength. The pump steering mirrors were set at Brewster's angle with respect to the cavity axis. The extraordinary pump beam was *s*-polarized and the ordinary signal and idler beams were *p*-polarized to take advantage of the high transmission of the pump mirrors at the Brewster's angle. Five pairs of OPO reflectors were used to cover the entire tuning range of the OPO.

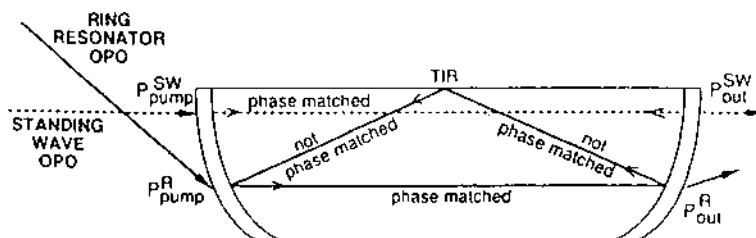


Figure 54 Monolithic MgO:LiNbO₃ singly resonant OPO. (From Ref. 33.)

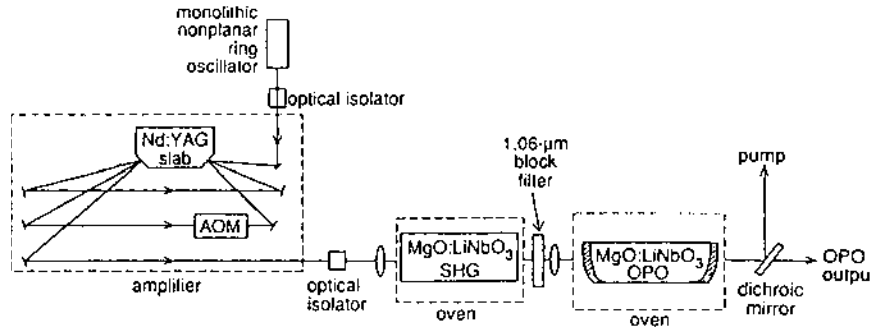


Figure 55 Schematic diagram of a monolithic MgO:LiNbO_3 based pulsed OPO system. (From Ref. 33.)

A two BBO crystal version of the above OPO [49] is shown in Fig. 57. The purpose of the two crystals is to compensate for the relatively large walk-off angle in BBO, which limits the efficiency. The first crystal (BBO1), with an aperture of $10 \times 10 \text{ mm}^2$ and an interaction length of 11.5 mm, is cut for type I

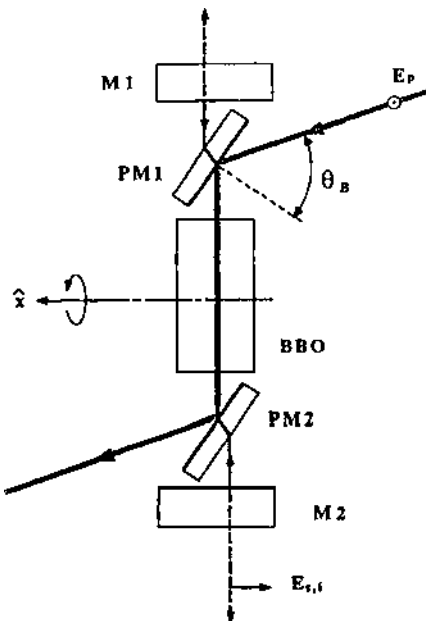


Figure 56 Schematic diagram of a 266 nm pumped BBO based pulsed OPO system. PM1 and PM2 = pump steering mirrors. (From Ref. 21).

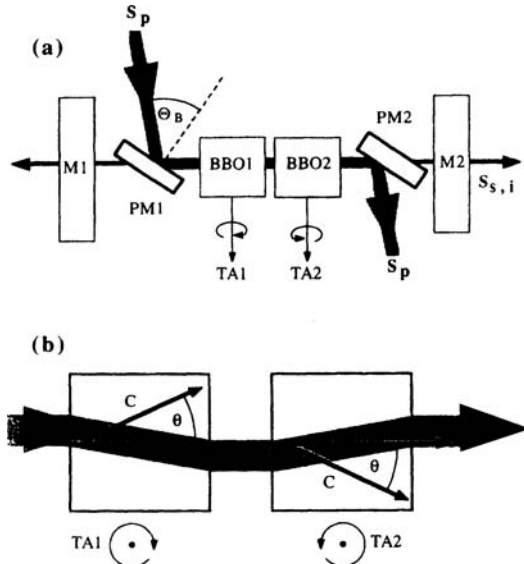


Figure 57 Schematic diagram of a 355 nm pumped two BBO crystal based pulsed OPO system. PM1 and PM2 = pump steering mirrors, TA1 and TA2 = crystal tuning axes. (From Ref. 49.)

phase matching with an angle of 30.2° between the entrance face normal and the optic axis. The second crystal is $10 \times 10 \times 9.5 \text{ mm}^3$ and cut at 29.3° . These crystals reside on separate rotation stages and are arranged with their optic axes at twice the phase matching angle relative to one another. In this manner the walk-off of the pump beam in the first crystal is compensated in the second crystal to improve the conversion efficiency, as illustrated in the figure. Tuning is accomplished by rotating both crystals. The pump steering mirrors in this experiment consisted of standard high reflectors ($>98\%$) at the 355 nm pump wavelength. Cavity mirror M1 was a standard, low damage threshold, broadband dielectric high reflector ($>90\%$ over 480–700 nm). For line width narrowing, this reflector was replaced with a 1,800 grooves/mm grating blazed at 26.7° , with the grooves perpendicular to the signal wave polarization. Mirror M2 was a 50% output coupler. All mirrors transmitted $>90\%$ of the infrared idler waves to ensure singly resonant operation. The cavity length was 55 mm.

A visible OPO pumped by a XeCl excimer laser [30] is illustrated in Fig. 58. The pump laser emits 10 ns, 1 Hz repetition rate pulses at 308 nm. The beam was linearly polarized with a rectangular cross-section. It was compressed by a Galilean telescope to an approximately $1 \times 2.5 \text{ mm}^2$ cross-section before entering the OPO as an ordinary wave. The nonlinear medium was type II single crystal of

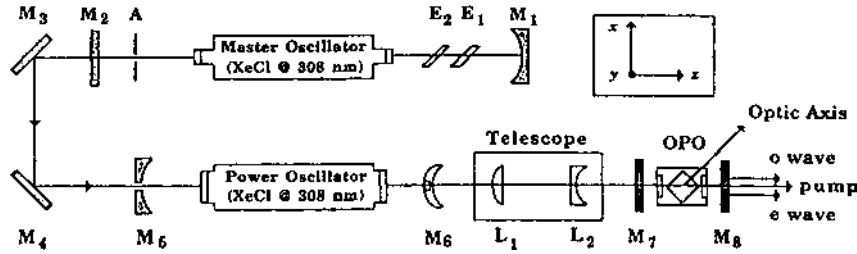


Figure 58 Schematic diagram of a 308 nm pumped urea based pulsed OPO system. A = aperture, Es = étalons. (From Ref. 30.)

urea with a 15 mm length and $12 \times 10 \text{ mm}^2$ aperture. The crystal was a polished on its (110) entrance and exit faces, then immersed in a cell containing *n*-hexane for index matching. The cell had uncoated quartz windows. The crystal was mounted near the 90° phase matching angle to minimize walk-off. Flat dichroic mirrors were chosen for the cavity mirrors with high reflectance (>95%) over 500–600 nm. The mirrors also had a transmittance of >95% at the pump wavelength and were antireflection coated on the back surfaces at 308 nm. The physical length of the OPO cavity was 54 mm.

A BBO OPO pumped by a visible source for near IR output [25] is shown in Fig. 59. The pump wavelength was 532 nm, obtained from frequency doubling

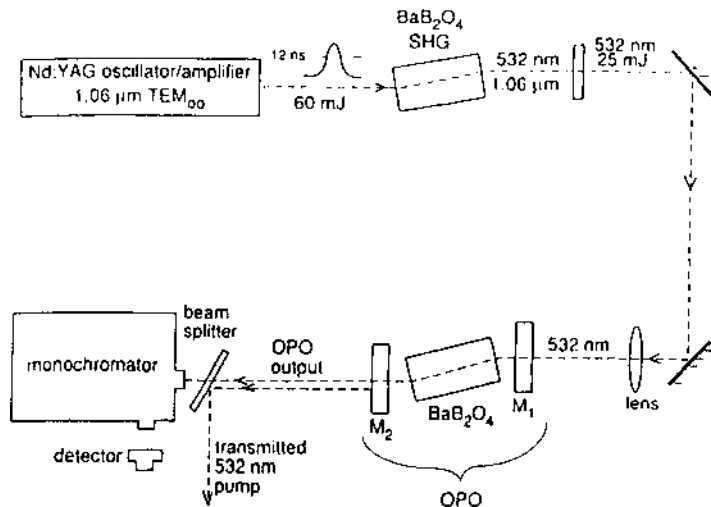


Figure 59 Schematic diagram of a 532 nm pumped BBO based pulsed OPO system. (From Ref. 25 © IEEE 1989.)

the fundamental output of an amplified TEM₀₀ mode Q-switched Nd:YAG laser. The 12 ns fundamental was converted to the second harmonic with 50% internal energy conversion efficiency in a 6.8 mm long BBO crystal. This green beam was then weakly focused into the OPO at a position that could be adjusted to achieve maximum gain. The OPO consisted of a simple two flat mirror resonator of 25 mm length. The mirror reflectances at the signal wave were 90% and 76%. The BBO crystal inserted in the OPO cavity was 9 mm long with its optic axis oriented at 20° with respect to the surface normal. The parallel end faces were polished and uncoated.

Excimer lasers are potentially useful pump sources for OPOs operating throughout the ultraviolet, visible, and near-infrared spectral region because of a variety of available UV pump wavelengths that allow relatively high efficiency and the potential for higher average power compared to frequency tripled Nd:YAG lasers. Figure 60 illustrates such a UV-NIR OPO system [22]. Because of the wide bandwidths associated with excimer lasers, this particular configuration employs a master oscillator/power oscillator combination to obtain high pump energy with a narrow linewidth. Line narrowing étalons and a spatial filter are used in the master oscillator to obtain a relatively spectrally pure seed signal, which is injected into the power oscillator. Spectral purity of the 308 nm pump energy (10 ns pulses at a 1 Hz repetition rate) from the power oscillator was better than 0.25 cm^{-1} . Polarization is controlled by a half-wave plate prior to the power oscillator to yield an extraordinary beam to pump the OPO. The emerging pump beam had a cross-section of $1 \times 2.5 \text{ cm}^2$, which was compressed by passing through an 8 × Galilean telescope to $1.2 \times 3 \text{ mm}^2$ before being launched into the OPO. The OPO consisted of a BBO crystal situated between a pair of flat dichroic mirrors separated by 28 mm. The crystal was cut for type I phase matching at a nominal internal propagation angle of 32° with respect to the optic axis. The crystal measured 12 mm in length with a $6 \times 8 \text{ mm}^2$ aperture. The faces were

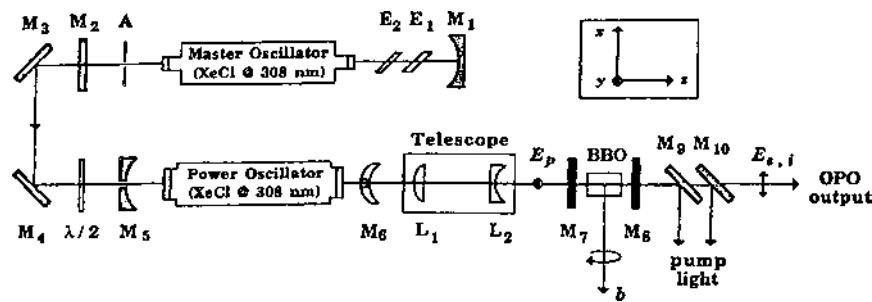


Figure 60 Schematic diagram of a 308 nm pumped BBO based pulsed OPO system. A = aperture, Es = étalons. (From Ref. 22 © IEEE 1990.)

polished but uncoated, and the crystal was mounted on a precision rotation stage for angle tuning. Three sets of dichroic mirrors were needed to cover the entire tuning range. The mirrors had a high reflectance of 90–95% over the signal wavelength ranges (320–370 nm, 420–480 nm, and 500–600 nm) and were highly transmitting at 308 nm.

Many applications of OPOs require a high average power system, since efficiency and signal-to-noise ratio typically scale with repetition rate. Figure 61 illustrates a high average power injection seeded OPO [50]. The pump laser is a single longitudinal mode Q-switched Nd:YAG laser producing 15 ns pulses at a 540 Hz repetition rate. After propagating over 6 m, the spectrally pure (120 MHz bandwidth) pump beam is imaged onto the OPO cavity with a zoom telescope. The OPO is seeded with a cw single mode 1500 nm color center laser.

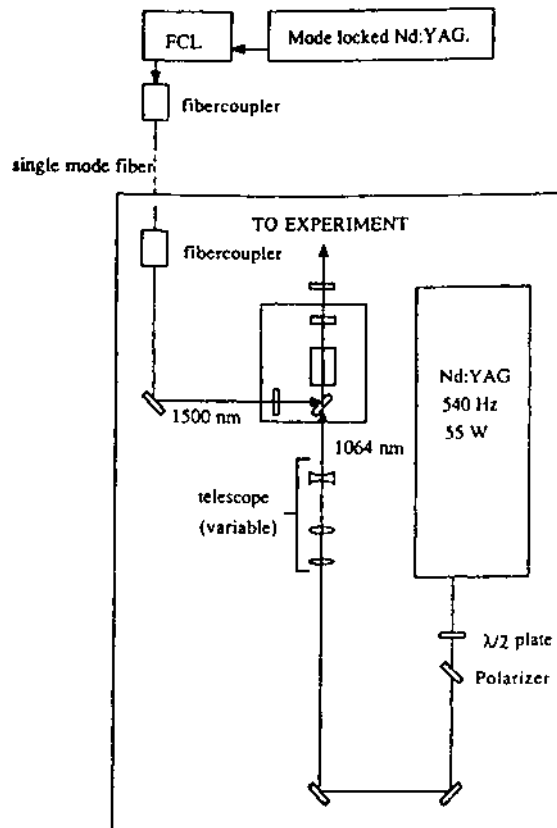


Figure 61 Schematic diagram of a 1064 nm pumped LiNbO_3 based pulsed OPO system with injection seeding at 1500 nm. FCL = color center laser. (From Ref. 50.)

The L-shaped OPO cavity consists of three dielectric mirrors and a LiNbO₃ crystal ($10 \times 10 \times 50 \text{ mm}^3$) as the nonlinear medium. The two input couplers are highly reflecting at 1500 nm, while the output coupler has a 50% reflectance at this wavelength. A piezoelectric transducer is applied to one of the input couplers to match the cavity modes to the seed frequency. The nonlinear crystal resides in a brass oven stabilized near 35°C and mounted on a rotation stage.

Another seed injected OPO for operation in the near-IR and mid-IR [51] is shown in Fig. 62. The introduction of dispersing elements in the OPO cavity to reduce the line width can raise the threshold of available crystals. Crystals such as LiNbO₃ suffer from low damage thresholds. Thus the technique of injection seeding is a means of obtaining narrow line widths without the use of dispersive elements in the cavity. The system shown in Fig. 62 uses DFG generated in a LiIO₃ crystal by mixing the outputs of a dye laser and a doubled Nd:YAG laser to provide the seed beam for the OPO. The OPO is pumped by the fundamental output of a Q-switched Nd:YAG laser operating at 10 Hz. The OPO consists of a LiNbO₃ crystal situated between two CaF₂ mirrors that are coated to reflect the signal at 1.4–1.8 μm and to transmit the idler at 2.7–4.2 μm. The 1064 nm pump beam is coupled into the OPO by two sapphire mirrors that are highly reflecting at 1064 nm but transmit the signal and idler wavelengths. The LiNbO₃ crystal is 50 mm in length and cut at 47°. A 3 mm thick Ge window situated at the output at the Brewster angle separates the signal and idler beams.

A doubly resonant OPO utilizing an LBO crystal [39] is shown in Fig. 63. The pump source is a diode pumped Nd:YLF laser that is frequency doubled to 523.5 nm in an LBO crystal. The 16 ns pump pulses at 523.5 nm are then

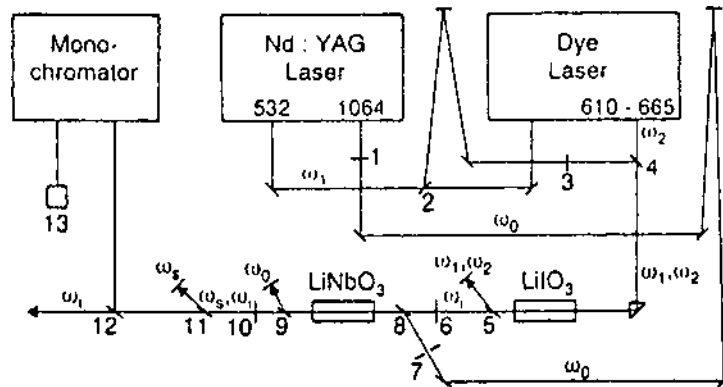


Figure 62 Schematic diagram of an injected seeded 1064 nm pumped LBO based pulsed OPO system. (From Ref. 51.)

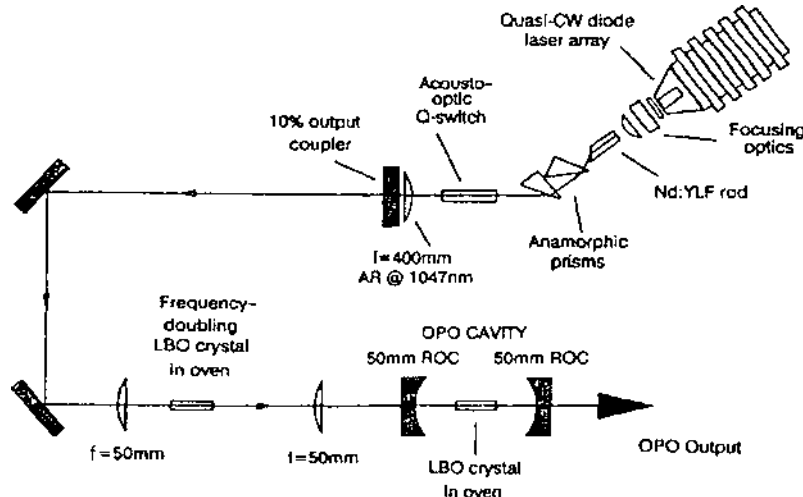


Figure 63 Schematic diagram of an all-solid state, 523.5 nm pumped LBO based pulsed OPO system. (From Ref. 39.)

focused by a 50 mm focal length lens to a spot size of approximately 15 μm inside the LBO crystal situated in the OPO cavity. The crystal length (12 mm) to confocal distance ratio was nearly optimum at a value of 2.84. The LBO crystal was placed at the intracavity focus of the resonator, which consisted of two 50 mm radius of curvature mirrors. Both mirrors were highly reflecting at 1047 nm and antireflection coated at 523.5 nm. Both $3 \times 3 \text{ mm}^2$ faces of the LiNbO₃ crystal were antireflection coated at both 1047 nm and 523.5 nm. The crystal, cut for type I NCPM in the $X-Y$ crystal plane ($\theta = 90^\circ$, $\phi = 0^\circ$), was placed in an oven with tuning accomplished by varying the temperature over a range of 156–166°C.

Without the introduction of wavelength dispersing elements in the cavity or injection seeding, the line width of a pulsed OPO can vary over a range of a few wave numbers to several hundred wave numbers and can vary as a function of output wavelength. An OPO that achieves single-frequency line widths of 0.02 cm^{-1} over its tuning range [52] is illustrated in Fig. 64. The resonator consists of a back mirror, a grating, and a tuning mirror. The 1800 grooves/mm holographic grating had deep modulation for optimum diffraction efficiency and was placed in the cavity at a grazing angle ($\sim 88^\circ$) with respect to the cavity axis. The tuning mirror was set to retroreflect the first order diffracted beam, and both the signal and the idler coupled out of the cavity by the zero order specular reflection of the grating. The pump beam was obtained by doubling the output of a 10 Hz, injection seeded, single

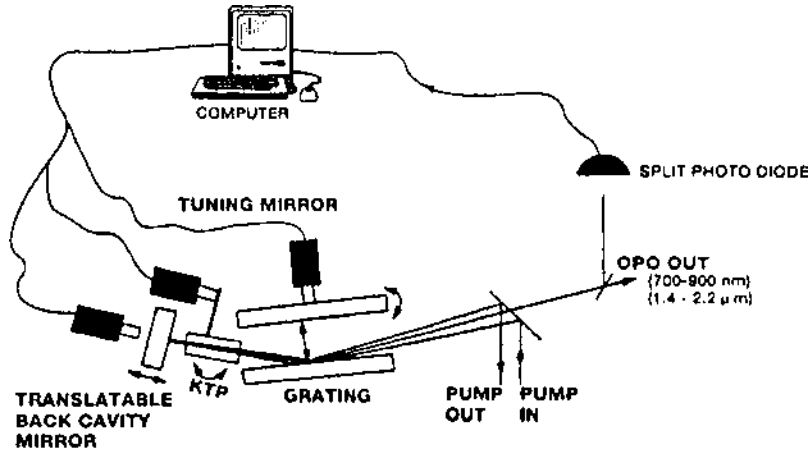


Figure 64 Schematic diagram of a single-frequency, 532 nm pumped KTP based pulsed OPO system. (From Ref. 52.)

longitudinal mode Nd:YAG laser. The 532 nm pulses were 6 ns wide, and the beam was reduced to a 1.3 mm diameter by a 1.8:1 telescope before pumping the KTP crystal of the OPO. The crystal resided in a 5 cm cavity (corresponding to a free spectral range of 0.1 cm^{-1}), which was kept as short as possible to optimize efficiency and longitudinal mode discrimination. Tuning over short ranges ($< 7 \text{ cm}^{-1}$) could be accomplished by rotating the tuning mirror alone. For longer tuning scans, the mirror and the KTP crystal had to be rotated simultaneously. Two KTP crystals were used. Both were $7 \times 7 \times 15 \text{ mm}^3$ in size. The crystals were cut for type II phase matching in the X-Z crystal plane with orientations of $\theta = 54^\circ$, $\phi = 0^\circ$ and $\theta = 65^\circ$, $\phi = 0^\circ$. Both were antireflection coated at the pump wavelength (532 nm) and the resonated wavelengths (700–900 nm).

Since the latter half of the 1990s there has been a virtual explosion of development in pulsed OPO systems. This includes new nonlinear crystals and new pump sources, including other OPOs. There has also been considerable interest in the development of tunable sources in the near and mid-infrared spectral regions. Examples are given in Table 26.

D. Synchronously Pumped OPOs

Several areas of research, such as studying carrier dynamics in semiconductors and performing time domain vibrational spectroscopy of molecules, require ultrashort optical pulses. Extending these types of optical sources into new

wavelength regions, including the IR, has provided a motivation for the development of synchronously pumped OPOs. This section describes some of the activities in this area. Some features of the OPOs discussed are included in Table 27.

The first reported OPO synchronously pumped with femtosecond pulses at 10^8 Hz [53] is depicted in Fig. 65. The OPO is situated within the cavity of a colliding pulse mode-locked (CPM) dye laser. This CPM laser was modified in the following way. The output coupler was replaced with a high reflector, a new intracavity focus was formed with the introduction to two 20 cm radii of curvature mirrors (for pumping the OPO), and the existing quartz prism pairs were separated by an additional 14 cm to compensate for the group velocity dispersion at 620 nm (pump wavelength) introduced by the nonlinear OPO crystal (KTP). The hydrothermally grown KTP was cut for type II phase matching at normal incidence, with single layer MgF₂ antireflection coatings on both faces. This crystal was placed in the new intracavity CPM focus, and tuned by rotating about a horizontal axis perpendicular to the CPM beam. The OPO cavity was formed into a ring by two 10 cm radii of curvature mirrors and two flat mirrors. One flat mirror was mounted on a piezoelectric transducer for fine adjustments of the cavity length. Three of the mirrors were highly reflecting over 820–920 nm, while the one flat mirror acted as a 1% output coupler. The ratio of signal to pump confocal parameters was less than one. Group velocity dispersion and pulse walk-off between signal and pump in the KTP resulted in consistently broader pulses than those of the CPM pump laser.

A dispersion compensated system to correct for these effects [54] is shown in Fig. 66. The cavity is nearly identical with that of Fig. 65, but a set of prisms and cavity length stabilization electronics have been added. The prisms (P) were equilateral, uncoated SF-14 flint glass, mounted for minimum deviation, which is approximately Brewster's angle in the near-IR. The prism separation was approximately 20 cm. By varying the amount of glass intercepted by the signal beam, the net cavity group velocity dispersion could be adjusted to zero for any wavelength. To minimize long-term drift of the pulse width caused by acoustic noise and other room fluctuations, the cavity length was actively stabilized. This was done by monitoring light leaking through one of the cavity mirrors. Such light was diffracted off a grating and incident on two photodiodes, with their difference signal typically set near zero. A change in the cavity length would produce a monotonic shift in the output spectrum. The error signal detected by the combination of the two photodiodes was fed back to the mirror transducer through a high-gain amplifier to compensate actively for the cavity change. This system was then able consistently to achieve transform limited 105 fs output pulses.

A 76 MHz synchronously pumped OPO in an external cavity [55] is shown in Fig. 67. The ring resonator was formed with two highly reflecting 20 cm radii

Table 27 Synchronously Pumped OPO Systems

Pump laser	Nonlinear crystal	Output energy/power	Conversion efficiency (%)	Tuning range	Line width	Pulse width	Ref.
CPM dye (R6G) 620 nm intracavity $\tau = 170$ fs, 100 MHz	KTiOPO ₄ (KTP)	2 mW, avg.	—	820–920 nm 1.9–2.54 μ m	—	220 fs	[53]
CPM dye (R6G) 620 nm intracavity GVD compensation $\tau = 170$ fs, 100 MHz	KTiOPO ₄ (KTP)	2 mW, avg.	—	720–4500 nm	—	105 fs	[54]
CPM dye (kiton red/malachite green) 645 nm $\tau = 150$ fs, 76 MHz 280 mW, avg.	KTiOPO ₄ (KTP)	30 mW, avg.	13 (internal)	1.2–1.34 μ m	—	220 fs	[55]
M-L Nd:YLF 2nd harm., 523 nm $\tau = 15$ ps, 325 MHz 570 mW, avg. 123 W, peak	KTiOPO ₄ (KTP)	10–40 mW, avg.	~ 7	$\lambda_s = 1020$ nm $\lambda_i = 1075$ nm	~ 99 nm	—	[56]
M-L Nd:YLF 2nd harm., 523 nm	KTiOPO ₄ (KTP)	42 mW, avg.	16	1.002–1.096 μ m	~ 0.77 nm	~ 1.5 ps	[19]

$\tau = 2 \text{ ps},$ 125 MHz $\sim 300 \text{ mW, avg.}$ $\sim 101 \text{ kW, peak}$	Q-Sw. M-L Nd:YLF 2nd harm., 523 nm	LiB ₃ O ₅ (LBO)	—	20 (internal)	652–2650 nm	$\sim 1\text{--}11 \text{ nm}$	—	[57]
$\tau = 55 \text{ ps}, 182 \text{ MHz}$ $\tau_{\text{av}} = 105 \text{ ns},$ 500 Hz	M-L Nd:YAG	LiB ₃ O ₅ (LBO)	—	26 (internal)	452–690 nm	—	6 ps	[28]
3rd harm., 355 nm $\tau = 9 \text{ ps},$ $\sim 130 \text{ MHz}$	M-L Ti:Al ₂ O ₃ 765 nm	KTiOPO ₄ (KTP)	185 mW, avg.	—	1.2–1.34 μm 1.78–2.1 μm	—	62 fs (ext com)	[58]
$\tau = 110 \text{ fs},$ 76MHz 800 mW, avg.	M-L Ti:Al ₂ O ₃ $\tau = 125 \text{ fs},$ 90MHz 2.5 W, avg.	KTiOPO ₄ (KTP)	115 mW	55	1.2–1.37 μm 1.8–2.15 μm	—	57 fs	[59]
Q-Sw. M-L Nd:YAG 2nd harm., 532 nm $\tau = 100 \text{ ps}, 100 \text{ MHz}$ $\tau_{\text{av}} = 230 \text{ ns}$	Q-Sw. M-L Nd:YAG 2nd harm., 532 nm $\tau = 100 \text{ ps}, 100 \text{ MHz}$ $\tau_{\text{av}} = 230 \text{ ns}$	LiB ₃ O ₅ (LBO)	— $\sim 180 \text{ mW, avg sig}$ $\sim 100 \text{ mW, avg idl}$	30	800–1700 nm	0.14 nm no grating 0.01 nm grating (80 mW, avg.)	$\leq 100 \text{ ps}$	[41]

(continued)

Table 27 Continued

Pump laser	Nonlinear crystal	Output energy/power	Conversion efficiency (%)	Tuning range	Line width	Pulse width	Ref.
600 mW, avg.							
M-L Nd:YLF 2nd harm., 523 nm $\tau = 2$ ps 290 mW, avg.	LiB ₃ O ₅ (LBO)	78 mW, avg.	27	800–1500 nm	~ 1.5 nm	1.5 ps	[40,60]
M-L Nd:YLF 2nd harm., 527 nm $\tau = 35$ ps, 76 MHz 5.6 W, avg.	LiB ₃ O ₅ (LBO)	1.6 W, avg.	55	740–930 nm (signal) 1220–1830 nm (idler)	0.06 nm	22 ps	[88]
M-L Ti:Al ₂ O ₃ 800 nm $\tau = 50$ fs, 2 W, avg.	β -BaB ₂ O ₄ (BBO)	13 nJ	—	570–600 nm	—	30 fs	[89]
M-L Ti:Al ₂ O ₃ 765 nm $\tau = 26$ fs, 80 MHz 800 mW, avg.	KTiOPO ₄ (KTP)	55 mW, avg.	—	~ 1.2 μ m	53 nm	34 fs	[90]
Q-Sw. M-L Nd:YAG 2nd harm., 532 nm $\tau = 145$ ps, 1 kHz $\tau_{\text{av}} = 260$ ns 5 W, avg.	AgGaS ₂ (AGS)	750 mW, (signal, avg.) 350 mW (idler, avg.)	19 (26, slope) 7	1.4–1.9 μ m (signal) 2.6–4.4 μ m (idler)	—	—	[91]

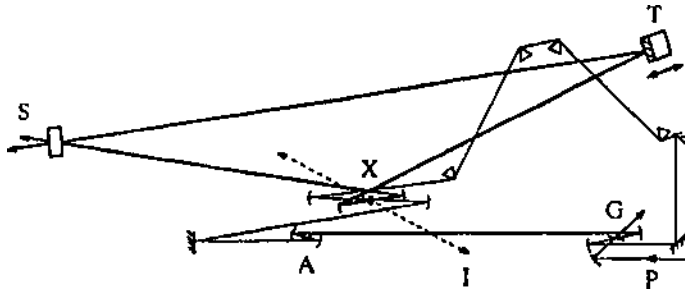


Figure 65 Schematic diagram of an intracavity KTP based OPO synchronously pumped by a CPM laser. Signal wave (S) beamline is bolded. I = idler beam, X = KTP crystal, T = piezoelectric transducer P = Ar ion laser pump beam, G = dye gain jet, A = dye saturable absorber jet. (From Ref. 53.)

of curvature mirrors, one highly reflecting plane mirror, and a flat 2% output coupler. The flat high reflector was mounted on a piezoelectric transducer for fine-tuning the cavity length. A 1.5 mm thick KTP crystal, cut for type II phase matching and antireflection coated at 1300 nm on both faces, was mounted on a rotation stage at the intracavity focus. The pump source was a dispersion

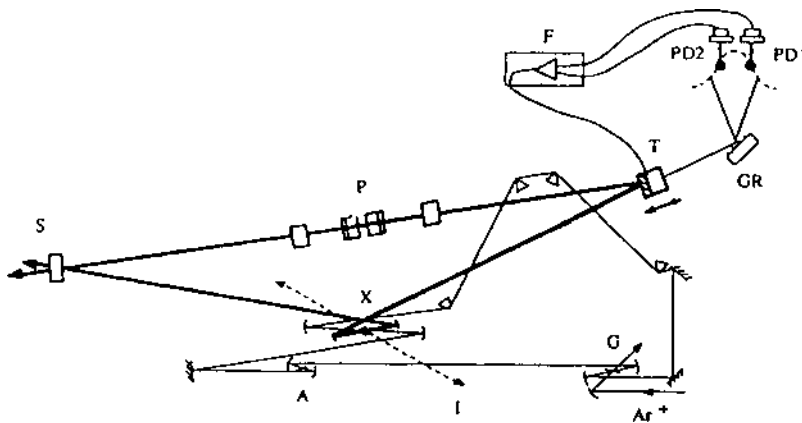


Figure 66 Schematic diagram of an intracavity KTP based OPO synchronously pumped by a CPM laser, with prism compensated group velocity dispersion (GVD) and actively stabilized cavity length. Signal wave (S) beamline is bolded. I = idler beam, X = KTP crystal, T = piezoelectric transducer, P = GVD compensation prism sequence, G = dye gain jet, A = dye saturable absorber jet, GR = grating PDs = photodiodes, F = feedback circuit. (From Ref. 54.)

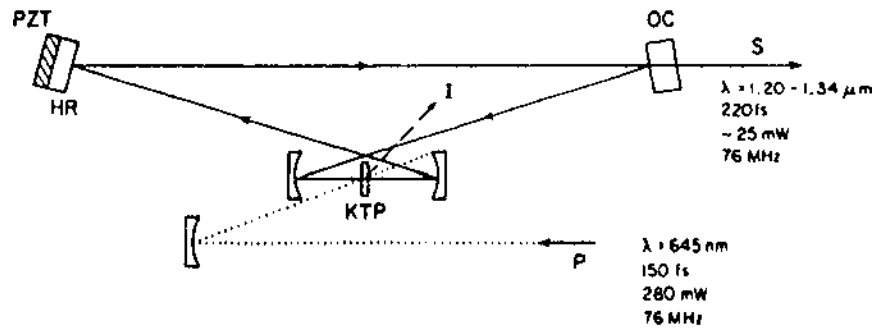


Figure 67 Schematic diagram of a 654 nm external synchronously pumped KTP based OPO. P = pump, S = signal, I = idler, HR = high reflector, PZT = piezoelectric transducer, OC = output coupler. (From Ref. 55.)

compensated hybirdly mode-locked dye laser producing 150 fs pulses at 645 nm. The pump beam was focused onto the KTP crystal noncollinearly with the signal beam (typically at 1.7°) to compensate partially for beam walk-off. The output signal wavelength was tuned by rotating the KTP crystal.

Many synchronously pumped OPOs are pumped with Q-switched mode-locked lasers to achieve the peak powers required for singly resonant OPOs. The finite pulse trains obtained are not optimal for all applications. The configuration shown in Fig. 68 illustrates a doubly resonant OPO pumped by a lower power but longer train of pulses from a cw mode-locked laser [56]. The pump was an FM mode-locked Nd:YLF laser, frequency doubled in an external cavity to produce a continuous train of mode-locked pulses at 523.5 nm at a repetition rate of 353 MHz. The width of each pulse was approximately 15 ps. The OPO folded cavity resonator was formed by a concave 15 cm radius of curvature mirror, a 10 cm radius of curvature folding mirror and a flat output coupler. All cavity mirrors were highly reflecting (>99%) over a range of 1020–1200 nm with >99% transmittance at 523.5 nm. The OPO cavity length was set at twice the length for synchronous pumping by the Nd:YLF laser. This was done to match the cavity confocal parameter close to that for minimum threshold. The nonlinear crystal was a $3 \times 3 \times 5$ mm³ KTP crystal, cut for collinear type II phase matching at normal incidence. Both faces of the crystal were broad band antireflection coated with a center wavelength of 1064 nm.

The requirement for simultaneous resonance of the signal and idler waves places stringent constraints on the pump laser and OPO cavity and often results in poor amplitude and frequency stability. The problem associated with pumping a singly resonant oscillator with cw mode-locked lasers is one of weak pump power. It is possible to overcome this limitation if higher-energy pump pulses are

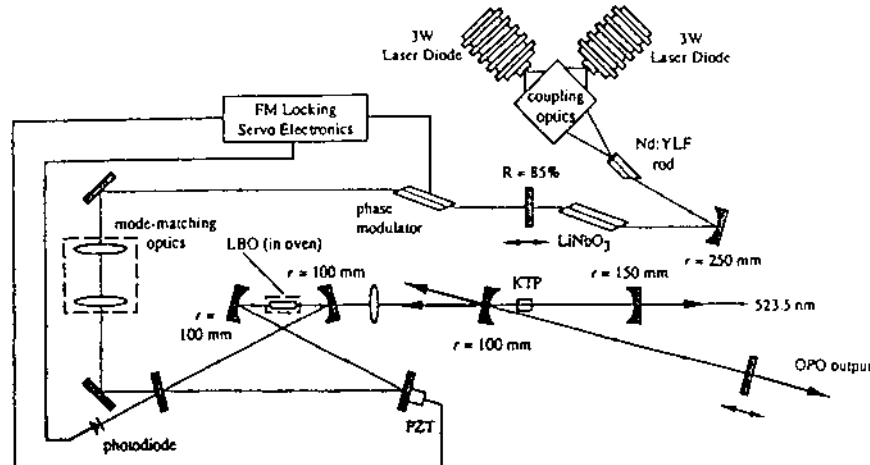


Figure 68 Schematic diagram of 523.5 nm synchronously pumped KTP based OPO. PZT = piezoelectric transducer. (From Ref. 56.)

short enough. Such a system pumped with picoseconds pulses [19] is illustrated in Fig. 69. The laser was a frequency doubled, self-starting additive-pulse mode-locked Nd:YLF laser pumped by a diode laser. The peak power at 532 nm was about 1.1 kW in 2 ps pulses. The OPO cavity was in a ring configuration with two 10 cm radius of curvature mirrors 99.7% reflecting at 1047 nm, and highly transmitting (90%) at the 523 nm pump wavelength. One flat high reflector was

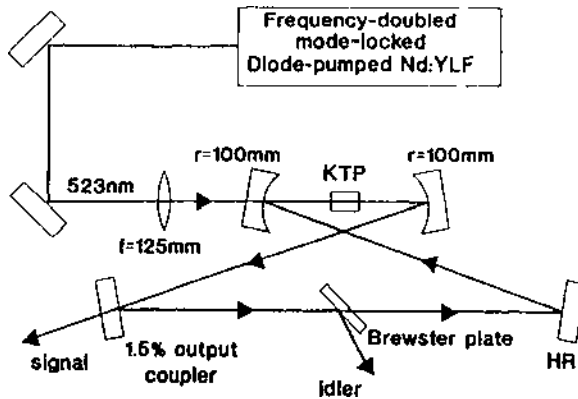


Figure 69 Schematic diagram of 523.5 nm synchronously pumped KTP based OPO. (From Ref. 19.)

mounted on a piezoelectric transducer for fine cavity length adjustments, and a 1.5% transmitting flat output coupler was mounted on a micrometer-driven translation stage. The angle of incidence on the curved cavity mirrors was kept to about 2.5° to minimize astigmatism. The nonlinear crystal was a $5 \times 5 \times 5 \text{ mm}^3$ KTP crystal, antireflection coated at 1047 nm and 523 nm on both faces. The crystal was cut for quasi-NCPM in the XY plane ($\theta = 90^\circ$, $\phi = 26^\circ$) and placed at the intracavity focus, designed for a $20 \mu\text{m}$ radius resonated beam. A 125 mm focal length lens focused the pump beam to an approximately $16 \mu\text{m}$ waist in the KTP. A Brewster angle plate was inserted in the cavity to discriminate against the idler wave.

A temperature tuned, NCPM LBO based OPO [57] is shown in Fig. 70. The pump source in this case was derived from a diode-pumped Nd:YLF laser that was FM mode-locked at 182 MHz and Q-switched at 500 Hz. The output of this laser was doubled to 523.5 nm, yielding a 105 ns Q-switched envelope of mode-locked pulses with an average pulse duration of 55 ps. The OPO cavity was a three-mirror ring resonator consisting of two 10 cm radius of curvature mirrors and a flat output coupler. This yielded a signal confocal parameter of approximately 6 mm. The cavity mirrors provided >99% reflectance over

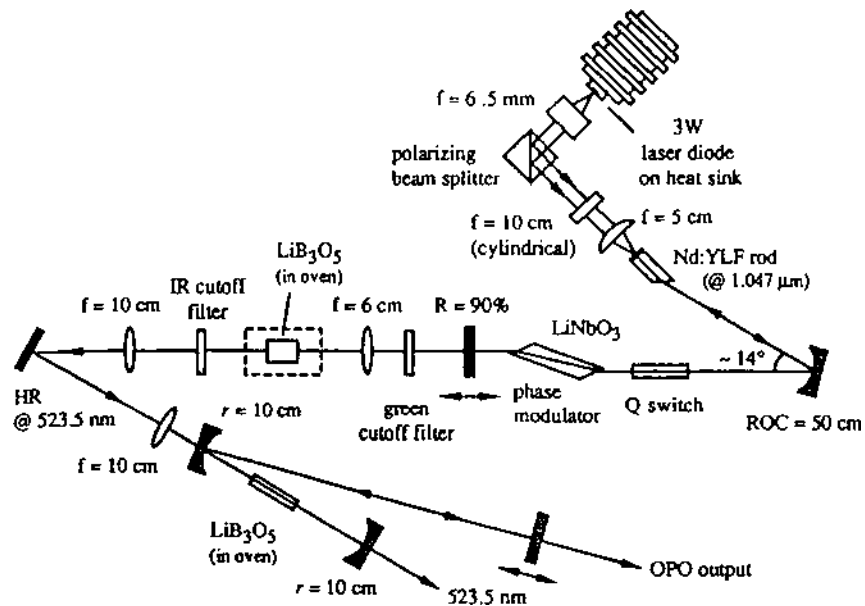


Figure 70 Schematic diagram of 523.5 nm synchronously pumped LBO based OPO. (From Ref. 57.)

the 650–800 nm signal wavelength range and were >85% transmitting at the pump wavelength. The pump beam was focused to a spot radius of approximately 15 μm so that the pump confocal parameter was matched closely to that of the signal. A 12 mm long LBO crystal with a $3 \times 3 \text{ mm}^2$ aperture was located inside an oven and placed at the intracavity focus. Both faces of the crystal were antireflection coated at 523.5 nm and 1047 nm. The crystal was cut for noncritical type I phase matching in the XY plane, with the surface normal along the X-axis.

Another LBO based system pumped in this case in the UV [28] is illustrated in Fig. 71. The output of a passive negative feedback mode-locked Nd:YAG laser was amplified in a three-stage Nd:YAG amplifier, and the third harmonic at 355 nm was obtained using a pair of KDP type II crystals. The result was a beam of 355 nm pulses with single pulse width of 9 ps. This beam was focused by a 1 m focal length lens into a $5 \times 5 \times 10.5 \text{ mm}^3$ LBO crystal, at an angle of 35 mr with respect to the resonator axis. The crystal was cut for type I phase matching ($\theta = 90^\circ, \phi = 39^\circ$). The resonator consisted of two identical spherical mirrors, with radii of curvature of 1 m and high reflectance (>99%) over 405–690 nm. The beam waist for this confocal resonator had a diameter of 400 μm and was closely matched to the pump waist diameter.

High repetition rate, ultrashort pulse CPM pumped systems are particularly suited for high signal-to-noise ratio time resolved spectrometry. The femtosecond dye pump lasers have some undesirable features, though, including high maintenance, poor mode quality, and delicate operation. The recently developed Kerr lens mode-locked Ti:sapphire lasers offer potentially dramatic improvements for pumping these types of OPOs. An OPO pumped with this type of laser [58] is illustrated in Fig. 72. The pump produces 110 fs pulses at a 76 MHz repetition rate with nearly 1 W of average power at 765 nm. The output of this

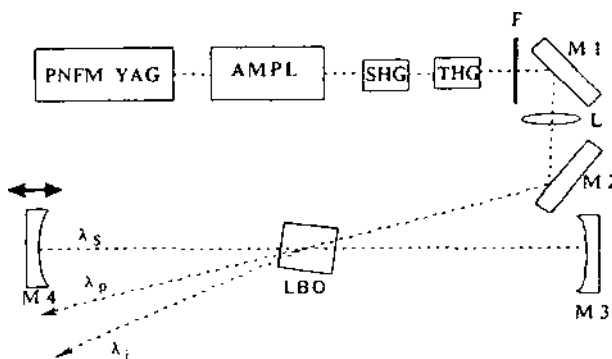


Figure 71 Schematic diagram of 355 nm synchronously pumped LBO based OPO. (From Ref. 28.)

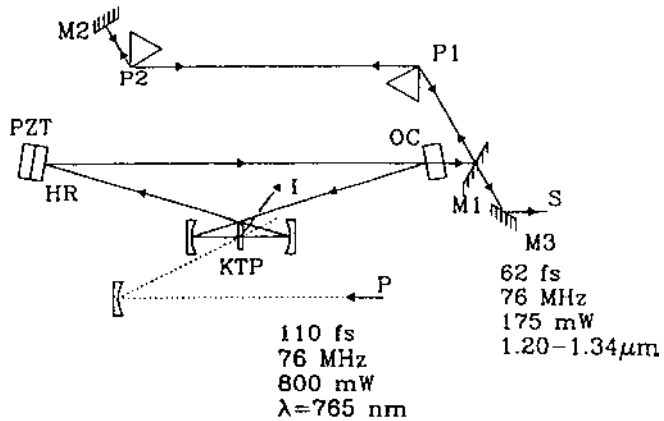


Figure 72 Schematic diagram of Ti:sapphire synchronously pumped KTP based OPO. P = pump, S = signal, I = idler, HR = high reflector, PZT = piezoelectric transducer, OC = output coupler, Ps = prisms. (From Ref. 58.)

laser is tunable between 720 nm and 1000 nm, with peak powers that can exceed 100 kW, crucial for pumping singly resonant OPOs. The OPO in Fig. 72 is a ring resonator type. A 1.5 mm thick KTP crystal, antireflection coated at 1300 nm, was cut for type II phase matching ($\theta = 67^\circ$) with propagation in the XZ plane and mounted at the intracavity focus of the resonator. The cavity consists of two highly reflecting 20 cm radius of curvature mirrors, a plane high reflector, and a 2% output coupler. The plane high reflector is mounted on a piezoelectric transducer for fine-tuning the cavity length. The high intracavity intensity produces self-phase modulation within the crystal, which leads to chirped pulses. Thus a pair of SF4 equilateral prisms are used to compress the pulses to a 62 fs width.

Another example of a Ti:sapphire synchronously pumped OPO [59] is given in Fig. 73. This self-mode-locked laser produced 125 fs pulses at a 90 MHz repetition rate with 2.5 W of average power when pumped with a 15 W argon ion laser. The Ti:sapphire laser was focused into a 1.15 mm KTP crystal using a 15 cm radius of curvature mirror. The crystal was cut for type II phase matching at $\theta = 47.5^\circ$ and $\phi = 0^\circ$ and antireflection coated at 1300 nm with MgF₂. The linear OPO cavity was formed using two 10 cm radius of curvature mirrors aligned for oscillation in the XZ-plane of the crystal to provide compensation for walk-off between the pump and signal beams. Two flat mirrors, one a 1% output coupler and the other mounted on a piezoelectric transducer for fine cavity length adjustment, completed the cavity. To compensate for group velocity dispersion, which puts a chirp on the signal pulses, an SF-14 prism pair was inserted in

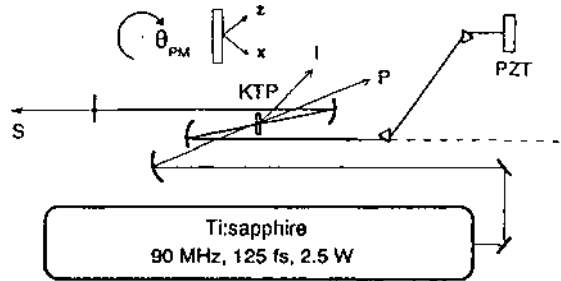


Figure 73 Schematic diagram of Ti:sapphire synchronously pumped KTP based OPO. P = pump, S = signal, I = idler, HR = high reflector, PZT = piezoelectric transducer. (From Ref. 59.)

the cavity as shown in the figure. The OPO output wavelength could be tuned by adjusting the cavity length, changing the pump wavelength, or rotating the KTP crystal.

A temperature tuned, synchronously pumped OPO [41] is illustrated in Fig. 74. The pump in this case was the frequency doubled output of a Q-switched mode-locked Nd:YAG laser, producing a 230 ns train of 23 mode-locked pulses at 532 nm. The singly resonant OPO was formed with two 30 cm radius of curvature mirrors that were >99% reflecting at the signal wavelengths, and two flat mirrors with reflectances of >99% and approximately 75% for the output coupler. An LBO crystal in a temperature- controlled oven was placed at the intracavity focus. The crystal had dimensions of $2.5 \times 3 \times 15 \text{ mm}^3$ and was cut for NCPM. The pump beam was focused to a 170 μm spot inside the crystal and

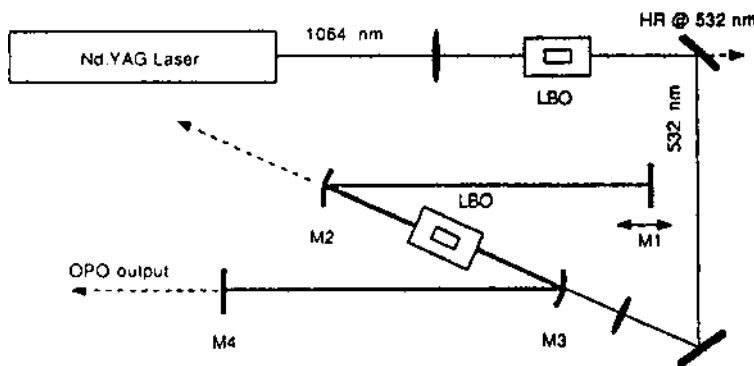


Figure 74 Schematic diagram of 532 nm synchronously pumped LBO based OPO. Output coupling mirror M4 replaceable with a Littrow grating. (From Ref. 41.)

closely matched to the focal spot of the signal beam. To achieve a narrow line width, the output coupler was replaced with an 1800 grooves/mm Littrow grating. The first order diffracted beam was retroreflected by a flat mirror, and the zero order diffraction provided the output coupling.

Another temperature tuned OPO based on an LBO nonlinear crystal [40,60] is shown in Fig. 75. This OPO was pumped with the second harmonic of a mode-locked Nd:YLF laser, with 2 ps pulse and peak power of 1.3 kW. The linear OPO cavity was formed with mirrors taken from a commercial Ti:sapphire laser (Spectra-Physics 3900). They were coated to be highly reflecting (>99.9%) over 800–1000 nm and highly transmitting (>96%) at 523 nm. They also had high transmittance (80–90%) over the 1100–1400 nm range. One flat high reflector was mounted on a micrometer-driven translation stage for coarse cavity length adjustment, while the other was mounted on a piezoelectric transducer for fine cavity length control. The $3 \times 3 \times 12$ mm³ LBO crystal was cut for type I NCPM and antireflection coated on both faces at 1047 nm and 523 nm. The crystal was mounted in an oven to control the temperature between ambient and 200°C with a stability of $\pm 1^\circ\text{C}$, for tuning the output wavelength, and placed at the intracavity focus where the resonated mode had a waist of 26 μm radius. The pump beam was focused through a 125 mm focal length lens to a 16 μm waist within the LBO crystal.

The latter half of the 1990s has witnessed a continued interest in the development of synchronously pumped OPO systems. Several additional examples are included in Table 27.

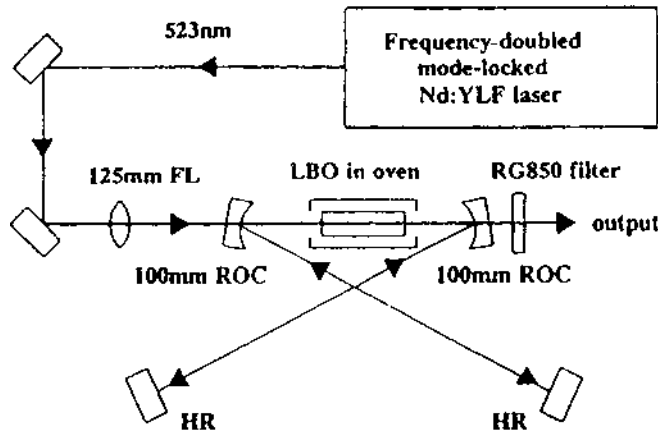


Figure 75 Schematic diagram of 523.5 nm synchronously pumped LBO based OPO. (From Ref. 60.)

E. Systems with Quasi-phase-matched Materials

Recently, a phenomenal amount of work has been directed toward the development of parametric systems based on quasi-phase-matched (QPM) materials. These efforts have benefited from the achievement of periodic poling of nonlinear crystals, which was extended from earlier work on periodic poling in waveguides. QPM materials offer distinct advantages. Since the restrictions of birefringent phase matching are removed, propagation along a principal crystal axis becomes feasible, where the largest nonlinear coefficients can be selected without the problems of beam walk-off. This results in highly efficient frequency conversion at modest pump energies and high pulse repetition frequencies. In turn, it reduces the likelihood of optical damage particularly for nanosecond pump sources. In fact, the high efficiency allows for the consideration of small, compact pump sources such as microchip lasers. Tuning in QPM-based systems can be achieved by recording multiple grating periods in the poled crystals. Fan-out gratings can also be employed. Temperature control provides a further tuning mechanism and also prevents photorefractive damage in periodically poled lithium niobate (PPLN), which is the most common QPM crystal. Recent work has also demonstrated the utility of other periodically poled materials.

QPM materials have been employed in OPG/OPA systems, cw OPOs, pulsed OPOs, and synchronously pumped OPOs. Several examples are summarized in Tables 28–31.

VI. SUMMARY AND SOME PRACTICAL CONSIDERATIONS

OPOs make very attractive all solid-state sources of continuously tunable radiation, from the UV to long wave infrared (LWIR). In the visible and near-IR they are replacing dye lasers, which tend to be both messy and cover only a small spectral range without a dye change. Already, commercially available OPOs provide spectral coverage from 410 nm to 2400 nm using a single type I BBO crystal pumped by the 355-nm third harmonic of a Nd:YAG laser. It may be remarked that with type I phase matching there is small gap near the degeneracy point (710 nm) that does not exist for type II phase matching. OPOs using the noncritically phase-matched (NCPM) KTP have become popular as a source of eye-safe 1.57- μm radiation for such applications as military training exercises and for wire avoidance for helicopters. OPOs are also very attractive for mid-infrared (MIR) and LWIR radiation sources for such applications as lidar and military countermeasures. For applications requiring continuous tunability in the 3–5 μm atmospheric window, the holmium laser-pumped ZnGeP₂ (ZGP) OPO has proved to be very useful [139].

Table 28 QPM-Based OPG/OPA Systems

Pump laser	Nonlinear medium ^a	Output energy/power	Conversion efficiency (%)	Tuning range	Line width	Pulse width	Ref.
Q-Sw Tm, Ho: YLF 2.051 μm $\tau = 50$ ns, 50 Hz 7 mJ/pulse 180 mW, avg.	PPLN (50 mm) $\Lambda = 25.5\text{--}28.7 \mu\text{m}$	30 mW	16.7	3.4–5.2 μm	—	—	[92]
Q-Sw Nd:YAG 1064 nm $\tau = 2.6$ ns, 120 Hz 650 μJ /pulse	PPLN (50 mm) $\Lambda = 28.5\text{--}29.9 \mu\text{m}$	~ 8 μJ	~ 8	6820–6220 cm^{-1} (signal) 2580–3180 cm^{-1} (idler)	0.05 cm^{-1}	2.5 ns	[93]
Q-Sw Nd:YAG 2nd harm., 532 nm $\tau = 2.5$ ns, 1.1 kHz 90 μJ /pulse 97 mW avg. Alexandrite, diode seed 786 nm $\tau = 0.5$ ns 5 mJ/pulse	PPLN (5 mm) $\Lambda = 10.1\text{--}13 \mu\text{m}$	12 mW, avg.	23	637–593 nm	0.15–0.32 nm	—	[94]
Er-doped fiber	PPLN (20 mm [2])	50 nJ	~ 39	1.31 μm	1.5 mm	2.7 ps	[96]

2nd harm., 676 nm $\tau = 2$ ps, 1.6 MHz 10 μ J/pulse diode seed, 1.31 m μ	$\Lambda = 18.3, 18.7 \mu\text{m}$			
Q-Sw Nd:YAG 1064 nm $\tau = 15$ ns, 1 kHz 750 μ J/pulse	PPLN (5 cm [2]) $\Lambda = 29.75 \mu\text{m}$ $\Lambda = 29.7-30.1 \mu\text{m}$	180 μ J (signal) 60 μ J (idler)	— $\lambda_s = 1.6 \mu\text{m}$ $\lambda_i = 3.3 \mu\text{m}$ 18 cm^{-1} tuning	0.08 cm^{-1} (idler) —
Q-Sw Nd: YAG 1064 nm $\tau = 5$ ns, 20 Hz 3 mJ/pulse Er-Yb:glass seed 1554 nm, 6 mW avg.	PPKTN (15 mm) $\Lambda = 35.6 \mu\text{m}$	0.61 mJ (signal) 0.15 mJ (idler) 71 mJ (signal, OPA)	38 (total OPG) 1544–1559 nm (signal) 3.1 (total, OPA) 1554 nm	0.65 nm —
M-L II:sapphire 800 nm $\tau = 80-100$ fs, 1 kHz 600 μ J/pulse Nd:YVO ₄ , 8- kW peak 1064-nm seed	PPKTN 10 mm $\Lambda = 27.5 \mu\text{m}$	5 μ J (idler)	40 (internal) 3.8 μm (idler)	$\sim 0.2 \mu\text{m}$ 210 fs

^a PPLN = periodically poled lithium niobate; PPKTN = periodically poled KTN (KTiOPO₄).

Table 29 QPM-Based Continuous Wave OPO Systems

Pump laser	Nonlinear medium ^a	Output power	Conversion efficiency (%)	Tuning range	Line width	Ref.	
AlGaAs diode 810 nm 75 mW	PPLN (50 mm) $A = 21.0\text{--}22.4 \mu\text{m}$	4.6 mW (idler)	6.5	1.06–1.19 μm (signal) 2.58–3.44 μm (idler)	—	[100]	
InGaAs diode 924 nm 2.25 W	PPLN (33 mm) $A = 26.0 \mu\text{m}$	200 mW (idler)	9	2.11 μm (56 GHz tuning) 5 MHz (idler)	<1 MHz (signal)	[101]	
Nd:YAG 1064 nm 3.7 W	PPLN (2.5 cm) $A = 30.34\text{--}30.66 \mu\text{m}$	450 mW (idler)	12	2.9–3.25 μm	140 MHz	[102]	
InGaAs MOPA 925 nm 2.5 W	PPLN (38 mm) $A = 26.0\text{--}26.6 \mu\text{m}$	480 mW (idler)	19	1.55–1.70 μm (signal) 2.03–2.29 μm (idler)	<1 MHz (signal) 5 MHz (idler)	[103]	
Nd:YVO ₄ 2nd harm., 532 nm 5 W	PPLN (53 mm)	~200 mW (signal)	~7 (signal)	917–988 nm (signal)	—	[104]	
Nd:YAG 1064 nm 11 W	$A = 6.5 \mu\text{m}$	~430 mW (idler)	~14 (idler)	1151–1267 nm (idler)	—		
Nd:YAG 1064 nm 1 W	PPLN (50 mm)	400 mW	~4	1.53–1.62 μm	<6 MHz	[105]	
$A = 29.1 \mu\text{m}$ (fan-out)							
PPLN (50 mm)		~295 mW (total)		~68 (total)		1.446–1.604 μm (signal)	
$A = 28.5\text{--}29.9 \mu\text{m}$						3.158–4.024 μm (idler)	

Diode 810 nm	PPLN (19 mm)	5 mW (signal)	5 (signal mode)	1.15–1.25 μm (signal)	—	[107]
100 mW (signal mode) 400 mW (multi mode)	$A = 21.0\text{--}22.4 \mu\text{m}$	39 mW (signal)	9.75 (multi mode)	2.31–2.66 μm (idler)	—	
Nd:YAG 2nd harm., 532,26 nm 430 mW	PPLT (25 mm)	60 mW	22 (total)	768–978 nm (signal)	<160 kHz	[108]
InGaAs MOPA 925 nm 2.3 W	PPLT (35 mm)	244 mW	1167–1733 nm (idler) ~11	1.55–2.3 μm	<10 MHz	[109]
Nd:YAG 2nd harm., 532 nm 93 mW	$A = 7.3\text{--}10.7 \mu\text{m}$ PPKTP (10 mm)	~6.5 mW (total)	~8	1037–1093 nm	—	[110]
Nd:YLF 2nd harm., 532 nm 200 mW	$A = 9.00 \mu\text{m}$ PPKTP (9 mm)	10 mW (idler)	5 (idler)	769.1–763.4 nm (signal)	~10 MHz	[111]
Ti:sapphire 840 nm 2.2 W (intracavity OPO)	$A = 9.55 \mu\text{m}$ PPRTA (4.5 mm) $A = 30 \mu\text{m}$	270 mw (idler) 930 mW (total)	43 (total)	1639.2–1665.7 nm (idler) 2.53–3.26 μm (idler) 1.13–1.27 μm (signal)	—	[112]
Ar ion pump, 8 W						

^a PPLN = periodically poled lithium niobate (LiNbO_3); PPLT = periodically poled lithium tantalite (LiTaO_3); PPKTP = periodically poled KTP (KTiOPO_4).

Table 30 QPM-Based Pulsed OPO Systems

Pump laser	Nonlinear medium ^a	Output energy/power	Conversion efficiency (%)	Tuning range	Line width	Pulse width	Ref.
Q-SW. Nd:YAG 1064 nm $\tau = 20\text{ ns}, 1\text{ kHz}$ 3.2 mJ/pulse	PPLN (17 mm)	338 μJ (idler)	15.4	3.22–3.7 μm	158 MHz	4 ns	[113]
$\Lambda = 29\text{ }\mu\text{m}$							
Q-SW. Nd:YAG 1064 nm $\tau = 120\text{ ns}, 1\text{--}5\text{ kHz}$ 1 mJ/pulse	PPLN (40 mm)	270 μj (total)	~ 8	1.529 and 1.546 μm	~ 0.1 μm	—	[114]
$\Lambda = 29.3\text{ & }29.5\text{ }\mu\text{m}$ (DAST crystal for DFG of 2 signals)							
Q-SW. Nd:YAG 1064 nm $\tau = 28\text{ ns}, 3\text{ kHz}$ 0.8 mJ/pulse	PPLN (2) (50 mm)	(53 fJ of DFG)		(120–160 μm , THz wave by DFG)			
$\Lambda = 28.5\text{--}29.9\text{ }\mu\text{m},$ $\Lambda = 30.0\text{--}31.2\text{ }\mu\text{m}$							
Q-SW. Nd:YAG 1064 nm $\tau = 120\text{ ns}, 1\text{ kHz}$ 1.6 W, avg.	PPLN (18 mm)	250 μJ (signal)	25	1450–1950 nm	0.3 cm^{-1}	—	[115]
$\Lambda = 30\text{ }\mu\text{m}$							
Q-SW. Nd:YAG 1064 nm $\tau = 3.5\text{ ns}, 30\text{ Hz}$ 300 μJ /pulse	PPLN (10 mm)	~ 260 mW, avg.	~ 16 (18.5, slope)	1.533–1.589 μm	—	—	[116]
$\Lambda = 26\text{--}31.5\text{ }\mu\text{m}$							
Q-SW. Nd:YAG 1064 nm $\tau = 3.5\text{ ns}, 30\text{ Hz}$ 300 μJ /pulse		~ 80 μJ , (signal)	~ 27	1.475–1.7 μm (signal)	~ 1–30 nm	3 ns	[117]

Nd:YAG, 1064 nm 1.2-W diode pump, or Nd:YVO ₄ , 1064 nm 2-W diode pump (monolithic OPO design, with LiTaO ₃ Q-switch)	PPLN (11 mm) $\Lambda = 30\text{--}31.2$	—	1540–3440 nm	—	11.4 ns (YAG) 1.65 ns (YVO ₄)	[118]
Er-doped fiber 2nd harm., 780 nm $\tau = 45\text{ ns}, 300\text{ Hz}$ 60 $\mu\text{J}/\text{pulse}$	PPLN (20 mm) $\Lambda = 19\text{--}20.5\text{ }\mu\text{m}$	~ 2 μJ	~ 6 (signal) (~ 10, slope)	945–1450 nm (signal) 1690– 4450 nm (idler)	—	[119]
Er-doped fiber 1.545–1.56 μm $\tau = 60\text{ ns}, 500\text{ Hz}$ 150 $\mu\text{J}/\text{pulse}$	PPLN (50 mm) $\Lambda = 32.4\text{--}$ 33.2 μm	8 μJ (idler)	18	2.55–2.7 μm (signal) 3.65– 3.96 μm (idler)	—	[120]
Q-SW Nd:YAG 1064 nm $\tau = 5.1\text{ ns}, 10\text{ Hz}$ 150 mJ/pulse	PPKTP (10 mm) $\Lambda 35.0\text{ }\mu\text{m}$ (cylindrical)	—	—	1517–2040 nm (signal) 2220– 3560 nm (idler)	—	[121]
Q-SW Nd:YAG 2nd harm., 523 nm $\tau = 5\text{ ns}, 20\text{ Hz}$ 0.5 mJ/pulse	PPKTP (8 mm) $\Lambda = 12.77\text{ }\mu\text{m}$	1.79 mJ	50 (signal)	631–641 nm 0.3 nm	—	[122]
Q-SW Nd:YAG 1064 nm $\tau = 5\text{ ns}, 20\text{ Hz}$ 16.2 mJ/pulse	PPKTP (8 mm) $\Lambda = 37.8\text{ }\mu\text{m}$	7 mJ (total)	45 (total)	1715–1745 nm (signal) 2803– 2726 nm (idler)	~ 15 nm (signal) —	[123] (continued)

Table 30 Continued

Pump laser	Nonlinear medium ^a	Output energy/power	Conversion efficiency (%)	Tuning range	Line width	Pulse width	Ref.
Q-SW, Nd:YAG 2nd harm., 523 nm $\tau = 5$ ns, 1.5 mJ/pulse	PPKTP (10 mm) $\Lambda = 9.01 \mu\text{m}$	—	13 (idler, axial Bessel beam) (27, total)	931–1241 nm (total)	—	—	[124]
Q-SW, Nd:YAG 1064 nm $\tau = 5$ ns, 20 Hz 4.5 mJ/pulse	PPKTP (2) (15 and 20 mm) $\Lambda = 38.5 \mu\text{m}$	1.8 mJ (total)	50	1.8–2.5 μm	—	—	[125]
Q-SW, Nd:YVO ₄ 1064 nm, $\tau = 5.5$ ns, 1 kHz 800 μJ /pulse	PPRTA (7 mm) $\Lambda = 40.2 \mu\text{m}$	45 μJ (signal) 11 μJ (idler)	6 (signal) 26	1577/sf/mm (signal) 1577 nm (signal)	~7–11 nm	—	[126]
Q-SW, Nd:YAG 1064 nm $\tau = 20$ ns, 10 Hz 65 mJ/pulse							
M-L Ti:sapphire	PPRTA (8 mm)	320 mW (signal) 113 mW	~25 (signal) ~9 (idler)	1.062–1.112 μm (signal) 3.35–5 μm (idler)	~3 nm (signal) ~35 nm (idler)	714 fs (signal) ~1 ps (idler)	[127]
780–910 nm $\tau = 1.5$ ps, 81 MHz 1.5 W, avg.	$\Lambda = 30 \mu\text{m}$						

^a PPLN = periodically poled lithium niobate (LiNbO_3); PPKTP = periodically poled KTP (KTiOPO_4); PPRTA = periodically poled RTA (RBTOAsO_4).

Table 31 QPM-Based Synchronously Pumped OPO Systems

Pump laser	Nonlinear medium ^a	Output energy/ power	Conversion efficiency (%)	Tuning range	Line width	Pulse width	Ref.
M-L-Ti:Al ₂ O ₃ 790 nm $\tau = 175$ fs, 110 MHz 1 W, avg.	PPLN (0.8 mm) $\Lambda = 19.75 \mu\text{m}$	20 mW, avg. (signal)	~ 5	1.4 μm (signal)	—	220 fs	[128]
M-L-InGaAs oscillator 927 nm $\tau = 20$ ps, 2.488 GHz 1 W, avg.	PPLN (38 mm) $\Lambda = 26.0\text{--}26.6 \mu\text{m}$	5 mW, avg. (signal)	< 1 (signal)	1531–1737 nm (signal)	1 nm	7.8 ps	[129]
M-L-Ti:Al ₂ O ₃ 840 nm $\tau = 45$ fs, 84.5 MHz 1 W, avg.	PPLN (aperiodic) (1 mm) $\Lambda = 22.96 \mu\text{m}$, avg. 21.89–23.55 μm , max chirp	5–10 mW, avg.	—	2.7–3.7 μm (idler)	> 500 nm	53 fs	[130]
M-L-Ti:Al ₂ O ₃ 800 nm $\tau = 100$ fs, 86 MHz, 1.5 W, avg.	PPLN (1 mm)	90 mW, avg. (signal)	12	0.975–1.54 μm (signal)	—	140 fs	[131]
M-L-Ti:Al ₂ O ₃ 810 nm $\tau = 100$ fs, 84 MHz, 1.5 W, avg.	PPLN (1 mm)	14.4 mW, avg. (idler)	—	910–1080 nm (signal)	—	~ 150 fs	[132]
M-L-Nd:YLF	PPLN (19 mm)	300 mW, avg. (signal)	30	1.6–1.9 μm (signal)	—	~ 3 ps	[133] (continued)

Table 31 Continued

Pump laser	Nonlinear medium ^a	Output energy/- power	Conversion efficiency (%)	Tuning range	Line width	Pulse width	Ref.
1064 nm $\tau = 4$ ps, 120 MHz 1 W, avg.	$\Lambda = 30\text{--}30.4 \mu\text{m}$	200 mW, avg. (signal)	22			~ 250 fs	
M-L Nd:YAG 1064 nm $\tau = 100$ ps, 76 MHz	PPLN (12 mm) $\Lambda = 29.75 \mu\text{m}$	3.3 W, avg. (idler)	~ 20 (idler)			—	[134]
M-L Nd:YLF 1064 nm 1 W, avg.	PPLN (19 mm) $\Lambda = 21\text{--}24 \mu\text{m}$	10 mW, avg. (idler)	—	5.3–6.3 μm (idler)	—	—	[135]
M-L Ti:Al ₂ O ₃ 835–1000 nm $\tau = 800$ fs, 80.5 MHz 250– 980 mW, avg.	PPLN (6 mm) $\Lambda = 21\text{--}22.4 \mu\text{m}$	280 mW, avg. (signal) ~ 60 mW, avg. (idler)	35 (signal) ~ 9 (idler)	1.004–1.040 μm (signal) 3.9–5.98 μm (idler)	~ 7 nm (signal)	0.4 ps (signal)	[136]
M-L Yd:YAG 1030 nm $\tau = 600$ fs, 35 MHz	PPLT (22 mm) $\Lambda = 28.3\text{--}29 \mu\text{m}$	2.3–2.7 W, avg. (signal)	~ 30	1429–1473 (signal) 3425–3670 nm (idler)	3–4 nm (signal)	700–900 fs	[137]
M-L Ti:Al ₂ O ₃ 758 nm $\tau = 215$ fs, 76 MHz 650 mW, avg.	PPKTP (7 mm) $\Lambda = 24 \mu\text{m}$	140 mW, avg. (signal)	22	1000–1235 nm (sig- nal)	—	330 fs	[138]

^a PPLN = periodically poled lithium niobate (LiNbO₃); PPLT = periodically poled lithium tantalite (LiTaO₃); PPKTP = periodically poled KTP (KTiOPO₄).

Lidar (light detection and ranging) applications have great need for a continuously tunable coherent radiation source for the LWIR 8–12- μm atmospheric transmission window. Many chemical species have distinguishing signatures in this window. Traditionally, the CO₂ laser has been used in this region. The CO₂ laser carries the advantage of large energies and high efficiency. The disadvantage is that the CO₂ laser emits only discrete lines over a limited spectral range and is, therefore, not able to meet lidar needs. The OPO, although a much weaker source, is able to cover the entire 8–12 μm range continuously. A number of different OPO schemes are able to generate tunable radiation in this range. Some of these schemes involve two-stage OPOs while others attempt parametric generation in a single step. So far no one scheme has emerged as the clear winner for lidar applications.

For lidar applications in both the visible and IR, the following factors enter into consideration:

1. Spectral coverage
2. Energy per pulse
3. Peak power
4. Pulse repetition frequency (PRF)
5. Spectral bandwidth
6. Output beam quality (M^2)
7. Beam stability during tuning
8. Pump laser maturity
9. Ease of system operation

In designing an OPO, a number of practical issue must be considered. These are outlined below.

A. Pump Laser Issues

The availability of a suitable pump laser is one of the most important considerations in designing an OPO. Currently, the Nd:YAG laser is the most mature commercially available laser. Typically it provides Q-switched, nanosecond pulse-width output at 1064 nm. The Nd:YAG output, along with its harmonics at 532 nm, 355 nm and 266 nm, have been very popular pump sources for OPOs from the UV to the IR. A summary of some examples of the use of the Nd:YAG laser and its harmonics being used as a pump for OPO generation are:

- 266 nm pumping BBO, LBO, →0.32 μm to 1.6 μm
- 355 nm pumping BBO, LBO → 0.4 μm to 2.5 μm
- 532 nm pumping KTP, KTA, BBO → 0.68 μm to 2.5 μm
- 1.064 μm pumping KTP, KTA, PPLN, AgGaS₂ → 1.5 μm to 10 μm

1.064 μm pumping tandem OPOs (e.g., KTA + AgGaSe₂) \rightarrow 1.5 μm to $> 14 \mu\text{m}$

The 2- μm Ho laser, pumped by a diode array-pumped thulium laser, has emerged as a promising pump for MIR [139] and LWIR [140,141] OPOs. The 2.8- μm Er:Cr:YSGG laser has also been used as a pump for OPOs in the same range [142]. Many other lasers, ranging in pulse widths from femtoseconds to continuous wave as described in Section V, have also been successfully used to pump OPOs.

B. Crystal Issues

The first requirement for an OPO crystal is, of course, phase-matching, which may be normally type I or II. Type II, generally speaking, gives higher dispersion and thereby leads to narrower linewidths for the OPO output. Type I provides greater tunability, but leads to wider linewidths, specially near the degeneracy point.

Another consideration is beam walk-off among the waves of differing polarizations inside the crystal. This problem is less severe when the beam diameters are large, but can limit the interaction length for smaller diameter beams. The problem of beam walk-off is alleviated when the propagation is along, or perpendicular to, a crystal axis [the so-called noncritical phase matching (NCPM)] at the expense of output wavelength choices. The introduction of QPM materials (e.g., PPLN) has helped alleviate the walk-off problem since phase-matched propagation may be along a crystal axis.

Absorption at any of the three waves can reduce the effective OPO again. In terms of sensitivity, absorption at the resonated wave is most serious followed by that at the pump.

Crystal damage long prevented OPOs from gaining acceptance as a viable source of tunable radiation. The development of damage-resistant KTP and BBO crystals and isomorphs changed the situation. For MIR and LWIR, the development of ZGP crystals has been very important. New developments of QPM materials also alleviates this problem because the larger nonlinear coefficients utilized lower the pump threshold.

C. Resonator Issues

Which wavelength to resonate in an OPO is an important question. In principle, either of the two wavelengths produced in the parametric process may be resonated while the other is generated to balance the energy and momentum with pump. Traditionally, because of the easier availability of optical coatings, it is the shorter wavelength that is resonated regardless of which wavelength is of interest.

Such a choice, however, is not always wise [141], especially when the longer wavelength is the one desired. This is especially true when the beam quality is important (e.g., for remote sensing). One reason is that the resonator Fresnel number, $w^2/L\lambda$ (where w is the beam radius, L the resonator length, and λ the resonated wavelength), becomes smaller when the longer wavelength is resonated. A second reason is that a small divergence of the shorter wavelength leads to a large divergence of the longer wavelength (shorter wave-vector) even for a diffraction-limited pump, as shown in Fig. 76. Third, when the pump phase front is not diffraction-limited, its imperfections are carried by the nonresonated beam.

Optical coatings. The presence of three wavelengths in the resonator simultaneously requires rather demanding trichroic optical coatings. First of all, the crystal must be coated with trichroic anti-reflection (AR) coatings. For a simple two-mirror SRO cavity, one desires the input mirror to be highly transmissive (HT) for the pump and highly reflective (HR) for the signal and the idler. The outcoupler is typically HR for the pump, a partial reflector for the signal and should be HT for the idler. Such coatings are often difficult to make, especially when OPO tuning is to be done over a large range. Sometimes one may get around the problem by taking advantage of the polarization differences among the waves. A judicious use of a polarizer in the resonator and/or an L-shaped resonator cavity can reduce demands on the coatings.

Tuning issues. In most OPO cavities, the output beam(s) position translates as the crystal is rotated for turning the output wavelength. This can be a major problem in remote sensing applications. Further, when the phase matching is not exactly collinear, as is the case with most double pump pass cavities, the nonresonated beam would steer as well as translate. Figure 77 shows a design that alleviates the output beam movement [141]. In this design, the output is taken from the rear of the resonator, whereas the beam translation occurs only at the silver (front) mirror.

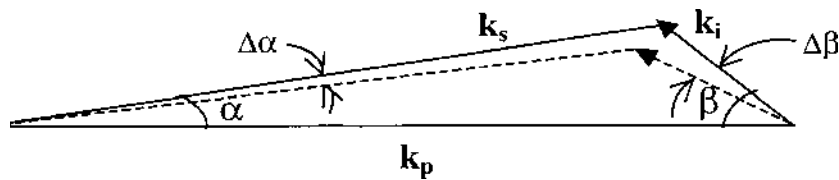


Figure 76 The phase matching condition means that any angular spread in the longer wave vector will cause a much bigger angular spread in the shorter wave vector (longer wavelength).

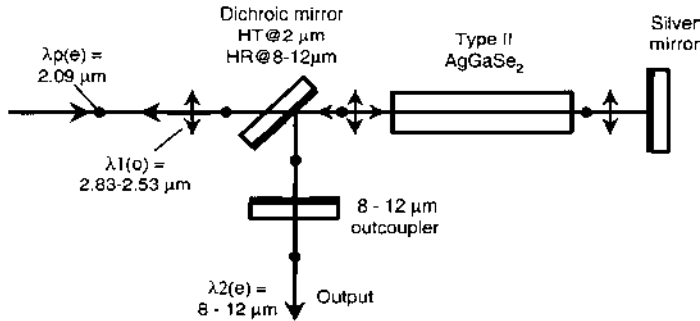


Figure 77 The Ho-laser pumped 100-Hz OPO achieved more than 40% quantum slope conversion efficiency, M^2 of 2.3, and a stationary beam during scanning.

D. Energy Conversion Efficiency Issues

Apart from the quantum conversion efficiency (i.e., fraction of pump photons converted), one also must contend with the quantum defect, which becomes especially severe, for example, in converting the 1.064 μm wavelength to 8–12 μm LWIR. For every LWIR photon generated, nine-tenths of the pump photon energy goes into the photon that is wasted. Schemes have been proposed to convert the energy of the would-be wasted photons into desired photons. The so-called “greater-than-100%” quantum conversion efficiency was demonstrated experimentally in PPLN generating MIR photons.

A 2-for-1 scheme. This scheme utilizes the more energetic photon in the OPO process as a pump for OPA/DFG to derive a second photon of the desired wavelength. This may be done either interactively or external to the resonator cavity. The intracavity DFG was used in the PPLN experiment mentioned above.

A 9-for-1 photon concept [143]. This concept, (shown Fig. 78) was presented by Allik et al. The KTA OPO generates photons at wavelengths of

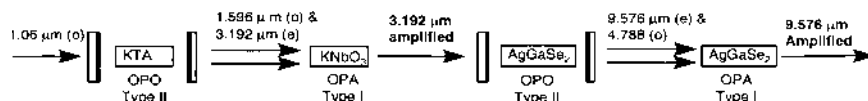


Figure 78 The first OPO and OPA combination seeks to generate three photons at 3.192 μm starting from one initial 1.064 μm photon. The subsequent OPO and OPA containing AgGaSe₂ strive to generate three-for-one photons at 9.576 μm .

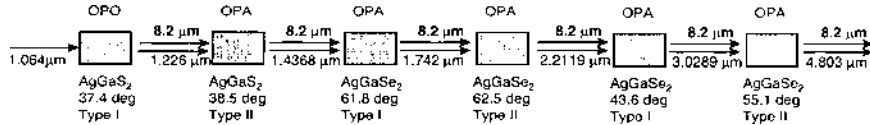


Figure 79 An example of how an idler of desired wavelength may be amplified by successive stage OPAs using signal wavelengths from a previous stage.

1.5 × and 3 × the pump wavelength. The type I OPA then seeks to add two more photons at the longer wavelength for each shorter wavelength photon destroyed.

Cascaded OPO/OPA concept [144]. The idea here is to effect amplification of the LWIR photons using the otherwise wasted photons produced in each previous stage (see Fig. 79).

REFERENCES

1. J. A. Giordmaine and R. C. Miller, Tunable coherent parametric oscillation in LiNbO₃ at optical frequencies, *Phys. Rev. Lett.* 14:973 (1965).
2. F. Zernike and J. E. Midwinter, *Applied Nonlinear Optics*, John Wiley, New York, 1973, pp. 170–171.
3. S. G. Anderson, Commercial OPO produces high energy tunable output, *Lazer Focus World* 16: April 1993.
4. M. Shimazu, Spectra-Physics unveils femtosecond OPO, *Photonics Spectra* 26: June 1993.
5. M. Shimazu, The optical parametric oscillator challenge, *Photonics Spectra* 51: May 1993.
6. W. H. Louisell, A. Yariv, and A. E. Siegman, Quantum fluctuations and noise in parametric processes, *Phys. Rev.* 124:1646 (1961).
7. Y. R. Shen, *Principles of Nonlinear Optics*, John Wiley, New York, 1984.
8. A. Yariv, *Quantum Electronics*, John Wiley, New York, 1989.
9. S. E. Harris, Tunable optical parametric oscillators, *Proc. IEEE* 57:2096 (1969).
10. R. L. Byer and S. E. Harris, Power and bandwidth of spontaneous parametric emission, *Phys. Rev.* 168:1064 (1968).
11. G. D. Boyd and D. A. Kleinman, Parametric interactions of focused gaussian light beams, *J. Appl. Phys.* 39:3597 (1968).
12. G. D. Boyd and A. Ashkin, Theory of parametric oscillator threshold with single-mode optical lasers and observation of amplification in LiNbO₃, *Phys. Rev.* 146:187 (1966).

13. J. E. Bjorkholm, A. Ashkin, and R. G. Smith, Improvement of optical parametric oscillators by nonresonant pump reflection, *IEEE J. Quant. Electron.* QE-6:797 (1970).
14. S. E. Harris, Threshold of multimode parametric oscillators, *IEEE J. Quant. Electron.* QE-2:701 (1966).
15. H. Hsu, Parametric interactions involving multiple elementary scattering processes, *J. Appl. Phys.* 38:1787 (1967).
16. A. E. Siegman, Nonlinear optical effects: an optical power limiter, *Appl. Opt.* 1:739 (1962).
17. J. E. Bjorkholm, Some effects of spatially nonuniform pumping in pulsed optical parametric oscillators, *IEEE J. Quant. Electron.* QE-7:109 (1971).
18. See references [9] and [43].
19. M. J. McCarthy and D. C. Hanna, Continuous-wave mode-locked singly resonant optical parametric oscillator synchronously pumped by a laser-diode-pumped Nd: YLF laser, *Opt. Lett.* 17:402 (1992).
20. H. He, Q. Zhao, J. Guo, Y. Lu, Y. Liu, and J. Wang, Picosecond optical parametric generation in flux grown KTP, *Opt. Comm.* 87:33 (1992).
21. W. R. Bosenberg, L. K. Cheng, and C. L. Tang, Ultraviolet optical parametric oscillation in β -BaB₂O₄, *Appl. Phys. Lett.* 54:13 (1989).
22. M. Ebrahimzadeh, A. J. Henderson, and M. H. Dunn, An excimer-pumped β -BaB₂O₄ optical parametric oscillator tunable from 354 nm to 2.370 μm , *IEEE J. Quant. Electron.* QE-26:1241 (1990).
23. Y. X. Fan, R. C. Eckardt, R. L. Byer, J. Nolting, and R. Wallenstein, Visible BaB₂O₄ optical parametric oscillator pumped at 355 nm by a single-axial-mode pulsed source, *Appl. Phys. Lett.* 53:2014 (1988).
24. J. Y. Zhang, J. Y. Huang, Y. R. Shen, and C. Chen, Optical parametric generation and amplification in barium borate and lithium triborate crystals, *J. Opt. Soc. Am. B* 10:1758 (1993).
25. Y. X. Fan, R. C. Eckardt, R. L. Byer, C. Chen, and A. D. Jiang, Barium borate optical parametric oscillator, *IEEE J. Quant. Electron.* QE-25:1196 (1989).
26. G. Robertson, A. Henderson, and M. H. Dunn, Broadly tunable LiB₃O₅ optical parametric oscillator, *Appl. Phys. Lett.* 60:271 (1992).
27. H.-J. Krause and W. Daum, Efficient parametric generation of high-power coherent picosecond pulses in lithium borate tunable from 0.405 to 2.4 μm , *Appl. Phys. Lett.* 60:2180 (1992).
28. V. Kubicek, Y. Takagi, K. Yoshihara, and G. C. Reali, Lithium triborate picosecond optical parametric oscillator, *Opt. Comm.* 91:93 (1992).
29. Y. Cui, D. E. Withers, C. F. Rae, C. J. Norrie, Y. Tang, B. D. Sinclair, W. Sibbel, and M. H. Dunn, Widely tunable all-solid-state optical parametric oscillator for the visible and near infrared, *Opt. Lett.* 18:122 (1992).
30. M. Ebrahimzadeh, M. H. Dunn, and F. Akerboom, Highly efficient visible urea optical parametric oscillator pumped by a XeCl excimer laser, *Opt. Lett.* 14:560 (1989).

31. D. Josse, S. X. Dou, J. Zyss, P. Andreazza, and A. Périgaud, Near-infrared optical parametric oscillation in a *N*-(4-nitrophenyl)-*L*-prolinol molecular crystal, *Appl. Phys. Lett.* 61:121 (1992).
32. K. L. Vodopyanov, Parametric generation of tunable infrared radiation in ZnGeP₂ and GaSe pumped at 3 μm, *J. Opt. Soc. Am. B* 10:1723 (1993).
33. W. J. Kozlovsky, E. K. Gustafson, R. C. Eckardt, and R. L. Byer, Efficient monolithic MgO:LiNbO₃ singly resonant optical parametric oscillator, *Opt. Lett.* 13:1102 (1988).
34. D. C. Gerstenberger and R. W. Wallace, Continuous-wave operation of a doubly resonant lithium niobate optical parametric oscillator system tunable from 966–1185 nm, *J. Opt. Soc. Am. B* 10:1681 (1993).
35. F. Hansom and D. Dick, Blue parametric generation from temperature-tuned LiNbO₃, *Opt. Lett.* 16:205 (1991).
36. Y. Cui, M. H. Dunn, C. J. Norrie, W. Sibbet, B. D. Sinclair, Y. Tang, and J. A. C. Terry, All-solid-state optical parametric oscillator for the visible, *Opt. Lett.* 17:646 (1992).
37. F. Huang, and L. Huang, Picosecond optical parametric generation and amplification in LiB₃O₅ and β-BaB₂O₄, *Appl. Phys. Lett.* 61:1769 (1992).
38. M. Ebrahimzadeh, G. J. Hall, and A. I. Ferguson, Broadly tunable, all-solid-state, visible and infrared picosecond optical parametric oscillator, *Opt. Lett.* 18:278 (1993).
39. G. J. Hall and A. I. Ferguson, LiB₃O₅ optical parametric oscillator pumped by a Q-switched frequency-doubled all-solid-state laser, *Opt. Lett.* 18:1511 (1993).
40. M. J. McCarthy, S. D. Butterworth, and D. C. Hanna, High-power widely-tunable picosecond pulses from an all-solid-state synchronously-pumped optical parametric oscillator, *Opt. Comm.* 102:297 (1993).
41. H. Zhou, J. Zhang, T. Chen, C. Chen, and Y. R. Shen, Picosecond, narrow-band, widely tunable optical parametric oscillator using a temperature-tuned lithium borate crystal, *Appl. Phys. Lett.* 62:1457 (1993).
42. G. P. Banfi, R. Danielius, A. Piskarskas, P. Di Trapani, P. Foggi, and R. Righini, Femtosecond traveling-wave parametric generation with lithium triborate, *Opt. Lett.* 18:1633 (1993).
43. R. L. Byer, Parametric oscillators nad nonlinear materials, *Nonlinear Optics* (P. G. Harper and B. S. Wherrett, eds), Academic Press, New York, 1977.
44. J. E. Pearson, U. Ganiel, and A. Yariv, Rise time of pulsed parametric oscillators, *IEEE J. Quant. Electron.* QE-8:433 (1972).
45. S. J. Brosnan and R. L. Byer, Optical parametric oscillator threshold and linewidth studies, *IEEE J. Quant. Electron.* QE-15:415 (1979).
46. E. C. Cheung nad and J. M. Liu, Theory of a synchronously pumped optical parametric oscillator in steady-state operation, *J. Opt. Soc. Am. B* 7:1385 (1990).
47. V. G. Dmitriev, G. G. Gurzadyan, and D. N. Nikogosyan, *Handbook of Nonlinear Optical Crystals*, Springer-Verlag, New York, 1991.
48. S. T. Yang, R. C. Eckardt, and R. L. Byer, Continuous-wave singly resonant optical parametric oscillator pumped by a single-frequency resonantly doubled Nd:YAG laser, *Opt. Lett.* 18:971 (1993).

49. W. R. Bosenberg, W. S. Pelouch, and C. L. Tang, High-efficiency and narrow-linewidth operation of a two-crystal β -BaB₂O₄ optical parametric oscillator, *Appl. Phys. Lett.* 55:1952 (1989).
50. D. C. Hovde, J. H. Timmermans, G. Scoles, and K. K. Lehmann, High power injection seeded optical parametric oscillator, *Opt. Comm.* 86:294 (1991).
51. F. Huisken, A. Kulcke, D. Voelkel, C. Laush, and J. M. Lisy, New infrared injection-seeded optical parametric oscillator with high energy and narrow bandwidth output, *Appl. Phys. Lett.* 62:805 (1993).
52. W. R. Bosenberg and D. R. Guyer, Single-frequency optical parametric oscillator, *Appl. Phys. Lett.* 61:387 (1992).
53. D. C. Edelstein, E. S. Wachman, and C. L. Tang, Broadly tunable high repetition rate femtosecond optical parametric oscillator, *Appl. Phys. Lett.* 54:1728 (1989).
54. E. S. Wachman, D. C. Edelstein, and C. L. Tang, Continuous-wave mode-locked and dispersion-compensated femtosecond optical parametric oscillator, *Opt. Lett.* 15:136 (1990).
55. G. Mak, Q. Fu, and H. M. van Driel, Externally pumped high repetition rate femtosecond infrared optical parametric oscillator, *Appl. Phys. Lett.* 60:542 (1992).
56. M. Ebrahimzadeh, G. P. A. Malcolm, and A. I. Ferguson, Continuous-wave mode-locked optical parametric oscillator synchronously pumped by a diode-laser-pumped solid-state laser, *Opt. Lett.* 17:183 (1992).
57. M. Ebrahimzadeh, G. J. Hall, and A. I. Ferguson, Singly resonant, all-solid-state, mode-locked LiB₃O₅ optical parametric oscillator tunable from 652 nm to 2.65 μm , *Opt. Lett.* 17:652 (1992).
58. Q. Fu, G. Mak, and H. M. van Driel, High-power, 62-fs infrared optical parametric oscillator synchronously pumped by a 76-MHz Ti:sapphire laser, *Opt. Lett.* 17:1006 (1992).
59. W. S. E. Pelouch, P. E. Powers, and C. L. Tang, Ti:sapphire-pumped, high-repetition-rate femtosecond optical parametric oscillator, *Opt. Lett.* 17:1070 (1992).
60. S. D. Butterworth, M. J. McCarthy, and D. C. Hanna, Widely tunable synchronously pumped optical parametric oscillator, *Opt. Lett.* 18:1429 (1993).
61. F. Rotermund, V. Petrov, F. Noack, L. Isaenko, A. Yelisseyev, and S. Lobanov, Optical parametric generation of femtosecond pulses up to 9 μm with LiInS₂ pumped at 800 nm, *Appl. Phys. Lett.* 78:2623 (2001).
62. J. Piel, M. Beutter, and E. Riedle, 20–50-fs pulses tunable across the near infrared from a blue-pumped noncollinear parametric amplifier, *Opt. Lett.* 25:180 (2000).
63. F. Rotermund and V. Petrov, Mercury thiogallate mid-infrared femtosecond optical parametric generator pumped at 1.25 μm by a Cr:forsterite regenerative amplifier, *Opt. Lett.* 25:746 (2000).
64. F. Rotermund, V. Petrov, F. Noack, M. Wittmann, and G. Korn, Laser-diode-seeded operation of a femtosecond optical parametric amplifier with MgO:LiNbO₃ and generation of 5-cycle pulses near 3 μm , *J. Opt. Soc. Am. B* 16:1539 (1999).

65. N. P. Barnes, K. E. Murray, M. G. Jani, P. G. Schunemann, and T. M. Pollak, ZnGeP₂ parametric amplifier, *J. Opt. Soc. Am. B* 15:232 (1998).
66. V. Petrov, F. Rotermund, F. Noack, and P. Schunemann, Femtosecond parametric generation in ZnGeP₂, *Opt. Lett.* 24:414 (1999).
67. A. Shirakawa, I. Sakane, and T. Kobayashi, Pulse-front-matched optical parametric amplification for sub-10-fs pulse generation tunable in the visible and near infrared, *Opt. Lett.* 23:1292 (1998).
68. G. Cerullo, M. Nisoli, S. Stagira, and S. De Silvestri, Sub-8-fs pulses from an ultrabroadband optical parametric amplifier in the visible, *Opt. Lett.* 23:1283 (1998).
69. A. Shirakawa, and T. Kobayashi, Noncollinearly phase-matched femtosecond optical parametric amplification with a 2000 cm⁻¹ bandwidth, *Appl. Phys. Lett.* 72:147 (1998).
70. K. Kawase, J. Shikata, K. Imai, and H. Ito, Transform-limited, narrow-linewidth, terahertz-wave parametric generator, *Appl. Phys. Lett.* 78:2819 (2001).
71. K. Kawase, H. Minamide, K. Imai, J. Shikata, and H. Ito, Injection-seeded terahertz-wave parametric generator with wide tunability, *Appl. Phys. Lett.* 80:195 (2002).
72. G. M. Gibson, R. S. Conroy, A. J. Kemp, B. D. Sinclair, M. J. Padgett, and M. H. Dunn, Microchip laser-pumped continuous-wave doubly resonant optical parametric oscillator, *Opt. Lett.* 23:517 (1998).
73. A. Douillet and J.-J. Zondy, Low-threshold, self-frequency-stabilized AgGaS₂ continuous-wave subharmonic optical parametric oscillator, *Opt. Lett.* 23:1259 (1998).
74. T. J. Edwards, G. A. Turnbull, M. H. Dunn, M. Ebrahimzadeh, and F. G. Colville, High-power, continuous-wave, singly resonant, intracavity optical parametric oscillator, *Appl. Phys. Lett.* 72:1527 (1998).
75. M. Tsunekane, S. Kimura, M. Kimura, N. Taguchi, and H. Inaba, Continuous-wave, broadband tuning from 788 to 1640 nm by a doubly resonant, MgO:LiNbO₃ optical parametric oscillator, *Appl. Phys. Lett.* 72:3414 (1998).
76. R. F. Wu, P. B. Phua, K. S. Lai, Y. L. Lim, E. Lau, A. Chng, C. Bonnin, and D. Lupinski, Compact 21-W 2-μm intracavity optical parametric oscillator, *Opt. Lett.* 25:1460 (2000).
77. O. Pacaud, J. P. Fève, B. Boulanger, and B. Ménaert, Cylindrical KTiOPO₄ crystal for enhanced angular tunability of phase-matched optical parametric oscillators, *Opt. Lett.* 25:737 (2000).
78. R. S. Conroy, C. F. Rae, G. J. Friel, M. H. Dunn, B. D. Sinclair, and J. M. Ley, Compact low-threshold Q-switched intracavity optical parametric oscillator, *Opt. Lett.* 23:1348 (1998).
79. M. S. Webb, P. F. Moulton, J. J. Kasinski, R. L. Burnham, G. Loiacono, and R. Stolzenberger, High-average-power KTiOAsO₄ optical parametric oscillator, *Opt. Lett.* 23:1161 (1998).
80. K. Imai, K. Kawase, J. Shikata, H. Minamide, and H. Ito, Injection-seeded terahertz-wave parametric oscillator, *Appl. Phys. Lett.* 78:1026 (2001).

81. B. Scherrer, I. Ribet, A. Godard, E. Rosencher, and M. Lefebvre, Dual-cavity doubly resonant optical parametric oscillators: demonstration of pulsed single-mode operation, *J. Opt. Soc. Am. B* 17:1716 (2000).
82. S.-D. Huang, C.-W. Hsu, D.-W. Huang, and C. C. Yang, Retracing behaviors of the phase-matching angle in noncollinear phase-matched optical parametric oscillators, *J. Opt. Soc. Am. B* 15:1375 (1998).
83. K. L. Vodopyanov, F. Ganikhanov, J. P. Maffetone, I. Zwieback, and W. Ruderman, ZnGeP₂ optical parametric oscillator with 3.8–12.4-μm tunability, *Opt. Lett.* 25:841 (2000).
84. F. Ganikhanov, T. Caughey, and K. L. Vodopyanov, Narrow-linewidth middle-infrared ZnGeP₂ optical parametric oscillator, *J. Opt. Soc. Am. B* 18:818 (2001).
85. P. A. Budni, L. A. Pomeranz, M. L. Lemons, C. A. Miller, J. R. Mosto, and E. P. Chicklis, Efficient mix-infrared laser using 1.9-μm-pumped Ho:YAG and ZnGeP₂ optical parametric oscillators, *J. Opt. Soc. Am. B* 17:723 (2000).
86. K. L. Vodopyanov, J. P. Maffetone, I. Zwieback, and W. Ruderman, AgGaS₂ optical parametric oscillator continuously tunable from 3.9 to 11.3 μm, *Appl. Phys. Lett.* 75:1204 (1999).
87. S. Khodja, D. Josse, and J. Zyss, Near-infrared optical parametric oscillation in an organomineral crystal, *J. Opt. Soc. Am. B* 15:751 (1998).
88. T. W. Tukker, C. Otto, and J. Greve, Design, optimization, and characterization of a narrow-bandwidth optical parametric oscillator, *J. Opt. Soc. Am. B* 16:90 (1999).
89. E. O. Potma, W. P. de Boeij, M. S. Pshenichnikov, and D. A. Wiersma, 30-fs, cavity-dumped optical parametric oscillator, *Opt. Lett.* 23:1763 (1998).
90. J. Hebling, X. P. Zhang, H. Giessen, J. Kuhl, and J. Seres, Pulse characteristics of an optical parametric oscillator pumped by sub-30-fs light pulses, *Opt. Lett.* 25:1055 (2000).
91. K. J. McEwan, High-power synchronously pumped AgGaS₂ optical parametric oscillator, *Opt. Lett.* 23:667 (1998).
92. G. Hansson and D. D. Smith, Optical parametric generation in 2-μm-wavelength-pumped periodically poled LiNbO₃, *Opt. Lett.* 25:1783 (2000).
93. K. W. Aniolek, R. L. Schmitt, T. J. Kulp, B. A. Richman, S. E. Bisson, and P. E. Powers, Microlaser-pumped periodically poled lithium niobate optical parametric generator-optical parametric amplifier, *Opt. Lett.* 25:557 (2000).
94. U. Bäder, J.-P. Meyn, J. Bartschke, T. Weber, A. Borsutzky, R. Wallenstein, R. G. Batchko, M. M. Fejer, and R. L. Byer, Nanosecond periodically poled lithium niobate optical parametric generator pumped at 532 nm by a single-frequency passively Q-switched Nd:YAG laser, *Opt. Lett.* 24:1608 (1999).
95. A. Galvanauskas, A. Hariharan, D. Harter, M. A. Arbore, and M. M. Fejer, High-energy femtosecond pulse amplification in a quasi-phase-matched parametric amplifier, *Opt. Lett.* 23:210 (1998).
96. P. E. Britton, J. G. R. Broderick, D. J. Richardson, P. G. R. Smith, G. W. Ross, and D. C. Hanna, Wavelength-tunable high-power picosecond pulses from a fiber-pumped diode-seeded high-gain parametric amplifier, *Opt. Lett.* 23:1588 (1998).

97. P. E. Powers, K. W. Anolek, T. J. Kulp, B. A. Richman, and S. E. Bisson, Periodically poled lithium niobate optical parametric amplifier seeded with the narrow-band filtered output of an optical parametric generator, *Opt. Lett.* 23:1886 (1998).
98. J. Hellström, G. Karlsson, V. Pasiskevicius, and F. Laurell, Optical parametric amplification in periodically poled KTiOPO₄ seeded by an Er-Yb:glass microchip laser, *Opt. Lett.* 26:352 (2001).
99. F. Rotermund, V. Petrov, F. Noack, V. Pasiskevicius, J. Hellström, and F. Laurell, Efficient femtosecond traveling-wave optical parametric amplification in periodically poled KTiOPO₄, *Opt. Lett.* 24:1874 (1999).
100. I. D. Lindsay, C. Petridis, M. H. Dunn, and M. Ebrahimzadeh, Continuous-wave pump-enhanced singly resonant optical parametric oscillator pumped by an extended-cavity diode laser, *Appl. Phys. Lett.* 78:871 (2001).
101. M. E. Klein, C. K. Laue, D.-H. Lee, K.-J. Boller, and R. Wallenstein, Diode-pumped singly resonant continuous-wave optical parametric oscillator with wide continuous tuning of the near-infrared idler wave, *Opt. Lett.* 25:490 (2000).
102. D. Chen, D. Hinkley, J. Pyo, J. Swenson, and R. Fields, Single-frequency low-threshold continuous-wave 3-μm periodically poled lithium niobate optical parametric oscillator, *J. Opt. Soc. Am. B* 15:1693 (1998).
103. M. E. Klein, D.-H. Lee, J.-P. Meyn, K.-J. Boller, and R. Wallenstein, Singly resonant continuous-wave optical parametric oscillator pumped by a diode laser, *Opt. Lett.* 24:1142 (1999).
104. R. G. Batchko, D. R. Weise, T. Plettner, G. D. Miller, M. M. Fejer, and R. L. Byer, Continuous-wave 532-nm-pumped singly resonant optical parametric oscillator based on periodically poled lithium niobate, *Opt. Lett.* 23:168 (1998).
105. P. E. Powers, T. J. Kulp, and S. E. Bisson, Continuous tuning of a continuous-wave periodically poled lithium niobate optical parametric oscillator by use of a fan-out grating design, *Opt. Lett.* 23:159 (1998).
106. D. J. M. Stothard, M. Ebrahimzadeh, and M. H. Dunn, Low-pump-threshold continuous-wave singly resonant optical parametric oscillator, *Opt. Lett.* 23:1895 (1998).
107. I. D. Lindsay, G. A. Turnbull, M. H. Dunn, and M. Ebrahimzadeh, Doubly resonant continuous-wave optical parametric oscillator pumped by a single-mode diode laser, *Opt. Lett.* 23:1889 (1998).
108. U. Strössner, A. Peters, J. Mlynek, S. Schiller, J.-P. Meyn, and R. Wallenstein, Single-frequency continuous-wave radiation from 0.77 to 1.73 μm generated by a green-pumped optical parametric oscillator with periodically poled LiTaO₃, *Opt. Lett.* 24:1602 (1999).
109. M. E. Klein, D.-H. Lee, J.-P. Meyn, B. Beier, K.-J. Boller, and R. Wallenstein, Diode-pumped continuous-wave widely tunable optical parametric oscillator based on periodically poled lithium tantalate, *Opt. Lett.* 23:831 (1998).
110. A. Garashi, A. Arie, A. Skliar, and G. Rosenman, Continuous-wave optical parametric oscillator based on periodically poled KTiOPO₄, *Opt. Lett.* 23:1739 (1998).

111. G. M. Gibson, M. Ebrahimzadeh, J. J. Padgett, and M. H. Dunn, Continuous-wave optical parametric oscillator based on periodically poled KTiOPO₄ and its application to spectroscopy, *Opt. Lett.* 24:397 (1999).
112. T. J. Edwards, G. A. Turnbull, M. H. Dunn, M. Ebrahimzadeh, H. Karlsson, G. Arvidsson, and F. Laurell, Continuous-wave singly resonant optical parametric oscillator based on periodically poled RbTiOAsO₄, *Opt. Lett.* 23:837 (1998).
113. S. T. Yang, and S. P. Velsko, Frequency-agile kilohertz repetition-rate optical parametric oscillator based on periodically poled lithium niobate, *Opt. Lett.* 24:133 (1999).
114. K. Kawase, T. Hatanaka, H. Takahashi, K. Nakamura, T. Taniuchi, and H. Ito, Tunable terahertz-wave generation from DAST crystal by dual signal-wave parametric oscillation of periodically poled lithium niobate, *Opt. Lett.* 25:1714 (2000).
115. C.-S. Yu and A. H. Kung, Grazing-incidence periodically poled LiNbO₃ optical parametric oscillator, *J. Opt. Soc. Am. B* 16:2233 (1999).
116. T. Hatanaka, K. Nakamura, T. Taniuchi, H. Ito, Y. Furukawa, and K. Kitamura, Quasi-phase-matched optical parametric oscillation with periodically poled stoichiometric LiTaO₃, *Opt. Lett.* 25:651 (2000).
117. M. J. Missey, V. Dominic, P. E. Powers, and K. L. Schepler, Periodically poled lithium niobate monolithic nanosecond optical parametric oscillators and generators, *Opt. Lett.* 24:1227 (1999).
118. R. S. Conroy, C. F. Rae, M. H. Dunn, B. D. Sinclair, and J. M. Ley, Compact, actively Q-switched optical parametric oscillator, *Opt. Lett.* 24:1614 (1999).
119. P. E. Britton, D. Taverner, K. Puech, D. J. Richardson, P. G. R. Smith, G. W. Ross, and D. C. Hanna, Optical parametric oscillation in periodically poled lithium niobate driven by a diode-pumped Q-switched erbium fiber laser, *Opt. Lett.* 23:582 (1998).
120. P. E. Britton, H. L. Offerhaus, D. J. Richardson, P. G. R. Smith, G. W. Ross, and D. C. Hanna, Parametric oscillator directly pumped by a 1.55-μm erbium-fiber laser, *Opt. Lett.* 24:975 (1999).
121. J.-P. Fève, O. Pacaud, B. Boulanger, B. Ménaert, J. Hellström, V. Pasiskevicius, and F. Laurell, Widely and continuously tunable optical parametric oscillator based on a cylindrical periodically poled KTiOPO₄, *Opt. Lett.* 26:1882 (2001).
122. V. Pasiskevicius, H. Karlsson, F. Laurell, R. Butkus, V. Smilgevičius, and A. Piskarskas, High-efficiency parametric oscillation and spectral control in the red spectral region with periodically poled KTiOPO₄, *Opt. Lett.* 26:710 (2001).
123. J. Hellström, V. Pasiskevicius, H. Karlsson, and F. Laurell, High-power optical parametric oscillation in large-aperture periodically poled KTiOPO₄, *Opt. Lett.* 25:174 (2000).
124. V. Pasiskevicius, H. Karlsson, J. A. Tellefsen, F. Laurell, R. Butkus, A. Piskarskas, V. Smilgevičius, and A. Stabinis, Singly resonant optical parametric oscillator in periodically poled KTiOPO₄ pumped by a Bessel beam, *Opt. Lett.* 25:969 (2000).

125. J. Hellström, V. Pasiskevicius, F. Laurell, and H. Karlsson, Efficient nanosecond optical parametric oscillators based on periodically poled KTP emitting in the 1.8–2.5- μm spectral region, *Opt. Lett.* 24:1233 (1999).
126. H. Karlsson, M. Olson, G. Arvidsson, F. Laurell, U. Bäder, A. Borsutzky, R. Wallenstein, S. Wickström, and M. Gustafsson, Nanosecond optical parametric oscillator based on large-aperture periodically poled RbTiOAsO_4 , *Opt. Lett.* 24:330 (1999).
127. G. T. Kennedy, D. T. Reid, A. Miller, M. Ebrahimzadeh, H. Karlsson, G. Arvidsson, and F. Laurell, Near- to mid-infrared picosecond optical parametric oscillator based on periodically poled RbTiOAsO_4 , *Opt. Lett.* 23:503 (1998).
128. X. Meng, J.-C. Diels, D. Kuehlke, R. Batchko, and R. Byer, Bidirectional, synchronously pumped, ring optical parametric oscillator, *Opt. Lett.* 26:265 (2001).
129. A. Robertson, M. E. Klein, M. A. Tremont, K.-J. Boller, and R. Wallenstein, 2.5-GHz repetition-rate singly resonant optical parametric oscillator synchronously pumped by a mode-locked diode oscillator amplifier system, *Opt. Lett.* 25:657 (2000).
130. T. Beddard, M. Ebrahimzadeh, T. D. Reid, and W. Sibbett, Five-optical-cycle pulse generation in the mid infrared from an optical parametric oscillator based on aperiodically poled lithium niobate, *Opt. Lett.* 25:1052 (2000).
131. G. McGowan, D. T. Reid, Z. E. Penman, M. Ebrahimzadeh, and W. Sibbett, Femtosecond optical parametric oscillator based on periodically poled lithium niobate, *J. Opt. Soc. Am. B* 15:694 (1998).
132. P. Loza-Alvarez, C. T. A. Brown, D. T. Reid, W. Sibbett, and M. Missey, High-repetition-rate ultrashort-pulse optical parametric oscillator continuously tunable from 2.8 to 6.8 μm , *Opt. Lett.* 24:1523 (1999).
133. L. Lefort, K. Puech, S. D. Butterworth, Y. P. Svirko, and D. C. Hanna, Generation of femtosecond pulses from order-of-magnitude pulse compression in a synchronously pumped optical parametric oscillator based on periodically poled lithium niobate, *Opt. Lett.* 24:28 (1999).
134. M. E. Dearborn, K. Koch, G. T. Moore, and J. C. Diels, Greater than 100% photon-conversion efficiency from an optical parametric oscillator with intracavity difference-frequency mixing, *Opt. Lett.* 23:759 (1998).
135. L. Lefort, K. Puech, G. W. Ross, Y. P. Svirko, and D. C. Hanna, Optical parametric oscillation out to 6.3 μm in periodically poled lithium niobate under strong idler absorption, *Appl. Phys. Lett.* 73:1610 (1998).
136. P. J. Phillips, S. Das, and M. Ebrahimzadeh, High-repetition-rate, all-solid-state, Ti:sapphire-pumped optical parametric oscillator for the mid-infrared, *Appl. Phys. Lett.* 77:469 (2000).
137. T. Südmeyer, J. Aus der Au, R. Paschotta, U. Keller, P. G. R. Smith, G. W. Ross, and D. C. Hanna, Femtosecond fiber-feedback optical parametric oscillator, *Opt. Lett.* 26:304 (2001).
138. T. Kartaloğlu, K. G. Köprülü, O. Aytür, M. Sundheimer, and W. P. Risk, Femtosecond optical parametric oscillator based on periodically poled KTiOPO_4 , *Opt. Lett.* 23:61 (1998).

139. P. A. Budni, L. A. Pomerang, M. L. Lemons, P. G. Schuneman, T. M. Pollack, J. R. Mosto, and E. P. Chicklis, Mid-IR laser based on ZnGeP₂ and nonsensitized Ho:YAG, *Trends Opt. Photon.* 26:454 (1999).
140. G. J. Quarles, C. L. Marquardt, and L. Esterowitz, 2-μm pumped AgGaSe₂ with continuous tuning 2.49–12.05 μm, *Proc. LEOS '90*:paper ELT7.1, Boston, MA (1990).
141. S. Chandra, M. E. Wager, T. H. Allik, and W. W. Hovis, 8–12 micron OPO pumped by a 2.09-micron holmium laser, *Trends Opt. Photon.* 39:496 (2000).
142. T. H. Allik, S. Chandra, D. M. Rines, P. G. Schunemann, J. A. Hutchinson, and R. Utano, Tunable 7–12 μm optical parametric oscillator using a Cr, Er:YSGG laser to pump CdSe and ZnGeP₂ crystals, *Opt. Lett.* 22:597 (1997).
143. T. H. Allik, S. Chandra, W. Horis, C. G. Simi, and J. A. Hutchinson, Advances in optical parametric oscillators with application to remote chemical sensing, *Proc. SPIE* 3383:58 (1998).

4

Characterization of Second Order Nonlinear Optical Materials

The previous two chapters have shown the importance of the nonlinear coefficient d_{eff} (or d_{ij}) for determining frequency conversion efficiencies as well as gain and thresholds for optical parametric devices. Another key optical parameter is the index of refraction, since the nonlinear optical figure of merit is actually d^2/n^3 , but more importantly the refractive index plays the pivotal role in determining phase matching for efficient frequency conversion.

The focus of this chapter is measurement techniques for characterizing the second order nonlinear coefficients of materials, although a brief discussion of index of refraction will be given. However, it should be noted that these are not the only parameters of a material that should be optimized for devices. Besides having a large nonlinear coefficient and appropriate refractive index (or birefringence) for phase matching, a good material should have very low absorption, good optical quality (i.e., highly uniform index of refraction), hardness and ability to take a high polish, good thermal conductivity to avoid thermal inhomogeneities that destroy phase matching and hurt beam quality, low two-photon absorption coefficient (see Chapter 9), and high laser damage threshold. There may be additional requirements as well, such as being processable for waveguides, etc. Although each of these topics is important for consideration in designing and fabricating devices, they are beyond the scope of this chapter.

The nonlinear coefficient, which again is two times the second order nonlinear susceptibility, will be referred to in this chapter as the effective value d_{eff} (defined in Chapter 2), as the tensor components d_{ij} , i.e., the reduced subscript

form (introduced in Chapter 1), which can be expressed in matrix form, or as just a scalar d . For small dispersion (i.e., Kleinman symmetry), d can be measured at a single wavelength, and the usual method is second harmonic generation. Both absolute methods for measuring d as well as relative techniques have been developed over the last several years, although the more common methods now are relative measurements. By this it is meant that two materials are measured, one the sample being characterized, and the other a well characterized and accepted (in the literature) standard material. The values of the d -coefficients are then determined in terms of the known value(s) of the standard material. Materials that are generally accepted as standard references today are $\text{NH}_4\text{H}_2\text{PO}_4$ (ammonium dihydrogen phosphate, ADP), KH_2PO_4 , (potassium dihydrogen phosphate, KDP), and SiO_2 , (quartz) for the visible and near infrared, and GaAs (gallium arsenide), Ag_3AsS_3 (proustite), and Ag_3SbS_3 (pyrargyrite) for the infrared. Both absolute and relative methods are discussed in this chapter.

It should be reiterated that accurately knowing the principal refractive indices $n_i(\lambda, T)$ ($i = X, Y, Z$), as well as the principal axes and optic axes of a material, is of paramount importance. This is so not only for the design of devices but is also crucial for some measurement techniques. Many optics textbooks, such as Born and Wolf [1], describe methods for accurately measuring these optical parameters. A brief summary of some of these methods is given here.

The optic axis(es) of a crystal can be found by viewing the material with a polarizing microscope and observing the resulting interference figure (isogyres and isochromates) [1]. The isogyres are in the form of dark crosses, while the isochromates form closed curves (bright and dark fringes) about the optic axis(es). The presence of one or two optic axes is readily apparent, signifying a uniaxial or biaxial crystal, respectively. The angle between the axes of a biaxial crystal can also be measured, taking into account the refracted light leaving the crystal. This can be analyzed and corrected for numerically once the principal refractive indices are known.

Several methods are available for determining the crystallographic axes of the crystal. These include X-ray diffraction and orientation, the shape of etch pits on the different faces of the crystal, and measurement of the piezoelectric effect [2]. These determinations are simpler once the optic axis(es) are known. The principal axes of the material are related to these crystallographic axes in a definite way for each point symmetry group (crystal class).

Born and Wolf [1] briefly discuss two methods for measuring the principal indices of refraction. One involves a measurement of the angle of deviation or total internal reflection in a prism cut from the material. This method is more convenient for uniaxial crystals but can be used for biaxial crystals as well. The other method involves immersing the crystal in a series of liquids with graded refractive indices. For two orthogonal polarizations of incident light, two different indices n' and n'' will make the crystal invisible. If the principal axes are

known, these measurements will yield the pairs (n_X, n_Y) , (n_X, n_Z) , and (n_Y, n_Z) . If the principal axes are not known, then a range of measurements on several crystals of the same material will yield lower bounds n'_1 , n''_1 and upper bounds n'_u , n''_u . If several such measurements are made, then it will generally be true that $n_X = n'_1$, $n_Y = n'_u = n''_1$, and $n_Z = n''_u$. For a uniaxial crystal, there will only be one lower and one upper bound which will correspond, respectively, to n^o and n^e for a positive uniaxial crystal, and to n^e and n^o for a negative uniaxial crystal. See Born and Wolf for more details.

With the n_i known as functions of wavelength and temperature, d_{eff} or d_{ij} can be measured by the techniques described in this chapter. Other parameters will often be required as well, such as the linear absorption coefficient and, of course, the sample length, which can be measured by standard techniques. Some parameters, such as the walk-off angle, can be measured or calculated from other measured parameters.

Two absolute measurement methods will be summarized:

- Phase matched method, and
- Parametric fluorescence method.

Relative methods for characterizing materials with respect to a standard, or for screening materials, will include:

- Maker fringe method, and
- Powder methods.

All of the above techniques are useful when the material is in the form of a single crystal. Often the material of interest exists only as a thin film. For these, the following techniques will be described:

- Thin film reflectance, and
- Poling (polymer films).

Finally, in the interest of developing new materials it is sometimes more convenient and appropriate to characterize the individual molecules of the material rather than the bulk material. This is especially true for organic materials since the bulk optical properties of organic crystals are largely determined by the individual molecular units. Relative methods for characterization of molecular parameters will include:

- Electric field induced second harmonic generation,
- Hyper-Rayleigh scattering, and
- Solvatochromatic measurements.

Appropriate to laboratory measurements, only SI units will be used for formulas in this chapter. Conversions to cgs units can be made by referring to Table 2 of Chapter 2.

I. BULK MATERIAL COEFFICIENTS

A. Phase Matched Method

The objective of this method is to obtain an absolute measurement of the d -coefficients by measuring the second harmonic power generated by radiating a crystal in a phase matched configuration and obtaining d_{eff} through inversion of the frequency conversion efficiency formula. The advantage of this method is that a convenient, readily measurable amount of second harmonic power is generated, because of phase matching, and that the absolute measurement, if done accurately, sets the material as a standard for other relative measurements. The disadvantage is that it requires a number of precise and difficult measurements. An excellent discussion of this method can be found in Kurtz [3].

Theory. Equations giving the conversion efficiency for SHG were presented in Chapter 2. It is convenient to establish conditions (i.e., the incident fundamental intensity) such that the nondepleted pump approximation is valid. This makes inversion of the conversion efficiency formula easier. In the phase matched method, d_{eff} is measured (see Tables 18 through 21 of Chapter 2), or a particular d_{ij} if phase matching allows. Two different regimes are considered: the weakly focused or thin crystal regime, and the tightly focused or thick crystal regime. Gaussian beams are assumed throughout the following.

In the weakly focused regime where diffraction and beam walk-off can be ignored, the plane wave approximation can be used. The advantage of this is that the equation is simpler. The disadvantage is that the second harmonic power generated is generally weaker. This can be significant because this method requires precise measurement of this power.

The conversion efficiency for this case was given in Chapter 2. However, in a real material that is not antireflection coated or immersed in an index matching fluid, which is not always feasible, Fresnel reflections at the crystal surfaces must be taken into account. The effective d -coefficient in terms of the actual measured fundamental and second harmonic powers is then given by

$$(d_{\text{eff}})^2 = \frac{\epsilon_0 c [(n_\omega + 1)^2 (n_{2\omega} + 1)]^2 \lambda_\omega^2 w_0^2 (\mathcal{P}_{2\omega})_{\text{out}}}{512\pi L^2 (\mathcal{P}_\omega)_{\text{in}}^2} \quad (1)$$

where w_0 is the $1/e^2$ beam radius at the waist of the incident fundamental beam. If there is absorption at the fundamental and second harmonic wavelengths, then Eq. (1) must be corrected for absorption by dividing by the following function:

$$H(\alpha_\omega, \alpha_{2\omega}) = \exp \left[- \left(\alpha_\omega + \frac{\alpha_{2\omega}}{2} \right) L \right] \frac{\sinh^2[(\alpha_\omega - \alpha_{2\omega}/2)L/2]}{[(\alpha_\omega - \alpha_{2\omega}/2)L/2]^2} \quad (2)$$

To Compute d_{eff} from Eq. (1), precise measurements of $(\mathcal{P}_\omega)_{\text{in}}$, $(\mathcal{P}_{2\omega})_{\text{out}}$, w_0 , n_ω ,

$n_{2\omega}$, and crystal thickness L are required. The refractive index measurements were discussed above. A discussion of beam waist measurements is given below.

Operation in the tightly focused regime has the advantage of increased fundamental intensity and higher second harmonic power. The disadvantage is that one must then be concerned with diffraction and double refraction. In the general case, the analysis of Boyd and Kleinman [4], discussed in Chapter 2, applies with corrections for reflection losses. Thus the second harmonic power measured in the far field under the conditions of tight focusing, and including absorption, is given by

$$\begin{aligned} (\mathcal{P}_{2\omega})_{\text{out}} = & \frac{1024\pi^2 n_\omega}{\epsilon_0 c [(n_\omega + 1)^2 (n_{2\omega} + 1)]^2 \lambda_\omega^3} (d_{\text{eff}})^2 (\mathcal{P}_\omega)_{\text{in}}^2 L \\ & \times \exp[-(\alpha_\omega + \alpha_{2\omega}/2)L] h(\sigma, \beta, \kappa, \xi, \mu) \end{aligned} \quad (3)$$

where $h(\sigma, \beta, \kappa, \xi, \mu)$, and all of the independent variables, were defined in Chapter 2. From an experimental point of view, Eq. (3) is not particularly easy to work with since the function $h(\sigma, \beta, \kappa, \xi, \mu)$, cannot be obtained in closed form. Also, in Boyd and Kleinman's work, they only plotted optimized forms of this function, which may not always apply under experimental conditions.

For these reasons, it is simpler to work in the weakly focused regime. However, it may not always be possible to avoid the effects of double refraction. In the weakly focused case, but including absorption and double refraction, Boyd et al. [5] have shown that, including Fresnel reflection losses,

$$(\mathcal{P}_{2\omega})_{\text{out}} = \frac{512\pi^2 (d_{\text{eff}})^2 L^2}{\epsilon_0 c [(n_\omega + 1)^2 (n_{2\omega} + 1)]^2 \lambda_\omega^2 w_0^2} e^{-\alpha_{2\omega} L} G(t, q) \quad (4)$$

The following definitions of the functions in Eq. (4) apply, given by Kurtz [3]:

$$G(t, q) = \exp\left[-\left(\alpha_\omega - \frac{\alpha_{2\omega}}{2}\right)L\right] g(t, q) \quad (5)$$

$$\begin{aligned} g(t, q) = & \frac{1}{2} \sqrt{\frac{\pi}{2}} \left[\frac{\exp(2q^2)}{t^2 q} \right] \left\{ \exp(2tq) \operatorname{erf}\left(\frac{t}{\sqrt{2}} + \sqrt{2}q\right) \right. \\ & \left. - \exp(-2tq) \operatorname{erf}\left[\frac{t}{\sqrt{2}} - \sqrt{2}q\right] - [\exp(2tq) + \exp(-2tq)] \operatorname{erf}(\sqrt{2}q) \right\} \end{aligned} \quad (6)$$

where

$$\operatorname{erf}(x) = \frac{2}{\sqrt{\pi}} \int_0^x e^{-y^2} dy \quad (7)$$

and t and q are normalized length and absorption parameters, respectively, defined by

$$t = \sqrt{2} \left(\frac{\rho L}{w_0} \right) \quad (8)$$

$$q = \left(\alpha_\omega - \frac{\alpha_{2\omega}}{2} \right) \frac{w_0}{2\sqrt{2}\rho} \quad (9)$$

and ρ is the walk-off angle. Kurtz [3] gives a plot of the function $G(t, q)$. For $t > 2(w_0 < 3\rho L)$, the effects of absorption become obvious for $q \geq 0.05$, and for $t \geq 0.5$ the effects of walk-off are significant. For the case of no absorption at either the fundamental or second harmonic (i.e., $q = 0$), then

$$G(t, 0) = \frac{\sin^2 \psi}{\psi^2} \quad (10)$$

$$\psi = \frac{\pi}{2} \frac{L}{L_c} \quad (11)$$

where L_c is the coherence length, and for small angular deviations about the phase matching angle θ_{pm} ,

$$\psi \approx (k_\omega L \sin \rho)(\theta - \theta_{pm}) \quad (12)$$

Experimental. It is important to verify the crystal orientation and polarizations of the beams, and see that the spherical angles θ, ϕ , are properly set for both the type of phase matching and the d_{eff} desired. As can be seen from Tables 19 and 21 of Chapter 2 (i.e., when Kleinman symmetry holds), various choices of angles of propagation and beam polarizations can yield different d_{eff} measurements and thereby obtain all of the nonzero d_{ij} .

One should verify that the experiment is in accord with the theory given above in the appropriate regimes of approximation. It is also important to check the quality of the crystal under measurement. This can be done by an angle (CPM) or temperature (NCPM) variation, and a determination that the second harmonic power is varying as $\sin^2 \psi / \psi^2$. This experimentally generated curve should be symmetric, for the weakly focused case, and the minima should lie precisely at values of $\psi_m = m\pi (m = 1, 2, 3, \dots)$.

A better quantitative measure of the overall curve's behavior can be obtained, however, in terms of the effective bandwidth [3]. This can be derived from the experimental curve as follows. Consider first the case of NCPM and temperature bandwidths. From the experimental curve, define

$$(\Delta T_{BW})_{exp} = \frac{\text{area under curve}}{\text{height of central peak}} \quad (13)$$

This is compared to the theoretical value

$$(\Delta T_{\text{BW}})_{\text{th}} = \frac{\lambda_{\omega}/2L}{(\partial n'_{2\omega}/\partial T)_{T_{\text{pm}}} - (\partial n''_{\omega}/\partial T)_{T_{\text{pm}}}} \quad (14)$$

where T_{pm} is the phase matching temperature, and the ' and '' refer to e (extraordinary) or o (ordinary). One should find that $(\Delta T_{\text{BW}})_{\text{exp}} \approx (\Delta T_{\text{BW}})_{\text{th}}$ to within a few percent. If this is not the case, it is a strong indication that the crystal is defective (i.e., has a spatially varying index of refraction) and must be replaced for a good characterization of the second order coefficients [5]. For CPM, an experimental angular bandwidth can be defined just as in Eq. (13) and should be compared to the theoretical value given by

$$(\Delta\theta_{\text{BW}})_{\text{th}} = \frac{\lambda_{\omega}/2L}{\sin p} \quad (15)$$

Again, one should see that $(\Delta\theta_{\text{BW}})_{\text{exp}} \approx (\Delta\theta_{\text{BW}})_{\text{th}}$ to within a few percent.

In the tight focusing regime, the phase matching curve is skewed and peaks in the region $\Delta k > 0$ (see Chapter 2, Section IV.C). One should consult the numerical analysis and plots of Ref. [4] for the correct behavior of the second harmonic power as temperature or angle are varied. Boyd and Kleinman [4] plot the function $(\xi/\pi^2)h(\sigma, 0, 0, \xi, 0)$ (i.e., no absorption, no double refraction, and focus in the center of the crystal) as a function of $\xi\sigma = \frac{1}{2}\Delta kL$ for $\xi = 0.50, 1.0, 2.838, 5.00$, and 50 ($\xi = L/b$ where b is the confocal parameter). It should be noted that the spot size w_0 measured in air is unchanged upon entering the nonlinear medium. However, the position of the beam waist is shifted in the $+z$ direction by an amount $f + (n_{\omega} - 1)(f - z')$, where f is the focal length of the focusing lens, and z' is the distance of the front face of the crystal from the lens. The confocal parameter b measured in air is increased to $n_{\omega}b$ in the crystal.

Once the experimenter is assured that the experiment is in accord with well-established theory and the crystal is of adequate quality, he must proceed with a precise characterization of the fundamental laser beam. This first calls for a measurement of the fundamental beam power. Large area precision power and energy meters that effectively integrate over the beam area are available for this task with accuracy better than 5%. One must assure that the beam underfills the detector and that the detector is unsaturated.

The next task is to measure the beam spot radius w_0 at focus. For tightly focused experiments, one should assure that the laser is operating in the lowest spatial order TEM₀₀ mode for accurate application of the above formulas. This is not so crucial for weakly focused experiments. However, a precise measurement of w_0 is still required. The generally preferred method for measuring the spot size w_0 is by scanning a knife edge (e.g., a razor blade) through the beam perpendicular to the beam axis. The measured transmitted power past the edge of

the knife is then fitted to an error function (i.e., the integral of a Gaussian) to determine w_0 . Generally, it is best to do this at several locations along the beam near focus to characterize the confocal parameter of the beam (i.e., twice the Rayleigh range, see Chapter 1), and to determine precisely where the waist is. The position of the waist for the weakly focused regime is not as crucial as in the tightly focused regime. However, it is important to determine that one is truly operating in the weakly focused regime to apply Eqs. (1) and (4).

Another important characteristic of the laser is its number m of longitudinal modes. This is perhaps one of the parameters that makes absolute measurements most difficult since for multimode pulsed lasers, the mode structure can vary from pulse to pulse. The second harmonic power generated will be enhanced by a factor of $[(2m - 1)/m]$ due to mode mixing when the crystal is pumped by a multimode laser [3]. Therefore a single longitudinal mode pump laser is desired. In earlier experiments this required the use of a cw laser, which resulted in very weak second harmonic signals. Now, however, narrow line width, single-mode seed-injection Q-switched lasers with high peak power are available that should be able to fill this role with much higher second harmonic conversion efficiency.

The final task is a measurement of the second harmonic power. First, the second harmonic output should be maximized by small temperature or angle adjustments. To assure that no fundamental is measured along with the second harmonic, these beams must be carefully separated by a combination of polarization and wavelength filtering. For measurements with a cw pump laser, a photomultiplier tube (PMT), for the visible and near-IR, calibrated at the second harmonic wavelength, is required. For the IR regime, a very sensitive bolometer is needed. With a seed-injected, Q-switched pump laser, other detection schemes may be possible. For example, consider a 1064 nm laser emitting 1 mJ pulses of 10 ns width. This corresponds to a peak power of approximately 100 kW. Assume that $2w_0 = 1$ cm, $d_{\text{eff}} = 1 \text{ pm/V}$, $L = 1$ cm, and $n_{2\omega} \approx n_\omega = 1.5$. The second harmonic peak power should then be of the order of 100 W, which would correspond to $\sim 500\text{--}1000$ nJ. This is measurable with precision silicon energy meters.

It is difficult to perform all of these measurements with high accuracy. However, with great care an accuracy of about 10% in d_{eff} should be possible. With a few materials now well characterized by this absolute method, it is more customary to perform relative measurements on new materials and compare them to these standard materials.

B. Parametric Fluorescence

This absolute measurement method was developed by Byer and Harris [6]. The objective is to measure the signal power generated in an optical parametric generation experiment and obtain d_{eff} through an inversion of the formulas given

in Table 2 of Chapter 3 for parametric fluorescence. This measurement technique has several advantages:

- Only the ratio of signal and pump powers need be measured, and not the absolute powers.
- The signal power generated is independent of the pump beam area.
- Only average power measurements are needed since the signal power is not affected by mode mixing and relative mode phases.
- There is no need to phase match to exact frequencies, so angle or temperature control is not as stringent.
- The effects of beam divergence and crystal imperfection are less important than in the phase matched method.

The disadvantages are that the signal power can be very weak, and a finite spectral distribution of signal power must be measured.

Theory. The equations for the signal power \mathcal{P}_s were given in Table 2 of Chapter 3. It is important to work in the small gain regime so that the signal power has a simple linear dependence on the solid angle of detection ($\pi\theta^2$). A measurement of the ratio $\mathcal{P}_s/\mathcal{P}_p$ (i.e., the ratio of signal to pump power), will yield the effective d -coefficient through

$$\frac{(d_{\text{eff}})^2}{|b|} = \frac{\epsilon_0 n_i n_p \lambda_i \lambda_s^4}{8\pi^2 h L} \frac{1}{\pi\theta^2} \frac{(\mathcal{P}_s)_{\text{out}} (n_s + 1)^2 (n_p + 1)^2}{(\mathcal{P}_p)_{\text{in}}} \frac{1}{16 n_s n_p} \quad (16)$$

where h is Planck's constant, and the last factor corrects for Fresnel reflection losses so that the ratio of powers is that of output signal power to input pump power. The parameter b is given by (see Chapter 3)

$$b = \frac{1}{c} \left[n_s - n_i + \omega_s \left(\frac{dn_s}{d\omega_s} \right)_{\omega_{s_0}} - \omega_i \left(\frac{dn_i}{d\omega_i} \right)_{\omega_{i_0}} \right] z \quad (17)$$

There are three potential ways to find b which can be cross-checked for accuracy [6]:

1. Calculate b from refractive index dispersion data (e.g., a Sellmeier equation).
2. Stop down the collection aperture in the experiment until the bandwidth $\Delta\omega_s$ of the signal becomes a constant independent of the collection angle θ . Then in terms of the measured bandwidth, $|b| = \pi/\Delta\omega_s L$.
3. Measure the bandwidth $\Delta\omega_s$ as a function of θ . The slope of the plot of $\Delta\omega_s$ versus θ^2 gives $a/|b|$, where $a = k_s k_p / 2k_i$.

Experimental. The experiment performed by Byer and Harris is shown in Fig. 1. The reference laser wavelength was matched to the peak wavelength of the signal power. Today this could be done with a tunable cw laser. The purpose of

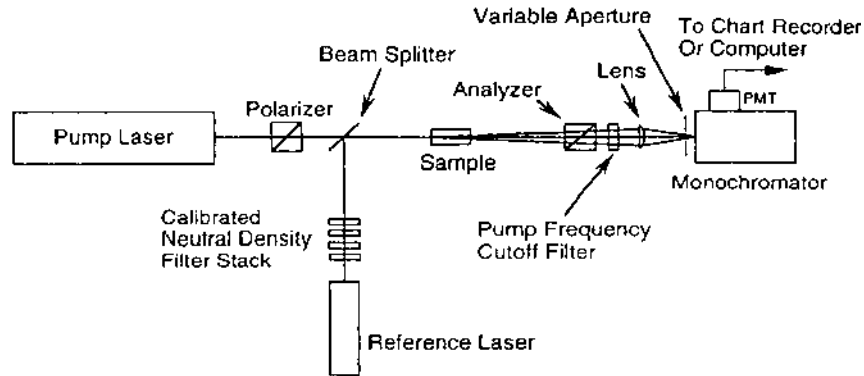


Figure 1 Typical experimental configuration for measuring d_{eff} by the parametric fluorescence method. (From Ref. 6).

the reference laser is to determine the ratio of the signal power to the pump power. The pump and reference powers can be measured by precision power meters. The reference laser is then attenuated with calibrated neutral density filters (i.e., calibrated at the reference wavelength) to a level where its signal, as measured by the PMT, matches that of the signal. This determines the ratio $\mathcal{P}_s/\mathcal{P}_p$.

The polarizer in conjunction with the crystal orientation sets the d_{eff} to be measured. The variable aperture stop in conjunction with the final lens sets the collection angle through $\theta = r/n_s f$, where r is the aperture radius and f is the lens focal length.

The signal spectral distribution is measured with the spectrometer. Today, the data would probably be digitized and stored on disk for later processing. With the parameter b determined by one of the methods described above, d_{eff} can be determined to a potential accuracy of 10% [3]. This accuracy will be limited by the knowledge of b and the accuracy of measuring θ .

C. Maker Fringe Method

This relative measurement technique is based on the experimentally generated bright and dark second harmonic fringes that result as a crystal is rotated about an axis perpendicular to the pump beam axis as first observed by Maker et al. [7]. Two experimental techniques have been developed over the last several years. One involves the rotation of a plane parallel slab. The second requires the sample to be in the form of a wedge that is translated along an axis perpendicular to the pump beam axis.

1. Plane Parallel Slab Rotation (Uniaxial Crystals)

The objective of this method is to measure the second harmonic power generated by a slab of material as a function of the angle of rotation (i.e., as a function of the angle of incidence θ of the fundamental beam), and compare this measurement to that of a standard, well-characterized material to obtain the d_{eff} of the sample. The advantages of this method are that it does not require precise absolute measurements of the fundamental and second harmonic powers, and it does not require knowledge of the longitudinal mode structure of the pump laser, since the effects of multiple modes are the same in the sample and the reference material. Its disadvantages include the requirement of a well-characterized reference that one can trust. It also requires a dual-beam technique to monitor any fluctuations in pump power. This increases the amount of optics and detectors in the experiment. Finally, it requires the additional measurement of coherence lengths.

Theory. The theory of Maker fringes was first given by Jerphagnon and Kurtz [8]. Their development is strictly valid only for isotropic (cubic) materials, or for uniaxial crystals for which the fundamental and second harmonic waves are both either parallel or perpendicular to the optic axis. However, assuming Kleinman symmetry, it is possible for any uniaxial crystal to choose the crystal orientation and the beam polarizations relative to the optic axis so that one component of the d tensor is isolated and measured. Extensions of the theory to biaxial crystals are given later (see below).

The geometry of the second order wave interaction was given in Fig. 36 of Chapter 2. Free and bound second harmonic waves are generated in the nonlinear medium. The sum of these fields (the transmitted second harmonic field in the medium) is given in Table 43 of Chapter 2 for the nonlinear polarization both parallel and perpendicular to the plane of incidence. Jerphagnon and Kurtz considered the transmitted second harmonic wave, which is propagated through the crystal of length L and then transmitted through the back face. Assuming that a weakly focused TEM₀₀ Gaussian pump beam is incident on the crystal in air (with $n_{2\omega} \approx n_\omega \approx 1$ in air), the measured second harmonic power, including multiple internal sample reflections, is given by [8]

$$(\mathcal{P}_{2\omega})_{\text{out}} = \mathcal{P}_M(\theta) \sin^2 \psi \quad (18)$$

where

$$\psi = \frac{2\pi}{\lambda_\omega} (n_\omega \cos \theta_\omega - n_{2\omega} \cos \theta_{2\omega}) L \equiv \frac{\pi}{2} \frac{L}{L_c(\theta)} \quad (19)$$

with $L_c(\theta)$ the angular dependent coherence length. The refractive indices are those of the nonlinear medium, while θ_ω is the angle of the transmitted fundamental wave with respect to the crystal normal (this is the same as the angle θ_s of the source polarization as defined in Chapter 2), and $\theta_{2\omega}$ is the angle of

the transmitted second harmonic free wave (θ_t as defined in Chapter 2). These angles are related to the incident angle through the nonlinear Snell law (see Chapter 2) by $n_\omega \sin\theta_\omega = n_{2\omega} \sin\theta_{2\omega} = \sin\theta$. $\mathcal{P}_M(\theta)$ is the envelope of peaks in the Maker fringe pattern and is given by

$$\begin{aligned}\mathcal{P}_M(\theta) = & \left(\frac{8}{\pi\epsilon_0 c w_0^2} \right) \left(\frac{1}{n_\omega^2 - n_{2\omega}^2} \right)^2 (d_{\text{eff}})^2 (\mathcal{P}_\omega)_{\text{in}}^2 t_\omega^4(\theta) \\ & \times T_{2\omega}(\theta) R(\theta) p^2(\theta) B(\theta)\end{aligned}\quad (20)$$

The parameters t_ω and $T_{2\omega}$ are related to Fresnel transmission factors, and are given by, for the fundamental polarized perpendicular to the plane of incidence (*s*-polarization)

$$t_\omega(\theta) = \frac{2 \cos\theta}{n_\omega \cos\theta_\omega + \cos\theta} \quad (21)$$

$$T_{2\omega}(\theta) = \frac{2n_{2\omega} \cos\theta_{2\omega} (\cos\theta + n_\omega \cos\theta_\omega)(n_\omega \cos\theta_\omega + n_{2\omega} \cos\theta_{2\omega})}{(n_{2\omega} \cos\theta_{2\omega} + \cos\theta)^3} \quad (22)$$

and for the fundamental polarized parallel to the plane of incidence *p*-polarization)

$$t_\omega(\theta) = \frac{2 \cos\theta}{n_\omega \cos\theta + \cos\theta_\omega} \quad (23)$$

$$T_{2\omega}(\theta) = \frac{2n_{2\omega} \cos\theta_{2\omega} (\cos\theta_\omega + n_\omega \cos\theta)(n_\omega \cos\theta_{2\omega} + n_{2\omega} \cos\theta_\omega)}{(n_{2\omega} \cos\theta + \cos\theta_{2\omega})^3} \quad (24)$$

The projection factor $p(\theta)$ takes into account the angular dependence of d_{eff} . As pointed out by Kurtz [3], it is possible to choose the orientation of the crystal principal axes, the rotation axis, and the fundamental polarization such that the nonlinear polarization is parallel to the rotation axis and a single d_{ij} is measured. Table 1 gives the various possibilities and the projection factor $p(\theta)$ for each case.

The multiple reflection factor $R(\theta)$ accounts for the fact that in a plane parallel slab both the fundamental and second harmonic waves can undergo multiple internal reflections. It is given by

$$R(\theta) = \frac{1}{(1 - r_{2\omega}^4)(1 - r_\omega^8)} \left\{ 1 + \frac{p_R^2(\theta)}{p^2(\theta)} r_{2\omega}^2 r_\omega^4 \right\} \quad (25)$$

where $r_{2\omega}$ and r_ω are Fresnel reflection coefficients, and at normal incidence $r_{2\omega} \approx r_\omega = (n_\omega - 1)/(n_\omega + 1)$. The projection factor for the reflected

Table 1 Geometries for Measuring d_{ij} in Uniaxial Crystals Using the Maker Fringe Method

d_{ij}	Point group	Sample orientation	Rotation axis	\hat{e}_ω	$\hat{e}_{2\omega}$	$p(\theta)$
d_{11}	3, 32, $\bar{6}$, $\bar{6}$ m2	(011)	$\ X$	$\ X$	$\ X$	1
d_{22}	3, 3 m, $\bar{6}$	(101)	$\ Y$	$\ Y$	$\ Y$	1
d_{33}	4, 4 mm, 3, 3 m, 6, 6 mm	(hk0)	$\ Z$	$\ Z$	$\ Z$	1
d_{31}	4, 4, 4 mm, 3, 3 m, 6, 6 mm	(hk0)	$\ Z$	$\perp Z$	$\ Z$	1
d_{36}	$\bar{4}$, $\bar{4}$ 2 m, 23, 43 m	(110)	$\ Z$	$\perp Z$	$\ Z$	$2 \cos(\theta_\omega + 45^\circ)$ $\times \cos(\theta_\omega - 45^\circ)$

Source: Adapted from Ref. 8.

fundamental wave is generally given by $p_R(\theta) \simeq p(\theta)$ [8]. For low index materials ($n_\omega, n_{2\omega} \leq 2$), $R(\theta) \simeq 1$.

The beam size factor $B(\theta)$ accounts for the fact that for finite size beams, the free and bound waves will separate as they propagate through the medium. This is not the walk-off effect introduced in Chapter 2 but a consequence of the fact that the fundamental is not at normal incidence. This factor is given, for weak focusing such that $L \gg w_0$, $B(\theta) \simeq 1$, by [8]

$$B(\theta) = \exp \left[- \left(\frac{L}{w_0} \right)^2 \cos^2 \theta (\tan \theta_\omega - \tan \theta_{2\omega})^2 \right] \quad (26)$$

In a Maker fringe experiment, a measurement of the fringe spacing yields the coherence length, while the envelope $\mathcal{P}_M(\theta)$ gives information about d_{eff} . Measurements of both the sample and the reference yield

$$d_{\text{eff}} = \left[\frac{\mathcal{P}_M(0)}{\mathcal{P}_M^{\text{ref}}(0)} \frac{\eta}{\eta^{\text{ref}}} \right]^{1/2} \frac{L_c^{\text{ref}}(0)}{L_c(0)} d_{\text{eff}}^{\text{ref}} \quad (27)$$

where

$$\eta = \frac{(n_\omega + 1)^3 (n_{2\omega} + 1)^3 (n_{2\omega} + n_\omega)}{128 n_{2\omega} R(0)} \quad (28)$$

Experimental. A typical experimental configuration for Maker fringe measurements is illustrated in Fig. 2. A reference material (e.g., quartz) in the reference arm of the experiment is set at a constant angle so that its output is at the peak of a Maker fringe. This second harmonic output is monitored to account for

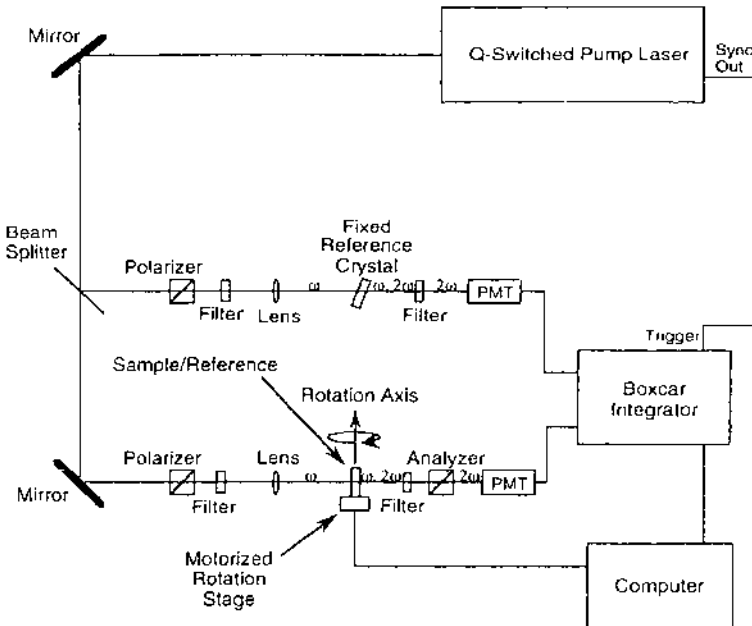


Figure 2 Typical experimental configuration for measuring d_{ij} by the Maker fringe method (sample rotation).

laser power fluctuations. The pump is typically a Q-switched laser with pulse width ~ 10 ns and wavelength selected so that the sample and reference are nonabsorbing at both the fundamental and the second harmonic wavelengths. The second harmonic signals are detected with PMTs, and gated integration (~ 10 pulses) is used (boxcar integrators) to improve the signal-to-noise ratio. The polarizers and analyzers are set for the d_{ij} desired for measurement and for reference. Both the sample and a reference crystal (e.g., quartz) are mounted on rotation stages, and the second harmonic is measured as a function of the angle of incidence. The signals are normalized to the second harmonic measured in the reference arm to factor out laser power fluctuations as well as the effects of mode mixing. An example of a Maker fringe pattern is shown in Fig. 3.

Jerphagnon and Kurtz [8] give an excellent discussion of experimental techniques. The theory assumes symmetric fringe patterns about $\theta = 0$, so it is necessary to position the crystal carefully to get symmetric fringes. The rotation axis of the crystal must be centered on the laser beam axis, perpendicular to it, and at the beam waist. The plane of incidence must also remain constant as the sample is rotated. Finally, the sample must be carefully oriented so that the rotation axis remains along a principal axis of the crystal. Adjustments can be made by monitoring a cw HeNe laser beam that is collinear with the pump beam.

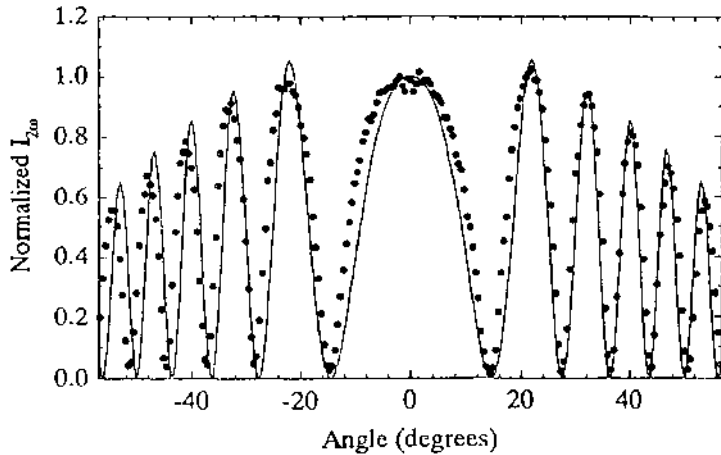


Figure 3 Example of Maker fringes in Y -cut quartz in the (010) orientation.

The measurements required are $L_c(0)$ and $\mathcal{P}_M(0)$ for both the sample and the reference. The coherence length is related to the distance between minima in the fringe pattern. The coherence length can be determined in the following manner [8]. The crystal length and refractive indices are generally known, but not with sufficient accuracy to obtain the coherence length, which is usually on the order of a few micrometers. Hence both L and $(n_\omega - n_{2\omega})$ are treated as adjustable parameters near $\theta = 0$ to fit the shape of the fringe pattern there and the first few minima. The minima at larger angles are then fitted by small adjustments of $(n_\omega - n_{2\omega})$ or L , depending on which is known more accurately. This procedure is iterated to converge to an approximately constant and accurate value of the coherence length at normal incidence $L_c(0)$.

The locus of maxima are then fitted by a least squared method to $\mathcal{P}_M(\theta)$ to obtain an accurate value of $\mathcal{P}_M(0)$. However, it may first be necessary to make some corrections to the peak heights. These may vary over the sample run because of laser fluctuations. This is corrected for by normalizing the corresponding measurements (in time) to those of the reference material set at a constant angle in the reference arm of the experiment. Another source of error is nonzero minima. These nonzero minima can be caused by surface defects in the sample (scratches, pits, etc.), by a finite pump beam divergence (i.e., the output power is averaged over a small angle $\delta\theta$ for each θ due to the finite angular spread of the beam), and by a small wedge in the sample (i.e., the output power is averaged over a small thickness δL because of a thickness variation over the beam spot). One should seek to minimize these effects. However, as pointed out by Jerphagnon and Kurtz, these accumulated effects can be corrected for by adding to each maximum the value of the adjacent minima.

2. Wedge Translation

The objective of this technique is to perform essentially the same measurements as in the Maker fringe method, except to replace the plane parallel slab rotation with a translation of a wedge-shape (i.e., prism) sample. This has two main advantages. First, it eliminates the multiple reflection factor $R(\theta)$, which is especially important in the IR, where materials can have larger refractive indices. Second, it also creates a larger phase mismatch for measuring the coherence length [3]. In the IR the coherence length is often so long that an insufficient number of fringes are generated by sample rotation. The disadvantage of this technique is that it requires the sample to be formed into the shape of a prism.

Theory. The Maker fringe experiment with wedge translation is essentially the same in motive and practice as that with sample rotation. The differences have to do with the shape and analysis of the fringe pattern that results.

The fundamental beam is incident on the wedge at normal incidence. Hence for weak focusing and negligible double refraction, the free and bound second harmonic waves travel collinearly in the sample. There is still a relative phase lag between these two waves, which is given by

$$\psi = \frac{\pi}{2} \frac{L(x)}{L_c(0)} = \frac{\pi}{2} \frac{L_0 + x \tan\theta_w}{L_c(0)} \quad (29)$$

where x is the translation distance along the incident face of the sample, θ_w is the wedge angle of the sample, and L_0 and $L_c(0)$ are the sample thickness and the coherence length, respectively, at the initial position $x = 0$ of the scan.

The measured second harmonic power is now given by [3]

$$(\mathcal{P}_{2\omega})_{\text{out}} = \mathcal{P}_M C(\eta, \psi) \quad (30)$$

where \mathcal{P}_M is the same as given earlier for sample rotations except that $t_\omega(\theta) = t_\omega(0)$, $T_{2\omega}(\theta) = T_{2\omega}(\theta_w)$, $R(\theta) = 1$, $p(\theta) = 1$, and $B(\theta) = 1$. The wedge function $C(\eta, \psi)$ is

$$C(\eta, \psi) = \frac{1}{2} \left[1 - \cos 2\psi \exp\left(\frac{-\pi^2 \eta^2}{16}\right) \right] \quad (31)$$

This function accounts for the small change in path length through the wedge over a finite beam diameter, with

$$\eta = \frac{w_0 \tan\theta_w}{L_c(0)} \quad (32)$$

For $\eta \ll 1$, $C(\eta, \psi) \rightarrow \sin^2\psi$ as in the Maker fringe pattern with sample rotations. Fitting the fringes to Eq. (31), the coherence length at $x = 0$ can be determined through Eq. (29). Measurements on both the sample and a reference material then

yield

$$d_{\text{eff}} = \left[\frac{\mathcal{P}_M C^{\text{ref}}(\eta, \psi)}{\mathcal{P}_M^{\text{ref}} C(\eta, \psi)} \right]^{1/2} \frac{(n_\omega + 1)^2 (n_{2\omega} + 1)}{[(n_\omega + 1)^2 (n_{2\omega} + 1)]^{\text{ref}}} \frac{L_c^{\text{ref}}(0)}{L_c(0)} d_{\text{eff}}^{\text{ref}} \quad (33)$$

In some materials absorption cannot be ignored. If $(\alpha_\omega - \alpha_{2\omega}/2)L \ll 1$, then Chemla and Kupecek found the following result, as given by Kurtz [3], for the measured second harmonic power from a wedge, assuming nonnormal incidence, exact boundary conditions, a finite beam diameter, and absorption:

$$\begin{aligned} (\mathcal{P}_{2\omega})_{\text{out}} = & \mathcal{P}_M(\theta) \left\{ \frac{1}{4} \exp \left[-\frac{\alpha_{2\omega} L(x)}{2 \cos \theta_{2\omega}} \right] + \frac{1}{4} \exp \left[-\frac{2\alpha_\omega L(x)}{\cos \theta_\omega} \right] \right. \\ & \left. - \frac{1}{2} \exp \left[-\left(\frac{\alpha_\omega}{\cos \theta_\omega} + \frac{\alpha_{2\omega}}{2 \cos \theta_{2\omega}} \right) L(x) \right] \cos \left[\frac{\pi L(x)}{L_c(\theta)} \right] F \left[\frac{\pi \Lambda}{L_c(\theta)} \right] \right\} \end{aligned} \quad (34)$$

where $\mathcal{P}_M(\theta)$ is as given for the slab rotation, with $R(\theta) = B(\theta) = 1$, and the wedge correction factor is given by

$$F \left[\frac{\pi \Lambda}{L_c(\theta)} \right] = \frac{2J_1[\pi \Lambda / L_c(\theta)]}{\pi \Lambda / L_c(\theta)} \quad (35)$$

with J_1 a first-order Bessel function. At normal incidence, $\Lambda = \eta L_c(0)$, while at the angle of minimum deviation through the prism, $\Lambda = w_0(\sin \theta_w / \cos \theta)$.

The effect of absorption is that the fringes are no longer of constant height in the wedge translation experiment. Figure 4 illustrates the shape of the wedge translation fringe pattern with and without absorption. The analysis of the fringe envelope must include the modification given by the factors in curly brackets of Eq. (34) when absorption is present.

3. Extension of Maker Fringe Method to Biaxial Crystals

Dou et al. [9] have extended the treatment of Maker fringes to include absorbing biaxial crystals. This is especially relevant to the characterization of newly developed organic crystals. They treat the crystals with laboratory axes x_1, x_2, x_3 such that x_1 and x_2 are along crystal principal axes in the plane of the sample surface, and x_3 is perpendicular to this plane. Rotations are taken to be about the x_2 -axis.

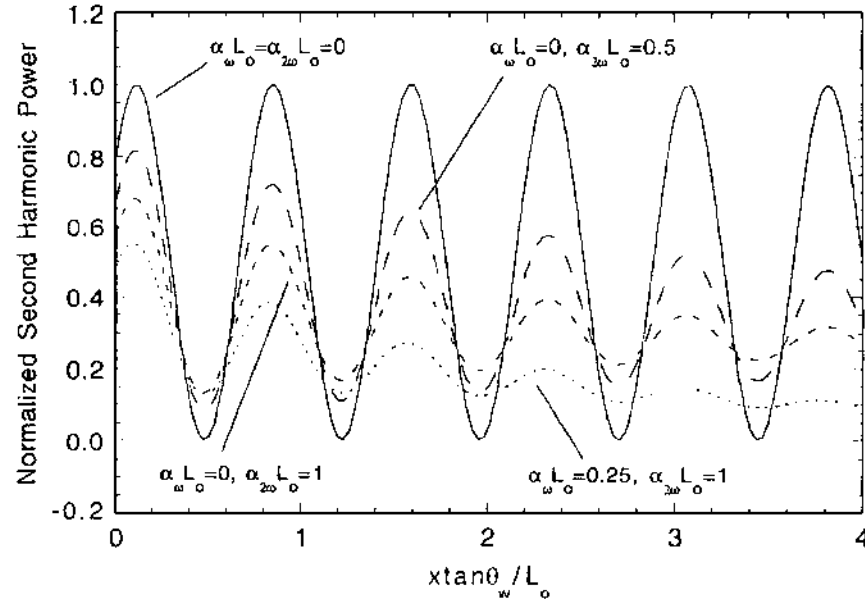


Figure 4 Theoretical calculation of Maker fringes in a wedge-shaped sample including absorption at ω and 2ω .

The measured second harmonic power can now be written as [9]

$$\begin{aligned} (\mathcal{P}_{2\omega})_{\text{out}} = & \frac{C(\mathcal{P}_\omega)_{\text{in}}^2}{n_\omega^2 w_0^2} R(\theta) b_0 b_1 \left\{ b_2 \exp\left(-\frac{\alpha_{2\omega} L}{\cos\theta_{2\omega}}\right) + \frac{1}{b_2} \exp\left(-\frac{2\alpha_\omega L}{\cos\theta_\omega}\right) \right. \\ & \left. - 2B(\theta) \exp\left(-\frac{\alpha_\omega L}{\cos\theta_\omega} - \frac{\alpha_{2\omega} L}{2\cos\theta_{2\omega}}\right) \cos 2\psi \right\} \end{aligned} \quad (36)$$

where C is an unimportant constant that will cancel when ratios are taken, and b_0 , b_1 , b_2 are new parameters defined below. Other parameters are as defined earlier.

When the nonlinear polarization is perpendicular to the plane of incidence, the following equations apply:

$$b_0 = \left(\frac{1}{n_{2\omega}^2 - n_\omega^2} \right)^2 \quad (37)$$

$$b_1 = \frac{2n_{2\omega} \cos\theta_{2\omega} (n_\omega \cos\theta_\omega + \cos\theta) (n_{2\omega} \cos\theta_{2\omega} + n_\omega \cos\theta_\omega)}{(n_{2\omega} \cos\theta_{2\omega} + \cos\theta)^3} |d_{\text{eff}}|_2^2 \quad (38)$$

$$b_2 = \frac{2n_{2\omega} \cos\theta_{2\omega} (n_\omega \cos\theta_\omega + \cos\theta)}{(n_{2\omega} \cos\theta_{2\omega} + \cos\theta)(n_{2\omega} \cos\theta_{2\omega} + n_\omega \cos\theta_\omega)} \quad (39)$$

In these equations, $n_{2\omega} = n_{2\omega,2}$, the principal index along x_2 .

For the nonlinear polarization parallel to the plane of incidence, a different set of equations apply:

$$b_0 = \left(\frac{1}{1 - n_\omega^2 (n_{2\omega,1}^{-2} \cos^2\theta_\omega + n_{2\omega,3}^{-2} \sin^2\theta_\omega)} \right)^2 \quad (40)$$

$$\begin{aligned} b_1 = & \frac{2n_{2\omega} \cos\theta_{2\omega} / n_{2\omega,1}^6 n_{2\omega,3}^4}{(n_{2\omega} n_{2\omega,1}^{-2} \cos\theta_{2\omega} + \cos\theta)^3} \times (M_1 |d_{\text{eff}}|_1 + M_2 |d_{\text{eff}}|_3 \sin\theta) \\ & \times (M_3 |d_{\text{eff}}|_1 + M_4 |d_{\text{eff}}|_3 \sin\theta) \end{aligned} \quad (41)$$

$$b_2 = \frac{2n_{2\omega} \cos\theta_{2\omega}}{n_{2\omega} \cos\theta_{2\omega} + n_{2\omega,1}^2 \cos\theta} \left(\frac{M_3 |d_{\text{eff}}|_1 + M_4 |d_{\text{eff}}|_3 \sin\theta}{M_1 |d_{\text{eff}}|_1 + M_2 |d_{\text{eff}}|_3 \sin\theta} \right) \quad (42)$$

$$M_1 = \sin^2\theta - n_{2\omega,3}^2 - \left(\frac{n_{2\omega,3}}{n_{2\omega,1}} \right)^2 n_\omega n_{2\omega} \cos\theta_\omega \cos\theta_{2\omega} \quad (43)$$

$$M_2 = n_\omega \cos\theta_\omega + n_{2\omega} \cos\theta_{2\omega} \quad (44)$$

$$M_3 = \sin^2\theta - n_{2\omega,3}^2 - n_{2\omega,3}^2 n_\omega \cos\theta_\omega \cos\theta \quad (45)$$

$$M_4 = n_\omega \cos\theta_\omega + n_{2\omega,1}^2 \cos\theta \quad (46)$$

$$n_{2\omega} = (n_{2\omega,1}^2 n_{2\omega,3}^2 - n_{2\omega,1}^2 \sin^2\theta + n_{2\omega,3}^2 \sin^2\theta)^{1/2} / n_{2\omega,3} \quad (47)$$

In these equations, $n_{2\omega,i}$ are the principal indices along the x_i -axes. In all of the equations above, $|d_{\text{eff}}|_i = |d_{\text{eff}}|$ for the nonlinear polarization vector projected along the x_i -axis.

Dou et al. point out that the sample orientation and beam polarizations can be chosen in such a way that $|d_{\text{eff}}|_1$ depends on no more than two d_{ij} coefficients, and $|d_{\text{eff}}|_2$ and $|d_{\text{eff}}|_3$ each depend on no more than one. Then three kinds of Maker fringe envelopes are possible for biaxial crystals:

1. Symmetric, peak at $\theta = 0$, depending on only one d_{ij}
2. Symmetric, zero at $\theta = 0$, depending on only one d_{ij}
3. Asymmetric, depending on two d_{ij} , but only one at $\theta = 0$.

Table 2 Geometries for Measuring d_{ij} in Biaxial Crystals of Point Group m Using the Maker Fringe Method

d_{ij}	MF kind	Sample orientation	Rotation axis		\hat{e}_ω	$\hat{e}_{2\omega}$
			axis	\hat{e}_ω		
d_{11}	1st	(001), (010)	$\ X$	$\ X$	$\ X$	
d_{12}	3rd	(001)	$\ X$	$\perp X$	$\ X$	
	3rd	(001)	$\ Y$	$\ Y$	$\perp Y$	
d_{13}	1st	(010)	$\ Z$	$\ Z$	$\perp Z$	
	2nd	(100)	$\ Z$	$\ Z$	$\perp Z$	
	1st	(010)	$\ X$	$\ X$	$\perp X$	
d_{31}	2nd	(001)	$\ X$	$\ X$	$\perp X$	
	3rd	(100)	$\ Z$	$\perp Z$	$\ Z$	
d_{32}	3rd	(100)	$\ Z$	$\perp Z$	$\ Z$	
	3rd	(100)	$\ Y$	$\ Y$	$\perp Y$	
d_{33}	1st	(100), (010)	$\ Z$	$\ Z$	$\ Z$	

Source: Adapted from Ref. 9.

Table 2 shows the experimental geometries for a monoclinic system, while Fig. 5 illustrates the behavior of the three kinds of Maker fringe patterns in biaxial crystals. The experimental methods are basically the same as described above for uniaxial crystals. Pavlides and Pugh [10] also give an extensive theoretical treatment of Maker fringes in crystals of low symmetry.

D. Powder Methods

1. Kurtz Powder Method

It is a difficult, time consuming, and costly endeavor to develop single-crystal growth methods for new materials. Therefore a relatively rapid and simple method of screening new candidate materials for frequency conversion applications prior to crystal growth and accurate characterization is needed. Kurtz and Perry [11] were the first to develop such a method. The advantage of their method is that it is inexpensive and not only provides a screening of some d_{ij} values but also determines if a material is phase matchable or not (by birefringence methods). The disadvantages are that the accuracy is not high ($\sim 25\%$), it misses some potentially large d_{ij} that are not phase matchable in the conventional sense, and it is difficult to use in an absorption region. Notwithstanding these problems, it has proven to be a very useful method for screening new materials that can occur in powder (i.e., small crystallite) form.

Theory. Kurtz and Perry developed a semiquantitative approach to the theory of SHG from powders, making the following assumptions:

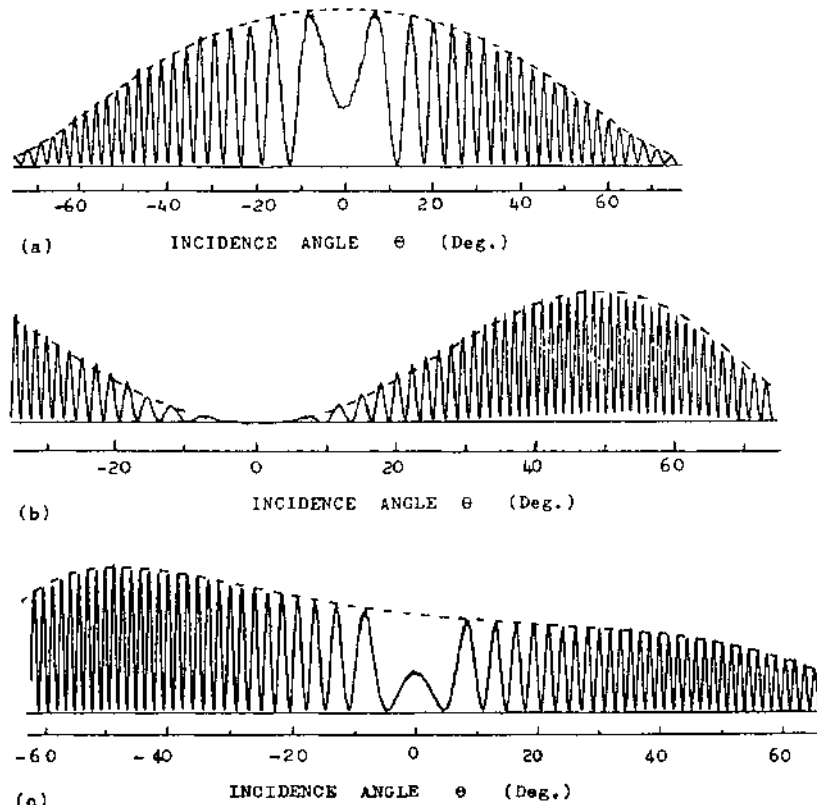


Figure 5 Maker fringes in the biaxial crystal thiosemicarbazide cadmium chloride monohydrate (point group m). (a) Maker fringes of the first kind for d_{33} . (b) Maker fringes of the second kind for d_{31} . (c) Maker fringes of the third kind for d_{32} . (From Ref. 9).

The particles are immersed in an index matching liquid.

The particles are single crystal, nearly identical in size, have random orientation, and are densely packed (no voids).

An infinite plane wave analysis with no pump depletion is valid with appropriate averaging over particles.

The first assumption was made to avoid tracking mathematically the scattered light from each particle, but is not an absolutely necessary experimental condition as long as nearly all of the second harmonic light is collected and measured.

Following the work of Bloembergen and Pershan [12], Kurtz and Perry showed that the second harmonic intensity generated by a single particle can be

related by, assuming no absorption and low dispersion,

$$I_{2\omega} \propto d^2 L_c^2 \sin^2 \left[\frac{\pi r}{2 L_c} \right] \quad (48)$$

where r is the particle size. To obtain the resultant second harmonic intensity radiating from a system of small particles, the approach depends on whether the particles are phase matchable or not.

Consider first nonphase matchable materials. One can define an average coherence length given by

$$\langle L_c \rangle = \left\langle \frac{\lambda_\omega}{4(n_{2\omega} - n_\omega)} \right\rangle \quad (49)$$

where the angle brackets define a suitable average over the particles with an average size $\langle r \rangle$. The second harmonic is generated effectively only over a distance $\langle L_c \rangle$. So, for $\langle r \rangle \gg \langle L_c \rangle$, one can assume that there is no phase correlation between the second harmonic fields generated by different particles. Hence the net second harmonic signal is found by summing over the intensities generated by each particle rather than by a sum over the fields. This is obtained by multiplying the single particle result by the average number of particles (i.e., $L/\langle r \rangle$) in the path length L of the cell. However, since the particles have random orientation, an average of d over the spherical angles (θ, ϕ) must first be performed. Kurtz and Perry [11] have computed this average for several crystal point symmetry groups. These results are shown in Table 3. Finally, if the rms deviation of r from $\langle r \rangle$ exceeds $\langle L_c \rangle$, the oscillatory behavior of the phase matching factor $\sin^2 \psi$ will smear out. The final result is (for nonphase matchable materials)

$$I_{2\omega} \propto \langle d^2 \rangle L \langle L_c \rangle \frac{\langle L_c \rangle}{\langle r \rangle} \quad (\langle r \rangle \gg \langle L_c \rangle) \quad (50)$$

For $\langle r \rangle \ll \langle L_c \rangle$, and for interparticle spacing $\ll \langle L_c \rangle$, there is some phase coherence in the second harmonic fields generated by different particles, but it

Table 3 Angle Averaged d -Coefficients for Several Point Symmetry Groups

Point group	Nonzero d_{ij}	$\langle d^2 \rangle$
32	$d_{11} = -d_{12} = -d_{26}$	$(50/105)(d_{11})^2$
$\bar{4}3m, \bar{4}2m$	$d_{14} = d_{25} = d_{36}$	$(5/7)(d_{14})^2$
6 mm, 4 mm	$d_{31} = d_{32} = d_{24} = d_{15}$	$(19/105)(d_{33})^2 + (26/105)d_{33}d_{31} + (114/105)(d_{15})^2$
3 m	$d_{31} = d_{32} = d_{24} = d_{15}$ $d_{21} = d_{16} = -d_{22}$	$(19/105)(d_{33})^2 + (26/105)d_{33}d_{31} + (114/105)(d_{15})^2 + (10/21)(d_{22})^2$

contains some degree of randomness because of randomly different particle sizes. Kurtz and Perry [11] then treated the nonlinear polarization wave as a one-dimensional random walk problem. The net result is (for nonphase matchable materials)

$$I_{2\omega} \propto \langle d^2 \rangle \frac{L}{\langle L_c \rangle} \frac{\langle r \rangle}{\langle L_c \rangle} \quad (\langle r \rangle \ll \langle L_c \rangle) \quad (51)$$

This randomness in phase between particles implies that the second harmonic generation is only quasi-phase matched. The degree of randomness (for a fixed length of sample) will be less for larger (and hence fewer) particles, as long as $\langle r \rangle \ll \langle L_c \rangle$. Thus in this regime the second harmonic intensity will increase with average particle size as indicated by Eq. (51). The behavior of the second harmonic intensity as a function of particle size for nonphase matchable materials is illustrated in Fig. 6.

Consider next materials that are phase matchable. For $\langle r \rangle \gg \langle L_c \rangle$, the major particle orientational dependence is now due to the sensitivity of the generated second harmonic to the phase matching. The coherence length in this case is given by

$$L_c = \frac{\lambda_\omega}{4(n'_{2\omega} - n''_\omega) \sin \theta_{pm}(\theta - \theta_{pm})} \quad (52)$$

where the ' and '' designate e or o depending on the type of crystal. Averaging over the coherence length and applying the plane wave result for $L/\langle r \rangle$ particles results in (for phase matchable materials)

$$I_{2\omega} \propto (d_{eff})^2 L \Lambda_{pm} \quad \left(\langle r \rangle \gg \frac{\Lambda_{pm}}{\sin \theta_{pm}} \right) \quad (53)$$

for $\langle r \rangle \gg \Lambda_{pm}/\sin \theta_{pm} = (\lambda_\omega/2n_\omega)/\sin \rho \approx \pi/k_\omega \rho$, where d_{eff} is the appropriate d -coefficient for phase matching, θ_{pm} is the phase matching angle relative to the optic axis of the crystal, and ρ is the walk-off angle. In the visible spectral region, $\Lambda_{pm} \sim 1-10 \mu\text{m}$. This result dominates over all other d -coefficients which are not phase matchable (i.e., for which $I_{2\omega} \propto \langle L_c \rangle/\langle r \rangle$). The result is that in this size regime, the second harmonic intensity for phase matchable particles is independent of particle size.

For $\langle r \rangle \leq \Lambda_{pm}/\sin \theta_{pm}$, an argument similar to that given for the nonphase matchable materials shows that again $I_{2\omega} \propto \langle r \rangle$. The behavior of the second harmonic intensity generated in a sample of phase matchable particles as a function of particle size is also shown in Fig. 6.

Experimental. A typical experimental configuration is shown in Fig. 7. The ground particles are passed through standard sieves to obtain the desired size, which can be characterized by standard optical microscopy. The particles are

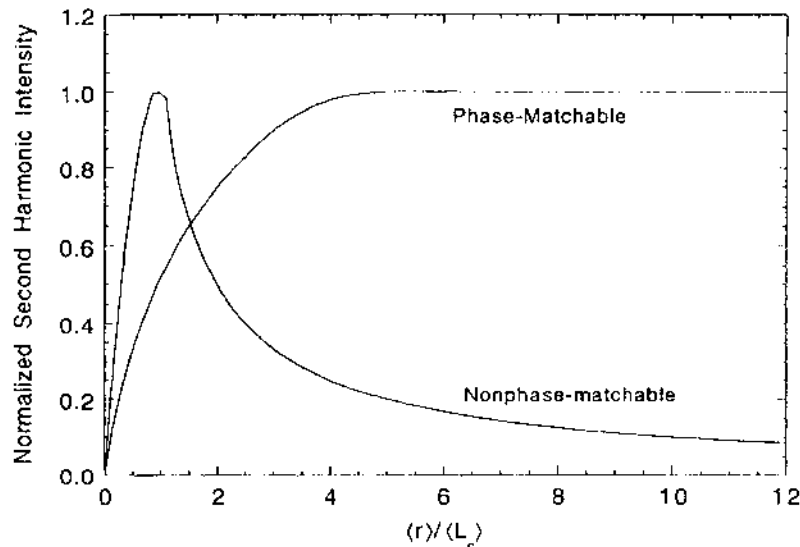


Figure 6 Normalized second harmonic intensity for a powder sample as a function of average particle size $\langle r \rangle$ normalized to the average coherence length $\langle L_c \rangle$. (From Ref. 11).

placed in a thin cell ($\sim 0.1\text{--}0.2$ mm) and should be sonicated to assure dense packing. A range of samples with different particle sizes are measured to test for phase matchability. Kurtz and Perry showed that in a densely packed sample the scattering pattern is roughly symmetric about the forward and backward directions, so only the forward lobe needs to be sampled. To be sure, though, one can place the sample in an integrating sphere and collect all of the generated second harmonic. This also increases the measurement sensitivity. For very weak signals, it is best to pack the particles densely in an index matching liquid. Then the second harmonic is strongly directed into a narrow forward lobe [11]. This gives increased sensitivity over low-efficiency integrating spheres.

The sample cell thickness and laser beam diameter should be chosen to assure operation in the $\langle r \rangle \ll L \ll 2w_0$ regime. This ensures a constant plane wave irradiance over a large number of particles for a significant statistical average.

Both the sample and a reference (e.g., quartz) are irradiated in separate arms of the experiment. The signal from the reference can be used to factor out random fluctuations in the laser peak power. A monochromator may be used to scan the signal over a narrow frequency band to assure that the signal is due to second harmonic generation and not two-photon fluorescence. (The SHG will have a very narrow bandwidth.) Finally, the signals are detected by

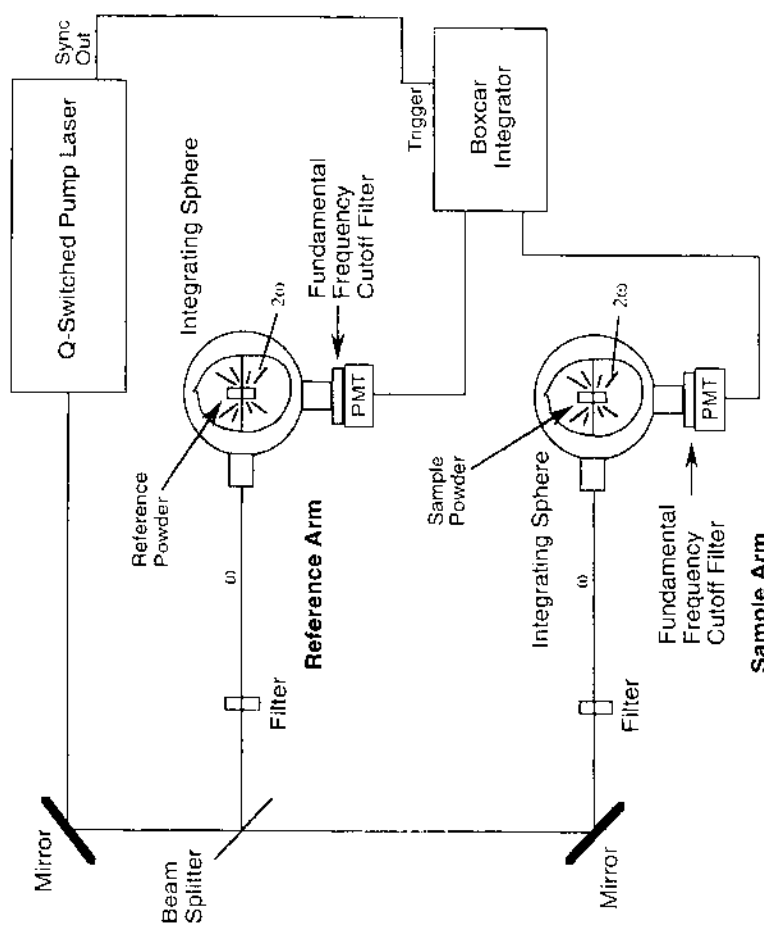


Figure 7 Typical experimental configuration for screening second order nonlinear optical materials in powder form. The samples can also be measured directly in air (without integrating spheres) or in a condenser system for efficiently collecting the light at 2ω .

photomultiplier tubes (PMTs) and then amplified and integrated over several pulses using boxcar integrators.

The results of this experiment give the value of d relative to the reference material with an accuracy $\sim 25\%$, and a determination of whether the material is phase matchable. For phase matchable materials, only the relative size of the d_{ij} contained in the d_{eff} for phase matching is sampled. Typically, one should rely on measurements for particle sizes $\langle r \rangle \geq 100 \mu\text{m}$ to obtain the relative value of d_{eff} .

2. Modified Powder Method

A new powder method has been developed recently due to Kiguchi et al. [13]. The objective of this method is to sample all of the d_{ij} , even those for which the material is not normally phase matched. These can be important for waveguide applications using either quasi-phase matching or Čerenkov phase matching. The powder sample is measured by reflection through a hemicylindrical prism. Every nonzero element of the second order susceptibility tensor is sampled and phase matched through Čerenkov phase matching. In this way no potentially large d -coefficients are overlooked when screening materials.

Theory. The geometry of the experiment for measuring the second harmonic on reflection from the powder sample/prism interface is shown in Fig. 8. Čerenkov phase matching (see Chapter 2) sets the angle for viewing the second harmonic through.

$$n_{\omega}^{\text{prism}} \sin\theta = n_{2\omega}^{\text{prism}} \sin\theta_m \quad (54)$$

where θ is the incident angle of the fundamental wave, and θ_m is the Čerenkov phase matching angle.

Because of the total internal reflection geometry, the fundamental has a penetration depth ξ into the sample:

$$\xi = \frac{\lambda_{\omega}}{2\pi n_{\omega}^{\text{prism}}} \left[\sin^2\theta - \left(\frac{n_{\omega}^{\text{sample}}}{n_{\omega}^{\text{prism}}} \right)^2 \right]^{-1/2} \quad (55)$$

The measured second harmonic power is then given by

$$\begin{aligned} (\mathcal{P}_{2\omega})_{\text{out}} \propto & \frac{(n_{\omega}^{\text{prism}})^2 (n_{2\omega}^{\text{prism}})}{[(n_{\omega}^{\text{prism}} + 1)^2 (n_{2\omega}^{\text{prism}} + 1)]^2} \frac{(d_{\text{eff}})^2}{(n_{\omega}^{\text{sample}})^2 (n_{2\omega}^{\text{sample}})} \\ & \times \xi^2 \cos\theta (\mathcal{P}_{\omega})_{\text{in}}^2 \end{aligned} \quad (56)$$

where $\cos\theta$ accounts for the projected area of the fundamental beam on the sample, and d_{eff} is a weighted sum of all nonzero tensor components with the weighting depending on the crystal orientation. Assuming random crystal

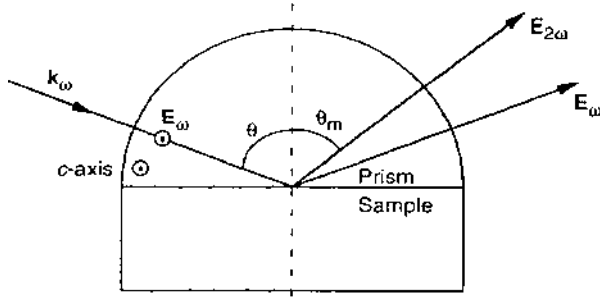


Figure 8 Sample configuration for a modified powder method using Čerenkov phase matching at the interface of the powder sample and a hemicylindrical prism. (From Ref. 13.)

orientation, an average over all angles is taken, and the results given in Table 3 can be used.

Experimental. The experimental configuration is similar to that used in the Kurtz method, with the prism/sample cell replacing the powder cell in one arm of the experiment. The hemicylindrical prism is placed in optical contact with the powder sample.

Note that the fundamental and second harmonic beams should be separated. A strong signal should be found at the phase matching angle, which depends on the incident angle through the phase matching relation in Eq. (54). The sample is compared to a reference powder (e.g., quartz or urea), which is also placed in the prism geometry.

E. Thin Film Reflectance

Sometimes new materials are available only in thin film form. This configuration is also desirable for waveguide applications. If the thin film is grown on a highly absorbing substrate, the Maker fringe method is not always feasible, since it is the transmitted second harmonic that is measured in such an experiment.

The second harmonic generated upon reflection from a surface has been treated by Bloembergen and Pershan [12], but the signal is generally very weak. Hase et al. [14] have extended the analysis of Bloembergen and Pershan to the case of a thin film for which the reflected second harmonic includes a coherent superposition of multiply reflected second harmonic waves as well as second harmonic reflected from the substrate surface. The analysis is performed in the nondepleted pump approximation and includes multiply reflected pump waves. The results of the analysis show that the second harmonic measured upon reflection is enhanced due to thin film interference.

The objective of this experimental method is to measure the second harmonic power by reflection from a thin film sample and use the analysis described above to find the d_{eff} of the thin film relative to that of the substrate. The advantage of this technique is that samples on highly absorbing substrates can be characterized, and the second harmonic signal is enhanced by thin film interference. The disadvantage is that the film must be grown on a well-characterized sample (n , α , and d_{eff}), and the refractive index and thickness of the film must be known to high accuracy.

Theory. The wave equation is solved in the manner shown by Bloembergen and Pershan [12]. Boundary conditions at each interface are included, and a coherent sum of multiple fundamental and second harmonic reflected waves is formed, taking into account the relative phase of each wave, which depends on the refractive index and thickness of the film. Reflections from both the film surface and the substrate surface are included.

Figure 9 shows an example of the second harmonic intensity reflected from a thin film (normalized to the second harmonic reflected from the substrate) as a function of film thickness. The fringes are due to interference effects in the thin film for both the fundamental and the second harmonic. The envelope of fringes varies periodically with a period that is twice the coherence length of the film. In an experiment, the measured second harmonic for different film thicknesses is fitted to the theoretical curve by varying the quantity $|d_{\text{eff}}^{\text{film}}/d_{\text{eff}}^{\text{substrate}}|$.

Experimental. Several sample films are prepared of varying thickness. The film index and thickness must be measured, for example by ellipsometry. The crystal (film) axis must be found and the beam polarizations set for obtaining

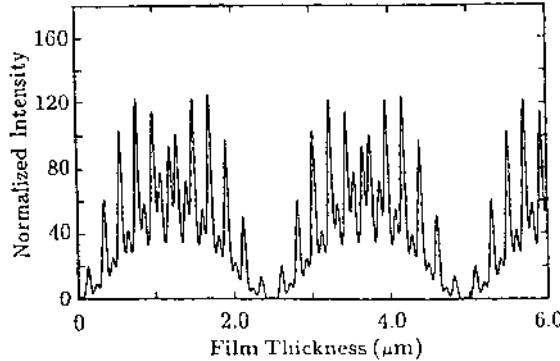


Figure 9 Theoretical calculation of reflected second harmonic intensity from a ZnSe film on a GaAs substrate as a function of film thickness. The fundamental wavelength was taken to be 1064 nm, and $|d_{36}^{\text{ZnSe}}/d_{36}^{\text{GaAs}}|^2 = (0.16)^2$ was used. (From Ref. 14).

the desired d_{eff} . The reflected second harmonic is detected with a photomultiplier and the signal fed to a gated integrator to enhance the signal-to-noise ratio.

A fit of experimental data for a ZnSe film grown on GaAs is shown in Fig. 10. The value of $d_{36} = 33 \pm 7 \text{ pm/V}$ for ZnSe obtained by this method is in agreement with the literature [14]. Most of the error in the measurement comes from the variability of the crystal axis from sample to sample (of varying thickness). A potential way to overcome this is to make a film of tapered thickness and sample the reflected second harmonic over various positions on the film. Other possibilities include scanning the incident angle or wavelength of the fundamental beam.

F. Poling

There has been a considerable amount of research undertaken over the past several years in the development of organic molecules with large hyperpolarizabilities for nonlinear optics applications. The first hyperpolarizability (see Section II.A) is applicable to second order frequency conversion processes. The macroscopic nonlinear properties of a medium depend on a properly oriented ensemble of these molecular units.

Several molecules with large first hyperpolarizability also have a strong permanent dipole moment. A collection of these molecules will therefore want to align antiparallel in pairs. Then, even though each molecular unit is acentric, the collection as a whole is centrosymmetric, and hence will have no macroscopic second order susceptibility.

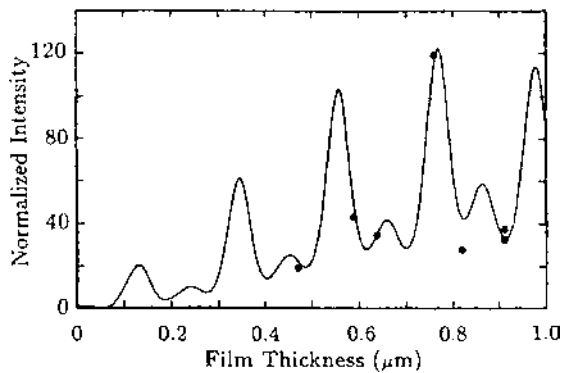


Figure 10 Experimental data fitted to a theoretical curve for second harmonic intensity reflected from ZnSe films of various thicknesses on GaAs substrates. The best fit is given by $|d_{36}^{\text{ZnSe}}/d_{36}^{\text{GaAs}}| = 0.16 \pm 0.032$, which yields $|d_{36}^{\text{ZnSe}}| = 33 \pm 7 \text{ pm/V}$. (From Ref. 14).

An approach that has been taken to overcome this problem is to dope the nonlinear molecules into a polymer and use the properties of the polymer to align the molecular dipoles for a macroscopic $\chi^{(2)}$. The nonlinear molecules can be mixed in as a guest in the host polymer, or covalently attached to individual monomer units. In either case, the nonlinear moiety retains some orientational freedom. The usual procedure is to raise the temperature of the polymer mixture above its glass transition point (T_g) while applying an external electric field. The nonlinear molecules align with the field through the interaction of their permanent dipole moments. This establishes a macroscopic order to break the symmetry that disallows second order processes. With the field applied, the temperature of the system is lowered to room temperature (i.e., below T_g) to lock in the field-established order, then the external field is turned off. Due to some internal free volume, the microscopic dipoles will relax to a larger degree of randomness over time but will eventually settle into a steady state with a nonzero order parameter. The result is a polymer with a macroscopic second order susceptibility.

The objective in a poling experiment is to monitor the second harmonic produced by a poled polymer film. This is often done *in situ* to study the kinetics of the system and observe the decay of the second harmonic after the poling field is turned off. This will determine if the polymer reaches a steady state with a nonzero second order susceptibility. Once a steady state is reached, a Maker fringe type of experiment is used to measure the nonzero d_{ij} components. The advantages of such an experiment are that it not only allows one to study the ordering and decay kinetics of such a system but also is more convenient than performing the measurements in a waveguide configuration (which may be the eventual application of the polymer), since the polymer film would normally require much improvement to be a good waveguide. The polymer can generally only be prepared as a thin ($\sim 1 \mu\text{m}$) film. The disadvantage is that since the optical path length is small, the second harmonic signal, though measurable, is small.

Theory. The typical geometry of the sample is that of a thin film on a centrosymmetric substrate, and the sample is immersed in air. The laser is incident from the film side of the sample. Other geometries are possible [15].

The analysis of Jerphagnon and Kurtz [8] that was applied to the Maker fringe analysis of a plane parallel slab can be modified slightly for this problem. For example, if the nonlinear polarization is perpendicular to the plane of incidence, so that the second harmonic is *s*-polarized, the measured second harmonic power can be written as [16]

$$(\mathcal{P}_{2\omega})_{\text{out}} = \frac{8\pi(d_{\text{eff}})^2}{\epsilon_0 c(n_{\omega}^f)^2 \lambda_{\omega}^2} \frac{(\mathcal{P}_{\omega})_{\text{in}}^2}{w_0^2} L_f^2 \frac{\sin^2 \psi}{\psi^2} T_{\omega}(\theta) T_{2\omega}^{(s)}(\theta) \quad (57)$$

where L_f is the film thickness, n_ω^f is the film index, the T_ω and $T_{2\omega}$ factors are combinations of Fresnel factors and are functions of the incident angle θ , and ψ was given in Section C. Because the film is thin and usually has low indices, the quantities used in Section C, $R(\theta)$ and $B(\theta)$, are approximately equal to 1.

For the case when the nonlinear polarization is parallel to the plane of incidence (second harmonic is *p*-polarized), the output power can be put in a similar form. In the spirit of the Jerphagnon and Kurtz analysis [8] (i.e., low dispersion), where $n_\omega \approx n_{2\omega}$, then $\theta_\omega \approx \theta_{2\omega}$ and thus $n_{2\omega} \cos\theta_\omega + n_\omega \cos\theta_{2\omega} \approx n_\omega \cos\theta_\omega + n_{2\omega} \cos\theta_{2\omega}$ in Eq. (24).

Finally, several organic polymer films are absorbing, at least at the second harmonic frequency, so absorption must be included in the same manner as in Chapter 2. Thus the following modification is made:

$$\frac{\sin^2\psi}{\psi^2} \rightarrow \exp\left\{-\left[\frac{\alpha_\omega}{\cos\theta_\omega^f} + \frac{\alpha_{2\omega}}{2\cos\theta_{2\omega}^f}\right]L_f\right\} \frac{\sin^2\psi + \sinh^2\sigma}{\psi^2 + \sigma^2} \quad (58)$$

where

$$\sigma = \left[\frac{\alpha_\omega}{\cos\theta_\omega^f} - \frac{\alpha_{2\omega}}{2\cos\theta_{2\omega}^f}\right] \frac{L_f}{2} \quad (59)$$

and the superscript or subscript f signifies a film quantity.

The output second harmonic power measured on the other side of the substrate, for *s*- or *p*-polarization, is given by

$$(\mathcal{P}_{2\omega}^{(s,p)})_{\text{out}} = \mathcal{P}_M^{(s,p)} F(L_f, \theta) \quad (60)$$

where, $F(L_f, \theta)$ is given by Eq. (58) above, and [16]

$$\mathcal{P}_M^{(s,p)} = \frac{8\pi(d_{\text{eff}})^2}{\epsilon_0 c (n_\omega^f)^2 \lambda_\omega^2} \frac{(\mathcal{P}_\omega)^2}{w_0^2} L_f^2 T_\omega^{(s,\phi,p)}(\theta) T_{2\omega}^{(s,p)}(\theta) \quad (61)$$

The Fresnel factor for the fundamental is given for *s*-, *p*-, or mixed (ϕ) polarization, where ϕ is the angle of the fundamental beam polarization measured with respect to the direction of *s*-polarization. It is given by

$$T_\omega^{(s,\phi,p)} = \begin{cases} (t_\omega^s)^4 & s - \text{polarization} \\ (t_\omega^s)^2 (t_\omega^p)^2 & \phi - \text{polarization} \\ (t_\omega^p)^4 & p - \text{polarization} \end{cases} \quad (62)$$

where

$$t_\omega^s = \frac{2 \cos\theta}{\cos\theta + n_\omega^f \cos\theta_\omega} \quad (63)$$

and

$$t_{\omega}^p = \frac{2 \cos \theta}{n_{\omega}^f \cos \theta + \cos \theta_{\omega}} \quad (64)$$

The Fresnel factors for the second harmonic are given by

$$\begin{aligned} T_{2\omega}^s(\theta) &= \frac{8n_{2\omega}^f \cos \theta_{2\omega}^f}{(n_{2\omega}^f \cos \theta_{2\omega}^f + n_{2\omega}^s \cos \theta_{2\omega}^s)^2 (n_{2\omega}^f \cos \theta_{2\omega}^f + n_{\omega}^f \cos \theta_{\omega}^f)} \\ &\times \left(\frac{\cos \theta + n_{\omega}^f \cos \theta_{\omega}^f}{\cos \theta + n_{2\omega}^f \cos \theta_{2\omega}^f} \right) \left(\frac{2n_{2\omega}^s \cos \theta_{2\omega}^s}{\cos \theta + n_{2\omega}^s \cos \theta_{2\omega}^s} \right)^2 \end{aligned} \quad (65)$$

and

$$\begin{aligned} T_{2\omega}^p(\theta) &= \frac{8n_{2\omega}^f \cos \theta_{2\omega}^f}{(n_{2\omega}^f \cos \theta_{2\omega}^s + n_{2\omega}^s \cos \theta_{2\omega}^f)^2 (n_{2\omega}^f \cos \theta_{2\omega}^f + n_{\omega}^f \cos \theta_{\omega}^f)} \\ &\times \left(\frac{n_{\omega}^f \cos \theta + \cos \theta_{\omega}^f}{n_{2\omega}^f \cos \theta + \cos \theta_{2\omega}^f} \right) \left(\frac{2n_{2\omega}^s \cos \theta_{2\omega}^s}{n_{2\omega}^s \cos \theta + \cos \theta_{2\omega}^s} \right)^2 \end{aligned} \quad (66)$$

where the superscript *s* on refractive indices and angles designates substrate quantities.

For the reference, usually a slab of quartz,

$$(\mathcal{P}_{2\omega}^{\text{ref}})_{\text{out}} = \mathcal{P}_M^{\text{ref}} \frac{\sin^2 \psi_{\text{ref}}}{\psi_{\text{ref}}^2} \quad (67)$$

where

$$\mathcal{P}_M^{\text{ref}} = \frac{8\pi(d_{\text{eff}}^{\text{ref}})^2}{\epsilon_0 c (n_{\omega}^{\text{ref}})^2 \lambda_{\omega}^2} \left(\frac{(\mathcal{P}_{\omega})_{\text{in}}}{w_0} \right)_{\text{ref}}^2 L_{\text{ref}}^2 T_{\omega}^{\text{ref}}(\theta) T_{2\omega}^{\text{ref}}(\theta) \quad (68)$$

The Fresnel factor T_{ω}^{ref} for the appropriate polarization will be given by Eqs. (62)–(64) with the substitution $n_{\omega}^f \rightarrow n_{\omega}^{\text{ref}}$, etc. For $T_{2\omega}^{\text{ref}}$, $n_{2\omega}^f \rightarrow n_{2\omega}^{\text{ref}}$, $n_{2\omega}^s \rightarrow 1$, $\theta_{2\omega}^s \rightarrow \theta$, $\theta_{\omega,2\omega}^f \rightarrow \theta_{\omega,2\omega}^{\text{ref}}$, and the last substrate factor in Eqs. (65) and (66) is replaced by 1.

The second harmonic signals are measured as functions of the incident angle. The film is too thin for Maker fringes to be formed. Nevertheless, an angular dependence is obtained, with peaks occurring at the nonlinear Brewster angle. Fitting the peak envelopes for the sample and reference, the d_{eff} for the sample is found from

$$\begin{aligned} (d_{\text{eff}})^2 &= \left(\frac{n_{\omega}^f}{n_{\omega}^{\text{ref}}} \right)^2 \left(\frac{\mathcal{P}_{\omega}^{\text{ref}} / w_0^{\text{ref}}}{\mathcal{P}_{\omega} / w_0} \right)_{\text{in}}^2 \left(\frac{L_{\text{ref}}}{L_f} \right)^2 \frac{T_{\omega}^{\text{ref}}(0) T_{2\omega}^{\text{ref}}(0)}{T_{\omega}^{(s,p)}(\theta') T_{2\omega}^{(s,p)}(\theta')} \\ &\times \frac{\mathcal{P}_M^{(s,p)}(\theta')}{\mathcal{P}_M^{\text{ref}}(0)} (d_{\text{eff}}^{\text{ref}})^2 \end{aligned} \quad (69)$$

The angle θ' for the sample envelope is usually chosen to coincide with one of the peaks in the data.

The applied field, normal to the plane of the film, establishes a symmetry axis in the film. The point symmetry group is ∞mm . Therefore, poled polymer films, like 4 mm and 6 mm crystals, have nonzero tensor elements $d_{15} = d_{24}$, $d_{31} = d_{32}$, and d_{33} . When Kleinman symmetry holds, $d_{15} = d_{31}$, and $d_{15}/d_{33} = 1/3$. But with absorbing films Kleinman symmetry cannot be assumed. The ratio d_{15}/d_{33} should be checked experimentally, and if it does not equal 0.33, then d_{31} must be measured independently.

The three independent, nonzero tensor elements can be found by making three independent measurements. These can be done by setting the incident fundamental at given polarizations and detecting either *s*- or *p*-polarized second harmonic. The d_{eff} of the sample for given polarizations and angle of incidence can be obtained through the direction cosine transforms as discussed in Chapter 2. However, it must be remembered that here the fundamental and second harmonic waves are not collinear in the film. The first two direction cosines must relate to the angle of propagation of the fundamental, while the third direction cosine relates the direction of propagation of the second harmonic.

The three independent measurements correspond to the following polarizations:

$$\hat{e}_\omega = (0, 1, 0) \quad \hat{e}_{2\omega} = (\cos\theta_{2\omega}, 0, \sin\theta_{2\omega}) \quad (s \rightarrow p)$$

$$\hat{e}_\omega = (\cos\theta_\omega \sin\phi, 0, \sin\theta_\omega \sin\phi); \quad \hat{e}_{2\omega} = (0, 1, 0) \quad (\phi \rightarrow s)$$

$$\hat{e}_\omega = (\cos\theta_\omega, 0, \sin\theta_\omega); \quad \hat{e}_{2\omega} = (\cos\theta_{2\omega}, 0, \sin\theta_{2\omega}) \quad (p \rightarrow p)$$

where (x, y, z) are the laboratory coordinates with y perpendicular to the plane of incidence. Thus $(0, 1, 0)$ is *s*-polarization, etc. In the parentheses at the right, the first symbol corresponds to the polarization of the incident fundamental, and the second symbol corresponds to the detected second harmonic. The corresponding d_{eff} for each measurement is

$$d_{\text{eff}} = d_{31} \sin\theta_{2\omega} \quad (s \rightarrow p)$$

$$d_{\text{eff}} = d_{15} \sin 2\phi \sin\theta_\omega \quad (\phi \rightarrow s)$$

$$d_{\text{eff}} = 2d_{15} \cos\theta_\omega \sin\theta_\omega \cos\theta_{2\omega} + (d_{31} \cos^2\theta_\omega + d_{33} \sin^2\theta_\omega) \sin\theta_{2\omega} \quad (p \rightarrow p)$$

It should be remembered that ϕ is *not* the azimuthal angle, which is 0 in this case, but the angle of the fundamental polarization with respect to the y -axis. Normally, $\phi = 45^\circ$ is chosen to maximize the second harmonic signal. With d_{31} and d_{15} measured in $(s \rightarrow p)$ and $(\phi \rightarrow s)$ experiments, respectively, the third independent measurement $(p \rightarrow p)$ determines d_{33} .

Experimental. The most common approach to studying SHG from poled polymer films is to employ corona onset poling at elevated temperatures (COPET). The polymer film is normally spin coated onto an indium tin oxide (ITO) coated glass substrate. The film thickness ($\sim 1 \mu\text{m}$) is measured with a stylus profilometer. The film/substrate sample is mounted on a sample stage for *in situ* heating and poling during the SHG experiment.

A typical sample stage is illustrated in Fig. 11. The corona electrode can be either a needle perpendicular to, or a thin wire (or two) parallel to the sample. The electrode material is typically tungsten, and in the case of the needle electrode, one end is etched in, for example, hydrofluoric acid to obtain a fine tip. The tungsten electrode is situated $\sim 1\text{--}2 \text{ cm}$ from the sample. The sample is clamped on the stage with a clear aperture for the beam line and is heated by electrical elements embedded in the stage. A thermocouple monitors the sample temperature, and a thermal controller feedback circuit keeps the temperature at a preset value.

A high voltage ($\sim 5\text{--}10 \text{ kV}$), either positive or negative, is applied to the tungsten electrode with the ITO kept at ground potential. A corona discharge in the air deposits charge on the film; image charges on the ground plane set up a field across the film. Low lateral conductivity in the film keeps the current through local conduction paths of the film low. This is the advantage of COPET. In parallel plate (contact) poling, a large lateral conductivity limits the maximum poling field [17].

A typical procedure is to strike a discharge and keep the poling current to a prescribed level (e.g., $\sim 1 \mu\text{A}$). Reference [17] describes a technique for measuring the actual poling field using a dual-arm corona poling apparatus. It is important to use a high-conductivity substrate like BK-7 glass or Pyrex, not fused silica, to maintain a high poling field. The corona discharge is established, and then the temperature is raised to a value greater than T_g , where it is held constant for a few minutes and then lowered back to room temperature. Finally, the corona discharge is extinguished. Usually, the second harmonic signal is monitored during this entire process to observe the rise and decay of the second harmonic signal. The film absorbance may also be monitored, with a cw laser (both polarized and unpolarized), to study the order parameter of the film.

After the film nonlinearity has reached a steady state, the d -coefficients can be measured. A typical experimental configuration is shown in Fig. 12. The SHG from the corona poled film is measured as a function of angle of incidence, and then this measurement is repeated with a reference slab, e.g., quartz. These measurements are performed in the sample arm of the experiment. In the other arm a reference, e.g., quartz again, set at an angle for maximum SHG, is continuously monitored during the sample and reference angular SHG measurements. The angular dependent measurements are normalized to their corresponding (in time) reference arm measurements to compensate for laser power fluctuations and mode mixing enhancements of the second harmonic signal (see Section I.A).

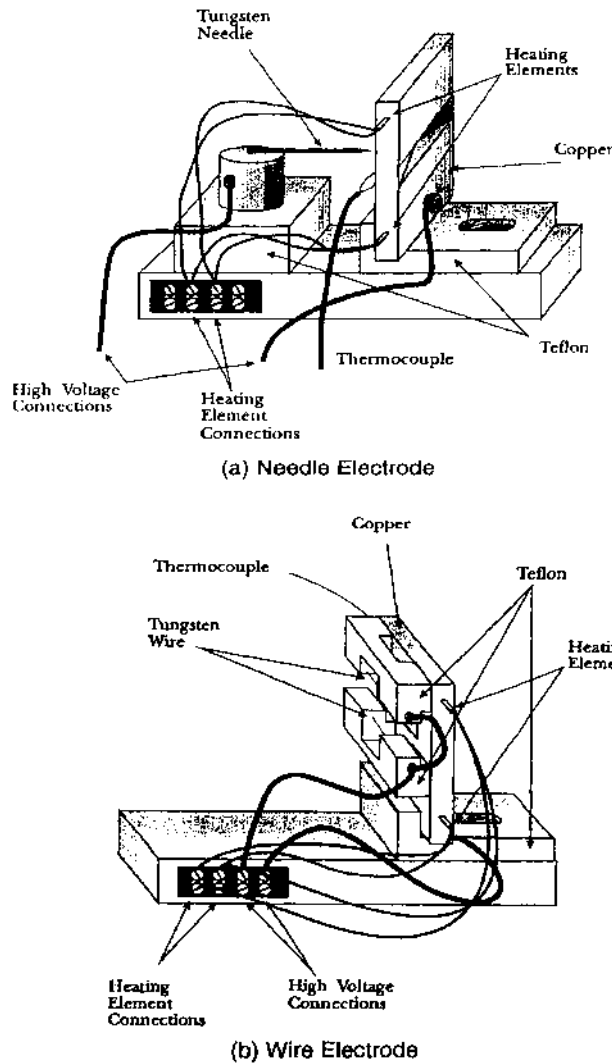


Figure 11 COPET sample stages. (a) Tungsten needle electrode sample stage. (b) Tungsten wire electrode sample stage.

The fundamental pump is usually derived from a Q-switched laser emitting 10–50 ns pulses of ~ 100 –200 mJ at a 10–50 Hz repetition rate. The beam is weakly focused to a 50–100 μm diameter spot at both the sample and the reference. The second harmonic power is detected with PMTs, and the signals are sent to boxcar

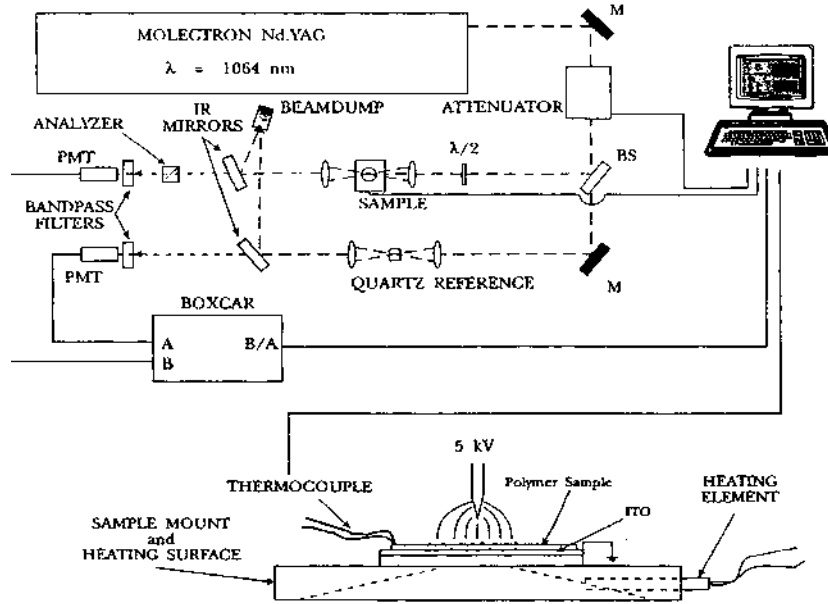


Figure 12 Typical experimental configuration for characterization of the second order nonlinear optical coefficients of corona-poled polymer films.

integrators for averaging (~ 10 pulses). The polarizer and analyzer are set appropriately for the d_{eff} desired from the measurement. An example of second harmonic data from a poled polymer film is given in Fig. 13

II. MOLECULAR COEFFICIENTS

A. EFISH

There has been considerable interest in developing organic materials with large nonlinear coefficients. As mentioned in the last section, the nonlinear coefficients in organic media is derived primarily from the individual molecular units. In organic crystals with weak molecular bonding [18],

$$\epsilon_0 \chi_{IJK}^{(2)} = \frac{N}{N_g} f_\omega^2 f_{2\omega} \sum_{l,m,n} \left(\sum_{s=1}^{N_g} (\hat{I} \cdot \hat{l})_s (\hat{J} \cdot \hat{m})_s (\hat{K} \cdot \hat{n})_s \right) \beta_{lmn} \quad (70)$$

where $(I, J, K) = (X, Y, Z)$ are crystal coordinates, and $(l, m, n) = (\xi, \eta, \zeta)$ are molecular coordinates. N_g is the number of equivalent sites s in the unit cell, and

$(\hat{l} \cdot \hat{l})_s$ etc. are direction cosines for site s , projecting the molecular coordinates onto the crystal coordinate system.

The key molecular nonlinear parameter is β_{lmn} , the first hyperpolarizability. The motive is to screen new organic materials for large β_{lmn} without the costly and difficult program of growing single organic crystals. In some cases, an ensemble of molecules will not form an acentric crystal because of the interaction of their permanent dipole moments (see Section 1.E). This places a restriction on the use of powder methods.

A convenient method of screening new materials is to place them in solution. However, a solution is centrosymmetric and hence will not produce a macroscopic $\chi^{(2)}$. The means of breaking the symmetry is to apply an external electric field to the solution. This produces an electric field induced second harmonic (EFISH).

All materials will produce an EFISH signal through their second molecular hyperpolarizability γ since EFISH is a third order nonlinear process. However, molecules that possess a permanent dipole moment μ will attempt to align with the applied dc field E_0 . In these cases, a measurement of the second harmonic will also yield the product $\mu \cdot \beta$. Therefore it is the vector part of β that is measured. Taking μ to be along the ζ -axis, this quantity is

$$\beta_\zeta = \beta_{\zeta\zeta\zeta} + \beta_{\zeta\zeta\xi} + \beta_{\zeta\xi\xi} \quad (71)$$

The element $\beta_{\zeta\zeta\zeta} = \beta_{CT}$ is the part of the hyperpolarizability along the charge transfer axis of the molecule. For molecules with strong electron donor and acceptor groups (at opposite ends of the molecule), β_{CT} accounts for most of β_ζ . In the following discussion, it will be understood that the quantity β means β_ζ .

Theory. In EFISH experiments, the fundamental is polarized along the direction of the applied dc field. Therefore the generated second harmonic will also be polarized along this direction, because of symmetry properties of an isotropic medium. The lowest order nonlinear response in isotropic systems is third order, so the nonlinear polarization at 2ω takes the simple form [19]

$$P_{2\omega} = \epsilon_0 \Gamma E_0 (A_\omega)^2 \quad (72)$$

$\Gamma = 3\chi_{zzzz}^{(3)}(-2\omega; 0, \omega, \omega)$ is the EFISH third order macroscopic susceptibility. It is related to the microscopic second hyperpolarizability by [19]

$$\epsilon_0 \Gamma = N f_0 (f_\omega)^2 f_{2\omega} \gamma' \quad (73)$$

where N is the number of molecules per unit volume, the f_s are local field factors (see below), and γ' is the effective second hyperpolarizability. It is given by an average over a Boltzmann molecular orientational distribution [20,21]:

$$\gamma' = \gamma + \frac{\mu \beta}{5k_B T} \quad (74)$$

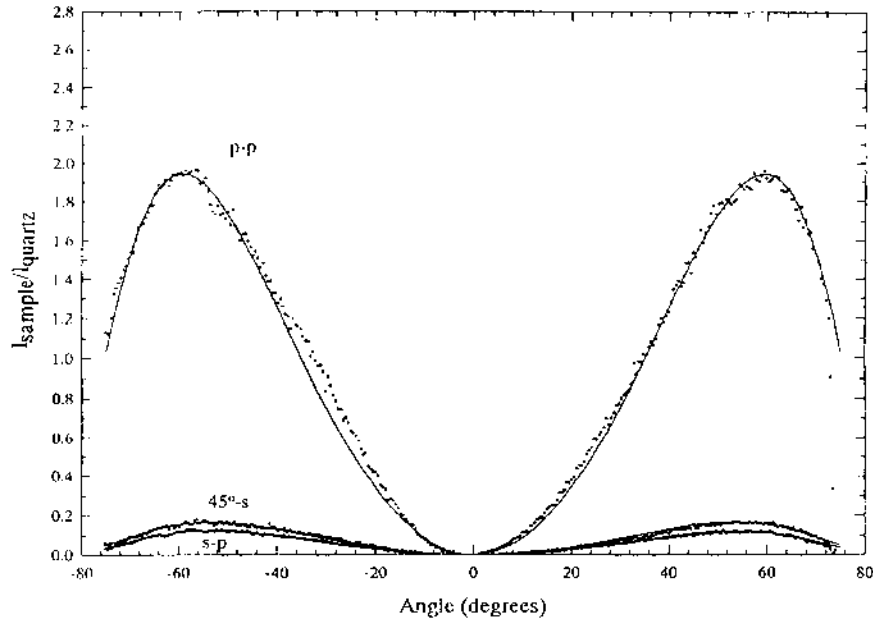


Figure 13 Example of poled polymer film SHG data for DANS in PMMA. The data is labeled by the fundamental second harmonic polarizations ($p-p$, $45^\circ-s$, $s-p$). The sample exhibits Kleinman symmetry ($d_{31} = d_{15}$, $d_{15} = 1/3d_{33}$).

where k_B is Boltzmann's constant (1.38×10^{-23} J/K), T is the temperature in kelvins (K), and $\gamma = \gamma_e + \gamma_v$ is the intrinsic second hyperpolarizability consisting of electronic and molecular vibrational parts, and is nonzero for all materials.

Experimentally, a uniform electric field must be applied to the liquid, for example, with parallel plate electrodes. As was pointed out by Levine and Bethea [20] and by Oudar [21], this cannot be done by simply immersing a pair of electrodes in the liquid. Although a large uniform field can be obtained in the interior region between the electrodes, near the edges of the electrodes the fringe fields become weak and eventually go to approximately zero a few electrode spacings away from the edges. In these regions, on either side of the electrodes (where the fundamental wave enters and exits the electrode region), the nonlinear polarization is essentially zero, so no bound second harmonic field is generated. With no bound field, no free field can be generated either. (See Chapter 2. It should be remembered that it is the free field that propagates to the far field and is detected.) Therefore, for measurable second harmonic, the liquid needs sharp

boundaries inside the electrodes, several electrode spacings away from the edges where the field is uniform.

The approach is to construct a cell with a wedge-shaped space, where the liquid will reside, bounded by windows (see Fig. 14). The wedge will be translated in a direction perpendicular to the incident fundamental beam to obtain Maker fringes as discussed in Section I.C. The cell windows are typically glass. The use of fused silica is discouraged since a small amount of residual order in this material will produce a measurable second harmonic even with no external field applied (i.e., far from the electrodes) [20]. The liquid/window boundaries should be well within the electrode region, several electrode spacings away from the edge of the electrodes.

Since the electrodes overlap the glass windows, there will be a bound second harmonic wave generated in the glass as well as in the liquid. The generated second harmonic that is measured is essentially due to the difference in the bound fields between the two media. For a weakly focused fundamental beam, the measured second harmonic power can be written as [21]

$$(P_{2\omega}^{\text{EFISH}})_{\text{out}} = P_M^{\text{EFISH}} \exp \left[- \left(\frac{2\alpha_\omega + \alpha_{2\omega}}{2} \right) L \right] (\sin^2 \psi + \sinh^2 \sigma) \quad (75)$$

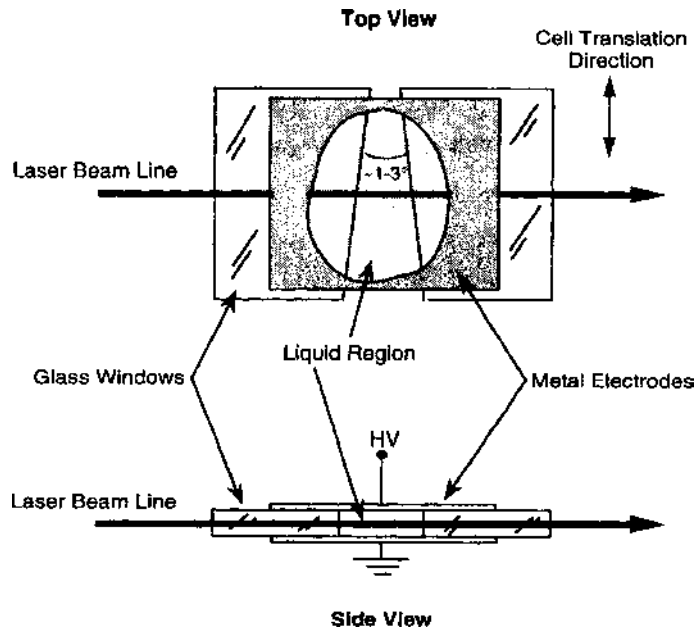


Figure 14 Example design of an EFISH wedge-shaped liquid cell configured with plane parallel electrodes.

where

$$\mathcal{P}_M^{\text{EFISH}} \propto \eta_{\text{EFISH}} (T_G \Gamma_G L_c^G - T_L \Gamma_L L_c^L)^2 E_0^2 \left(\frac{\mathcal{P}_\omega}{w_0} \right)_{\text{in}}^2 \quad (76)$$

$$\eta_{\text{EFISH}} = \left(\frac{2n_{2\omega}^G}{1 + n_{2\omega}^G} \right) \left(\frac{2}{1 + n_\omega^G} \right)^4 \left(\frac{1}{n_{2\omega}^G + n_{2\omega}^L} \right)^2 \quad (77)$$

$$T_G = \frac{n_\omega^G + n_\omega^L}{n_{2\omega}^G + n_\omega^G} \quad T_L = \left(\frac{2n_\omega^G}{n_\omega^G + n_\omega^L} \right)^2 \quad (78)$$

In the above equations it should be noted that the wedge angle θ_w , is small so $\cos\theta_w \approx 1$, and the measured power can be assumed independent of angle (so long as $n^G \approx n^L$ for both ω and 2ω). The superscripts and subscripts G and L signify glass and liquid quantities, respectively, and all other factors have been defined previously. It should be noted that the absorption coefficients as well as σ and ψ are liquid parameters.

A measurement is also performed on a reference wedge, typically quartz cut so that the d_{11} coefficient is dominant. The measured second harmonic power from the quartz, assumed to be in air with a small wedge angle, is expressed as

$$(\mathcal{P}_{2\omega}^Q)_{\text{out}} = \mathcal{P}_M^Q \sin^2 \psi_Q \quad (79)$$

where

$$\mathcal{P}_M^Q \propto \eta_Q (d_{11} L_c^Q)^2 \left(\frac{\mathcal{P}_\omega}{w_0} \right)_{\text{in}}^2 \quad (80)$$

$$\eta_Q = \frac{1}{[(n_\omega^Q + 1)^2 (n_{2\omega}^Q + 1)]^2} \left(\frac{1}{n_{2\omega}^Q + n_\omega^Q} \right)^2 \quad (81)$$

Equations (75) and (79) are fitted to the Maker fringe data to obtain coherence lengths and envelopes. An example of EFISH data is given in Fig. 15. The coherence length and third order susceptibility for the glass must be obtained from a separate experiment. Finally, Γ_L is found from, assuming that different fundamental intensities are used in the EFISH and the quartz reference measurements,

$$\begin{aligned} \Gamma_L &= \left(\frac{T_G L_c^G}{T_L L_c^L} \right) \Gamma_G \\ &\pm \left(\frac{\eta_Q}{\eta_{\text{EFISH}}} \right)^{1/2} \frac{(\mathcal{P}_\omega/w_0)_Q}{(\mathcal{P}_\omega/w_0)_{\text{EFISH}}} \left(\frac{\mathcal{P}_M^{\text{EFISH}}}{\mathcal{P}_M^Q} \right)^{1/2} \frac{1}{T_L} \frac{L_c^Q d_{11}^Q}{L_c^L E_0} \end{aligned} \quad (82)$$

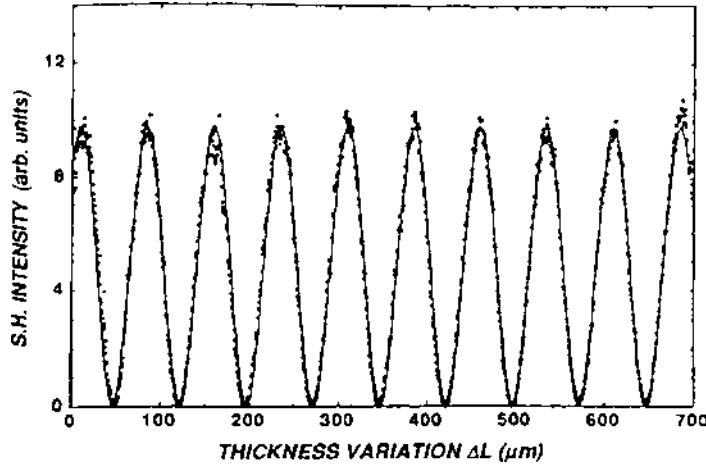


Figure 15 Example of Maker fringes measured in an EFISH experiment at $\lambda_{\omega} = 1318$ nm for a 10 wt% solution of 2-cyclooctylamino-5-nitropyridine in 1,4-dioxane. (From Ref. [24]).

In Eq. (82), the \pm sign comes from the fact that only the magnitude $(T_G \Gamma_G L_c^G - T_L \Gamma_L L_c^L)^2$ is measured. Experimentally, one can use several methods to determine the proper sign [20]. One method is to dilute the liquid with a linear liquid (e.g., a small nonpolar molecular liquid) and observe whether the second harmonic signal increases or decreases. One can also mix the liquid with a reference liquid for which the magnitude and sign of Γ_L is known (e.g., nitrobenzene) [20].

Once the macroscopic quantity Γ_L is found, one must proceed to determine the microscopic quantities. To do this, the local field factors must be known. Further complications arise when these factors, which depend on refractive indices and dielectric constants, become functions of the concentration of the nonlinear solute molecules. These come about due to solute–solute, solvent–solute, and solvent–solvent interactions. Singer and Garito [22] developed an infinite dilution extrapolation method to factor out these effects as well as reduce systematic errors associated with concentration dependent measurements.

For a two-component solution (solute, solvent), the macroscopic susceptibility is related to the microscopic parameters through

$$\epsilon_0 \Gamma_L = N_{sv} f_0^{sv} (f_{2\omega}^{sv})^2 f_{2\omega}^{sv} \gamma'_{sv} + N_{sl} f_0^{sl} (f_{2\omega}^{sl})^2 f_{2\omega}^{sl} \gamma'_{sl} \quad (83)$$

where sv = solvent, sl = solute, and

$$\gamma'_{sl} = \gamma_{sl} + \frac{\mu_{sl} \beta_{sl}}{5k_B T} \quad (84)$$

The desired quantity is β_{sl} of the solute molecules. The dc local field factor

depends on the linear static dielectric constant, and the optical local field factors depend on the refractive indices. Hence, in addition to the usual optical measurements, one must measure the dielectric constant and the molecular dipole moment.

For optical local field factors, dispersion can be ignored (i.e., $n_{2\omega} \approx n_\omega$). Therefore the local field factors for both ω and 2ω will be designated by f_∞ , where ∞ implies frequencies very large compared to dc. There exist two formalisms: Debye (for nonassociating liquids, e.g., no hydrogen bonding or other polarity) and Onsager (appropriate for polar liquids). In the Debye formalism,

$$f_0^{\text{sv}} = f_0^{\text{sl}} = f_{\text{sv}}^* = f_{\text{sl}}^* = \frac{\epsilon + 2}{3} \quad (85)$$

$$f_\infty^{\text{sv}} = f_\infty^{\text{sl}} = \frac{n^2 + 2}{3} \quad (86)$$

where ϵ and n are the static dielectric constant and refractive index, respectively, of the solution and hence are measurable. The parameter f^* is the local field factor associated with the permanent dipole moment (see below). In the Onsager formalism,

$$f_0^i = \frac{\epsilon(n_i^2 + 2)}{n_i^2 + 2\epsilon} \quad (87)$$

$$f_i^* = \frac{\epsilon(2\epsilon + 1)(n_i^2 + 2)}{3(n_i^2 + 2\epsilon)^2} \quad (88)$$

$$f_\infty^i = \frac{n^2(n_i^2 + 2)}{n_i^2 + 2n^2} \quad (89)$$

where $i = \{\text{sv}, \text{sl}\}$. Singer and Garito [22] have shown that mixed local field factors agree well with experiment, where f_0^i and f_i^* are given by the Onsager relations, and f_∞^i are given by the Debye relations.

For a two-component solution with polar molecules, the static dielectric constant is given by

$$\epsilon_0(\epsilon - 1) = N_{\text{sv}}\alpha_{\text{sv}}f_0^{\text{sv}} + \frac{N_{\text{sv}}\mu_{\text{sv}}^2 f_{\text{sv}}^*}{3k_B T} + N_{\text{sl}}\alpha_{\text{sl}}f_0^{\text{sl}} + \frac{N_{\text{sl}}\mu_{\text{sl}}^2 f_{\text{sl}}^*}{3k_B T} \quad (90)$$

where α_i are the linear microscopic polarizabilities. The number density can be expressed as $N_i = (\rho_i/M_i)N_A = (\rho w_i/M_i)N_A$, where ρ_i is the density of the component i in the solution, M_i is the molecular weight, and w_i is the weight fraction ($= m_i/m$, with m_i the mass of component i and m the total mass). N_A is Avogadro's number, and ρ is the total density of the liquid solution. With

a two-component solution, only the weight fraction w of the solute needs to be specified, since $1 - w$ is then the weight fraction of the solvent. Thus the static dielectric constant, as well as the refractive index, can be expressed as functions of the measurable quantities w and ρ .

Expanding Eq. (90) in a Taylor series about $w = 0$ and keeping terms to lowest order in w yields an expression for the infinite dilution extrapolation:

$$\begin{aligned} \frac{\rho_{sv} N_A}{\epsilon_0 M_{sl}} \left(\alpha_{sl} f_0^{sv} + \frac{\mu_{sl}^2 f_*^{sv}}{3k_B T} \right) &= \epsilon_{sv} - 1 + \left(\frac{\partial \epsilon}{\partial w} \right)_0 + (\epsilon_{sv} - 1) \frac{\rho_{sv}}{\rho^2} \left(\frac{\partial \rho}{\partial w} \right)_0 - (n_{sv}^2 - 1) \\ &\times \frac{1}{f_0^{sv}} \left(\frac{\partial f_0^{sv}}{\partial w} \right)_0 - (\epsilon_{sv} - n_{sv}^2) \frac{1}{f_*^{sv}} \left(\frac{\partial f_*^{sv}}{\partial w} \right)_0 \end{aligned} \quad (91)$$

From the Onsager relations:

$$\left(\frac{\partial f_0^{sv}}{\partial w} \right)_0 = \frac{n_{sv}^2 (n_{sv}^2 + 2)}{(n_{sv}^2 + 2\epsilon)^2} \left(\frac{\partial \epsilon}{\partial w} \right)_0 \quad (92)$$

$$\left(\frac{\partial f_*^{sv}}{\partial w} \right)_0 = [n_{sv}^2 (4\epsilon + 1) - 2\epsilon] \frac{n_{sv}^2 + 2}{3(n_{sv}^2 + 2\epsilon)^2} \left(\frac{\partial \epsilon}{\partial w} \right)_0 \quad (93)$$

For Debye liquids:

$$\left(\frac{\partial f_0^{sv}}{\partial w} \right)_0 = \left(\frac{\partial f_*^{sv}}{\partial w} \right)_0 = \frac{1}{3} \left(\frac{\partial \epsilon}{\partial w} \right)_0 \quad (94)$$

The subscripts 0 on the partial derivatives indicate $w = 0$, i.e., the extrapolation to infinite dilution.

In a similar way, the refractive index of the solution is expressed by

$$\epsilon_0 (n^2 - 1) = N_{sv} \alpha_{sv} f_\infty^{sv} + N_{sl} \alpha_{sl} f_\infty^{sl} \quad (95)$$

Performing the same analysis as above yields [22]

$$\begin{aligned} \frac{\rho_{sv} N_A}{\epsilon_0 M_{sl}} \alpha_{sl} f_\infty^{sv} &= 2n \left(\frac{\partial n}{\partial w} \right)_0 - (n_{sv}^2 - 1) \frac{\rho_{sv}}{\rho^2} \left(\frac{\partial \rho}{\partial w} \right)_0 - (n_{sv}^2 - 1) \\ &\times \left[\frac{1}{f_\infty^{sv}} \left(\frac{\partial f_\infty^{sv}}{\partial w} \right)_0 - 1 \right] \end{aligned} \quad (96)$$

From the Debye relations:

$$\left(\frac{\partial f_\infty^{sv}}{\partial w} \right)_0 = \frac{2}{3} n \left(\frac{\partial n}{\partial w} \right)_0 \quad (97)$$

In Eqs. (91) and (96), the two unknowns are α_{sl} and μ_{sl} . All other quantities are measurable or are constants. Hence α_{sl} is found from Eq. (96). This value is then used in Eq. (91) to find μ_{sl} .

It remains to determine the effective second hyperpolarizability γ'_{sl} of the solute before the first hyperpolarizability β_{sl} , can be found. This comes from an analysis of Eq. (83). Again, expanding in a Taylor series and keeping only terms to first order in w ,

$$\begin{aligned} \frac{\rho_{sv} N_A}{\epsilon_0 M_{sl}} f_0^{sv} (f_\infty^{sv})^3 \gamma'_{sl} = & \left(\frac{\partial \Gamma_L}{\partial w} \right)_0 - \Gamma_L^{sv} \frac{\rho_{sv}}{\rho^2} \left(\frac{\partial \rho}{\partial w} \right)_0 \\ & - \frac{\Gamma_L^{sv}}{\epsilon_0} \left\{ \frac{1}{f_0^{sv}} \left(\frac{\partial f_0^{sv}}{\partial w} \right)_0 + \frac{3}{f_\infty^{sv}} \left(\frac{\partial f_\infty^{sv}}{\partial w} \right)_0 - 1 \right\} \end{aligned} \quad (98)$$

The desired quantity, β_{sl} , can now be found from Eq. (84), assuming that γ_{sl} for the solute is known. There are two approaches. One is to ignore γ_{sl} , which is usually possible for highly conjugated molecules, since this quantity is small in comparison to the product $(\mu\beta)_{sl}$ [22]. The other approach is to obtain γ_{sl} , through another measurement [21,23] (e.g., four-wave mixing, third harmonic generation, etc.; see Chapter 7).

Experimental. The pertinent experimental quantities are measured in solution as a function of the solute weight fraction w , i.e., $\Gamma_L(w)$, $n(w)$, $\epsilon(w)$, and $\rho(w)$. The neat solvent values are given as $\Gamma_L^{sv} = \Gamma_L(0)$, $n_{sv} = n(0)$, $\epsilon_{sv} = \epsilon(0)$, and $\rho_{sv} = \rho(0)$. These quantities are plotted as functions of w and the data fitted to analytical functions (e.g., linear or quadratic [22] functions). Then the slopes are computed near $w = 0$ to find the infinite dilution factors: $(\partial \Gamma_L / \partial w)_0$, $(\partial n / \partial w)_0$, $(\partial \epsilon / \partial w)_0$, and $(\partial \rho / \partial w)_0$.

The solution dielectric constant ϵ can be measured using a capacitance bridge. The solution refractive index n can be measured by measuring the angular deviation of a laser beam passing through a solution-filled hollow glass prism.

Γ_L is measured by an experimental method nearly identical to the wedge Maker fringe method discussed above in Section I.C. The main difference is in the details of the EFISH cell.

The cell geometry was shown in Fig. 14. It consists of two thin ($\sim 1-3$ mm) glass pieces cut at small angles and placed together to form a small wedge ($\sim 1-3^\circ$) air space for the liquid. The liquid area should be adequately covered by a pair of plane electrodes (e.g., gold, stainless steel, etc., chosen so that no electrochemical reactions contaminate the liquid sample) placed on either side of the wedged windows. An open cell is often totally immersed in the liquid of interest so that no bubbles are trapped in the wedge region.

Voltage pulses of 1–10 kV (fields $\sim 10-50$ kV/cm) are applied to the cell with durations in the range of a few microseconds to a few milliseconds. Pulsed high voltage (HV) is used to avoid current flow in the liquid. These HV pulses are

synchronized with the Q-switched pulses from the incident laser. The laser pulses are typically a few millijoules in 10–50 ns.

The second harmonic pulses are detected with PMTs, and the signals are averaged in a boxcar integrator. The electronic instruments and components used in the experiment should be shielded from electromagnetic interference (EMI) generated by the HV pulses. The laser pulse should be timed to arrive at the EFISH cell at a time near the center of the HV pulse. By avoiding the rising and falling regions of the HV pulse, EMI in the detection electronics can be minimized.

The Maker fringes are fit to Eq. (75) to obtain the coherence length and envelope of the peak heights for the liquid. Γ_L is then determined with the help of Eq. (82). To use this equation, Γ_G must be known. This can be measured in a separate EFISH experiment on a single wedge-shaped piece of glass. The glass piece should be small enough that it is completely covered with the electrodes, its boundaries being several electrode spacings away from the electrode edges. Alternatively, one can take Γ_G from the literature. Bossherd et al. [24] have given the following values for BK-7 glass at three different wavelengths:

$$\Gamma_G(1064 \text{ nm}) = (3.58 \pm 0.05) \times 10^{-22} \text{ m}^2/\text{V}^2$$

$$\Gamma_G(1318 \text{ nm}) = (3.69 \pm 0.05) \times 10^{-22} \text{ m}^2/\text{V}^2$$

$$\Gamma_G(1907 \text{ nm}) = (3.86 \pm 0.05) \times 10^{-22} \text{ m}^2/\text{V}^2$$

They also give the following coherence lengths:

$$L_c^G(1064 \text{ nm}) = 20.56 \pm 0.03 \mu\text{m}$$

$$L_c^G(1318 \text{ nm}) = 30.00 \pm 0.04 \mu\text{m}$$

$$L_c^G(1907 \text{ nm}) = 39.12 \pm 0.04 \mu\text{m}$$

Finally, they measured the coherence lengths for quartz and found:

$$L_c^Q(1064 \text{ nm}) = 20.9 \pm 0.4 \mu\text{m}$$

$$L_c^Q(1318 \text{ nm}) = 30.2 \pm 0.6 \mu\text{m}$$

$$L_c^Q(1907 \text{ nm}) = 36.3 \pm 0.5 \mu\text{m}$$

Also, $d_{11}^Q = 0.4 \text{ pm/V}$ [24].

Finally, the pertinent microscopic quantities are obtained from the measured macroscopic quantities through Eqs. (91), (96), and (98). It is noted that in the literature the dipole moment is often quoted in Debye (D) units. For reference, 1D = $3.34 \times 10^{-30} \text{ C}\text{-m}$ (coulomb-meters).

Modified EFISH. Uemiya et al. [25] have reported a modified EFISH experiment in which the EFISH signal from the glass is eliminated. In their experiment, the sharp boundary for the liquid is obtained by placing the liquid sample between glass windows coated with ITO. The dc field is applied across the liquid, and the incident laser (*p*-polarized) propagates at an angle with respect to the field direction. Thus the field is strong and uniform across the entire path of the laser through the liquid (no fringe fields), and a detectable second harmonic is generated with no contribution from the glass.

The second harmonic is measured as the sample cell is rotated about an axis perpendicular to the dc field. The analysis is just like that for a plane parallel slab Maker fringe experiment. The nonlinear susceptibility now goes as $\Gamma_L \rightarrow \Gamma_L \sin^2 \theta_\omega$, where $n_\omega^L \sin \theta_\omega = \sin \theta$ with θ the incident angle of the laser.

Eliminating the contribution of Γ_G from the second harmonic measurement makes it easier to characterize very dilute solutions with nonpolar (i.e., $\beta = 0$) solvents. It also obviates the need to determine the sign of β for the solution. Measuring $\Gamma_L(w)$ allows one to use the infinite dilution extrapolation technique, and also yields Γ_{sv} by extrapolation to $w = 0$, which can be very small.

To calibrate the measurements, a reference liquid is used in the cell. Uemiya et al. [25] used nitrobenzene for which $\beta = 2.04 \times 10^{-30}$ esu = 7.57×10^{-51} C-m³/V², and $\mu = 4.07$ D = 1.36×10^{-29} C-m.

B. Hyper-Rayleigh Scattering

Although EFISH is a well established method for characterizing the first hyperpolarizability of organic molecules, it has some limitations. Among these are that the molecules must possess a permanent dipole moment, and they must not ionize in solution. These limitations cause some potentially interesting materials to be overlooked. In addition, its complexity (specialized cells, high-voltage pulses, Maker fringe analysis, etc.) makes it a somewhat arduous task for screening several materials. The newly developed technique of hyper-Rayleigh scattering (HRS) offers a method that alleviates some of these difficulties.

HRS is the scattering of light at frequency 2ω when a liquid sample is irradiated by light at frequency ω . This is a parametric frequency conversion process and does not involve two-photon fluorescence.

The objective of the HRS method is to determine the first hyperpolarizability β of molecules in solution by measuring the second harmonic scattered light as a function of concentration. The advantages of this technique are several: it does not require a dc applied field; it offers a means of measuring the nonvector part of β (i.e., where μ and the vector part of β make an arbitrary angle); the second harmonic scattered light is proportional to β^2 , so it does not require measuring (or neglecting) γ or μ ; it can use an internal solvent reference for calibration. One important implication of the fact that this method does not

require an external field is that it can be used to characterize nonpolar (e.g., octupolar) and ionic samples. It also has several disadvantages: the scattered second harmonic is weak and requires sensitive detection; it requires high fundamental intensity, hence it must be focused and the scattered second harmonic observed from the focal volume; the detection system is sensitive to this focal position, which can change with each solution measured because of differing refractive index; the high intensity used must not be so high that it introduces complications like stimulated Raman or Brillouin scattering, self-focusing, or dielectric breakdown in the liquid.

Theory. HRS is due to orientational fluctuations of asymmetric molecules in solution, which give rise to an average asymmetry, on a microscopic scale, in an isotropic liquid [26]. Thus the light scattered from such a system can have a component at the second harmonic of the incident light that, unlike ordinary scattering, depends only on the first hyperpolarizability of the solute molecules, and varies quadratically with the incident intensity.

Taking the fundamental wave to be polarized along the x -axis, and the HRS wave to be observed at 90° (along the y -axis), the i th component ($i = x$ or z) of the second harmonic intensity is given by [27]

$$I_{2\omega,i} = \frac{4\pi^2}{\epsilon_0^3 n_\omega^2 c \lambda_\omega^4} f_\omega^4 f_{2\omega}^2 I_\omega^2 \times \sum_m N_m \left[\sum_{jk} \sum_{j'k'} (\hat{j} \cdot \hat{e}_\omega)(\hat{k} \cdot \hat{e}_\omega)(\hat{j}' \cdot \hat{e}_\omega)(\hat{k}' \cdot \hat{e}_\omega) \langle \beta_{ijk} \beta_{ij'k'} \rangle \right]_m \quad (99)$$

where \hat{e}_ω is the unit vector for the polarization of the fundamental beam, and the angle brackets imply an average over molecular orientations, with β_{ijk} in the laboratory frame obtained from β_{lmn} in the molecular frame by a transformation using the direction cosines for the projection of the molecular axes onto the laboratory axes.

A typical experiment employs a linearly polarized fundamental wave (say along z), with the detected second harmonic polarized along the same direction. Then the only component of the hyperpolarizability tensor measured is $\langle \beta_{zzz}^2 \rangle$. For asymmetric conjugated π -electron systems, $\beta_{\zeta\zeta\zeta}$ is dominant, so $\langle \beta_{zzz}^2 \rangle \propto \beta_{\zeta\zeta\zeta}^2$ [26,27].

A linear detection system measures a signal $S_{2\omega} \propto I_{2\omega}$. So, for a two-component system (solute, solvent), one can write [26]

$$S_{2\omega} = G[N_{sv}(\beta_{\zeta\zeta\zeta}^2)_{sv} + N_{sl}(\beta_{\zeta\zeta\zeta}^2)_{sl}]I_\omega^2 \quad (100)$$

where the constant G accounts for the averages over direction cosines, electronic measuring instrument factors, and other constants. The basic assumption of

the measurements is that for dilute solutions, the refractive indices as well as the solvent number density N_{sv} do not change significantly with solute density. Then, a plot of the signal $S_{2\omega}$ as a function of N_{sl} yields a straight line with a slope b_1 and an intercept b_0 . Thus

$$(\beta_{\zeta\zeta\zeta}^2)_{sl} = \left(\frac{b_1}{b_0}\right) N_{sv} (\beta_{\zeta\zeta\zeta}^2)_{sv} = \left(\frac{b_1}{b_0}\right) \frac{\rho_{sv} N_A}{M_{sv}} (\beta_{\zeta\zeta\zeta}^2)_{sv} \quad (101)$$

With the solvent value of $\beta_{\zeta\zeta\zeta}$ known, this is used as an internal reference to determine that of the solute.

Heesink et al. [27] have studied HRS with an elliptically polarized fundamental wave. They show that by measuring depolarization ratios, e.g.,

$$D_{zz}^{zx} = \frac{I_{2\omega}(\hat{e}_\omega = \hat{z}, \hat{e}_{2\omega} = \hat{x})}{I_{2\omega}(\hat{e}_\omega = \hat{z}, \hat{e}_{2\omega} = \hat{z})} \quad (102)$$

and so on, information about ratios between hyperpolarizability tensor components (e.g., $\beta_{\zeta\zeta\zeta}/\beta_{\zeta\zeta\zeta}$), including their signs, can be found.

Experimental. A typical experimental configuration is shown in Fig. 16. A seed injected, Q-switched laser (~ 10 ns, 100 mJ/pulse, 10 Hz repetition rate) is used to pump the HRS cell. Seed injection is desirable for its smooth temporal profile, since intensity spikes in the pulse will be magnified quadratically in the HRS second harmonic signal [26]. The incident intensity is controlled by a half-wave plate polarizer combination. The desired input polarization is also selected by the polarizer. The incident fundamental intensity is monitored with a photodiode or energy meter.

The incident laser is focused into the sample liquid contained in a thermostatted cylindrical cell. The use of a long focal length lens avoids significant focal shifts with different solutions (i.e., different refractive indices) [26]. The focal region should stay within the focus of the condenser system. The incident intensity should be chosen to avoid stimulated Raman and Brillouin scattering, self-focusing, and dielectric breakdown, but large enough to obtain a detectable signal with a dynamic range of ~ 1000 .

The condenser system, consisting of a concave mirror, with its focus at the interaction focal volume, and a lens, is used to efficiently collect the scattered light. High pass cutoff and narrow bandpass (~ 5 nm) filters isolate the second harmonic frequency, which is detected with a PMT, and the signal passed to a gated integrator for averaging.

The data should be checked for a quadratic dependence on I_ω to verify that it is due to HRS. An example of HRS data is given in Fig. 17. The signal $S_{2\omega}$ is measured as a function of N_{sl} using a solvent with a well-characterized β . Clays and Persoons [26] have measured three solvents at 1064 nm with the following

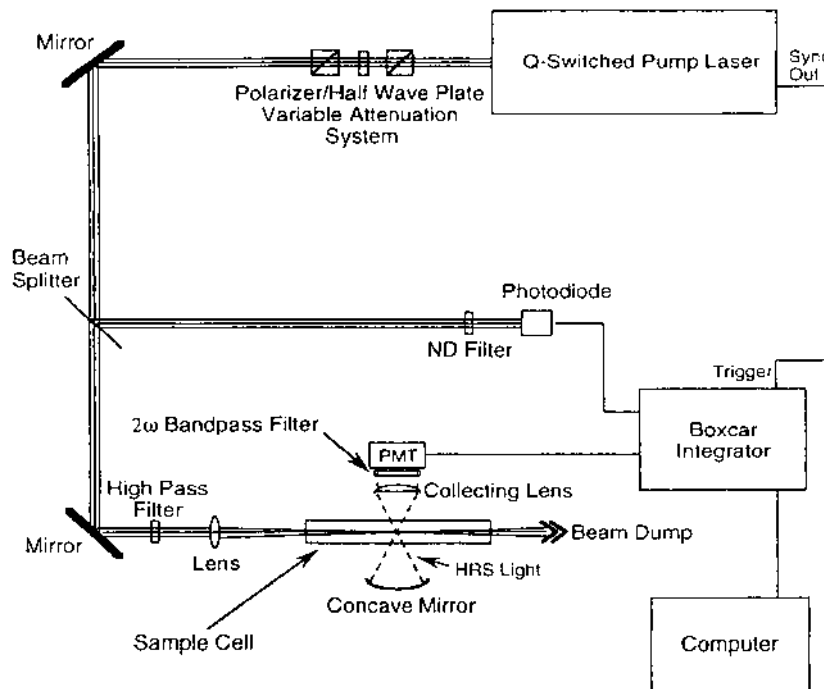


Figure 16 Typical experimental configuration for characterizing the first hyperpolarizability β of molecules in solution by the hyper-Rayleigh scattering method. (From Ref. [26]).

hyperpolarizabilities:

$$\text{Chloroform } \beta = -(0.49 \pm 0.05) \times 10^{-30} \text{ esu}$$

$$\text{Methanol } \beta = +(0.69 \pm 0.07) \times 10^{-30} \text{ esu}$$

$$\text{Nitromethane } \beta = +(1.82 \pm 0.33) \times 10^{-30} \text{ esu}$$

To obtain SI units, the conversion $\beta(\text{SI}) = [(3.71 \times 10^{-21})\beta(\text{esu})] \text{ C}\cdot\text{m}^3/\text{V}^2$ should be used.

C. Solvatochromatic Measurements

Theory. Solvatochromism provides a method for screening new nonlinear organic materials without performing any laser measurements. It is based on the two-level microscopic model of the first hyperpolarizability. When both

the fundamental and second harmonic frequencies are far from resonance with the first absorption band of a molecule, the infinite sum-over-states quantum perturbation expression for β can be reduced to a consideration of just two states: the ground and first excited states [24,28]. The result of this model is an expression for β in terms of other measurable microscopic quantities:

$$\beta_{\zeta\zeta} = \beta_{CT} = \frac{3}{2\hbar^2} \frac{\omega_{eg}^2}{(\omega_{eg}^2 - 4\omega^2)(\omega_{eg}^2 - \omega^2)} (\mu_e - \mu_g)(\mu_{eg})^2 \quad (103)$$

where $\hbar\omega_{eg}$ is the ground to excited state transition energy, μ_{eg} is the transition dipole moment, and μ_g and μ_e are the dipole moments of the ground and excited states, respectively. These quantities are all measurable.

The first two quantities can be measured with a spectrophotometer. The transition energy is related to the λ_{max} of the first absorption band ($\omega_{eg} = 2\pi c/\lambda_{max}$) in the UV-VIS absorption spectrum of the molecule. The transition dipole moment can be related to the area under the spectrum. With the molar extinction coefficient defined by $\epsilon_M(\omega) = -\log T(\omega)/CL$, where $T(\omega)$ is the measured spectral transmittance, C the concentration in moles/m³, and L the path length in m [24],

$$\int \epsilon_M(\omega) d\omega = \frac{2\pi^2 \omega_{eg}^{\sin} N_A f^2}{3 \ln 10 \epsilon_0 c h n} (\mu_{eg})^2 \quad (104)$$

where ω_{eg}^{\sin} is the transition frequency measured in the solvent of choice, h is Planck's constant, f is the Lorentz local field factor, and n is the refractive index of the solution (assuming no dispersion).

The ground state dipole moment is obtained by concentration dependent measurements of the static dielectric constant and the index of refraction with extrapolation to infinite dilution as discussed in Section II.A. The most critical measurement is that of the excited state dipole moment. It is obtained by measuring the solvatochromatic shift of λ_{max} of the solute in different solvents of varying polarity and dielectric constant. This shift is given by [24]

$$\begin{aligned} \hbar(\omega_{eg}^{\sin} - \omega_{eg}^v) = & -\frac{1}{4\pi\epsilon_0 a^3} \left[2(\mu_e^{sl} - \mu_g^{sl}) \mu_g^{sl} \left(\frac{\epsilon_{sv} - 1}{\epsilon_{sv} + 1} - \frac{n_{sv}^2 - 1}{n_{sv}^2 + 2} \right) \right. \\ & \left. + [(\mu_e^{sl})^2 - (\mu_g^{sl})^2] \frac{n_{sv}^2 - 1}{n_{sv}^2 + 1} \right] \end{aligned} \quad (105)$$

where ω_{eg}^v is the transition frequency in the vapor phase of the solute molecules, and $a = r_{sl} + \frac{1}{2}r_{sv}$ is the radius of an equivalent spherical volume for the solute

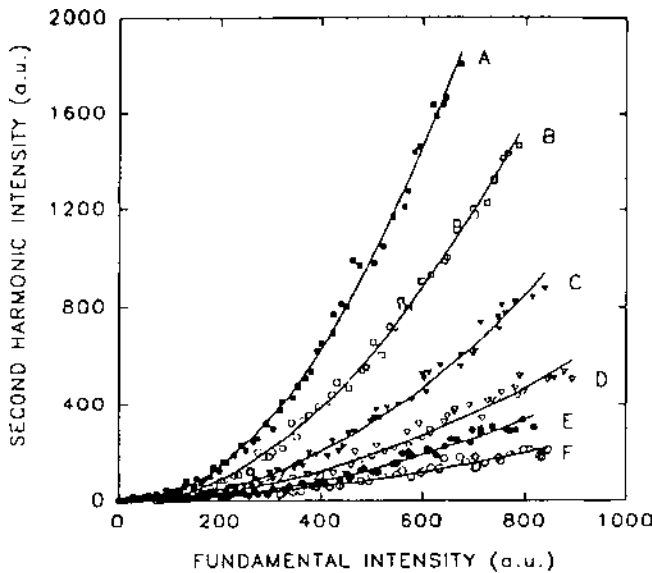


Figure 17 Example of HRS data for *para*-nitroaniline in methanol at 293K for differing number densities. (A) $92 \times 10^{-18} \text{ cm}^{-3}$. (B) $46 \times 10^{-18} \text{ cm}^{-3}$. (C) $23 \times 10^{-18} \text{ cm}^{-3}$. (D) $9.2 \times 10^{-18} \text{ cm}^{-3}$. (E) $4.6 \times 10^{-18} \text{ cm}^{-3}$. (F) $1.8 \times 10^{-18} \text{ cm}^{-3}$. The solid lines are curve fits to the data. The data display a quadratic dependence on $I_{2\omega}$. (From Ref. 26).

molecules with

$$r_{\text{sl}} = \left(\frac{3M_{\text{sl}}}{4\pi N_A \rho_{\text{sl}}} \right)^{1/3} \quad r_{\text{sv}} = \left(\frac{3M_{\text{sv}}}{4\pi N_A \rho_{\text{sv}}} \right)^{1/3} \quad (106)$$

for the solute and solvent molecules, respectively.

Experimental. The absorption spectrum of the solute–solvent system, for which β_{CT} of the solute molecules is desired, is measured in a standard way using a spectrophotometer. The neat solvent in an identical cuvette should be measured as a background to obtain a baseline for the spectral scan. The λ_{max} can be read directly from the spectrum, while to obtain μ_{eg} , the area under the spectral molar extinction coefficient curve must be measured. This can be done numerically, or by assuming a Lorentzian shape and measuring the peak $\varepsilon_{\text{M}}^{\text{peak}}$ and the width $\Delta\omega_{\text{FWHM}}$ of the curve, and then determining the area analytically [area = $\frac{1}{2}\pi(\Delta\omega)_{\text{FWHM}}\varepsilon_{\text{M}}^{\text{peak}}$].

The ground state dipole moment is found through the experimental and analytical techniques discussed under EFISH (see Section II.A). Finally, the excited state dipole moment is found by measuring the absorption spectrum for

the solute in several different solvents of varying polarity and dielectric constant. The dielectric constant and refractive index for each solvent must be known or measured. Three independent measurements are sufficient to determine the three unknowns μ_e^{sl} , μ_g^{sl} , and ω_{eg}^v . The value of μ_g^{sl} can be checked against capacitance bridge measurements for accuracy. Overdetermining the data with additional solvent shift measurements improves the accuracy [24].

One of the largest sources of error in the solvatochromic method is in the assumption of the equivalent radius a for the solute molecule since it enters Eq. (105) as a cubed value. For long conjugated molecules, the assumption of an equivalent sphere is probably inadequate, and the solvatochromic method will work better for small, nearly spherical molecules [24]. Although its accuracy is not as good generally as EFISH or HRS, it is useful for screening new organic materials of comparable size.

REFERENCES

1. M. Born and E. Wolf, *Principles of Optics*, 5th ed., Pergamon Press, New York, 1975, p. 702.
2. F. Zernike and J. E. Midwinter, *Applied Nonlinear Optics*, John Wiley, New York, 1973, p. 17 (see also references therein).
3. S. E. Kurtz, Measurement of nonlinear optical susceptibilities. *Quantum Electronics*, Vol I, Part A, (H. Rabin, and C. L. Tang, eds.), Academic Press: New York, pp. 209–281.
4. G. D. Boyd and D. A. Kleinman, Parametric Interactions of Focused Gaussian Light Beams, *J. Appl. Phys.* 39:3597 (1968).
5. G. D. Boyd, A. Ashkin, J. M. Dziedzic, and D. A. Kleinman, Second-harmonic generation of light with double refraction, *Phys. Rev.* 137:A1305 (1965).
6. R. L. Byer and S. E. Harris, Power and bandwidth of spontaneous parametric emission, *Phys. Rev.* 168:1064 (1968).
7. P. D. Maker, R. W. Terhune, M. Nisennoff, and C. M. Savage, Effects of dispersion and focusing on the production of optical harmonics, *Phys. Rev. Lett.* 8:21 (1962).
8. J. Jerphagnon and S. E. Kurtz, Maker fringes: A detailed comparison of theory and experiment for isotropic and uniaxial crystals, *J. Appl. Phys.* 41:1667 (1970).
9. S. X. Dou, M. H. Jiang, Z. S. Shao, and X. T. Tao, Maker fringes in biaxial crystals and the nonlinear optical coefficients of thiosemicarbazide cadmium chloride monohydrate, *Appl. Phys. Lett.* 54:1101 (1989).
10. P. Pavlides and D. Pugh, General theory of maker fringes in crystals of low symmetry, *J. Phys.: Condens. Matter* 3:967 (1991).
11. S. K. Kurtz and T. T. Perry, A powder technique for the evaluation of nonlinear optical materials, *J. Appl. Phys.* 39:3798 (1968).
12. N. Bloembergen and P. S. Pershan, Light waves at the boundary of nonlinear media, *Phys. Rev.* 128:606 (1962).

13. M. Kiguchi, M. Kato, M. Okunaka, and Y. Taniguchi, New method of measuring second harmonic generation efficiency using powder crystals, *Appl. Phys. Lett.* 60:1933 (1992).
14. Y. Hase, K. Kumata, S. S. Kano, M. Ohashi, T. Kondo, R. Ito, and Y. Shiraki, New method for determining the nonlinear optical coefficients of thin films, *Appl. Phys. Lett.* 61:145 (1992).
15. M. G. Kuzyk, K. D. Singer, H. E. Zahn, and L. A. King, Second-order nonlinear-optical tensor properties of poled films under stress, *J. Opt. Soc. Am. B* 6:742 (1989).
16. L. M. Hayden, G. F. Sauter, F. R. Ore, P. L. Pasillas, J. M. Hoover, G. A. Lindsey and R. A. Henry, Second-order nonlinear optical measurements in guest-host and sidechain polymers, *J. Appl. Phys.* 68:456 (1990).
17. A. Knoesen, N. E. Molau, D. R. Yankelevich, M. A. Mortazavi, and H. Dienes, Corona-poled nonlinear polymeric films: in situ electric field measurement, characterization and ultrashortpulse applications, *Inl. J. Nonlinear Opt. Phys.* 1:73 (1992).
18. P. N. Prasad and D. J. Williams, *Introduction to Nonlinear Optical Effects in Molecules and Polymers*, John Wiley, New York, 1991, pp. 60–61.
19. C. G. Bethea, Experimental technique of dc induced shg in liquids: measurement of the nonlinearity of CH_2I_2 , *Appl. Opt.* 14:1447 (1975).
20. B. F. Levine and C. G. Bethea, Second and third order hyperpolarizabilities of organic molecules, *J. Chem. Phys.* 63:2666 (1975).
21. J. L. Oudar, Optical nonlinearities of conjugated molecules. stilbene derivatives and highly polar aromatic compounds, *J. Chem. Phys.* 67:446 (1977).
22. K. D. Singer and A. F. Garito, Measurements of molecular second order optical susceptibilities using dc induced second harmonic generation, *J. Chem. Phys.* 75:3572 (1981).
23. L.-T. Chang, W. Tam, S. H. Stevenson, G. R. Meredith, G. Rikken, and S. R. Marder, Experimental investigations of organic molecular nonlinear optical polarizabilities. 1. methods and results on benzene and stilbene derivatives, *J. Phys. Chem.* 95:10632 (1991).
24. Ch. Bossherd, G. Knöpfle, P. Prêtre, and P. Günter, Second-Order Polarizabilities of Nitropyridine Derivatives Determined with Electric-Field-Induced Second-Harmonic Generation and a Solvatochromic Method: A Comparative Study, *J. Appl. Phys.* 71:1594 (1992).
25. T. Uemiya, N. Uenishi, and S. Umegaki, Modified method of electricfield induced secondharmonic generation, *J. Appl. Phys.* 73:12 (1993).
26. K. Clays and A. Persoons, Hyper-Rayleigh scattering in solution, *Rev. Sci. Instrum.* 63:3285 (1992).
27. G. L. T. Heesink, A. G. T. Ruiter, N. F. van Hulst, and B. Bölger, Determination of hyperpolarizability tensor components by depolarized hyper rayleigh scattering, *Phys. Rev. Lett.* 71:999 (1993).
28. M. S. Paley, J. M. Harris, H. Looser, J. C. Baumert, G. C. Bjorklund, D. Jundt, and R. J. Twieg, A solvatochromatic method for determining secondorder polarizabilities of organic molecules, *J. Org. Chem.* 54:3774 (1989).

5

Properties of Selected Second Order Nonlinear Optical Materials

This chapter presents data for several second order materials. Sections I and II give nonlinear optical coefficients for inorganic and organic crystals, respectively. First hyperpolarizability data for selected organic molecules are given in Section III. This chapter does not contain detailed refractive index dispersion data, absorption data, or other physical parameters of materials important for several applications (such as thermooptic coefficients, two-photon absorption coefficients, thermal conductivities, etc.). Two excellent sources containing this type of information in table, chart, and page formats are S. Singh [23] and V. G. Dmitriev, G. G. Gurzadyan, and D. N. Nikogosyan [176].

I. INORGANIC CRYSTALS

Table 1 gives d -coefficients as well as refractive index data for several selected inorganic crystals. Both uniaxial and biaxial crystals are included. The materials are presented in alphabetical order.

II. ORGANIC CRYSTALS

Table 2 gives d -coefficients as well as refractive index data for several selected organic crystals. Both uniaxial and biaxial crystals are included. The materials are presented in alphabetical order.

Table 1 Second-Order Nonlinear Optical Coefficients of Some Selected Inorganic Crystals

Material	Abbr.	Symmetry class λ_{ω} (nm)	n_o	n_{2o}	d (pm/V)	Ref.
Aluminum nitride		6mm	1064 $n^o = 1.431$ $n^e = 1.447$	$n^o = 1.445$ $n^e = 1.463$	$d_{33} = 7.4$	[9,10]
Ammonium deuterium arsenate	AD*A	$\bar{4}2m$	1064 $n^o = 1.552$ $n^e = 1.506$	$d_{33} = 8.0$ $d_{36} = 0.40$	$d_{31} = 0.2$	[10,1]
Ammonium dihydrogen arsenate	ADA	$\bar{4}2m$	1064 $n^o = 1.555$ $n^e = 1.508$	$d_{36} = 0.43$	$d_{33} = 8.0$	[1]
Ammonium deuterium phosphate	AD*P	$\bar{4}2m$	1064 $n^o = 1.505$ $n^e = 1.466$	$d_{36} = 0.52$	$d_{31} = 0.2$	[2]
Ammonium dihydrogen phosphate	ADP	$\bar{4}2m$	1064 $n^o = 1.507$ $n^e = 1.468$	$d_{36} = 0.53$	$d_{33} = 8.0$	[3]
Antimony niobate		mm2	1058	$d_{32} = 4.7$	$d_{32} = 4.7$	[8]
Antimony tantalate		mm2	1058	$d_{32} = 4.1$	$d_{32} = 4.1$	[8]
Barium–sodium borate		mm2	1064 $n_X = 2.257$ $n_Y = 2.257$	$d_{31} = -13.2$ $d_{33} = -18.2$	$n_X = 2.368$ $n_Y = 2.367$	[7]
β -Barium borate	BBO	3m	1064 $n^o = 1.655$ $n^e = 1.543$	$d_{11} = 1.6$ $d_{22} = 2.1$	$n_Z = 2.250$ $n^o = 1.675$ $n^e = 1.556$	[4]
β -Barium borate	BBO	3m	1064 $n^o = 1.6544$ $n^e = 1.5422$	$d_{31} = 0.15$	$d_{22} = 2.24$ $d_{22} = 2.2;$	[164]
β -Barium borate	BBO	3m	1064 $n^o = 1.6501$ $n^e = 1.5402$	$d_{31} = 0.15$	$d_{31} = 2.0$ (type I); $d_{31} = 1.4$ (type II)	[165]
β -Barium borate	BBO	3m	1319	$d_{22} = 1.87-1.91$	$d_{22} = 1.87-1.91$	[164]
β -Barium borate	BBO	3m	1313 $n^o = 1.6661$ $n^e = 1.5492$	$d_{22} = 1.9;$ $d_{31} = 1.7$ (type I); $d_{31} = 1.3$ (type II)	$d_{22} = 1.9;$ $d_{31} = 1.7$ (type I); $d_{31} = 1.3$ (type II)	[165]

β -Barium borate	BBO	3m	852	$n^o = 1.6591$; $n_e = 1.6878$ $n^e = 1.5447$ $n^e = 1.5643$	$d_{22} = 2.3$; $d_{eff} = 2.0$ (type I); $d_{eff} = 1.2$ (type II)	[165]
β -Barium borate	BBO	3m	532	$n^o = 1.6743$; $n_o = 1.7574$ $n^e = 1.5548$ $n^e = 1.6129$	$d_{22} = 2.6$; $d_{eff} = 1.6$ (type I); $d_{eff} = 0.04$ (type II)	[165]
Beryllium sulfate		$\bar{4}2m$	1064	$n^o = 1.463$; $n^o = 1.475$ $n^e = 1.426$ $n^e = 1.435$	$d_{36} = 0.25$	[6]
Cadmium gallium sulfide		$\bar{4}$	1064	2.327	2.453	$d_{36} = 25.6$
Cadmium germanium arsenide		$\bar{4}2m$	10,600	$n^o = 3.505$; $n^o = 3.530$ $n^e = 3.591$ $n^e = 3.621$	$d_{36} = 235$	[3,12]
Cadmium germanium phosphide		$\bar{4}2m$	10,600	3.142	3.198	$d_{36} = 162$
Cadmium selenide		6mm	10,600	$n^o = 2.427$; $n^o = 2.462$ $n^e = 2.445$ $n^e = 2.482$	$d_{15} = 18$	[3,13]
Cadmium sulfide		6mm	1064	2.34	2.65	$d_{15} = 44.0$; $d_{31} = 40.2$;
Cadmium telluride		$\bar{4}3m$	10,600	2.69	2.71	$d_{33} = 77.9$
Cesium deuterium phosphate	CD*P	$\bar{4}2m$	1064	$n^o = 1.550$; $n^o = 1.569$ $n^e = 1.534$ $n^e = 1.550$	$d_{14} = 168$ $d_{36} = 0.40$	[17] [11]
Cesium dihydrogen phosphate	CDP	$\bar{4}2m$	1064	$n^o = 1.551$; $n^o = 1.573$ $n^e = 1.536$ $n^e = 1.552$	$d_{36} = 0.40$	[11]
$\text{CsLiB}_6\text{O}_{10}$	CLBO	$\bar{4}2m$	1064	$n^o = n^o = 1.48501$; $n^e = 1.49824$ $= 1.43507$ $= 1.44506$	$d_{36} = 0.7$; $d_{eff} = 0.38$ (type I); $d_{eff} = 0.67$ (type II)	[166]

(continued)

Table 1 Continued

Material	Abbr.	Symmetry class	λ_{ω} (nm)	n_{ω}	$n_{2\omega}$	d (pm/V)	Ref.
CsLiB ₆ O ₁₀	CLBO	$\bar{4}2m$	852	$n^o = 1.48848; n^e = 1.43741$	$n^o = 1.50492; n^e = 1.45177$	$d_{14} = 0.69;$ $d_{36} = 0.83;$ $d_{\text{eff}} = 0.48$ (type I); $d_{\text{eff}} = 0.74$ (type II)	[166]
CsLiB ₆ O ₁₀	CLBO	$\bar{4}2m$	532	$n^o = 1.49824; n^e = 1.44506$	$n^o = 1.54584; n^e = 1.48456$	$d_{36} = 0.92;$ $d_{\text{eff}} = 0.92$ (type I)	[166]
Cesium titanyl arsenate, CsTiOAsO ₄	CTA	mm2	1064	$n_X = 1.850;$ $n_Y = 1.865;$ $n_Z = 1.920$	$n_X = 1.899;$ $n_Y = 1.916;$ $n_Z = 1.988$	$d_{31} = 2.1;$ $d_{32} = 3.4;$ $d_{33} = 18.1$	[18,49]
Cinnabar, HgS		32	10,600	$n^o = 2.594;$ $n^e = 2.845$	$n^o = 2.628;$ $n^e = 2.888$	$d_{11} = 50.2$	[16]
Copper gallium arsenide		$\bar{4}2m$	10,600	2.695	2.722	$d_{36} = 44.2$	[20]
Copper gallium sulfide		$\bar{4}2m$	10,600	2.436	2.475	$d_{36} = 14.5$	[19]
Copper indium sulfide		$\bar{4}2m$	10,600	2.531	2.558	$d_{36} = 10.6$	[19]
Fused silica (polished glass)			1064			$d_{33} = 0.185$	[21]
Gadolinium molybdate		mm2	1064			$d_{15} = -2.62;$ $d_{24} = 2.58;$ $d_{31} = -2.49;$ $d_{33} = -0.044;$	[23]
Gallium antimonide		$\bar{4}3m$	10,600	3.8	3.82	$d_{36} = 2.42$	[24]
Gallium arsenide		$\bar{4}3m$	10,600	3.27	3.30	$d_{14} = 628$ $d_{14} = 368.7$	[25]

Gallium phosphide	$\bar{4}3m$	1064	3.1	3.51	$d_{14} = 147 - 220$	[14]
Gallium selenide	$\bar{6}2m$	10,600	$n^o = 2.814;$ $n^e = 2.439$	$n^o = 2.834;$ $n^e = 2.460$	$d_{22} = 54.4$	[3,22]
Hexagonal silicon carbide, α -SiC		1064			$d_{31} = \pm 2.51;$ $d_{33} = \pm 25.1$	[26]
Indium antimonide	$\bar{4}3m$	10,600	3.955	3.54	$d_{14} = 1634$	[29]
Indium arsenide	$\bar{4}3m$	10,600	3.49	4.24	$d_{14} = 419$	[25]
Indium phosphide	$\bar{4}3m$	1058	3.44	4.24	$d_{14} = 143.5$	[28]
α -Iodic acid, α -HIO ₃	222	1065	$n_X = 1.951;$ $n_Y = 1.928;$ $n_Z = 1.813$	$n_X = 2.012;$ $n_Y = 1.983;$ $n_Z = 1.855$	$d_{36} = 4.1$	[29]
LaCa ₄ O (BO ₃) ₃	LaCOB	m	1064	—	—	
Lead niobate	mm2		1064		$d_{12} = 0.26 \pm 0.04;$ $d_{32} = 1.69 \pm 0.17;$ $d_{\text{eff}} = 0.52 \pm 0.05$	[167]
Lithium indium sulfide	mm2		10,600		$d_{15} = 5.9;$ $d_{24} = -5.4;$ $d_{31} = 6.5;$ $d_{32} = -5.9;$ $d_{33} = -8.9$	[33]
Li _{0.96} In _{1.06} S _{1.98}	mm2		5000	—	$d_{31} = 9.9;$ $d_{32} = 8.6;$ $d_{33} = 15.8$	[34]
Li _{0.86} In _{1.04} S _{1.98}	mm2		5000	—	$d_{\text{eff}} = 3.4 \pm 0.2$ (type II)	[168]
				—	$d_{\text{eff}} = 3.2 \pm 0.2$ (type II)	[168]

(continued)

Table 1 Continued

Material	Abbr.	Symmetry class	λ_{o} (nm)	n_{o}	$n_{2\text{o}}$	d (pm/V)	Ref.
Lithium iodate	6	1064	$n^{\text{o}} = 1.857;$ $n^{\text{e}} = 1.717$	$n^{\text{o}} = 1.898;$ $n^{\text{e}} = 1.748$	$d_{15} = -5.53;$ $d_{31} = -7.11;$ $d_{33} = -7.02$	[3]	
Lithium iodate	6	1319	—	—	$d_{31} = 3.90$	[164]	
Lithium iodate	6	1064	—	—	$d_{14} = 0.19 \pm 0.06;$ $d_{31} = 4.2 \pm 0.3$	[169]	
Lithium iodate	6	806	—	—	$d_{31} = 5.23 \pm 0.52$	[164]	
		1318			$d_{31} = -6.82;$ $d_{33} = -6.75$	[31]	
		2120			$d_{31} = -6.43;$ $d_{33} = -6.41;$ $d_{31} = -8.41$		
		694	$n^{\text{o}} = 1.875;$ $n^{\text{e}} = 1.730$	$n_X = 1.367;$ $n_Y = 1.468;$ $n_Z = 1.504$	$d_{31} = 0.4;$ $d_{32} = -1.16;$ $d_{33} = 1.68$	[3,32]	
Lithium formate	LFM	mm2	1064	$n_X = 1.359;$ $n_Y = 1.468;$ $n_Z = 1.504$	$d_{31} = 0.4;$ $d_{32} = -1.16;$ $d_{33} = 1.68$		
Lithium niobate	3m	1064	$n^{\text{o}} = 2.234;$ $n^{\text{e}} = 2.155$	$n^{\text{o}} = 2.325;$ $n^{\text{e}} = 2.233$	$d_{31} = -5.95;$ $d_{33} = -34.4$		
		1150			$d_{31} = -5.77$	[31]	
		1318			$d_{33} = -33.4$		
		2120			$d_{33} = -31.8$		
					$d_{32} = -29.1$		

Table 1 Continued

Material	Abbr.	Symmetry class	λ_{ω} (nm)	n_{o}	$n_{2\omega}$	d (pm/V)	Ref.
Potassium dihydrogen phosphate	KDP	42m	1064			$d_{36} = 0.270$	[164]
Potassium dihydrogen phosphate	KDP	$\bar{4}2\text{m}$	1064			$d_{14} = 0.387 \pm 0.03;$ $d_{\text{eff}} = 0.375 \pm 0.04$	[169]
Potassium dihydrogen phosphate	KDP	$\bar{4}2\text{m}$	1319	$n^{\text{o}} = 2.208;$ $n^{\text{e}} = 2.112$	$n^{\text{o}} = 2.328;$ $n^{\text{e}} = 2.197$	$d_{36} = 0.227$ (type I)	[164]
Potassium lithium niobate	KDP	4mm	1064	$n^{\text{o}} = 2.220;$ $n^{\text{e}} = 2.119$	$n_X = 2.381;$ $n_Y = 2.323;$ $n_Z = 2.203$	$d_{15} = -17.1;$ $d_{24} = -16.5;$ $d_{31} = -18.3;$ $d_{32} = -15.8;$ $d_{33} = -27.4$	[40]
Potassium niobate	mm2		1064	$n_X = 2.258;$ $n_Y = 2.220;$ $n_Z = 2.119$	$n_X = 2.381;$ $n_Y = 2.323;$ $n_Z = 2.203$	$d_{15} = -17.1;$ $d_{24} = -16.5;$ $d_{31} = -18.3;$ $d_{32} = -15.8;$ $d_{33} = -27.4$	[40]
Potassium pentaborate	KB5	mm2	1064	$n_X = 1.479;$ $n_Y = 1.427;$ $n_Z = 1.414$	$n_X = 1.489;$ $n_Y = 1.436;$ $n_Z = 1.423$	$d_{31} = 0.046;$ $d_{36} = 0.003$	[45]
Deuterated potassium pentaborate	DKB5	mm2		$n_X = 1.413;$ $n_Z = 1.479$	$n_X = 1.422;$ $n_Z = 1.489$	$d_{31} = 0.046;$ $d_{36} = 0.004$	[45]
Potassium sodium barium niobate		4mm	1064	2.260	2.264	$d_{31} = 14$	[47]
Potassium titanyl arsenate	KTA	mm2	1064	$n_X = 1.782;$ $n_Y = 1.789;$ $n_Z = 1.868$	$n_X = 1.823;$ $n_Y = 1.835;$ $n_Z = 1.930$	$d_{31} = 4.2;$ $d_{32} = 2.8;$ $d_{33} = 16.2$	[39]

Potassium titanyl phosphate	KTP	mm2	880	$d_{15} = 3.92;$ $d_{24} = 2.04;$ $d_{31} = 4.74;$ $d_{32} = 2.76;$ $d_{33} = 18.5$	[41]
			1064	$n_x = 1.738;$ $n_y = 1.745;$ $n_z = 1.830$	$n_x = 1.779;$ $n_y = 1.790;$ $n_z = 1.887$
				$d_{15} = 1.91;$ $d_{24} = 3.64;$ $d_{31} = 2.54;$ $d_{32} = 4.53;$ $d_{33} = 16.9$	
Potassium titanyl phosphate	KTP	mm2	1319	$d_{24} = 2.88 \pm 0.2$	[164]
Proustite, Ag_3AsS_3	3m	10,600	$n^o = 2.697;$ $n^e = 2.503$	$d_{15} = 11;$ $d_{22} = 18$	[44]
Pyragyrate, Ag_3SbS_3	3m	10,600	$n^o = 2.735;$ $n^e = 2.614$	$d_{22} = 13.4;$ $d_{31} = 12.6$	[48]
Rubidium deuterium arsenate	$\bar{4}2m$	1064	$n^o = 1.539;$ $n^e = 1.509$	$d_{36} = 0.31$	[1]
Rubidium deuterium phosphate	$\bar{4}2m$	1064	$n^o = 1.491;$ $n^e = 1.468$	$d_{36} = 0.38$	[1]
Rubidium dihydrogen phosphate	$\bar{4}2m$	1064	$n^o = 1.492;$ $n^e = 1.470$	$d_{36} = 0.40$	[3,50]
Rubidium titanyl arsenate	RTA	mm2	694	$n = 1.481$	
			1064	$d_{36} = 0.39$	[51]
				$d_{31} = 3.8;$ $d_{32} = 2.3;$ $d_{33} = 15.8$	[49]

(continued)

Table 1 Continued

Material	Abbr.	Symmetry class	λ_{ω} (nm)	n_o	n_{2o}	d (pm/V)	Ref.
Rubidium tityanyl phosphate	RTP	mm2	1064	$n_x = 1.764;$ $n_y = 1.773;$ $n_z = 1.850$	$n_x = 1.805;$ $n_y = 1.817;$ $n_z = 1.910$	$d_{31} = 4.1;$ $d_{32} = 3.3;$ $d_{33} = 17.1$	[49]
Selenium		32	10,600	$n^o = 2.64;$ $n^e = 3.48$		$d_{11} = 100$	[52]
Silver gallium selenide	$\bar{4}2m$		28,000	$n^o = 2.592;$ $n^e = 2.559$	$n^o = 2.614;$ $n^e = 2.582$	$d_{11} = 185$ $d_{36} = 33$	[53] [3,20]
Silver gallium sulfide	$\bar{4}2m$		10,600	$n^o = 2.316;$ $n^e = 2.347$	$n^o = 2.383;$ $n^e = 2.341$	$d_{14} = 57;$ $d_{36} = 20$	[56,57]
Silver iodide	6mm		1064	1318	2.104	2.200	$d_{36} = 23.6$ $d_{31} = 8.2;$ $d_{33} = -16.8$
Silver thiogallate	$\bar{4}2m$		10,600	$n^o = 2.347;$ $n^e = 2.292$	$n^o = 2.395;$ $n^e = 2.342$	$d_{36} = 13$	[58]
Sodium nitrite	mm2		1064			$d_{15} = 0.07;$ $d_{24} = 1.8;$ $d_{31} = 0.07;$ $d_{32} = 1.9;$ $d_{33} = 0.9$	[55]

Strontium barium niobate (thin film) $\text{Sr}_x\text{Ba}_{1-x}\text{Nb}_2\text{O}_6$ ($x = 0.4$)	SBN		$d_{\text{eff}} \sim 3.0$	[59]
Tellurium		32	10,600 $n^o = 4.798;$ $n^e = 6.248;$ $n^o = 4.781;$ $n^e = 6.226$	$d_{11} = 650$ [3]
			28,000 $n^o = 4.790;$ $n^e = 6.238$	$d_{11} = 570$ [60]
YCa ₄ O (BO ₃) ₃	YCOB	m	1064 —	— [172]
Zinc germanium phosphide		42m	10,600 $n^o = 3.073;$ $n^e = 3.112$	$d_{32} = 1.36;$ $d_{33} = 0.93$ [3,62]
Zinc oxide		6mm	1064 1.95 2.05	$d_{36} = 75$ [14]
Zinc selenide		43m	10,600 2.42 2.43	$d_{33} = 18.0;$ $d_{35} = 54$ [65]
Zinc selenide (thin film on GaAs)			1064 3.175	$d_{14} = 78$ $d_{36} = 33$ [63]
Zinc silicon arsenide α -Zinc sulfide		42m 6mm	10,600 1064	$d_{36} = 108.5;$ $d_{15} = 7;$ $d_{33} = 14$ [12] [64]
Zinc telluride Zinc tris (thiourea) sulfate	ZTS	43m mm2	10,600 2.69 2.70 $n_x = 1.631;$ $n_y = 1.694;$ $n_z = 1.698$	$d_{14} = 90$ $d_{31} = 0.35;$ $d_{32} = 0.31;$ $d_{33} = 0.23$ [66] [36,37]

Table 2 Second Order Nonlinear Optical Coefficients of Selected Organic Crystals

Material	Abbreviation	Symmetry class	λ_{wo} (nm)	n_{o}	$n_{2\text{o}}$	d (pm/V)	Ref.
2-Amino-5-nitropyridinium dihydrogen phosphate	2ANPDP	mm2	1064	$n_x = 1.583;$ $n_y = 1.621;$ $n_z = 1.696$	$n_x = 1.647$ $n_y = 1.660;$ $n_z = 1.779$	$d_{15} = 1;$ $d_{24} = 7$	[67]
2-Amino-5-nitropyridinium dihydrogen phosphate-arsenate (x = 0.2 – 1.0)	2ANPDP _{(1-x)As_x}	mm2	1064	$n_x = 1.586$ $n_y = 1.628$ $n_z = 1.705$	$n_x = 1.649;$ $n_y = 1.669;$ $n_z = 1.790;$ (x = 0.2)	$d_{\text{eff}} = 1.7$ (type II)	[173]
Acenaphthalene		mm2	694.3				[73]
8-(4'-Acetylphenyl)-1,4-dioxa-8-azaspiro[4,5]-dione	APDA	mm2	1064	$n_x = 1.55;$ $n_y = 1.64$	$n_x = 1.57;$ $n_y = 1.68$	$d_{31} = 0.14;$ $d_{33} = 1.2$ $d_{32} = 7;$ $d_{33} = 50$	[67]
2-Adamantylamino-5-nitropyridine	AANP	mm2	1064	$n_z = 1.66$ $n_x = 1.59;$ $n_y = 1.67;$	$n_z = 1.72$ $n_x = 1.61;$ $n_y = 1.77;$	$d_{\text{eff}} = 14.9$ $d_{31} = 54.4;$ $d_{33} = 40.8$	[67] [68]
2-Adamantylamino-5-nitropyridine	AANP	mm2	1320	$n_x = 1.636;$ $n_y = 1.644;$	$n_x = 1.657;$ $n_y = 1.7026;$	$d_{\text{eff}} = 17.9;$ (type II)	[174]
2-Adamantylamino-5-nitropyridine	AANP	mm2	1550	$n_z = 1.744$ $n_x = 1.6361;$ $n_y = 1.6419;$ $n_z = 1.704$	$n_z = 1.8242$ $n_x = 1.6523;$ $n_y = 1.6766;$ $n_z = 1.7878$	$d_{\text{eff}} = 8.6$; (type II)	[174]

Ammonium malate	m	600			$d_{32} = 0.45$	[71]
Ammonium oxylate monohydrate	222	1064	1.480	1.600	$d_{14} = 0.37$	[72]
Ammonium tartrate	2	1153			$d_{21} = 0.24;$	[70]
<i>m</i> -Anniophenol	AP	mm2	1064		$d_{36} = 0.25$	[74]
					$d_{15} = 0.98;$	
					$d_{24} = 1.27$	
Aromatic polyurea					$d_{31} = 1.03$	
Barium formate	222	1064	$n_x = 1.621;$	$n_x = 1.641;$	$d_{32} = 1.44;$	[75]
			$n_y = 1.582;$	$n_y = 1.602;$	$d_{33} = 1.48$	
Benzanthracene	2	694.3	$n_z = 1.559$	$n_z = 1.577$	$d_{24} = 1.27$	
					$d_{31} = 0.5;$	
					$d_{32} = 1.5;$	
					$d_{33} = 2.2$	
Benzophenone	222	694.3	1.66	1.70	$d_{31} = 0.92;$	[69]
2,5-Bis(benzylidene) cyclopentanone	BBCP	222	1064	$n_x = 1.471;$	$d_{33} = 3.4$	
				$n_y = 1.738;$	$d_{14} = 0.11;$	[80]
				$n_z = 1.762$	$d_{25} = 0.11;$	
					$d_{36} = 0.11$	
					$d_{21} = 0.064;$	[73]
					$d_{22} = 0.0096;$	
					$d_{16} = 0.003$	
					$d_{36} = 0.35$	[81]
					$d_{14} = 7$	
					$n_x = 1.596;$	
					$n_y = 1.827;$	
					$n_z = 1.850$	

(continued)

Table 2 Continued

Material	Abbreviation	Symmetry class	λ_{o} (nm)	n_{o}	n_{20}	d (pm/V)	Ref.
2,6-Bis(<i>p</i> -methylbenzylidene)-4- <i>tert</i> -butylcyclohexanone	MBBCH	mm2	1064	$n_y = 1.557;$ $n_z = 1.712$	$n_x = 1.596;$ $n_y = 1.711;$ $n_z = 1.950$	$d_{31} = 15;$ $d_{32} = 12;$ $d_{33} = 4$	[81]
Bisphenol-A-4-amino-4'-nitrotolane			1064			$d_{31} = 25;$ $d_{33} = 89$	[76]
Bisphenol-A-diglycidylether-4-nitro-1,2-phenylenediamine	Bis-A-NPDA		1064	1.602		$d_{31} = 3.0;$ $d_{33} = 13.5$	[77]
4-Bromo-4'-methoxychalcone	BMC	m	1064			$d_{13} = 90$	[78]
2-Bromo-4'-nitroaniline		mm2	1064			$d_{15} = 4.51;$ $d_{24} = 11.48;$ $d_{31} = 6.15;$ $d_{32} = 1.44;$ $d_{33} = 1.48;$	[74]
<i>m</i> -Bromonitroaniline	BNB	mm2	1064			$d_{31} = 2.6;$ $d_{32} = 2.9;$ $d_{33} = 5.1$	[75]
Buckminsterfullerene, C ₆₀			1064	$n_x = 1.447;$ $n_y = 1.663$	$n_x = 1.493;$ $n_y = 1.710$	$d_{33} = 0.88$	[79]
Chalcone derivative R ₁ = CH ₃ CH ₂ O, R ₂ = OCH ₃		mm2	1064	$n_z = 1.850$	$n_z = 1.983$	$d_{\text{eff}} = 3.5$ (type I) $d_{\text{eff}} = 5.7$ (type II)	[85]
<i>m</i> -Chloronitrobenzene	CNB	mm2	1064			$d_{31} = 2.9;$ $d_{32} = 2.6;$ $d_{33} = 5.0$	[75]

2-Cyano-3-(2-methoxyphenyl) propenoic acid methyl ester	CMP-M	2	1064	1.781	1.897	$d_{22} = 29$	[82]
2-Cyclooctylamino-5-nitro pyridine	COANP	mm2	1064	$n_x = 1.604;$ $n_y = 1.636;$ $n_z = 1.715$	$n_x = 1.697;$ $n_y = 1.710;$ $n_z = 1.1872$	$d_{31} = 32;$ $d_{33} = 14$	[83,84]
$\text{C}_{17}\text{H}_{17}\text{NO}_2\text{S}$ /aromatic polyimide (44.6% chromophore density)			1064	1.630	1.815	$d_{33} = 45.7$	[86]
$\text{C}_{17}\text{H}_{17}\text{NO}_2\text{S}$ /aromatic polyimide (51.0% chromophore density)			1064	1.625	1.781	$d_{33} = 60.7$	[86]
Dicyanovinyllazo dimethyl methacrylate	DCV-MMA		1580			$d_{33} = 21.4$	[89]
D-Glucose		222	1064			$d_{14} = 0.32$	[14]
2,4-Diaminotolane	DMC	mm2	1064	1.593	1.767	$d_{31} = 0.4$	[95]
7-Diethylamino-4-methylcoumarin		2	1064			$d_{21} = 4.1;$ $d_{22} = 1.6;$ $d_{23} = 0.53;$ $d_{25} = 0.61$	[92]
N,N -(Diglycidyl)-4-nitroaniline+ N -(2-aminophenyl-4-nitroaniline)	NNDN-NAN		1064			$d_{31} = 16;$ $d_{33} = 50$	[114]
1,4-Diiodobenzene		mm2		694.3		$d_{32} = 2.70;$ $d_{33} = 0.83$	[73]

(continued)

Table 2 Continued

Material	Abbreviation	Symmetry class	λ_{ω} (nm)	n_{ω}	$n_{2\omega}$	d (pm/V)	Ref.
4'-Dimethylamino- <i>N</i> -methyl-4-stilbazolium tosylate	DAST	m	1064			$d_{11} = 600;$ $d_{12} = 30;$ $d_{22} = 10$	[90]
1-(4-Dimethylamino-phenyl)-4,4-dicyano-1,3-butadiene/PMMA ($3.2 \times 10^{20} \text{ cm}^{-3}$)						$d_{15} = 5.3;$ $d_{31} = 4.4;$ $d_{33} = 11$	[91]
<i>m</i> -Dinitrobenzene		mm2	694.3			$d_{31} = 3.39;$ $d_{32} = 2.32;$ $d_{33} = 3.11$	[73]
Disperse red #1/polymethyl methacrylate ($1.1 \times 10^{20} \text{ cm}^{-3}$)	DR1/PMMA		1064			$d_{15} = 3.2;$ $d_{31} = 2.7;$ $d_{33} = 6.8$	[91]
Disperse red #1/polymethyl methacrylate ($2.3 \times 10^{20} \text{ cm}^{-3}$)	DR1/PMMA		1064			$d_{15} = 3.1;$ $d_{31} = 2.9;$ $d_{33} = 9.0$	[91]
Disperse orange #3/poly methyl methacrylate ($3.0 \times 10^{20} \text{ cm}^{-3}$)	DR3/PMMA		1064			$d_{15} = 2.1;$ $d_{31} = 1.8;$ $d_{33} = 5.8$	[91]
4-(<i>N,N</i> -Dimethylamino)-3-acetamido-nitrobenzene	DAN	2	1064	$n_X = 1.517;$ $n_Y = 1.636;$ $n_Z = 1.843$	$n_X = 1.554;$ $n_Y = 1.732;$ $n_Z = 2.107$	$d_{21} = 2;$ $d_{22} = 5;$ $d_{23} = 50;$ $d_{25} = 2;$ $d_{\text{eff}} = 27$ (type I)	[113]

3,5-Dimethyl-1-(4-nitrophenyl) pyrazole	DMNP	mm2	884	$n_x = 1.513;$ $n_y = 1.696;$ $n_z = 1.793$	$n_x = 1.567;$ $n_y = 1.822;$ $n_z = 1.1997$	$d_{33} = 29;$ $d_{36} = 90$	[87]
1,8-Dinitronaphthalene		222	694.3	$n_x = 1.489;$ $n_y = 1.504;$ $n_z = 1.519$	$n_x = 1.569;$ $n_y = 1.569;$ $n_z = 1.570$	$d_{25} = 0.35;$ $d_{36} = 0.35$ $d_{21} = 0.12;$ $d_{22} = 4.1;$ $d_{25} = 0.18$	[73]
Dipotassium tartrate hemihydrate		2	694.3	$n_x = 1.489;$ $n_y = 1.504;$ $n_z = 1.519$	$n_x = 1.569;$ $n_y = 1.569;$ $n_z = 1.570$	$d_{21} = 0.12;$ $d_{22} = 4.1;$ $d_{25} = 0.18$	[93]
2-Docosylamino-5-nitropyridine	DCANP		1064	1.574	$d_{31} = 2;$ $d_{33} = 8$	$d_{31} = 2;$ $d_{33} = 8$	[88]
<i>n</i> -Docosyl-2-methyl-4-nitroaniline	DCMNA		1318		$d_{33} = 6$	$d_{31} = 0.04;$ $d_{33} = 0.5$	[115]
D-Threonine		222	1064		$d_{33} = 0.5$	$d_{14} = 0.4;$ $d_{25} = 0.4;$ $d_{36} = 0.4$	[94]
4-[<i>N</i> -Ethyl- <i>N</i> -(2-hydroxyethyl)]amino-4'-nitroazobenzene/poly methyl methacrylate	DR1/PMMA		1580		$d_{33} = 2.6$		[116]
Glutamic acid hydrochloride 4-Hexyloxy-4'-nitrostilbene/methyl methacrylate (waveguide)	HNS-MNA	222	1064	1.555 (TE); 1.554 (TM)	1.606 (TE); 1.605 (TM)	$d_{36} = 0.17$ $d_{33} = 6.7$	[96] [97]
Hippuric acid		222	694.3	1.561	1.78	$d_{36} = 2.5$	[98]

(continued)

Table 2 Continued

Material	Abbreviation	Symmetry class	λ_{o} (nm)	n_{o}	$n_{2\omega}$	d (pm/V)	Ref.
Idoform sulfur		3m	1064			$d_{22} = 8.79;$ $d_{31} = 3.2;$ $d_{33} = 1.66$	[99]
L-Arginine phosphate monohydrate	LAP	m	1064	$n_x = 1.497;$ $n_y = 1.559;$ $n_z = 1.567$	$n_x = 1.512;$ $n_y = 1.579;$ $n_z = 1.588$	$d_{11} = 0.40;$ $d_{22} = 0.92;$ $d_{23} = -0.84;$ $d_{25} = -0.58$	[100]
L-Histidine tetrafluoroborate	HFB	2	1064	$n_x = 1.465;$ $n_y = 1.527;$ $n_z = 1.561$	$n_x = 1.483;$ $n_y = 1.544;$ $n_z = 1.581$	$d_{\text{eff}} = 2$ (type I)	[101]
L-N-(5-nitro-2-pyridyl) leucinol	NPLO	2	1064	$n_x = 1.451;$ $n_y = 1.598;$ $n_z = 1.812$	$n_x = 1.507;$ $n_y = 1.667;$ $n_z = 2.068$	$d_{\text{eff}} = 37$ (type I); $d_{\text{eff}} = 3$ (type II)	[102]
L-Pyrrolidone-2-carboxylic acid	L-PCA	222	532	$n_x = 1.484;$ $n_y = 1.508;$ $n_z = 1.615$	$n_x = 1.498;$ $n_y = 1.521;$ $n_z = 1.637$	$d_{14} = 0.32$	[103]
Meta-dinitrobenzene	mDNB	mm2	1064	$n_x = 1.471;$ $n_y = 1.654;$ $n_z = 1.709$	$n_x = 1.491;$ $n_y = 1.698;$ $n_z = 1.759$	$d_{31} = 1.78;$ $d_{32} = 2.7;$ $d_{33} = 7.4$	[112]
Meta-nitroaniline	mNA	mm2	1064	$n_x = 1.631;$ $n_y = 1.678;$ $n_z = 1.719$	$n_x = 1.705;$ $n_y = 1.738;$ $n_z = 1.798$	$d_{31} = 20;$ $d_{32} = 1.6;$ $d_{33} = 21$	[111]
3-Methoxy-4-hydroxy benzaldehyde	MHBA	2	1064			$d_{\text{eff}} = 8.0$	[104]

(-2-(α -Methylbenzyl-amino)-5-nitropyridine	MBANP	2	1064	1.748	1.884	$d_{16} = 14$; $d_{21} = 14$;	[105]
Methyl-(2,4-dinitrophenyl)-amino-2-propanoate	MAP	2	1064	$n_x = 1.508$; $n_y = 1.599$; $n_z = 1.844$	$n_x = 1.557$; $n_y = 1.710$; $n_z = 2.035$	$d_{22} = 14$; $d_{21} = 16.7$; $d_{22} = 18.4$; $d_{23} = 3.68$;	[109]
3-Methyl-4-methoxy-4'-nitro-stilbene	MMONS	mm2	1064	$n_x = 1.530$; $n_y = 1.630$; $n_z = 1.961$	$n_x = 1.605$; $n_y = 1.770$; $n_z = 2.352$	$d_{25} = -0.54$; $d_{15} = 68-78$; $d_{31} = 50.6$;	[106]
3-Methyl-4-methoxy-4'-nitrostilbene	MMONS	mm2	1320	$n_x = 1.530$; $n_y = 1.630$; $n_z = 1.961$	$n_x = 1.605$; $n_y = 1.770$; $n_z = 2.352$	$d_{33} = 227$; $d_{24} = 75 \pm 5$; $d_{33} = 195 \pm 10$	[175]
2-Methyl-4-nitro-N-methylaniline	MNMA	mm2	1064			$d_{24} = 12$; $d_{32} = 13$;	[107]
2-Methyl-4-nitroaniline	MNA	m	1064	1.8	2.2	$d_{33} = 3$; $d_{11} = 184$;	[110]
3-Methyl-4-nitropyridine-1-oxide	POM	222	1064	$n_x = 1.625$; $n_y = 1.668$; $n_z = 1.829$	$n_x = 1.660$; $n_y = 1.750$; $n_z = 1.997$	$d_{12} = 26.7$; $d_{36} = 10$	[108]
<i>N</i> -(4-Nitro-2-penidiny)-phenylalnininol	NPPA	2	1064			$d_{23} = 31$; $d_{34} = 25$; $d_{\text{eff}} = 19$; (type I); $d_{\text{eff}} = 22$; (type II)	[117]

(continued)

Table 2 Continued

Material	Abbreviation	Symmetry class	λ_{ω} (nm)	n_{ω}	$n_{2\omega}$	d (pm/V)	Ref.
4-Nitrophenol sodium [Na] salt dihydrate	NPNa	mm2	1064			$d_{\text{eff}} = 5.0$	[120]
<i>N</i> -(4-Nitrophenyl)-acetonitrile	NPAN	mm2				(type I) $d_{21} = 200$	[119]
2-(<i>p</i> -Nitrophenyl)-4,5-bis(<i>p</i> -hydroxyphenyl)oxazole/fluorinated polyimide	TNON/fluorinated polyimide		1217	1.57		$d_{31} = 1.6;$ $d_{33} = 49$	[121]
<i>N</i> -(4-Nitrophenyl)-(S)-prolinol	NPP	2	1064			$d_{21} = 84;$ $d_{22} = 29$	[118]
<i>N</i> -(4-Nitrophenyl)-(L)-prolinol	NPP	2		1.68		$d_{21} = 84$	[119]
5-Nitouracil	5-NU	222		$n_X = 1.852;$ $n_Y = 1.680;$ $n_Z = 1.534$	$n_X = 1.936;$ $n_Y = 1.731;$ $n_Z = 1.560$	$d_{36} = 7.1$	[119]
4-Oxy-4'-nitrostilbene/ methyl methacrylate Phenanthrene	P ₆ CS/MMA		1340	1.587	1.621	$d_{33} = 8.97$	[127]
<i>N</i> -Phenylated aromatic polyurea		2	694.3			$d_{16} = 0.003;$ $d_{21} = 0.013;$ $d_{22} = 0.026$ $d_{31} = 1.68;$ $d_{33} = 5.44$	[73] [124]

Poly{1-methyl-4-[2-[4-(6-((methacryloxy)hexyl)oxy)phenyl]vinyl]pyridinium tetraphenylborate}	HP6B	$d_{33} = 37.9$	[127]
Poly{1-methyl-4-[2-[4-(10-(methacryloxy)hexyl)oxy]phenyl]vinyl]pyridinium tetraphenylborate}	HP10B	$d_{33} = 22.8$	[127]
Poly{1-methyl-4-[2-[4-(2-(4-(10-(methacryloxy)hexyl)oxy)phenyl]vinyl]pyridinium tetraphenylborate}	HP0B	$d_{33} = 16.3$	[127]
Poly- <i>p</i> -nitroaniline	1064	$d_{31} = 4;$ $d_{33} = 19$	[125]
Polysiloxane copolymer Potassium maleate	m 630	$d_{11} = 2.2$ $d_{11} = 6.62;$ $d_{12} = 0.6;$ $d_{13} = 0.66;$ $d_{15} = 2.52;$ $d_{24} = 1.39;$ $d_{26} = 0.53;$ $d_{31} = 0.66;$ $d_{32} = 2.52;$ $d_{33} = 3.97;$ $d_{35} = 0.26$	[126] [128]

(continued)

Table 2 Continued

Material	Abbreviation	Symmetry class	λ_{o} (nm)	n_{o}	$n_{2\omega}$	d (pm/V)	Ref.
2-(<i>N</i> -Prolinol)-5-nitropyridine	PNP	2	1064	$n_x = 1.880;$ $n_y = 1.732;$ $n_z = 1.456$	$n_x = 2.117;$ $n_y = 1.853;$ $n_z = 1.471$	$d_{21} = 48;$ $d_{22} = 17$	[123]
Strontium formate		222	1064	1.545	1.553	$d_{14} = 0.51$	[129]
Strontium formate dihydrate		222	1064	1.488	1.517	$d_{14} = 0.33$	[129]
Thienylchalcone	T-17	2	1064	$n_x = 1.640;$ $n_y = 1.692;$ $n_z = 1.767$	$n_x = 1.731;$ $n_y = 1.740;$ $n_z = 1.863$	$d_{\text{eff}} = 7.1$	[130]
Thiosemicarbazide cadmium chloride monohydrate	TSCCC	m	1064	$n_x = 1.650;$ $n_y = 1.715;$ $n_z = 1.739$	$n_x = 1.678;$ $n_y = 1.752;$ $n_z = 1.777$	$d_{11} = 0.098;$ $d_{12} = 0.35;$ $d_{13} = \pm 0.12;$ $d_{31} = -1.2;$ $d_{32} = 1.2;$ $d_{33} = -1.8$	[131]
<i>m</i> -Tolylendiamine	MTD	mm2	1064			$d_{15} = 0.37;$ $d_{32} = 0.94;$ $d_{33} = 0.66$	[95]
4-Tricyanovinyl- <i>N</i> , <i>N</i> -dimethylaniline/PMMMA ($3.2 \times 10^{20} \text{ cm}^{-3}$)			1064			$d_{15} = 7.7;$ $d_{31} = 6.1;$ $d_{33} = 16$	[91]

Table 3 First Hyperpolarizability Data for Selected Organic Molecules

Molecule	Solvent	λ (nm)	μ_0 (D)	$(10^{-40} \text{ m}^4/\text{V})$	β (10^{-30} esu)	Method	Ref.
4-Amino-4'-nitrodiphenyl sulfide	Dioxane	1064	6.44	26	EFISH	[133]	
4-Amino-4'-nitrodiphenyl sulfide	Benzene	1064	6.07	26	EFISH	[133]	
4-Amino-4'-nitrodiphenyl sulfide	Acetone	1064	6.3	27	EFISH	[133]	
4-Amino-4'-nitrodiphenyl sulfide	Methanol	1064	6.3	28	EFISH	[133]	
4-Amino-4'-nitrodiphenyl oxide	Dioxane	1064	6.19	15	EFISH	[133]	
4-Amino-4'-nitrodiphenyl selenide	Dioxane	1064	5.89	27	EFISH	[133]	
4-Amino-4'-nitrodiphenyl telluride	Dioxane	1064	5.6	27	EFISH	[133]	
2-Nitrotripycene	CH_2Cl_2	1064	4.0 ± 0.2	10 ± 3	EFISH	[134]	
Water	(neat)	1064	1.82	0.046	EFISH	[135]	
<i>p</i> -Nitroaniline	Methanol	1064	7.2	20–24.5	EFISH	[135]	
<i>p</i> -Nitroaniline (175°C)	(melt)	1064	7.2	21.1	EFISH	[135]	
<i>m</i> -Dinitrobenzene	Benzene	1064	4.1	1.07	EFISH	[135]	
<i>m</i> -Dinitrobenzene (140°C)	(melt)	1064	4.1	2.3	EFISH	[135]	
<i>para</i> -Substituted benzene (D = CH_3 , A = CN)*	Dimethyl sulfoxide	1064	4.41–4.47	2.95–2.91	EFISH	[136]	
<i>para</i> -Substituted benzene (D = OCH_3 , A = CN)*	Dimethyl sulfoxide	1064	4.76–4.82	4.83–4.77	EFISH	[136]	
<i>para</i> -Substituted benzene (D = NH_2 , A = CN)*	Dimethyl sulfoxide	1064	5.92	13.34	EFISH	[136]	
<i>para</i> -Substituted benzene (D = $\text{N}(\text{CH}_3)_2$, A = CN)*	Dimethyl sulfoxide	1064	6.60	14.24	EFISH	[136]	
<i>para</i> -Substituted benzene (D = NH_2 , A = COCH_3)*	Dimethyl sulfoxide	1064	4.54	2.40	EFISH	[136]	

(continued)

Table 3 Continued

Molecule	Solvent	λ (nm)	μ_0 (D)	β ($10^{-40} \text{ m}^4/\text{V}$)	β (10^{-30} esu)	Method	Ref.
<i>para</i> -Substituted benzene (D = CH_3 , A = NO_2)*	Dimethyl sulfoxide	1064	3.62–4.49	9.12–7.35	EFISH	[136]	
<i>para</i> -Substituted benzene (D = OCH_3 , A = NO_2)*	Dimethyl sulfoxide	1064	4.05–4.98	17.53–14.26	EFISH	[136]	
<i>para</i> -Substituted benzene (D = NH_2 , A = NO_2)*	Dimethyl sulfoxide	1064	6.00–6.23	47.67–45.91	EFISH	[136]	
<i>para</i> -Substituted benzene (D = $\text{N}(\text{CH}_3)_2$, A = NO_2)*	Dimethyl sulfoxide	1064	6.73–6.93	52.75–51.23	EFISH	[136]	
Urea	Water	1064	4.56	0.45 ± 0.12	EFISH	[137]	
Urea	DMF	1064	4.56	0.30 ± 0.09	EFISH	[137]	
Urea	DMSO	1064	4.56	0.29 ± 0.03	EFISH	[137]	
Monomethylurea	Water	1064	4.34	0.45 ± 0.16	EFISH	[137]	
Monomethylurea	DMF	1064	4.34	0.65 ± 0.12	EFISH	[137]	
Monomethylurea	DMSO	1064	4.34	0.43 ± 0.04	EFISH	[137]	
<i>N,N'</i> -Dimethylurea	Water	1064	4.66	0.6 ± 0.3	EFISH	[137]	
<i>N,N'</i> -Dimethylurea	DMF	1064	4.66	0.28 ± 0.20	EFISH	[137]	
<i>N,N'</i> -Dimethylurea	DMSO	1064	4.66	0.18 ± 0.13	EFISH	[137]	
Tetramethylurea (neat)	1064	3.92	20.1 ± 6.0	EFISH	[137]		
<i>N-t</i> -Butyl-(4-nitrophenyl) nitrone	Acetone	1340	6.7	12 ± 1	EFISH	[138]	
2-(4-Nitrophenyl)-4,4,5,5-tetramethyl-4,5-dihydro-1 <i>H</i> -imidazoly-1-oxyl-3-oxide	Acetone	1064	6.8	9.4 ± 1.0	EFISH	[138]	
4-Nitrostilbene	Benzene	1340	4.56	6.24 ± 0.10	EFISH	[139]	
		1064	29 ± 10	EFISH		[139]	

4-Aminostilbene	Benzene	1064	2.07	12 ± 7	EFISH	[139]
4-Dimethylaminostilbene	Benzene	1064	2.4	29 ± 8	EFISH	[139]
4-Chlorostilbene	Benzene	1064	1.5	3.6 ± 2.0	EFISH	[139]
4-Chloro-4'-nitrostilbene	Chloroform	1064	3.1	39 ± 10	EFISH	[139]
4-Chloro-4'-dimethylamino-stilbene	Chloroform	1064	4.02	42 ± 10	EFISH	[139]
4-Nitro-4'-aminostilbene	Acetone	1064	7.54	260 ± 35	EFISH	[139]
4-Nitro-4'-dimethylamino-stilbene	Acetone	1064	7.42	450 ± 90	EFISH	[139]
<i>para</i> -Dimethylamino- β nitrostilbene	Chloroform	1064	7.9	220 ± 40	EFISH	[139]
<i>para</i> -Dimethylamino-phenyl,	Chloroform	1064	8.8	630 ± 160	EFISH	[139]
4-nitrostilbene						
<i>p</i> -Nitroaniline	1,4-Dioxane	1907	9.6 ± 0.5		EFISH	[140]
		1370	11.8 ± 0.3			
		1064	16.9 ± 0.4			
2-Methyl-4-nitroaniline	(neat)	909	25 ± 1			
	(neat)	830	40 ± 3			
	1,4-Dioxane	1907	9.5 ± 0.5		EFISH	[140]
		1370	12.8 ± 0.5			
		1064	16.7 ± 0.5			
<i>o</i> -Nitroaniline	(neat)	909	27 ± 1			
<i>m</i> -Nitroaniline	(neat)	830	45 ± 4			
<i>p</i> -Nitroaniline	(neat)	1318	5.0	6.4	EFISH	[140]
Nitrobenzene	(neat)	1318	5.5	4.2	EFISH	[140]
Aniline	(neat)	1318	7.2	21.1	EFISH	[140]
<i>N</i> -Octadecyl-merocyanine	Methanol	1318	4.1	19.7	EFISH	[140]
1% Methanol/pyridine		1318	1.5	7.9	EFISH	[140]
				—418, —214 [†]	—100, —51.0 [†]	[142]
				—543, —155 [†]	—130, —37.0 [†]	

(continued)

Table 3 Continued

Molecule	Solvent	λ (nm)	μ_0 (D)	β ($10^{-40} \text{ m}^4/\text{V}$)	β (10^{-30} esu)	Method	Ref.
<i>N</i> -Methyl-merocyanine	Pyridine			-880, -142 [†]	-210, -34.0 [†]		
3-Methyl-4-nitropyridine <i>N</i> -oxide	DMSO (neat)	1890	8	-4000	-950	EFISH	[143]
4- <i>N,N</i> -Dimethylamino-pyridine	Chloroform	1064		35.6	8.5 ± 2.0	EFISH	[144]
<i>N</i> -oxide				21	5.0	EFISH	[145]
4'- <i>N,N</i> -Dimethylamino-4'-azastilbene	Chloroform	1064		2090	500	EFISH	[145]
<i>N</i> -oxide	Benzene	1318		40 ± 15%	9.6 ± 15%	EFISH	[146]
Pyridine-I ₂ CT	9:1 Benzene/pyridine	1318		58 ± 15%	4.5 ± 15%	EFISH	[147]
Pyridine-ICl CT	Dioxane	1318		18.8 ± 15%	EFISH	[147]	
4-Aminopyridine-I ₂ CT	DMSO	1064		-1000 ± 250 - 240 ± 60	EFISH	[148]	
2-(4-Dicyanomethylene cyclohexa-2,5-dienylidene) imidazolidine	Dichloroethylene	1064	8000	2090 ± 50% ^{± 50%}	EFISH	[149]	
Poly-γ-benzyl-L-glutamate	Chloroform	1907		3.5	0.5	EFISH	[150]
Me ₂ NCHO							
Me ₂ N(CH = CH)CHO				6.3	3.3		
Et ₂ N(CH = CH) ₂ CHO				6.5	20		
Me ₂ N(CH = CH) ₃ CHO				6.9	53		
Me ₂ NCH = CCN) ₂				7.6	1.0		
Me ₂ (CH = CH)CH = C(CN) ₂				8.9	6.1		
Et ₂ N(CH = CH) ₂ CH = C(CN) ₂				10.7	45		
Me ₂ N(CH = CH) ₃ CH = C(CN) ₂				9.9	211		
Me ₂ NC ₆ H ₄ CHO				5.1	6.3		

$\text{Me}_2\text{NC}_6\text{H}_4\text{CH} = \text{CHCHO}$	5.6	30	[151]
$\text{Me}_2\text{NC}_6\text{H}_4\text{CH} = \text{C}(\text{CN})_2$	7.8	32	
$\text{Me}_2\text{NC}_6\text{H}_4\text{CH} = \text{CHCH} = \text{C}(\text{CN})_2$	8.4	82	
1,8-Naphthylene-(3'-amino)benzimidazole-4,5-dicarboxy- <i>N</i> -(2,5-di- <i>tert</i> -butylphenylimide)	4.1	93 ± 10	EFIGH
(solid polyimide)	1907		
2-Cyclooctylamino-5-nitropyridine	1,4-Dioxane	6.8	EFIGH [152]
	1064	92 ± 18	
	1318	50 ± 9	
	1907	46 ± 7	
2-Dorosylamino-5-nitropyridine	1,4-Dioxane	6.7	EFIGH [152]
	1064	54 ± 11	
	1318	39 ± 7	
	1907	25 ± 4	
2-(<i>N</i> -Prolinol)-5-nitropyridine	1,4-Dioxane	7.2	EFIGH [152]
	1064	76 ± 15	
	1318	47 ± 9	
	1907	47 ± 7	
2-Methyl-4-nitroaniline	1,4-Dioxane	7.4	EFIGH [152]
	1064	77 ± 16	
	1318	38 ± 7	
	1907	32 ± 5	
4-(<i>N,N</i> -Dimethylamino)-3-acetamidonitrobenzene	1,4-Dioxane	7.38	18.2 Modified [153]
2-Methyl-4-nitroaniline	1,4-Dioxane	5.68	EFIGH Modified [153]
(-)2- α -Methylbenzyl-amino)-5-nitropyridine	1,4-Dioxane	6.13	13.0 EFIGH Modified [153]
2-(<i>N</i> -Prolinol)-5-nitropyridine	1,4-Dioxane	5.51	14.6 EFIGH Modified [153]
<i>para</i> -Nitroaniline	Chloroform	1064	17.0 EFIGH Modified [153]
			HRS 23 [154]

Table 3 Continued

Molecule	Solvent	λ (nm)	μ_0 (D)	β ($10^{-40} \text{ m}^4/\text{V}$)	β (10^{-30} esu)	Method	Ref.
4-Methoxy-4'-nitrostilbene	Chloroform	1064		105	HRS	[154]	
4-Hydroxy-4'-nitrostilbene	Chloroform	1064		95	HRS	[154]	
Tricyanomethanide ion $[\text{CCN}]_3^-$	Water	1064		7 ± 1.5	HRS	[155]	
	Methanol			7 ± 1.5			
	Ethanol			7 ± 1.5			
4-Nitroaniline	Dioxane	1064	7.13	17	Solv.	[156]	
		1907		9.6			
4-(Dimethylamino)-1-nitrobenzene	Dioxane	1064	7.14	22	Solv.	[156]	
		1907		12			
3-Acetamido-4-(dimethylamino)-1-nitrobenzene	Dioxane	1064	8.10	16	Solv.	[156]	
		1907		9.5			
2-(Dimethylamino)-5-nitropyridine	Dioxane	1064	5.97	23	Solv.	[156]	
		1907		13			
4-Pyrrolidino-nitrobenzene	Dioxane	1064	7.50	34	Solv.	[156]	
		1907		17			
4-Nitroanisole	Dioxane	1064	5.34	5.7	Solv.	[156]	
		1907		4			
Methyl 4-nitrophenyl sulfide	Dioxane	1064	4.61	10.6	Solv.	[156]	
		1907		6.7			
4-(Dimethylamino)-4'-nitrostilbene	Dioxane	1064	7.10	323	Solv.	[156]	
2-(<i>p</i> -Nitrophenyl)-4,5-bis(<i>p</i> -hydroxyphenyl) oxazole	1,4-Dioxane	1344	7.7	36	EFISH	[158]	

^{*}D, donor; A, acceptor.[†]Corrected for dispersion.

III. ORGANIC MOLECULES

Table 3 gives first hyperpolarizability as well as permanent electric dipole data for several selected organic molecules in various solvents. The materials are not presented in alphabetical order. (Note: Under methods used, EFISH = electric field induced second harmonic, HRS = hyper-Rayleigh scattering, and Solv. = solvatochromism.)

This list is certainly not inclusive of the large amount of literature on these measurements. Rather it is representative of the values presented in the literature through 1995. For additional data, see Cheng et al. [158,159] for measurements on several substituted benzenes, disubstituted benzenes, *para* substituted benzenes, as well as various 4-methoxy-4'-nitroarenes, mono and 4-4'-disubstituted stilbenes; see Steigman et al. [160] for measurements on various diphenylacetylenes; and see Moylan et al. [161] for measurements on various substituted triphenylimidazoles and triphenyloxazoles.

A word of caution is in order concerning the system of units for the first hyperpolarizability β . In the literature references used in Table 3, the conversion given between SI and cgs units is

$$\beta(\text{SI}) = \frac{4\pi}{3 \times 10^{10}} \beta(\text{cgs})$$

However, Prasad and Williams [162] give a numerical conversion formula that is equivalent to

$$\beta(\text{SI}) = \frac{4\pi\epsilon_0}{3 \times 10^{10}} \beta(\text{cgs})$$

This author prefers the latter conversion formula since it is consistent with using the factor of ϵ_0 in the definition of the nonlinear polarization and second order susceptibility. To make this conversion, simply multiply the SI numbers and units in Table 3 by $\epsilon_0 (= 8.85 \times 10^{-2} \text{C/V} \cdot \text{m})$. The physical units of β will then be $\text{C} - \text{m}^3/\text{V}^2 = \text{C}^3 - \text{m}^3/\text{J}^2$. See Boyd [163] also for a discussion of the two different conventions, in SI units, of either employing or not employing ϵ_0 in the definition of higher order susceptibilities.

REFERENCES

1. D. Eimerl, Electro-optic, linear, and nonlinear optical properties of KDP and its isomorphs, *Ferroelectrics* 72:95 (1987); K. W. Kirby and L. G. DeShazer, Refractive indices of 14 nonlinear crystals isomorphic to KH_2PO_4 , *J. Opt. Soc. Am. B* 4: 1072 (1987).

2. V. S. Suvorov, A. S. Sonin, and I. S. Rez, Some nuclear optical properties of crystals of the KDP group, *Sov. Phys. JETP* 26:33 (1968).
3. B. F. Levine and C. G. Bethea, Nonlinear susceptibility of GaP; relative measurement and use of measured values to determine a better absolute value, *Appl. Phys. Lett.* 20:272 (1972).
4. D. Eimerl, L. Davis, S. Velsko, E.K. Graham, and A. Zalkin, Optical, mechanical, and thermal properties of barium borate, *J. Appl. Phys.* 62: 1968; (1987); K. Kato, Second harmonic generation to 2048 Å in β -BaB₂O₄, *IEEE J. Quant. Electron. QE-22*: 1013 (1986); C. Chen, B. Wu, G. You, and Y. Huang, paper MCC5, *Proc. XIII International Quantum Electronics Conference*, 1984.
5. Y.X. Fan, R.C. Eckardt, R.L. Byer, C. Chen, and A.D. Jiang, Barium borate optical parametric oscillator, *IEEE J. Quant. Electron. QE-25*: 1196 (1989); C. Chen, Y.X. Fan, R.C. Eckardt, and R.L. Byer, Recent developments in barium borate, *Proc. SPIE 681*: 12 (1986).
6. K. Kato, Second harmonic generation at 2660 X in BeSO₄·4H₂O, *Appl. Phys. Lett.* 33:413 (1978).
7. S. Singh, D. A. Draegert, and J. E. Geusic, Optical and ferroelectric properties of barium sodium niobate, *Phys. Rev. B* 2:2709 (1970).
8. V. I. Popolitov, L. A. Ivanova, S. Yu. Stephanovitch, V. V. Chetchkin, A. N. Lobachev, and Yu. N. Venevtsev, Ferroelectrics ABO₄: synthesis of single crystals and ceramics; dielectric and nonlinear optical properties, *Ferroelectrics* 8:519 (1974).
9. Y. Fujii, S. Yoshida, S. Misawa, S. Maekawa, and T. Sakudo, Nonlinear optical susceptibilities of AlN Film, *Appl. Phys. Lett.* 31:815 (1977).
10. D. Blanc, A. M. Bouchoux, C. Plumereau, and A. Cachard, Phase-matched frequency doubling in an aluminum nitride waveguide with a tunable laser source, *Appl. Phys. Lett.* 66:659 (1995).
11. K. Kato, Second-harmonic generation in CDA and CD*A, *IEEE J. Quant. Electron. QE-10*:616 (1974).
12. G. D. Boyd, E. Buechler, F. G. Storz, and J. H. Wernick, Linear and nonlinear optical properties of ternary A^{II}B^{IV}C₂^V chalcopyrite semiconductors, *IEEE J. Quant. Electron. QE-8*:419 (1972).
13. G. D. Boyd, W. B. Grandrud, and E. Buechler, Phase-matched up conversion of 10.6-μm radiation in ZnGeP₂, *Appl. Phys. Lett.* 18:446 (1971).
14. S. K. Kurtz and T. T. Perry, A Powder technique for the evaluation of nonlinear optical materials, *J. Appl. Phys.* 39:3798 (1968).
15. B. F. Levine, C. G. Bethea, and H. M. Kasper, Nonlinear optical susceptibility of thiogallate CdGaS₄, *IEEE J. Quant. Electron. QE-10*:904 (1974).
16. G. D. Boyd, T. J. Bridges, and E. G. Burkhardt, Up-conversion of 10.6 μm radiation to the visible and second harmonic generation in HgS, *IEEE J. Quant. Electron. QE-4*:515 (1968).
17. C.K.N. Patel, Optical harmonic generation in the infrared using a CO₂ laser, *Phys. Rev. Lett.* 16: 613 (1966); R. C. Miller and W. A. Nordland, Absolute sips of second harmonic generation coefficients of piezoelectric crystals, *Phys. Rev. B* 2: 4896 (1970).

18. L.T. Cheng, L. K. Cheng, J. D. Bierlein, and F. C. Zumsteg, Nonlinear optical and electro-optical properties of single crystal CsTiOAsO₄, *Appl. Phys. Lett.* 63:2618 (1993).
19. G. D. Boyd, H. Kasper, and J. H. McFee, Linear and nonlinear optical properties of AgGaS₂, CuGaS₂, and CuInS₂, and theory of the wedge technique for the measurement of nonlinear coefficients, *IEEE J. Quant. Electron.* 7:563 (1971).
20. G. D. Boyd, H. M. Kasper, J. H. McFee, and F. G. Storz, Linear and nonlinear optical properties of some ternary selenides, *IEEE J. Quant. Electron.* QE-8:900 (1972).
21. H. Nasu, H. Okamoto, K. Kurachi, J. Matsuoka, and K. Kamiya, Second-harmonic generation from electrically poled SiO₂ glasses: effects of OH concentration, defects, and poling conditions, *J. Opt. Soc. A. B* 12:644 (1995).
22. G.D. Boyd, E. Buechler, F.G. Storz, Linear and nonlinear optical properties of ZnGeP₂ and CdSe, *Appl. Phys. Lett.* 18: 301 (1971); G.B. Abdullaev, L.A. Kulevsky, A.M. Prokhorov, A.D. Savelev, E. Yu. Salaev, and V. V. Smirnov, GaSe, a new effective material for nonlinear optics *JEPT Lett.* 16: 90 (1972).
23. R.C. Miller, W.A. Nordland, K. Nassau, Nonlinear optical properties of Gd₂(MoO₄)₃ and Tb₂ (MoO₄)₃, *Ferroelectrics* 2: 97 (1971); R.C. Miller and W.A. Nordland, Absolute signs of second harmonic generation coefficients of piezoelectric crystals, *Phys. Rev. B* 2: 4896 (1970); S. Singh, Nonlinear Optical Properties, *Handbook of Laser Science and Technology*, Vol. III, Optical Materials, Part 1 (M. J. Weber, ed.), CRC Press, Inc., Boca Raton, 1986.
24. J. J. Wynne and N. Bloembergen, Measurement of the lowest order nonlinear susceptibility in III-V semiconductors by second harmonic generation with a CO₂ laser, *Phys. Rev.* 188:1211 (1969).
25. C. K. N. Patel, Optical harmonic generation in the infrared using a CO₂ laser, *Phys. Rev. Lett.* 16:613 (1966).
26. P. M. Lundquist, W. P. Lin, G. K. Wong, M. Razeghi, and J. B. Ketterson, Second harmonic generation in hexagonal silicon carbide, *Appl. Phys. Lett.* 66:1883 (1995).
27. J. J. Wynne, Dispersion of the lowest-order optical nonlinearity in InSb, *Phys. Rev. Lett.* 27:17 (1971).
28. R. Braunstein and N. Ockman, *Interactions of Coherent Optical Radiation with Solids*, Final Report, Contract N ONR-4128100, ARPA Order #306-62, Department of the Navy, Washington, DC, 1964.,
29. R. A. Andrews, IR image parametric up-conversion, *IEEE J. Quant. Electron.* QE-6:68 (1970).
30. C. Chen, Y. Wu, A. Jiang, B. Wu, G. You, R. Li, and S. Lin, New nonlinear optical crystal Li₃BO₅, *J. Opt. Soc. Am. B* 6: 616 (1989); S. Lin, Z. Sun, B. Wu, and C. Chen, The nonlinear optical characteristics of a Li₃BO₅ crystal, *J. Appl. Phys.* 67: 634 (1990); S.P. Velsko, M. Webb, L. Davis, and C. Huang, Phase matched harmonic generation in lithium triborate, *IEEE J. Quant. Electron.* 27: 2182 (1991); K. Kato, Tunable UV generation to 0.2325 μm in Li₃BO₅, *IEEE J. Quant. Electron.* 26: 1173 (1990).
31. M.M. Choy and R.L. Byer, Accurate second order susceptibility measurements of visible and infrared nonlinear crystals, *Phys. Rev. B* 14: 1693 (1976); S.K. Kurtz,

- J. Jerphagnon, and M.M. Choy, Nonlinear Dielectric Susceptibilities, *Landolt-Bornstein*, Group 3, Vol. 11, Springer, Berlin, 1979, pp. 641–743; J. Jerphagnon, S.K. Kurtz, and J.L. Oudar, Nonlinear Dielectric Susceptibilities, *Landolt-Bornstein*, Group 3, Vol. 18, Springer, Berlin, 1984, pp. 456–506.
32. S. Singh, W. A. Bonner, J. R. Potopowitz, and L. G. Van Uitert, Nonlinear optical susceptibility of lithium formate monohydrate, *Appl. Phys. Lett.* 17:292 (1970).
 33. S. Singh, W.A. Bonner, J.R. Potopowitz, and L.G. Van Uitert, Nonlinear optical properties of lead niobate, *Proc. Electrochemical Society Meeting*, Los Angeles, May 1970.
 34. G. D. Boyd, H. M. Kasper, and J. H. McFee, Linear and nonlinear optical properties of LiInS₂, *J. Appl. Phys.* 44:2809 (1973).
 35. V. V. Badikov, I. N. Matveev, S. M. Pshenichnikov, O. V. Rychik, N. K. Trotsenko, N. D. Ustinov, and S. I. Shcherbakov, *Sov. J. Quant. Electron.* 10:1300 (1980).
 36. B. F. Levine, C. G. Bethea, H. M. Kasper, and F. A. Thiel, Nonlinear optical susceptibility of HgGa₂S₄, *IEEE Correspondence Ann.* No.606QE008:367 (1976).
 37. S. Kielich, Optical harmonic generation and laser light frequency mixing processes in nonlinear media, *Opto-electronics* 2:125 (1970).
 38. M. M. Choy and R. L. Byer, Accurate second-order susceptibility measurements of visible and infrared nonlinear crystals, *Phys. Rev. B* 14:1693 (1976).
 39. L.-T. Cheng, L.K. Cheng, and J.D. Bierlein, Linear and nonlinear optical properties of the arsenate isomorphs of KTP, *Proc. SPIE 1863* (1993); J.D. Bierlein, H. Vanherzele, and A.A. Ballman, Linear and nonlinear optical properties of flux grown KTiOAsO₄, *Appl. Phys. Lett.* 54: 783 (1989).
 40. B. Zysset, I. Biaggio, and P. Gunter, Refractive indices of orthorhombic KnbO₃ I: Dispersion and temperature dependence, *J. Opt. Soc. Am. B* 9: 380 (1992); I. Biaggio, P. Kerkoc, L.S. Wu, P. Gunter, and B. Zysset, Refractive indices of orthorhombic KNbO₃ II: Phase matching configurations for nonlinear optical interactions, *J. Opt. Soc. Am. B* 9: 507 (1992).
 41. L.-T. Cheng, L.K. Cheng, J.D. Bierlein, Linear and nonlinear optical properties of the arsenate isomorphs of KTP, *Proc. SPIE 1863* (1993); J.D. Bierlein and H. Vanherzele, Potassium titanyl phosphate: properties and new applications, *J. Opt. Soc. Am. B* 6: 622 (1989); H. Vanherzele and J.D. Bierlein, Magnitude of the nonlinear optical coefficients of KTiOPO₄, *Opt. Lett.* 17: 982 (1992); T.Y. Fan, C.E. Huang, B.Q. Hu, R.C. Edkardt, Y.X. Fan, R.L. Byer, and R.S. Feigelson, Second harmonic generation and accurate index of refraction measurements in flux-grown KTiOPO₄, *Appl. Opt.* 26: 2390 (1987); H.Y. Shen, Y.P. Zhou, W.X. Lin, Z.D. Zeng, R.R. Zeng, G. F. Yu, C.F. Huang, A.D. Jiang, S.Q. Jia, and D.Z. Shen, Second harmonic generation and sum frequency mixing of dual wavelength Nd:YAlO₃ laser in flux grown KTiOPO₄ crystals, *IEEE J. Quant. Electron.* 28: 48 (1992).
 42. K.W. Kirby and L.G. DeShazer, Refractive indices of 14 nonlinear crystals isomorphic to KH₂PO₄, *J. Opt. Soc. Am. B* 4: 1072 (1987); V.S. Suvorov, A.S. Sonin, and I.S. Rez, Some nonlinear optical properties of crystals of the KDP groups, *Sov. Phys. JEPT* 26: 23 (1968); R.C. Miller, Optical second harmonic generation in piezoelectric crystals, *Appl. Phys. Lett.* 5: 17 (1964).

43. S. Singh, Nonlinear Optical Materials, *Handbook of Lasers with Selected Data on Optical Technology* (R. J. Pressley, ed), CRC, Cleveland, 1971; L.G. Van Uitert, S. Singh, H.J. Levinstein, J.E. Geusic, and W.A. Bonner, A new and stable nonlinear optical material, *Appl. Phys. Lett.* 11: 161 (1967); Errata: A new and stable nonlinear optical material, *Appl. Phys. Lett.* 12: 224 (1968).
44. K.F. Hulme, P. Jones, P.H. Davies, and M.V. Hobden, Synthetic proustite (Ag_3AsS_3): a new crystal for optical mixing, *Appl. Phys. Lett.* 10: 133 (1967); D.S. Chemla, P.I. Kubicek, and C.A. Schwartz, Redetermination of the nonlinear optical coefficients of proustite by comparison with pyrargyrite and gallium arsenide, *Opt. Commun.* 7: 225 (1973).
45. D. N. Nikogosyan and G. G. Gurzadyan, Crystals for nonlinear optics, *Sov. J. Quant. Electron.* 17:970 (1987).
46. B. Tofield, G. R. Crane, and J. G. Bergman, Structural aspects of nonlinear optics: optical properties of $\text{K}_2\text{H}(\text{IO}_3)_2\text{Cl}$ and related compounds, *J. Chem. Soc. Faraday Trans. II* 70:1488 (1974).
47. A. W. Smith, G. Burns, and D. F. O'Kane, Optical and ferroelectric properties of $\text{K}_x\text{Na}_{1-x}\text{Ba}_2\text{Nb}_5\text{O}_{15}$, *J. Appl. Phys.* 42:250 (1971).
48. W. B. Gandrud, G. D. Boyd, J. H. McFee, and F. H. Wehmeier, Nonlinear optical properties of Ag_3SbS_3 , *Appl. Phys. Lett.* 16:59 (1970).
49. L.T. Cheng, L.K. Cheng, and J.D. Bierlein, Linear and nonlinear optical properties of the arsenate isomorphs of KTP, *Proc. SPIE* 1863 (1993).
50. J. E. Pearson, J. A. Evans, and A. Jariv, Measurement of the relative nonlinear coefficients of KDP, RDP, RDA, and LiIO_3 , *Opt. Commun.* 4:366 (1972).
51. K. Kato, High efficient UV generation at 3472 Å in RDA, *IEEE J. Quant. Electron.* QE-10:622 (1974).
52. G. W. Day, Linear and nonlinear optical properties of trigonal selenium, *Appl. Phys. Lett.* 18:347 (1971).
53. G. H. Sherman and P. D. Coleman, Measurement of the second-harmonic-generation nonlinear susceptibilities of Se, CdTe, and InSb at 28.0 μm by comparison with Te, *J. Appl. Phys.* 44:238 (1973).
54. P. J. Kupecek, C. A. Schwartz, and D. S. Chemla, Silver thiogallate (AgGaS_2). I. Nonlinear optical properties, *IEEE J. Quant. Electron.* QE-10:540 (1974).
55. K. Inoue, and T. Ishidate, Temperature dependence of optical nonlinear susceptibility of NaNO_2 , *Ferroelectrics* 7:105 (1974).
56. D. S. Chemla, P. L. Kupecek, D. S. Robertson, and R. C. Smith, Silver thiogallate. A new material with potential for infrared devices, *Opt. Commun.* 3:29 (1971), see also Ref. 57.
57. E. C. Cheung, K. Koch, G. T. Moore, and J. M. Liu, Measurements of second-order nonlinear optical coefficients from the spectral brightness of parametric fluorescence, *Opt. Lett.* 19:168 (1994).
58. B. F. Levine, W. A. Nordland, and W. J. Shiever, Nonlinear optical susceptibility of AgI, *IEEE J. Quant. Electron.* QE-9:468 (1973).
59. M. J. Nystrom, B. W. Wessels, W. P. Lin, G. K. Wong, D. A. Neumayer, and T. J. Marks, Nonlinear optical properties of textured strontium barium niobate thin films

- prepared by metalorganic chemical vapor deposition, *Appl. Phys. Lett.* 66:1726 (1995).
- 60. G. H. Sherman and P. D. Coleman, Absolute measurement of the second-harmonic generation nonlinear susceptibility of tellurium at 28.0 μm , *IEEE J. Quant. Electron.* QE-9:403 (1973).
 - 61. H.O. Marcy, L.F. Warren, M.S. Webb, C.A. Ebbers, S.P. Velsco, G.C. Kennedy, and G.-C. Catella, Second harmonic generation in zinc tris (thio urea) sulfate, *Appl. Opt.*, 31: 5051 (1992); U.B. Ramabadran, D.E. Zelmon, and G.C. Kennedy, Electro-optic, piezoelectric, and dielectric properties of zinc tris thio urea sulfate, *Appl. Phys. Lett.* 60: 2590 (1992).
 - 62. G. D. Boyd, E. Buechler, and F. G. Storz, Linear and nonlinear optical properties of ZnGeP₂ and CdSe, *Appl. Phys. Lett.* 18:301 (1971).
 - 63. Y. Hase, K. Kumata, S. S. Kano, M. Ohashi, T. Kondo, R. Ito, and Y. Shiraki, New method for determining the nonlinear optical coefficients of thin films, *Appl. Phys. Lett.* 61:145 (1992).
 - 64. R.C. Miller, S.C. Abrahams, R.L. Barns, J.L. Bernstein, and W.A. Nordland, Absolute signs of the second harmonic generation, electro-optic, and piezoelectric coefficients of CuCl and ZnS, *Solid State Commun.* 9: 1463 (1971); S. Singh, Nonlinear Optical Properties, *Handbook of Laser Science and Technology*, Vol. III, Optical Materials, Part 1 (M. J. Weber, ed.), CRC Press, Inc., Boca Raton, 1986.
 - 65. C. K. N. Patel, Optical harmonic generation in the infrared using a CO₂ laser, *Phys. Rev. Lett.* 16:613 (1966), see also Ref. 26.
 - 66. R.K. Chang, J. Ducuing, and N. Bloembergen, Dispersion of the optical nonlinearity in semiconductors, *Phys. Rev. Lett.* 15: 415 (1965); R.C. Miller and W.A. Nordland, Absolute signs of second harmonic generation coefficients of piezoelectric crystals, *Phys. Rev. B* 2: 4896 (1970).
 - 67. M. Sagawa, H. Kagawa, A. Kakuta, and M. Kaji, Generation of a violet phase-matched second-harmonic wave with a new organic single crystal, 8-(4'-acetylphenyl)-1,4-dioxa-8-azaspiro[4.5]decane, *Appl. Phys. Lett.* 63:1877 (1993).
 - 68. S. Tomaru, S. Matsumoto, T. Kurihara, H. Suzuki, N. Ooba, and T. Kaino, Nonlinear optical properties of 2-adamantylamino-5-nitropyridine crystals, *Appl. Phys. Lett.* 58:2583 (1991).
 - 69. K. Kajikawa, H. Nagamori, H. Takezoe, A. Fukuda, S. Ukishama, Y. Takhashi, M. Iijima, and E. Fukuda, Optical second harmonic generation from poled thin films of aromatic polyurea prepared by vapor deposition polymerization, *Jpn. J. Appl. Phys.* 30:L1737 (1991).
 - 70. T. Mitsui, K. Iio, K. Hamono, and S. Sawada, Optical second harmonic generation in ammonium tartrate, *Opt. Commun.* 9:322 (1973).
 - 71. K. Betzler, H. Hess, and P. Loose, Optical second harmonic generation in organic crystals: urea and ammonium malate, *J. Mol. Struct.* 47:393 (1978).
 - 72. A. N. Izrailenko, R. Yu. Orlov, and V. A. Koptsiuk, Ammonium oxalate—a new nonlinear optical material, *Sov. Phys. Crystallogr.* 13:136 (1968).
 - 73. J. R. Gott, Effect of molecular structure on optical second harmonic generation from organic crystals, *J. Phys. B* 4:116 (1971).

74. P. D. Southgate and D. S. Hall, Second harmonic generation and Miller's delta parameter in a series of benzene derivatives, *J. Appl. Phys.* 43:2765 (1972).
75. A. Carenco, J. Jerphagnon, and A. Perigaud, Nonlinear optical properties of some m-disubstituted benzene, *J. Chem. Phys.* 66:3806 (1977).
76. D. Jungbauer, I. Teraoka, D. Y. Yoon, B. Reck, J. D. Swalen, and R. Twieg, Second order nonlinear optical properties and relaxation characteristics of poled linear epoxy polymers with tolane chromophores, *J. Appl. Phys.* 69:8011 (1991).
77. M. Eich, B. Reck, D. Y. Yoon, C. G. Wilson, and G. C. Bjorklund, Novel second order nonlinear optical polymers via chemical crosslinking induced vitrification under electric field, *J. Appl. Phys.* 66:3241 (1989).
78. G. J. Zhang, T. Kinoshita, K. Sasaki, A. Goto, and A. Nakayama, *Proc. CLEO*, Baltimore, 1989.
79. W. J. Blau, H. J. Byrne, D. J. Cardin, T. J. Dennis, J. P. Hare, H. W. Kroto, R. Taylor, and D. R. M. Walton, Large infrared nonlinear optical response of C_{60} , *Phys. Rev. Lett.* 67:1423 (1991).
80. P. S. Bechthold and S. Haussuhl, Nonlinear optical properties of orthorhombic barium formate and magnesium barium fluoride, *Appl. Phys.* 14:403 (1977).
81. J. Kawamata, K. Inoue, and T. Inabe, Salient nonlinear optical properties of novel organic crystals comprising π -conjugated ketones, *Appl. Phys. Lett.* 66:3102 (1995).
82. H. Nakatani, H. Hayashi, and T. Hidaka, Linear and nonlinear optical properties of 2-cyano-3-(2-methoxyphenyl)-2-propenoic acid methyl ester, *Jpn. J. Appl. Phys.* 31:1802 (1992).
83. Ch. Bosshard, K. Sutter, P. Gunter, and G. Chapuis, Linear and nonlinear optical properties of 2-cyclo-octyl-amino-5-nitropyridine, *J. Opt. Soc. Am. B* 6:721 (1989).
84. R. Quintero-Torres and M. Thakur, Second-harmonic generation in single-crystal films of an organic material, *Opt. Lett.* 19:87 (1994).
85. Y. Kitaoka, T. Sasaki, S. Nakai, A. Yokotani, Y. Goto, and M. Nakayama, Laser properties of new organic nonlinear optical crystal chalcone derivatives, *Appl. Phys. Lett.* 56:2074 (1990).
86. D. Yu, A. Gharavi, and L. Yu, Novel second-order nonlinear optical, aromatic, and aliphatic polyimides exhibiting high-temperature stability, *Appl. Phys. Lett.* 66:1050 (1995).
87. A. Harada, Y. Okazaki, K. Kamiyami, and S. Umegaki, Generation of blue coherent light from a continuous wave semiconductor laser using an organic crystal-cored fiber, *Appl. Phys. Lett.* 59:1535 (1991).
88. Ch. Bosshard, M. Kupfer, P. Gunter, S. Pasquier, S. Zahir, and M. Seifert, Optical wave guiding and nonlinear optics in high quality 2-docosyl-amino-5-nitropyridine Langmuir-Blodgett films, *Appl. Phys. Lett.* 56:1204 (1990).
89. K. D. Singer, M. G. Kuzyk, W. R. Holland, J. E. Sohn, S. J. Lalama, R. B. Commizolli, G. E. Katz, and M. L. Schilling, Electro-optic phase modulation and optical second harmonic generation in corona poled polymer films, *Appl. Phys. Lett.* 53:1800 (1988).

90. J. W. Perry, S. R. Marder, E. T. Sleva, C. Yakymyshyn, K. R. Stewart, and E. P. Boden, Organic salts with large electro-optic coefficients, *Proc. SPIE* 1560:301 (1991).
91. L. M. Hayden, G. F. Sauter, F. R. Ore, P. L. Pasillas, J. M. Hoover, G. A. Lindsay, and R. A. Henry, Second-order nonlinear optical measurements in guest-host and side-chain polymers, *J. Appl. Phys.* 68:456 (1990).
92. P. D. Southgate and D. S. Hall, Nonlinear optical susceptibility of a crystalline coumarin dye, *J. Appl. Phys.* 42:4480 (1971).
93. A. Sonin, A. A. Filimonov, and V. S. Suvorov, Generation of the second harmonic of ruby laser radiation in some crystals, *Sov. Phys. Solid State* 10:1481 (1968).
94. S. Singh, W. A. Bonner, T. Kyle, J. R. Potopowicz, and L. G. Van Uitert, Second harmonic generation in D-threonine, *Opt. Commun.* 5:131 (1972).
95. V. D. Shigorin, G. P. Shipulo, S. S. Grazhulene, L. A. Musikhin, and V. Sh. Shekhtman, Nonlinear optical properties of molecular crystals of metatolylenediamine, *Sov. J. Quant. Electron.* 5:1393 (1976).
96. M. Nelson and M. Delfino, Nonlinear dielectric susceptibilities, *Landolt and Bornstein Data Series* 11:671 (1979).
97. Y. Shuto, H. Takara, M. Amano, and T. Kaino, Noncollinearly phase-matched second harmonic generation in stilbene-dye-attached polymer thin films, *Jpn. J. Appl. Phys.* 28:2508 (1989).
98. R. Y. Orlov, Hippuric acid as a source of second harmonics in the optical range, *Sov. Phys. Crystallogr.* 11:410 (1966).
99. A. Samoc, M. Samoc, P. N. Prasad, and A. K. Cizio, Second harmonic generation in the crystalline complex antimony tri-iodide-sulfur, *J. Opt. Soc. Am. B* 9:1819 (1992).
100. D. Eimerl, S. Velsko, L. Davis, F. Wang, G. Loizcono, and G. Kennedy, Deuterated L-arginine phosphate: a new efficient nonlinear crystal, *IEEE J. Quant. Electron.* 25:179 (1989).
101. H. O. Marcy, M. J. Rosker, L. F. Warren, P. H. Cunningham, C. A. Thomas, L. A. DeLoach, S. P. Velsko, C. A. Ebbers, J.-H. Lao, and M. G. Kanatzidis, L-histidine tetrafluoroborate: a solution-grown semiorganic crystal for nonlinear frequency conversion, *Opt. Lett.* 20:252 (1995).
102. T. Ukachi, T. Shigemoto, H. Komatsu, and T. Sugiyama, Crystal growth, and characterization of a new organic nonlinear-optical material: L-N-(5-nitor-2-pyridyl)leucinol, *J. Opt. Soc. Am. B* 10:1372 (1993).
103. M. Kitazawa, R. Higuchi, M. Takahashi, T. Wada, and H. Sasabe, Ultraviolet generation 266 nm in a novel organic nonlinear optical crystal: L-pyrrolidone-2-carboxylic acid, *Appl. Phys. Lett.* 64:2477 (1994).
104. X. T. Tao, D. R. Yuan, N. Zhang, M. H. Jiang, and Z. S. Shao, Novel organic molecular at second harmonic generation crystal: 3-methoxy-4-hydroxy-benzaldehyde, *Appl. Phys. Lett.* 60:1415 (1992).
105. T. Kondo, R. Morita, N. Ogasawara, S. Umegaki, and R. Ito, A nonlinear optical organic crystal for wave guiding SHG devices (-2)-(α-methylbenzyl-amino)-5-nitropyridine (MBANP), *Jpn. J. Appl. Phys.* 28:1622 (1989).

106. J. D. Bierlein, L. K. Cheng, Y. Wang, and W. Tam, Linear and nonlinear optical properties of 3-methyl-4'-methoxy-4-stilbene, *Appl. Phys. Lett.* 56:424 (1990).
107. K. Sutter, Ch. Bosshard, M. Ehrensperger, P. Gunter, and R. J. Twieg, Nonlinear optical and electro-optical effects in 2-methyl-4-nitro-N-methylalanile (MNMA) crystals, *IEEE J. Quant. Electron.* 24:2362 (1988).
108. J. Zyss, D. S. Chemla, and J. F. Nicoud, Demonstration of efficient nonlinear optical crystals with vanishing molecular dipole moment: second-harmonic generation in 3-methyl-4-nitropyridine-1-oxide, *J. Chem. Phys.* 74:4800 (1981).
109. J. L. Oudar and R. Hierle, An efficient organic crystal for nonlinear optics-Methyl-2,4-dinitrophenyl-aminopropanoate, *J. Appl. Phys.* 48:2699 (1977).
110. B. F. Levine, C. G. Bethea, C. D. Thurmond, R. T. Lynch, and J. L. Bernstein, An organic crystal with an exceptionally large optical second-harmonic coefficient: 2-methyl-4-nitroaniline, *J. Appl. Phys.* 50:2523 (1979).
111. B. L. Davydov, L. B. Koreneva, and E. A. Lavrovsky, An efficient frequency doubler of neodymium laser radiation, employing a molecular crystal of metanitroaniline, *Radio Eng. Electron. Phys.* 19:130 (1974).
112. G. S. Belikova, M. P. Golovey, V. D. Shigorin, and G. P. Shipulo, Optical second-harmonic generation in meta-dinitrobenzene, *Opt. Spectrosc. (USSR)* 38:441 (1975).
113. P. Kerkoc, M. Zgonik, K. Sutter, Ch. Bosshard, and P. Gunter, 4-(*N,N*-Dimethylamino)-3-acetamidonitrobenzene single crystals for nonlinear optical applications, *J. Opt. Soc. Am. B* 7: 313 (1990); J.C. Baumert, R.J. Twieg, G.C. Bjorklund, J.A. Logan, and C.W. Dirk, Crystal growth and characterization of 4-(*N,N*-Dimethylamino)-3-acetamidonitrobenzene, a new organic material for nonlinear optics, *Appl. Phys. Lett.* 51: 1484 (1987).
114. D. Junbauer, B. Reck, R. Twieg, D. Y. Yoon, C. G. Wilson, and J. D. Swalen, Highly efficient and stable nonlinear opical polymers via chemical cross-linking under electric field, *Appl. Phys. Lett.* 56:2610 (1990).
115. V. A. Howarth, N. Asai, N. Kishii, and I. Fujiwara, Optical second harmonic generation in Langmuir Blodgett films of *n*-docosy-2-methyl-4-nitroaniline, *Appl. Phys. Lett.* 61:1616 (1992).
116. K. D. Singer, J. E. Sohn, and S. J. Lalama, Second harmonic generation in poled polymer films, *Appl. Phys. Lett.* 49:248 (1986).
117. K. Sutter, J. Hulliger, E. Knopfle, N. Saupper, and P. Gunter, Nonlinear optical properties of *N*-(4-nitro-2-pyridinyl)phenylaninol (NPPA) crystals, *Proc. CLEO* 10:478 (1991).
118. J. Zyss, F. Nicoud, and M. Coquillay, Chirality and hydrogen bonding in molecular crystals for phase-matched second harmoinc generation: *N*-(4-nitrophenyl)-(L)-prolinol, *J. Chem. Phys.* 81:4160 (1984).
119. D. Xu, M. H. Jiang, X. T. Tao, Z. S. Shao, J. T. Lin, and B. H. T. Chai, The investigation of new nonlinear organometallic complex crystals—correlation between optical properties and structural radicals, *Proc. SPIE* 1104:188 (1989).
120. H. Minemoto, Y. Ozaki, and N. Sonoda, Intracavity second-harmonic generation using a deuterated organic ionic crystal, *Appl. Phys. Lett.* 63:3565 (1993).

121. S. F. Hubbard, K. D. Singer, F. Li, S. Z. D. Cheng, and F. W. Harris, Nonlinear optical studies of a fluorinated poled polyimide guest–host system, *Appl. Phys. Lett.* 65:256 (1994).
122. G. Khanarian, R. A. Norwood, D. Haos, B. Feueur, and D. Karim, Phase matched second-harmonic generation in a polymer waveguide, *Appl. Phys. Lett.* 57:977 (1990).
123. K. Sutter, Ch. Bosshard, W. S. Wang, G. S. Surmely, and P. Gunter, Linear and nonlinear properties of 2-(*N*-prolinol)-5-nitropyridine, *Appl. Phys. Lett.* 53:1779 (1988).
124. H. S. Nalwa, T. Watanabe, A. Kakuta, A. Mukoh, and S. Miyata, Second-order nonlinear optical properties of an aromatic polyurea exhibiting optical transparency down to 300 nm, *Appl. Phys. Lett.* 62:3223 (1993).
125. M. Eich, A. Sen, H. Looser, G. C. Bjorklund, J. D. Swalen, R. Twieg, and D. Y. Yoon, Corona poling and real-time second harmonic generation study of a novel covalently functionalized amorphous nonlinear optical polymer, *J. Appl. Phys.* 66:2559 (1989).
126. S. H. Ou, J. A. Mann, and J. B. Lando, Nonlinear optical studies of polar polymeric Langmuir Schaefer films, *Appl. Phys. Lett.* 61:2284 (1992).
127. D. H. Choi, W. M. K. P. Wijekoon, H. M. Kim, and P. N. Prasad, Second-order nonlinear optical effects in novel polymethacrylates containing a molecular–ionic chromophore in the side chain, *Chem. Mater.* 6:234 (1994).
128. L. Schuler, K. Betzler, H. Hesse, and S. Kapphan, Phase-matched second harmonic generation in potassium malate, *Opt. Commun.* 43:157 (1982).
129. V. Deserno and S. Haussuhl, Phase-matchable optical nonlinearity in strontium formate and strontium formate dehydrate, *IEEE J. Quant. Electron.* QE-8:608 (1972).
130. Y. Kitaoka, T. Sasaki, S. Nakai, and Y. Goto, New nonlinear optical crystal thienyl chalcone and its harmonic generation properties, *Appl. Phys. Lett.* 59:20 (1991).
131. S. X. Dou, M. H. Jiang, Z. S. Shao, and X. T. Tao, Maker fringes in biaxial crystals and the nonlinear optical coefficients of thiosemicarbazide cadmium chloride monohydrate, *Appl. Phys. Lett.* 54:1101 (1989).
132. K. Betzler, H. Hesse, and P. Loose, Optical second harmonic generation in organic crystals: urea and ammonium–malate, *J. Mol. Struct.* 47:393 (1978).
133. D. W. Robinson, H. Abdel-Halim, S. Inoue, M. Kimura, and D. O. Cowan, Hyperpolarizabilities of 4-amino-4'-nitrodiphenyl sulfide and all of its chalcogen analogues, *J. Chem. Phys.* 90:3427 (1989).
134. S. Norvez and M. Barzoukas, Nonlinear optical properties of triptycene derivatives, *Chem. Phys. Lett.* 165:41 (1990).
135. B. F. Levine and G. Bethea, Effects on hyperpolarizabilities of molecular interactions in associating liquid mixtures, *J. Chem. Phys.* 65:2429 (1976).
136. A. Dulcic and C. Sauteret, The regularities observed in the second order hyperpolarizabilities of variously disubstituted benzenes, *J. Chem. Phys.* 69:3453 (1978).

137. I. Ledoux and J. Zyss, Influence of the molecular environment in solution measurements of the second-order optical susceptibility for urea and derivatives, *Chem. Phys.* 73:203 (1982).
138. J.-F. Nicoud, C. Serbutoviez, G. Puccetti, I. Ledoux, and J. Zyss, Hyperpolarizability of new nitro-aromatic-N-oxide species: nonlinear optical properties of a ferromagnetic organic material, *Chem. Phys. Lett.* 175:257 (1990).
139. J. L. Oudar, Optical nonlinearities of conjugated molecules. Stilbene derivatives and highly polar aromatic compounds, *J. Chem. Phys.* 67:446 (1977).
140. C. C. Teng and A. F. Garito, Dispersion of the nonlinear second-order optical susceptibility of organic systems, *Phys. Rev. B.* 28:6766 (1983).
141. B. F. Levine, Donor-acceptor charge transfer contributions to the second order hyperpolarizability, *Chem. Phys. Lett.* 37:516 (1976).
142. B. F. Levine, C. G. Bethea, E. Wasserman, and L. Leenders, Solvent dependent hyperpolarisability of a merocyanine dye, *J. Chem. Phys.* 68:5042 (1978).
143. A. Dulcie and C. Flytzanis, A new class of conjugated molecules with large second order polarizability, *Opt. Commun.* 25:402 (1978).
144. J. Zyss and J. L. Oudar, Relations between microscopic and macroscopic lowest-order optical nonlinearities of molecular-crystals with one-dimensional or two-dimensional units, *Phys. Rev. A* 26:2028 (1982).
145. J. Zyss, D. S. Chemla, and J.-F. Nicoud, Demonstration of efficient nonlinear optical crystals with vanishing molecular dipole moment: second-harmonic generation, *J. Chem. Phys.* 74:4800 (1981).
146. B. F. Levine and C. G. Bethea, Hyperpolarizability of the pyridine–iodine charge transfer complex, *J. Chem. Phys.* 65:2439 (1976).
147. B. F. Levine and C. G. Bethea, Charge transfer complexes and hyperpolarizabilities, *J. Chem. Phys.* 66:1070 (1977).
148. S. J. Lalama, K. D. Singer, A. F. Garito, and K. N. Desai, Exceptional second-order nonlinear optical susceptibilities of quinoid systems, *Appl. Phys. Lett.* 39:940 (1981).
149. B. F. Levine and C. G. Bethea, Second order hyperpolarizability of a polypeptide alpha-helix: poly gamma -benzyl-L-glutamate, *J. Chem. Phys.* 65:1989 (1976).
150. S. R. Marder, C. B. Gorman, B. G. Tiemann, and L.-T. Cheng, Stronger acceptors can diminish nonlinear optical response in simple donor–acceptor polyenes, *J. Am. Chem. Soc.* 115:3006 (1993).
151. R. F. Shi, M. H. Wu, S. Yamada, Y. M. Cai, and A. F. Garito, Dispersion of second-order optical properties of new high thermal stability guest chromophores, *Appl. Phys. Lett.* 63:1173 (1993).
152. Ch. Bosshard, G. Knopfle, P. Pretre, and P. Gunter, Second-order polarizabilities of nitropyridine derivatives determined with electric-field-induced second-harmonic generation and a solvatochromic method: A comparative study, *J. Appl. Phys.* 71:1594 (1992).
153. T. Uemiya, N. Uenishi, and S. Umegaki, Modified method of electric-field induced second-harmonic generation, *J. App. Phys.* 73:12 (1993).
154. K. Clays and A. Persoons, Hyper-Rayleigh scattering in solution, *Rev. Sci. Instrum.* 63:3285 (1992).

155. T. Verbiest, K. Clays, A. Persoons, F. Meyers, and J. L. Bredas, Determination of the hyperpolarizability of an octopolar molecular ion by hyper-Rayleigh scattering, *Opt. Lett.* 18:525 (1993).
156. M. S. Paley, J. M. Harris, H. Looser, J. C. Baumert, G. C. Bjorklund, D. Jundt, and R. J. Tweig, A solvatochromic method for determining second-order polarizabilities of organic molecules, *J. Org. Chem.* 54:3774 (1989).
157. S. F. Hubbard, K. D. Singer, F. Li, S. Z. D. Cheng, and F. W. Harris, Nonlinear optical studies of a fluorinated poled polyimide guest–host system, *Appl. Phys. Lett.* 65:265 (1994).
158. L.-T. Cheng, W. Tam, G. R. Merideth, G. L. J. A. Rikken, and E. W. Meijer, Nonresonant EFISH and THG studies of nonlinear optical property and molecular structure relations of benzene, stilbene, and other arene derivatives, *Proc. SPIE* 1147:61 (1989).
159. L.-T. Cheng, W. Tam, S. H. Stevenson, G. R. Meredith, G. Rikken, and S. R. Marder, Experimental investigations of organic molecular nonlinear optical polarizabilities, *J. Chem. Phys.* 95:10631 (1991).
160. A. E. Stiegman, E. Graham, K. J. Perry, L. R. Khundkar, S.-T. Cheng, and J. W. Perry, The electronic structure and second-order nonlinear optical properties of donor–acceptor acetylenes, *J. Am. Chem. Soc.* 113:7658 (1991).
161. C. R. Moylan, R. D. Miller, R. J. Twieg, K. M. Betterton, V. Y. Lee, T. J. Matray, and C. Nguyen, Synthesis and nonlinear optical properties of donor–acceptor substituted triaryl azole derivatives, *Chem. Mater.* 5:1499 (1993).
162. P. N. Prasad and D. J. Williams, *Introduction to nonlinear optical effects in molecules and polymers*, John Wiley & Sons, Inc., New York, 1991, p. 303.
163. R. W. Boyd, *Nonlinear Optics*, Academic Press Inc., New York, 1992, pp. 429–432.
164. W. J. Alford and A. V. Smith, Wavelength variation of the second-order nonlinear coefficients of KNbO_3 , KTiOPO_4 , KTiOAsO_4 , LiNbO_3 , LiIO_3 , $\beta\text{-BaB}_2\text{O}_4$, KH_2PO_4 , and LiB_3O_5 crystals: a test of Miller wavelength scaling, *J. Opt. Soc. Am. B* 18:524 (2001).
165. I. Shoji, H. Nakamura, K. Ohdaira, T. Kondo, R. Ito, T. Okamoto, K. Tatsuki, and S. Kubota, Absolute measurement of second-order nonlinear-optical coefficients of $\beta\text{-BaB}_2\text{O}_4$ for visible to ultraviolet second-harmonic wavelengths, *J. Opt. Soc. Am. B* 16:620 (1999).
166. I. Shoji, H. Nakamura, R. Ito, T. Kondo, M. Yoshimura, Y. Mori, and T. Sasaki, Absolute measurement of second-order nonlinear-optical coefficients of $\text{CsLiB}_6\text{O}_{10}$ for visible-to-ultraviolet second-harmonic wavelengths, *J. Opt. Soc. Am. B* 18:302 (2001).
167. J. J. Adams, C. A. Ebbers, K. I. Schaffers, and S. A. Payne, Nonlinear optical properties of $\text{LaCa}_4\text{O}(\text{BO}_3)_3$, *Opt. Lett.* 26:217 (2001).
168. G. H. M. Knippels, A. F. G. van der Meer, A. M. MacLeod, A. Yelisseyev, L. Isaenko, S. Lobanov, I. Thénot, and J.-J. Zondy, Mid-infrared (2.75–6.0- μm) second-harmonic generation in LiInS_2 , *Opt. Lett.* 26:617 (2001).

169. R. J. Gehr and A. V. Smith, Separated-beam nonphase-matched second-harmonic method of characterizing nonlinear optical crystals, *J. Opt. Soc. Am. B* 15:2298 (1998).
170. G. A. Wagoner, P. D. Persans, E. A. Van Wagenen, and G. M. Korenowski, Second-harmonic generation in molybdenum disulfide, *J. Opt. Soc. Am. B* 15:1017 (1998).
171. N. Ye, W. Zeng, J. Jiang, B. Wu, C. Chen, B. Feng, and X. Zhang, New nonlinear optical crystal K₂Al₂B₂O₇, *J. Opt. Soc. Am. B* 17: 764 (2000); New nonlinear optical crystal K₂Al₂B₂O₇: errata, *J. Opt. Soc. Am. B* 18: 122 (2001).
172. C. Chen, Z. Shao, J. Jiang, J. Wei, J. Lin, J. Wang, N. Ye, J. Lv, B. Wu, M. Jiang, M. Yoshimura, Y. Mori, and T. Sasaki, Determination of the nonlinear optical coefficients of YCa₄O(BO₃)₃ crystal, *J. Opt. Soc. Am. B* 17:566 (2000).
173. J. Zaccaro, A. Ibanez, and M. Chamel, Linear and second-order nonlinear optical characterizations of the solid solution 2-amino-5-nitropyridinium dihydrogenphosphate–arsenate 2A5NPDP_(1-x)As_x(0 ≤ x ≤ 1), *J. Opt. Soc. Am. B* 16:1385 (1999).
174. A. Yokoo, I. Yokohama, H. Kobayashi, and T. Kaino, Linear and nonlinear optical properties of the organic nonlinear optical crystal 2-adamantylamino-5-nitropyridine, *J. Opt. Soc. Am. B* 15:432 (1998).
175. S. Tan, A. K. Bhowmik, S. Sodah, and M. Thakur, Nonlinear optical studies of 3-methyl-4-methoxy-4'-nitrostilbene single-crystal films, *Appl. Phys. Lett.* 77:827 (2000).
176. V. G. Dmitriev, G. G. Gurzadyn, and D. N. Nikogosyan, *Handbook of Nonlinear Optical Crystals*, Springer-Verlag, New York, 1991.

6

Nonlinear Index of Refraction

Many of the interesting phenomena of nonlinear optics derive their behavior from the nonlinear index of refraction. It has led to a variety of fascinating applications. It is also central to many fundamental scientific investigations, such as chaos theory and quantum optics.

Several diverse physical effects contribute to the nonlinear index of refraction. Generally, it can be defined as a change in the refractive index or the spatial distribution of the refractive index of a medium due to the presence of optical waves. There are several different types of effects that fall under this general definition.

Optical Kerr effect. This effect is directly related to the third order nonlinear polarization. The change in index is proportional to the time average of the optical electric field squared, $\langle \mathbf{E}^{(\sim)}(\mathbf{r}, t) \cdot \mathbf{E}^{(\sim)}(\mathbf{r}, t) \rangle$. Another way to say this is that the change in index depends linearly on the optical intensity.

Nonlocal effects. In this case, the index change again depends on the time averaged field, or the intensity, but is due to a gradient in the field or long range order in the medium. The gradient could be caused by, for example, a focused beam or the superposition of coherent beams producing an interference pattern of bright and dark fringes. Long range order exists, for example, in liquid crystals. In these materials, if a molecule experiences a force due to the presence of an electromagnetic wave, intermolecular interactions cause molecules a relatively long distance away to be also affected by the force.

Saturation. In this type of effect, the change in index accompanies absorption of optical energy by the medium. Thus this case involves optical loss. For small enough intensities, the index change is approximately proportional to the intensity.

Changes in physical properties of a medium. In some instances an intense optical wave will induce changes in some physical property of a medium. Examples are the temperature or the concentration of a particular species. The index change will often be proportional to the intensity but may also depend on the time integrated intensity, that is, the fluence.

Cascading effects. An effective change in index can result from a combination of second order effects, or a sequential effect of linear and second order phenomena. An example of the former is the change in optical phase of the pump wave in a general second harmonic generation or frequency mixing process. The photorefractive effect, discussed below, is an example of the latter. In processes utilizing this effect, the index change does not depend on the magnitude of the intensity but rather on the spatial modulation of the intensity.

The nonlinear index of refraction has generated significant scientific and technological interest. It has been utilized in or considered for a variety of applications:

- Nonlinear spectroscopy,
- Correcting optical distortions,
- Optical switching,
- Optical logic gates,
- Optical data processing,
- Optical communications,
- Optical limiting,
- Passive laser mode-locking, and
- Waveguide switches and modulators.

These applications derive from several phenomena that have been discovered and are related to the nonlinear refractive index. These occur through a modulation of the phase or amplitude of an intense optical wave propagating through a nonlinear medium.

The nonlinear index of refraction can also produce detrimental effects, such as unwanted phase aberrations or even optical damage. Thus it becomes an important consideration in any experiment or application employing the manipulation of intense optical beams.

This chapter describes many of the physical processes contributing to the nonlinear index of refraction as well as many of the resulting optical phenomena. First, important definitions and notation are given. Then, many of the physical mechanisms producing the nonlinear index are discussed, with formulas given relating the index change to important microscopic and macroscopic parameters. Finally, the formulas for important parameters in nonlinear optical phenomena resulting from the nonlinear index are presented and discussed.

I. DEFINITIONS AND NOTATION

The general dependence of the nonlinear refractive index on intensity can be expressed as

$$n(\mathbf{r}, t) = n_0(\mathbf{r}, t) + \Delta n[I(\mathbf{r}, t)] \quad (1)$$

This equation indicates that the change in the refractive index Δn over its value at low intensities n_0 has a functional dependence on the intensity $I(\mathbf{r}, t)$. This dependence is made more explicit in the following paragraphs. The majority of phenomena considered occur in isotropic materials. Thus, unless stated otherwise, most of the formulas that follow apply to isotropic media.

Kerr-like media. In this case the nonlinear index change can be written as

$$\Delta n = n_2 \langle \mathbf{E}^{(\sim)} \cdot \mathbf{E}^{(\sim)} \rangle \quad (2)$$

where n_2 is called the nonlinear index coefficient, and the angle brackets indicate a time average over at least one optical cycle. It will be remembered that $\mathbf{E}^{(\sim)}$ is the total real optical field, including the rapidly varying oscillatory behavior. These oscillations are too rapid to observe at optical frequencies: only the time averaged effect is observed. Thus the nonlinear index of refraction depends on the slowly time varying complex amplitude $\mathbf{E}(\mathbf{r}, t)$.

At this point, the result of Eq. (2) will depend on the convention used to describe the real field in complex notation. Following the notation for the expansion of the nonlinear polarization as a power series in the electric field, given in Chapter 1, the result is $\Delta n = 2n_2|\mathbf{E}|^2$. Some authors prefer to write the real field as $\mathbf{E}^{(\sim)}(\mathbf{r}, t) = (1/2)\mathbf{E}(\mathbf{r}, t)e^{-i\omega t} + \text{c.c.}$ With this notation, the result of Eq. (2) is $\Delta n = (1/2)n_2|\mathbf{E}|^2$. Both expressions are valid as long as the expression for the field and related expressions, e.g., the intensity, are consistent. For example, for the former case, $I = 2\epsilon_0 n_0 c |\mathbf{E}|^2$, while for the latter, $I = (1/2)\epsilon_0 n_0 c |\mathbf{E}|^2$, with both expressions in SI units. The reader is cautioned to be aware that these conventions are sometimes mixed together in the literature on nonlinear optics. In this book, the former convention will be adhered to unless explicitly stated otherwise.

Since $I \propto |\mathbf{E}|^2$, it is sometimes convenient to express the nonlinear index in terms of intensity. In this case, the index change is expressed by

$$\Delta n = n_2^I I \quad (3)$$

where n_2^I is the nonlinear index intensity coefficient. In the literature this constant is often called γ or sometimes just n_2 . Although it is often possible to distinguish the intensity coefficient from the field-squared coefficient by their context (they also have different physical units), the two will be identified differently here to avoid confusion. The use of γ is avoided since this also is used for other quantities in expressions of the nonlinear index coefficient (see below).

The nonlinear index coefficient is related to the third order nonlinear susceptibility that appears in the expansion to third order of the nonlinear polarization. From Chapter 1, the i th component ($i = x, y, z$) of this third order polarization for a single wave of frequency ω is given by

$$P_i^{(3)}(\omega) = 3\epsilon_0 \sum_{jkl} \chi_{ijkl}^{(3)}(-\omega; \omega, \omega, -\omega) E_j(\omega) E_k(\omega) E_l^*(\omega) \quad (4)$$

This nonlinear polarization leads to a self-induced index change of the type described above in Eq. (2). Another case of importance is that of a strong wave at frequency ω inducing an index change for a weak probe beam at frequency ω' . For this case the third order polarization is written as

$$P_i^{(3)}(\omega') = 6\epsilon_0 \sum_{jkl} \chi_{ijkl}^{(3)}(-\omega'; \omega', \omega, -\omega) E_j(\omega') E_k(\omega) E_l^*(\omega) \quad (5)$$

Note the difference in degeneracy factor since all four frequencies in the argument of the susceptibility are different in Eq. (5). As noted by Boyd [1], the degeneracy factor will also be 6 even if $\omega' = \omega$, as long as there are two physically distinguishable fields present, such as when the weak probe field propagates in a different direction from the pump field.

Recall from Chapter 1 that, from the symmetry properties of an isotropic medium, the only nonzero independent components of the third order susceptibility are χ_{iijj} , χ_{ijji} , and χ_{ijji} with $\chi_{iiii} = \chi_{iijj} + \chi_{ijji} + \chi_{ijji}$ for all i and j . For a single linearly polarized beam or two parallel linearly polarized beams, n_2 is proportional to χ_{iiii} . The existence of off-diagonal terms in the third order susceptibility indicates the possibility of a nonlinearly induced birefringence in isotropic materials through the third order polarization. This will occur for elliptically polarized waves, or for two beams of nonparallel linear polarization.

Expressions that relate n_2 to the third order susceptibility are given in Table 1 in both SI and cgs units. Although for linear polarization n_2 is written in terms of χ_{xxxx} , it could equivalently be expressed in terms of χ_{yyyy} or χ_{zzzz} . It should also be noted that these expressions were developed in an attempt to be consistent with the way the real field is expressed in complex notation for both the nonlinear index and for the third order polarization. As noted above, this can be in terms of either $\mathbf{E}(\mathbf{r}, t)$ or $(1/2)\mathbf{E}(\mathbf{r}, t)$. As long as the field is expressed in the same way for both formulations, i.e., Eqs. (2), (4), and (5), the expressions in Table 1 will be the same. However, some authors choose to expand the nonlinear polarization in $\mathbf{E}(\mathbf{r}, t)$ but express the nonlinear index for a field in terms of $(1/2)\mathbf{E}(\mathbf{r}, t)$. In this latter case, the expressions for n_2 in Table 1 would all be larger by a factor of 4. Finally, for linear polarization note that the nonlinear index change experienced by a weak probe beam of frequency ω' induced by

Table 1 Formulas Relating n_2 and $\chi^{(3)}$ for Isotropic Materials

	SI	cgs
Self-action		
Linear polarization	$n_2 = \frac{3}{4n_0} \chi_{xxxx}^{(3)}(-\omega; \omega, \omega, -\omega)$	$n_2 = \frac{3\pi}{n_0} \chi_{xxxx}^{(3)}(-\omega; \omega, \omega, -\omega)$
$\Delta n = 2n_2 E ^2$	$= \frac{3}{4n_0} (2\chi_{xxyy}^{(3)} + \chi_{yyxx}^{(3)})$	$= \frac{3\pi}{n_0} (2\chi_{xxyy}^{(3)} + \chi_{yyxx}^{(3)})$
Circular polarization	$n_2^{cir} = \frac{3}{2n_0} \chi_{xxyy}^{(3)}(-\omega; \omega, \omega, -\omega)$	$n_2^{cir} = \frac{6\pi}{n_0} \chi_{xxyy}^{(3)}(-\omega; \omega, \omega, -\omega)$
$\Delta n_{\pm} = 2n_2^{cir} E_{\pm} ^2$	$\Delta n_+ = \frac{3}{n_0} [\chi_{xxyy}^{(3)} E_+ ^2 + (\chi_{xxyy}^{(3)} + \chi_{yyxx}^{(3)}) E_- ^2]$	$\Delta n_+ = \frac{12\pi}{n_0} [\chi_{xxyy}^{(3)} E_+ ^2 + (\chi_{xxyy}^{(3)} + \chi_{yyxx}^{(3)}) E_- ^2]$
Elliptical polarization	$\Delta n_- = \frac{3}{n_0} [\chi_{xxyy}^{(3)} E_- ^2 + (\chi_{xxyy}^{(3)} + \chi_{yyxx}^{(3)}) E_+ ^2]$	$\Delta n_- = \frac{12\pi}{n_0} [\chi_{xxyy}^{(3)} E_- ^2 + (\chi_{xxyy}^{(3)} + \chi_{yyxx}^{(3)}) E_+ ^2]$
Cross-action		
Linear polarization	$n_2^{(weak)} = \frac{3}{2n_0} \chi_{xxxx}^{(3)}(-\omega'; \omega', \omega, -\omega)$	$n_2^{(weak)} = \frac{6\pi}{n_0} \chi_{xxxx}^{(3)}(-\omega'; \omega', \omega, -\omega)$
$\Delta n(\omega') = 2n_2^{(weak)} E ^2$		
Self-action		
Intensity coefficient	$n_2^I = \frac{n_2}{\epsilon_0 n_0 c}$	$n_2^I = \frac{4\pi n_2}{n_0 c}$
$\Delta n = n_2^I I$		

a strong beam of frequency ω is twice as large as the self-induced index change experienced by the strong beam.

The nonlinear index change for a circularly polarized beam is weaker than that of a linearly polarized beam, as it depends on only one component of the susceptibility tensor. This index change is also the same for both right-handed and left-handed polarizations.

For an arbitrary elliptical polarization, a circular birefringence is induced in the material. In this situation, the index change Δn_+ , experienced by the left circularly polarized component of the field is generally not equal to the index change Δn_- experienced by the right circularly polarized component. This leads to an intensity induced rotation of the polarization ellipse of the beam. These changes are not conveniently expressed in terms of an n_2 but rather in terms of the third order susceptibility components.

The nonlinear index intensity coefficient is directly related to n_2 in the same way that the intensity is related to the square of the modulus of the field. Table 1 also gives these relations in both SI and cgs units.

Non-Kerr-like media. In Kerr-like media the nonlinear index change exhibits a linear dependence on the optical intensity. In some materials, the dependence is not as simple. Generally, it can be stated that the index change is some function of the intensity, i.e.,

$$\Delta n = f(I) \quad (6)$$

For sufficiently small intensities, depending on the properties of the medium, Eq. (6) can be expanded in a power series of I . The leading term will be linear in I , and thus for sufficiently small intensities, the medium will be Kerr-like and thus the index change can be expressed in terms of an n_2 . For larger intensities this is not possible. An example of this is a medium exhibiting saturable absorption (i.e., where the absorption coefficient of the medium decreases with increasing intensity).

Quasi-Kerr-like media. In these materials it is possible to obtain an expression for the nonlinear index change as a linear function of the intensity. One example was given above for non-Kerr-like materials at low intensities. Other examples exist wherein a physical change in the medium, brought on by the accumulated energy or fluence (integrated intensity) from an optical wave deposited in the medium, causes a change in the index of refraction. In some cases it is possible to express this index change as a linear function of the intensity, which would give the appearance that the medium is Kerr-like. An example of this is a thermal nonlinearity. A further example is that of a cascaded second order effect where there is an intensity dependent shift of the optical phase of a wave. This is possible in, for example, second harmonic generation that is not phase matched. The phase shift can be expressed in terms of an effective index change proportional to intensity, which gives the appearance that the medium is Kerr-like.

Intensity modulation effects. In this case, the index change is not directly dependent on the absolute intensity but rather on the relative modulation of the intensity. The index change can be expressed by

$$\Delta n(\mathbf{r}) \propto \frac{\delta I(\mathbf{r})}{I_0} \quad (7)$$

where I_0 is the total spatially averaged intensity and δI is the spatially modulated part of the intensity, i.e., $I(\mathbf{r}) = I_0 + \delta I(\mathbf{r})$. An example of this type of effect is observed in photorefractive media.

The physical units, in both SI and cgs systems, of several parameters appearing in formulas for the nonlinear index and related phenomena are given in Table 2. SI units are most appropriate for experiments, but cgs units often appear in the literature in theoretical developments and sometimes in experimental data. Sometimes the units are mixed, such as when expressing intensity in W/cm^2 .

Table 2 Physical Units of Important Physical Parameters Utilized in Formulas Related to the Nonlinear Index of Refraction

Physical parameter	SI	cgs
Dipole moment, transition moment	$[\mu] = \text{C}\cdot\text{m}$	$[\mu] = \text{sC}\cdot\text{cm} = \text{sV}\cdot\text{cm}^2$
Linear polarizability	$[\alpha] = \text{C}\cdot\text{m}^2/\text{V}$	$[\alpha] = \text{cm}^3$
Second hyperpolarizability	$[\gamma] = \text{C}\cdot\text{m}^4/\text{V}^3$	$[\gamma] = \text{cm}^5/\text{sV}^2$
Third order polarization	$[P^{(3)}] = \text{C}/\text{m}^2$	$[P^{(3)}] = \text{sV}/\text{cm} = (\text{erg}/\text{cm}^3)^{1/2}$
Electric field	$[E] = \text{V}/\text{m}$	$[E] = \text{sV}/\text{cm} = (\text{erg}/\text{cm}^3)^{1/2}$
Third order susceptibility	$[\chi^{(3)}] = \text{m}^2/\text{V}^2$	$[\chi^{(3)}] = \text{cm}^2/\text{sV}^2$ = $\text{cm}^3/\text{erg} = \text{esu}$
Nonlinear index of refraction (field coefficient)	$[n_2] = \text{m}^2/\text{V}^2$	$[n_2] = \text{cm}^2/\text{sV}^2$ = $\text{cm}^3/\text{erg} = \text{esu}$
Nonlinear index of refraction (intensity coefficient)	$[n_2^I] = \text{m}^2/\text{W}$	$[n_2^I] = \text{cm}^2\cdot\text{s}/\text{erg}$
Vacuum permittivity	$[\epsilon_0] = \text{F}/\text{m} = \text{C}/\text{V}\cdot\text{m}$	—
Distance, length	$[z] = [r] = [L] = \text{m}$	$[z] = [r] = [L] = \text{cm}$
Speed of light	$[c] = \text{m}/\text{s}$	$[c] = \text{cm}/\text{s}$
Wavelength	$[\lambda] = \text{m}$	$[\lambda] = \text{cm}$
Wave vector	$[k] = \text{m}^{-1}$	$[k] = \text{cm}^{-1}$
Absorption coefficient	$[\alpha] = \text{m}^{-1}$	$[\alpha] = \text{cm}^{-1}$
Planck's constant	$[\hbar] = [h/2\pi] = \text{J}\cdot\text{s}$	$[\hbar] = [h/2\pi] = \text{erg}\cdot\text{s}$
Intensity	$[I] = \text{W}/\text{m}^2$	$[I] = \text{erg}/\text{s}\cdot\text{cm}^2$
Power	$[\mathcal{P}] = \text{W}$	$[\mathcal{P}] = \text{erg}/\text{s}$

Formulas for converting parameters in cgs units to SI units, and for some mixed units, are given in Table 3.

II. PHYSICAL MECHANISMS

Several physical mechanisms that contribute to the nonlinear index of refraction are discussed below. Formulas for n_2 and $\chi^{(3)}$ in terms of other physical parameters for the various mechanisms are summarized in Tables 4 and 5, respectively.

A. Electronic Polarization

This mechanism involves a distortion of the electron cloud about an atom or molecule by the optical field. If the atom or molecule is highly polarizable, then it can exhibit a significant electronic nonlinearity.

Table 3 Conversion Formulas Between the SI and cgs Systems of Units for Several Physical Parameters Utilized in Nonlinear Index of Refraction Processes

μ	$(SI) = \frac{1}{3} \times 10^{-11} \mu$	(cgs)
α	$(SI) = \left(\frac{1}{3}\right)^2 \times 10^{-15} \alpha$	(cgs)
γ	$(SI) = \left(\frac{1}{3}\right)^4 \times 10^{-23} \gamma$	(cgs)
$P^{(3)}$	$(SI) = \frac{1}{3} \times 10^{-5} P^{(3)}$	(cgs)
E	$(SI) = 3 \times 10^4 E$	(cgs)
$\chi^{(3)}$	$(SI) = \frac{4\pi}{3^2} \times 10^{-8} \chi^{(3)}$	(cgs)
n_2	$(SI) = \left(\frac{1}{3}\right)^2 \times 10^{-8} n_2$	(cgs)
n_2^I	$(SI) = 10^3 n_2^I$	(cgs)
n_2^I	$(cm^2/W) = 10^4 n_2^I(SI) = 10^7 n_2^I$	(cgs)
L	$(SI) = 10^{-2} L(cgs)$	
c	$(SI) = 10^{-2} c$	(cgs)
λ	$(SI) = 10^{-2} \lambda$	(cgs)
k	$(SI) = 10^2 k$	(cgs)
α	$(SI) = 10^2 \alpha$	(cgs)
I	$(SI) = 10^{-3} I$	(cgs)
I	$(W/cm^2) = 10^{-4} I(SI) = 10^{-7} I$	(cgs)
\mathcal{P}	$(SI) = 10^{-7} \mathcal{P}$	(cgs)

The nonlinear susceptibility is related to the second hyperpolarizability, which is a microscopic parameter. The microscopic dipole moment for any material can, under certain circumstances, be expanded in a power series of the local field at the site of the dipole:

$$\mu_p = \mu_p^0 + \sum_q \alpha_{pq} E_q^{\text{loc}} + D^{(2)} \sum_{qr} \beta_{pqr} E_q^{\text{loc}} E_r^{\text{loc}} + D^{(3)} \sum_{qrs} \gamma_{pqrs} E_q^{\text{loc}} E_r^{\text{loc}} E_s^{\text{loc}} \quad (8)$$

where μ_p is the p th component of the total dipole moment, and μ_p^0 is the p th component of the permanent dipole moment, if one exists. The terms under the summation symbols are the various orders of the induced dipole moment, with $D^{(n)}$ the degeneracy for the n th order term. The third order nonlinearity derives from the second hyperpolarizability:

$$\begin{aligned} \varepsilon_0 \chi_{ijkl}^{(3)}(-\omega; \omega, \omega, -\omega) = \\ f^4 \sum_m N_m \left[\sum_{pqrs} \langle (\hat{i} \cdot \hat{p})(\hat{j} \cdot \hat{q})(\hat{k} \cdot \hat{r})(\hat{l} \cdot \hat{s}) \rangle_m \gamma_{pqrs}^m(-\omega; \omega, \omega, -\omega) \right] \end{aligned} \quad (9)$$

where m ranges over the number of species making up the material. The angular brackets indicate an orientational average over the direction cosines relating

Table 4 Formulas for n_2 or n_2^I Due to Various Physical Mechanisms^a

Physical mechanism	SI	cgs
Electronic polarization	$n_2 = \frac{3}{4n_0} \chi_{xxxx}^{(3)}(-\omega; \omega, \omega, -\omega)$	$n_2 = \frac{3\pi}{n_0} \chi_{xxxx}^{(3)}(-\omega; \omega, \omega, -\omega)$
Raman-induced Kerr effect [g_s = Stokes gain coefficient]	$ n_2 = \frac{\varepsilon_0 n_0 c \lambda_s}{8\pi} g_s$	$ n_2 = \frac{n_0 c \lambda_s}{32\pi^2} g_s$
Molecular reorientation $f = (n_0^2 + 2)/3$	$n_2 = \frac{f^4 N}{\varepsilon_0 n_0} \left[\frac{(\alpha_{\eta\eta} - \alpha_{\zeta\zeta})^2 + (\alpha_{\zeta\xi} - \alpha_{\xi\xi})^2}{90k_B T} + (\alpha_{\xi\xi} - \alpha_{\zeta\zeta})^2 \right]$	$n_2 = \frac{4\pi f^4 N}{n_0} \left[(\alpha_{\xi\xi} - \alpha_{\eta\eta})^2 + (\alpha_{\eta\eta} - \alpha_{\zeta\zeta})^2 + (\alpha_{\zeta\xi} - \alpha_{\xi\xi})^2 \right] / 90k_B T$
No axial symmetry	$n_2 = \frac{f^4 N}{\varepsilon_0 n_0} \left[\frac{(\alpha_{ } - \alpha_{\perp})^2}{45k_B T} \right]$	$n_2 = \frac{4\pi f^4 N}{n_0} \left[\frac{(\alpha_{ } - \alpha_{\perp})^2}{45k_B T} \right]$
Axial symmetry	$n_2 = \frac{f^4 N}{\varepsilon_0 n_0} \left[\frac{(\alpha_{ } - \alpha_{\perp})^2}{45k_B T} \right]$	$n_2 = \frac{4\pi f^4 N}{n_0} \left[\frac{(\alpha_{ } - \alpha_{\perp})^2}{45k_B T} \right]$
Axial symmetry (pretransitional behaviour)	$n_2^I(z) = \frac{(\Delta\varepsilon/\varepsilon_0)^2 \sin^2 2\beta}{4K_C} (Lz - z^2)$	$n_2^I(z) = \frac{(\Delta\varepsilon)^2 \sin^2 2\beta}{4K_C} (Lz - z^2)$
(homeotropically aligned liquid crystal cell)	$\langle n_2^I \rangle = \frac{(\Delta\varepsilon/\varepsilon_0)^2 L^2 \sin^2 2\beta}{24K_C}$	$\langle n_2^I \rangle = \frac{(\Delta\varepsilon)^2 L^2 \sin^2 2\beta}{24K_C}$
Electrostriction Homogeneously broadened two-level system steady state	$n_2 = \frac{\varepsilon_0}{36\nu_a^2 p} \frac{[(n_0^2 + 2)(n_0^2 - 1)]^2}{n_0}$	$n_2 = \frac{1}{144\pi\nu_a^2 p} \frac{[(n_0^2 + 2)(n_0^2 - 1)]^2}{n_0}$
	$n_2 = \frac{\alpha_{00}}{4(\omega_{eg}/c)n_0} \left[\frac{T_2\Delta}{(1 + T_2^2\Delta^2)^2} \right] \frac{1}{ E_s^0 ^2}$	$n_2 = \frac{\alpha_{00}}{4(\omega_{eg}/c)n_0} \left[\frac{T_2\Delta}{(1 + T_2^2\Delta^2)^2} \right] \frac{1}{ E_s^0 ^2}$

(continued)

Table 4 Continued

Physical mechanism	SI	cgs
Homogeneously broadened two-level system	$n_2 = \frac{1}{2n_0} \frac{N \mu_{\text{eg}} ^4}{\varepsilon_0(\hbar\Delta)^3}$	$n_2 = \frac{2\pi N \mu_{\text{eg}} ^4}{n_0 (\hbar\Delta)^3}$
Adiabatic following		
Semiconductors		
Free carrier absorption (m_e = effective mass)	$n_2^l = -\frac{e^2 \tau_R \alpha_0}{2m_e \varepsilon_0 r_0 \hbar \omega^3}$	$n_2^l = -\frac{2\pi e^2 \tau_R \alpha_0}{m_e r_0 \hbar \omega^3}$
Band filling	$n_2^l = \left[\frac{d(\Delta n)}{dI} \right]_{I=0}$	$n_2^l = \left[\frac{d(\Delta n)}{dI} \right]_{I=0}$
	$\Delta n(\omega, I) = \frac{c}{\pi} \times \text{P.V.} \int_0^\infty \frac{\Delta \alpha(\omega', I)}{(\omega')^2 - \omega^2} d\omega'$	$\Delta n(\omega, I) = \frac{c}{\pi} \times \text{P.V.} \int_0^\infty \frac{\Delta \alpha(\omega', I)}{(\omega')^2 - \omega^2} d\omega'$
Thermal	$n_2^l = \frac{\alpha \tau}{\rho C} \frac{dn}{dT}$	$n_2^l = \frac{\alpha \tau}{\rho C} \frac{dn}{dT}$
Cascaded SHG	$n_2^l(\omega) = \frac{4\pi \sigma_{\text{eff}}^2}{\varepsilon_0 n_\omega^2 n_{2\omega} c \lambda_\omega \Delta k}$	$n_2^l(\omega) = \frac{256\pi^4 d_{\text{eff}}^2}{n_\omega^2 n_{2\omega} c \lambda_\omega \Delta k}$
Photorefractive effect (sinusoidal index modulation due to two interfering waves)	$\Delta n(x) = -n_0^3 r_{\text{eff}} \left(\frac{E_D}{1 + E_D/E_N} \right) \times \frac{\sqrt{I/I_0}}{I_1 + I_2} \sin Kx$	
	$E_D = \frac{k_B T K}{e}$	
	$E_N = \frac{e N_A}{\varepsilon_{\text{dc}} K}$	

^a Parameters are defined in the text.

Table 5 Formulas for $\chi^{(3)}$ in SI Units Due to Various Physical Processes^a

Physical mechanism	
Electronic polarization	$\chi_{iiii}^{(3)}(-\omega; \omega, \omega, -\omega) = \frac{f^4 N}{\epsilon_0} \gamma_{iiii}(-\omega; \omega, \omega, -\omega)$ $\gamma_{iiii} \equiv \gamma$ $\gamma_{ijj} = \gamma_{iij} = \gamma_{iji} = \frac{1}{3} \gamma$
Molecular reorientation	$\chi_{ijk}^{(3)}(-\omega; \omega, \omega, -\omega) = \frac{f^4 N}{\epsilon_0} [3(\delta_{ij}\delta_{ki} + \delta_{ik}\delta_{ji}) - 2\delta_{il}\delta_{jk}]$ $\times \left[\frac{(\alpha_{\xi\xi} - \alpha_{\eta\eta})^2 + (\alpha_{\eta\eta} - \alpha_{\zeta\zeta})^2 + (\alpha_{\xi\xi} - \alpha_{\zeta\zeta})^2}{270k_B T} \right]$ $\chi_{iij}^{(3)} = \chi_{iji}^{(3)} = \frac{f^4 N}{\epsilon_0} \left[\frac{(\alpha_{\xi\xi} - \alpha_{\eta\eta})^2 + (\alpha_{\eta\eta} - \alpha_{\zeta\zeta})^2 + (\alpha_{\xi\xi} - \alpha_{\zeta\zeta})^2}{90k_B T} \right]$ $\chi_{iji}^{(3)} = -\frac{f^4 N}{\epsilon_0} \left[\frac{(\alpha_{\xi\xi} - \alpha_{\eta\eta})^2 + (\alpha_{\eta\eta} - \alpha_{\zeta\zeta})^2 + (\alpha_{\xi\xi} - \alpha_{\zeta\zeta})^2}{135k_B T} \right]$
Electrostriction	$\chi_{iiii}^{(3)} = \frac{1}{\epsilon_0} \frac{\gamma_e}{v_a^2} \frac{\partial \epsilon}{\partial \rho} = \frac{\epsilon_0}{27v_a^2 \rho} (n_0^2 + 2)^2 (n_0^2 - 1)^2$
Homogeneously broadened two-level system Steady state	$\chi(E ^2) = \frac{\alpha_{00}}{\omega_{eg}/c} \frac{-T_2 \Delta + i}{1 + (T_2 \Delta)^2 + E ^2/ E_s^0 ^2}$ $\chi^{(1)} = \frac{\alpha_{00}}{\omega_{eg}/c} \frac{-T_2 \Delta + i}{1 + (T_2 \Delta)^2}$ $\chi^{(3)} = \frac{\alpha_{00}}{3\omega_{eg}/c} \frac{T_2 \Delta - i}{[1 + (T_2 \Delta)^2]^2} \frac{1}{ E_s^0 ^2} = -\frac{\chi^{(1)}}{3 E_s^{\Delta} ^2}$
Adiabatic following	$\chi^{(3)} = \frac{2N \mu_{eg} ^4}{3\epsilon_0(\hbar\Delta)^3}$

^a Parameters are defined in the text.

the atomic or molecular coordinates $\{\xi\eta\zeta\}$ to the laboratory coordinates $\{xyz\}$; γ_{pqrs}^m is the second hyperpolarizability for species m, N_m is the number of atomic or molecular units of species m per unit volume, and f is a local field factor.

For a centrosymmetric material, the third order term is the lowest order nonlinearity. If the atomic or molecular unit is symmetric, it has no preferred direction of axes. Hence the laboratory system, defined by the vector properties of the applied fields, determines the coordinate system of the microscopic system. The direction cosines are thus all equal to 1, and for a single species Eq. (9) reduces to the expression given in Table 5. The local field factor is then simply

$$f = \frac{n_0^2 + 2}{3} \quad (10)$$

where again n_0 is the linear index of refraction.

The second hyperpolarizability can be computed from quantum mechanics using perturbation theory. The full expression contains 48 terms, all related to a product of four transition dipole moment matrix elements (in the numerators) and energy level transition frequencies (in the denominators). This full expression is not in itself particularly useful for calculations since, in general, the matrix elements and the transition frequencies (i.e., electron energy levels) must further be computed in terms of the basis set of states of the system. This is not a trivial problem, and various *ab initio* and semiempirical methods have been developed to make these calculations [2,3]. The calculations are numerical in nature, since no simple analytical formulas can be found, and they generally require powerful computational methods and long computation times. These computational methods are beyond the scope of this book, and the reader is referred to the literature for further details [2].

When the optical frequency is close to a single or two-photon resonance, then a few terms dominate the contribution to the second hyperpolarizability. Boyd [1] gives an excellent discussion of these terms. Under these conditions, the single beam n_2 is due primarily to the second hyperpolarizability given by

$$\gamma_{iii}(-\omega; \omega, \omega, -\omega) = \frac{2}{3\hbar^3} \left[\sum'_{abc} \frac{\mu_{gc}^i \mu_{cb}^i \mu_{ba}^i \mu_{ag}^i}{(\omega_{cg} - \omega)(\omega_{bg} - 2\omega)(\omega_{ag} - \omega)} - \sum_{ac} \frac{\mu_{gc}^i \mu_{cg}^i \mu_{ga}^i \mu_{ag}^i}{(\omega_{cg} - \omega)(\omega_{ag} - \omega)(\omega_{ag} - \omega)} \right] \quad (11)$$

where the sums are over a complete basis set of the system, with g representing the ground state and a, b, c representing higher lying excited states. The prime on the first summation signifies that $b = g$ is excluded from the sum. The μ_{ab}^i are the i th components of the transition moment matrix element between states a and b, etc., and $\omega_{ag} = \omega_a - \omega_g$ is the transition frequency between states a and g, etc., where $\hbar\omega_a$ is the energy level of state a, and similarly for other states. It can be seen that the first term contains a two-photon resonance, whereas the second term contains only single photon resonances.

As discussed by Boyd [1], when ω is smaller than any resonance of the system, the two-photon resonant term tends to give rise to a positive n_2 , since the linear polarizability of excited states tend to be larger than that of the ground state (i.e., the electrons spend more time further away from the nuclei). On the other hand, a single photon resonance will generally give rise to a negative n_2 , since a single photon resonance will cause a partial depletion of the ground state leading to a decrease in the molecular polarizability (see Section II.E).

For nonresonant electronic processes in transparent dielectrics, a typical value for the second hyperpolarizability is $\gamma \sim 10^{-36}$ esu $\sim 10^{-61}$ C-m⁴/V³,

although large organic molecules can have $\gamma \sim (100's \text{ to } 1000's) \times 10^{-36} \text{ esu}$. Typically, $\chi^{(3)} \sim 10^{-14} \text{ esu} \sim 10^{-22} \text{ m}^2/\text{V}^2$, and $n_2 \sim 10^{-13} \text{ esu} \sim 10^{-22} \text{ to } 10^{-21} \text{ m}^2/\text{V}^2$. Some polymeric systems have been developed with nonresonant $\chi^{(3)} \sim 10^{-12} \text{ to } 10^{-10} \text{ esu} \sim 10^{-20} \text{ to } 10^{-18} \text{ m}^2/\text{V}^2$. Nonresonant electronic processes are very fast, with typical time responses $\sim 10^{-15} \text{ s}$.

B. Raman Induced Kerr Effect

This effect is related to stimulated Raman scattering (see Chapter 14) and is an example of a strong beam inducing a refractive index change for a weak probe beam. The strong beam incident on a Raman active medium is from a laser at frequency ω_L . A weak probe beam of frequency ω_S is also incident on the medium. The weak beam is referred to as the Stokes beam with $\omega_S < \omega_L$.

Linear Raman scattering is a two-photon process wherein a laser photon scatters into a Stokes photon, which is down-shifted in frequency from the laser frequency by an amount equal to a Raman active mode in the medium, e.g., a molecular vibrational quantum (see Fig. 1). Stimulated Raman scattering is a four-photon process wherein a Stokes beam incident on the Raman active medium is amplified. The gain in the Stokes beam is at the expense of photons lost from the laser beam. However, for a strong laser beam and weak Stokes beam, the laser field can be treated as approximately constant (nondepleted pump approximation).

Stimulated Raman scattering can be described as a third order nonlinear process. The third order polarization at the Stokes frequency is given by

$$P_S^{(3)} = 6\epsilon_0\chi_R^{(3)}(-\omega_S; \omega_S, \omega_L, -\omega_L)E_S|E_L|^2 \quad (12)$$

where all fields are linearly polarized and are parallel. The subscript R signifies a Raman susceptibility, which is a complex quantity. The Raman gain factor is

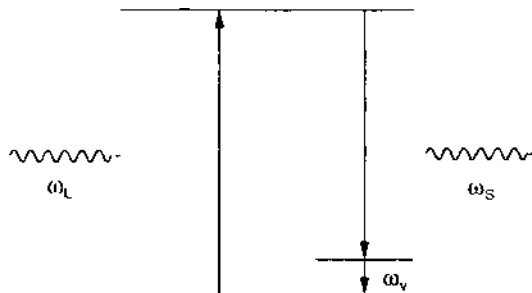


Figure 1 Schematic diagram of Raman scattering.

related to the imaginary part of this susceptibility:

$$G(\omega_S) = -\frac{6\omega_S}{n_S c} \text{Im}[\chi_R^{(3)}(-\omega_S; \omega_S, \omega_L, -\omega_L)] |E_L|^2 \quad (13)$$

where n_S is the linear index of refraction at the Stokes frequency, and the exponential gain factor $G(\omega_S)$ has units of m^{-1} . The real and imaginary parts of $\chi_R^{(3)}$ are related through a Kramers–Kronig relation.

The frequency dependence of the gain factor displays a Raman resonance:

$$G(\omega_S) = \frac{(\Gamma/2)^2 G^{\text{peak}}}{[\omega_S - (\omega_L - \omega_V)]^2 + (\Gamma/2)^2} \quad (14)$$

where G^{peak} is the peak gain, Γ is the Raman linewidth (FWHM), and $\omega_L - \omega_V$ is the Raman resonance. The nonlinear index coefficient is related to the real part of $\chi_R^{(3)}$ and can be expressed in terms of the gain coefficient g_s , which is the gain factor $G(\omega_S)$ per unit (laser) intensity. When the probe (Stokes) frequency ω_S is within $\pm \Gamma/2$ of resonance, the approximate relation shown in Table 5 is obtained. Note that $\text{Re}[\chi_R^{(3)}]$ will change sign as the Stokes frequency is swept through resonance.

For typical values of $g_s \sim 3 \times 10^{-11} \text{ m/W}$, $n_L \sim n_S \sim 1.5$, $\lambda_S \sim 10^{-6} \text{ m}$, the real part of the third order Raman susceptibility has a typical value of $|\text{Re}[\chi_R^{(3)}]| \sim 10^{-20} \text{ m}^2/\text{V}^2$. This is about two orders of magnitude larger than typical nonresonant electronic processes because of the resonant nature of the Raman effect. The response times of these effects are of the order of the lifetime of the Raman induced material excitation (e.g., a higher lying vibrational state in the ground electronic manifold of states of a molecule), and is typically $\sim 10^{-12} \text{ s}$.

C. Molecular Orientational Effects

Anisotropic molecules (i.e., displaying an anisotropic linear polarizability tensor) will tend to exhibit an optically isotropic behavior in the bulk when they are disordered, i.e., when their orientations are randomly distributed. This is true of several liquids (e.g., CS_2) and of liquid crystals above the transition to a mesoscopic phase.

When a strong electric field is applied to such a system, the induced dipole moments of the molecules experience a torque attempting to align the most polarizable axis with the applied field, working against the thermal fluctuation forces (i.e., molecular collisions). An incident optical wave polarized along the direction of the strong field will experience an increase in the local index of refraction, since it sees, on the average, more highly polarizable molecules than when the strong alignment field is absent. The situation is depicted schematically in Fig. 2.

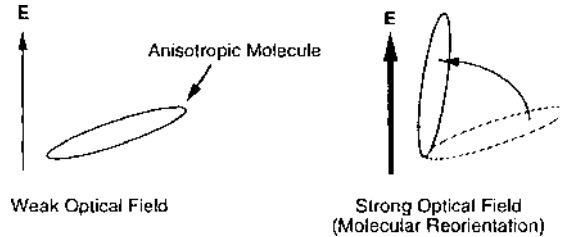


Figure 2 Anisotropic molecular reorientation by a strong electric field.

When the applied field is dc, this effect is called the Kerr effect. Similarly, the field could be due to a strong optical wave. The system then responds not to the instantaneous field but to the time averaged field squared, as in Eq. (1), and the effect is then termed the ac or optical Kerr effect. When the alignment field and the incident optical field are one and the same, this leads to a self-induced refractive index change expressible by an n_2 as long as the induced dipole-electric field interaction energy is small compared to the thermal energy, which is typically the case.

The induced dipole moment of an anisotropic molecule can be expressed in terms of the principal polarizability components corresponding to the principal axes of the molecule: $\alpha_{\xi\xi}$, $\alpha_{\eta\eta}$, and $\alpha_{\zeta\zeta}$. When a strong field is applied to such a system, the system will attempt to minimize the electrical energy ($-\frac{1}{2}\int \mu \cdot dE^{(2)}$) by aligning the most polarizable axis (usually designated by the ζ -axis) to the field. The result is a new thermal equilibrium state of the system. The average polarizability of the medium in this new state can be calculated assuming a Boltzmann distribution of molecular orientations. To lowest order in $|E|^2$, the average polarizability is given by a linear term $\langle \alpha_0 \rangle = \frac{1}{3}(\alpha_{\xi\xi} + \alpha_{\eta\eta} + \alpha_{\zeta\zeta})$ plus a nonlinear term proportional to $|E|^2$. The nonlinear term can thus be expressed in terms of a third order susceptibility, which is given in Table 5.

For axially symmetric molecules (e.g., CS_2), $\alpha_{\xi\xi} = \alpha_{\eta\eta} \equiv \alpha_{\perp}$ and $\alpha_{\zeta\zeta} \equiv \alpha_{\parallel}$. Then writing $\Delta\alpha = \alpha_{\parallel} - \alpha_{\perp}$, the factor containing the molecular polarizability components becomes

$$\frac{(\alpha_{\xi\xi} - \alpha_{\eta\eta})^2 + (\alpha_{\eta\eta} - \alpha_{\zeta\zeta})^2 + (\alpha_{\xi\xi} - \alpha_{\zeta\zeta})^2}{270k_B T} \rightarrow \frac{(\Delta\alpha)^2}{135k_B T} \quad (15)$$

where k_B is Boltzmann's constant ($1.38 \times 10^{-23} \text{ J/K} = 1.38 \times 10^{-16} \text{ erg/K}$), and T is the temperature in kelvins (K).

The usual self-induced nonlinear index coefficient n_2 is given in terms of $\chi_{iiji}^{(3)}(-\omega; \omega, \omega, -\omega)$ where $i = x, y$, or z . For this so-called degenerate case,

$$\chi_{iiji}^{(3)}(-\omega; \omega, \omega, -\omega) = \chi_{ijij}^{(3)}(-\omega; \omega, \omega, -\omega) \quad (16)$$

for all i, j , which can be seen to follow from the intrinsic permutation symmetry of the nonlinear susceptibility (see Chapter 1), and

$$\chi_{ijji}^{(3)}(-\omega; \omega, \omega, -\omega) = 6\chi_{iiji}^{(3)}(-\omega; \omega, \omega, -\omega) \quad (17)$$

for all i, j for molecular reorientation processes.

The situation is somewhat different for the case of a strong pump induced nonlinear index for a weak probe. In this case the susceptibility $\chi_{iiii}^{(3)}(-\omega'; \omega', \omega, -\omega) = \chi_{iiji}^{(3)}(-\omega'; \omega', \omega, -\omega) + \chi_{ijji}^{(3)}(-\omega'; \omega', \omega, -\omega) + \chi_{ijji}^{(3)}(-\omega'; \omega, \omega, -\omega) = \chi_{iiji}^{(3)}(-\omega, \omega, \omega, -\omega)$, i.e., it is equal to its degenerate counterpart, ignoring dispersion, but the relations between its three nonzero components is different from those of the degenerate case:

$$\begin{aligned} \chi_{ijji}^{(3)}(-\omega'; \omega', \omega, -\omega) &= \chi_{iiji}^{(3)}(-\omega'; \omega', \omega, -\omega) \\ &= -\frac{2}{3}\chi_{iiji}^{(3)}(-\omega'; \omega', \omega, -\omega) \end{aligned} \quad (18)$$

The significance of this is as follows. As stated earlier, the nonlinear index coefficient for the weak probe, when the pump and probe are copolarized, is twice as large as the self-induced index coefficient for the pump, i.e.,

$$(n_2^{(\text{weak})})_{ii} = 2n_2 \quad (19)$$

while the index coefficient for a cross-polarized pump and probe is

$$(n_2^{(\text{weak})})_{ij} = -\frac{1}{2}(n_2^{(\text{weak})})_{ii} \quad (20)$$

These equations are true for the nondegenerate case as well as the degenerate case when the pump and probe are physically distinguishable fields. The situation in Eq. (20) arises for molecular reorientation processes because the strong pump tends to align molecules along its polarization axis, while the probe samples the index perpendicular to this direction. Hence it sees an index reduced from the no-pump situation since, on the average, the molecules it samples have a smaller polarizability. This is depicted schematically in Fig. 3. Note that in a molecular reorientation process, the net polarizability of the medium has not increased. The optical field merely rearranges the polarizability present among the various tensor components.

Typical nonlinearities associated with small anisotropic molecular systems are $\chi^{(3)} \sim 10^{-13}-10^{-12}$ esu $\sim 10^{-22}-10^{-21}$ m²/V², and $n_2 \sim 10^{-12}-10^{-11}$ esu $\sim 10^{-21}-10^{-20}$ m²/V². The response time is $\sim 10^{-12}$ s. Liquid crystals in their isotropic phase will exhibit larger nonlinearities but with slower response times. These materials are particularly interesting in their mesoscopic phase or near the transition to such a phase.

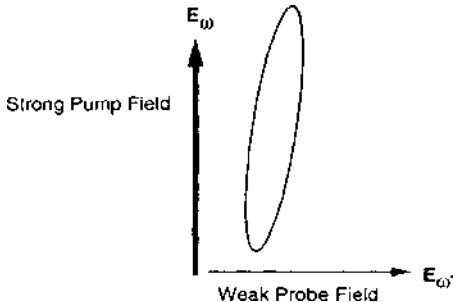


Figure 3 Molecular reorientation by a strong pump field probed with a weak orthogonally polarized field.

A system of axially symmetric liquid crystal molecules will exhibit a pretransitional behavior near its isotropic-to-nematic transition in which the optical nonlinearity can grow very large. The susceptibility is very temperature dependent in this case as shown in Table 5. It can be seen that as the temperature is lowered, the susceptibility increases as $(T - T^*)^{-1}$, where T^* is a fictitious second order phase transition temperature approximately equal to the critical temperature for the isotropic-to-nematic transition.

The parameter a in the expression for the susceptibility is a constant in the expansion of the free energy F of the system in terms of an order parameter Q [3,4,5]:

$$F = F_0 + \frac{1}{2}a(T - T^*)Q^2 + \frac{1}{3}BQ^3 + \dots - \text{const.} \times Q|\mathbf{E}|^2 \quad (21)$$

The order parameter is defined by

$$Q = \frac{3}{2} \left\langle \cos^2 \theta - \frac{1}{3} \right\rangle \quad (22)$$

where θ is the angle between the long axis of the molecule and the direction of the optical electric field. The maximum order parameter is 1.

In the nematic phase, liquid crystal molecules are highly correlated and act cooperatively. This is the origin of the large nonlinearity observed in this phase. Pretransitional behavior describes the system optical response as this transition is approached. The apparent divergence in the susceptibility with temperature is a manifestation of the gradual transition from the isotropic to the nematic phase. The nonlinear index of refraction can increase by orders of magnitude as this transition is approached, but the response of the system exhibits a critical slowing

down with a response time given by

$$\tau = \frac{\eta}{a(T - T^*)} \quad (23)$$

where η is the coefficient of viscosity. In the pretransition region, the nonlinear index coefficient can approach $n_2 \sim 10^{-9}$ esu, but the response time is $\sim 10^{-7}$ s.

In the nematic phase, the cooperative behavior of the liquid crystal molecules produces a nonlocal response. This results in a nonlinear index that is a function of position. An example taken from Khoo and Wu [5] is illustrated in Fig. 4. This depicts an optical wave propagating through a homeotropically aligned nematic liquid crystal cell of thickness L . The wave vector of the field makes an angle β with respect to the average liquid crystal director field (the direction of the long molecular axis). The nonlinear index intensity coefficient is given in Table 4. This expression is valid for small angle distortions of the nematic director field. Note that this index coefficient is z dependent, where the z -axis coincides with the average nematic director orientation.

For computational purposes in devices, the average nonlinear index coefficient over the cell thickness is of interest. This is also given in Table 4. Now note that the coefficient varies quadratically with the cell thickness. The anisotropy parameter $\Delta\epsilon$ is the difference in the optical dielectric constants measured parallel to and perpendicular to the long molecular axis. K is a typical elastic restoring force constant for the nematic (the splay constant in this example).

Khoo and Wu [5] give some typical values for the parameters associated with a liquid crystal cell (in cgs units): $\Delta\epsilon = 0.6$, $K = 10^{-6}$ dyn, $L = 10^{-2}$ cm,

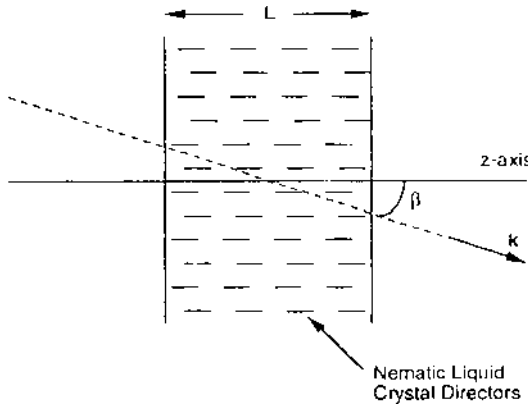


Figure 4 Schematic diagram of a wave propagating through a homeotropically aligned nematic liquid crystal cell.

$\beta = 45^\circ$. These yield an average index coefficient of $\langle n_2^I \rangle = 5 \times 10^{-11} \text{ cm}^2\text{-s/erg} = 5 \times 10^{-4} \text{ cm}^2/\text{W}$. This is about 10 orders of magnitude larger than the n_2^I achieved with small anisotropic molecular systems (e.g., CS_2). However, the response time ($\sim 10^{-3}\text{--}10^{-2}$ s) is much longer.

The equation given in Table 4 indicates that the nonlinear index change is zero when $\beta = 0$. However, for this case with a homeotropically aligned liquid crystal cell, there is a highly nonlinear refractive index change above a critical intensity. This change is associated with the Fredericks transition. See Ref. 5 for more details on this highly nonlinear phenomenon.

D. Electrostriction

Electrostriction is a phenomenon that depends on the presence of an inhomogeneous intensity, i.e., a spatially varying, time averaged electric field. This would occur, for example, in the superposition of coherent waves to form an interference pattern of bright and dark fringes, or along the transverse direction to a propagating Gaussian shaped beam. Such an inhomogeneous field produces a force on the molecules or atoms comprising a system called the electrostrictive force.

The electrostrictive force is proportional to the gradient of the square modulus of the electric field. The constant of proportionality, $(1/2)\gamma_e$, is given in terms of the electrostrictive coefficient, where

$$\gamma_e = \rho \left(\frac{\partial \epsilon}{\partial \rho} \right) \quad (24)$$

with ρ the mass density and $\epsilon = \epsilon_0 n_0^2$. This force can be understood from the fact that the induced dipoles in the medium will experience a translational force in a nonuniform field that is proportional to the gradient of the field. (Dipoles will not experience such a force in a uniform field, although they may experience a torque). The force is such as to move the dipoles into a region of higher intensity. This produces an increase in local density resulting in an increase of the refractive index locally. Thus even a system of isotropic molecules will be electrostrictive.

The nonlinear index coefficient is proportional to $\chi_{xxx}^{(3)}$ and is given in Table 4, where v_a is the acoustic velocity in the medium. For an electrostrictive medium, the following properties of the susceptibility hold:

$$\begin{aligned} \chi_{ijj}^{(3)}(-\omega; \omega, \omega, -\omega) &= \chi_{iji}^{(3)}(-\omega; \omega, \omega, -\omega) \\ &= \frac{1}{2} \chi_{iii}^{(3)}(-\omega; \omega, \omega, -\omega) \\ \chi_{iji}^{(3)}(-\omega; \omega, \omega, -\omega) &= 0 \end{aligned} \quad (25)$$

For typical values given by $v_a \sim 10^4$ m/s, $\rho \sim 10^3$ kg/m³, $n_0 \sim 1.4$, the electrostriction contribution to the nonlinear index coefficient is $n_2 \sim 10^{-19}$ m²/V². This is of the same order as the molecular reorientational contribution. The response time, however, is of the order of 10^{-9} s, i.e., about three orders of magnitude slower than the molecular reorientational response time.

E. Population Redistribution

When the frequency of incident radiation is near a resonant energy transition of an atom or molecule, then real transitions are induced. This means that electrons can occupy real excited states for a finite period of time. This is called a population redistribution. Since the optical polarization is ordinarily determined by the total number of atoms or molecules in the ground electronic state (for low intensity light), this population redistribution produces a change in the index of refraction. This effect can be seen in atomic vapors, molecular gases, liquid solutions of organic molecules, transparent dielectric solids doped with metal ions or color centers, and semiconductors.

In some situations, the near-resonant interaction can be described as if the material had only two energy levels. This is because the resonant interaction between the radiatively connected ground and excited states is so strong that other nonresonant interactions can be ignored. It is assumed that the resonant frequency for a transition from the excited state to a higher lying state is far removed from that of the ground and excited states. The situation of semiconductors, with finite valence and conduction energy bands, is somewhat different depending on the time scale of the optical interaction.

Two-level systems. This deceptively simple looking system is illustrated in Fig. 5. The two levels are the ground (g) and excited (e) states. The resonant transition frequency connecting these states is defined by ω_{eg} . The system is also

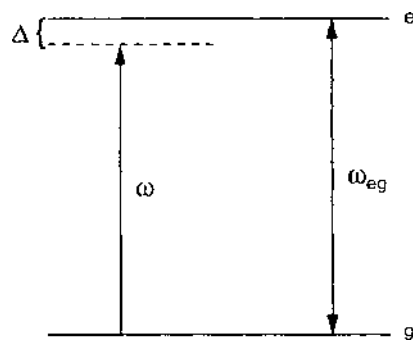


Figure 5 A two-level system.

characterized by a transition dipole moment, μ_{eg} , and an equilibrium population difference $\Delta N^{eq} = (N_g - N_e)^{eq}$, where N_g^{eq} and N_e^{eq} are the number densities of atoms or molecules in the ground and excited states, respectively, long after or before the radiation is incident on the medium. The transition dipole moment has a characteristic dephasing lifetime T_2 , which is related to the homogeneous line width (FWHM) of the transition by $\Delta\omega_{FWHM} = 2\pi/T_2$. A nonequilibrium population difference will decay to its equilibrium value in a time of the order of a characteristic time defined as T_1 .

The average dipole moment of such a system described above is usually derived by density matrix theory. The polarization is then given as the average dipole moment per unit volume. In two particular time regimes, defined as the steady-state and the adiabatic following regimes, the resulting polarization P can be written as a constant times the applied field E . The susceptibility of the system is then given by $\epsilon_0\chi = P/E$.

The steady-state regime is examined first. Here the optical field has been applied for a time long compared to T_1 and T_2 . Thus all optically induced transient effects have been damped out. This regime is typical of the response of a two-level system to a cw laser.

The applied optical field is close to resonance, and a detuning parameter is defined by

$$\Delta = \omega - \omega_{eg} \quad (26)$$

Since the frequency is near resonance, the susceptibility will be complex, with its real part related to the index of refraction and its imaginary part related to the absorption coefficient. The susceptibility is also proportional to the non-equilibrium population difference, which is itself dependent on the intensity of the incident radiation due to optically induced resonant transitions from the ground to excited states (i.e., absorption). The result is an intensity dependent susceptibility given by

$$\chi = \frac{\alpha_{00}}{\omega_{eg}/c} \frac{i - T_2\Delta}{1 + (T_2\Delta)^2 + |E|^2/|E_s^0|^2} \quad (27)$$

where α_{00} is the ordinary (linear) absorption coefficient at line center ($\Delta = 0$, $|E|/|E_s^0| \ll 1$), which is given by

$$\alpha_{00} = \frac{\omega_{eg} |\mu_{eg}|^2 T_2 \Delta N^{eq}}{\epsilon_0 c \hbar} \quad (28)$$

(Equation (28) is valid for an atomic vapor or molecular gas where the linear index of refraction is approximately 1. For molecules in solution or doped in a solid dielectric, the expression for χ should include the local field factors appropriate to the host medium.) A saturation field at line center, determined by

microscopic parameters, is defined by

$$|E_s^0|^2 = \frac{\hbar^2}{4|\mu_{eg}|^2 T_1 T_2} \quad (29)$$

Thus it can be seen that when the applied optical field is small compared to the line center saturation field, the susceptibility is essentially independent of intensity and has a characteristic Lorentzian line shape.

When the applied field is larger, but still small compared to the saturation field, the denominator in Eq. (27) can be expressed as a binomial expansion in terms of the quantity $|E|^2/|E_s^0|^2$. To lowest order in this parameter, the resulting expression for χ has a term independent of the applied field, and a term proportional to $|E|^2$. The former is identified with the linear susceptibility $\chi^{(1)}$. The latter term, through the relationship of the nonlinear polarization, i.e.,

$$P^{(3)} = 3\epsilon_0 \chi^{(3)}(-\omega; \omega, \omega, -\omega) E |E|^2 \quad (30)$$

determines the third order susceptibility $\chi^{(3)}$. These expressions are given in Table 5, and the corresponding expressions for n_2 are in Table 4.

Note that $\chi^{(3)}$ can be expressed compactly in terms of $\chi^{(1)}$ and an off-resonance saturation field defined by

$$|E_s^\Delta|^2 = |E_s^0|^2 [1 + (T_2 \Delta)^2] \quad (31)$$

Furthermore, it is useful to define corresponding saturation intensities by

$$\begin{aligned} I_s^0 &= 2\epsilon_0 n_0 c |E_s^0|^2 \\ I_s^\Delta &= 2\epsilon_0 n_0 c |E_s^\Delta|^2 \end{aligned} \quad (32)$$

Alkali metal vapors exhibit some of the largest resonant nonlinearities. Consider, for example, the $3s \rightarrow 3p$ transition in atomic sodium vapor at a frequency corresponding to a wavelength of 589 nm. The transition dipole moment is approximately $|\mu_{eg}| \approx 2.5ea_0 = 2.0 \times 10^{-29}$ C-m, where a_0 is the Bohr radius. Assuming $N = 10^{20} \text{ m}^{-3}$ and negligible collisional line broadening so that $T_2 \approx 2T_1 = 32 \text{ ns}$, the unsaturated line center absorption coefficient is $\alpha_{00} = 1.5 \times 10^7 \text{ m}^{-1}$. This corresponds to a $1/e$ absorption depth of less than 1 μm . Let the incident radiation have a frequency below the transition frequency of 1 cm^{-1} . Then the detuning parameter would be $\Delta = -6\pi \times 10^{10} \text{ rad/s}$. From Table 5, the real part of $\chi^{(1)}$ is 2.3×10^{-4} . Hence the linear index of refraction is approximately 1, and local field factors can be ignored. The line center saturation field is then approximately 100 V/m, corresponding to a line center saturation intensity of only 70 W/m^2 . The off-resonance saturation intensity corresponding to this detuning is $36 \text{ MW/m}^2 = 3.6 \text{ kW/cm}^2$. Finally, the value of $\chi^{(3)}$ is then

$-1.6 \times 10^{-16} \text{ m}^2/\text{V}^2$, which corresponds to $n_2 = -1.2 \times 10^{-16} \text{ m}^2/\text{V}^2$. The nonlinear index coefficient is negative because saturation causes the index to decrease for this detuning, as illustrated in Fig. 6.

The magnitude of this n_2 is 4 or 5 orders of magnitude larger than those corresponding to molecular reorientation, but the response time is $\sim T_2$, which for the alkali metal vapors in the noncollisionally line broadened regime is tens of nanoseconds. The effective T_2 can be reduced by introducing a foreign gas (e.g., a noble gas), but this would also raise the saturation intensity. For atoms of comparable dipole moment (i.e., oscillator strength) doped in liquid solutions or solids, the nonlinear index coefficient will be smaller because of the high damping rates induced by molecular or phonon collisions. This reduces the effective T_2 and increases the saturation intensity.

The adiabatic following regime applies to short pulses rather than cw laser beams. It is assumed that the pulse width τ_p satisfies the inequality $\tau_p \ll T_1, T_2$. Also, the detuning is assumed to be such that $|\Delta| >> T_2^{-1}, \tau_p^{-1}, |\mu_{eg}| |E|/\hbar$. In other words, the detuning is large compared to the homogeneous line width, any Fourier component of the pulse, and the so-called Rabi frequency $\Omega = |\mu_{eg}| |E|/\hbar$ (which leads to power broadening of the line width). The polarization

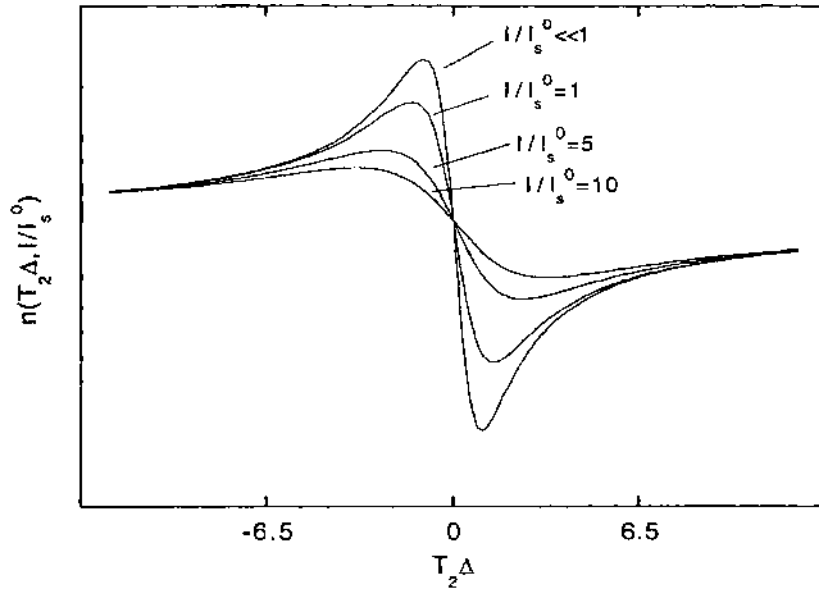


Figure 6 Refractive index of a two-level system as a function of normalized detuning from line center, parameterized by the ratio of incident intensity to the saturation intensity.

can then be written in terms of the Rabi frequency as

$$P = -\frac{\Omega\Delta}{2\Delta^2} \frac{N|\mu_{eg}|}{(1 + |\Omega|^2/\Delta^2)^{1/2}} \quad (33)$$

Expanding the denominator again leads to a third order term that yields the expression for $\chi^{(3)}$ given in Table 5.

Note that the polarization is real in the adiabatic following regime. This is because of the conditions assumed above, which imply that the pulse is far enough from resonance that negligible absorption results, and the pulse is so short that no atomic or molecular relaxation (i.e., damping) can occur for the duration of the pulse. The nonlinear response of the medium then adiabatically follows the optical pulse in time.

Semiconductors. These materials have proved to be very rich and fruitful media for nonlinear optical research and potential applications. They exhibit bound electronic nonlinear effects like wide gap dielectrics (these can be described by the equations in Section II.A), but some of the larger effects are due to electron population redistribution.

One of the main differences in semiconductors over transparent dielectrics is that semiconductors can have a small population of free carriers at thermal equilibrium. These carriers can absorb electromagnetic radiation as they scatter from the lattice. Accompanying this free carrier absorption is a free carrier index of refraction. The refractive index depends directly on the plasma frequency, which itself is a function of the free carrier density. Linear absorption of a photon of energy $\hbar\omega > \mathcal{E}_g$, where \mathcal{E}_g is the energy gap between the valence and conduction bands, promotes electrons to the conduction band, increasing the electron population density. Hence the plasma frequency is modified, producing an intensity dependent change in the refractive index. The resulting nonlinear index coefficient is given in Table 4.

The ω^{-3} dependence makes this effect particularly strong in the infrared. Typical values are $n_2' \sim 10^{-6} \text{ cm}^2/\text{W}$. Note that α is the linear absorption coefficient across the energy gap, m_e the electron effective mass, and $\tau_R \sim 10 \text{ ns}$ is the electron–hole recombination time.

Linear absorption across the energy gap will produce a redistribution of electron and hole densities. This causes a change in the linear absorption $\Delta\alpha(\omega, I)$ which is intensity dependent. Two time regimes are of interest. For pulses short compared to the intravalley scattering time, the system will respond just like an ensemble of two level absorbers. These cases can be treated by the theory for two-level systems given earlier. This phenomenon is called state filling. It may be observed when subpicosecond pulses are used to excite the semiconductor. For pulses long compared to the intravalley scattering time, the nonlinear effects are due to band filling.

The intensity dependent absorption change is not easily computed for the band filling regime. However, it is readily measured as a function of frequency, or photon energy. Then, as shown in Table 4, the index change can be computed by the Kramers–Kronig relation. This relates $\Delta\alpha(\omega, I)$ to $\Delta n(\omega, I)$ through the integrals given in Table 4, where P.V. stands for the Cauchy principal value of the integral defined by

$$P.V. \int_A^B f(x)dx = \lim_{\epsilon \rightarrow 0} \left[\int_A^{a-\epsilon} f(x)dx + \int_{a+\epsilon}^B f(x)dx \right] \quad (34)$$

where a is a singularity of the function $f(x)$ on the real axis. The nonlinear index coefficient is given by the derivative of $\Delta n(\omega, I)$ with respect to intensity I in the limit when $I \rightarrow 0$.

Butcher and Cotter [6] outline a model for computing $\Delta\alpha(\omega, I)$ for direct gap group IV and III–V semiconductors. The free electron density is determined by a simple rate equation:

$$\frac{dN_e}{dt} = \frac{\alpha I}{\hbar\omega} - \frac{(N_e - N_e^{eq})}{\tau_R} \quad (35)$$

The resulting electron density (which is intensity dependent) changes the Fermi levels of the conduction and valence bands. This in turn changes the absorption coefficient and refractive index. The problem must be solved self-consistently. The intensity scale for significant changes in the linear optical properties is determined by the saturation intensity given by

$$I_s = \frac{\epsilon_0 n_0 c m_e \mathcal{E}_g \Gamma_{cv}}{e^2 \tau_R} \quad (36)$$

where Γ_{cv} is the transition line width and e is the electron charge. Typical values of I_s are on the order of 10^3 W/cm^2 . With $\tau_R \sim 10\text{--}50 \text{ ns}$, typical nonlinear index coefficients for the band filling regime in direct gap semiconductors are $n_2^I \sim 10^{-6}\text{--}10^{-4} \text{ cm}^2/\text{W}$.

The Coulomb interaction between an excited electron and hole can strongly modify the absorption edge of a semiconductor. When the electron and hole form a bound state known as an exciton, an additional line spectrum appears for $\hbar\omega < \mathcal{E}_g$. The photogeneration of free carriers results in an electric field that screens (i.e., reduces the effectiveness of) the field binding the exciton. This strongly saturates the exciton absorption, producing a large change in the refractive index. Formulas for the resulting n_2^I are the same as for the band filling effect, assuming that the intensity dependent change in absorption coefficient as a function of frequency or photon energy can be measured. Butcher and Cotter [6] also give the outline of a theory for computing this exciton saturation effect. The results must be obtained numerically. Typical values are $n_2^I \sim 10^{-6} \text{ cm}^2/\text{W}$.

The above discussion has related the properties of bulk semiconductors. Large nonlinear effects have also been observed in artificially produced semiconductors such as multiple quantum wells and quantum dots. Quantum well materials consist of multiple alternating thin layers (~ 10 nm) of different semiconductor materials. In the thin dimension, quantum confinement effects produce exciton resonances that are sharper than the corresponding ones in bulk semiconductors and are more easily saturated. This results in large optical nonlinearities. Nonlinear index coefficients as large as $n_2^l = -2 \times 10^{-4} \text{ cm}^2/\text{W}$ have been measured. Again, the equations displayed for band filling effects can be used to compute n_2^l if the nonlinear absorption can be measured as a function of frequency. The recovery time of the nonlinear index in quantum wells can be of the order of tens of nanoseconds, or ~ 100 ps for proton-bombarded materials.

Quantum dots are small semiconductor particles with dimensions of a few nanometers. Quantum confinement produces a large separation in energy states with the result that state filling effects dominate the optical nonlinearities. Thus the system is treated as a two-level system as described above. Typical experiments have been performed on semiconductor doped glasses that have a range of particle sizes. This produces an inhomogeneous broadening of the absorption lines with a much higher saturation intensity than homogeneous broadened systems. However, typical measured values give $n_2^l \sim 10^{-12} - 10^{-11} \text{ cm}^2/\text{W}$ with recovery times ~ 10 ps. This fast recovery time is believed to be related to the small size of the semiconductor particles (e.g., surface state effects or large free carrier capture cross-sections by deep lying traps). The development of smaller, more uniformly sized particles with lower saturation intensities promises higher nonlinearities with fast recovery rates.

The nonlinear optics of metallic quantum dots has also been studied. There are no simple formulas for computing the nonlinear index coefficients. The metal spheres support a surface plasmon mode. The nonlinear susceptibility is enhanced when the frequency of the incident optical intensity approaches the resonant frequency of the surface plasmon. Colloidal silver and gold particles have been studied experimentally. Typical values are $\chi^{(3)} \sim 10^{-9}$ to $10^{-8} \text{ esu} \sim 10^{-17}$ to $10^{-16} \text{ m}^2/\text{V}^2$.

F. Thermal Contributions

The nonlinear index intensity coefficient due to thermal contributions in the steady state is shown in Table 4. The change in index due to a temperature rise ΔT can be expressed by

$$\Delta n = \frac{dn}{dT} \Delta T \quad (37)$$

where dn/dT is called the thermooptic coefficient. In most liquids and solids it is

due to a density change (i.e., expansion) with temperature. Since the density decreases in expansion and the refractive index is proportional to density, this contribution to dn/dT is generally negative. In some semiconductors, the absorption band edge will red-shift with temperature (Franz–Keldish effect). This produces a positive thermo-optic coefficient.

In the formula given in Table 4, α is the linear absorption coefficient. This could be an intrinsic absorption of the material, or absorption due to impurities. However, any material that has some appreciable absorption will exhibit a thermal nonlinear index of refraction in the steady state. The time constant τ represents the thermal diffusion time in the steady state. For times short compared to the diffusion time, it may represent the laser pulse width. Thus thermal contributions can cause an index change even for short times before a steady state is reached. This is because this index change is proportional to the total energy deposited in the medium (i.e., the integral of the intensity) and increases with time. The quantity $\alpha\tau I$ represents the energy per unit volume absorbed in the material and converted to heat. Thus the index change is in reality fluence dependent. The specific heat C times the mass density ρ converts this energy absorbed into a temperature change ΔT .

Typical values of $|dn/dT|$ range from 10^{-6} to 10^{-3} K^{-1} . The larger values usually correspond to a liquid crystal near the nematic-to-isotropic transition. For $\alpha \sim 10^2 \text{ m}^{-1}$, $\tau \sim 10^{-4} \text{ s}$, $\rho \sim 10^3 \text{ kg/m}^3$, $C \sim 10^3 \text{ J/kg-K}$, and $dn/dT \sim -10^{-4}$; the nonlinear index intensity coefficient is $n_2^I \sim -10^{-12} \text{ m}^2/\text{W}$ and can thus be substantial.

G. Cascaded Second Order Effects

Second order nonlinear optical processes in noncentrosymmetric media were discussed in Chapter 2. It was noted that when perfect phase matching is not achieved, there will be a flow of power between the pump wave(s) and the newly generated frequency wave(s) as the generated wave(s) propagate periodically in and out of phase with the driving nonlinear polarization. This will impress a phase retardation on the pump wave(s) that is intensity dependent.

Consider second harmonic generation as an example of a quasi-self-induced phase retardation. When there is not perfect phase matching, the second harmonic will beat with the fundamental to generate a wave at the fundamental frequency that is in phase quadrature with the incident fundamental wave. The net result is an additional phase retardation impressed on the fundamental. As the incident fundamental intensity increases, a greater fraction of it is converted into the second harmonic within a coherence length. Thus a larger phase retardation is impressed on the fundamental. Such a process is a quasi-third order process

(i.e., nonlinear index of refraction) due to a cascaded second order effect, with an effective third order susceptibility written as $[\chi^{(3)}(-\omega; \omega, \omega, -\omega)]_{\text{eff}} = \chi^{(2)}(-\omega; 2\omega, -\omega) : \chi^{(2)}(-2\omega; \omega, \omega)$.

In the nondepleted pump regime, the pump intensity is essentially constant as a function of position and always large compared to the second harmonic intensity. Under these conditions, the net phase retardation induced by the cascaded process when the wave has traveled through a crystal of length L is given by

$$\Delta\varphi = -\frac{\Delta k L}{2} \left\{ 1 - \left[1 + \left(\frac{2\kappa\sqrt{I_\omega}}{\Delta k} \right)^2 \right]^{1/2} \right\} \quad (38)$$

where $\Delta k = 2k_\omega - k_{2\omega}$, and

$$\kappa = \frac{2\omega d_{\text{eff}}}{\sqrt{2\epsilon_0 n_\omega^2 n_{2\omega} c^3}} \quad (39)$$

In terms of the vacuum wave vector, this phase change is equivalent to a refractive index change, i.e., $\Delta\varphi = (\omega/c)\Delta n L$. For small enough pump intensity, or large enough phase mismatch, Eq. (38) can be expanded, and to lowest order the resulting Δn is proportional to I_ω . Thus an effective n_2^l can be defined, and its expression is given in Table 4.

Note that the effective nonlinear index intensity coefficient can be either positive or negative depending on the sign of the phase mismatch. In the literature, the phase mismatch is often defined as the negative of that defined above. However, it will always be true that $(n_2^l)_{\text{eff}}$ for SHG will be positive if $n_\omega > n_{2\omega}$ and negative if $n_\omega < n_{2\omega}$.

This effective nonlinear index coefficient can be substantial, with a typical value of $(n_2^l)_{\text{eff}} \sim 10^{-14} \text{ cm}^2/\text{W}$, and feasibly a factor of 1,000 times larger in realistic materials (i.e., for $d_{\text{eff}} \sim 50 \text{ pm/V}$). However, as the incident intensity increases [i.e., $I_\omega \sim (\Delta k/2\kappa)^2$], the expression in Table 4 is no longer valid. Then the expression for the net phase retardation given by Eq. (38) must be used, and the material is not Kerr-like. In general, when pump depletion cannot be ignored, then the coupled wave equations given in Chapter 2 must be solved numerically to find the net nonlinear phase retardation.

It is also noted that other non-phase matched second order processes, such as sum- and difference-frequency generation, produce nonlinear phase shifts. These processes can be considered as equivalent to a strong pump wave inducing a nonlinear index for a weak probe wave.

H. Photorefractive Effect

The photorefractive effect is the last example of a physical mechanism involved in an intensity induced refractive index change. Unlike the previous examples, the index change is not dependent on the magnitude of the intensity that produces it. Rather, it is a nonlocal change in refractive index due to a spatial variation of intensity. It was first observed in 1966 in electro-optic crystals and was described as “optical damage” [7].

The photorefractive effect is often encountered in a situation where two coherent waves of intensities, I_1 and I_2 , overlap and produce interference fringes. The case discussed here is the degenerate one where the frequencies of both waves are the same. The z -components of their wave vectors are parallel, but the x -components point in opposite directions. The intensity pattern produced in the region of the overlap of these two waves is given by

$$I(x) = I_1 + I_2 + 2\sqrt{I_1 I_2} \cos Kx \quad (40)$$

where $K = 2\pi/\Lambda$, and Λ is the fringe spacing. This intensity pattern is stationary in the photorefractive medium.

The photorefractive medium is modeled as a wide gap semiconductor that is normally transparent at the frequency of the incident radiation. However, the semiconductor contains donor and acceptor impurities (electrons or holes), whose energies lie within the forbidden gap of the semiconductor. It is assumed that $N_D \gg N_A$, where N_D and N_A are the number densities of donor and acceptor species, respectively. A small number of donors are thermally ionized, and in the dark the number of these ionized donors equals N_A . The acceptors maintain charge neutrality, but do not contribute directly to the photorefractive effect.

The neutral donors are photoionized by the incident light and create free carriers. Charge transport ensues due to diffusion. If an external field is applied, there will also be a drift current. The discussion here assumes only diffusion. After diffusing a small distance through the crystal, the free carriers can be trapped by ionized donors. In the steady state, this will occur in the dark regions of the intensity pattern. Thus, a space charge density pattern is established. The formation of this space charge density leads to the buildup of an internal space charge field. This field forms an index grating by the linear electro-optic (Pockels) effect. Thus, the medium must be noncentrosymmetric to be photorefractive.

The change in refractive index due to an applied electric field via the Pockels effect is written as

$$\Delta \left(\frac{1}{n^2} \right)_{ij} = \sum_k r_{ijk} E_k \quad (41)$$

where r_{ijk} are elements of the Pockels tensor, which is related to the second order susceptibility $\chi_{ijk}^{(2)}(-\omega; \omega, 0)$, and the subscripts i, j , and k range over x, y, z . In the photorefractive effect, the applied field is the internal space charge field, which is determined by the intensity interference pattern and physical properties of the medium. An externally applied field can modify the space charge field.

In a simple one-dimensional model of the photorefractive effect, the index of refraction can be considered a scalar quantity. For small modulation depth $2(I_1 I_2)^{1/2}/(I_1 + I_2)$, a closed form solution for the refractive index change can be obtained [8] and is given in Table 4, where r_{eff} is an effective Pockels coefficient depending on the polarization and the crystal orientation. (This coefficient can be determined in an analogous way to d_{eff} , as described in Chapter 2, through the use of direction cosines relating the crystal principal axes to the laboratory axes.)

Several things are noted about the refractive index grating $\Delta n(x)$. First, as mentioned earlier, it depends on the intensity only through the modulation depth. The index modulation thus goes to zero when either I_1 or I_2 is zero, and is a maximum when $I_1 = I_2$ (i.e., maximum fringe contrast).

Second, it is noted that $\Delta n(x)$ is $\pi/2$ radians out of phase with the intensity pattern that produced it. This result, due to the diffusion of charge and subsequent trapping in dark regions, leads to a transfer of energy between the two waves incident on the medium. This has several interesting consequences that can be used in a variety of applications (see Section III).

The phase difference between the index modulation and intensity pattern can be understood by a closer examination of the band transport model. For the sake of discussion, assume that the charge carriers are electrons. Free electrons are photogenerated in the bright fringes of the intensity pattern. This creates a free-charge density gradient and leads to diffusion of the electrons, which are then trapped by ionized donors in the dark fringes at a distance of one-half grating period away. Thus, a charge separation is created yielding a charge density grating (alternating positive and negative charge density) that is in phase with the intensity pattern. The charge separation results in a space charge electric field. In the vicinity of the peaks and valleys of the charge density grating, the charge distribution is symmetric. Hence, at the peaks and valleys the field on either side is of equal strength but pointing in the opposite direction. Consequently, the net field here must be zero. On the other hand, in the vicinity of the zeroes of the space charge grating, the charge distribution is asymmetric. The field on either side of these points is of equal strength and pointing in the same direction, and the net field is thus a maximum. For an adjacent zero at a distance $\Lambda/2$ away, the same condition holds except that the net field points in the opposite direction. Hence, the space charge field also forms in an

alternating positive and negative pattern that is $\pi/2$ radians out of phase with the space charge grating and the intensity fringe pattern.

Finally, the band transport model yields an expression for the space charge field amplitude that can be written as

$$E_{sc} = \left(\frac{1}{E_D} + \frac{1}{E_N} \right)^{-1} \quad (42)$$

where E_D and E_N are called the diffusion field and the saturation field, respectively. Expressions for these are given in Table 4. Consequently, the space charge field is less than the smaller of these two fields.

The names given to these fields originated from the physical processes producing them. When a charge density gradient is established charges diffuse in a direction opposite the gradient, creating a diffusion current and leading to charge separation. This charge separation sets up an electric field that opposes the diffusion and establishes a drift current in the opposite direction. The electric field that yields a steady-state net current of zero is called the diffusion field. The steeper the charge density gradient, the stronger this field must be. Thus $E_D \propto \Lambda^{-1}$, and increases for small grating period and decreases for large grating period.

The saturation field E_N is the maximum possible electric field for a given space charge density. By integration of Poisson's equation it is proportional to $eN_A\Lambda/2\pi$, which is the effective areal space charge density (i.e., it has units of coulombs per unit area). Thus, E_N increases with grating spacing since, for a given peak space charge (volume) density eN_A , the net charge contributing to the field increases with Λ .

As a result of these dependencies on Λ , for large grating spacing (small K), $E_D \ll E_N$ and the space charge field approaches E_D . On the other hand, for small grating spacing (large K), $E_D \gg E_N$ and the space charge field approaches E_N . Consequently, the amplitude of $\Delta n(x)$ has a maximum that is reached for a grating wave vector $K_{max} = (e^2 N_A / \epsilon k_B T)^{1/2}$, where e is the electron charge, ϵ is the average (dc) dielectric constant, k_B is Boltzman's constant, and T is the absolute temperature. The maximum space charge field amplitude is given by $E_{sc,max} = (N_A k_B T / 4\epsilon)^{1/2}$.

An externally applied field can modify the strength of the space charge field. When $E_N \ll E_D$ the modification is negligible. However, when $E_N \gg E_D$ and the applied field is large compared to both E_N and E_D , then the space charge field amplitude approaches E_N instead of E_D , as it does in the case with no external field. In general, the application of an external field will also shift the relative phase between the index grating and the intensity grating.

The magnitudes of the diffusion and saturation fields can be substantial, ranging from a few to hundreds of kilovolts per centimeter. (Note that the strength of the saturation field is inversely proportional to the dielectric constant and will

thus be smaller in a high dielectric material.) Consequently, the amplitude of the index modulation due to the photorefractive effect can be quite large compared to the nonlinear index changes described earlier for a given incident intensity. However, the process is in comparison quite slow, ranging from tens of microseconds to tens of seconds to reach a steady state (assuming an incident intensity $\sim 1 \text{ W/cm}^2$), depending on the material. The effect depends on charge separation and requires the absorption of at least one photon to separate a charged pair. Thus, the time required to reach a given space charge density is dependent on the photon flux. The actual response time for a given situation is inversely proportional to the incident intensity. It will also depend on other material and geometry parameters, such as the absorption cross section, the quantum efficiency (fraction of photoexcitations resulting in charge separation), the refractive index, the Pockels coefficient, and the grating spacing [8].

III. RELATED PHENOMENA AND APPLICATIONS

The discussion above illustrates several mechanisms whereby the incident light produces a change in the optical properties of a medium. This section examines the reaction of the medium back on the light and describes many of the electromagnetic phenomena resulting from a nonlinear index of refraction.

A. Optical Kerr Effect

Polarized optical radiation can induce a symmetry axis in an isotropic medium. Thus a birefringence is induced by an intense beam of light. This birefringence can lead to two interesting phenomena, intensity induced linear birefringence and ellipse rotation; the two are collectively referred to as the optical Kerr effect. The Kerr effect refers to a birefringence induced by an applied electric field where the index change is second order in the field strength. In the optical Kerr effect, the field derives from the optical frequency electromagnetic wave.

Induced linear birefringence. Consider an isotropic nonlinear medium wherein a strong pump beam at frequency ω and a weak probe beam at frequency ω' propagate collinearly. Both beams are linearly polarized, but the probe polarization is at a 45° angle with respect to the pump polarization. The strong pump establishes an extraordinary axis in the isotropic medium through the nonlinear index of refraction. The probe, which is assumed to be too weak to produce an index change of its own, thus sees the medium as an intensity dependent retardation plate. The two orthogonal components of the probe field will experience a different phase retardation, so that the output probe at the end of the medium will be, in general, elliptically polarized.

The induced linear birefringence is given by the formula in Table 6. It depends on the quantity $\chi_{xyxy}^{(3)} + \chi_{xyyx}^{(3)}$. Thus a measurement of the retardation can yield this quantity for the medium. The net phase retardation at ω' induced by the intensity at ω is also given in Table 6. An application of this effect is an intensity-controlled fast optical shutter. When the material is between parallel polarizers, extinction of the transmitted probe beam occurs at a pump intensity that leads to a net nonlinear phase retardation of $\Delta\varphi = \pi$. If the response of the medium is sufficiently fast, the time response of the shutter will follow the pump pulse temporal profile.

Ellipse rotation. Consider now a single optical beam incident on an isotropic nonlinear medium. For both linearly and circularly polarized light, the third order nonlinear polarization $\mathbf{P}^{(3)}$ has the same vector character as the applied field $\mathbf{E}^{(\sim)}$. Thus the induced birefringence produces no change in the polarization state of the optical field. However, an elliptically polarized wave induces a nonlinear polarization that mixes the left and right circularly polarized components of the wave. The induced circular birefringence Δn_c is given by the formula in Table 6. Note that this quantity depends only on the tensor component $\chi_{xyyx}^{(3)}$. E_+ and E_- are the complex field amplitudes of the left and right circularly polarized components, respectively, of the elliptically polarized wave. The circular birefringence produces a rotation of the polarization ellipse (ellipse axes) through an angle θ_c , which is also given in Table 6. A measurement of this rotation angle gives a measure of the $\chi_{xyyx}^{(3)}$ tensor component for the medium.

Table 6 Formulas Related to the Optical Kerr Effect (SI units)

Induced linear birefringence

Pump (ω) and probe (ω')

$$\begin{aligned}\text{Induced birefringence} \quad \Delta n(\omega') &= \frac{3(\chi_{xyxy}^{(3)} + \chi_{xyyx}^{(3)})}{n_0} |E(\omega)|^2 \\ &= \frac{3(\chi_{xyxy}^{(3)} + \chi_{xyyx}^{(3)})}{2\epsilon_0 n_0^2 c} I_\omega\end{aligned}$$

$$\text{Nonlinear phase retardation} \quad \Delta\varphi(\omega') = \frac{3\omega' L}{2\epsilon_0 n_0^2 c^2} (\chi_{xyxy}^{(3)} + \chi_{xyyx}^{(3)}) I_\omega$$

Probe transmittance

$$(\text{through parallel polarizers}) \quad I_{\omega'}(L) = I_{\omega'}(0) \cos^2 \left[\frac{1}{2} \Delta\varphi(\omega') \right]$$

Induced circular birefringence

Single elliptically polarized beam

$$\text{Induced birefringence} \quad \Delta n_c = -\frac{3\chi_{xyyx}^{(3)}}{n_0} (|E_+|^2 - |E_-|^2)$$

$$\text{Nonlinear phase retardation} \quad \theta_c = \frac{\pi \Delta n_c L}{\lambda}$$

B. Four-Wave Mixing

Four-wave mixing refers to the interaction of four waves in a nonlinear medium via the third order polarization. When the waves have different frequencies, the process can be used to generate new frequencies. However, several interesting effects are observed when all the waves have the same frequency. This is referred to as the degenerate case.

Degenerate four-wave mixing in centrosymmetric media. Degenerate four-wave mixing (DFWM) in isotropic media having a center of symmetry is nice to study because it avoids the complications of birefringence and the competing effects of second order processes. Two geometries used in studying this phenomenon are illustrated in Fig. 7. The first is called the backward geometry, since two of the waves travel in the backward direction and two travel in the forward direction. In the second case, all four waves travel in the forward direction, hence its name. This latter case is useful only for thin samples, as will be shown, since it is not phase matched.

The backward geometry is considered first. Two counterpropagating strong pump beams are labeled as the forward pump and the backward pump as shown in Fig. 7a. A third wave called the probe beam is incident at some angle θ to the direction of the forward pump. A fourth beam, called the conjugate beam, is generated in the process and propagates counter to the probe beam.

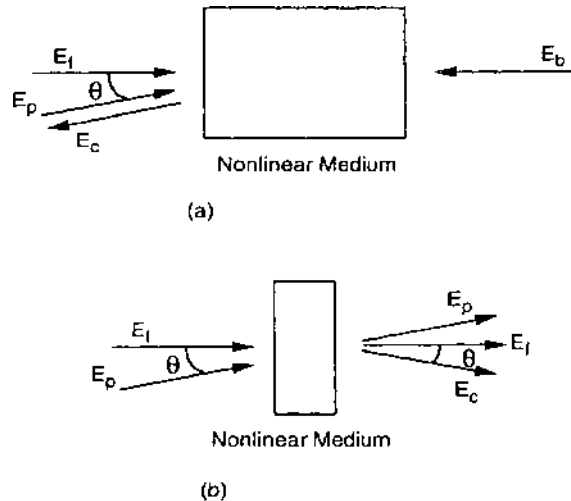


Figure 7 Two configurations for observing degenerate four-wave mixing. (a) Backward geometry. (b) Forward geometry.

The interaction of these waves will generate a third order polarization oscillating at the same frequency ω given by

$$P_c^{(3)} = 6\epsilon_0 \chi_{\text{eff}}^{(3)} A_f A_b A_p^* \exp[i(\mathbf{k}_f + \mathbf{k}_b - \mathbf{k}_p) \cdot \mathbf{r}] \quad (43)$$

where

$$\chi_{\text{eff}}^{(3)} = \hat{e}_c \cdot \chi^{(3)}(-\omega; \omega, \omega, -\omega) : \hat{e}_f \hat{e}_b \hat{e}_p^* \quad (44)$$

The polarization is proportional to the conjugate (negative frequency component) of the probe wave so that the net frequency is ω . Note that the degeneracy factor is 6 even though two of the incident waves have the same frequency since they are two distinct fields, traveling in opposite directions. Note that because $\mathbf{k}_f = -\mathbf{k}_b$ and $\mathbf{k}_p = -\mathbf{k}_c$, the DFWM process is automatically phase matched.

Similar third order polarizations can be written for the other three waves. Because of permutation symmetry for this nonresonant process, they will all have the same $\chi_{\text{eff}}^{(3)}$.

The third order polarization couples the four waves. Substituting the expressions for the nonlinear polarization into the wave equation and employing the slowly varying amplitude approximation yields four first order coupled differential equations that describe the spatial evolution of the waves in this process. The usual case involving strong pump beams of approximately equal amplitude allows one to ignore the pump beam equations. This is the nondepleted pump regime where A_f and A_b are approximately constant throughout the medium. The equations for the probe and conjugate waves are then given by

$$\frac{dA_p}{dz} = i\kappa A_c^* \quad (45)$$

and

$$\frac{dA_c^*}{dz} = i\kappa^* A_p \quad (46)$$

where

$$\kappa = \frac{3\omega}{n_0 c} \chi_{\text{eff}}^{(3)} A_f A_b \quad (47)$$

is called the coupling coefficient. In deriving these equations, it is assumed that the angle θ between the probe and forward pump beams is small. Otherwise, the left-hand sides of Eqs. (44) and (45) should be multiplied by $\cos \theta$.

The usual boundary conditions are that the input wave amplitudes are $A_p(0)$ nonzero and $A_c(L) = 0$. Using these conditions, the solutions to the coupled wave

equations are given by

$$A_p(z) = \frac{\cos[|\kappa|(z - L)]}{\cos(|\kappa|L)} A_p(0) \quad (48)$$

$$A_c(z) = -i \frac{\kappa \sin[|\kappa|(z - L)]}{|\kappa| \cos(|\kappa|L)} A_p^*(0) \quad (49)$$

Note that the output wave $A_p(L)$ is amplified by a factor of $1/\cos(|\kappa|L)$. However, the real interest is in the conjugate wave whose output $A_c(0)$ is proportional to the complex conjugate of the incident probe wave. This conjugate wave has been called the time reversed probe wave. It travels in the opposite direction of the probe wave and has exactly the time-reversed phase. It is often referred to as the “reflected” conjugate wave, and the medium in which DFWM occurs is called a “phase conjugate mirror.”

A phase conjugate mirror has several unique properties compared to an ordinary mirror. For example, it functions as a retroreflector for any incident angle. Also, for any angle, if the incident wave is converging (spherical phase curvature), then the reflected wave is diverging along the same path. Any phase distortion $\varphi(\mathbf{r})$ impressed on the incident probe, for example by propagating through an inhomogeneous medium (e.g., turbulence), will result in exactly the opposite phase $-\varphi(\mathbf{r})$ impressed on the reflected wave traveling backward through the distorting medium. Thus the wave emerging from the inhomogeneous medium will have no phase distortions. All of these special effects occur because the conjugate phase of the incident probe beam is impressed on the reflected beam. This is why it is called the conjugate wave.

Another interesting facet of the wave reflected from a phase conjugate mirror is that it can have a larger amplitude than the incident probe. This occurs when $\pi/4 < |\kappa L| < \pi/2$, as can be seen from Eq. (49). Thus both the probe and conjugate waves experience gain under these pump conditions. In fact, when $|\kappa L| \rightarrow \pi/2$ the gain $\rightarrow \infty$. This has an analog in electronic circuitry and refers to the situation where an amplifier bursts into oscillation, i.e., there is a finite output for zero input. Actually, the input is quantum fluctuations (noise). Thus one has the interesting phenomenon of a mirrorless oscillator. The energy for amplifying the beams comes from the pump beams. When the amplification is large, the pumps can no longer be considered nondepleted.

It is useful to define a conjugate reflectance by the ratio of the intensities, I_c/I_p . Expressions for this quantity are given in Table 7. Note that $R \rightarrow \infty$ as $|\kappa L| \rightarrow \pi/2$, reflecting once again the oscillation condition. For small values of $|\kappa L|$ it is noted that $R \sim |\kappa L|^2$. This form is useful in measurements of $\chi_{\text{eff}}^{(3)}$, as will be discussed in Chapter 7.

Table 7 Formulas Related to Four-Wave Mixing^a

Process	Phase conjugate reflectance
DFWM in centrosymmetric media	
No absorption	$R = \tan^2 \kappa L$ $R \approx (\kappa L)^2 \quad \kappa L \ll 1$ $\kappa = \frac{3\omega}{n_0 c} \chi_{\text{eff}}^{(3)} A_f A_b \quad (\text{SI})$ $\kappa = \frac{12\pi\omega}{n_0 c} \chi_{\text{eff}}^{(3)} A_f A_b \quad (\text{cgs})$
Effect of background linear absorption	$R = \frac{4 \kappa L ^2 e^{-\alpha L} \tan^2 \kappa_{\text{eff}} L}{ \alpha L \tan \kappa_{\text{eff}} L + 2\kappa_{\text{eff}} L ^2}$ $\kappa_{\text{eff}} = \sqrt{ \kappa ^2 e^{-\alpha L} - (\alpha/2)^2}$ $R \approx \frac{ \kappa L_{\text{eff}} ^2 e^{-\alpha L}}{1 - e^{-\alpha L}} \quad \kappa L ^2 e^{-\alpha L} \ll (\alpha L/2)^2$ $L_{\text{eff}} = \frac{\alpha}{\tan^2 \kappa' L}$ $R = \frac{\tan^2 \kappa' L}{1 + \eta^2 \sec^2 \kappa' L}$ $\kappa' = \frac{ \kappa \sqrt{1 + \eta^2}}{I_f - I_b}$ $\eta = \frac{4\sqrt{I_f I_b}}{I_f + I_b}$ $R = \frac{\sinh^2 \frac{1}{4} \gamma L}{\cosh^2 [\frac{1}{4} \gamma L - \ln(I_b/I_f)^{1/2}]} \quad (\text{see Section III.c})$ $\gamma = \frac{\pi}{n_0 \epsilon_0 \lambda \cos \theta} \hat{e}_p \cdot \boldsymbol{\epsilon}_1 \cdot \hat{e}_f$ $R = \left \frac{\kappa \sinh \gamma L}{\gamma \cos \gamma L + \alpha \sin \gamma L} \right ^2$ $\gamma = \sqrt{ \kappa ^2 - \alpha^2}$
DFWM in photorefractive media (ignoring absorption) (θ = angle between \mathbf{k}_f and \mathbf{k}_p)	$\kappa = \alpha_{00} \frac{T_2 \Delta - i}{1 + (T_2 \Delta)^2} \frac{2(I_f I_b)^{1/2}/I_s^\Delta}{\{(1 + (I_f + I_b)/I_s^\Delta)^2 - 4I_f I_b/(I_s^\Delta)^2\}^{3/2}}$ $R = \left \frac{(\kappa/\gamma) \tan \gamma L}{1 + (\alpha/\gamma) \tan \gamma L} \right ^2 \quad \kappa ^2 > \alpha^2$ $R = \left \frac{(\kappa/\gamma) \tanh \gamma L}{1 + (\alpha/\gamma) \tanh \gamma L} \right ^2 \quad \kappa ^2 < \alpha^2$
DFWM in two-level media	$R(\delta\omega/\omega) = \frac{\tan^2 \kappa' L}{1 + x^2 \sec^2 \kappa' L}$ $\kappa' = \kappa \sqrt{1 + x^2}$ $x = \frac{k \delta\omega}{ \kappa \omega}$
Nearly DFWM in centrosymmetric media	$R(\omega_1) = \frac{\lambda_2 n_2}{\lambda_1 n_1} \tan^2 \kappa L$
Non-DFWM in centrosymmetric media	
Phase conjugate reflectance (Fig. 15)	

(continued)

Table 7 Continued

Process	Phase conjugate reflectance
Signal amplification (s = signal, p = pump) (Fig. 14)	$\kappa = 3 \left(\frac{\omega_1 \omega_2}{n_1 n_2 c^2} \right)^{1/2} \chi_{\text{eff}}^{(3)} A_3^* A_4$ $I_s(L) = I_s(0) \exp[2Re(G)]$ $G(L) = i \frac{3\omega_s}{n_s c} \chi_{\text{eff}}^{(3)} A_{p1} A_{p2} L e^{i(\Delta k \cdot \hat{z})L/2} \frac{\sin[(\Delta k \cdot \hat{z})L/2]}{(\Delta k \cdot \hat{z})L/2}$ $Re(G) = - \frac{3\omega_s}{n_s c} \text{Im}(\chi_{\text{eff}}^{(3)}) A_p ^2 L, (\Delta k \cdot \hat{z})L \ll 1$ $= - \frac{3\omega_s \text{Im}(\chi_{\text{eff}}^{(3)})}{2\epsilon_0 n_p n_s c^2} I_p L \quad A_{p1} = A_{p2} = A_p $

^a Parameters defined in the text. DFWM, degenerate four-wave mixing. (Nondepleted pump approximation.)

Effects of linear nonresonant absorption. If there is some background linear absorption in the medium, the above equations must be modified. This could be due to a nonresonant interaction where the frequency is in the far wings of the absorption line, or it could be due to impurity absorption. For a linear absorption coefficient α , the resulting expression for the conjugate reflectance is given in Table 7. The approximate expression corresponds to the condition $|\kappa L|^2 \exp(-\alpha L) \ll (-\alpha L/2)^2$ and is given in terms of an effective length $L_{\text{eff}} < L$, which is determined by the absorption coefficient: $L_{\text{eff}} = [1 - \exp(-\alpha L)]/\alpha$.

Real-time holography and polarization effects. Some aspects of DFWM can be interpreted as real-time holography [3,9]. This can be observed by rewriting the third order polarization driving the conjugate beam, making use of the symmetry properties of $\chi_{ijkl}^{(3)}$ in an isotropic medium:

$$\mathbf{P}_c^{(3)} = 6\epsilon_0 [\chi_{xyxy}^{(3)} (\mathbf{E}_f \cdot \mathbf{E}_p^*) \mathbf{E}_b + \chi_{xxyy}^{(3)} (\mathbf{E}_b \cdot \mathbf{E}_p^*) \mathbf{E}_f + \chi_{yyxy}^{(3)} (\mathbf{E}_f \cdot \mathbf{E}_b) \mathbf{E}_p^*] \quad (50)$$

Thus the conjugate wave is due to three independent contributions represented by the three terms in Eq. (50). Note that any one of these contributions can be observed in isolation by appropriately choosing the polarizations of the three incident waves. The first term is selected by choosing $\hat{e}_f \parallel \hat{e}_p \perp \hat{e}_b$. The conjugate wave is then polarized parallel to \hat{e}_b . Similarly, the second and third terms are isolated by the choices $\hat{e}_b \parallel \hat{e}_p \perp \hat{e}_f$ and $\hat{e}_f \parallel \hat{e}_b \perp \hat{e}_p$, respectively. In each case, the conjugate wave assumes the polarization of the last of the unit vector triplets.

The first term of Eq. (50) is interpreted as the scattering of the backward pump beam from a Bragg grating written by the interference of the forward pump and probe beams, where the phase grating is recorded through the nonlinear index of refraction. Similarly, the second term corresponds to a Bragg grating written by the interference pattern due to the overlap of the backward pump and probe

beams, which then scatters the forward pump beam. In both cases these are time independent stationary gratings in space, the first having a coarse grating spacing and the second having a fine grating spacing. These are illustrated in Fig. 8. The scattered pump beams are always counter propagating to the incident probe beam because of the angular selectivity of the Bragg gratings and the phase matching of the interaction.

This real-time grating picture also helps explain the phase conjugation of the reflected beam. This is illustrated in Fig. 9. If the phase of the probe beam is distorted, this phase distortion is imprinted in the phase gratings recorded by the interference of the probe with both pump beams. Each pump beam acts as a reading beam for this hologram. Since each pump beam reads from the opposite direction of the other pump, its scattered component carries the phase information present in the hologram, but in an exactly opposite sense to that of the incident probe, as illustrated in Fig. 9.

The last term in Eq. (50) does not bear any analogy to holography. There are two ways in which it can be interpreted, both of which are valid depending on the type of medium in which the interaction takes place. In its present form, written in Eq. (50) it is apparent that the forward and backward waves will interfere to form a grating stationary in space. However, since the conjugate of either wave is not involved, this grating is not time independent but rather oscillates at 2ω . Secondly, the probe wave is not incident at the correct angle for Bragg scattering into 180° . Therefore at first glance a grating interpretation does not appear to be appropriate.

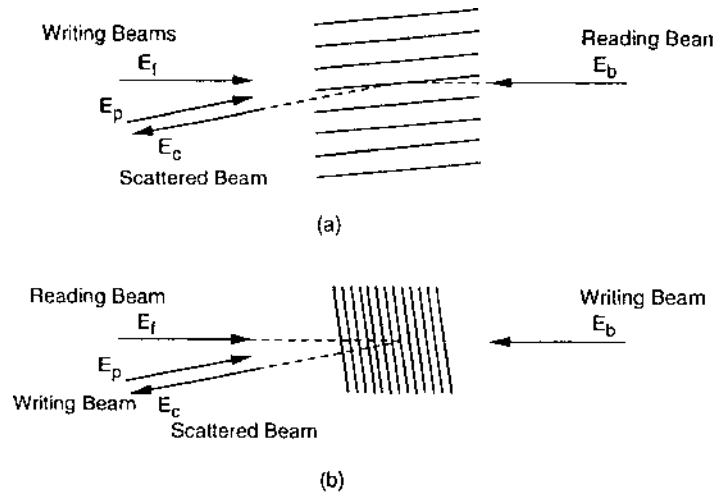


Figure 8 Real-time holographic gratings recorded in a nonlinear medium by degenerate four-wave mixing. (a) Coarse grating. (b) Fine grating.

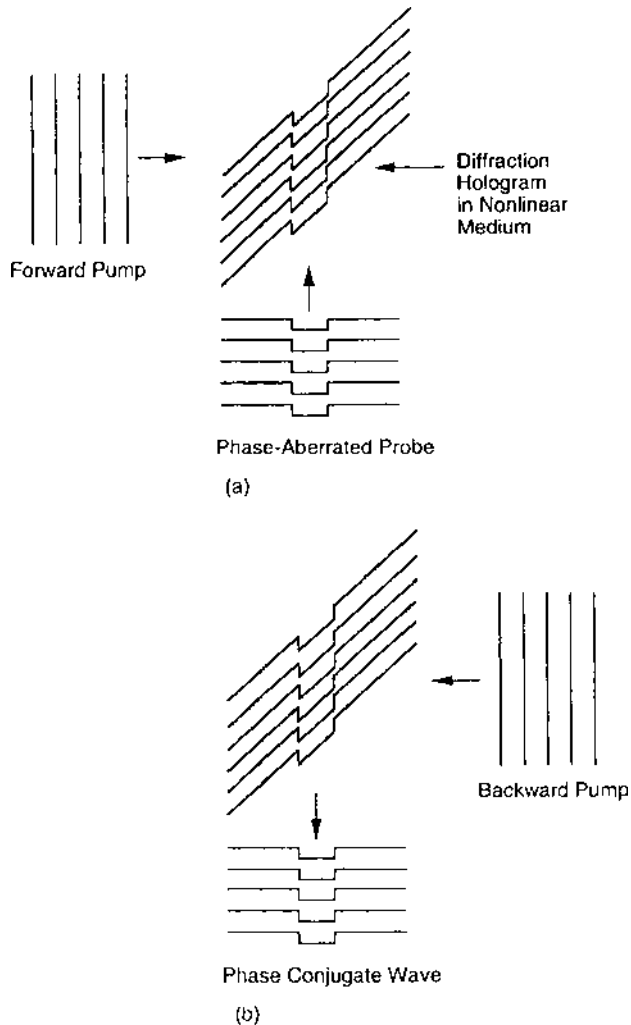


Figure 9 Grating formation and readout (phase conjugate wave) for a phase-distorted probe wave. (a) Grating recording. (b) Grating readout.

Rather the phase conjugate beam is due to a scattering of the probe from a two-photon excitation [10]. This term will thus be strong when the material has a nearby two-photon absorption resonance. Quantum mechanical considerations indicate that if the two-photon resonance is strong, then the material will be put into a two-photon coherent state (i.e., a superposition of the ground and

two-photon excited states). This coherent state will oscillate at 2ω . The incident probe photon stimulates a scattering of two photons from this state: one in the forward probe direction and one in the backward probe direction. The most efficient scattering takes place along the direction that is phase matched and along the direction that will achieve gain (i.e., along the probe beam axis).

Even when a two-photon resonance is not nearby, the last term in Eq. (50) can make a significant contribution to the conjugate wave. To see this, first rewrite this term as $\chi_{xyyx}^{(3)} \mathbf{E}_f \cdot (\mathbf{E}_b \mathbf{E}_p^*)$. This now has the appearance of the forward beam scattered from a tensor grating formed by the backward pump and probe beams. This grating is again independent of time and stationary in space. However, it is fundamentally different from those described earlier. Since the backward pump and probe wave are assumed to be polarized orthogonally, their superposition will not produce interference fringes. They will, however, produce a field vector whose direction varies periodically along the phase front of the forward pump wave. A medium of anisotropic molecules will attempt to reorient with this rocking polarization and thus produce a periodically modulated birefringence that scatters the forward beam in the direction opposite to the probe propagation. Likewise, the forward pump and probe beams will also form such a grating to scatter the backward pump. These types of gratings are called orientation gratings [11,12]. A medium with anisotropic absorption will also respond to these vector patterns and produce strong orientation gratings.

Effects of two-photon absorption. This grating picture takes on more interesting aspects when strong two-photon absorption is present. It should be noted that the conjugate reflectance is related only to the modulus of the third order susceptibility through the factor $|\kappa|$. The third order susceptibility is complex, in general. Its real part relates to the nonlinear index coefficient discussed above. The imaginary part gives rise to two-photon absorption (see Chapter 9). Thus the diffraction gratings referred to earlier are made up of two contributions that are in phase quadrature (i.e., $\pi/2$ radians out of phase). Thus they contribute independently in a time averaged sense. The refractive index part creates a phase grating. The two-photon absorption part creates what is known as an amplitude grating that contributes to Bragg scattering but also produces optical loss.

It is possible to observe this amplitude grating in solutions using picosecond pulses. In a solution, the conjugate signal is due to nonlinearities contributed by both solvent and solute molecules. Usually, the solvent is chosen to have negligible two-photon absorption. If the real parts of the solvent and solute contributions to $\chi^{(3)}$ have opposite signs, then for some concentration of solute, the two real parts will cancel. The detected conjugate signal then comes from scattering off the amplitude grating due to the imaginary part of $\chi^{(3)}$. To see this effect, the conjugate signal must be measured as a function of concentration [2].

Strong two-photon absorption can lead to other changes in the linear optical properties of the medium. This cascading of effects of different orders creates an effective fifth order process in the medium. One example is the creation of a thermal grating due to the heating of the medium caused by the two-photon absorption amplitude grating. As discussed in Section II.F, the resultant temperature distribution will produce an index distribution through the thermooptic effect. Another possibility is a concentration grating of new species with a different linear susceptibility than that of the surrounding medium. This could be a two-photon excited state, a triplet state of the molecule, or possibly a different conformation of the molecule.

The index amplitude corresponding to the phase grating created by this effective fifth order effect can have the opposite sign of that due to the real part of $\chi^{(3)}$, i.e., the two phase gratings can be π radians out of phase. When this is the case, at some pump intensity the two gratings will have the same strength and thus wash each other out. All that is left is the two-photon amplitude grating to scatter the incoming pump beams. When the DFWM process is created with optical pulses, this washout will not be instantaneous, since the fifth order phase grating takes some time to build up. The growth of this grating can be observed using nanosecond pulses. Depending on the pulse width and the energy in the pulses, it is possible to isolate the amplitude grating. The effect is easy to see by capturing and digitizing the phase conjugate pulse. The pulse exhibits a double peak, where the dip corresponds to the point in time when the phase gratings disappear [13]. This point will move to earlier times in the pulse as the pump pulse energy is increased. Examples are shown in Fig. 10.

Effects of unbalanced pump beams. All of the effects described above assumed equal pump amplitudes. When this is not the case, the conjugate reflectance is affected even for nondepleted pumps. The expression for the conjugate reflectance under these conditions is given in Table 7.

To be complete, the nonlinear polarizations leading to self-action and cross-action of the beams (i.e., optical Kerr effect) should be included in the coupled wave equations. These were ignored in the treatment above. The self-action of each beam just contributes a constant phase shift to the waves and hence does not create any observable effect to the DFWM process, unless polarization effects are detected. Hence these can safely be ignored. The combined effects of self-action and cross-action cannot be ignored when the pump beams are unequal.

This combination produces a z dependent phase shift, proportional to the asymmetry in the pump beam intensities, which appears in the product of the pump amplitudes. This adds a phase term to the coupling coefficient κ , which has the effect of introducing a phase mismatch between the driving nonlinear polarization and the phase conjugate wave. Hence this produces a decrease in the efficiency of the conjugate wave production. This intensity dependent phase

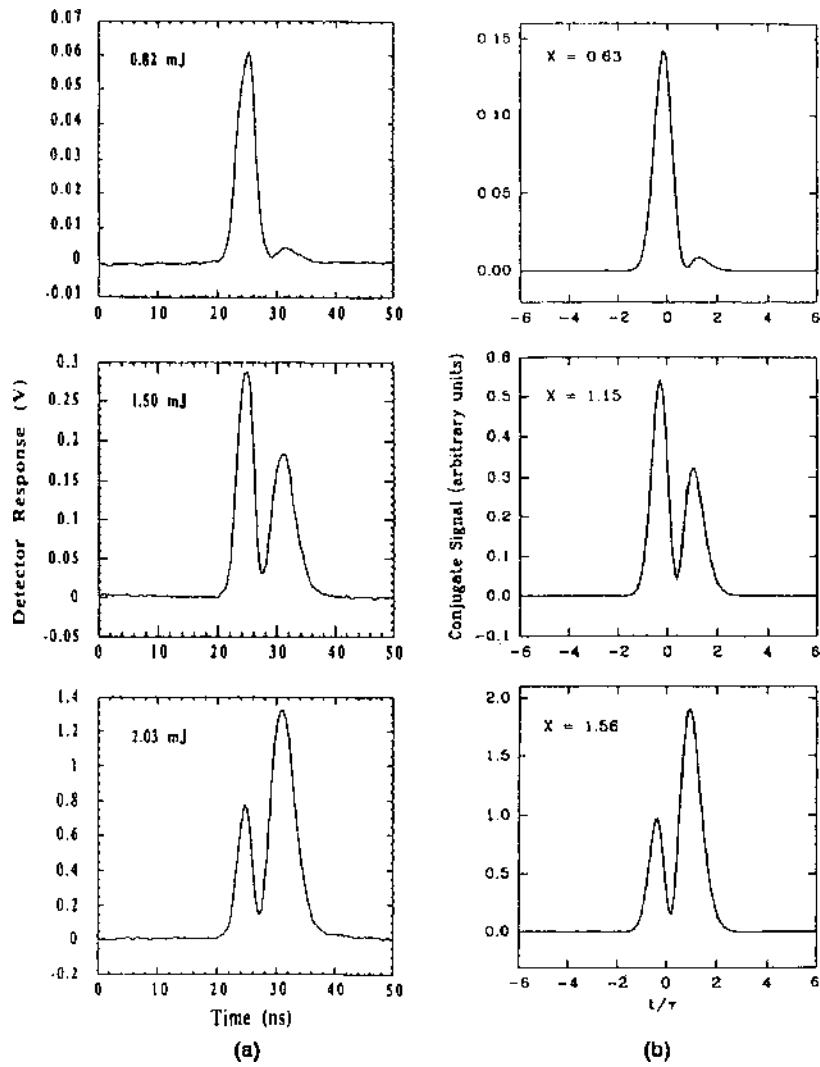


Figure 10 Effects of two-photon absorption on pulsed degenerate four-wave mixing in the nanosecond regime (solution of diphenyl butadiene in chloroform). The left set of plots are experimental data showing the effects of increasing pump energy, and the right set are theoretical calculations. The parameter X is proportional to pump energy, and both X and pump energy are in the ratio of 1:1.83:2.48 (From Ref. 13.)

mismatch can be offset by an intentionally introduced linear phase mismatch. This could be, for example, a small angle adjustment of the pump beams from exact counterpropagation, or a small frequency shift in the probe wave.

Pump depletion [14]. The four coupled-wave equations cannot be solved analytically when pump depletion is included. Numerical analyses predict that it is possible to fully convert the power of one of the pump waves into the conjugate wave. However, full conversion is only possible if the two pump intensities are equal and if the incident probe intensity is small compared to $[(4/3)\epsilon_0 n_0 c I_f(0)/\chi_{xxx}^{(3)}]^{1/2}$. Oscillation is still possible but will be suppressed for a nonzero input probe intensity. For increasing pump intensity, power will flow back and forth from the pump waves to the probe and conjugate waves.

DFWM in photorefractive media [8]. The sinusoidal index modulation recorded in a photorefractive medium by two interfering waves was described in Section II.H. In the notation of backward DFWM, these recording waves correspond to the forward pump and probe beams. This coarse phase grating (a “transmission grating”) scatters a beam propagating counter to the forward pump beam into the direction of the phase conjugate beam in the backward DFWM geometry. Simultaneously, the backward wave records a fine grating (a “reflection grating”) by interfering with the probe beam, which then scatters the forward pump in the direction of the conjugate beam. In many practical situations, this grating contributes negligibly to the phase conjugate signal since, in the limit of small K , the space charge field responsible for the index modulation is small in comparison to that associated with the coarse grating.

The index modulation is due to the photorefractive effect. This is a real stationary spatial modulation. Hence, there is no two-photon coherence or orientation grating contributing to the DFWM process in photorefractive media. There are, however, some unique aspects of the photorefractive effect that also make DFWM different in these media.

As noted in Section II.H, the index modulation is shifted in phase by $\pi/2$ radians from the intensity pattern that recorded it. Section III.C describes how this leads to a coupling between the two recording beams. This coupling produces a one-way power flow from one recording beam to the other. Thus, the conjugate wave is due not only to the scattering of a third wave incident on the medium, like that described above for Kerr media, but also due to this self-scattering process called two-beam coupling.

The expression for the phase conjugate reflectance due to DFWM in photorefractive media in the nondepleted pump approximation, including the effects of unequal pump intensities, is given in Table 7. Only contributions from the coarse grating have been included. Note that for symmetric pumping, the reflectance is always less than one. Larger reflectances are obtained using asymmetric pumping. Still, the reflectance cannot be driven to ∞ where oscillation occurs. To achieve this condition, a phase shift other than $\pm \pi/2$

between the phase grating and the intensity modulation, as well as unequal pump intensities, must be obtained. Such a phase shift can be achieved by applying an external field or making the frequencies of the interacting waves nondegenerate.

Some of the differences between DFWM in Kerr media and photorefractive media bear repeating. In Kerr media, the phase conjugate reflectance increases with pump intensity. This is not so in photorefractive media since the coupling coefficient is independent of intensity. For a 1:1 pump beam ratio the reflectance in Kerr media can go to ∞ , producing oscillation. The oscillation condition is defined by a critical index modulation (coupling coefficient) achieved at some finite pump intensity. In a photorefractive medium the reflectance never exceeds unity for this pump ratio. Whereas a pump beam imbalance is detrimental to the reflectance in Kerr media, it can produce a reflectance $\gg 1$ in photorefractive media. The condition for maximum reflectance is $\gamma L = 2 \ln(I_b/I_f)$. This condition is also required for self-oscillation. In addition, oscillation requires a particular value of not only the index modulation (which in this case is independent of pump intensity), but also a particular phase difference unequal to $\pm \pi/2$ between the phase grating and the intensity modulation.

The gratings in photorefractive DFWM are actually tensor gratings, determined by the polarizations of the recording beams and the orientation of the crystal. The conjugate reflectance as well as its polarization will depend on these factors. Additional aspects of wave mixing in photorefractive media are quite extensive, and the reader is referred to the literature for further details [8].

Resonant saturation case. The nonlinear refractive index of a two-level system was taken up in section II.E. Only the case of homogeneous absorption line broadening is considered here.

Both amplitude and index gratings are recorded near resonance. The conjugate reflectance is given in Table 7. The effective coupling coefficient is related to the saturable index and the saturable absorption coefficient.

The conjugate reflectance does not necessarily increase without limit in this case because of saturation. When $|\kappa|^2 > (\alpha/2)^2$, then R can become infinite when $\tan \gamma L = -2\gamma/\alpha$, where $\gamma^2 = |\kappa|^2 - (\alpha/2)^2$, κ is the complex coupling coefficient, and α is the saturable absorption coefficient. (Expressions for these quantities are given in Table 7.) When $|\kappa|^2 < (\alpha/2)^2$, R cannot become infinite for any value of γL [15].

A pure amplitude grating is possible at resonance ($\Delta = 0$). The general behavior of the reflectance for such gratings is shown in Fig. 11. For $I > I_s^\Delta$, the reflectance decreases, since the absorption coefficient, acting like the coupling coefficient in this case, saturates and becomes smaller. Also, as $\alpha_0(0)L$ increases, where $\alpha_0(0) \propto N$ (number density) is the on-resonance low-intensity absorption coefficient, the reflectance increases due to an increase in N (i.e., more absorbers). However, this is eventually offset by increased absorption of the probe

and conjugate waves, so increasing $\alpha_0(0)L$ gives diminishing returns. Here the reflectance can never exceed unity.

The reflectance can only exceed unity by detuning from line center, if this is done while also increasing the density. Figure 11 shows this effect by plotting the reflectance as a function of I/I_s^Δ for different values of $\alpha_0(0)L/(1 + T_2^2\Delta^2)$. The cost of increased reflectance is a higher pump intensity requirement, since the saturation intensity scales as $1 + T_2^2\Delta^2$.

The above discussion ignores the absorption of the pump beams. It turns out that this is significant for $I/I_s^\Delta < 1$. At higher intensities, saturation makes pump losses insignificant.

Motion of the atoms in a gas can have a significant effect on the conjugate reflectance. This is due to two effects. One is that Doppler broadening (inhomogeneous broadening) causes the absorption to saturate as $(1 + I/I_s^\Delta)^{-1/2}$ rather than $(1 + I/I_s^\Delta)^{-1}$. The other reason is that the motion tends to wash out the fine grating. Details of these processes can be found in the literature [11]. The effects of equal beam intensities and pump depletion are also discussed in Ref. 11.

Forward conjugate wave generation. Forward DFWM was discussed briefly above. It is illustrated again in more detail in Fig. 12. Forward DFWM involves only a single pump beam, the forward pump shown in the figure. The probe beam is incident on the medium from the same side and overlaps the forward pump. The output waves include, in addition to the transmitted pump and probe, a conjugate wave and a fourth wave called the auxiliary wave. In actuality, for an optically thin medium, there can be a multitude of output waves. The pump and probe waves write an index grating in the nonlinear medium that self-diffracts these waves. The scattering from this optically thin nonlinear grating corresponds to Raman–Nath diffraction, which produces a multitude of diffracted waves. For most practical situations, consideration of the waves depicted in Fig. 12 is sufficient.

The usual situation is that of a strong pump and a weak probe. Thus $|E_f| \gg |E_p|$, which implies that $|E_f| \gg |E_c|$ and $|E_c| \gg |E_a|$ also [5]. Under these conditions, the pump can be considered nondepleted, and only wave equations for E_f , E_p , and E_c need to be solved. The complex wave amplitudes are determined to be

$$A_f(z) = |A_f(0)|\exp(i\kappa z) \quad (51)$$

$$A_p(z) = A_p(0)\exp\left[i\left(\kappa + \frac{\Delta k}{2}\right)z\right]\left[\cosh(gz) + i\frac{(\kappa - \Delta k/2)}{g}\sinh(gz)\right] \quad (52)$$

$$A_c(z) = i\frac{\kappa}{g}A_p^*(0)\exp[i(\kappa + \Delta k/2)z]\sinh(gz) \quad (53)$$

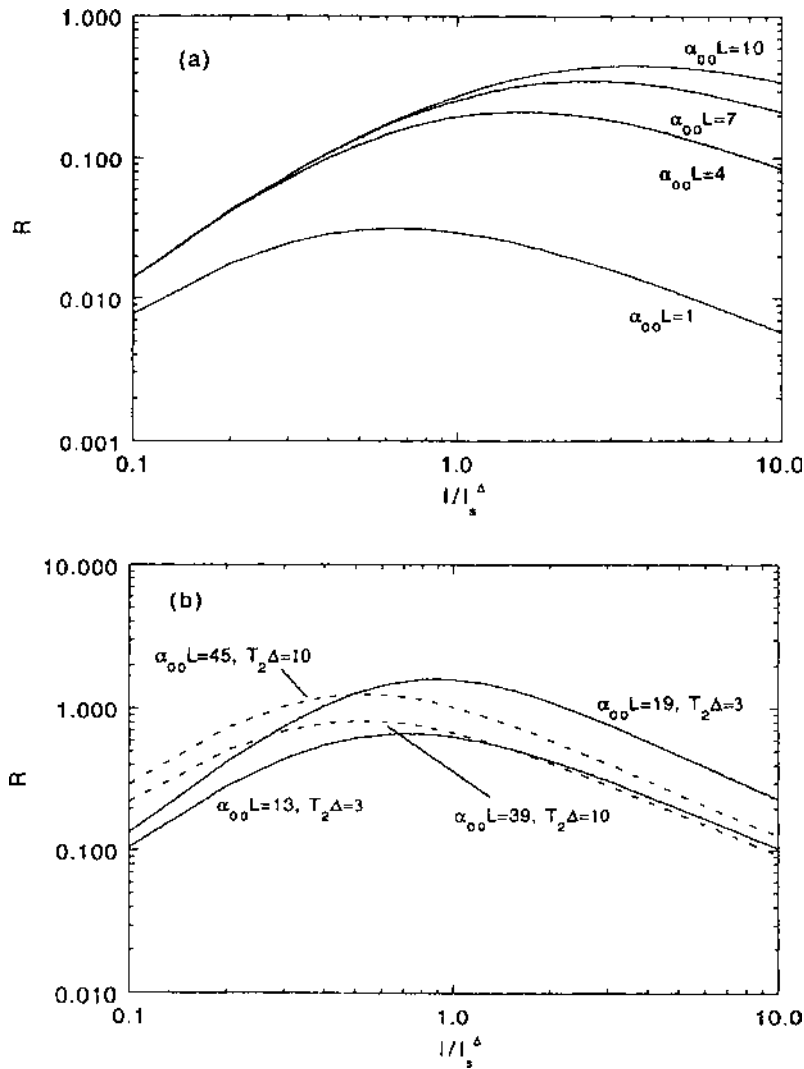


Figure 11 Phase conjugate reflectance in a homogeneously broadened two-level system as a function of intensity. (a) Pure amplitude gratings ($T_2\Delta = 0$). (b) Mixed amplitude and phase gratings ($T_2\Delta \neq 0$).

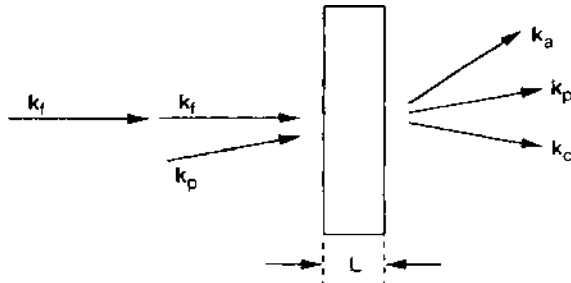


Figure 12 Forward degenerate four-wave mixing in a thin nonlinear medium.

where

$$\kappa = \frac{3\omega}{n_0 c} \chi_{\text{eff}}^{(3)} |A_f(0)|^2 \quad (54)$$

is the nonlinear coupling coefficient,

$$\Delta k = (2\mathbf{k}_f - \mathbf{k}_p - \mathbf{k}_c) \cdot \hat{\mathbf{z}} \quad (55)$$

is the phase mismatch, and

$$g = \sqrt{\Delta k \left(\kappa - \frac{\Delta k}{4} \right)} \quad (56)$$

Notice that all of the waves experience a nonlinear phase shift due to the strong pump beam. Also, the conjugate wave is proportional to the complex conjugate of the input probe wave. If the medium is thin, so that $\Delta k L$ is small, this wave can be appreciable. The probe wave is amplified by the interaction with a gain factor G given by

$$G = \frac{I_p(L)}{I_p(0)} = 1 + \frac{\kappa^2}{g^2} [\cosh^2(gL) - 1] \quad (57)$$

Nearly degenerate four-wave mixing. In this case, the pump waves have frequency ω , while the incident probe wave is taken to have a frequency $\omega - \delta\omega$, where $\delta\omega/\omega \ll 1$. This introduces a small phase mismatch to the interaction, which profoundly affects the conjugate reflectance. The corresponding formula is given in Table 7. This is shown plotted in Fig. 13 as a function of $k\delta\omega/\omega|\kappa|$. It can be seen that now the conjugate mirror acts as narrow band reflector, with a peak at

$\delta\omega = 0$ and a bandwidth of

$$(\delta\omega)_{\text{FWHM}} = \frac{2c|\kappa|}{n_0} \left[1 + R_{\text{peak}} - (2 + R_{\text{peak}}) \frac{\tan^{-1} \sqrt{R_{\text{peak}}}}{\sqrt{R_{\text{peak}}}} \right]^{-1/2} \quad (58)$$

for $\delta\omega/\omega \ll 1$, where $R_{\text{peak}} = \tan^2 |\kappa L|$.

Nondegenerate four-wave mixing. For completely nondegenerate frequencies, other geometries must be considered to obtain efficient wave mixing. Two examples are considered here.

The first is illustrated in Fig. 14. Here two pump beams of frequency ω_p and a signal beam of frequency ω_s are incident on an isotropic medium. The third order susceptibility that couples the waves and gives rise to an output signal wave $E_s(L)$ is $\chi_{ijkl}^{(3)}(-\omega_s; \omega_s, \omega_p, -\omega_p)$. The pump waves are designated E_{p1} and E_{p2} since, although they have the same frequency, they may be distinct fields having unique directions and polarizations. The phase mismatch is thus $\Delta\mathbf{k} = \mathbf{k}_{p1} - \mathbf{k}_{p2}$.

In the nondepleted pump approximation the output signal field is related to the input signal field by an exponential factor $G(L)$ (see Table 7). Note that this factor is related to a sine function, which accounts for the phase mismatch just as in second order frequency mixing processes. Thus the factor $G(L)$ is effective only over a distance of the order of a coherence length. If the geometry is such that phase matching is achieved, or if the material is thin compared to a coherence

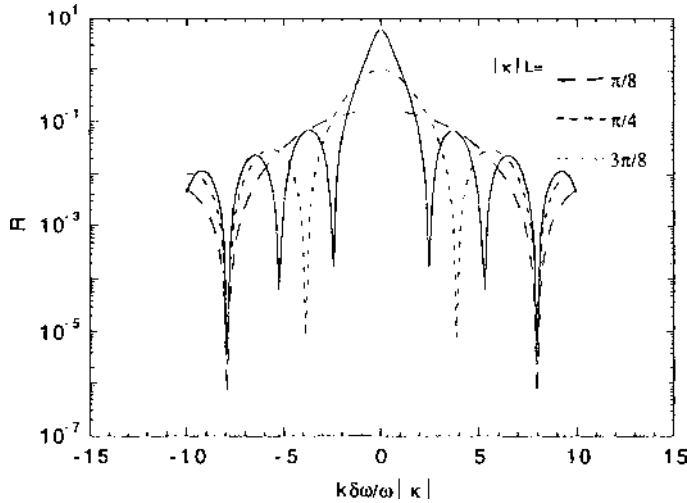


Figure 13 Narrow band phase conjugate reflectance as a function of detuning from exact phase matching for nearly degenerate four-wave mixing.



Figure 14 Nondegenerate four-wave mixing geometry for gain or loss processes.

length, then the signal wave will experience gain or loss depending on the sign of $\text{Im}(\chi_{\text{eff}}^{(3)})$, where $\chi_{\text{eff}}^{(3)} = \hat{e}_s \cdot \chi^{(3)} : \hat{e}_s \hat{e}_{p1} \hat{e}_{p2}^*$. A negative imaginary part corresponds to gain, while a positive imaginary part corresponds to loss. A specific example of this is stimulated Raman scattering, for which $\chi_{\text{eff}}^{(3)}$ is resonantly enhanced and phase matching is automatically satisfied (see Chapter 14).

A second nondegenerate four-wave mixing example is shown in Fig. 15, where the input waves are the pump waves E_3 and E_4 and the signal waves $E_1(0)$ traveling to the right and $E_2(L)$ traveling to the left. The frequencies are such that $\omega_4 = \omega_1 + \omega_2 + \omega_3$. Hence the signal waves couple to the pump waves in the combination $E_3^* E_4$ (i.e., $\omega_1 = \omega_4 - \omega_3 - \omega_2$ and $\omega_2 = \omega_4 - \omega_3 - \omega_1$). A typical phase matching geometry for this process is shown in Fig. 15, where the signal waves are counterpropagating. Nondepleted pumps are assumed.

The two signal waves are coupled in the interaction, and the output wave amplitudes are given by

$$A_1(L) = \frac{A_1(0)}{\cos|\kappa L|} + i \frac{\kappa}{|\kappa|} \left(\frac{\omega_1 n_2}{\omega_2 n_1} \right)^{1/2} A_2^*(L) \tan|\kappa L| \quad (59)$$

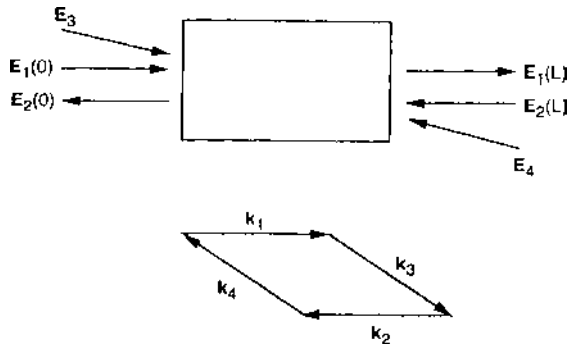


Figure 15 Nondegenerate four-wave mixing geometry for a mirrorless parametric oscillation process.

$$A_2^*(0) = -i \frac{|\kappa|}{\kappa} \left(\frac{\omega_2 n_1}{\omega_1 n_2} \right)^{1/2} A_1(0) \tan |\kappa L| + \frac{A_2^*(L)}{\cos |\kappa L|} \quad (60)$$

where

$$\kappa = 3 \left(\frac{\omega_1 \omega_2}{n_1 n_2 c^2} \right)^{1/2} \chi_{\text{eff}}^{(3)} A_3^* A_4 \quad (61)$$

is the complex coupling coefficient. An interesting case is when $A_2(L) = 0$. Then Eq. (60) predicts that the output field $A_2(0)$ is proportional to the complex conjugate of the input signal wave $A_1(0)$. The conjugate reflectance, given in Table 7, looks formally the same as in the DFWM case, except that it is scaled by the ratio of the wavelengths and refractive indices.

An even more interesting situation occurs when both input signal waves are zero. Note that when the pump intensities are sufficiently high so that $|\kappa L| = \pi/2$, Eqs. (59) and (60) predict infinite gains for the signal waves. This is the oscillation condition once again. This case thus corresponds to a third order mirrorless optical parametric oscillator. The feedback is provided by the counterpropagating coupled waves.

Optical phase conjugation. One of the most studied applications of DFWM is the correction of beam (phase) aberrations by phase conjugation. The properties of the phase conjugate wave that are exploited were described above. The probe beam, which passes through an aberrating medium, is incident on a phase conjugate mirror. The reflected phase conjugate wave passes back through the aberrating medium in the opposite direction. Since the phase is reversed on this wave, the aberrating medium then cleans up the phase aberrations. This is illustrated in Fig. 16.

The assumption of infinite plane waves and nondepleted pump waves gives the impression that the process of phase conjugation is exact. Actually, this is not the case, and several factors limit the quality, or fidelity, of the phase conjugation. Some of these are listed in Table 8. A discussion of these is beyond the scope of this book. They are adequately treated in the literature on optical phase conjugation [16].

The literature on other applications of optical phase conjugation is also extensive. The richness and diversity of these ideas is illustrated in Table 9. It should be noted that in some cases these ideas have been investigated utilizing the phase conjugation attributes of stimulated Brillouin scattering (see Chapter 15) rather than DFWM. However, the ideas are quite general and independent of the choice of nonlinear medium.

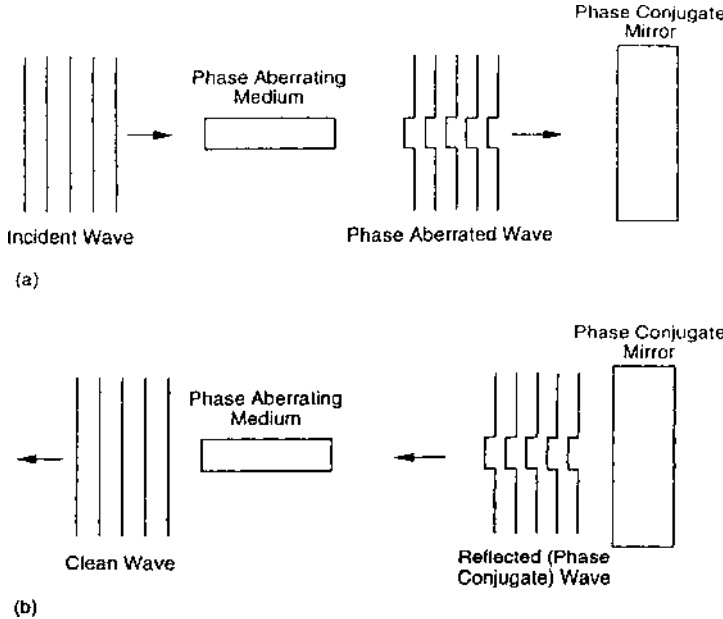


Figure 16 Illustration of aberrated phase cleanup by optical phase conjugation. (a) Phase aberrated wave incident on phase conjugate mirror. (b) Cleaned up phase aberrated wave reflected from phase conjugate mirror.

Table 8 Some Factors Affecting the Quality of Phase-Corrected Beam Aberrations by Optical Phase Conjugation [14]

Factor	Ref.
Limiting aperture (preventing some rays from reaching interaction region)	[62–64]
Nonexact retrace of conjugate beam through aberrating medium	[65]
Motion of aberrating medium	[14]
Nonlinear phase shifts	
Phase mismatch	[66]
Self-focusing/defocusing	[63,67]
Birefringence (ellipse rotation)	[68]
Phase aberration of pump beam(s)	[65,69,70]
Saturation	[63,71,72]

Table 9 Some Applications of Optical Phase Conjugation

Aberration compensation (phase, polarization)
Lensless imaging (high resolution photolithography)
Spatial information processing
Image addition, subtraction, differentiation (edge enhancement), integration
Spatial signal convolution and correlation
Intensity filtering
Logic and digital processing of binary signals
Coherent optical processing (using iterative algorithms)
Frequency filtering
Temporal signal processing
Pulse envelope shaping
Optical gating and time delay control
Pulse envelope time reversal
Temporal signal convolution and correlation
Pulse spreading compensation
Phase conjugate resonators
Photorefractive phase conjugators
Self-pumped
Mutually pumped
Phase conjugate Fabry–Perot interferometer (retroreflected intensity has same form as transmitted intensity for ordinary Fabry–Perot)
Phase conjugate Michelson interferometer (output intensity is always zero, retroreflection is phase conjugate of input; useful for parallel image subtraction)
Phase conjugate Sagnac interferometer (output intensity is zero for 50/50 beam splitter; useful for detecting nonreciprocal phase shift due to rotation of interferometer)
Phase conjugate Mach–Zehnder interferometer (useful for image subtraction)

C. Two-Beam Coupling

This phenomenon involves the interaction of two waves in a nonlinear medium with a nonreciprocal transfer of energy from one wave to the other. Photorefractive and Kerr media are considered.

Photorefractive media. Two beams are incident on a photorefractive crystal as illustrated in Fig. 17. They cross at an angle 2θ in the crystal. As described above in Section II.H, these beams write an index grating in the crystal that is phase shifted from the sinusoidal intensity pattern. The beams self-diffract from this grating by Bragg scattering. One beam is amplified, and the other is attenuated. The direction of energy flow depends on the phase of the grating and the orientation of the crystal.

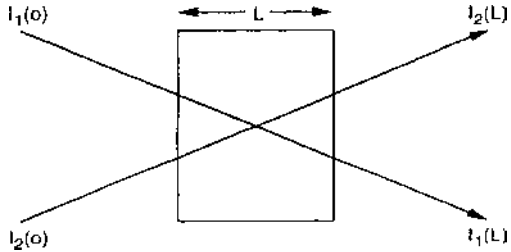


Figure 17 Two-beam coupling in a photorefractive medium.

For the configuration shown in Fig. 17, called codirectional beam coupling, the coupled wave equations are given by

$$\frac{dI_1}{dz} = -\gamma \frac{I_1 I_2}{I_1 + I_2} - \alpha I_1 \quad (62)$$

and

$$\frac{dI_2}{dz} = \gamma \frac{I_1 I_2}{I_1 + I_2} - \alpha I_2 \quad (63)$$

where α is the linear absorption coefficient, assumed to be the same for both beams, and γ is the photorefractive coupling coefficient. In terms of a sinusoidal dielectric grating with amplitude ϵ_1 [8], this coefficient is given by

$$\gamma = \frac{\pi}{n_0 \epsilon_0 \lambda \cos \theta} \hat{e}_1 \cdot \epsilon_1 \cdot \hat{e}_2 \quad (64)$$

where the components of the tensor grating amplitude are given by

$$(\epsilon_1)_{ij} \exp(i\varphi) = -2 \sum_k \epsilon_0 \mathbf{n}_i^2 \mathbf{n}_j^2 \mathbf{r}_{ijk} E_k^{sc} \quad (65)$$

The phase of the grating is φ , which is determined by the space charge field, of which E_k^{sc} is the k th component, and r_{ijk} is the component of the electrooptic tensor (Pockels coefficient). The direction of power flow is determined by the sign of γ , which can be reversed by rotating the crystal through 180° . For a space charge field that is determined by charge diffusion only, the phase is $\varphi = \pi/2$. The expression for the diffusion-controlled space charge field was given in Section II.H. Examples of the coupling coefficient for specific cases for crystals of point group symmetry 4mm (e.g., BaTiO₃ or strontium barium niobate [SBN]) and for cubic crystals are given in Table 10.

The solutions of Eqs. (62) and (63) for codirectional beam coupling in a photorefractive medium are given in Table 11 in terms of the input intensity ratio,

Table 10 Form of the Coupling Coefficient γ for Photorefractive Two-Beam Coupling for Two-Crystal Classes

<i>4mm (Plane of incidence = ac plane of crystal)</i>	
(1) Incident light polarized \perp plane of incidence (α = angle between K and <i>c</i> -axis)	$\gamma = -\frac{2\pi}{\lambda \cos \theta} (n^\circ)^3 r_{13} E^{\text{sc}} \cos \alpha$
(2) Incident light polarized \parallel plane of incidence (α = angle between K and <i>c</i> -axis)	$\gamma = -\frac{2\pi}{n\lambda \cos \theta} [\cos \theta_1 \cos \theta_2 (n^\circ)^4 r_{13} \cos \alpha + (n^\circ)^2 (n^\circ)^2 r_{42} \sin \alpha \sin 2\alpha + \sin \theta_1 \sin \theta_2 (n^\circ)^4 r_{33} \cos \alpha] E^{\text{sc}}$ $\theta_1 = 90^\circ + \theta - \alpha$ $\theta_2 = 90^\circ - \theta - \alpha$
<i>43m (Cubic crystals)</i>	
$\gamma = \frac{\pi}{\lambda} n^3 r_{41} E^{\text{sc}}$	

Table 11 Formulas Related to Two-Beam Coupling in Photorefractive and Kerr Media

<i>Photorefractive media (degenerate codirectional coupling)</i>	
$I_1(L) = I_1(0) \frac{1+m^{-1}}{1+m^{-1}e^{\gamma L}} e^{-\alpha L}$	
$I_2(L) = I_2(0) \frac{1+m}{1+me^{-\gamma L}} e^{-\alpha L}$	
$m = \frac{I_1(0)}{I_2(0)}$	
<i>Photorefractive media (degenerate contradirectional coupling)</i>	
$I_1(L) = I_1(0) \frac{1+m^{-1}}{1+m^{-1}e^{\gamma L}} e^{-\alpha L}$	
$I_2(0) = I_2(L) \frac{1+m}{1+me^{-\gamma L}} e^{-\alpha L}$	
$m = \frac{I_1(0)}{I_2(L)}$	
$\alpha \ll \gamma$	
<i>Kerr media (nondegenerate codirectional coupling)</i>	
$I_1(L) = I_1(0) \frac{1+m^{-1}}{1+m^{-1} \exp[(\gamma/\alpha)(1-e^{-\alpha L})]} e^{-\alpha L}$	
$I_2(L) = I_2(0) \frac{1+m}{1+m \exp[-(\gamma/\alpha)(1-e^{-\alpha L})]} e^{-\alpha L}$	
$m = \frac{I_1(0)}{I_2(0)}$	
$\gamma = \frac{2\pi}{\lambda \cos \theta} \frac{n_2^l}{[1+(\Omega\tau)^2]^{1/2}} [I_1(0) + I_2(0)] \sin \varphi$	
$\varphi = -\tan^{-1}(\Omega\tau)$	

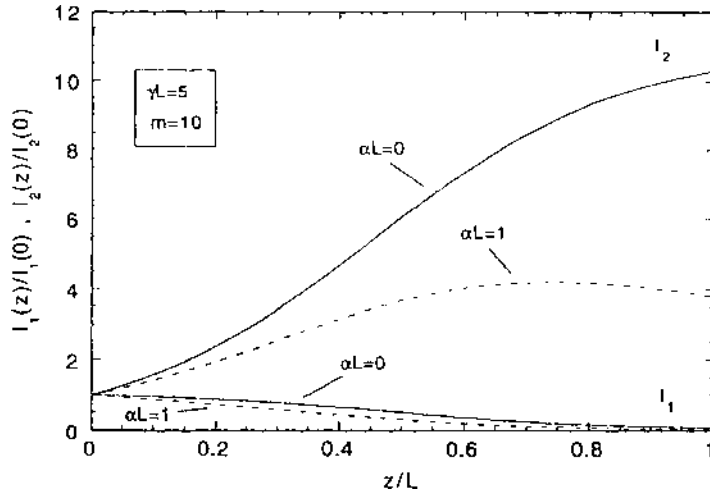


Figure 18 Intensities I_1 and I_2 as functions of z for two-beam coupling in a photorefractive medium.

$m = I_1(0)/I_2(0)$. The behavior of these solutions is shown in Fig. 18. Beam amplification requires that $\gamma > \alpha$. For large m , $I_2(z) \approx I_1(0)\exp[(\gamma - \alpha)z]$. The amplification of beam 2 is given by a gain factor G :

$$G = \frac{I_2(L)}{I_2(0)} = \frac{1 + m}{1 + m \exp(-\gamma L)} e^{-\alpha L} \quad (66)$$

In contradirectional beam coupling, the two beams are incident on the crystal from opposite directions. Both beams are assumed to make an angle θ with respect to the z -axis. The coupled equations are nearly identical to Eqs. (62) and (63), except for I_2 the signs of γ and α are reversed. These equations cannot be solved exactly except for $\alpha = 0$. However, provided that $\alpha \ll \gamma$, the resulting approximated solutions have the identical form as those for codirectional coupling [8]. It should be noted now that the two input waves are $I_1(0)$ and $I_2(L)$, and $m = I_1(0)/I_2(L)$. Defining transmittances $T_1 = I_1(0)/I_1(L)$ and $T_2 = I_2(L)/I_2(0)$, it is noted that $T_2 = T_1 \exp(\gamma L)$. Thus, for $\gamma L \gg 1$, beam 1 traveling to the right is strongly attenuated, and beam 2 traveling to the left is amplified. This nonreciprocal transmission has no analog in linear optics and has a potential application for a one-way viewing window.

When the beams are nondegenerate (i.e., $\omega_1 \neq \omega_2$), a traveling grating is produced with velocity $V = \Omega\Lambda/2\pi$, where Λ is the grating spacing and $\Omega = \omega_2 - \omega_1$. This causes an additional phase shift, with the net phase shift

given by

$$\varphi = \varphi_0 - \tan^{-1}(\Omega\tau) \quad (67)$$

where φ_0 is the phase shift for $\Omega = 0$ and τ is the response time of the photorefractive medium. For a diffusion controlled space charge field, the two-beam gain decreases as Ω increases. This is because φ is at the optimum value of $\pi/2$ for $\Omega = 0$. When an external field is applied to optimize the space charge field (and hence the index modulation), $\varphi_0 \neq \pi/2$. Thus in this case the nondegeneracy can be exploited to drive the phase shift to $\pi/2$ and enhance the gain.

In the situations described above, the input waves were assumed to have the same polarization. When this is not the case, an anisotropic two-wave mixing can occur that mixes waves of different polarization (cross-polarization coupling) [8]. However, this coupling is generally small in birefringent materials because the optical anisotropy creates different Bragg conditions for the two independent polarization states. Cross-polarization coupling can be significant however in cubic materials, such as GaAs. The faster photorefractive response in these materials makes this case of much interest. (See Ref. 8 for more details.)

Nondegenerate two-beam coupling in Kerr media. As mentioned above, the interference of two nondegenerate waves creates a traveling interference pattern. In a Kerr medium, this produces a traveling index grating through the nonlinear index of refraction. The index pattern for codirectional beam coupling can be written as

$$n = n_0 + \Delta n_0 + 2\{n'_2 e^{i\varphi} A_1^* A_2 \exp[i(\mathbf{K} \cdot \mathbf{r} - \Omega t)] + \text{c.c.}\} \quad (68)$$

where

$$|\mathbf{K}| = |\mathbf{k}_2 - \mathbf{k}_1| = \frac{2\pi}{\Lambda} \quad (69)$$

and Δn_0 is a uniform nonlinear index change. The phase φ indicates the degree to which the index grating is temporally delayed (spatially shifted) with respect to the interference pattern and is a result of the finite material response time τ . Assuming a steady-state model in which the grating is written instantaneously but decays with a time constant τ [17],

$$n'_2 e^{i\varphi} = \frac{n_2}{1 + i\Omega\tau} \quad (70)$$

and therefore

$$\varphi = -\tan^{-1}(\Omega\tau) = -\tan^{-1}\left(2\pi \frac{V\tau}{\Lambda}\right) \quad (71)$$

while $n_2' = n_2/(1 + \Omega^2\tau^2)^{1/2}$. Thus if the distance traveled by the grating in a time τ is large compared to Λ , then $\varphi \rightarrow -\pi/2$.

The solutions to the coupled wave equations are given in Table 11, where m is again the input intensity ratio. Notice the similarity to the solutions for two-beam coupling in a photorefractive medium. Hence again there is a nonreciprocal energy transfer from one wave to the other. The coupling coefficient in this case is given by

$$\gamma = \frac{2\pi}{\lambda \cos \theta} \frac{n_2'}{[1 + (\Omega\tau)^2]^{1/2}} [I_1(0) + I_2(0)] \sin \varphi \quad (72)$$

where λ is the mean wavelength. Notice in this case that the coupling coefficient depends on the total input intensity, unlike the photorefractive case, for which the coupling coefficient depends on the intensity ratio. Also note that the coupling is zero if $\varphi = 0$. Thus there is no energy transfer between the waves when the frequencies are degenerate, in which case there is no phase shift between the grating and the interference pattern.

In the lossless regime ($\alpha = 0$), the transmittances of the two beams are

$$T_1 = \frac{I_1(L)}{I_1(0)} = \frac{1 + m^{-1}}{1 + m^{-1} \exp(\gamma L)} \quad (73)$$

$$T_2 = \frac{I_2(L)}{I_2(0)} = \frac{1 + m}{1 + m \exp(-\gamma L)} \quad (74)$$

The behavior of these solutions is illustrated in Fig. 19. For $n_2 > 0$, the low-frequency wave will always see gain at the expense of the high-frequency wave.

As pointed out by Yeh [17], there is no cross-coupling of the phases in nondegenerate two-beam coupling in Kerr media. Thus a phase aberrated beam can be used to amplify a “clean” beam without introducing any phase distortions.

Two-beam coupling of chirped pulses in Kerr media. A particular case of nondegenerate two-beam coupling occurs in time-delayed two-beam experiments using chirped pulses. Pulses exhibiting linear frequency chirp have an instantaneous frequency given by $\omega(t) = \omega_0 + bt$, where ω_0 is the center frequency of the pulse and b is the linear chirp coefficient. For $b > 0$, the leading edge of such a pulse is red-shifted from the center frequency (obtained at the peak of the pulse) while the trailing edge is blue-shifted. Consequently, when one pulse is delayed in time relative to the other pulse, the instantaneous frequencies of the two pulses are nondegenerate where they overlap spatially. The coupling between two such pulses can be described by equations analogous to those given above, in terms of integrated pulse energy instead of instantaneous intensity, with the substitution $\Omega \rightarrow 2b\tau_d$, where τ_d is the delay time between the two pulses. As the delay time is swept from positive to negative values, the sign of the coupling coefficient changes sign. Thus, energy flows first from one pulse to the other, then

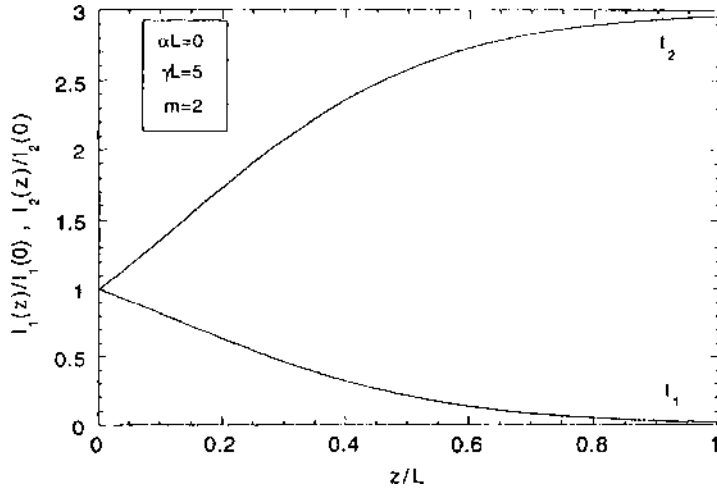


Figure 19 Intensities I_1 and I_2 as functions of z for nondegenerate two-beam coupling in a Kerr medium.

reverses as the delay between them is reversed. The energy flow is always from the high-frequency beam to the low-frequency beam as long as both $n_2 > 0$ and $b > 0$.

Applications. Several applications have been explored utilizing two-beam coupling. Some of these are listed in Table 12. Although most of these have exploited the large gain in photorefractive media, the flexible rejection filter has been investigated using Kerr media as well. Such a filter can be used for protecting optical sensors from high-intensity lasers. By using the codirectional

Table 12 Some Applications of Two-Beam Coupling

-
- Flexible rejection filter
 - “One way” window
 - Photorefractive resonators (self-adjusting phase)
 - Optical computing
 - Optical interconnects
 - Optical neural networks
 - Image amplification
 - Laser beam clean-up
 - Spatial light modulators
-

beam coupling described above, the filter selectively responds to coherent radiation by transferring the laser beam energy to a beam dump while the weak beam is directed to the sensor's detector. Since two-beam coupling is a coherent process, the filter does not respond to ordinary scene radiation which is broadband and incoherent. Other applications listed in Table 12 are more thoroughly discussed in the literature [8].

D. Optical Bistability

The first optical bistability experiments were performed using a Fabry–Perot interferometer with a nonlinear material situated between the two mirrors of the cavity [18]. Much of the interest in this phenomenon has centered around this nonlinear étalon.

A Fabry–Perot étalon is a narrow-band transmission filter. The spectral location of the transmission peak can be swept in frequency, or wavelength, by varying the optical path length between the cavity mirrors. This can be accomplished by varying the physical distance between the mirrors, or by varying the index of refraction of the medium between the mirrors. If the medium has an intensity dependent index of refraction, then light can be used to tune the cavity.

Steady-state optical bistability in a Fabry–Perot. The simplest Fabry–Perot consists of two partially transmitting mirrors separated by a distance L and filled with a dielectric material. The intensity of light I_t transmitted by this device for an incident intensity of I_i is given by

$$\frac{I_t}{I_i} = \frac{T^2}{T^2 + 4R \sin^2 \varphi / 2} \quad (75)$$

where T and R are the mirror transmittance and reflectance, respectively, and $\varphi = 4\pi nL/\lambda$. If $n = n_0 + n_2^l I_c$, where I_c is the internal cavity intensity, then this phase becomes intensity dependent. The cavity intensity is related simply to the device transmitted intensity by $I_t = TI_c$. Thus

$$\varphi = 4\pi n_0 \frac{L}{\lambda} + \frac{(4\pi L/\lambda)n_2^l}{T} I_t = \varphi_0 + 2aI_t \quad (76)$$

The equation for the transmitted light intensity from a nonlinear Fabry–Perot is shown in Table 13.

This solution for I_t is a transcendental equation and cannot be simplified. A graphical solution is illustrated in Fig. 20. The curve in this figure is the Fabry–Perot Airy function [19] and depends on I_t . The straight lines are of the form $y = I_t/I_i$, i.e., they have zero intercept and are parameterized by the slope I_i^{-1} . Thus a vertical line would correspond to $I_i = 0$, and as $I_i \rightarrow \infty$ the line becomes horizontal. The solution for any given I_i is the intersection of the straight line with

Table 13 Formulas Related to Optical Bistability

Nonlinear dispersive Fabry–Perot étalon (Kerr-like media)

Optical bistability

$$\frac{I_t}{I_i} = \frac{T^2}{T^2 + 4R\sin^2\left(\frac{1}{2}\varphi_0 + aI_t\right)}$$

$$I_i = I_t \left[1 + \frac{4R}{T^2} \sin^2\left(\frac{1}{2}\varphi_0 + aI_t\right) \right]$$

$$a = \frac{2\pi L n_2^l}{\lambda T}$$

Differential gain

$$\frac{dI_t}{dI_i} \approx \left[1 + 4a\left(\frac{R}{T}\right)^2 (2aI_t + \theta)I_t + \left(\frac{R}{T}\right)^2 (2aI_t + \theta)^2 \right]^{-1}$$

$$\left(\frac{dI_t}{dI_i} \right)_{\max} \approx \left[1 - \left(\frac{R}{T}\right)^2 \theta^2 / 3 \right]^{-1} \text{ at } I_t = -\theta/3a$$

Nonlinear dispersive distributed feedback system (Kerr-like media)

$$J_i = y_3(J_i) + \frac{y_3(J_t) - y_2(J_t)}{[y_1(J_t) - y_2(J_t)][y_1(J_t) - y_3(J_t)]^{-1} \operatorname{sn}^2(u, \gamma) - 1}$$

$$y_1 > y_2 > y_3 > y_4 = \text{roots of } Q(y) = 0, \text{ Eq. (80)}$$

$$u = 2[(y_1 - y_3)(y_2 - y_4)]^{1/2}$$

$$\gamma = \frac{(y_1 - y_2)(y_3 - y_4)}{(y_1 - y_3)(y_2 - y_4)}$$

$$y = I_f/I_c \quad J_i = I_i/I_c \quad J_c = I_t/I_c$$

$$I_c = \frac{2\epsilon_0 n_0^2 c \lambda}{3\pi n_2 L} = \frac{2n_0 \lambda}{3\pi n_2^l L}$$

Mixed absorptive and dispersive ring cavity (two-level system) (ℓ_{NL} = length of nonlinear medium in cavity)

$$I_i = I_t \left\{ \left[1 + \frac{\alpha_{00}\ell_{NL}}{2T} \frac{1}{1 + (T_2\Delta)^2 + I_t/TI_s^\Delta} \right]^2 \left[\frac{\alpha_{00}\ell_{NL}}{2T} \frac{T_2\Delta}{1 + (T_2\Delta)^2 + I_t/TI_s^\Delta} - \frac{\alpha R}{T} \right]^2 \right\}$$

the Airy function. Note that for some incident intensities, the output is multivalued for a single input intensity. When two of these states are stable, i.e., they settle into a nearby steady state when subjected to minor perturbations, the system is said to be bistable. The intensity regime of these states, if indeed two states rather than just one exist, depends on the original phase of the system at low intensities, i.e., on φ_0 .

For the situation depicted in Fig. 20, as the incident intensity increases, the output intensity increases only slightly (points a and b), since the filter is detuned

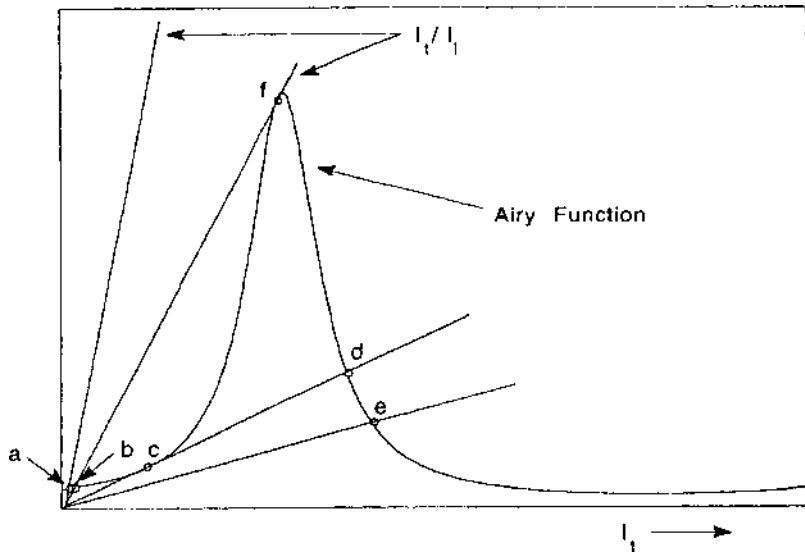


Figure 20 A graphical solution of intensity transmitted through a nonlinear Fabry–Perot étalon, illustrating optical bistability.

from resonance. At point c , a minor increase in I_t causes the output to jump to a high value. This is called optical switching. For further increases in I_t , the transmitted intensity increases only slightly. This is a power limiting region, since the increasing light intensity is tuning the filter away from resonance, decreasing its transmittance. As I_t is now decreased, the output remains high until the point f is reached. This is the region of bistability. Since the device has been put in a high transmittance state, the internal cavity intensity is high enough to keep it there over a limited range of input intensity. A minor drop of input intensity at point f causes the device to switch down to low transmittance. Thus as the incident intensity is ramped up and down, the device output traces out a hysteresis curve, which has come to be the signature of optical bistability.

It is also possible to obtain a graphical solution by plotting the equation in Table 13 as a function $I_t(I_i)$, with I_t as the independent variable, and then inverting the axes. This is illustrated in Fig. 21, where the solutions are given for various values of φ_0 . The three cases shown illustrate the three different operating conditions of the nonlinear Fabry–Perot: (a) power limiting, (b) differential gain, and (c) optical bistability. The negative slope region in Fig. 21c has been shown to be unstable [20]. Therefore the output makes discontinuous jumps at these turning points as discussed above.

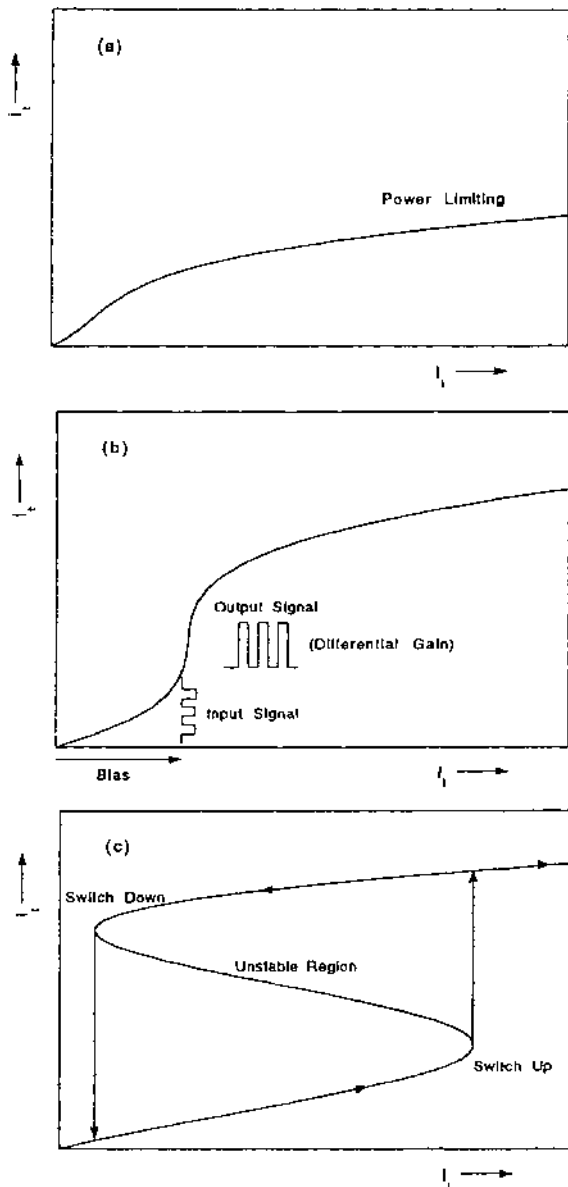


Figure 21 Transmitted intensity as a function of incident intensity for a nonlinear Fabry-Perot étalon for various detunings from resonance. (a) Power limiter; (b) optical transistor; and (c) optical switching and bistability.

The differential gain region has been proposed as an optical transistor. If the system is biased by a light beam so that the output is near the knee of this curve, then a small variation in this beam, or an input by another beam, will result in a relatively large output variation. This is illustrated in Fig. 21b.

Further insight into the differential gain and bistable regions can be obtained by an approximate analysis of the system when it is near resonance [18]. The relation between the input and output fields, E_i and E_t , for the Fabry–Perot is

$$E_i = \frac{1 - Re^{i\varphi}}{T} E_t \quad (77)$$

Take the phase to be $\varphi = 2M\pi + \theta + 2aI_t$, where M is an integer and $\theta + 2aI_t \ll 2M\pi$. Thus θ is the original detuning of the Fabry–Perot from resonance. Expanding the exponential in Eq. (77) to lowest order in θ , taking the derivative of this expression, and inverting yields the result for the differential gain dI_t/dI_i shown in Table 13. The differential gain will have the maximum value shown when the input intensity is such that $I_t = -\theta/3a$. This maximum gain will approach infinity as $(\theta R/T)^2 \rightarrow 3$. Thus the cavity detuning and finesse (i.e., mirror reflectance) set the conditions for the differential gain mode [$(\theta R/T)^2 \leq 3$] or the optical bistability mode [$(\theta R/T)^2 > 3$].

Optical bistability in distributed feedback systems. The minimum requirements for optical bistability are illustrated in the Fabry–Perot device: a nonlinear transmission with positive feedback. In a Fabry–Perot, the feedback is provided at two points: the cavity mirrors. In a Bragg filter, for example, a hologram, the feedback is distributed throughout the device. If the material is nonlinear, this type of system will also exhibit optical bistability as well as power limiting and differential gain [21].

In the steady-state analysis of the Fabry–Perot device, the cavity intensity was taken as a constant between the mirrors. Ignoring the spatial variation of the standing wave gives what is sometimes called the mean field approximation. Gibbs [20] discusses some of the effects of standing waves. However, the mean field approximation is adequate to analyze the main properties of the device.

For a distributed feedback (DFB) device, standing wave effects are still ignored. The envelope of the internal intensity is, however, not spatially uniform in these types of systems. This spatial nonuniformity cannot be ignored, so the analysis is somewhat more involved [21].

The index distribution for a nonlinear DFB device is taken to be

$$n(z) = n_0 + n_1 \cos 2Kz + 2n_2 |E(z)|^2 \quad (78)$$

where $n_1 \ll n_0$ is the amplitude of an index grating with a grating spacing of $\Lambda = \pi/K$. A coupling coefficient $\kappa = \pi n_1/\lambda$ and phase mismatch $\Delta k = k - K$ are defined, where κ couples forward and backward traveling waves of wave

vector $k = n_0\omega/c$ in the DFB device. Thus the total complex field amplitude is taken to consist of forward and backward propagating waves:

$$E(z) = A_f(z)e^{ikz} + A_b(z)e^{-ikz} \quad (79)$$

These forms for the field and index of refraction are substituted into the wave equation and result in two coupled first order differential equations for the forward and backward waves in the slowly varying amplitude approximation. These can be solved exactly, and the solution for the transmitted intensity $I_t = I_f(L)$ is given in Table 13 in terms of normalized intensities.

The normalization is in terms of a characteristic intensity

$$I_c = \frac{2\epsilon_0 n_0^2 c \lambda}{3\pi n_2 L} = \frac{2n_0 \lambda}{3\pi n_2' L} \quad (80)$$

which sets the intensity scale for nonlinear operation. The parameters $y_1 > y_2 > y_3 > y_4$ are roots of a fourth order polynomial $Q(y)$,

$$Q(y) = (y - J_t)[(\kappa L)^2 y - (y - J_t)(\Delta k L + 2y)^2] \quad (81)$$

where $y = I_f/I_c$, and are thus functions of the normalized transmitted intensity J_t . The solution $J_i(J_t)$ is given in terms of a Jacobi elliptic sine function, which was introduced in Chapter 2.

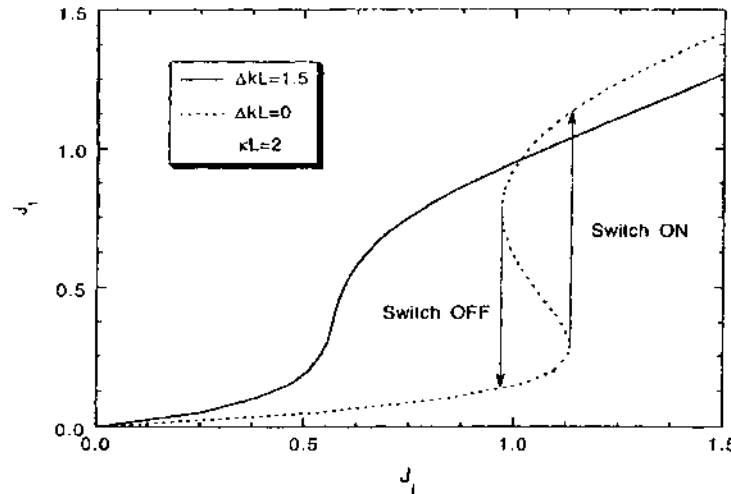


Figure 22 Transmitted intensity as a function of incident intensity of nonlinear distributed feedback device (Bragg reflector), illustrating optical bistability.

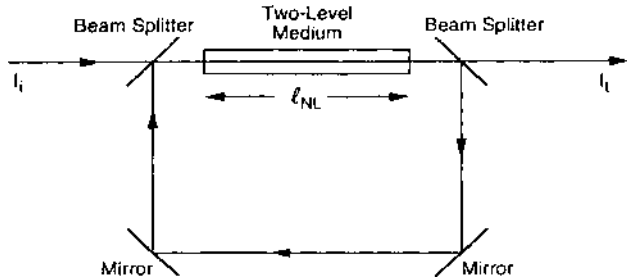


Figure 23 Ring cavity optically bistable device.

The behavior of these solutions is shown in the plot of Fig. 22. Negative slope regions are again unstable. The parameters determining regions of differential gain and optical bistability are now κL and $\Delta k L$, which correspond to R and θ for the Fabry–Perot. Note that although the Bragg filter is a narrow band *reflection* filter, while the Fabry–Perot is a narrow band *transmission* filter, both can exhibit optical bistability. The key features are nonlinear transmission and positive feedback.

Mean field model of a ring cavity filled with a two-level system. Bonifacio and Lugiato [22] considered a nonlinear ring cavity as illustrated in Fig. 23, where the nonlinear medium is a two-level system (e.g., sodium vapor near resonance). Using the terms defined for two-level systems in Section II.E, the solution $I_l(I_t)$ to the analysis of this ring cavity system, which avoids standing-wave effects, is given in Table 13. This solution is for a homogeneously broadened two-level system. To include inhomogeneous broadening (e.g., Doppler broadening), the line shape should be integrated over a suitable distribution function (see Ref. 20).

The ring cavity/two-level medium forms a mixed bistable system. The first term in the solution $I_l(I_t)$ corresponds to that of a pure absorptive bistable system when $\Delta = \theta = 0$, where θ was defined above for a pure dispersive bistable system (no nonlinear absorption). The properties of saturable absorption are discussed further in Chapter 9. The second term corresponds to a pure dispersive bistable system when $T_2 \Delta \gg 1$. The first observations of optical bistability were performed with atomic sodium vapor in a Fabry–Perot with the dispersive part dominating [18]. The behavior of the solutions for this model are illustrated in Fig. 24.

Other approaches. Since the initial studies of a nonlinear Fabry–Perot with a two-level atomic vapor, several systems have been demonstrated to exhibit optical bistability. Some of these are listed in Table 14. Nonlinearities exploited include population redistribution in gases and semiconductors (both band filling and exciton saturation effects), Kerr nonlinearities in liquids, electrostrictive

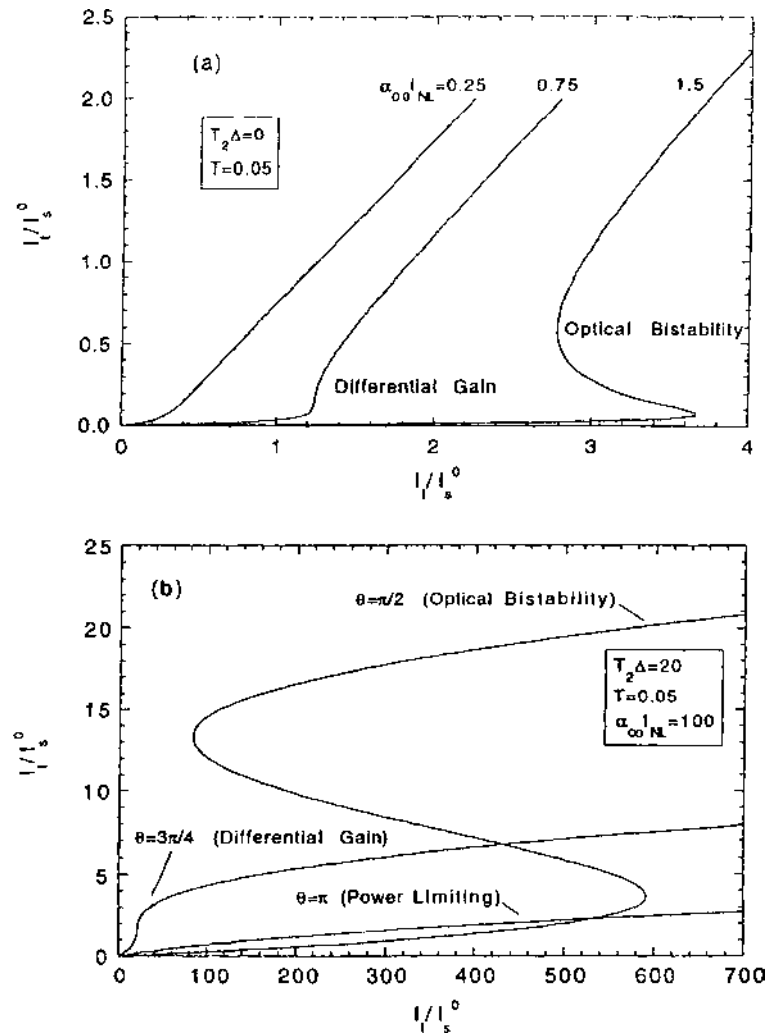


Figure 24 Transmitted vs. incident intensity for a two-level system in a ring cavity. (a) Pure absorptive system and (b) mixed absorptive and dispersive system.

effects in particle suspensions, thermal nonlinearities, electrooptic effects in solids and liquid crystals, as well as magnetooptic and acoustooptic effects. These latter devices are hybrid in the sense that the positive feedback is not obtained directly from the transmitted light but rather indirectly through an electronic signal proportional to the transmitted intensity. Several different

Table 14 Additional Optical Bistable Devices

Device	Ref.
Semiconductor étalons	
GaAs	[73–75]
GaAs–GaAlAs multiple quantum well	[76]
InSb	[77]
ZnS/ZnSe interference filters (thermal effects)	[78–80]
Color filters, dyes (Fabry–Perot)	[74,80–82]
Self-trapping, self-lensing, self-bending	[83–85]
Others not strictly related to n_2	[20]
Hybrid devices (electronic feedback)	
Pockels cell Fabry–Perot	[86–89]
Pockels cell polarization modulator	[90,91]
Pockels cell Mach–Zehnder interferometer	[92]
Pockels cell Michelson interferometer	[93]
Magneto-optic modulator	[94]
Acousto-optic modulator	[95]
Electro-optic scattering	[96]

optical phenomena have been exploited, including interference, polarization rotation, focusing, and scattering. Again, the key features are a nonlinear transmission as a function of some control variable proportional to the transmitted light intensity, and positive feedback to the system.

Transient effects. The above discussion summarizes the steady-state operation of optical bistable systems. Transient effects can arise when the system is pumped by a pulsed light source, or when pumped by a cw source and instabilities set in. A few of these effects are cited below.

Bischofberger and Shen [23] studied the effects of a nonlinear Fabry–Perot containing a Kerr medium when pumped with a pulsed laser. They examined these effects theoretically and experimentally in the power limiting, differential gain, and optical bistability regions. The effects observed depend on relations between three fundamental time constants: the round-trip cavity time for light $t_R = 2nL/c$, the response time of the nonlinearity in the medium τ_M , and the pulse width τ_p of the laser.

The basic results of the analysis of these transient effects can be summarized as follows. For $t_R \ll \tau_p \ll \tau_M$, there is a “bistability” in all regions (power limiting, differential gain, and optical bistability), but no sharp switching as the pulse ramps up and then down. This is illustrated in Fig. 25. Basically, the system response lags the optical pulse as it propagates through, and there is not enough time for a quasi-steady state to form. When $\tau_M \ll t_R \ll \tau_p$, quasi-steady

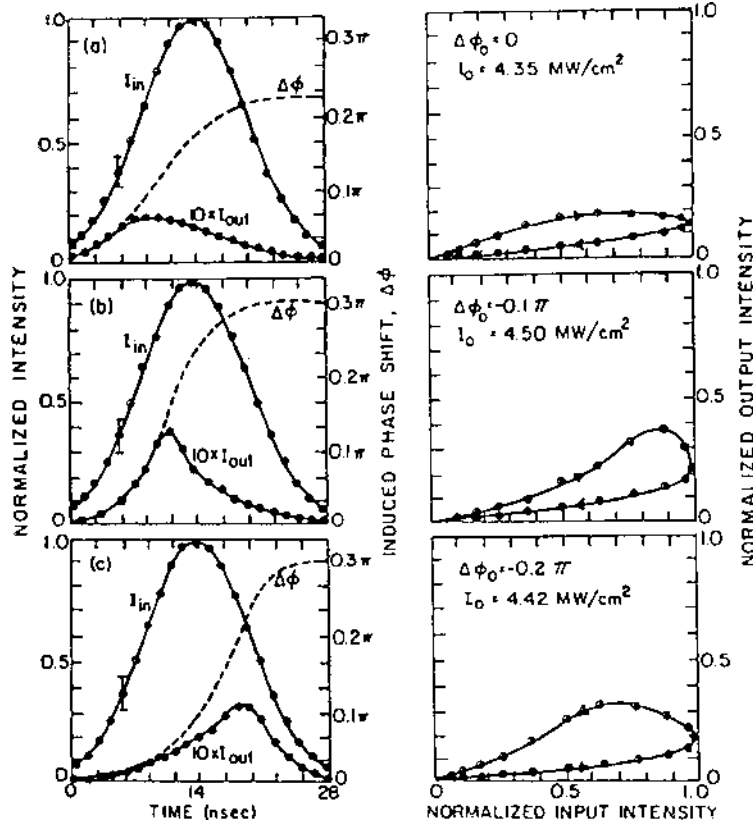


Figure 25 Transient effects in a nonlinear Fabry-Perot for $t_R \ll \tau_p \ll \tau_M$ [$t_R = 0.11$ ns, $\tau_p = 14$ ns, $\tau_M = 145$ ns (liquid crystal MBBA)]. (From Ref. 23.)

state regions of power limiting, differential gain, and optical bistability can be observed. However, in the switch up region of the bistable curve, there is overshoot and ringing. These effects are illustrated in Fig. 26. Optical switching is more effective (i.e., sharper) in cavities with high finesse, but the over-shoot and ringing are more evident [23].

Gibbs [20] reviews some of the literature covering other aspects of transient behavior associated with optical switching. This includes pulse shortening and pulse reshaping effects.

Optical bistability has some aspects that parallel those of phase transitions, such as abrupt switching and hysteresis. Another is a phenomenon called critical slowing down, first predicted by Bonifacio and Lugiato [24]. This refers to

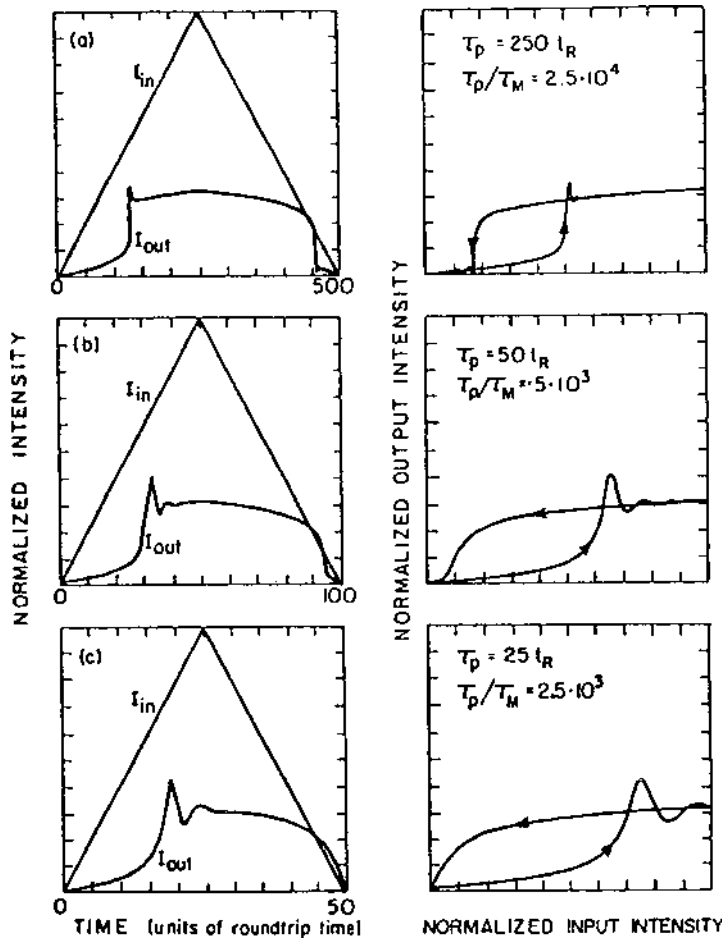


Figure 26 Computer simulations of transient effects in the switching and optical bistability behavior of a nonlinear Fabry-Perot for $\tau_M \ll t_R \ll \tau_p$ ($\tau_M = 0.01t_R$). (From Ref. 23.)

the power or intensity required to switch a bistable device ON, and the time it takes for the device to assume this ON state. Basically, if the input intensity is much larger than the switch ON intensity corresponding to the steady state, the system responds quickly, limited only by intrinsic time restraints such as the cavity build-up time in a Fabry-Perot. However, if the input intensity is only slightly greater than the steady-state switch ON value, the system response slows down. The switch ON time actually diverges as the input intensity approaches

the steady-state switch ON value from above. This is called critical slowing down and has been observed experimentally in a hybrid system by Garmire et al. [25], in an absorptive bistable system by Grant and Kimble [26], and in a thermal dispersive system (interference filter) by Karpushko and Sinitsyn [27].

The above discussion relates transient effects to the results of pulsed inputs. Transient effects also arise due to intrinsic instabilities of the system when the input is cw. One such effect is evident when there are two nonlinear contributions to the system response of differing sign and differing time constants [28]. An example would be a slightly absorbing material that exhibits a fast, positive Kerr response and a slow, negative thermal response. In such a system, biased for optical bistability, as the cw beam is turned on, the system finds itself in the ON state after a short transient response. The high transmission state produces absorption with a slowly responding thermal effect. The opposite sign of this nonlinearity causes the operating point on the optical bistability curve to drift, and the device eventually switches OFF. The resulting low transmission allows the device to cool and reset the optical bistability operating point. When this occurs, the fast Kerr nonlinearity causes the device to switch ON again, and the entire sequence recurs. The result is regenerative pulsations in the output for a steady cw input (i.e., the system functions as a relaxation oscillator). The period of oscillations depends on the time constants involved. Gibbs [20] discusses several other cases.

Another type of instability, called the Ikeda instability [29], can set in for cw inputs with $t_R \gg \tau_M$. In this case, the nonlinear response of the medium adiabatically follows the field. The instability sets in at high intensities in the bistable region. Although Ikeda first explored this instability theoretically for dispersive optically bistable systems in cavities, the results are perfectly general to all bistable systems and were first studied experimentally in a hybrid optical bistable system [30]. This system consisted of a Pockels cell based polarization modulator with electronic feedback proportional to the output intensity, but deliberately delayed electronically to satisfy the condition $t_R \gg \tau_M$, where now t_R refers to the feedback time of the device.

The Ikeda instability can be understood as follows. The device is assumed to be in a high transmission state. As the incident intensity is increased above some threshold, it reaches a value at which it would switch to a low transmission in the steady state. However, since the feedback is slow, light does not see this state until after a delay time t_R when the transmission switches to a low value. Since the transmission is now low, the intensity is not sufficient to keep it in this state. But since the feedback is not instantaneous, the transmission is kept low for a time t_R before it switches high again. The situation is now as it started, and the process continues. The result is that the output intensity oscillates with a period $2t_R$ even though the input is cw.

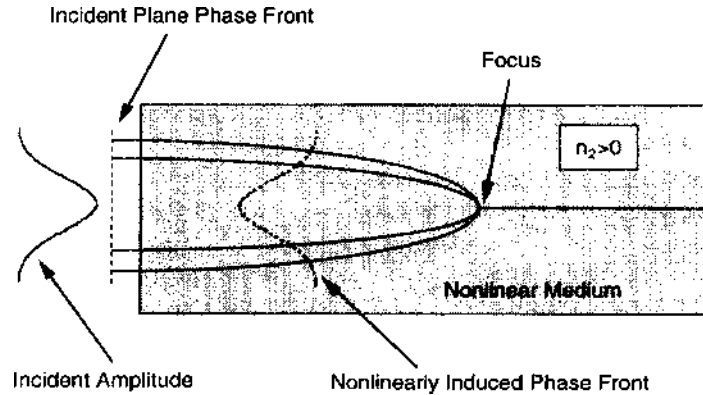


Figure 27 Self-focusing of a nonuniform beam of light in a nonlinear medium.

At a higher input intensity, another instability sets in, which produces a slightly modified oscillation pattern with a period of $4t_R$. As the system is driven even harder, the time required for the waveform to reproduce itself continues to double. So, at each bifurcation, the period doubles in the sequence $2t_R, 4t_R, 8t_R, 16t_R, \dots$, etc. This period doubling rapidly leads to a situation where the waveform does not repeat itself at all. This is called optical chaos. It is a phenomenon in which a completely deterministic nonlinear system exhibits apparently random behavior. Optical chaos has generated considerable interest since its behavior corresponds to phenomena in quite different systems, e.g., turbulence in fluids, fluctuations in population growth, chaotic behavior in financial markets, and apparent random behavior in biological systems.

E. Self-Focusing

Self-focusing occurs when a light beam of nonuniform intensity falls on a medium with a nonlinear index of refraction. As illustrated in Fig. 27, since the nonlinear index follows the shape of the beam (for local effects without saturation), an index gradient is induced in the medium. For a positive nonlinearity, this means that a greater index, and hence larger phase retardation, is induced on-axis than in the wings of the beam. This has the effect of creating a positive lens that tends to focus the beam.

Thin media. A wave with a plane phase front and a Gaussian amplitude distribution incident on a thin nonlinear medium will induce an index modulation

Table 15 Formulas Related to Self-Focusing in Kerr-Like Media*Thin nonlinear medium*

Nonlinear lens focal length for incident Gaussian beam with planar phase front (paraxial approximation)

$$f = \frac{n_0 w^2}{4n_2^I I_0 L}$$

Field distribution at far field point z' due to thin nonlinear medium at point z of Gaussian beam ($\Delta z = z' - z$)

$$\begin{aligned} E(z', r, t) &= E(z, 0, t) \sum_{m=0}^{\infty} \frac{[i\Delta\varphi(z, t)]^m}{m!} \frac{w_{m0}}{w_m} \exp\left(-\frac{r^2}{w_m^2} + i\frac{kr^2}{2R_m} + i\theta_m\right) \\ \Delta\varphi(z, t) &= \frac{(2\pi/\lambda)n_2^I I_0(t)}{1 + (z/z_R)^2} \\ w_{m0}^2 &= \frac{w^2(z)}{2m+1} \\ w_m^2 &= w_{m0}^2 \left[g^2 + \left(\frac{\Delta z}{\Delta z_m}\right)^2 \right] \\ g &= 1 + \frac{\Delta z}{z[1 + (z_R/z)^2]} \\ \Delta z_m &= kw_{m0}^2/2 \\ R_m &= \Delta z \left[1 - \frac{g}{g^2 + (\Delta z/\Delta z_m)^2} \right]^{-1} \\ \theta_m &= \tan^{-1} \left[\frac{(\Delta z/\Delta z_m)}{g} \right] \end{aligned}$$

Thick nonlinear medium

Critical power for self-trapping ($n_2 > 0$)

$$\mathcal{P}_{cr2} = \frac{(1.22\lambda)^2 \pi \epsilon_0 c}{32n_2} \quad (\text{SI}) \quad \mathcal{P}_{cr2} = \frac{(1.22\lambda)^2 c}{128n_2} \quad (\text{cgs})$$

Paraxial approximation of critical power for catastrophic self-focusing ($n_2 > 0$)

$$\mathcal{P}_{cr1} = \frac{\epsilon_0 c \lambda^2}{8\pi n_2} \quad (\text{SI}) \quad \mathcal{P}_{cr1} = \frac{c \lambda^2}{32\pi^2 n_2} \quad (\text{cgs})$$

Self-focusing distance (beam collapse) in paraxial approximation

$$\text{Plane wave front } z_{f\infty} = \frac{\pi w_0^2 / \lambda}{[(\mathcal{P}/\mathcal{P}_{cr1}) - 1]^{1/2}}$$

$$\text{Curved wave front } (R = \text{radius of curvature}) \quad z_f = \frac{R}{(R/z_{f\infty}) - 1}$$

(continued)

Table 15 Continued

Whole beam self-focusing critical powers
“Weak” focus
$\mathcal{P}_1 \approx \mathcal{P}_{\text{cr1}}$
Collapsed beam
$\mathcal{P}_2 \approx \mathcal{P}_{\text{cr2}}$
Whole beam self-focusing distance (beam collapse)
$z_{f\infty} = \frac{0.369\pi w_0^2/\lambda}{(\mathcal{P}/\mathcal{P}_2)^{1/2} - 0.858}$

given by

$$n = n_0 + n_2^I I_0 \exp\left(\frac{-2r^2}{w^2}\right) \quad (82)$$

where I_0 is the on-axis intensity. For distances not too far from the axis (paraxial approximation), the exponential can be expanded to lowest order:

$$n \approx n_0 \left(1 - \frac{2n_2^I I_0 r^2}{n_0 w^2}\right) \quad (83)$$

It can be shown [31] that a medium with a parabolic index profile like that in Eq. (83) will cause an incident plane wave to come to a focus. In the thin lens approximation appropriate to the assumption of a thin medium, the nonlinear focal length of this medium is given by the expression shown in Table 15. Note that the focal length decreases in magnitude with increasing on-axis intensity. Also, the lens is converging if $n_2^I > 0$, and diverging if $n_2^I < 0$, as expected.

If the incident beam has a finite phase curvature, then the above formulas will be less accurate. In general, a phase shift is impressed on the beam given by (for a TEM₀₀ Gaussian beam)

$$\Delta\phi(z, r, t) = \frac{(2\pi/\lambda)n_2^I I_0(t)L}{1 + (z/z_R)^2} \exp\left[\frac{-2r^2}{w^2(z)}\right] \equiv \Delta\phi(z, t) \exp\left[\frac{-2r^2}{w^2(z)}\right] \quad (84)$$

where $w(z)$ is the z dependent beam radius, z_R is the Rayleigh range, $I_0(t)$ is the time dependent on-axis intensity, and $z = 0$ is taken at the beam waist. The field that is then propagated to a new position z' , with $\Delta z = z' - z$, is given by the set of equations in Table 15. If the phase distortion is weak, then only a few terms in the infinite sum need to be retained to calculate the resulting field amplitude and phase distribution. This set of equations is the starting point for Z-scan analysis [32], which is a measurement technique for characterizing n_2^I (see Chapter 7).

Thick media ($n_2 > 0$). In thick media, the beam can actually come to focus within the medium. This can have a significant impact on the material as well as on the beam.

A simple analysis can be performed on a cw beam with a top-hat profile. The beam induces a waveguide (i.e., focusing exactly balances diffraction) at a critical power. An expression for this power, called $\mathcal{P}_{\text{cr}2}$, is given in Table 15. This is often referred to as self-trapping. Self-trapping is power dependent rather than intensity dependent since, for a given beam power, both diffraction and self-focusing are beam area dependent and tend to offset one another for $n_2' > 0$.

When the beam has a Gaussian profile, the analysis is not so simple. However, for distances not too far from the axis, a paraxial approximation can again be employed. A critical power for self-trapping (focusing balancing diffraction) can again be found, given by the expression for $\mathcal{P}_{\text{cr}1}$ shown in Table 15. Note the similarity between the two critical powers, but $\mathcal{P}_{\text{cr}1} < \mathcal{P}_{\text{cr}2}$.

For $\mathcal{P} > \mathcal{P}_{\text{cr}2}$, the beam will catastrophically focus (shrink to zero cross section) within the medium if the medium is sufficiently thick. Within the paraxial approximation, this focusing distance can be calculated, and for an incident plane wave it is shown by the expression for $z_{\text{f}\infty}$ in Table 15. (The subscript ∞ implies that the wave incident on the medium has an infinite radius of curvature.) Note that as $\mathcal{P} \rightarrow \mathcal{P}_{\text{cr}1}$, the focal distance approaches infinity in agreement with the condition of self-trapping.

If the phase of the incident wave has a finite radius of curvature R , then the corresponding focal distance is given by the expression for z_f given in Table 15 within the paraxial approximation. The convention is taken that $R < 0$ implies that the incident wave is converging, while $R > 0$ implies that it is diverging. Thus a converging (diverging) wave will collapse to a focus at a distance $z < z_{\text{f}\infty}$ ($z > z_{\text{f}\infty}$).

Dawes and Marburger [33] have conducted a numerical analysis of whole-beam self-focusing for Gaussian beams. They find that the phenomenon is characterized by two critical powers. The first, which they call \mathcal{P}_1 , is just $\mathcal{P}_{\text{cr}1}$ determined in the paraxial approximation. The second, called \mathcal{P}_2 , differs numerically by only about 1% from $\mathcal{P}_{\text{cr}2}$ determined from the top-hat beam self-trapping analysis. For incident optical power in the range $\mathcal{P}_1 < \mathcal{P} < \mathcal{P}_2$, the on-axis intensity rises as the beam comes to a “weak” focus and then falls off as the beam diffracts. When $\mathcal{P} > \mathcal{P}_2$, the beam catastrophically collapses. The focal distance for an incident plane wave is given approximately by the expression for $z_{\text{f}\infty}$ in Table 15, which applies to whole-beam self-focusing.

It should be noted that the beam collapsing to zero dimension is a mathematical concept. Physically, this does not happen. Instead, as the beam collapses, the intensity becomes so large that other nonlinear processes are triggered. This includes such phenomena as stimulated Raman scattering, dielectric breakdown, plasma formation, and permanent laser damage (if the medium is a solid). These processes rob energy from the beam and may severely distort its phase as well. This prevents the beam from further collapsing.

Self-focusing can also lead to a phenomenon known as filamentation, in which the beam becomes unstable and breaks into several tiny filaments. This occurs for beams that do not have a smooth spatial variation. Actually, this is true for nearly all beams, since a microscopic distortion of dimension Λ can become unstable if the beam power is high enough. Indeed, if the power contained within a cylinder of this dimension (residing within the beam) exceeds P_2 , that part of the beam will begin to collapse and break into a filament. This sets a critical size on the original distortion given by $\Lambda_c = (4P_2/\pi I_0)^{1/2}$ for filamentation, where I_0 is the mean peak intensity of the whole beam.

When self-focusing occurs in a two-level system, a cw beam can actually collapse to a finite diameter and then propagate as a self-trapped beam. This is because as the beam intensity increases, the nonlinear index eventually saturates and cannot increase any further even if the intensity increases. Hence this acts as an internal damping mechanism, and the beam settles into a steady state with a constant diameter.

Beam collapse followed by self-trapping also *appears* to happen with nanosecond pulse propagation in a nonsaturable Kerr medium. As pointed out by Shen [3], however, what appears to be self-trapping is actually the locus of moving foci in the medium due to quasi-steady-state self-focusing. As illustrated in Fig. 28, some point on the incident pulse comes to focus first. Earlier points on the pulse have longer self-focusing distances and hence come to focus farther away and at later times. Points closer to the peak of the pulse have a shorter self-focusing distance, but arrive later than the original point. Thus the original focus appears to split into two, one part moving forward in the beam, and the other

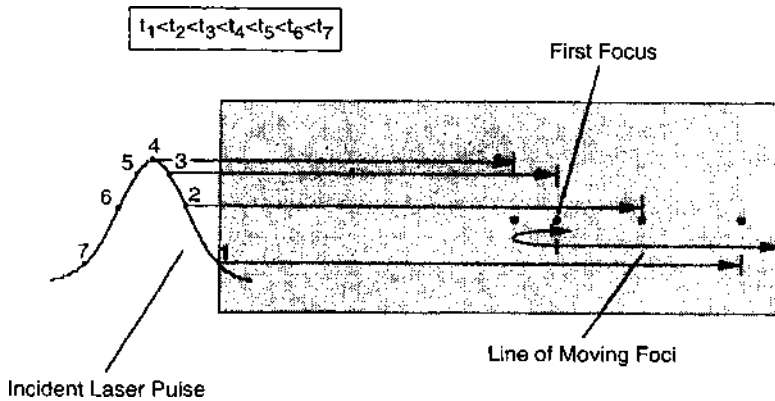


Figure 28 Schematic illustration of the track of moving foci in quasi-cw self-focusing of pulsed light.

moving backward. Eventually, the backward moving focus turns around and moves forward as points later in the pulse with longer self-focusing distances come to focus. To the eye, the moving foci appear as a continuous line, or as a self-trapped beam. As Shen has noted [3], at the turning point where the backward moving focus changes direction, the focus spends the greatest amount of time. This is the point where laser damage is likely to occur.

Thick media ($n_2 < 0$). For thick media with negative nonlinearities, the beam will not collapse but rather will diverge due to the negative lens effect. For most cases, when the temperature increases the index will decrease. Thus in a medium that absorbs part of a Gaussian beam, the index on axis is smaller than that in the wings, and the beam thus diverges. This is called thermal blooming.

Negative nonlinearities can also occur in resonant systems. For example, in a two-level system when the frequency is tuned below resonance, the index of refraction decreases due to saturation. Hence in a two-level gas, beam collapse can only be seen when the frequency is tuned to a frequency greater than the resonance frequency. In semiconductors the index coefficient is often negative, for absorption near the band edge, or for exciton saturation, or in some cases for two-photon absorption. These cases will lead to a defocusing similar to thermal blooming.

Applications. Often, self-focusing is undesirable, since it may lead to laser damage. There have been some device applications, however. The most common is optical limiting. This is illustrated in Fig. 29 for both positive and negative nonlinearities. The nonlinear medium is situated between two lenses. Low-intensity light is collected by the second lens and imaged through an aperture to a detector. High-intensity light will produce self-focusing. For $n_2 > 0$, this will result in beam collapse and phase distortion such that the light is not focused by the second lens but defocused in the aperture plane. Thus the power transmitted by the aperture to the detector is limited, and the detector is thus protected from the high-intensity radiation. Such an optical limiter has been constructed using materials like CS_2 [34]. In the negative n_2 case, the beam diverges more rapidly from the intermediate focus rather than collapsing. The result at the aperture plane is, however, the same: a defocused beam. The advantage of this type of limiter over the previous example is that it is self-protecting (i.e., the light is defocused inside the medium leading to lower intensity there that is less likely to cause laser damage). This is important when the medium is solid and the damage would be permanent. Such a limiter has been demonstrated for picosecond pulses using ZnSe as the nonlinear medium [35]. For limiting against cw and nanosecond pulses, thermal blooming in solutions with a small amount of absorbing dye has been demonstrated [36]. For such a limiter, a solvent with a high thermooptic coefficient and low heat capacity is the best choice.

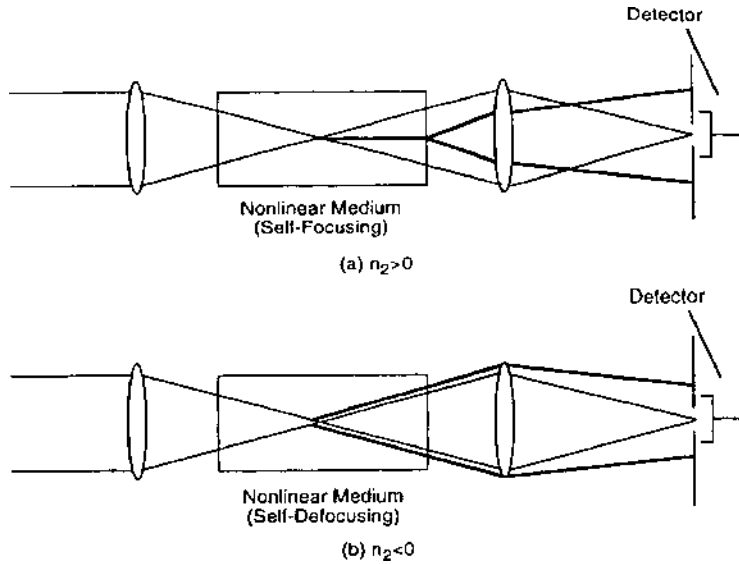


Figure 29 Optical limiters based on self-focusing. (a) $n_2 > 0$ and (b) $n_2 < 0$.

F. Beam Bending and Fanning

Other self-action effects observed with optical beams include self-bending (Kerr media) and beam fanning (photorefractive media). The self-bending in Kerr media is due to half-beam effects. In photorefractive media, whole-beam effects contribute to fanning.

Self-bending in Kerr media. In these effects, a beam block obscures half of the beam incident on a Kerr medium. For a slab beam (of infinite extent in the y -direction) with a right triangular profile in the x -direction [$I(x) = I_0(1 - x/w_0)$] that propagates in the z -direction through a thin medium, a prism is induced in the medium, which deflects the beam. The angle of deflection θ_{NL} measured in the far field is given by

$$\frac{\theta_{NL}}{\theta_d} = -\frac{\pi n_2^l I_0 L}{\lambda} \quad (85)$$

where $\theta_d = \lambda/\pi w_0$ is the far field diffraction angle of the beam. The direction of the deflected beam is to the opposite side of the axis on which the semitriangular beam is incident for $n_2^l > 0$ (positive prism). It turns out that the self-deflection angle for a slab semi-Gaussian beam is approximately equal to that given by this

equation. For a three-dimensional semi-Gaussian beam, this equation is still a fairly good approximation [37].

If the Kerr medium is thin and transparent, and the incident beam is a three-dimensional semi-Gaussian beam, then the on-axis far-field intensity is described by the relation

$$I_{\text{on-axis}} \propto \frac{\lambda w_0^4}{2\pi n_2^l L} [C^2(\Theta) + S^2(\Theta)] \quad (86)$$

where $\Theta = (4n_2^l I_0 L / \lambda)^{1/2}$. $C(\Theta)$ and $S(\Theta)$ are the Fresnel integral functions given by

$$C(\Theta) = \frac{1}{\sqrt{2\pi}} \int_0^{\Theta^2} \frac{\cos u}{\sqrt{u}} du \quad (87)$$

$$S(\Theta) = \frac{1}{\sqrt{2\pi}} \int_0^{\Theta^2} \frac{\sin u}{\sqrt{u}} du$$

Beam fanning in photorefractive media. When a single beam is incident on a photorefractive medium at some angle with respect to the *c*-axis of the crystal, a set of beams fans out asymmetrically from the main beam in the direction of the *c*-axis. This phenomenon is a whole-beam effect, not a semibeam effect as described above, and is illustrated in Fig. 30.

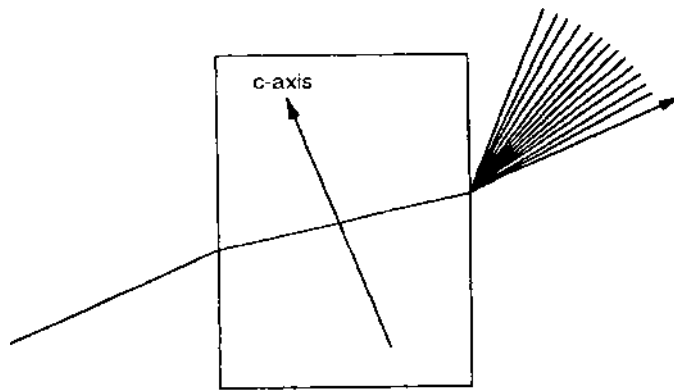


Figure 30 Schematic illustration of beam-fanning in a photorefractive medium.

Two theories have been put forth to explain this phenomenon. One, due to Feinberg [38], is a single-beam, deterministic, defocusing process. The other is a random scattering, multiple two-wave mixing process.

In the first theory, a Gaussian beam illuminates the crystal. This creates free carriers, as described above in Section II.H, which are transported by diffusion and subsequently trapped in the wings of the beam. This symmetric charge distribution leads to an asymmetric space charge field:

$$\mathbf{E}_{sc}(x, y) = \frac{-4k_B T(x\hat{x} + y\hat{y})}{e\pi w_0^2} \exp\left[-2\left(\frac{x^2 + y^2}{w_0^2}\right)\right] \quad (88)$$

\mathbf{E}_{sc} produces an asymmetric refractive index profile via the Pockels effect, which creates a prism in the material. This causes the beam to be deflected asymmetrically.

Because of the tensor nature of the electrooptic effect, the beam fanning can be stronger in one dimension than in another (i.e., the fanned beam can be in the form of a sheet). The strength of the fanning can also be a function of the incident polarization.

The above analysis is valid for a thin sample and has been extended to thick media by Banerjee and Liu [39]. This model gives reasonable agreement with some experimental data and is probably accurate as one source of beam fanning in photorefractive media.

Fanning has also been hypothesized as a two-beam coupling phenomenon accompanied by weak wave amplification [40,41], where the weak wave arises due to random scattering of the incident beam from surface or volume imperfections, charge density fluctuations, etc. Some aspects of this model have been confirmed experimentally by Zhang et al. [42].

The scattered wave travels out in a different direction from the incident beam. Since the two waves are coherent, they interfere and write a photorefractive grating in the usual manner. The two waves are coupled due to the phase shift of the grating with respect the interference pattern that recorded it. Waves scattered in the direction of the *c*-axis are amplified. As the scattered beam grows from noise, the modulation depth of the grating increases, which causes the two-beam coupling gain to increase. After many scattering events, a broad fan of beams develops and robs energy from the main beam.

Segev et al. [43] have extended the photorefractive two-beam coupling analysis presented earlier to the pair-wise coupling of *N* beams. The coupling coefficients depend on the angle between the beams and the *c*-axis as well as r_{eff} for the propagation direction, crystal orientation, and polarization. Noise is added in their model phenomenologically. The system of equations (sometimes for > 20 waves) is solved numerically, and the results show good agreement with several

beam fanning experiments [43]. This model has also been extended to describe the temporal evolution of beam fanning [44].

Applications. Beam fanning is sometimes detrimental, and some techniques have been developed to suppress it [45]. However, it can be used to advantage in some applications. A self-fanned beam that undergoes total internal reflection at the corner of the photorefractive crystal will propagate in the proper direction to achieve four-wave mixing with only one input beam. This leads to the concept of a self-pumped phase conjugate mirror [46]. Another application is the coherent beam excisor. Only coherent light will fan out, so this process discriminates coherent light from an incoherent background. The fanning is asymmetric and for large two-beam coupling gains can direct most of the energy in a coherent beam in one direction to a beam dump. This excises the beam and creates an optical power limiter for protection of sensitive optical sensors from harmfully high laser intensity [46].

Optical limiting by beam self-bending in Kerr media has also been discussed [47]. In this case, however, half of the incident beam must be masked to produce the asymmetry necessary for self-bending.

G. Nonlinear Phase Modulation and Solitons

Self-phase modulation (SPM). When an intense optical pulse propagates through a nonlinear medium, it gains an additional phase due to the nonlinear index of refraction. This was seen above in the optical Kerr effect, four-wave mixing, etc. If the intensity is time dependent (i.e., a short pulse), then the self-induced phase is also time dependent. For an ultrashort pulse with a center frequency ω_0 , the nonlinear phase shift is written as

$$\varphi_{NL}(t) = -\frac{\omega_0}{c} n_2^I I(t) L \quad (89)$$

The negative sign is inserted for convenience. If the material exhibits absorption at the wavelength of interest, then let $L \rightarrow L_{eff} = (1 - e^{-\alpha L})/\alpha$.

If the pulse envelope is slowly varying, an instantaneous frequency shift can be introduced by $\omega(t)t = [\omega_0 + \delta\omega(t)]t$, where $\delta\omega(t) = d\varphi_{NL}/dt$. The leading edge of the pulse has a negative slope, the peak has a zero slope, and the trailing edge of the pulse has a positive slope. Thus, the frequency shift near the peak of the pulse is zero. The leading edge is red-shifted while the trailing edge is blue-shifted. This is illustrated in Fig. 31.

Note that since $\varphi_{NL}(t)$ follows the pulse, φ_{max} occurs at the peak of the pulse. We can write $\varphi_{max} = \gamma \mathcal{P}_0 L_{eff} = L_{eff}/L_{NL}$, where $\gamma = \omega_0 n_2^I / c A_{eff}$. \mathcal{P}_0 is the peak power of the pulse, and A_{eff} is an effective area; for a Gaussian beam it would be $\pi w^2/2$, and for a guided wave it would be the effective mode area given

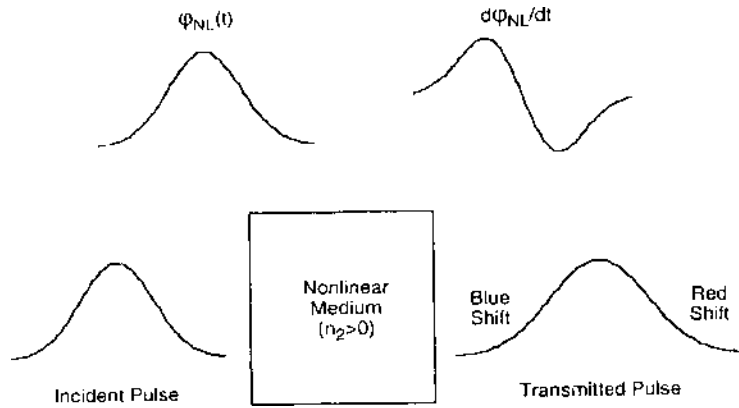


Figure 31 Self-phase modulation and frequency shifts in a nonlinear medium irradiated with a short optical pulse.

by

$$A_{eff} = \frac{\left[\int \int |a(x, y)|^2 dx dy \right]^2}{\int \int |a(x, y)|^4 dx dy}$$

where $a(x, y)$ is the normalized mode distribution across the waveguide. $L_{NL} = (\gamma P_0)^{-1}$ is the effective propagation distance for which $\phi_{max} = 1$ radian.

If the pulse has a rise and fall time of τ_0 , then the maximum frequency shift is $\delta\omega_{max} \approx \Delta\phi_{max}/\tau_0$ and $\Delta\phi_{max}$ corresponds to the difference between the peak and valley in the frequency plot of Fig. 31. Self-phase modulation becomes important when $\Delta\phi_{max} \geq 2\pi$. For example, for radiation of mean wavelength $1 \mu\text{m}$ propagating through a medium of length 1 cm with $n_2^l \sim 10^{-14} \text{ cm}^2/\text{W}$, this would require a peak intensity of $> 10 \text{ GW/cm}^2$. This is not unreasonable for picosecond and sub-picosecond pulses.

The instantaneous frequency shift $\delta\omega(t)$ implies that there is a frequency chirp impressed upon the pulse that increases with L_{eff} . A self-modulated pulse will have a broadened spectrum of frequencies. The spectrum is given by the Fourier transform of the phase-modulated pulse and the extent of spectral broadening depends on the shape of the pulse. A Gaussian pulse, for example, with intensity time dependence $\exp[-(t/\tau_0)^2]$, would experience a frequency chirp given by

$$\delta\omega(t) = \frac{2t}{\tau_0^2 L_{NL}} \exp[-(t/\tau_0)^2]. \quad (90)$$

Note that the chirp has the same sign as n_2^l and is approximately linear over the central region of the pulse. For nearly square (super Gaussian) pulses, the chirp is considerably larger near the leading and trailing edges of the pulse and approximately zero over the central pulse region.

As \mathcal{P}_0 increases, the broadened pulse eventually displays an oscillatory structure in the frequency domain, with a number of peaks that is nearly proportional to φ_{\max} . Qualitatively, this is due to constructive and destructive interference of different points in the pulse that have the same chirp but different phase. Note that SPM can enhance or decrease chirp that is already present in the pulse.

If the medium through which the pulse passes has normal group velocity dispersion (GVD), then the pulse will also spread out in time. This is true regardless of SPM, but the nonlinear interaction increases the effect. To analyze these effects, a unitless parameter is introduced:

$$N^2 = \frac{\gamma \mathcal{P}_0 \tau_0^2}{|k_2|} = \frac{L_D}{L_{NL}} \quad (91)$$

where

$$k_2 = \left(\frac{d^2 k}{d \omega^2} \right)_{\omega_0} \quad (92)$$

is the group velocity dispersion coefficient, and $L_D = \tau_0^2 / |k_2|$ is the dispersion length over which pulse spreading by GVD becomes significant. SPM can enhance pulse broadening due to GVD ($k_2 > 0$, normal dispersion) or inhibit it ($k_2 < 0$, anomalous dispersion). In the latter case, a Gaussian-shaped pulse initially broadens and then evolves into a sech^2 pulse, characteristic of the fundamental soliton (see below).

For $N \ll 1$ SPM dominates, but can enhance GVD effects because of the frequency chirp impressed on the pulse. In regions of normal GVD, a nearly rectangular pulse can be formed with an approximately linear chirp across the pulse. The pulse develops fine structure (oscillations) near its edges because of GVD. This is called optical wave breaking. For $k_2 > 0$, red-shifted light travels faster and catches up with blue light. The two different frequency components are coherent and interfere, creating oscillations. This process can be understood as four-wave mixing: fields at frequencies ω_1 and ω_2 interact via the third order polarization and create waves at new frequencies $2\omega_1 - \omega_2$ and $2\omega_2 - \omega_1$ in the pulse wings. Side lobes show up in the pulse frequency spectrum.

Additional phenomena appear for ultrashort pulses in the highly nonlinear regime. One of these is an effect called self-steepening. This involves higher order dispersion and depends on the first derivative $\partial P_{NL} / \partial t$ of the nonlinear polarization, which is usually ignored for most other process discussed in this

book. An intensity dependent group velocity is introduced, which causes the peak of the pulse to travel slower than the pulse wings. This pushes the peak toward the trailing edge of the pulse.

SPM effects can be deleterious in some circumstances. For example, in high-speed optical data transmission pulse broadening can produce a smearing out of individual bits, leading to higher bit error rates. However, in certain cases SPM can be put to advantage.

One application of self-phase modulation is super continuum generation [48]. This is useful for transient time-resolved spectroscopy. In such an experiment, an intense ultrashort pulse is split into two parts. One is incident on the sample under study and excites it by absorption. The other pulse is focused into a transparent nonlinear medium, such as a heavy water mixture or ethylene glycol. The output is frequency broadened over a wide spectral range (as much as $>100\text{ nm}$), but remains as a relatively short pulse. This output pulse is time-delayed relative to the pump pulse that excited the sample, and probes the resulting transmission of the sample. The transmitted pulse is then dispersed by a grating and recorded, for example with a CCD camera. The result is a complete excited state absorption spectrum obtained in a single laser shot. The dynamics of the excited state can then be monitored by repeating the experiment as a function of delay time between the pump and super continuum probe pulses.

Cross-phase modulation. When two or more waves interact in a third order medium, the phase of one wave can be modulated by the intensity of the other wave(s). This is called cross-phase modulation (XPM). The interacting waves can be of different frequencies, or of the same frequency but orthogonal polarization. The latter effect was treated previously under the Kerr effect or polarization ellipse rotation. Here, the effects of nondegeneracy and propagation in a medium that has a linear birefringence are discussed.

When the dominant contribution to the third order polarization in a centrosymmetric medium is electronic in origin, the three independent components of the third order susceptibility are nearly equal. Under these conditions, XPM induces an index modulation of the two orthogonal components (E_x, E_y) of an input wave, given by

$$\Delta n_x = 2n_2(|E_x|^2 + \frac{2}{3}|E_y|^2) \quad (93)$$

$$\Delta n_y = 2n_2(|E_y|^2 + \frac{2}{3}|E_x|^2)$$

Consider propagation in a uniaxial medium. If the polarization of the input wave is close to the direction of the fast axis (smaller index), then the nonlinear contribution to the birefringence decreases the net birefringence relative to

the intrinsic value. As the input power is increased, it is possible for the nonlinear birefringence to cancel the intrinsic birefringence or even change the sign of the net birefringence. Thus large changes to the output polarization state (and large changes in intensity transmitted through a polarizer) are possible for small changes in input power or input polarization state. This is called polarization instability. It occurs when the input peak power is large enough to make $L_{NL} \sim L_B$, where $L_B = 2\pi/\Delta k = 2\pi/(k_{slow} - k_{fast})$ is called the intrinsic polarization beat length. A critical power \mathcal{P}_c is defined at which the effective beat length goes to infinity, and is given by

$$\mathcal{P}_c = \frac{3}{2} \frac{\Delta k}{\gamma} \quad (94)$$

For small fluctuations about \mathcal{P}_c the effective beat length can change dramatically. This instability can lead to chaotic output polarization if the intrinsic birefringence is periodically modulated. Such modulation can occur, for example, in an optical fiber during fabrication by rocking the preform or periodically inducing stress.

Now consider the interaction of two waves of the same polarization but at different frequencies. For cw beams or sufficiently long pulses, the steady-state form of the complex wave amplitudes exhibits a constant magnitude (meaning no energy transfer between the waves), but a nonlinear phase, which is given by

$$\begin{aligned} \varphi_{NL1} &= \frac{\omega_1 n_2^I}{c} (I_1 + 2I_2)L \\ \varphi_{NL2} &= \frac{\omega_2 n_2^I}{c} (I_2 + 2I_1)L \end{aligned} \quad (95)$$

The accumulated phase in each beam depends on the intensity in both beams. It turns out, however, that this steady state can be unstable with respect to weak, time dependent perturbations. Under certain conditions, weak perturbations can experience exponential gain as the wave propagates leading to substantial changes in the magnitude of the wave amplitude. This effect is called modulation instability.

Analysis of these perturbations requires the time dependent wave equation for an ultrashort pulse, including the effects of GVD. The necessary condition for modulation instability can be written as

$$(\Omega_1^2/\Omega_{c1}^2 \pm 1)(\Omega_2^2/\Omega_{c2}^2 \pm 1) < 4 \quad (96)$$

where Ω_j ($j = 1, 2$) are the frequencies of the perturbations (typically in the THz regime) on each wave, the \pm sign corresponds to whether

the corresponding GVD coefficient is positive or negative, and

$$\Omega_{cj} = \sqrt{\frac{4\gamma_j \mathcal{P}_j}{|k_{2j}|}} \quad (97)$$

Over the range of frequencies satisfying the relation in Eq. (96), perturbations will experience a power dependent gain. If the perturbations are purposefully launched as weak probe beams at frequencies Ω_1 and Ω_2 , then the cw or long pulses will exhibit temporal modulations with period $2\pi/\Omega_j$. This can be considered a nondegenerate four-wave mixing process with gain, as discussed in Section III.B, with XPM providing the phase matching. The perturbations can also originate from spontaneous emission or thermally generated photons. In this case, perturbations at frequencies that correspond to maxima in the gain spectrum will build up most rapidly.

Finally, notice that the effects of both SPM and XPM will be present simultaneously when more than one wave is present. For ultrashort pulses this can lead to increased spectral broadening over that due to SPM alone, as well as asymmetric spectral broadening and asymmetric temporal changes to a symmetric input pulse.

Solitons. A steady-state optical wave that undergoes self-phase modulation while propagating in a medium with anomalous group velocity dispersion is unstable when subject to small perturbations [49]. The wave breaks into a string of periodic pulses. This is modulation instability as described above, except in the case of SPM it only occurs in the region of anomalous GVD. The growth of such instability by SPM is not possible under normal GVD, and thus waves in this regime are stable against weak perturbations.

In the negative group velocity dispersion region (e.g., for wavelengths $> 1.3 \mu\text{m}$ in fused silica optical fibers), there exists a condition where the propagation of a single short pulse is very stable. In fact, the pulse will propagate with constant shape and amplitude over essentially unlimited distance, limited only by linear adsorption in the medium. Such a pulse is called an optical soliton.

The nonlinear wave equation for an optical pulse propagating in the z -direction is shown in Table 16. The second derivative with respect to time of the slowly varying amplitude is included for group velocity dispersion effects. The time variable is written in terms of the retarded time $\tau = t - z/v_g$, where v_g is the group velocity of the pulse. This equation is often called the nonlinear Schrödinger equation.

A solution admitted by this equation is the fundamental soliton solution given in Table 16, where $t_{\text{FWHM}} = 1.76\tau_0$ is the width of the input pulse. This hyperbolic secant pulse will propagate without spreading or diminishing in amplitude provided the amplitude and phase are given by the expressions in

Table 16 Formulas Related to Optical Solitons

<i>Optical solitons</i>	
Nonlinear Schrödinger equation	
$\frac{\partial A}{\partial z} + \frac{i}{2} k_2 \frac{\partial^2 A}{\partial \tau^2} = i \frac{2\omega_0 n_2}{c} A ^2 A$	
$k_2 = \left(\frac{d^2 k}{d\omega^2} \right)_{\omega_0} = \left(-\frac{1}{v_g^2} \frac{dv_s}{d\omega} \right)_{\omega_0}$	
$\tau = t - z/v_g$	
Fundamental soliton solution	
$A(z, \tau) = A_0 \operatorname{sech}(\tau/\tau_0) \exp(i\kappa z)$	
$ A_0 ^2 = -\frac{k_2}{\gamma \tau_0^2} = -\frac{k_2 c}{2n_2 \omega_0 \tau_0^2}$	
$\kappa = -\frac{k_2}{2\tau_0^2}$	
<i>Spatial solitons</i>	
Nonlinear Schrödinger equation	
$\frac{\partial A}{\partial z} - \frac{i}{2k} \frac{\partial^2 A}{\partial x^2} = i \frac{2n_2 k}{n_0} A ^2 A$	
Fundamental spatial soliton solution	
$A(x, z) = A_0 \operatorname{sech}(x/w) \exp(i\kappa z)$	
$ A_0 ^2 = \frac{n_0}{2n_2} \left(\frac{1}{kw} \right)^2$	
$\kappa = \frac{1}{kw^2}$	

the table. Note that this means that k_2 and n_2 must have opposite signs. Thus, for a positive nonlinearity (e.g., the electronic third order nonlinearity in a glass fiber), this requires operation in the negative GVD region.

If the input intensity is slightly higher than needed for the fundamental soliton, then the pulse will shed some energy and eventually settle into the fundamental soliton. Thus, these pulses are very robust. At significantly higher intensities, higher order solitons can appear [49]. The input pulse will asymptotically approach the form of the n th order soliton, where n is the integer part of N , given by Eq. (91). The n th order solitons, for $n > 1$, change shape as they propagate, but recover to their original shape within a soliton period given

by

$$z_0 = \frac{\pi\tau_0^2}{2|k_2|} = 0.322 \frac{\pi t_{FWHM}^2}{2|k_2|} \quad (98)$$

The solitons described above are called bright solitons and have been observed experimentally [50]. They are the result of the interplay between self-phase modulation and anomalous group velocity dispersion. Interaction between self-phase modulation and *normal* group velocity dispersion ($k_2 > 0$) can lead to a phenomenon known as dark solitons. This is a pulse with a hole in the center that does not change shape as it propagates. The fundamental dark soliton takes the form $A(z, \tau) = A_0 \tanh(\tau/\tau_0) \exp(ikz)$. These have also been observed experimentally [51,52].

Spatial solitons. The nonlinear wave equation for a cw beam that varies rapidly in one space dimension (e.g., in a slab waveguide), such that its second order spatial derivative cannot be ignored, has the exact same form as the nonlinear Schrödinger equation introduced above. It follows that this wave equation admits the fundamental soliton solution given in Table 16, where w is the radius of the incident hyperbolic secant beam. This beam propagates in the nonlinear medium without spreading by diffraction (i.e., it is self-guided). This is reminiscent of the self-trapping described under Section III.E. However, the spatial soliton is stable with respect to minor perturbations.

Analogous to optical solitons (pulses) both bright and dark spatial solitons have been studied [53,54]. The generation of dark spatial solitons requires that a π -step phase or amplitude step be impressed on the input beam. The use of a spatial soliton to guide another beam has also been explored [55–57].

Early studies of the total reflection of a Gaussian beam from an interface between a linear medium and a nonlinear medium indicated that a spatial soliton could be propagated into the nonlinear medium for certain intensities [58]. These ideas have now been explored for propagation in a linear slab waveguide that is bounded on one side by a linear substrate and on the other side by a nonlinear cladding. For a positive nonlinearity, it has been determined that spatial solitons can be emitted into the nonlinear cladding where they propagate away from the waveguide [59–61]. Above a critical threshold intensity, the mode switches from a stable guided mode to a cladding mode. The soliton radiates away into the cladding, leaving a diminished guided mode in the waveguide. For increased incident intensity, there exist several thresholds for the emission of 1,2,3,... solitons, which shed energy from the guided mode.

Several applications based on soliton emission have been suggested [59]. These include optical limiting of the guided mode as excess energy is propagated into the cladding by the emitted solitons. Fast angular scanning of beams has also been proposed since the solitons propagate away from the waveguide at angles

that are intensity dependent. It also appears possible that coupling an emitted soliton into another nearby waveguide can form the basis for optical switches. Optical logic gates based on light intensity may then be constructed.

H. Nonlinear Optics in Fibers

Nonlinear optical effects are particularly efficient in optical fibers despite the relatively small nonlinear refractive index coefficient ($n_2 = 2.3 \times 10^{-22} \text{ m}^2/\text{V}^2$ or $n_2^I = 3.2 \times 10^{-16} \text{ cm}^2/\text{W}$ for silica fibers). The reason for this is that the spot size of radiation propagated in a single mode fiber is small ($\sim 2\text{--}4 \mu\text{m}$), this small spot size is maintained over a long interaction length by waveguiding, and the loss of optical fibers due to absorption and scattering can be quite small. The product IL_{eff} for a fiber can be $\sim 10^7\text{--}10^9$ times that in the same material in bulk form [49]. The primary reason is that for a correspondingly small spot size in the bulk material, diffraction severely limits the interaction length.

The phenomena discussed above (SPM, XPM, and solitons) are all quite efficient in optical fibers and have been studied extensively. Several other phenomena and applications have also been investigated. Agrawal [49] has devoted an entire book to the subject. Here two applications involving the nonlinear optics of ultrashort pulses in fibers are described.

Pulse compression. The principle of optical pulse compression is to pass a chirped pulse through a dispersive delay line. For a positive chirp pulse (i.e., blue-shifted frequencies in the trailing edge of the pulse), a negative GVD is required. As such a pulse travels in this medium, the red components in the leading edge of the pulse are delayed with respect to the blue components in the trailing edge. This slowing down of the front edge of the pulse compared to the end of the pulse causes the pulse to be compressed.

One of the most common pulse compressors is comprised of a fiber-grating pair. The fiber provides a positive, nearly linear chirp on the pulse through the combined effects of SPM and GVD. The diffraction grating pair provides an effective medium with negative GVD that is required to compress the positive chirp pulse. Light incident on the first grating is diffracted to the second grating, which then diffracts the light to the output. Because of the dispersive properties of the gratings, blue light travels a shorter distance and catches up with the red light, resulting in a compressed pulse. One drawback of this configuration is that due to the angular dispersion of wavelengths from a grating, the beam spreads spatially in one dimension. To overcome this, it is common to reflect the light from the second grating back through the compressor and pick off the compressed pulse with a beam splitter. This double-pass configuration mitigates the beam spreading and provides additional compression. The reflecting mirror is slightly tilted to avoid sending the pulse back through the fiber.

Fiber-grating pair compressors have yielded optical pulses with a width of a few femtoseconds. The detailed theory of their operation has been worked through numerical simulations. The objective of the compressor is to obtain a large compression factor in a high quality pulse, where nearly all of the pulse energy is maintained within the compressed pulse. This requires optimization of the fiber length to obtain the proper balance of SPM and GVD. Numerical simulations have shown that an optimum fiber length is given approximately by $(6L_DL_{NL})^{1/2}$ (i.e., approximately the geometric mean of the dispersion length and nonlinear length associated with the fiber).

Solitons in optical communications. One of the most important potential applications of optical solitons is high-speed data transmission in optical fibers. Short pulses that travel a long distance in fibers (several km) broaden due to group velocity dispersion and/or self-phase modulation. This limits the speed (bits/second) of data transmission since eventually the pulses spread into one another and can no longer be resolved. Solitons do not spread and hence can theoretically travel longer distances and/or have shorter widths for increased data transmission speed.

To preserve the soliton character of the pulses, a balance between the nonlinear and dispersive effects of the fiber must be maintained (i.e., the peak power of the pulses must be sustained). Therefore, optical loss in the fiber, although low, causes the width of the fundamental soliton to increase with the distance propagated. Numerical simulations show that over long distances ($>> L_D$) the broadening is nearly linear with distance, though smaller than that in a linear medium. To provide data transmission over long distance (~ 1000 km), without the use of electronic repeaters, soliton schemes require repeater amplifiers to periodically boost the optical power and reshape the pulse.

Ideally, a pulse is launched in a soliton-based communication system with no chirp. In practice this is difficult to achieve. An initial chirp superimposed on the SPM induced chirp disturbs the balance between SPM and GVD needed for soliton propagation. Although solitons are stable for a weak initial chirp, some pulse energy is shed. Above a critical chirp value (dependent on the soliton order), the soliton can be destroyed.

The nonlinearity that provides the basis for soliton production also leads to interaction between solitons separated by small intervals of time. A soliton pair (separated by a time interval determined by the bit rate), launched with zero relative phase and equal amplitude, tend to attract one another. They will periodically collapse into a single soliton. If the relative phase of the pair is $\pi/4$, they will repel each other and become more separated in time as they propagate. Stable transmission can be achieved if soliton pairs are launched with unequal amplitudes.

The trend in fiber optic communications is to multiplex several channels at different wavelengths. This is known as wavelength division multiplexing

(WDM). To fully utilize the available bandwidth of the fiber, several densely spaced (in wavelength) signals will be propagated over a single fiber at the same time. Soliton propagation requires a small but finite dispersion. It is difficult to fabricate fibers that maintain this small dispersion value over the whole bandwidth of the fiber, however, it is not difficult to make a composite fiber with alternating sections of positive and negative GVD.

As a pulse enters the first section of such a fiber, it broadens and becomes chirped in one direction. Upon entering the second section, the opposite sign of the GVD produces an opposite chirp, causing the pulse to compress and become unchirped. Propagating further, the pulse once again broadens and becomes chirped in the opposite sense. It then enters the third fiber section where the opposite dispersion once again counteracts the effects of the previous section. In this manner, a stable soliton forms and "breathes" periodically, oscillating between large and narrow pulse width. The repeat length of the fibers of alternating GVD is usually the same as the spacing between erbium optical amplifiers—about 80 to 100 km.

These solitons are called dispersion-managed solitons. Dispersion-managed solitons are Gaussian shaped pulses whose shape is preserved as they propagate. Gaussian pulses have a much faster decay in the wings of the pulse than the hyperbolic-secant shaped pulses. There may thus be less interaction between neighboring soliton pairs, allowing the possibility of higher bit rates.

REFERENCES

1. R. W. Boyd, *Nonlinear Optics*, Academic Press, New York, 1992.
2. P. N. Prasad and D. J. Williams, *Introduction to Nonlinear Optical Effects in Molecules and Polymers*, John Wiley, New York, 1991.
3. Y. R. Shen, *The Principles of Nonlinear Optics*, John Wiley, New York, 1984.
4. P. G. de Gennes, Short range order effects in the isotropic phase of nematics and cholesterics, *Mol. Cryst. Liq. Cryst.* 12:193 (1971).
5. I. C. Khoo and S.-T. Wu, *Optics and Nonlinear Optics of Liquid Crystals*, World Scientific, Singapore, 1993.
6. P. N. Butcher and D. Cotter, *The Elements of Nonlinear Optics*, Cambridge Univ. Press, New York, 1990.
7. A. Ashkin, G. D. Boyd, J. M. Dziedzic, R. G. Smith, A. A. Ballman, J. J. Levin-stein, and K. Nassau, Optically induced refractive index inhomogeneities in LiNbO_3 and LiTaO_3 , *Appl. Phys. Lett.* 9:72 (1966).
8. P. Yeh, *Introduction to Photorefractive Nonlinear Optics*, John Wiley, New York, 1993.
9. D. M. Pepper and A. Yariv, Optical phase conjugation using three-wave and four-wave mixing via elastic photon scattering in transparent media, *Optical Phase Conjugation* (R. A. Fisher, ed), Academic Press, New York, 1983, pp. 24–78.

10. R. K. Jain and M. B. Klein, Degenerate four-wave mixing in semiconductors, *Optical Phase Conjugation* (R. A. Fisher, ed), Academic Press, New York, 1983, pp. 307–416.
11. C. Moloney and W. Blau, Resonant third-order hyperpolarizabilities of large organic molecules, *J. Opt. Soc. Am. B* 4:1035 (1987).
12. K. J. McEwan and K. J. Harrison, Polarization and material dependence of degenerate four-wave mixing transients in molecular fluids, *Mol. Phys.* 69:1025 (1990).
13. P. A. Fleitz, R. L. Sutherland, L. V. Natarajan, T. Pottenger, and N. C. Fernelius, Effects of two-photon absorption on degenerate four-wave mixing in solutions of diphenyl polyenes, *Opt. Lett.* 17:716 (1992).
14. J. F. Reintjes, *Nonlinear Optical Parametric Processes in Liquids and Gases*, Academic Press, New York, 1984, pp. 376–377.
15. R. L. Abrams, J. F. Lam, R. C. Lind, D. G. Steel, and P. F. Liao, Phase conjugation and high resolution spectroscopy by resonant degenerate four-wave mixing, *Optical Phase Conjugation* (R. A. Fisher, ed), Academic Press, New York, 1983, pp. 211–284.
16. *Optical Phase Conjugation* (R. A. Fisher, ed), Academic Press, New York, 1983.
17. P. Yeh, Exact solution of a nonlinear model of two-wave mixing in kerr media, *J. Opt. Soc. Am. B* 3:747 (1986).
18. H. M. Gibbs, S. L. McCall, and T. N. C. Venkatesan, Differential gain and bistability using a sodium-filled Fabry–Parot interferometer, *Phys. Rev. Lett.* 36:1135 (1976).
19. M. Born, and E. Wolf, Principles of optics, 5th Ed., Pergamon Press, New York, 1975, pp. 325–327.
20. H. M. Gibbs, *Optical Bistability: Controlling Light with Light*, Academic Press, New York, 1985.
21. H. G. Winful, J. H. Marburger, and E. Garmire, Theory of bistability in nonlinear distributed feedback structures, *Appl. Phys. Lett.* 35:379 (1979).
22. R. Bonifacio, and L. A. Lugiato, Cooperative effects and bistability in resonance fluorescence, *Opt. Commun.* 19:172 (1976).
23. T. Bischofberger, and Y. R. Shen, Theoretical and experimental study of the dynamic behavior of a nonlinear Fabry–Perot interferometer, *Phys. Rev. A* 19:1169 (1979).
24. R. Bonifacio, and L. A. Lugiato, Optical bistability and cooperative effects in resonance fluorescence, *Phys. Rev. A* 18:1129 (1978).
25. E. Garmire, J. H. Marburger, S. D. Allen, and H. E. Winful, Transient response of hybrid bistable optical devices, *Appl. Phys. Lett.* 34:374 (1979).
26. D. E. Grant, and H. J. Kimble, Transient response in absorptive bistability, *Opt. Commun.* 44:415 (1983).
27. F. V. Karpushko, and G. V. Sinitsyn, An optical logic element for integrated optics in a nonlinear semiconductor interferometer, *J. Appl. Spectrosc. USSR* 29:1323 (1978).
28. S. L. McCall, Instability and regenerative pulsation phenomena in fabry–perot nonlinear optic media devices, *Appl. Phys. Lett.* 32:284 (1978).
29. K. Ikeda, Multiple-valued stationary state and its instability of the transmitted light by a ring cavity system, *Opt. Commun.* 30:257 (1979).

30. H. M. Gibbs, F. A. Hopf, D. L. Kaplan, and R. L. Shoemaker, Observation of chaos in optical bistability, *Phys. Rev. Lett.* 46:474 (1981).
31. A. Yariv, Quantum electronics, 3rd ed., John Wiley, New York, 1989, pp. 106–113.
32. M. Sheik-Bahae, A. A. Said, T. H. Wei, D. J. Hagan, and E. W. Van Stryland, Sensitive measurement of optical nonlinearities using a single beam, *IEEE J. Quantum Electron.* QE-26:760 (1989).
33. E. L. Dawes and J. H. Marburger, Computer studies in self-focusing, *Phys. Rev.* 179:862 (1969).
34. W. E. Williams, M. J. Soileau, and E. W. Van Stryland, Optical switching and n_2 measurements in CS_2 , *Opt. Commun.* 50:256 (1984).
35. D. J. Hagan, E. W. Van Stryland, M. J. Soileau, Y. Y. Wu, and S. Guhu, Self-protecting semiconductor optical limiter, *Opt. Lett.* 13:315 (1988).
36. B. L. Justus, A. L. Huston, and A. J. Campillo, Broadband thermal optical limiter, *Appl. Phys. Lett.* 63:1483 (1993).
37. G. A. Swartzlander, H. Yin, and A. E. Kaplan, Self-bending of a cw laser beam in sodium vapor, *Opt. Lett.* 13:1011 (1988).
38. J. Feinberg, Asymmetric self-defocusing of an optical beam from the photorefractive effect, *J. Opt. Soc. Am.* 72:46 (1982).
39. P. P. Banerjee and J.-J. Liu, Perturbational analysis of steady-state and transient beam fanning in thin and thick photorefractive media, *J. Opt. Soc. Am. B* 10:1417 (1993).
40. E. M. Avakyan, K. G. Belabaev, and S. G. Odulov, Polarization-anisotropic light induced scattering $\text{LiNbO}_3:\text{Fe}$ crystals, *Sov. Phys. Solid State* 25:1887 (1983).
41. V. V. Vorsnov, Photo-induced light scattering in cesium-doped variant strontium niobate crystals, *Sov. J. Quantum Electron.* 10:1346 (1980).
42. G. Zhang, Q.-X. Li, P.-P. Ho, S. Liu, Z. K. Wu, and R. R. Alfano, Dependence of specklon on the laser beam size via photo-induced light scattering in $\text{LiNbO}_3:\text{Fe}$, *Appl. Opt.* 25:2955 (1986).
43. M. Segev, Y. Ophir, and B. Fischer, Nonlinear multi two-wave mixing, the fanning process, and its bleaching in photorefractive media, *Opt. Commun.* 77:265 (1990).
44. M. Segev, D. Engin, A. Yariv, and G. C. Valley, Temporal evolution of fanning in photorefractive materials, *Opt. Lett.* 18:956 (1993).
45. W. S. Rabinovich, B. J. Feldman, and G. C. Gilbreath, Suppression of photorefractive beam fanning using achromatic gratings, *Opt. Lett.* 16:1147 (1991).
46. D. M. Pepper, J. Feinberg, and N. V. Kukhtarev, The photorefractive effect, *Sci. Am.* 263:34 (1990).
47. G. A. Swartzlander and A. E. Kaplan, Self-deflection of laser beams in a thin nonlinear film, *J. Opt. Soc. Am. B* 5:765 (1988).
48. R. R. Alfano, *The Super-Continuum Laser Source*, Springer-Verlag, New York, 1989.
49. G. P. Agrawal, *Nonlinear Fiber Optics*, Academic Press, New York, 1989.
50. L. F. Mollenauer, R. H. Stolen, and J. P. Gordon, Experimental observation of picosecond pulse narrowing and solitons in optical fibers, *Phys. Rev. Lett.* 45:1095 (1980).

51. P. Emplit, J. P. Hamaide, F. Reynand, C. Froehly, and A. Barthelemy, Picosecond steps and dark pulses through nonlinear single mode fibers, *Opt. Commun.* 62:374 (1987).
52. D. Krökel, N. J. Halas, G. Giuliani, and D. Grischkowsky, Dark-pulse propagation in optical fibers, *Phys. Rev. Lett.* 60:29 (1988).
53. J. J. Aitchison, A. M. Weiner, Y. Silberberg, M. K. Oliver, J. L. Jackel, D. E. Leaird, E. M. Vogel, and P. W. E. Smith, Observation of spatial optical solitons in a nonlinear glass waveguide, *Opt. Lett.* 15:471 (1990).
54. G. R. Allan, S. R. Skinner, D. R. Andersen, and A. L. Smirl, Observation of fundamental dark spatial solitons in semiconductors using picosecond pulses, *Opt. Lett.* 16:156 (1991).
55. B. Luther-Davies and Y. Xiaoping, Waveguides and Y junctions formed in bulk media by using dark spatial solitons, *Opt. Lett.* 17:496 (1992).
56. R. De La Fuente, A. Barthelemy, and C. Froehly, Spatial-soliton-induced guided waves in a homogeneous nonlinear Kerr medium, *Opt. Lett.* 16:793 (1991).
57. M. Shalaby and A. Barthelemy, Experimental spatial soliton trapping and switching, *Opt. Lett.* 16:1472 (1991).
58. W. J. Tomlinson, J. P. Gordon, P. W. Smith, and A. E. Kaplan, Reflection of a Gaussian beam at a nonlinear interface, *Appl. Opt.* 21:2041 (1982).
59. E. M. Wright, G. I. Stegeman, C. T. Seaton, J. V. Moloney, and A. D. Boardman, Multisoliton emission from a nonlinear waveguide, *Phys. Rev. A* 34:4442 (1986).
60. M. A. Gubbel, E. M. Wright, G. I. Stegeman, C. T. Seaton, and J. V. Moloney, Numerical study of soliton emission from a nonlinear waveguide, *J. Opt. Soc. Am. B* 4:1837 (1987).
61. H. E. Hernández-Figueroa, F. D. Pasquale, R. D. Ettinger, F. A. Fernández, and J. B. Davies, Controlled spatial bright soliton emission from a nonlinear waveguide, *Opt. Lett.* 19:326 (1994).
62. R. W. Hellwarth, Generation of time-reversed wave fronts by nonlinear refraction, *J. Opt. Soc. Am.* 67:1 (1977).
63. D. M. Bloom, P. F. Liao, and N. P. Economou, Observation of amplified reflection by degenerate four-wave mixing in atomic sodium vapor, *Opt. Lett.* 2:58 (1978).
64. M. D. Levenson, High-resolution imaging by wave-front conjugation, *Opt. Lett.* 5:182 (1980).
65. D. M. Bloom and G. C. Bjorkland, Conjugate wave-front generation and image reconstruction by four-wave mixing, *Appl. Phys. Lett.* 31:592 (1977).
66. J. H. Marburger and J. F. Lam, Effect of nonlinear index changes on degenerate four-wave mixing, *Appl. Phys. Lett.* 35:249 (1979).
67. F. A. Hopf, A. Tomita, and T. Liepmann, Quality of phase conjugation in silicon, *Opt. Commun.* 37:72 (1981).
68. D. M. Pepper, D. Fekete, and A. Yariv, Observation of amplified phase-conjugate reflection and optical parametric oscillation by degenerate four-wave mixing in a transparent medium, *Appl. Phys. Lett.* 33:41 (1978).
69. V. N. Blaschuk, B. Ya. Zel'dovich, and V. V. Shkunov, Four-wave wavefront reversal in a coded reference wave field, *Sov. J. Quantum Electron.* 10:1494 (1980).

70. A. Yariv and T. L. Koch, One-way coherent imaging through a distorting median using four-wave mixing, *Opt. Lett.* 7:113 (1982).
71. D. Grischkowsky, N. S. Shiren, and R. J. Bennett, Generation of time-reversed wave fronts using a resonantly enhanced electronic nonlinearity, *Appl. Phys. Lett.* 33:805 (1978).
72. A. Tomita, Phase conjugation using gain saturation of a Nd:YAG laser, *Appl. Phys. Lett.* 34:463 (1979).
73. H. M. Gibbs, A. C. Gossard, S. L. McCall, A. Passner, W. Wiegmann, and T. N. C. Venkatesan, Saturation of the free exciton resonance in gaas, *Solid State Commun.* 30:271 (1979).
74. H. M. Gibbs, S. L. McCall, A. C. Gossard, A. Passner, W. Wiegmann, and T. N. C. Venkatesan, Controlling light with light: optical bistability and optical modulation, *Laser Spectroscopy IV* (H. Walther, and K. W. Rothe, eds), Springer-Verlag, Berlin, 1980, p. 441.
75. H. M. Gibbs, S. L. McCall, T. N. C. Venkatesan, A. C. Gossard, A. Passner, and W. Wiegmann, Optical bistability in semiconductors, *Appl. Phys. Lett.* 35:451 (1979).
76. H. M. Gibbs, S. S. Tarn, J. L. Jewell, D. A. Weinberger, K. Tai, A. C. Gossard, S. L. McCall, A. Passner, and W. Wiegmann, Room temperature excitonic bistability in a GaAs–GaAlAs superlattice étalon, *Appl. Phys. Lett.* 41:221 (1982).
77. D. A. B. Miller, S. D. Smith, and A. Johnston, Optical bistability and signal amplification in a semiconductor crystal: applications of new low-power effects in InSb, *Appl. Phys. Lett.* 35:658 (1979).
78. F. V. Karpushko and G. V. Sinitsyn, An optical logic element for integrated optics in a nonlinear semiconductor interferometer, *J. Appl. Spectrosc. USSR* 29:1323 (1978).
79. F. V. Darpushko and G. V. Sinitsyn, Switching of laser emission spectrum by an external optical signal, *Sov. J. Quantum Electron.* 9:520 (1979).
80. S. L. McCall and H. M. Gibbs, Optical bistability via thermal effects in a glass filter, *J. Opt. Soc. Am.* 68:1378 (1979).
81. Z.-F. Zhu and E. Garmire, Optical bistability in BDN dye, *IEEE J. Quantum Electron.* QE-19:1495 (1983).
82. Z.-F. Zhu and E. Garmire, Optical bistability in four-level nonradiative dyes, *Opt. Commun.* 46:61 (1983).
83. J. E. Bjorkholm, P. W. Smith, W. J. Tomlinson, D. B. Pearson, P. J. Moloney, and A. E. Kaplan, Optical bistability based on self-focusing, *IEFE J. Quantum Electron.* QE-17:118 (1981).
84. P. W. Smith, A. Ashkin, J. E. Bjorkholm, and D. J. Eilenberger, Studies of self-focusing bistable devices using liquid suspensions of dielectric particles, *Opt. Lett.* 10:131 (1984).
85. K. Tai, H. M. Gibbs, N. Peyghambarian, and A. Mysyrowicz, Mirrorless dispersive optical bistability due to cross trapping of counterpropagating beams in sodium vapor, *Opt. Lett.* 10:220 (1985).
86. P. W. Smith and E. H. Turner, Bistable Fabry–Perot resonator, *J. Opt. Soc. Am.* 67:250 (1977).
87. P. W. Smith and E. H. Turner, A bistable Fabry–Perot resonator, *Appl. Phys. Lett.* 30:280 (1977).

88. P. W. Smith and E. H. Turner, Bistable Fabry–Perot devices, *IEEE J. Quantum Electron.* QE-13:42 (1977).
89. P. W. Smith, E. H. Turner, and P. J. Moloney, Electro-optic nonlinear Fabry–Perot devices, *IEEE J. Quantum Electron.* QE-14:207 (1978).
90. J. H. Marburger, S. D. Allen, E. Garmire, M. Levenson, and H. Winful, Optical bistability without mirrors, *J. Opt. Soc. Am.* 68:642 (1978).
91. E. Garmire, J. H. Marburger, and S. D. Allen, Incoherent mirrorless bistable optical devices, *Appl. Phys. Lett.* 32:320 (1978).
92. H. Ito, Y. Ogawa, and H. Inaba, Integrated bistable optical device using Mach–Zehnder interferometric optical waveguide, *Electron. Lett.* 15:283 (1979).
93. C. F. Li and J. R. Ji, Demonstration of optical bistability using a Michelson interferometer, *IEEE J. Quantum Electron.* QE-17:1317 (1981).
94. S. Umegaki, H. Inoue, and T. Yoshino, Optical bistability using a magneto-optic modulator, *Appl. Phys. Lett.* 38:752 (1981).
95. J. Chrostowski, R. Vallee, and C. Delisle, Self-pulsing and chaos in acousto-optic bistability, *Can. J. Phys.* 61:1143 (1983).
96. R. L. Sutherland, Optical limiters, switches and filters based on polymer dispersed liquid crystals, *Proc. Soc. Photo-Instrum. Eng. (SPIE)* 1080:83 (1989).

7

Characterization of Nonlinear Refractive Index Materials

As seen in the previous chapter, the nonlinear index of refraction, or the third order susceptibility, is an important parameter in the applications of nonlinear optics. It leads to a variety of phenomena. These phenomena, once understood, can in turn be used to measure the nonlinear index coefficient or $\chi^{(3)}$. This chapter describes several such characterization methods for studying materials exhibiting a nonlinear index of refraction.

As in the characterization of second order materials, the linear index of refraction and linear absorption coefficient must be known in most cases. These are obtained by ordinary measurement methods [1] or taken from the literature.

The measurement methods discussed below yield n_2 , n_2^I , or $\chi^{(3)}$, depending on which most naturally occurs in the theory. The relationships between these parameters are given in Chapter 6. Methods also yield the second hyperpolarizability γ by appropriate application of microscopic formulas that require the local field correction factors. Usually, the Lorentz form of the local field factor is assumed.

The following techniques are discussed:

- Degenerate four-wave mixing,
- Nearly degenerate three-wave mixing,
- Z-scan,
- Optical Kerr effect and ellipse rotation,
- Interferometric methods,
- Two-beam coupling,

Beam self-bending, and
Third harmonic generation.

The last method is included as the preferred technique for probing the pure nonresonant electronic contribution to the nonlinear refractive index.

I. DEGENERATE FOUR-WAVE MIXING

The phenomenon of optical phase conjugation by degenerate four-wave mixing (DFWM) was treated in Chapter 6, Section III.B. In this process, three coherent waves are incident on a nonlinear medium, and a fourth wave (the phase conjugate) is generated. The strength of this phase conjugate wave is dependent on a coupling coefficient κ that is proportional to the effective $\chi^{(3)}$ for the interaction. Hence measurements of the phase conjugate intensity can yield the $\chi^{(3)}$ tensor components of the medium.

This is a popular method for characterizing third order nonlinear materials and has been used extensively. Both backward and forward DFWM geometries can be employed, with the choice depending on experimental conditions. Using various combinations of polarizations for the four beams employed in the experiment, it is possible to measure all of the independent $\chi^{(3)}$ tensor components of an isotropic material.

The objective of the experiment is to measure the intensity of the phase conjugate beam or equivalently the phase conjugate reflectance. The formulas given in Chapter 6, Table 7, can then be inverted to extract the value of $\chi_{\text{eff}}^{(3)}$, which is further related to the various tensor components by the polarization of the beams and the geometry of the experiment. Both absolute and relative measurement of $\chi^{(3)}$ are possible.

This technique has several advantages. The phase conjugate beam is readily distinguishable by spatial separation from the other interacting beams. Under reasonable experimental conditions, the detected signal has a characteristic dependence on the laser intensity ($I_c \propto I^3$ or $R \propto I^2$), which can easily be checked for verification that the experiment is working. Samples can be in a variety of forms, and all the independent $\chi_{ijkl}^{(3)}$ can be measured in a single experimental setup (for isotropic materials). The beams employed in the experiment need not necessarily be true TEM₀₀ Gaussian modes as long as they are well characterized. Moreover, the time dependence of the nonlinearity can be readily studied, and other material parameters besides $\chi^{(3)}$ can sometimes be measured.

The disadvantages of this technique include the fact that only the modulus of $\chi^{(3)}$ (i.e., $|\chi^{(3)}|$) can generally be measured; the technique must in general be supplemented with another measurement to extract the real and imaginary parts

of $\chi^{(3)}$. Another disadvantage is the alignment sensitivity of the three incident beams on the sample. The angles of the beams and their overlap within the sample must be carefully controlled. This is especially true for time resolved measurements where the time of arrival of the pulse in one beam is varied with respect to the other two incident pulses. Finally, the backward DFWM geometry, that most commonly used, employs counterpropagating pump beams with inevitable feedback of optical energy into the laser cavity. Steps must be taken to ensure that this feedback does not disturb the stability of the laser (e.g., feedback is restricted to times between the output pulses of the laser).

A. Theory

Off-resonance measurements in isotropic media. Many applications of nonlinear refractive index materials require nonresonant conditions with no linear absorption. Hence this is a common experimental condition.

The theory and formulas for phase conjugate reflectance in nonabsorbing isotropic media were given in Chapter 6, Section III.B. Pump laser conditions are normally chosen so that $|\kappa L| \ll 1$, where κ is the DFWM coupling coefficient. For the usual conditions where $I_f = I_b = I_{\text{pump}}$,

$$|\kappa L|^2 = \left(\frac{3\pi L}{\epsilon_0 n_0^2 c \lambda} \right)^2 (\chi_{\text{eff}}^{(3)})^2 I_{\text{pump}}^2 \quad (1)$$

where n_0 is the linear refractive index of the sample of length L , and λ is the wavelength of the interacting light. Hence the phase conjugate reflectance is proportional to the square of the pump intensity. Measurements of this reflectance can thus be fitted to an equation of the form

$$R = b I_{\text{pump}}^2 \quad (2)$$

where b is a coefficient determined by the least-squares fit of Eq. (2) to the data. The effective $\chi^{(3)}$ for the measurement is then found from

$$\chi_{\text{eff}}^{(3)} = \frac{\epsilon_0 n_0^2 c \lambda}{3\pi L} \sqrt{b} \quad (3)$$

Alternatively, the phase conjugate intensity can be measured rather than the reflectance. If the probe intensity is related to the pump intensity by $I_p = \eta I_{\text{pump}}$, then $I_c = \eta |\kappa L|^2 I_{\text{pump}}$. The data can thus be fitted to an equation of the form

$$I_c = b' I_{\text{pump}}^3 \quad (4)$$

and

$$\chi_{\text{eff}}^{(3)} = \frac{\epsilon_0 n_0^2 c \lambda}{3\pi L} \sqrt{\frac{b'}{\eta}} \quad (5)$$

The methods just described require precise measurements of the pump intensity. Thus the beam $1/e^2$ radius and, for pulsed lasers, the pulse width must be measured with high accuracy. It is more common to make measurements with respect to a standard and thus avoid the need to characterize precisely these laser parameters.

In relative measurements, the same experiment described above is performed on a standard, well-characterized third order nonlinear material under conditions identical to those of the sample. However, the peak intensity is proportional to the average power or pulse energy, which are more easily measured. Thus to within a proportionality constant that is the same in both measurements, of the sample and of the standard, the conjugate power or energy or the conjugate reflectance data can be fitted to a formula of the form

$$R = b\mathcal{P}_{\text{pump}}^2 \quad \text{or} \quad R = b\mathcal{E}_{\text{pump}}^2 \quad (6)$$

where $\mathcal{P}_{\text{pump}}$ is the average pump power and $\mathcal{E}_{\text{pump}}$ is the pump pulse energy. Similar expressions for the conjugate power (energy) proportional to the third power of the pump power (energy) can also be used for data fitting. An example of DFWM data taken with CS_2 is shown in Fig. 1. Once both the sample and reference data have been fitted to a formula of the form of Eq. (6), the sample susceptibility is given by

$$\chi_{\text{eff}}^{(3)} = \left(\frac{n_0}{n_{\text{ref}}}\right)^2 \left(\frac{L_{\text{ref}}}{L}\right) \left(\frac{b}{b_{\text{ref}}}\right)^{1/2} \chi_{\text{eff}}^{(3)} \quad (7)$$

where the subscript ref refers to reference quantities.

An often used reference material is carbon disulfide (CS_2). The nonlinear index coefficient n_2 has been measured by several groups. Most groups agree that for CS_2 , this value is $n_2 = (1.2 \pm 0.1) \times 10^{-11}$ esu [2–4] = $1.3 \times 10^{-20} \text{ m}^2/\text{V}^2$, or $n_2' = (3.1 \pm 0.2) \times 10^{-14} \text{ cm}^2/\text{W}$ [5,6]. This value is relatively independent of wavelength over the visible and near infrared region and is also valid for picosecond and nanosecond regimes. However, Xuan et al. [7] have measured a value approximately 33% larger than this value using 25 ps pulses.

The appropriate value for $\chi_{\text{xxxx}}^{(3)}$ depends on the formula one uses to convert n_2 to $\chi^{(3)}$. Using the convention and formulas given in Chapter 6 with the most common values of n_2 quoted above yields $\chi_{\text{xxxx}}^{(3)} = 2.0 \times 10^{-12}$ esu = $2.8 \times 10^{-20} \text{ m}^2/\text{V}^2$. A value of $n_0 = 1.6$ for CS_2 has been used. The reader should note, however, that some authors use a value of $\chi_{\text{xxxx}}^{(3)}$ that is a factor of

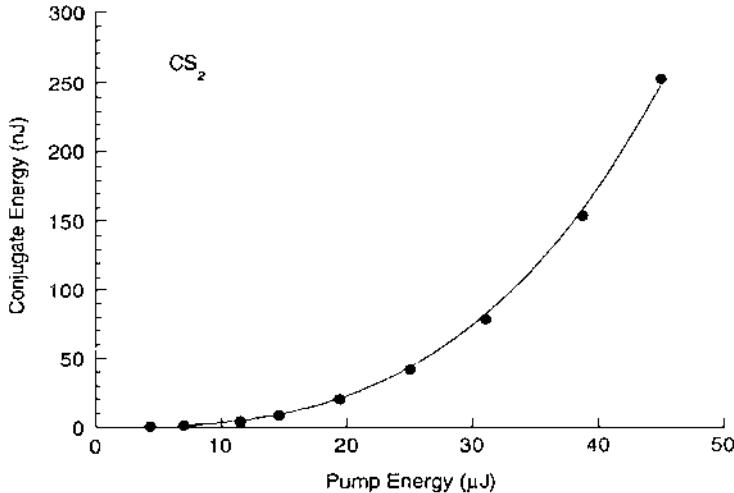


Figure 1 Phase conjugate pulse energy as a function of pump pulse energy as collected by degenerate four-wave mixing in carbon disulfide using a 35 ps frequency-doubled Nd:YAG laser. The data are fitted to a cubic equation of the form $y = bx^3$.

4 smaller than these values. Also, some use the value due to Xuan et al. [7], which is a factor of 1.33/4 times the value quoted here. To avoid confusion, one should always state the value of n_2 and the relation between n_2 and $\chi^{(3)}$ being used. Finally, other well-characterized materials are available and can be used as standards. Some of these are listed in Chapter 8.

In some cases, linear scattering can add a constant baseline to the phase conjugate reflectance. One should then fit the data to a formula of the form [5]

$$R = b_3 I_{\text{pump}}^2 + b_1 \quad \text{or} \quad I_c = b'_3 I_{\text{pump}}^3 + b'_1 I_{\text{pump}} \quad (8)$$

The linear coefficient b_1 (or b'_1) accounts for the linear scattering contribution to the detected signal, while the nonlinear coefficient b_3 (or b'_3) is used in the formulas given above to obtain $\chi^{(3)}$, Eqs. (3) and (5). For relative measurements, the same forms given in Eq. (8) can be used in terms of measured average power or measured pulse energy.

The same reference value $\chi_{\text{xxx}}^{(3)}(\text{ref})$ can be used for finding all tensor components of the sample under investigation. For isotropic media, Table 1 shows the various beam polarizations used to obtain the independent tensor components of $\chi^{(3)}$.

Effects of linear absorption. When the wavelength of the laser used in the measurements is in the tail of an absorption band of the sample, or if absorbing

Table 1 Relative Phase Conjugate (C), Forward Pump (F), Backward Pump (B), and Probe (P) Polarization Directions for Measuring the Various Tensor Components of $\chi^{(3)}$ in an Isotropic Medium

C	F	B	P	$\chi_{ijkl}^{(3)}$
↑	↑	↑	↑	xxxx
↑	↑	→	→	xxyy
↑	→	↑	→	xyxy
↑	→	→	↑	xyyx

impurities are present in the sample, then the phase conjugate signal will be modified. Formulas showing the effect of linear absorption on the phase conjugate reflectance were given in Chapter 6, Section III.B. The linear absorption coefficient must be taken into account to extract the true value of $\chi^{(3)}$.

Generally, one would operate in a regime where $|\kappa L| \ll \alpha L \ll 1$. Under these conditions, the formulas given in Eq. (6) can be used for data fitting (assuming relative measurements), and then the effective $\chi^{(3)}$ is found from

$$\chi_{\text{eff}}^{(3)} = \left(\frac{n_0}{n_{\text{ref}}}\right)^2 \left(\frac{L_{\text{ref}}}{L}\right) \left(\frac{b}{b_{\text{ref}}}\right)^{1/2} \frac{\alpha L \exp(\alpha L/2)}{1 - \exp(-\alpha L)} \chi_{\text{ref}}^{(3)} \quad (9)$$

It has been assumed that the reference has no linear absorption, and thus α is the linear absorption coefficient of the sample.

If the linear absorption becomes substantial ($\alpha L \sim 1$), then Eq. (9) will no longer be appropriate. It is likely that the material is then not Kerr-like, and $\chi^{(3)}$ could be due to population redistribution (i.e., the gratings are population gratings with both amplitude and phase components). The data should reflect this by showing a departure from a cubic dependence on pump intensity (average power or energy). Formulas in Chapter 6, Section III.B, should be consulted for the effective $\chi^{(3)}$ or n_2 for a two-level saturable system. Even if the material remains Kerr-like, strong linear absorption can produce thermal gratings that add to the phase conjugate signal. The data must then be appropriately analyzed to extract the true $\chi^{(3)}$ of the medium (see below).

Effects of two-photon absorption. As mentioned earlier, DFWM reveals the modulus of $\chi^{(3)}$ in measurements. Often, $\chi^{(3)}$ has a nonnegligible imaginary component. This is related to the two-photon absorption coefficient. Thus although the sample may appear to be transparent at low optical power, it could have substantial two-photon absorption manifest at the higher intensities

used in the measurements. This absorption can lead to contributions to the phase conjugate signal from effects such as thermal gratings [8], excited state species concentration gratings [9], or free carrier gratings in semiconductors [10].

The net effect of two-photon absorption is to produce an effective fifth order nonlinear refractive index at high intensities. This effective fifth order process is actually a cascading of third order and first order processes ($\chi^{(3)}$: $\chi^{(1)}$). In other words, the phase conjugate signal can have contributions from linear scattering by both phase (linear index) and amplitude (linear absorption) gratings, which have in turn been produced by two-photon absorption. This part of the signal will, in general, depend on the fifth power of the pump intensity.

It should be noted that the production of additional linear gratings is really dependent on absorbed energy rather than instantaneous intensity. However, for sufficiently short pulses (typically $\ll 1$ ns), the dependence of the data can be related to the peak power of the pump laser. Thus the data can be fitted to a formula of the form [10].

$$I_c = b_3 I_{\text{pump}}^3 + b_5 I_{\text{pump}}^5 \quad (10)$$

In this equation, I_{pump} is the peak intensity. The coefficient b_3 can thus be used in Eq. (6) to extract $\chi^{(3)}$.

It should be noted that in nanosecond DFWM experiments, two-photon absorption can significantly modify the temporal shape of the phase conjugate pulse. Thus the peak phase conjugate intensity is not a good quantity for determining $\chi^{(3)}$. In some cases, though, it is still possible to use DFWM data not only to extract $\chi^{(3)}$ but also to resolve its real and imaginary components [11]. This is further described below and in Chapter 10.

Temporal effects. For absolute measurements of $\chi^{(3)}$, it is necessary to know the beam spot size, the pulse energy, and the pulse shape. Two generally assumed pulse shapes are Gaussian [$\exp(-t^2/\tau^2)$] and hyperbolic secant squared [$\text{sech}^2(t/\tau)$], where τ is related to the pulse width and can be determined experimentally. For these types of pulses, the pump energy is related to the peak pump intensity by

$$\mathcal{E}_{\text{pump}} = \begin{cases} \frac{\pi w^2}{2} \sqrt{\pi \tau} I_{\text{pump}} & \text{Gaus} \\ \frac{\pi w^2}{2} 2\tau I_{\text{pump}} & \text{sech}^2 \end{cases} \quad (11)$$

where w is the $1/e^2$ radius of the beam. A measurement of the phase conjugate

pulse energy will then yield a value that in theory is proportional to

$$\mathcal{E}_c \propto \begin{cases} \frac{4}{3\sqrt{3}\pi^3} \frac{1}{w^4\tau^2} \mathcal{E}_{\text{pump}}^3 & \text{Gaus} \\ \frac{8}{45\pi^2} \frac{1}{w^4\tau^2} \mathcal{E}_{\text{pump}}^3 & \text{sech}^2 \end{cases} \quad (12)$$

For an instantaneous response (Kerr-like medium), the phase conjugate pulse should be narrower by a factor of $3^{-1/2}$ from the pump pulse width if the pump pulse shape is Gaussian. This factor will also be approximately true if the pump pulse has a hyperbolic secant squared shape. A conjugate pulse substantially broader than this indicates the presence of slower processes that may be adding to the signal or dominating it. This must then be accounted for in the data analysis, or eliminated experimentally by using shorter pulses.

As discussed above, both linear and two-photon absorption can lead to additional gratings that depend on the time integral of $I_{\text{pump}}(t)$ or $[I_{\text{pump}}(t)]^2$. If the slow nonlinearity has the same sign as the fast Kerr-like nonlinearity, then this added signal has the effect of broadening the conjugate pulse. On the other hand, if the slow and fast nonlinearities have opposite sign, the conjugate pulse will be distorted and can look like a double-peaked pulse [8,11–13]. For linear absorption, the relative position and ratio of the two peaks will remain constant as a function of pump energy. However, for two-photon absorption, both the position and the ratio will change as the pump energy increases [8], with the slow nonlinearity dominating at high pump energies. An example of the linear absorption effect is shown in Fig. 2. For this case, CS_2 was doped with some carbon particles to illustrate thermal effects. This is contrasted with the case of two-photon absorption effects in diphenylbutadiene, which was also illustrated in the last chapter (see Fig. 10 of Chapter 6).

This pulse distortion complicates the data analysis. To extract the true $\chi^{(3)}$ of the sample, a model must be assumed for the slow nonlinearity, which is then fitted to the pulse shape [11]. An example of this for two-photon absorption in solutions of diphenylbutadiene in chloroform is given in Fig. 3. In this example, the imaginary part of $\chi^{(3)}$ must be assumed or measured in another experiment. In some cases, it is possible to obtain this from the same DFWM experiment [11]. This subject is taken up in Chapter 10.

If the optical pulses used in the experiment are short compared to the response time of the slow nonlinearity, then this part of the conjugate signal will be negligible and safely ignored when all of the pulses from the three beams are coincident in time. The measured $\chi^{(3)}$ is then referred to as the instantaneous response of the medium (i.e., its Kerr-like response). A time resolved DFWM experiment, where one pulse is delayed in time with respect to the other two, can then be used to resolve and separately measure both the fast and the slow

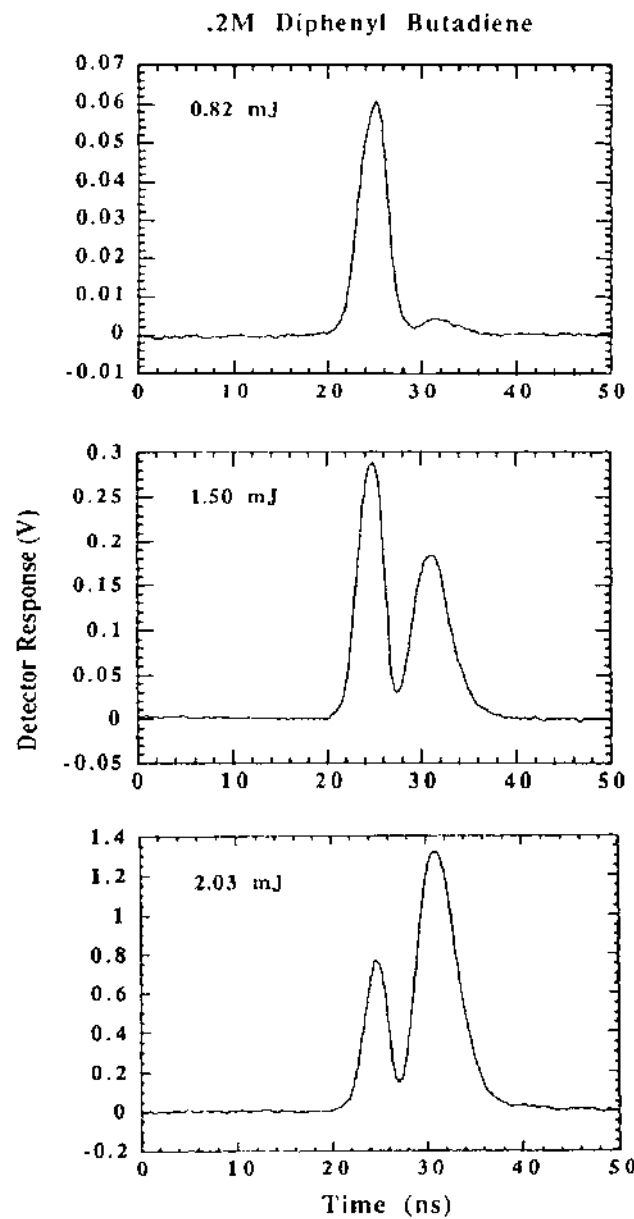


Figure 2 Temporal effects in the phase conjugate pulse (nanosecond regime) due to two-photon absorption in diphenylbutadiene and single-photon absorption in carbon particle-doped CS₂.

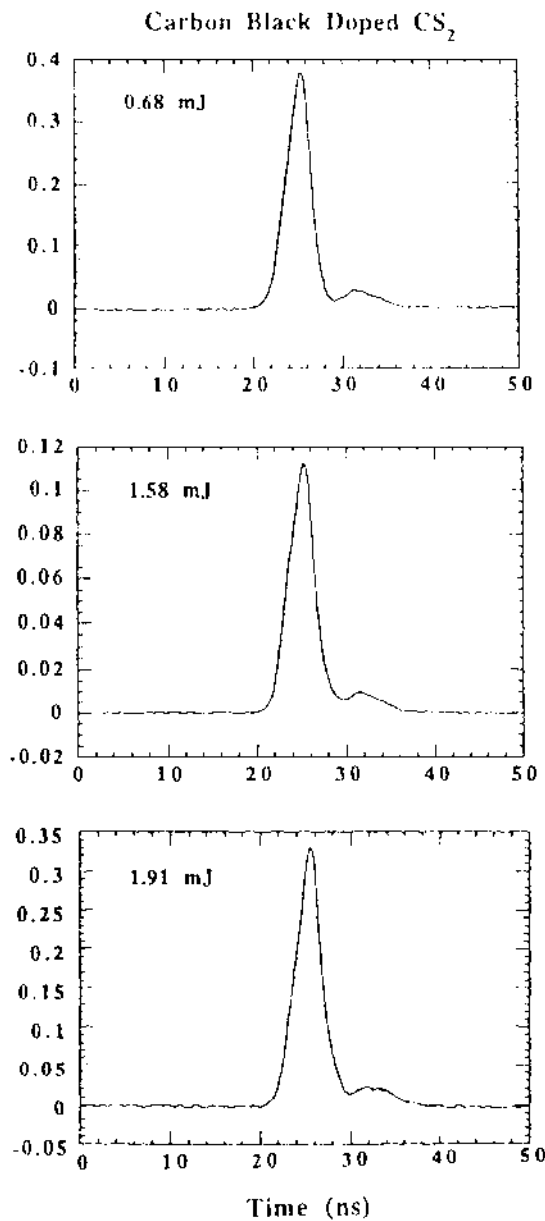


Figure 2 Continued.

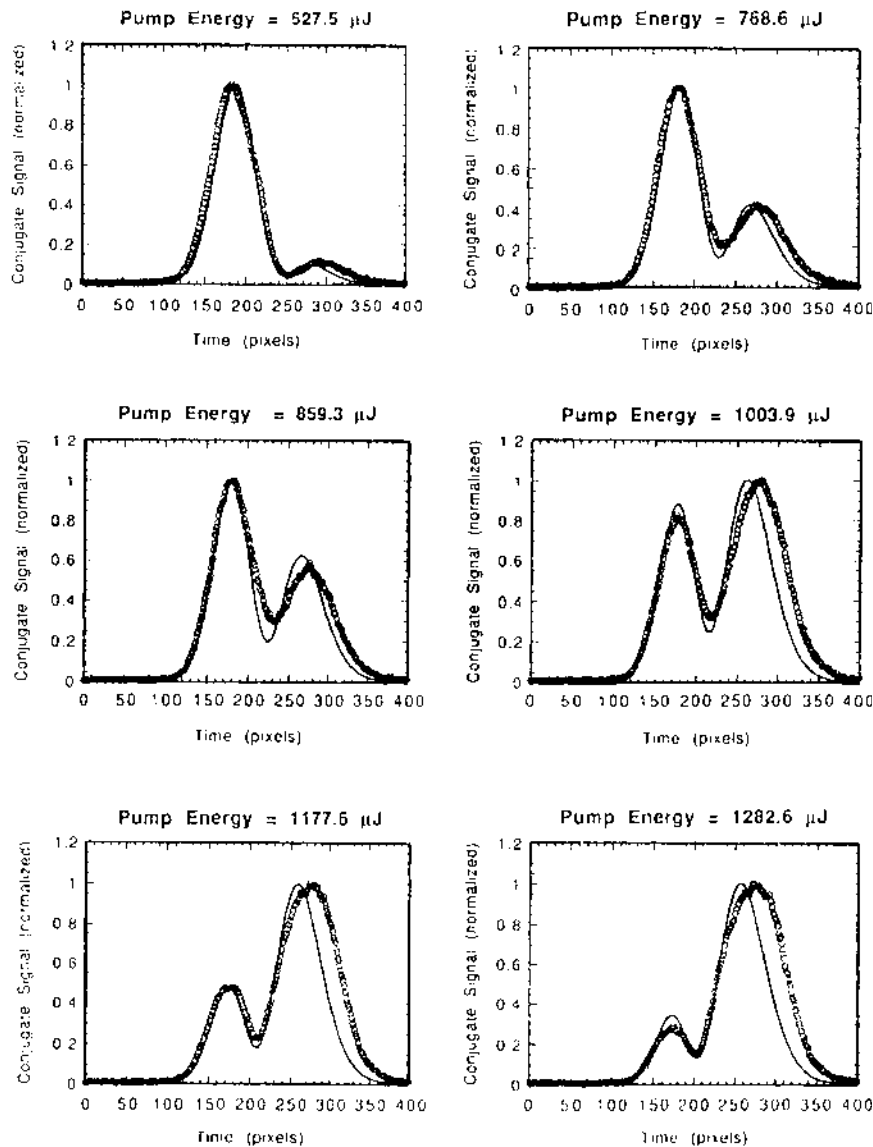


Figure 3 Data fits to phase conjugate pulses affected by two-photon absorption in solutions of diphenylbutadiene (double-peak pulse behavior). A model including two-photon induced diffraction gratings is employed to extract the third order susceptibility value of the solution. (From Ref. 11.)

response of the medium. An example of such time resolved measurements is shown in Fig. 4.

If two-photon absorption is occurring, then separate DFWM experiments at zero time delay and long time delay can resolve the $\chi^{(3)}$ and effective $\chi^{(5)}$ values. The zero time delay data are fitted to a cubic dependence on pump intensity, while the long time delay data are fitted to a fifth-power dependence [10].

Time delay experiments can also be used to measure intrinsic decay rates of the material, such as excited state population decay rate in a two-level system and charge carrier diffusion or recombination rates in semiconductors. If the pulse width is large compared to the decay time constant of the medium, then a quasi-steady state is reached during the pulse, and a time delay experiment will yield a symmetric response about the zero time delay. When the pulse width used is shorter or comparable to the decay time, then the data will be asymmetric about the zero time delay, showing a sharp rise for negative delays and a slower fall for positive delays [14,15]. In the latter case, a model of the system must be assumed and the data fitted to this model to extract the $\chi^{(3)}$ and the decay time constant.

Absorption (linear or nonlinear) can produce acoustic (density) gratings. The long time delay signal will then display oscillations at acoustic periods (usually ~ 1 ns). An example of this is shown in Fig. 5. Usually, the long time delay signal will be due to a mixture of population and acoustic gratings. Under

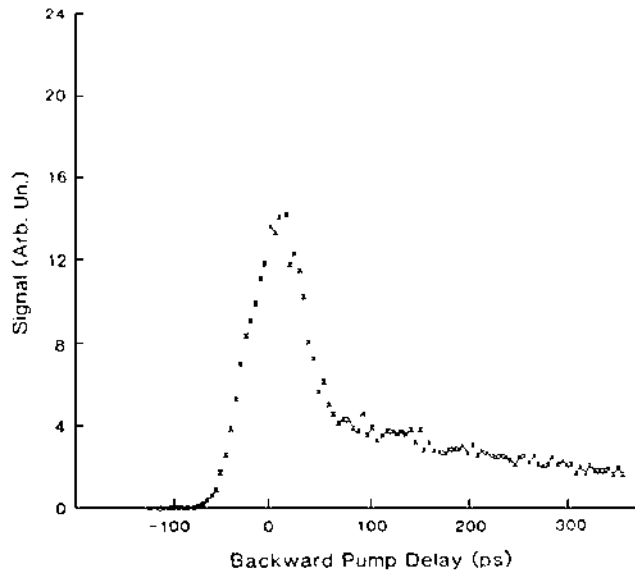


Figure 4 An example of a time-resolved phase conjugate signal obtained by degenerate four-wave mixing. (From Ref. 10. © 1991 IEEE.)

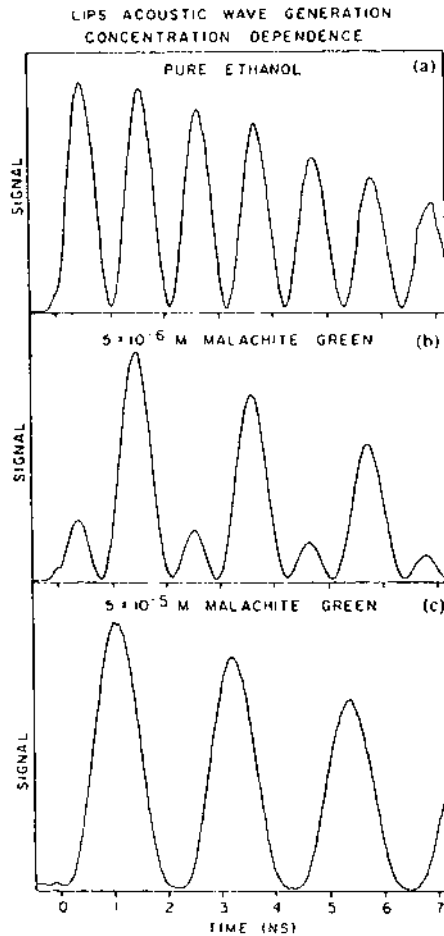


Figure 5 An example of picosecond laser induced photoacoustic gratings in liquids. In this particular case the pump and probe wavelengths are different. (From Ref. 16. © 1986 IEEE.)

some conditions, it is possible for these two contributions to interfere and wash out the acoustic ringing [16]. The time dependent diffraction efficiency $\eta(t)$ can be modeled by [17]

$$\begin{aligned} \eta(t) \sim & (e^{-\gamma t})^2 + \left\{ C e^{-\gamma t} + P [\Omega^{-2}(1 - \cos \Omega t) \right. \\ & \left. - (\gamma^2 + \Omega^2)^{-1} \left(\frac{\gamma}{\Omega \sin \Omega t} - \cos \Omega t + e^{-\gamma t} \right)] \right\}^2 \end{aligned} \quad (13)$$

where only one decay channel has been assumed with decay constant γ . The acoustic frequency is given by Ω , while C and P are constants with $C = 2(\omega - \omega_0)/\gamma$. The frequency ω corresponds to the laser frequency used in the experiment, and ω_0 is a resonance frequency of the material. The parameter P is related to properties of the material and the experimental conditions. The data are fitted to Eq. (13) by adjusting C , P , Ω , and γ .

Forward DFWM. The measured phase conjugate signal will be proportional to L^2 , where L is the sample thickness. When the sample is thin, it is often necessary to focus the incident beams to improve the signal-to-noise ratio. Under certain conditions, a forward geometry is then preferred. There are two possibilities.

The first possibility was illustrated in Chapter 6, Fig. 12. This configuration involves only a single pump beam and a probe beam incident at an angle θ with respect to the pump. The generated phase conjugate beam will propagate at an angle $-\theta$ with respect to the pump and can be easily resolved spatially if θ is larger than the diffraction angle. This is not a phase matched process, and for small angles $\Delta k \approx k\theta^2$. Under conditions where $|\kappa L| \ll 1$ and $\Delta kL \ll 1$, Eq. (6) can be used to extract $\chi^{(3)}$. The condition on the sample thickness is then $L \ll \lambda/\theta^2$, where λ is the laser wavelength.

An alternative phase matched geometry that avoids this sample thickness restriction is illustrated in Fig. 6. This is the so-called folded boxcars configuration [14]. Two pump beams cross at an angle in the sample. In the figure, these are shown in the yz -plane. The probe beam crosses the sample in a plane perpendicular to the pump beam plane. The phase matched conjugate beam is generated in this same plane (xz -plane as illustrated in Fig. 6). The only restriction on sample thickness in this case is that it be small compared to the confocal parameter of the laser. The formulas given above for backward DFWM can again be used for this configuration to extract $\chi^{(3)}$.

Anisotropic media. In isotropic media, principal axes are basically defined by the polarizations of the interacting beams, and the various tensor components of $\chi^{(3)}$ can be readily extracted independent of sample orientation. For anisotropic media, the principal axes are determined by the crystallographic axes, and the measured $\chi_{\text{eff}}^{(3)}$ will depend on sample orientation as well as beam polarization.

The nonlinear polarization driving the conjugate wave is given in laboratory coordinates by

$$(P_c^{(3)})_i = 3\epsilon_0 \sum_{jkl} \sum_{IJKL} (\hat{i} \cdot \hat{I})(\hat{j} \cdot \hat{J})(\hat{k} \cdot \hat{K})(\hat{l} \cdot \hat{L}) \chi_{IJKL}^{(3)} (E_f)_j (E_b)_k (E_p^*)_l \quad (14)$$

where $\{IJKL\} = \{XYZ\}$ are crystal coordinates. The dot products of unit vectors in each coordinate system are the direction cosines introduced in Chapter 2 and

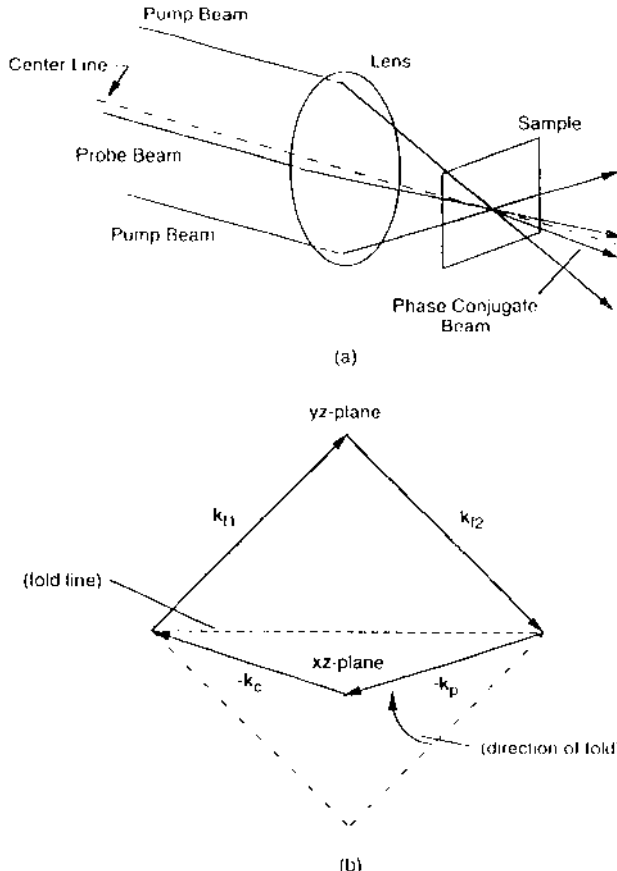


Figure 6 Folded boxcars form of forward degenerate four-wave mixing. (a) Experimental configuration. (b) Phase matching diagram illustrating the folded box.

are given in terms of the spherical angles θ, ϕ by Eq. (52) of Chapter 2. In general, one selects laboratory coordinates (x, y) by the various beam polarizations (the z -components of the fields can be ignored for small angles between the forward pump and probe beams). The effective $\chi^{(3)}$ measured for that configuration is then given in terms of the tensor components in the principal axis coordinate system and the appropriate direction cosines. For example, with all beam polarizations parallel along x ,

$$\chi_{\text{eff}}^{(3)}(\hat{x}, \hat{x}, \hat{x}, \hat{x}) = \sum_{IJKL} (\hat{x} \cdot \hat{I})(\hat{x} \cdot \hat{J})(\hat{x} \cdot \hat{K})(\hat{x} \cdot \hat{L}) \chi_{IJKL}^{(3)} \quad (15)$$

By selecting various combinations of beam polarization and sample orientation, the various tensor components can be characterized. Maker and Terhune [18] give expressions for cubic crystals and crystals of class 32, 3m, and $\bar{3}$ m. Adair et al. [19] also give expressions for cubic crystals. DeSalvo et al. [20] show expressions for crystals of class m3m, mm2, and $\bar{4}3$ m, while Rao et al. [21] give expressions for an orthorhombic polymer film.

Second hyperpolarizability. Often the quantity of interest is the microscopic parameter characterizing the individual molecules known as the second hyperpolarizability. This is the case for screening materials in solution form. For a single species in a dilute solution, the measured susceptibility when all beams are of parallel polarization is given by

$$\chi_{xxxx}^{(3)} = (\chi_{xxxx}^{(3)})_{sv} + \frac{f^4 N_{sl} \langle \gamma_{sl} \rangle}{\epsilon_0} \quad (16)$$

where sv stands for solvent and sl for solute. The first quantity on the right-hand side of Eq. (16) is thus the susceptibility of the solvent. N_{sl} is the number density of solute molecules, $\langle \gamma_{sl} \rangle$ represents an angular orientational average of the second hyperpolarizability tensor for the solute molecules, and f is a local field factor given by

$$f = \frac{n_0^2 + 2}{3} \quad (17)$$

where n_0 is the linear refractive index of the solution.

To obtain the hyperpolarizability, the solvent susceptibility must be known. These have been tabulated for several common organic solvents. Some of these are listed in Chapter 8. The number density (cm^{-3}) is given in terms of the molar concentration C (moles/liter) by $N_A C \times 10^{-3}$, where N_A is Avogadro's number.

The part of the measured effective $\chi^{(3)}$ due to the solute may have the same or opposite sign as that due to the solvent. This relative sign must be determined for an accurate characterization of the solute. A method for determining this is to perform a concentration study of the effective $\chi^{(3)}$ of the solution [22]. If the solvent and solute contributions have opposite sign, then the net effective $\chi^{(3)}$ will decrease initially from that of the neat solvent as the concentration of solute is increased. The qualitative behavior is illustrated in Fig. 7. If neither solvent or solute display two-photon absorption, then $\chi_{eff}^{(3)} = 0$ at some concentration. By fitting the measured susceptibility to Eq. (16) with the measured concentration, the value of $\langle \gamma_{sl} \rangle$ may be determined.

If $\chi_{eff}^{(3)}$ has a nonzero minimum as a function of concentration, this indicates that the solute has an imaginary component to its hyperpolarizability, assuming that the solvent does not exhibit two-photon absorption. Thus the concentration dependence can also be used to resolve both the real and imaginary parts.

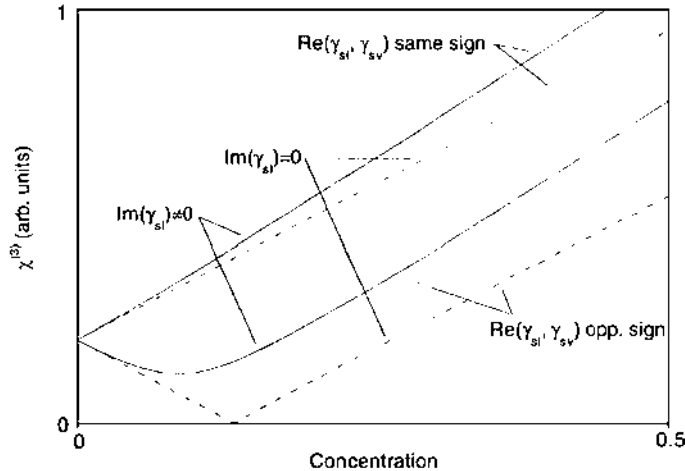


Figure 7 Illustration of the concentration dependence of the third order susceptibility of a liquid solution when the imaginary part of the solute hyperpolarizability is both zero and nonzero, and when the real part of the hyperpolarizability of the solute and solvent are of the same and opposite signs.

B. Experimental

A typical experimental setup for DFWM is shown in Fig. 8. This illustrates the backward geometry. The forward geometry, other than the directions of the various beams, will have many of the same features.

All of the interacting beams are derived from the same laser by the appropriate use of beam splitters. The path lengths of the various beams may differ prior to arrival at the sample but should not be more than the coherence length of the laser. This is because the beams must coherently interact in the sample to generate the phase conjugate beam.

The laser wavelength and pulse width should be selected for the particular phenomenon under study in the sample, i.e., resonant or nonresonant nonlinearities, electronic or molecular motion mechanisms, nonlinear index decay kinetics, etc. The laser pulse repetition frequency (PRF) is also an important consideration. Normally, the PRF is chosen to be relatively low (~ 10 Hz) to avoid cumulative energy (e.g., thermal) effects.

Normally, the laser is operated at its maximum output, since this provides for a more stable operation. The beam is then attenuated to desired power or energy for the experiment. A typical attenuator involves a half-wave plate and polarizer combination as shown in Fig. 8. Polarization choices for each individual beam can be selected by half-wave plates and/or polarizers in each beam line.

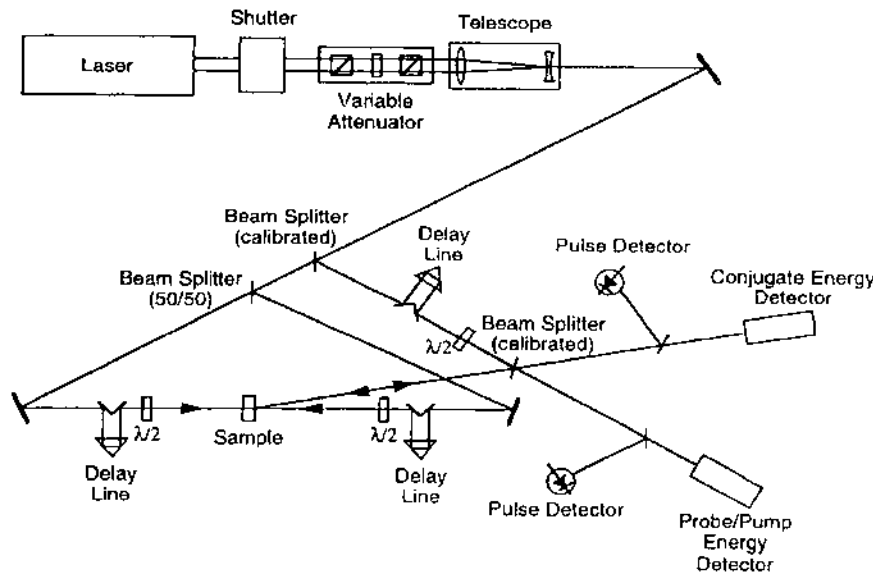


Figure 8 Schematic diagram of a degenerate four-wave mixing experiment.

Telescopes and lenses are often used to adjust the beam size for the desired range of intensities in the experiment.

Often a small fraction of the beam is picked off with a beam splitter (e.g., uncoated glass or pellicle slide) to serve as the probe beam. The remaining beam is split by a 50/50 beam splitter into two beams that are directed by beam steering optics to serve as the counterpropagating pump beams in the sample. Each beam can have an optical delay line for time resolved studies. A delay line usually consists of a 90° prism or retroreflector mounted on a precision translation stage. The precision of the linear translation will determine the accuracy of the time delay, and the range of translation will determine the net delay time available.

A beam splitter directs the probe beam at the desired angle with respect to the forward pump beam into the sample. The same beam splitter will serve to transmit the generated conjugate beam to its detector. All beam splitters must be calibrated so that energy or power measurements can be translated into the actual beam energy/power used in or compared to theoretical computations. Detectors are typically precision energy or power meters, or photodiodes calibrated against energy meters. These detectors need not have a fast response time, but they should be linear over as wide a range as possible. Calibrated neutral density filters are often used to keep the detectors in their linear range as the laser pump power is varied. Finally, pulse waveforms are also often monitored with fast photodiodes. These must have a response time that is short compared to the rise

time of the laser pulse. The waveform monitor (e.g., transient digitizer or streak camera) must also have sufficient bandwidth to faithfully reproduce the shape of the detected pulse.

For absolute measurements, the beam spatial profile and pulse shape as well as beam energy/power must be carefully measured. These parameters are usually where the greatest experimental error resides. Beam size in a DFWM experiment typically ranges from a few millimeters down to a few hundred micrometers. For this size of beam, a CCD camera coupled to a frame grabber and computer can be used to characterize the beam spatial profile. Software packages exist that will automatically determine the beam $1/e^2$ radius in two orthogonal directions as well as the quality of the beam fit to a Gaussian TEM₀₀ mode. Alternatively, one can scan a pinhole, slit, or knife edge across the beam in two orthogonal directions and fit the detected energy to an appropriate mathematical function (e.g., a Gaussian for a pinhole scan, or an error function for a knife edge scan). Care must be taken that the pinhole or slit be small compared to the beam size, or the result must be properly deconvolved before fitting the result to a Gaussian. Once the beam is properly characterized, the $1/e^2$ radius may be used to compute intensity or fluence values.

The pulse width and shape must also be carefully monitored to compute power or intensity. The necessary instrumentation depends on the pulse duration and PRF. For nanosecond pulses, a wide bandwidth (i.e., ~ 500 –1,000 MHz) transient digitizer is useful for low PRFs (~ 1 –1,000 Hz). For very high PRFs (~ 1 –100 MHz) a wide bandwidth sampling scope is useful. When the pulse width is in the range of ~ 1 ps to 10 ns, a streak camera may be used. An autocorrelator must be used when the pulses are shorter (i.e., a few picoseconds down to a few femtoseconds).

Peak intensities are usually required for absolute measurements. These can be determined from the measurements described above. Peak voltage and voltage waveform from a fast photodiode along with pulse energy measurements are sufficient to determine the peak optical power \mathcal{P}_0 through the relation

$$\frac{\mathcal{P}_0}{\mathcal{E}} = \frac{V_0}{\int V(t) dt} \quad (18)$$

where \mathcal{E} is the measured pulse energy, V_0 is the peak voltage, and the integral over $V(t)$ is the area under the voltage waveform. The peak intensity is then determined by $I_0 = 2\mathcal{P}_0/\pi w^2$, where w is the measured $1/e^2$ radius of the beam.

If the pulse shape cannot be continuously monitored for each pulse, then the pulse shape must be assumed to remain constant for data analysis. Measured pulses can often be fitted with high accuracy to analytical functions such as a Gaussian or a hyperbolic secant squared. These forms will often work for seed-injected Q-switched lasers or transform-limited outputs from mode-locked lasers.

Analytical formulas can then be used to compute peak powers if the pulse width t_{FWHM} (full width at half maximum) is carefully characterized. The following formulas apply:

$$\mathcal{P}_0 = \begin{cases} \frac{2\sqrt{\ln 2}\mathcal{E}}{\sqrt{\pi}t_{\text{FWHM}}} & \text{Gaus} \\ \frac{\ln(1 + \sqrt{2})\mathcal{E}}{t_{\text{FWHM}}} & \text{sech}^2 \end{cases} \quad (19)$$

Assuming the medium is Kerr-like (i.e., responds instantaneously to the optical pulses), then the conjugate pulse will be narrower by a factor of $(3)^{-1/2}$ for Gaussian pulses and approximately by this factor for sech^2 pulses.

The beams must be properly overlapped in the sample, both spatially and temporally. Spatial alignment can be facilitated by directing each beam through a pinhole at the sample location and maximizing the transmission through the pinhole. However, the pump beams must be truly counterpropagating to assure phase matching. This can be done by translating the pinhole along the pump beam axis and determining that the transmission of both pump beams through the pinhole is maximum. The pump beams must have nearly identical powers as well to avoid an intensity induced phase mismatch. Temporal overlap can be accomplished by varying beam path lengths to maximize the conjugate beam power.

Beam overlap affects the maximum sample thickness L that can be characterized. First, one should assure that $L < ct_{\text{FWHM}}$, (i.e., that the pulses overlap through the entire sample). Otherwise, the actual length of overlap should be used in the formulas given above for analyzing the data. Second, the angle of beam intersection and beam width set a limit on the sample thickness. As illustrated in Fig. 9, for beams of diameter $2w$ that intersect at an angle θ , the maximum sample thickness is determined by $L < 2w/\sin \theta$, where θ is measured *inside* the sample and is thus reduced according to Snell's law from the angle of incidence in air. The grating spacing used in the experiment can be varied by varying θ , with the coarse grating spacing given by $\Lambda_c = \lambda/2n_0 \sin(\theta/2)$ and the fine grating spacing given by $\Lambda_f = \lambda/2n_0 \cos(\theta/2)$.

The experiment is run by varying the pump and probe energies in proportional amounts over an extended range and measuring the conjugate energy. The detected signals can be digitized and averaged using boxcar integrators or simply stored on a computer and averaged later. Since the measured conjugate signal depends on the pump energy to the third power, small fluctuations in the pump energy will be magnified in the conjugate energy. Fluctuations can be reduced and accuracy increased by averaging over several pulses (e.g., ~ 10 –100 pulses). A typical procedure may be to keep the pump energy relatively fixed (i.e., keep the beam attenuator in the experiment at a fixed setting) for several pulses.

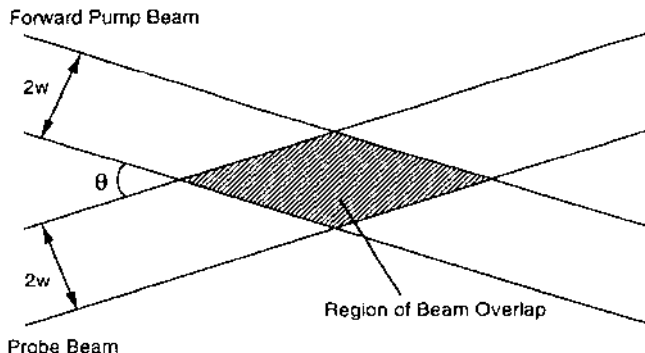


Figure 9 Illustration of the overlap of the forward pump and probe beams in a degenerate four-wave mixing experiment.

Compute the average pulse energy and its standard deviation. Then only keep those data for which the pulse energy varies by no more than one-half a standard deviation from the average. Proceed to the next attenuator setting and repeat the procedure. Variations on this theme are possible, but techniques such as this will reduce the scatter in the data. These measurements should be supplemented with temporal waveform or time delay measurements to examine the presence of fast or slow processes in the measurements.

A check on the consistency of the data in the experiment can be made by assuring that the conjugate signal varies as the appropriate power of the pump power or energy. The data should be fitted by a least squares technique to the appropriate power law as discussed in the theory section above. The closer the fit to the theory, the more accurate will be the value of $\chi^{(3)}$ obtained. Before analyzing the data, the pump power or energy should be corrected for Fresnel reflection losses at the sample's first surface.

Usually, two-photon absorption losses can be safely ignored if the product $q = \beta I_{\text{pump}} L$ is small (i.e., $q \ll 1$), where β is the two-photon absorption coefficient. This can be accomplished by controlling the pump intensity and/or the sample thickness. If this is not the case, then the conjugate signal should be divided by a factor of $T_{NL}^3 = [q^{-1} \ln(1 + q)]^3$ to account for the loss in each beam due to two-photon absorption. The coefficient β will have to be determined from other measurements (see Chapter 10).

Finally, to reduce the data and find the value of $\chi^{(3)}$ the values of the linear index n_0 and absorption coefficient α will need to be known or measured by standard techniques. If all measurements are carefully done, an experimental accuracy of 10–30% should be achievable.

II. NEARLY DEGENERATE THREE-WAVE MIXING

Nearly degenerate three-wave mixing is a form of four-wave mixing in which two of the waves are derived from the same beam. A strong pump beam at ω interacts with a weak probe beam at $\omega - \Delta\omega$ to produce a new wave at $2\omega - (\omega - \Delta\omega) = \omega + \Delta\omega$, where $\Delta\omega \ll \omega$. Under these conditions,

$$\chi_{xxxx}^{(3)}(-\omega; \omega, \omega, -\omega) \approx \chi_{xxxx}^{(3)}(-\omega - \Delta\omega; \omega, \omega, -\omega + \Delta\omega) \quad (20)$$

where the latter susceptibility is that governing the three-wave mixing process.

The intensity of the newly generated wave is proportional to the absolute square of the susceptibility in Eq. (20). Thus a measurement of this intensity provides a measure of the susceptibility, which is related to the degenerate form of $\chi^{(3)}$ through the approximate relationship of Eq. (20). The advantage of this technique is that it is nearly phase matched for forward collinear propagation of all three waves. This greatly simplifies the beam alignment in the experiment. The disadvantage is that waves of nearly equal frequency must be separated to measure the newly generated wave intensity.

A. Theory

Adair et al. [23] developed this technique for a relatively rapid assessment of glass hosts for laser media. They determined that the approximate relationship in Eq. (20) will hold for frequency shifts up to $\Delta\omega \sim 60 \text{ cm}^{-1}$. Under normal conditions, this will result in a small phase mismatch. The phase matching diagram for the nearly degenerate three-wave mixing process is shown in Fig. 10.

The phase mismatch Δk is given by

$$\Delta k \approx - \left[2 \left(\frac{dn}{d\omega} \right) + \omega \left(\frac{d^2n}{d\omega^2} \right) \right] \frac{(\Delta\omega)^2}{c} \quad (21)$$

The two terms in square brackets are comparable. With $(dn/d\omega) = -(\lambda^2/2\pi c) \times (dn/d\lambda)$, and with typical values of $(dn/d\lambda) \sim 500 \text{ cm}^{-1}$ and $\Delta\omega = 60 \text{ cm}^{-1}$, a typical phase mismatch will be $\Delta k \sim 0.1 \text{ cm}^{-1}$. This limits the sample length to $L < |\Delta k|^{-1} \sim 10 \text{ cm}^{-1}$. Note that if the probe and signal beams make a small



Figure 10 Phase matching diagram for a nearly degenerate three-wave mixing process.

angle (~ 0.1 mr) with respect to the pump beam, then the phase mismatch can be made to be approximately zero.

The generated signal intensity at $\omega + \Delta\omega$ is given by

$$I_+ \propto \frac{1}{n_0^4} |\chi_{xxxx}^{(3)}(-\omega - \Delta\omega; \omega, \omega, -\omega + \Delta\omega)|^2 I_p^2 I_- L^2 \quad (22)$$

where $I_{+(-)}$ is the intensity of the upshifted (downshifted) frequency, and I_p is the pump intensity. The objective of the experiment is to make several measurements of the signal intensity for constant pump and probe intensities. This is done for both the sample and a reference material (e.g., CS₂). The averages of the measured intensities (or pulse energies, if the spot size is the same in both reference and sample) are then used to compute the sample susceptibility by

$$\chi_{xxxx}^{(3)} = \left(\frac{n}{n_{ref}} \right)^2 \frac{L_{ref}}{L} \left(\frac{1 - R_{ref}}{1 - R} \right)^2 \left(\frac{\bar{I}_+}{\bar{I}_+^{ref}} \right)^{1/2} [\chi_{xxxx}^{(3)}]_{ref} \quad (23)$$

$R = [(1 - n)/(1 + n)]^2$ is the Fresnel reflectance of the sample or reference material. The expected accuracy of the measurement is $\sim 15\text{--}20\%$.

B. Experimental

A schematic diagram of the experiment is show in Fig. 11. Nanosecond laser pulses may be used since thermal and electrostriction processes are not expected to contribute to the generation of the upshifted signal frequency. The process is primarily electronic, with a small nuclear contribution.

Two different wavelengths must be used, with a frequency separation of $\leq 60\text{ cm}^{-1}$. In the experiment of Adair et al. [23] the pump beam was the fundamental from a Nd:YAG laser at $1.064\text{ }\mu\text{m}$, while the other wavelength at $1.071\text{ }\mu\text{m}$ was obtained by Raman-shifting the output of a dye laser ($0.567\text{ }\mu\text{m}$) pumped by the second harmonic of the Nd:YAG laser. The two beams are combined by beam splitters and adjusted to overlap spatially and temporally. Phase matching is obtained by adjusting angles and lenses to maximize the generated signal. The beams are then lightly focused into the sample/reference to a diameter of the order of a few hundred micrometers.

The sample and reference are irradiated simultaneously in separate beam paths. The two generated signal beams are then vertically separated and passed through a double monochrometer. The output signals are physically separated and detected by PMTs connected to boxcar integrators for signal averaging. The background can be subtracted out by blocking the probe beam and measuring the residual pump energy that leaks into the PMTs. After the background has been subtracted, averages of the signal energy or intensity from both the sample and

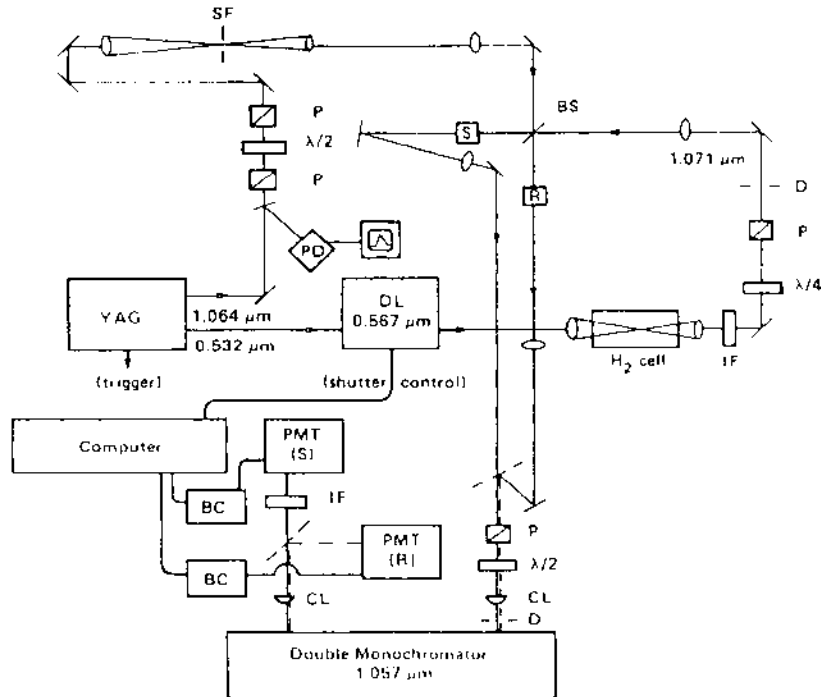


Figure 11 Schematic diagram of nearly degenerate three-wave mixing experiment. The two wavelengths are from a Nd:YAG laser and the Raman-shifted (H_2 cell) output of a dye laser. The sample and reference are labeled by S and R, respectively. (From Ref. 23, University of California, Lawrence Livermore National Laboratory and the Department of Energy.)

the reference are computed. These values are then used in Eq. (23) to compute the unknown susceptibility.

III. Z-SCAN

Pure refractive Z-scan. The phenomenon of the self-focusing of an intense Gaussian beam in a nonlinear medium was treated in Chapter 6, Section III.E. The resulting beam distortion can be measured and used to extract the value of n_2 for the medium. Whole-beam distortion measurements in the far field have been used as a method for measuring n_2 , but the technique is difficult and not very sensitive [3].

In 1989, Sheik-bahae et al. [4] developed a sensitive self-focusing measurement technique that involves focusing a laser beam through a thin sample and detecting the light transmitted by a small aperture in the far field. This simple method is illustrated in Fig. 12. The far-field aperture transmittance is measured for a constant laser input as the sample is scanned along the z -direction through the focus of the lens. Hence the measurement method has come to be known as the Z-scan.

Formulas for the self-focusing of light in a thin medium were given in Table 15 of Chapter 6. The medium acts like an intensity dependent lens. As it is scanned along the beam path, its effective focal length will change, since the incident intensity is changing. This change will be reflected in the intensity distribution at the aperture in the far field. The amount of energy transmitted by the aperture will depend on the sample location on the z -axis and on the sign of n_2 .

Consider, for example, a material with a positive n_2 . When the sample is far from the focus, the intensity in the sample is small, and since the sample is thin, the energy transmitted through the aperture remains approximately constant. As the sample gets nearer the focus, the intensity is high enough to produce a positive lensing effect. For $z < 0$, this lensing causes the beam to come to focus earlier, so that it diverges more rapidly in the far field. The result is that the aperture transmittance decreases. On the other hand, for $z > 0$, the positive lensing causes the beam divergence to decrease, resulting in an increased aperture transmittance. Near $z = 0$ a thin lens has little effect on a focused beam, and the aperture transmittance returns to its low intensity value. The net Z-scan yields a dispersion-shaped transmittance curve, as illustrated in Fig. 13. Obviously, a negative n_2 material will produce a similar curve, but with the peak and valley reversed about $z = 0$.

The aperture transmittance as a function of sample position depends on the magnitude and the sign of n_2 . This is the basis of the Z-scan technique.

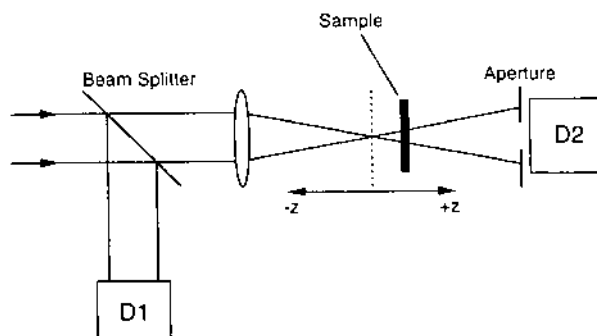


Figure 12 Schematic illustration of the Z-scan method. (From Ref. 4, © 1990 IEEE.)

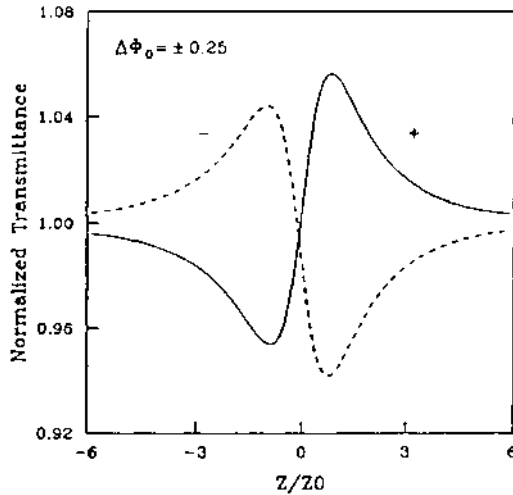


Figure 13 Illustration of the Z-scan normalized transmittance curve for an on-axis phase shift of $\Delta\Phi_0 = \pm 0.25$. The linear aperture transmittance is assumed to be $S = 0.01$ for this case. The quantity z_0 is equal to the Rayleigh range. (From Ref. 4, © 1990 IEEE.)

The nonlinear medium impresses a phase distortion on the electric field of the transmitted light. The field distribution after propagating to the far field was given in Chapter 6, Table 15. Using these formulas, the transmitted aperture power and/or energy can be computed. The objective of the Z-scan technique is to measure this transmittance and extract n_2 by inversion of the formula for the aperture transmittance.

The Z-scan has several advantages. Among these is its simplicity. As a single-beam technique, it has no difficult alignment other than keeping the beam centered on the aperture. As stated above, it can be used to determine both the magnitude and the sign of n_2 . The sign is obvious from the shape of the transmittance curve. Under rather general conditions that are easily fulfilled, the data analysis is quick and simple, making it a good method for screening new nonlinear materials. Under certain conditions, it is possible to isolate the nonlinear refractive and nonlinear absorptive contributions to the far-field transmittance. Thus, unlike most DFWM methods, the Z-scan can determine both the real and the imaginary parts of $\chi^{(3)}$. The technique is also highly sensitive, capable of resolving a phase distortion of $\sim \lambda/300$ in samples of high optical quality. Finally, the Z-scan can also be modified to study nonlinearities on different time scales as well as higher order contributions.

Disadvantages of the technique include the fact that it requires a high quality Gaussian TEM₀₀ beam for absolute measurements. The analysis must be

different if the beam is non-Gaussian. It is possible to relax the requirements on beam shape when relative measurements against a standard material are performed. Sample distortions or wedges, or a tilting of the sample during translation, can cause the beam to walk off the far-field aperture. This produces unwanted fluctuations in the detected signal. Even if these are kept under control, beam jitter will produce the same effect. A second reference arm can be employed to subtract out the effects of beam jitter. The technique cannot be used to measure off-diagonal elements of the susceptibility tensor except when a second nondegenerate frequency beam is employed. Such a technique is useful for measuring the time dependence of nonlinearities, but this detracts from the simplicity and elegance of the method. The introduction of a second beam of a different frequency requires careful alignment of the two beams, taking into account differences in spot sizes and focal positions due to chromatic aberration, and physical separation and filtering of the beams prior to detection.

A. Theory

It is assumed that a Gaussian TEM₀₀ beam is incident on a thin nonlinear medium (i.e., $L \ll z_R$, where z_R is the Rayleigh range of the beam in air). Hence the amplitude of the beam is unchanged by diffraction or nonlinear focusing within the medium. The amplitude may be changed by linear or nonlinear absorption (see Chapters 9 and 10). However, the phase of the incident wave is distorted, and the nonlinear phase $\Delta\varphi(r, z, t)$ impressed on the wave follows the shape of the incident beam:

$$\Delta\varphi(r, z, t) = \Delta\varphi(z, t) \exp\left[-\frac{2r^2}{w^2(z)}\right] \quad (24)$$

where

$$w(z) = w_0 \sqrt{1 + \left(\frac{z}{z_R}\right)^2} \quad (25)$$

$$\Delta\varphi(z, t) = \frac{\Delta\Phi_0(t)}{1 + (z/z_R)^2} \quad (26)$$

$$\Delta\Phi_0(t) = \frac{2\pi}{\lambda} n_2^I I_0(t) L_{\text{eff}} \quad (27)$$

$$L_{\text{eff}} = \frac{1 - \exp(-\alpha L)}{\alpha} \quad (28)$$

$I_0(t) = I(0, 0, t)$ is the on-axis intensity at focus, w_0 is the $1/e^2$ beam radius at focus, z is the sample position relative to the beam focus ($z = 0$), and α is the linear absorption coefficient.

The phase-distorted beam is propagated to the far-field aperture position z_a . One can obtain this by application of Huygens's principle. Sheik-bahae et al. [4] employ a Gaussian decomposition method. The resulting field distribution is given by the expressions in Chapter 6, Table 15 for the far field due to external self-focusing by a thin nonlinear medium, with z' in those expressions set equal to z_a .

The quantity of interest is the optical power transmitted by the aperture. An expression for this can be obtained in terms of the peak on-axis phase shift $\Delta\Phi_0(t)$, and the normalized quantities $\zeta = z/z_R$, $\zeta_a = z_a/z_R$, and $\rho = r_a/w_0$, where r_a is the aperture radius. The transmitted power is given by

$$\mathcal{P}_t[\Delta\Phi_0(t)] = \mathcal{P}_i(t)G(\zeta, t) e^{-\alpha L} \quad (29)$$

$$G(\zeta, t) = \sum_{m=0}^{\infty} \sum_{m'=0}^{\infty} (-1)^m h_{mm'} [i\Delta\Phi_0(t)]^{m+m'} \times \left\{ \frac{1 - \exp[-(1 + \zeta^2)(\kappa_m^* + \kappa_{m'})\rho_a^2]}{\kappa_m^* + \kappa_{m'}} \right\} \quad (30)$$

$$h_{mm'} = \frac{2(1 + \zeta^2)^{-(m+m')} e^{i(\theta_m - \theta_{m'})}}{m! m'! \sqrt{[(2m+1)^2(\zeta_a - \zeta)^2 + (1 + \zeta_a \zeta)^2][(2m'+1)^2(\zeta_a - \zeta)^2 + (1 + \zeta_a \zeta)^2]}} \quad (31)$$

$$\kappa_m = \frac{(2m+1) + i(1 + \zeta_a \zeta)(\zeta_a - \zeta)^{-1}}{(2m+1)^2(\zeta_a - \zeta)^2 + (1 + \zeta_a \zeta)^2} \quad (32)$$

$$\theta_m = \tan^{-1} \left[\frac{(2m+1)(\zeta_a - \zeta)}{1 + \zeta_a \zeta} \right] \quad (33)$$

The power incident on the sample is

$$\mathcal{P}_i(t) = \frac{\pi w_0^2}{2} I_0(t) \quad (34)$$

Finally, it is the optical energy and not the instantaneous power that is detected. So a normalized energy transmittance is defined by

$$T(\zeta) = \frac{\int_{-\infty}^{\infty} \mathcal{P}_i[\Delta\Phi_0(t)]dt}{S \int_{-\infty}^{\infty} \mathcal{P}_i(t)dt} \quad (35)$$

where S is the linear aperture transmittance (i.e., for $z \gg |z_R|$). Note that the normalized aperture radius can be given in terms of S by $\rho_a^2 = \frac{1}{2}(1 + \zeta_a^2) \ln(1 - Se^{\alpha L})^{-1}$.

The measured normalized energy transmittance from a Z-scan experiment can be fitted to Eqs. (29)–(35) to find n_2^l . However, for small on-axis phase shifts, it is possible to keep only terms linear in $\Delta\Phi_0(t)$ in Eq. (30). The normalized energy transmittance is then given as

$$T(\zeta) \approx 1 - \frac{e^{-\alpha L} F(\zeta)}{S} \langle \Delta\Phi_0 \rangle \quad (36)$$

where

$$\langle \Delta\Phi_0 \rangle = \frac{\int_{-\infty}^{\infty} \Delta\Phi_0(t) \mathcal{P}_i(t) dt}{\int_{-\infty}^{\infty} \mathcal{P}_i(t) dt} \quad (37)$$

and

$$F(\zeta) = 2\text{Re} \left\{ ih_{10}(\zeta) \left[\frac{1 - \exp[-(1 + \zeta^2)(\kappa_1^* + \kappa_0)\rho_a^2]}{\kappa_1^* + \kappa_0} \right] \right\} \quad (38)$$

Equation (36) can be written in a simple analytical form when the far field aperture is very small. For $S \ll 1$, this expression becomes

$$T(\zeta) \approx 1 - \frac{4\zeta}{(\zeta^2 + 9)(\zeta^2 + 1)} \langle \Delta\Phi_0 \rangle \quad (39)$$

Under appropriate experimental conditions, data can be fit to Eq. (39) to extract the nonlinear index coefficient.

Sheik-bahae et al. [4] have shown that a useful experimental parameter is the difference in the peak and valley transmittance values: $\Delta T_{p-v} = T(\zeta_p) - T(\zeta_v)$, where ζ_p and ζ_v give the z positions corresponding to the maximum and minimum $T(\zeta)$ values. It can be seen from Eq. (36) that this quantity is proportional to $\langle \Delta\Phi_0 \rangle$ for small on-axis phase shifts. Sheik-bahae et al. have determined through numerical analysis that for $|\Delta\Phi_0| < \pi$, the following approximation is valid to within 3%:

$$\Delta T_{p-v} \approx 0.405(1 - S)^{0.25} \langle \Delta\Phi_0 \rangle \quad (40)$$

For a Gaussian-shaped pulse, $\langle \Delta\Phi_0 \rangle = \Delta\Phi_0/\sqrt{2}$, while for a hyperbolic secant squared pulse, $\langle \Delta\Phi_0 \rangle = 2\Delta\Phi_0/3$, where $\Delta\Phi_0$ is now the peak on-axis phase shift. Thus a simplified analysis of the Z-scan measurement involves finding ΔT_{p-v} and using Eq. (40) to determine $\langle \Delta\Phi_0 \rangle$. Then, depending on the pulse shape, the nonlinear index coefficient is determined by

$$n_2^I \simeq a \frac{\lambda w_0^2}{L_{\text{eff}}} \frac{t_{\text{FWHM}}}{\mathcal{E}_i} \langle \Delta\Phi_0 \rangle \quad (41)$$

where t_{FWHM} is the measured pulse width (full width at half maximum), \mathcal{E}_i is the measured incident pulse energy corrected for Fresnel reflection at the front sample surface, and

$$a = \begin{cases} 0.38 & \text{Gaus} \\ 0.43 & \text{sech}^2 \end{cases} \quad (42)$$

Sheik-bahae et al. [4] have also determined that if the nonlinearity is cumulative (i.e., depends on the integrated intensity, such as a thermal nonlinearity), then

$$\langle \Delta\Phi_0 \rangle = \frac{2}{\lambda w_0^2} L_{\text{eff}} A \mathcal{E}_i \quad (43)$$

A is a proportionality constant determined by the physical mechanism of the accumulative nonlinearity. It can be determined by a measurement of ΔT_{p-v} using Eqs. (39) and (42), as long as $|\Delta\Phi_0| < \pi$.

Effects of nonlinear absorption. Nonlinear absorption will distort the shape of the Z-scan transmittance curve. Two-photon absorption will enhance the valley and reduce the peak. Saturable absorption will produce the opposite effect.

When two-photon absorption is present, it reduces the intensity in the sample as a function of the z -position of the sample. It also distorts the amplitude, which further affects the beam shape in the far field. To account for two-photon absorption, the previous theoretical expressions are modified by multiplying the factor $h_{mm'}$ [see Eq. (30)] by an additional factor $f_{mm'}$, where [4]

$$f_{mm'} = \prod_{n=0}^m \prod_{n'=0}^{m'} \left[1 - i(2n-1) \frac{\lambda\beta}{4\pi n_2^I} \right] \left[1 + i(2n'-1) \frac{\lambda\beta}{4\pi n_2^I} \right] \quad (44)$$

with $f_{00} = 1$, and β is the two-photon absorption coefficient (see Chapter 9). To recover n_2^I , β must be found from another measurement

One technique for determining β is to perform an open aperture Z-scan (see Chapter 10). Open aperture implies that all the energy transmitted by the sample

is collected and detected. Thus in this case the nonlinear transmittance is due to absorption loss only. As can be seen from Eq. (40), $\Delta T_{p-v} = 0$ when $S = 1$. Sheik-bahae et al. [4] have shown that, to within 10% accuracy, the pure refractive Z-scan transmittance curve can be recovered by a simple procedure, as long as $\beta L_{\text{eff}} I_0(0) \leq 1$ and $\lambda \beta / 4\pi n_2^l \leq 1$. The first condition can be met by an adjustment of the incident intensity. The second condition depends on the material. The procedure involves performing both an open and a closed aperture Z-scan. (“Closed” implies partially closed, as in a pure refractive Z-scan measurement.) The closed aperture data are then divided by the open aperture data. This will produce a Z-scan transmittance curve which approximates a purely refractive transmittance curve. In this way, β need not be known to obtain an estimate of n_2^l .

For a two-level system that exhibits saturable absorption, the intensity absorption coefficient is given by

$$\alpha(I) = \frac{\alpha_0}{1 + I/I_s} \approx \alpha_0(1 - I/I_s) = \alpha_0 - (\alpha_0/I_s)I \quad (45)$$

The approximation in Eq. (45) holds true when $I \ll I_s$, where I_s is the saturation intensity (see Chapter 6 or 9). The linear absorption coefficient in this case is designated by α_0 . Note that under the condition specified for the incident intensity, the term $-(\alpha_0/I_s)$ functions as an effective negative two-absorption coefficient (see, for example, [24]). Thus the discussion for two-photon absorption above applies, with the substitution $\beta \rightarrow -\beta$.

Higher order effects. Single- or two-photon absorption can populate new electronic states of the material under study. For example, this could be an excited bound state in a molecule, or a free carrier state in a semiconductor. A significant population redistribution will produce an additional change in the refractive index. The net change can be written as [25]

$$\Delta n = n_2^l I + \sigma_r N_e(I) \quad (46)$$

where σ_r is defined as the refractive index change per unit excited state charge per unit volume and has units of m^3 or cm^3 . $N_e(I)$ is the intensity dependent number density of charges in the excited state.

Assuming that the incident laser pulse width is short compared to all decay times of the excited state,

$$N_e(I) = \frac{\alpha}{\hbar\omega} \int_{-\infty}^t I(t') dt' \quad (47)$$

for single-photon pumped excited states, and

$$N_e(I) = \frac{\beta}{2\hbar\omega} \int_{-\infty}^t I^2(t') dt' \quad (48)$$

for excited states pumped by two-photon absorption. These expressions are now substituted into Eqs. (46) and (27) to compute the on-axis phase change.

When the excited state is pumped by single-photon absorption [26], the integrals are straightforward, and the average on-axis phase shift becomes

$$\langle \Delta\Phi_0 \rangle = \frac{2\pi L_{\text{eff}}}{\lambda} \left(n_2^I + \frac{\alpha\sigma_r \lambda t_{\text{FWHM}}}{2hc} b \right) a I_0 \quad (49)$$

where $a = 1/\sqrt{2}$ for Gaussian and $a = 2/3$ for hyperbolic secant squared pulses, and

$$b = \begin{cases} \sqrt{\frac{\pi}{2\ln 2}} & \text{Gaus} \\ \frac{3}{2\ln(1 + \sqrt{2})} & \text{sech}^2 \end{cases} \quad (50)$$

Hence the analysis follows as before, relating the measured ΔT_{p-v} to Eq. (49). However, now one obtains an effective nonlinear index coefficient. Generally, this formula is useful when characterizing molecules in solution. The n_2^I is due to the solvent, and the σ_r is due to the solute. The former parameter can be obtained by a Z-scan measurement of the neat solvent. The latter then is determined by a Z-scan measurement of the solution.

For the two-photon pumped case, the situation is not quite as simple. The nonlinear phase change is now given by [25]

$$\Delta\varphi(r, z, t) = \frac{2\pi n_2^I}{\lambda\beta} \ln[1 + q(r, z, t)] + \frac{\pi\sigma_r}{hc\beta} \int_{-\infty}^t H(t') dt' \quad (51)$$

where

$$H(t) = \alpha \ln[1 + q(r, z, t)] - \frac{q(r, z, t)}{L_{\text{eff}}} \left[1 - \frac{\exp(-\alpha L)}{1 + q(r, z, t)} \right] \quad (52)$$

and

$$q(r, z, t) = \beta I_i(r, z, t) L_{\text{eff}} \quad (53)$$

The field at the aperture cannot be determined by the Gaussian decomposition

method. Instead, Huygens's principle is applied, and the aperture field is [25]

$$\begin{aligned} E_a(\rho, t) &= i \frac{2}{(\zeta_a - \zeta)} \exp\left(i \frac{\rho^2}{\zeta_a - \zeta}\right) \\ &\times \int_0^\infty \rho' d\rho' E_t(\rho', \zeta, t) \exp\left(i \frac{\rho'^2}{\zeta_a - \zeta}\right) J_0\left(\frac{2\rho\rho'}{\zeta_a - \zeta}\right) \end{aligned} \quad (54)$$

$$E_t(\rho, \zeta, t) = \frac{E_i(\rho, \zeta, t) e^{-\alpha L}}{\sqrt{1 + q(\rho, \zeta, t)}} e^{i\Delta\varphi(\rho, \zeta, t)} \quad (55)$$

where

$$E_i(\rho, \zeta, t) = \frac{E_0(t)}{1 + \zeta^2} \exp\left[-\left(\frac{1 + i\zeta}{1 + \zeta^2}\right)\rho^2 - i\tan^{-1}\zeta\right] \quad (56)$$

The normalized Z-scan transmittance $T(\zeta)$ is once again determined as in Eq. (35). Assuming β is known, a two-parameter fit of the data using $T(\zeta)$ with Eqs. (51)–(56) is performed to extract n_2^l and σ_r .

Said et al. [25] have developed a simplified method to extract these parameters from Z-scan measurements performed at different pulse energies. The refractive index contribution from the two-photon pumped excited state is a cascaded $\chi^{(3)} : \chi^{(1)}$ effect, or an effective $\chi^{(5)}$ process. Assuming that the net on-axis phase shift can be written as a simple sum of the third order and effective fifth order phase shifts, the following procedure can yield estimates of n_2^l and σ_r to within 10% of the values determined by a fit to the complete theory.

For each pulse energy, the closed aperture scan is divided by the open aperture scan. Then, ΔT_{p-v} is determined. This quantity is divided by $0.406(1 - S)^{0.25}(2\pi L_{\text{eff}}/\lambda)aI_0$, where $a = 1/\sqrt{2}$ for Gaussian pulses and $a = 2/3$ for hyperbolic secant squared pulses. In computing L_{eff} , an effective linear absorption coefficient given by $\alpha + \beta I_0$ is used, where I_0 is the peak on-axis intensity determined by the pulse energy and spot size at the waist. This yields a simple equation for the on-axis index change, which is given by

$$\frac{\Delta n}{I_0} = n_2^l + C\sigma_r I_0 \quad (57)$$

where

$$C \cong \begin{cases} 0.14\beta t_{\text{FWHM}}/\hbar\omega & \text{Gaus} \\ 0.15\beta t_{\text{FWHM}}/\hbar\omega & \text{sech}^2 \end{cases} \quad (58)$$

Thus a plot of the quantity $\Delta n/I_0$ should be a straight line. Fitting the data to such an equation yields n_2^l as the intercept, with the slope proportional to σ_r .

Nondegenerate (two-color) Z-scan. Sheik-bahae et al. [27] have extended the Z-scan to the measurement of nondegenerate nonlinearities. This technique employs two beams of different frequencies (colors). One is used to pump the medium (the excitation beam), and the other is used to probe the nonlinearity. The transmittance of the probe through a far-field aperture is the main quantity measured.

This method may be used to measure the weak retardation nonlinear index:

$$(n_2^I)_{\text{ep}}^{(\text{weak})} \propto \chi_{\text{xyy}}^{(3)}(-\omega_p; \omega_p, \omega_e, -\omega_e) \quad (59)$$

where the subscript ep signifies the polarization states of the excitation and probe beams, respectively, which are given, for example, by y and x in Eq. (59). The peak on-axis phase shift for the two-color Z-scan is given by [27]

$$\Delta\Phi_{\text{ep}} = \frac{2\pi}{\lambda_p} (n_2^I)_{\text{ep}}^{(\text{weak})} I_{e0} \frac{1 - \exp(-\alpha_e L)}{\alpha_e} \quad (60)$$

where $I_{e0}(t)$ is the on-axis intensity of the excitation beam.

Full analytical expressions describing the Z-scan transmittance in terms of the different beam sizes, pulse widths, and focal lengths (due to chromatic aberration) can be obtained. The nonlinear phase shift $\Delta\varphi$ is given in terms of $I_e(\rho, \zeta, t)$, with $\zeta \rightarrow \zeta + \zeta_c$, where ζ_c corrects for the axial shift of the foci of the two beams (which can be ~ 1 mm) due to chromatic aberration [28]. The remaining terms in Eqs. (35) and (51)–(56) are given in terms of the probe field, with $\lambda_p, w_p, \zeta_p, \beta_{\text{ep}}$, and $(t_{\text{FWHM}})_p$ corresponding to probe quantities.

A time delay between the arrival of the two pulses can be accounted for by the substitution $t \rightarrow t - t_d$ in the expression for the excitation pulse, where t_d is the time delay. For one- or two-photon pumped population redistribution and decay effects, a model must be assumed to describe the kinetics of the system. The coupled system of equations, including those describing the Z-scan, must then be solved and fitted to the data to extract physical parameters [28]. This method can thus be useful for studying the dynamics of nonlinearities, but it is not as useful as DFWM when the frequencies of the two beams are degenerate. Coherence effects between the two beams then complicate the analysis [28].

In the case studied by Sheik-bahae et al. [27], where the probe beam was obtained from the excitation beam by second harmonic generation, they obtained an approximate expression for ΔT_{p-v} , analogous to that for the single beam Z-scan, which applies for a pure refractive two-color Z-scan with very small apertures and small chromatic aberration:

$$\Delta T_{p-v} \simeq 0.42(1 - S)^{0.35} \langle \Delta\Phi_{\text{ep}} \rangle \quad (61)$$

In this particular case, $\langle \Delta\Phi_{\text{ep}} \rangle = a\Delta\Phi_{\text{ep}}$, where $a = (3/2)^{-1/2}$ for Gaussian

pulses, and $a = 4/5$ for hyperbolic secant squared pulses. The reader should be cautioned, however, that these factors hold only for the specific case when the probe is generated from the pump by second harmonic generation.

When two-photon absorption is present, then the pure refractive Z-scan transmittance can be approximated by dividing a closed aperture scan by an open aperture scan. This procedure is valid when β_{ee} is negligible, but β_{ep} is not, as long as the two-photon absorption is not too large (see *Effects of nonlinear absorption* above).

Anisotropic media. The theory given above can be applied to probing $n_2(\theta) \sim \text{Re}[\chi_{\text{eff}}^{(3)}(\theta)]$ in anisotropic media, where θ is the angle between the polarization of the incident beam and a crystallographic axis of the medium [20]. A Z-scan is conducted in the usual manner. Then the sample is positioned at the z value corresponding to the peak in the transmittance curve. This peak transmittance is measured as the sample (or the incident polarization direction) is rotated about the propagation direction. The procedure is repeated for the position corresponding to the valley transmittance. A plot of $\Delta T_{p-v}(\theta)$ is then fitted to theoretical expressions of $\chi_{\text{eff}}^{(3)}(\theta)$. Various elements of the third order susceptibility tensor can be obtained in this manner, depending on the orientation of the sample.

Thick samples. Chapple et al. [29] have extended the analysis of the Z-scan to thick ($\geq z_R$) samples. (See also Ref. 30.) As illustrated in Fig. 14, the sensitivity of the measurement for a given peak incident intensity can be enhanced as the sample thickness is increased. However, the analysis of thick samples is computationally intensive. Consequently, in most cases, it is probably best to use thin samples for characterization of material nonlinearities.

Top-hat beams. With several lasers, it is not always possible to achieve a TEM₀₀ Gaussian spatial mode. However, it is often possible, if the beam profile is sufficiently smooth, to expand the beam and clip it with an aperture of diameter d to approximate a top-hat spatial profile. Zhao and Palfy-Muhoray [6] have analyzed the Z-scan using such a beam profile.

Defining the spot size as $w_0 = f/d$, where f is the focal length of the lens, the field at the focus of the lens can be written as

$$E(r, z = 0, t) = E_0(t) \frac{2J_1(\pi r/w_0)}{\pi r/w_0} \quad (62)$$

where $E_0(t)$ is the on-axis field at focus and J_1 is a first order Bessel function. The peak on-axis phase shift is defined as previously, and the analysis proceeds as before for an ordinary Z-scan. Fig. 15 shows the results for a top-hat Z-scan in CS₂. The normalized transmittance is actually about 2.5 times more sensitive than that obtained with a Gaussian beam.

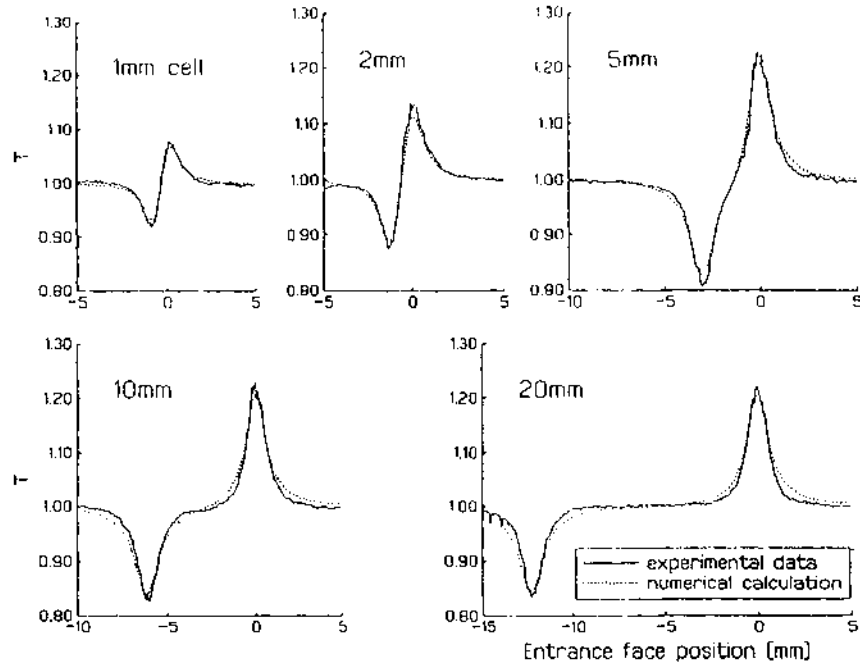


Figure 14 Z-scan theory and measurements in CS_2 as functions of sample thickness. (From Ref. 29.)

The relationship between $\langle \Delta\Phi_0 \rangle$ and ΔT_{p-v} is no longer linear in this case. However, for $|\Delta\Phi_0| < \pi$, Zhao and Palfy-Muhoray [6] have shown that a simple empirical relation given by

$$\langle \Delta\Phi_0 \rangle \approx 2.7 \tanh^{-1} \left[\frac{\Delta T_{p-v}}{2.8(1-S)^{1.14}} \right] \quad (63)$$

holds to within 1% of the extract theory.

EZ-scan. As described above, the Z-scan gives a simple measurement of the on-axis phase shift. This quantity is proportional to the sample thickness and thus is small for very thin samples. To improve the signal-to-noise ratio in these types of samples, the incident intensity must be increased. However, this is ultimately limited by the damage threshold of the sample. Consequently, samples much thinner than 1 mm cannot easily be characterized using Z-scan, even if they have large nonlinearities.

A need to characterize samples in thin film form has motivated the development of the EZ-scan [31]. In this technique, the far-field aperture is

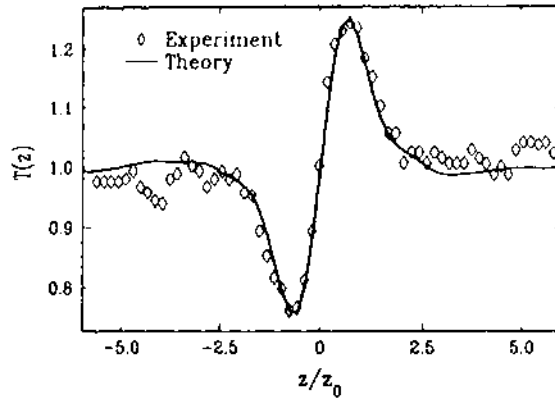


Figure 15 Results of a Z-scan measurement in CS_2 using a top-hat beam. (From Ref. 6.)

replaced by an obscuration, and the transmittance of the beam about this obscuration is measured. The image of the beam in the far field after this obscuration qualitatively resembles a solar eclipse. Hence the measurement method has been given the name eclipsed Z-scan (EZ-scan). The technique is based on the premise that the wings of the far-field beam that has been focused through a nonlinear medium are more proportionally distorted than the center of the beam. Thus a measurement of the transmittance about an obscuration should provide a more sensitive measure of the nonlinear phase distortion than a measurement of the transmittance through an aperture.

The analysis of the EZ-scan is directly analogous to that of the Z-scan. The normalized transmittance about the obscuration can be obtained with the help of Eqs. (24)–(33) by replacing the quantity in curly brackets in Eq. (30) by

$$\frac{\exp[-(1 + \zeta^2)(\kappa_m^* + \kappa_{m'}\rho_0^2)]}{\kappa_m^* + \kappa_{m'}} \quad (64)$$

where $\rho_0 = r_o/w_0$, with r_o being the radius of the obscuration, typically $1.5\text{--}2.0 \times$ the far-field beam radius in the linear regime ($S \sim 95\text{--}99\%$).

The peak–valley normalized transmittance again has a nearly linear dependence on the on-axis phase shift for $|\Delta\Phi_0| \leq 0.2$. Xia et al. [31] have determined this relationship to be

$$\Delta T_{p-v} \approx 0.68(1 - S)^{-0.44}\langle|\Delta\Phi_0|\rangle \quad (65)$$

where S is now the amount of light *blocked* in the linear regime.

B. Experimental

A generic experimental diagram for a Z-scan measurement is shown in Fig. 16. The choice of lasers depends primarily on the material under study and the physical mechanisms being explored. However, to avoid cumulative (multiple pulse) thermal effects, especially in linearly absorbing samples, the laser PRF should be quite low (< 1 Hz) [24].

The laser beam used in the experiment needs to be carefully characterized. One of the most critical measurements is spot size. This can be accomplished by scanning the beam transversely in two orthogonal dimensions with a knife edge, pinhole, or slit, and measuring the transmitted energy. Fitting these scans to the appropriate mathematical function (e.g., Gaussian, error function, Airy disc, etc.) will yield the beam radius (e.g., $1/e^2$ value for Gaussian beams). These measurements should be performed at several z positions before and after the focal point (without the sample in place) so that the focal point, beam waist, and Rayleigh range can be uniquely determined. For a Gaussian beam, the measured beam radius should follow a $(1 + z^2/z_R^2)^{1/2}$ dependence. An additional check on the beam parameters can be made by performing a Z-scan on a reference Kerr material such as CS₂. For a Gaussian beam, the difference in z positions of the sample for the peak and valley transmittance should be $\Delta z_{p-v} \approx 1.7z_R$ [4], and for a top-hat beam, $\Delta z_{p-v} \approx 1.4z_R$.

Two other critical parameters of the laser are the pulse shape and width (full width at half-maximum). These can be determined by monitoring the pulse with a fast photodiode and transient digitizer (for nanosecond pulses), or using a streak camera (for nanosecond or picosecond pulses) or autocorrelator (for picosecond and femtosecond pulses). Pulses from stable lasers often have approximate Gaussian or hyperbolic secant squared shapes. The pulse waveform from the instruments listed above can be fitted to these mathematical formulas to characterize t_{FWHM} accurately and also determine the correct numerical factors related to pulse shape to use in the formulas for data analysis. If the pulse width is subject to variations, it is wise to continuously monitor the pulse shape during the experiment. An average pulse width can then be determined. Data corresponding to pulse widths that differ from the average by more than half a standard deviation could then be discarded. Tighter or weaker constraints can be adopted depending on the level of accuracy desired.

Incident and transmitted energy measurements should be made with energy meters or photodiodes calibrated to energy meters. Since the incident intensity is assumed to vary only with z in a Z-scan measurement, it is imperative that the pulse energy remain constant during the Z-scan. Averages of the pulse energy (incident and transmitted) for several pulses (10–100) at each z position will reduce the scatter in the data. Again, data for which the incident pulse energy

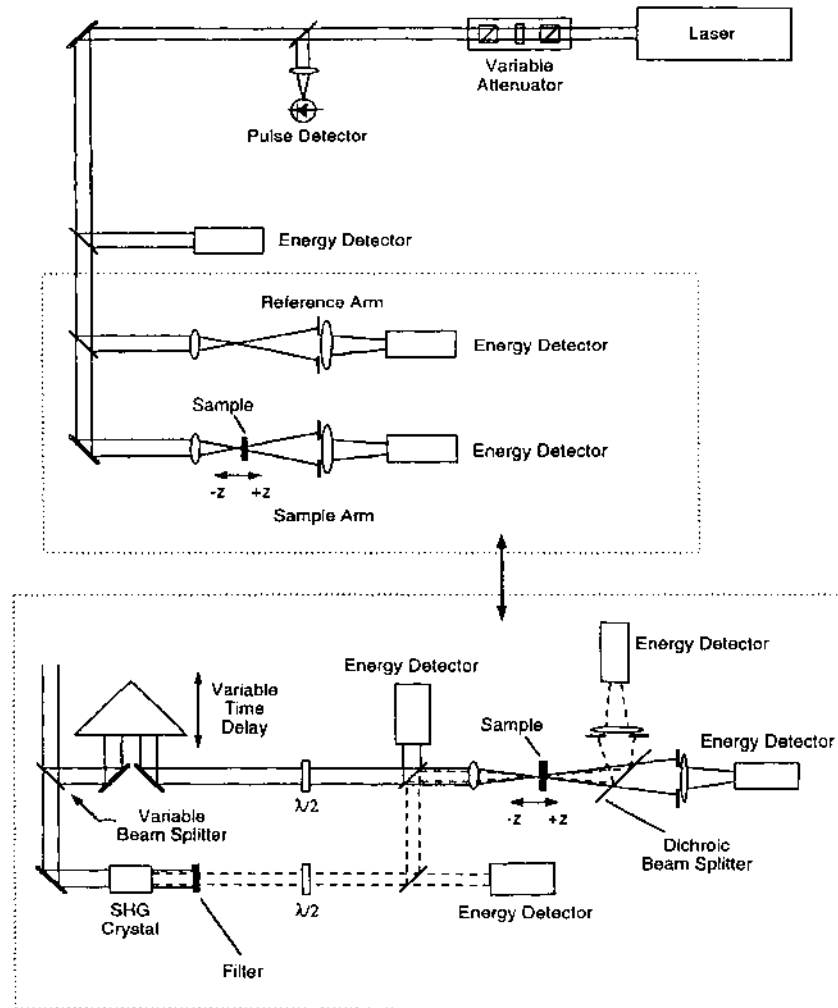


Figure 16 Schematic diagram of Z-scan experiment. The top figure represents a generic Z-scan. The bottom diagram (in the dashed box), taken from Ref. 27, would replace the generic setup to perform time resolved two-color Z-scan measurements.

deviates from the mean by some value (say, half a standard deviation) can be discarded to improve the accuracy.

Another source of scatter in the data is beam pointing jitter during the experiment. Using a reference arm, as shown in Fig. 16, with identical lens and aperture (or obscuration, for EZ-scan) as the sample arm, can reduce this scatter.

Each measurement is normalized to the transmittance in the reference arm to factor out fluctuations due to beam pointing jitter. This is particularly useful for EZ-scan measurements, since the linear transmittance is small in such an experiment, and small fluctuations can produce greater errors in the measurements.

The linear aperture transmittance S needs to be established. This can be accomplished by making aperture transmittance measurements for $|z| \gg z_R$, or performing a Z-scan at a very low pulse energy. In either case, it should be determined that the transmittance is relatively constant as a function of z , so that the linear regime is established and S is thus a good number. The value of S will automatically account for Fresnel reflections and linear absorption losses.

A low-energy Z-scan can also be useful for establishing a background signal. This is particularly helpful if the sample has poor optical quality (e.g., surface or volume imperfections that produce scattering of the beam). The low-energy scan data are then subtracted from the high-energy scan data prior to data analysis [4]. With proper attention to calibration of all significant experimental parameters, an overall accuracy of 10–15% in the measured n_2^I is achievable.

It is usually wise to perform both closed and open Z-scans to account properly for any nonlinear absorption that may be present. When making an open aperture Z-scan, it is important to assure that all of the transmitted energy is collected and directed to the detector. A large area lens situated after the aperture can be useful for both open and closed aperture scans if the detector area is small.

It is not always apparent from a single Z-scan measurement whether the nonlinearity being probed is instantaneous (i.e., Kerr-like) or cumulative (e.g., thermal). Performing the experiments using different pulse widths, but equal energy, can help determine if the nonlinearity is intensity or fluence dependent [26]. Time delay measurements are also useful for studying the time dependence of the nonlinearity and determining the physical mechanisms at work.

Relative Z-scan measurements can be made by first performing a Z-scan on a reference material. An example of such Z-scan reference data using toluene is given in Fig. 17. Following Z-scan measurements on the sample, the peak–valley transmittance for both sample and reference can then be used to determine the nonlinear index coefficient for the sample using

$$(n_2^I)_s = \frac{\mathcal{E}_r}{\mathcal{E}_s} \frac{1 - R_r}{1 - R_s} \frac{L_{\text{eff}}^r}{L_{\text{eff}}^s} \frac{\Delta T_{\text{p-v}}^s}{\Delta T_{\text{p-v}}^r} (n_2^I)_r \quad (66)$$

where the subscripts s and r refer to sample and reference quantities, respectively.

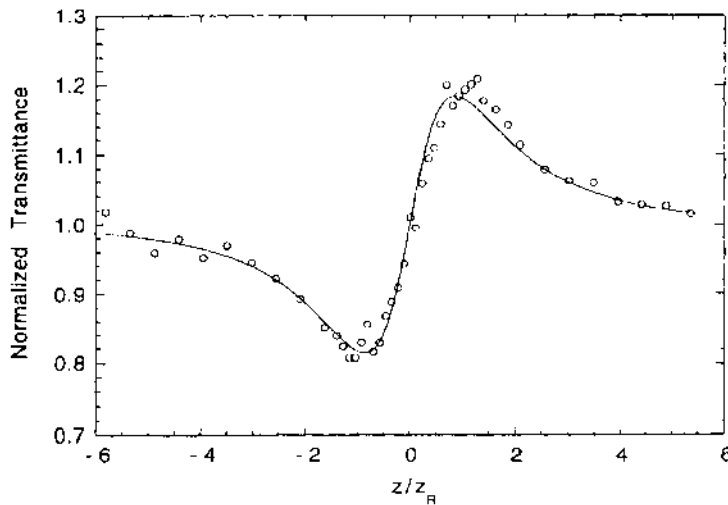


Figure 17 Example of a Z-scan in toluene, which can be used as a reference material in relative Z-scan measurements.

The energy ratio in this equation accounts for the fact that different pulse energies may be required in each Z-scan to optimize the signal-to-noise ratio and operate in a regime where the linear relation between peak–valley transmittance and on-axis phase shift is valid. R is the front-surface Fresnel reflectance and properly accounts for the actual intensity inside the sample and reference materials.

Experimental considerations are the same as described above when characterizing anisotropic samples. In addition, once the peak and valley transmittance positions have been established, the sample is placed at these positions for further characterization. These measurements consist of monitoring the aperture transmittance as the sample is rotated about its normal axis. (Alternatively, the incident beam polarization could be rotated.) The angular dependence is fitted to a theoretical formula that depends on the experimental geometry and structure of the sample.

A technique for adding a two-color time delay capability to the ordinary Z-scan method is illustrated in Fig. 16. In this example, developed by Sheik-bahae et al. [27,28], the second color probe beam is produced by second harmonic generation. The probe can actually be at any wavelength. The intensity ratio and beam polarization can be controlled by the appropriate use of beam splitters and half-wave plate/polarizer combinations. Pulse widths and spot sizes for each beam must be carefully measured in this technique. An achromatic lens will reduce the chromatic aberration, but the axial shift in focus for the two beams

should still be carefully measured and used in the data analysis (see *Nondegenerate Z-scan* above).

A zero time delay closed aperture Z-scan will determine the peak and valley transmittance positions. If nonlinear absorption is present, the closed aperture Z-scan should be normalized to an open aperture scan. These scans can be performed simultaneously by placing a beam splitter in the transmitted probe beam and directing the split beams to two different detectors, one with and one without an aperture. The sample is then set alternately at the peak and valley transmittance positions, and transmittance measurements at a constant z position are then performed as the time delay t_d between the pump and the probe is scanned. The difference between the two sets of data determines $\Delta T_{p-v}(t_d)$, which is proportional to $\Delta n(t_d)$. This quantity is then used to study the time dependence of the nonlinearity.

Wang et al. [28] give some precautions when performing time delay two-color Z-scan measurements. To maximize the time delay used in the experiment, the beam divergence prior to the focusing lens must be minimized. This optimizes the range over which the delayed beam will have an approximately constant focal position and waist size. Spatial overlap of the two beams is also crucial. This can be optimized by propagating the two beams over a long distance through several apertures to assure that they are propagating collinearly. Similarly, the transmission through several apertures prior to focus after the lens can be checked to assure alignment. Wang et al. made final fine adjustments in the spatial overlap of the two beams by maximizing the probe transmittance change when the two beams propagate through a nonlinear absorber placed at the common focus.

Finally, it should be noted that multiple internal sample reflections can modify the Z-scan measurements. Sutherland [32] has modeled these étalon effects and describes potential anomalies that can appear in the data.

IV. OPTICAL KERR GATE AND ELLIPSE ROTATION

These two phenomena are based on optically induced birefringence in third order isotropic media and were discussed in Chapter 6, Section III.A. Some of the earliest characterization techniques were based on these effects [33–35].

The nonlinearly induced birefringence affects the polarization properties of optical waves propagating through the medium. The objective of these methods is to transmit light of a known polarization state through the nonlinear material and then measure the resultant intensity of the light that passes through a final polarizer. The nonlinear susceptibility is obtained by inversion of the formulas given in Chapter 6, Table 6.

Although these are straightforward measurement techniques, neither one can independently determine all of the tensor components of $\chi^{(3)}$. Two different experiments (optical Kerr gate and ellipse rotation) are required to fully characterize the material. The experiments have a simpler alignment than DFWM but are not as simple as the Z-scan. However, under general conditions the data analysis is rather simple, and the experiments readily lend themselves to time resolved (pump–probe time delay) and nondegenerate frequency measurements. One of their greatest utilities is the ability to measure both the real and the imaginary parts of $\chi^{(3)}$ as functions of optical frequency. These subjects will be taken up in Chapter 10 under the topic of nonlinear absorption measurements.

A. Theory

Kerr gate. The optical Kerr gate consists of a third order nonlinear medium placed between crossed polarizers. A strong pump beam at frequency ω propagates collinearly or at a small angle with respect to a weak probe beam at frequency ω' . The polarization of the probe is typically set at 45° with respect to the pump polarization.

It is assumed that the nonlinear refractive index change is due only to the pump beam. The birefringence induced by this beam impresses a phase difference between the two orthogonal probe components as they propagate through the medium. The phase difference after propagation through a medium of length L is given by

$$\Delta\varphi(\omega') = \frac{3\pi L}{\epsilon_0 n_0^2 c \lambda_{\omega'}} [\chi_{xxyy}^{(3)}(-\omega'; \omega', \omega, -\omega) + \chi_{yyxx}^{(3)}(-\omega'; \omega', \omega, -\omega)] I_\omega \quad (67)$$

where I_ω is the pump intensity. For a sufficiently small nonlinear phase shift and negligible pump loss, the intensity of the probe transmitted by the final polarizer is

$$I_{\omega'}(L) = I_{\omega'}(0) \left(\frac{\Delta\varphi}{2} \right)^2 \quad (68)$$

In a typical experiment, it is the pulse energy and not the intensity that is measured. Forming the energy transmittance ratio, from Eqs. (67) and (68),

$$T = \frac{\mathcal{E}_{\omega'}(L)}{\mathcal{E}_{\omega'}(0)} \propto C \mathcal{E}_\omega^2 \quad (69)$$

The constant C is given by

$$C = \left[\frac{3\pi L}{2\epsilon_0 n_0^2 c \lambda_{\omega'}} (\chi_{xxyy}^{(3)} + \chi_{yyxx}^{(3)}) \right]^2 \quad (70)$$

Thus measuring T as a function of \mathcal{E}_ω and fitting the data to Eq. (69) will determine C to within a proportionality constant. Similar measurements can be performed on a reference material for which $\chi_{xxyy}^{(3)}$ and $\chi_{xyyx}^{(3)}$ are known. Then the susceptibility of the sample is determined from

$$|\chi_{xxyy}^{(3)} + \chi_{xyyx}^{(3)}|_s = \left(\frac{n_0^s}{n_0^r}\right)^2 \frac{L_r}{L_s} \left(\frac{C_s}{C_r}\right)^{1/2} |\chi_{xxyy}^{(3)} + \chi_{xyyx}^{(3)}|_r \quad (71)$$

where the subscripts and superscripts s and r refer to sample and reference, respectively. If there is appreciable absorption, then the right-hand side of Eq. (71) is multiplied by $\exp[\alpha_\omega^s L_s - \alpha_\omega^r L_r]$, and the sample–reference length ratio becomes a ratio of effective lengths, i.e., $L_{\text{eff}} = [1 - \exp(-\alpha_\omega L)]/\alpha_\omega$, for both the sample and reference.

For an isotropic material, $\chi_{xxxx}^{(3)} = \chi_{xxyy}^{(3)} + \chi_{xyxy}^{(3)} + \chi_{xyyx}^{(3)} = 2\chi_{xxyy}^{(3)} + \chi_{xyyx}^{(3)}$, where the last equality follows from the equality $\chi_{xyxy}^{(3)} = \chi_{xyyx}^{(3)}$. Also,

$$\frac{\chi_{xyyx}^{(3)}}{\chi_{xxyy}^{(3)}} = \begin{cases} 6 & \text{molecular reorientation} \\ 1 & \text{nonresonant electronic} \\ 0 & \text{electrostriction} \end{cases} \quad (72)$$

for the physical mechanisms given that dominate the process [36]. Thus if one process is dominant, and if one can independently measure $\chi_{xyyx}^{(3)}$, then $\chi_{xxxx}^{(3)}$ can be uniquely determined. This is possible by performing a polarization ellipse rotation experiment.

Ellipse rotation. This is single-beam experiment performed with an elliptically polarized wave. For example, consider a linearly polarized wave incident on a quarter-wave plate with its direction of polarization making an angle θ with respect to the fast axis of the wave plate. This creates an elliptically polarized beam with left-circularly and right-circularly polarized components E_+ and E_- , respectively. (Another way to create an elliptically polarized beam is by use of a Fresnel romb [34] or an eighth-wave plate [33].) The induced circular birefringence in the medium is proportional to (see Chapter 6, Table 6) $|E_+|^2 - |E_-|^2 = |E_0|^2 \sin(2\theta)$, where E_0 is the amplitude of the incident linearly polarized wave. The beam transmitted through the nonlinear medium is passed through a second quarter-wave plate oriented identically to the first. Finally, the beam is passed through a polarizer oriented for extinction of the beam in the absence of the nonlinear sample. For a small induced circular birefringence, the rotation θ_c of the polarization ellipse is small. Thus the transmittance through

the final polarizer can be written as

$$T \simeq \theta_c^2 = \left(\frac{3\pi L}{2\epsilon_0 n_0^2 c \lambda} |\chi_{xyyx}^{(3)}| I_0 \sin 2\theta \right)^2 \quad (73)$$

Measuring pulse energies, the energy transmittance ratio is then

$$T = \frac{\mathcal{E}_t}{\mathcal{E}_0} \propto C \mathcal{E}_0^2 \quad (74)$$

where

$$C = \left(\frac{3\pi L}{2\epsilon_0 n_0^2 c \lambda} |\chi_{xyyx}^{(3)}| \sin 2\theta \right)^2 \quad (75)$$

Thus measuring T as a function of \mathcal{E}_0 and fitting the data to Eq. (74) will determine C to within a proportionality constant. Performing the same measurements on a reference material will determine the sample nonlinear susceptibility through the relation

$$|\chi_{xyyx}^{(3)}|_s = \left(\frac{n_0^s}{n_0^r} \right)^2 \frac{L_r}{L_s} \left(\frac{C_s}{C_r} \right)^{1/2} |\chi_{xyyx}^{(3)}|_r \quad (76)$$

Notice that the optical Kerr gate and the ellipse rotation methods yield the modulus of $\chi^{(3)}$ components. Techniques have also been developed that separately measure the real and imaginary parts of $\chi^{(3)}$ using the optical Kerr gate method. These will be discussed in Chapter 10.

B. Experimental

Optical Kerr gate. A typical setup for an optical Kerr gate experiment is illustrated in Fig. 18. The pump and probe frequencies can be obtained from two different lasers (the probe can even be a cw laser, such as a HeNe laser), or they can be derived from the same laser by splitting the output and sending one beam through a frequency converter (e.g., an SHG cell or a Raman shifter). In the latter case, the residual pump should be filtered from the probe beam.

An attenuator (neutral density filters or a half-wave plate/polarizer combination) controls the incident pump intensity, which is varied in the experiment.

Half-wave plates and polarizers in the pump and probe paths set the desired polarization of each beam incident on the sample. Normally, the probe polarization is set at a 45° angle with respect to the pump polarization.

The pump and probe can be aligned collinearly through the sample by an appropriate beam splitter, or they can be made to cross in the sample at a small

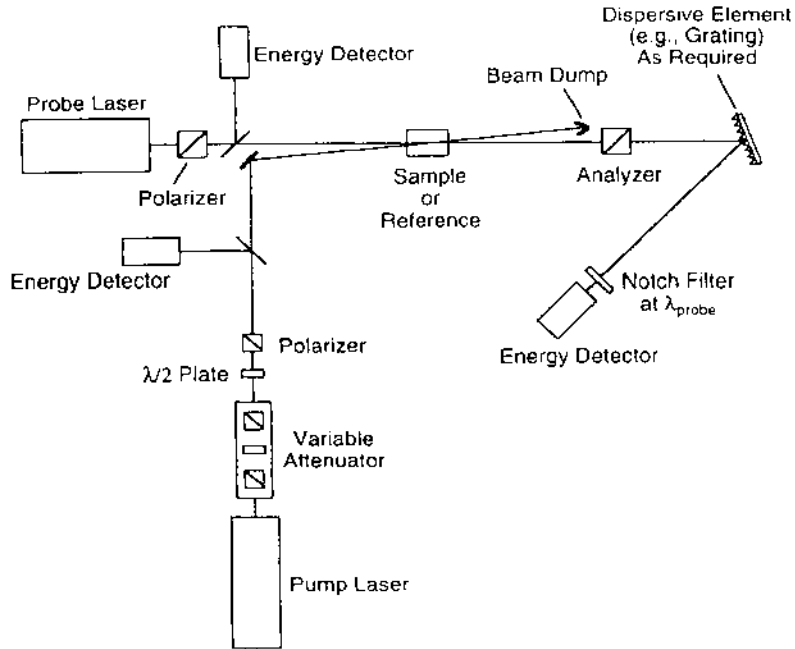


Figure 18 Schematic diagram of an optical Kerr gate experiment.

angle. In either case, they should achieve good spatial and temporal overlap. It is important that the degree of overlap be the same in both the sample and the reference. Also, one pulse can be delayed with respect to the other to study the time dependence of the nonlinearity.

The analyzer (final polarizer) is set to be crossed to the incident probe polarization. Then at low pump energy, the probe energy detector sees a null. As the pump energy is increased, the probe detector will give a signal that increases quadratically with pump energy. If the pump and probe cross at an angle, then the two beams can be separated spatially before detection. If they are collinear, then a frequency dispersion device (e.g., a grating) must be used to separate them spatially. In either case, a notch transmission filter (Fabry–Perot type) should be placed in front of the probe detector to filter out scattered pump light.

Three detectors are required to measure the incident pump and probe energies and the final transmitted probe energy. The probe energy transmittance ratio as a function of pump energy is then fitted to an equation of the form of Eq. (69) for data analysis and extraction of the $\chi^{(3)}$ values.

One of the utilities of the optical Kerr gate technique is that the probe can be a continuum of frequencies. An approach that is possible with short pulses

(picosecond to subpicosecond) is to focus the probe beam through a water or heavy water mixture, or any other suitable liquid, to generate a white light continuum prior to it passing through the sample. The transmitted probe is then sent to a spectrograph and optical multichannel analyzer to separately measure the transmittance for each resolvable frequency interval of the spectrograph. This will yield a measurement of the nondegenerate $\chi^{(3)}$ values as functions of frequency over a fairly large frequency range. If the pump is sufficiently intense, then it need not be focused into the sample. Under these conditions, there is no chromatic aberration that needs to be accounted for as in the two-color Z-scan.

Ellipse rotation. This single-beam experimental technique is illustrated in Fig. 19. An attenuator again sets the incident laser energy that is varied in the experiment. A half-wave plate and/or a polarizer can be used to set the pump polarization. This is incident on a birefringent element that sets the desired elliptical polarization incident on the sample. For example, this element can be a quarter-wave plate (see Section IV.A above), an eighth-wave plate, or a Fresnel romb.

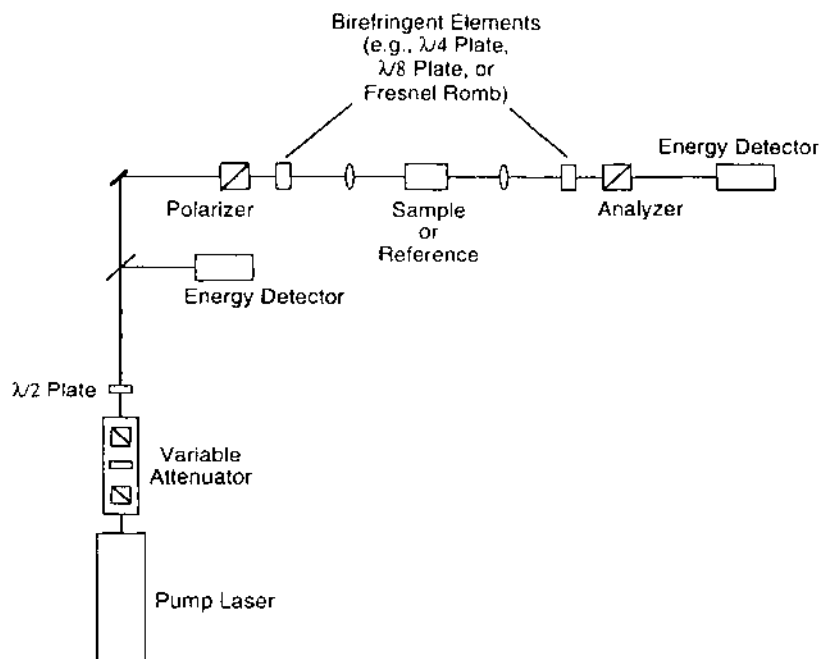


Figure 19 Schematic diagram of a nonlinear polarization ellipse rotation experiment.

The beam is then passed through the sample. It can be focused if desired to increase the intensity. The sample should have a very small intrinsic birefringence. For liquid samples in a glass cell, the cell windows need to be free from stress induced birefringence.

The output beam is then directed to another birefringent element identical to the input birefringent element. For low incident energies, this would render the beam linearly polarized. The analyzer (output polarizer) is set in a crossed position to this polarization direction so that the output energy meter detects a null value. As the incident energy increases, the output signal will increase quadratically with input. The output-to-input ratio as a function of incident energy can then be fitted to an equation of the form of Eq. (74) for data analysis to extract the $\chi^{(3)}$ value.

V. INTERFEROMETRIC METHODS

Several interferometric methods have been developed for characterizing the nonlinear index of refraction. All are based on the interference of at least two beams, one of which experiences an intensity dependent phase delay due to propagation through a nonlinear medium. Two examples are discussed here. Other examples can be found in the literature (see, for example, Refs. [38–40].)

A. Nonlinear Mach–Zehnder Interferometer

Moran et al. [2] developed a time resolved Mach–Zehnder interferometric method, illustrated in Fig. 20, for characterizing third order materials. The sample is placed in one arm and a reference material in the other arm of the interferometer. The objective is to measure the interference fringe distortion as the intensity is increased. This is done in the following way.

First, the optical path lengths in the two arms, in the linear regime, are set equal by monitoring the pulse arrival time from each arm at the interference plane with a streak camera. In the linear regime, the interference fringes form in parallel planes as illustrated in Fig. 21. Note that the output of the streak camera shows time in one sweep dimension and distance in the other sweep dimension. The time dimension runs parallel to the fringes.

Now as the intensity is increased, each arm experiences a nonlinear phase delay that follows the shape of the pulse, assuming the nonlinear response is instantaneous. If one arm experiences a larger delay, then the fringes will shift in the camera plane, following the shape of the pulse. The fringe shift will be negligible near the beginning and end of the pulse, with a maximum at the pulse peak. The result is that the fringe pattern will be bowed, either up or down,

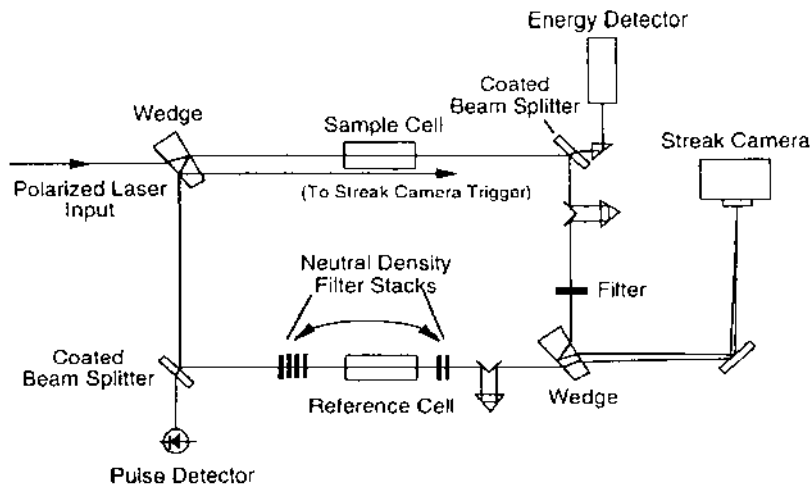


Figure 20 Schematic diagram of a nonlinear Mach-Zehnder experiment for characterizing the third order susceptibility of materials relative to a reference material. (From Ref. 2, © 1975 IEEE.)

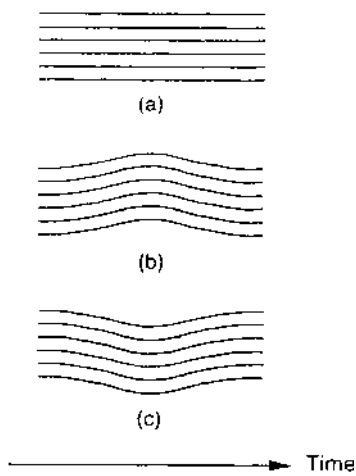


Figure 21 Illustration of the time resolved interference fringes as seen on a streak camera for the experiment in Fig. 20. (a) The optical path length in the two arms of the interferometer are exactly equal. (b) The nonlinear phase delay in the sample arm is greater than the nonlinear phase delay in the reference arm. (c) The nonlinear phase delay in the sample arm is less than the nonlinear phase delay in the reference arm.

depending on which arm experiences the larger phase shift. This is illustrated in Fig. 21.

Calibrated neutral density filters are positioned in the reference arm of the interferometer. The goal is to rearrange these filters from in front to in back of the reference material, as shown in Fig. 20, or vice versa, until the fringe pattern shows no distortion. Note that this changes only the intensity in the reference material but not the net intensity in the reference arm.

When there is no distortion in the fringe pattern, the nonlinear phase shift $\varphi_{NL}(t) = (2\pi L/\lambda)n_2^I I(t)$ of each arm is equal for all times. Then, if the spot size of the beam in each arm is the same, it is not necessary to measure the absolute intensity but only the pulse energy in each arm. The nonlinear index is then simply given by

$$(n_2^I)_s = \frac{\mathcal{E}_r L_r}{\mathcal{E}_s L_s} (n_2^I)_r \quad (77)$$

where the subscripts s and r signify sample and reference quantities, respectively; \mathcal{E} is the pulse energy, and L is the material thickness.

This method, like all interferometric methods, requires precise alignment of the beams to obtain good quality fringes. It also requires careful tweaking to equalize the optical path length in each arm. However, once aligned, the measurement and data analysis are straightforward. The measurement accuracy is limited by the resolution of the camera to measure the fringe shift. According to Moran et al. [2], a relative accuracy of 10% is possible.

B. Nonlinear Jamin Interferometer

This interferometric technique [7] is illustrated in Fig. 22. A laser beam is split into weak probe and strong pump beam. The probe beam is appropriately polarized and further split into two beams at the first mirror of the interferometer as shown in the figure. These two beams traverse the sample in parallel propagation, with equal path lengths, and then recombine at the second mirror of the interferometer. Their interference is manifested as fringes in the final camera plane.

The pump beam, appropriately polarized, is also passed through the sample and crosses one probe beam at a small angle. The angle is such that the intersection regime of these two beams is longer than the sample thickness. Thus the pump induces a nonlinear phase shift of one probe relative to the other probe. This shows up as a shift of the interference fringes in the camera plane.

With the pump and probe coincident in time, a measurement of the relative fringe displacement is made: $\delta = \Delta\Lambda/\Lambda$, where Λ is the fringe spacing. This yields the net index modulation on the one probe beam, which is related to

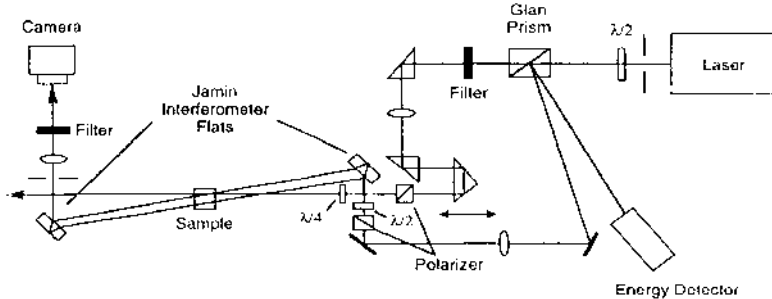


Figure 22 Schematic diagram of a nonlinear Jamin interferometer for measuring the nonlinear refractive index in materials. (From Ref. 7.)

the nonlinear index coefficient by

$$\Delta n = \frac{\lambda}{L} \delta = (n_2^I)^{(\text{weak})} I_{\text{pump}} \quad (78)$$

where L is the sample thickness and I_{pump} is the pump intensity.

Since this is a pump–probe method, it is the weak retardation nonlinear index that is measured (see Chapter 6, Section I). This method requires the absolute calibration of the pump intensity. The absolute probe intensities, however, are not required.

VI. CHIRPED-PULSE TWO-BEAM COUPLING

Two-beam coupling refers to phenomena where two beams interact in a nonlinear medium resulting in an exchange of energy between them. This subject was treated in Section III.C of Chapter 6. Two-beam coupling can occur in a general pump–probe experiment. In such an experiment, a strong pump induces an effect in a nonlinear medium, the results of which are probed by a second weak beam. These types of methods are often used to characterize the nonlinear absorption properties of materials, as described in Chapter 10. To observe transient effects and decay times of nonlinear excitations, the probe pulse is delayed in time with respect to the pump, and the evolution of the optical properties of the medium are monitored as the delay time is varied. In general, the delay time is swept from negative values (i.e., probe arriving before pump) to positive values to establish the time origin (the exact overlap of the two pulses). The evolution of the system is followed for long delay times, with the two pulses well-separated in time. For the short time when the pulses overlap, however, the nonlinearity can

induce an interaction between them. For example, if the frequencies of the pulses are unequal and the medium has a positive nonlinear index coefficient with a finite response time, then by the results of Chapter 6, Section III.C, energy will flow from the higher frequency pulse to the lower frequency pulse.

Consider the case of pulses with a positive linear chirp. The leading edge of such a pulse is red-shifted from the center frequency, and the trailing edge is blue-shifted. When the probe precedes the pump, its instantaneous frequency at any part of the pulse is higher than that of the corresponding point of the pump, and thus energy flows from the probe to the pump. At the point of exact pulse overlap, the frequencies are everywhere degenerate, and there is no coupling between the pulses. As the probe trails the pump, its instantaneous frequency is lower, and hence energy flows from the pump back to the probe. Thus, if the probe energy is monitored as a function of delay time, it will trace out a dispersion-like curve. An analysis of this curve can yield the nonlinear coefficients of the medium and, in certain circumstances, the response time of the medium.

Tang and Sutherland [41] presented a general theory for pump–probe experiments using chirped pulses, where $\chi^{(3)}$ is, in general, complex. Sutherland et al. [42] reported measurements of $\chi^{(3)}$ for organic materials using this technique. Dogariu et al. [43] conducted an extensive study of two-beam coupling with chirped pulses in a medium with a real $\chi^{(3)}$, using various combinations of the polarization of the two beams. The measurement technique presented here will assume the pump and probe are orthogonally polarized and will consider only a real $\chi^{(3)}$. An extension of the method to complex $\chi^{(3)}$ will be presented in Chapter 10.

A. Theory

Consider two beams of orthogonal polarization, derived from the same laser, that cross at an angle 2θ in a third order nonlinear medium. The beams consist of chirped pulses with instantaneous frequency $\omega(t) = \omega_0 + bt$, where b is the chirp coefficient. The pump (excitation) pulse has energy \mathcal{E}_e and is much stronger than the probe pulse. The probe pulse is delayed from the pump pulse by a time τ_d , and the time response of $\chi^{(3)}$ is assumed to follow a Debye relaxation equation with time constant τ_m . The two-beam coupling coefficient is given by

$$\gamma(\tau_d) = \frac{6\pi}{\epsilon_0 n_0^2 c \lambda \cos\theta} (\chi_{xxyy}^{(3)} + \chi_{xyxy}^{(3)}) \left[\frac{2b\tau_m\tau_d}{1 + (2b\tau_m\tau_d)^2} \right] \quad (79)$$

The probe intensity satisfies the following equation:

$$\frac{dI_p}{dz} = \gamma(\tau_d) I_e(t + \tau_d) I_p(t) \quad (80)$$

where the subscripts e and p stand for excitation and probe, respectively. The laser is assumed to have Gaussian spatial and temporal profiles so that $I_{e,p}(r, t) \propto \exp[-2(r/w_{e,p})^2]\exp[-(t/\tau_L)^2]$, where $2\tau_L$ is the laser 1/e pulse width. The beams may have different spot sizes, but they have the same time dependence since they are derived from the same laser. The pulse energies are measured, and the probe pulse transmittance is defined by $T = \mathcal{E}_p(L)/\mathcal{E}_p(0)$, where L is the sample thickness. Assuming a nondepleted pump and $\gamma I_e L \ll 1$, the probe transmittance is given by

$$T(\tau_d) = 1 + \frac{2\gamma(\tau_d)L}{\sqrt{2\pi^3(w_e^2 + w_p^2)\tau_L}} \mathcal{E}_e \exp(-\tau_d^2/2\tau_L^2) \quad (81)$$

A plot of Eq. (81) is given in Fig. 23. The maximum and minimum transmittance can be found by differentiating Eq. (81), using Eq. (79) to find the corresponding values of the time delay (τ_{\max} and τ_{\min} , respectively). A simplification occurs when $\tau_L \gg (2b\tau_m)^{-1}$ (i.e., for relatively long laser pulses). In this case, $\tau_{\max} = -\tau_{\min} = (2b\tau_m)^{-1}$. Substituting this result into Eqs. (79) and (81), $\chi^{(3)}$ values can

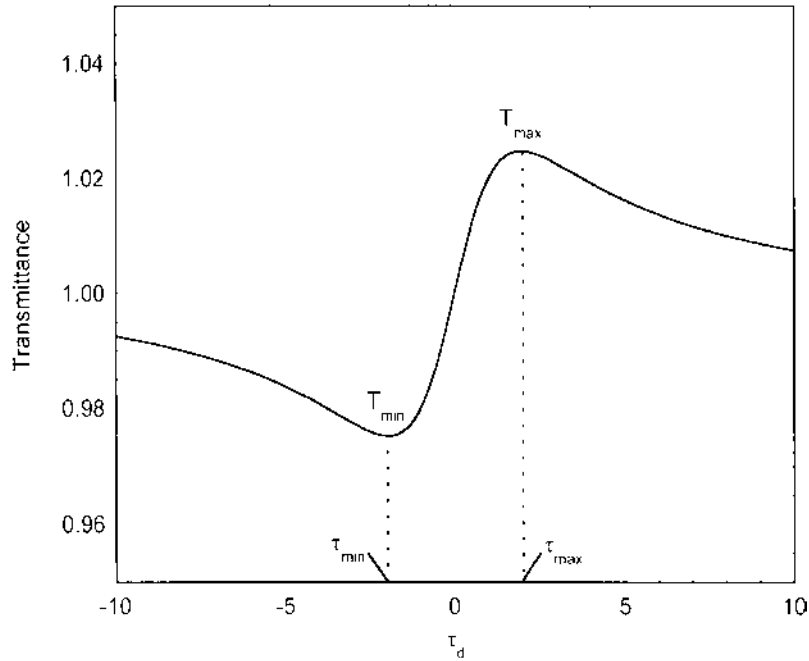


Figure 23 Transmittance as a function of probe delay time for a two-beam coupling experiment using chirped pulses.

be obtained by measuring the transmittance difference at the peak and valley of the curve in Fig. 23, for example,

$$\chi_{xxyy}^{(3)} + \chi_{yyxy}^{(3)} = \frac{\sqrt{2\pi}\epsilon_0 n_0^2 c \lambda \cos \theta (w_e^2 + w_p^2) \tau_L}{12 \mathcal{E}_e L} \exp[(\tau_{\max}^2 / 2\tau_L^2)] (T_{\max} - T_{\min}) \quad (82)$$

Note that τ_{\max} is a measured quantity corresponding to the value of τ_d at T_{\max} . Hence, the nonlinear susceptibility elements can be found even when the chirp coefficient or the material response time is unknown. Note further that $\tau_{\max} - \tau_{\min} = (b\tau_m)^{-1}$ so either the chirp coefficient or the response time can be obtained from a simple measurement if the other quantity is known.

B. Experimental

An experimental arrangement for two-beam coupling is shown in Fig. 24. Both beams are derived from the same laser by the appropriate use of beam splitters. The laser wavelength and pulse width should be selected for the time scale of the particular phenomenon in the sample under study. To simplify the analysis, as described above, the pulse width should be chosen to be large compared with

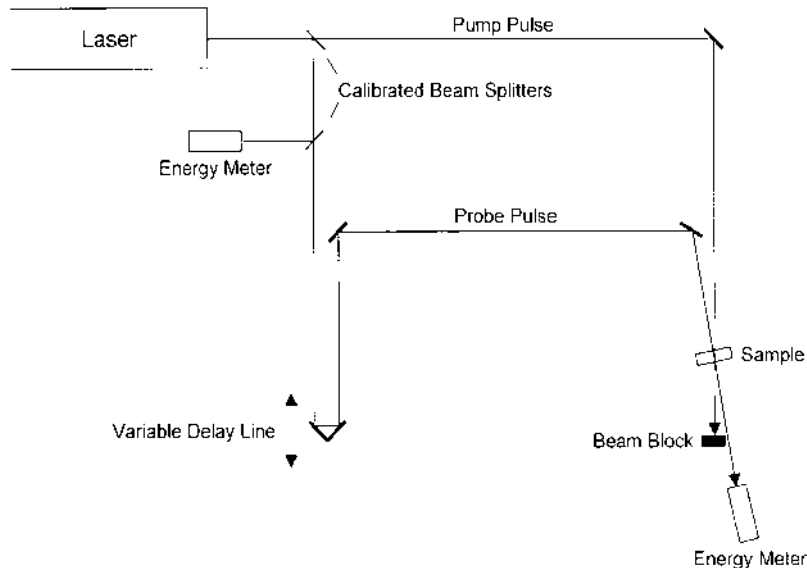


Figure 24 Schematic diagram of a two-beam coupling experiment using chirped pulses.

the inverse product of the chirp coefficient and material response time. An order-of-magnitude guess for the response time may be made based on physical considerations. The laser chirp can then be determined by methods outlined in Ref. [43], or a calibration experiment can be performed on a material with known response time (e.g., CS₂) to obtain the laser chirp coefficient. The laser pulse repetition frequency (PRF) is also an important consideration. Normally, the PRF is chosen to be relatively low (~ 10 Hz) to avoid cumulative energy effects (e.g., thermal).

Normally, the laser is operated at its maximum output since this provides for a more stable operation. The beam is then attenuated to the desired energy for the experiment. In the two-beam coupling method, the laser pump energy remains fixed. Half-wave plates in each beam line may be used to select the polarization for each individual beam. Telescopes and lenses are often used to adjust the beam size for the desired range of intensities in the experiment.

A small fraction of the laser output is picked off with a beam splitter (e.g., uncoated glass or pelicle slide) to serve as the probe beam. Typically, the probe energy will be $\sim 1\text{--}10\%$ of the pump energy. The probe is passed through an optical delay line, which usually consists of a 90° prism or retroreflector mounted on a precision translation stage. The precision of the linear translation will determine the accuracy of the time delay, and the range of translation will determine the net delay time available. The range of delay time should be large compared to the laser pulse width (at least 3–5 pulse widths), in both positive and negative delay directions.

The two beams are passed through the sample at a small angle. The choice of angle will depend to some extent on sample thickness to provide good beam overlap, as discussed in Section I.B. However, care must also be given to avoid forward four-wave mixing. Efficient forward four-wave mixing requires phase matching, which can be avoided by choosing an angle smaller than λ/n_0L . The incident pump and probe and transmitted probe energies are measured. Detectors are typically precision energy meters or photodiodes that are calibrated against energy meters. These detectors need not have a fast response time, but should be operated within their linear range. Finally, the pulse waveform must be measured and fit to a Gaussian or other mathematical form to determine the pulse width. This can be done with a fast photodiode and a transient digitizer for nanosecond pulses, or a streak camera or autocorrelator for shorter pulses.

For absolute measurements, the beam spatial profile and pulse shape as well as beam energy must be carefully measured. These parameters are usually where the greatest experimental error resides. Beam size typically ranges from a few millimeters down to a few hundred micrometers. For this size of beam, a CCD camera coupled to a frame grabber and computer can be used to

characterize the beam spatial profile. Software packages exist that will automatically determine the beam $1/e^2$ radius in two orthogonal directions as well as the quality of the beam fit to a Gaussian TEM₀₀ mode. Alternatively, the beam radius can be obtained by scanning a pinhole, slit, or knife edge across the beam in two orthogonal directions and fitting the detected energy to an appropriate mathematical function (e.g., a Gaussian for a pinhole scan, or an error function for a knife edge scan). Care must be taken that the pinhole or slit be small compared to the beam size, or the result must be properly deconvolved before fitting the result to a Gaussian.

The experiment is run by stepping the delay time from negative (i.e., probe arriving prior to pump) to positive values in increments small compared to the pulse width, and measuring the pulse energies at each step. For this experiment, it is desired that the pump energy remain constant over the entire experiment. Fluctuations can be reduced and accuracy increased by averaging over several pulses (e.g., $\sim 10\text{--}100$ pulses). A typical procedure may be to keep the delay time fixed for several pulses. Compute the average pulse energy and its standard deviation. Then only keep those data for which the pulse energy varies by no more than one-half of a standard deviation from the average. Proceed to the next delay time and repeat the procedure. Variations on this theme are possible, but techniques such as this will reduce the scatter in the data.

A plot of the data should yield a curve similar to that shown in Fig. 23. If enough parameters are known, the data can be fit directly to the theory, given by Eqs. (79) and (81). However, if the pulse width is sufficiently long, then the approximations given above apply. Then, one need only to determine T_{\max} and T_{\min} , and the corresponding delay times τ_{\max} and τ_{\min} , to find the components of $\chi^{(3)}$ as well as the chirp-response time product.

This type of experiment has been used with femtosecond pulses to probe the third order susceptibility associated with bound electronic and Raman nonlinearities [44,45]. Chirp and pulse width can be controlled through the use of self-phase modulation and dispersive delay lines. However, as noted by Smolorz and Wise [45], chirp-free two-beam coupling can occur in nonlinear media when using ultrashort pulses. The pump excites the nonlinear index, and the delayed response effectively chirps the probe pulse. However, such a signal is generally much smaller than that induced by pulses that have even a small chirp coefficient and may safely be ignored.

VII. BEAM SELF-BENDING

Ding et al. [46] reported an interesting single-beam method for measuring the nonlinear index of refraction based on nonlinear beam bending. The method is illustrated in Fig. 25.

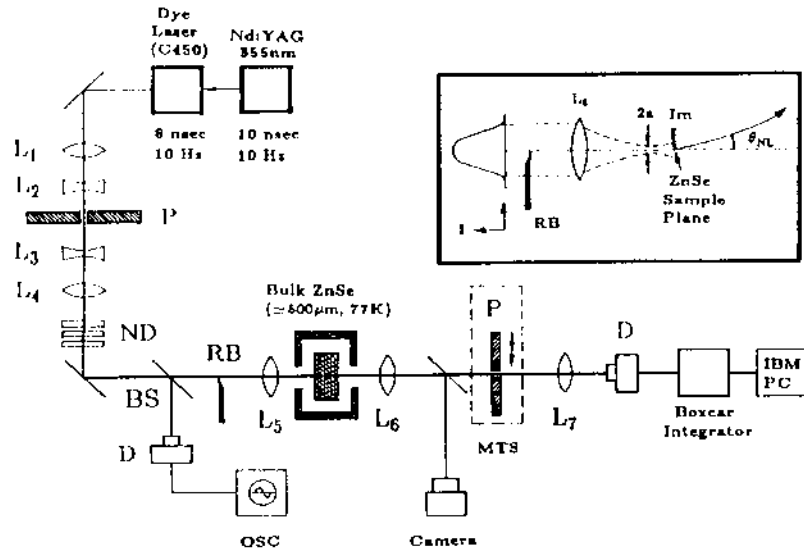


Figure 25 Schematic diagram for a nonlinear beam-bending experiment for measuring the nonlinear refractive index in materials (e.g., ZnSe). RB is a razor blade that obscures half of a Gaussian beam prior to focusing the beam into the sample. (From Ref. 41.)

A razor blade obscures one-half of the laser beam, which is then focused onto the sample. The nonlinear index produces a prism effect that causes the beam to be deflected by an angle θ_{NL} in the far field given by

$$\theta_{NL} = \frac{n_2^l I_0 L}{w_0} \quad (83)$$

where L is the sample thickness, I_0 is the peak intensity in the sample plane, and w_0 is the beam radius at the waist (in the sample, measured in the absence of the razor blade). Equation (83) applies exactly for a triangular beam but is accurate to within 10% for a semi-Gaussian beam.

The output beam is collimated and then scanned with a pinhole to determine the net deflection caused by self-bending. The sign of the nonlinearity is immediately obvious from the direction of the beam deflection (see Chapter 6, Section III.F). The average of several pulses through the pinhole at a single position improves the accuracy of the measurement. Equation (83) is then used to find the value of n_2^l .

This technique has the advantage of using a single laser beam. Its accuracy is limited by the ability to measure small angular beam deviations in

the far field. It is subject to some of the same beam jitter limitations as the Z-scan method.

VIII. THIRD HARMONIC GENERATION

All of the previous methods discussed in this chapter are based on a perturbation of the normal linear regime propagation of an optical beam, i.e., they are related to perturbations of the index of refraction. These methods are thus subject to all physical mechanisms that modify the refractive index. For molecular liquids, these include, in addition to pure electronic effects, molecular density, orientation, and correlation effects [47]. Hence the characterization of the medium in terms of a $\chi^{(3)}$ is a characterization with respect to the optical phenomenon utilized. For most situations, if the intended use of the material is based on perturbations to the refractive index, then this characterization is not only adequate but also appropriate.

It is often desirable, however, to study molecular hyperpolarizabilities and determine the pure electronic behavior. For example, one may want to test molecular orbital calculations of hyperpolarizabilities or bond additivity models, study interactions (correlations) of molecules, or supply the electronic second hyperpolarizability required to complete the first hyperpolarizability characterization using EFISH (see Chapter 4, Section II.A) [48].

Third harmonic generation (THG) has been developed to characterize the pure electronic third order susceptibility in centrosymmetric materials. No other mechanism but the pure nonresonant electron cloud distortion can respond rapidly enough to produce a nonlinear polarization oscillating at the third harmonic of the incident wave. Therefore even nanosecond laser pulses can be used in the characterization without the problem of competing or interfering mechanisms.

The THG method is similar in many respects to characterization of second order materials by SHG. However, there are at least two additional complications. First, all media are third order and hence will generate the third harmonic. This includes glass windows surrounding a liquid sample, and even the air surrounding the sample or sample cell. These additional contributions interfere coherently with the third harmonic generated in the sample and complicate the data analysis. Second, focused beams in an (approximately) infinite medium produce no net third harmonic. In essence, the third harmonic generated prior to focus is π radians out of phase with that generated after focus. To deal with these problems, the sample must be properly located with respect to the incident beam.

Several THG techniques for liquid cells have been developed. All involve some THG from the glass windows that interferes with the THG from the liquid. Therefore the window material must be separately characterized and the window THG included in the analysis of the liquid.

Meredith et al. [47] have developed a technique using a three-media cell, consisting of two wedged glass windows surrounding a wedged liquid chamber. (The wedges are utilized to study Maker fringes. See Chapter 4 and below.) The sample is placed in a vacuum chamber to avoid THG from air. The sample cell must thus be vacuum sealed. It sits with the front surface near the focal position of a long focal length lens. This avoids the problem mentioned above with respect to focused Gaussian beams and also allows a plane wave approximation in the analysis. This technique produces complex Maker fringes and requires a multiparameter (>4) fit of the data to extract the $\chi^{(3)}$ of the liquid. Also, these measurements must be supplemented with a separate Maker fringe experiment of the liquid alone using a wedged cell with flat windows.

Thalhammer and Penzkofer [49] also have used a three-media cell wherein the liquid compartment has a wedge, but the windows are flat. In this case, they employ a slight tilt of the cell with precisely polished windows so that the incident light sees an integer multiple of the coherence length in each window. Thus the THG contributions from the windows are zero. Their sealed cell is also placed in a vacuum in a slightly divergent beam for approximate plane wave analysis. This method produces simple sinusoidal Maker fringes and requires fewer free parameters to fit the data. However, it requires high precision in polishing the windows and positioning the cell. Also, the cell is only appropriate for one incident wavelength.

Meredith et al. [50] have proposed a simpler technique that can be used when the liquid is slightly absorbing at the fundamental wavelength. They use a long cell, which assures depletion of the pump and avoids TEG from the back window. The back window can thus be a flat. However, the path length of the sample must be long (several centimeters), and the cell is still placed in a vacuum to avoid THG contributions from air.

A much simpler technique has been developed by Kajzar and Messier [51] with only two free parameters that must be fitted to the data. These are $\chi^{(3)}$ and L_c , the coherence length, each of which can be separately determined from the same data. The sample can be placed in air, and the liquids can be slightly absorbing at both the fundamental and the third harmonic. This technique is described further below.

A. Theory

The sample cell used in this method is illustrated in the inset to Fig. 26. The liquid compartment is wedged (wedge angle = θ_w) with a thickness at any point that is small compared to the confocal parameter of the incident focused laser beam. Hence the beam in the liquid can be treated as a plane wave. The cell windows, however, are thick compared to the Rayleigh range of the focused laser, with plane air-glass interfaces. Thus the intensity at the air-glass interfaces is low

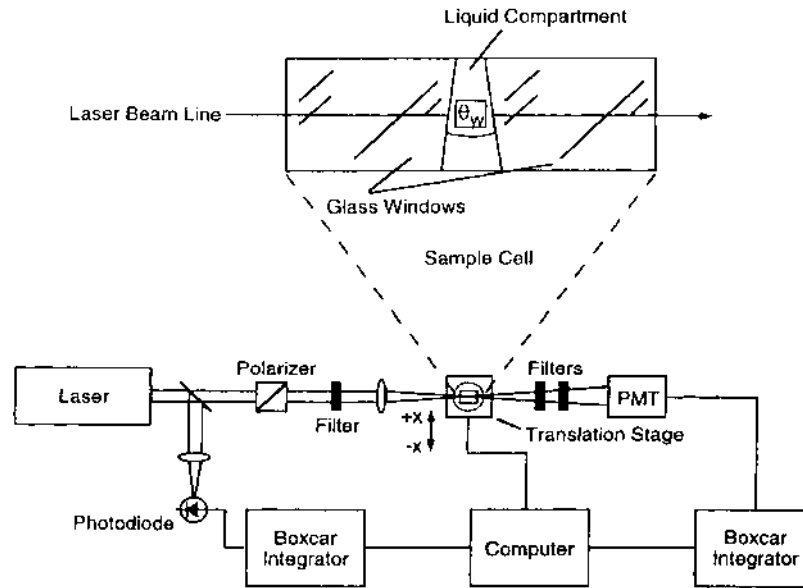


Figure 26 Schematic diagram of a third harmonic generation experiment for measuring the third order susceptibility of liquids by the Maker fringe method. The inset shows the configuration of the sample cell. (From Ref. 46.)

enough that the THG contribution from the air can be safely ignored. With a small wedge angle and with small differences between the refractive indices of the glass and the liquid, any prismatic deviation of the beams is negligible.

If the widows were in close contact with no dispersive material between them, then there would be no net third harmonic generated, since $E_{3\omega}^{G1} \simeq -E_{3\omega}^{G2}$ [51]. However, a dispersive liquid between the windows introduces a phase mismatch such that

$$E_{3\omega}^{G2} = -E_{3\omega}^{G1} e^{i\Delta\psi} (t_{\omega}^{GL} t_{\omega}^{LG})^3 \quad (84)$$

where

$$t_{\omega}^{ij} = \frac{2n_{\omega}^i}{n_{\omega}^i + n_{\omega}^j} \quad i, j = G, L \quad (85)$$

$$|\Delta\psi(x)| = \pi \frac{L(x)}{L_c} \quad (86)$$

$$L_c = \frac{\lambda_{\omega}}{6|n_{\omega}^L - n_{3\omega}^L|} \quad (87)$$

and

$$L(x) = L_0 + 2x \tan\left(\frac{\theta_w}{2}\right) \quad (88)$$

In Eq. (88), the parameter x is the transverse displacement of the wedged cell (for measuring Maker fringes), and L_0 is $L(x)$ at the position where $x = 0$. The superscripts G and L refer to glass and liquid quantities, respectively.

The third harmonic field in the liquid is found by a generalization of the plane wave analysis for SHG given in Chapter 4. The resultant field at the cell output is a coherent sum of the fields generated in the first window ($E_{3\omega}^{G1}$), in the liquid ($E_{3\omega}^L$), and in the second window ($E_{3\omega}^{G2}$), appropriately taking into account the interface transmittances:

$$E_{3\omega} = t_{3\omega}^{GL} t_{3\omega}^{LG} t_{3\omega}^{GA} E_{3\omega}^{G1} + t_{3\omega}^{LG} t_{3\omega}^{GA} E_{3\omega}^L + t_{3\omega}^{GA} E_{3\omega}^{G2} \quad (89)$$

where Eq. (85) is used for $t_{3\omega}^{GA}$ with $i = G$ and $j = A$ for air ($n^A \approx 1$ for all frequencies).

Generalizing the results of Kajzar and Messier to the analysis presented in Chapter 4, Eq. (34), which includes the effects of absorption and finite beam width, yields

$$\begin{aligned} \mathcal{P}_{3\omega}(x) = & \frac{\mathcal{P}_M}{2} \left\{ \frac{1}{2} \exp\left(-\frac{3\alpha_\omega L}{2}\right) + \frac{1}{2} \exp\left(-\frac{\alpha_{3\omega} L}{2}\right) \right. \\ & \left. - \exp\left[-\frac{(3\alpha_\omega + \alpha_{3\omega})L}{2}\right] \cos\left(\pi \frac{L(x)}{L_c}\right) \frac{2J_1[\pi w_0 \tan \theta_w / L_c]}{\pi w_0 \tan \theta_w / L_c} \right\} \end{aligned} \quad (90)$$

where α_ω and $\alpha_{3\omega}$ are the linear absorption coefficients at the fundamental and third harmonic, respectively. The factor involving the first order Bessel function J_1 accounts for the reduction in Maker fringe contrast due to a finite beam width of $2w_0$ at the focus. When the absorption at both frequencies is negligible and w_0 or θ_w are sufficiently small, the factor in curly brackets reduces to simply $2 \sin^2(\Delta\psi/2)$.

The factor in curly brackets yields the Maker fringes, while \mathcal{P}_M gives the envelope of the fringes. A two-parameter fit of the measured values $\mathcal{P}_{3\omega}(x)$ will yield the coherence length L_c and \mathcal{P}_M . The envelope function is given by the relation

$$\begin{aligned} \mathcal{P}_{3\omega} \propto & A^2 + B^2 + 2AB \cos \Delta\psi \approx (1 - \rho)^2 \sin^2\left(\frac{\Delta\psi}{2}\right) \\ & \equiv \mathcal{P}_M \sin^2\left(\frac{\Delta\psi}{2}\right) \end{aligned} \quad (91)$$

for negligible absorption and beam width, where

$$A = t_{3\omega}^{\text{GL}} t_{3\omega}^{\text{LG}} - t_{3\omega}^{\text{GL}} \left(\frac{n_{\omega}^{\text{L}} + n_{3\omega}^{\text{L}}}{n_{3\omega}^{\text{L}} + n_{3\omega}^{\text{G}}} \right) \rho \approx 1 - \rho \quad (92)$$

$$B = t_{3\omega}^{\text{GL}} \left(\frac{n_{\omega}^{\text{L}} + n_{3\omega}^{\text{L}}}{n_{3\omega}^{\text{L}} + n_{3\omega}^{\text{G}}} \right) \rho - (t_{\omega}^{\text{GL}} t_{\omega}^{\text{LG}})^3 \approx \rho - 1 \quad (93)$$

and

$$\rho = \left(\frac{n_{\omega}^{\text{G}} + n_{3\omega}^{\text{G}}}{n_{\omega}^{\text{L}} + n_{3\omega}^{\text{L}}} \right) \frac{L_c^{\text{L}} \chi_{\text{L}}^{(3)}}{L_c^{\text{G}} \chi_{\text{G}}^{(3)}} \approx \frac{L_c^{\text{L}} \chi_{\text{L}}^{(3)}}{L_c^{\text{G}} \chi_{\text{G}}^{(3)}} \quad (94)$$

The approximate forms in Eqs. (92)–(94) are valid when the refractive indices of the glass and liquid at both ω and 3ω do not differ greatly. \mathcal{P}_M will thus be proportional to $(1 - \rho)^2$ as well when absorption and finite beam width effects cannot be ignored.

When the Maker fringe experiment is repeated for a reference liquid, then the sample susceptibility is given by

$$\chi_s^{(3)} = \left[1 - \left(1 - \frac{L_c^{\text{r}} \chi_{\text{r}}^{(3)}}{L_c^{\text{G}} \chi_{\text{G}}^{(3)}} \right) \left(\frac{\mathcal{P}_M^{\text{s}}}{\mathcal{P}_M^{\text{r}}} \right)^{1/2} \right] \frac{L_c^{\text{G}}}{L_c^{\text{s}}} \chi_{\text{G}}^{(3)} \quad (95)$$

where it is understood that $\chi^{(3)} = \chi_{xxxx}^{(3)}$ ($-3\omega; \omega, \omega, \omega$). Thus the coherence lengths L_c^{r} and L_c^{G} , and the susceptibilities $\chi_{\text{r}}^{(3)}$ and $\chi_{\text{G}}^{(3)}$, for the reference liquid and glass window material, respectively, must be accurately known.

B. Experimental

A typical experimental setup is illustrated in Fig. 26. For studying organic molecular liquids, the laser is typically a Nd:YAG (at 1064 nm) or a combination of Nd:YAG and dye lasers with Raman shifters to obtain wavelengths in the near infrared. It is generally desired that the third harmonic wavelength be in the visible or near ultraviolet to facilitate detection and avoid strong UV absorption lines typical in organic materials. The pulse width can be in the nanosecond regime. A seed-injection laser is usually desired for stability and single-mode operation. Pulses should be monitored to factor out strong fluctuations. The incident laser is linearly polarized to yield a measurement of $\chi_{xxxx}^{(3)}$. A typical laser pulse repetition rate is 10–30 Hz.

The sample cell is shown in the insert to Fig. 26. As stated above, the liquid compartment is small compared to the laser confocal parameter, and the faces of the windows are at distance from the focus which is large compared to the Rayleigh

range. The sample is positioned near the focus of the beam, but the exact position is not critical as long as the reference is placed in the same position [51].

The output is filtered to pass only 3ω and then detected with a photomultiplier tube. The signal is averaged with a boxcar integrator and then stored on a computer for analysis. The Maker fringe data for both the sample and the reference are fitted to the expressions given by Eq. (90) to obtain L_c and \mathcal{P}_M . Using Eq. (95), the susceptibility of the sample is determined. The appropriate values of coherence length and susceptibility for the reference and window materials must be found from separate measurements or from literature values. Kajzar and Messier used fused silica windows and chloroform as a reference liquid. For a fundamental beam at 1064 nm, the following values apply [51]:

$$\begin{aligned} \text{Fused silica: } L_c &= 6.6 \mu\text{m}, \chi^{(3)} = 3.1 \times 10^{-14} \text{ esu} \\ \text{Chloroform: } L_c &= 5.2 \mu\text{m}, \chi^{(3)} = 7.0 \times 10^{-14} \text{ esu} \end{aligned}$$

Several experimental cautions that were discussed in Chapter 4, Section I.C apply as well to the THG method. One can also extend the SHG Maker fringe experiment and analysis for rotation of plane parallel slabs to THG. This technique would be appropriate to the characterization of samples in thin film form [52].

REFERENCES

1. M. Born and E. Wolf, *Principles of Optics*, 5th ed., Pergamon Press, New York, 1975, p. 702.
2. M. J. Moran, C.-Y. She, and R. L. Carman, Interferometric measurements of the nonlinear refractive-index coefficient relative to CS_2 in laser-system-related materials, *IEEE J. Quant. Electron.* QE-11:259 (1975).
3. M. J. Soileau, W. F. Williams, and E. W. Van Stryland, Optical power limiter with picosecond response time, *IEEE J. Quant. Electron.* QE-19:731 (1983).
4. M. Sheik-bahae, A. A. Said, T. H. Wei, D. J. Hagan, and E. W. Van Stryland, Sensitive measurement of optical nonlinearities using a single beam, *IEEE J. Quant. Electron.* 26:760 (1989).
5. S. R. Friberg and P. W. Smith, Nonlinear optical glasses for ultrafast optical switches, *IEEE J. Quant. Electron.* QE-23:2089 (1987).
6. W. Zhao and P. Palffy-Muhoray, Z-scan technique using top-hat beams, *Appl. Phys. Lett.* 63:1613 (1993).
7. N. P. Xuan, J.-L. Ferrier, J. Gazengel, and G. Rivoire, Picosecond measurements of the third-order susceptibility tensor in liquids, *Opt. Commun.* 51:433 (1984).
8. P. A. Fleitz, R. L. Sutherland, L. V. Natarajan, T. Pottenger, and N. C. Fernelius, Effects of two-photon-absorption on degenerate four-wave mixing in solutions of diphenyl polyenes, *Opt. Lett.* 17:716 (1992).
9. M. Zhao, Y. Cui, M. Samoc, P. N. Prasad, M. R. Unroe, and B. A. Reinhardt, Influence of two-photon absorption on third-order nonlinear optical processes as

- studied by degenerate four-wave mixing: the study of soluble didecyloxy substituted polyphenyls, *J. Chem. Phys.* 95:3991 (1991).
- 10. E. J. Canto-Said, D. J. Hagan, and E. W. Van Stryland, Degenerate four-wave mixing measurements of high order nonlinearities in semiconductors, *IEEE J. Quant. Electron.* 27:2274 (1991).
 - 11. R. L. Sutherland, E. Rea, L. V. Natarajan, T. Pottenger, and P. A. Fleitz, Two-photon absorption and second hyperpolarizability measurements in diphenylbutadiene by degenerate four-wave mixing, *J. Chem. Phys.* 98:2593 (1993).
 - 12. P. W. Smith, W. J. Thomlinson, D. J. Eilenberger, and P. J. Maloney, Measurement of electronic optical Kerr coefficients, *Opt. Lett.* 6:581 (1981).
 - 13. K. J. McEwan, K. J. Harrison, and P. A. Madden, Polarisation and material dependence of degenerate four-wave mixing transients in molecular fluids, *Mol. Phys.* 69:1025 (1990).
 - 14. G. M. Carter, Excited-state dynamics and temporally resolved nonresonant nonlinear-optical processes in polydiacetylenes, *J. Opt. Soc. Am. B* 4:1018 (1987).
 - 15. G. M. Carter, J. V. Hryniwicz, M. K. Thakur, Y. J. Chen, and S. E. Meyler, Nonlinear optical processes in polydiacetylene measured with femtosecond duration laser pulses, *Appl. Phys. Lett.* 49:998 (1986).
 - 16. M. D. Fayer, Picosecond holographic grating generation of ultrasonic waves, *IEEE J. Quant. Electron.* QE-22:1437 (1986).
 - 17. S. K. Ghoshel, P. Chopra, B. P. Singh, J. Swiatkiewicz, and P. N. Prasad, Picosecond degenerate four-wave mixing study of nonlinear optical properties of the poly-*N*-vinyl carbazole: 2,4,7-trinitrofluorenone composite polymer photoconductor, *J. Chem. Phys.* 90:5078 (1989).
 - 18. P. D. Maker and R. W. Terhune, Study of optical effects due to an induced polarization third-order in the electric field strength, *Phys. Rev.* 137:801 (1965).
 - 19. R. Adair, L. L. Chase, and S. A. Payne, Nonlinear refractive index of optical crystals, *Phys. Rev. B* 39:3337 (1989).
 - 20. R. DeSalvo, M. Sheik-bahae, A. A. Said, D. J. Hagan, and E. W. Van Stryland, Z-scan measurements of the anisotropy of nonlinear refraction and absorption in crystals, *Opt. Lett.* 18:194 (1993).
 - 21. D. N. Rao, J. Swiatkiewicz, P. Chopra, S. K. Ghoshel, and P. N. Prasad, Third order nonlinear optical interactions in thin films of poly-*p*-phenylenebenzobisthiazole polymer investigated by picosecond and subpicosecond degenerate four wave mixing, *Appl. Phys. Lett.* 48:1187 (1986).
 - 22. P. N. Prasad and D. J. Williams, *Introduction to Nonlinear Optical Effects in Molecules and Polymers*, John Wiley, New York, 1991, pp. 218–220.
 - 23. R. Adair, L. L. Chase, and S. A. Payne, Nonlinear refractive index measurements of glasses using three-wave mixing, *J. Opt. Soc. Am. B* 4:875 (1987).
 - 24. L. Yang, R. Dorsinville, Q. Z. Wang, P. X. Ye, R. R. Alfano, R. Zambini, and C. Taliani, Excited-state nonlinearity in polythiophene thin films investigated by the Z-scan technique, *Opt. Lett.* 17:323 (1992).
 - 25. A. A. Said, M. Sheik-bahae, D. J. Hagan, T. H. Wei, J. Wang, J. Young, and E. W. Van Stryland, Determination of bound-electronic and free-carrier nonlinearities in ZnSe, GaAs, CdTe, and ZnTe, *J. Opt. Soc. Am. B* 9:405 (1992).

26. T. H. Wei, D. J. Hagan, M. J. Sence, E. W. Van Stryland, J. W. Perry, and D. R. Coulter, Direct measurements of nonlinear absorption and refraction in solutions of phthalocyanines, *Appl. Phys. B* 54:46 (1992).
27. M. Sheik-bahae, J. Wang, R. DeSalvo, D. J. Hagan, and E. W. Van Stryland, Measurement of nondegenerate nonlinearities using a two-color Z-scan, *Opt. Lett.* 17:258 (1992).
28. J. Wang, M. Sheik-bahae, A. A. Said, D. J. Hagan, and E. W. Van Stryland, Time-resolved Z-scan measurements of optical nonlinearities, *J. Opt. Soc. Am. B* 11:1009 (1994).
29. P. B. Chapple, J. Staromlynska, and R. G. McDuff, Z-scan studies in the thin- and the thick-sample limits, *J. Opt. Soc. Am. B* 11:975 (1994).
30. M. Sheik-bahae, A. A. Said, D. J. Hagan, M. J. Soileau, and E. W. Van Stryland, Nonlinear refraction and optical limiting in thick media, *Opt. Eng.* 30:1228 (1991).
31. T. Xia, D. J. Hagan, M. Sheik-bahae, and E. W. Van Stryland, Eclipsing Z-scan measurement of a $\lambda/10^4$ wave-front distortion, *Opt. Lett.* 19:317 (1994).
32. R. L. Sutherland, Effects of multiple internal sample reflections on nonlinear refractive Z-scan measurements, *Appl. Opt.* 33:5576 (1994).
33. P. D. Maker, R. W. Terhune, and C. M. Savage, Intensity-dependent changes in the refractive index of liquids, *Phys. Rev. Lett.* 12:507 (1964).
34. R. W. Hellwarth, A. Owyoung, and N. George, Origin of the nonlinear refractive index of liquid CCl_4 , *Phys. Rev. A* 4:2342 (1971).
35. G. K. L. Wong and Y. R. Shen, Study of pretransitional behavior of laser-field-induced molecular alignment in isotropic nematic substance, *Phys. Rev. A* 10:1277 (1974).
36. P. P. Ho and R. R. Alfano, Optical Kerr effect in liquids, *Phys. Rev. A* 20:2170 (1979).
37. R. W. Boyd, *Nonlinear Optics*, Academic Press, New York, 1992, p. 167.
38. H. Uchiki and T. Kobayashi, New method for the measurement of electro-optic constant of polycarbonate films doped with 4-diethylamino-4'-nitrostilbene molecules, *Nonlinear Optical Properties of Polymers*, Materials Research Society Symposium Proceedings, Vol 109 (A. J. Heeger, J. Orenstein, and D. R. Ulrich, eds), Materials Research Society, Pittsburgh, 1988, pp. 373–378.
39. S. M. Saltiel, B. Van Wonterghem, and P. M. Rentzepis, Measurement of $\chi^{(3)}$ and phase shift of nonlinear media by means of a phase-conjugate interferometer, *Opt. Lett.* 14:183 (1989).
40. T. Hattori, H. Okawa, T. Wada, and H. Sasabe, Subpicosecond interferometric measurement of the nonlinear refractive index of poly(3-hexylthiophene), *Opt. Lett.* 17:1560 (1992).
41. N. Tang and R. L. Sutherland, Time-domain theory for pump–probe experiments with chirped pulses, *J. Opt. Soc. Am. B* 14:3412 (1997).
42. R. L. Sutherland, D. G. McLean, S. M. Kirkpatrick, P. A. Fleitz, S. Chandra, and M. C. Brant, Multiphoton absorption and optical limiting, *Multiphoton and Light Driven Multielectron Processes in Organics: New Phenomena, Materials and Applications* (F. Kajzar and M. V. Agranovich, eds), NATO Science Series 3. High

- Technology, Vol 79, Kluwer Academic Publishers, Dordrecht, The Netherlands, 2000, pp. 67–81.
- 43. A. Dogariu, T. Xia, A. A. Said, E. W. Van Stryland, and N. Bloembergen, Purely refractive transient energy transfer by stimulated Rayleigh-Wing scattering, *J. Opt. Soc. Am. B* 14:796 (1997).
 - 44. A. Dogariu and D. J. Hagan, Low frequency Raman gain measurements using chirped pulses, *Opt. Express* 1:73 (1997).
 - 45. S. Smolorz and F. Wise, Femtosecond two-beam coupling energy transfer from Raman and electronic nonlinearities, *J. Opt. Soc. Am. B* 17:1636 (2000).
 - 46. Y. J. Ding, C. L. Guo, G. A. Swartzlander, Jr., J. B. Khurgin, and A. E. Kaplan, Spectral measurement of the nonlinear refractive index in ZnSe using self-bending of a pulsed laser beam, *Opt. Lett.* 15:1431 (1990).
 - 47. G. R. Meredith, B. Buchalter, and C. Hanzlik, Third order optical susceptibility determination by third harmonic generation. I, *J. Chem. Phys.* 78:1533 (1983).
 - 48. F. Kajzar and J. Messier, Third-harmonic generation in liquids, *Phys. Rev. A* 32:2352 (1985).
 - 49. M. Thalhammer and A. Penzkofer, Measurement of third-order nonlinear susceptibilities by non-phase matched third-harmonic generation, *Appl. Phys. B* 32:137 (1983).
 - 50. G. R. Meredith, B. Buchalter, and C. Hanzlik, Third-order optical susceptibility determination by third harmonic generation. II, *J. Chem. Phys.* 78:1543 (1983).
 - 51. F. Kajzar and J. Messier, Original technique for third-harmonic-generation measurements in liquids, *Rev. Sci. Instrum.* 58:2081 (1987).
 - 52. W. E. Torruellas, R. Zanoni, G. I. Stegeman, G. R. Möhlmann, R. W. P. Erdhuisen, and W. H. G. Horsthuis, The cubic susceptibility dispersion of alkoxy-nitro-stilbene (MONS) and di-alkyl-amino-nitro-stilbene (DANS) side chain substituted polymers: comparison with the two-level model, *J. Chem. Phys.* 94:6851 (1991).

8

Optical Properties of Selected Third Order Nonlinear Optical Materials

This chapter presents nonlinear refractive index data for several third order materials. These data have been extracted from several sources, including original references and secondary sources. Some very useful sources containing a considerable listing of materials and data can be found in Refs. 1–4. Chang [5] has surveyed materials for fast self-induced refractive index changes. Some of his tabulated data are incorporated here by permission.

The purpose of this chapter is not to be exhaustive but rather to present data on a wide selection of common materials, as well as on a few new interesting materials. A more complete list of data, many of historical significance, is given in Refs. 1–4.

Section I of this chapter contains data on molecular gases and atomic vapors. Section II gives data on several common liquids. Data on selected solid dielectrics and partially transparent metallic colloid suspensions are given in Section III. Section IV contains data on several selected semiconductor materials. Section V concentrates on organic materials, while Section VI presents second hyperpolarizability data for several organic materials.

I. MOLECULAR GASES AND ATOMIC VAPORS

Third order susceptibility data for several common gases are given in Table 1, measured by several methods. Since $\chi^{(3)}$ varies with pressure or gas density, most

Table 1 Nonlinear Refractive Index and Third order Susceptibility Data for Selected Atomic Vapors and Molecular Gases

Material	λ (nm)	Pulse width (ns)	n_0	$(10^{-25} \text{ m}^2/\text{V}^2)^a$	n_2 (10^{-16} esu)	n_2^l ($10^{-16} \text{ cm}^2/\text{W}$)	$\chi_{\text{ext}}^{(3)}$ ($10^{-20} \text{ m}^3/\text{V}^2$)	$\chi_{\text{ext}}^{(3)}$ (10^{-18} esu) ^b	Method ^c	Ref.
Argon	676, 584	~1–10	1.0					9.46/am	CRS	[6]
Argon	607, 532	~1–10	1.0					9.6/am	CARS	[7,8]
Argon	694	~1–10	1.0					9.2/am	EFISH	[9]
Argon	683, 532	~1–10	1.0					10.6/am	CARS	[10]
Argon	976, 694	~1–10	1.0					9.31/am	CARS	[11]
Acetylene	532	8	1.0					50.9/am	CARS	[12]
Carbon dioxide	532	8	1.0					11.8/am	CARS	[12]
Carbon dioxide	694	~1–10	1.0					10.6/am	EFISH	[9]
Carbon dioxide	683, 532	~10	1.0					9.1/am	CARS	[12]
Carbon dioxide	683, 532	~1–10	1.0					12.3/am	CARS	[10]
Carbon dioxide	976, 694	~1–10	1.0					12.0/am	CARS	[11]
Methane	532	8	1.0					22.7/am	CARS	[12]
Methane	694	~1–10	1.0					25.6/am	EFISH	[9]
Methane	683, 532	~10	1.0					31.3/am	CARS	[12]
Methane	683, 532	~1–10	1.0					26.6/am	CARS	[10]

Methane	976, 694	~1–10	1.0	17.7/am	CARS	[11]
Nitrogen (N ₂)	532 8	1.0		7.90/am	CARS	[12]
Nitrogen (N ₂)	607, 532	~1–10	1.0	8.5/am	CARS	[7.8]
Nitrogen (N ₂)	694	~1–10	1.0	7.2/am	EFISH	[9]
Nitrogen (N ₂)	683,	~1–10	1.0	7.0/am	CARS	[12]
Nitrogen (N ₂)	532	~1–10	1.0	8.47/am	CARS	[10]
Nitrogen (N ₂)	683,	~1–10	1.0	8.11/am	CARS	[11]
Nitrogen (N ₂)	532	~1–10	1.0	7.98/am	CARS	[12]
Nitrogen (N ₂)	976, 694	~1–10	1.0	7.6/am	EFISH	[9]
Oxygen (O ₂)	532 8	1.0		7.7/am	CARS	[12]
Oxygen (O ₂)	694	~1–10	1.0	11.4/am	CARS	[10]
Oxygen (O ₂)	683, 532	~10	1.0	7.81/am	CARS	[11]
Oxygen (O ₂)	683,	~1–10	1.0	88.7/am	CARS	[12]
Oxygen (O ₂)	532	~1–10	1.0	80/am	CARS	[7.8]
Propane	694	1.0		84.6/am	EFISH	[9]
Propane	607, 532	~1–10	1.0	12.3/am	CARS	[12]
Propane Carbon monoxide	694 532 8	~1–10	1.0	13.6/am	EFISH	[9]
Carbon monoxide	694	~1–10	1.0			

(continued)

Table 1 Continued.

Material	λ (nm)	Pulse width (ns)	n_0	$(10^{-25} \text{ m}^2/\text{V}^2)^a$	(10^{-16} esu)	n'_2 ($10^{-16} \text{ cm}^2/\text{W}$)	$(10^{-20} \text{ m}^2/\text{V}^2)$	$\chi_{\text{ext}}^{(3)}$ (10^{-18} esu) ^b	$\chi^{(3)}$ Method ^c	Ref.
Carbon monoxide	683, 532	~1–10	1.0					12.5/am	CARS	[10]
Carbon monoxide	976, 694	~1–10	1.0					11.8/am	CARS	[11]
Freon	532	8	1.0					7.15/am	CARS	[12]
Freon	694	~1–10	1.0					8.9/am	EFISH	[9]
Hydrogen (H_2)	532	8	1.0					5.90/am	CARS	[12]
Hydrogen (H_2)	676,	~1–10	1.0					5.34/am	CRS	[6]
Hydrogen (H_2)	584							5.4/am	EFISH	[9]
Hydrogen (H_2)	694	~1–10	1.0					6.9/am	CARS	[12]
Hydrogen (H_2)	683, 532	~10	1.0						SF	[13]
Air (1 atm)	1064	30	1.0	2.8	$2.5 \times 10^{-14} \text{ N(cm}^{-3}\text{)}$					[14]
Sodium vapor	589	ew	1.0		$0.27 \times 10^{-14} \text{ N(cm}^{-3}\text{)}$					
Cesium vapor	1064	0.03	1.0		$-1.4 \times 10^{-14} \times 10^{-14} \text{ N(cm}^{-3}\text{)}$					[15]
Rubidium vapor	795	6	1.0		$-1.1 \times 10^{-5} \times 10^{-14} \text{ N(cm}^{-3}\text{)}$					
Iodine vapor (I_2)	694	10	1.0	6300	5700				SF	[17]

^a Calculated.^b am = amagat (1 amagat = 0.044617 gram-mole/liter = 2.7037×10^{19} molecules/cm³).^c CRS, coherent Raman spectroscopy; CARS, coherent anti-Stokes Raman spectroscopy; EFISH, electric field induced second harmonic; SF, self-focusing; DFWM, degenerate four-wave mixing.

nonresonant data are given in units of per amagat. One amagat is the concentration of 1 atmosphere of an ideal gas at a temperature of 273.16K.

Table 1 includes values of n_2 for a few atomic vapors. Note that n_2 depends on vapor concentration but is also very sensitive to wavelength. Atomic vapors (particularly alkali vapors) have very sharp spectral lines and only become interesting nonlinear materials for radiation near these absorption lines. These materials then behave as nearly ideal two-level systems.

Chang [5] has gathered specific data on two-level atomic vapors that can be used to compute the nonlinear optical response, using methods presented in Chapter 6, Section II.E. Although the list given here in Table 2 is not exhaustive, it is representative of what can be done with atomic vapors. The first column gives the atomic absorber, and the second gives the upper state involved in the two-level transition. The line center absorption wavelength is given in the third column, while the fourth and fifth columns present the line width and oscillator strength, respectively, of the transition. The line width in this case is the Doppler-broadened width for the typical temperature given in column seven. The oscillator strength is related to the absorption cross section, given in column six, by $\sigma(\text{cm}^2) = 5.1285 \times 10^{-11} f T_2(\text{ns})$, with T_2 the dipole phase coherence lifetime [5] (see Chapter 6, Section II.E). A typical population difference density is given in column eight. The product of the line center saturation intensity and the total ground state recovery time τ is recorded in the ninth column. Column ten contains typical values of τ . Typically $T_2 < \tau$, and τ depends on the local environment of the atom. Quenching agents can be used to reduce τ as well as drive the value of T_2 toward τ . Typical quenching agents are given in column eleven. References originally given by Chang are included in column twelve of the table.

T_2 can be varied from $\sim 1\text{ ps}$ to $> 100\text{ ps}$ by varying the vapor and/or buffer gas (e.g., nitrogen gas) pressure (before Doppler broadening becomes important). Note that T_2 is related to the homogeneous line width by $\Delta\nu_{\text{homo}} = 1/\pi T_2$. Formulas can be found in Chapter 6, Section II.E (see therein Tables 1 and 5) for calculating effective $\chi^{(3)}$ and n_2 values of two-level systems.

Molecular two-level systems have much smaller oscillator strengths than atomic vapors. However, they allow resonant nonlinearities at near-infrared and mid-infrared wavelengths to be accessed. Generally, for these systems $T_2 \geq 1\text{ ns}$ and $\tau \geq 1\text{ }\mu\text{s}$. Data for some molecular gases are given in Table 3, using the same format as Table 2.

Table 2 Data for Computing Nonlinear Refractive Index in Two-Level Systems: Atomic Vapors

Absorber	Upper state	λ (nm) ^a	$\Delta\nu$ (cm^{-1}) ^b	f^c	σ (cm^2) ^d	T_2 (ns) ^e	T (K) ^f	Typical ΔN (cm^{-3}) ^g	$I_{\text{so}} \cdot \tau$ (W-nm/cm ²) ^h	Typical τ (ns) ⁱ	Quenching agent	Ref.
Li	2P _{3/2}	671	0.09	0.50	2.65×10^{-11}	T_2	>450	> 10^6	$5.6/T_2$	≥ 1	N ₂	[99–101]
	2P _{1/2}	671	0.09	0.25	1.33×10^{-11}	T_2	>450	> 10^6	$11/T_2$	≥ 1	N ₂	[102–105]
Na	3P _{3/2}	589	0.05	0.65	3.45×10^{-11}	T_2	>300	> 10^6	$4.9/T_2$	≥ 1	N ₂	
	3P _{1/2}	590	0.05	0.33	1.73×10^{-11}	T_2	>300	> 10^6	$9.7/T_2$	≥ 1	N ₂	
K	4P _{3/2}	767	0.026	0.70	3.72×10^{-11}	T_2	>300	> 10^9	$3.5/T_2$	≥ 1	N ₂	
	4P _{1/2}	777	0.026	0.35	1.86×10^{-11}	T_2	>300	> 10^9	$6.9/T_2$	≥ 1	N ₂	
Rb	5P _{3/2}	405	0.049	0.010	5.13×10^{-13}	T_2	>300	> 10^9	$478/T_2$	≥ 1		
	5P _{1/2}	405	0.049	0.005	2.56×10^{-13}	T_2	>300	> 10^9	$958/T_2$	≥ 1		
Cs	6P _{3/2}	870	0.017	0.72	3.82×10^{-11}	T_2	>300	> 10^{10}	$3.3/T_2$	≥ 1	N ₂	[106]
	6P _{1/2}	795	0.017	0.36	1.91×10^{-11}	T_2	>300	> 10^{10}	$6.5/T_2$	≥ 1	N ₂	
Cs	6P _{3/2}	420	0.032	0.012	6.15×10^{-13}	T_2	>300	> 10^{10}	$384/T_2$	≥ 1		
	6P _{1/2}	422	0.032	0.006	3.08×10^{-13}	T_2	>300	> 10^{10}	$764/T_2$	≥ 1		
Cs	7P _{3/2}	456	0.024	0.017	8.72×10^{-13}	T_2	>300	> 3×10^9	$2.7/T_2$	≥ 1		
	7P _{1/2}	459	0.023	0.003	1.44×10^{-13}	T_2	>300	> 3×10^9	$5.3/T_2$	≥ 1		
Cs	7P _{3/2}	456	0.024	0.017	8.72×10^{-13}	T_2	>300	> 3×10^9	$250/T_2$	≥ 1		
	7P _{1/2}	459	0.023	0.003	1.44×10^{-13}	T_2	>300	> 3×10^9	$1500/T_2$	≥ 1		

Source: Adapted from Ref. 5.

^a Absorption wavelength.^b Doppler-broadened line width (FWHM).^c Oscillator strength.^d Absorption cross-section.^e Phase coherence time.^f Temperature.^g Population difference.^h Line center saturation intensity.ⁱ Typical ground state recovery time.

Table 3 Data for Computing Nonlinear Refractive Index in Two-Level Systems: Molecular Gases

Absorber	Upper state	λ (nm) ^a	$\Delta\nu$ (cm ⁻¹) ^b	σ (cm ²) ^d	T_2 (ns) ^e	T (K) ^f	ΔN (cm ⁻³) ^g	$I_{s0} \tau$ (W·ns/cm ²) ^h	Typical τ (ns) ⁱ	Quenching agent	Ref.
Na ₂	$A^1\Sigma_u^+$	600–700	0.04	~ 0.05	$2.6 \times 10^{-12} T_2$	>400	$>10^7$	$59/T_2$	≥ 1	N ₂	[107,108]
	$B^1\Pi_u$	450–510	0.05	~ 0.05	$2.6 \times 10^{-12} T_2$	>400	$>10^7$	$80/T_2$	≥ 1	N ₂	[109]
K ₂	$A^1\Sigma_u$	770–860	0.02	~ 0.05	$2.6 \times 10^{-12} T_2$	>400	$>10^8$	$30/T_2$	≥ 1	N ₂	[108–110]
	$B^1\Pi_u$	630–670	0.023	~ 0.03	$1.5 \times 10^{-10} T_2$	>400	$>10^8$	$50/T_2$	≥ 1	N ₂	[108–110]
Rb ₂	$B^1\Pi_u$	650–700	0.017	~ 0.03	$1.5 \times 10^{-13} T_2$	>400	$>10^9$	$530/T_2$	≥ 1	N ₂	[108–110]
	$C^1\Pi_u$	470–490	0.022	0.004	$2.0 \times 10^{-13} T_2$	>400	$>10^9$	$20/T_2$	≥ 1	N ₂	[108–110]
Li ₂	$A^1\Sigma_u^+$	650–750	~1	0.08	$3.6 \times 10^{-12} T_2$	>600	$>10^8$	$2100/T_2$	≥ 1	N ₂	[111–113]
	$B^1\Pi_u$	450–540	~1	0.001	$5.1 \times 10^{-14} T_2$	>600	$>10^8$	$2.4 \times 10^4 T_2$	≥ 1	C ₃ D ₈ or C ₄ D ₁₀	[115,116]
I ₂	$B^3\Pi_u^+$	510–770	0.014	$\sim 1.3 \times 10^{-4}$	$6.7 \times 10^{-15} T_2$	>300	$\sim 10^{14}$	$7.6 \times 10^3 T_2$	≥ 1	C ₃ D ₈ or C ₄ D ₁₀	[116,117]
	v_3	$\sim 4.26 \times 10^3$	$(\pi c T_2)^{-1}$	$\sim 6.0 \times 10^{-5}$	$6.7 \times 10^{-15} T_2$	300	$<10^{18}$	$1.3 \times 10^4 T_2$	≥ 1	C ₃ H ₁₀ or C ₆ H ₁₄	[116,118–123]
CO ₂	v_3	$\sim 4.50 \times 10^3$	$(\pi c T_2)^{-1}$	$\sim 3.5 \times 10^{-5}$	$1.8 \times 10^{-15} T_2$	300	$<10^{18}$	$1.5 \times 10^4 T_2$	≥ 1	C ₅ H ₁₀ or C ₆ H ₁₄	[116,123–126]
	v_3	$\sim 10.5 \times 10^3$	$(\pi c T_2)^{-1}$	$\sim 1.3 \times 10^{-5}$	$6.4 \times 10^{-15} T_2$	300	$<10^{18}$	$2.0 \times 10^4 T_2$	≥ 1	C ₆ H ₁₄ self	[116,123–126]
N ₂ O	v_7	$\sim 9.54 \times 10^3$	$(\pi c T_2)^{-1}$	$\sim 1.0 \times 10^{-5}$	$5.1 \times 10^{-16} T_2$	300	$<10^{18}$	$5.3 \times 10^4 T_2$	≥ 1	self	[116,127]
	v_7	$\sim 3.34 \times 10^3$	$(\pi c T_2)^{-1}$	0.81	$5.6 \times 10^{-15} T_2$	300	$<10^{18}$				
NH ₃	v_5	$\sim 3.39 \times 10^3$	$(\pi c T_2)^{-1}$	0.39	$2.2 \times 10^{-15} T_2$	300	$<10^{18}$	$1.3 \times 10^4 T_2$	≥ 1	self	
				0.017							
				0.003							

Source: Adapted from Ref. 5.

^a Absorption wavelength.^b Doppler-broadened line width (FWHM) except homogeneous line width when indicated by the factor T_2 .^c Oscillator strength.^d Absorption cross-section.^e Phase coherence time.^f Temperature.^g Population difference.^h Line center saturation intensity.ⁱ Typical ground state recovery time.

II. LIQUIDS

A. Dye Solutions

Dyes can also be approximated as two-level systems when the intersystem crossing rate is small compared to the fluorescent rate. This assures that the buildup of triplet states is minimal, and the interaction can be described as between only the ground and the excited singlet states. Absorptive transitions are often very strong in these systems with large oscillator strengths. Typically $T_2 \geq 0.1$ ps, and the quenching agent quenches the triplet state to recover the ground singlet state quickly, since the phosphorescent rate is slow (lifetime of the lowest triplet is typically ~ 1 μ s). Pertinent data for two-level dye systems are given in Table 4. Note that the line width (column four) in this table is the homogeneous line width of the transition.

Dyes often also have large nonresonant values of $\chi^{(3)}$, and some have been measured. Table 5 gives some examples. See Ref. 4b for more data.

Although these values are reported as nonresonant data, the linear absorption can still be significant, especially in applications. A figure of merit often quoted is $\chi^{(3)}/\alpha$ or n_2/α , where α is the linear absorption coefficient. For applications of these materials, α should always be measured at the intended wavelength.

For example, β -carotene is cited as a two-level system near 420–480 nm in Table 4. However, these large organic molecules often have a large Q-band absorption in the near-infrared. Note from Table 5 that n_2^l for β -carotene is significantly larger at 1064 nm than at 532 nm, even though at a lower concentration. However, the laser pulse width can also have an effect. For long pulse widths (>1 ns), there is the possibility of contributions to n_2 from electrostrictive, molecular reorientation, and thermal effects. These phenomena are less prevalent for pulses <1 ns. All possible effects must be kept in mind when interpreting or applying nonlinearities.

B. Neat Liquids

Table 6 presents data for several common solvents. Again, a more complete listing can be found in Refs. 1–4. Original references are included in the table. Note that several sources for carbon disulfide have been given since its value is often quoted as a standard.

The linear refractive index is also given in some references in addition to nonlinear data. When these linear data are not available, values were taken from Ref. 177. In these cases the value of the index is quoted at the sodium D line (589.3 nm). Therefore, due to dispersion, the value of n_0 may not be accurate to two decimal places for the stated wavelength (where the nonlinearity was

Table 4 Data for Computing Nonlinear Reference Index in Two-Level Systems: Organic Dyes

Absorber	Upper state	λ (nm) ^a	$\Delta\nu$ (cm ⁻¹) ^b	f^c	σ (cm ²) ^d	T (K) ^e	Typical ΔN (cm ⁻³) ^f	$I_{s0}\tau$ (W·ns/cm ²) ^g	Typical τ (ns) ^h	Quenching agent	Ref.
3-Phenylbenzo-furan in cyclohexane	S ₁	307	1800	0.41	1.23 × 10 ⁻¹⁶	300	<10 ¹⁸	2.4 × 10 ⁶	1.8	O ₂ ⁱ	[128]
3,3''-Dimethyl- <i>P</i> -quarter-phenyl in cyclohexane	S ₁	296	1800	0.41	1.27 × 10 ⁻¹⁶	300	<10 ¹⁸	2.4 × 10 ⁶	1.8	O ₂ ⁱ	[128]
3,3''-Dimethyl-3',3'- <i>P</i> -quarter-phenyl in cyclohexane	S ₁	323	2700	0.82	1.12 × 10 ⁻¹⁶	300	<10 ¹⁸	1.9 × 10 ⁶	1.0	O ₂ ⁱ	[128]
Di(3-ethylheptyl)- <i>p</i> -quinophenyl in cyclohexane	S ₁	297	2700	0.56	2.4 × 10 ⁻¹⁶	300	<10 ¹⁸	1.9 × 10 ⁶	1.0	O ₂ ⁱ	[128]
PPF in cyclohexane	S ₁	306	5300	$\Sigma = 2.3$	2.4 × 10 ⁻¹⁶	300	<10 ¹⁸	1.4 × 10 ⁶	0.8	O ₂ ⁱ	[128]
Rhodamine 101 in ethanol	S ₁	341	1200	0.19	8.5 × 10 ⁻¹⁷	300	<10 ¹⁸	2.2 × 10 ⁶	1.2	O ₂ ⁱ	[128]
Rhodamine B in glycerol	S ₁	326	1600	0.55	1.4 × 10 ⁻¹⁶	300	<10 ¹⁸	2.2 × 10 ⁶	1.2	O ₂ ⁱ	[129]
Rhodamine B in ethanol	S ₁	576	1200	0.97	4.4 × 10 ⁻¹⁶	300	<10 ¹⁸	3.9 × 10 ⁵	8 ^j	O ₂ ⁱ	[128,130]
Rhodamine 6G perchlorate in ethanol	S ₁	554	1200	~1	4.8 × 10 ⁻¹⁶	300	<10 ¹⁸	3.7 × 10 ⁵	7 ^j	O ₂ ⁱ	[128]
Coumarin 102 in ethanol	S ₁	554	1200	~1	4.8 × 10 ⁻¹⁶	300	<10 ¹⁸	3.7 × 10 ⁵	3.2	O ₂ ⁱ	[128]
Cresyl violet perchlorate in ethanol	S ₁	530	~1200	0.95	4.3 × 10 ⁻¹⁶	300	<10 ¹⁸	4.4 × 10 ⁵	3.9	O ₂ ⁱ	[128–130]
Oxazine 1 perchlorate in ethanol	S ₁	389	3600	0.55	8.3 × 10 ⁻¹⁷	300	<10 ¹⁸	1.5 × 10 ⁶	<4	O ₂ ⁱ	[129,131]
	S ₁	601	1900	0.94	2.7 × 10 ⁻¹⁶	300	<10 ¹⁸	6.0 × 10 ⁵	<6	O ₂ ⁱ	[129,130]
	S ₁	645	1100	0.97	4.8 × 10 ⁻¹⁶	300	<10 ¹⁸	3.2 × 10 ⁵	<7	O ₂ ⁱ	[129,130]

(continued)

Table 4 Continued.

Absorber	Upper state	λ (nm) ^a	$\Delta\nu$ (cm ⁻¹) ^b	f^c	σ (cm ²) ^d	T (K) ^e	Typical ΔN (cm ⁻³) ^f	$I_{\text{g0}} \tau$ (W·ns/cm ²) ^g	Typical τ (ns) ^h	Quenching agent	Ref.
Pyromin B perchlorate in ethanol	S ₁	553	~2000	$\Sigma = 1.6$	4.3×10^{-16}	300	$< 10^{18}$	4.2×10^5	< 6	O ₂ ⁱ	[129,132]
Cryptocyanine in propanol	S ₁	700	1100	$\Sigma = 1.6$	8×10^{-16}	300	$< 10^{18}$	1.8×10^5	0.044	O ₂ ^j	[133,134]
β -Carotene in hexane	S ₁	420–480	4200	$\Sigma = 3$	5.2×10^{-16}	300	$< 10^{18}$	4.2×10^5		O ₂ ^j	[135]

Source: Adapted from Ref. 5.

^a Absorption wavelength.^b Homogeneous line width (FWHM).^c Oscillator strength.^d Absorption cross-section.^e Temperature.^f Population difference.^g Line center saturation intensity.^h Typical ground state recovery time.ⁱ Also, cyclooctatetraene or cycloheptatriene [133,139].^j Radiative lifetime.

Table 5 Nonlinear Refractive Index and Third Order Susceptibility Data for Selected Liquid Solutions

Material/solvent ^a	λ (nm)	Pulse width (ns)	n_0	$(10^{-20} \text{ m}^2/\text{V}^2)^b$	n_2 (10^{-13} esu)	n_2' ($10^{-16} \text{ cm}^2/\text{W}$)	$(10^{-20} \text{ m}^2/\text{V}^2)$	$\chi_{xxx}^{(3)}$ (10^{-13} esu)	$\chi_{xxx}^{(3)}$ (10^{-13} esu)	Method ^c	Ref.
α, β -unsaturated ketone derivative/ toluene ($R = \text{NO}_2$, $5-20 \times 10^{-3}$ M)	1064 532	7		1360 – 1730				326 – 413	ZS	[182]	
α, β -unsaturated ketone derivative/ toluene ($R = \text{CN}$, $5-20 \times 10^{-3}$ M)	1064 532	7		2240 – 852				535 – 203	ZS	[182]	
2-(9-Carbazole)ethyl methacrylate & 3-(2-methacryloxy) carbonyl 7 diethylamino-coumarine/ tetrahydrofuran (20 g/l)	532	0.030			0.47				DFWM	[183]	
Carbon nanotubes/ (polypyrrol & <i>m</i> -cresyl with ethanol) (0.08 mg/ml)	1064 532	0.030				1.2456 2.1685	DFWM	1.2456 2.1685	[186]		
Carbon nanotubes/ (polypyrrol & <i>m</i> -cresyl with ethanol) (0.08 mg/ml)	1064 532	8				242.9 58.6	DFWM	242.9 58.6	[186]		

(continued)

Table 5 Continued.

Material/solvent ^a	λ (nm)	Pulse width (ns)	n_0	n_2 ($10^{-20} \text{ m}^2/\text{V}^2$) ^b	n_2 (10^{-13} esu)	n_2^l ($10^{-16} \text{ cm}^2/\text{W}$)	$\chi_{ext}^{(3)}$ ($10^{-20} \text{ m}^2/\text{V}^2$)	$\chi_{ext}^{(3)}$ (10^{-13} esu)	Method ^c	Ref.
β -Carotene/carbon disulfide ($5.7 \times 10^{19} \text{ cm}^3$)	1064 532	10	106		25,000				TWM	[18]
β -Carotene/ethanol ($2.0 \times 10^{23} \text{ cm}^3$)		0.16	1.3	0.12		(33.4) ^b	0.2		DFWM	[19,20]
Dihydrogen	532	0.08–0.20				40			DFWM	[22]
Hypocrellin A/ terephthalocyanine/ toluene ($3.86 \times 10^{-4} \text{ M}$)		532					−1.44		ZS	[184]
Hypocrellin A/ ethanol ($7.7 \times 10^{-5} \text{ M}$)		0.040					−0.47		ZS	[184]
Hypocrellin A/ ethanol ($2.0 \times 10^{-5} \text{ M}$)	1064	0.040								
Lead-phthalocyanine/ chloroform (0.73 M)	1064	0.035					2000		DFWM	[23]
Magnesium octamethyl- tetraphenylporphyrin/ tetrahydrofuran ($10^{-5} - 10^{-4} \text{ g/ml}$)	532	17					80,000		DFWM	[19]
<i>p</i> -N,N'-dimethylaniine tetrahydrofulvalene derivative ^a (0.7 mole/m ³)		0.030					11.4 ± 0.5		DFWM	[185]
<i>p</i> -N,N'-dimethylaniine tetrahydrofulvalene derivative ^b (1.3 mole/m ³)	532	0.030					9.5 ± 0.5		DFWM	[185]

Nigrosine/water ($4.2 \times 10^{21} \text{ cm}^3$)	532	0.16	1.3		2.6	DFWM [20,22]
Physiological saline	532	0.06	1.33	0.020	1.8 ± 0.6	ZS [178]
Platinum-phthalocyanine/chloroform (0.73 M)	1064	0.035				DFWM [23]
Polyaniline emeraldine base/dimethylsulfoxide (1.3 mg/ml)	532	0.070		-200		ZS [181]
Polyaniline leucoenine alidine base/ dimethylsulfoxide (1.3 mg/ml)	532	0.070		-400		ZS [181]
Poly(3-methoxy- N-vinyl carbazole)/ tetrahydrofuran (20 g/l)	532	0.030			0.19	DFWM [183]
Poly(N-vinyl carbazole)/ tetrahydrofuran (20 g/l)	532	0.030			0.1	DFWM [183]
Tetrabenzoporphyrin/ tetrahydrofuran (10^{-5} – $10^{-4} \text{ g}/\text{ml}$)	532	17			30,000	DFWM [19]
Tetrakis(cumylophenoxyl) phthalocyanine/ chloroform (0.73 M)	1064	0.035			40	DFWM [23]
Vitreous humor (human)	532	0.06	1.3	0.016	1.4 ± 0.4	ZS [178]
Vitreous humor (rabbit)	532	0.06	1.3	0.030	2.7 ± 0.6	ZS [178]
Zinc tetraphenylporphyrin/ toluene ($2.29 \times 10^{-4} \text{ M}$)	532	0.08–0.20			20	DFWM [22]

^a M = mole/liter.^b Calculated.^c DFWM, degenerate four-wave mixing; TWM, three-wave mixing; ZS, Z-scan.

Chlorobenzene	590, 560	3	1.52			0.30	TWM [30]
Chlorobenzene	1320	0.7	1.50	44	40	110	NLI [29]
Chlorobenzene	532	0.030			192	NLI [188]	
Chloroform	532	0.025	1.46 (D)			0.19	NLI [39]
Chloroform	1064, 532	0.01	1.46 (D)	11.8	10.6	OKE [25]	
Cyclohexane	532	0.025	1.45 (D)			0.09	NLI [39]
Cyclohexane	1064, 532	0.01	1.45 (D)	4.3	3.9	OKE [25]	
Dichlorobenzene	1320	0.7	1.53	46	41	110	NLI [29]
Dimethyl methane	1320	0.7	1.69	66	59	150	NLI [29]
Dimethyl ketone	532	0.030			32	NLI [188]	
Ethanol	694	10	1.36 (D)			1.4	NLI [24]
Ethanol	1064, 532	0.01	1.36 (D)	2.8	2.5	OKE [25]	
Formic acid	1064, 532	0.01	1.37 (D)	11	10	OKE [25]	
Glycerin	694	10	1.47 (D)			1.4	NLI [24]
Glycerin	1064, 532	0.01	1.47 (D)	2.8	2.5	OKE [25]	
Hexadecane	1064,	0.01	1.43 (D)	17.2	15.5	OKE [25]	
Iodobenzene	532						
Methanol	1320	0.7	1.59	77	69	180	NLI [29]
Methanol	1064, 532	0.01	1.33 (D)	2.4	2.2	OKE [25]	
Methyl-methacrylate	1064, 532	0.025				0.077 ± 0.0072 OKE	[187]
Nitrobenzene	532	0.025	1.56 (D)			1.3	NLI [39]
Nitrobenzene	1064, 532	0.01	1.56 (D)	278	250	OKE [25]	
Nitrobenzene	1064, 532	0.025				0.925 ± 0.033 OKE	[187]

(continued)

Table 6 Continued.

Material	λ (nm)	Pulse width (ns)	n_0^a	$n_2^{b, D}$ ($10^{-22} \text{ m}^2/\text{V}^2$)	$n_2^{D, Z}$ (10^{-13} esu)	n_2^l ($10^{-16} \text{ cm}^2/\text{W}$)	$\chi_{\text{xx}}^{(3)}$ ($10^{-20} \text{ m}^2/\text{V}^2$)	$\chi_{\text{xx}}^{(3)}$ (10^{-13} esu)	Method ^c	Ref.
Nitrobenzene	1054, 527	0.006	1.56 (D)	233	210				OKE	[32]
Nitrobenzol	532	0.030	1.55 (D)	300	270	245			NLI	[188]
Nitrotoluene	1064, 532	0.01	1.40 (D)	6.1	5.5				OKE	[25]
Octane	1064, 532	0.01	1.43 (D)	4.6	4.1				OKE	[25]
Octanol	1064, 532	0.01	1.36 (D)	4.7	4.2				OKE	[25]
Pentane	1064, 532	0.01	1.39 (D)	3.0	2.7				OKE	[25]
Propanol	1064, 532	0.01	1.59	122	110	280			NLI	[29]
Quinoline	1320	0.7	1.50 (D)					0.38	NLI	[39]
Toluene	532	0.025	1.50 (D)	67	60				OKE	[25]
Toluene	1064, 532	0.01	1.40 (D)	9.1	8.2				OKE	[25]
Trichloroethane	1064, 532	0.01	1.44 (D)						SF	[34]
Water	532	0.021	1.33 (D)	1.9	1.7				OKE	[25]
Water	1064, 532	0.01	1.33 (D)	1.4	1.3					
Water (heavy)	532	0.06	1.33 (D)	1.4	1.3 ± 0.6				ZS	[178]
Xylene	694	10	1.33 (D)	2.2	2.0			4.4	SF	[34]
									NLI	[24]

^a (D) = sodium D line (589.3 nm) [177].^b Calculated.^c OKE, optical Kerr effect; THZS, top hat Z-scan; NLI, nonlinear interferometry; SF, self-focusing; TWM, three-wave mixing; ZS, Z-scan.

measured). Usually, the values of n_0 should be accurate to at least one decimal place.

Several methods have been employed in these measurements. Most of these were discussed in Chapter 7. Note that NLI includes both time resolved and time integrated nonlinear interferometry. Different types of interferometers have been reported in the literature (e.g., Mach-Zehnder, Jamin, etc.).

Absolute measurements of the nonlinear refractive index are often conveniently reported in intensity units, since the intensity of the measurement is readily measurable. When relative measurements are performed, the values are often reported in esu (cgs units), since historically the values for standard materials were given in these units. Many prefer SI units. Therefore n_2 has been computed in these units and included in the table.

III. SOLID DIELECTRICS

A. Transparent Dielectrics

Optical data for some selected wide band gap insulator crystals are given in Table 7. References 1–4 contain several additional materials. This table contains some new data as well as data tabulated previously. Again, the linear index is sometimes given in the references. When these data are not available, values were taken from Ref. 177. As stated earlier, in these cases the value of the index is quoted at the sodium D line (589.3 nm). Therefore, due to dispersion, the value of n_0 may not be accurate to two decimal places for the stated wavelength (where the nonlinearity was measured). Usually, the values of n_0 should be accurate to at least one decimal place.

As stated above, most nonlinear index data are reported in intensity units or esu (cgs units). Therefore calculated values in SI units are included in the table.

The most common methods used for these data were three-wave mixing, nonlinear interferometry, and Z-scan. These methods were discussed in Chapter 7.

Table 8 presents data for several types of optical glasses, mostly from Refs. 51 and 53. Linear refractive index data, when available, were taken from several sources. The methods primarily used in these cases were three-wave mixing and degenerate four-wave mixing. Some optical fiber data at one of the communication wavelengths are also given for interest. References 2 and 4a give further examples of glass data, including estimates of linear refractive index not contained in Table 8.

Table 7 Nonlinear Refractive Index and Third Order Susceptibility Data for Selected Wide Bandgap Crystals

Material	Pulse width (ns)	λ (nm)	n_0^a	$n_2 \cdot 10^{-22} \text{ m}^2/\text{V}^2$ ^b	$n_2 \cdot 10^{-13} \text{ esu}$	$n_2^l \cdot 10^{-16} \text{ cm}^2/\text{W}$	$n_2^l \cdot 10^{-22} \text{ m}^2/\text{V}^2$	$\chi_{xx}^{(3)} \cdot 10^{-13} \text{ esu}$	$\chi_{xx}^{(3)} \cdot 10^{-13} \text{ esu}$	Method ^c	Ref.
Aluminum oxide ($E \perp c$)	1064	3	1.75	1.37	1.23					TWM	[40]
Aluminum oxide ($E \parallel c$)	1064	3	1.75	1.4	1.3					TWM	[40]
Aluminum oxide	1064	0.028	1.75	3.2	2.9					ZS	[41]
Aluminum oxide	532	0.02	1.8	3.7	3.3					ZS	[41]
Aluminum oxide	355	0.016	1.8	4.1	3.7					ZS	[41]
Barium fluoride	575	4	1.47 (D)								
Barium fluoride	1064	0.125	1.47 (D)	1.11		2.85				NLI	[42]
Barium fluoride	532	0.021	1.48	8.17		2.08				ZS	[43]
(100) Barium fluoride											
(010) Barium fluoride	532	0.021	1.48	8.17		2.08				ZS	[43]
(110) Beryllium aluminum oxide	1064	3	1.73	1.62	1.46					TWM	[40]

γ -cadmium fluoride	575	4	1.56 (D)	0.145	TWM	[27]	
γ -cadmium fluoride	1064	3	1.56 (D)	0.145	TWM	[40]	
(100)					NLI	[42]	
γ -cadmium fluoride	1064	0.125	1.56 (D)	1.60	TWM	[40]	
Calcium carbonate	1064	3	1.64	1.23	TWM	[40]	
($E \perp c$)					TWM	[40]	
γ -calcium carbonate ($E \parallel c$)	1064	3	1.48	0.92	0.043	TWM	[40]
γ -calcium fluoride	575	4	1.43 (D)	1.43 (D)	0.043	TWM	[27]
γ -calcium fluoride	1064	3	1.43 (D)	0.48	0.043	TWM	[40]
(100)					TWM	[40]	
γ -calcium oxide	1064	3	1.83	5.8	0.043	TWM	[40]
(100)					TWM	[40]	
γ -cerium fluoride	1064	3	~1.6	1.44	0.043	NLI	[42]
γ -cerium fluoride	1064	0.125	~1.6	1.72	0.046	TWM	[45]
γ -cesium chloride	1064, 532	0.006	1.64 (D)	3.8 × 10 ⁷	0.086	TWM	[46]
γ -chromium dioxide	632.8	cw		3.6 × 10 ⁸		ZS	[46]
doped gadolinium aluminum oxide	611.9			1.4 × 10 ⁹			
	604			1.9 × 10 ⁹			
	594			1.8 × 10 ⁹			
	514.5						

Table 7 Continued.

Material	λ (nm)	Pulse width (ns)	n_0^a	$(10^{-22} \text{ m}^2/\text{V}^2)^b$	n_2 (10^{-13} esu)	n_2^l ($10^{-16} \text{ cm}^2/\text{W}$)	$\chi_{\text{ext}}^{(3)}$ ($10^{-22} \text{ m}^2/\text{V}^2$)	$\chi_{\text{ext}}^{(3)}$ (10^{-13} esu)	Method ^c	Ref.
Diamond	545	4	2.42 (D)					0.46	TWM	[27]
Erbium oxide	1064	3	1.96	5.03	4.53				TWM	[40]
Gallium oxide	1064	3	1.96	6.4	5.8				TWM	[40]
Lanthanum fluoride (Ell_c)	1064	3	1.60	1.6	1.4				TWM	[40]
Lanthanum fluoride	1064	0.125	1.60	1.68	1.51	3.95			NLI	[42]
Lead fluoride	1064	0.125	1.76	5.49	4.94				NLI	[42]
Lithium chloride	1064, 532	0.006	1.66 (D)					0.069	TWM	[45]
Lithium fluoride	1064	3	1.39 (D)	0.29	0.26				TWM	[40]
Lithium fluoride	1064	0.028	1.39 (D)	0.30	0.81				ZS	[47]
Lithium fluoride	532	0.02	1.39 (D)	0.33	0.9				ZS	[47]
Magnesium aluminum oxide	1064	3	1.72	1.7	1.5				TWM	[40]
Magnesium fluoride	1064	0.125	1.38 (D)	0.33	0.30	0.92			NLI	[42,44]
Magnesium fluoride	1064	0.028	1.38 (D)	0.22		0.61			ZS	[47]
Magnesium fluoride	532	0.027	1.38 (D)	0.28	0.25				ZS	[47]

Magnesium fluoride	355	0.016	1.4	0.26	0.69	ZS	[41]
Magnesium oxide	1064	3	1.72	1.79	1.61	TWM	[40]
Potassium bromide	1064	3	1.54	3.26	2.93	TWM	[40]
Potassium chloride	1064	3	1.48	2.23	2.01	TWM	[40]
Potassium dihydrogen phosphate ($E \perp c$)	1064	3	1.49	0.87	0.78	TWM	[40]
Potassium dihydrogen phosphate ($E \parallel c$)	1064	3	1.46	0.80	0.72	TWM	[40]
Potassium fluoride	1064, 532	0.006	1.36 (D)			0.014	TWM
Potassium iodide	1064, 532	0.006	1.68 (D)			0.38	TWM
Potassium titanyl phosphate (100)	1064	0.03	1.74	9.89	21.4	$\text{Re}^d = 23.2$	ZS
Potassium titanyl phosphate (010)	1064	0.03	1.74	8.36	18.1		ZS
Potassium titanyl phosphate (110)	1064	0.03	1.74	6.42	13.9		ZS
Ruby	514.5	cw	1.76			1.2×10^8	ZS

(continued)

Table 7 Continued.

Material	λ (nm)	Pulse width (ns)	n_0^a	$n_2^{b,c}$ ($10^{-22} \text{ m}^2/\text{V}^2$) ^b	$n_2^{d,e}$ (10^{-13} esu)	n_2^f ($10^{-16} \text{ cm}^2/\text{W}$)	$\chi_{\text{ext}}^{(3)}$ ($10^{-22} \text{ m}^2/\text{V}^2$)	$\chi_{\text{ext}}^{(3)}$ (10^{-13} esu)	Method ^c	Ref.
Silicon dioxide ($E \perp c$)	1064	3	1.53	1.24	1.12				TWM	[40]
Silicon dioxide ($E \parallel c$)	1064	3	1.54	1.29	1.16				TWM	[40]
Silver chloride	1064	3	2.02	25.9	23.3				TWM	[40]
Sodium bromide	1064	3	1.62	3.62	3.26				TWM	[40]
Sodium chloride	1064	3	1.53	1.78	1.59				TWM	[40]
Sodium fluoride	1064	3	1.32	0.38	0.34				TWM	[40]
Sodium fluoride	1064	0.125	1.32	0.48		1.37			NLI	[42]
Strontium fluoride	575	4	1.44 (D)				0.044		TWM	[27]
Strontium fluoride	1064	3	1.43	0.56	0.50				TWM	[40]
Strontium fluoride	1064	0.125	1.43	0.67		1.76			NLI	[42]

Strontium oxide (110)	1064	3	1.81 (D) ^a	5.63	5.07	TWM	[40]
Strontium titanium oxide	1064	3	2.31	29.7	26.7	TWM	[40]
Titanium dioxide ($E \perp c$)	532	5	2.66	-718	-646 ± 80	ZS	[48]
Titanium dioxide ($E \parallel c$)	532	5	2.97	-839	-755 ± 94	ZS	[48]
Titanium dioxide	1064	3	2.48	62.0	55.8	TWM	[40]
Titanium dioxide	1064	0.08	2.48	132	200	DFWM	[53]
Ytrrium oxide	1064	3	1.92	2.92	5.33	TWM	[40]
Zirconium oxide	1064	3	2.12	6.4	5.8	TWM	[40]
Zirconium oxide	1064	0.045	2.12	8.9	8	SF	[49]
Zirconium oxide	1064	0.03	2.12	6.7	6	SF	[50]

^a (D) = sodium D line (589.3 nm) [177].^b Calculated.^c DFWM, degenerate four-wave mixing; SF, self-focusing; NLI, nonlinear interferometry; ZS, Z-scan; TWM, three-wave mixing.^d Re, real part.

Table 8 Nonlinear Refractive Index and Third Order Susceptibility Data for Selected Glasses

Material	λ (nm)	Pulse width (ns)	n_0	$(10^{-22} m^2/V^2)^a$	n_2 (10^{-13} esu)	n_2' ($10^{-16} cm^2/W$)	$n_2^{(3)}$ ($10^{-22} m^2/V^2$)	$\chi_{xxx}^{(3)}$ (10^{-13} esu)	Method ^b	Ref.
Aluminate L-65	1064	3			2.93	2.64			TWM	[51]
As ₂ S ₃ -chalcogenide	1550 1300	100×10^{-6}	2-2.5			180 180			ZS	[189]
As ₄₀ S ₆₀ -chalcogenide	1250 1500	~fs	2.45			650 540			TBC	[194]
As ₄₀ S ₅₀ Se ₁₀ -chalcogenide	1250 1500	~fs	2.49			1000 940			TBC	[194]
As ₄₀ S ₅₀ Se ₂₀ -chalcogenide	1250 1500	~fs	2.55			900 740			TBC	[194]
As ₄₀ S ₅₀ Se ₃₀ -chalcogenide	1250 1500	~fs	2.62			1500 1100			TBC	[194]
As ₄₀ S ₅₀ Se ₄₀ -chalcogenide	1250 1500	~fs	2.70			2300 1400			TBC	[194]
As ₄₀ Se ₆₀ -chalcogenide	1250 1500	~fs	2.81			3000 2300			TBC	[194]

As ₃₉ Se ₆₁ - chalcogenide	1250 1500	~fs	2.81	TBC	[194]
As ₄₀ Se ₅₅ Cu ₅ -chalcogenide	1250 1500	~fs	2.93	TBC	[194]
As ₂₅ S ₅ Te ₂₀ - chalcogenide	1250 1500	~fs	2.52	TBC	[194]
Bi ₂ O ₃ - B ₂ O ₃ - SiO ₂ - (60-20- 20 mol.-%)	1900	6	2.04	51	THG [191]
Bi ₂ O ₃ - B ₂ O ₃ - SiO ₂ -(65-20- 15 mol.-%)	1900	6	2.08	67	THG [191]
Bi ₂ O ₃ - B ₂ O ₃ - SiO ₂ -(70-20- 10 mol.-%)	1900	6	2.13	75	THG [191]
Bi ₂ O ₃ - B ₂ O ₃ - SiO ₂ -(75-20- 5 mol.-%)	1900	6	2.16	79	THG [191]
Bi ₂ O ₃ - B ₂ O ₃ - SiO ₂ -(77.5-20- 2.5 mol.-%)	1900	6	2.21	92	THG [191]
Borate L-109 (Kigre)	1064	3	2.09	TWM	[51]
			1.88		

(continued)

Table 8 Continued.

Material	λ (nm)	Pulse width (ns)	n_0	$(10^{-22} \text{ m}^2/\text{V}^2)^a$	n_2 (10^{-13} esu)	n_2^l ($10^{-16} \text{ cm}^2/\text{W}$)	$\chi_{\text{xxx}}^{(3)}$ ($10^{-22} \text{ m}^2/\text{V}^2$)	$\chi_{\text{xxx}}^{(3)}$ (10^{-13} esu)	Method ^b	Ref.
Borsilicate BK-7 (Schott)	1064	3	1.52	1.44	1.30				TWM	[51]
Fluorophosphate E-115 (Owens-Illinois)	1064	3		0.89	0.80				TWM	[51]
Fluorophosphate E-131 (Owens-Illinois)	1064	3		0.68	0.61				TWM	[51]
Fluorophosphate E-132 (Owens-Illinois)	1064	3		0.78	0.70				TWM	[51]
Fluorophosphate E-133 (Owens-Illinois)	1064	3		0.76	0.68				TWM	[51]

Fluoro-phosphate K-1172 (Owens-Illinois)	1064	3	0.79	0.71	TWM	[51]
Fluorozirconate 9028	1064	3	1.34	1.21	TWM	[51]
Germanium silica (8 wt-% GeO ₂)	800	16×10^{-6}		0.883	TBC	[225]
Germanium silica (19 wt-% GeO ₂)	800	16×10^{-6}		0.915	TBC	[225]
Germanium silica (36 wt-% GeO ₂)	800	16×10^{-6}		0.988	TBC	[225]
Germanium silica (50 wt-% GeO ₂)	800	16×10^{-6}	1.13		TBC	[225]
GeS ₂ -chal cogenide	1550 1300	100×10^{-6} 2-2.5		92 80	ZS	[189]
LaSfF ₃ (Schott)- La,Zn,B	638	130×10^{-6}	1.81	2.6	OKE	[190]
LaSfF ₈ (Schott)- La, B	638	130×10^{-6}	1.81	4.8	OKE	[190]

(continued)

Table 8 Continued.

Material	λ (nm)	Pulse width (ns)	n_0	$(10^{-22} \text{ m}^2/\text{V}^2)^a$	n_2 (10^{-13} esu)	n_2^l ($10^{-16} \text{ cm}^2/\text{W}$)	$(10^{-22} \text{ m}^2/\text{V}^2)$	$\chi_{\text{ext}}^{(3)}$ (10^{-13} esu)	$\chi_{\text{ext}}^{(3)}$ ($10^{-22} \text{ m}^2/\text{V}^2$)	Method ^b	Ref.
LaSF32 (Schott)- Ti,Nb,Ba	638	130×10^{-6}	1.80		4.6					OKE	[190]
LaSFN9 (Schott)- Ti,I,a, Ba,B	638	130×10^{-6}	1.85		4.3					OKE	[190]
LaSFN18 (Schott)- Nb,Ia,B	638	130×10^{-6}	1.91		6.6					OKE	[190]
Lead gallate (40 Pb:40 Bi:20 Ga)	1064	0.1	2.45 (D)							DFWM	[179]
Lead gallate (40 Pb:35 Bi:25 Ga)	1064	0.1	2.45 (D)							DFWM	[179]
Lead silicate SF-56 (Schott)	1064	0.08	1.75	12.1	26					DFWM	[53]
Lead silicate SF-57 (Schott)	1064	0.08	1.81	19.7	41					DFWM	[53]
Lead silicate SF-58 (Schott)	1064	0.08	1.88	24.5	49					DFWM	[53]

Lead silicate SF-59 (Schott)	1064	0.08	1.91	34.5	68	DFWM [53]
Phosphate LHG-5 (Hoya)	1064	3		1.60	1.44	TWM [51]
Phosphate LHG-6 (Hoya)	1064	3		1.24	1.12	TWM [51]
Phosphate P-108 (Kigre)	1064	3		1.42	1.28	TWM [51]
Phosphate 5037 (Hoya)	1064	3		1.73	1.56	TWM [51]
Phosphate 5038 (Hoya)	1064	3		1.90	1.71	TWM [51]
Silica (Dynasil 4001)	1064	3		0.94	0.85	TWM [51]
Silica (SiO ₂)	532	0.030			2.5	NLI [188]
Silica fiber	1319	0.11	1.46	2.62	2.36	SPM [52]
Silica fiber (dispersion shifted)	1319	0.11	1.46	2.91	2.62	SPM [52]
Silica fiber (single- mode, 10.5 km)	1472	cw		23.00	OKE [195]	(continued)

Table 8 Continued.

Material	λ (nm)	Pulse width (ns)	n_0	$(10^{-22} \text{ m}^2/\text{V}^2)^a$	n_2 (10^{-13} esu)	n_2^l ($10^{-16} \text{ cm}^2/\text{W}$)	$\chi_{xx}^{(3)}$ ($10^{-22} \text{ m}^2/\text{V}^2$)	$\chi_{xx}^{(3)}$ (10^{-13} esu)	Method ^b	Ref.
Silica fiber (single-mode, 20.5 km)	1472	cw	2100						OKE	[195]
Silica fiber (dispersion-shifted, 10.5 km)	1472	cw	2300						OKE	[195]
Silica fiber (dispersion-shifted, 20.5 km)	1472	cw	2100						OKE	[195]
Silica fiber (20 mol-% GeO_2)	1064	cw							NLI	[192]
Silicate C2828 (American Optical)	1064	3	1.53		1.71	1.54			TWM	[51]
Silicate ED-2 (Owens-Illinois)	1064	3	1.57		1.76	1.58			TWM	[51]
Silicate ED-3 (Owens-Illinois)	1064	3			1.70	1.53			TWM	[51]
Silicate ED-8 (Owens-Illinois)	1064	3			1.88	1.69			TWM	[51]
Silicate FR-5 (Hoya)	1064	3			2.14	1.93			TWM	[51]

Silicate LG-650 (Schott)	1064	3	1.60	1.44	TWM	[51]
Silicate O-246 (Kigre)	1064	3	1.46	1.31	TWM	[51]
Silicate S7606 (Schott)	1064	3	1.74	1.57	TWM	[51]
Silicate SF-6 (Schott)	1064	3	1.77	8.9	TWM	[51]
Tellurite 3151 (Rigre)	1064	3	27	24	TWM	[51]
Tellurite K-1261 SF6 (Schott)-Pb	1064	3	26	23	TWM	[51]
SFL6 (Schott)-Ti,Nb,Ba	638	130×10^{-6}	1.80	9.7	OKE	[190]
SF11 (Schott)-Pb	638	130×10^{-6}	1.80	6.8	OKE	[190]
SF56 (Schott)-Pb	638	130×10^{-6}	1.78	5.1	OKE	[190]
SFL56 (Schott)-Ti,Nb,Zr	638	130×10^{-6}	1.78	7.7	OKE	[190]
SF57 (Schott)-Pb	638	130×10^{-6}	1.85	5.1	OKE	[190]
SFL57 (Schott)-Ti,Nb,Ba	638	130×10^{-6}	1.85	9.6	OKE	[190]
SF58 (Schott)-Pb,B	638	130×10^{-6}	1.92	6.5	OKE	[190]
SF59 (Schott)-Pb,B	638	130×10^{-6}	1.95	15.4	OKE	[190]
SF59 (Schott)	1500			18.2	TBC	[193]
TeO ₂ -chalcogenide	1550	100×10^{-6}	2-2.5	38	ZS	[189]
	1300			40		
Thallium gallate (20 Tl:60 Bi:20 Ga)	1064	0.1	2.45 (D)	4.4	DFWM	[179]

(continued)

Table 8 Continued.

Material	λ (nm)	Pulse width (ns)	n_0	n_2 ($10^{-22} \text{ m}^2/\text{V}^2$) ^a	n_2 (10^{-13} esu)	n_2' ($10^{-16} \text{ cm}^2/\text{W}$)	$\chi_{\text{ext}}^{(3)}$ ($10^{-22} \text{ m}^2/\text{V}^2$)	$\chi_{\text{ext}}^{(3)}$ (10^{-13} esu)	Method ^b	Ref.
Thallium gallate (25 Tl:55 Bi:20 Ga)	1064	0.1	2.45 (D)						DFWM	[179]
Thallium gallate (30 Tl:50 Bi:20 Ga)	1064	0.1	2.45 (D)						DFWM	[179]
Thallium gallate (35 Tl:45 Bi:20 Ga)	1064	0.1	2.45 (D)						DFWM	[179]
Thallium gallate (40 Tl:60 Bi:20 Ga)	1064	0.1	2.45 (D)						DFWM	[179]
Thallium gallate (45 Tl:55 Bi:20 Ga)	1064	0.1	2.45 (D)						DFWM	[179]

Thallium-lead gallate (20 Tl:20 Pb:40 Bi:20 Ga)	1064	0.1	2.45 (D) ^a		4.8	DFWM [179]
Titanium Silicate FD-6	1064	0.08	1.77 ^b	14.6	31	DFWM [53]
Titanium Silicate FD-60	1064	0.08	1.77 ^b	9.4	20	DFWM [53]
Titanium Silicate FDS-9	1064	0.08	1.81 ^b	10.5	22	DFWM [53]

^a Calculated.^b DFWM, degenerate four-wave mixing; TWM, three-wave mixing; SPM, self-phase modulation; TBC, two-beam coupling; THG, third harmonic generation; NLI, nonlinear intereformetry; OKE, optical Kerr effect.

Adair et al. [51] compared their data to nonlinear index coefficients computed using the semiempirical formula

$$n_2(10^{-13} \text{ esu}) = \frac{68(n_d - 1)(n_d^2 + 2)^2}{v_d \{1.52 + [(n_d^2 + 2)(n_d + 1)/6n_d]v_d\}^{1/2}}$$

and found good agreement. In this formula, v_d is the Abbe number defined by

$$v_d = \frac{n_d - 1}{n_F - n_c}$$

where n_d , n_F , and n_c are refractive indices at wavelengths $\lambda_d = 587.6 \text{ nm}$, $\lambda_F = 486.1 \text{ nm}$, and $\lambda_c = 656.3 \text{ nm}$, respectively. This formula is derived using the Clausius–Mossotti equation to describe a medium with one polarizable constituent, assuming that the second hyperpolarizability γ is related to the linear polarizability α by $\gamma = Q\alpha^2$. Q is an empirically determined constant. This indicates that the above semiempirical formula may be useful for estimating n_2 for a variety of glass compositions with parameters normally supplied by the manufacturer.

B. Metal Colloids, Metal Ions, and Color Centers

Small metal colloid composite materials have generated some interest in the NLO community, primarily because of a plasmon resonance enhanced $\chi^{(3)}$. Quantum confinement effects in very small particles may also play a role in the nonlinearity. Table 9 gives data on several metal colloid suspensions in both solids and liquids.

Metal ion doped wideband crystals have been developed as laser media. For some applications that allow long response times (1~ms), these ions may be interesting two-level systems. Table 10, adapted from the work of Chang [5], presents data for computing the effective nonlinearity for some of these types of materials. This table is organized in the same fashion as Tables 2, 3, and 4. Comments similar to those stated in Sections I and II.A apply here. The total ground state recovery time for these materials is on the order of 1 ms.

Table 10 also includes data for color centers. Most color centers are unstable under high excitation energy at room temperature. The use of some color centers requires cryogenic temperatures, but large oscillator strengths $\sim 0.1 – 1$ are possible.

Table 9 Nonlinear Refractive Index and Third Order Susceptibility Data for Selected Metal Colloid Suspensions

Material ^a /host	λ (nm)	Pulse width (ns)	n_0	$(10^{-20} \text{ m}^2/\text{V}^2)$	(10^{-13} esu)	n_2^{l} ($10^{-10} \text{ cm}^2/\text{W}$)	$\chi_{\text{ext}}^{(3)}$ ($10^{-20} \text{ m}^2/\text{V}^2$)	$\chi_{\text{ext}}^{(3)}$ (10^{-30} esu)	Method ^b	Ref.
Cobalt/glass (silica) ($R = 1.5$)	770	1.30×10^{-6}				1.8			ZS	[199]
Copper/glass ($R = 2.5$, $f = 17.6 \times 10^{-4}$)	~ 565 -580	7					0.13	DFWM	[54]	
Copper/glass ($R = 2.8$, $f = 12.6 \times 10^{-4}$)	~ 565 -580	7					0.18	DFWM	[54]	
Copper/glass ($R = 3.4$, $f = 122.3 \times 10^{-4}$)	~ 565 -580	7					0.44	DFWM	[54]	
Copper/glass ($R = 4.0$, $f = 14.0 \times 10^{-4}$)	~ 565 -580	7					0.35	DFWM	[54]	
Copper/glass ($R = 5.5$, $f = 128.2 \times 10^{-4}$)	~ 565 -580	7					1.2	DFWM	[54]	
Copper/glass ($R = 7.3$, $f = 42.7 \times 10^{-4}$)	~ 565 -580	7					2.2	DFWM	[54]	
Copper/glass ($R = 7.5$, $f = 5.3 \times 10^{-4}$)	~ 565 -580	7					0.31	DFWM	[54]	
Copper/glass ($R = 7.8$, $f = 18.8 \times 10^{-4}$)	~ 565 -580	7					1.2	DFWM	[54]	
Copper/glass ($R = 10.6$, $f = 32.9 \times 10^{-4}$)	~ 565 -580	7					3.5	DFWM	[54]	
Copper/glass ($R = 11.2$, $f = 24.0 \times 10^{-4}$)	~ 565 -580	7					3.3	DFWM	[54]	
Copper/glass ($R = 12.2$, $f = 31.6 \times 10^{-4}$)	~ 565 -580	7					5.8	DFWM	[54]	
Copper/glass ($R = 12.5$, $f = 43.4 \times 10^{-4}$)	~ 565 -580	7					6.5	DFWM	[54]	
Copper/glass ($R = 21.3$, $f = 17.8 \times 10^{-4}$)	~ 565 -580	7					4.6	DFWM	[54]	

(continued)

Table 9 Continued.

Material ^a /host	λ (nm)	Pulse width (ns)	n_0	$(10^{-20} \text{ m}^2/\text{V}^2)$	n_2 (10^{-13} esu)	n_2^l ($10^{-10} \text{ cm}^2/\text{W}$)	$\chi_{\text{ext}}^{(3)}$ ($10^{-20} \text{ m}^2/\text{V}^2$)	$\chi_{\text{ext}}^{(3)}$ (10^{-8} esu)	Method ^b	Ref.
Copper/glass ($R = 24.6$, $f = 4.7 \times 10^{-4}$)	~565–580	7							DFWM	[54]
Copper/glass ($R = 29.0$, $f = 15.6 \times 10^{-4}$)	~565–580	7							DFWM	[54]
Copper/glass ($R = 32.3$, $f = 18.9 \times 10^{-4}$)	~565–580	7							DFWM	[54]
Copper/glass ($R = 40.2$, $f = 8.3 \times 10^{-4}$)	~565–580	7							DFWM	[54]
Copper/glass ($R = 47.7, 25.8 \times 10^{-4}$)	~565–580	7							DFWM	[54]
Copper/glass (alumina) ($R = 2.5 - 3$)	585	0.012							DFWM	[201]
Copper/silica	600–570	0.006				2.0–4.2				
($R = 2.5 - 12.5$, $f = .075 \times 10^{-4}$)						$\text{Re}^c \sim 1.1 -$ 2.3	ZS	ZS	[55]	
Copper/glass (silica) ($R = 1.1$, $f = 4 \times 10^{-2}$)	1064 532	0.006				0.024 ± 0.003		ZS	[196]	
Copper/glass (silica)	770	1.30×10^{-6}				0.030 ± 0.003				
Copper–nickel/glass (silica) ($R \sim 5$)	1064	0.006	1.96			0.5 < 0.05		ZS	[200]	
Copper–nickel/glass (silica)	770	1.30×10^{-6}				6.8		ZS	[197]	
Gold/acetone ($R = 2.5$, $f = 2.1 \times 10^{-4}$)	562	0.005				1.6 ± 1.5		DFWM	[56]	

Gold/acetone ($R = 2.5$, $f = 2.1 \times 10^{-4}$)	569	0.005	13 ± 0.3	DFWM [56]
Gold/acetone ($R = 2.5$, $f = 2.1 \times 10^{-4}$)	575	0.005	10 ± 0.2	DFWM [56]
Gold/acetone ($R = 2.5$, $f = 2.1 \times 10^{-4}$)	581	0.005	$8.7 \pm .02$	DFWM [56]
Gold/acetone ($R = 2.5$, $f = 2.1 \times 10^{-4}$)	587	0.005	$7.0 \pm .02$	DFWM [56]
Gold/acetone ($R = 2.5$, $f = 2.1 \times 10^{-4}$)	594	0.005	4.6 ± 0.3	DFWM [56]
Gold/acetone ($R = 2.5$, $f = 2.1 \times 10^{-4}$)	600	0.005	$3.5 \pm .09$	DFWM [56]
Gold/acetone ($R = 2.5$, $f = 2.1 \times 10^{-4}$)	606	0.005	$3.2 \pm .08$	DFWM [56]
Gold/glass (titania thin film) ($f = 38\%$)	532	200×10^{-6}	>2	DFWM [208]
	630		2^{-3}	
Nickel/glass (silica)	670		2^{-5}	
Silver/glass ($R = 2.1$, $f = 15.1 \times 10^{-5}$)	770	130×10^{-6}	1-7	ZS [209]
Silver/glass ($R = 3.0$, $f = 30.0 \times 10^{-5}$)	~415-430	7	0.031	DFWM [56]
Silver/glass ($R = 3.3$, $f = 33.5 \times 10^{-5}$)	~415-430	7	0.13	DFWM [56]
Silver/glass ($R = 4.0$, $f = 0.7 \times 10^{-5}$)	~415-430	7	0.36	DFWM [56]
Silver/glass ($R = 4.9$, $f = 48.4 \times 10^{-5}$)	~415-430	7	0.012	DFWM [56]
Silver/glass ($R = 5.2$, $f = 35.1 \times 10^{-5}$)	~415-430	7	1.2	DFWM [56]
Silver/glass ($R = 5.4$, $f = 2.6 \times 10^{-5}$)	~415-430	7	1.1	DFWM [56]
			0.11	DFWM [56]

(continued)

Table 9 Continued.

Material ^a /host	λ (nm)	Pulse width (ns)	n_0	$(10^{-20} \text{ m}^2/\text{V}^2)$	n_2 (10^{-13} esu)	$(10^{-10} \text{ cm}^2/\text{W})$	n_2^f ($10^{-20} \text{ m}^2/\text{V}^2$)	$\chi_{\text{ext}}^{(3)}$ (10^{-8} esu)	$\chi_{\text{ext}}^{(3)}$ ($10^{-20} \text{ m}^2/\text{V}^2$)	Method ^b	Ref.
Silver/glass ($R = 5.7$, $f = 22.5 \times 10^{-5}$)	~ 415 –430	7								1.3	DFWM [56]
Silver/glass ($R = 6.0$, $f = 27.3 \times 10^{-5}$)	~ 415 –430	7								1.8	DFWM [56]
Silver/glass ($R = 6.4$, $f = 24.2 \times 10^{-5}$)	~ 415 –430	7								1.9	DFWM [56]
Silver/glass ($R = 8.8$, $f = 25.6 \times 10^{-5}$)	~ 415 –430	7								3.3	DFWM [56]
Silver/glass ($R = 10.4$, $f = 26.6 \times 10^{-5}$)	~ 415 –430	7								4.4	DFWM [56]
Silver/glass ($R = 10.9$, $f = 27.7 \times 10^{-5}$)	~ 415 –430	7								7.6	DFWM [56]
Silver/glass ($R = 11.3$, $f = 18.7 \times 10^{-5}$)	~ 415 –430	7								6.1	DFWM [56]
Silver/glass ($R = 12.1$, $f = 24.0 \times 10^{-5}$)	~ 415 –430	7								11	DFWM [56]
Silver/glass ($R = 13.0$, $f = 13.9 \times 10^{-5}$)	~ 415 –430	7								6.2	DFWM [56]
Silver/glass ($R = 15.3$, $f = 9.5 \times 10^{-5}$)	~ 415 –430	7								4.6	DFWM [56]
Silver/glass (silica) ($R = 3$, $f = 3 \times 10^{-4}$)	388, white			500×10^{-6}		2400				TAS [198]	

^a R , particle radius (nm); f , volume fraction.^b DFWM, degenerate four-wave mixing; ZS, Z-scan; TAS, transient absorption spectroscopy.^c Re, real part.

Table 10 Data for Computing Nonlinear Refractive Index in Two-Level Systems: Metal Ions and Color Centers

Absorber	Upper state	λ (nm) ^a	$\Delta\nu$ (cm ⁻¹) ^b	$f(10^{-5})^c$	σ (cm ²) ^d	$T(K)^e$	Typical ΔN (cm ⁻³) ^f	I_{oT} (W·ns/cm ²) ^g	Typical τ (ns) ^h	Quenching agent	Ref.
Nd ³⁺ in POCl ₃	⁴ F _{3/2}	862.8	30	0.52	9.6×10^{-20}	100	$< 10^{20}$	1.2×10^9	2.6×10^5		[140]
Nd ³⁺ in YAG	⁴ F _{3/2}	869.0	12.5	0.34	4.1×10^{-20}	300	$< 10^{21}$	2.8×10^9			[141,142]
Cr ³⁺ in Al ₂ O ₃	⁴ G _{3/2}	561			9×10^{-20}	300	$< 10^{21}$	2.0×10^9			
	² E(E)	694.3	14	0.044	1.7×10^{-20}	300	$< 10^{20}$	8.4×10^9	$\sim 10^6$		[143,144]
Yb ³⁺ in YGG	² E(A)	696.9	10	0.022	1.2×10^{-20}	300	$< 10^{20}$	1.2×10^{10}			
Er ³⁺ in YGG	⁴ F ₂	560	2230	74	1.8×10^{-19}	300	$< 10^{20}$	9.9×10^8			
C _o ²⁺ in ZnS	⁴ F ₁	410	2970	110	2.05×10^{-19}	300	$< 10^{20}$	1.2×10^9			
C _o ²⁺ in ZnO	² F _{5/2}	969.5	50	0.069	7.4×10^{-21}	300	$< 10^{21}$	1.4×10^{10}			
C _o ²⁺ in CdS	⁴ I _{13/2}	1460	20	0.022	6.0×10^{-21}	300	$< 10^{21}$	1.1×10^{10}			
	⁴ T _{1(P)}	728	1400	1300	5.1×10^{-18}	300	$< 10^{19}$	2.7×10^7			[146]
	⁴ T _{1(P)}	653	2300	520	1.23×10^{-18}	300	$< 10^{19}$	1.3×10^8			[147]
	⁴ T ₂	611	1700	80	3.6×10^{-18}	300	$< 10^{19}$	1.6×10^7			[148]

(continued)

Table 10 Continued.

Absorber	Upper state	λ (nm) ^a	$\Delta\nu$ (cm ⁻¹) ^b	$f(10^{-5})^c$	σ (cm ²) ^d	$T(K)^e$	Typical ΔN (cm ⁻³) ^f	$I_o\tau$ (W·ns/cm ²) ^g	Typical τ (ns) ^h	Quenching agent	Ref.
Ni ²⁺ in ZnS	$^3T_1(P)$	765	2000	1900×10^{-18}	5.2×10^{-18}	300	$< 10^{19}$	2.4×10^7			[147]
Ni ²⁺ in ZnO	$^3T_1(P)$	800	1500	160	5.8×10^{-19}	300	$< 10^{19}$	2.7×10^8			[147]
M center in CaF ₂	618	900	$> 10^4$	$> 6 \times 10^{-17}$	300		$< 3.2 \times 10^6$		36		[149,150]
M center in LiF	445	2840	$\sim 2 \times 10^4$	$\sim 4 \times 10^{-17}$	300		5.6×10^6		17.2		[151,152]
M center in NaF	507	2580	$\sim 3 \times 10^4$	$\sim 6 \times 10^{-17}$	300	$< 10^7$	3.3×10^6		12.3		[152,153]
F ⁺ center in NaF	740	1600	$\sim 2 \times 10^4$	$\sim 1 \times 10^{-16}$	77	$\leq 10^{17}$	1.3×10^6		31		[154]
F _A center in KCl:Li	F _{A1}	626	1050	9×10^4	$\sim 4.7 \times 10^{-16}$	77	$\leq 10^{17}$	3.4×10^5	80		[155]

Source: Adapted from Ref. [5].

^a Absorption wavelength.^b Homogeneous line width (FWHM).^c Oscillator strength.^d Absorption cross-section.^e Temperature.^f Population difference.^g Line center saturation intensity.^h Typical ground state recovery time.

IV. SEMICONDUCTORS

A. Bulk Semiconductors

Considerable interest has been generated in the use of semiconductor materials for third order NLO because of strong nonlinearities in many of these materials. However, these nonlinearities are also associated with strong nonlinear absorption (see Chapters 9 and 13). Several nonlinear mechanisms can be at work in these materials, depending on the wavelength and pulse width of the incident light (see Chapter 6).

Table 11 lists data for selected common semiconductor materials. Several additional ones can be found in Refs. 1–4a. Table 11 contains some new data as well as some data tabulated previously. Again, n_2 has been calculated in SI units and included in the table.

B. Semiconductor Doped Materials

Considerable interest has also been generated in recent years in quantum-confined semiconductor systems (e.g., quantum dots). These were briefly discussed in Chapter 6, Section II.E. Representative third order susceptibility data on small semiconductor particle doped systems are given in Table 12.

C. Impurity Photoconductors and Excitons

Semiconductors have also been considered as two-level systems. Data taken from Chang [5] are presented in Table 13.

Impurity photoconductors have been developed as high-speed infrared detectors. They must generally be operated at cryogenic temperatures. Among room temperature absorbers, intervalence band transitions in Ge, GaAs, and ZnTe are quite strong. Typical ground state recovery times are ~ 1 ps due to phonon scattering of holes. This, unfortunately, leads to high saturation intensities.

Operation at cryogenic temperatures allows very strong exciton transitions in semiconductors to be considered. These have very low saturation intensities. Data for a few of these transitions in different systems are included in Table 13. Chang [5] gives a good discussion of the trade-offs of absorption, response speed, sample thickness, and the useful nonlinear phase shift for applications in these materials.

(text continues on p. 564)

Table 11 Nonlinear Refractive Index and Third Order Susceptibility Data for Selected Bulk Semiconductors

Material	λ (nm)	Pulse width (ns)	n_0	n_2 (10^{-20} m ² /V ²) ^a	n_2^l (10^{-13} esu)	n_2^l (10^{-16} cm ² /W)	$\chi^{(3)}$ (10^{-20} m ² /V ²)	$\chi^{(3)}_{\text{ext}}$ (10^{-13} esu)	Method ^b	Ref.
Arsenic sulfide (amorphous film)	633	cw		7.6×10^{11}					ZS	[205]
Cadmium sulfide ($E \perp c$)	1064	3	2.33	3.38	304				TWM	[40]
Cadmium sulfide ($E \parallel c$)	1064	3	2.34	3.14	283				TWM	[40]
Cadmium sulfide	532	0.03	2.34	-28	-3400				ZS	[57]
Cadmium sulfide	610	1.25×10^{-4}		-5.6	-500				ZS	[58]
Cadmium sulfide	1270	8.0×10^{-5}		0.44	40				ZS	[58]
Cadmium sulfide	780	7.5×10^{-5}		1.1	95				ZS	[58]
Cadmium sulfide selenide (CdS _{0.5} Se _{0.5})	1064	0.03	2.45	11.0	1000				ZS	[57]
Cadmium selenide	1064	0.03	2.56	-1.0	-90				ZS	[57]
Cadmium telluride	1064	0.04	2.84	-22	-2000				ZS	[59]
Cadmium telluride	1064	0.04	2.84	-23	-2100	-3100			DFWM	[60]
Gallium arsenide	1064	0.04	3.47	-30	-2700				ZS	[59]
Gallium arsenide antimonide (<i>n</i> -GaSb)	2100	80						-1.6×10^6	ZS	[204]
Gallium indium arsenide antimonide (Ga _{0.87} In _{0.13} As _{0.11})	2100	80						-3.5×10^6	DFWM	[204]
Gallium nitride	527		0.0025					-11.0×10^7	ZS	[204]
								-4.0×10^7	DFWM (270K)	[203]
									ZS	[203]

Gallium phosphide	577	0.0027			2100	YWM	[61]
Germanium	10,600	0.06	3.47	30	ZS	[57]	
Indium antimonide	10,600	4000	3.95	-1800	ZS	[62]	
Silicon (porous)	9600	4000	3.95	-1700	ZS	[62]	
Silicon (anorphous film)	665	0.5	4.1		$\text{Re}^c = 27,500$	[63]	
	532	0.07	4.1		$ \chi^{(3)} = \frac{(5.1 \pm 1.0)}{\times 10^6}$	[64]	
Silicon (nanocluster film)	9000	2500		73.0×10^6	ZS	[206]	
SrSrBi ₂ Ta ₂ O ₉ (thin film)	1064	0.038	2.225	-1.9×10^7	8.02×10^6	[207]	
SrSrBi ₂ Ta ₂ O ₉ (thin film)	1064	0.038	2.29	-3.58×10^7	6.93×10^6	ZS	
Strontium cuprous oxide ($E b$)	532		2.29	-3.84×10^7	5.18×10^6	ZS	[209]
Zn _x Sn _{1-x} O ₂ (E $\perp c$)	1700		$\sim 200 \times 10^{-6}$	5000		ZS	[202]
Zn _x Sn _{1-x} O ₂ (E $\parallel c$)	1064	3	1.99	0.28	25	TWM	[40]
Zn _x Sn _{1-x} O ₂ (E $\parallel c$)	1064	3	1.96	0.26	23	TWM	[40]
Zn _x Sn _{1-x} O ₂ (E $\parallel c$)	446	8	2.7	1.4×10^6	1.9×10^8	SB	[65]
Zn _x Sn _{1-x} O ₂ (E $\parallel c$)	447.6	8	2.7	4.4×10^5	6.1×10^7	SB	[65]
Zn _x Sn _{1-x} O ₂ (E $\parallel c$)	1064	0.04	2.48		18	DFWM	[60]
Zn _x Sn _{1-x} O ₂ (E $\parallel c$)	1064	0.03	2.48	1.9		ZS	[57]
Zn _x Sn _{1-x} O ₂ (E $\parallel c$)	532	0.03	2.70		± 30	DFWM	[60]

Table 11 Continued.

Material	λ (nm)	Pulse width (ns)	n_0	$n_2^{(1)}$ (10^{-20} m 2 /V 2) ^a	$n_2^{(2)}$ (10^{-13} esu)	$n_2^{(l)}$ (10^{-16} cm 2 /W)	$\chi_{\text{ext}}^{(3)}$ (10^{-20} m 2 /V 2)	$\chi_{\text{ext}}^{(3)}$ (10^{-13} esu)	Method ^b	Ref.
Zinc selenide	532	0.027	2.70	-4.9	-440				ZS	[59]
Zinc selenide	610	1.25×10^{-4}		<22					ZS	[58]
Zinc selenide	1270	8.0×10^{-5}	0.39	35					ZS	[58]
Zinc selenide	780	7.5×10^{-5}	1.1	100					ZS	[58]
Zinc sulfide	1064	3	2.29	0.52	47				TWM	[40]
<i>(E\perp c)</i>										
Zinc sulfide	1064	3	2.29	0.54	49				TWM	[40]
<i>(E c)</i>										
Zinc sulfide	610	1.25×10^{-4}	0.37	33					ZS	[58]
Zinc sulfide	1270	8.0×10^{-5}	0.19	17					ZS	[58]
Zinc sulfide	780	7.5×10^{-5}	0.23	21					ZS	[58]
Zinc telluride	1064	0.04	2.79	9.2	830				ZS	[59]

^a Calculated.^b DFWM, degenerate four-wave mixing; TWM, three-wave mixing; SB, self-bending; ZS, Z-scan.^c Re, Real part.

Table 12 Nonlinear Refractive Index and Third Order Susceptibility Data for Selected Semiconductor Doped Materials

Material ^a /host	λ (nm)	Pulse width (ns)	n_0	$(10^{-22} \text{ m}^2/\text{V}^2)$	n_2 (10^{-12} esu)	n_2' $(10^{-12} \text{ cm}^2/\text{W})$	n_2'' $(10^{-22} \text{ m}^2/\text{V}^2)$	$\chi_{xxz}^{(3)}$ (10^{-12} esu)	$\chi_{xxx}^{(3)}$ (10^{-12} esu)	Method ^b	Ref.
Cadmium sulfide (encapsulated) zeolite A	1900	8	1.47					4.1	THG	[66]	
Cadmium sulfide (encapsulated) zeolite X	1900	8	1.50					11	THG	[66]	
Cadmium sulfide selenide/glass Schott GG495 ($R = 2.1, f = 5.2 \times 10^{-3}$)	1090, 1064	0.03			7.44				TWM	[67]	
Cadmium sulfide selenide/glass Schott OG570 ($R = 3.5, f = 3.5 \times 10^{-3}$)	1090, 1064	0.03			8.13				TWM	[67]	
Cadmium sulfide selenide/glass Schott OG540 ($R = 3.0, f = 4.7 \times 10^{-3}$)	1090, 1064	0.03			8.09				TWM	[67]	
Cadmium sulfide selenide/glass Schott RG610 ($R = 3.1, f = 2.9 \times 10^{-3}$)	1090, 1064	0.03			7.91				TWM	[67]	
Cadmium sulfide selenide/glass Schott RG630 ($R = 3.7, f = 3.2 \times 10^{-3}$)	1090, 1064	0.03			8.24				TWM	[67]	
Cadmium sulfide selenide/glass Schott RG665 ($R = 6.5, f = 3.5 \times 10^{-3}$)	1090, 1064	0.03			7.95				TWM	[67]	
Cadmium sulfide selenide/glass Schott RG695 ($R = 4.3, f = 1.6 \times 10^{-3}$)	1090, 1064	0.03			6.76				TWM	[67]	
Cadmium sulfide selenide/glass Schott RG715 ($R = 5.5, f = 3.2 \times 10^{-3}$)	1090, 1064	0.03			7.55				TWM	[67]	
Cadmium sulfide selenide/glass	1090,	0.03			7.86				TWM	[67]	

(continued)

Table 12 Continued.

Cadmium telluride/glass	1090, 1064	0.03	6.17	TWM	[67]
Schott R2 ($R = 6.9, f = 1.7 \times 10^{-3}$)					
Cadmium telluride/glass	1090, 1064	0.03	5.85	TWM	[67]
Schott R3 ($R = 9.8, f = 1.7 \times 10^{-3}$)					
Cadmium telluride/glass	1090, 1064	0.03	5.74	TWM	[67]
Schott R4 ($R = 14, f = 1.6 \times 10^{-3}$)					
Cadmium telluride/glass	532	0.08	7	NLI	[68]
Schott OG530					
Germanium/Infrasil ($R = 1.5, 9.7$ wt-% Ge)	800	100×10^{-6}	0.27	DFWM	[212]
Germanium/silica ($R = 3.0, 8$ at-% Ge)	532	650×10^{-6}	0.69	ZS	[210]
Germanium/silica ($R = 3.0, 12.5$ at-% Ge)	532	0.035	2.6	ZS	[210]
Germanium/silica ($R = 3.0, 14.7$ at-% Ge)	532	0.035	4.1	ZS	[210]
Germanium/silica ($R = 3.0, 27.5$ at-% Ge)	1064	0.1	4.2	ZS	[210]
Indium phosphide/vycor glass ($R \sim 2, f \sim 0.03$)			8.2	ZS	[210]
			-2.1	ZS	[69]

^a R , particle radius (nm); f , volume fraction.^b THG, third harmonic generation; TWM, three-wave mixing; ZS, Z-scan; TBC, two-beam coupling.

Table 13 Data for Computing Nonlinear Refractive Index in Two-Level Systems: Impurity Photoconductors and Excitons

Absorber	Transition ^a	λ (nm) ^b	$\Delta\nu$ (cm ⁻¹) ^c	f^d	σ (cm ²) ^e	T (K) ^f	Typical ΔN (cm ⁻³) ^g	$I_{s0}\tau$ (W·ns/cm ²) ^h	Typical τ (ns) ⁱ	Quenching agent	Ref.
Cu in <i>p</i> -ZnSe	V → A	1380	5000	0.3	3.5×10^{-17}	300	$< 10^{18}$	2.0×10^6	9^j		[156,157]
Cu in ZnS	V → A	730	8800	~1	1.6×10^{-16}	80	$< 10^{18}$	8.5×10^5			[158,159]
P in ZnTe	V(SO) → A	1170	890	0.1	6.1×10^{-17}	<100	$< 10^{19}$	1.4×10^6			[160,161]
	V(SO) → A(top)	1170	1370	0.08	3.3×10^{-17}	300	$< 10^{19}$	2.6×10^6			
Zn in GaAs	V(SO) → A(HH)	3020	2400	~0.3	7×10^{-17}	300	$< 10^{18}$	4.7×10^5	$\sim 10^{-3}$		[162,163]
In or Ga in Ge	V(SO) → A(top)	3400	1800	~0.4	1.3×10^{-16}	300	$< 10^{18}$	2.2×10^5	$\sim 10^{-3}$		[164,165]
Au in Ge	V → A	5000			8×10^{-17}	80	$< 10^{16}$	2.5×10^5	≥ 1	As or Sb	[166,167]
Hg in Ge	V → A	11,000			3.9×10^{-16}	30	$< 10^{16}$	2.3×10^4	≥ 1	As or Sb	[166,167]
Cu in Ge	V → A	22,000			1.0×10^{-15}	5	$< 10^{16}$	4.5×10^3	≥ 0.5	As or Sb	[166,167]
In in Si	V → A	4800			3.3×10^{-17}	80		6.3×10^4			166,167
Ga in Si	V → A	15,000			5×10^{-16}	10	$< 10^{19}$	1.3×10^4			[166,167]
Al in Si	V → A	15,000			8×10^{-16}	10		8.3×10^3			[166,167]
B in Si	V → A	23,000			1.4×10^{-15}	5	$< 10^{20}$	3.1×10^3			[166,167]
P in Si	D → C	27,000			1.7×10^{-15}	5	$< 10^{20}$	2.2×10^3			[166,167]

<i>n</i> -Gap Bound exciton in GaP:N	C → C A	2900 537	18 0.033	1.0 × 10 ⁻¹⁵ 5 × 10 ⁻¹⁹	300 77	< 10 ¹⁹ < 10 ¹⁹	1.8 × 10 ⁵ ~1	— GaP lattice	[168,169] [169,170]
Bound exciton in GaP:S	A	538	7.4	7 × 10 ⁻¹⁶	5 × 10 ⁻¹⁹	77	3.7 × 10 ⁸	— [171]	
Intrinsic exciton in CdS	A($\hbar = 1$) $E \perp c$ B($\hbar = 1$) $E \perp c$ B($\hbar = 1$) $E \parallel c$	487 485 485	39.5 37.5 ~40	3.92 ^k 2.18 ^k 2.40 ^k	5.4 × 10 ⁻¹⁴ 3.2 × 10 ⁻¹⁴ 3.2 × 10 ⁻¹⁴	77 77 77	1.3 × 10 ¹⁹ 1.3 × 10 ¹⁹ 1.3 × 10 ¹⁹	3.8 × 10 ³ 6.4 × 10 ³ 6.4 × 10 ³	1.8 ^j 3.2 ^j 2.9 ^j
Intrinsic exciton in ZnO	A($\hbar = 1$) $E \perp c$ B($\hbar = 1$) $E \parallel c$ C($\hbar = 1$) $E \parallel c$	365 361 357	17.7 13.7 72.5	6.25 ^k 8.33 ^k 2.08 ^k	1.9 × 10 ⁻¹³ 3.3 × 10 ⁻¹³ 1.6 × 10 ⁻¹⁴	4.2 4.2 4.2	3 × 10 ¹⁹ 3 × 10 ¹⁹ 3 × 10 ¹⁹	1.4 × 10 ³ 8.3 × 10 ² 1.7 × 10 ⁴	0.32 ^j 0.23 ^j 0.92 ^j

Source: Adapted from Ref. [5].

^aV, valence band; A, acceptor; D, donor; C, conduction band; SO, split off band; HH, heavy hole.

^bAbsorption wavelength.

^cHomogeneous line width (FWHM).

^dOscillator strength.

^eAbsorption cross-section.

^fTemperature.

^gPopulation difference.

^hLine center saturation intensity.

ⁱTypical ground state recovery time.

^jRadiative lifetime.

^kEffective value per exciton.

Table 14 Nonlinear Refractive Index and Third Order Susceptibility Data for Selected organic Crystals, Polymers, and Thin Films

Material ^a	λ (nm)	Pulse width (ns)	n_0	n_{20} ($10^{-20} \text{ m}^2/\text{V}^2$)	n_2 (10^{-12} esu)	n'_2 ($10^{-12} \text{ cm}^2/\text{W}$)	$\chi_{\text{ext}}^{(3)}$ ($10^{-20} \text{ m}^2/\text{V}^2$)	$\chi_{\text{ext}}^{(3)}$ (10^{-12} esu)	Method ^b
Bacteriorhodopsin [TF]	632	cw							6 $\times 10^{11}$ DFWM [70]
Buckminsterfullerene C ₆₀ [TF]	1064	0.035	2.0						7 DFWM [71]
Buckminsterfullerene C ₆₀ [TF]	1064		2.0						200 THG [72]
A-(NO ₂) ₄ -D-NH-C ₆ H ₃₃ -substituted azobenzene poly(methyl methacrylate) [PTF]	632.8	cw			6×10^8		4×10^8	ZS, DF- WM	[73]
Disperse Red 1 (0.1 M) in PMMA [PTF]	570	0.020			-3.0×10^5	-2.0×10^5			ZS [216]
Perylenetetracarboxylic dianhydride [TF]	602	0.0004							200 DFWM [78]
Phthalocyanine (axially modified composite) [TF]	532	0.07					13.3 ± 1.5	DFWM [85]	
Polyaniline emeraldine base in polyvinyl-alcohol acetate/glu-taraldehyde [PTF]	532	0.070					-0.2		ZS [181]

Polyaniline leuco-	532	0.070	-0.4	ZS	[181]
meradine base in polyvinyl-					
alcohol acetate-					
glutaraldehyde					
[PTF]	595	0.0007		33,000	DFWM [180]
Polydiacetylene (CH ₂) ₉ OCO-					
NHCH ₂ OCOC ₄ ⁻					
H ₉ [PTF]	641	0.0007		12,000	DFWM [180]
Polydiacetylene (CH ₂) ₉ OCO-					
NHCH ₂ OCOC ₄ ⁻					
H ₉ [PTF]	707	0.0007		2000	DFWM [180]
Polydiacetylene (CH ₂) ₉ OCO-					
NHCH ₂ OCOC ₄ ⁻					
H ₉ [PTF]	720	200 × 10 ⁻⁶	2.382	39	SPM [213]
Poly-[2,4 hexa-					
diyne-1,6 diol-					
bis-(<i>p</i> -toluene					
sulfonate)] [SC] ⁺					
	736		2.301	27	
	760		2.215	20	
	777		2.187	16	
	800		2.122	13	
	820		2.090	11	
	836		2.068	10	
	860		2.040	10	
	877		2.023	10	
	900		2.003	10	
	920		1.988	10	
	1064		1.911	10	

(continued)

Table 14 Continued.

Material ^a	λ (nm)	Pulse width (ns)	n_0	$(10^{-20} m^7/V^2)$	n_2 (10^{-12} esu)	n_2' ($10^{-12} \text{cm}^2/W$)	$\chi_{xxz}^{(3)}$ ($10^{-20} m^2/V^2$)	$\chi_{yyx}^{(3)}$ (10^{-12} esu)	Method ^b
Poly(3-hexyl thiophene) [PTF]	602	0.0006			-6000				NLI [79]
Poly(α -[5,5'-bithio-phendiy] benzylidene-block- α -[5,5'-bithio-phenyl-quinodimethanediyl]) [SL]	532	0.025	1.81						DFWM [74]
Poly(α -[5,5'-bithio-phendiy] <i>p</i> -acetoxybenzylidene-block- α -[5,5'-bithio-phenyl-quinodimethanediyl]) [SL]	532	0.025	1.76						DFWM [74]
Poly bis(<i>p</i> -toluenesulfonate) of 2,4-hexadiyne-1,6-dio polydicylenene [SC]	651.5	0.006	3.0						DFWM [75]
Poly bis(<i>p</i> -toluenesulfonate) of 2,4-hexadiyne-1,6-dio polydicylenene [SC]	661	0.006	3.0						DFWM [75]

Poly bis(<i>p</i> -toluene sulfonate) of 2,4-hexadiyne-1,6-diol polydicytlenole [SC]	671	0.006	3.0	2317	DFWM	[75]
Poly bis(<i>p</i> -toluene sulfonate) of 2,4-hexadiyne-1,6-diol polydicytlenole [SC]	681	0.006	3.0	1025	DFWM	[75]
Poly bis(<i>p</i> -toluene sulfonate) of 2,4-hexadiyne-1,6-diol polydicytlenole [SC]	691	0.006	3.0	380	DFWM	[75]
Poly bis (<i>p</i> -toluene sulfonate) of 2,4-hexadiyne-1,6-diol polydicytlenole [SC]	701.5	0.006	3.0	500	DFWM	[75]
Poly(di- <i>n</i> -hexylgermane) [PTF]	1064			4.6	THG	[76]
Poly(di- <i>n</i> -hexylsialane) [PTF]	1907			1.53	THG	[76]
Polydithieno(3,2- <i>b</i> ,2',3'- <i>b</i>)thiophene [PTF]	530	0.008	2.0	6.42	THG	[77]
Polydithieno(3,2- <i>b</i> ,2',3'- <i>b</i>)thiophene [PTF]	585	0.008	2.0	1.8	THG	[77]
				11,400	DFWM	[77]
				770	DFWM	[77]

(continued)

Table 14 Continued.

Material ^a	λ (nm)	Pulse width (ns)	n_0	$(10^{-20} m^2/V^2)$	n_2 (10^{-12} esu)	$(10^{-20} m^2/V^2)$	n_2^l (10^{-12} cm 2 /W)	$\chi_{xx}^{(3)}$ ($10^{-20} m^2/V^2$)	$\chi_{xx}^{(3)}$ ($10^{-20} esu$)	Method ^b	Ref.
Polydithieno(3,2- <i>b</i> ,2',3'- <i>b</i>)thio-phenne [PTF]	605	0.008	2.0							DFWM	[77]
Polydithieno(3,2- <i>b</i> ,2',3'- <i>b</i>)thio-phenne [PTF]	630	0.008	2.0							DFWM	[77]
Polydithieno(3,2- <i>b</i> ,2',3'- <i>b</i>)thio-phenne [PTF]	1060	0.008	2.0							DFWM	[77]
Polydithieno(3,2- <i>b</i> ,2',3'- <i>b</i>)thio-phenne [PTF]	590	0.015						5900	DFWM	[80]	
Polydithieno(3,2- <i>b</i> ,2',3'- <i>b</i>)thio-phenne [PTF]	595	0.015						6100	DFWM	[80]	
Polydithieno(3,2- <i>b</i> ,2',3'- <i>b</i>)thio-phenne [PTF]	600	0.015						4200	DFWM	[80]	
Poly-N-vinyl carbazole:2,4,7-trinitrofluorenone composite [PTF], mole ratio 2:1	1064 1907	0.002	1.33				10 5.86	THG THG	THG	[77]	
	602							20 ± 2	DFWM	[78]	

Poly- <i>N</i> -vinyl carbazole:2,4,7-trinitrofluorenone composite [PTF], mole ratio 4:1	602	0.002	1.33	12 ± 1	DFWM [78]
Poly- <i>N</i> -vinyl carbazole:2,4,7-trinitrofluorenone composite [PTF], mole ratio 8:1	602	0.002	1.33	7.4 ± 0.7	DFWM [78]
Poly- <i>N</i> -vinyl carbazole:2,4,7-trinitrofluorenone composite [PTF], mole ratio 16:1	602	0.002	1.33	3.4 ± 0.3	DFWM [78]
Poly- <i>N</i> -vinyl carbazole:2,4,7-trinitrofluorenone composite [PTF], mole ratio 32:1	602	0.002	1.33	2.0 ± 0.2	DFWM [78]
Poly- <i>p</i> -phenylene benzobisthiazole [PTF]	604, 585	0.008		$xxxx = 5.4$	DFWM [81]
Poly- <i>p</i> -phenylene vinylene) [PTF] $\lambda_{max} \sim 375\text{--}$ 460 nm ^c	585 800	1.25×10^{-4}	1.59^- 1.61 (TE)	$yyyy = 7.2$	DFWM [82]
			$\sim 0.8\text{--}1.1$		

(continued)

Table 14 Continued.

Material ^a	λ (nm)	Pulse width (ns)	n_0	$(10^{-20} m^2/V^2)$	n_{12} (10^{-12} esu)	n'_2 ($10^{-12} cm^2/W$)	$\chi_{\text{ext}}^{(3)}$ ($10^{-20} m^3/V^2$)	$\chi_{\text{ext}}^{(3)}$ (10^{-2} esu)	Method ^b	Ref.
				1.92– 2.30						
Polythieno(3,2- <i>b</i>) thiophene [PTFI]	530	0.015							6000	DFWM [80]
Polythieno(3,2- <i>b</i>) thiophene [PTFI]	585	0.015							4200	DFWM [80]
Polythieno(3,2- <i>b</i>) thiophene [PTFI]	590	0.015							3000	DFWM [80]
Polythieno(3,2- <i>b</i>) thiophene [PTFI]	595	0.015							3500	DFWM [80]
Polythieno(3,2- <i>b</i>) thiophene [PTFI]	600	0.015							2900	DFWM [80]
Polythieno(3,2- <i>b</i>) thiophene [PTFI]	605	0.015							3100	DFWM [80]
Polythiophene [PTF]	530	0.008	2.0						6700	DFWM [77]
Polythiophene [PTF]	585	0.008	2.0						5500	DFWM [77]
Polythiophene [PTF]	605	0.008	2.0						3000	DFWM [77]
Polythiophene [PTF]	630	0.008	2.0						700	DFWM [77]
Polythiophene [PTF]	1060	0.008	2.0						30	DFWM [77]
Polythiophene [PTF]	590	0.015	2.0						3500	DFWM [82]
Polythiophene [PTF]	595	0.015	2.0						3800	DFWM [82]

Polythiophene	600	0.015	2.0		3100	DFWM [82]
[PTF]					ZS	[83]
Polythiophene	532	0.03	1.89			
[PTF]					DFWM	[215]
Polythiophene 366-79 ($\lambda_{\max} = 727$)	800	100×10^{-6}		\$20		
[PTF]					DFWM	[215]
Polythiophene 366-80 ($\lambda_{\max} = 739$)	800	100×10^{-6}		410		
[PTF]					DFWM	[215]
Polythiophene 366-143	800	100×10^{-6}		360		
($\lambda_{\max} = 1015$)					DFWM	[215]
[PTF]						
Polythiophene 366-144	800	100×10^{-6}		1100		
($\lambda_{\max} = 985$)					DFWM	[215]
[PTF]						
Polythiophene 366-146	800	100×10^{-6}		110		
($\lambda_{\max} = 596$)					DFWM	[215]
[PTF]						
Polythiophene 366-150	800	100×10^{-6}		1800		
($\lambda_{\max} = 673$)					DFWM	[215]
[PTF]						
Polythiophene 366-172	800	100×10^{-6}		4700		
($\lambda_{\max} = 673$)					DFWM	[215]
[PTF]						
Polythiophene 366-189	800	100×10^{-6}		8400		
($\lambda_{\max} = 683$)					DFWM	[215]
[PTF]						

(continued)

Table 14 Continued.

Material ^a	λ (nm)	Pulse width (ns)	n_0	$(10^{-20} \text{ m}^2/\text{V}^2)$	n_2 (10^{-12} esu)	n_2' ($10^{-12} \text{ cm}^2/\text{W}$)	$\chi_{\text{ext}}^{(3)}$ ($10^{-20} \text{ n}^2/\text{V}^2$)	$\chi_{\text{ext}}^{(3)}$ (10^{-12} esu)	Method ^b	Ref.
Poly(vinyl-alco-hol)-glutaraldehyde-polyaniline [PTF]	532	0.02								[84]
750 μm thick					-6.4					
350 μm thick					-2.9					
250 μm thick					-2.1					
Squarylium dye <i>J</i> aggregates,										
dipropylamino bases [TF]	805		90×10^{-6}		3.7×10^4					[214]
Squarylium dye <i>J</i> aggregates, dibutylamino bases [TF]	805		90×10^{-6}		4.2×10^4					[214]
<i>p</i> -Toluene sulfate [SC]	1064		0.035			5 \pm 1				[86]
<i>p</i> -Toluene sulfate [SC]	1300		0.1			3.2 ± 0.3				[86]

^a [SC], single crystal; [SL], superlattice; [TF], thin film; [PTF], polymer thin film; A, acceptor; D, donor.^b DFWM, degenerate four-wave mixing; NLI, nonlinear interferometry; THG, third harmonic generation; ZS, Z-scan. SPM, self-phase modulation.^c n_2 varies with λ_{max} .

Table 15 Molecular Second Hyperpolarizability Data for Some Selected Organic Materials

Molecule ^a	Solvent	λ (nm)	$\gamma(10^{-61} \text{ C} - \text{m}^4/\text{V}^3)$	$\gamma(10^{-36} \text{ esu})$	Method ^b	Ref.
Acetone	(neat)	1054	3.2		THG	[87]
Acetone	(neat)	1907		1.88	THG	[88]
Acetonitrile	(neat)	1910		0.87	THG	[89]
Allo-ocimene	(neat)	1054	21.6		THG	[87]
Allo-ocimene	(neat)	1890		9.7 \pm 1.7	THG	[90]
<i>trans</i> -4-(4-Aminostyryl)-1-methylpyridinium iodide	methanol	532		4.1×10^5	DFWM	[217]
Aniline	(neat)	1910		$\text{Re}^c(\gamma) = 3.6 \times 10^5$	ZS	
2-Anilinonaphthalene-6-sulfonic acid	ethanol	780		5.71	THG	[89]
β -Carotene	carbon disulfide	1064		4.3×10^4	NLI	[221]
Benzene (monomer)	tetrahydrofuran	602		4600	DFWM	[18]
Benzene (dimer)	tetrahydrofuran	602		5.5	DFWM	[91]
Benzene (trimer)	tetrahydrofuran	602		29	DFWM	[91]
Benzene	(neat)	1054		85	DFWM	[91]
Benzene	(neat)	1907		14.8	THG	[87]
Benzene	(neat)	1910		4.07	THG	[88]
Benzene	(neat)	1054		3.85	THG	[89]
Benzonitrile	(neat)	1054		7.1	THG	[87]
Bromobenzene	(neat)	1910		5.40	THG	[89]
Buckminsterfullerene C ₆₀	(solid)	1064		300	DFWM	[71]
Carbon disulfide	(neat)	1054		15.1	THG	[87]
Carbon disulfide	(neat)	1910		4.4	THG	[92]
Carbon tetrachloride	(neat)	1054		5.9	THG	[87]

(continued)

Table 15 Continued.

Molecule ^a	Solvent	λ (nm)	$\gamma(10^{-61} \text{ C} - \text{m}^4/\text{V}^3)$	$\gamma(10^{-36} \text{ esu})$	Method ^b	Ref.
Carbon tetrachloride	(neat)	1907		3.36	THG	[88]
Carbon tetrachloride	(neat)	1910		3.09	THG	[92]
Chlorobenzene	(neat)	1910		4.34	THG	[89]
Chloroform	(neat)	1907		2.27	THG	[88]
Chloroform	(neat)	1910		2.29	THG	[92]
Cyanobenzene	(neat)	1910		4.11	THG	[89]
Cyclohexane	(neat)	1097		3.02	THG	[88]
Dicarbon tetrachloride (C_2Cl_4)	(neat)	1910		3.70	THG	[92]
Dichloromethane	(neat)	1907		1.55	THG	[88]
Didecyloxy substituted <i>p</i> -poly-phenyl (monomer)	tetrahydrofuran	602		22	DFWM	[93]
Didecyloxy substituted <i>p</i> -poly-phenyl (trimer)	tetrahydrofuran	602		69	DFWM	[93]
Didecyloxy substituted <i>p</i> -poly-phenyl (pentamer)	tetrahydrofuran	602		350	DFWM	[93]
Didecyloxy substituted <i>p</i> -poly-phenyl (heptamer)	tetrahydrofuran	602		$\text{Re}^{\text{c}} = -3300$	DFWM	[93]
Didodecyltrimethylammonium-Au(dmit) ₂ (2C12-Au)	acetone	830		2.2×10^4	OKE	[220]
<i>trans</i> -4-[4-Dimethylamino]styryl]-1-methylpyridinium iodide	methanol	532		1.6×10^5 $\text{Re}^{\text{c}}(\gamma) = 7.4 \times 10^5$	DFWM ZS	[217]
Dimethylformamide	(neat)	1907		2.03	THG	[88]
Diphenylbutadiene	Chloroform	532		$\text{Re}^{\text{c}} = 410 \pm 80$	DFWM	[95]
1,1'-Disityrlferrocene	tetrahydrofuran	602		270 ± 26	DFWM	[94]

Endohedral metallofullerene (Er ₂ @C ₈₂ -isomer III)	carbon disulfide	1064	$\gamma_{xyyx} = -48.7 \times 10^4$	DFWM	[224]
Ethanol	(neat)	1054	1.95	THG	[87]
Ethanol	(neat)	1907	1.44	THG	[88]
Ethanol	(neat)	1910	1.33	THG	[89]
Europium bis(phthalocyanine)	chloroform	1064	220,000	DWFM	[96]
Europium bis(phthalocyanine)	chloroform	1064	280,000	DWFM	[96]
Ferrocene	tetrahydrofuran	602	16.1 ± 1.8	DWFM	[94]
	acetonitrile	532	0.55×10^5	DFWM	[94]
<i>trans</i> -4-[4-(1-Ferrocenyl)styryl]-1-methylpyridinium iodide	methanol	532	2.1×10^5	DFWM	[217]
<i>trans</i> -4-[2-(1-Ferrocenyl)vinyl]-1-methylpyridinium iodide	(neat)	1910	$Re^c(\gamma) = 1.1 \times 10^5$	ZS	
Fluorobenzene	tetrahydrofuran	602	3.19	THG	[89]
1-Formyl-1',1''-(1,4-phenylene-2,1-ethenediyl)bisferrocene	tetrahydrofuran	602	925 ± 86	DFWM	[94]
1-Formyl-1'-styrylferrrocene	tetrahydrofuran	602	305 ± 36	DFWM	[94]
Gadolinium bis(phthalocyanine)	chloroform	1064	220,000	DFWM	[96]
Gadolinium bis(phthalocyanine)	chloroform	1064	280,000	DFWM	[96]
1,5-Hexadiene	(neat)	1054	7.1	THG	[87]
<i>c,t</i> 2,4-Hexadiene	(neat)	1054	14.4	THG	[87]
<i>t,t</i> 2,4-Hexadiene	(neat)	1054	10.4	THG	[87]
2-(2'-Hydroxyphenyl) benzoxazole	cyclohexane	1064,532	3100	TCZS	[219]
Hypocrellin A	ethanol	1064	-1.4×10^5	ZS	[184]

(continued)

Table 15 Continued.

Molecule ^a	Solvent	λ (nm)	$\gamma(10^{-61} \text{ C} - \text{m}^4/\text{V}^3)$	$\text{Re}^c(\gamma) = 1.8 \times 10^5$	$\gamma(10^{-36} \text{ esu})$	Method ^b	Ref.
Indole squarylium	carbon tetrachloride (neat)	660 1910		8.19		OKE	[187]
Iodobenzene	chloroform	1064		340,000		THG	[89]
Lutetium bis(phthalocyanine)	chloroform	1064		220,000		DFWM	[96]
Lutetium bis(phthalocyanine) ion						DFWM	[96]
Methanol	(neat)	1054	0.93			THG	[87]
Methanol	(neat)	1907		0.87		THG	[88]
Methanol	(neat)	1910		0.80		THG	[89]
Methylcyclohexane	(neat)	1910		3.97		THG	[89]
Neodymium bis(phthalocyanine)	chloroform	1064		150,000		DFWM	[96]
Nitrobenzene	(neat)	1054	14.9			THG	[87]
Nitrobenzene	(neat)	1907				THG	[88]
Nitrobenzene	(neat)	1910				THG	[89]
2-Nitrotoluene	(neat)	1054	11.8	6.57		THG	[87]
<i>N</i> -hexane	(neat)	1907		5.37		THG	[88]
Pentaazadentate porphyrin-lidé metal complex		532		4.17		DFWM	[222]
$[(R\text{-APPC})\text{M}]Cl_n$					2.6 $\times 10^5$		
$R = OCH_3C_6H_3$, M = Cd, n = 1	methanol						
$R = CO_2NaC_6H_3$, M = Cd, n = 1	methanol				4.3 $\times 10^5$		
$R = C_6H_4$, M = Cd, n = 1	methanol				4.8 $\times 10^5$		
$R = ClC_6H_3$, M = Cd, n = 1	methanol				5.6 $\times 10^5$		

$R = \text{NO}_2\text{C}_6\text{H}_3$, M = Cd, n = 1	methanol	7.5×10^5	
$R = \text{C}_{10}\text{H}_6$, M = Cd, n = 1	methanol	12.0×10^5	
$R = (\text{NC})_2\text{C}_2$, M = Cd, n = 1	chloroform	3.4×10^5	
$R = \text{C}_6\text{H}_4$, M = Pd, n = 1	methanol	1.1×10^5	
$R = \text{C}_6\text{H}_4$, M = Sm, n = 2	chloroform	1.4×10^5	
Pentaazadentate porphyrin-lide metal complex	methanol	532	DFWM [218]
[$(R\text{-APPC})\text{Cd}]\text{Cl}$			
$R =$ dibenzophenone			
$R = \text{C}_6\text{H}_4$			
<i>p</i> -Phenyl (monomer)	tetrahydrofuran	602	DFWM [97]
<i>p</i> -Phenyl (dimer)	tetrahydrofuran	602	DFWM [97]
<i>p</i> -Phenyl (trimer)	tetrahydrofuran	602	DFWM [97]
<i>p</i> -Pentaphenyl	tetrahydrofuran	602	DFWM [97]
<i>p</i> -Pentaphenyl 1,1'--(1,4-Phenylenedi-2,1- ethenediyi)bifluorene	tetrahydrofuran	602	DFWM [97]
Phthalocyanine monomethacry- late	carbon teta- chloride	670	$\text{Re}^{\text{c}}(\gamma) = -7.88 \times 10^5$
Poly(ferrocenylenevinylene- phenylenevinylene)	tetrahydrofuran	602	OKE [187]
2-Propanol	(neat)	1910	1550 ± 270
2-Propanone	(neat)	1910	DFWM [97]
6-Propionyl-2-dimethylamine	ethanol	780	
naphthalene			
Pyridine	(neat)	1907	THG [89]
Pyridine	(neat)	1910	THG [89]

(continued)

Table 15 Continued.

Molecule ^a	Solvent	λ (nm)	$\gamma(10^{-61} \text{ C} - \text{m}^4/\text{V}^3)$	$\gamma(10^{-36} \text{ esu})$	Method ^b	Ref.
Retinal	(molten) carbon disulfide	1064 1064	160 2300	DFWM DFWM	[18]	[18]
Retinoic acid	(molten)	1064	44	DFWM DFWM	[18]	[18]
Retinol	(molten)	1064	140	DFWM DFWM	[18]	[18]
Retinol acetate	carbon disulfide	1064	130	DFWM DFWM	[18]	[18]
Retinol acetate	chloroform	1064	480,000	DFWM DFWM	[96]	[96]
Scandium bis(phthalocyanine)	chloroform	1064	200,000	DFWM DFWM	[96]	[96]
Scandium bis(phthalocyanine) ion	tetrahydrofuran	602	16.9 ± 0.8	DFWM DFWM	[94]	[94]
Styrene	tetrahydrofuran	602 2100	85.5 ± 19.8 2000 ± 100	THG THG	[223]	[223]
1-Styrylferrocene						
Tetraethylmethane derivative						
D = [<i>p</i> -(CH ₃) ₂ NC ₆ H ₄ -] A = (<i>p</i> -NO ₂ C ₆ H ₄ -)						
symmetry: 2mm (C _{2v})						
Tetraethylethylene derivative						
D = [<i>p</i> -(CH ₃) ₂ NC ₆ H ₄ -] A = (<i>p</i> -NO ₂ C ₆ H ₄ -)						
symmetry: 2/m (C _{2h})						
Tetraethylethylene derivative						
D = [<i>p</i> -(CH ₃) ₂ NC ₆ H ₄ -] A = (<i>p</i> -NO ₂ C ₆ H ₄ -)						
symmetry: m2m (C _{2v})						
Tetraethylethylene derivative						
D = [<i>p</i> -(CH ₃) ₂ NC ₆ H ₄ -] A = (<i>p</i> -NO ₂ C ₆ H ₄ -)						
symmetry: 2/m (C _{2h})						

		[223]		
D = [<i>p</i> -(CH ₃) ₂ NC ₆ H ₄ -] A = (<i>p</i> -NO _{2C₆H₄-) A' = (<i>p</i>-NO_{2C₆SH₄-)}}				
symmetry: m (C ₈)				
Tetraethyllethene derivative D = [<i>p</i> -(CH ₃) ₂ NC ₆ H ₄ -] A' = (<i>p</i> -NO _{2C₃SH₄-)}	2100	2200 ± 100	THG	[223]
symmetry: 2mm (C _{2v})				
Tetrahydrofuran	(neat)	1910	2.24	DFWM [89]
Toluene	(neat)	1054	6.7	THG [87]
Thiophene (monomer)	(neat)	1910	4.55	THG [89]
Thiophene (dimer)	tetrahydrofuran	602	4.1	DFWM [98]
Thiophene (trimer)	tetrahydrofuran	602	22	DFWM [98]
Thiophene (tetramer)	tetrahydrofuran	602	160	DFWM [98]
Thiophene (pentamer)	tetrahydrofuran	602	800	DFWM [98]
Thiophene (hexamer)	tetrahydrofuran	602	2600	DFWM [98]
<i>trans</i> -Retinal	(molten)	1890	10,000	DFWM [98]
<i>trans</i> -Retinol	(molten)	1890	90 ± 20	THG [90]
<i>trans</i> -Stilbene	tetrahydrofuran	602	46 ± 12	THG [90]
Water	(neat)	1054	41.6 ± 4.9	DFWM [94]
Ytterbium bis(phthalocyanine)	chloroform	1064	0.57	THG [87]
Yttrium bis(phthalocyanine)	chloroform	1064	410,000	DFWM [96]
Yttrium bis(phthalocyanine) ion	chloroform	1064	260,000	DFWM [96]
			220,000	DFWM [96]

^aD, donor; A, acceptor.^bDFWM, degenerate four-wave mixing; THG, third harmonic generation; NLI, nonlinear interferometry; OKE, Optical Kerr effect; TCZS, two-color Z-scan; ZS, Z-scan.^cRe, real part.

V. ORGANIC MATERIALS

Much interest has also been generated in the development of organic materials for third order NLO, primarily systems with delocalized π electrons for large, very fast nonresonant $\chi^{(3)}$ response. Table 14 presents data for several selected organic single crystals, polymers, and thin films.

Note that $\chi^{(3)}$ can be quite large in these systems. However, this can often be due to a near-resonance enhancement, implying that linear absorption can be significant. Again, $\chi^{(3)}/\alpha$ is a good figure of merit.

Two-photon and three-photon absorption also are present in several of these types of materials (see Chapters 9 and 13). Large values of these coefficients place limits on the usefulness of these materials in all-optical switches due to the resultant losses.

VI. MOLECULAR SECOND HYPERPOLARIZABILITY DATA

Due to the high interest in organic systems for third order NLO, several materials are under development. It is often easier to obtain data on these systems in solution form. This way materials may be readily screened before the difficult processing of materials into single crystals or high quality thin films.

Table 15 presents some representative second hyperpolarizability (γ) data for both large molecular systems and some common solvents. Note that one method commonly used to characterize these materials is third harmonic generation. This method is often used to isolate the pure electronic response of the molecule, since the interest is in the fast nonresonant response. Caution should be exercised, however, in extrapolating these values to the anticipated value of $\chi^{(3)}$ or n_2 at the measurement wavelength because of dispersion. This is particularly so in many cases because either the fundamental wavelength or the third harmonic wavelength may be near an absorption band of the material. Intermediate resonances (i.e., at 2ω) may also be present that could enhance the value of γ measured using this technique.

REFERENCES

1. S. Singh, Nonlinear and harmonic generation materials, *Handbook of Laser Science and Technology*, Vol 3, Optical Materials, Part 1 (M. J. Weber, eds), CRC Press, Boca Raton, FL, 1986, pp. 3–228.
2. W. L. Smith, Nonlinear refractive index, *Handbook of Laser Science and Technology*, Vol 3 Optical Materials, Part 1 (M. J. Weber, ed), CRC Press, Boca Raton, FL, 1986, pp. 259–282.

3. S. Singh, Organic and inorganic materials, *Handbook of Laser Science and Technology*, Suppl., 2: Optical Materials (M. J. Weber, ed), CRC Press, Boca Raton, FL, 1995, pp. 147–249.
4. (a) L. Chase and E.W. Van Stryland, Inorganic materials, *Handbook of Laser Science and Technology*, Suppl. 2: Optical Materials (M. J. Weber, ed), CRC Press, Boca Raton, FL, 1995, pp. 269–288; (b) A.F. Garito and M. Kuzyk, Organic materials, *Handbook of Laser Science and Technology*, Suppl. 2: Optical Materials (M. J. Weber, ed), CRC Press, Boca Raton, FL, 1995, pp. 289–298.
5. T. Y. Chang, Fast self-induced refractive index changes in optical media: a survey, *Opt. Eng.* 20:220 (1981).
6. G. J. Rosasco and W. S. Hurst, Measurement of resonant and nonresonant third-order nonlinear susceptibilities by coherent Raman spectroscopy, *Phys. Rev. A* 32:281 (1985).
7. R. L. Farrow, and L. A. Rahn, Interpreting coherent anti-Stokes Raman spectra measured with multimode Nd:YAG pump lasers, *J. Opt. Soc. Am. B* 2:903 (1985).
8. R. L. Farrow, R. P. Lucht, and L. A. Rahn, Measurements on nonresonant third-order susceptibilities of gases using coherent anti-Stokes Raman spectroscopy, *J. Opt. Soc. Am. B* 4:1241 (1987).
9. D. P. Shelton and J. E. Rice, Measurements and calculations of the hyperpolarizabilities of atoms and small molecules in the gas phase, *Chem. Rev.* 94:3 (1994).
10. T. Lundein, S. Y. Hou, and J. W. Nibler, Nonresonant third-order susceptibilities for various gases, *J. Chem. Phys.* 79:6301 (1983).
11. W. G. Rado, The nonlinear third-order dielectric susceptibility coefficients of gases and optical third-harmonic generation, *Appl. Phys. Lett.* 11:123 (1967).
12. J. W. Hahn and E. S. Lee, Measurement of nonresonant third-order susceptibilities of various gases by the nonlinear interferometric technique, *J. Opt Soc. Am. B* 12:1021 (1995).
13. D. V. Vlasov, R. A. Garaev, V. V. Korobkin, and R. V. Serov, Measurement of nonlinear polarizability of air, *Sov. Phys. JETP* 49:1033 (1979).
14. J. E. Bjorkholm and A. Ashkin, CW self-focusing and self-trapping of light in sodium vapor, *Phys. Rev. Lett.* 32:129 (1974).
15. R. H. Lehmberg, J. Reintjes, and R. C. Eckardt, Negative nonlinear susceptibility of cesium vapor around 1.06 μm , *Phys. Rev. A* 13:1095 (1976).
16. D. Grischkowsky, N. S. Shiren, and R. J. Bennett, Generation of time-reversed wave fronts using a resonantly enhanced electronic nonlinearity, *Appl. Phys. Lett.* 33:805 (1978).
17. A. B. Villaverde, Saturable absorption and self-focusing effects in molecular iodine vapour, *J. Phys. B* 13:1817 (1980).
18. P. W. Smith, W. J. Tomlinson, E. J. Eilenberger, and P. J. Maloney, Measurement of electronic optical Kerr coefficients, *Opt. Lett.* 6:581 (1981).
19. D. V. G. L. N. Rao, F. J. Aranda, J. F. Roach, and D. E. Remy, Third-order nonlinear optical interactions of some benzoporphyrins, *Appl. Phys. Lett.* 58:1241 (1991).

20. C. Maloney and W. Blau, Resonant third-order hyperpolarizabilities of large organic molecules, *J. Opt. Soc. Am. B* 4:1035 (1987).
21. C. S. Winter, C. A. S. Hill, and A. E. Underhill, Near resonance optical nonlinearities in nickel dithiolene complexes, *Appl. Phys. Lett.* 58:107 (1991).
22. C. Maloney, H. Byrne, W. M. Dennis, and W. Blau, Picosecond optical phase conjugation using conjugated organic molecules, *Chem. Phys.* 21:21 (1988).
23. J. S. Shirk, J. R. Lindle, F. J. Bartoli, C. A. Hoffman, Z. H. Kafafi, and W. A. Snow, Off-resonant third-order optical nonlinearities of metal-substituted phthalocyanines, *Appl. Phys. Lett.* 55:1287 (1989).
24. A. P. Veduta and B. P. Kirsanov, Variation of the refractive index of liquids and glasses in a high intensity field of a ruby laser, *Sov. Phys. JEPT* 27:736 (1968).
25. P. P. Ho and R. R. Alfano, Optical Kerr effect in liquids, *Phys. Rev. A* 20:2170 (1979).
26. A. Owyong and P. S. Peercy, Precise characterization of the Raman nonlinearity in benzene using nonlinear interferometry, *J. Appl. Phys.* 48:674 (1977).
27. M. D. Levenson and N. Bloembergen, Dispersion of the nonlinear optical susceptibility tensor in centrosymmetric media, *Phys. Rev. B* 10:4447 (1974).
28. M. D. Levenson, Feasibility of measuring the nonlinear index of refraction by third-order frequency mixing, *IEEE J. Quant. Electron. QE-10:110* (1974).
29. K. J. Witte, M. Galanti, and R. Volk, n_2 -Measurements at $1.32\text{ }\mu\text{m}$ of some organic compounds usable as solvents in a saturable absorber for an atomic iodine laser, *Opt. Commun.* 34:278 (1980).
30. M. D. Levenson and N. Bloembergen, Dispersion of the nonlinear optical susceptibilities of organic liquids and solutions, *J. Chem. Phys.* 60:1323 (1974).
31. M. J. Moran, C.-Y. She, and R. L. Carman, Interferometric measurements of the nonlinear refractive-index coefficient relative to CS_2 in laser-system-related materials, *J. Quant. Electron. QE-11:259* (1975).
32. P. P. Ho, P. Y. Lu, and R. R. Alfano, Oscillatory optically induced Kerr kinetics in nitrobenzene, *Opt. Commun.* 30:426 (1979).
33. J. J. Song and M. D. Levenson, Electronic and orientational contributions to the optical Kerr constant determined by coherent Raman techniques, *J. Appl. Phys.* 48:3496 (1977).
34. W. L. Smith, P. Liu, and N. Bloembergen, Superbroadening in H_2O and D_2O by self-focused picosecond pulses from a YA1G:Nd laser, *Phys. Rev. A* 15:2396 (1977).
35. I. Golub, Y. Beaudoin, and S. L. Chin, Nonlinear refraction in CS_2 at $10.6\text{ }\mu\text{m}$, *Opt. Lett.* 13:488 (1988).
36. W. Zhao and P. Palffy-Muhoray, Z-scan technique using top-hat beams, *Appl. Phys. Lett.* 63:1613 (1993).
37. P. B. Chapple, J. Staromlynska, and R. G. McDuff, Z-scan studies in the thin- and the thick-sample limits, *J. Opt. Soc. Am. B* 11:975 (1994).
38. M. Sheik-Bahae, A. A. Said, T.-H. Wei, D. J. Hagan, and E. W. Van Stryland, Sensitive measurement of optical nonlinearities using a single beam, *IEEE J. Quant. Electron.* 26:760 (1990).

39. N. P. Xuan, J.-L. Ferrier, J. Gazengel, and G. Rivoire, Picosecond measurements of the third order susceptibility tensor in liquids, *Opt. Commun.* 51:433 (1984).
40. R. Adair, L. L. Chase, and S. A. Payne, Nonlinear refractive index of optical crystals, *Phys. Rev. B* 39:3337 (1989).
41. M. Sheik-bahae, J. R. DeSalvo, A. A. Said, D. J. Hagan, M. J. Soileau, and E. W. Van Stryland, Nonlinear refraction in UV transmitting materials, *Proc. SPIE* 1624:25 (1992).
42. D. Milam, M. J. Weber, and A. J. Glass, Nonlinear refractive index of fluoride crystals, *Appl. Phys. Lett.* 31:822 (1977).
43. R. DeSalvo, M. Sheik-Bahae, A. A. Said, D. J. Hagan, and E. W. Van Stryland, Z-scan measurements of the anisotropy of nonlinear refraction and absorption in crystals, *Opt. Lett.* 18:194 (1993).
44. D. Milam and M. J. Weber, Tune-resolved interferometric measurements of the nonlinear refractive index in laser materials, *Opt. Commun.* 18:172 (1976).
45. A. Penzkofer, J. Schmailzi, and H. Glas, Four-wave mixing in alkali halide crystals and aqueous solutions, *Appl. Phys. B* 29:37 (1982).
46. L. C. Oliveira and S. C. Zilio, Single-beam time-resolved Z-scan measurements of slow absorbers, *Appl. Phys. Lett.* 65:2121 (1994).
47. E. W. Van Stryland, Dispersion of n_2 in solids, *Proc. SPIE* 1441:430 (1991).
48. Y. Watanabe, M. Ohnishi, and T. Tsuchiya, Measurement of nonlinear absorption and refraction in titanium dioxide single crystal by using a phase distortion method, *Appl. Phys. Lett.* 66:3431 (1995).
49. N. Mansour, M. J. Soileau, and E. W. Van Stryland, Picosecond damage in Y_2O_3 stabilized zirconia, *Laser-Induced Damage in Optical Materials*, NBS Special Publication 727, National Bureau of Standards, Washington, D.C., 1984, p. 31.
50. S. Guha, N. Mansour, and M. J. Soileau, Direct n_2 measurement in yttria stabilized cubic zirconia, *Laser-Induced Damage in Optical Materials*, NBS Special Publication 746, National Bureau of Standards, Washington, D.C., 1985, p. 80.
51. R. Adair, L. L. Chase, and S. A. Payne, Nonlinear refractive index measurements of glasses using three-wave frequency mixing, *J. Opt. Soc. Am. B* 4:875 (1987).
52. K. S. Kim, R. H. Stolen, W. A. Reed, and K. W. Quoi, Measurement of the nonlinear index of silica-core and dispersion-shifted fibers, *Opt. Lett.* 19:257 (1994).
53. S. R. Friberg and P. W. Smith, Nonlinear optical glasses for ultrafast optical switches, *IEEE J. Quant. Electron.* QE-23:2089 (1987).
54. K. Uchida, S. Kaneko, S. Omi, C. Hata, H. Tanji, Y. Asahara, and A. J. Ikushima, Optical nonlinearities of a high concentration of small metal particles dispersed in glass: copper and silver particles, *J. Opt. Soc. Am. B* 11:1236 (1994).
55. R. F. Haglund, Jr., L. Yang, R. H. Magruder, III, J. E. Wittig, K. Becker, and R. A. Zehr, Picosecond nonlinear optical response of a Cu:silica nanocluster composite, *Opt. Lett.* 18:373 (1993).
56. K. Puech, W. Blau, A. Grund, C. Bubeck, and G. Cardenas, Picosecond degenerate four-wave mixing in colloidal solutions of gold nanoparticles at high repetition rates, *Opt. Lett.* 20:1613 (1995).

57. M. Sheik-Bahae, A. A. Said, T.-H. Wei, Y. Y. Wu, D. J. Hagan, M. J. Soileau, and E. W. Van Stryland, Z-scan: a simple and sensitive technique for nonlinear refraction measurements, *Proc. SPIE* 1148:41 (1989).
58. T. D. Krauss and F. W. Wise, Femtosecond measurement of nonlinear absorption and refraction in CdS, ZnSe, and ZnS, *Appl. Phys. Lett.* 65:1739 (1994).
59. A. A. Said, M. Sheik-Bahae, D. J. Hagan, T. H. Wei, J. Wang, J. Young, and E. W. Van Stryland, Determination of bound-electronic and free-carrier nonlinearities in ZnSe, GaAs, CdTe, and ZnTe, *J. Opt. Soc. Am. B* 9:405 (1992).
60. E. J. Canto-Said, D. J. Hagan, J. Young, and E. W. Van Stryland, Degenerate four-wave mixing measurements of high-order nonlinearities in semiconductors, *IEEE J. Quant. Electron.* 27:2274 (1991).
61. B. K. Rhee, W. E. Bron, and J. Kuhl, Determination of third-order nonlinear susceptibility $\chi^{(3)}$ through measurements in the picosecond time domain, *Phys. Rev. B* 30:7358 (1984).
62. A. E. Smith, R. G. McDuff, and N. R. Heckenberg, Nonlinear optical parameters for InSb at 10.6 and 9.6 μm with microsecond pulses, *J. Opt. Soc. Am. B* 12:393 (1995).
63. F. Z. Henari, K. Morgenstern, W. J. Blau, V. A. Karavanskii, and V. S. Dneprovskii, Third-order optical nonlinearity and all-optical switching in porous silicon, *Appl. Phys. Lett.* 67:323 (1995).
64. R. M. Ribeiro, W. Margulis, C. A. F. Leite, I. Guedes, L. Misoguti, and V. S. Bagnato, Nonlinear optical response of hydrogenated amorphous silicon films studied by laser induced transient gratings, *Appl. Phys. Lett.* 66:1089 (1995).
65. Y. J. Ding, C. L. Guo, G. A. Swartzlander, Jr., J. B. Khurgin, and A. E. Kaplan, Spectral measurement of the nonlinear refractive index in ZnSe using self-bending of a pulsed laser beam, *Opt. Lett.* 15:1431 (1990).
66. N. Sugimoto, A. Koiwai, S. Hyodo, T. Hioki, and S. Noda, Nonresonant third-order nonlinear optical susceptibility of CdS clusters encapsulated in zeolite A and X, *Appl. Phys. Lett.* 66:923 (1995).
67. G. P. Banfi, V. Degiorgio, D. Fortusini, and H. M. Tan, Third-order nonlinearity of semiconductor doped glasses at frequencies below band gap, *Appl. Phys. Lett.* 67:13 (1995).
68. S. M. Saltiel, B. Van Wonterghem, and R. M. Rentzepis, Measurement of $\chi^{(3)}$ and phase shift of nonlinear media by means of a phase-conjugate interferometer, *Opt. Lett.* 14:183 (1989).
69. M. D. Dvorak, B. L. Justus, D. K. Gaskill, and D. G. Hendershot, Nonlinear absorption and refraction of quantum confined InP nanocrystals grown in porous glass, *Appl. Phys. Lett.* 66:804 (1995).
70. F. J. Aranda, R. Garimella, N. F. McCarthy, D. N. Rao, Z. Chen, J. A. Akkara, D. L. Kaplan, and J. F. Roach, All-optical light modulation in bacteriorhodopsin films, *Appl. Phys. Lett.* 67:599 (1995).
71. Z. H. Kafafi, J. R. Lindle, R. G. S. Pong, F. J. Bartoli, L. J. Lingg, and J. Milliken, Off-resonant nonlinear optical properties of C_{60} studied by degenerate four-wave mixing, *Chem. Phys. Lett.* 188:492 (1992).

72. H. Hoshi, N. Nakamura, Y. Maruyama, T. Nakagawa, S. Suzuki, H. Shiromaru, and Y. Achiba, Optical second- and third-harmonic generations in C₆₀ film, *Jpn. J. Appl. Phys.* 30:L1397 (1991).
73. H. Fei, Z. Wei, Q. Yang, Y. Che, Y. Shen, X. Fu, and L. Qiu, Low-power phase conjugation in push-pull azobenzene compounds, *Opt. Lett.* 20:1518 (1995).
74. S. A. Jenekhe, W.-C. Chen, S. Lo, and S. R. Flom, Large third-order optical nonlinearities in organic polymer superlattices, *Appl. Phys. Lett.* 57:126 (1990).
75. G. M. Carter, M. K. Thakur, Y. J. Chen, and J. V. Hryniewicz, Time and wavelength resolved nonlinear optical spectroscopy of a polydiacetylene in the solid state using picosecond dye laser pulses, *Appl. Phys. Lett.* 47:457 (1985).
76. J. C. Baumert, G. C. Bjorklund, D. H. Jundt, M. C. Jurich, H. Looser, R. D. Miller, J. Rabolt, J. Sooriyakumaran, J. D. Swalen, and R. J. Twieg, Temperature dependence of the third-order nonlinear optical susceptibilities in polysilanes and polygermanes, *Appl. Phys. Lett.* 53:1147 (1988).
77. R. Dorsinville, L. Yang, R. R. Alfano, R. Zamboni, R. Danieli, G. Ruani, and C. Taliani, Nonlinear-optical response of polythiophene films using four-wave mixing techniques, *Opt. Lett.* 14:1321 (1989).
78. M. Samoc and P. N. Prasad, Dynamics of resonant third-order optical nonlinearity in perlylene tetracarboxylic dianhydride studied by monitoring first- and second-order diffractions in subpicosecond degenerate four-wave mixing, *J. Chem. Phys.* 91:6643 (1989).
79. T. Hattori, H. Okawa, T. Wada, and H. Sasabe, Subpicosecond interferometric measurement of the nonlinear refractive index of poly(3-hexylthiophene), *Opt. Lett.* 17:1560 (1992).
80. L. Yang, R. Dorsinville, Q. Z. Wang, W. K. Zou, P. P. Ho, N. L. Yang, R. R. Alfano, R. Zamboni, R. Danieli, G. Ruani, and C. Taliani, Third-order optical nonlinearity in polycondensed thiophene-based polymers and polysilane polymers, *J. Opt. Soc. Am. B* 6:753 (1989).
81. D. N. Rao, J. Swiatkiewicz, P. Chopra, S. K. Ghoshai, and P. N. Prasad, Third order nonlinear optical interactions in thin films of poly-*p*-phenylenebenzobisthiazole polymer investigated by picosecond and subpicosecond degenerate four wave mixing, *Appl. Phys. Lett.* 48:1187 (1986).
82. A. Samoc, M. Samoc, M. Woodruff, and B. Luther-Davies, Tuning the properties of poly(*p*-phenylenevinylene) for use in all-optical switching, *Opt. Lett.* 20:1241 (1995).
83. L. Yang, R. Dorsinville, P. X. Ye, R. R. Alfano, R. Zamboni, and C. Taliani, Excited-state nonlinearity in polythiophene thin films investigated by the Z-scan technique, *Opt. Lett.* 17:323 (1992).
84. D. V. Petrov, A. S. L. Gomes, C. B. de Araujo, J. M. de Souza, W. M. de Azevedo, J. V. de Melo, and F. B. Diniz, Nonlinear-optical properties of a poly(vinylalcohol)-polyaniline interpenetrating polymer network, *Opt. Lett.* 20:554 (1995).
85. B. K. Mandal, B. Bihari, A. K. Sinha, M. Kamath, and L. Chen, Third-order nonlinear optical response in a multilayered phthalocyanine composite, *App. Phys. Lett.* 66:932 (1995).

86. B. L. Lawrence, M. Cha, W. E. Torruellas, G. I. Stegeman, S. Etemad, G. Baker, and R. Kajzar, Measurement of the complex nonlinear refractive index of single crystal *p*-toluene sulfonate at 1064 nm, *App. Phys. Lett.* 64:2773 (1994).
87. M. Thalhammer and A. Penzkofer, Measurement of third-order nonlinear susceptibilities by non-phase matched third-harmonic generation, *Appl. Phys. B* 32:137 (1983).
88. F. Kajzar and J. Messier, Third-harmonic generation in liquids, *Phys. Rev. A* 32:2352 (1985).
89. G. R. Meredith, B. Buchalter, and C. Hanzlik, Third-order susceptibility determination by third harmonic generation. II, *J. Chem. Phys.* 78:1543 (1983).
90. J. P. Hermann and J. Duccing, Third-order polarizabilities of long-chain molecules, *J. Appl. Phys.* 45:5100 (1974).
91. P. N. Prasad, E. Perrin, and M. Samoc, A coupled anharmonic oscillator model for optical nonlinearities of conjugated organic structures, *J. Chem. Phys.* 91:2360 (1989).
92. G. R. Meredith, B. Buchalter, and C. Hanzlik, Third-order susceptibility determination by third harmonic generation. I, *J. Chem. Phys.* 78:1533 (1983).
93. M. Zhao, Y. Cui, M. Samoc, P. N. Prasad, M. R. Unroe, and B. A. Reinhardt, Influence of two-photon absorption on third-order nonlinear optical processes as studied by degenerate four-wave mixing: the study of soluble didecyloxy substituted polyphenyls, *J. Chem. Phys.* 95:3991 (1991).
94. S. Ghosal, M. Samoc, P. N. Prasad, and J. J. Tufariello, Optical nonlinearities of organometallic structures: aryl and vinyl derivatives of ferrocene, *J. Phys. Chem.* 94:2847 (1990).
95. R. L. Sutherland, E. Rea, L. V. Natarajan, T. Pottenger, and P. A. Fleitz, Two-photon absorption and second hyperpolarizability measurements in diphenylbutadiene by degenerate four-wave mixing, *J. Chem. Phys.* 98:2593 (1993).
96. J. S. Shirk, J. R. Lindle, F. J. Bartoli, and M. E. Boyle, Third-order optical nonlinearities of bis(phthalocyanines), *J. Phys. Chem.* 96:5847 (1992).
97. M.-T. Zhao, M. Samoc, B. P. Singh, and P. N. Prasad, Study of third-order microscopic optical nonlinearities in sequentially built and systematically derivatized structures, *J. Phys. Chem.* 93:7916 (1989).
98. M.-T. Zhao, B. P. Singh, and P. N. Prasad, A systematic study of polarizability and microscopic third-order optical nonlinearity in thophene oligomers, *J. Chem. Phys.* 89:5535 (1988).
99. J. Si, Y. Wang, J. Zhao, P. Ye, D. Wang, W. Sun, and S. Dong, Fluence dependence of nonlinear optical response of cadmium texaphyrin, *Appl. Phys. Lett.* 67:1975 (1995).
100. C. E. Moore, *Atomic Energy Levels*, U.S. Dept. of Commerce, NBS, U.S. GPO, Washington, D.C., 1958.
101. E. M. Anderson and V. A. Zilitis, *Opt. Spectrosc.* 16:99 (1964).
102. E. M. Anderson and V. A. Zilitis, *Opt. Spectrosc.* 16:211 (1964).
103. B. P. Kibble, G. Copley, and L. Krause, Inelastic collisions between excited alkali atoms and molecules. II. The quenching of sodium resonance radiation by N₂, H₂, HD, and D₂, *Phys. Rev.* 159:11 (1967).

104. T. F. Gallagher, W. E. Cooke, and S. A. Edelstein, Collisional deactivation of the 5s and 4p states of Na by N₂, *Phys. Rev. A* 17:125 (1978).
105. W. Shutz, *A. Phys.* 45:30 (1927).
106. F. Birabon, B. Cagnac, and G. Grynberg, *J. Phys. (Paris) Lett.* 36:41 (1975).
107. J. A. Bellisio, P. Davidovits, and P. J. Kindlmann, *J. Chem. Phys.* 48:2376 (1968).
108. W. Demtroder, M. McClintock, and R. N. Zare, Spectroscopy of Na₂ using laser-induced fluorescence, *J. Chem. Phys.* 51:5495 (1968).
109. M. McClintock, W. Demtroder, and R. N. Zare, Level-crossing studies of Na₂ using laser-induced fluorescence, *J. Chem. Phys.* 51:5509 (1968).
110. M. A. Henesian, R. L. Herbst, and R. L. Byer, Optically pumped superfluorescent Na₂ molecular laser, *J. Appl. Phys.* 47:1515 (1976).
111. W. H. Evans, R. Jacobson, T. R. Munson, and D. D. Wagman, *J. Res. Natl. Bur. Std.* 55:83 (1955).
112. P. Kusch and M. M. Hessel, Analysis of B1- π - μ -X1- sigmagt band system of Na₂, *J. Chem. Phys.* 68:2591 (1978).
113. Landolt-Bornstein-Zahlenwerte und Funktionen, *J. Band Atom und Molekular Physik*, 3 Teil, Springer-Verlag, Berlin, 1951, pp. 9–10.
114. J. I. Steinfeld, R. N. Zare, L. Jones, M. Lesk, and W. Klemperer, *J. Chem. Phys.* 42:25 (1965).
115. R. J. LeRoy, Molecular constants and internuclear potential of ground-state molecular iodine (vibrational energies, rotational constants and internuclear potential of ground state molecular iodine, using reanalyzed spectroscopic data), *J. Chem. Phys.* 52:2683 (1970).
116. A. Chutjian, J. K. Link, and L. Brewer, *J. Chem. Phys.* 46:2666 (1967).
117. R. L. Byer, R. L. Herbst, H. Kildal, and M. D. Levenson, Optically pumped molecular iodine vapor-phase laser, *Appl. Phys. Lett.* 20:463 (1972).
118. R. Oberly, K. N. Rao, Y. H. Hahn, and T. K. McCubbin, Jr., *J. Mol. Spectrosc.* 25:138 (1968).
119. L. M. Sverdlov, M. A. Kovner, and E. P. Krainov, *Vibrational Spectra of Poly-atomic Molecules*, John Wiley, New York, 1974.
120. E. K. Plyler, E. D. Tidwell, and A. B. Maki, *J. Res. Natl Bur. Std. A* 68:79 (1964).
121. J. S. Garing, H. H. Nielsen, and K. N. Rao, *J. Mol. Spectrosc.* 3:496 (1959).
122. H. M. Mould, W. C. Price, and G. R. Wilkinson, *Spectrochim. Acta* 15:313 (1959).
123. F. Shimizu, Stark spectroscopy of NH₃v₂ band by 10- μ m CO₂ and N₂O lasers, *J. Chem. Phys.* 52:3572 (1970).
124. T. Shimizu, F. O. Shimizu, R. Turner, and T. Oka, Pressure broadening measurement of the v₂¹R-(0,0) transition of ¹⁵NH₃ by a CO₂, *J. Chem. Phys.* 55:2822 (1971).
125. J. S. Murphy and J. E. Boggs, Collision broadening of rotational absorption lines. IV. Pressure broadening of the ammonia inversion spectrum, *J. Chem. Phys.* 50:3320 (1969).
126. T. Y. Chang and C. Lin, Effects of buffer gases on an optically pumped CH₃F FIR laser, *J. Opt. Soc. Am.* 66:362 (1976).
127. W. L. Smith and I. M. Mills, *J. Mol. Spectrosc.* 11:11 (1963).

128. S. M. Freund, G. Duxbury, M. Romheld, J. T. Tiedje, and T. Oka, Laser Stark spectroscopy in the 10 μm region: the ν_3 bands of CH_3F , *J. Mol. Spectrosc.* 52:38 (1974).
129. G. Birnbaum, *Adv. Chem. Phys.* 12:487 (1967).
130. L. G. Smith, *J. Chem. Phys.* 50:139 (1969).
131. I. B. Berlman, *Handbook of Fluorescence Spectra of Aromatic Molecules*, Academic Press, New York, 1971.
132. *Eastman Organic Chemicals*, Catalog No. 49, Eastman Kodak Co., Rochester, New York, 1977.
133. K. H. Drexhage, Structure and properties of laser dyes, *Dye Lasers*, 2nd ed., (F. P. Schafer, ed), Springer-Verlag, New York, 1977.
134. K. H. Drexhage, Fluorescence efficiency of laser dyes, *J. Res. NBS* 80A:421 (1976).
135. W. C. Holmes and A. R. Peterson, *J. Chem. Phys.* 36:1248 (1962).
136. M. L. Spaeth and W. R. Sooy, Fluorescence and bleaching of organic dyes for a passive Q-switch laser. (Organic dyes fluorescence and bleaching by passive Q switched ruby laser radiation in various dye-solvent combinations, measuring lifetimes), *J. Chem. Phys.* 48:2315 (1968).
137. P. Kafalas, J. I. Masters, and E. M. E. Murray, *J. Appl. Phys.* 35:2349 (1964).
138. L. Zechmeister and A. Polgar, *J. Am. Chem. Soc.* 65:1522 (1943).
139. F. P. Schafer, Principles of dye laser operation, *Dye Lasers*, 2nd ed., (F. P. Schafer, ed), Springer-Verlag, New York, 1977.
140. C. Brecher and K. W. French, Comparison of aprotic solvents for trivalent neodymium ion liquid laser systems. Selenium oxychloride and phosphorus oxychloride, *J. Phys. Chem.* 73:1785 (1969).
141. A. A. Kaminski, *Sov. Phys. JETP* 24:33 (1967).
142. H. G. Danielmeyer, *Lasers* (A. K. Levine, and A. J. DeMaria, eds), Marcel Dekker, New York, 1976.
143. D. C. Cronemeyer, Optical absorption characteristics of pink ruby, *J. Opt. Soc. Am.* 56:1703 (1966).
144. D. E. McCumber and M. D. Sturge, *J. Appl. Phys.* 34:1682 (1963).
145. R. Pappalardo and D. L. Wood, *J. Chem. Phys.* 33:1734 (1960).
146. R. Pappalardo, *Z. Physik* 173:374 (1963).
147. H. A. Weakliem, *J. Chem. Phys.* 36:2117 (1962).
148. R. Pappalardo and R. E. Dietz, Absorption spectra of transition ions in CdS crystals, *Phys. Rev.* 123:1188 (1961).
149. L. M. Lisitsyn, L. A. Lisitsyna, M. I. Kalinin, V. M. Reiterov, and V. A. Federov, *Opt. Spectrosc.* 43:539 (1977).
150. J. H. Beaumont and W. Hayes, M centres in alkaline earth fluorides, *Proc. Roy. Soc. A* 309:41 (1969).
151. J. Nahum and D. A. Wiegand, Optical properties of some F-aggregate centers in LiF, *Phys. Rev.* 154:817 (1967).
152. L. Bosi, C. Bussolati, and G. Spinolo, Lifetime studies on the relaxed excited state of color centers, *Phys. Rev. B* 1:890 (1970).
153. K. Amenu-Kpodou and T. J. Neubert, *J. Phys. Chem. Solids* 26:1615 (1965).

154. L. F. Mollenauer and D. M. Bloom, Broadly tunable cw lasers using F^{2+} centers for the 1.26–1.48 and 0.82–1.07 μm bands, *Opt. Lett.* 3:48 (1978).
155. F. Luty, In *Physics of Color Centers* (W. B. Fowler, ed), Academic Press, New York, 1968.
156. G. B. Stringfellow and R. M. Bube, Photoelectronic properties of ZnSe crystals, *Phys. Rev.* 171:903 (1968).
157. H. G. Grimmeiss, C. Ovren, W. Ludwig, and R. Mach, Identification of deep centres in ZnSe, *J. Appl. Phys.* 48:5122 (1977).
158. R. Bowers and N. T. Melamed, Luminescent centers in ZnS: Cu: Cl phosphors, *Phys. Rev.* 99:1781 (1955).
159. I. Broser and K. H. Franke, *J. Phys. Chem. Solids* 26:1013 (1965).
160. N. Watanabe and S. Usui, *Jpn. J. Appl. Phys.* 5:569 (1966).
161. N. Watanabe, Infrared absorption in p-type semiconductors with zincblende structure—Application to zinc telluride, *J. Phys. Soc. Jpn.* 21:713 (1966).
162. G. Picus, E. Burstein, B. W. Henvis, and M. Hass, *J. Phys. Chem. Solids* 8:282 (1959).
163. R. Braunstein and E. O. Kane, *J. Phys. Chem. Solids* 23:1423 (1962).
164. H. B. Briggs and R. C. Fletcher, Absorption of infrared light by free carriers in germanium, *Phys. Rev.* 91:1342 (1953).
165. W. Kaiser, R. J. Collins, and H. Y. Fan, Infrared absorption in p-type germanium, *Phys. Rev.* 91:1380 (1953).
166. R. H. Bube, *Photoconductivity of Solids*, John Wiley, New York, 1960.
167. P. R. Bratt, In *Semiconductors and Semimetals*, Infrared Detectors II, Vol 12 (R. K. Willardson and A. C. Beer, eds), Academic Press, New York, 1977.
168. J. I. Pankove, *Optical Processes in Semiconductors*, Prentice-Hall, Englewood Cliffs, N.J., 1971.
169. W. G. Spitzer, M. Gershenson, C. J. Frosch, and D. F. Gibbs, *J. Phys. Chem. Solids* 11:339 (1959).
170. R. F. Leheny and J. Shah, Optical pumping in nitrogen-doped GaP, *Phys. Rev. B* 12:3268 (1975).
171. Y. Kaifu, T. Komatsu, and Y. Takemura, Temperature dependence of the optical absorption of bound excitons in GaP:N and GaP:S crystals, *J. Phys. Soc. Jpn.* 38:791 (1975).
172. D. G. Thomas, and J. J. Hopfield, Exciton spectrum of cadmium sulfide, *Phys. Rev.* 116:573 (1959).
173. E. Gutsche and J. Voigt, *II-VI Semiconducting Compounds* (D. G. Thomas, ed), W. A. Benjamin, New York, 1967, pp. 337–348.
174. J. J. Hopfield and D. G. Thomas, Fine structure and magneto-optic effects in the exciton spectrum of cadmium sulfide, *Phys. Rev.* 122:35 (1961).
175. Y. S. Park, C. W. Litton, T. C. Collins, and D. C. Reynolds, Exciton spectrum of ZnO, *Phys. Rev.* 143:512 (1966).
176. D. C. Reynolds, *Optical Properties of Solids*, Ch. 10 (S. Nudelman and S. S. Mitra, eds), Plenum Press, New York, 1969.
177. *CRC Handbook of Chemistry and Physics*, 53rd ed., (R. C. Weast, ed), CRC Press, Cleveland, Ohio, 1972.

178. B. A. Rockwell, W. P. Roach, M. E. Rogers, M. W. Mayo, C. A. Toth, C. P. Gain, and G. D. Noojin, Nonlinear refraction in vitreous humor, *Opt. Lett.* 18:1792 (1993).
179. J. Yumoto, S. G. Lee, B. Kippelen, N. Peyghambarian, B. G. Aitken, and N. F. Borrelli, Enhancement of optical nonlinearity of heavy-metal oxide glasses by replacing lead and bismuth with thallium, *Appl. Phys. Lett.* 63:2630 (1993).
180. S. Molyneux, A. K. Kar, B. S. Wherrett, T. L. Axon, and D. Bloor, Near-resonant refractive nonlinearity in polydiacetylene 9-BCMU thin films, *Opt. Lett.* 18:2093 (1993).
181. G. S. Maciel, A. G. Bezerra, Jr., N. Rakov, C. B. de Araújo, A. S. L. Gomes, and W. M. de Azevedo, Third-order nonlinear optical properties of undoped polyaniline solutions and films probed at 532 nm, *J. Opt. Soc. Am. B* 18:1099 (2001).
182. J. Zhou, E. Y. B. Pun, and X. H. Zhang, Nonlinear optical refractive indices and absorption coefficients of α,β -unsaturated ketone derivatives, *J. Opt. Soc. Am. B* 18:1456 (2001).
183. I. Fuks, B. Derkowska, B. Sahraoui, S. Niziol, J. Sanetra, D. Bogdal, and J. Pielichowski, Third-order nonlinear optical susceptibility of polymers based on carbazole derivatives, *J. Opt. Soc. Am. B* 19:89 (2002).
184. X. Shang, Y. Liu, G. Tang, G. Zhang, and W. Chen, Optical nonlinearities of hypocrellin A with the excitation of nanosecond pulses, *J. Opt. Soc. Am. B* 15:1502 (1998).
185. B. Sahraoui, X. Nguyen Phu, M. Sallé, and A. Gorgues, Electronic and nuclear contributions to the third-order nonlinear optical susceptibilities of new *p*-*N,N'*-dimethylaniline tetrathiafulvalene derivatives, *Opt. Lett.* 23:1811 (1998).
186. X. Liu, J. Si, B. Chang, G. Xu, Q. Yang, Z. Pan, S. Xie, P. Ye, J. Fan, and M. Wan, Third-order optical nonlinearity of the carbon nanotubes, *Appl. Phys. Lett.* 74:164 (1999).
187. S. R. Vigil and M. G. Kuzyk, Absolute molecular optical Kerr effect spectroscopy of dilute organic solutions and neat organic liquids, *J. Opt. Soc. Am. B* 18:679 (2001).
188. G. Boudebs, M. Chis, and X. N. Phu, Third-order susceptibility measurement by a new Mach-Zehnder interferometry technique, *J. Opt. Soc. Am. B* 18:623 (2001).
189. K. S. Bindra, H. T. Bookey, A. K. Kar, B. S. Wherrett, X. Liu, and A. Jha, Nonlinear optical properties of chalcogenide glasses: Observation of multiphoton absorption, *Appl. Phys. Lett.* 79:1939 (2001).
190. J. E. Aber, M. C. Newstein, and B. A. Garetz, Femtosecond optical Kerr effect measurements in silicate glasses, *J. Opt. Soc. Am. B* 17:120 (2000).
191. N. Sugimoto, H. Kanbara, S. Fujiwara, K. Tanaka, Y. Shimizugawa, and K. Hirao, Third-order optical nonlinearities and their ultrafast response in $\text{Bi}_2\text{O}_3\text{-B}_2\text{O}_3\text{-SiO}_2$ glasses, *J. Opt. Soc. Am. B* 16:1904 (1999).
192. D. Monzón-Hernández, A. N. Starodumov, Yu. O. Barmenkov, I. Torees-Gómez, and F. Mendoza-Santoyo, Continuous-wave measurement of the fiber nonlinear refractive index, *Opt. Lett.* 23:1274 (1998).

193. M. O. Martin, L. Canioni, and L. Sarger, Measurements of complex third-order optical susceptibility in a collinear pump-probe experiment, *Opt. Lett.* 23:1874 (1998).
194. J. M. Harbold, F.Ö. Ilday, F. W. Wise, J. S. Sanghera, V. Q. Nguyen, L. B. Shaw, and I. D. Aggarwal, Highly nonlinear As-S-Se glasses for all-optical switching, *Opt. Lett.* 27:119 (2002).
195. J. Subías, J. Pelayo, R. Alonso, F. Villuendas, and C. Heras, Electrostriction-free n₂ measurement in single-mode optical fibers based on nonlinear-polarization evolution, *J. Opt. Soc. Am. B* 19:390 (2002).
196. G. Battaglin, P. Calvelli, E. Cattaruzza, F. Gonella, R. Polloni, G. Mattei, and P. Mazzoldi, Z-scan study of the nonlinear refractive index of copper nanocluster composite silica glass, *Appl. Phys. Lett.* 78:3953 (2001).
197. G. Battaglin, P. Calvelli, E. Cattaruzza, R. Polloni, E. Borsella, T. Cesca, F. Gonella, and P. Mazzoldi, Laser-irradiation effects during Z-scan measurement on metal nanocluster composite glasses, *J. Opt. Soc. Am. B* 17:213 (2000).
198. Y. Hamanaka, A. Nakamura, S. Omi, N. Del Fatti, F. Vallée, and C. Flytzanis, Ultrafast response of nonlinear refractive index of silver nanocrystals embedded in glass, *Appl. Phys. Lett.* 75:1712 (1999).
199. E. Cattaruzza, F. Gonella, G. Mattei, P. Mazzoldi, D. Gatteschi, C. Sangregorio, M. Falconieri, G. Salvetti, and G. Battaglin, Cobalt nanoclusters in silica glass: Nonlinear optical and magnetic properties, *Appl. Phys. Lett.* 73:1176 (1998).
200. M. Falconieri, G. Salvetti, E. Cattaruzza, F. Gonella, G. Mattei, P. Mazzoldi, M. Piovesan, G. Battaglin, and R. Polloni, Large third-order optical nonlinearity of nanocluster-doped glass formed by ion implantation of copper and nickel in silica, *Appl. Phys. Lett.* 73:288 (1998).
201. R. de Nalda, R. del Coso, J. Requejo-Isidro, J. Olivares, A. Suarez-Garcia, J. Solis, and C. N. Afonso, Limits to the determination of the nonlinear refractive index by the Z-scan method, *J. Opt. Soc. Am. B* 19:289 (2002).
202. M. Ashida, T. Ogasawara, Y. Tokura, S. Uchida, S. Mazumdar, and M. Kuwata-Gonokami, One-dimensional cuprate as a nonlinear optical material for ultrafast all-optical switching, *Appl. Phys. Lett.* 78:2831 (2001).
203. A. Pačebutas, A. Stalnionis, A. Krotkus, T. Suski, P. Perlin, and M. Leszczynski, Picosecond Z-scan measurements on bulk GaN crystals, *Appl. Phys. Lett.* 78:4118 (2001).
204. M. D. Turner, W. B. Roh, and K. L. Schepler, Nonlinear optical properties of GaSb and GaInAsSb and their application for phase conjugation in degenerate four-wave mixing, *J. Opt. Soc. Am. B* 17:790 (2000).
205. C. H. Kwak, Y. L. Lee, and S. G. Kim, Analysis of asymmetric Z-scan measurement for large optical nonlinearities in an amorphous As₂S₃ thin film, *J. Opt. Soc. Am. B* 16:600 (1999).
206. S. Vijayalakshmi, J. Sturmann, and H. Grebel, Linear and nonlinear properties of laser-ablated Si films in the 9.0–9.6-μm wavelength region, *J. Opt. Soc. Am. B* 16:1286 (1999).

207. W. F. Zhang, M. S. Zhang, Z. Yin, Y. Z. Gu, Z. L. Du, and B. L. Yu, Large third-order optical nonlinearity in $\text{SrBi}_2\text{Ta}_2\text{O}_9$ thin films by pulsed laser deposition, *Appl. Phys. Lett.* 75:902 (1999).
208. H. B. Liao, R. F. Xiao, H. Wang, K. S. Wong, and G. K. L. Wong, Large third-order optical nonlinearity in Au:TiO₂ composite films measured on a femtosecond time scale, *Appl. Phys. Lett.* 72:1817 (1998).
209. Y. Z. Gu, W. F. Zhang, D. H. Gu, and F. X. Gan, Nonlinear response and optical limiting in $\text{SrBi}_2\text{Ta}_2\text{O}_9$ thin films, *Opt. Lett.* 26:1788 (2001).
210. Y. X. Jie, Y. N. Xiong, A. T. S. Wee, C. H. A. Huan, and W. Ji, Dynamics of optical nonlinearity of Ge nanocrystals in a silica matrix, *Appl. Phys. Lett.* 77:3926 (2000).
211. J.-K. Wang, T.-L. Chiu, C.-H. Chi, and C.-K. Sun, Nonlinear refraction and absorption measurements with chirped femtosecond laser pulses: experiments and simulations, *J. Opt. Soc. Am. B* 16:651 (1999).
212. A. Dowd, R. G. Elliman, M. Samoc, and B. Luther-Davies, Nonlinear optical response of Ge nanocrystals in a silica matrix, *Appl. Phys. Lett.* 74:239 (1999).
213. A. K. Bhowmik and M. Thakur, Self-phase modulation in polydiacetylene single crystal measured at 720–1064 nm, *Opt. Lett.* 26:902 (2001).
214. S. Tatsuura and O. Wada, Large $\chi^{(3)}$ of squarylium dye J aggregates measured using the Z-scan technique, *Appl. Phys. Lett.* 79:2517 (2001).
215. W. Schrof, S. Rozouvan, T. Hartmann, H. Möhwald, V. Belov, and E. Van Keuren, Nonlinear optical properties of novel low-bandgap polythiophenes, *J. Opt. Soc. Am. B* 15:889 (1998).
216. R. Rangel-Rojo, S. Yamada, H. Matsuda, and D. Yankelevich, Large near-resonance third-order nonlinearity in an azobenzene-functionalized polymer film, *Appl. Phys. Lett.* 72:1021 (1998).
217. W. Sun, C. M. Lawson, G. M. Graty, C. Zhan, and D. Wang, Degenerate four-wave mixing and Z-scan measurements of stilbazolium derivatives, *Appl. Phys. Lett.* 78:1817 (2001).
218. W. Sun, C. C. Byeon, C. M. Lawson, G. M. Gray, and D. Wang, Third-order nonlinear optical properties of an expanded porphyrin cadmium complex, *Appl. Phys. Lett.* 77:1759 (2000).
219. X. Shang, G. Tang, G. Zhang, Y. Liu, W. Chen, B. Yang, and X. Zhang, Optical nonlinearities and transient dynamics of 2-(2'-hydroxyphenyl)benzoxazole studied by single-beam and time-resolved two-color Z-scan techniques, *J. Opt. Soc. Am. B* 15:854 (1998).
220. S. Wang, W. Huang, T. Zhang, H. Yang, Q. Gong, Y. Okuma, M. Horikiri, and Y. F. Miura, Third-order nonlinear optical properties of didodecyldimethylammonium-Au(dmit)₂, *Appl. Phys. Lett.* 75:1845 (1999).
221. M. Yamashita, S. Kikuma, Y. Yamaoka, H. Murakami, R. Morita, and H. Shigekawa, Nonresonant femtosecond second hyperpolarizabilities of intramolecular charge-transfer molecules with great excited- and ground-state dipole-moment differences, *Appl. Phys. Lett.* 75:28 (1999).
222. W. Sun, C. C. Byeon, C. M. Lawson, G. M. Gray, and D. Wang, Third-Order susceptibilities of asymmetric pentaazadentate porphyrin-like metal complexes, *Appl. Phys. Lett.* 74:3254 (1999).

223. U. Gubler, R. Spreiter, Ch. Bosshard, P. Günter, R. R. Tykwienski, and F. Diederich, Two-dimensionally conjugated molecules: The importance of low molecular symmetry for large third-order nonlinear optical effects, *Appl. Phys. Lett.* 73:2396 (1998).
224. J. R. Helfin, D. Marciu, C. Figura, S. Wang, P. Burbank, S. Stevenson, and H. C. Dorn, Enhanced nonlinear optical response of an endohedral metallofullerene through metal-to-cage charge transfer, *Appl. Phys. Lett.* 72:2788 (1998).
225. S. Smolorz, F. Wise, and N. F. Borrelli, Measurement of the nonlinear optical response of optical fiber materials by use of spectrally resolved two-beam coupling, *Opt. Lett.* 24:1103 (1999).

9

Nonlinear Absorption

The intense monochromatic radiation from a laser can induce profound changes in the optical properties of a material. Nonlinear absorption refers to the change in transmittance of a material as a function of intensity or fluence. At sufficiently high intensities, the probability of a material absorbing more than one photon before relaxing to the ground state can be greatly enhanced. As early as 1931, Göppert-Mayer derived the two-photon transition probability in a system using second order quantum perturbation theory [1]. Since the invention of the laser, not only has this phenomenon of the simultaneous absorption of two photons been observed in a wide variety of materials, multiphoton (>2) absorption has also been widely studied. In addition, population redistribution induced by intense laser fields leads to interesting counterplays of stimulated emission and absorption, complicated energy transitions in complex molecular systems, and the generation of free carriers in solids. These phenomena are manifested optically in a reduced (saturable) or increased (reverse saturable) absorption.

The many different effects produced by nonlinear absorption in the frequency dependent transmittance of a material have led to several applications in science and technology. These include such diverse areas as nonlinear spectroscopy and optical limiting. In the sections that follow, several of the formulas and phenomena pertinent to an understanding of simultaneous multiphoton absorption, cumulative multistep absorption, and absorption effects associated with population redistributions are discussed. The last section briefly describes some applications.

Several parameters and their physical units, both SI and cgs, that appear in formulas related to nonlinear absorption are given in Table 1. SI units are the most appropriate for experiments, but cgs units often appear in the literature in

Table 1 Physical Units of Important Parameters Utilized in Formulas Related to Nonlinear Absorption

Physical parameter	SI	cgs
Linear absorption cross-section	$[\sigma] = \text{m}^2$	$[\sigma] = \text{cm}^2$
Two-photon absorption cross-section	$[\sigma_2] = \text{m}^4\text{-s/}$ photon-molecule	$[\sigma_2] = \text{cm}^4\text{-s/}$ photon-molecule
Linear absorption coefficient	$[\alpha] = \text{m}^{-1}$	$[\alpha] = \text{cm}^{-1}$
Two-photon absorption coefficient	$[\beta] = \text{m/W}$	$[\beta] = \text{cm-s/erg}$
Three-photon absorption coefficient	$[\gamma] = \text{m}^3/\text{W}^2$	$[\gamma] = \text{cm}^3\text{-s}^2/\text{erg}^2$
Third order susceptibility	$[\chi^{(3)}] = \text{m}^2/\text{V}^2$	$[\chi^{(3)}] = \text{cm}^2/\text{sV}^2$ $= \text{cm}^3/\text{erg} = \text{esu}$
Fifth order susceptibility	$[\chi^{(5)}] = \text{m}^4/\text{V}^4$	$[\chi^{(5)}] = \text{cm}^4/\text{sV}^4$ $= \text{cm}^6/\text{erg}^2 = \text{esu}$
Vacuum permittivity	$[\epsilon_0] = \text{F/m} = \text{C/V-m}$	—
Distance, length	$[z] = [L] = \text{m}$	$[z] = [L] = \text{cm}$
Speed of light	$[c] = \text{m/s}$	$[c] = \text{cm/s}$
Wavelength	$[\lambda] = \text{m}$	$[\lambda] = \text{cm}$
Wave vector	$[k] = \text{m}^{-1}$	$[k] = \text{cm}^{-1}$
Planck's constant	$[\hbar] = [h/2\pi] = \text{J-s}$	$[\hbar] = [h/2\pi] = \text{erg-s}$
Electric field	$[E] = \text{V/m}$	$[E] = \text{sV/cm}$ $= (\text{erg}/\text{cm}^3)^{1/2}$
Intensity	$[I] = \text{W/m}^2$	$[I] = \text{erg/s-cm}^2$
Fluence	$[F] = \text{J/m}^2$	$[F] = \text{erg/cm}^2$
Power	$[\mathcal{P}] = \text{W}$	$[\mathcal{P}] = \text{erg/s}$
Energy	$[\mathcal{E}] = \text{J}$	$[\mathcal{E}] = \text{erg}$

theoretical developments and sometimes in experimental data. Often the units are mixed, such as when expressing fluence in J/cm^2 . Formulas for converting parameters in cgs units to SI units, and for some mixed units, are given in Table 2.

I. TWO-PHOTON ABSORPTION

Two-photon absorption (TPA) involves a transition from the ground state of a system to a higher-lying state by the simultaneous absorption of two photons from an incident radiation field or fields. This process involves different selection rules than those of single-photon absorption. Hence TPA spectroscopy complements linear absorption spectroscopy in studying the excited states of systems.

Table 2 Conversion Formulas Between the SI and cgs Systems of Units for Several Physical Parameters Utilized in Nonlinear Absorption Processes

σ	(SI) = $10^{-4}\sigma$	(cgs)
σ_2	(SI) = $10^{-8}\sigma_2$	(cgs)
α	(SI) = $10^2\alpha$	(cgs)
β	(SI) = $10^5\beta$	(cgs)
β (cm/W)	= $10^2\beta$	(SI) = $10^7\beta$ (cgs)
γ	(SI) = $10^8\gamma$	(cgs)
γ (cm ³ /W ²)	= $10^6\gamma$	(SI) = $10^{14}\gamma$ (cgs)
$\chi^{(3)}$	= $\frac{4\pi}{3^2} \times 10^{-8}\chi^{(3)}$	(cgs)
$\chi^{(5)}$	= $\frac{4\pi}{3^4} \times 10^{-16}\chi^{(5)}$	(cgs)
L	(SI) = $10^{-2}L$	(cgs)
c	(SI) = $10^{-2}c$	(cgs)
λ	(SI) = $10^{-2}\lambda$	(cgs)
k	(SI) = 10^2k	(cgs)
E	(SI) = 3×10^4E	(cgs)
I	(SI) = $10^{-3}I$	(cgs)
I	(W/cm ²) = $10^{-4}I$	(SI) = $10^{-7}I$ (cgs)
F	(SI) = $10^{-3}F$	(cgs)
F	(J/cm ²) = $10^{-4}F$	(SI) = $10^{-7}F$ (cgs)
\mathcal{P}	(SI) = $10^{-7}\mathcal{P}$	(cgs)
\mathcal{E}	(SI) = $10^{-7}\mathcal{E}$	(cgs)

Two possible situations are illustrated in Fig. 1. In the first, two photons from the same optical field oscillating at frequency ω are absorbed to make the transition, which is approximately resonant at 2ω . In the second situation, two optical fields at frequencies ω_e and ω_p are present, and one photon from each field is absorbed for the transition, which is approximately resonant at $\omega_e + \omega_p$. The first field in this case can be thought of as the pump or excitation beam, with a subscript e, while the second can be thought of as the probe beam, with subscript p. In both cases, the intermediate (or virtual) state is not real (i.e., does not involve a real stationary state of the system). Hence the system must absorb the two photons simultaneously. This makes the process sensitive to the instantaneous optical intensity.

Although the transition does not involve a real intermediate state, often there are impurities present that will produce a small amount of linear absorption. It should be understood that this absorption does not contribute to the transition to the final state of the process but only serves as an additional loss mechanism. Two-step absorption involving a single photon pumped intermediate state is described as excited state absorption, a subject discussed below in Section V.

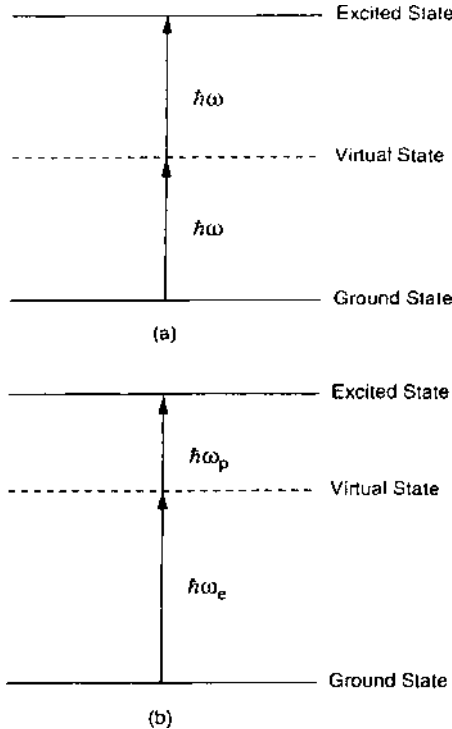


Figure 1 Schematic diagram of two-photon absorption (TPA). (a) Self-TPA. (b) Pump–probe TPA.

A. Single Beam Two-Photon Absorption

The nonlinear absorption in this case is proportional to the square of the instantaneous intensity. The differential equation describing the optical loss is given by

$$\frac{dI}{dz} = -\alpha I - \beta I^2 \quad (1)$$

where α is the linear absorption coefficient due to the presence of impurities and β is the two-photon absorption coefficient.

The TPA coefficient β is a macroscopic parameter characterizing the material. Often, there is interest in the individual molecular TPA property that is described by the TPA cross-section σ_2 . The relation between β and σ_2 is given in Table 3, where N is the number density of molecules in the system, and $\hbar\omega$ is the energy of photons in the incident optical field.

Table 3 Formulas Related to Two-Photon Absorption of a Single Beam

Two-photon absorption coefficient	$\beta = \frac{3\pi}{\epsilon_0 n^2 c \lambda} \text{Im}[\chi_{xxxx}^{(3)}(-\omega; \omega, \omega, -\omega)]$ (SI)
	$\beta = \frac{48\pi^3}{n^2 c \lambda} \text{Im}[\chi_{xxxx}^{(3)}(-\omega; \omega, \omega, -\omega)]$ (cgs)
Two-photon absorption cross-section	$\sigma_2 = \frac{\hbar\omega\beta}{N}$
Energy transmittance CW top-hat beam	$T = \frac{(1-R)^2 \exp(-\alpha L)}{1+q_0} \quad q_0 = \beta(1-R)I_0 L_{\text{eff}} \quad L_{\text{eff}} = \frac{1-\exp(-\alpha L)}{\alpha}$
CW Gaussian beam	$T = \frac{(1-R)^2 \exp(-\alpha L)}{q_0} \ln(1+q_0)$
Pulsed Gaussian beam General	$T = \frac{(1-R)^2 \exp(-\alpha L)}{\sqrt{\pi}q_0} \int_{-\infty}^{\infty} \ln[1+q_0 \exp(-x^2)] dx \quad (\text{Gaus})$
	$T = \frac{(1-R)^2 \exp(-\alpha L)}{2q_0} \int_{-\infty}^{\infty} \ln[1+q_0 \operatorname{sech}^2(x)] dx \quad (\operatorname{sech}^2)$
$q_0 < 1$	$T = (1-R)^2 e^{-\alpha L} \sum_{m=0}^{\infty} (-1)^m \frac{q_0^m}{(m+1)^{3/2}} \quad (\text{Gaus})$
	$T = (1-R)^2 e^{-\alpha L} \sum_{m=0}^{\infty} (-1)^m \frac{q_0^m}{m+1} \prod_{n=0}^m \left[\frac{2(m-n)+\delta_{mn}}{2(m-n)+1} \right] \quad (\operatorname{sech}^2)$
	$\delta_{mn} = \begin{cases} 1 & m=n \\ 0 & m \neq n \end{cases}$

The TPA coefficient is also related to the third order susceptibility. This relationship is also given in Table 3, in both SI and cgs units. Note that it is the imaginary part of $\chi^{(3)}$ that determines the strength of the nonlinear absorption. Hence the susceptibility is complex, meaning that one of the resonant frequency denominators is near zero and hence the imaginary part of the transition frequency ($i\gamma_{\text{ge}}$, where γ_{ge} is the line width of the transition) is not negligible, as is assumed in purely reactive phenomena (see, e.g., the nonlinear refractive index, Chapter 6). This frequency denominator corresponds to the energy transition of the system, which is resonant near $2\hbar\omega$. Also, it is assumed that the incident light is linearly polarized and the medium is centrosymmetric so that only the $xxxx$ component of the susceptibility is relevant.

The principal quantity of interest in a measurement is the net transmittance of the material to light at frequency ω . Expressions for this quantity are given in Table 3 in various levels of approximation. The physical quantity usually measured is the optical energy. Thus the transmittance T is defined as the ratio of the transmitted and incident energies. The parameter R is the Fresnel reflection at the interface of the material with air, while in all cases I_0 corresponds to the peak on-axis intensity incident on the material from air.

The three cases presented in the table correspond to (1) a cw beam with a top-hat beam profile, (2) a cw beam with a Gaussian beam spatial profile, and (3) a pulsed Gaussian beam. For the cw beam, the transmitted and incident beam energies are determined by the instantaneous peak intensity, the beam areas, and an integration time associated with the detector. For the pulsed beam, the integration time is assumed to be long with respect to the pulse width t_{FWHM} (full-width at half-maximum). Hence the limits of integration extend to $\pm\infty$.

In the pulsed beam case, explicit expressions are given for two mathematical forms often encountered for the optical pulse: a Gaussian shaped pulse and a hyperbolic secant squared shaped pulse. In each case, the pulse is centered at time $t = 0$, and the time is scaled by a parameter τ . This parameter is the $1/e$ pulse half-width for a Gaussian pulse, and approximately the same for a hyperbolic secant squared pulse. The parameter usually measured and reported, however, is the full width at half maximum. The relation between τ and t_{FWHM} for both of these types of pulses is given by

$$\begin{aligned}\tau &= \frac{t_{\text{FWHM}}}{2\sqrt{\ln 2}} \quad \text{Gaus} \\ \tau &= \frac{t_{\text{FWHM}}}{2 \ln(1 + \sqrt{2})} \quad \text{sech}^2\end{aligned}\tag{2}$$

For the pulsed Gaussian beam case, the transmittance is left in terms of an integral over all time. This integral must in general be evaluated numerically. However, when the parameter $q_0 < 1$, where $q_0 = \beta(1 - R)I_0L$, the logarithm function can be expanded in a Taylor series and the result integrated term by term. The results for Gaussian and hyperbolic secant squared pulses are shown in Table 3. Usually, only a few terms of the infinite sums need to be retained for an accurate result. This form of the transmittance is often useful when fitting the theory to experimental data. A comparison of the transmittance for each of these cases is shown in Fig. 2.

B. Two-Beam Two-Photon Absorption

This process, depicted in Fig. 1(b), involves the simultaneous absorption of two photons of different frequencies. These are designated as the pump or excitation frequency ω_e and the probe frequency ω_p . The intensity in each of these beams can be comparable, but more often $I_p \ll I_e$.

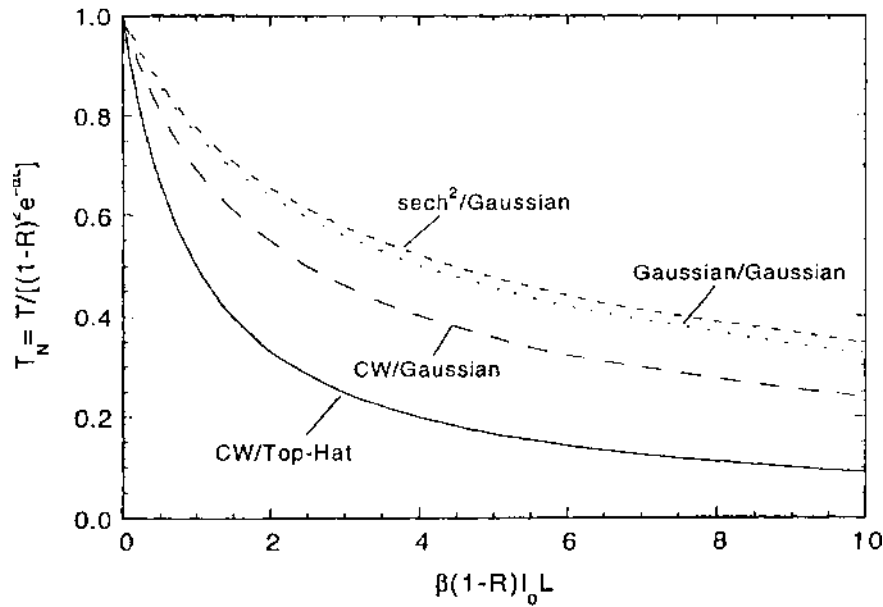


Figure 2 Energy transmittance as a function of incident peak intensity for various beam and pulse shapes.

The TPA coefficients involved in this process are again related to the third order susceptibility. The symmetry relation shown in Table 4 means that a single TPA coefficient relates the absorption of photons from both beams. The fact that the excitation and probe fields can have orthogonal polarization implies that this nonlinear process can lead to an induced dichroism in the material.

The differential equations describing the attenuation of the beams are

$$\begin{aligned} \frac{dI_e}{dz} &= -\alpha_e I_e - 2\left(\frac{\omega_e}{\omega_p}\right)^{1/2} \beta_{ep} I_e I_p - \beta_{ee} I_e^2 \\ \frac{dI_p}{dz} &= -\alpha_p I_p - 2\left(\frac{\omega_p}{\omega_e}\right)^{1/2} \beta_{pe} I_p I_e - \beta_{pp} I_p^2 \end{aligned} \quad (3)$$

The first and last terms in these equations describe the linear and self-induced two-photon absorption, respectively, while the middle terms are what give rise to induced dichroism. In what follows, linear absorption will be ignored.

Two situations are considered. First, the excitation photon energy is less than half the energy of the first two-photon allowed transition. Thus the term

Table 4 Formulas Related to Two-Beam Two-Photon Absorption

Two-photon absorption coefficient	$\beta_{ep} = \frac{3\pi}{\epsilon_0 n_e n_p c \sqrt{\lambda_e \lambda_p}} \text{Im}(\chi_{ep}^{(3)}) \quad (\text{SI})$
	$\beta_{ep} = \frac{48\pi^3}{n_e n_p c \sqrt{\lambda_e \lambda_p}} \text{Im}(\chi_{ep}^{(3)}) \quad (\text{cgs})$
	$\chi_{ep}^{(3)} = \chi_{iijj}^{(3)}(-\omega_e; \omega_e, \omega_p, -\omega_p) = \chi_{jjii}^{(3)}(-\omega_p; \omega_p, \omega_e, -\omega_e)$
	$i = \text{pump polarization direction}$
	$j = \text{probe polarization direction}$
Transmitted intensity	
Pump	$I_e(L) = (1 - R_e)^2 \left[\frac{(I_{e0}/\omega_e) - (I_{p0}/\omega_p)}{(I_{e0}/\omega_e) - (I_{p0}/\omega_p) \exp(-\mu L)} \right] I_{e0}$
	$\mu = 2\sqrt{\omega_e \omega_p} \beta_{ep} (1 - R_e) \left[\frac{I_{e0}}{\omega_e} - \frac{I_{p0}}{\omega_p} \right]$
Probe	$I_p(L) = (1 - R_p)^2 \left[\frac{(I_{e0}/\omega_e) - (I_{p0}/\omega_p)}{(I_{e0}/\omega_e) \exp(+\mu L) - (I_{p0}/\omega_p)} \right] I_{p0}$
Probe ($I_{e0} \gg I_{p0}$)	$I_p(L) \approx I_{p0} \exp(-\mu L)$
Probe energy transmittance	$\mu \approx 2\sqrt{\frac{\lambda_e}{\lambda_p}} \beta_{ep} (1 - R_e) I_{e0}$
Negligible pump self-TPA	$T = (1 - R_p)^2 \exp(-\Gamma_0)$
CW top-hat beam	$\Gamma_0 \approx 2\sqrt{\frac{\lambda_e}{\lambda_p}} \beta_{ep} (1 - R_e) I_{e0} L$
CW Gaussian beam	$T = (1 - R_p)^2 \sum_{m=0}^{\infty} \frac{(-\Gamma_0)^m \eta}{(m + \eta)m!}$
	$\eta = \left(\frac{w_e}{w_p} \right)^2$
Pulsed Gaussian beam	$T = (1 - R_p)^2 \sum_{m=0}^{\infty} \frac{(-\Gamma_0)^m \eta}{(m + \eta)m! \sqrt{m + 1}} \quad (\text{Gaus})$
	$T = (1 - R_p)^2 \sum_{m=0}^{\infty} \frac{(-\Gamma_0)^m \eta}{(m + \eta)m!} \prod_{n=0}^m \left[\frac{2(m - n) + \delta_{mn}}{2(m - n) + 1} \right] \quad (\text{sech}^2)$
Pulsed pump, cw probe ($\Delta t = \text{detector integration time}$)	$T = (1 - R_p)^2 \left\{ 1 + 1.06 \frac{t_{\text{FWHM}}}{\Delta t} \sum_{m=1}^{\infty} \frac{(-\Gamma_0)^m \eta}{(m + \eta)m! \sqrt{m}} \right\} \quad (\text{Gaus})$
	$T = (1 - R_p)^2 \left\{ 1 + 1.13 \frac{t_{\text{FWHM}}}{\Delta t} \sum_{m=1}^{\infty} \frac{(-\Gamma_0)^m \eta}{(m + \eta)m!} \right. \times \prod_{n=1}^m \left[\frac{2(m - n) + \delta_{mn}}{2(m - n) + 1} \right] \left. \right\} \quad (\text{sech}^2)$
Dominant pump self-TPA	
CW top-hat beam	$T = (1 - R_p)^2 \left(\frac{1}{1 + q_{e0}} \right)^r$

(continued)

Table 4 Continued

	$q_{e0} = \beta_{ee}(1 - R_e)I_{e0}L, \quad r = 2\sqrt{\frac{\lambda_e}{\lambda_p}}\frac{\beta_{ep}}{\beta_{ee}}$
CW Gaussian beam (general)	$T = (1 - R_p)\eta \int_0^1 \left(\frac{1}{1 + q_{e0}y}\right)^r y^{\eta-1} dy$
CW Gaussian beam ($q_{e0} < .8, \eta \sim 1$)	$T = (1 - R_p)^2 \sum_{m=0}^{\infty} \frac{(-q_{e0})^m \eta}{(m + \eta)m!(r - 1)} \prod_{m'=0}^m (r + m' - 1)$
Pulsed Gaussian beam (general)	$T = (1 - R_p)^2 \frac{\eta}{\sqrt{\pi}} \int_{-\infty}^{\infty} \int_0^1 \left(\frac{1}{1 + q_{e0}y \exp(-x^2)}\right)^r y^{\eta-1} dy dx \quad (\text{Gaus})$
Pulsed Gaussian beam ($q_{e0} < .8, \eta \sim 1$)	$T = (1 - R_p)^2 \frac{\eta}{2} \int_{-\infty}^{\infty} \int_0^1 \left(\frac{1}{1 + q_{e0}y \operatorname{sech}^2(x)}\right)^r y^{\eta-1} dy dx \quad (\operatorname{sech}^2)$
Pulsed pump, cw probe ($\Delta t = \text{detector}$ integration time) ($q_{e0} < .8, \eta \sim 1$)	$T = (1 - R_p)^2 \sum_{m=0}^{\infty} \frac{(-q_{e0})^m \eta}{(m + \eta)m!\sqrt{m+1}(r - 1)} \prod_{m'=0}^m (r + m' - 1) \quad (\text{Gaus})$ $T = (1 - R_p)^2 \sum_{m=0}^{\infty} \frac{(-q_{e0})^m \eta}{(m + \eta)m!(r - 1)} \prod_{m'=0}^m (r + m' - 1)$ $\times \prod_{n=0}^m \left[\frac{2(m-n)+\delta_{mn}}{2(m-n)+1} \right] \quad (\operatorname{sech}^2)$ $T = (1 - R_p)^2 \left\{ 1 + 1.06 \frac{t_{\text{FWHM}}}{\Delta t} \sum_{m=1}^{\infty} \frac{(-q_{e0})^m \eta}{(m + \eta)m!\sqrt{m+1}(r - 1)} \right\} \times \prod_{m'=1}^m (r + m' - 1) = (\text{Gaus})$ $T = (1 - R_p)^2 \left\{ 1 + 1.13 \frac{t_{\text{FWHM}}}{\Delta t} \sum_{m=1}^{\infty} \frac{(-q_{e0})^m \eta}{(m + \eta)m!(r - 1)} \right\} \times \prod_{m'=1}^m (r + m' - 1) \prod_{n=1}^m \left[\frac{2(m-n)+\delta_{mn}}{2(m-n)+1} \right] \right\} = (\operatorname{sech}^2)$

involving β_{ee} can be ignored. Also, the self-induced absorption term involving β_{pp} is ignored since the probe is assumed to be weak relative to the excitation beam. In the second situation, self-induced TPA by the excitation beam is allowed, and the induced dichroism by the probe on the pump is assumed to be negligible. This implies that the excitation beam can pump allowed two-photon states both by itself (at $2\omega_e$) and in conjunction with the probe (at $\omega_e + \omega_p$). This is possible when there is a large density of two-photon allowed states, such as occurs in the conduction band of semiconductors and in the excited state spectrum of polyatomic molecules.

Equations for the transmittance of the probe beam in each of these situations are given in Table 4, for the cases of cw top-hat beams, cw Gaussian beams, and pulsed Gaussian beams. Formulas are appropriately corrected for

Fresnel reflections at the material–air interfaces for both the probe (R_p) and the excitation source (R_e). Usually, the beams are pulsed to increase the incident power to observe this nonlinear process. But both beams need not be pulsed, since to observe the induced dichroism only the excitation intensity needs to be high. The special case of a cw probe is thus included in Table 4, with Δt being the integration time of the energy detector for the probe.

For the case of negligible self-TPA by the excitation beam, the probe experiences exponential loss, with the exponential loss factor Γ_0 given in Table 4. When the two beams have finite width (e.g., Gaussian profiles), then the process of attenuation of the probe will be more or less efficient depending on the degree of beam overlap. This is illustrated by the plots in Fig. 3, which shows the transmittance for Gaussian beams with Gaussian shaped pulses, where the parameter η is the ratio of beam areas (excitation-to-probe). It is assumed in this plot that the pulse widths are equal. For the special case where the excitation beam is large compared to the probe ($\eta \gg 1$), the probe transmittance sees a simple exponential loss with a peak excitation intensity dependent exponent [$T \rightarrow (1 - R_p)^2 \exp(-\Gamma_0)$], i.e., as if the excitation beam has a top-hat profile.

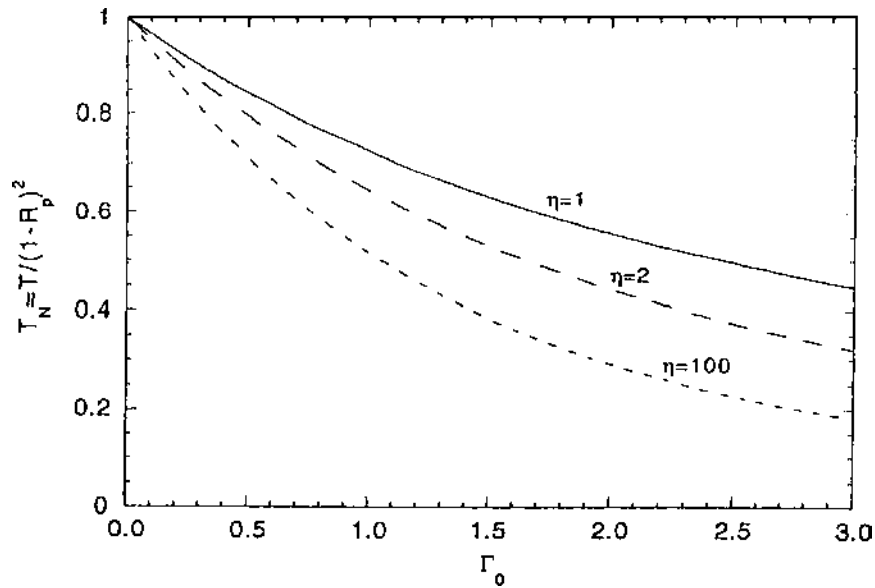


Figure 3 Probe energy transmittance as a function of pump peak intensity when pump self-TPA is negligible. The beams are assumed to have a Gaussian spatial profile and a Gaussian pulse shape, with the same pulse width.

When the beams are of equal size ($\eta = 1$), the probe transmittance goes as $(1 - R_p)^2[1 - \exp(-\Gamma_0)]/\Gamma_0$.

When self-TPA dominates the loss terms for the excitation beam, the probe sees an intensity dependent loss reminiscent of the self-TPA loss given by the transmittance equations in Table 3. This case is also given in Table 4. Note that the transmittance depends on the parameter $r = 2(\lambda_e/\lambda_p)^{1/2}\beta_{ep}/\beta_{ee}$. When the beam sizes are equal and $r \rightarrow 1$, the probe sees just the single beam transmittance due to excitation beam self-TPA. The general expressions for unequal beam sizes are given in Table 4. The behavior of the probe normalized transmittance as a function of $q_{e0} = \beta_{ee}(1 - R_e)I_{e0}L$ for a Gaussian beam and Gaussian pulse shape for various beam area ratios η is shown in Fig. 4.

II. THREE-PHOTON ABSORPTION

The phenomenon of resonant three-photon absorption (3PA) is illustrated in Fig. 5. Three cases are shown involving one, two, and three fields. Only the single field case is treated here.

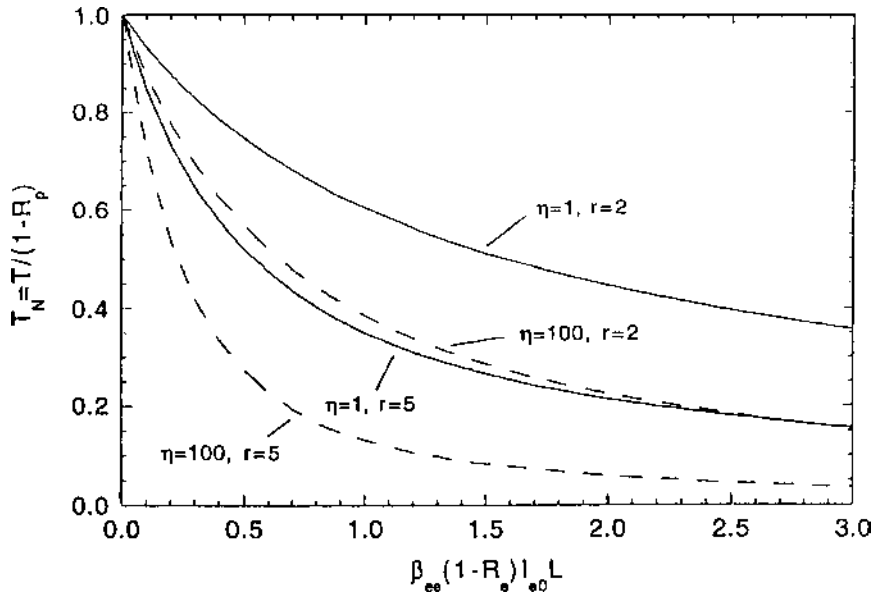


Figure 4 Probe energy transmittance as a function of pump peak intensity including the effects of pump self-TPA. The beams are assumed to have a Gaussian spatial profile and a Gaussian pulse shape, with the same pulse width.

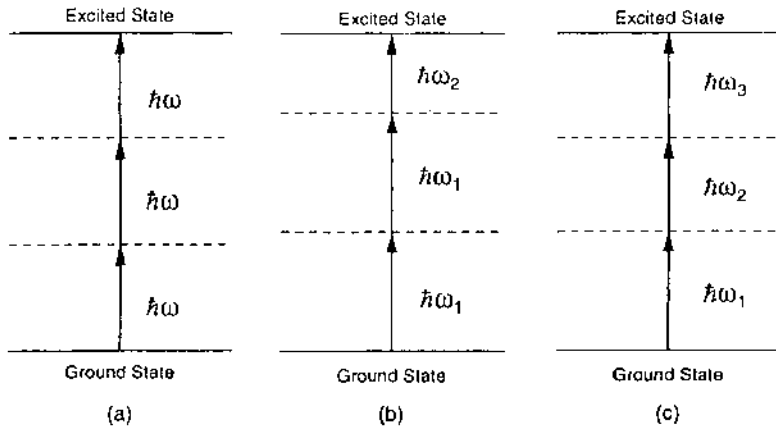


Figure 5 Schematic diagram of three-photon absorption (3PA). (a) Single beam self-3PA; (b) two-beam 3PA; and (c) three-beam 3PA.

Assuming that impurities introduce some background linear absorption, the equation describing the attenuation of a beam experiencing 3PA is given by

$$\frac{dI}{dz} = -\alpha I - \gamma I^3 \quad (4)$$

where γ is the 3PA coefficient. Three-photon absorption is a fifth order nonlinear process, and γ is related to the fifth order susceptibility as shown in Table 5. Again, the beam is assumed to be linearly polarized, and the medium is centrosymmetric.

Equation (4) is readily solved, and expressions for the transmittance of a cw top-hat beam, a cw Gaussian beam, and a pulsed Gaussian beam are given in Table 5. The key parameter here is $p_0 = [2\gamma(1-R)^2 I_0^2 L'_{\text{eff}}]^{1/2}$, where in this case $L'_{\text{eff}} = [1 - \exp(-2\alpha L)]/2\alpha$, which reduces to L when $\alpha L \ll 1$. When $p_0 < 1$, the expressions for the pulse transmittance can be expanded in infinite series. These expressions, which may be useful for fitting the theory to data, are also given in Table 5. A comparison of the normalized transmittance as function of p_0 for the various types of beams is given in Fig. 6.

III. MULTIPHOTON ABSORPTION

The results of the previous two sections can be extended to an arbitrary number of absorbed photons. Multiphoton absorption refers to the simultaneous absorption of n photons from a single beam or multiple beams.

Table 5 Formulas Related to Three-Photon Absorption of a Single Beam

Three-photon absorption coefficient	$\gamma = \frac{5\pi}{\epsilon_0^2 n^3 c^2 \lambda} \text{Im}[\chi_{xxxxx}^{(5)}(-\omega; \omega, \omega, \omega, -\omega, -\omega)] = (\text{SI})$
Energy transmittance	$T = \frac{(1-R)^2 \exp(-\alpha L)}{\sqrt{1+p_0^2}} \quad p_0 = \sqrt{2\gamma(1-R)^2 I_0^2 L_{\text{eff}}}$
CW top-hat beam	$L'_{\text{eff}} = \frac{1 - \exp(-2\alpha L)}{2\alpha}$
CW Gaussian beam	$T = \frac{(1-R)^2 \exp(-\alpha L)}{\sqrt{\pi} p_0} \ln(\sqrt{1+p_0^2} + p_0)$
Pulsed Gaussian beam	$T = \frac{(1-R)^2 \exp(-\alpha L)}{\sqrt{\pi} p_0} \int_{-\infty}^{\infty} \ln \left[\sqrt{1+p_0^2 \exp(-2x^2)} + p_0 \exp(-x^2) \right] dx \quad (\text{Gaus})$
General	$T = \frac{(1-R)^2 \exp(-\alpha L)}{2p_0} \int_{-\infty}^{\infty} \ln \left[\sqrt{1+p_0^2 \operatorname{sech}^4(x)} + p_0 \operatorname{sech}^2(x) \right] dx \quad (\operatorname{sech}^2)$
$p_0 < 1$	$T = (1-R)^2 e^{-\alpha L} \sum_{m=1}^{\infty} (-1)^{m-1} \frac{p_0^{2m-2}}{(2m-1)! \sqrt{2m-1}} \quad (\text{Gaus})$
	$T = (1-R)^2 e^{-\alpha L} \sum_{m=1}^{\infty} (-1)^{m-1} \frac{p_0^{m-2}}{(2m-1)} \times \prod_{n=1}^m \left[\frac{4(m-n) + \delta_{mn}}{4(m-n) + 1} \right] \prod_{n'=1}^m \left[\frac{4(m-n' - \frac{1}{2}) + \delta_{mn'}}{4(m-n' - \frac{1}{2}) + 1} \right] \quad (\operatorname{sech}^2)$

The analog to Eqs. (1) and (4) for the absorption of $n+1$ photons from a single optical beam is

$$\frac{dI}{dz} = -(\alpha + \gamma^{(n+1)} I^n) I \quad (5)$$

where $\gamma^{(n+1)}$ is the $(n+1)$ -photon absorption coefficient and has units of $\text{m}^{2n-1}/\text{W}^n$. The intensity transmitted through a material of length L and surface reflectance R is thus given by

$$I(L) = \frac{(1-R)^2 I_0 \exp(-\alpha L)}{[1+p_0^n]^{1/n}} \quad (6)$$

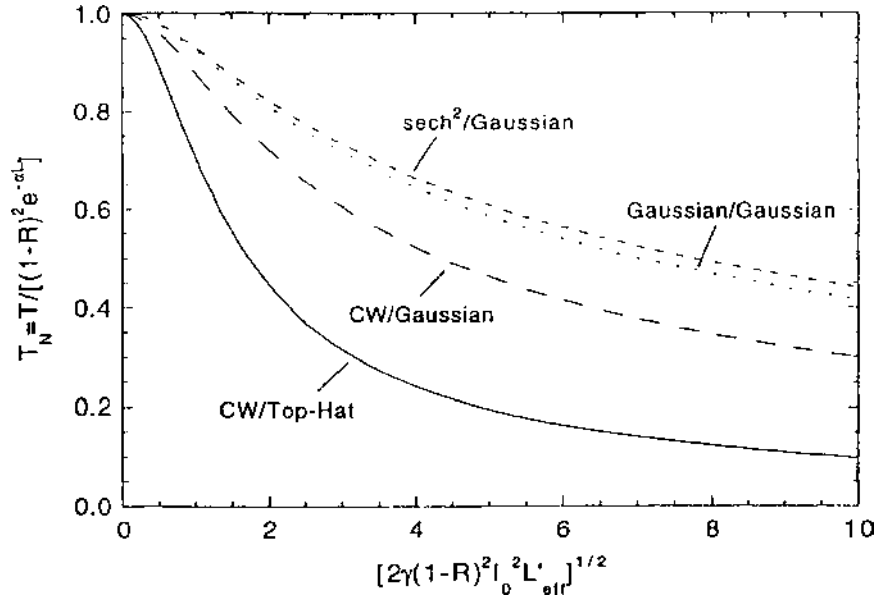


Figure 6 Single beam energy transmittance as a function of incident peak intensity for various beam and pulse shapes.

with

$$p_0^n = n\gamma^{(n+1)} \left(\frac{1 - \exp(-n\alpha L)}{n\alpha} \right) (1 - R)^n I_0^n \quad (7)$$

Nonresonant multiphoton absorption is usually very weak for $n \geq 3$. It can, however, be significant in semiconductors, especially narrow band gap materials.

Shen [2] gives the transition probability rate per molecule for a nonresonant n -photon transition as

$$W^{(n)} = \frac{\sigma^{(n)} I_1(\omega_1) I_2(\omega_2) \cdots I_n(\omega_n)}{\hbar^n \omega_1 \omega_2 \cdots \omega_n} \quad (8)$$

where $\sigma^{(n)}$ (assumed a scalar quantity) is the n -photon absorption cross-section. For nonresonant transitions, $|\sigma^{(n+1)} / \sigma^{(n)}| \sim 10^{-34}$ [2]. Therefore $\sigma^{(n+1)} I / \hbar \omega \sim 10^{-6} \sigma^{(n)}$ for $I \sim 1 \text{ GW/cm}^2$. Thus very high intensities are required to excite multiphoton absorption. This is usually accompanied by avalanche ionization and breakdown in condensed matter.

The n th order absorption cross-section can be enhanced by many orders of magnitude by the presence of intermediate resonances. However, resonances

imply finite lifetimes of intermediate states. Thus a population rate equation approach must be employed to compute intermediate populations, including all decay rates (see Section V below). The process thus becomes fluence-driven rather than intensity-driven. If there are m intermediate resonances, then the process is called an $(m + 1)$ -step n -photon transition.

Intermediate resonances are the key to multiphoton dissociation of polyatomic molecules. Multiphoton dissociation has been observed with tens of photons of IR radiation [2]. This corresponds in some cases to only a few J/cm^2 ($\sim 10 \text{ MW}/\text{cm}^2$). This was not understood at first, because absorption of so many photons would ordinarily require much higher intensities unless there are many intermediate resonances. However, in molecular systems the anharmonic shift of vibrational levels with energy would lead to a nonresonance condition after the absorption of a few photons. Now this multiphoton excitation is understood as a sequence of the following mechanisms [2].

Vibration–rotation transitions follow the selection rules $\Delta\nu = \pm 1$ and $\Delta J = 0, \pm 1$, where ν is the vibration quantum number and J is the total angular momentum quantum number. A photon resonant with the first vibrational transition is not resonant with the second transition because of the anharmonic energy shift. However, associated with each vibrational level is a large number of closely spaced rotational energy levels. Thus a near-resonance transition is possible through the following mechanisms:

- Addition or removal of rotational energy through $|\Delta J| = 1$,
- Anharmonic coupling between degenerate vibrational modes inducing energy level splittings partially compensating for the anharmonic shift,
- Forbidden transitions, though weak, that can participate at high intensity levels, and
- Power broadening of levels (see Section IV), which further reduces the energy mismatch.

Thus it is possible to excite through intermediate resonances vibrational levels selectively from $\nu = 0$ to $\nu = 3–6$ in polyatomic molecules.

Another aspect of polyatomic molecules is that the density of states increases rapidly with energy due to the large number of vibrational and rotational modes, forming a quasi-continuum of states after a few vibrational transitions. With $3n - 6$ vibrational modes for $n \geq 3$, energy levels in polyatomic molecules are already forming a quasi-continuum by $\nu = 3–6$. Thus, by the mechanisms described above, stepwise near-resonant absorption is possible in polyatomic molecules up to the quasi-continuum.

For example, in SF_6 [2], the density of states is $g(E) \sim 100 \text{ states}/\text{cm}^{-1}$ at $E = 4000 \text{ cm}^{-1}$ (above the ground state), and $g(E) \sim 1000 \text{ states}/\text{cm}^{-1}$ at $E = 5000 \text{ cm}^{-1}$. This corresponds to $\sim 4–5$ photons at $10.6 \mu\text{m}$.

Multiphoton absorption in the quasi-continuum is essentially stepwise resonant because of the large density of states. Multiphoton transitions through the quasi-continuum to the true continuum lead to molecular dissociation. The excess energy absorbed is carried away by the molecular fragments as internal and kinetic energy. More details can be found in Shen (Chapter 23) [2] and the references cited therein.

IV. NONLINEAR ABSORPTION IN TWO-LEVEL SYSTEMS

The nonlinear refractive index of a simple two-level system, illustrated in Fig. 7, was discussed in Chapter 6, Section II.E. There it was shown that the intensity dependence of the refractive index was due to a redistribution of the population of the two energy levels in a collection of two-level systems. The population redistribution will also produce a reduction in the absorption of a high-intensity beam of light.

As photons from the incident light pump electrons into the upper energy level, the ground state becomes depleted. Population of the upper state also leads to spontaneous and stimulated emission of photons. The net result is that the system cannot absorb as large a fraction of the incident light as it can under low-intensity conditions. This process is called saturable absorption [2–5].

Two cases of saturable absorption in two-level systems are considered. The first is called a homogeneously broadened system. The term broadening refers to

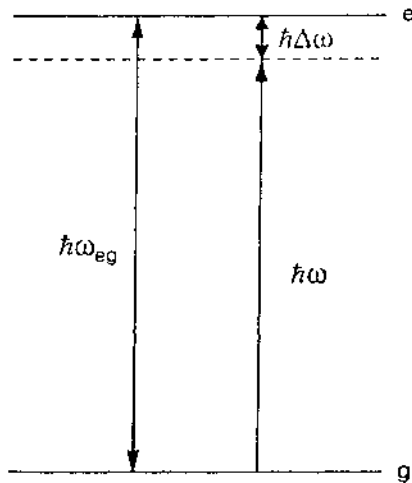


Figure 7 Schematic diagram of a two-level system.

the width (usually measured in frequency units, Hz or cm^{-1}) of the absorption spectrum. In a homogeneously broadened system, all of the atoms or molecules comprising the system have the same resonant frequency, corresponding to the energy difference of the two levels. The width of the absorption line is determined by microscopic damping factors in the low-intensity regime. The damping factor or relaxation rate is written as $(T_2)^{-1}$, where T_2 is the phase coherence lifetime of the state of the system consisting of a superposition of the ground and excited states formed by interaction with the incident light. This lifetime is usually limited by collisions with other particles or phonons, or ultimately by the quantum uncertainty principle in the absence of collisions. The width of a two-level system under these conditions is called its natural line width. Under high-intensity radiation, the width of a homogeneously broadened absorption line will be broadened by the incident intensity. This is called power broadening.

In an inhomogeneously broadened system, some internal property of the system causes atoms or molecules of the system to have different resonant frequencies. For example, in a gas there will be a distribution of molecular velocities resulting in one group of molecules seeing a different incident frequency from another group moving at a different velocity due to the Doppler shift. This type of broadening is called Doppler broadening. In a solid material, an inhomogeneous strain distribution can also produce inhomogeneous broadening. The width of an inhomogeneously broadened line is usually much greater than the natural line width of the system. These systems thus do not display power broadening at high intensity levels.

Steady-state absorption in these two types of system is described first. This will be followed by a brief discussion of time dependent absorption and transient effects.

A. Homogeneous Broadening

In the high-intensity regime, electrons are pumped from the ground state into the excited state of the system. The difference in population between the ground and excited states is thus reduced from its equilibrium value. This causes a reduction in the absorption coefficient.

An expression for the intensity dependent absorption in the steady state is given in Table 6. In this formula, α_{00} is the absorption coefficient of the system at exact resonance in the low intensity regime ($I \ll I_s^0$), and I_s^0 is the saturation intensity of the system. I_s^0 is given in terms of the transition dipole moment μ_{eg} of the system and of the product of lifetimes T_1 and T_2 , where T_1 is the lifetime of the population in the upper state (see Chapter 6, Section II.E). Also, $\omega \asymp \omega_{eg} = \omega_e - \omega_g$, and $\Delta\omega = \omega - \omega_{eg}$.

Table 6 Formulas Related to Saturable Absorption in Two-Level Systems

Absorption coefficient	
Homogeneous broadening	$\alpha(I) = \frac{\alpha_{00}}{1 + (\Delta\omega T_2)^2 + I/I_s^0} = \frac{\alpha_0}{1 + I/I_s^\Delta}$ $\alpha_0 = \frac{\alpha_{00}}{1 + (\Delta\omega T_2)^2}$ $I_s^\Delta = I_s^0[1 + (\Delta\omega T_2)^2]$
Inhomogeneous broadening	$\alpha(I) = \frac{\alpha_0}{\sqrt{1 + I/I_s^0}}$ $\frac{T}{T_0} = \exp[(I_0/I_s^\Delta)(1 - T)]$ $\frac{\sqrt{1 + T_0/I_s^0} - 1}{\sqrt{1 + T_0/I_s^0} + 1} = T_0 \left[\frac{\sqrt{1 + I_0/I_s^0} - 1}{\sqrt{1 + I_0/I_s^0} + 1} \right] \exp \left[2 \left(\sqrt{1 + \frac{I_0}{I_s^0}} - \sqrt{1 + \frac{T_0}{I_s^0}} \right) \right]$
Intensity transmittance (steady state)	
Homogeneous broadening	
Inhomogeneous broadening	
Pump/probe absorption coefficient	$\alpha(\omega', I_\omega) = \alpha_0(\omega') \left[\frac{1 + (\Delta\omega T_2)^2}{1 + (\Delta\omega T_2)^2 + I_\omega/I_s^0} \right]$ ω = pump frequency ω' = probe frequency
Homogeneous broadening (weak probe)	
Inhomogeneous broadening	
Weak probe (hole burning)	$\alpha(\omega', I_\omega) = \alpha_0(\omega') \left[\frac{(\omega - \omega')^2 + (1/T_2)^2}{(\omega - \omega')^2 + (1/T_2)^2(1 + I_\omega/I_s^0)} \right]$
Equal counterpropagating beams (Lamp dip, $I/I_s^0 \ll 1$)	$\alpha(\omega, I) = \alpha_0(\omega) \left[\frac{1}{2} \frac{I}{I_s^0} \frac{1}{1 + (\Delta\omega T_2)^2} \right]$
Short pulse transmitted intensity ($T_2 \ll t_{FWHM} \ll T_1$)	$I(L, t) = \frac{I_0(t - L/c)}{1 + (T_0^{-1} - 1) \exp \left[-\frac{1}{F_s} \int_{-\infty}^{t-L/c} I_0(t') dt' \right]}$

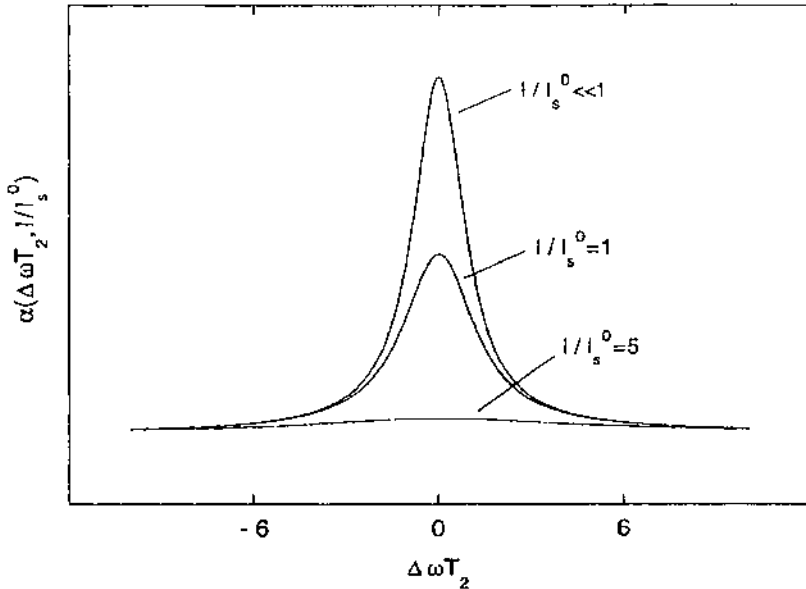


Figure 8 Intensity dependent absorption coefficient for a homogeneously broadened line for various intensities relative to the saturation intensity.

Figure 8 illustrates the effect of intensity on the absorption line of a homogeneously broadened two-level system. Note that the saturation intensity is defined as the value of the incident intensity that causes a reduction of the peak absorption coefficient by a factor of 2.

The normalized line shape function $g(\nu)$ for a homogeneously broadened system in the low-intensity regime is given by

$$g(\nu) = \frac{(1/2\pi^2 T_2)}{(\nu - \nu_{eg})^2 + (1/2\pi T_2)^2} \quad (9)$$

with

$$\int_{-\infty}^{\infty} g(\nu) d\nu = 1 \quad (10)$$

The line width $\Delta\nu$ (FWHM) is then $(\pi T_2)^{-1}$. From the expression for the absorption coefficient in Table 6, it can be seen that in the high-intensity regime the line width is increased by a factor of $(1 + I/I_s^0)^{1/2}$. This phenomenon is called power broadening.

When $\Delta\omega \neq 0$, it is convenient to write the intensity dependent absorption coefficient in terms of

$$\alpha_0 = \frac{\alpha_{00}}{1 + (\Delta\omega T_2)^2} \quad (11)$$

the off-resonance linear absorption coefficient, and

$$I_s^\Delta = I_s^0 [1 + (\Delta\omega T_2)^2] \quad (12)$$

the detuned saturation intensity. The resulting expression for $\alpha(I)$ is given in Table 6.

The attenuation of the incident light is now described by

$$\frac{dI}{dz} = -\alpha(I)I = -\frac{\alpha_0}{1 + I/I_s^\Delta} I \quad (13)$$

Solving for the intensity transmitted through a material of thickness L , the intensity transmittance $T = I(L)/I_0$ is given in Table 6, where I_0 is the incident intensity. For a cw top-hat beam, this would also be the energy transmittance. $T_0 = \exp(-\alpha_0 L)$ is the linear transmittance.

The nonlinear transmittance as a function of I_0/I_s^0 is shown in Fig. 9 for various values of T_0 . Both on-resonance and off-resonance cases are illustrated.

B. Inhomogeneous Broadening

The intensity dependent absorption coefficient for an inhomogeneously broadened transition is given in Table 6. The inhomogeneous absorption line saturates more slowly, with the intensity dependence going as $(1 + I/I_s^0)^{-1/2}$. A small group of atoms or molecules seeing the same incident frequency will saturate as a group as $(1 + I/I_s^\Delta)^{-1}$. But power broadening will cause other groups seeing a slightly different frequency to participate in the absorption. This results in the slower saturation indicated by the square root in the formula for the absorption coefficient. Note that in this case, $\alpha_0(\omega)$ is the linear absorption coefficient of the inhomogeneously broadened line. For example, with Doppler broadening, the shape of $\alpha_0(\omega)$ is Gaussian.

An expression for the intensity transmittance is also given in Table 6. Plots of T as a function of I_0/I_s^0 for various values of T_0 are shown in Fig. 10.

A common situation in nonlinear spectroscopy is to pump a two-level system with a strong beam at frequency ω and then probe the resultant absorption coefficient with a weak beam at ω' . The formula for the homogeneously broadened absorption coefficient seen by the probe is given in Table 6. The shape of the absorption is similar to what the probe would see without the pump present, though reduced due to the population redistribution produced by the pump.

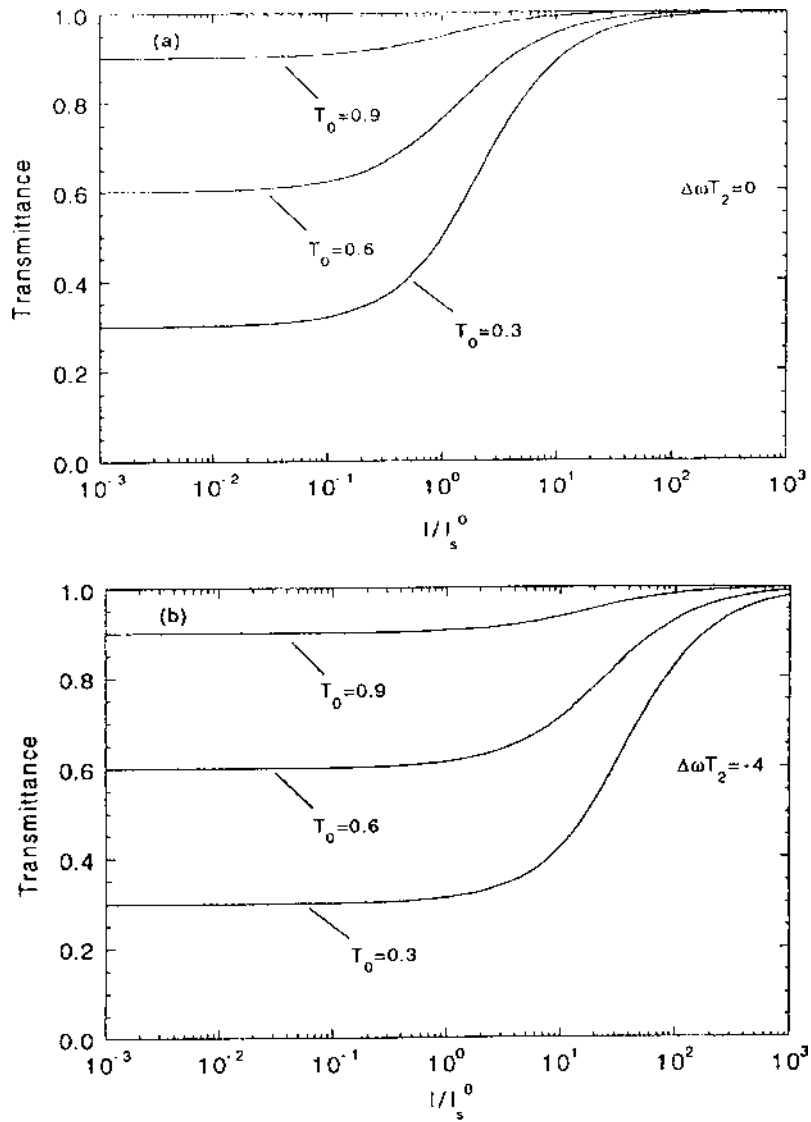


Figure 9 Intensity transmittance as a function of incident intensity in a homogeneously broadened system for on-resonance and off-resonance conditions.

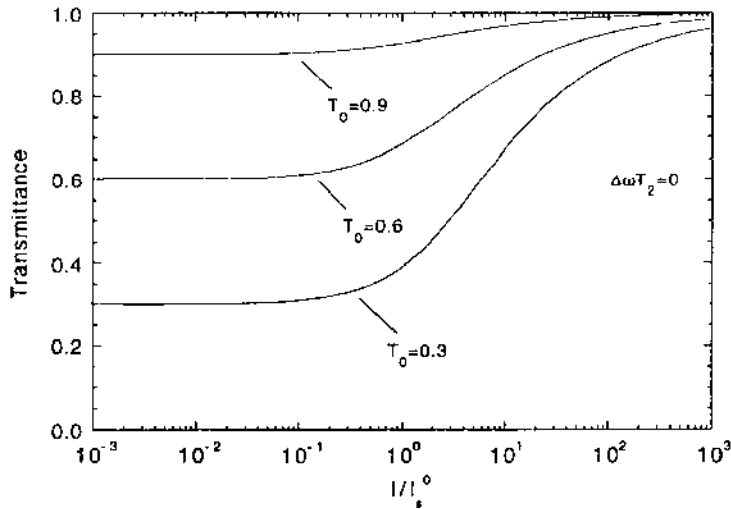


Figure 10 Intensity transmittance as a function of incident intensity in an inhomogeneously broadened system.

In other words, the pump depletes the ground state uniformly in a homogeneously broadened transition so the probe sees fewer electrons to excite into the upper state.

The situation is vastly different for an inhomogeneously broadened line. The absorption coefficient for this case is also given in Table 6. (The coherent interaction of the pump and probe when they have the same frequency has been ignored in this equation [2].) In this case, when $|\omega - \omega'| \gg T_2^{-1}$, the natural line width $\alpha(\omega')$ has approximately the same shape as $\alpha_0(\omega')$, though slightly reduced in magnitude. However, when $\omega' \sim \omega$, $\alpha(\omega')$ is more severely reduced by a factor of $\sim (1 + I_\omega/I_s^0)^{-1}$. As illustrated in Fig. 11, it appears as if the pump beam has burned a hole in the absorption line. This process is called hole burning, and the width of the hole is

$$\Delta\omega_{\text{hole}} = \frac{2}{T_2} \sqrt{1 + \frac{I_\omega}{I_s^0}} \quad (14)$$

When coherence effects between the pump and probe for $\omega' \sim \omega$ are included, the hole burning is less severe. As long as $I_\omega/I_s^0 \leq 1$, the equation in Table 6 gives a very good approximation for the depth of the hole burned into the absorption line. However, for $I_\omega/I_s^0 > 1$, the depth of the hole is smaller than indicated by this formula. See Ref. 2 for more details.

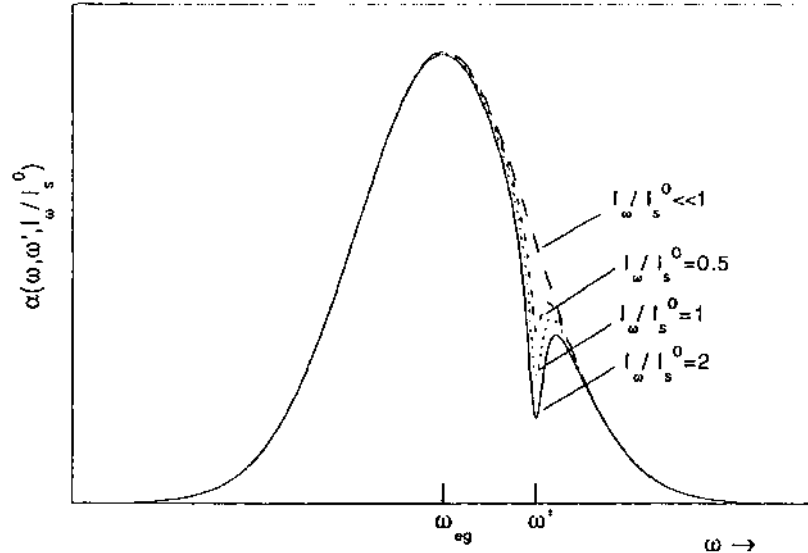


Figure 11 Hole burning in an inhomogeneously broadened absorption line.

Interesting new effects occur when the pump and probe have equal frequency, equal intensity, and travel in opposite directions through a two-level saturable absorber. Shen [2] treats the Doppler broadening case, the most common one, and shows that, in the weak saturation regime ($I_\omega/I_s^0 \ll 1$), the absorption coefficient seen by each beam is given by the expression in Table 6.

When the frequency in each beam is detuned from the resonant transition so that $|\omega - \omega_{eg}| \gg (T_2)^{-1}$, then the absorption coefficient is slightly reduced so that $\alpha(\omega) \sim \alpha_0(\omega)(1 - \frac{1}{2}I/I_s^0)$. However, for $|\omega - \omega_{eg}| \sim (T_2)^{-1}$, an absorption hole appears at line center with a depth of $\frac{1}{2}\alpha_0(\omega)I/I_s^0$ and a width equal to the natural line width $2/T_2$. This is called the Lamb dip.

C. Short Pulse Effects

Nonlinear transmittance. Consider now the case of a short pulse propagating in a two-level medium at exact resonance ($\omega = \omega_{eg}$) [6,7]. The pulse width is such that $T_2 \ll t_{FWHM} \ll T_1$. This implies that the phase coherence of the superposition state (mixed ground and excited states) has decayed away, but the pulse is shorter than the decay time of the upper state population.

The absorption of light in this situation is described by (for plane waves)

$$\frac{\partial I}{\partial z} + \frac{1}{c} \frac{\partial I}{\partial t} = -\sigma \Delta N(z, t) I(z, t) \quad (15)$$

where $\Delta N = N_g - N_e$ is the difference in the population densities of the two levels, and $\sigma = \alpha_0/N$ is the absorption cross-section for the transition, with N being the total density of particles. The second term on the left-hand side of Eq. (15) is comparable to the first and must be included when $ct_{\text{FWHM}} \leq L$, where L is the length of the medium.

In the time regime specified above, the population difference satisfies a simple rate equation:

$$\frac{\partial \Delta N}{\partial t} = -\frac{2\sigma}{\hbar\omega} I(z, t) N(z, t) \quad (16)$$

In general, Eqs. (15) and (16) must be solved simultaneously, with the initial boundary condition $\Delta N(0, -\infty) \simeq N_g \simeq N$. The solution for the intensity at the output of the material is given in Table 6.

The quantity $I_0(t - L/c)$ is the intensity at the input to the medium evaluated at a time retarded by the transit time through the medium. $T_0 = \exp(-\sigma NL)$ is the linear transmittance, and

$$F_s = \frac{\hbar\omega}{2\sigma} \quad (17)$$

is called the saturation fluence. (Note that in the steady state it is the saturation intensity $I_s = \hbar\omega/2\sigma T_1$ that plays the key role. In the pulsed case, with $t_{\text{FWHM}} \ll T_1$, it is not the intensity but the accumulated energy or fluence that is important.) When the accumulated fluence is small compared to F_s , the transmitted intensity goes as $I(L, t) \rightarrow T_0 I_0(t - L/c)$. However, when the accumulated fluence is large compared to the saturation fluence, $I(L, t) \rightarrow I_0(t - L/c)$.

Whereas two-photon absorption flattens and broadens the transmitted pulse, saturable absorption sharpens it. For large fluences, however, the transmitted pulse will approximate the shape of the incident pulse. This is illustrated in Fig. 12.

The population difference as a function of z and t is given by

$$\Delta N(z, t) = \frac{\exp(\alpha_0 z) \Delta N_0}{\exp\left[\frac{1}{F_s} \int_{-\infty}^{t-z/c} I_0(t') dt'\right] + \exp(\alpha_0 z) - 1} \quad (18)$$

When the accumulated fluence is small compared to F_s , the population density is approximately equal to its initial value $\Delta N_0 \simeq N$. For large fluences, $\Delta N(z, t) \rightarrow 0$ everywhere. In other words, the strong beam equalizes the population

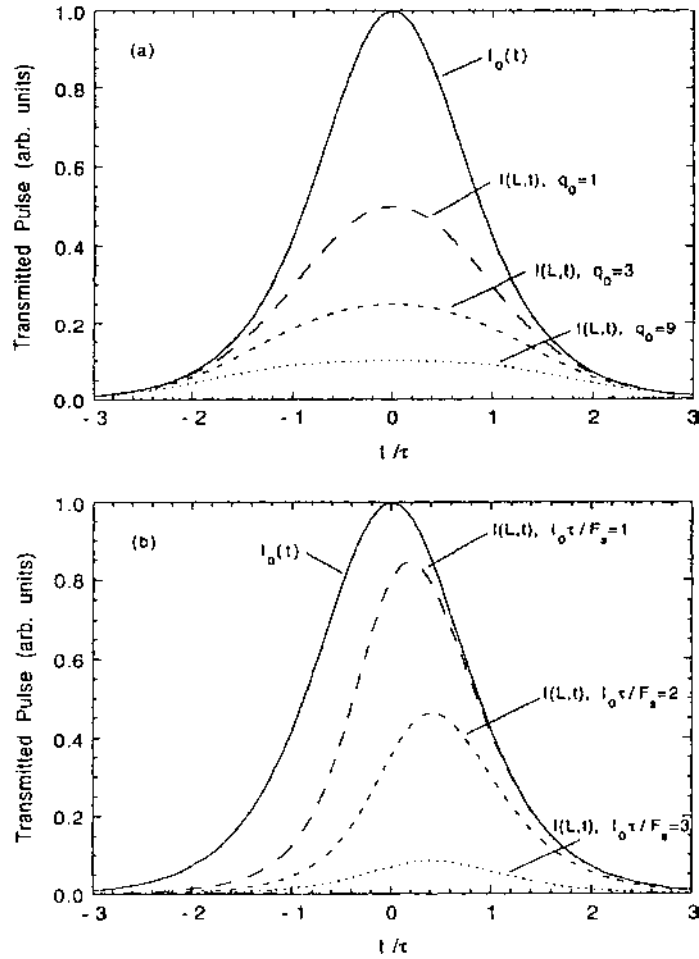


Figure 12 A comparison of transmitted pulse effects in (a) two-photon absorption and (b) saturable absorption.

distribution between the two levels everywhere so that there is no absorption, and the beam bleaches a transparent path through the medium.

Resonance fluorescence. In a two-level medium, the levels are radiatively coupled, so that when the system is excited, its upper state will decay emitting photons. This process is called fluorescence. (The upper state decay time is T_1 , although this is not necessarily the reciprocal of the fluorescence rate. In some

cases, the system can undergo a nonradiative decay, such as by inelastic collisions with other atoms or molecules.)

When an atom is driven strongly at resonance, stimulated emission can balance absorption, and as was noted above it is possible to drive the population difference to zero. When the incident light is detuned from exact resonance, the steady-state population assumes a value reduced from its equilibrium value by the power broadened line shape:

$$\Delta N^{\text{ss}} \rightarrow \frac{\Delta N^{\text{eq}}[1 + (\Delta\omega T_2)^2]}{1 + (\Delta\omega T_2)^2 + I/I_s} \rightarrow \frac{\Delta N^{\text{eq}}[1 + (\Delta\omega T_2)^2]}{1 + (\Delta\omega T_2)^2 + |\Omega|^2 T_1 T_2} \quad (19)$$

$\Omega = 2\mu_{eg}E/\hbar$ is called the (complex) Rabi frequency.

The strong population redistribution and interaction of the medium with the near-resonant light causes profound changes in the resonance fluorescence. In the steady state, the strong optical field E produces ac Stark shifts of the energy levels of the system [3,4]. This causes sidebands to appear in the resonance fluorescence spectrum. The emission spectrum has a central peak at the resonance frequency, with two weaker sidebands appearing at $\omega_{eg} \pm |\Omega|$. In other words, the Stark splitting of the energy levels is given by the Rabi frequency times \hbar .

Transient effects. A step input pulse will cause ΔN to oscillate at the Rabi frequency as the system is driven coherently between its upper and lower levels by absorption and stimulated emission [3,5]. Damping causes the oscillations to die out in a characteristic dipole dephasing time T_2 , so ΔN approaches a steady state given by Eq. (19). These damped oscillations appear in the transient resonance fluorescence. These effects are referred to as optical nutation and free induction decay [8] from their two-level spin magnetic resonance analogs.

Photon echoes. When an inhomogeneously broadened system is excited with optically short pulses near resonance, new pulse effects occur under special conditions. If the first pulse at time t is such that $\int_{-\infty}^{\infty} \Omega(t)dt = \pi$, and this is followed at a time $t + T$ later by a second pulse with $\int_{-\infty}^{\infty} \Omega(t)dt = 2\pi$, where $\Omega(t)$ is the time dependent Rabi frequency, then at $t + 2T$ later a superradiant pulse is emitted by the system. This pulse is called a photon echo [2,5,8–10]. Photon echoes have several interesting properties and can be used in spectroscopic studies of materials. For more details, see Ref. 5.

Self-induced transparency. When a two-level system is driven coherently near resonance by a short optical pulse, the so-called area theorem [5] is satisfied, which states that

$$\frac{dA}{dz} = -\frac{\alpha_{00}}{2} \sin A \quad (20)$$

where

$$A = \frac{1}{2} \int_{-\infty}^{\infty} \Omega(t) dt \quad (21)$$

is called the pulse area. For weak pulses, $\sin A \approx A$, and $A(z) \rightarrow A(0)\exp(-\alpha_0 z/2)$. In other words, the pulse is attenuated by linear absorption.

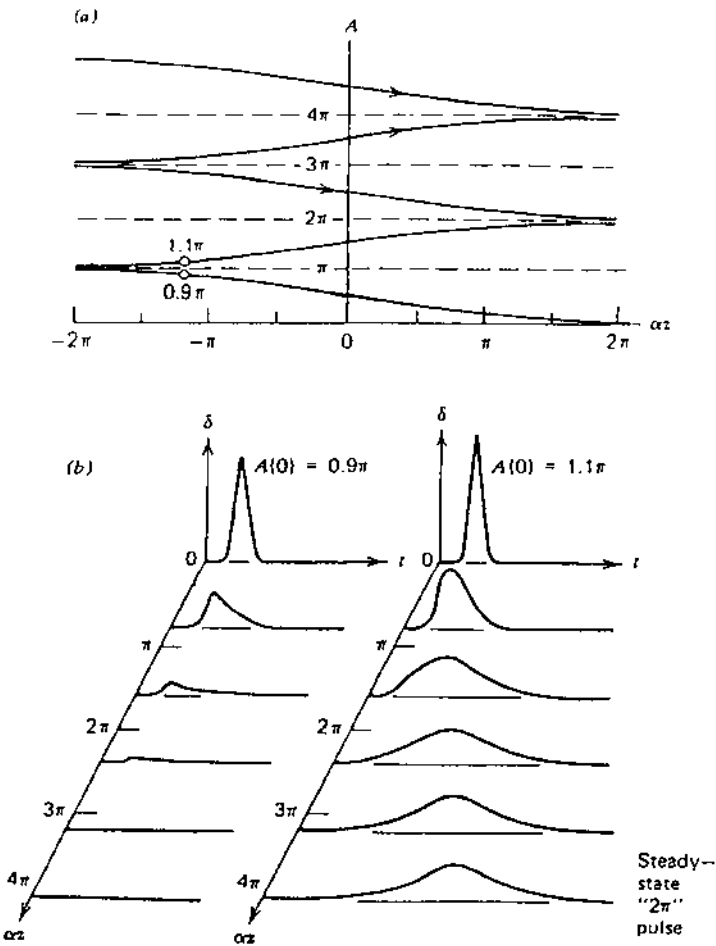


Figure 13 Self-induced transparency pulse area plots. (a) For $\alpha > 0$, the pulse area will evolve with increasing distance z toward the nearest even multiple of π . The entry face of the medium may be at any value of z . (b) Evolution of inputs $A(0) = 0.9\pi$ and $A(0) = 1.1\pi$ with distance. (From Ref. 12.)

In general, equilibrium solutions ($dA/dz = 0$) are possible when $A = m\pi$ ($m = 1, 2, 3, \dots$) [5,11,12]. Odd m solutions are unstable with respect to small fluctuations in A , while even m solutions are stable. Thus a pulse of arbitrary area will approach a shape that yields an area given by the nearest even integer multiple of π . Figure 13, taken from Ref. 12, illustrates this for two different incident pulses.

For a pulse with $A = 2\pi$ resonantly driving an ensemble of two-level systems, atoms make a transition to the upper state during the rising part of the pulse, and then they transition back to the ground state during the latter half of the pulse. The net result is propagation of a pulse with constant width, shape, and energy through an arbitrary length of an ordinarily absorbing medium. This phenomenon is called self-induced transparency. The steady-state pulse has a hyperbolic secant squared shape but travels at a very low velocity, as much as three orders of magnitude smaller than c [5].

V. EXCITED STATE ABSORPTION

When the incident intensity is well above the saturation intensity, then the excited state can become significantly populated. In systems such as polyatomic molecules and semiconductors, there is a high density of states near the state involved in the excitation. The excited electron can rapidly make a transition to one of these states before it eventually transitions back to the ground state. There are also a number of higher-lying states that may be radiatively coupled to these intermediate states, and for which the energy differences are in near-resonance with the incident photon energy. Therefore, before the electron completely relaxes to the ground state, it may experience absorption that promotes it to a higher-lying state. This process is called excited state absorption. It is observable when the incident intensity is sufficient to deplete the ground state significantly.

When the absorption cross-section of the excited state is smaller than that of the ground state, the transmission of the system will be increased when the system is highly excited. This process is called saturable absorption (SA). It is similar to, but more complex than, saturable absorption in a simple two-level system. Generally, two-level saturable absorption will be approximated when the incident pulse is shorter than the decay time for any energy relaxation channel available to the excited electron, and when the transition to any higher lying state is not resonantly enhanced.

When the absorption cross-section of the excited state is larger than that of the ground state, then the system will be less transmissive when excited. This gives the opposite result as saturable absorption and is thus called reverse saturable absorption (RSA).

In semiconductors, the absorption of a photon with energy greater than the band gap will promote an electron to the conduction band, where it is a free carrier and can contribute to current flow when a field is applied. The excited electron will rapidly thermalize and relax to the bottom of the conduction band. From there it will recombine with an excited hole in the valence band after a characteristic recombination time. However, at sufficiently high intensities, it can with high probability absorb another photon while it is still in the conduction band. This process is called free carrier absorption. It has similar qualitative characteristics to reverse saturable absorption.

These three processes are discussed further below. Both steady-state absorption and pulsed excitation are considered.

A. Saturable Absorption

A simplified energy level diagram of a polyatomic molecule is given in Fig. 14[13–16]. This is usually called a five-level model of the molecule, referring to five distinct electronic states, and is adequate to explain the nonlinear absorption

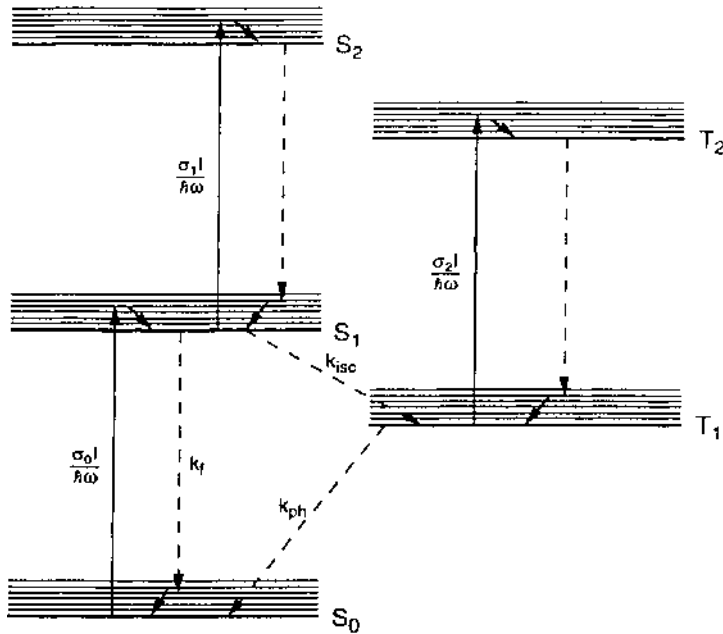


Figure 14 Schematic diagram of a five-level system.

over a wide range of incident intensity. Within each electronic state, there exists a manifold of very dense vibrational–rotational states. When an electron is promoted from one electronic state to another, it will generally transition to one of these vibrational–rotational states. However, with very little energy transfer, collisions will rapidly thermalize the electron, and it will drop to the lowest-lying vibrational–rotational level within the electronic manifold of states. From this state, it can either experience absorption of another photon or relax to any of a number of lower-energy states.

The ground electronic state is called a singlet state. These states have a pair of electrons with antiparallel spins. Selection rules disallow any radiative energy transition for which one of these spins would flip, producing a pair of electrons with parallel spins. Thus absorption from the ground state causes a transition only to another singlet electronic state. The same is true for absorption of fluorescence from a higher-lying singlet state.

It is possible to produce a spin flip by external processes such as collisions with paramagnetic ions, or internal processes such as strong spin–orbit coupling. Under such conditions, the first excited electronic state may make a radiationless transition to a lower-lying triplet state (i.e., a state with a pair of electrons having parallel spins). (The symmetric spatial factor of the singlet two-electron wave function results in an electron pair at equal molecular coordinates along the symmetry axis of the molecule, but residing in upper and lower lobes of the π -orbital. This close proximity results in a higher (Coulombic) energy state than that of the antisymmetric triplet spatial wave function, which preferentially places the electrons at unequal molecular coordinates [13].) A radiative transition from this state is allowed by selection rules only to another triplet state. Hence one speaks of singlet–singlet and triplet–triplet radiative transitions in such molecular systems.

The process of absorption in a five-level system is as follows. Absorption of an incident photon promotes an electron to the first excited singlet state. From this state, one of three things may happen. The electron can relax to the ground state by a radiative or nonradiative transition. The net rate constant for this transition is given by the parameter k_f . Another possibility is for the electron to undergo a spin-flip transition to a triplet state. This process is called intersystem crossing and has a rate constant k_{isc} . The third possibility is that the molecule may absorb another photon, which promotes the electron to a higher-lying singlet state, from which it then relaxes back to the first excited singlet state.

For an electron in the lowest triplet state, two possibilities exist. It may relax by another spin-flip transition to the ground state. This occurs by a process called phosphorescence and has an associated rate constant k_{ph} . The other possibility is that the molecule absorbs another photon, promoting the electron to a higher-lying triplet state. The electron then relaxes back to the lowest triplet state.

Relaxation rates from higher-lying singlet and triplet states are generally very large [13,14]. It is normally assumed that these rates are so large that the population densities of these states, designated by S_2 and T_2 in Fig. 14, are very small and can be ignored. Stimulated emission from excited states is also ignored, since the absorption normally promotes the electron to vibronic levels well above the bottom of the manifold, and relaxation to the bottom vibronic level is very fast.

With these assumptions, rate equations may easily be written for the population densities of the three most important states, S_0 and S_1 (the ground and first excited singlet states, respectively), and T_1 (the first excited triplet state). Introducing the dimensionless quantities $S_0 = N_{S0}/N$, $S_1 = N_{S1}/N$, and $T_1 = N_{T1}/N$, where N_{S0} , N_{S1} , and N_{T1} are the population densities of the S_0 , S_1 , and T_1 states, respectively, and N is the total number density of molecules, the following equations apply:

$$\frac{\partial S_0}{\partial t} = -\frac{\sigma_0 I}{\hbar\omega} S_0 + k_f S_1 + k_{ph} T_1 \quad (22)$$

$$\frac{\partial S_1}{\partial t} = \frac{\sigma_0 I}{\hbar\omega} S_0 - k_f S_1 - k_{isc} S_1 \quad (23)$$

$$\frac{\partial T_1}{\partial t} = k_{isc} S_1 - k_{ph} T_1 \quad (24)$$

The attenuation of the incident light is described by

$$\frac{\partial I}{\partial z} = -\sigma_0 S_0 NI - \sigma_1 S_1 NI - \sigma_2 T_1 NI \quad (25)$$

In these equations, $I(z, t)$ is the light intensity, and σ_0 , σ_1 , and σ_2 are the absorption cross-sections for the ground, first excited singlet, and first excited triplet states, respectively. Also, by conservation of number density, $S_0 + S_1 + T_1 = 1$.

Steady state. In the steady state, Eqs. (22–24) are set equal to zero. An immediate consequence of this is the result that $T_1 = gS_1$, where $g = k_{isc}/k_{ph}$. Normally, the intersystem crossing rate is orders of magnitude larger than the phosphorescence rate (e.g., $k_{isc} \sim 10^9 \text{ s}^{-1}$ and $k_{ph} \sim 10^6 \text{ s}^{-1}$). Thus g is a large number and indicates that the triplet state acts as an electron trap with $T_1 \gg S_1$. Hence the nonlinear absorption in the steady state is determined primarily by the triplet cross-section.

An expression for the steady-state intensity transmittance is given in Table 7. The parameters $\delta_1 = (\sigma_1 - \sigma_0)/\sigma_0$ and $\delta_2 = (\sigma_2 - \sigma_0)/\sigma_0$ measure the relative differences in the cross-sections of the singlet and triplet states, respectively, over that of the ground state. Generally, one would not expect

Table 7 Formulas Related to Excited State Absorption in Polyatomic Molecules and Semiconductors

Saturation and reverse saturable absorption Steady state (intensity transmittance)	$\frac{T_0}{T} = \frac{[1 + [1 + \delta_1 + g(1 + \delta_2)]I_0/I_s]^\kappa}{[1 + [1 + \delta_1 + g(1 + \delta_2)]I_0/I_s]}$
	$\kappa = \frac{\delta_1 + g\delta_2}{1 + g + \delta_1 + g\delta_2}$
	$\delta_i = \frac{\sigma_i - \sigma_0}{\sigma_0}$ ($i = 1, 2$)
	$g = \frac{k_{\text{sc}}}{k_{\text{ph}}}$
	$I_s = \frac{\hbar\omega}{\sigma_0}(k_f + k_{\text{sc}})$
	SA: $\delta_i < 0$
	RSA: $\delta_i > 0$
Pulsed excitation ($F \ll F_s$)	$T = \frac{(1 - R)^2 \exp(-\alpha_0 L)}{1 + (1 - R)[1 - \exp(-\alpha_0 L)]\delta_{\text{eff}} F_0 / 2F_s}$
Energy transmittance (top-hat beam)	$F_s = \frac{\hbar\omega}{\sigma_0}$
	$\delta_{\text{eff}} = \frac{\sigma_{\text{eff}} - \sigma_0}{\sigma_0}$
	$\sigma_{\text{eff}} = \frac{[\sigma_1 - \sigma_0 - \phi_f(\sigma_2 - \sigma_0)]\eta^2 - (1 - e^{-\eta})}{\eta^2}$
	$\eta = (k_f + k_{\text{sc}}) \text{FWHM}$
	$\sigma_{\text{eff}} \rightarrow \sigma_1 (\eta \ll 1)$
	$\sigma_{\text{eff}} \rightarrow \phi_f \sigma_2 (\eta \gg 1)$
Energy transmittance (Gaussian beam)	$T = \frac{(1 - R)^2 \exp(-\alpha_0 L)}{q} \ln(1 + q)$
Free carrier absorption (pulsed excitation)	$q = (1 - R)[1 - \exp(-\alpha_0 L)]\delta_{\text{eff}} F_0 / 2F_s$
Energy transmittance (top-hat beam)	$T = \frac{(1 - R)^2 \exp(-\alpha_0 L)}{1 + (1 - R)[1 - \exp(-\alpha_0 L)]F_0 / 2F_s}$
	$F_s = \frac{\hbar\omega}{\sigma_c}$
	$\sigma_c = \frac{e^2}{\varepsilon_0 I_0 c m^* \omega^2 \tau}$
	m^* = effective carrier mass
	τ = free carrier decay time (mean collision time)
Energy transmittance (Gaussian beam)	$T = \frac{(1 - R)^2 \exp(-\alpha_0 L)}{q} \ln(1 + q)$
	$q = (1 - R)[1 - \exp(-\alpha_0 L)]F_0 / 2F_s$

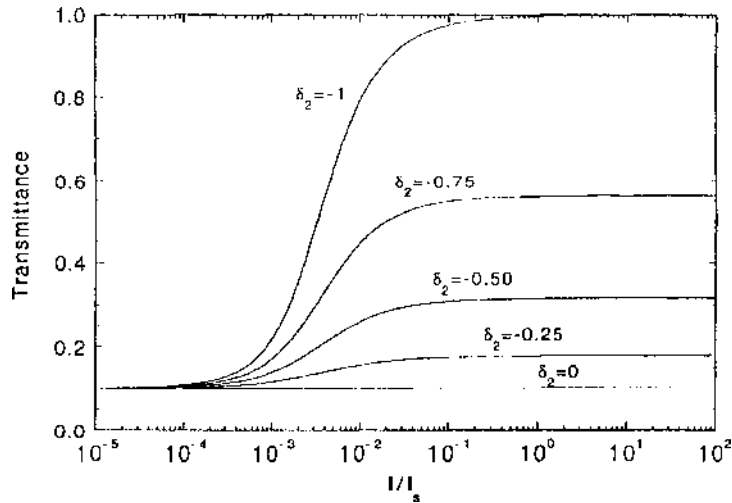


Figure 15 Steady-state intensity transmittance illustrating saturable absorption in a five-level system.

δ_1 and δ_2 to differ greatly in magnitude. But the triplet enhancement factor g makes δ_2 the most important parameter. If $\delta_2 < 0$, then the system will exhibit saturable absorption in the steady state. This is illustrated in the intensity transmittance plots in Fig. 15. The saturation intensity I_s gives a measure of the incident intensity required for bleaching to be observed. Note that I_s is determined by properties of the first excited singlet state, i.e., by the $S_0 \leftarrow S_1$ cross-section, and by the total relaxation time $\tau_1 = (k_f + k_{isc})^{-1}$ of the S_1 state.

Pulsed excitation. When the incident optical pulse width is of the order of the first excited singlet state relaxation time, then the nonlinear absorption characteristics will depend more critically on the $S_1 \leftarrow S_2$ absorption cross-section. If $t_{FWHM} \ll \tau_1$, then the nonlinear absorption will be primarily singlet–singlet. Conversely, when $t_{FWHM} \gg \tau_1$, triplet–triplet absorption will dominate.

The rate equations and the intensity attenuation equation must be solved simultaneously in the pulsed case. In general, this must be done numerically. However, when the incident pulse fluence is small compared to the saturation fluence, defined by $F_s = \hbar\omega/\sigma_0$, then approximate expressions for the energy transmittance can be found.

For very short pulses, there is insufficient time for decay to the triplet state, so $T_1 \approx 0$ and the decay terms in Eq. (23) can be ignored. With the incident fluence small compared to F_s , $S_0 \approx 1$. Then, Eqs. (23) and (25) can be integrated

over time to obtain the following equation for the pulse fluence:

$$\frac{\partial F}{\partial z} = -\alpha_0 \left[1 + \frac{\delta_1 F}{2 F_s} \right] F \quad (26)$$

where $\alpha_0 = \sigma_0 N$ is the linear absorption coefficient.

When the pulse is long compared to τ_1 but short compared to k_{ph}^{-1} , S_1 will reach a quasi-steady state and be small compared to T_1 . Then, under the conditions described above, an equation for the pulse fluence attenuation similar to Eq. (26) can be found:

$$\frac{\partial F}{\partial z} = -\alpha_0 \left[1 + \frac{\phi_T \delta_2}{2 F_s} F \right] F \quad (27)$$

where $\phi_T = k_{isc}/(k_f + k_{isc})$. This parameter is called the triplet quantum yield and is a number between 0 and 1.

For the intermediate pulse width case, it is possible to obtain an approximate equation like Eqs. (26) and (27) in terms of a parameter $\eta = (k_f + k_{isc})t_{FWHM}$. Defining $\delta_{eff} = (\sigma_{eff} - \sigma_0)/\sigma_0$, with

$$\sigma_{eff} = \frac{[\sigma_1 - \sigma_0 - \phi_T(\sigma_2 - \sigma_0)][\eta - (1 - e^{-\eta})] + \phi_T(\sigma_2 - \sigma_0)\eta^2/2}{\eta^2} \quad (28)$$

the pulse fluence attenuation is described by

$$\frac{\partial F}{\partial z} = -\alpha_0 \left[1 + \frac{\delta_{eff}}{2 F_s} F \right] F \quad (29)$$

For $\eta \ll 1$, Eq. (29) reduces to Eq. (26), while for $\eta \gg 1$, it reduces to Eq. (27).

The solutions to these equations are given in Table 7. The energy transmittance for a Gaussian beam is also given in this table.

B. Reverse Saturable Absorption

In a material exhibiting reverse saturable absorption (RSA), the excited state absorption cross-sections are larger than the ground state cross-section. Thus all of the equations described above and in Table 7 apply with $\delta_1, \delta_2 > 0$.

Examples of steady-state RSA intensity transmittance are shown in Fig. 16. Again, δ_2 or triplet-triplet absorption dominates for large g . It should be noted that it is possible to have SA or RSA even if δ_1 and δ_2 have opposite signs, depending on which level dominates.

SA and RSA in the same molecule have been observed. Higher-order singlet-singlet absorption must be invoked to explain this phenomenon [17]. In essence, the population of an intermediate singlet state (e.g., S_1) goes through

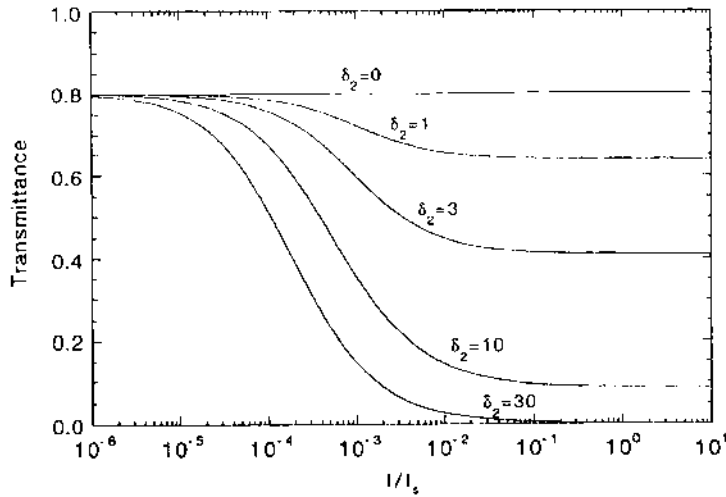


Figure 16 Steady-state intensity transmittance illustrating reverse saturable absorption in a five-level system.

a maximum as the incident intensity increases, with a higher state S_n being increasingly populated at the highest intensities.

For pulsed excitation, Eqs. (26–29) again apply for $F_0 \ll F_s$. The solutions to these equations are given in Table 7. For arbitrary fluence inputs, the rate equations and intensity attenuation equation must be solved simultaneously on a computer. An example of these solutions for RSA in a C₆₀-toluene solution (buckminsterfullerene) is given in Fig. 17. Note that for very high fluences ($>1\text{ J/cm}^2$) the five-level model is inadequate to explain the data, particularly for the nanosecond case. In this case, higher-level singlet–singlet or triplet–triplet absorption may be playing a significant role.

C. Free Carrier Absorption

Once free carriers are generated by linear absorption in semiconductors, they may experience phonon assisted absorption to higher-lying (lower-lying) states in the conduction (valence) band. This process is called free carrier absorption.

In the weak absorption regime, the attenuation may be described by

$$\frac{\partial I}{\partial z} = -\alpha_0 I - \sigma_c N_c(I)I \quad (30)$$

where $N_c(I)$ is the intensity dependent carrier density, and σ_c is the free carrier cross-section. This quantity is given in Table 7. Note that it has the $1/\omega^2$

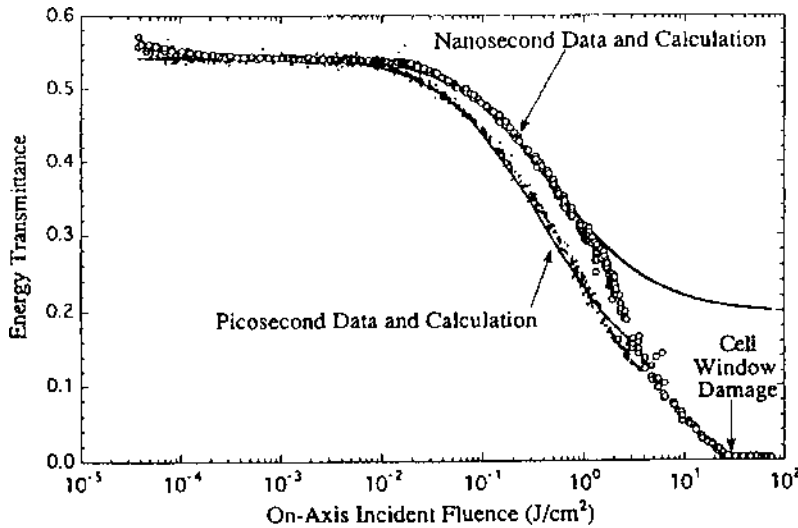


Figure 17 Nonlinear energy transmittance as a function of incident pulse fluence for a C₆₀-toluene solution. The data are for nanosecond and picosecond pulse experiments, and the solid curves are numerical solutions of the rate equations and the optical energy transport equation. (From Ref. 65.)

dependence of a high-frequency conductivity (ω is the optical frequency) and thus is most important for infrared radiation in semiconductors.

The free carrier density is governed by a rate equation given by

$$\frac{\partial N_c}{\partial t} = \frac{\alpha_0 I}{\hbar\omega} - \frac{N_c}{\tau_c} \quad (31)$$

where τ_c is the free carrier relaxation time due to electron–hole recombination and carrier diffusion. In the general case, Eqs. (30) and (31) must be solved numerically to determine the transmittance of the material.

When the incident pulse is short compared to the carrier relaxation time, the latter term may be neglected in Eq. (31), and Eqs. (30) and (31) may be integrated over time to obtain the fluence attenuation equation

$$\frac{\partial F}{\partial z} = -\alpha_0 \left(1 + \frac{F}{2F_s}\right) F \quad (32)$$

where $F_s = \hbar\omega/\sigma_c$ is the saturation fluence. (Note that the cross-section involved in this definition of saturation fluence is the free carrier cross-section and not

the linear absorption cross-section as in the discussion of SA and RSA in polyatomic molecules above.)

Solutions to Eq. (32) are given in Table 7. The energy transmittance of top-hat and Gaussian-beam profiles are included.

D. Two-Photon Assisted Excited State Absorption

When two-photon absorption is particularly strong in a material, it can lead to significant population of a two-photon allowed state. Often there are allowed radiative transitions from this state to higher-lying states of the system (i.e., excited state absorption can ensue from the two-photon pumped state.) This occurs both in polyatomic molecules and in semiconductors.

The attenuation and excited state population equations are given by

$$\frac{\partial I}{\partial z} = -\alpha I - \beta I^2 - \sigma NI \quad (33)$$

and

$$\frac{\partial N}{\partial t} = \frac{\beta I^2}{2\hbar\omega} - \frac{N}{\tau_1} \quad (34)$$

where α is the linear absorption coefficient for impurity absorbers, and τ_1 represents the lifetime of two-photon excited states. These equations must be solved numerically to determine the nonlinear transmittance of the system.

VI. APPLICATIONS

A. Multiphoton Spectroscopy

Lasers have been a boon to the field of spectroscopy, not only because of their narrow line width but also because their high intensity can be used to excite states through nonlinear absorption. Two-photon absorption was used early on to study exciton models in the alkali halides [18,19]. It was also useful for studying the spectral dispersion of exciton—polaritons [20]. TPA allows scientists to probe states of excitonic molecules that are not accessible by single-photon absorption [2].

Physical chemists have been interested in TPA for quantum chemical studies and validation of molecular orbital calculations. Centrosymmetric molecules have electronic states of definite parity, designated as gerade (g) or ungerade (u). Transitions of g–g states or u–u states are forbidden by single-photon absorption but are accessible by TPA. Thus the energy ordering of these states is possible through two-photon spectroscopy. Also, although molecules are randomly oriented in gases and liquids, TPA with $\omega_1 \neq \omega_2$ has polarization

properties that allow a determination of the symmetry of excited states [21]. Several techniques have been developed to study TPA spectra in polyatomic molecules [22–27].

Letokhov and Chebotayev [28] discuss two-photon selection rules for the total angular momentum (J) and magnetic (M) quantum numbers. Three-photon transitions follow the same selection rules as single-photon transitions. However, nonlinear absorption of three photons allows the probing of states that could be accessed by absorption of a single photon of equivalent energy, but where such radiation cannot propagate through cell windows, air, etc.

Multiphoton spectroscopy can also be used to study high Rydberg states in atomic systems. For example, Demtröder [29] discusses multiphoton ionization spectroscopy of alkali metal atoms. Highly excited atoms can be ionized by, for example, field ionization, photoionization, collisional (impact) ionization, etc. Demtröder describes an atomic vapor cell with a thin wire inserted through the window of the cell and negatively biased with respect to the cell walls. Thermionic emission from the wire leads to a space-charge limited current through an external circuit. Ions produced by laser excitation (multiphoton absorption) partially neutralize the space charge, allowing increased electron current. This offers a sensitive detection of the multiphoton transition states in the atomic vapor.

Two-photon spectroscopy has also been useful for validating theoretical models in semiconductors. (See the review by Worlock [30] and also Ref. 31.) Accurate knowledge of the TPA spectrum is valuable in the development of all-optical switches, since TPA imposes fundamental limitations on semiconductor devices [32]. Two- and three-photon absorption is very evident in semiconductors and is often accompanied by free carrier absorption at high intensities [33].

Two- and three-photon absorption has been shown to adversely affect the performance of all-optical waveguide switches in GaAlAs [34]. Yang et al. [35] discuss two-photon and three-photon absorption figures of merit for nonlinear directional coupling switches. The two-photon figure of merit is given by $T = 2\beta\lambda/n_2$, where λ is the incident wavelength and n_2 is the nonlinear refractive index coefficient (see Chapter 6). A small value of T is desired to limit the losses due to TPA. The three-photon figure of merit is given as $V \propto \lambda\gamma/n_2$, where the proportionality constant contains parameters dependent on device design. Knowledge of the 3PA coefficient γ is crucial for limiting three-photon losses. Careful analysis of these figures of merit has led to the demonstration of an all-optical switch at optical communication wavelengths ($\lambda = 1.55 \mu\text{m}$) in GaAlAs without multiphoton absorption losses [36].

B. Q-Switching and Mode-Locking

Saturable absorber dyes have been used extensively in laser cavities for passive Q-switching and mode-locking [37–43]. At low intensities, the dye presents a high loss to the internal cavity radiation by linear absorption. A high intensity will deplete the ground state and bleach a path through the dye. Thus the dye favors the oscillation of high peak power pulses. This is the mechanism of passive Q-switching or mode-locking.

A review of spectroscopic properties of complex molecules for saturable absorption was given by Giuliano and Hess in 1967 [14]. During investigations of bleachable dyes, Giuliano and Hess discovered some molecules that exhibited both saturable absorption and reverse saturable absorption effects in the same molecule [17]. They also discovered some systems in which RSA predominates [14]. Although RSA was considered earlier for power stabilization in Q-switched lasers, in recent years it has been applied more to optical limiting (see Section VII.D). There has been considerable interest in using saturable absorption for high-resolution nonlinear spectroscopy.

C. High-Resolution Doppler-Free Spectroscopy

Spectroscopy has been a key tool in studying the structure of matter. Some effects, such as isotope shifts and hyperfine structure, produce subtle changes in the optical absorption spectrum of materials. Other spectral properties, such as the natural line width of a transition or collisional broadening of a line, which contain interesting information about the material or a particular phenomenon, are also hidden in a typical absorption spectrum. Even with spectrally pure (narrow line width) radiation sources, inhomogeneous broadening of the transitions masks many of these fine structures in the spectrum. In atomic and molecular gases, the Doppler effect is the principal cause of this inhomogeneous broadening.

This broadening mechanism is due to the thermal motion of the individual atoms or molecules. A particle moving at a velocity v in the presence of an optical field of frequency ω will see a field that is frequency shifted, either up or down depending on the direction of the velocity with respect to the direction of the optical beam. This is called the Doppler effect. Relative to a fixed laboratory frame, for which the optical frequency is a fixed quantity, the particle will appear to have a shifted transition frequency. In a gas at thermal equilibrium, the particles have a Maxwellian (i.e., Gaussian) distribution of velocities. Thus each group of particles moving at approximately the same velocity will have its own transition frequency that is shifted from that of a particle at rest (the true transition frequency) by an amount dependent on that velocity. This is the origin of the inhomogeneous broadening of the absorption line.

Nonlinear absorption can be used to excite selectively only a particular velocity group within a Maxwell distribution. This was noted in Section IV under the discussion of spectral hole burning. For example, consider hole burning produced by two counterpropagating beams in the weak saturation regime ($I \ll I_s$). If v is the component of velocity along the axis of beam propagation for a particular group of particles, and if $|\omega_{eg} - (1 \pm v/c)\omega| \leq \Delta\omega$, where $\Delta\omega$ is the *homogeneous* width of the line, then particles with velocity $\pm v$ will be resonantly excited. If the incident frequency in both beams is tuned to ω_{eg} , then the velocity of the group of particles resonantly excited goes to zero ($v \rightarrow 0$). In other words, the beams interact with a group of particles that have zero longitudinal velocity. Thus the interaction is free of the Doppler effect, and the saturated absorption (hole burning) displays a Doppler-free spectrum.

Liao and Bjorkholm [44] discuss experimental techniques for Doppler-free spectroscopy. With counterpropagating cw pump–probe beams, the pump is chopped at audio frequencies and phase sensitive detection is used to monitor the probe. If pulsed lasers are used, then a time delayed probe can be employed to measure the lifetime associated with spectral diffusion. When the counterpropagating beams have different frequencies, then they will interact with the same group of particles, but with $v \neq 0$. Under this condition, collisional broadening of the absorption line as a function of v can be studied as the laser frequencies are tuned.

These methods are valid in the weak saturation regime where ac Stark splitting of the absorption lines and other nonlinear refractive index effects are negligible. In general, other line broadening and shifting mechanisms will be present and must be taken into account. These include, for example, power broadening, divergence and noncollinearity of the laser beams, transit times of the particles through the beams, the second order Doppler effect, and particle recoil. Several related techniques have been developed to account for these mechanisms and are discussed in Ref. 44.

The above methods are collectively referred to as saturation spectroscopy. It is used to study many structural effects and other phenomena in atomic and molecular systems. Some of these include isotopic structure, Zeeman and Stark effects, and forbidden transitions in atomic systems. In molecules it is used to study level structures, vibrational–rotational transitions, hyperfine structure, Zeeman and Stark effects in vibrational–rotational transitions, and isotopic shifts. Letokhov and Chebotayev [28] give a good discussion of these.

Demtröder [29] discusses additional saturation spectroscopy techniques. For example, polarization saturation spectroscopy utilizes a circularly polarized pump to depopulate magnetic sublevels selectively. He also discusses coherent transient spectroscopy (i.e., photon echoes and optical nutation/free induction decay), which is useful for studying optical relaxation phenomena.

Two-photon absorption can also be utilized to achieve Doppler-free spectra [44]. For two counterpropagating waves of frequencies ω_1 and ω_2 , a group of particles moving at velocity v will see frequencies $\omega'_1 = (1 + v/c)\omega_1$ and $\omega'_2 = (1 - v/c)\omega_2$. The two-photon transition is resonant at the frequency $\omega'_1 + \omega'_2 = \omega_1 + \omega_2 + (\omega_1 - \omega_2)v/c$. When $\omega_1 = \omega_2$, the first order Doppler effect is eliminated independent of the velocity v . Thus all particles in the Maxwell velocity distribution are simultaneously resonant, in contrast to saturation spectroscopy, wherein a single velocity group is selectively excited. Velocity dependent TPA from each single beam is also present but is much weaker than the Doppler-free line. It appears as a broad background to the Doppler-free signal.

The situation where $\omega_1 \neq \omega_2$ can also be useful if an intermediate resonance enhances the absorption. This results in a residual Doppler spectrum with magnitude proportional to $\omega_1 - \omega_2$. However, Doppler-free operation is still possible if both ω_1 and $\omega_1 + \omega_2$ are simultaneously resonant [44].

Letokhov and Chebotayev [28] discuss the second order Doppler effect in TPA spectroscopy. They also describe power shifts and power broadening in two-photon resonant transitions.

D. Optical Limiting

Optical limiters display a decreasing transmittance as a function of intensity or fluence. These types of devices have been discussed for applications in optical pulse shaping and smoothing and pulse compression [45,46]. However, the greatest amount of interest in optical limiters in recent years has been for optical sensor protection.

Several reviews of optical limiter materials and devices have been published since 1989, including those by Wood et al. [47–49], Tutt and Boggess [50], and Hermann and Staromlynski [51]. Several physical mechanisms have been exploited for optical limiting, including the nonlinear index of refraction (see Chapter 6, Sections III.E and III.F). Those based primarily on nonlinear absorption are considered here.

The operation of an ideal optical limiter is illustrated in Fig. 18a. For low incident intensity or fluence, the device has a linear transmittance. For some materials, e.g., two-photon absorbers, this transmittance may be near 100%, and the input–output curve would have a slope of 45°. On the other hand, RSA materials require a certain amount of linear absorption, and thus the input–output slope in the linear regime would be <45°.

At some critical intensity or threshold in an ideal limiter, the transmittance changes abruptly and exhibits an inverse intensity or fluence dependence. Thus the output is clamped at some value that would presumably be less than the amount required to damage the sensor. This critical point is called the threshold

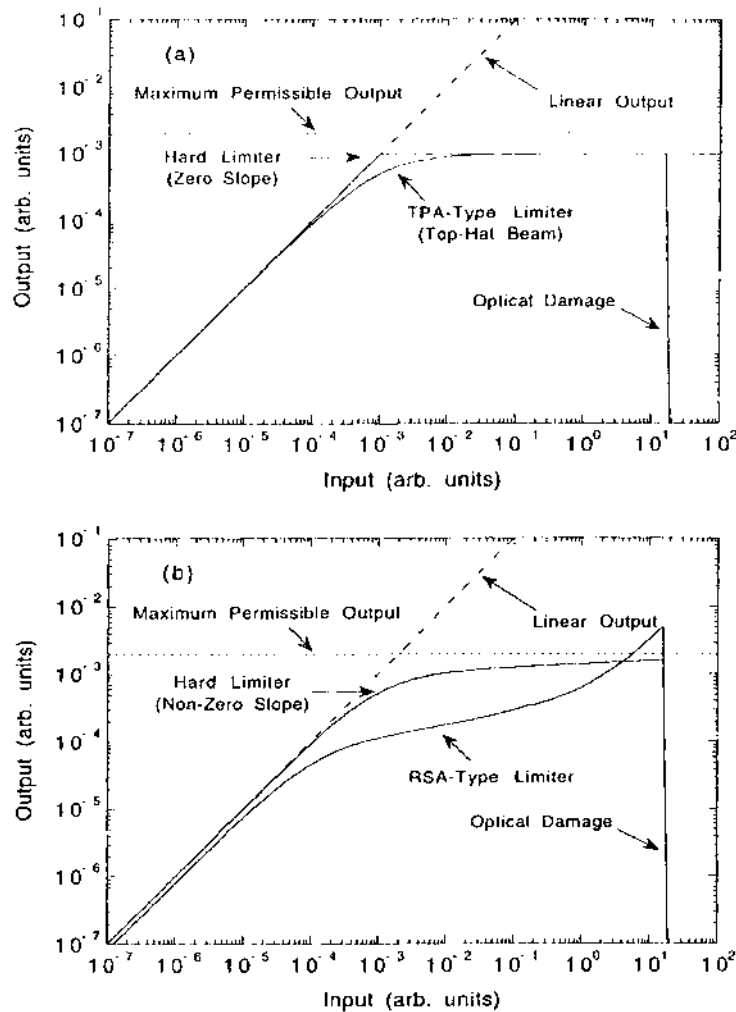


Figure 18 Input–output characteristics of an optical limiter. (a) Ideal optical limiter and (b) realistic optical limiter.

of the device, while the clamped output is called the limiting value of intensity or fluence.

In a real material, illustrated in Fig. 18a and b, this transition is not so abrupt. The definition of threshold is thus not quite as precise, although one approach is to define it as the input intensity or fluence for which the transmittance decreases by a factor of 2 from its value in the linear regime. Also,

in a real material, the output is not always clamped at a constant value, but the input–output slope is decreased as shown in Fig. 18b. Often this is simply the result of the incident beam having a Gaussian rather than a top-hat spatial profile.

An optical limiter must provide protection over a wide range of incident intensity or fluence. Thus if the input–output slope is nonzero, at some input above threshold the device will fail to provide protection. In some cases, the material itself may be damaged if its damage threshold is below this point, or the intensity/fluence dependent transmittance may approach a constant asymptote so that the input–output slope again increases. Any one of these situations will define a maximum input for which the device will provide effective limiting. The ratio of this input value to the threshold is called the dynamic range of the limiter.

Therefore, two desirable attributes of an optical limiter are low threshold and wide dynamic range. In addition, since the device is usually passive and must respond to pulses of arbitrary duration, a fast optical response is required. Also, since optical sensors usually have wide spectral passbands, the device should have a broadband response. Other requirements may include low insertion loss (high linear transmittance), optical clarity (low optical scatter or haze), color neutrality, and robustness (i.e., resistance to damage and degradation due to humidity, temperature swings, etc.). These many requirements place severe restrictions on materials, and development of optical limiter materials is an active research area.

There has been considerable activity in RSA materials for optical limiting. Systems that have been developed and studied include Cr³⁺-doped alexandrite [45], indanthrones [52], phthalocyanines and naphthalocyanines [53–55], heavy atom substituted phthalocyanines [56], iron-tricobalt cluster complexes [57–59], platinum poly-ynes [60], metallotetraporphyrins [60], King's complex (cyclopentadienyliron carbonyl tetramer) [61–64], fullerenes [63–70], and *N*-methylthioaridone [63]. All of these materials tend to exhibit the nonideal limiting behavior illustrated in Fig. 8b. They have low fluence thresholds due to their dependence on linear absorption, but they also exhibit linear loss (less than ideal insertion loss) because of this. The rollover of the fluence dependent transmittance in these materials is determined by $\sigma_{\text{eff}} - \sigma_0$, while the maximum optical density for fluences above the saturation fluence is determined by $\sigma_{\text{eff}}/\sigma_0$. Thus these materials may also be thought of as fluence dependent optical switches, being driven from a high transmittance for $F \ll F_s$ to a low transmittance for $F > F_s$. Miles discusses some potential designs for optical limiters using RSA materials [71].

Two-photon absorbers and materials for which excited state absorption follows two-photon transitions to an excited state (e.g., free carrier absorption) have also been extensively studied for optical limiting. Optical limiting in solutions of diphenyl polyenes [72] was originally attributed to self-focusing, but later studies indicated that TPA plays a significant if not dominant role in these

materials [26,73]. At intensities greater than 100 MW/cm^2 , ESA is also probably contributing to the optical limiting. TPA optical limiting has also been observed in solutions of dithienyl polyenes [74]. Thresholds for TPA materials depend on β and are generally much higher than those observed in RSA materials. However, TPA materials do not saturate as readily as RSA materials. TPA followed by ESA is particularly attractive for optical limiting.

TPA followed by free carrier absorption (FCA) has been shown to yield optical limiting in the IR for a variety of semiconductors. These include InSb [33,75–82], HgCdTe [81–83], InAs [79], Si [84], GaP [50], CdSe [31], CdTe [31], and GaAs [85]. The limiting in GaAs was partially attributed to nonlinear refractive index effects. Similar combined TPA/FCA and nonlinear refraction effects in the visible have been studied in ZnSe [86]. IR optical limiting in Ge has been attributed to seven-photon absorption followed by FCA [87].

REFERENCES

1. M. Göppert-Meyer, *Ann. Phys.* 9:273 (1931).
2. Y. R. Shen, *The Principles of Nonlinear Optics*, John Wiley, New York, 1984, pp. 334–336, 437–446.
3. R. W. Boyd, *Nonlinear Optics*, Academic Press, New York, 1992, pp. 191–239.
4. P. N. Butcher and D. Cotter, *The Elements of Nonlinear Optics*, Cambridge Univ. Press, 1990, pp. 150–210.
5. A. Yariv, *Quantum Electronics*, 3rd ed., John Wiley, New York, 1989, pp. 155–182, 342–377.
6. P. G. Kryukov and V. S. Letokhov, Propagation of a light pulse in a resonantly amplifying (absorbing) medium, *Sov. Phys.-Usp.* 12:641 (1970).
7. N. G. Basov and V. S. Letokhov, Change of light-pulse shape by nonlinear amplification, *Sov. Phys.-Dok.* 11:222 (1966).
8. R. G. Brewer and R. L. Shoemaker, Photon echoes and optical nutation in molecules, *Phys. Rev.* 27:632 (1971).
9. N. A. Kurnit, I. D. Abella, and S. R. Hartman, Observation of a photon echo, *Phys. Rev. Lett.* 13:567 (1964).
10. I. D. Abella, N. A. Kurnit, and S. R. Hartman, Photon echoes, *Phys. Rev.* 141:391 (1966).
11. S. L. McCall and E. L. Hahn, Self-induced transparency by pulsed coherent light, *Phys. Rev. Lett.* 18:908 (1967).
12. S. L. McCall and E. L. Hahn, Pulse-area pulse-energy description of a traveling wave laser amplifier, *Phys. Rev. A*2:961 (1970).
13. F. P. Schäfer, Principles of dye laser operation, *Dye Lasers* (F. P. Schäfer, ed), Springer-Verlag, New York, 1977, pp. 9–32.
14. C. R. Giuliano and L. D. Hess, Nonlinear absorption of light: optical saturation of electronic transitions in organic molecules with high intensity laser radiation, *IEEE J. Quantum Electr.* QE-3:358 (1967).

15. L. Huff and L. G. DeShazer, Nonlinear absorption behavior of indanthrone dyes: comparison of optical saturation and photochemical processes, *J. Appl. Phys.* 40:4336 (1969).
16. L. Huff and L. G. DeShazer, Saturation of optical transitions in organic compounds by laser flux, *J. Opt. Soc. Am.* 60:157 (1970).
17. C. R. Giuliano and L. D. Hess, Nonlinear absorption of light. Positive and negative saturation effects in the same absorber, *Appl. Phys. Lett.* 12:292 (1968).
18. J. J. Hopfield, J. M. Worlock, and K. J. Park, *Phys. Rev. Lett.* 11:414 (1963).
19. J. J. Hopfield and J. M. Worlock, *Phys. Rev.* 137:A1455 (1959).
20. D. Fröhlich, E. Mohler, and P. Wiesner, *Phys. Rev. Lett.* 26:554 (1971).
21. W. M. McClain, *J. Chem. Phys.* 55:2789 (1971).
22. W. M. McClain, *Ann. Rev. Phys. Chem.* 31:559 (1980).
23. R. J. M. Anderson, G. R. Holton, and W. M. McClain, Two-photon absorptivities of the all trans α,ω -diphenyl polyenes from stilbene to diphenyl octatetraene via three-wave mixing, *J. Chem. Phys.* 70:4310 (1979).
24. R. L. Swofford and W. M. McClain, Two-photon absorption studies of diphenylbutadiene: the location of the 1A_g excited state, *J. Chem. Phys.* 59:5740 (1973).
25. H. L. Fang, T. L. Gustafson, and R. L. Swofford, Two-photon absorption photothermal spectroscopy using a synchronously pumped picosecond dye laser. Thermal lensing spectra of naphthalene and diphenylbutadiene, *J. Chem. Phys.* 78:1663 (1983).
26. R. L. Sutherland, E. Rea, L. V. Natarajan, T. Pottenger, and P. A. Fleitz, Two-photon absorption and second hyperpolarizability measurements in diphenylbutadiene by degenerate four-wave mixing, *J. Chem. Phys.* 98:2593 (1993).
27. A. J. Twarowski and D. S. Kliger, Multiphoton absorption spectra using thermal blooming, *Chem. Phys.* 20:253 (1977).
28. V. S. Letokhov and V. P. Chebotayev, *Nonlinear Laser Spectroscopy*, Springer-Verlag, New York, 1977, pp. 142, 156, 159–161, 166–174, 317–328, 332–343.
29. W. Demtröder, *Laser Spectroscopy*, Springer-Verlag, Berlin, 1982, pp. 441–442, 505–518, 573–582.
30. J. M. Worlock, *Laser Handbook*: Vol II (T. Arecchi and F. Schulz-Debois, eds), North-Holland, Amsterdam, 1972, p. 1323.
31. A. F. Stewert and M. Bas, Intensity-dependent absorption in semiconductors, *Appl. Phys. Lett.* 37:1040 (1980).
32. J. A. Bogler, A. K. Kar, B. J. Wherrett, R. DeSalvo, D. C. Hutchings, and D. J. Hagan, Nondegenerate two-photon absorption spectra of ZnSe, ZnS, and ZnO, *Opt. Commun.* 97:203 (1993).
33. M. Sheik-bahae, P. Mukherjee, and H. S. Kwok, Two-photon and three-photon absorption coefficients of InSb, *J. Opt. Soc. Am. B* 3:379 (1986).
34. J. S. Aitchison, A. Villeneuve, and G. I. Stegeman, All-optical switching in a nonlinear GaAlAs X junction, *Opt. Lett.* 18:1153 (1993).
35. C. C. Yang, A. Villeneuve, G. I. Stegeman, and T. J. Aitchison, Effects of three-photon absorption on nonlinear directional coupling, *Opt. Lett.* 17:710 (1992).

36. K. Al-hemyari, A. Villeneuve, J. U. Kang, J. S. Aitchison, C. N. Ironside, and I. Stegeman, Ultrafast all-optical switching in GaAlAs directional couplers at 1.55 μm without multiphoton absorption, *Appl. Phys. Lett.* 63:3562 (1993).
37. H. Mocker and R. J. Collins, Mode competition and self-locking effects in a Q-switched ruby laser, *Appl. Phys. Lett.* 7:720 (1965).
38. P. Kafalas, J. I. Masters, and E. M. E. Murray, *J. Appl. Phys.* 35:2349 (1964).
39. B. H. Soffer and R. H. Hoskins, *Nature* 204:276 (1964).
40. G. Bret and G. Gires, *Appl. Phys. Lett.* 4:175 (1964).
41. A. J. DeMaria, D. A. Stetser, and H. Heynan, *Appl. Phys. Lett.* 8:174 (1966).
42. J. Schwartz, C. S. Naiman, and R. K. Chang, Effects of internal induced absorption on laser emission, *Appl. Phys. Lett.* 11:242 (1967).
43. R. H. Pantell and J. Warszawski, Laser power stabilization by means of nonlinear absorption, *Appl. Phys. Lett.* 11:213 (1967).
44. P. F. Liao and J. E. Bjorkholm, Doppler-free laser spectroscopy, *Methods of Experimental Physics: Vol. 15, Part B, Quantum Electronics* (C. L. Tang, ed), Academic Press, New York, 1979, pp. 232–248.
45. D. J. Harter, M. L. Shand, and Y. B. Band, Power/energy limiter using reverse saturable absorption, *J. Appl. Phys.* 56:865 (1984).
46. Y. B. Band, D. J. Harter, and R. Bavli, *Chem. Phys. Lett.* 126:280 (1986).
47. G. L. Wood, A. A. Said, D. J. Hagan, M. J. Soileau, and E. W. Van Stryland, *Proc. Soc. Photo-Opt. Eng.* 1105:154 (1989).
48. G. L. Wood, W. W. Clark III, and E. J. Sharp, *Proc. Soc. Photo-Opt. Eng.* 1307:376 (1990).
49. G. L. Wood, A. G. Mott, and E. J. Sharp, *Proc. Soc. Photo-Opt. Eng.* 1692:2 (1992).
50. L. W. Tutt and T. F. Boggess, A review of optical limiting mechanisms and devices using organics, fullerenes, semiconductors, and other materials, *Prog. Quant. Electr.* 17:299 (1993).
51. J. A. Hermann and J. Staromlynska, Trends in optical switches, limiters, and discriminators, *Int. J. Nonlin. Opt. Phys.* 2:271 (1993).
52. R. C. Hoffman, K. A. Stetyck, R. S. Potember, and D. G. McLean, Reverse saturable absorbers: indanthrone and its derivatives, *J. Opt. Soc. Am. B* 6:772 (1989).
53. T. H. Wei, D. J. Hagan, M. J. Sence, E. W. Van Stryland, J. W. Perry, and D. R. Coulter, Direct measurement of nonlinear absorption and refraction in solutions of phthalocyanines, *Appl. Phys. B* 54:46 (1992).
54. J. S. Shirk, J. R. Lindle, F. J. Bartoli, Z. H. Kafafi, A. W. Snow, and M. E. Boyle, *Int. J. Nonlin. Opt. Phys.* 1:699 (1992).
55. D. R. Coulter, V. M. Miskowski, J. W. Perry, T. H. Wei, E. W. Van Stryland, and D. J. Hagan, Optical limiting in solutions of metallo-phthalocyanines and naphthalocyanines, *Proc. Soc. Photo-Opt. Eng.* 1105:42 (1989).
56. J. W. Perry, K. Mansour, S. R. Marder, K. J. Perry, D. Alvarez, Jr., and I. Choong, Enhanced reverse saturable absorption and optical limiting in heavy-atom-substituted phthalocyanines, *Opt. Lett.* 19:625 (1994).
57. L. W. Tutt, S. W. McCahon, and M. B. Klein, Optimization of optical limiting properties of organometallic compound, *Proc. Soc. Photo-Opt. Eng.* 1307:315 (1990).

58. S. W. McCahon, L. W. Tutt, M. B. Klein, and G. C. Valley, Optical limiting with reverse saturable absorbers, *Proc. Soc. Photo-Opt. Eng.* 1307:304 (1990).
59. L. W. Tutt and S. W. McCahon, Reverse saturable absorption in metal cluster compounds, *Opt. Lett.* 15:700 (1990).
60. S. Guha, K. Kang, D. Porter, J. F. Roach, D. E. Remy, F. J. Aranda, and D. V. G. L. N. Rao, Third-order optical nonlinearities of metallotetrabenzoporphyrins and a platinum poly-yne, *Opt. Lett.* 17:264 (1992).
61. G. R. Allan, D. R. Labergerie, S. J. Rychnovsky, T. F. Boggess, A. L. Smirl, and L. W. Tutt, Picosecond reverse saturable absorption in King's complex $[(\text{CH}_5\text{H}_5)\text{Fe}(\text{CO})]_4$, *J. Phys. Chem.* 96:6313 (1992).
62. T. F. Boggess, G. R. Allan, S. J. Rychnovsky, D. R. Labergerie, C. H. Venzke, A. L. Smirl, L. W. Tutt, A. R. Kost, S. W. McCahon, and M. B. Klein, Picosecond investigations of optical limiting mechanisms in King's complex, *Opt. Eng.* 32:1063 (1993).
63. A. Kost, L. Tutt, M. B. Klein, T. K. Dougherty, and W. E. Silas, Optical limiting with C_{60} in polymethyl methacrylate, *Opt. Lett.* 18:334 (1993).
64. L. W. Tutt and A. Kost, Optical limiting performance of C_{60} and C_{70} solutions, *Nature* 356:225 (1992).
65. D. G. McLean, R. L. Sutherland, M. C. Brant, D. M. Brandelik, P. A. Fleitz, and T. Pottenger, Nonlinear absorption study of a C_{60} -toluene solution, *Opt. Lett.* 18:858 (1993).
66. D. Brandelik, D. McLean, M. Schmitt, B. Epling, C. Colclasure, V. Tondiglia, R. Pachter, K. Obermeier, and R. Crane, *Proc. Mat. Res. Soc.* 247:361 (1991).
67. S. R. Flom, R. G. S. Pong, F. J. Bartoli, and Z. H. Kafafi, *Phys. Rev. B* 46:15598 (1992).
68. M. P. Joshi, S. R. Mishra, H. S. Rawat, S. C. Mehendale, and K. C. Rustagi, *Appl. Phys. Lett.* 62:1763 (1993).
69. F. Bentiregna, M. Canva, P. Georges, A. Brun, F. Chaput, L. Malier, and J.-P. Boilot, *Appl. Phys. Lett.* 62:1721 (1993).
70. B. L. Justus, Z. H. Kafafi, and A. L. Huston, Excited-state absorption-enhanced thermal optical limiting in C_{60} , *Opt. Lett.* 18:1603 (1993).
71. P. A. Miles, Bottleneck political limiters: the optimal use of excited-state absorbers, *Appl. Opt.* 33:6965 (1944).
72. T. J. Bunning, L. V. Natarajan, M. G. Schmitt, B. P. Epling, and R. L. Crane, Optical limiting in solutions of diphenyl polyenes, *Appl. Opt.* 30:4341 (1991).
73. P. A. Fleitz, R. L. Sutherland, L. V. Natarajan, T. Pottenger, and N. C. Fernelius, Effects of two-photon absorption on degenerate four-wave mixing in solutions of diphenyl polyenes, *Opt. Lett.* 17:716 (1992).
74. L. V. Natarajan, R. L. Sutherland, M. G. Schmitt, M. C. Brant, D. G. McLean, P. A. Fleitz, T. J. Bunning, and R. L. Crane, Optical limiting in solutions of dithienyl polyenes, *Proc. Soc. Photo-Opt. Eng.* 1853:99 (1993).
75. J. F. Figueira, C. D. Cantrell, J. P. Rink, and P. R. Furman, Time-resolved pump depletion in n -InSb Raman spin-flip laser, *Appl. Phys. Lett.* 28:398 (1976).
76. A. F. Gibson, C. B. Hatch, P. N. Maggs, D. R. Tilley, and A. C. Walker, Two-photon absorption in InSb and Ge, *J. Phys. C* 9:3259 (1976).

77. H. J. Fossum and D. B. Chang, Two-photon excitation rate in InSb, *Phys. Rev. B* 8:2842 (1973).
78. J. Dempsey, J. Smith, G. O. Holah, and A. Miller, Nonlinear absorption and pulse shaping in InSb, *Opt. Commun.* 26:265 (1978).
79. S. A. Jamison and A. V. Nurmiikko, Avalanche formation and high-intensity infrared transmission limit in InAs, InSb, and $Hg_{1-x}Cd_xTe$, *Phys. Rev. B* 19:5185 (1979).
80. J. M. Doviak, A. F. Gibson, M. F. Kimitt, and A. C. Walker, Two-photon absorption in InSb at $10.6\text{ }\mu\text{m}$, *J. Phys. C* 6:593 (1973).
81. A. Miller, A. Johnson, J. Dempsey, J. Smith, C. R. Pidgeon, and G. D. Holah, Two-photon absorption in InSb and $Hg_{1-x}Cd_xTe$, *J. Phys. C* 12:4389 (1979).
82. A. M. Johnson, C. R. Pidgeon, and J. Dempsey, Frequency dependence of two-photon absorption in InSb and $Hg_{1-x}Cd_xTe$, *Phys. Rev. B* 22:825 (1980).
83. S. A. Jamison and A. V. Nurmiikko, High-intensity transmission limit in $Hg_{1-x}Cd_xTe$, *Appl. Phys. Lett.* 33:182 (1978).
84. T. F. Boggess, S. C. Moss, I. W. Boyd, and A. L. Smirl, Nonlinear optical energy regulation by nonlinear refraction and absorption in silicon, *Opt. Lett.* 9:291 (1984).
85. T. F. Boggess, A. L. Smirl, S. C. Moss, I. W. Boyd, and E. W. Van Stryland, *IEEE J. Quantum Electr.* 21:488 (1985).
86. A. A. Said, M. Sheik-bahae, D. J. Hagan, E. J. Canto-Said, Y. Y. Wu, J. Young, T. H. Wei, and E. W. Van Stryland, Nonlinearities in semiconductors for optical limiting, *Proc. Soc. Photo-Opt. Instrum. Eng.* 1307:294 (1990).
87. S. Y. Yuen, R. L. Aggarwal, and B. Lax, Saturation of transmitted intensity of CO₂ laser pulses in germanium, *J. Appl. Phys.* 51:1146 (1980).

10

Experimental Techniques in Nonlinear Absorption

Nonlinear absorption plays an important role in the applications of nonlinear optics. In some devices it is detrimental, limiting the usefulness of device operation at high intensities. Such is the case of all-optical waveguide switches. On the other hand, devices such as optical limiters rely on strong nonlinear absorption for effective performance, as discussed in the last chapter. Nonlinear absorption has also been employed to enhance the optical spectroscopic study of materials. The phenomena produced by nonlinear absorption can in turn be used to measure the associated materials parameters. This chapter describes several such characterization methods.

As in all nonlinear optical characterization methods discussed in previous chapters, linear properties of materials, such as linear index of refraction and linear absorption coefficient, must be known in most cases. Standard measurement techniques [1] can be used to obtain these, or in many cases they can be taken from the literature.

Measurement methods discussed in this chapter generally yield nonlinear absorption coefficients (e.g., β , γ , or $\text{Im}(\chi^{(3)})$), depending on which parameter occurs most naturally in the theory. The relationships between these parameters are given in Chapter 9. Microscopic parameters of the medium, such as the two-photon cross-section σ_2 , excited state cross-sections (e.g., σ_s , σ_T , σ_{eff}), and so forth, can be obtained from the measurements if the concentration or molecular number density of the sample is known.

The following techniques are discussed:

Transmission measurements

- Three-wave mixing
- Two-photon fluorescence
- Photothermal techniques
- Degenerate four-wave mixing
- Heterodyned Kerr effect measurements
- Chirped-pulse pump–probe technique

The last two methods are useful for determining both the real and the imaginary components of the third-order susceptibility. The former of course relates to the nonlinear refractive index, while the latter yields the two-photon absorption coefficient.

I. TRANSMISSION MEASUREMENTS

The most obvious effect of nonlinear absorption is a change in the transmission of a material with increasing intensity or fluence. If this change can be measured, then the equations given in Chapter 9 can be inverted to obtain the two-photon absorption coefficient β , the excited state cross-section σ_{ex} , etc. Thus this technique can be used to characterize two- and three-photon absorption materials and excited state absorption materials.

The advantages of this method include its straightforward experimental and analysis techniques. In addition, it is directly amenable to pump–probe methods for studying wavelength and time dependencies. Its chief disadvantage is that it involves measuring a small change in a large background, since the nonlinear transmittance change is generally a small fraction of the linear transmittance. This is reflected in a large uncertainty in the extracted nonlinear coefficients. Nevertheless, under certain conditions the change is significant, and the technique is a popular one because of its simplicity.

A. Theory

Multiphoton absorption. Although in principle all multiphoton absorption coefficients could be measured, those of order higher than two- or three-photon absorption are generally too small to measure. With the exception of gases and some semiconductors, the direct measurement of higher-order coefficients would require intensities of such magnitude that the material would be damaged.

In most cases, a Gaussian beam is employed in the measurement. Two situations are considered. In both cases the sample length is assumed to be small compared to the Rayleigh length of the Gaussian beam. In one case, the sample is fixed, and the intensity is increased in the experiment. In the second case, the beam power or energy is held constant, and the sample is translated along the beam to increase the intensity incident on the sample. This is the Z-scan

technique discussed in Chapter 7; it is often used for nonlinear refractive index measurements.

The measured nonlinear transmittance is normalized with respect to the linear transmittance (measured at very low intensity). For two-photon absorption, this normalized transmittance is given by

$$T_N = \frac{1}{aq(\zeta)} \int_{-\infty}^{\infty} \ln[1 + q(\zeta)f(x)]dx \quad (1)$$

where

$$q(\zeta) = \frac{\beta(1 - R)I_0L_{\text{eff}}}{1 + \zeta^2} \quad (2)$$

and $\zeta = z/z_R$ with z_R being the Rayleigh range. R is the Fresnel reflectance of the front sample surface, I_0 is the on-axis intensity at the focus of the incident beam in air, and

$$L_{\text{eff}} = \frac{1 - \exp(-\alpha L)}{\alpha} \quad (3)$$

with α the linear absorption coefficient and L the sample thickness. Finally, for a Gaussian-shaped pulse, $f(x) = \exp(-x^2)$, while for a hyperbolic secant squared pulse, $f(x) = \text{sech}^2(x)$, and

$$a = \begin{cases} \sqrt{\pi} & \text{Gaus} \\ 2 & \text{sech}^2 \end{cases} \quad (4)$$

For fixed sample measurements, $\zeta = 0$ and the on-axis intensity I_0 is varied. In the Z-scan technique, I_0 is held fixed while ζ is varied. In either case, the data are fitted to Eqs. (1–4) to extract β . Under arbitrary conditions, Eq. (1) must be solved numerically. However, when $q_0 = \beta(1 - R)I_0L < 1$ the following approximation may be used:

$$T_N = \sum_{m=0}^{\infty} \frac{[-q(\zeta)]^m}{(m+1)^{3/2}} \quad (5)$$

for Gaussian pulses, and

$$T_N = \sum_{m=0}^{\infty} \frac{[-q(\zeta)]^m}{m+1} \prod_{n=0}^m \left[\frac{2(m-n) + \delta_{mn}}{2(m-n) + 1} \right] \quad (6)$$

for hyperbolic secant squared pulses, with $\delta_{mn} = 1$ for $m = n$ and zero otherwise.

For three-photon absorption, the normalized transmittance is given by

$$T_N = \frac{1}{ap(\zeta)} \int_{-\infty}^{\infty} \ln[\sqrt{1 + p^2(\zeta)f(x)} + p(\zeta)f(x)]dx \quad (7)$$

where

$$p(\zeta) = \sqrt{2\gamma(1 - R)^2 I^2(\zeta) L'_{\text{eff}}} \quad (8)$$

and

$$L'_{\text{eff}} = \frac{1 - \exp(-2\alpha L)}{2\alpha} \quad (9)$$

Again, $f(x)$ describes the pulse shape as given above, and Eqs. (7–9) must generally be solved numerically to extract the three-photon absorption coefficient γ . When $p_0 = [2\gamma(1 - R)^2 I_0^2 L'_{\text{eff}}]^{1/2} < 1$, the following approximations may be used:

$$T_N = \sum_{m=1}^{\infty} (-1)^{m-1} \frac{p^{2m-2}(\zeta)}{(2m-1)! \sqrt{2m-1}} \quad (10)$$

for a Gaussian-shaped pulse, and

$$\begin{aligned} T_N = & \sum_{m=1}^{\infty} (-1)^{m-1} \frac{p^{m-2}(\zeta)}{(2m-1)!} \\ & \times \prod_{n=1}^m \left[\frac{4(m-n) + \delta_{mn}}{4(m-n) + 1} \right] \prod_{n'=1}^m \left[\frac{4(m-n'-\frac{1}{2}) + \delta_{mn'}}{4(m-n'-\frac{1}{2}) + 1} \right] \end{aligned} \quad (11)$$

for a hyperbolic secant squared pulse. Again, for fixed sample measurements, $\zeta = 0$ and I_0 is varied, while with the Z-scan technique, I_0 is held fixed and ζ is varied.

In two-photon spectroscopy, pump–probe methods are often employed. It is generally allowable to assume that $I_e \gg I_p$, where I_e is the pump (excite) beam intensity, and I_p is the probe beam intensity. The self-induced two-photon absorption coefficient β_{ee} is measured in a separate single beam experiment as described above. The two-beam two-photon absorption coefficient β_{ep} , defined in Chapter 9, Table 4, is measured in the pump–probe experiment. Two cases are generally considered. The first is such that β_{ee} is negligible (e.g., when the pump photon energy is less than half the band gap energy in a semiconductor). The second case is when β_{ee} is nonnegligible, and two-photon loss due to the pump beam alone must also be considered.

When self-TPA by the pump can be ignored, the normalized probe transmittance is given by (for pulsed Gaussian beams)

$$T_N = \sum_{m=0}^{\infty} \frac{[-\Gamma(\zeta)]^m \eta}{(m + \eta)m! \sqrt{m+1}} \quad (12)$$

for a Gaussian pulse, and

$$T_N = \sum_{m=0}^{\infty} \frac{[-\Gamma(\zeta)]^m \eta}{(m + \eta)m!} \prod_{n=0}^m \left[\frac{2(m-n) + \delta_{mn}}{2(m-n) + 1} \right] \quad (13)$$

for a hyperbolic secant squared pulse, where

$$\Gamma(\zeta) \simeq 2 \sqrt{\frac{\lambda_e}{\lambda_p}} \beta_{ep} (1 - R_e) I_e(\zeta) L \quad (14)$$

and

$$\eta = \left(\frac{w_e}{w_p} \right)^2 \quad (15)$$

is the ratio of the beam areas (pump-to-probe). These equations apply to the case where the pump and probe have essentially the same time behavior (i.e., derived from the same laser). For the situation in which the probe is a cw beam, refer to the formulas given in Chapter 9, Table 4. Also, when the probe beam is small compared to the pump beam, the formulas for the normalized transmittance become essentially independent of η .

When self-TPA by the pump cannot be safely ignored, then the normalized probe transmittance is given by

$$T_N = \frac{\eta}{a} \int_{-\infty}^{\infty} \int_0^1 \left(\frac{1}{1 + q_e(\zeta)yf(x)} \right)^r y^{\eta-1} dy dx \quad (16)$$

where

$$q_e(\zeta) = \beta_{ee}(1 - R_e) I_e(\zeta) L_{eff} \quad (17)$$

and

$$r = 2 \sqrt{\frac{\lambda_e}{\lambda_p}} \frac{\beta_{ep}}{\beta_{ee}} \quad (18)$$

while $f(x)$ again describes the pulse shape. These equations must be solved numerically to extract β_{ep} . Under certain restricted conditions, other approximations may be used. For these and conditions where the probe is a cw beam, refer to the formulas in Chapter 9, Table 4.

Excited state/free carrier absorption. Single beam excited state absorption experiments with organic materials and free carrier absorption experiments with semiconductors are very similar. For purposes of analysis, it is preferred to operate in a regime where the incident fluence is small compared to the saturation fluence, which was defined in Chapter 9. For excited state absorption, this depends on the photon energy and the ground state absorption cross-section. Therefore this parameter is readily computed from linear absorption measurements and should be known *a priori*. For free carrier absorption, the critical fluence depends instead on the free carrier absorption cross-section. This cannot be known *a priori* and must await the results of the nonlinear absorption experiment. Once a value is extracted for the free carrier cross-section, the critical fluence should be calculated and checked against incident fluence values used in the experiment to assure that any approximations utilized in the data analysis are valid.

For ESA and FCA it is useful to define a normalized change in transmittance $\Delta T_N = 1 - T/T_0$, where T_0 is the linear transmittance. For ESA, this quantity is given by

$$\Delta T_N = \frac{(\sigma_{\text{eff}} - \sigma_0)\alpha L_{\text{eff}}(1 - R)F(\zeta)}{4\hbar\omega} \quad (19)$$

where σ_{eff} is the effective excited state cross-section defined in Chapter 9 for a five-level model of a polyatomic molecule. It is a combination of excited singlet and triplet cross-sections. When the incident laser pulse width is shorter than the first excited singlet state lifetime, then σ_{eff} reduces to σ_1 , the excited singlet–singlet cross-section. On the other hand, when the incident pulse width is long compared to the singlet lifetime, σ_{eff} becomes $\phi_T\sigma_2$, the effective triplet–triplet cross-section, where ϕ_T is the triplet quantum yield. Thus, in terms of the measured normalized transmittance change,

$$\sigma_{\text{eff}} = \sigma_0 + \frac{4\hbar\omega\Delta T_N}{\alpha L_{\text{eff}}(1 - R)F(\zeta)} \quad (20)$$

where $F(\zeta)$ is the incident fluence (in air).

With FCA, it is useful if the incident laser pulse is short compared to the free carrier relaxation time. Then an analytical expression for the transmittance can be obtained, as given in Chapter 9, Table 4. Under this condition for FCA, a similar relation holds for the normalized transmittance as in Eq. (19). The free carrier cross-section is thus given by

$$\sigma_c = \frac{4\hbar\omega\Delta T_N}{\alpha L_{\text{eff}}(1 - R)F(\zeta)} \quad (21)$$

Often of interest in ESA is the excited state spectrum as a function of time. The time-delayed pump–probe method lends itself to this type of measurement.

From these experiments it is possible to obtain both the excited singlet–singlet and triplet–triplet cross-sections as functions of wavelength. Generally, the pump (or excite) beam is fixed at a single wavelength while the wavelength of a weak probe beam is varied. In ESA pump–probe experiments, the nonlinear absorption of the pump cannot be ignored, even when the incident fluence is well below the saturation fluence.

To simplify the analysis, the incident fluence is kept below the saturation fluence, and the probe fluence is assumed to be small compared to the pump fluence. Then a simple analytical expression for the transmittance can be obtained. These expressions can easily be extended to all probe wavelengths. In this case, it is helpful to express the results in terms of a change in the optical density (OD). Optical density is defined by $OD = -\log(T)$, where the base 10 logarithm is used. The change in OD is simply $\Delta OD = -\log(T/T_0)$.

To obtain the singlet–singlet excited state cross-section, the instantaneous ($t = 0$) transmittance is measured, using a pulse much shorter than the excited singlet lifetime. The instantaneous change in optical density is then given by

$$\Delta OD(0) = \frac{\alpha_0^p L_{\text{eff}}^e}{2.3} \frac{\sigma_1^p - \sigma_0^p}{\sigma_0^p} \frac{\sigma_0^e F_{e0}}{\hbar\omega_e} \quad (22)$$

From the measured optical density the excited singlet cross-section is then extracted:

$$\sigma_1^p = \sigma_0^p \left[1 + \frac{2.3}{\alpha_0^p L_{\text{eff}}^e} \frac{\hbar\omega_e}{\sigma_0^e F_{e0}} \Delta OD(0) \right] \quad (23)$$

Similarly, by sending the probe pulse through a long delay line that produces a delay time long compared to the excited singlet lifetime ($t \rightarrow \infty$), the optical density $\Delta OD(\infty)$ produced by pure triplet–triplet absorption can be obtained. The physical parameter that can be extracted in this case is

$$\phi_T \sigma_2^p = \sigma_0^p \left[1 + \frac{2.3}{\alpha_0^p L_{\text{eff}}^e} \frac{\hbar\omega_e}{\sigma_0^e F_{e0}} \Delta OD(\infty) \right] \quad (24)$$

To obtain σ_2 uniquely requires an independent assessment of the triplet quantum yield (i.e., branching ratio for the fluorescence and intersystem crossing rates).

Two-photon assisted ESA. At sufficiently high intensities, excited state absorption from a two-photon pumped state can be observed [2]. Under certain conditions it is possible to measure this excited state absorption cross-section in addition to the TPA coefficient.

When the incident pulse width is short compared to the decay time of the two-photon pumped excited state, the number density for the excited state is

given by

$$N_{\text{ex}}(I) = \frac{\beta}{2\hbar\omega} \int_{-\infty}^t I^2(t') dt' \quad (25)$$

An effective (intensity dependent) TPA coefficient can be defined as

$$\beta_{\text{eff}}(I) = \beta + s(I) \quad (26)$$

where

$$s(I) = \frac{\sigma_{\text{ex}} N_{\text{ex}}(I)}{I} \quad (27)$$

To obtain an analytical expression for data analysis, the quantity in Eq. (27) is replaced by its average over space and time:

$$\langle s \rangle = \frac{\int_{-\infty}^{\infty} \int_0^L \int_0^{\infty} s(I) I^2(r, z, t) r dr dz dt}{\int_{-\infty}^{\infty} \int_0^L \int_0^{\infty} I^2(r, z, t) r dr dz dt} \quad (28)$$

As a further approximation, the intensity $I(r, z, t)$ used in finding this average is assumed to be given by TPA alone. Then an effective TPA coefficient parameterized by the incident peak on-axis intensity can be found:

$$\beta_{\text{eff}}(I_0) = \beta \left[1 + \frac{\sigma_{\text{ex}} t_{\text{eff}} I_0}{2\hbar\omega} G(q_0) \right] \quad (29)$$

where $G(q_0)$ is some function of $q_0 = \beta(1 - R)I_0 L_{\text{eff}}$, and t_{eff} is an effective integration time. For example, if $I(t) \sim \text{sech}^2(t/\tau)$, then $t_{\text{eff}} = 2\tau/3$.

An analytical approximation for $G(q_0)$ can be found by first solving for $\langle s \rangle$ exactly (numerically) and then finding a good polynomial fit to the exact curve. Over the range $0 \leq q_0 \leq 3$, the following approximation to third order holds extremely well:

$$G(q_0) \approx 1 - 0.33q_0 + 0.096q_0^2 - 0.012q_0^3 \quad (30)$$

Given the effective TPA coefficient, the nonlinear transmittance can be computed using the formulas given above for TPA. A series of measurements at different incident intensities will yield β_{eff} as a function of I_0 . Fitting these data to Eqs. (29–30) allows the simultaneous extraction of β and σ_{ex} . Figure 1 illustrates how well the approximate effective TPA transmittance matches the exact transmittance for two-photon assisted ESA for different values of the excited state cross-section.

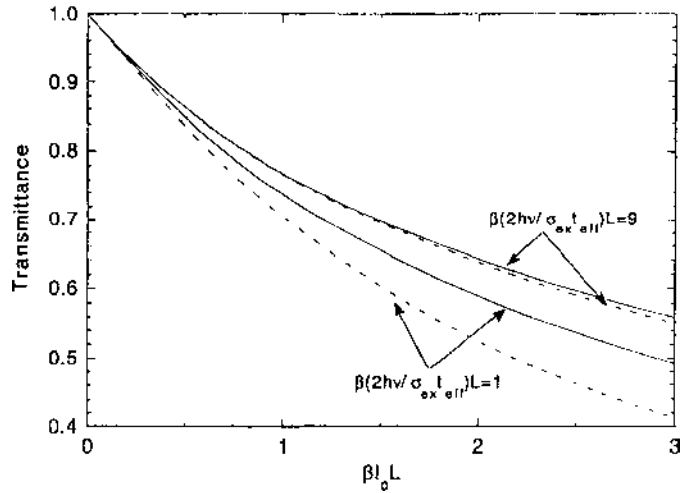


Figure 1 Transmittance as a function of $\beta I_0 L$ for material exhibiting excited state absorption from a two-photon pumped state. The solid line is exact theory, while the dashed line is the approximate model discussed in the text.

B. Experimental

A major objective of a nonlinear transmission experiment is to maximize the ratio $\Delta T/T_0$. Sample, laser, and beam geometry all come into consideration when designing an experiment.

Thick samples offer increased sensitivity for low concentrations of absorbing species and for low intensities [3]. Sometimes low concentrations are unavoidable because of low solubility in available solvents (for solution samples). Low intensities are sometimes desired to avoid complications of excited state absorption from two-photon pumped states. Thick samples require a larger quantity of material, however, and also demand that the laser beam be collimated over a longer distance. This sets a lower limit on the spot size, which in turn limits the incident intensity for a given pulse energy.

With thin samples, one can get by with a much smaller quantity of material, but harder beam focusing is generally required to make up for the decreased path length. Although this makes beam control easier and eases pulse energy restrictions, it makes ESA more likely and potentially presents a laser induced surface damage problem. Thin samples can offer the convenience of high sensitivity with minimal material in some circumstances, however, and are in the form desired for Z-scan measurements. For ease of analysis in the latter case,

the sample should be thin enough that the beam shape within the sample does not change significantly due to diffraction or self-focusing (self-defocusing).

When contemplating lasers for nonlinear transmission experiments, several things should be considered. First, picosecond pulses achieve higher peak intensities at lower energies than nanosecond pulses. This can be important for both sensitivity and damage considerations. The laser wavelength is also important and needs to be chosen depending on the energy of the two-photon allowed states under study, or possibly on the band gap of semiconductors being examined. It is often advantageous to operate the laser at a low pulse repetition rate to avoid sample heating. Thermal effects can cause a blooming of the beam, which under certain circumstances may cause some energy to miss the sensitive portions of detectors due to beam clipping. If not noticed, this will appear to make the material more nonlinearly absorbing than it actually is.

Thick sample experiments. An example of a thick sample experimental diagram is given in Fig. 2. In a thick sample ($\sim 10\text{--}20\text{ cm}$) care must be taken to insure that the laser beam is reasonably collimated over the length of the sample. This requires a confocal beam parameter longer than the sample. For distances farther away from focus than a Rayleigh range, the beam diverges too rapidly to stay well collimated within the sample. Therefore samples this thick are not amenable to Z-scan measurements.

The basic objective of a nonlinear transmission experiment is to measure incident and transmitted laser pulse energies and form their ratio to obtain the sample transmittance. This requires the use of calibrated beam splitters, as shown

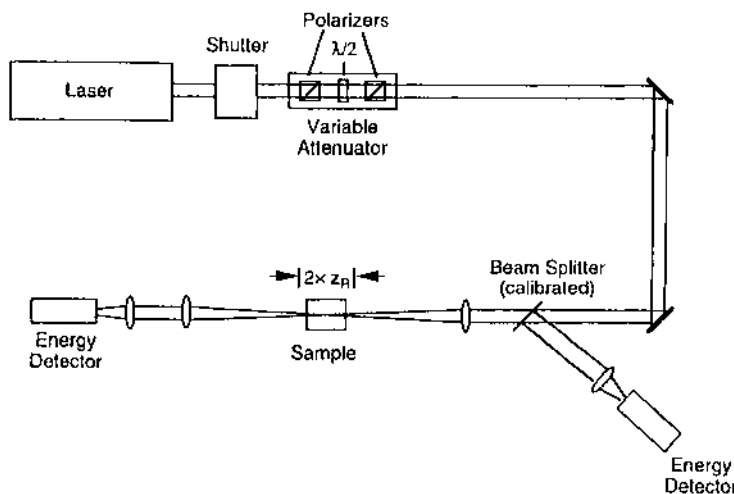


Figure 2 Thick sample nonlinear transmission experiment.

in Fig. 2, to accurately sample the incident and transmitted energies. The front sample surface reflectance must also be known to account properly for the true energy incident in the bulk of the sample. Energy probes (silicon or pyroelectric) or photodiodes calibrated to energy meters are required. Care should be taken to insure that all of the transmitted energy (or a calibrated sample of the beam) is collected by the energy probe. Refocusing lenses or large area ($\sim 1\text{ cm}^2$) probes are generally used for this purpose. Calibrated neutral density filters are sometimes required to keep the probes within their linear operating regime over a wide dynamic range.

In a thick sample experiment, the incident laser energy is varied, and the transmittance found as a function of incident energy. This incident laser energy can be varied by an appropriate attenuator system, such as a half-wave-plate/polarizer combination as shown in the figure.

For ESA and FCA measurements, the on-axis beam fluence is a key parameter. Therefore the beam spatial profile must be characterized. A TEM_{00} Gaussian is usually preferred to facilitate the analysis, although other approaches have been used. For example, Tutt and McCahon [4] used a technique wherein they image the output of the amplifier rod in a Nd:YAG laser onto their sample. This yields an approximate top-hat profile that considerably simplifies the analysis.

For Gaussian beams, the beam profile must be carefully measured. For beam diameters greater than or on the order of $100\text{ }\mu\text{m}$, this is most easily accomplished using a CCD camera coupled to a frame grabber and image digitizer system. Beam analysis software is available that will fit the data to a Gaussian profile and yield statistics about the beam (including the goodness of the fit). The most crucial parameter is the $1/e^2$ beam diameter $2w$ in two orthogonal directions. The on-axis fluence, assuming cylindrical beam symmetry, is then given by

$$F_0 = \frac{2\mathcal{E}}{\pi w^2} \quad (31)$$

where \mathcal{E} is the measured pulse energy.

For smaller beams, a scanning knife edge, slit, or pinhole can be used to characterize the beam. A pinhole scan, in both the x - and the y -direction, yields the most information about the beam. In all cases, the object is mounted on a translation stage and scanned orthogonally to the beam, with an energy probe sampling the transmitted energy. The data can then be fitted to a Gaussian profile to find the $1/e^2$ beam diameter. For slits and pinholes, the size of the aperture should be small compared to the beam size to avoid convolution effects.

In TPA and 3PA experiments, the crucial parameter is the on-axis peak intensity, so the pulse profile and width are required. For nanosecond pulses, a fast photodiode coupled to a wide bandwidth (500–1000 MHz) transient digitizer

(for low repetition rate lasers) or sampling oscilloscope (for high repetition rate lasers) can be used. With picosecond lasers, an autocorrelator or streak camera is required. Often the pulse shape can be approximated by and fitted to either a Gaussian or a sech^2 function. In either case, the full width at half maximum pulse width (t_{FWHM}) is the typical characteristic measured. The on-axis peak intensity is found from

$$I_0 = \frac{4\sqrt{\ln 2} \mathcal{E}}{\pi^{3/2} w^2 t_{\text{FWHM}}} \quad (32)$$

for a Gaussian pulse and

$$I_0 = \frac{2 \ln(1 + \sqrt{2}) \mathcal{E}}{\pi w^2 t_{\text{FWHM}}} \quad (33)$$

for a sech^2 pulse.

An example of nonlinear transmittance data due to two-photon absorption in a thick cell (10 cm) experiment [5] is given in Fig. 3. In this particular case, the sample is a 0.2 M solution of diphenylbutadiene in chloroform, and the incident intensity was kept low enough to avoid two-photon assisted ESA. Note that the solution is dilute enough that the sensitivity of the experiment is low even for this cell thickness.

Examples of nonlinear transmittance data in an ESA experiment [6] are shown in Fig. 4. The sensitivity of ESA experiments, since they couple directly to

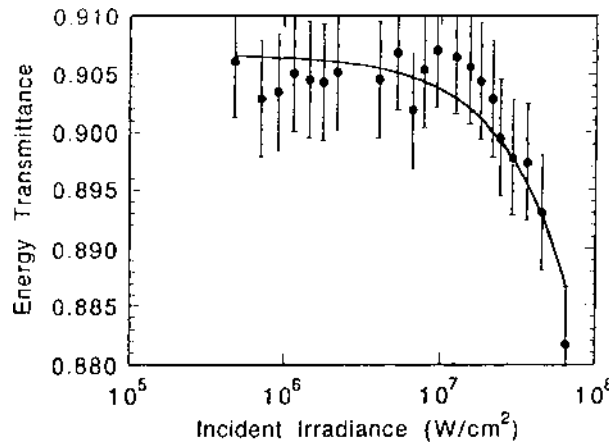


Figure 3 Energy transmittance at 532 nm (10 ns) due to two-photon absorption as a function of incident peak, on-axis irradiance for a 10 cm cell containing a 0.2 M solution of diphenylbutadiene in chloroform. (From Ref. 5.)

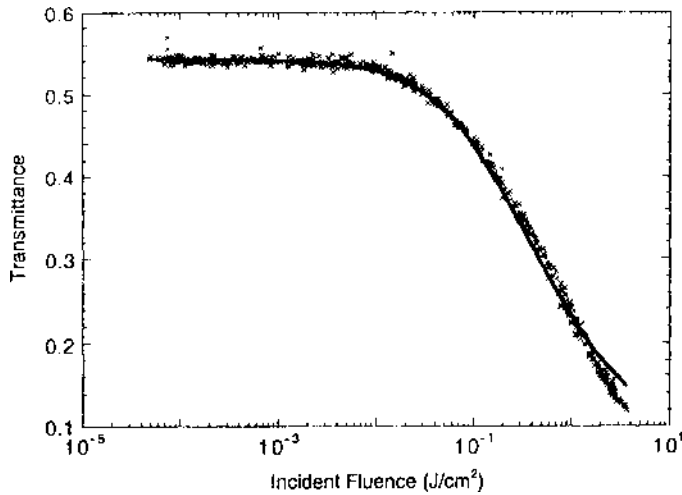


Figure 4 Energy transmittance at 532 nm (30 ps) due to excited state absorption as a function of incident on-axis fluence for a 2.59 mM solution of C_{60} in toluene.

the linear absorption of the material (i.e., basically a two-step resonant process), is much higher, and consequently thinner samples may be used. For the data in Fig. 4, the sample cells were 1 cm thick, even though the solutions were in the millimolar concentration range.

Thin sample experiments. A Z-scan nonlinear transmission experiment for thin samples is illustrated in Fig. 5. Closed aperture Z-scans were discussed in Chapter 7. For nonlinear absorption measurements, an open aperture configuration must be used. In fact, care must be taken that all of the energy is

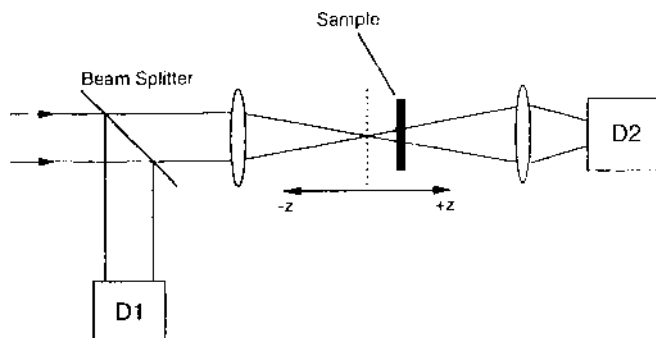


Figure 5 Z-scan experimental setup. (Adapted from Ref. 7. © 1990 IEEE.)

collected by the detector, since Z-scan measurements are very sensitive to nonlinear refractive effects that will spread the transmitted beam. An additional large aperture collecting lens before the detector may be required, especially since nonlinear absorption can produce thermal lensing in some cases, which may lead to strong defocusing of the beam.

The same characterizations of beam and pulse parameters described above are also required for Z-scan measurements. However, since the Z-scan analysis explicitly assumes Gaussian beam propagation, it is important to assure that the incident beam follows this behavior. This can be done by measuring the beam spot size as a function of distance from the focusing lens, on either side of the focal position, and verifying that this follows the $(1 + \zeta^2)^{1/2}$ behavior of a Gaussian beam, as illustrated in Fig. 6. Another check on the Gaussian nature of the beam is to perform a closed aperture Z-scan on a standard Kerr material, such as CS₂, as described in Chapter 7, and measure the distance between the peak and the valley of the normalized transmittance curve. For a Gaussian beam, this distance should be approximately $1.7z_R$ [7]. The Rayleigh range z_R can be determined independently by measuring the $1/e^2$ radius w_0 at focus and applying the formula $z_R = \pi w_0^2 / \lambda$.

An example of open aperture Z-scan data [7] in a TPA material (ZnSe) is given in Fig. 7. The data can be fitted to the equations given above using a single parameter variation to extract β . At high intensities it is possible to observe ESA from a two-photon pumped state [8], as illustrated in Fig. 8. Note that the effective TPA coefficient increases with increasing on-axis peak intensity at the

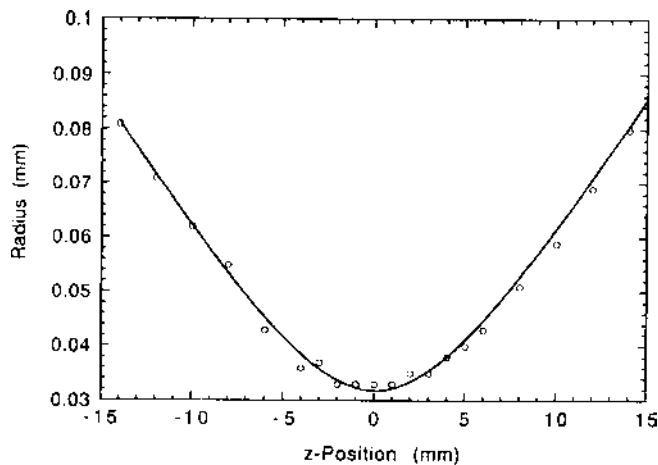


Figure 6 Spot radius ($1/e^2$) of a focused Gaussian beam as a function of position along the axis. The theoretical fit corresponds to the propagation of a Gaussian beam.

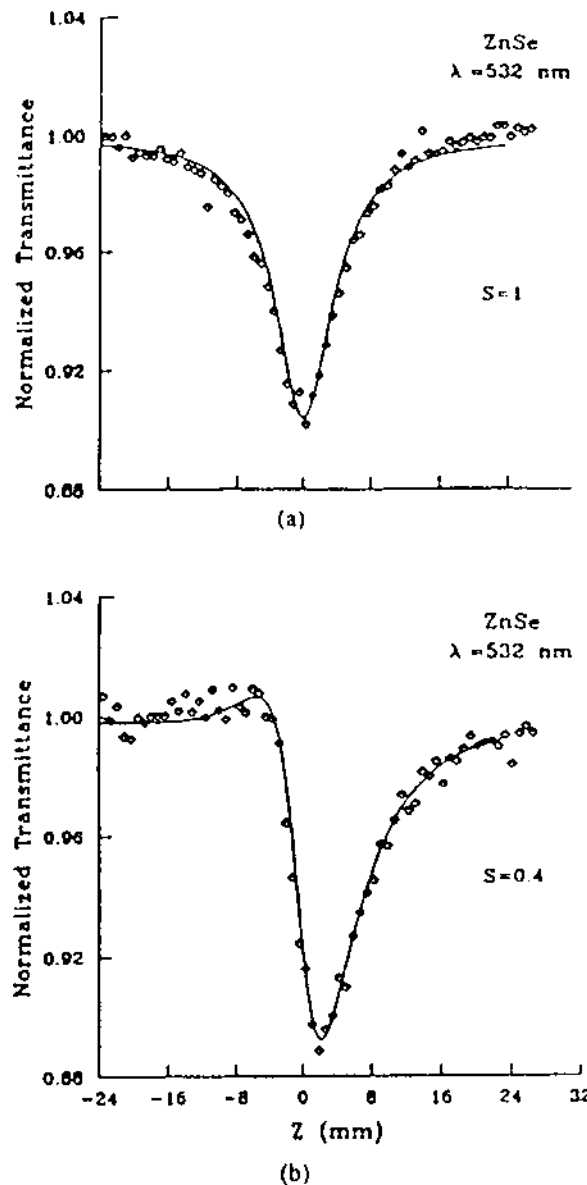


Figure 7 Z-scan data in ZnSe at 532 nm. (a) Open aperture illustrating two-photon absorption. (b) Closed aperture illustrating combined effects of two-photon absorption and nonlinear refraction. (From Ref. 7. © 1990 IEEE.)

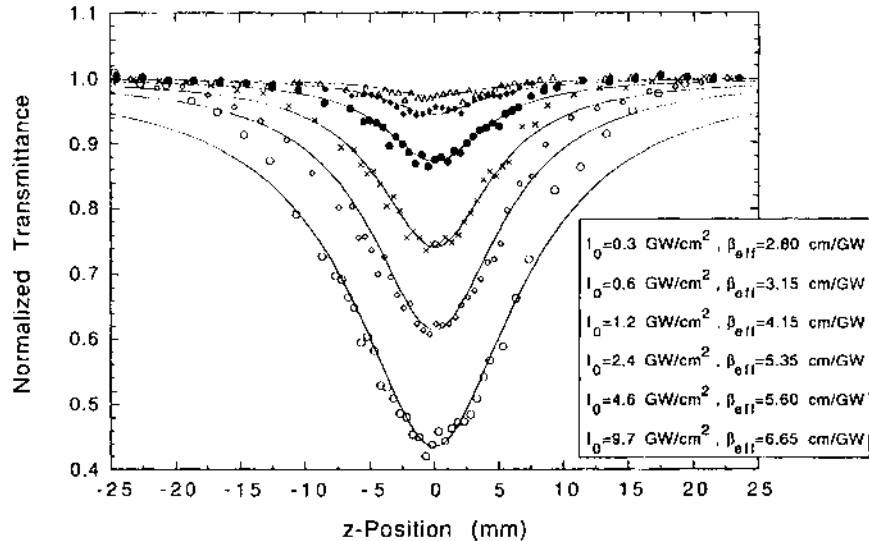


Figure 8 Open aperture Z-scan data at 532 nm (35 ps) in molten diphenylbutadiene at various on-axis peak irradiances illustrating two-photon absorption followed by excited state absorption.

focal position. The sample in this particular case was molten diphenyl-butadiene in a 1 mm thick cell.

An example of pure ESA Z-scan data for a phthalocyanine solution [9] is shown in Fig. 9. ESA is verified by the strict fluence dependence of the nonlinear absorption. For two different pulse widths with identical pulse energy, the Z-scan traces virtually overlap [9]. On the other hand, TPA depends on the peak on-axis intensity and would be different for the two pulse widths. The minimum in the Z-scan trace corresponds directly to the focal position where the on-axis fluence is a maximum. Using Eq. (20), the excited state cross-section can be determined.

Pump-probe experiments. The experiments described above involve single wavelength, single beam techniques. To perform two-photon or excited state spectroscopy, a tunable or broadband source is required. Generally, it is simpler to have one strong pump source at a fixed wavelength to reach the nonlinear regime, and derive the tunable or broadband radiation from a weaker source. This is the basis for pump–probe two-beam experiments.

These types of experiments can be employed for both TPA and ESA studies. The relatively weak probe can be a tunable laser or even narrow spectral band incoherent light derived from a monochromator. An increasingly popular approach, however, is to generate a continuum of frequencies with a short pulse

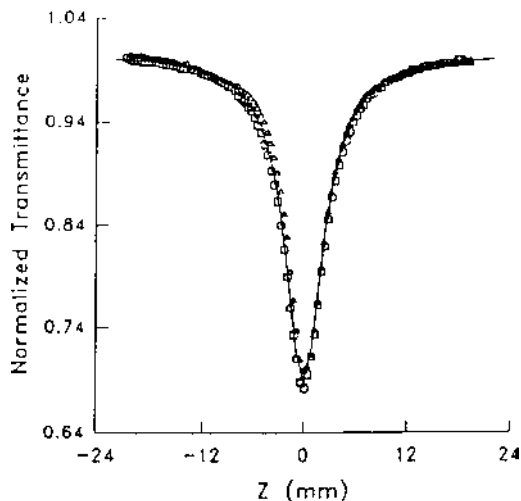


Figure 9 Open aperture Z-scan data at 532 nm in a 1.3 mM solution of chloroaluminum phthalocyanine in methanol illustrating excited state absorption. The squares correspond to 29 ps pulses and the triangles to 61 ps pulses, both at 1.16 μJ . This demonstrates that the nonlinear absorption is strictly fluence dependent, not intensity dependent, and thus ESA, not TPA. (From Ref. 9, Fig. 3, Copyright © Springer-Verlag 1992.)

of light derived from the pump laser [10]. This technique allows a full nonlinear absorption spectrum to be generated on a single laser shot, and offers the potential for observing how the spectrum changes in time after the pump pulse has excited the medium. This white light transient absorption experiment will be described here.

A typical white light pump–probe experiment is illustrated in Fig. 10. The laser system will typically consist of a mode-locked Nd:YAG laser that synchronously pumps a dye laser. A portion of the 1064 nm beam (\sim a few nJ) is directed into a Nd:YAG regenerative amplifier where it is amplified up to approximately 50 mJ at a pulse repetition rate of \sim 10 Hz. The output is frequency doubled and used to pump a dye amplifier (typically three amplification stages). The dye amplifier is used to amplify the output of the dye laser. A gain of $\sim 10^6$ is typical. Hence the final output pulse has an energy of \sim 1–2 mJ with a pulse width of a few picoseconds. In some cases, the pulse can be shortened to a few hundred femtoseconds.

A portion of the pump beam is picked off by a beam splitter and directed to a cell containing water, a heavy water mixture, or perhaps ethylene glycol. The intense short pulse generates a continuum of frequencies, which can cover several hundred nanometers, by the nonlinear process of self-phase modulation [11].

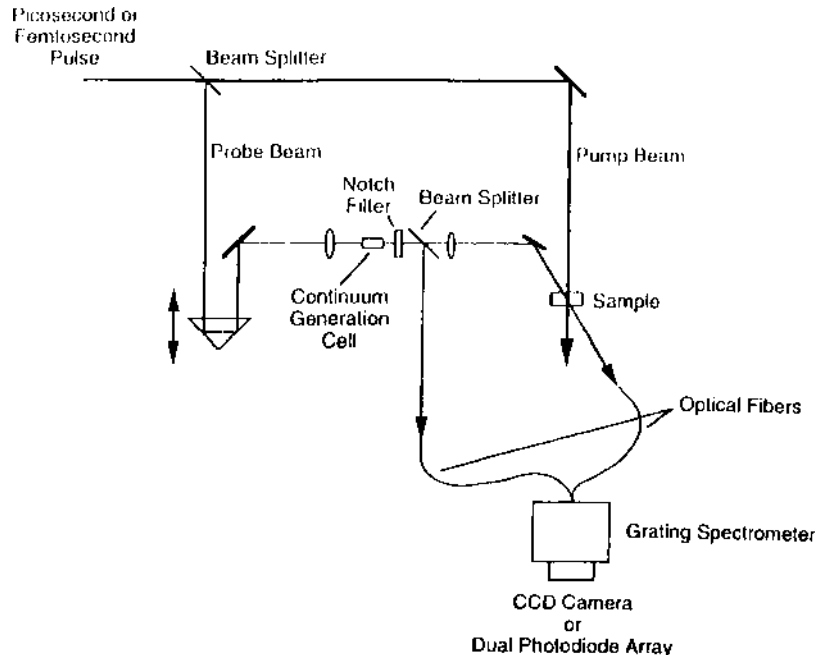


Figure 10 White light continuum pump–probe transient absorption spectroscopy experiment.

This process was discussed in Chapter 6. A notch filter can be placed directly after this white light continuum generation cell to filter out the residual light at the pump frequency.

The probe pulse is sent through an appropriate delay line for time delay experiments. This is better done before the continuum generation to avoid dispersive broadening of the pulse. The pump and probe beams are then made to overlap in the sample. It is usually desired that the probe be smaller in size than the pump to examine a more uniform excitation region [10]. A typical spot size for the pump beam is ~ 100 s of μm . Reflective optics work better for focusing the continuum probe to avoid chromatic aberrations.

A portion of the continuum pulse is split off directly after the white light generation cell and is used as a reference. Both the reference and the beam transmitted through the sample are collected using optical fibers and coupled to a grating spectrometer. Both dispersed beams are then sent to a dual photodiode array or separate locations on a CCD camera. If the beams are registered properly, the wavelength of the spectrum can be correlated to pixel position, and

the strength of the signal at each pixel is proportional to the intensity of light at that wavelength.

By establishing a baseline signal with the sample absent, the two spectra with the sample present can be compared to find the nonlinear spectral transmittance of the sample. With prior knowledge of the linear transmittance of the sample (e.g., from spectrophotometer data), the $\Delta OD(\lambda, t)$ can be computed and used in conjunction with Eqs. (23) and (24) to determine the excited state cross-sections for an ESA experiment. Care should be taken to keep the pump fluence below the saturation fluence so that the approximations used to simplify this analysis remain valid. Also, the probe intensity should be small ($\sim 1\%$) compared to the pump. With further knowledge of the pulse widths and pulse shapes, Eqs. (12–18) can be employed to determine TPA coefficients in a two-photon spectroscopy experiment.

II. THREE-WAVE MIXING

Three-wave mixing (TWM) is an older name for the now traditional coherent anti-Stokes Raman scattering (CARS) [12]. However, the interest is not in the Raman spectra but in the interference between Raman and other two-photon resonant processes. This technique is also very closely related to the nearly degenerate three-wave mixing technique, discussed in Chapter 7, Section 2, which is used for characterizing the third order susceptibility of materials.

In the TWM method, two beams of frequencies ω and $\omega - \Delta\omega$ are made to overlap in the sample and produce a new beam at frequency $\omega + \Delta\omega$. The objective is to measure the intensity of the beam at this new frequency, which is proportional to the absolute square of the third order susceptibility. When coupled with ordinary Raman scattering measurements, the imaginary part of the susceptibility can be found, and hence the TPA coefficient.

The advantages of this technique include its generation of a signal with a low background, in contrast with nonlinear transmissions methods. Since the process is phase matchable, significant signals can be produced, and even cw lasers may be employed if photon counting is used [12]. The phase matching geometry is like that employed in a CARS experiment (see below).

One principal disadvantage of the technique is that the generated signal is often close in frequency to that of the incident lasers. The generated beam must be spatially and spectrally resolved from the much more intense pump beams. Furthermore, the technique requires further knowledge of the real part of the susceptibility and the differential Raman scattering cross-sections for both the solvent and the solution.

A. Theory

For Raman scattering due to one mode energetic enough that only the ground state is significantly populated at room temperature, the Stokes shifted beam intensity is related to the intensity of the incident beam at frequency ω by

$$\frac{I(\omega - \Delta\omega)}{I(\omega)} \propto \text{Im} \left[\frac{A_j}{\Delta\omega - \omega_j - i\Gamma_j} \right] \quad (34)$$

where ω_j is the center frequency of the j th Raman resonance, and $2\Gamma_j$ is the full width at half maximum of the j th Raman resonance, assuming a Lorentzian line shape. The scattering amplitude is given by

$$A_j = \frac{N(d\sigma_j/d\Omega)_{\max}}{12hc\omega_s^4} \quad (35)$$

N is the molecular density, $\lambda_s = 2\pi c/\omega_s$ is the mean scattered wavelength, and $(d\sigma_j/d\Omega)_{\max}$ is the maximum angle dependent absolute differential scattering cross-section for the j th Raman mode, integrated over the scattering frequency.

The parameters ω_j and Γ_j for each resonance can be found by fitting the relative Raman spectra obtained experimentally to the imaginary part of a sum of complex Lorentzians [12]. Raman spectra of the neat solvent and the solution under study are collected. The scattering amplitude A_j for all resonances is scaled to resonances for which $(d\sigma_j/d\Omega)_{\max}$ is known.

In the TWM experiment, with all laser line widths small compared to the widths of Raman resonances, the anti-Stokes line is generated with

$$I(\omega + \Delta\omega) \propto |3\chi_{xxxx}^{(3)}(-\omega - \Delta\omega; \omega, \omega, -\omega + \Delta\omega)|^2 I^2(\omega) I(\omega - \Delta\omega) \quad (36)$$

where $\chi_{xxxx}^{(3)}(-\omega - \Delta\omega; \omega, \omega, -\omega + \Delta\omega)$ is the third order susceptibility governing the process, assuming all beam polarizations are parallel. As discussed in Chapter 7, Section 2, if the generated signal is compared with the TWM signal produced in a reference material (e.g., CS_2), then the susceptibility of the sample is determined by

$$\chi_{xxxx}^{(3)} = \left(\frac{n}{n_{\text{ref}}} \right)^2 \frac{L_{\text{ref}}}{L} \left(\frac{1 - R_{\text{ref}}}{1 - R} \right)^2 \left[\frac{I(\omega + \Delta\omega)}{I_{\text{ref}}(\omega + \Delta\omega)} \right]^{1/2} [\chi_{xxxx}^{(3)}]_{\text{ref}} \quad (37)$$

R is the surface Fresnel reflectance, and L is the thickness of the sample or reference. For ω constant or variable over a small range, for which the variation of the two-photon absorption cross-section σ_2 is negligible, the susceptibility has the following contributions:

$$\chi^{(3)} = \chi_{\text{NR}}^{(3)\prime} + i\chi_{\text{NR}}^{(3)\prime\prime} + \sum_j \frac{A_j}{\Delta\omega - \omega_j - i\Gamma_j} \quad (38)$$

Note that the Raman resonances contribute to the signal as well as ordinary third order susceptibility components, which are nearly resonant at 2ω . The primed component is the real part of this susceptibility and is related to the nonlinear index of refraction (Chapter 6). The TPA coefficient is proportional to the imaginary component given as the double-primed symbol. This latter coefficient will be due only to the solute if the solvent is judiciously chosen to have negligible TPA at the measurement wavelength.

The phase matching condition for the TWM experiment is given by

$$\mathbf{k}(\omega + \Delta\omega) = 2\mathbf{k}(\omega) - \mathbf{k}(\omega - \Delta\omega) \quad (39)$$

The phase matching diagram is illustrated in Fig. 11. If the sample thickness is such that $L < |\Delta\mathbf{k}|^{-1}$, where $\Delta\mathbf{k}$ is the phase mismatch, then collinear phase matching is allowed, as in the case of nearly degenerate three-wave mixing (Chapter 7, Section 2).

TWM data at $\omega + \Delta\omega$ are fitted to Eqs. (36) and (38) by varying $\chi_{\text{NR}}^{(3)}$ and $\chi_{\text{NR}}^{(3)\prime\prime}$. The imaginary part, $\chi_{\text{NR}}^{(3)\prime\prime}$, is determined uniquely by accounting for A_j , ω_j , and Γ_j from independent Raman scattering measurements. The weakest spectral regions occur where the real parts of the solute and solvent susceptibilities nearly cancel, leaving the signal determined primarily by the imaginary part of the susceptibility for the solute [12]. Since these areas contain the most information about $\chi_{\text{NR}}^{(3)\prime\prime}$, the photon counting time should be increased here to keep the signal quality equal to that of the stronger spectral regions. The two-photon cross-section is then given by

$$\sigma_2 = 3\chi_{\text{NR}}^{(3)\prime\prime} \frac{\pi h}{\epsilon_0 n^2 \lambda^2 N} \quad (40)$$

B. Experimental

The experimental setup for this technique is very similar to that shown in Chapter 7, Fig. 11 for nearly degenerate three-wave mixing. Nanosecond lasers may be used, since thermal and electrostriction processes are not expected to

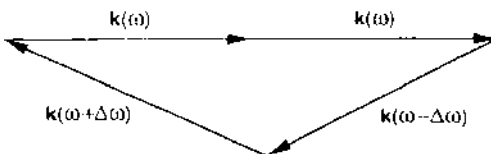


Figure 11 Phase matching diagram for the three-wave mixing two-photon absorption measurement technique.

contribute to the generation of the unshifted frequency. Two different wavelengths must be used. For two-photon spectroscopy using the TWM technique, tunable lasers are normally desired to center the frequencies on specific Raman resonances and to find cancellation of the real parts of the solvent and solute susceptibilities.

The two beams are adjusted to overlap spatially and temporally in the sample. Phase matching can be achieved by adjusting the angles and focusing lenses to maximize the generated signal. If the anti-Stokes shifted frequency is too large for collinear phase matching, then a configuration like that in Fig. 12, from Anderson et al. [12], may be used. This achieves the CARS phase matching as shown schematically in Fig. 11. The beams are lightly focused into the sample or reference to a diameter of the order of a few hundred micrometers.

The sample and reference are irradiated simultaneously in separate beam paths. The two anti-Stokes shifted beams are then separated spatially and passed through a double monochrometer. The output signals are physically separated and detected by PMTs connected to boxcar integrators. When cw lasers of several hundred milliwatts of power are used, long counting times are required. By blocking each beam successively and measuring the residual energy from the other beam, an average background signal can be subtracted from the desired signals. Following background subtraction, average signal energy or intensity values from both the sample and the reference are computed. These values can then be used in Eq. (37) to compute the desired susceptibility.

Before performing the final data fit according to the prescription given in the previous section, Raman spectra from the neat solvent and the solution must be collected in an independent experiment. The same lasers are used, and the Raman signal is collected at an angle of 90° with respect to the incident laser. With care, an accuracy of $\sim 15\text{--}20\%$ in the value of σ_2 may be obtained with the TWM measurement technique over the spectral region desired.

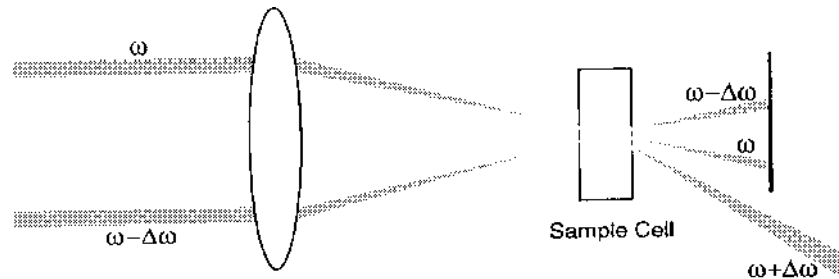


Figure 12 Focusing arrangement for achieving phase matching in the three-wave mixing experiment.

III. TWO-PHOTON FLUORESCENCE

Two-photon fluorescence, or two-photon excitation as it is sometimes called, was one of the earliest forms of two-photon spectroscopy, complementing two-photon absorption spectroscopy. Single photon fluorescence emission from two-photon excited states is measured. Strong fluorescence at a particular frequency indicates strong TPA at one-half that frequency, assuming no frequency shifts in the molecule under study.

The objective of this technique is to measure the two-photon fluorescence intensity (usually by photon counting methods) as a function of the energy of the incident photons. Comparing the fluorescence intensity to that of a reference material allows an estimation of the TPA cross-section σ_2 . The fluorescence spectrum shows the origin of two-photon allowed states ($\sigma_2 \gg 1 \times 10^{-50} \text{ cm}^4 \text{s}/\text{photon-molecule}$). In addition, measurements using incident light of linear and circular polarization allow a determination of the polarization ratio, defined by

$$\Omega = \frac{\sigma_2^{\text{cir}}}{\sigma_2^{\text{lin}}} \quad (41)$$

This ratio gives information regarding the symmetry of excited vibronic states [13].

The advantages of this technique include its convenience for spectroscopy, when tunable laser sources are used. It also allows the measurement of the signal against a low background, in contrast to nonlinear transmission methods. Its disadvantages include a low signal level (photon counting regime), and that some materials have very low quantum fluorescence yields. The quantum yield may also vary with wavelength. Moreover, available calibration methods may result in large errors in the absolute value of the TPA cross-section [14]. These errors are less significant when measuring Ω .

A typical experimental arrangement is shown in Fig. 13 [15,16]. The wavelength of the excitation laser is chosen for the two-photon spectral region desired. If the material under study exhibits strong self-absorption in the UV region, then the laser wavelength must be restricted to the red and near-IR spectral regions. For near-IR wavelengths, a Ti:sapphire laser may be used. Dye lasers are frequently used, however, with cyanines used for IR output, and oxazines for the red spectrum. The laser is usually pulsed to obtain a high peak power for the nonlinear excitation.

The laser is directed and focused into the sample. A tight focus is normally used, such that the sample length is much greater than the laser confocal parameter. This avoids strong two-photon excitation or fluorescence of the sample windows. The fluorescence emission is collected at 90° with respect to

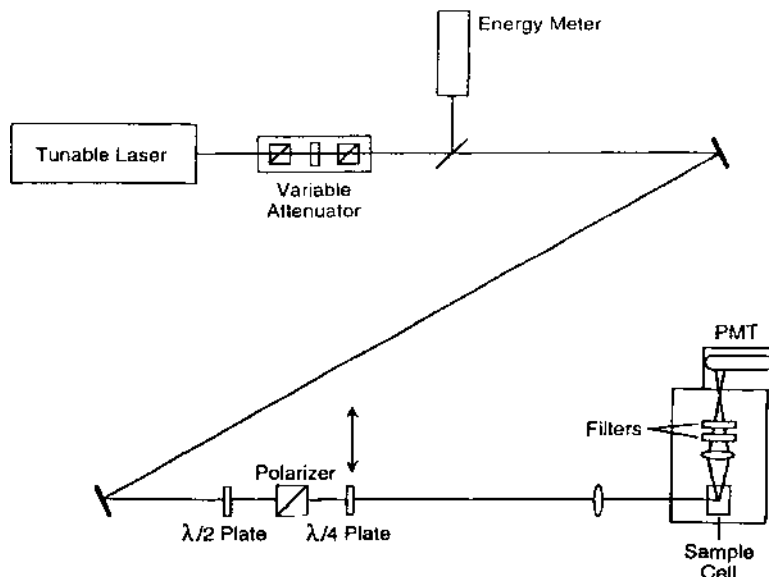


Figure 13 Two-photon fluorescence experimental setup.

the incident laser beam, with the collection volume restricted to the center of the sample. Red and near-IR filters are used to attenuate any linearly scattered laser energy, and the fluorescence is detected with a PMT (photomultiplier tube). (Often, the light incident on the PMT is defocused to avoid saturation of the tube.)

An identical reference arm is set up to calibrate the system, and the measurement of the fluorescence is compared to the reference to obtain the TPA cross-section. The reference is a well-characterized two-photon absorber (e.g., sodium fluorescein in water [16]). The incident laser energy and pulse waveform are measured to obtain the incident excitation intensity. The output of the PMT is amplified and the peak height, assumed proportional to the fluorescence intensity, is measured. Normally, an average of ≥ 10 shots is obtained.

To verify that the signal is due to two-photon fluorescence, a plot of $\log(I_F)$ vs. $\log(I_L)$ is generated at several representative wavelengths, where I_F and I_L are the fluorescence and laser intensities, respectively. A slope of 2 in these plots indicates that the signal is due to two-photon excitation [15–17]. Finally, a plot of $\ln(I_F/I_L^2)$ as a function of wavelength yields the two-photon excitation spectrum [17–19], and a comparison of these data with the reference will yield an estimation of σ_2 at each wavelength.

A combination of polarizers, half-wave plates, and quarter-wave plates in the laser beam allows for polarization studies. After measuring σ_2 , for both linear

and circular polarization, the polarization ratio Ω is obtained. A value of $\Omega = 3/2$ must be obtained for a transition to a vibronic state of B_g symmetry, and less than $3/2$ for an A_g state [16].

IV. PHOTOTHERMAL METHODS

Some, if not most, of the energy absorbed through either a linear or a nonlinear process is converted to heat. This internal change in energy of the material is measurable either as a direct change in temperature or in an optical property that depends on temperature. Thus temperature changes can be related back to absorption coefficients. Two photothermal methods for measuring nonlinear absorption are considered here. One monitors changes in the refractive index of the material due to temperature excursions, while the second one involves a direct measurement of the temperature change.

A. Thermal Blooming

Thermal contributions to the nonlinear refractive index were discussed in Chapter 6. Energy absorbed by the medium from an optical beam with a symmetric radial profile and a peak intensity or fluence on-axis produces a radially symmetric temperature distribution. A radial index profile results from this temperature gradient. The ensuing distortion of the beam is called thermal lensing. Normally, the change in index is negative for a rise in temperature, and the lensing induced is like that of a defocusing lens. The beam expands in both the near and the far field as a result, and the phenomenon has been referred to as thermal blooming.

For small temperature changes in the medium at the focus of a laser beam, changes in the far-field intensity distribution can be observed. Thus thermal blooming was developed as a sensitive technique for measuring small linear absorption in materials [20]. Long et al. [21] further developed a two-beam pump–probe thermal blooming method. A strong pump beam with a tunable wavelength was used to measure the spectral absorption of a material, while a weak fixed wavelength beam was used to monitor the thermal lens that developed. Twarowski and Kliger [22] subsequently extended this two-beam method to the case of m -photon absorption.

The objective of a thermal blooming experiment is to induce a thermal lens in a material by nonlinear absorption (e.g., TPA) from a strong pump beam, and then monitor changes in the on-axis intensity of a probe beam in the far field. The changes in the far-field intensity can be related to the nonlinear absorption coefficient in the medium. The advantages of this technique are that it involves a simple experimental setup, and that experimental conditions related to

assumptions and approximations in the theory of the measurement are easily satisfied. The far-field intensity is sensitive to the nonlinear absorption and can easily be detected. Disadvantages include the alignment and overlap of the common focus of two beams of different wavelengths. Additional thermal parameters of the material must also be known or measured to calibrate the experiment. Also, the quantum fluorescence yield must be measured if it is too large to be neglected.

Theory. The optical configuration of the sample for a thermal blooming experiment is shown in Fig. 14. The sample is situated near the focus of the lens, and an aperture in the far field limits the amount of transmitted light that reaches a detector. The experimental setup is very similar to the Z-scan technique discussed in Chapter 7.

Several assumptions are required in the theory of this measurement [22]. First, the fraction of light absorbed is assumed to be small enough that the light absorbed per unit length is constant over the sample path. A thin sample is assumed such that the radius of the pump beam is also approximately constant over the sample path. Since the amount of light absorbed is small, it is assumed that the temperature change is also small ($\Delta T \ll 1$) so that an approximate expansion of the refractive index with temperature can be used: $n(T) \approx n_0 + (dn/dT)\Delta T$. Both pump and probe beams are taken to be TEM₀₀ Gaussian modes, and the pinhole aperture in the far field is small compared to the far-field probe beam $1/e^2$ radius. The distance d to the aperture is larger than the induced focal length in the sample, and the aperture is definitely in the far field ($d \gg z_R$, where z_R is the Rayleigh range of the focused probe beam).

For m -photon absorption, the maximum change in the time dependent on-axis probe intensity occurs when the sample is placed at the position $z' = -2(2m+1)^{-1/2}z_R$, where the origin $z=0$ is taken to be at the waist of the common beam focus [22]. With the pump pulse centered at time $t=0$, and its pulse width small compared to the thermal time constant of the medium,

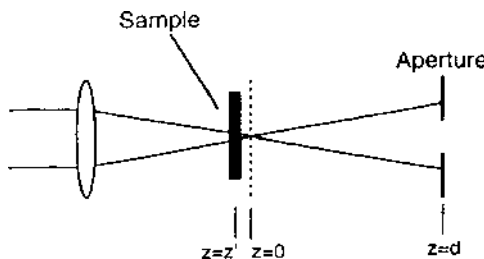


Figure 14 Thermal blooming experimental geometry.

the relative change in the on-axis far-field probe intensity from $t = 0$ to $t = \infty$ is given by [22]

$$\frac{I_p(d, 0) - I_p(d, \infty)}{I_p(d, 0)} \simeq \frac{2^{m+3} m^2}{\sqrt{2m+1}} \left(\frac{2m+1}{2m+2} \right)^{m+1} \frac{dn}{dT} \frac{LD\sigma_m hcH}{\pi^{m-1} w_{0e}^{2m} k_T \lambda_e^2} \quad (42)$$

where L is the sample thickness, D is the thermal diffusivity of the sample, σ_m is the m -photon absorption cross-section, h is Planck's constant, c is the speed of light, k_T is the sample thermal conductivity, λ_e is the pump (excite) beam wavelength, and w_{0e} is the radius of the pump beam waist. H is a quantity defined by

$$H = \left(\frac{\lambda_e}{hc} \right)^m \int [\mathcal{P}(t)]^m dt \quad (43)$$

where $\mathcal{P}(t)$ is the instantaneous pump power. For a Gaussian-shaped pump pulse of energy \mathcal{E} , $H = (\pi/m)^{1/2} (\lambda_e/hc)^m \tau (\mathcal{E}/\pi^{1/2} \tau)^m$ with τ the 1/e half-width of the pulse. The m -dependent prefactor in Eq. (42) has a value of 33.1 for $m = 2$ (TPA), and 127.6 for $m = 3$ (3PA). Once the relative change in on-axis intensity at the far-field $z = d$ has been measured, Eq. (42) can be inverted to find σ_m .

Experimental. A typical experimental configuration is illustrated in Fig. 15 [23]. Care should be taken with respect to the geometry of the experiment and the conditions of the sample so that all of the assumptions listed in the theoretical discussion above are satisfied.

The pump laser is usually tunable (e.g., a dye laser) to obtain the m -photon spectrum of the sample. The probe laser is preferably a cw laser with a fixed

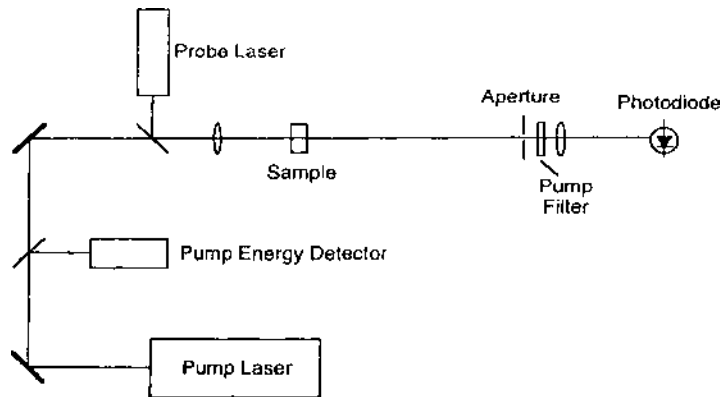


Figure 15 Thermal blooming experimental arrangement for measuring nonlinear absorption.

wavelength to facilitate timing synchronization with the pump and a constant probe focus. Both beams are focused into the sample at the same spot with comparable beam sizes. Suitable probes monitor the incident pump and transmitted probe pulses. The incident pump energy is also measured. Finally, a filter is in place at the far-field probe detector to selectively attenuate the pump signal to an acceptably low value. The time dependent probe signal transmitted through the far-field aperture is captured and digitized.

With the probe signal captured, a plot of the quantity $\{I_p(t)/[I_p(t) - I_p(\infty)]\}^{1/2}$ vs. t should yield a straight line. The slope of this line is $t_{th}/2m$, where $t_{th} = w_e^2/4D$ is the thermal time constant of the sample. Thus a measurement of this slope will yield the thermal diffusivity D of the sample [23].

A plot of the quantity $[I_p(0) - I_p(\infty)]/I_p(0)$ vs. \mathcal{E} should be quadratic for TPA [23]. This will be true if the temporal profile of the pump pulse is constant from pulse to pulse. Once this quantity is measured, Eq. (42) is inverted to obtain the two-photon cross-section σ_2 .

Fang et al. [24] have extended these techniques with the use of sync-pumped picosecond dye lasers. Although these lasers have a low peak power, their high repetition rate results in an integration of TPA by the individual picosecond pulses due to the relatively slow thermal decay in the medium. The low peak power also ensures that competing nonlinear effects (e.g., the Kerr effect) are absent. The high pulse-to-pulse stability of sync-pumped dye lasers results in a high signal-to-noise ratio for the detection of far-field intensity changes. Chopping the beam also allows for sensitive phase detection schemes like those used in ordinary linear photothermal measurements. A single photon transition in the material can also be used to calibrate the measurement of σ_2 [24]. The experimental configuration is similar to that described above. The pump laser beam is chopped, however, and the probe laser intensity is monitored using a lock-in amplifier.

B. Laser Calorimetry

The laser calorimeter is a device developed to measure small absorption in samples. This instrument is capable of detecting absorptions less than one part in 10^5 using a 1 W laser (linear absorption) [25]. When TPA is present, the calorimeter can be used to measure the total absorption (linear plus nonlinear) and hence determine the TPA coefficient. The advantage of this technique is that it measures a large change (the added absorption due to TPA) in a small quantity (total absorption). Its chief disadvantage is that care must be taken to ensure that the sample is thermally isolated from its surroundings to avoid thermal losses that introduce inaccuracies into the measurement. This complicates the experiment.

A typical experimental setup is shown in Fig. 16 [25]. The sample, in an evacuated chamber, is fitted with a thermocouple probe to monitor temperature

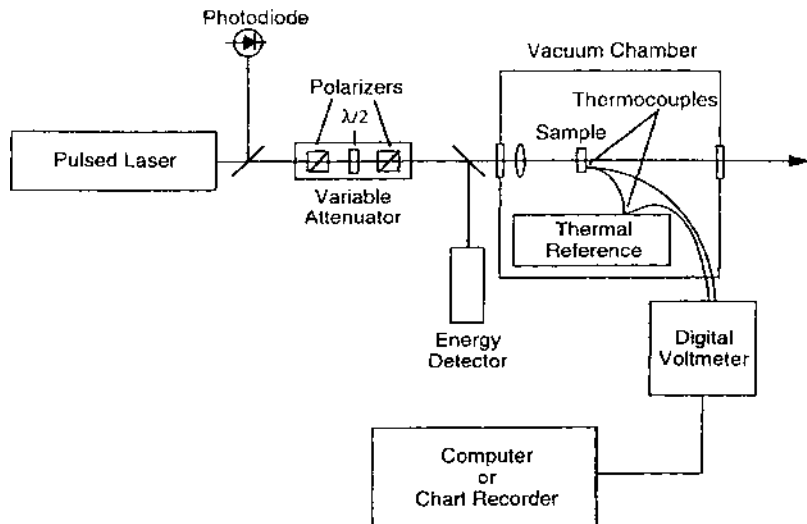


Figure 16 Experimental setup for a laser calorimetry measurement of two-photon absorption. (Adapted from Ref. 25.)

changes. A chart recorder or digitized voltage signals can be used to monitor the temperature rise of the sample due to a sequence of incident Q-switched pulses. The calorimeter responds to the total average power absorbed. The incident pulse energy, pulse width, and spot size are also recorded to obtain the peak on-axis intensity.

For small total absorption [i.e., $(\alpha + \beta I)L \ll 1$], the total absorption as a function of incident intensity will be a straight line. The vertical intercept yields α , while β is determined by the slope [25]. For high index materials, reflection from the rear surface of the sample can significantly affect the computed absorption coefficients. Bass et al. [25] describe a numerical computation technique to account for this in the data, assuming only a single rear surface reflection.

V. DEGENERATE FOUR-WAVE MIXING

Degenerate four-wave mixing (DFWM), described in Chapters 6 and 7, has been developed for characterizing the third order susceptibility of materials. As discussed in Chapter 7, the standard DFWM technique only measures the modulus of $\chi^{(3)}$. However, it was shown in a set of experiments on diphenyl polyenes that TPA produces a double peak response in the phase conjugate signal

produced by nanosecond pulses [26]. A theoretical analysis of this effect reveals that the minimum between the two peaks of the pulse does not go to zero if the imaginary part of the susceptibility is nonzero. At the particular point in time when this minimum occurs, the phase conjugate signal is due to scattering of the pump beams from a pure two-photon absorption grating [26].

The objective of the DFWM technique with nanosecond pulses, for measuring TPA, is to monitor the signal at the minimum between the two peaks of the phase conjugate pulse as a function of pump energy. The phase conjugate reflectance from this pure amplitude grating will be proportional to the imaginary part of $\chi^{(3)}$, which is of course proportional to β .

This technique has several advantages in its favor. First, it utilizes the standard DFWM experimental method. The generated signal is strong and easy to detect, i.e., energy probes can be used instead of the photomultiplier tubes required in fluorescence techniques. It measures a large signal relative to a weak background in contrast to nonlinear transmission methods. The experiment is calibrated in the usual way with a nonabsorbing nonlinear material (e.g., CS₂). Finally, as discussed in Chapter 7, the real part of the susceptibility can also be obtained from the same data. Its chief disadvantage lies in the pulse detection and monitoring using a streak camera, as described below.

A. Theory

The theory of DFWM was given in Chapter 6. The process may be examined in terms of real-time holography. In this picture, the interference of the probe and the two pump beams (forward and backward pumps) writes gratings in the medium due to its nonlinear refractive index. This produces a scattering of the pump beams in the direction of the conjugate beam, counterpropagating to the direction of the probe beam. Since $\chi^{(3)}$ is complex, in general, these gratings consist of a combination of phase and amplitude gratings. The amplitude grating depends on the imaginary part of $\chi^{(3)}$ and thus on the TPA coefficient β .

Strong TPA will modify the linear optical properties of the medium. The cascading of third order optical properties like TPA with linear optical properties (e.g., the index of refraction) yields an effective fifth order nonlinear process. The spatial dependence of these optical modulations is determined by the interfering optical fields. Hence additional TPA induced optical gratings will be superimposed on the usual gratings present in the DFWM experiment.

These new gratings are assumed to be pure phase gratings and also scatter the pump beams in the direction of the phase conjugate [5]. Thus the signal measured carries information about the TPA induced gratings as well as the ordinary $\chi^{(3)}$ gratings of the medium. The dynamical processes associated with the formation of these gratings have finite decay times. Two possibilities have been considered: population gratings (creation of excited species) and thermal

gratings [5]. For optical pulses with pulse widths short compared to these decay times, the time dependence of the induced optical modulation is independent of the particular type of induced grating (i.e., population or thermal).

Assuming Gaussian-shaped pulses (usually valid for Q-switched nanosecond lasers), the time dependence of the index modulation due to TPA induced processes can be analytically determined. A time dependent phase conjugate reflectance is defined by

$$R(t) = \frac{I_c(t)}{I_{p0}} \quad (44)$$

where $I_c(t)$ is the time dependent conjugate wave intensity and I_{p0} is the peak value of the time dependent probe intensity. The conjugate reflectance then depends on the pump energy $\mathcal{E}_{\text{pump}}$, which is assumed equal in each pump beam and is given by [5]

$$\begin{aligned} R(t) = & \left(\frac{6L}{\sqrt{\pi}\epsilon_0 n^2 c \lambda w^2 \tau} \right)^2 (\{\chi_R^{(3)}[G(t) + A\mathcal{E}_{\text{pump}}H(t)]\}^2 \\ & + \{\chi_I^{(3)}G(t)\}^2) G(t) \mathcal{E}_{\text{pump}}^2 \end{aligned} \quad (45)$$

In this expression, L is the sample thickness, w is the $1/e^2$ beam radius, and $G(t)$ is the pulse shape given by

$$G(t) = \exp[-(t/\tau)^2] \quad (46)$$

with τ the pulse $1/e$ half-width. $\chi_R^{(3)}$ and $\chi_I^{(3)}$ are the real and imaginary parts of the third order susceptibility, and

$$H(t) = \left(\frac{\sqrt{\pi}\tau}{\sqrt{8}} \right) [1 + \operatorname{erf}(\sqrt{2}t/\tau)] \quad (47)$$

with

$$\operatorname{erf}(x) = \frac{2}{\sqrt{\pi}} \int_0^x \exp(-u^2) du \quad (48)$$

being the error function.

The parameter A in Eq. (45) depends on several experimental parameters, and $R(t)$ will have a minimum within the laser pulse profile if A is negative. The temporal position t_{\min} of this minimum is given by the solution of the equation

$$G(t) + A\mathcal{E}_{\text{pump}}H(t) = 0 \quad (49)$$

and is thus a function of the pump energy. By measuring t_{\min} as a function of $\mathcal{E}_{\text{pump}}$, the parameter A may be determined.

Now, by the definition of t_{\min} ,

$$R(t_{\min}) = BG^3(t_{\min})\mathcal{E}_{\text{pump}}^2 \quad (50)$$

where

$$B = \left(\frac{6L\chi_l^{(3)}}{\sqrt{\pi}\epsilon_0 n^2 c \lambda w^2 \tau} \right)^2 \quad (51)$$

The parameter B can be obtained by measuring $R(t_{\min})$ as a function of pump energy and fitting the data to Eq. (50). The measurement can be calibrated by measuring the peak conjugate reflectance of a standard material (e.g., CS_2) that does not exhibit TPA and hence has a single peak phase conjugate pulse. For the reference material,

$$R_{\text{ref}}(0) = B_{\text{ref}}\mathcal{E}_{\text{pump}}^2 \quad (52)$$

The imaginary part of the susceptibility is then found from

$$\chi_l^{(3)} = \sqrt{\frac{B}{B_{\text{ref}}}} \left(\frac{n}{n_{\text{ref}}} \right)^2 \left(\frac{L_{\text{ref}}}{L} \right) |\chi_{\text{ref}}^{(3)}| \quad (53)$$

where the subscript ref always refers to a reference quantity. Finally, the TPA coefficient is related to $\chi_l^{(3)}$ by

$$\beta = \frac{3\pi\chi_l^{(3)}}{\epsilon_0 n^2 c \lambda} \quad (54)$$

With the imaginary part of the susceptibility and the parameter A thus determined, the pulse shape can be fitted to Eq. (45) to determine the real part of the susceptibility. This was discussed in Chapter 7.

B. Experimental

The DFWM experimental technique for measuring $\chi^{(3)}$ was described in Chapter 7. The experimental method described here utilizes a setup similar to that shown in Fig. 17 [5]. The light source in this case is a seed-injected Q-switched laser producing smooth nanosecond pulses. The shutter selects pulses for the experiment at a < 1 Hz rate to avoid cumulative pulse effects. The polarizer/half-wave plate combination sets the total energy in the pump and probe beams, while the actual beam energies are then determined by calibrated beam splitters in the experiment. Probe and conjugate pulse energies are measured with calibrated energy meters.

The theory given in Section A above assumes plane waves of infinite extent, whereas the experiment employs finite beams with Gaussian spatial

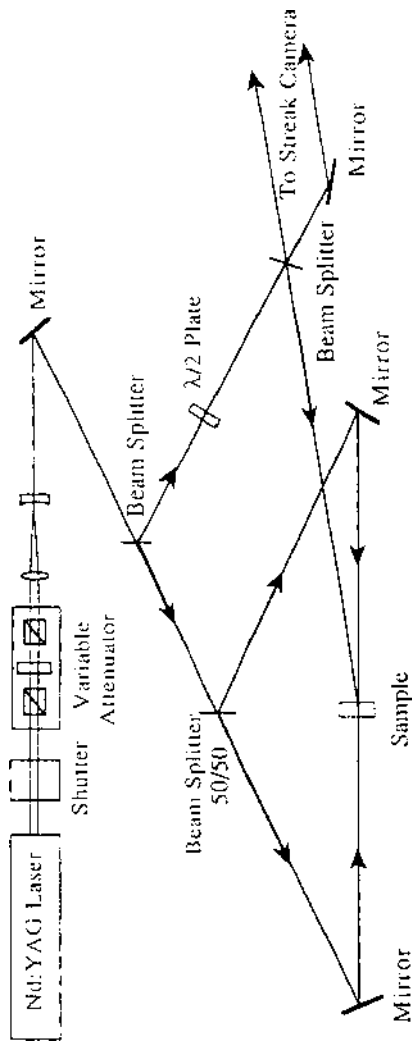


Figure 17 Degenerate four-wave mixing experiment for measuring two-photon absorption. (From Ref. 5.)

profiles. Since the phase conjugate beam is due to a superposition of third order and effective fifth order effects, its temporal profile is dependent on the local intensity. Each space point of the beam will have its own temporal profile, although this will vary only as a function of the radial coordinate, since the beam has axial symmetry. To obtain good agreement with the theory, the on-axis temporal profiles of the probe and phase conjugate beams must be compared, for both the sample and the reference. This comparison requires a good registration of the temporal and spatial profiles of both beams, which can be obtained by the method described below.

Probe and phase conjugate beams are directed to a streak camera as illustrated in Fig. 18. The beams are first centered on the streak camera slit and are individually attenuated to produce comparable amplitude streaks and prevent saturation of the streak camera photocathode. The voltage signals obtained from the streak camera are then referenced to the pulse energy measurements. To obtain the necessary time and space references, the probe polarization is set orthogonal to the polarization of the pump beams, and the streaks for the probe and phase conjugate beams are recorded. This is done each time the pump energy is changed. Under these conditions no TPA induced gratings can be written in the sample, and the phase conjugate signal is due only to the $\chi_{yyx}^{(3)}$ component of the susceptibility [5]. Thus the time and space dependencies of the phase conjugate signal show a smooth, single peak behavior. This allows the on-axis spatial and peak temporal positions of both beams to be uniquely determined and registered, as illustrated in Fig. 19 [5]. With these signals recorded and stored in computer memory, the probe polarization is again set parallel to the pump polarization, and measurements are repeated at the same pump energy. The same procedure is used for measurements of the reference material.

The first part of the data analysis is to determine t_{\min} as a function of E_{pump} . With the probe and phase conjugate signals temporally and spatially registered, the time pixel associated with t_{\min} is located by striking a horizontal line through

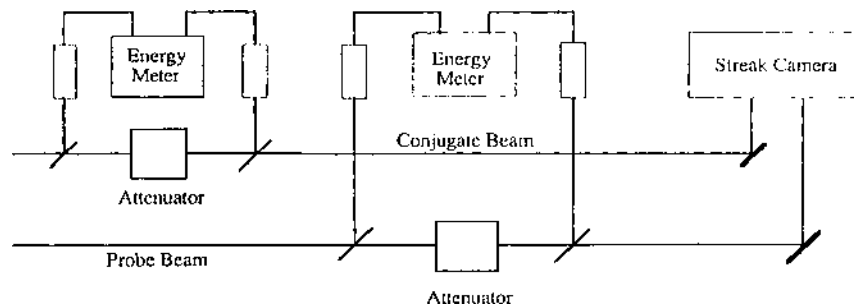


Figure 18 Streak camera setup for the DFWM experiment shown in Fig. 17.

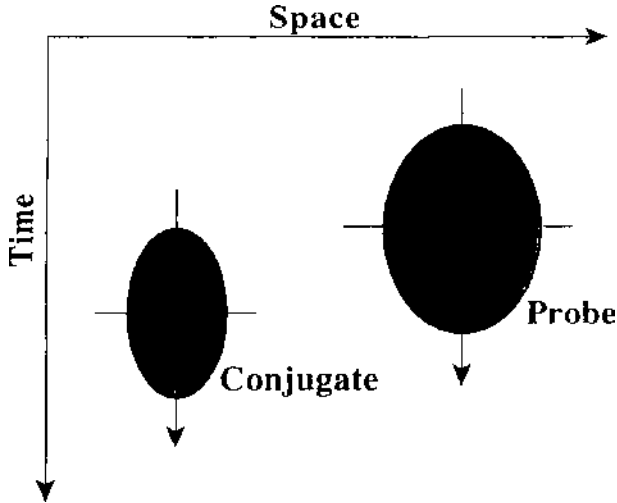


Figure 19 Illustration of the probe and phase conjugate streaks in the experiment of Figs 17 and 18, illustrating the time and space registration of the peak on-axis signals. (From Ref. 5.)

the temporal waveform and seeking the minimum signal voltage level for which the line intersects the waveform at three points. The middle intersection point is identified as t_{\min} [5]. Fitting a plot of t_{\min} as a function of $\mathcal{E}_{\text{pump}}$ to the solution of Eq. (49) yields the parameter A . With this parameter determined, a pump energy dependent t_{\min} can be determined to obtain $G(t_{\min})$ for the later data analysis. This allows a smoother fit of data for $R(t_{\min})$.

To determine the parameter B from Eq. (50), the voltage signal levels must be calibrated against the pulse energy measurements. Since the beams are centered on the camera slit, the streak camera integrates the beam over the slit width Δy . The recorded signal $S(x, t)$ is proportional to the beam intensity

$$S(x, t) = b\Delta y I(x, 0, t) \quad (55)$$

where b is a constant and $I(x, y, t) \approx I(x, 0, t)$ over the narrow slit width. Assuming axial symmetry for the beam implies that

$$b = \frac{2\pi}{\mathcal{E}\Delta y} \int_{-\infty}^{\infty} \int_0^{\infty} S(x, t) x dx dt \quad (56)$$

The integration can be performed numerically with

$$\begin{aligned} & \int_{-\infty}^{\infty} \int_0^{\infty} S(x, t) x dx dt \\ & \approx \frac{1}{2} \Delta x_{\text{pixel}} \Delta t_{\text{pixel}} \sum_{x-\text{pixels}} \sum_{t-\text{pixels}} S(x - x_0, t - t_0) |x - x_0| \end{aligned} \quad (57)$$

where (x_0, t_0) are the pixels defining the origin.

Now

$$R(t_{\min}) = \frac{I_c(0, 0, t_{\min})}{I_p(0, 0, 0)} \approx \frac{b_p}{b_c} \frac{S_c(x_0, t_0 + t_{\min})}{S_p(x_0, t_0)} \quad (58)$$

With $R(t_{\min})$ determined by Eq. (58), this quantity is then plotted as a function of pump energy. The data are then fitted to Eq. (50) to determine the parameter B . An example of these data for a solution of diphenyl butadiene in chloroform is given in Fig. 20 [5]. Similar procedures are used to find B_{ref} for the reference measurement. Then Eqs. (53) and (54) may be used to find the imaginary part of the susceptibility and hence β .

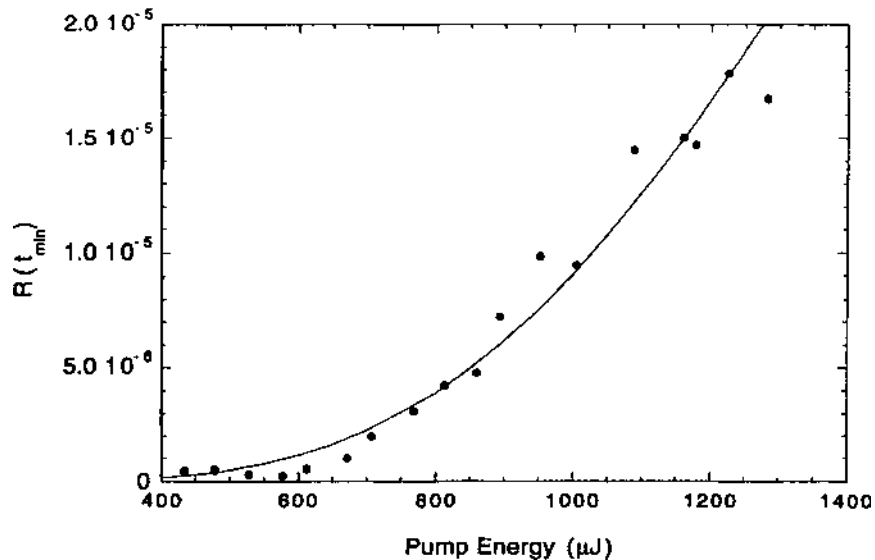


Figure 20 $R(t_{\min})$ as a function of pump energy in the measurement of TPA by DFWM. (From Ref. 5.)

C. Picosecond Measurements

The experiment described in the two sections above requires the use of nanosecond pulses. This is because the TPA induced phase gratings that interfere with the ordinary $\chi^{(3)}$ gratings take time of the order of nanoseconds to develop. Thus at some point in time the TPA induced gratings cancel the ordinary phase gratings, leaving only the contribution to the phase conjugate signal from the pure TPA amplitude gratings.

In a solution, it is also possible to get a cancellation of the pure phase gratings due to the solvent and solute having real hyperpolarizabilities of opposite sign [27]. Then the cancellation is good over the whole pulse, even in the picosecond case, and occurs at a particular concentration of the solute. This can be seen in the full expression for the effective susceptibility of a solution:

$$|\chi_{\text{eff}}^{(3)}| = f^4 [(N_{\text{sv}}\gamma_{\text{sv}} + N_{\text{sl,r}})^2 + (N_{\text{sl}}\gamma_{\text{sl,i}})^2]^{1/2} \quad (59)$$

In this expression, the subscripts sv and sl stand for solvent and solute, respectively. N represents the concentration (number density) and γ the second hyperpolarizability of the solvent and solute. The subscripts r and i signify real and imaginary parts, respectively, and f is the local field factor (see Chapters 6 and 7). It is assumed that the imaginary part of the solvent hyperpolarizability is zero, i.e., the solvent exhibits no appreciable TPA. Note that if the real parts of the solvent and solute hyperpolarizabilities have opposite signs, they will cancel each other at some concentration. Then the phase conjugate signal will be due to the imaginary part of the solute hyperpolarizability alone.

The objective of this method then is to perform an ordinary DFWM experiment, as described in Chapter 7, using picosecond pulses, and measure the effective susceptibility as a function of concentration. These data are fitted to Eq. (59). Normally it will be possible to assume that the solvent number density remains approximately constant. This is true if the solute hyperpolarizability is much larger in magnitude than that of the solvent. The minimum in the curve that fits the data will yield the imaginary part of the second hyperpolarizability of the solute [28].

The advantage of this technique lies in its simplicity, i.e., it is a standard $\chi^{(3)}$ characterization method and enjoys all of the advantages of that method. Its chief disadvantages are that it requires several lengthy measurements for different sample concentrations (which may be limited by solubility problems) and that it requires that the real parts of the solvent and solute hyperpolarizabilities have opposite signs, which may not be known *a priori*.

VI. HETERODYNED KERR EFFECT MEASUREMENTS

Optical Kerr effect measurements for characterizing the nonlinear refractive index were described in Chapter 7. Actually, in such an experiment, only the modulus of the third order susceptibility is measured. If the material has a substantial imaginary component of the susceptibility, then nonlinear dichroism (related to TPA) as well as nonlinear birefringence (related to the nonlinear index) will contribute to the signal measured. In ordinary Kerr effect measurements, there is no way to separate the real and imaginary parts of the susceptibility and uniquely characterize them.

Orczyk et al. [29] developed an optical heterodyned measurement technique that allows this separation to be performed. The method employs a local oscillator beam that mixes with the Kerr effect signal. Appropriate optical phase adjustments between this local oscillator and the nonlinear response of the medium may be used to enhance selectively the contribution from either the real or the imaginary part of the third order susceptibility.

The obvious advantage in this technique is that it allows the use of a standard $\chi^{(3)}$ characterization method, but with the added significance that the real and imaginary parts can be separated and measured through simple experimental adjustments. It also has the advantage that it measures a relatively large signal against a small background. One disadvantage is the complication added by the heterodyning method. Also, it does not allow a measurement of the $\chi_{xxxx}^{(3)}$ component; hence it does not give a measure of β but rather the two-photon equivalent of a dichroic absorption coefficient. These coefficients come into play in orthogonally polarized pump–probe beam experiments (see Chapter 9).

A. Theory

The theory of optical Kerr effect measurements was given in Chapter 7. Recall that in such an experiment, a strong linearly polarized beam pumps the medium, and a weak beam probes changes in the birefringence. For an isotropic medium, the initial birefringence is zero. The probe polarization is generally set at an angle of 45° with respect to the pump polarization. The transmitted probe is sent through another polarizer that is oriented at 90° with respect to the input probe polarization. Induced birefringence (as well as induced dichroism) produces a small component of the probe field in the direction of this polarizer axis.

In the method developed by Orczyk et al., this last polarizer is rotated by a small angle ϕ from true orthogonality and hence passes a small portion of the probe component in the direction of the original probe polarization. This field, which is approximately equal to the value of the incident probe field, constitutes the local oscillator field (at the same frequency of the desired cross-polarized signal field). If the third order susceptibility is complex, the part of the desired

signal field that is due to the imaginary part of $\chi^{(3)}$ is in phase with the local oscillator field. The part of this field due to the real part of $\chi^{(3)}$ is $\pi/2$ radians out of phase [29].

The introduction of a quarter-wave plate between the sample and the final polarizer (analyzer) in the experiment imposes a fixed $\pi/2$ phase bias between the local oscillator and the Kerr signal. Thus the net field that would be detected after passage through a sample of thickness L and after the analyzer is [29]

$$E(L) \propto E_{\text{LO}}(0)\sin\phi + E_{\text{K}}(L)\cos\phi \quad (60)$$

without the quarter-wave plate, and

$$E(L) \propto E_{\text{LO}}(0)\sin\phi + iE_{\text{K}}(L)\cos\phi \quad (61)$$

in the presence of the quarter-wave plate, where the LO and K subscripts refer to local oscillator and Kerr signal quantities, respectively. The detected intensity is proportional to $E(L)E^*(L)$ and hence contains terms proportional to $\cos^2\phi$, $\sin^2\phi$, and $\sin\phi\cos\phi$. For small ϕ , only terms to first order in ϕ need to be retained. The net result is that with and without the $\pi/2$ phase bias present, the detected intensity contains ϕ dependent terms given by [29]

$$I_0 \propto \chi_{\text{R}}^{(3)} I_{\text{pump}} I_{\text{probe}}(0)\phi \quad (62)$$

and

$$I_{\pi/2} \propto \chi_{\text{I}}^{(3)} I_{\text{pump}} I_{\text{probe}}(0)\phi \quad (63)$$

respectively. Thus simply removing or replacing the quarter-wave plate in the experiment allows independent measurements of the real and imaginary parts of an effective $\chi^{(3)} = \chi_{\text{xyxy}}^{(3)} + \chi_{\text{xxyy}}^{(3)}$.

Thus, in the experiment, the net heterodyned signal is measured as a function of ϕ over a small range of angles. The data are then least-squares fitted to an equation of the form $I(L) = a + b\phi$. The experiment is repeated with a known reference material that exhibits only a real susceptibility. Finally, the real and imaginary parts of $\chi^{(3)}$ for the sample can be determined from

$$\begin{aligned} (\chi_{\text{xxyy}}^{(3)} + \chi_{\text{xyxy}}^{(3)})_{\text{R}} &= \left(\frac{I_{\text{pump}}^{\text{ref}} I_{\text{probe}}^{\text{ref}}}{I_{\text{pump}} I_{\text{probe}}} \right) \left(\frac{L_{\text{ref}}}{L} \right) \left(\frac{n}{n_{\text{ref}}} \right)^2 \left(\frac{b_0}{b_0^{\text{ref}}} \right) (\chi_{\text{xxyy}}^{(3)} \\ &\quad + \chi_{\text{xyxy}}^{(3)})_{\text{ref}} \end{aligned} \quad (64)$$

and

$$\begin{aligned}
 (\chi_{xxyy}^{(3)} + \chi_{xyxy}^{(3)})_I = & \left(\frac{I_{\text{pump}}^{\text{ref}} I_{\text{probe}}^{\text{ref}}}{I_{\text{pump}} I_{\text{probe}}} \right) \left(\frac{L_{\text{ref}}}{L} \right) \left(\frac{n}{n_{\text{ref}}} \right)^2 \left(\frac{b_{\pi/2}}{b_{\pi/2}^{\text{ref}}} \right) (\chi_{xxyy}^{(3)} \\
 & + \chi_{xyxy}^{(3)}_{\text{ref}})
 \end{aligned} \quad (65)$$

where the subscripts 0 and $\pi/2$ on the b coefficient refer to the situation of the quarter-wave plate absent and present, respectively.

B. Experimental

A typical experiment is illustrated in Fig. 21 [29]. This experimental setup is very similar to the optical Kerr gate experiment described in Chapter 7. The main differences are the introduction of the quarter-wave plate before the analyzer and the use of phase sensitive detection by chopping the pump beam and detecting with a lock-in amplifier.

The laser source used by Orczyk et al. was an amplified colliding pulse mode-locked dye laser producing 60 fs pulses at an 8 kHz rate. Typical pulse energies are $\sim 50 \mu\text{J}$. The beam is split into two parts, with the pump beam a factor of ~ 30 stronger than the probe. Pump and probe polarizations are set at an angle of 45° . The quarter-wave plate is selected or deselected depending on the measurement of real or imaginary $\chi^{(3)}$ components.

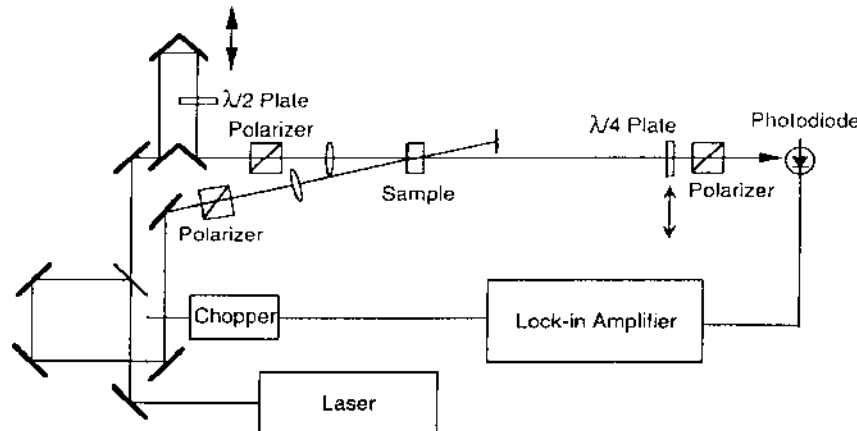


Figure 21 Heterodyned optical Kerr effect experiment for measuring the real and imaginary parts of $\chi^{(3)}$. (Adapted from Ref. 29.)

Data are collected as a function of the analyzer angle ϕ and fitted to a straight line. Measurements are then repeated with the reference. A typical reference material may be CS₂. Orczyk et al. used tetrahydrofuran, for which $\chi_{xxxx}^{(3)} = 3.7 \times 10^{-14}$ esu and $n = 1.4070$ [29].

Pfeffer et al. [30] have employed a similar technique for measuring the real and imaginary parts of $\chi^{(3)}$ using the optical Kerr effect. Their analysis is somewhat different, although the underlying physics is much the same. In their experiments, the probe is the white light continuum generated by focusing frequency doubled 33 ps pulses from a Nd:YAG laser into a D₂O cell. The Kerr signal is then fed to a spectrometer coupled to an optical multichannel analyzer. They were thus able to obtain a two-photon spectrum of the sample in a single pulse. (See Ref. [30] for details.)

VII. CHIRPED-PULSE PUMP–PROBE TECHNIQUE

A pump–probe technique using chirped pulses for measuring $\chi^{(3)}$, based on two-beam coupling, was described in Chapter 7. The technique involves measuring the transmittance of a weak probe pulse when the sample is pumped by a strong pulse. The transmittance is measured as a function of the delay time between pump and probe. As the delay time is varied, the transmittance traces out a dispersion-like curve, and an analysis of the curve yields third order susceptibility. In the nondepleted pump, the small signal regime, the difference between the peak and valley (T_{\max} and T_{\min} , respectively) in the transmittance curve is directly proportional to $\chi^{(3)}$ (or, a combination of $\chi^{(3)}$ components). In this section, the two-beam coupling treatment is extended to the case of a complex third order susceptibility (i.e., where two-photon absorption is present). The advantages of this method are that it allows simultaneous measurements of real and imaginary $\chi^{(3)}$ components as well as the response time of the real nonlinearity. It can also be performed with relatively long pulses (i.e., long compared to the response time of the medium). In fact, long pulses simplify the analysis. Its chief disadvantage is that it requires characterization of the laser chirp (for real $\chi^{(3)}$ and response time measurements), or calibration against a reference with known response time.

A. Theory

Tang and Sutherland [32] presented a general theory for pump–probe experiments using chirped pulses, where $\chi^{(3)}$ is, in general, complex. Consider here two beams of orthogonal polarization, derived from the same laser, that cross at an angle 2θ in a third order nonlinear medium. The beams consist of chirped pulses with instantaneous frequency $\omega(t) = \omega_0 + bt$, where b is the chirp

coefficient. The pump (excitation) pulse has energy \mathcal{E}_e and is much stronger than the probe pulse. The probe pulse is delayed from the pump pulse by a time τ_d , and the time response of $\chi^{(3)}$ is assumed to follow a Debye relaxation equation with time constant τ_m . An extension of the treatment in Chapter 7, Section VI leads to the following equation for the probe intensity:

$$\frac{dI_p}{dz} = [\gamma(\tau_d) - 2\beta_{ep}]I_e(t + \tau_d)I_p(t) \quad (66)$$

where

$$\gamma(\tau_d) = \frac{6\pi}{\epsilon_0 n_0^2 c \lambda \cos \theta} \operatorname{Re}(\chi_{xxyy}^{(3)} + \chi_{xyxy}^{(3)}) \left[\frac{2b\tau_m \tau_d}{1 + (2b\tau_m \tau_d)^2} \right] \quad (67)$$

and β_{ep} is the two-photon absorption coefficient for the probe beam induced by the pump (excitation) beam, given by

$$\beta_{ep} = \frac{3\pi}{\epsilon_0 n_0^2 c \lambda \cos \theta} \operatorname{Im}(\chi_{xxyy}^{(3)} + \chi_{xyxy}^{(3)}) \quad (68)$$

The laser is assumed to have Gaussian spatial and temporal profiles, so that $I_{e,p}(r, t) \propto \exp[-2(r/w_{e,p})^2] \exp[-(t/\tau_L)^2]$, where $2\tau_L$ is the laser 1/e pulse width. The beams may have different spot sizes, but they have the same time dependence since they are derived from the same laser. The pulse energies are measured, and the probe pulse transmittance is defined by $T = \mathcal{E}_p(L)/\mathcal{E}_p(0)$, where L is the sample thickness. Assuming a nondepleted pump and $\gamma I_e L \ll 1$, the probe transmittance is given by

$$T(\tau_d) = 1 + \Delta T_r(\tau_d) + \Delta T_a(\tau_d) \quad (69)$$

$$\Delta T_r(\tau_d) = \frac{2\gamma(\tau_d)L}{\sqrt{2}\pi^{3/2}(w_e^2 + w_p^2)\tau_L} \mathcal{E}_e \exp(-\tau_d^2/2\tau_L^2) \quad (70)$$

$$\Delta T_a(\tau_d) = -\frac{4\beta_{pe}L}{\sqrt{2}\pi^{3/2}(w_e^2 + w_p^2)\tau_L} \mathcal{E}_e \exp(-\tau_d^2/2\tau_L^2). \quad (71)$$

A plot of Eq. (71) is given in Fig. 22. When $\tau_L \gg (2b\tau_m)^{-1}$, i.e., for relatively

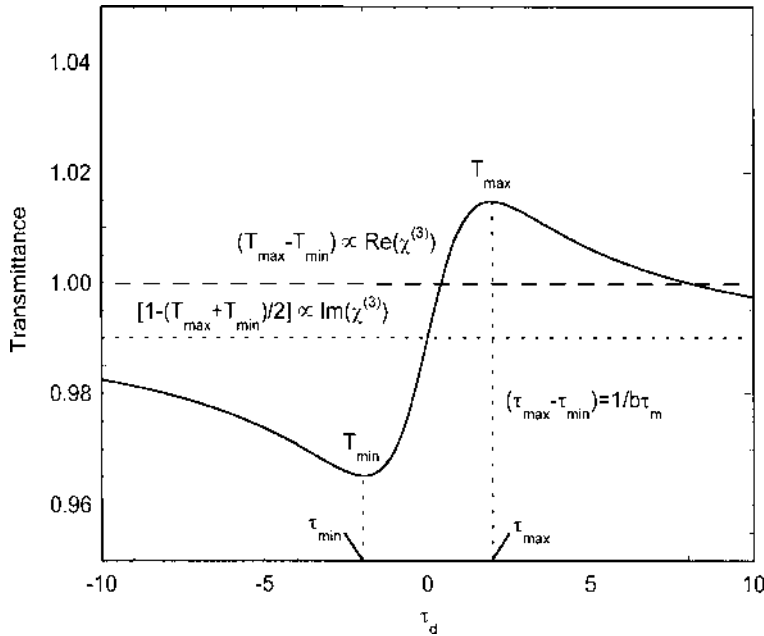


Figure 22 Transmittance as a function of probe delay time for a chirped-pulse pump–probe experiment measuring both the real and imaginary parts of $\chi^{(3)}$.

long laser pulses,

$$\tau_{\max} - \tau_{\min} = \frac{1}{b\tau_m} \quad (72)$$

$$\begin{aligned} \text{Re}(\chi_{xxyy}^{(3)} + \chi_{xyxy}^{(3)}) &= \frac{\sqrt{2\pi}\epsilon_0 n_0^2 c \lambda \cos\theta (w_e^2 + w_p^2) \tau_L}{12\epsilon_e L} \exp[(\tau_{\max}^2 / 2\tau_L^2)] \\ &\times (T_{\max} - T_{\min}) \end{aligned} \quad (73)$$

$$\beta_{pe} = \frac{\sqrt{2}\pi^{3/2} (w_e^2 + w_p^2) \tau_L}{4\epsilon_e L} \exp[(\tau_{\max}^2 / 2\tau_L^2)] [1 - (T_{\max} + T_{\min})/2]. \quad (74)$$

Note that τ_{\max} is a measured quantity corresponding to the value of τ_d at T_{\max} . Hence, the nonlinear susceptibility elements and the TPA coefficient can be found even when the chirp coefficient or the material response time is unknown. Note further by Eq. (72) that either the chirp coefficient or the response time can be obtained from a simple measurement if the other quantity is known.

B. Experimental

An experimental arrangement for this method was given in Fig. 24 of Chapter 7. Both beams are derived from the same laser by the appropriate use of beam splitters. The laser wavelength and pulse width should be selected for the time scale of the particular phenomenon in the sample under study. To simplify the analysis, as described above, the pulse width should be chosen to be large compared with the inverse product of the chirp coefficient and material response time. A description of the experimental method is given in Section VI of Chapter 7. The experiment is basically the same as detailed there. An additional analysis (as discussed above) yields the two-photon absorption coefficient as well.

REFERENCES

1. M. Born and E. Wolf, *Principles of Optics*, 5th ed., Pergamon Press, New York, 1975, p. 702.
2. A. A. Said, M. Sheik-bahae, D. J. Hagan, T. H. Wei, J. Wang, J. Young, and E. W. Van Stryland, Determination of bound-electronic and free-carrier nonlinearities in ZnSe, GaAs, CdTe, and ZnTe, *J. Opt. Soc. Am. B* 9:405 (1992).
3. J. Kleinschmidt, S. Rentsch, W. Tottleben, and B. Wilhelmi, Measurement of strong nonlinear absorption in stilbene-chloroform solutions, explained by the superposition of two-photon absorption and one-photon absorption from the excited state, *Chem. Phys. Lett.* 24:133 (1974).
4. L. W. Tutt and S. W. McCahon, Reverse saturable absorption in metal cluster compounds, *Opt. Lett.* 15:700 (1990).
5. R. L. Sutherland, E. Rea, L. V. Natarajan, T. Pottenger, and P. A. Fleitz, Two-photon absorption and second hyperpolarizability measurements in diphenylbutadiene by degenerate four-wave mixing, *J. Chem. Phys.* 98:2593 (1993).
6. D. G. McLean, R. L. Sutherland, M. C. Brant, D. M. Brandelik, P. A. Fleitz, and T. Pottenger, Nonlinear absorption study of a C₆₀-toluene solution, *Opt. Lett.* 18:858 (1993).
7. M. Sheik-bahae, A. A. Said, T. H. Wei, D. J. Hagan, and E. W. Van Stryland, Sensitive measurement of optical nonlinearities using a single beam, *IEEE J. Quant. Electron.* 26:760 (1989).
8. P. A. Fleitz, R. L. Sutherland, and T. J. Bunning, Z-scan measurements on molten diphenylbutadiene in the isotropic liquid state, *Proc. Mat. Res. Soc.* 374:211 (1995).
9. T. H. Wei, D. J. Hagan, M. J. Sence, E. W. Van Stryland, J. W. Perry, and D. R. Coulter, Direct measurements of nonlinear absorption and refraction in solutions of phthalocyanines, *Appl. Phys. B* 54:46 (1992).
10. See, e.g., J. A. Bolger, A. K. Kar, B. S. Wherrett, R. DeSalvo, D. C. Hutchings, and D. J. Hagan, Nondegenerate two-photon absorption spectra of ZnSe, ZnS, and ZnO, *Opt. Commun.* 97:203 (1993).

11. Y. R. Shen, *The Principles of Nonlinear Optics*, John Wiley, New York, 1984, pp. 324–328.
12. R. J. M. Anderson, G. R. Holtom, and W. M. McClain, Two-photon absorptivities of the all trans α , ω -diphenylpolyenes from stilbene to diphenyloctatetraene via three wave mixing, *J. Chem. Phys.* 70:4310 (1979).
13. A. P. Aleksansrov, V. I. Bredikhin, and V. N. Genkin, Two-photon absorption by centrally symmetric organic molecules, *Sov. Phys. JETP* 33:1078 (1971).
14. R. L. Swofford and W. M. McClain, New two-photon absorption spectrometer and its application to diphenylbutadiene, *Rev. Sci. Instrum.* 46:246 (1975).
15. J. A. Bennett and R. R. Birge, Two-photon spectroscopy of diphenylbutadiene. The nature of the lowest-lying ${}^1A_g^*$ $\pi\pi^*$ state, *J. Chem. Phys.* 73:4234 (1980).
16. G. R. Holtom and W. M. McClain, Two-photon excitation spectra of the low energy excited states of diphenylhexatriene and diphenyloctatetraene, *Chem. Phys. Lett.* 44:436 (1976).
17. H. L.-B. Fang, R. J. Thrash, and G. E. Leroi, Observation of the low-energy 1A_g state of diphenylhexatriene by two-photon excitation spectroscopy, *Chem. Phys. Lett.* 57:59 (1978).
18. H. L. B. Fang, R. J. Thrash, and G. E. Leroi, Observation of “hidden” electronic states by two-photon excitation spectroscopy: confirmation of the low-energy 1A_g state of diphenyloctatetraene, *J. Chem. Phys.* 67:3389 (1977).
19. R. L. Swofford and W. M. McClean, Two-photon absorption studies of diphenylbutadiene: the location of a 1A_g excited state, *J. Chem. Phys.* 59:5740 (1973).
20. D. M. Friedrich and W. M. McClean, Polarization and assignment of the two-photon spectrum of benzene vapor, *Chem. Phys. Lett.* 32:541 (1975).
21. M. E. Long, R. L. Swofford, and A. C. Albrecht, Thermal lens technique: A new method of absorption spectroscopy, *Science* 191:183 (1976).
22. A. J. Twarowski and D. S. Kliger, Multiphoton absorption spectra using thermal blooming. I. Theory, *Chem. Phys.* 20:253 (1977).
23. A. J. Twarowski and D. S. Kliger, Multiphoton absorption spectra using thermal blooming. II. Two-photon spectrum of benzene, *Chem. Phys.* 20:259 (1977).
24. H. L. Fang, T. L. Gustafson, and R. L. Swofford, Two-photon absorption photo thermal spectroscopy using a synchronously pumped picosecond dye laser. Thermal lensing spectra of naphthalene and diphenylbutadiene, *J. Chem. Phys.* 78:1663 (1983).
25. M. Bass, E. W. Van Stryland, and A. F. Stewart, Laser calorimetric measurement of two-photon absorption, *Appl. Phys. Lett.* 34:142 (1979).
26. P. A. Fleitz, R. L. Sutherland, L. V. Natarajan, T. Pottenger, and N. C. Fernelius, Effects of two-photon absorption on degenerate four-wave mixing in solutions of diphenyl polyenes, *Opt. Lett.* 17:716 (1992).
27. P. N. Prasad and D. J. Williams, *Introduction to Nonlinear Optical Effects in Molecules and Polymers*, John Wiley, New York, 1991, pp. 218–220.
28. M. Zhao, Y. Cui, M. Samoc, P. N. Prasad, M. R. Unroe, and B. A. Reinhardt, Influence of two-photon absorption on third-order nonlinear optical processes as studied by degenerate four-wave mixing: the study of soluble didecyloxy substituted polyphenyls, *J. Chem. Phys.* 95:3991 (1991).

29. M. E. Orczyk, M. Samoc, J. Swiatkiewicz, M. Tomoaia-Cotisel, and P. N. Prasad, Optical heterodyning of the phase-tuned femtosecond optical Kerr gate signal for the determination of complex third-order susceptibilities, *Appl. Phys. Lett.* 60:2837 (1992).
30. N. Pfeffer, F. Charra, and J. M. Nunzi, Phase and frequency resolution of picosecond optical Kerr nonlinearities, *Opt. Lett.* 16:1987 (1991).
31. P. B. Chapple, J. Staromlynska, and R. G. McDuff, Z-scan studies in the thin- and thick-sample limits, *J. Opt. Soc. Am. B* 11:975 (1944).
32. N. Tang and R. L. Sutherland, Time-domain theory for pump–probe experiments with chirped pulses, *J. Opt. Soc. Am. B* 14:3412 (1997).

11

Ultrafast Characterization Techniques

Sean Kirkpatrick

*U.S. Air Force Research Laboratory,
Wright Patterson Air Force Base, Ohio, U.S.A.*

In the previous chapter, several experimental techniques for measuring the nonlinear optical parameters of various types of materials were illustrated. It was mentioned that most of those parameters are absorptive in nature and that the theoretical basis for these parameters and their interrelationships were detailed in Chapter 9. As the measurements of these parameters arise from intensity variations of an incident laser beam, accurate absorptive experimental measurement require high peak intensities. With the advent of new, commercially available ultrafast laser systems (pulse widths < 250 fs, pulse energies ~ 1 mJ), this type of nonlinear measurement has become more prevalent. However, the appeal of using a versatile ultrafast laser for many types of nonlinear measurements comes at the expense of the difficulty with which they are conducted.

The very property that is required to make fine, accurate nonlinear measurements (i.e., short pulse widths and high peak intensities), make working with ultrafast lasers a challenging task. Typical unfocused emission intensities of these types of lasers are on the order of tens to hundreds of gigawatts per square centimeter (assuming a single-stage amplifier). At this level of intensity, normal coated mirrors generally ablate. Apart from the obvious damage-oriented problems, a few more subtle problems can arise. For example, BK-7 glass is the most common substrate for mirrors and lenses. BK-7 glass has a nonlinear refractive index coefficient of $n_2^l \sim 4 \times 10^{-16} \text{ cm}^2/\text{W}$ in the near infrared, and its effects are readily observable under this scale of intensity. Self-phase modulation, self-focusing, and group velocity dispersion effects can all work

toward changing the pulse from its original state into something that can lead not only to incorrect measurements, but can also become quite useless.

In this chapter we will discuss some of these effects in detail as they apply to ultrafast lasers, and then explore some specific measurement techniques and the special considerations that are necessary to make them successful. As an ultrafast pulse provides a nearly ideal temporal delta function compared to the dynamic response of many processes in the material system, the techniques we will discuss will include both static and transient response measurements.

I. WAVE THEORY AND RELATED PHENOMENA FOR ULTRASHORT PULSES

In the following sections, we review the propagation equation as it applies to ultrashort pulse phenomena. A review of Chapters 1, 6, 7, and 9 is warranted. In this discussion, only third order nonlinearities are considered as they primarily have an intensity dependence which is easily attainable with ultrashort pulses. A full, detailed analysis of short-pulse propagation inclusive of all possible linear and nonlinear effects requires a beam propagation code and numerical solution. Subsequently, each effect is treated independently, with nonlinear absorption treated at the end. For the following discussion, we use the form of the electric field given by

$$E(z, t) = A(z, t)\exp(iK \cdot r - i\omega_0 t) + \text{c.c.} \quad (1)$$

A. Nonlinear Wave Equation

We begin with a review of the nonlinear wave equation in the absence of nonlinear absorption and under some typical assumptions. These assumptions are: 1) pulse propagation is primarily along the $+z$ direction, 2) the transverse components are slowly varying, 3) the z -component of the envelope is slowly varying, and 4) the nonlinearity arises from the third order susceptibility only. Under these conditions, the nonlinear wave equation can be written as

$$\left[\frac{\partial A}{\partial z} + k_1 \frac{\partial A}{\partial t} \right] + \frac{i}{2} k_2 \frac{\partial^2 A}{\partial t^2} = i \frac{2\omega_0 n_2}{c} |A|^2 A \quad (2)$$

where k_1 is the inverse of the group velocity, k_2 is the group velocity dispersion coefficient, and n_2 is the nonlinear refractive index coefficient. Furthermore, by introducing the retarded time given as $\tau = t - z/v_g$, and $\zeta = z$, the nonlinear wave equation (or nonlinear Schrödinger equation) reduces to the form give in

Chapter 6, Table 16, as

$$\frac{\partial A}{\partial \zeta} + \frac{i}{2} k_2 \frac{\partial^2 A}{\partial \tau^2} = i \frac{2\omega_0 n_2}{c} |A|^2 A \quad (3)$$

Examination of Eq. (2) above shows that the terms in brackets describe the envelope propagation, while the next term is responsible for pulse broadening due to group velocity dispersion (GVD). The term on the right-hand side is responsible for spectral broadening due to self-phase modulation as well as other nonlinear refractive index effects discussed earlier. The following discussion centers on two extreme cases, with and without GVD effects, aimed at illustrating certain problems that arise due to the pulse width and due to peak intensity.

B. Group Velocity Dispersion

The first case of interest is for materials in which the nonlinearity is small, resulting in pulse propagation dominated by the group velocity dispersion. To review, the group velocity dispersion term describes the variation of group velocity through a material as a function of wavelength or frequency. In normal dispersion, the red wavelengths travel faster than the blue wavelengths. The reverse is true for anomalous dispersion. An ultrafast pulse necessarily has a large spectral width. As a consequence, GVD can affect the propagation of an ultrafast pulse by introducing a phase delay as a function of wavelength (or chirp), and by changing the pulse width.

In the case of GVD dominated propagation, Eq. (3) reduces to

$$\frac{\partial A(\zeta, \tau)}{\partial \zeta} + \frac{i}{2} k_2 \frac{\partial^2 A(\zeta, \tau)}{\partial \tau^2} \approx 0 \quad (4)$$

There are two methods of solution to this equation, in the time domain or in the frequency domain. We begin with the frequency domain by performing a Fourier transform of Eq. (4)

$$\begin{aligned} \tilde{A}(\zeta, \Omega) &= \int_{-\infty}^{\infty} A(\zeta, \tau) \exp(i\Omega\tau) d\tau \\ A(\zeta, \tau) &= \frac{1}{2\pi} \int_{-\infty}^{\infty} \tilde{A}(\zeta, \Omega) \exp(-i\Omega\tau) d\Omega \end{aligned} \quad (5)$$

The propagation equation [Eq. (4)] is transformed to

$$\frac{1}{2\pi} \int_{-\infty}^{\infty} \left[\frac{\partial \tilde{A}(\zeta, \Omega)}{\partial \zeta} + i \frac{k_2}{2} \Omega^2 \tilde{A}(\zeta, \Omega) \right] \exp(-i\Omega\tau) d\Omega = 0 \quad (6)$$

Equation (6) is true when the integrand is equal to 0. The result can be solved

analytically to give

$$\tilde{A}(\zeta, \Omega) = \tilde{A}(0, \Omega) \exp\left(-i \frac{k_2}{2} \Omega^2 \zeta\right) \quad (7)$$

where $A(\zeta, \tau)$ is found via Eq. (5).

To illustrate the concepts of chirp and pulse broadening, consider a Gaussian input field having a pulse envelope form given by $A(\zeta, \tau) = A(\zeta) \exp[-(\tau/\sqrt{2}\tau_0)^2]$ with pulse width τ_0 . To solve Eq. (7), we first find $\tilde{A}(\zeta = 0, \Omega)$ from Eq. (5) giving

$$\tilde{A}(0, \Omega) = \sqrt{2\pi}\tau_0 A(0) \exp[-(\Omega\tau_0/\sqrt{2})^2] \quad (8)$$

Substituting Eq. (8) back into Eq. (7) and taking the inverse Fourier transform, we find

$$A(\zeta, \tau) = \frac{\tau_0}{\sqrt{2}\xi} A(0) \exp[-(\tau/2\xi)^2] \quad (9)$$

where $\xi^2 = (\tau_0^2 + ik_2\zeta)/2$. By rewriting $\xi = |\xi| \exp[-i\varphi(\zeta)]$, substituting into the solution given by Eq. (9), and simplifying, one can write the field amplitude as

$$A(\zeta, \tau) = A(0)[1 + (\zeta/L_d)^2]^{-1/4} \exp[i\varphi(\zeta) + i\psi(\zeta, \tau) - (\tau/\sqrt{2}\tau_{eff})^2] \quad (10)$$

where $\varphi(\zeta) = 1/2 \tan^{-1}(\zeta/L_d)$, $\psi(\zeta, \tau) = \zeta\tau^2/2\tau_{eff}^2 L_d$, $\tau_{eff}^2 = \tau_0^2[1 + (\zeta/L_d)^2]$, and $L_d = \tau_0^2/k_2$ is a characteristic distance over which the group velocity dispersion effects become significant, sometimes referred to as the dispersive spreading length [1]. It can immediately be seen that the temporal pulse width has now changed to τ_{eff} , and is a function of the propagation distance through the material. Note that this pulse width spreading is proportional to the group velocity dispersion coefficient through L_d . For example, the group velocity dispersion coefficient for silica fiber at 1.55 μm is 20 ps^2/km . Propagation of a 5-ns pulse down 10 km of fiber will result in negligible pulse broadening, while the comparable propagation of 30-ps and 100-fs pulses will result in effective pulse widths of 31 ps and 2 ns, respectively. It should be obvious that without compensating effects, high bit rate errors would occur in an optical transmission channel for higher baud rates requiring short pulse propagation [2].

Rewriting Eq. (10) in the form

$$A(\zeta, \tau) = A(0)[1 + (\zeta/L_d)^2]^{-1/4} \exp[i\varphi(\zeta) + iC\tau^2 - (\tau/\sqrt{2}\tau_{eff})^2] \quad (11)$$

shows that the propagated Gaussian pulse now has a linear chirp coefficient C given by [3,4]

$$C = \frac{\zeta}{2\tau_{eff}^2 L_d} \quad (12)$$

The chirp coefficient defines how the phase of each frequency component develops as it propagates a given length, and is dependent on k_2 as well as inversely dependent on the initial pulse width. Shorter pulses have stronger chirp due to GVD.

C. Self-Phase Modulation

We next consider the case where GVD is negligible and only the nonlinearity on the right-hand side of Eq. (3) exists. This is the case where self-phase modulation is said to dominate. Self-phase modulation was introduced in Chapter 6 with respect to soliton propagation. The typical solution to this equation is given under several assumptions, which should be reiterated. First, it has been implicitly assumed that we are examining linearly polarized light, that we are in an isotropic and nonmagnetic medium, and that we are far from resonance, making $\chi^{(3)}$ frequency independent. Results will vary when dealing with situations other than this. Under these conditions, Eq. (3) reduces to the form

$$\frac{\partial A}{\partial \zeta} = i \frac{2\omega_0 n_2}{c} |A|^2 A \quad (13)$$

With the substitution $A(\zeta, \tau) = a(\zeta)F(\tau)$, it can be shown through rather straightforward manipulation that a solution to this equation (following the convention of Alfano [4] with the additional assumption that the induced nonlinear phase is not explicitly dependent on time), is given by

$$A(\zeta, \tau) = a_0 F(\tau) \exp[i(2\omega_0 n_2 a_0^2/c) F^2(\tau) \zeta] \quad (14)$$

where $a_0 = |a(0)|$, and $F(\tau)$ is the temporal envelop of the incident pulse for materials with a nonlinear response somewhat longer than the pure electronic response. For a pure electronic response, the optical cycles must be included. This can be important when dealing with ultrashort pulse phenomena which can only be affected by responses on the order of the pulse width (i.e., pure electronic). Note that in this case, the intensity is related to defined parameters by

$$I(\tau) = 2n_0 \epsilon_0 c |A|^2 = 2n_0 \epsilon_0 c a_0^2 F^2(\tau) \quad (15)$$

This leads to an equivalent nonlinear phase term as given by Eq. (88), Chapter 6, but without the sign convention adopted there. In this form, the local and instantaneous frequency is given by $\omega(\tau) = \omega_0 - \delta\omega(\tau)$. Using the solution above, this becomes

$$\omega(\tau) = \omega_0 - \frac{2\omega_0 n_2}{c} a_0^2 \zeta \frac{dF^2(\tau)}{d\tau} \quad (16)$$

As before, for a positive n_2 , the leading edge is red-shifted and the trailing edge is

blue-shifted. The frequency spectrum can be determined by taking the Fourier transform of Eq. (14), $A(\zeta, \Omega)$. From this frequency spectrum, the intensity distribution can then be found from the Poynting vector, $S(\zeta, \Omega)$. These relations are given in Eq. (17), and interested readers are referred to books by Alfano and Jackson [4,5]:

$$\begin{aligned} A(\zeta, \Omega) &= \int_{-\infty}^{\infty} A(\zeta, \tau) \exp(i\Omega\tau) d\tau \\ S(\zeta, \Omega) &= 2n_0 c \epsilon_0 |A(\zeta, \Omega)|^2 \end{aligned} \quad (17)$$

There are two approaches to determining whether experimental conditions warrant concern over self-phase modulation. The first requires numerical calculation based on the above formalism and Eq. (17). However, apart from it being numerically intensive to calculate this spectrum at all potential focal regions in the experiment, a more thorough approach is necessary, including GVD effects which can either enhance or amplify the frequency shifts. The second approach is a back-of-the-envelope type of calculation. Although not effective in borderline cases, it can give a good measure of the importance of this effect most of the time. We consider the first case where we calculate the intensity spectrum of an ultrashort pulse passing through a focus in a typical material such as quartz. This is not an uncommon occurrence, such as when using quartz cuvettes or windows.

We consider, as a moderate case, a 100-fs pulse centered at 800 nm, having a pulse energy of 10 μJ . The pulse is focused to a spot with a 50- μm radius. Using the value of the nonlinear refractive index $4 \times 10^{-16} \text{ cm}^2/\text{W}$ and a path length of 1 cm, the intensity spectrum is calculated as outlined above. Figure 1 shows the calculated normalized intensity spectrum versus wavelength of the incident and transmitted pulses. As can be seen, a significant frequency shift has occurred, resulting in an increase in the spectral content of the transmitted pulse. The full width of the transmitted pulse is about $6.1 \times 10^{14} \text{ s}^{-1}$, over an order of magnitude larger than the incident bandwidth limit. Unless created intentionally, this type of self-phase modulation could be detrimental to the intended experiment, having both a larger frequency spectrum and a longer pulse width as determined by the group velocity dispersion of the system.

We next consider the approximate case where we find the maximum bandwidth increase from the above formalism. Beginning with the instantaneous frequency within the pulse, we calculate the maximum frequency shift by finding the critical points of Eq. (16), i.e., the inflection points of the incident pulse at τ_1

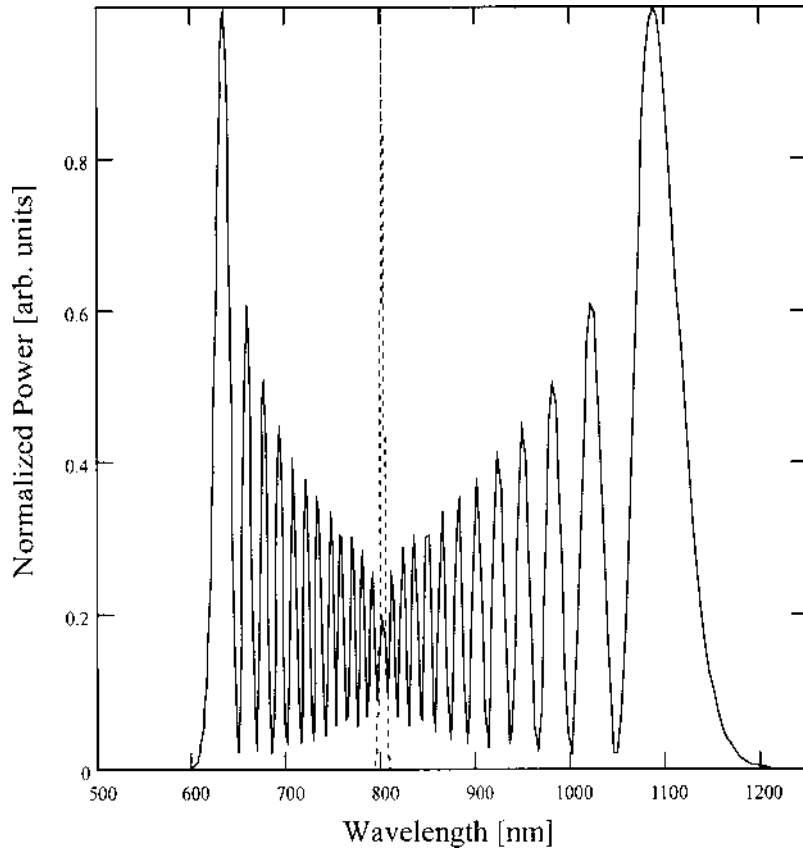


Figure 1 Normalized power spectrum of a self-phase modulated pulse (solid line) compared to the incident pulse spectrum (dotted line).

and τ_2 :

$$\Delta\omega_{\max} = \frac{2\omega_0 n_2 a_0^2 \zeta}{c} \left[\frac{dF^2(\tau)}{d\tau} \Big|_{\tau_1} - \frac{dF^2(\tau)}{d\tau} \Big|_{\tau_2} \right] \quad (18)$$

For a Gaussian pulse envelope where $F(\tau) = \exp(-\tau^2/2\tau_0^2)$, the maximum frequency shift is found to be

$$\Delta\omega_{\max} = \frac{4\omega_0 n_2 a_0^2 \zeta}{c\tau_0} \sqrt{2} e^{-1/2} \quad (19)$$

Using the same parameters as before, this is equal to a frequency shift of

$\Delta\omega_{\max} = 6.8 \times 10^{14} \text{ s}^{-1}$, in close agreement to the exact value calculated above. For a center wavelength of 800 nm, such a frequency shift would correspond to a wavelength shift of about 710 nm to 920 nm, and in the presence of GVD, the resulting pulse width would be significantly different than the original 100 fs.

D. Self-Focusing and Self-Trapping

Two other important nonlinear processes, having significant impact in ultrafast characterization techniques, are self-focusing and self-trapping. These processes are a result of the nonlinear refractive response of the medium to the high peak intensity profile of an ultrashort pulse. Both processes have been discussed in Chapter 6, and so only the highlights are presented here in relation to ultrafast pulses.

In a simple nonlinear transmission or fluorescence experiment (discussed below), the incident beam is typically collimated with a planar wave front incident on the sample. As the transmission and fluorescence intensity is dependent on the intensity within the sample, a key concern is whether or not there is the possibility for self-focusing within the sample. In this case, self-focusing will give incorrect results by increasing the intensity beyond the desired and calculated level. For such an experimental arrangement, the conditional equation of interest is the self-focusing distance in the paraxial approximation for a plane wave front, given in Table 15 of Chapter 6:

$$z_{f\infty} = \frac{z_R}{\sqrt{(\mathcal{P}/\mathcal{P}_{cr1}) - 1}} \quad (20)$$

where z_R is the Rayleigh range, and the critical power \mathcal{P}_{cr1} is given in either cgs or SI units. Typical optical elements, sample cuvettes, or windows are made of borosilicate crown glass or fused silica. These two materials have nonlinear refractive index coefficients of $1.5 \times 10^{-13} \text{ esu}$ ($4.4 \times 10^{-16} \text{ cm}^2/\text{W}$) and $1.2 \times 10^{-13} \text{ esu}$ ($3.5 \times 10^{-16} \text{ cm}^2/\text{W}$), respectively [8]. Using the value of borosilicate glass, we find a critical power of $\sim 400 \text{ kW}$. While this seems moderately high, keep in mind that a typical Ti:Sapphire ultrafast laser system, with a single stage amplifier, can create 100-fs pulses with pulse energies in the millijoule range. From these parameters, the peak power is found to be 10 GW. At this high-peak power, the self-focusing distance is found from Eq. (20) to be $6.3 \times 10^{-3} z_R$, while at a lower pulse energy of $1 \mu\text{J}$, self-focusing occurs at $0.2 z_R$. In the previously mentioned experiments, depending on configuration (see below), it is possible to use a beam waist ranging from $100 \mu\text{m}$ ($z_R \approx 4 \text{ cm}$) to 0.5 cm ($z_R \approx 9800 \text{ cm}$) at the sample with a corresponding energy range of $1 \mu\text{J}$ to 1 mJ . At the high energy end, self-focusing would occur within approximately $240 \mu\text{m}$ for a Rayleigh range of 4 cm , while for a Rayleigh range of 9800 cm , self-focusing would occur within about 60 cm . In the case of the lower energy range,

the corresponding self-focusing distances are 0.8 cm and 20 m. Apart from thin films, sample lengths are typically within the range of 0.5 mm to 1 cm, determined by the available spectroscopic cell lengths for liquids and typical polishing thickness for crystals and glasses. In the nonlinear fluorescence experiment the fluorescence is usually collected at 90° to the pump direction, necessitating a longer cell length to geometrically optimize the signal level to the collection optics. It should be noted that our calculations are based only on the nonlinearity inherent in the glass or silica substrates used in conjunction with the samples to be examined. Generally, these materials will have a larger intrinsic nonlinear susceptibility and, hence, refractive index than the substrates used with them. Thus the distance required for self-focusing will inevitably be shorter than what we have calculated. Using these calculations as a guide, we find that for the longer path lengths needed for nonlinear fluorescence (discussed below), low concentration testing, or typical crystal/glass sample sizes, self-focusing can readily occur for the entire energy range available for testing if a smaller waist at the sample is used. While increasing the waist at the sample can alleviate the concern over this phenomenon, such an increase can lead to other experimental difficulties such as increased scatter and lower imaging efficiency of the nonlinear fluorescence signal.

We have thus far concerned ourselves with only collimated beams at a sample. It is often the case that a focused geometry is used instead, as in a Z-scan experiment. In such a case, the self-focusing distance is again given in Table 15 of Chapter 6 for the curved wave front:

$$z_f = \frac{R}{(R/z_{f\infty}) - 1} \quad (21)$$

where R is the radius of curvature. Note that for any converging wave ($R < 0$), the beam will focus in a distance $z < z_{f\infty}$. For example, using a moderately focused beam with a radius of curvature of 10 cm, a 1-mJ pulse with a 0.5-cm waist at the input surface ($z_{f\infty} = 60$ cm) will self-focus at a distance of 8.6 cm. While this distance does not lie within typical sample lengths, it is close enough to a standard 1 cm sample cell to cause nonuniformity of the intensity within the sample with possibly misleading results.

With respect to a Z-scan experiment, too high a peak intensity or too long a path length can create a situation where self-focusing becomes evident. It is also the case that self-trapping, the physical balance between diffraction and self-focusing, can lead to difficulties. However, such a situation is generally easier to recognize, as the resulting closed aperture trace has a characteristic profile as shown for the thick sample data in Figure 14 of Chapter 7. Self-trapping will occur when the peak power within the sample approaches P_{erl} in Eq. (20). For the case of a 100-fs pulse through a glass substrate, this corresponds to ~ 40 nJ, whereas for a 2-ps pulse the required energy is ~ 0.8 μ J. The former pulse width

and energy level are easily attainable using a standard Ti:Sapphire oscillator and pulse stretcher; no amplifier is necessary. The latter is attained from amplification after pulse stretching; no compression is necessary. Alternatively, a compressed Nd:YLF laser with or without regenerative amplification will also suffice. See below for further discussion.

E. Two-Photon Absorption

Thus far, we have examined phenomena related to the nonlinear refractive index. The use of ultrashort pulses having high peak intensities allows easy access to the intensity-dependent refractive index and related processes. We now examine the imaginary part of $\chi^{(3)}$, namely two-photon absorption. The high photon density in an ultrashort pulse increases the probability of a multiphoton absorption event significantly. The general equations governing two-photon absorption were discussed in Chapter 9, and its use in Z-scan measurements in Chapter 7. In this section we review the relevant expressions as well as examine new conditions under which saturation of the TPA process can occur. We also note that throughout this chapter we use the conventional units for the two-photon absorption coefficient (cm/GW) and cross-section (cm^4/GW). To change to Göppert-Meyer units ($\text{GM} = \text{cm}^4 \cdot \text{s}/(\text{photon-molecule})$), one only needs to take the two-photon cross section in units of cm^4/W and multiply by the energy per photon. Typically, these numbers are reported as some number times $10^{-21} \text{ cm}^4/\text{GW}$ and 10^{-50} GM .

Nonlinear transmission and Z-scan. The two easiest methods of measuring the two-photon absorption coefficient are a simple nonlinear transmission (NLT) experiment or a Z-scan experiment. A typical pulsed nonlinear transmission experiment (also referred to as a nonlinear absorption experiment) uses a collimated-beam geometry to measure the transmission of a thin sample. The transmission is then governed by (Gaussian pulse)

$$T = (1 - R)^2 \exp(-\alpha_0 L) \sum_{m=0}^{\infty} \frac{(-q_0)^m}{(m + 1)^{3/2}} \quad (22)$$

where $q_0 = (1 - R)\beta I_0 L_{\text{eff}}$ and is assumed to be less than 1. L_{eff} is the effective path length and is defined in Table 3 of Chapter 9. A carefully calibrated measurement of input intensity and transmission can be fit to Eq. (22) to obtain the two-photon coefficient β . As the experiment uses an unfocused geometry, problems with self-focusing, trapping, and subsequent self-phase modulation are not a problem, even for pulses down to the tens of femtoseconds. In contrast, a typical pulsed Z-scan experiment uses a focused-beam geometry and moves the sample through the focal point, again measuring the transmission as a function of

peak intensity. The resulting data is fit to

$$T = (1 - R)^2 \exp(-\alpha_0 L) \sum_{m=0}^{\infty} \frac{(-q'_0)^m}{(m + 1)^{3/2}} \quad (23)$$

where $q'_0 = q_0/(1 + z/z_R)$, z_R being the Rayleigh range and z being the translation distance of the sample relative to the focus. Again, a careful measurement of the peak on-axis intensity gives the two-photon absorption coefficient. In this case, however, as the sample is moved through a focus, other nonlinear processes such as supercontinuum generation can occur with as little as hundreds of nanojoules of energy in a 100-fs pulse.

In both cases, a tunable laser is ideal in order to obtain dispersion data on the TPA process. Unfortunately, tuning over a large spectral region can be a lengthy process. Therefore, it is desirable to look at many frequencies simultaneously. Such an experiment is the nondegenerate two-photon absorption measurement using a single frequency pump and supercontinuum pulse as a probe. This is discussed further in the “Experimental techniques” section below. The governing transmission equations were discussed in Chapter 9, and are summarized in Table 4 of that chapter.

Nonlinear fluorescence. Another alternative to measuring a single frequency two-photon absorption cross-section is the nonlinear fluorescence measurement. Although a fairly straightforward measurement, the resulting data may be difficult to interpret, yet provide much more insight than a nonlinear transmission or absorption experiment. In this experiment, a two-photon absorption event results in fluorescence from either the two-photon state or a closely coupled one-photon state. Just as two-photon absorption can give information regarding same-parity states, nonlinear fluorescence can give information regarding a third state. If the two-photon state couples closely to a nearby one-photon state (opposite parity of ground state), then the fluorescence that ensues should have the same shape as the linearly excited (at twice the frequency) fluorescence. However, fluorescence from the two-photon state (same parity as ground state) can occur to an intermediate state of opposite parity to the ground state, and same parity as the one-photon state. In this case the spectrum would not resemble the linearly excited fluorescence. Such processes are similar to the Orbach process in solid state spectroscopy [6]. Information regarding vibrational spectra, dipole moments of transition, and photo-induced chemical reactions may also be obtained.

Consider a simple three-level model with two-photon absorption from the ground state to the second excited state, resulting in a one-photon emission from the second excited state to the first excited state. Assuming no linear absorption, no stimulated emission, and no degeneracy, the rate equations and propagation

equation governing the system and the pulse propagation are given by

$$\begin{aligned}\frac{dN_2}{dt} &= \frac{\sigma_{TPA}I^2}{2\hbar\omega_0}N_0 - \frac{N_2}{\tau_{21}} - \frac{N_2}{\tau_{20}} \\ \frac{dN_1}{dt} &= \frac{N_2}{\tau_{21}} - \frac{N_1}{\tau_{10}} \\ \frac{dN_0}{dt} &= -\frac{dN_1}{dt} - \frac{dN_2}{dt} \\ \frac{\partial I}{\partial z} + \frac{1}{c} \frac{\partial I}{\partial t} &= -\sigma_{TPA}N_0I^2\end{aligned}\quad (24)$$

where τ_{ij}^{-1} is the decay rate of the i th state to the j th state, and σ_{TPA} is the two-photon absorption cross section. Under short pulse excitation, such that $\tau_p \ll \tau_{ij}$, the excited state population N_2 can be approximated as [7]

$$N_2 \approx \frac{\sigma_{TPA}N_T}{2\hbar\omega_0} \int I^2(t') dt' \quad (25)$$

where N_T is the total concentration of TPA absorbers. The integration limits extend to plus and minus the inverse of the repetition rate of the experiment, which should be much longer than the total relaxation time of the system and may then be taken as infinity. For a Gaussian pulse with peak intensity I_0 , Eq. (25) can be evaluated to give

$$N_2 \approx \frac{\sigma_{TPA}N_T\tau_p I_0^2}{2\hbar\omega_0} \sqrt{\frac{\pi}{2}} \quad (26)$$

For simplicity, assume that we are measuring the fluorescence from state 2 to state 1 and that the two fluorescence lines (bands in reality) are spectrally separate. The number of photons M_{21} emitted into this fluorescence line per unit time can be written as

$$\frac{dM_{21}}{dt} = \frac{N_2}{\tau_{21}} \quad (27)$$

In addition, assuming no loss of population within an ultrafast pulsed excitation, the decay of the two-photon excited state is now governed by

$$\frac{dN_2}{dt} = -\frac{N_2}{\tau_{21}} - \frac{N_2}{\tau_{20}} \quad (28)$$

The total energy emitted in the fluorescence band per excitation pulse can be found from integrating Eqs. (27) and (28) over time, space (collection volume),

and frequency. Thus the total collected energy within the spectral line is found to be

$$\mathcal{E}_{pulse} = \int \omega g(\omega) \frac{\sigma_{TPA} N_T \tau_p I_0^2}{2\omega_0} \sqrt{\frac{\pi}{2}} \left[\frac{\tau_{21}^{-1}}{\tau_{20}^{-1} + \tau_{21}^{-1}} \right] V d\omega \quad (29)$$

where $g(\omega)$ is the lineshape of the fluorescence band, and V is the collection volume of the radiated energy flux determined by $V = c\tau_{21}A$, with A the area of the detector and c the speed of light. Note that other factors such as collection optics should also be included. The fluorescence or quantum yield, φ_f , is defined by the ratio in the square brackets in Eq. (29). It should be noted that the fluorescence yield may or may not be the same as the corresponding one-photon fluorescence yield, depending on the coupling between the states.

A typical detector gives a response in volts determined by the responsivity of the detector (A/W) and the input resistance to a monitoring device. In this case, the total integrated signal S (measured in volts) is determined by

$$S = \mathcal{R} \mathcal{E}_{pulse} r Z \quad (30)$$

where \mathcal{R} is the responsivity of the detector in A/W, r is the repetition rate of the experiment, and Z is the input resistance of the monitor. Substituting Eq. (29) into (30), we get the measured integrated fluorescence resulting from the two-photon excitation,

$$S = \int \omega g(\omega) R r Z \frac{\sigma_{TPA} N_T \tau_p I_0^2}{2\omega_0} \sqrt{\frac{\pi}{2}} \varphi_f c \tau_{21} A d\omega \quad (31)$$

Note the square dependence on the input intensity.

A measurement of the integrated fluorescence versus pump intensity should give a quadratic dependence for a dominant two-photon absorption process as discussed below. A fit to the allometric equation Cx^b should return a b value of 2 and a coefficient C , which can be used in conjunction with Eq. (31) to find either the TPA cross section or the nonlinear fluorescence quantum yield, provided σ_{TPA} is known.

Saturated two-photon absorption. Linear saturated absorption is well understood and often treated in nonlinear optics texts [8,9]. The theoretical treatment of a homogeneously broadened two-level system, under steady state conditions, leads to an intensity dependent linear absorption coefficient α^h given by

$$\alpha^h = \frac{\alpha_0}{1 + I/I_s^h} \quad (32)$$

where the homogeneous saturation intensity at line center is given by

$$I_s^h = \frac{\hbar\omega}{\tau\sigma_0(1 + g_k/g_n)} \quad (33)$$

Here, $g_k(g_n)$ is the electronic degeneracy of the upper (lower) state, τ_0 is the lifetime of the upper state, ω is the excitation frequency, and $\alpha_0(\sigma_0)$ is the linear absorption coefficient (cross section). Boyd has shown that in the case of linear saturated absorption, many saturable absorbers are imperfect and do not obey the typical intensity dependent absorption coefficient given by Eqs. (32)-(33), but instead obey

$$\alpha^h = \frac{\alpha_0}{1 + I/I_s^h} + \alpha_1 \quad (34)$$

where α_1 is a constant denoting the above-saturation linear absorption coefficient linked to the background absorption of the host material [8]. The constant background absorption coefficient does not show saturation due to the high concentration of the host material relative to the photon density.

Homogeneously broadened saturated two-photon absorption coefficient. We consider an analogous derivation of the two-photon saturation coefficient and its application to ultrafast measurements of the TPA behavior of a model chromophore. Similar saturation effects have been modeled via a density matrix approach with respect to optical phase conjugation [10], a semiperturbative approach with respect to molecular quantum wires [11], and a hyperbolic approximation based on Eq. (32) for bulk semiconductors [12]. This section derives the saturated two-photon absorption coefficient for both a homogeneously broadened and an inhomogeneously broadened system by extending the linear rate equation analysis for the two-level system to the nonlinear regime. The effects of excited state absorption are then examined and a comparison of our model to the TPA behavior of GFP is presented.

From quantum mechanics, the transition rate of a two-photon absorption event from a state $|n\rangle$ to a state $|k\rangle$ is

$$W_{nk} = \sum_m \left[\frac{\mu_{nm}\mu_{mk}}{\omega_{mn} - \omega} \right]^2 \frac{2\pi|E|^4 g(\omega_{kn})}{8\hbar^4} \quad (35)$$

where a normalized homogeneously broadened lineshape, $g(\omega_{kn})$, is assumed. Using the definition of intensity (see Ref. 13; note the departure from the convention used in this book) as $I = 2\epsilon_0 n_0 c |E|^2$, with n_0 being the linear index of refraction, the two-photon absorption transition rate can be rewritten as

$$W_{nk} = \frac{\sigma_{TPA} I^2}{2\hbar\omega} \quad (36)$$

where the two-photon absorption cross section is given in units of cm^4/GW and embodies the dipole moments, lineshape, and constant factors in Eq. (35). If both linear absorption and excited state absorption are ignored, then the rate equations governing this two-level system are

$$\frac{dN_k}{dt} = -W_{nk} \left(N_k - \frac{g_k}{g_n} N_n \right) - \frac{N_k}{\tau_{kn}} \quad (37)$$

$$\frac{dN_n}{dt} = -\frac{dN_k}{dt}$$

where τ_{kn} is the lifetime of the upper state, and $g_k (g_n)$ is the electronic degeneracy of the upper (lower) state. Using the localized coordinate transformations $\zeta = z$ and $\eta = z - ct$, the propagation equation is then taken to be (again, assuming negligible linear absorption)

$$\frac{dI}{d\zeta} = 2\hbar\omega W_{nk} \left(N_k - \frac{g_k}{g_n} N_n \right) = \sigma_{TPA} \Delta N I^2 \quad (38)$$

where $\Delta N = N_k - (g_k/g_n)N_n$. If it is assumed that we have at least a quasi-steady state regime, then using the localized coordinate transformations, Eqs. (37) can be rewritten as

$$\frac{d\Delta N}{d\eta} = - \left(1 + \frac{g_k}{g_n} \right) W_{nk} \Delta N - \left(\frac{(g_k/g_n)N_0 + \Delta N}{\tau_{kn}} \right) = 0 \quad (39)$$

where $N_0 = N_k + N_n$ is the total concentration of the two-photon absorbers. Extending the derivation given by Yariv [9] for the linear saturated absorption model, we can solve for the equilibrium population inversion ΔN^{eq} from Eq. (39), and substitute it into Eq. (38). It follows that for a homogeneously broadened system, the propagation equation dominated by two-photon absorption is given by

$$\frac{dI}{d\zeta} = \frac{-\sigma_{TPA} I^2 (g_k/g_n) N_0}{1 + (I/I_s^h)^2} \quad (40)$$

where we have identified the homogeneous saturation intensity as

$$I_s^h = \sqrt{\frac{2\hbar\omega}{\tau_{kn}\sigma_{TPA}(1 + g_k/g_n)}} \quad (41)$$

The homogeneously broadened effective two-photon absorption coefficient can then be identified from Eq. (40) as

$$\beta_{eff}^h(I) = \frac{\sigma_{TPA}(g_k/g_n)N_0}{1 + (I/I_s^h)^2} \quad (42)$$

Note that at low intensities, this reduces to the normal definition of the two-photon absorption coefficient in terms of the cross section.

Inhomogeneously broadened saturated two-photon absorption coefficient. If we continue to follow the analogous derivation of the *linear* saturated absorption coefficient, it is straightforward to show that the inhomogeneously broadened system will have a saturated two-photon absorption coefficient given by

$$\beta_{eff}^{ih}(I) = \int_{-\infty}^{\infty} \beta_{eff}^h(I, \omega - \omega_{kn}) p(\omega_{kn}) d\omega_{kn} \quad (43)$$

where $p(\omega_{kn})$ is the probability of a homogeneous class of absorbers having a central frequency of ω_{kn} , and $\omega - \omega_{kn}$ has explicitly been included in the argument of the homogeneous TPA coefficient to point out the dependence buried in the homogeneous lineshape, $g(\omega_{kn})$, of the TPA cross section. Under the approximation that the inhomogeneous lineshape is slowly varying with respect to the homogeneous lineshape (assumed to be a Lorentzian), evaluation of Eq. (43) results in

$$\beta_{eff}^{ih}(I) = \frac{\sigma_{TPA}^{ih}(g_k/g_n)N_0}{\sqrt{1 + (I/I_s^{ih})^2}} \quad (44)$$

where σ_{TPA}^{ih} and the inhomogeneous saturation intensity are defined by

$$\begin{aligned} \sigma_{TPA}^{ih} &= \sum_m p(2\omega) \left[\frac{\mu_{nm}\mu_{mk}}{\omega_{mn} - \omega} \right]^2 \frac{2\pi^2\omega}{\hbar^3\epsilon_0^2 n_0^2 c^2} \\ I_s^{ih} &= \sqrt{\frac{\hbar\omega\pi\Delta\omega p(2\omega)}{\tau_{kn}(1 + g_k/g_n)\sigma_{TPA}^{ih}}} \end{aligned} \quad (45)$$

Here, $p(2\omega)$ is the probability density of a homogeneous class of absorbers having a central frequency of 2ω . Analogously, this is normalized inhomogeneous lineshape function. The quantity $\Delta\omega$ is related to the dephasing time of the excitation (i.e., the width of the homogeneous lineshape, $g(\omega_{kn})$). The semi-classical expressions derived in Eqs. (42–45) are similar to those found from a purely quantum mechanical approach given by Ref. 10. We again note that if the intensity is very low compared to the saturation intensity, then Eq. (44) reduces to the typical expression.

Excited state absorption and background contributions. Until now, we have been examining the saturation behavior of the chromophore nonlinearity. Noting that, in general, the observed saturation does not go to zero, it is assumed that a second contribution, that of the host background, is contributing to the nonlinear absorption similar to the linear case of Eq. (34). Apart from an additional constant TPA coefficient, the effective nonlinear coefficient usually has a finite nonzero slope above the saturation intensity indicating the existence of excited state absorption. To fully model the system, we consider the general case of excited state absorption following a two-photon absorption event. For a three-level system, in the absence of stimulated emission (and subsequently from saturation), it can be shown that under short pulse excitation, the two-photon excited state population can be found from evaluating Eq. (25),

$$N_k \approx \frac{\sigma_{TPA}(g_k/g_n)N_0\tau_p I_0^2}{2\hbar\omega} \sqrt{\frac{\pi}{2}} \quad (46)$$

where τ_p is the pulse width, and I_0 is the peak intensity from a Gaussian pulse. Assuming the excited state absorption depends only on the two-photon excited state population, N_k , the propagation equation becomes (linear absorption negligible)

$$\frac{dI}{d\xi} = -\sigma_{TPA} \frac{g_k}{g_n} N_0 I^2 - \sigma_{ESA} N_k I \quad (47)$$

Substituting Eq. (46) into Eq. (47), factoring out I^2 , and performing a Taylor series expansion on the Gaussian pulse profile, one can identify (to lowest order) the effective two-photon absorption coefficient as (see Chapter 10):

$$\beta_{eff}^h(I \ll I_s^h) = \beta_0^h \left(1 + \frac{\sigma_{ESA}\tau_p I_0}{2\hbar\omega} \sqrt{\frac{\pi}{2}} \right) \quad (48)$$

where $\beta_0^h = \sigma_{TPA}(g_k/g_n)N_0$. The linear dependence of the two-photon absorption coefficient on intensity is manifested in typical Z-scan or nonlinear transmission experiments where the excitation energy is varied and the effective TPA coefficient measured as a function of intensity. The resulting data are fitted to a straight line where the y-intercept yields the TPA coefficient and the slope is proportional to the excited state absorption cross section. It can again be shown that the analogous inhomogeneous expression of Eq. (48) can be found from evaluation of Eq. (43), resulting in

$$\beta_{eff}^{ih}(I) = \sigma_{TPA}^{ih} \frac{g_k}{g_n} N_0 \left(1 + \frac{\sigma_{ESA}\tau_p I_0}{2\hbar\omega} \sqrt{\frac{\pi}{2}} \right) \quad (49)$$

where we have assumed that the excited state absorption cross section is nearly constant, such as occurs for excitation into or near the continuum or into conduction bands.

Effective two-photon absorption coefficient. Taking into account the background absorption of a host material, it has already been noted that linear saturable absorbers behave according to Eq. (34). It is reasonable to expect that saturation of a two-photon absorber in a host background would behave similarly. Thus, for a system of absorbers having a low concentration compared to the photon density, the former saturation model (Eqs. (42) or (44)) would dominate. As the intensity is increased beyond the saturation intensity, any intrinsic TPA and ESA of the host material background become observable, allowing the latter (Eqs. (48) or (49)) to dominate. Under these conditions, it is expected that a measurement of the effective two-photon absorption coefficient using standard Z-scan routines will yield data fitting Eqs. (42) or (44) at low intensities (but comparable to the saturation intensity), and fitting Eq. (48) or (49) at higher intensities. Subsequently, the cross section (or TPA coefficient) appearing in Eq. (48) or (49) is expected to be related to the host material, and is not expected to be the same as in Eqs. (42) or (44), such that for $\sigma_{ESA} = 0$ an expression similar to Eq. (34) is obtained. The choice of the final form of the effective TPA coefficient will depend on whether the system is homogeneously or inhomogeneously broadened within the timeframe of the experiment (i.e., within ~ 100 fs). For the case of a homogeneously broadened system, a measurement of the TPA coefficient versus intensity should follow the form of

$$\beta_{eff}^h(I) = \frac{\beta_0^h}{1 + (I/I_s^h)^2} + \beta_0^{h,host} \left(1 + \frac{\sigma_{ESA}\tau_p I_0}{2\hbar\omega} \sqrt{\frac{\pi}{2}} \right) \quad (50)$$

The analogous inhomogeneously broadened system will have the form

$$\beta_{eff}^{ih}(I) = \frac{\beta_0^{ih}}{\sqrt{1 + (I/I_s^{ih})^2}} + \beta_0^{ih,host} \left(1 + \frac{\sigma_{ESA}\tau_p I_0}{2\hbar\omega} \sqrt{\frac{\pi}{2}} \right) \quad (51)$$

Here, we have designated the above-saturation TPA coefficient with a “host” in the superscript analogous to Eq. (34) for distinction. The excited state absorption cross section can be linked to either the host or dopant species, depending on the coupling between the two-photon states of the host and dopant.

Coupled Z-scan and nonlinear fluorescence. A recent adaptation of the Z-scan and nonlinear fluorescence experiments detailed above consists of fiber-coupling the translation stage to a spectrometer. A standard Z-scan stage is adapted with a large collection optic and cylindrical lens at 90° to the propagation direction. A microscope objective is then used to focus the fluorescence into a fiber coupled to a spectrometer. Since the path lengths of the spectroscopic cells

are usually 1 cm or less (see discussion in Section IV), there is often plenty of light to observe. As the experiment proceeds, both the open and closed aperture Z-scan data are collected as well as the nonlinear fluorescence at each step. In this case, the intensity variation for the NLF results from the changing beam waist given by standard Gaussian beam propagation. It then becomes important to relate the nonlinear fluorescence to the shrinking active volume of the experiment. To do this, we need to calculate the total number of excited molecules as a function of the sample position.

The total number of excited molecules resulting from the two-photon excitation within the active volume of the sample is given by

$$N_{\text{molecules}} = \int N_{\text{TPA}} d^3 r \quad (52)$$

where for short pulse excitation in the absence of saturation, N_{TPA} is given by Eq. (26) with the notation $I_0 = I_0(\rho, z)$. In this equation, the integration volume is over the active area of the sample in a cuvette of length L . Substituting Eq. (26) into Eq. (52) above yields

$$N_{\text{molecules}} = \int \frac{N_T \sigma_{\text{TPA}} I_0^2(\rho, z) \tau_p}{2\hbar\omega_0} \sqrt{\frac{\pi}{2}} d^3 r \quad (53)$$

where the constants are defined under Eq. (26). Assuming a Gaussian spatial profile, the intensity can be represented as

$$I_0(\rho, z) = \frac{2\mathcal{E}}{\tau_p \pi w^2(z)} \exp[-2(\rho/w(z))^2] \quad (54)$$

where $w(z) = w_0 \sqrt{1 + (z/z_R)^2}$, z_R is the Rayleigh range, w_0 is the waist at focus, and \mathcal{E} is the incident energy. In cylindrical coordinates, it follows that the total number of excited molecules within the active volume of a two-photon absorbing sample is given by

$$N_{\text{molecules}} = \iiint \frac{N_T \sigma_{\text{TPA}} 2\mathcal{E}^2 \exp[-4(\rho/w(z))^2]}{\hbar\omega_0 \tau_p \pi^2 w^4(z)} \sqrt{\frac{\pi}{2}} dz \rho d\rho d\theta \quad (55)$$

Evaluating the ρ and θ integrals, we find

$$N_{\text{molecules}} = \int \frac{N_T \sigma_{\text{TPA}} \mathcal{E}^2}{2\hbar\omega_0 \tau_p \pi w^2(z)} \sqrt{\frac{\pi}{2}} dz \quad (56)$$

where the limits of integration extend from z' to $z' + L$, z' being the sample position along the translation stage of the Z-scan experiment. The total integrated fluorescence is then found in a similar fashion leading up to Eq. (29). Assuming that \mathcal{E} is constant, we find from Eq. (6) that the integrated fluorescence resulting

from two-photon absorption is linearly dependent on the local (at z') intensity. A log–log plot of the resulting data shows a slope of 1.

Similarly, the number density of molecules resulting from a short pulse one-photon excitation is represented by,

$$N_{\text{OPA}} \approx \frac{N_T \sigma_{\text{GSA}} I_0(\rho, z) \tau_p}{\hbar \omega_0} \sqrt{\pi} \quad (57)$$

Thus the total number of excited molecules within the active volume is given by,

$$N_{\text{molecules}} = \int \frac{N_T \sigma_{\text{GSA}} \mathcal{E}}{\hbar \omega_0} \sqrt{\pi} dz \quad (58)$$

The limits of integration again span from z' to $z' + L$. As can be seen from Eq. (58), the number of molecules is simply a constant number for linear fluorescence. Therefore, when the integrated fluorescence of a sample is graphed on a log–log plot, the resulting line has a slope of zero. In performing the combination experiment, simultaneous measurements of the NLF with the Z-scan data gives additional information regarding the relative contributions of one-photon and two-photon states.

If one further extends the theory by including the possibility of nonlinear saturation, as described above, then the total number of molecules in the excited state behaves as

$$N_{\text{molecules}} = \iint \frac{N_T \sigma_{\text{TPA}} I_0^2(t, \rho, z) \tau_p}{2 \hbar \omega_0 \sqrt{1 + (I_0(t, \rho, z)/I_s^{ih})^2}} dt d^3 r \quad (59)$$

where I_s^{ih} is the inhomogeneous saturation intensity. The total detected signal can then be found from a similar analysis to the discussion leading up to Eq. (31). With modest incident energies (of order 1 μJ), saturation effects can be clearly visible from the integrated NLF.

II. SPECIAL EXPERIMENTAL CONSIDERATIONS

The setup and execution of any optical experiment usually contains one or more of the following components: reflecting optics, refracting optics, and detectors. In the successful execution of an ultrafast pulse experiment, some extra consideration should be given towards the effects of these components on the pulse as well as the effects of the pulse on the components. In considering which type of optics to use, one must consider the pulse parameters of the system. Commercially available ultrafast systems are dominated by Ti:sapphire (700–900 nm) having pulse widths ranging from about 30–200 fs depending on the options. Frequency doubling allows these systems to reach the

350–450 nm range. While other ultrafast systems are available, none are so common or versatile, and therefore we will restrict our discussions to components relating to these lasers. In this section we examine some of the practical concerns using the formalisms discussed above. For a more thorough theoretical description of these effects, the reader is referred to references [15] and [3].

A. Reflective Optics

Most likely, the first thing an ultrafast pulse is going to encounter when exiting the cavity is a mirror. There are three main concerns regarding a mirror: the damage threshold, self-phase modulation(SPM), and GVD. Whether the system in use is just an oscillator or an amplified and compressed laser will determine the choice of mirror with respect to damage threshold, and to some extent SPM. The effects of GVD, however, will always be present and are dependent on pulse width as defined by Eq. (10).

The selection of mirrors for the near infrared wavelength range is either a protected metal (aluminum or silver) front surface mirror or a dielectric coating. Both of the protected metal mirrors have high reflectivity in the infrared region, however the protected silver generally has a higher damage threshold (see, for example, optical specifications from commercial catalogs). Oscillator peak pulse intensities are typically on the order of tens of megawatts per square centimeter, while amplified peak pulse intensities can range from hundreds of megawatts per square centimeter for 300-fs pulses to tens of gigawatts per square centimeter for 30-fs pulses. The not so obvious problem with protected metal mirrors is the oxidation effect under prolonged exposure to the high intensities common to ultrafast pulses. It is generally found that the protective layer covering the metal is slowly ablated allowing oxygen to penetrate the metal layer and tarnish the mirror, resulting in greatly reduced performance and eventual damage. Prolonged life can be given to these mirrors by enclosing them in a nitrogen atmosphere. Dielectric mirrors, on the other hand, have a comparable reflectance and a very high damage threshold in comparison, without the problems associated with metals. Their main drawback, however, is that they are usually an order of magnitude more expensive.

The effects of GVD on a Gaussian pulse were discussed in Section I.B. For the case of a typical dielectric stack mirror, the GVD coefficient across the infrared wavelength range is shown in Fig. 2 (typically tens of $\text{fs}^2/\mu\text{m}$). Using these values in Eq. (10) above, one can calculate that the effective pulse width resulting from reflection of a 700-nm, 100-fs pulse, incident on a 100- μm stack, is approximately 120 fs, and the center wavelength shift is about 6 nm with little effect on the bandwidth. The effect is less for a comparable pulse at 800 nm and beyond, while for a shorter pulse (30 fs) the effect is dramatically larger giving an

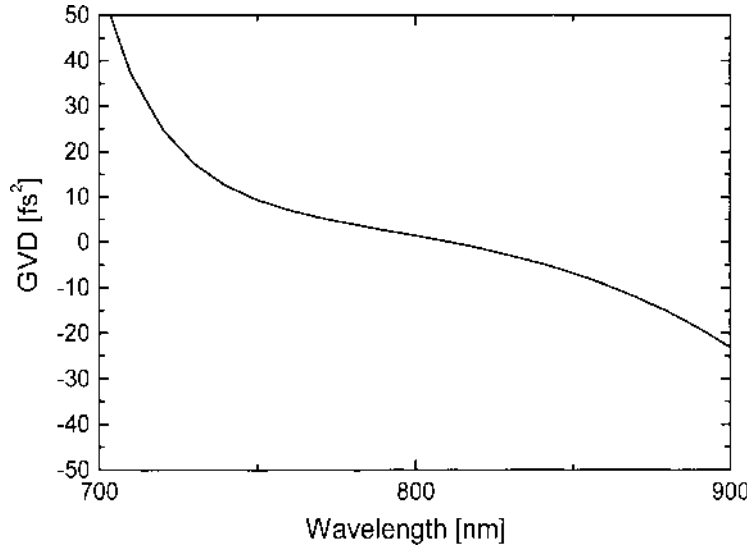


Figure 2 Typical group velocity dispersion coefficient versus wavelength for a dielectric stack mirror.

effective pulse width of 240 fs and a wavelength shift of 17 nm, with an accompanying bandwidth increase of a few percent. Metal mirrors typically have a lower GVD coefficient around a few $\text{fs}^2/\mu\text{m}$, making the GVD effects on the pulse somewhat less than the dielectric case.

The self-phase modulation of an ultrafast pulse by any optical component can be estimated by calculating a critical intensity where the effect becomes noticeable. We can make use of Eq. (19) to define this critical intensity where the maximum frequency shift due to SPM is equal to the bandwidth limit ($\Delta\omega_b = 2\pi/\tau_0$) of the pulse (i.e., where $\Delta\omega_{\max} \approx \Delta\omega_b$). Beyond this intensity, the spectrum of the pulse will broaden beyond the limit. Using the definition of peak intensity $I_0 = 2n_0\epsilon_0 c a_0^2$ in Eq. (19), we can write

$$\frac{2\omega_0 n_2 I_0 \zeta}{c \tau_0 n_0 \epsilon_0 c} (\sqrt{2} e^{-1/2}) = \frac{2\pi}{\tau_0} \quad (60)$$

Solving for $I_{\text{cr}} = I_0$ where this equality holds true, one finds that

$$I_{\text{cr}} = \frac{\lambda_0}{1.716 \zeta n_2} \quad (61)$$

where λ_0 is the center wavelength in free space. For example, aluminum oxide has a nonlinear refractive index coefficient of about $7.2 \times 10^{-16} \text{ cm}^2/\text{W}$ at

800 nm. The propagation depth of the reflected wave from a coated surface of this material is taken to be the skin depth of the metal [5]. In this case, the skin depth is on the order of a few micrometers, giving a critical intensity of over 60 TW/cm^2 —usually beyond the damage threshold of the coating. In other words, although the mirror surface itself may cause some SPM of the reflected wave, ablation of the surface and subsequent propagation of the pulse into the substrate can very easily cause SPM as demonstrated below. Usually damage to a mirror is more noticeable by the supercontinuum generation visible downstream than by the appearance of a small spot on the mirror, often only observable under magnification. The case of the dielectric stack is comparable.

While the metal mirrors affect an ultrafast pulse less than the dielectric stack, the pulse affects the metal mirrors significantly more. In view of these considerations, the preference is to use dielectric mirrors whenever possible for pulse widths of 100 fs or less, while metal mirrors can be used for longer pulse widths provided the peak intensity is below the damage threshold.

B. Refractive Optics

The next practical concern is the use of refractive optics to focus and collimate an ultrafast pulse. The most common materials for these optical components are BK7 glass and fused silica. The GVD coefficients for BK7 and fused silica at 800 nm are $45 \text{ ps}^2/\text{km}$ and $36 \text{ ps}^2/\text{km}$, respectively [3], while the nonlinear coefficients are $4.4 \times 10^{-16} \text{ cm}^2/\text{W}$ and $3.5 \times 10^{-16} \text{ cm}^2/\text{W}$, respectively [8]. Intuitively, one would like to use only thin lenses to minimize the interaction lengths relative to the characteristic lengths of GVD and SPM.

Damage to refracting optics is less of a problem than to mirrors unless a reflected focus occurs within the lens, or unless the self-focusing threshold is surpassed. The former can be avoided by using the proper antireflection coatings and plano-type optics. The latter can be avoided by controlling the peak power relative to the critical power (typically a few hundred kilowatts) discussed in Section I.D, relative to the self-focusing distance in Eqs. (60) and (61) (typically in the mm range). Using thin lenses, on the order of a few millimeters thick, and keeping the incident peak power low, damage due to self-focusing within refractive optics is usually not a problem for pulse widths longer than 100 fs.

Prior to the onset of damage due to self-focusing, one will usually observe supercontinuum generation due to SPM. For example, using Eq. (61), a 3-mm thick lens of fused silica would have a critical intensity threshold of about 440 GW/cm^2 in the near IR ($\sim 800 \text{ nm}$). For a 100-fs pulse, this corresponds to a fluence of 44 mJ/cm^2 . A 4% retroreflection of a $500\text{-}\mu\text{J}$ pulse need only have a beam waist of about $120 \text{ }\mu\text{m}$ to cross this threshold within the lens. Alternatively, a $500\text{-}\mu\text{J}$ pulse need only have a waist of about $600 \text{ }\mu\text{m}$ within a lens to cross

the threshold. Once this threshold is surpassed, the group-velocity dispersion of the optic will consequently broaden the supercontinuum pulse, creating a spectrally and temporally broader pulse delivered to the sample in the experiment. Caution must therefore be exercised when setting up an optical configuration in order to avoid this problem. Alternatively, one can pre-chirp the incident pulse to have the optical chain compensate [14]. It is usually more efficient to avoid the problem if possible.

C. Detectors

The measurement of nonlinear phenomena by ultrafast techniques requires the accurate knowledge of the pulse profile at the sample interface. Unfortunately, the evolution of beam profiling instruments has not been able to keep up with the rapid evolution and affordability of ultrafast, high-energy lasers. In this section, we briefly cover some of the problems relevant to detectors and comment on some possible solutions.

Due to the physical limitations on electronic measurement of the temporal dynamics of subpicosecond pulses, we are left with optical characterization of the profile. There are two domains in which this can occur—time or frequency, with respect to a given order of a correlation function. The methods employed usually involve a nonlinear crystal, calibrated detectors, and/or spectral analysis. Several authors have excellent detailed articles and books on the various methods, and the interested reader is referred to them [15–17]. Here, we comment on the problems common to these methods. Direct detection of the pulse with a semiconductor detector is a common practice, either for characterization of the pulse or for triggering purposes. The most evident problems of this approach are saturation, single pulse damage, and cumulative damage due to high repetition rates (MHz) compared to the sweep rates of small area devices ($<100 \mu\text{m}^2$). For example, with regards to the optical component of the characterization technique (usually a nonlinear crystal), the effects of GVD and SPM are very important due to the obvious broadening effects detailed above. With respect to pump-probe experiments, autocorrelation of the pulse at the sample interaction plane is the easiest and most efficient method of pulse characterization downstream of the optical train. However, care must be exercised in selecting the crystal for this purpose as crystal thickness is an optimized parameter for ultrafast autocorrelators due to the extreme GVD) that can cause broadening of such a short pulse ($<100 \text{ fs}$). Alternative methods of *in situ* pulse profiling are illustrated below, and readers are referred to Rullière's book [15] on femtosecond pulses for more information.

III. EXPERIMENTAL TECHNIQUES

Thus far we have reviewed and detailed some of the important theoretical aspects of using ultrafast laser pulses and some of the special experimental considerations needed in ultrafast nonlinear characterization of materials. Here we detail some of the more common experiments that can be performed, making note of the nuances of using ultrafast pulses.

A. Ultrafast Z-Scan

The general aspects pertaining to the standard Z-scan experiment were detailed in Chapter 7. In this section, we discuss the experiment with respect to ultrafast pulses. The main advantage of using femtosecond pulses can be found from considering the time responses of the different contributing processes to the nonlinear refractive index. These have been well characterized in the literature and summarized in Boyd's book [18,8]. The intrinsic response of the material due to the electronic contribution to the third order nonlinearity occurs on the time scale characterized by the electron orbit (i.e., a femtosecond time scale). In order to probe such a response to extract significant structure-property relationships, without the obscurity of longer time scale processes such as excited state absorption, molecular reorientation, multiple reflection effects, and thermal lensing, one has to probe the system with ultrafast pulses. For example, on the time scale of a single pulse (<100 fs), there is essentially not enough time for molecules to reorient or for a thermal lens to form. In addition, étalon effects are mitigated by the short coherence lengths (μm) compared to typical sample path lengths (mm). However, using femtosecond pulses in the standard Z-scan experiment can easily result in several problems stemming from SPM and thermal blooming (repetition rate dependent) due to the high nonlinearity of the materials under study. Using the formalisms developed earlier, we will detail some of these effects as well as some solutions to either overcome them or make good use of them.

A generic schematic of a standard Z-scan experiment is presented in Fig. 3. We begin with a review of the experiment. A beam is focused coaxial with a translation stage such that the focus occurs at the center of the stage. At the end of the stage, in the far field, a beam splitter is placed. One portion of the beam is focused into a detector (named the open aperture detector) and the second beam is centered on an aperture with a detector behind to measure the transmitted energy through the aperture (named the closed aperture detector). A calibrated energy meter measures the input of the pulse prior to the stage. Phase sensitive detection is usually the best and provides the highest sensitivity. The sample is fixed to the translation stage and moved down the axis of the beam. As the sample passes

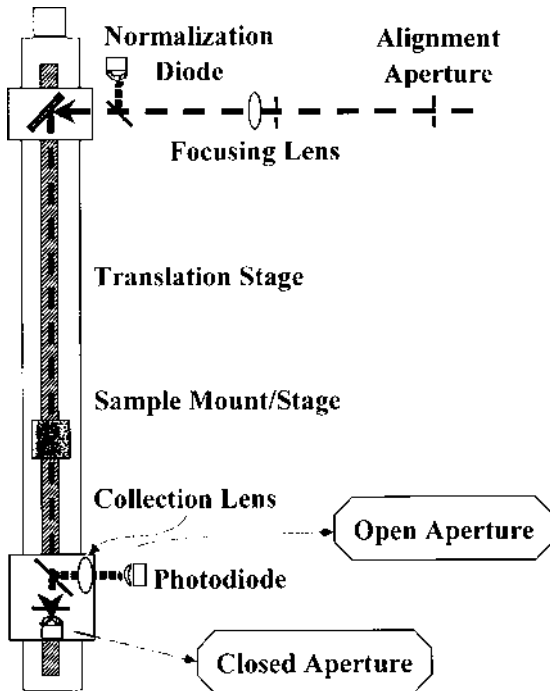


Figure 3 Z-scan experimental setup.

through the focus, the intensity progressively increases by virtue of the decreasing beam size. The open aperture detector will see only changes in the transmission due to a reduction (or increase) of the absolute number of photons (energy) from the pulse due to nonlinear absorption processes. These can include two-photon absorption, excited state absorption, or saturated absorption. The closed aperture detector will see changes in the transmitted energy through the aperture due to the reduction (or increase) in the photon number (energy) as seen by the open aperture detector, as well as the reduction of transmitted photons through the aperture due to changes in the spot size resulting primarily from the nonlinear refractive index. The resulting data for the open aperture detector can be fit to Eq. (23) above with the nonlinear coefficient, β , replaced by $\beta_{eff}^{th}(I)$ as defined by Eq. (49), assuming only one excited state absorption event from the two-photon state and no saturation. The intercept is the intrinsic TPA coefficient while the slope is proportional to the excited state absorption cross section from the TPA state. One or two-photon saturation effects can be taken care of by the appropriate substitution of the effective two-photon absorption coefficient illustrated above [Eq. (51)] and in Chapter 10. Typical open-aperture data, showing both

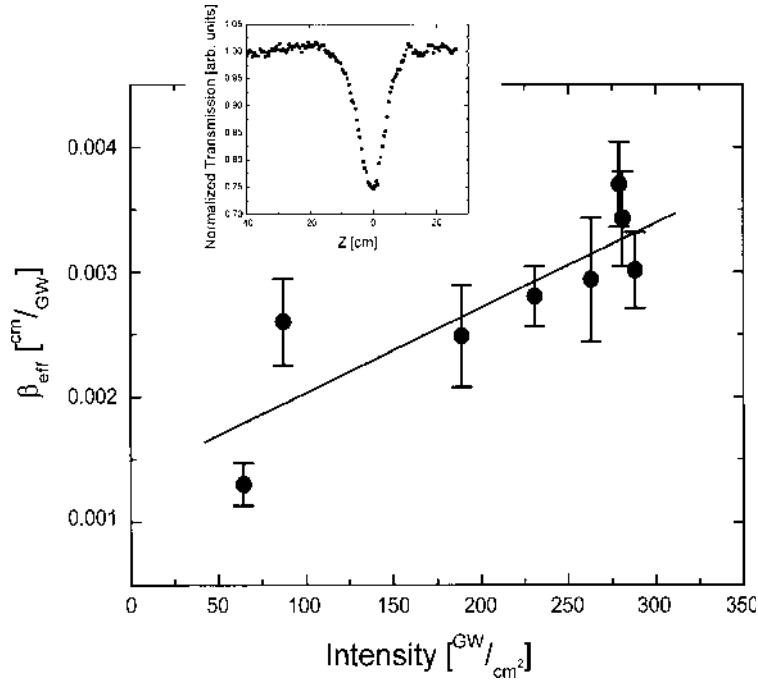


Figure 4 Typical open aperture Z-scan data and resulting intensity dependence of the effective two-photon coefficient.

the intrinsic two-photon absorption and the excited state absorption, is given in Fig. 4, while saturated open-aperture data is shown in Fig. 5.

While this technique has been widely used to measure the effective third order nonlinearity in a vast number of materials, some important details need to be considered when using an ultrafast pulse to measure the intrinsic nonlinearity. In the conventional setup, where nanosecond and picosecond pulses are used, it is desirable to have the translation stage as short as possible to minimize the effects of moving an optical wedge (the sample) along the axis of a directed beam. Even the most expensive matched spectroscopic cells still have a slight wedge, which can walk a beam off target on a long lever arm. Ultimately, the length of the translation determines the focal length of the focusing optic and consequently the sample path length. In order to use the thin sample approximation for developing the theoretical functions above, the sample length must be shorter than the Rayleigh range. However, when switching to an ultrafast pulse, extra consideration of the focal length must be taken into account. Primarily, as one is trying to measure samples with a high nonlinear refractive index, a short focal

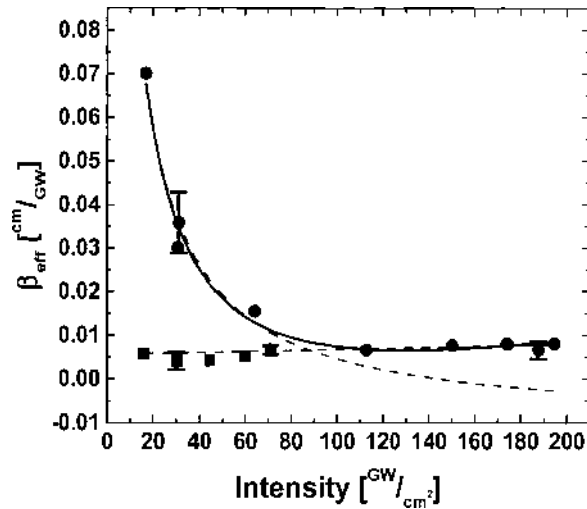


Figure 5 Saturated two-photon absorption coefficient for GFP (circles) versus intensity. The solid curve is a fit to Eq. (51). The circles are data for a control protein. The two dashed curves are fits to Eqs. (44) and (49).

length in conjunction with an ultrafast pulse will undoubtedly lead to self-phase modulation, or supercontinuum generation. For example, using a path length of 1 mm and a typical sample nonlinearity of $10^{-15} \text{ cm}^2/\text{W}$ (an order of magnitude higher than the glass surrounding the sample), from Eq. (53) we find that the threshold intensity for supercontinuum generation is about 466 GW/cm^2 . In a typical configuration, the translation stage may be configured for a Rayleigh range of twice the sample length (e.g., 2 mm). In that case, the input energy required to meet the critical intensity for self-phase modulation is $0.75 \mu\text{J}$. This means that for this particular setup and experiment, $0.75 \mu\text{J}$ is the limit of useful input energy. As a consequence, the detectors in the far field must necessarily be sensitive to the low nanojoule range in order to get the dynamic range required to separate the intrinsic TPA coefficient from the excited state absorption as defined by Eq. (49). Typical nanojoule-sensitive energy meters or cooled semiconductor detectors run in the thousands of dollars, making practical considerations such as cost a significant problem. In addition to SPM, catastrophic self-focusing would almost be a certainty, as the peak power ($< 7.5 \text{ MW}$) exceeds the critical power typical of glass (400 kW) used to house the sample, and the short Rayleigh range would give a focusing distance to within the sample. If self-focusing occurs, the spot size within the sample decreases, causing the intensity to increase, and as before, causing a stronger self-focusing effect. It should be obvious that a higher

intensity will cause a stronger two-photon absorption, further decreasing the pulse transmission. Coupled to the two-photon absorption is the ease with which cumulative thermal build up can occur from a high repetition rate and a short focus. Ti:sapphire systems typically run in the 100-MHz range (oscillator) or in the kilohertz range (amplified). In either case, this repetition rate is in general too fast. Since the two-photon state and the corresponding one-photon state are necessarily not the same by virtue of parity, there is a high probability that some thermal energy will be released by the coupling of these two states in proportion to the number of excited states formed (high peak intensities). Without giving the system enough time for the heat to diffuse out of the focal region, a steady-state thermal lens will form very quickly. Such a thermal lens will manifest itself as a high nonlinear refractive index leading again to erroneous intrinsic measurements. All of these processes can quickly play off of one another, causing either catastrophic sample damage, or just plain bad data.

A practical solution to these problems can be found by going to a longer translation stage and a longer Rayleigh range. It is not uncommon to use up to a meter translation and an optical arrangement having a Rayleigh range of 10 cm. In such a setup, the dynamic range of useful input energy rises up to tens of microjoules allowing the use of room temperature photodiodes or energy meters for measurement. In addition, the longer Rayleigh range allows for longer sample path lengths. However, care should be exercised as the thin sample approximations can more easily be violated due to self-focusing/trapping. Increasing the Rayleigh range (the waist at focus) also decreases the probability that SPM will occur, while maintaining the intensity level required to measure a signal. Either chopping or reducing the repetition rate can mitigate the problem with thermal lensing. While the reader may note that this solution is not restricted to the long translation stage setup, there is an advantage in this case. If we consider that the net thermal loading per pulse is some fraction of the incident pulse fluence, then for a fixed energy, increasing the beam waist by a factor of 10 will decrease the thermal load delivered to the system, per pulse, by a factor of 100. For a fixed repetition rate, the cumulative buildup of thermal energy to some given threshold will take 100 times longer in the long Rayleigh range setup. Therefore, all things being equal, one would need to reduce the repetition rate of the low f-number setup by a factor of 100 from that of the high f-number setup to nullify the same thermal problem.

While a long translation stage appears to solve several concerns of an ultrafast pulse Z-scan, there is one inherent problem that arises. A long translation stage means a long lever arm, causing beam walk off due to wedged samples to be a major problem. To some extent this can be answered by using shorter sample path lengths, but then higher concentrations of materials are needed to compensate. Subsequently, the setup of choice will necessarily be a balance

between the ability of the researcher to align and maintain a long lever arm and the ability to compensate for lower energies necessary with short lever arms.

B. Nonlinear Fluorescence

A simple three-level model detailing the measurement of nonlinear fluorescence was presented in Section I.E above. One general experimental setup for ultrafast nonlinear fluorescence measurement is shown in Fig. 6. Note that it is important to have accurate knowledge of the input pulse and corresponding intensity at the sample in order to correctly fit data to Eq. (31). Therefore, a sample is excited in an unfocused geometry, although the beam diameter can be telescopied to give the appropriate intensity range. Intensity attenuation should be performed prior to telescoping using a single variable attenuator (metal coated) or a pair of high intensity ultrafast polarizers. Inserting multiple neutral density filters can be problematic, as these glasses are either dye doped or semiconductor doped, giving them high nonlinearities that can cause SPM or pulse broadening as discussed in Section III. As in all fluorescence measurements, fluorescence is collected at 90° to the pump axis to avoid laser scatter. A dielectric notch filter is recommended to block the fundamental. A calibration is necessary to determine the collection volume in Eq. (31), as well as a lifetime measurement of the emitting state. In the most controlled circumstances, a pair of phased shutters is used to collect single pulse events. Nonlinear fluorescence is collected on a CCD (or a scanning spectrometer and PMT) as a function of incident intensity. As a result, several processes can be observed. These include, but are not limited to normal two-photon emission, two-photon saturation, vibrational modes and nonlinear photochemical reactions.

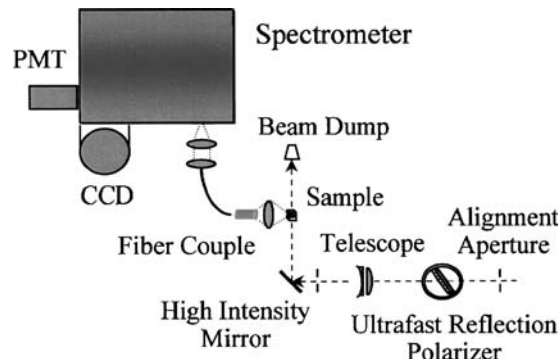


Figure 6 Nonlinear fluorescence experimental setup.

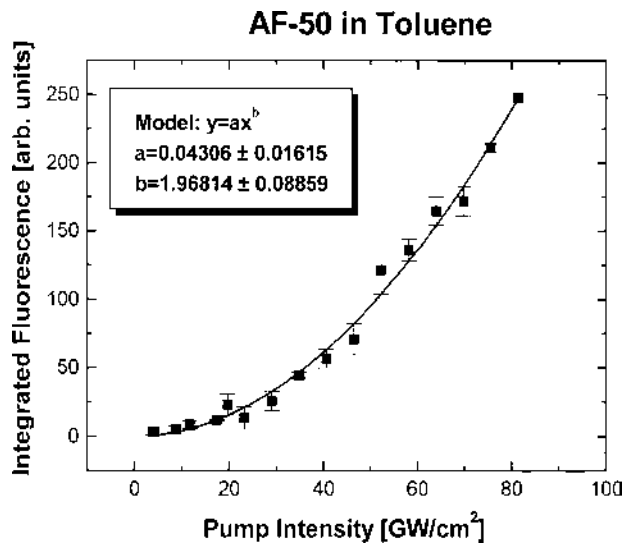


Figure 7 Integrated nonlinear fluorescence with theoretical fit (solid line).

In Figures 7–10 we illustrate several of these processes. Figure 7 shows a typical nonlinear fluorescence scan resulting from a “well-behaved” material, AF50 in toluene [19,20]. The fit (solid line) to the data has an exponent of 2, clearly indicating two-photon absorption. Assuming a three-level model and

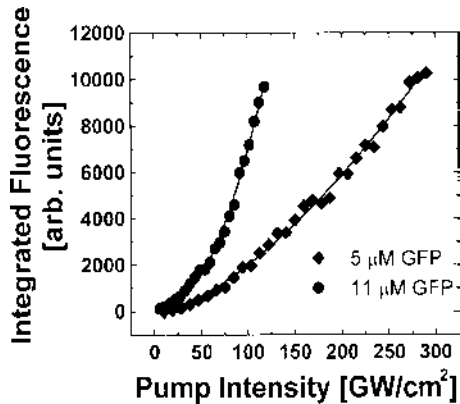


Figure 8 Integrated nonlinear fluorescence of GFP showing saturation at low concentration.

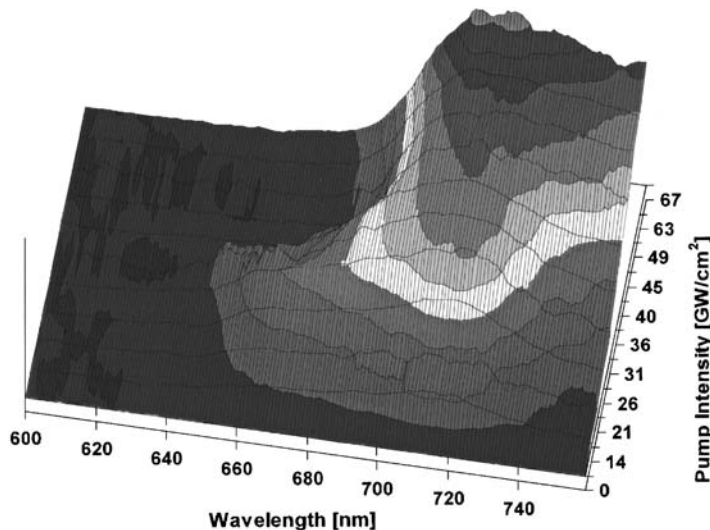


Figure 9 Nonlinear fluorescence of tetraphenylporphyrin showing a photo-induced chemical reaction at high intensity.

a fluorescence quantum yield of 0.8, the two-photon absorption cross section is found from Eq. (31) to be $0.14 \times 10^{-20} \text{ cm}^4/\text{GW}$, in close agreement to the Z-scan measurements of AF50 ($\sim 0.2 \times 10^{-20} \text{ cm}^4/\text{GW}$). Figure 8 shows the same experiment performed on two concentrations of the biological chromophore GFP (green fluorescent protein). As can be seen from the fits, the lower concentration data shows saturation resulting in an exponent of 1.3, while the higher concentration shows no saturation with a nominal exponent of 2. As saturation is evident here, Eq. (31) cannot be applied directly to this case. Instead, an exact rate model analysis similar to that leading up to Eq. (42) is useful. However, it should be noted that one would need to further perform an inhomogeneous statistical analysis to match the data. In this case, it is easier to perform the Z-scan analysis demonstrating the saturation of the two-photon coefficient as in Fig. 5. Figure 9 shows an irreversible nonlinear photochemical change. The material of interest here is tetraphenylporphyrin in chloroform. At low intensities, the nonlinear fluorescence has two characteristic peaks centered at about 670 nm and 720 nm. Note that as the intensity is increased, the blue peak disappears and the red peak begins to broaden and red shift. The effect is irreversible and was found to be linked to a degradation of the chromophore resulting from nonlinear excitation of the solvent (chloroform). Figure 10 shows the linear absorbance (dashed) and the linear fluorescence spectrum (dotted) of octobromotetrphenyl porphyrin as compared to the nonlinear fluorescence (solid). The two peaks occurring in

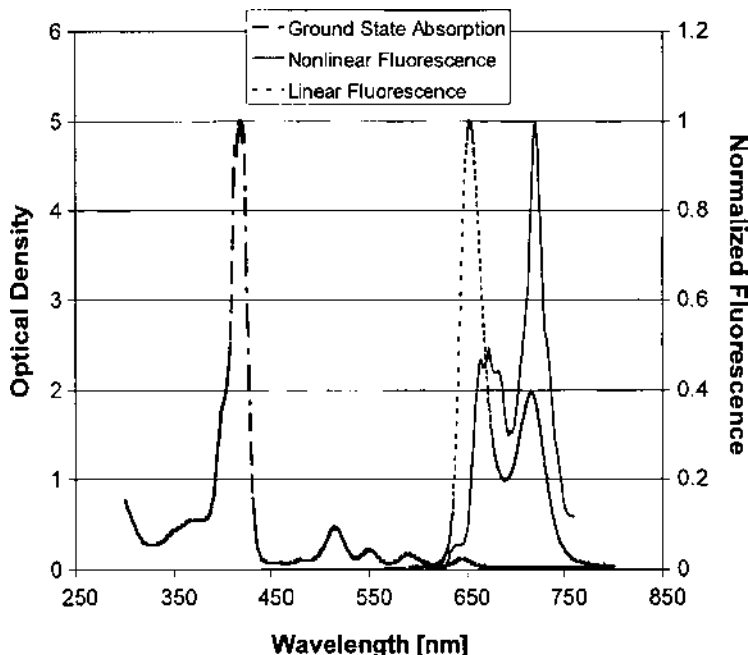


Figure 10 Nonlinear fluorescence spectrum compared to linear fluorescence spectrum illustrating a variation in vibrational modes.

the linear spectrum have been attributed to the 1 and 0 vibrational modes of the porphyrin [21]. Note that in the nonlinear case, the relative intensities of these peaks are reversed, possibly indicating a localized nonequilibrium hot spot. These data illustrate the scope of information available from this experiment.

As mentioned previously, it should be obvious that the nonlinear fluorescence and Z-scan experimental techniques can be combined by fiber coupling a spectrometer and CCD camera at 90° to the propagation direction. If aligned properly, the fluorescence coupling should be constant along the propagation path, while the pump intensity changes as a function of position by virtue of the changing spot size. The overall increase in processing time is minimal as the instruments can be triggered to pass data independently. The total data increase can be substantial as both incident pulse monitoring for SPM, as well as photochemical measurements, can be obtained simultaneously.

As an example, Fig. 11 shows the integrated NLF of a typical two-photon chromophore resulting from a fiber-coupled Z-scan experiment. It can clearly be seen that for lower intensities (far from focus) the NLF behaves as expected with a slope of ~ 1 . As the sample approaches focus, saturation effects become visible

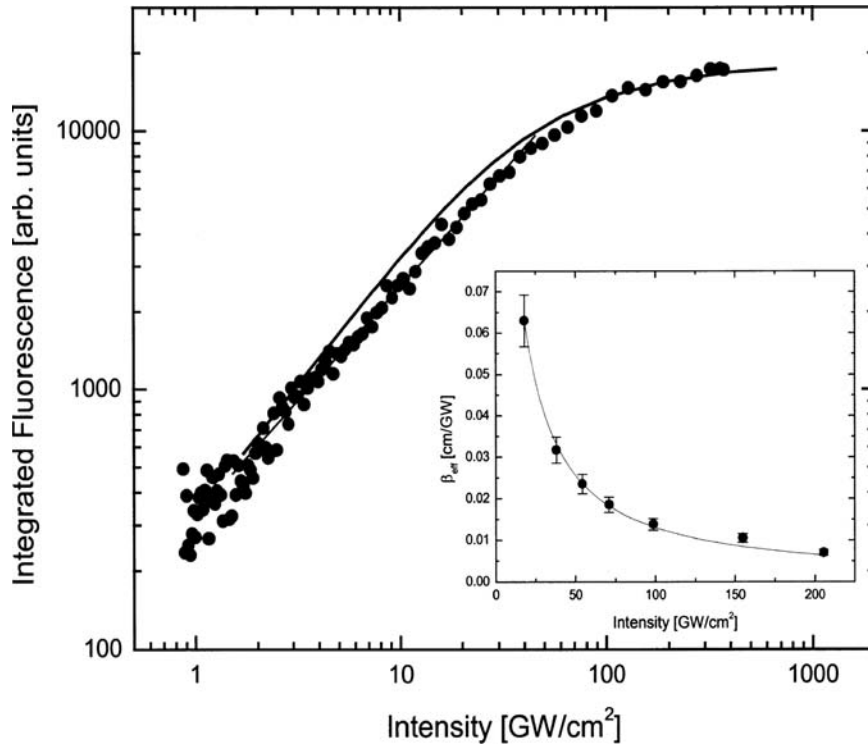


Figure 11 Integrated nonlinear fluorescence obtained from a fiber-coupled Z-scan experiment. Solid line is a fit to Eq. (59). Inset shows results of Z-scan open aperture experiment clearly showing saturation. Solid line is fit to Eq. (44).

as the signal becomes constant. The solid line is the fit to the data numerically solving Eq. (59). As an additional note, the measurement of the effective two-photon absorption cross section also shows saturation effects as described by Eq. (44) and illustrated by the inset to Fig. 11. The solid line is the fit to Eq. (44). An advantage to this technique is the sensitivity of the NLF to saturation effects, which may be masked in the open-aperture data by noise, photodegradation, and moderate saturation intensities (a negative slope in the effective two-photon absorption coefficient measurement over the incident intensity range).

C. Nonlinear Transmission

As indicated in Section I.E, a standard nonlinear transmission experiment uses a collimated beam to probe the two-photon absorption coefficient of a material.

When using an amplified ultrafast pulse for this experiment, the spot size is not required to be exceptionally small in order to probe the nonlinearity. As a result, the problems associated with pushing the threshold for white light generation and self-focusing can be avoided. There are primarily two separate experimental arrangements that one might use. The first uses the beam as it exits the compressor, namely as a pulsed Gaussian beam. The incident and transmitted pulse energy can be measured using a pair of calibrated diodes or energy meters in conjunction with two thin beam splitters as illustrated in Fig. 12. Again, phase sensitive detection is best here. The resulting transmission can be plotted versus incident intensity and fit to Eq. (22) for a Gaussian pulse. As this technique and the open aperture Z-scan technique are similar in nature, a brief comparison is justified. In a nonlinear transmission experiment, the pump beam is set to some collimated waist size such that at maximum energy, neither the damage threshold nor any unwanted nonlinear thresholds are reached. This often results in spot sizes on the order of square millimeters. Subsequently, to see a nonlinear change in the transmission, one needs to have pulse energies in the hundreds of microjoules (i.e., intensities in the hundreds of gigawatts per square centimeter). The advantage is that no moving parts are required, however data sampling is limited to the availability of discrete energy sampling. In contrast, an open-aperture Z-scan experiment can be performed using as little as hundreds of nanojoules of energy in an appropriate geometry as discussed above. Some advantages here are that both excited state absorption information and statistical sampling become easier. For comparison, a typical set of data for tetraphenylporphyrin in toluene is shown in Fig. 13(a) (Z-scan) and Fig. 13(b) (nonlinear transmission). The Z-scan data were taken with 1 μJ of energy, while the NLT data were taken with pulse energies up to 1 mJ.

The second experimental arrangement is generally used when the spatial response of the material is also desired, for example to check for concentration homogeneity within a solid. In this instance, some spatial filtering of the incident beam is required in order to produce a well-defined top hat profile. Additional

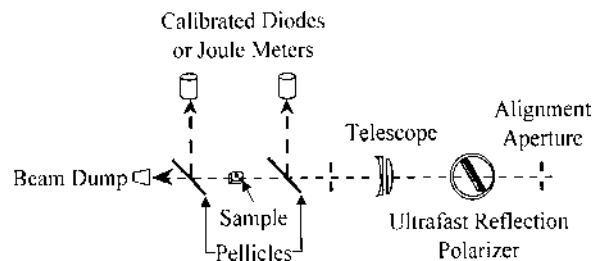


Figure 12 Nonlinear transmission experimental setup.

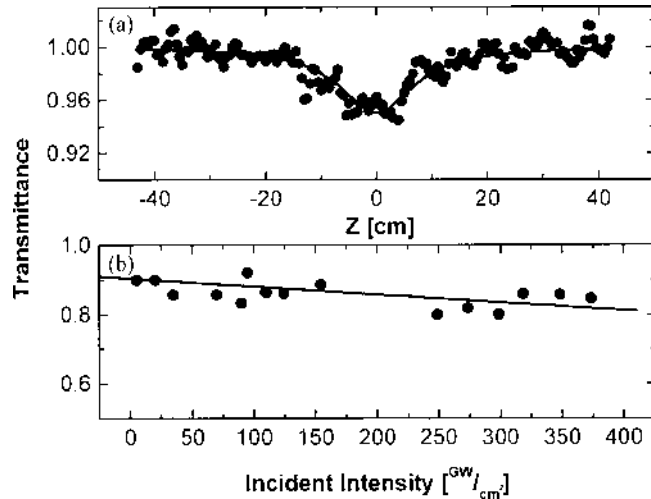


Figure 13 Nonlinear transmission data compared to open aperture Z-scan data.

complexity is added, as the transmitted pulse needs to be imaged onto a CCD camera.

There are two main issues to deal with when performing this experiment with ultrafast pulses: spatial filtering and CCD saturation or damage. First, in order to obtain a top-hat profile, one usually overfills an on-axis iris and collimates the output beam. If the initial pulse energy is high enough, this method may be used and still allow a large enough dynamic range to perform the measurement. However, additional spatial filtering employing focusing has to be avoided as the ionization intensity of air is easily surpassed causing spatial distortions of the pulse as well as phase modulation. In addition, attempting to pass a focused ultrafast pulse through a pinhole is only successful using a few microjoules of energy before the damage threshold of the pinhole is reached. In this regime, it is almost impossible to see the nonlinearity. In regards to the CCD, an upper limit to the total fluence of the top hat beam is determined ultimately by the saturation fluence threshold of the camera for a direct view measurement, where the CCD camera is placed directly at the output. However, this is usually not necessary, and neutral density filtering can be used to increase the dynamic range of the measurement. For the case where only one CCD camera is available (for measurement at the output), the incident beam must necessarily be well characterized and stable over long periods of time in order to extract the transmission. Commercial femtosecond laser systems having a pulse width of less than 100 fs and amplified energy up to a couple of millijoules typically have pulse-to-pulse energy stability of a 2% or less. Unless the differential nonlinear

transmission across the spot is larger than a few percent, this method of measurement will be inaccurate. The best method would employ two calibrated CCD cameras to measure the incident pulse and the transmitted pulse allowing for single pulse-to-pulse normalization. Practical considerations, specifically cost associated with cooled cameras, can make this impractical. An alternative is to use a single camera with a large enough detector area to image two spots onto one camera. This method still allows for single pulse-to-pulse normalization using one camera. One possible setup was illustrated earlier in Chapter 10, Figure 10 with respect to a transient white light absorption experiment, and is further discussed below. Some problems associated with this method include charge drift and matching the dynamic range of the incident and transmitted spots.

D. Transient White Light Absorption Spectroscopy

Transient white light absorption spectroscopy is a technique that makes use of supercontinuum generation in a pump-probe setup to measure the excited state dynamics of a material. The resolution of the temporal dynamics is determined by the optical delay resolution of the particular setup as well as the overall chirp of the supercontinuum pulse. A schematic of a typical transient white light absorption experiment is shown in Fig. 14. Unless otherwise noted, all optics are low dispersion, high intensity optics designed for use with femtosecond pulses as indicated in Section II. In this case, a commercial femtosecond Ti:sapphire laser

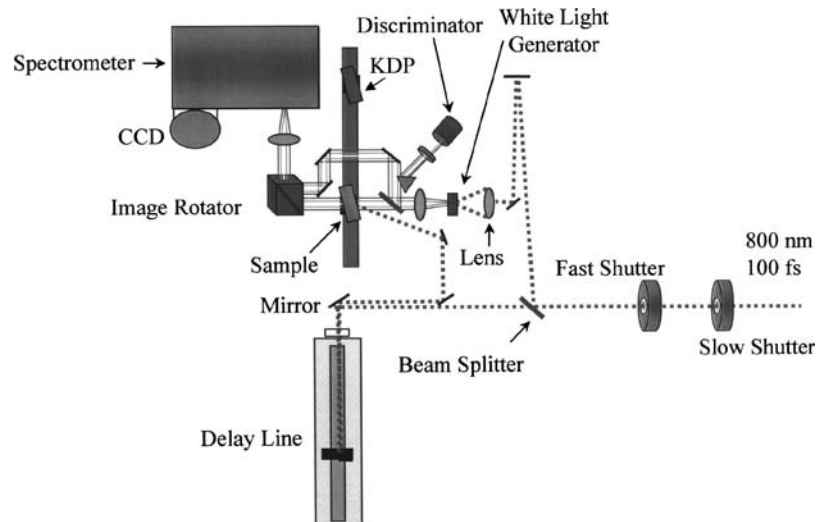


Figure 14 Transient white light absorption experimental setup.

with regenerative amplifier is used to generate bandwidth limited 90-fs pulses, centered at 800 nm with typical pulse energies between 0.95–1.0 mJ. A pair of phased shutters is used in conjunction with the variable repetition rate of the regenerative amplifier to obtain single pulses.

As the pump frequency can change from sample to sample, it may be necessary to use an OPA for frequency conversion of the fundamental. This should not cause too much concern, as it takes only a few microjoules to generate a supercontinuum pulse as illustrated in Section I.C. This can usually be derived from residual fundamental energy in the OPA. For the present discussion, the sample illustrating the technique has an absorption band at 800 nm, and therefore it is not necessary to use an OPA for frequency conversion. Instead, the pulse is split in two by an ultrafast beam splitter (70/30). The higher energy pulse is used as a pump beam and is propagated down a variable delay line. The lower energy pulse (designated seed pulse) is propagated along a fix delay line and is used to generate a white light supercontinuum in the single filament regime. The single filament regime is the result of self-trapping as described above in Section I.D. Note that this setup is contrary to a typical two-color pump-probe experiment where the probe pulse is delayed relative to a fixed pump. This is because the generation of the supercontinuum is highly nonlinear both in intensity and in bandwidth, requiring a stable input pulse. In this case, a supercontinuum pulse is generated by focusing the seed pulse into a 5-mm flowing water cell. The white light pulse is collimated using a matched achromatic lens, giving a spot size of 0.5 mm². In most cases, it is beneficial to incorporate a hardware discriminator circuit to determine when data should be collected (i.e., when the supercontinuum is of sufficient bandwidth and intensity). Therefore, a small pick-off prism is used to select a portion of the probe pulse and send it through a short pass filter with a cutoff wavelength of 500 nm. An amplified photodiode collects the remaining signal and sends it to a discriminator circuit with a variable threshold. The probe beam is split into signal and reference beams and both are imaged onto a spectrometer. A liquid nitrogen CCD array collects the signal at the repetition rate of the phased shutters, but does not pass the data along to the computer unless it receives a trigger pulse from the discriminator circuit telling the CCD controller that the supercontinuum just observed is within the desired bandwidth and intensity limits. A variation of this can use a discriminator with both upper and lower limits, depending on the stability of the probe pulse. The net result is an increase in the signal-to-noise ratio by nearly an order of magnitude.

It is desirable to collect as many wavelengths simultaneously as possible in order to get a good picture of the dynamics occurring within the sample. However, care must be taken to avoid ground state saturation from the probe pulse and multiple order signals on a low groove density grating. Some authors elect to use a tunable étalon to select single probe wavelengths from the supercontinuum and then to detect them on two cooled PMTs in order to

normalize out background electrical noise, shot noise, fluorescence, and scattering [22,23]. In this example, the probe beam is split into two beams, one (designated signal pulse) of which makes an angle of 20° with the pump beam at the sample cell. The other beam is used as a reference pulse and is propagated around the cell. An alternative arrangement sends the reference pulse through an empty portion of the cell or substrate. This allows for the effects of the glass or substrate to be removed. Both beams are imaged onto two separate regions of the CCD detector and collected simultaneously to give single pulse normalization. If possible, it is preferred to have the probes fiber-coupled to the spectrometer in order to ensure a good separation between the imaging regions of the chip. A 600 g/mm grating and appropriate long and short pass filters are used to probe a given wavelength region. This also allows one to adjust probe intensity to match the dynamic range of the detection setup as the supercontinuum peaks in intensity at the generation wavelength of 800 nm and spans from 400–1100 nm. Selection of a smaller wavelength region also prevents higher order diffraction images within the spectrometer from obscuring the signal, while allowing for a larger spectral range to be measured simultaneously. The zero time delay of the experiment is set using a KDP crystal and maximizing the SHG signal by varying the optical delay line.

In order to obtain accurate spectra, four configurations, are used to collect data. First, a spectrum (designated I_c) is taken with no sample in the path. This gives the calibration curve of the reference pulse relative to the signal pulse and should correspond to the optical density of the beam splitter. If sufficient supercontinuum pulse stability is achieved, then this calibration needs only to be taken once with, for example, an empty sample cell. Second, a spectrum (designated I_g) is taken of the sample with no pump beam. These two spectra combined give the ground state absorbance and correspond to that taken by a commercial UV-VIS spectrophotometer. Third, a spectrum (designated I_p) is taken with the pump beam overlapping the signal pulse at the sample cell. Finally, a spectrum (designated I_s) is taken with the pump incident on the sample, but with both probes blocked. This last spectrum gives the amount of fluorescence and scatter caused by the pump pulse on both regions of the CCD. The ground state and excited state absorbances of the sample are then given by

$$A_{GSA} = -\log_{10} \left(\frac{I_g^{sig}/I_g^{ref}}{I_c^{sig}/I_c^{ref}} \right) \quad (62)$$

$$A_{ESA} = -\log_{10} \left(\frac{(I_p^{sig} - I_s^{sig})/(I_p^{ref} - I_s^{ref})}{I_g^{sig}/I_g^{ref}} \right) \quad (63)$$

where the superscript indicates either the signal or reference region of the detector. Use of this method can eliminate most sources of noise by using the same detector and optical path for single pulse normalization, giving an excellent signal-to-noise ratio throughout most of the probe spectrum. Collection of the absorbance as a function of the optical path difference between the pump and probe pulses gives the transient absorption of the material.

It should be noted, however, that the absolute zero delay between the pump and probe is valid only for the residual fundamental wavelengths. The actual zero for every wavelength is determined by the chirp inherent in the supercontinuum pulse. Therefore, the data must be deconvolved or temporally adjusted for the chirp of the probe. Some authors have suggested methods of experimentally removing the chirp of the probe instead of from the data, however this leads to additional difficulty in an already complex experiment. For systems in which the dynamics occur much slower than the chirp of the supercontinuum, and for which multi-wave mixing can be ignored, such measures are unnecessary.

A representative set of data at a single time delay is shown in Fig. 15. This particular material is a lead phthalocyanine in a 13- μm film. Note the increase in the absorbance attributed to a charge separated excited state. It was found that this state only existed for about 1 ps [24]. Figure 16 shows a complete transient absorption spectrum illustrating the singlet state absorption of a two-photon absorbing molecule, AF-380. In this case, it was found that the long time increase

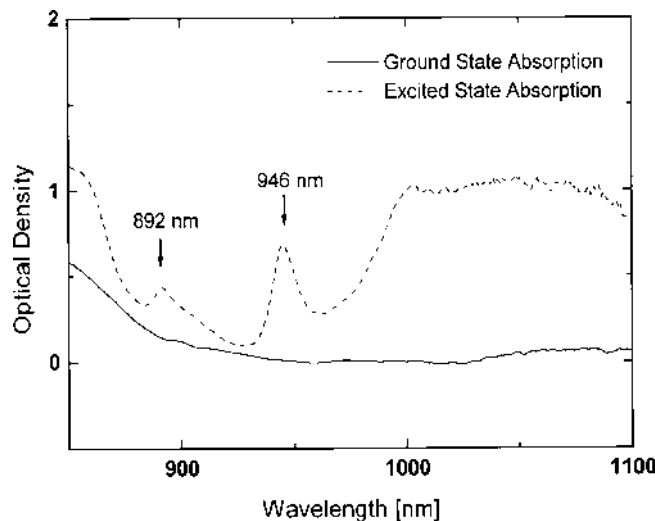


Figure 15 Typical white light absorption spectra at several time delays.

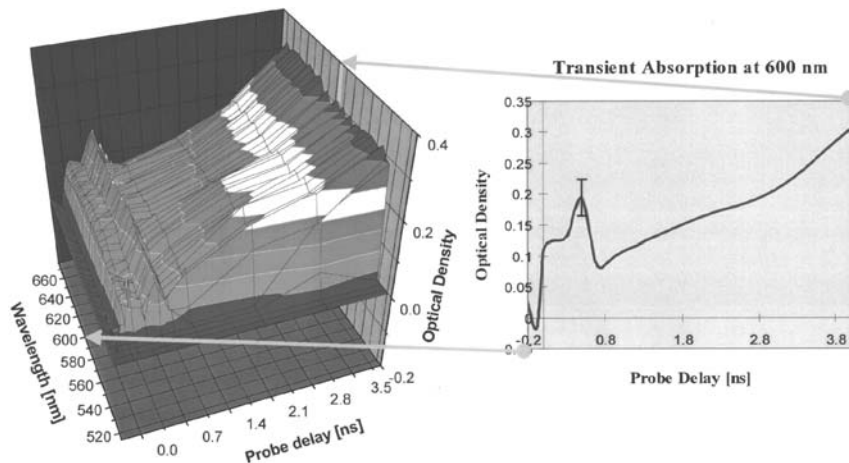


Figure 16 Transient absorption spectrum of an AFX chromophore.

in absorbance is attributed to a photo-induced free carrier population resulting from excited state absorption out of the two-photon state.

E. Two-Photon Absorption Spectroscopy

One of the most important nonlinear measurements, the two-photon absorption cross section, is generally thought to be of limited value unless measured at many different wavelengths, leading to a degenerate (same frequency) two-photon absorption spectrum. One way of making such a set of measurements is to use a frequency conversion process, such as optical parametric amplification, to generate a tunable ultrafast source, and then run a series of Z-scan measurements at various wavelengths. It should be obvious from the previous discussions that such an endeavor would be time consuming, costly, and inefficient. An alternative method, which can give a nondegenerate (different frequencies) two-photon absorption spectrum, is to make use of supercontinuum generation. Using the exact same experimental setup as in transient white light absorption spectroscopy, the nondegenerate TPA spectrum can be measured simply by running the delay only through the supercontinuum pulse width, as defined by the group velocity dispersion and self-phase modulation of the white light generator. For the case of a sapphire plate, the resulting pulse width is typically ~ 2 ps, corresponding to a few millimeters of translation. The drawback here is that there is no direct correlation between the degenerate and nondegenerate cross sections due to the sampling of

different third order susceptibility tensor elements. However, such a spectrum may be used as a more rapid screening method to find trends in the nondegenerate spectrum that are of interest in the degenerate case. Several authors have made use of this technique to gain insight into the major spectral features of the material of interest, and then use a tunable Z-scan experiment to measure the degenerate cross section near the peaks of interest [25,26].

F. Nonlinear Photo-Induced Free Carrier Generation

The generation of free carriers by the absorption of a photon is a well understood process having strong application in semiconductor physics [27,28]. This knowledge base has recently been extended to organic devices similar in design to conventional semiconductor devices, such as electronic and light-emitting organic diodes, photovoltaic cells, and photoconducting polymers [29–32]. In the linear case, if a photon is absorbed having energy above the material bandgap, then the production of a free carrier in the conduction band of the material results. The nonlinear analogue to this process is the generation of a conduction band free carrier by the absorption of two or more photons, either simultaneously or through excited state absorption. This process can be used as an additional tool for material characterization and is discussed in this section.

Some two-photon absorbing chromophores, for example the class consisting of donor and acceptor moieties, can behave like a current source when put into thin film form due to aggregate extended states, energy transfer, or hopping of the carrier. While the exact nature of the mobility of the free carrier is material dependent, these mechanisms are fairly well understood, and the interested reader is referred to the appropriate literature sources [33,34]. For the purposes of this section, we are interested in the nonlinear generation process and the resulting measurement. As mentioned above, the nonlinear generation event, in its simplest form, can take on two different pathways. First, two-photon absorption to an excited state is followed by one-photon excited state absorption into the conduction band. The second is two-photon absorption into an excited state, which is within $k_B T$ of the conduction band. Here T is the local temperature. These processes are schematically shown via a configurational coordinate diagram in Fig. 17.

To illustrate this mechanism, the measurement technique, and the theory, we will use a model chromophore which has been highly investigated due to its use in femtosecond–nanosecond characterization comparisons, quantum molecular modeling, ultrafast holographic two-photon induced polymerization, and structure–property investigations [35–40]. The energy level diagram proposed for this particular chromophore, AF-380, is shown in Fig. 18, taking into account either possible excited state absorption scenario detailed in

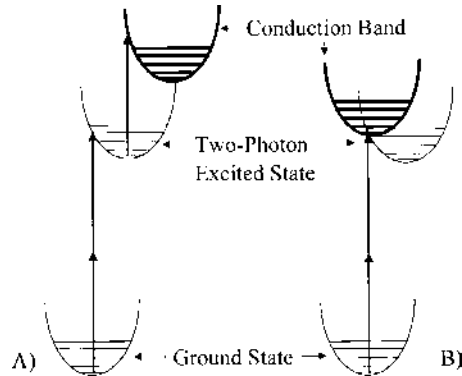


Figure 17 Possible excited state absorption paths associated with free carrier generation.

Fig. 17. The energy levels have the following characteristics. State 1 is the first excited state reached through a two-photon absorption process at 790 nm. State 2 is assumed to be an intermediate state between the first excited state and the fluorescing level 3 associated with the linear fluorescence band (centered around 514 nm). Based on the decrease in the observed ESA, it is assumed that 2 has much weaker ESA [35]. The upper level 4 is considered to

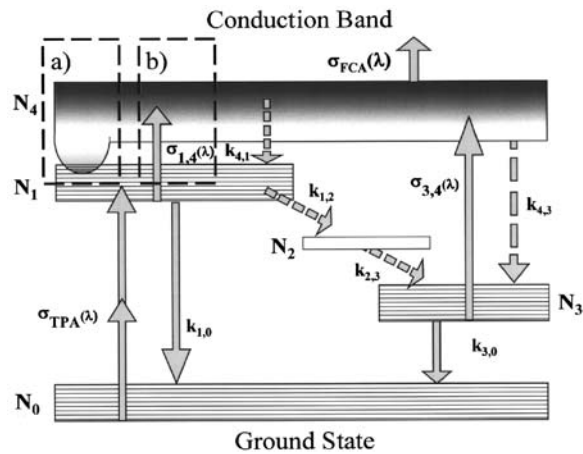


Figure 18 Energy level diagram of model two-photon molecule with two ESA pathways from Fig. 17.

be the conduction band and can be populated from either 1 or 3. The absorption cross section from level I to level J is given by $\sigma_{I,J}$. Similarly, the relaxation rate from state I to state J is given by $R_{I,J}$. Ultrafast Z-scan measurements and fluorescence lifetime measurements give the values of the two-photon absorption cross section, σ_{TPA} , the first effective excited state absorption cross section, σ_{ESA} , and the fluorescence lifetime of state 3, $1/R_{3,0}$ as $8.1 \times 10^{-21} \text{ cm}^4/\text{GW}$, $2 \times 10^{-17} \text{ cm}^2$, and 2.9 ns, respectively. This leaves five free parameters. One may argue that if 4 is truly in the continuum, then the relaxation rates to 1 and 3 are proportional to the energy gap between them. Due to the width of these bands, it is not unreasonable to assume that the relaxation rates to each of these levels from 4 are very similar. We also note that previous authors have observed long-lived free carrier formation of similar triarylamines, normally on the millisecond time scale and some as long as hours [30,41]. Therefore, a reasonable estimate of the lifetime of 4 could be at least a few milliseconds. Ideally one would like to use the transient white light data (Fig. 16) to fit the remaining parameters. However, there are too many adjustable parameters for this to be convincingly quantitative. The model does, however, qualitatively reproduce the structure of the transient absorption measurement as shown in Fig. 19, using moderate values for the ESA cross section ($\sim 10^{-17} \text{ cm}^2$) and relaxation rates into and out of state 2 based on the white light data (hundreds of picoseconds to nanoseconds).

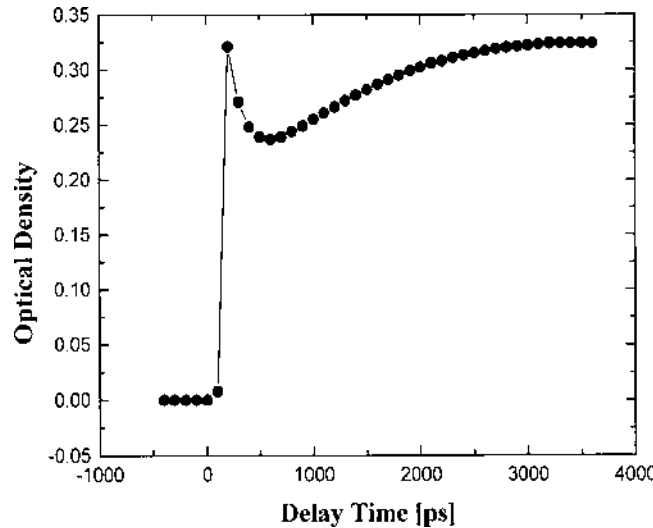


Figure 19 Rate model results demonstrating qualitative agreement with Fig. 16.

The following general set of rate equations describes the model indicated in Fig. 18, taking into account the possibility of either ESA event of Fig. 17:

$$\begin{aligned}\frac{dN_0}{dt} &= -\frac{\sigma_{TPA}I^2(t)N_0}{2\hbar\omega_0} + R_{1,0}N_1 + R_{3,0}N_3 \\ \frac{dN_1}{dt} &= \frac{\sigma_{TPA}I^2(t)N_0}{2\hbar\omega_0}(1-\eta) - R_{1,0}N_1 - R_{1,2}N_1 - \frac{\sigma_{1,4}I(t)N_1}{\hbar\omega_0} \\ \frac{dN_2}{dt} &= R_{1,2}N_1 - R_{2,3}N_2 \\ \frac{dN_3}{dt} &= R_{2,3}N_2 - R_{3,0}N_3 - \frac{\sigma_{3,4}I(t)N_3}{\hbar\omega_0} + R_{4,3}N_4 \\ \frac{dN_4}{dt} &= \frac{\sigma_{3,4}I(t)N_3}{\hbar\omega_0} - R_{4,3}N_4 + \eta \frac{\sigma_{TPA}I^2(t)N_0}{2\hbar\omega_0} + \frac{\sigma_{1,4}I(t)N_1}{\hbar\omega_0}\end{aligned}\quad (64)$$

Here, the fraction of the two-photon population that contributes to the photo-induced current is given by the Boltzmann distribution for electrons

$$\eta = \frac{1}{1 + \exp(-\Delta\mathcal{E}/k_B T)} \quad (65)$$

where $\Delta\mathcal{E}$ is the energy gap between the two-photon state and the continuum level (i.e., the conduction band). In the event that the two-photon state lies within a thermally accessible energy gap, then it is assumed that the one-photon excited state absorption cross section $\sigma_{1,4}$ is zero. Conversely, if the gap is not thermally accessible, then a third photon is necessary to make the transition, and $\sigma_{1,4}$ is not zero, but η is.

In a typical semiconductor photodetector, the photo-induced current in a device limited by the transit-time spread is given by [42]

$$i(t) = -\frac{Q}{d}v(t) = -\frac{Q}{\tau_e} \quad (66)$$

where Q is the total charge, d is the separation between the electrodes, $v(t)$ is the drift velocity of the electrons, and τ_e is the transit time of the electrons. The total charge is given by the integral of the charge density over the generation volume as

$$Q = \iiint \rho d^3r \quad (67)$$

which for uniform illumination reduces to $Q = \rho V_G$, where V_G is the total generation volume of the device. From the model given above, the total charge

density is just the integral of the rate of change of N_4 over time multiplied by the charge of the electron, q_e ,

$$\rho = \int q_e \frac{dN_4}{dt} dt \quad (68)$$

Under ultrashort pulse excitation, assuming a thermally accessible conduction band ($\sigma_{1,4} = 0$, $\eta \neq 0$) Eqs. (64) and (68) reduce to

$$\rho \approx \int \eta q_e \frac{\sigma_{TPA} I^2(t) N_0}{2\hbar\omega_0} dt \approx \eta q_e \frac{\sigma_{TPA} N_0 \tau_0}{2\hbar\omega_0} \sqrt{\frac{\pi}{2}} I_0^2 \quad (69)$$

and the total charge Q can then be found from Eq. (67). If, however, we assume that a third photon ESA event is necessary to reach the conduction band ($\sigma_{1,4} \neq 0$, $\eta = 0$), then Eqs. (64) and (68) can be reduced to the following using a perturbative expansion:

$$\rho \approx q_e \frac{\sigma_{1,4} \sigma_{TPA} N_0 \tau_0}{2(\hbar\omega_0)^2} \sqrt{\frac{\pi}{2}} I_0^3 \quad (70)$$

The total charge Q can again be found from Eq. (67). It should be noted that the difference in the intensity dependence is manifest as expected. A measure of

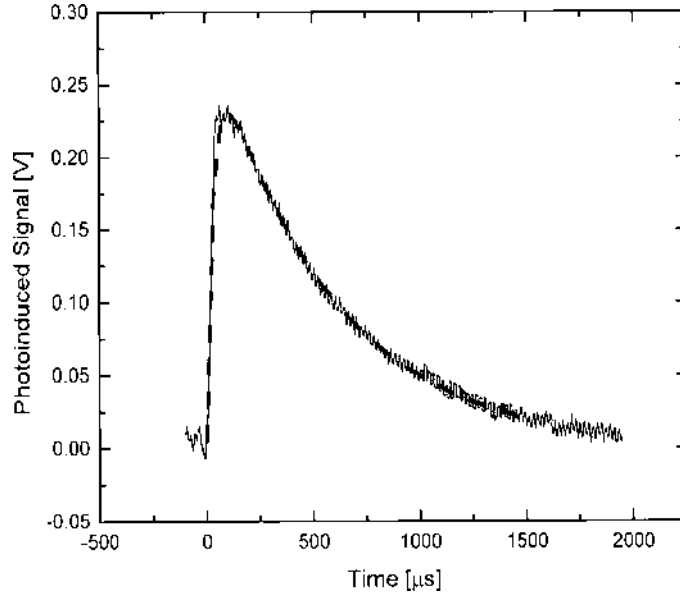


Figure 20 Transient photo-induced current response of a thin film two-photon dye.

the total photo-induced charge as a function of intensity should then determine which view of the energy level dynamics is appropriate.

For this measurement, the film configuration of the device is essentially that of a PIN diode. The device response resulting from uniform illumination of an ultrashort pulse is thus given by

$$V(t) = \begin{cases} V_0 \exp(-t/\tau_1)[1 - \exp(-t/\tau_2)] & t > 0 \\ 0 & t < 0 \end{cases} \quad (71)$$

where τ_1 and τ_2 are the fall and rise times respectively, and V_0 is the peak voltage. Figure 20 shows a typical transient response from the device. The rise and fall times for this particular device were found to be 40 μs and 560 μs , respectively. Recall from linear system theory that this response is a convolution of the impulse response function of the device and the signal generated by the optical pulse. From Eq. (71), the total detected charge is found from integrating

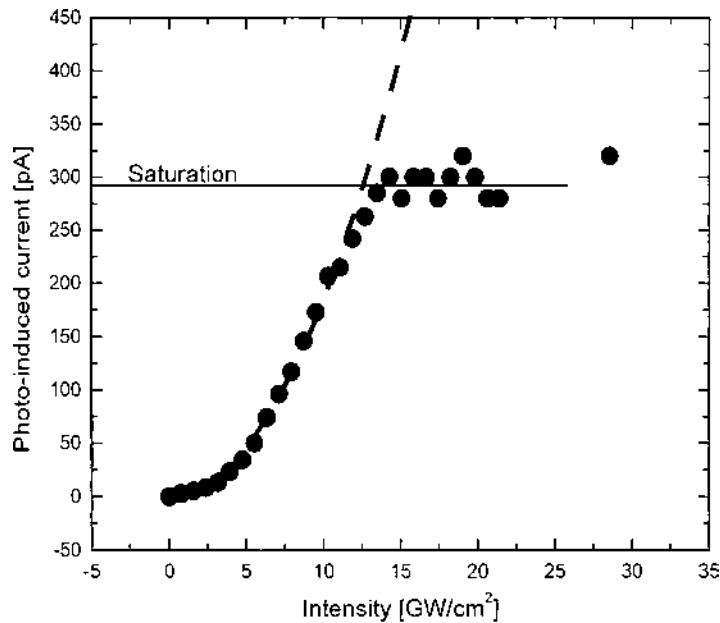


Figure 21 Intensity dependence of nonlinear photo-induced current. Saturation is evident at the dotted line.

the resulting current over time, i.e.,

$$Q = \int \frac{V(t)}{R_L} dt \quad (72)$$

where R_L is the load resistance. From the measurement, a plot of the result of Eq. (72) can be fit to the total charge calculated from Eqs. (67) and (69) to give the fraction η of the two-photon population contributing to the photo-induced current. Alternatively, the result can be fit to Eqs. (67) and (70) to give the singlet excited state cross-section, $\sigma_{1,4}$. In addition, the impulse response function of the device can be deconvolved from the device response, Eq. (71), and the transient of the signal obtained. The result is compared to the solution N_4 of the rate Eqs. (64), and the recombination rate $R_{4,3}$ obtained (under short pulse excitation, no ESA from N_3 to N_4 occurs).

Figure 21 shows the intensity dependence of the total photo-induced current for the model chromophore AF-380. The result of an allometric fit, $y = Ax^b$, gives an exponent of $b = 1.8$. This implies that the two-photon state lies very near the conduction band of the material. Subsequently the dynamics outlined in Fig. 17b give the relevant picture. Three photons are not necessary to reach the conduction band. From the fit in Fig. 21 and using Eq. (69), the fraction of the two-photon state population contributing to the conduction band comes out

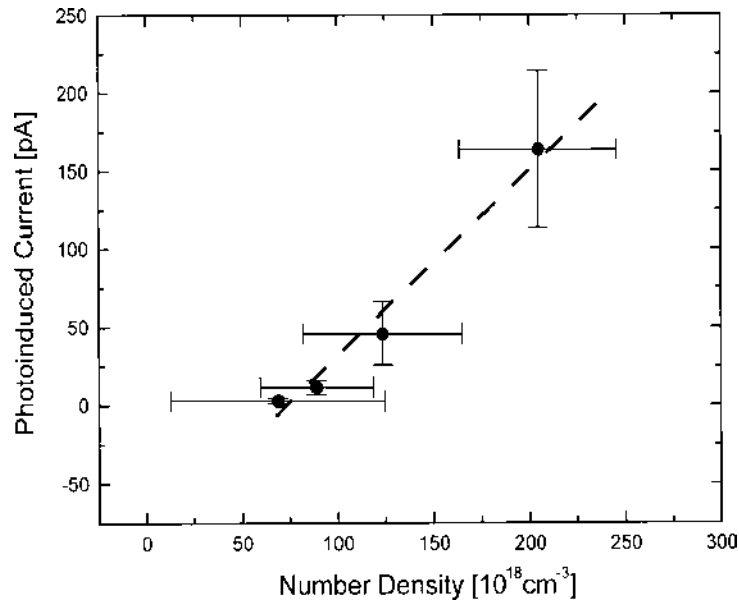


Figure 22 Concentration dependence of nonlinear photo-induced current.

to be $\eta = 6\%$.

A series of similar devices containing an increasing amount of AF-380 was also measured to determine the concentration dependence of the nonlinear photo-induced current. Absolute concentration of the active region was determined by linear absorption. Figure 22 gives the resulting plot clearly showing a linear concentration dependence to within experimental error, consistent with the model. There does appear to be a slight cubic correction term to the linear concentration dependence, which may be attributed to Auger recombination processes [43].

IV. CONCLUDING REMARKS

The previous descriptions of several common ultrafast experimental techniques should serve as a guide in the use of ultrashort pulses for spectroscopic applications. It is important to keep in mind the wide range of nonlinear interactions that can affect the application of the pulse in both frequency and time. With care, a femtosecond laser system can be used as an ideal spectroscopic tool, tapping into the strengths of nonlinear optics, and opening new realms of nonlinear, high intensity phenomena.

REFERENCES

1. V. G. Dmitriev, G. G. Gurzadyan, and D. N. Nikogosyan, *Handbook of Nonlinear Optical Crystals*, 2nd ed., Springer-Verlag, New York, 1997, pp. 3–65.
2. G. P. Agrawal, *Nonlinear Fiber Optics*, 2nd ed., Academic Press, San Diego, 1995, pp. 164–179.
3. J. C. Diels and W. Rudolph, *Ultrashort Laser Pulse Phenomena*, Academic Press, San Diego, 1996, pp. 12–22.
4. R. R. Alfano, *The Supercontinuum Laser Source*, Springer-Verlag, New York, 1989, pp. 34–40, 184–187.
5. J. D. Jackson, *Classical Electrodynamics*, 2nd ed., John Wiley, New York, 1975, p. 237.
6. W. M. Yen, *Laser Spectroscopy of Solids*, 2nd ed., Springer-Verlag, Berlin, 1986, pp. 18–22.
7. See Chapter 9, Section IV. C.
8. R. W. Boyd, *Nonlinear Optics*, Academic Press, New York, 1992, pp. 162–178.
9. A. Yariv, *Quantum Electronics*, 2nd ed., John Wiley, New York, 1989, pp. 176–182.
10. M. Kauranen, D. J. Gauthier, M. S. Malcuit, and R. W. Boyd, Polarization properties of optical phase conjugation by two-photon resonant degenerate four-wave mixing, *Phys. Rev. A* 40:1908 (1989).

11. W. E. Torruellas, B. L. Lawrence, G. I. Stegeman, and G. Baker, Two-photon saturation in the band gap of a molecular quantum wire, *Optics Lett.* 21:1777 (1996).
12. J. F. Lami, P. Gilliot, and C. Hirlmann, Observation of interband two-photon absorption saturation in CdS, *Phys. Rev. Lett.* 77:1637 (1996).
13. R. W. Boyd, *Nonlinear Optics*, Academic Press, New York, 1992, p. 432.
14. A. M. Weiner, Femtosecond pulse processing, *Opt. Quantum Electron.* 32:473 (2000).
15. C. Rullière, *Femtosecond Laser Pulses*, Springer-Verlag, Berlin, 1998, pp. 177–200.
16. R. W. Eason and A. Miller, *Nonlinear Optics in Signal Processing*, Chapman and Hall, London, 1993, pp. 391–401.
17. R. Trebino, K. W. DeLong, D. N. Fittinghoff, J. N. Sweetser, M. A. Krumbügel, and B. A. Richman, Measuring ultrashort laser pulses in the time-frequency domain using frequency resolved optical gating, *Rev. Sci. Instrum.* 68:3277 (1997).
18. R. W. Boyd, *Nonlinear Optics*, Academic Press, New York, 1992, p. 163.
19. F. Kajzar and M. V. Agranovich, *Multiphoton and Light Driven Processes in Organics: New Phenomena, Materials, and Applications, NATO Advanced Research Workshop*, Kluwer Academic Publishers, Dordrecht, The Netherlands, 2000, pp. 67–81.
20. J. W. Baur, G. Das, M. D. Alexander, Jr., R. Kannan, R. A. Vaia, Loon-Seng Tan, P. N. Prasad, L. Yaun, J. Swiatkiewicz, S. M. Kirkpatrick, C. M. Clark, and D. J. Pikas, The influence of pulse-width and chemical structure on the two-photon absorbing properties of amino-fluorene molecules, *J. Phys. Chem.* (2001), in press.
21. R. A. Reed, R. Purrello, K. Prendergast, and T. G. Spiro, Resonance Raman characterization of the radical anion and triplet states of zinc tetraphenylporphine, *J. Phys. Chem.* 95:9720 (1991).
22. Y. H. Meyer M. Pittman, and P. Plaza, Transient absorption of symmetrical carbocyanines, *J. Photochem. Photobiol. A* 114:1 (1988).
23. Y. H. Meyer and P. Plaza, Ultrafast excited singlet state absorption/gain spectroscopy of perylene in solution, *Chem. Phys.* 200:235 (1995).
24. S. M. Kirkpatrick, C. Clark, E. S. Pooler, J. S. Shirk, R. L. Sutherland, and P. A. Fleitz, Ultrafast transient white light absorption spectroscopy of novel materials for optical limiting, *Proc. SPIE* 3798:123 (1999).
25. T. Itaka and T. Ebisuzaki, Non-degenerate two photon absorption spectra of Si nanocrystallites, *Microelectron.* 47:321 (1999).
26. F. Kajzar and M. V. Agranovich, eds, *Multiphoton and Light Driven Processes in Organics: New Phenomena, Materials, and Applications*, Kluwer Academic Publishers, Dordrecht, The Netherlands, 2000, pp. 39–52.
27. S. L. Chuang, *Physics of Optoelectronic Devices*, Wiley and Sons, New York, 1995, pp. 35–49.
28. J. I. Pankove, *Optical Processes in Semiconductors*, Dover, New York, 1971, pp. 34–81.
29. H. Sirringhaus, T. Kawasw, R. H. Friend, T. Shimoda, M. Inbasekaran, W. Wu, and E. P. Woo, High-resolution inkjet printing of all-polymer transistor circuits, *Science* 290:2123 (2000).

30. H. Vestweber, J. Pommerene, R. Sander, R. F. Mahrt, A. Greiner, W. Heitz, and H. Bässler, Majority carrier injection from ITO anodes into organic light-emitting diodes based upon polymer blends, *Synth. Met.* 68:263 (1995).
31. P. Gomez-Romero, Hybrid organic-inorganic materials—in search of synergic activity, *Adv. Mater.* 13:163 (2001).
32. D. Abramavicius, V. Gulbinas, A. Ruseckas, and L. Undzenas, Geminate charge pair recombination in sensitized photoconducting polymer, *J. Chem. Phys.* 111:5611 (1999).
33. B. Henderson and G. F. Imbush, *Optical Spectroscopy of Inorganic Solids*, Clarendon press, Oxford, 1989, pp. 445–475.
34. W. M. Yen, ed, Laser spectroscopy of solids II, Springer-Verlag, Berlin, 1989, pp. 77–119.
35. S. M. Kirkpatrick, C. Clark, and R. L. Sutherland, Singlet state absorption spectra of novel nonlinear materials, *Mat. Res. Soc. Symp. Proc.* 597:333 (1999).
36. M. P. Joshi, J. Swiatkiewicz, F. Xu, P. N. Prasad, B. A. Reinhardt, and R. Kannan, Energy transfer coupling of two-photon absorption and reverse saturable absorption for enhanced optical power limiting, *Opt. Lett.* 23:1742 (1998).
37. S. M. Kirkpatrick, J. W. Baur, C. M. Clark, L. R. Denny, D. W. Tomlin, B. R. Reinhardt, R. Kannan, and M. O. Stone, Holographic recording using two-photon induced photopolymerization, *Rapid Comm. Appl. Phys. A* 69:461 (1999).
38. S. M. Kirkpatrick, L. R. Denny, and M. O. Stone, Ultrafast holographic recording using two-photon induced photopolymerization, *Proc. SPIE* 3951:102 (2000).
39. B. A. Reinhardt, L. L. Brott, S. J. Clarson, A. G. Dillard, J. C. Bhatt, R. Kannan, L. Yuan, G. S. He, and P. N. Prasad, *Chem. Mater.* 10:1863 (1998).
40. J. W. Baur, M. D. Alexander, Jr., M. Banach, L.R.D., B. A. Reinhardt, R. A. Vaia, P. A. Fleitz, and S. M. Kirkpatrick, Molecular environment effects on two-photon absorbing heterocyclic chromophores, *Chem. Mater.* 11:2899 (1999).
41. J. Louis, J. F. Hartwig, and A. L. Fry, Discrete high molecular weight triarylamine dendrimers prepared by palladium-catalyzed amination, *J. Am. Chem. Soc.* 119:11695 (1997).
42. B. E. A. Saleh and M. C. Teich, *Fundamentals of Photonics*, John Wiley and Sons, New York, 1991, pp. 648–693.
43. S. L. Chuang, *Physics of Optoelectronic Devices*, John Wiley and Sons, New York, 1995, pp. 40–42.

12

Laser Flash Photolysis

Daniel G. McLean

Science Applications International Corporation, Dayton, Ohio, U.S.A.

Laser flash photolysis (LFP) is a mature technique [1] for the characterization of photophysical and photochemical properties. It can be applied to a large range of organic, organometallic, and even inorganic materials. It is useful in a large range of materials development applications including, but not limited to artificial photosynthesis, photodynamic therapy, optical limiting, photoconductive materials, and optical memory materials. Several reviews [2–7] are available in the literature. The main purpose here is to provide a starting point to set up or to understand the results of such an experiment along with an idea of the errors and limitations.

There are two main divisions of how the technique may be done. One method uses the time-resolving power of the detection system and a continuous probe source. These techniques have benefited from much faster sampling oscilloscopes and detectors, resulting in time resolution easily in the nanosecond range and often extending to the picosecond domain. This is the main method of choice for long lifetime states or processes including nanosecond to seconds or even hours. The other main methods are pump–probe techniques where the probe is short in time to provide the temporal resolution. This probe acts like a strobe over which the dynamics are averaged but gives time resolution on the order of the pulse width. It is necessary to create a short white light pulse in order to perform spectroscopic investigations. These are usually in the picosecond or femtosecond time regime. These are the techniques of choice for studying singlet states, transition states, or even vibronic manifold dynamics. (Ultrafast techniques were reviewed in Chapter 11.) This chapter will focus on techniques using the time resolution of the detection system. The most common method is generally termed nanosecond LFP.

I. PHOTOPHYSICAL AND PHOTOCHEMICAL PROCESSES

A summary review of the possible photophysical and photochemical processes is necessary to understand the LFP experiment and general results. A much deeper understanding of the processes and interactions is needed for an accurate and unambiguous interpretation of results. This is given in the literature [8–10].

A. Absorption

A Jablonski diagram of many of the possible processes is shown in Fig. 1. The first process to understand is that of absorption. Absorption commonly occurs from the lowest vibrational state of an occupied molecular orbital into a higher vibronic harmonic of an unoccupied electronic state. The probability that a given wavelength photon will produce an excited state is determined by the dipole moment matrix element between the electronic states, the Frank–Condon factors, inhomogeneous broadening, and even the excitation intensity. The transition probability will also be sensitive to molecular agglomeration, interactions between species, solvent interactions, and, through these, the temperature. The most common metric of transition probability for chemists is the molar extinction coefficient, ϵ . This is directly related to the physicist's notation of cross section,

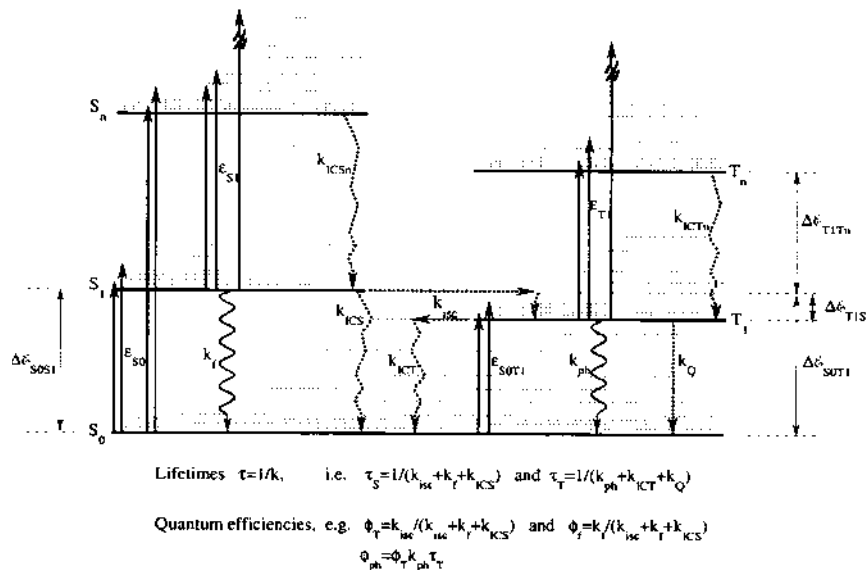


Figure 1 A Jablonski diagram of the most common intramolecular processes.

σ , through the two Beer's law representations, $T = 10^{-\epsilon M/\ell} = e^{-\sigma N \ell}$, where ℓ , M , and N are the path length (cm), concentration (moles/liter), and molecular number density (cm^{-3}), respectively. The concentration and molecular number density are proportional through Avagadro's number. Thus, the cross section may be calculated from the molar extinction coefficient by $\sigma(\text{cm}^2) = 3.82 \times 10^{-21} \epsilon (\text{liter/mole}\cdot\text{cm})$.

The ground state is a singlet state, with a few exceptions. Thus, transitions from this state will be to higher singlet states, $S_0 \rightarrow S_n$. The transition from the highest occupied molecular orbital (HOMO) to the lowest unoccupied molecular orbital (LUMO) via the lowest vibrational states defines the fundamental absorption edge of the molecule. A direct singlet to triplet transition ($S_0 \rightarrow T_n$) is possible in strong spin-orbit influenced molecules, but with low intensity. In many molecules, the fundamental transition is not allowed due to symmetry considerations, causing this transition to be weak. Other absorption features are attributable to (n,π^*) transitions, CT complexes, and high order aggregates. Finally, a measured absorption spectrum may be compromised by the presence of scattering centers such as particulate or agglomerates. A fundamental understanding of the ground state absorption spectrum, the source of the various features, and the extinction coefficient spectrum is necessary for an accurate interpretation and judicious choice of operating conditions of the laser flash photolysis experiment.

B. Radiative Relaxations

The two primary emission mechanisms are fluorescence and phosphorescence. Fluorescence is emission from a singlet excited state (k_f) and phosphorescence is emission from the triplet excited state (k_p). The observed emission rate is really the sum of all rates affecting the population of the emitting state. An unambiguous determination of the radiative rate is difficult because it is difficult to determine comprehensively all of the rates affecting the emitting populations.

C. Internal Conversions

Internal conversion (k_{ICS} and k_{ICT}) is the process of relaxation through the many vibrational states available for each electronic state. The relaxation rate becomes large when the density of these vibrational states is large. The density increases for higher electronic states and when electronic states are closer together. This is the primary reason that Kasha's rule holds, which states that fluorescence is almost universally from the S_1 excited state independent of excitation wavelength. This rate is usually large, exceeding 10^{12} s^{-1} [9].

D. Singlet–Triplet Manifold Conversion

The singlet to triplet manifold conversion is called intersystem crossing, k_{ICS} . This conversion is actually two processes that include both spin flip and internal conversion. The prohibition of spin flip that makes this a nonallowed process is broken by any spin-orbit mediating process. The most well known is the heavy atom effect. This is an interaction energy Hamiltonian between the spin and orbital momentum of each electron, and has the form

$$\sum_k \xi(r_k) \mathbf{L}_k \cdot \mathbf{S}_k \quad (1)$$

where \mathbf{L} is the orbital angular momentum operator, \mathbf{S} the spin angular momentum operator, and ξ the relativistic precession energy [11]. This sum is zero for any filled electronic level.

E. Energy Transfer

Energy transfer can occur from an excited molecule to one with a lower energy state, and some times even to those with higher energy states, via three possible processes. The first is radiative transfer where one molecule emits a photon that is absorbed by a second molecule. This process operates over extremely large distances between molecules whose emission and absorption bands overlap. The other two nonradiative processes are mediated by a Hamiltonian consisting of a Coulombic interaction and an exchange interaction. The Coulombic interaction leads to a process termed variously as induced dipole–dipole, long range, or Förster energy transfer. Since the electric field of the electron extends further than the wave function, this process operates over distances much larger than that of the exchange process. The exchange interaction leads to a process termed variously as collision, short range, or Dexter energy transfer.

II. EXPERIMENTAL METHODS

The purpose of this experiment is to measure triplet state processes and final chemical species. This is achieved using array detection methods that allow either simultaneous time or wavelength samples giving fast data acquisition. The detection systems primarily reach from subnanosecond to millisecond time scales.

A. Experimental Arrangements

The experiment is designed to measure the absorbance in a sample both before and immediately following an excitation pulse. There are three arrangements in

common use. The most common and oldest arrangement uses transverse pumping and monitors the probe transmission. A second method also monitors the transmission of the probe, but uses longitudinal or collinear pumping. The third method uses transverse pumping and monitors the reflection of the probe from the sample.

An experimental layout for the transverse pump–probe transmission arrangement is shown in Fig. 2. The probe is a cw xenon lamp focused into a cuvette that is masked such that the light passes immediately inside the side window of the cuvette. A high power handling shutter absorbs most of the probe power, and a fast shutter is used to set the probe pulse duration, which is typically ~ 3 ms. (The probe power is always at least a factor of 10^4 less than the pump power.) A lens is used to collect and focus the transmitted probe radiation into a monochromator. Filters before the sample eliminate unnecessary probe UV irradiation of the sample and eliminate second-order grating transmission artifacts. A narrow band rejection filter is also used at the monochromator entrance to eliminate any scattered pump light.

A Q-switched laser pulse is used to excite the sample through the side window (i.e. transverse pumping). The pump beam is shaped using a combination of spherical, cylindrical, or prism optics to fill the side aperture (e.g., 3 mm \times 10 mm). The sample holder, shown as a magnified inset in Fig. 2, forces

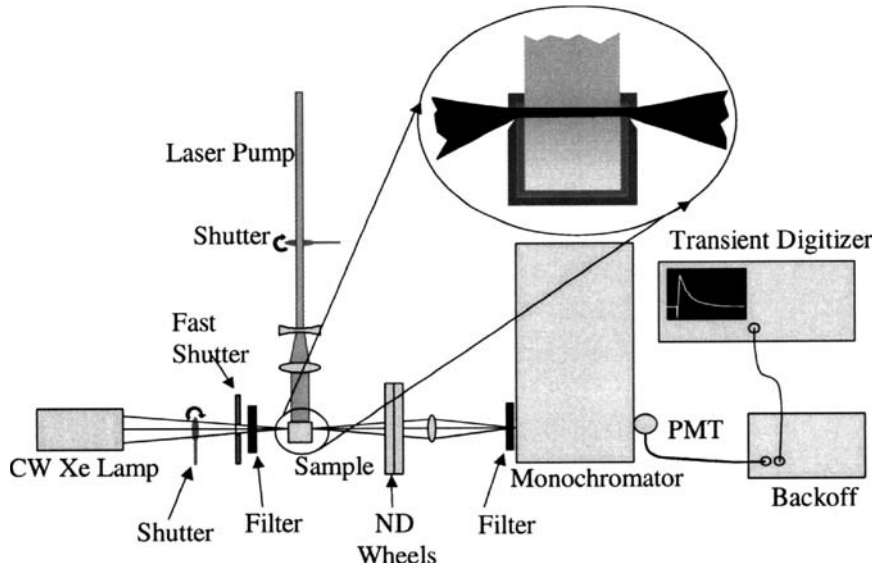


Figure 2 The experiment layout and sample holder configuration.

the excitation and probe regions to overlap. It also discriminates against noncollimated probe light to insure a valid absorbance measurement.

A photomultiplier tube, wired to be linear for currents as high as 5 mA, detects the spectral radiation. A backoff circuit from a design by Janata [12,13] is used to produce a null signal background. The transmitted probe light is proportional to the linear transmission and is sampled ($\sim 100 \mu\text{s}$) before the laser pulse. The backoff circuit generates a current of opposite sign to this photocurrent and is applied to the signal, giving a null current. Neutral density filters are used to adjust the current in the photomultiplier tube (PMT) to be in the optimum linearity range. Thus, the full dynamic range of the digitizing oscilloscope is used to measure the laser induced transient. The differential voltages are converted to differential absorbance for curve fitting and data analysis. The time dependent signal is acquired at each wavelength and assembled to make a time dependent spectral array.

Two other pump configurations are also in use. One is the longitudinal pumping scheme, shown in Fig. 3. Here the pump and probe beams are nearly collinear. This is used for thin films of strongly absorbing materials. The other configuration is the diffuse reflectance method. This may be used for opaque samples and powdered samples.

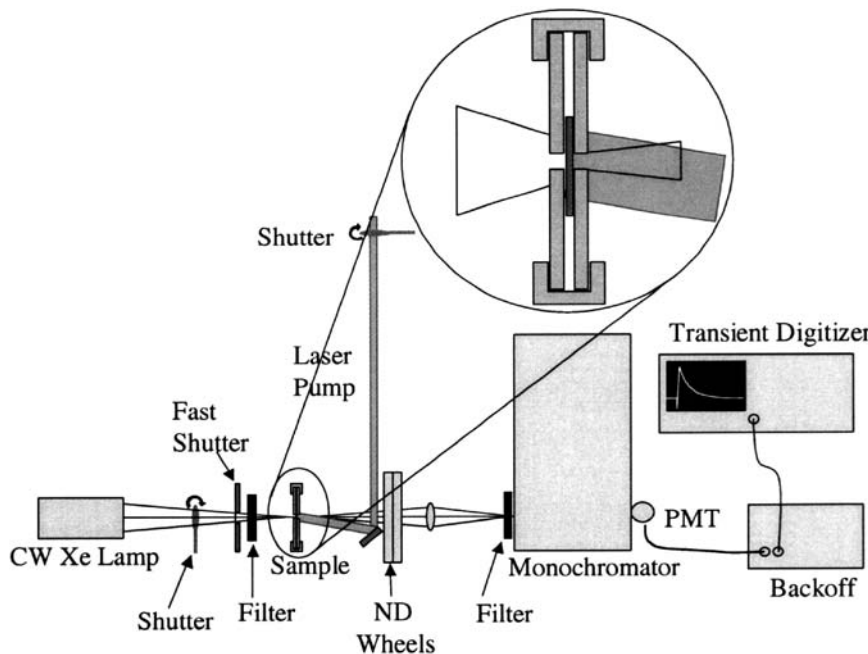


Figure 3 The layout for longitudinal pumping of thin solid samples.

B. Probe

Sources. The selection of the probe white light source is a critical part of an experiment design. This source is one of the main determinants of the noise in the system and consequently a major determinant of the sensitivity of the experiment to small changes in the absorbance. To reduce shot noise, one selects as high as an intensity as possible. This is generally achieved with pulsed sources. Even if cw sources are used, it is necessary to use shutters to limit their duration because of detector saturation effects. A xenon arc lamp has become the almost universal source. A tungsten–halogen lamp can also be used, especially in the infrared.

There are two common types of housing for the arc lamp. One is an elliptical reflector with the arc placed at one focus. This will collect a very large fraction of the light and focus it to the second focus of the reflector. The second type of housing uses a spherical reflector behind the arc and refractive optics to collect and collimate the radiation. In addition to the two types of optics, sources can be purchased with the arc, either horizontal or vertical. In general, the vertical arrangement is better since the deposition of the metal evaporated from the arc is near to the ends and does not occlude the arc as it accumulates. The horizontal arrangement, however, does not require a turning mirror and is thus a little simpler and less expensive. Common suppliers of these include Photon Technology, Inc. (PTI, Lawrenceville, NJ) and Oriel (Stratford, CT).

One consideration is the power output of the lamp. These are generally available in 75, 150, and 500 W levels. A larger arc length is required as the power increases. This leads to the curious effect that the most powerful lamps do not provide the most intense illumination of the sample and thus the greatest probe level. One should choose an arc or filament length similar to the size of the sample illumination area in order to optimize the usable brightness.

Pulsed light sources may be purchased as a unit, or a pulser circuit may be added to a cw source. Pulsed sources with power suitable for laser flash photolysis are available from Applied Photophysics Limited (Leatherhead, Surrey, UK). A circuit design supplied by Kirk Schanze [14,15] may be added to a PTI lamp. The LED driver is no longer available, and one replacement is Model 779A from Analog Modules (Longwood, FL). Removal of the protection diode allows its use as a negative polarity source.

The curves shown in Fig. 4 compare the spectral brightness of the cw-xenon lamp, the pulsed-xenon lamp, and the quartz tungsten halogen lamp. It can be seen that as the xenon current density increases (in going from cw to long-arc-pulsed to short-arc-pulsed), the blue and ultraviolet content increase. For the same power output, the tungsten halogen source filament is usually larger than the corresponding Xe arc, giving it significantly lower brightness.

Shutters. Shutters are often required in an LFP experiment. This is especially true if a cw probe source is used. Sources such as these have an average

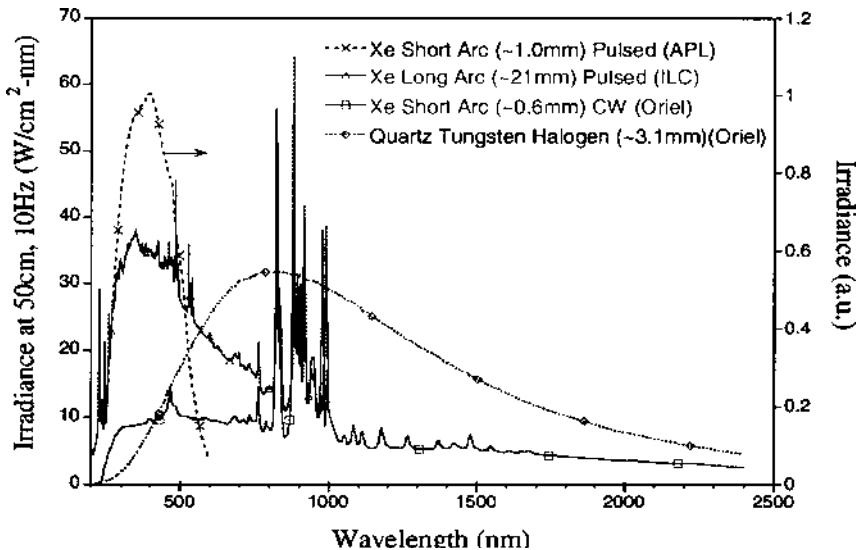


Figure 4 Comparison of lamp sources. The source dimensions are geometric averages.

power of up to 150 W and are typical. This requires a large heat load to be handled by the shutter, even if a small fraction is absorbed. Consequently, a pair of shutters are used for cw sources. One shutter is slow and handles the power while the other is a high-speed mechanical shutter. One method of making a simple, relatively high-speed shutter is to use a rotating solenoid with an attached paddle. A solid state relay is used in an RLC circuit, such as is shown in Fig. 5, to perform and optimize the switching characteristics. It is possible to achieve 5–10 ms switching times. The paddle can be optimized for speed or power handling by attaching mirrors or absorbing glass to tailor absorption or reflection of energy. One of the fastest and most configuration-flexible mechanical shutters is dual leaf shutters like those made by Vincent Associates (Rochester, NY). Switching times of ~1 ms are achievable for small apertures. The shutters are not needed if the lamp is pulsed and has negligible simmer light.

Shutters are also often needed to select laser pulses. As stated earlier, rotating solenoid shutters can be tailored for laser use. An electromagnet-driven grazing incidence shutter (made by NMI, Sunnyvale, CA) can handle very large laser pulse energies.

There are other shutters types, such as galvanometer, liquid crystal, and electro-optic (see Table 1). These have advantages and disadvantages, but are not commonly used.

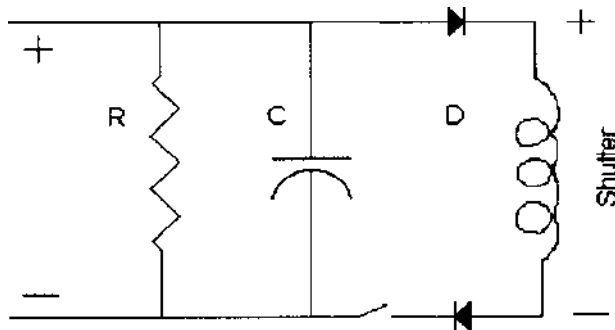


Figure 5 An RLC circuit diagram to optimize switching of rotating solenoid shutters.

Optics. First we treat the optics for the probe beam and then the optics for the laser, which are often quite different. The probe is usually a broadband incoherent source. Thus there are less restrictions on the power handling requirements and more on the design and control of the optical radiation divergence. A starting point for the design of the optical system is the principle of *etendue*, or optical invariant [16]. This principle states that the product of an object's size and solid angle is invariant as the radiation is passed through an optical system, unless it is reduced by some optical element. After that limiting optical element, the invariant is again maintained at this reduced value for the rest of the optical system. A system may then be optimized by matching the invariant of the source, detector, and all aperture planes throughout the system. Common limiting elements are the source size, sample apertures, collecting optics, and the spectrometer.

Table 1 Types of Shutters for the LFP Experiment

Shutter type	Min. time window	Max. rep. rate	Features
Rotating solenoid	5–10 ms	5–10 Hz	Very customizable, cheap
Leaf shutter	1 ms	100 Hz	Fast, flexible configuration
Ferroelectric liquid crystal	15 μ s	5 kHz	Uncertain power handling, changes transmission spectrum of light, polarization required
Electro-optic	2–5 ns	\sim kHz	Requires high voltage switching, polarization, operates at one wavelength
Galvanometer	1 ms	kHz	Operates at frequency or resonance

The optical elements may be refractive or reflective. In general, the reflectivity of the best mirror is not as good as the transmissivity of the best antireflection-coated optic for the broad spectral bands required. Achromatic lenses are only needed if they are the limiting element of the invariant at important probe wavelengths. High spectral resolution requires a narrow slit width and thus may force a requirement for achromatic lenses. Adding optics before a relatively thick sample can improve the optical invariant at the output of the sample.

Filters. Two kinds of filters are required in the probe beam. The most common need is for order sorting filters to prevent the second order reflection of the grating from being detected. Glass lowpass filters from Schott (Mainz, Germany) or Corning (Corning, New York) are commonly used.

The laser light is sometimes scattered into the probe beam. If it is necessary to test the material close to the wavelength, a notch filter is required. Raman notch filters are available at many wavelengths. Another method is to program the scan to skip the pump laser wavelength. A second monochromator will reduce the Rayleigh scattering of the laser and allow testing to wavelengths nearer to the laser line, however, it will likely cause a severe attenuation of the probe signal.

Input intensity control. The detection system has a range where the linearity of the response and signal-to-noise ratio are optimal. Operation in this region will give the best results. Two methods are commonly applied. One is to control the light intensity via controlled attenuation, and the second is to change the gain of the detection system to match the linearity range to the intensity of the probe light.

The light intensity may be controlled by neutral density filters or by using broadband polarization techniques. The neutral density filters may be the Inconel type. Both automated and manual multiposition filter wheels are available. A sequence of filters having optical density values of 0.1, 0.2, 0.3, 0.4, and 0.5 in one six-position wheel and 0.6, 1.2, 1.8, 2.4, and 3.0 in a second tandem wheel give attenuation values up to 3.6 in steps of 0.1. Another scheme uses a filter of 0.05, 0.6, 1.2, 1.8, and 2.4 in the second wheel to give attenuation up to 2.9 with steps of 0.05 at the high transmission values. Any attenuation of the signal beam will mean higher shot noise and thus a lower signal-to-noise ratio for the experiment.

The voltage on the PMT may be varied to match the gain to the light intensity to give a constant output [6,7]. This gives a continually variable system that can respond extremely fast to change. The system uses all of the available light in order to maximize the signal-to-noise ratio. However, PMTs do not preserve linearity as the voltage is varied. An extremely careful design of the PMT divider circuit is required to maintain linearity while the gain is adjusted, and this must be verified over the entire light level range for confidence in the measurements.

C. Pump

Sources. There are many laser sources now available for use in nanosecond laser flash photolysis. These sources are rapidly developing, yielding more compact and more efficient lasers, more wavelengths, shorter pulse widths, increased stability, and increased repetition rate.

The workhorse laser has traditionally been the flashlamp pumped, Q-switched Nd:YAG laser. This is commonly used with second-harmonic generation crystals to give a wavelength of 532 nm and third harmonic generation crystals to give a wavelength of 355 nm. Sometimes a fourth harmonic crystal is used to produce the 266 nm wavelength. It is fortuitous that usually one of these three wavelengths is significantly absorbed by just about any molecule. This enables one to use a simple laser to excite a large number of materials. Recent developments include laser seeding to give, essentially, single longitudinal mode output and thus smooth pulse envelopes, laser diode pumping to give much better efficiency and stability, and Gaussian mirrors to improve the M^2 of the laser and reduce beam divergence. The lasers are also decreasing in price for the commodity type configurations.

The Nd:YAG is also the workhorse to pump an optical parametric oscillator (OPO). These devices are pumped by one of the harmonic wavelengths. The OPO is designed to produce two resonances whose frequencies add to the frequency of the pump radiation. Thus these two frequencies gain energy from the pump and produce radiation at different wavelengths (see Table 2). Frequencies that are larger than half of the pump frequency are called signal frequencies and those smaller than half the pump frequency are called idler frequencies. For example, an OPO pumped with 355-nm radiation has a degeneracy point (wavelength corresponding to half the pump frequency) of 710 nm. Signal wavelengths are shorter than 710 nm and commonly extend to 410 nm. The idler wavelengths are longer than 710 nm and may extend to 2.5 μm . Near the degeneracy wavelength, the two oscillating frequencies are almost identical, and the conditions for momentum conservation become sensitive to extremely minor imperfections in the optics, giving conditions where any direction can satisfy momentum conservation. This gives highly divergent beams and unstable power conditions.

Table 2 OPO Pump, Signal, and Idler Wavelengths for the LFP Experiment

Pump wavelength (nm)	Doubled-signal range (nm)	Doubled-idler range (nm)	Signal range (nm)	Idler range (nm)
532	340–480	550–770	680–1000	1100–2500
355	210–310	360–900	420–680	720–2400
266	160–205	270–650	320–510	540–1500

near the degeneracy wavelength. One major difference between OPO designs is the linewidth of the oscillator. This is especially critical if the OPO is used in atomic spectroscopy or if very tight focusing is needed, but a narrow linewidth is generally not needed for laser flash photolysis.

The output of the Nd:YAG, its harmonics, and OPOs may be combined in nonlinear crystals to give a very wide range of wavelengths. These combinations are often used to reach into the UV domain. Since the harmonic conversion of the fundamental Nd:YAG wavelength is not 100% efficient, and in fact it is usually on the order of 50%, a very significant amount of energy is available at either 532 nm or 1064 nm. These leftover beams may be combined with the OPO output to shift the wavelength to shorter values. For example, the output of a 355-nm pumped OPO may be combined with the leftover 1064-nm radiation to shift the laser tuning range from 420–680 nm to 301–414 nm. The wavelengths add reciprocally,

$$\frac{1}{\lambda_{\text{resultant}}} = \frac{1}{\lambda_{\text{OPO}}} + \frac{1}{\lambda_{\text{pump}}} \quad (2)$$

It is also possible to use a nonlinear crystal to frequency double the output of the OPO. However, for a broad line OPO this produces almost negligible power.

Optics. High power lasers require specialized optics to handle this power without damage. Damage can be to the coatings, to the substrate, or to other objects that the laser beam hits. The coherence of the laser allows for special optical methods to control the propagation.

The available optics tend to divide into several domains, depending on the laser being used. One characteristic is the wavelength range, with the two most common being UV (200–400 nm) or visible-near IR (400–1100 nm). A second domain is characterized by whether the laser is a fixed line laser such as Nd:YAG and its harmonics, or is tunable such as an OPO. A third characteristic is whether it is pulsed or cw, but the LFP technique uses pulsed lasers almost exclusively.

Elements. Three different forms of lenses are available. These are plano-covex (concave), bi-convex (concave), and best form. In this application the plano variety is usually sufficient since the laser is used to illuminate large areas, and thus tight focusing is not required. The plano variety is well-suited to infinite conjugate ratios, that is, the ratio of the object to image distance. The lens is oriented such that the most curved surface faces the long conjugate distance (i.e., the collimated beam), to minimize spherical aberration [16]. The laser is a point source and well-collimated, giving rise to large conjugate distances. The biconvex lenses are best used in near unity conjugate ratio situations. The best form lenses are used for near diffraction limited focusing of the laser. The spot size achievable with these is still limited by the M^2 of the laser.

Beam expansion, collimation, and shaping are done with telescopes. The degree of collimation achievable depends on the M^2 of the laser. Often it is advantageous to purchase computer-optimized telescopes. These are widely

available for various expansion ratios and wavelength ranges. They may be purchased with the zoom (expansion ratio) adjustable and the wavelength focusing motorized, or with purely manual adjustment. Cylindrical telescopes may be used to expand or contract the beam in one dimension. These can give rise to very significant astigmatism, where either the horizontal or vertical radii of curvature are different from the other. Astigmatism gives rise to large spot sizes and distorted focal regions. A pair of Littrow prisms may be used to build an anamorphic beam expander/compressor. The prisms are very wavelength sensitive, and alignment of such a prism expander is not simple. Such an expander is not recommended for use at multiple wavelengths or for variable beam expansion.

Polarizing optics are extremely effective in most laser systems for control of the radiation. It is critical that they and their coatings be designed specifically for laser use, as many are absorptive and can be easily damaged by laser radiation. There are a wide range of polarizers available. One should carefully consider the extinction ratio since it will determine the maximum and minimum radiation levels in an attenuator. For any thick prism-based polarizer, it is necessary to carefully align the normal of the prism face to the rotation axis of the mechanical rotator to minimize beam pointing variation with rotation angle.

Design. In designing an optical system to control propagation of the beam to the sample, it is best to understand Gaussian beam propagation and the properties of the laser beam. The simplest method is called the ABCD law and is fully described by Yariv [17]. In this method the complex beam radius is propagated from a beam waist through various elements to a desired plane. It applies only to true Gaussian, TEM₀₀ beams. The complex radius of curvature at a beam waist is

$$q_0 = i \frac{\pi w_0^2 n}{\lambda} \quad (3)$$

where w_0 is the 1/e² radius of the beam at the waist, n is the refractive index, and λ is the wavelength in air. The complex radius of curvature after an element, characterized by the coefficients A , B , C , and D , is

$$q_1 = \frac{Aq_0 + B}{Cq_0 + D} \quad (4)$$

The coefficients may all be complex. The complex radius of curvature can be expressed in measurable quantities as

$$\frac{1}{q_1} = \frac{1}{R_1} + i \frac{\lambda}{\pi w_1^2 n_1} \quad (5)$$

where R_1 is the real radius of curvature of the phase front at the new location, and w_1 is the 1/e² radius at the new location. Thus, by evaluating the real and

imaginary parts of the complex beam radius one can calculate the properties of the beam as a result of the optical element. Three basic ABCD matrices are

$$\begin{bmatrix} 1 & d \\ 0 & 1 \end{bmatrix} \text{ propagation over distance } d$$

$$\begin{bmatrix} 1 & 0 \\ -1/f & 1 \end{bmatrix} \text{ through a thin lens of focal length } f, f > 0 \text{ converging} \quad (6)$$

$$\begin{bmatrix} 1 & 0 \\ 0 & n_1/n_2 \end{bmatrix} \text{ through a dielectric interface from } n_1 \text{ to } n_2$$

Multiple elements may be combined by matrix multiplication.

Coatings. It is critical that the coatings on all laser optics be designed and manufactured for use in the laser. These coatings should come with a specific damage threshold rating, and are suspect if no rating is given. One needs to calculate specifically the irradiance or pulse energy density (fluence) of the laser before specifying the coating. These coatings should only be purchased from those experienced with optics for use in lasers. A common problem in the past has been the humidity sensitivity of the coatings. In specifying a coating, one should double check that it is not humidity sensitive.

Most laser coatings are for specific wavelengths. Dielectric stack coatings can be designed for fairly large wavelength ranges. For the largest wavelength range, a single layer MgF₂ coating is often used. In general, as the coating bandwidth gets wider, the performance, either transmittance or reflectance, gets worse.

Attenuation. Most of the time it is best to have the ability to control the amount of laser pump radiation incident on the sample. Attenuation systems can be based on polarization, absorption, or reflection. The simplest polarizer system uses a single polarizer and the fact that most lasers are linearly polarized to achieve attenuation. This has two disadvantages: first, that the electric field vector changes direction when the polarizer is rotated, and second, for thick calcite polarizers (e.g., Glan-laser polarizers), the beam can change direction or position as the polarizer is rotated. An improved system uses a $\lambda/2$ waveplate before a fixed polarizer to rotate the electric field and thus keep the output field direction constant, and does not allow the beam to change direction or position. This has the disadvantage that most waveplates are only effective for a single wavelength. Some achromatic waveplates are available but may be limited either to low laser powers, or may have limited retardation accuracy. Absorption-based attenuation systems may use absorbing glass neutral density (ND) filters as a stack or in

wheels. Great caution must be exercised since these filters are very susceptible to bleaching at laser intensities or fracture due to heating by absorption of the laser beam. Reflection-based attenuators can be in several forms. One commercial system uses two counter-rotating plates to give variable attenuation without walking the beam. Reflective ND filters usually cannot be used because of their low damage threshold for pulsed lasers. One system uses stacks of plates to attenuate by Fresnel losses. If a high index material such as sapphire is used, large attenuation can be achieved. This can be positioned using wheels or by manually adding plates. Figure 6 shows one design of an adapter to go in a filter wheel that requires 400- μm sapphire plates, offsetting them at an angle to prevent back-reflection into the laser while eliminating beam walk. This gives neutral attenuation from 200 nm to 5 μm . In all cases a beam dump must be positioned to accept the rejected energy for all beams.

D. Sample Holders

The design, construction, and alignment of a good sample holder is critical to obtaining the best measurements. These cell holders are often designed to do more than just hold the cell or sample. One common purpose is to build masking

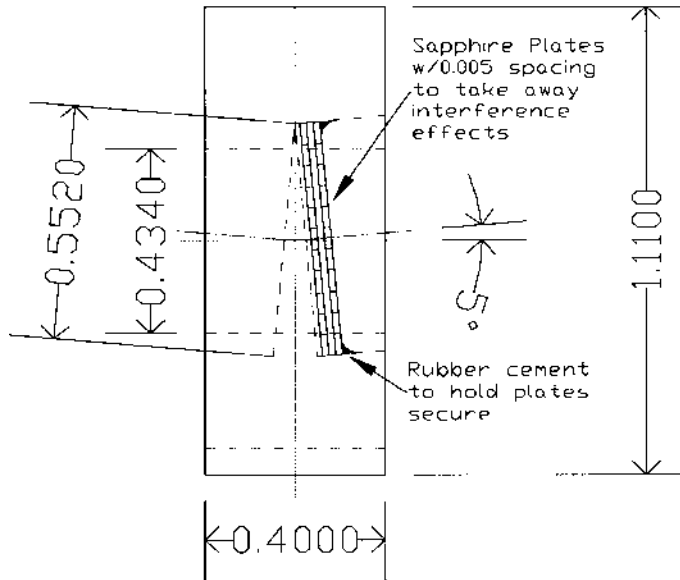


Figure 6 Adapter for sapphire plates in filter wheel for broadband attenuation control.

into the holder to insure the overlap of the pump and probe regions in the sample. A design that includes these functions is shown in Fig. 7. Other purposes may be to enable temperature control, stirring, or motion of solid samples.

It is best to have the pumped region near the surface of the sample and to be as uniform as possible. A mirror to reflect transmitted radiation back through the cell will make the pump profile more uniform. However, the uniformity along the longitudinal (depth) into the cell will change due to deviations from Beer's law at high pump intensities. A good solution is to use low enough concentrations that the pump is not severely depleted in passing through the sample. Absorbances of 0.1 to 0.3 in a 1-cm cell will keep the depletion to less than 10% over 1 mm.

The masking should also prevent pump or probe radiation from entering the cell walls. The cell is positioned so that the front surface is parallel to the probe beam in order to insure an accurate transmission measurement. The slits at the probe entrance and exit surfaces control the depth of the pump region and thus the amount of excitation variation due to Beer's law. The exit slit will also determine the amount of fluorescence radiation passed through to the detector. If the probe

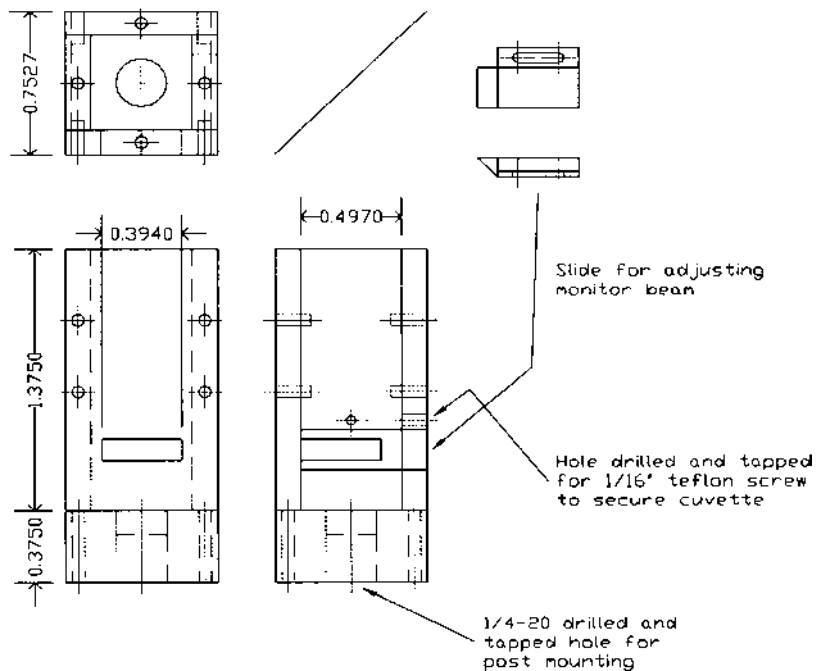


Figure 7 Sample holder design.

beam is well-collimated, this slit may be moved further from the sample with little loss of probe beam intensity while causing a large decrease in fluorescence radiation. A rear escape window allows monitoring of incident energy without a sample, or energy transmitted with a sample in place.

A Peltier temperature-controlled cell holder with four-window access is available from Quantum Northwest (Spokane, WA) (Model Flash 200). Many standard slit configurations are available and the holder includes horizontal and vertical translation, a stirrer, and the option of adding an acoustic pressure transducer.

E. Deoxygenation

Freeze-pump-thaw. The most reliable method for deoxygenation of a liquid sample is the freeze–pump–thaw method. In this method the sample is held in a vessel that can be immersed in liquid nitrogen (LN) and is connected to a vacuum manifold through a valve. The valve is closed and the sample immersed in LN. All of the liquid and vapor condense out except the oxygen and nitrogen, which will have a substantial vapor pressure. The valve is opened while the sample is immersed in LN and the gas pumped out to a pressure of $\leq 10^{-3}$ torr. The valve is closed and the sample allowed to thaw. At higher temperatures, the solubility of the gases decreases and any dissolved gas is released. After it is completely thawed, it is immersed in LN again, and then pumped out. This cycle is repeated at least three times. It is important to monitor the pressure to ensure a good vacuum at all times. A sample vessel and manifold are shown in Fig. 8.

Bubbling. Bubbling with an inert gas, either nitrogen or argon, may also be used to deoxygenate samples, but is much less effective than the freeze–pump–thaw method even when done with extreme care. In this technique oxygen diffuses out of solution in order to come to equilibrium with the gas in the bubble. However, the diffusion is slow and the bubble moves quickly due to buoyancy, making it inefficient in removing gas. It takes vigorous bubbling, which in turn leads to very significant solvent loss and, consequently, knowledge of the concentration. This may be somewhat ameliorated by bubbling the inert gas through the neat solvent first in order to saturate it with vapor. It is important that tubing carrying the gas not be oxygen permeable, such as copper. It is also necessary to scrub the gas using an oxygen filter, since even small concentrations will give large reductions in the measured triplet lifetimes, especially long lifetimes.

F. Spectrometers

The choice of which spectrometer to use and how to use the spectrometer is critical to taking the best data. The first choice is whether an imaging or

nonimaging spectrometer is needed. The imaging spectrometer is needed if more than one channel of spectral data will be taken at the same time. This would be used for a CCD detector or if multiple fiber optic channels and discrete detectors are planned. The nonimaging spectrometers are useful for single channel spectral information and usually are less expensive.

A critical choice is the f-number of the spectrometer. The lower the f-number, the more light gathering and ultimately the narrower the line width achievable by the spectrometer. For low light signals it is important to use the fastest (i.e., lowest f-number) spectrometer affordable. For laser flash photolysis on condensed matter at room temperature, the line width is usually not a critical

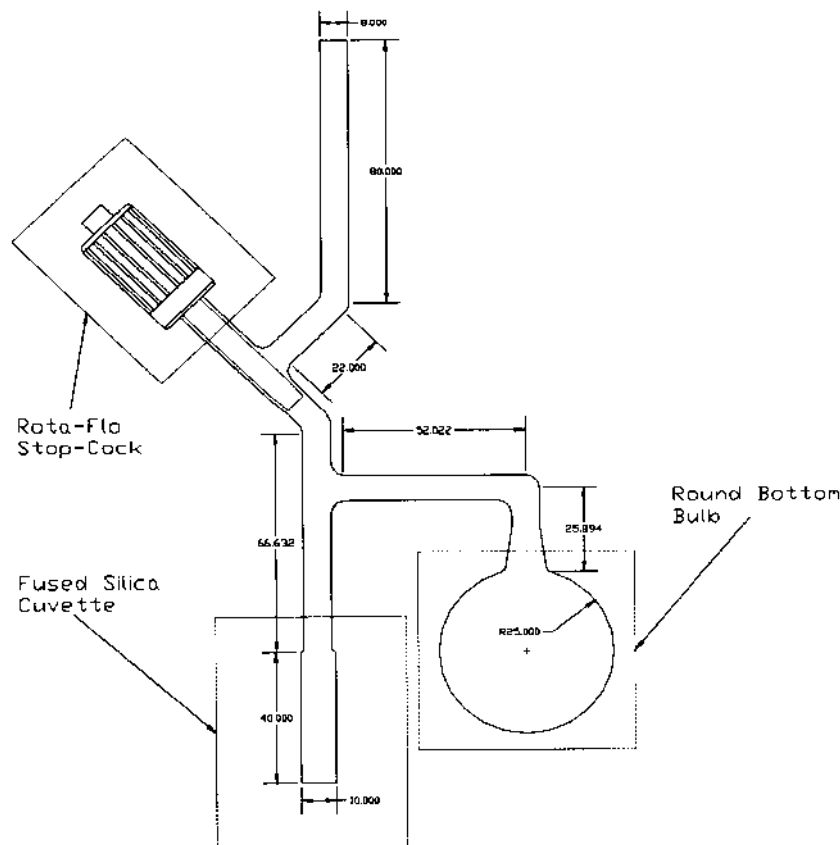


Figure 8 Sketch of a typical freeze–pump–thaw vessel made of glass using standard glass fittings and adapters.

issue. In addition, many spectrometers are made with a speed of $\sim f/4$ which is usually sufficient for laser flash photolysis.

Gratings come in three different types and many different line spacings and blaze angles. The holographically ruled, ion-etched grating has the lowest scattering and highest efficiency, but is also the most expensive. The classically ruled grating gives very high efficiency, but can produce significant scattering that is detrimental to high optical density (or absorbance) and narrow line width measurements. It is usually the least expensive and is available in the widest range of line spacing. The holographic grating has very low scattering but also low efficiency. For intermediate optical densities from 0.1 to 2 and intermediate line widths from 3 to 10 nm (such as is common in laser flash photolysis experiments), the classically ruled grating is often best. Many spectrometers have multiple gratings. This enables one to optimize the gratings over a wider wavelength range, or to enable continuous scans over a wide range. However, one can work with a single grating if it is chosen wisely. The blaze determines the center wavelength of the grating. One must also be aware that some gratings, especially classically ruled gratings, can have wavelength regions where the efficiency is drastically less than other areas, giving artifacts in the measured spectra unless corrected by using a known, smoothly varying light source such as a tungsten filament.

Spectrometers can be purchased with multiple input and output ports. This offers the ability to switch easily between multiple sources and detectors. Sources are either free space propagated or fiber optically coupled. The ports can be configured to switch between single point detectors, multiple point detectors (such as optical fiber coupled multiple channels), or large array detectors such as CCDs. Alternatively, they are used to switch between wavelength regions where one detector is for the visible and one for the IR.

Computer interfacing should also be considered. The two most common interfaces are the IEEE-488 and RS232 interfaces. In general, only small amounts of data will be transferred. Either of these interfaces is sufficient. Newer interfaces provide more bandwidth than is actually needed. IEEE-488 is the easiest to use. Related to this is the availability of stand-alone control software for the spectrometer or modules that make control via LabView or some other programming interface easier.

G. Detector Systems

There are three classes of detectors—single point temporal detectors, linear array spectral detectors, and combination spectral–temporal detectors. There are detectors for each wavelength regime within each class.

One should determine the fastest event to resolve. This is determined by the photoprocesses to be measured. The detection system is then designed to have

the necessary instrument response function. This is a convolution of laser pulse width and detection system bandwidth. There are three regimes defined by a combination of laser and detection systems. The first is a Q-switched laser (4–10-ns pulselwidth), a PMT (0.6–2-ns risetime) and relatively fast [~ 5 gigasamples/second (GS/s)] sampling oscilloscope. This combination is limited by the laser pulse width. The second regime is the modelocked laser, a microchannel plate-PMT (MCP-PMT), and a high-end real-time sampling oscilloscope (20 GS/s–6 GHz amplifiers). This system is limited by the scope and MCP-PMT. The third system would consist of a femtosecond Kerr-lens modellocked Ti:sapphire laser (~ 50 –150-fs pulse width) and a streak camera (up to 0.2-ps resolution). Faster systems require pump–probe techniques, which are covered elsewhere in this book. The second system costs approximately four to five times the price of the first system and gives about $40\times$ shorter time resolution. In some materials this higher time resolution would be sufficient to measure the excited singlet state and directly observe intersystem crossing. The third system costs approximately two to three times the second system and gives almost $500\times$ better time resolution. In all cases the complexity and difficulty of the systems increases dramatically as the time resolution increases. This system easily resolves most singlet states, and even hot electron effects.

Temporal detectors. Temporal detectors provide a single time varying signal. The detectors may be extremely small, as in fast PIN photodiodes having dimensions of $\sim 100\text{ }\mu\text{m}$, or large area ultrasensitive PMTs with an area of several square centimeters. Those detectors with internal electronic gain have the lowest noise.

Visible detectors. The most common single point, temporal detector used in laser flash photolysis in the visible range is the PMT. The internal gain, large area, and high speed make this a nearly ideal detector. It is capable of gains as high as 10^7 , but this is rarely needed. The spectral range for traditional design PMTs extends from 185 nm to 900 nm. An old Ag-O-Cs (S1) style photocathode can be sensitive to 1000 nm, but at the cost of a large increase in noise and lower sensitivity.

The PMT consists of a photocathode material that, when immersed in an electric field and struck by a photon, emits an electron. This electron is accelerated by the electric field and guided to a dynode. The dynode is coated with a material that emits two or more electrons when struck with a sufficiently energetic electron. The electron can easily be accelerated to tens or hundreds of electron volts. The emission of multiple electrons causes the number of electrons to be multiplied at each dynode stage. The electrons are then focused and accelerated to the next dynode stage by the geometric design of the dynodes. A PMT can have 5 to 12 dynode stages. As the number of electrons in a cloud emitted from each dynode increases from dynode to dynode, the size of the cloud also tends to increase due to electron repulsion. This is counteracted by the electric field that focuses the cloud. The risetime of the standard side window PMT is 1–2 ns.

It is customary to wire the PMT for a lower gain and higher current handling capability in order to reduce shot noise. The circuit must be designed carefully to prevent the electron cloud from spreading in space. Thus the electric field must become larger as the cloud number increases. The large number of electrons emitted from the later dynode stages puts a large strain on power supplies to provide the high currents. It is advantageous to have a large field at the initial stage since the loss of any of the initial electrons emitted from the photocathode gives rise to a large noise factor. It is not recommended, although often done in practice, to collect the generated current from any dynode since the tube is balanced and designed to collect from the anode. Special tubes with fewer dynodes are the best solution for high current applications such as laser flash photolysis, but are expensive. One technique to maintain the system in a linear condition under varying incident light levels is to vary the PMT gain as a function of light level to produce a constant output. This is best done by varying the voltage division in the middle group of dynodes, while keeping the initial and final accelerating voltages the same.

Figure 9 gives a design for a voltage divider using nine dynodes. This is definitely not an optimal design. Guidance on the design of dividers is given in much more detail in handbooks supplied by the PMT suppliers—Hamamatsu (Bridgewater, NJ), Burle (Lancaster, PA), and Phillips (Slaterstown, RI). A typical tube in use is the Hamamatsu R928 Multialkali. The GaAs tubes have a longer red response, but cannot handle the high currents.

There are compact PMTs available that give comparable multiplication to the larger PMTs with rise times down to 600 ps. Microchannel plate PMTs can have risetimes as low as 100 ps.

Large area avalanche photodiodes (APDs) are now available with internal gains of several hundred. These detectors have electron generation quantum efficiencies of nearly 100%, which is ten times better than most PMTs. The gain is almost what is achievable using five dynodes in a PMT, but the APD is capable of much higher currents. The silicon APD sensitivity extends out to about 1000 nm. These seem to be likely candidates for use in an LFP experiment, but none have been reported to date.

IR detection. The traditional laser flash photolysis detector in the near IR range has been the solid-state germanium detector coupled to high gain electronics. The minimum possible gain and bandwidth are used in order to minimize noise. For singlet oxygen fluorescence measurements, extremely high gain is required, and this forces the bandwidth to be reduced to ~ 1 MHz, which in turn negates the ability to detect fast transients. InGaAs detectors are increasingly the detector of choice. These are now available in thermoelectrically and LN-cooled versions.

LFP techniques have been developed [18–20] using both dispersive and transform spectrometers for the IR portion of the spectrum. In these instruments,

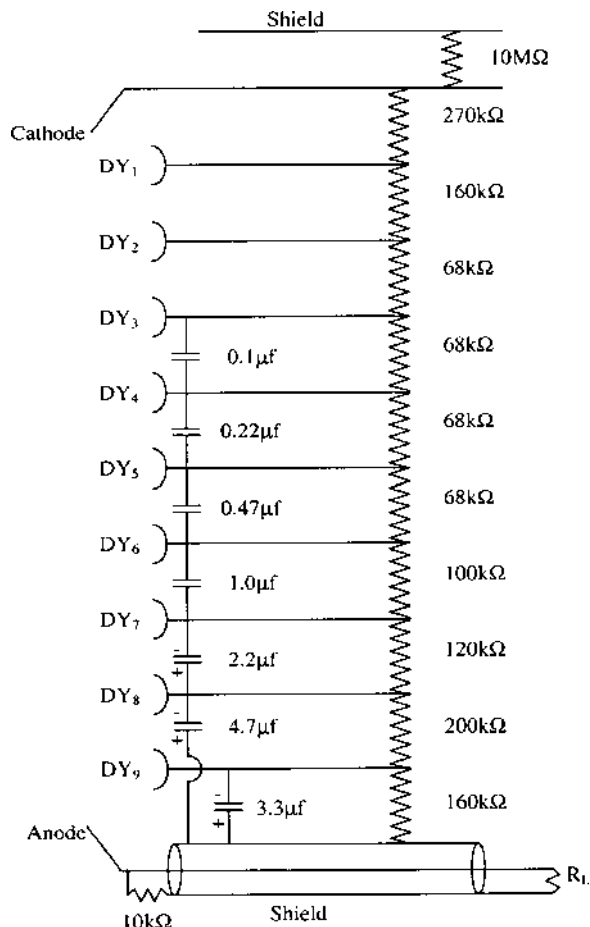


Figure 9 Wiring diagram for high current PMT using all nine dynodes.

a UV or visible laser pulse excites the molecule, and the transmission is probed in the infrared over the region of $700\text{--}4000\text{ cm}^{-1}$. These vibrational spectra are much easier to compare to quantum chemical calculations, and in many ways provide a more direct method to identify the species created. These techniques rely on mercury cadmium telluride (MCT), lead sulfide (PbS), lead selenide (PbSe), or indium antimonide (InSb) detectors.

Oscilloscopes. The temporal detectors need a digitizing oscilloscope to acquire the data. Digitizing rates of 1 GS/s give a Nyquist frequency of 500 MHz and are sufficient for a rise time of $\sim 1\text{ ns}$. Single shot digitizers in excess of 10 GS/sec are available if needed.

Digital oscilloscopes built onto a PC card are now available. The price is not that much different than the stand-alone scopes, however, the data transfer rate can be 10 to 100 times faster for the PC card compared to IEEE-488 based instruments that have only about 1-Mb/s transfer rates.

In all cases it is best to use a backoff circuit. This circuit negates the signal from the radiation transmitted through the unexcited sample and enables one to measure just the transient induced by the excitation. This then is a measurement against a zero background. The backoff circuit of Janata [12,13] is one of the best to use. Backoff may also be accomplished using the DC offset feature of many oscilloscopes. To do this, the sensitivity of the scope would be set to a low value and a waveform acquired of the unexcited sample. The offset would be used to force this essentially flat waveform to be centered around 0 V. Then the sensitivity would be increased and the transient signal recorded. This is more time consuming, and there is a limit to the amount of DC offset available, especially for the highest recording sensitivities. Without a backoff circuit or using DC offset, the entire waveform would be recorded, and the transient riding on a large background signal would need to be extracted. To see small signals, a large number of digitizing levels are required. Most digitizers have 8 to 9 bits, which are extended by averaging.

Spatial/chromatic. Instead of taking a single wavelength and measuring its variation over time, one may measure the entire spectrum over a small time slice. The chosen time slice is varied with respect to the laser excitation pulse, and the spectrum assembled to again give full time dependent spectral arrays. The advantage of measuring the spectrum over a small time slice is that much higher spectral resolution can be obtained. This is good for identifying narrow features or identifying excited state species. In order to sample only a narrow time slice, a gated CCD is needed. This gating is almost always done with a microchannel plate intensifier. The intensifier may be gated to slices < 10 ns. This is clearly sufficient time resolution for many processes, but many spectra would need to be acquired to achieve good time resolution. It may also be very difficult to determine complex kinetics using this method. This spectral technique also has the disadvantage of a narrow wavelength bandwidth, that is limited because intensifiers require a photocathode. The spatial detectors do not enable one to use a backoff type device. Thus a large portion of the dynamic range of the CCD is used in measuring the uninteresting background signal. This implies that one must get the best dynamic range of the intensified CCD (ICCD) affordable. Another disadvantage is the much higher cost of ICCD compared to single point temporal detectors. In summary, the temporal detectors give very high temporal resolution and low spectral resolution at very moderate cost. The spectral detectors give high spectral resolution and low temporal resolution at much higher cost.

Other CCD intensification technologies, such as electron bombardment and on-chip multiplication, are of little use in LFP because what is really needed is

gating and, as of this writing, such technologies have not been implemented. The electron bombardment scheme should in principle be gatable. Again, cooled CCD and back-illuminated CCDs are of little use since the light level in LFP is generally strong. Deep well CCDs are of use for their extra dynamic range, but only if the intensifier dynamic range is greater.

Streak camera. The streak camera allows one to obtain both temporal and wavelength information at the same time. Thus data is acquired much faster, and this allows one to use much fewer excitation pulses, which can be critical for unstable materials.

The streak camera consists of a slit aperture, followed by a re-imaging lens system that places the slit image onto a photocathode. The photocathode generates an electron cloud that is accelerated and focused onto an MCP intensifier. The cloud from the MCP is still in the shape of a slit and retains the distribution of intensity information along the slit. This slit distribution is then swept at high speed by deflecting electrodes across a fluorescent screen. Light is emitted from the screen and detected by a CCD. The resulting CCD image contains spatial information in one dimension and temporal information in the other dimension. If a spectrograph is coupled to the input of the streak camera, one may map the spectral information along the slit and thus give a wavelength–time distribution out of the streak camera.

The wavelength of operation of the camera is similar to that of available photocathodes for PMTs. The cameras and readout system can be extremely expensive. However, there is no other detection system that can approach the temporal resolution of this instrument. Triggering of streak cameras often requires many passes of the excitation beam up and down the table to provide the time delay for the streak to start while synchronized. One concern is the wavelength resolution achievable. At most, one part in 500 is resolvable, but under many conditions only one part in ~ 20 is achievable. This depends on how the camera is operated and the quality and matching of the readout CCD detector. Finally, since no backoff system is available, a large background signal will consume much of the limited dynamic range of the streak camera. New cameras are available with dynamic range, under some conditions, of 10,000:1, making the possibility of this system much more attractive.

H. Timing Control System

This experiment requires the timing control of a rather large number of events. A typical timing sequence is listed in Table 3. Time delay generators have been developed to provide the type of control needed. These are available either as stand alone units or as PC cards that mount inside a computer. Some of the signals need to be at TTL voltage levels, but others may be needed at voltages up to 15 V.

Table 3 A Typical Timing Sequence for the Nanosecond LFP Experiment

Event	Start time (ms)	Stop time (ms)	Acceptable jitter (ms)	Repetition rate (Hz)
Laser lamp charge	0			10
Probe slow shutter	85	95	1.0	2-5
Laser shutter	85	95	1.0	2-5
Probe fast shutter	89	92	0.01	2-5
Laser lamp fire	90		0.001	10
Backoff trigger	90.163		0.005	2-5
Laser Q-switch fire	90.263		0.001	2-5
Energy meter trigger	90.263		0.1	2-5
Oscilloscope trigger	90.263000		0.000001	2-5

The different repetition rates require either divide by N circuits or gating. Table 4 gives a list of several instruments that can be used for timing control.

I. Data Acquisition

It is most efficient to automate the data acquisition and control of the experiment. The acquisition process starts with a measurement of the ground state absorption spectrum. It is advisable to obtain these data on the same sample and with the same spectral bandwidth as the LFP experiment in order to facilitate calculations and comparison of the ground state and excited state data. From this one can decide the optimum wavelength range to run. Next, a background run of just the solvent in the LFP experiment is performed. This is to assess the maximum intensity of the probe beam, correct for lamp and grating spectral distributions, test for any luminescence of the solvent, and finally test for electromagnetic interference from the laser source.

It is best to keep the light intensity on the detector in the center of its linear range. The probe source, grating, and sample can have a wide range of transmittances making it necessary to readjust the probe light level during a wavelength scan. This process is automated. Two common methods are to use neutral density filters in the probe beam, or to vary the gain of the detector to give a constant output as measured before the excitation pulse. This requires one or a few pulses of the probe beam to be measured and the intensity adjusted accordingly. The probe source can have wavelengths that cause permanent damage to the sample, which is minimized by filtering, and thus exposure to the probe beam is also minimized by carefully predicting the necessary filter from a few pulses.

Table 4 Timing Control Sources

Manufacturer	Model	Time resolution	Independent timers	Output	Repetition rate
Stanford Research Systems	DG535	5 ps	4	4 V in 50Ω (optional to 40 V in high Z)	1 MHz
Berkeley Nucleonics Corp.	555	1 ns	16	6 V in 50Ω (optional to 35 V in high Z)	1 MHz
Quantum Composer	9314	10 ns	8	10 V in 50Ω (20 V in high Z)	100 kHz
National Instruments	NI6608	12.5 ns	8	2.4 V	N/A

It is best to use the maximum sensitivity of the digital oscilloscope. The sensitivity is adjusted so as to not clip the noise, as this distorts the averaging statistics. An autoscaling procedure can be written that uses the persistence in the digital scope to find the maximum recorded voltages. Again a delicate balance is needed between overexposing the sample to excitation energy and determining the optimum sensitivity setting. It is best to use a few pulses and then apply a safety factor to allow for variations that may be larger than the small set of pulses tested. If the data transfer process is fast enough, each waveform can be assessed individually as to whether it should be kept. A typical assessment factor would be selecting the laser pulse energy in a narrow range. However, it is better to stabilize the laser energy.

Lasers and harmonic generation crystals operate best under continuous conditions. Thus flashlamps and Q-switches are operated at the designed repetition rate, and the beam controlled by an external shutter.

The language used to write control programs is an important choice. Options include LabView, C++, VisualBasic, and LabWindows CVI. LabView has the advantage that learning it is extremely fast and the code is easy to read. It can also incorporate C++ or VisualBasic subroutines to give more flexibility. It can, however, be very cumbersome to execute highly nested looping schemes. In general, the other options are more difficult to learn but give greater flexibility.

Several options are available for the data acquisition and control interface. The most common has been the IEEE–GPIB interface. A very wide range of instruments is available with this interface, and setting up a system can be quite easy. However, the interface is now considered to be very slow, especially for large data sets now available from digital oscilloscopes. The RS232 interface is still useful with some instruments. Ethernet 10/100 Base T is now available on

some instruments. This gives a better data transfer bandwidth and can allow these instruments to be controlled remotely via an Internet connection. Some new interfaces, such as USB and Firewire, can give superb data transfer rate, however, these are not ideally suited for control because of inherent time lags.

III. DATA ANALYSIS

A. Data Reduction

The raw data obtained by the LFP experiment are in the form of a transient voltage waveform. If a backoff unit is used, the baseline will have a zero-voltage reference at the point in time where the backoff was applied. In fact, the backoff may not be accurately calibrated and there can be a few mV error in the zero position. The photophysical properties are best related to the differential change in absorbance, or optical density. The backoff supplies a measurement of the transmitted probe intensity at the test wavelength before laser excitation. This is also the DC offset value if no backoff is used. Therefore, the ratio of the voltages before and after excitation gives the transient transmission of the sample,

$$T(t) = \frac{V}{V_0} = \frac{i}{i_0} \quad (7)$$

where V represents the voltages, i represents the currents through the respective loads producing the voltages, and the subscript 0 implies a measurement without excitation. It is more common to use the current parameters than the voltages. The ratio of the current difference gives the differential transmission and the negative log gives the differential absorbance,

$$\Delta A = \log\left(1 - \frac{i}{i_0}\right) \quad (8)$$

Inaccuracies in the probe beam are corrected by performing a baseline correction. There are at least three sources of systematic error in the baseline. As mentioned earlier, the backoff or DC offset value may not be perfect. The background signal may change in time giving a curved baseline. There are often noise sources, especially Q-switch electromagnetic interference (EMI) noise, which is picked up by the detectors and observed in the baseline. These can be easily corrected if they do not vary. Their variation should be tested. At the least, their mean variation can be corrected. If their variation is severe, either they must be eliminated by more careful design and control of the sources of the noise, or by construction of an extremely well-matched detector circuit that can produce the identical baseline but without the transient signal. The latter is a much more difficult approach than the former.

The main method is to measure the background signal without the laser excitation. This is averaged and taken under the exact same conditions as that with the laser excitation. To remove EMI noise requires that the laser Q-switch be fired during background acquisition. This in turn requires that shutters and not the Q-switch trigger be used to control the presence of the laser pulse. The EMI is generally very short lived and is not a concern for time scales greater than 1 μs . The acquisition of a baseline under matching conditions can double the time it takes to acquire data. If a cw probe beam is used, the baseline can be made extremely flat and time invariant. In this case a baseline is acquired at the beginning of a data run and applied to all waveforms. A pulsed probe is tested for the baseline stability. If it is stable, a test at the beginning of a run is sufficient. Testing is done with very large averaging and high sensitivity to pick up the small deviations. The small DC error in any waveform may be corrected by averaging the baseline signal that is obtained before the laser pulse excites the sample. This requires that the trigger point be adjusted to provide sufficient baseline values, and also that one knows where the leading edge of the laser pulse occurs relative to the trigger point. The transient absorption with these corrections is

$$\Delta A = \log \left(1 - \frac{(i - e_{\text{SDC}}) - (i_b - e_{\text{bDC}})}{i_0 + e_{\text{DC}}} \right) \quad (9)$$

where e_{SDC} and e_{bDC} are the DC errors in the signal and the baseline, respectively, and i_b is the baseline.

B. Kinetic Analysis

Curve fitting. A nonlinear curve fitting method is used to extract the decay information from the ΔA waveform. For most tests, the laser pulse and the formation of a triplet state are much faster than the decay of the triplet or resulting species. This allows one to model just the decay process without modeling the formation process as long as the instrument bandwidth is also chosen to give a risetime much shorter than the decay time of the measured species.

Decay models. A single exponential fit of the data is represented by

$$\Delta A = (A_0 - A_F)e^{-kt} + A_F \quad (10)$$

where A_0 , A_F , and k are the peak differential absorbance signal extrapolated to time zero, the final differential absorbance signal at long times, and the decay rate of the single exponential process, respectively. Time zero is chosen at the point where the laser intensity arises to a level greater than the noise. The zero point in time is not critical in assessing the decay rate from the fit, since a shift in the zero time is equivalent to a change in the prefactor giving the same functional form. Near the peak of an absorbance waveform the decay may not be explicitly

exponential due to a convolution with the pulse profile and the excited state formation kinetics. Thus it is best to fit data at least one pulse width delayed from the peak of the absorbance waveform. This decay profile may then be used to extrapolate back to the zero point to obtain an accurate A_0 .

A bi-exponential fit of the data is represented by

$$\Delta A = (A_0 - A_2)e^{-k_1 t} + (A_2 - A_F)e^{-k_2 t} + A_F \quad (11)$$

where A_0 , A_2 , A_F , k_1 , and k_2 are the peak differential absorbance signal extrapolated to time zero, the actual time zero absorbance, the final differential absorbance signal at long times, and the decay rates of the single exponential processes, respectively. The same discussion and procedures as given for the single exponential model concerning the time zero point applies to this functional decay model as well.

A single exponential with bimolecular annihilation fit of the data is represented by

$$\Delta A = \frac{(A_0 - A_F)e^{-kt}}{1 + 2(A_0 - A_F)r(1 - e^{-kt})} + A_F \quad (12)$$

where A_0 , A_F , k , and r are the peak differential absorbance signal extrapolated to time zero, the final differential absorbance signal at long times, the decay rate of the single exponential process, and the ratio of the triplet-triplet annihilation rate to the excited triplet decay rate, respectively.

Identification of processes. One must identify the decay processes and the nature of the excited states produced in order to correctly interpret the interactions involved in the decay process. There are a large number of possible decay processes, but in the nanosecond time scale many are not observable. Thus the identification of the nature of the excited state observed is the first priority. Because of the prevalence of the triplet state formation, several tools have been developed to test this nature.

The most direct method is to observe the emission of the sample. The emission can be prompt fluorescence (from the singlet state), phosphorescence (from the triplet state), delayed fluorescence, charge transfer (CT) emission, or emission from some other species created in the solution. The spectral features and decay rates are the primary ways of identifying the nature of the emission. Prompt fluorescence is the first and fastest decay process after the excitation pulse. This emission will have a peak near to but red-shifted from the fundamental absorption in the ground state spectrum. Rarely, fluorescence will occur from the S_2 state and will be near to but red-shifted from the second absorption peak of the ground state spectrum. This emission spectrum will show evidence of vibrational overtones, which become more distinct at lower

temperatures. A plot of the absorption spectrum and the fluorescence spectrum on a wavenumber axis is often symmetric about the fundamental transition.

The phosphorescence band is shifted to a much larger degree than the fluorescence band from the fundamental absorption peak. This spectrum will also show evidence of vibrational overtones and will be much longer lived. The efficiency of emission from the triplet state is often low and requires low temperatures to observe. Materials with strong phosphorescence often have a very weak absorption tail in the ground state spectrum due to a direct S_0 to T_1 transition. The feature will be symmetric with the phosphorescence band on a wavenumber scale. This feature, if attributable to a direct S_0 to T_1 transition, will not produce prompt fluorescence emission. The presence of a phosphorescence band that mirrors a weak ground state feature is a very strong indication of triplet formation. The phosphorescence decay rate matches the decay rate of the triplet excited state absorption. Thus a measurement of both of these decay rates in the LFP experiment can give conclusive evidence that a triplet state has formed.

Delayed fluorescence occurs because of back-transfer of energy from a higher triplet state to the singlet manifold. It has a spectral distribution that matches the prompt fluorescence, but a lifetime more closely matching the triplet state lifetime. The presence of this feature indicates that a strong spin-orbit coupling is likely present and is enhanced by an energy level resonance between higher singlet and triplet states.

Luminescence may also be observed from CT states. This luminescence is usually broad and featureless. The presence of such a feature in the luminescence spectrum is a clear indication that a CT process is involved in the kinetics.

Oxygen is a ubiquitous quencher of triplet states in liquid solutions. Pure solvents generally have a large enough HOMO–LUMO gap that energy transfer from the excited solute is extremely unlikely. Thus the dissolved oxygen, which has a very low lying excited singlet state, becomes the most prevalent quencher of excited states. Oxygen also is an efficient scavenger of free electrons leading to its quenching of radical anions. Nitrous oxide (N_2O), has been used to quench the formation of radicals without quenching the triplet state [3].

Sensitization can also be used to identify the triplet state. This can be done by adding an acceptor of low energy. By judicious choice of acceptor and laser excitation wavelength one can often excite only the unknown species and then detect the known acceptor. By using several acceptor materials one is able to measure the triplet energy of the unknown. Similarly, one may excite a donor having energy greater than the unknown. Energy transfer to the unknown will produce the same differential spectrum as measured by excitation of the unknown alone.

Global analysis. Global analysis refers to mathematical methods that work on an array of data, which in this case is absorbance or differential absorbance versus time and wavelength. Several steps are involved with the first

being factor analysis using singular value decomposition. This is a method to extract the basis set for the array of data values (i.e., the eigenvector spectra associated with each kinetic behavior). This method is chosen since there are generally many more wavelength and time samples than there are chemical species and decay rates, and the problem is thus over determined, causing some eigenvalues to be of nearly zero weight and thus singular. Often there are only a few eigenvectors with significant values. These are correlated to the species in the mixture or to a systematic system signature such as a baseline drift or a spectral background. The real eigenvectors are thus easily identified. The other eigenvalues are set to zero and the noise vectors, consequently, are eliminated. Various tests have been derived to indicate which eigenvalues are significant and need to be retained [21].

The temporal component of these spectral eigenvectors is then analyzed using a specific kinetic model. The model can be zeroth order, first order, second order, or any combination of these. It is necessary to have some understanding of the expected processes since more than one model may give a reasonable fit. The quality of fit is decided by an inspection or tests of the residuals.

Two programs are available for spectral work. These are Global Works by OLIS (Bogart, GA) and Specfit by Spectrum Software Associates (Manlbarough, MA).

C. Calibration of Triplet Extinction Coefficients

One often wishes to obtain distinct molecular properties of the species excited. The measured differential absorbance spectrum is a function of the concentrations and the extinction coefficients of the species. The mixing of these parameters makes their individual extraction difficult. Many methods have been developed to extract quantitative triplet extinction coefficients. A large number of these methods were detailed by Carmichael and Hug [22]. We describe here two of the most common and widely applicable methods.

Energy transfer. In this method a triplet energy donor is added to the solution with the unknown and selectively excited by the pump radiation. The availability of a suitable donor is critical to the success of this method. The donor must have (1) high triplet yield, (2) a much stronger absorption at the pump wavelength than the unknown, (3) well known triplet and singlet extinction coefficients at the same wavelength, and (4) a triplet energy greater than the unknown. A series of solutions are made varying the concentration of the unknown. The kinetics of these solutions are measured and the decay coefficient k_{obs} extracted. One calculates the quenching fraction, f_q , according to

$$f_q = \frac{k_{obs} - k_d}{k_{obs}} \quad (13)$$

where k_d and k_{obs} are energy donor decay rates in the absence, and presence, of the energy accepting unknown, respectively. The differential extinction coefficients are related to the differential absorbance and quenching fraction via

$$\Delta A_U^0 = \Delta A_R^0 \frac{\Delta \varepsilon_U}{\Delta \varepsilon_R} f_q \quad (14)$$

where ΔA_U^0 , ΔA_R^0 , $\Delta \varepsilon_U$, and $\Delta \varepsilon_R$ are the differential absorbance of the unknown and reference donor at $t = 0$, respectively, and differential extinction coefficient of the unknown and reference, respectively. One can determine $\Delta \varepsilon_U$ from a plot ΔA_U^0 versus f_q . It is difficult to find a suitable donor, especially when only a limited number of pump wavelengths is available. These kinetics must be measured in well deoxygenated samples, and it is important to eliminate second order decay of the donor by limiting the donor concentration and excitation pulse energy. It is also possible to use an energy acceptor for the energy transfer.

Singlet depletion. The singlet depletion technique is built on the assumption that the absorption resonances of the excited state are distinctly different from those of the ground state. It requires that one measure the differential absorbance in a region or regions where the ground state has absorption. Assuming that the absorbance is measured at a time after the excited singlet state is empty, that no photoproducts are formed, and that all excited electrons migrate to the lowest triplet state, the differential absorbance is written as

$$\Delta A(\lambda) = (\varepsilon_T^*(\lambda) - \varepsilon_S(\lambda)) [{}^3M^*] \ell \quad (15)$$

where $\varepsilon_T^*(\lambda)$, $\varepsilon_S(\lambda)$, $[{}^3M^*]$, and ℓ are the first excited triplet state molar extinction coefficient, the ground singlet state molar extinction coefficient, the first excited triplet state concentration, and the path length, respectively. Thus the ground state absorption features will give a negative contribution to the measured $\Delta A(\lambda)$, producing negative peaks where the ground state is more strongly absorbing than the excited triplet state. These negative peaks have the same shape as the ground state spectrum. Equation (15) can be recast as,

$$\varepsilon_T^*(\lambda) = \frac{\Delta A(\lambda)}{[{}^3M^*] \ell} + \varepsilon_S(\lambda) \quad (16)$$

The technique is then used to form the $\varepsilon_S(\lambda)$ spectra by taking a well-measured ground state spectrum, $\varepsilon_S(\lambda)$, and adding the $\Delta A(\lambda)$ adjusted by varying $[{}^3M^*]$ as a parameter to remove the apparent negative peaks in the $\varepsilon_T^*(\lambda)$ spectra. Several methods have been developed to estimate $[{}^3M^*]$ [22]. One method not mentioned, which is just the embodiment of the original assumption in the method, is to minimize the correlation of $\varepsilon_S(\lambda)$ and $\varepsilon_T^*(\lambda)$ in a region around a ground state absorption feature. This is an objective and robust method. It must also be pointed

out that it is absolutely necessary that the $\varepsilon_S(\lambda)$ and $\Delta A(\lambda)$ spectra be measured under the exact same spectroscopic conditions, especially the spectral bandwidth. One limitation not often mentioned is that for those molecules that are excited to the S_1 state and relax back to S_0 , a large amount of thermal energy must be dissipated. This, coupled with the fact that many molecules have a relatively strong thermochromic behavior, means that one cannot necessarily null out the ground state resonances in the triplet state construction due to thermal differences. Thus, it is necessary to minimize the laser pulse energy and photon energy, if possible.

D. Triplet Quantum Yields

Absorbed quanta. The triplet yield is estimated using the triplet concentration measured by either energy transfer or singlet depletion. The triplet yield is

$$\phi_T = \frac{[{}^3M^*]}{[{}^1M^*]} \quad (17)$$

where $[{}^1M^*]$ is the concentration of excited singlets created by the laser pulse. One must estimate $[{}^1M^*]$. The first estimate, giving an upper limit to ϕ_T , is to assume complete conversion to the excited singlet state and uses $[{}^1M^0]$ as the concentration excited. A more accurate method is to measure the $[{}^3M^*]$ at low energies and calculate $[{}^1M^*]$ according to

$$[{}^1M^*] = [{}^1M^0] \frac{\mathcal{E}}{A} \frac{\varepsilon_S(\lambda_{\text{pump}}) \ln(10)}{6.02 \times 10^{20} \hbar \omega_{\text{pump}}} \quad (18)$$

where \mathcal{E} , $\varepsilon_S(\lambda_{\text{pump}})$, ω_{pump} are the pulse energy in excitation area A , the molar extinction coefficient at the pump wavelength, and the pump frequency, respectively. The excitation energy must be such that

$$\mathcal{E} \ll \frac{A \varepsilon_S(\lambda_{\text{pump}}) \ln(10)}{6.02 \times 10^{20} \hbar \omega_{\text{pump}}} \quad (19)$$

The limit of excitation energy is also determined from a plot of ΔA versus \mathcal{E} . At the energy where this plot is no longer linear, saturation effects are beginning and the excitation energy is too high.

Comparative method. The principle of this technique is that the concentration of triplet formed in a solution of some sample with unknown ϕ_T^U is compared with the concentration formed by the same number of quanta in a solution of some standard with a known ϕ_T^R and $\Delta \varepsilon_T^R$. The unknown triplet yield is

determined from

$$\phi_T^U = \phi_T^R \frac{\Delta A_T^U \Delta A_T^R}{\Delta \epsilon_T^R \Delta \epsilon_T^U} \quad (20)$$

Low excitation energy is again required as described in the previous section. Suitable reference materials are listed by Carmichael and Hug [22], and Murov [23].

Heavy atom fluorescence quenching. This method compares the change in fluorescence intensity of a molecule in solution, caused by adding a given concentration of heavy atom quencher, with the increase in triplet state absorption resulting from such addition of quencher observed by flash photolysis. This is applicable to materials that have a rather long singlet state lifetime. Suitable heavy atom quenchers are alkyl halides, dimethyl mercury, cesium iodide, and xenon. The triplet yield is

$$\phi_T = \left(\frac{\phi_F^0}{\phi_F} - 1 \right) \Bigg/ \left(\frac{\Delta A_T \phi_F^0}{\Delta A_T^0 \phi_F} - 1 \right) \quad (21)$$

where ϕ_F^0 , ϕ_F , ΔA_T^0 , ΔA_T are the fluorescence yield without and with quencher, and the differential absorbance at time zero without and with the quencher, respectively.

E. Triplet Energy

Phosphorescence and absorption. The triplet energy is determined from the phosphorescence spectrum and the absorption feature of the direct $S_0 \rightarrow T_1$ transition. This is a graphical technique best done by plotting both normalized spectra versus wavenumbers and identifying the point where the two spectra cross as the 0–0 transition.

Energy transfer. As discussed earlier, the triplet energy is identified by testing the ability of the unknown to sensitize known reference materials and thus bracketing the energy.

IV. ERRORS AND CORRECTIONS

The errors associated with a good laser flash photolysis experiment can be broken down into those associated with having a known ground state concentration of known species, producing a known excited state population, and in measuring the excited state population over time and wavelength. We treat these in the order in which they are encountered.

A. Producing a Known Ground State Population

Solute. The experiment begins with the material to test. It is critical that the purity of the sample be known (i.e., it must be measured). The methods are beyond the scope of this book, but H-nuclear magnetic resonance, C¹³-nuclear magnetic resonance, elemental analysis, FTIR spectroscopy, GC-mass spectrometry, HPLC, X-ray crystallography, and Raman spectroscopy can all contribute to the knowledge of the sample.

Obviously, for characterization of molecular properties one must know the molecular mass. Specifically one must know the molecular mass of the chromophore for which one wishes to attain the molecular properties. This is important in polymeric work. For these types of materials it is important to determine, through study of monomeric or oligomeric forms, the operational chromophore. Impurities will disrupt the ability to quantify the number of chromophore units in solution.

It is possible to predict for some materials (e.g., by the solubility parameter), likely solvent systems for the solute. Careful consideration of the form of the molecule and the likelihood of dimerization should be made before selection of the solvent.

Liquid samples. Liquid solutions are the simplest to make and often the easiest to work with in order to minimize errors. It was mentioned earlier that one should select a solvent that is compatible chemically with the molecule under study. The solvent should also be chosen to be stable under illumination conditions. For example, it is often the case that solvents containing halogens, such as chlorine, readily lose the chlorine as an ion under illumination, which reacts with the solute changing its properties. Finally, it is important that the solvents be pure. Impurities can react with the solute or can fluoresce.

Besides the obvious need for quantitative preparative techniques in making solutions, one must insure that agglomeration of the solute and complexation with the solvent has not occurred in the solution to be tested. This is why most experiments are done at micromolar concentrations. If there is any doubt that the solute is monodisperse, a range of concentrations is tested and the spectra run to inspect for agglomeration effects (i.e., increased scattering at longer wavelengths).

It is important to quantitatively measure the ground state absorption spectrum. This is done in a series of samples, preferably by varying the path length and using the same concentration that will be tested in the LFP experiment. It is important that the same spectral bandwidth be used as in the LFP experiment and that careful wavelength calibration is maintained.

Degradation of samples can occur in the LFP experiment. If this is the case for the materials being tested, then a flow cell is used with a reservoir of pure sample.

Solid samples. Solid samples provide several difficulties in addition to those presented for liquid samples. Since the molecule is physically confined and the diffusion of quenching materials is slowed, one commonly finds a much longer lifetime in solid samples. This implies that the excited state has a longer time to undergo reactions. In general, degradation is a more vexing problem in the solid state. Samples must be physically moved for each test point if degradation occurs. The long lifetime also increases the probability of energy transfer to and from the matrix. Solubility of a molecule in the monomeric state of a polymer host does not guarantee that it will remain monodisperse as the polymerization reaction occurs. The solute is often susceptible to the same reaction as the monomer, which then degrades the molecule of interest. All of these problems should be tested and addressed before commencing LFP measurements.

B. Producing A Controlled Excited State Population

Excitation beam. Many models assume that the pump region is uniformly irradiated throughout the volume, and that the excited state species are uniformly distributed throughout the pump volume. The first requirement then is that the excitation beam be of uniform intensity in the probe region. The pump is well-collimated using anamorphic prisms or a telescope with cylindrical optics. The beam is expanded to provide a small variation in intensity across the probe region. This requires a certain loss of energy in the beam. The pump beam is masked so that the pump radiation is not incident on the cell walls, in order to prevent fluorescence from the cuvette from entering the probe beam path. The pump and probe regions are precisely overlapped.

A nonuniform profile does not contribute to an error as long as the concentration of excited species is linearly related to the pump intensity. The problem arises that nonuniform high intensity regions will become nonlinear before the low intensity regions. This forces one to operate at lower pulse energies and thus at smaller signals. If the intensity is uniform, better signals can be obtained. A few percent variation in intensity will matter little, but a 50% variation will force one to live with just half of the possible signal.

Nonlinear effects are determined by the rate constants of the various intramolecular processes and the excitation rates. These are defined in three regions: (I) $k_{\text{ex}} < k_{\text{T}}$, (II) $k_{\text{S}} > k_{\text{ex}} > k_{\text{T}}$, (III) $k_{\text{ex}} > k_{\text{S}} > k_{\text{T}}$, and, within the second and third regions, sub regions for (IIb) $k_{\text{T}_{\text{nex}}} > k_{\text{ICTn}}$, (IIIb) $k_{\text{S}_{\text{nex}}} > k_{\text{ICSn}}$, where $k_{\text{ex}} = 2303\epsilon_{\text{S}0}(\lambda)I$, with I in Einstein/cm², k_{ex} is the excitation rate out of the ground state at the pump wavelength, k_{S} is the first excited singlet decay rate, k_{T} is the first excited triplet decay rate, $k_{\text{S}_{\text{nex}}}$ is the excitation rate from the first

excited singlet to higher singlets at the pump wavelength, $k_{T_{\text{nex}}}$ is the excitation rate from the first excited triplet to higher triplets at the pump wavelength, k_{ICS_n} is the internal conversion from higher excited singlets to the first excited singlet, and k_{ICT_n} is the internal conversion from higher excited triplets to the first excited triplet. These dividing points for the regions are shown in Table 5.

In region (I) the triplet is proportional to the excitation energy and there is no depletion of the ground state. This is the linear region.

Region (II) is a nonlinear region where the triplet state population is still determined by the pulse energy, but it is no longer linearly dependent on the energy. In this region the population of the triplet state is significant and can lead to two problems. First, if the triplet state is more absorbing than the ground state at the same wavelength, then the absorption depth of the pump beam can be dramatically shortened leading to energy absorption at the front surface of the cell, significantly more heating, and a much higher excitation rate into the higher excited states. The distribution of the triplet in the cell will no longer follow Beer's law and is not easily known without extensive modeling of the coupled differential rate equations. Because of the significant triplet state population, one can expect a significantly higher probability of forming reaction products. If the triplet state is less absorbing than the ground state, then the pump will bleach through the sample and produce a much lower triplet state concentration than expected. However, the triplet state distribution will in fact become more uniform.

Region (IIb) is caused by the higher excitation rate in materials where absorption increases in the triplet state at the pump wavelength. It is possible for the triplet state extinction coefficient to be 100 times or more larger than the

Table 5 Nonlinear Regions and the Intensities That Determine Them

Region	I (Einstein/cm ²) limits
I	$I < \frac{k_T}{2303\varepsilon_{S0}(\lambda_{\text{pump}})}$
II	$\frac{k_T}{2303\varepsilon_{S0}(\lambda_{\text{pump}})} < I < \frac{k_S}{2303\varepsilon_{S0}(\lambda_{\text{pump}})}$
IIb	$I > \frac{k_{\text{ICT}_n}}{2303\varepsilon_{T1}(\lambda_{\text{pump}})}$
III	$I < \frac{k_S}{2303\varepsilon_{S0}(\lambda_{\text{pump}})}$
IIIb	$I > \frac{k_{\text{ICS}_n}}{2303\varepsilon_{S1}(\lambda_{\text{pump}})}$

ground state extinction coefficient, and thus the excitation rate would increase by the same factor. If this new excitation rate exceeds the internal conversion decay rate from the higher excited triplet states, real populations will accumulate in the higher excited states. This will produce a dramatic increase in the reactivity of the absorbing species. The process would first affect the peak of the pulse. The rate, k_{ICTn} , and the molar extinction coefficient, $\epsilon_{T1}(\lambda_{\text{pump}})$ are not usually known, although k_{ICTn} is reported to be $\sim 10^{12} \text{ s}^{-1}$ [8]. The molar extinction coefficient can be measured by the same experiment at low intensities using a different pump wavelength.

Region (III) begins where the excitation rate from the ground state exceeds the first excited singlet state decay rate. At this intensity the first excited singlet state will begin to fill. The population in the first excited singlet state may also have a larger or smaller extinction coefficient than the ground state, leading to bleaching or increased absorption. The same effects seen in Region (II) would now occur, but are due to the singlet states.

Region (IIIb) begins where the excitation rate from the first excited singlet state is greater than the internal conversion rate from the higher singlet states to the first excited singlet state. Again, much higher reactivities and ionization would be expected.

The pump wavelength should be selected carefully. This is determined by the desire to preferentially excite the solute of interest, the absorption depth, concentration achievable, concentration necessary to avoid triplet-triplet annihilation, and decomposition sensitivity. In general, lower concentrations, lower pulse energies, longer pulse widths, and longer wavelengths are preferred. These are limited by the signal-to-noise ratio available, the desired temporal resolution, and laser wavelengths available.

Quenching effects. One must be aware of and avoid quenching effects for an accurate determination of kinetics. Oxygen is an ubiquitous quencher unless great care is taken to avoid it. Also very common is the occurrence of triplet-triplet annihilation. This occurs for high concentrations and high pump energies. One requires that the total diffusion-limited quenching rate be much less than the observed decay rate. The total diffusion rate is [9]

$$k_D[{}^3M^*] = 2 \times 10^5 \frac{T}{\eta} [{}^3M^*] \ll k_T \quad (22)$$

and the excited state concentration is estimated from [24]

$$[{}^3M^*] = [{}^1M^0][1 - \exp(-k_{\text{ex}}k_{\text{isc}}\tau_p/(k_{\text{ex}} + k_s))] \quad (23)$$

Similarly quenching may be done by the ground state species, which requires a dilute solution to reduce this rate below other rates of interest. A large number of

other quenching processes that can affect the kinetics are possible, and the reader is referred to the text by Birks [8] for a comprehensive (though somewhat dated) treatment.

C. Measuring the Excited State Population

Probe beam. The LFP experiment is basically a transmission measurement and thus the principal parameter is the ratio of intensities before and after excitation. This in fact obviates the need for an absolute measurement of the ground state spectrum. It is critical that the region of the sample probed be the same before and after excitation and that the probe region overlap the pump region. The probe beam is assumed to probe the entire excitation region and therefore must be uniform in intensity. Good shot noise performance requires a well-collimated beam through the sample region. The probe beam temporal variation must be stable from shot to shot, or, better yet, invariant. For cw lamps, a feedback circuit may stabilize the power level if long decays are measured. For pulsed work, a stable pulse profile enables one to characterize the baseline time behavior and correct for it.

Collection optics. The collection optics that transfer the transmitted probe radiation to the spectrometer are a critical part of the experiment design. Many materials are highly fluorescent and thus produce high levels of irradiance beyond the baseline level expected for the system. This often prohibits one from measuring the differential absorbance accurately. First, insuring good collimation of the probe beam, and then placing an aperture displaced from the sample, may ameliorate this problem. This aperture reduces the f-number of the collection optics and thus discriminates against fluorescence, but if the probe is well-collimated, much less attenuation of the probe than fluorescence will be seen.

Spectroscopy. There are several common problems of which to be aware. One is overfilling the grating that causes undue scattering in the spectrometer. Underfilling the grating also reduces the spectral resolution, although this is often not too severe a problem. Careful calibration of the wavelength must be done at many wavelengths throughout the detection band. A common error is inadvertent detection of harmonics of the grating. Order sorting filters must be carefully considered to ensure second order bands are not passed to the detector. Many times, especially in the IR, more than one filter is required as some filters have secondary transmission bands where the light source is intense. Scatter of pump radiation into the spectrometer is also a common problem. Several Raman filters are available that can eliminate the problem, or a double monochromator may be employed.

Detection. It is important that all detectors and the associated digitizing equipment be operated in the linear range. This should be tested as best as possible by varying the probe intensity over a wide range and by coupling some scattered pump light into the detector to test impulse response over a wide range. In all cases, rebound may be found in the detectors or ringing due to impedance mismatch when they are tested over a wide range. Careful attention to impedance matching and shielding will alleviate much of this problem. A common problem with PMTs is the charging of dynodes upon high exposure. This is particularly a problem with a highly fluorescent sample, and data should be examined carefully under these conditions for artifacts.

Noise analysis. There are several noise sources and methods for reducing their effect. Shot noise arises from the stochastic incidence of photons on the detectors. This requires a higher flux of photons to reduce it. This is achieved by a more powerful probe source and careful optics design, but is ultimately limited by the detector flux handling capability (i.e., higher flux while maintaining linearity). Reducing the time exposure to the probe will increase the PMT flux handling capability. Pulsing the source with narrower windows and faster rise times does this. Minimizing the gain of the PMT also increases the input flux handling capability. Finally, better PMT wiring will improve the flux capability. Other detectors, such as avalanche photodiodes, can handle higher flux, but have less amplification and may require more electronic amplification resulting in more 1/f noise.

EMI noise, the radio frequency signal due to fast Q-switching electronics, is best eliminated at the laser source by shielding and good electronics design. Prevention of ground loops is important to keep EMI from invading the detection system. Time shifting the optical from the electronic pulse can be done but is not easy because large delays are required. Subtracting the EMI signal measured without an optical signal can be done if it is stable. A study of the laser operating conditions and their effect on EMI can be used to minimize this noise.

The pump laser pulse energy often varies from shot to shot. For experiments done in the linear region and for exponential decays this is not a problem. Normalization of the signal by measuring the individual pulse energies can be done, but may also make noise worse if the signal is not proportional to the laser energy. In the nonlinear region, the absorbance is not proportional to the pulse energy and normalization is not technically correct. Thus, windowing the data, by rejecting data obtained where the laser pulse energy is outside of the preset window, is required.

One of the best methods of noise reduction is to reduce the bandwidth of the detection system to the minimum necessary to observe the transient of interest. This can be done by an electronic passband filter at the DSO input or by digital filtering of the measured waveform.

Averaging, the universal noise eliminator, dramatically increases the time needed to acquire data. This also requires stability of the material and the experiment. Material stability is an often overlooked problem.

REFERENCES

1. R. G. W. Norrish and G. Porter, Chemical reactions produced by very high light intensities, *Nature* 164:658 (1949).
2. J. C. Scaiano, *CRC Handbook of Organic Photochemistry*, Vol. 1 (J. C. Scaiano, ed), CRC Press, Boca Raton, FL, 1989, p. 438.
3. R. V. Bensasson, E. J. Land, and T. G. Truscott, *Flash Photolysis and Pulse Radiolysis*, Pergamon Press, New York, 1983, p. 236.
4. G. Porter, *Chemistry in Microtime: Selected Writings on Flash Photolysis, Free Radicals, and the Excited State*, Imperial College Press, London, 1997, p. 541.
5. R. W. Redmond, Photophysical techniques used in photobiology and photomedicine, *Photobiology in Medicine*, Plenum Press, New York, 1994, pp. 1–28.
6. D. E. Lynch, The Determination of photophysical and photochemical parameters by pulsed photoacoustic microcalorimetry, flash photolysis, and single beam, 77K, DETE, *Chemistry*, Wayne State University, Detroit, 1990, p. 112.
7. A. Berinstain, Development of laser techniques for applications in biomolecules and cellular systems, *Chemistry*, University of Ottawa, Ottawa, 1997, p. 242.
8. J. B. Birks, *Photophysics of Aromatic Molecules*, Wiley-Interscience, John Wiley & Sons Ltd., London, 1970, p. 704.
9. N. J. Turro, *Modern Molecular Photochemistry*, University Science Books, Sausalito, CA, 1991.
10. S. P. McGlynn, F. J. Smith, and G. Cilento, Some aspects of the triplet state, *Photochem. Photobiol.* 3:269 (1964).
11. L. I. Schiff, *Quantum Mechanics*, 3rd ed., 1968, p. 544.
12. E. Janata, Baseline compensation circuit for measurement of transient signals, *Rev. Sci. Instrum.* 57:273 (1986).
13. E. Janata, Instrumentation of Kinetic Spectroscopy-8. The use of baseline compensation in the sub nanosecond time domain, *Radiat. Phys. Chem.* 39:319 (1992).
14. B. W. Hodgson and J. P. Keene, Some characteristics of a pulsed xenon lamp for use as a light source in kinetic spectra photometer, *Rev. Sci. Instrum.* 43:493 (1972).
15. T. Hviid and S. O. Nielson, 35 volt, 150 ampere pulse generation with droop control for pulsing xenon arcs, *Rev. Sci. Instrum.* 43:1198 (1972).
16. W. J. Smith, *Modern Optical Engineering: The Design of Optical Systems*, 2nd ed., 1990, p. 524.
17. A. Yariv, *Quantum Electronics*, 2nd ed., 1975, p. 570.
18. B. D. Moore, et al. Fast Time-resolved ftir detection of short-lived photochemical transient species in solution: a direct comparison with IR laser spectroscopy, *J. Phys. Chem.* 89:850 (1985).
19. K. H. Iwata, Construction of a versatile microsecond time-resolved infrared spectrometer, *Appl. Spectrosc.* 44:1431 (1990).

20. T. Yuzawa, et al. Nanosecond Time-resolved infrared spectrometry with a dispersive scanning spectrometer, *Appl. Spectrosc.* 48:684 (1994).
21. E. R. Malinkowski, *Factor Analysis in Chemistry*, 2nd ed., John Wiley, New York, 1991.
22. I. Carmichael and G. L. Hug, Triplet–triplet absorption spectra of organic molecules in condensed phases, *J. Phys. Chem. Ref. Data* 15:1 (1986).
23. S. L. Murov, I. Carmichael, and G. L. Hug, *Handbook of Photochemistry*, 2nd ed., Marcel Dekker, Inc., New York, 1993, p. 420.
24. I. Carmichael and G. L. Hug, A note on the total depletion method of measuring extinction coefficients of triplet–triplet transitions, *J. Phys. Chem. Ref. Data* 89:4036 (1985).

13

Nonlinear Absorption Properties of Selected Materials

This chapter presents nonlinear absorption parameters of several selected materials. The data are extracted from several sources, including original references and secondary sources. An excellent listing of two-photon absorption data can be found in Refs.[1–3]. Tables in these references include sources for relative two-photon spectra as well as absolute two-photon absorption coefficients.

Sections I–IV contain nonlinear absorption coefficients for several selected materials. Data have been restricted to single beam measurements. Therefore these are true nonlinear coefficients at the reported wavelengths for these materials. Van Stryland and Chase [2] have discussed the problems of measuring nonlinear absorption coefficients, and state that picosecond pulse, or shorter, measurements are usually more reliable. Therefore, most of the data reported here, where possible, were measured at < 1 ns. This is not the case for all of the data, however, and some longer pulse (i.e., > 1 ns) measurements are included when short pulse data could not be found.

Section V gives two-photon absorption cross-sections for several organic molecules. Finally, photophysical data for some reverse saturable absorption materials are listed in Section VI.

I. WIDE BANDGAP INSULATOR MATERIALS

Table 1 lists two-photon absorption coefficients for several selected wide bandgap materials. These include mostly crystals but also some glasses.

Table 1 Nonlinear Absorption Coefficients for Selected Wide Bandgap Insulator Materials

Material	λ (nm)	β (10^{-9} cm/W)	γ (10^{-21} cm 3 /W 2)	Method ^a	Ref.
Aluminum oxide	355	<0.0016		NLT	[4]
Aluminum oxide	308	0.0276		NLT	[5]
Aluminum oxide	266	0.27		NLT	[4]
Arsenic trisulfide glass	1115	0.003		NLT	[80]
	1485	0.011			
	1730	0.08			
	1920	4			
	2165	5			
	2350	15			
	2475	30			
			2.0	ZS	[85]
Arsenic trisulfide glass	1550				
	1300				
	633	1.6×10^9 (cw)		ZS	[88]
Arsenic trisulfide (amorphous)					
	1250	0.16		TBC	[91]
	1550	<0.030			
	1250	0.14		TBC	[91]
	1550	0.16			
	1250	0.22		TBC	[91]
	1550	0.060			
	1250	0.38		TBC	[91]
	1550	0.15			
	1250	0.04		TBC	[91]
	1550	0.25			
	1250	1.4		TBC	[91]
	1550	0.14			

As ₄₀ Se ₆₀	1250 1550 1550 1550 1550 355 266 248 1064 266 355 266 781.5	2.8 0.14 0.28 0.29 0.15 <0.0036 <0.0040 0.11 51.7 0.24 <0.042 1.6 0.064	TBC [91] TBC [91] TBC [91] NLT [6] NLT [6] NLT [7] ZS [82] NLT [4] NLT [6] NLT [6] TBC [89]
RG610	308 266 1064 807 308 248 248 1300 264 532	0.032 0.00092 <0.02 59.3 $(9.2 \pm 2.3) \times 10^{-4}$ 0.74 1.6 ± 0.3 0.014 0.55 0.42 ± 0.03 190	NLT [5] NLT [4] ZS [82] TBC [89] NLT [8] NLT [11] NLT [13] ZS [85] NLT [84] ZS [86]
Calcium fluoride			
Cerium-doped barium titanate			
Chromium-doped LiSGaF			
Diamond			
Diamond			
Fused silica			
Germanium sulfide glass			
Germanium-doped silica (3.5 mol-% Ge)			
Germanium-doped silica (8 at-% Ge)			

(continued)

Table 1 Continued

Material	λ (nm)	β (10^{-9} cm/W)	γ (10^{-21} cm 3 /W 2)	Method ^a	Ref.
(12.5 at-% Ge)	240				
(14.7 at-% Ge)	290				
(27.5 at-% Ge)	760				
Herasil glass (Heraeus)		0.018 ± 0.002			[84]
Infrasil glass (Heraeus)	264	0.021 ± 0.002			[84]
Lithium fluoride	266	< 0.02			[4]
Potassium bromide	266	2.0			[4]
Potassium chloride	266	2.2			[4]
Potassium iodide	355	7.3			[4]
Potassium iodide	348	8.0			[9]
Potassium iodide	266	3.7			[4]
Potassium niobate	846	0.032 ± 0.005			[83]
Potassium titanyl phosphate (100)	532	0.24		ZS	[10]
Potassium titanyl phosphate (010)	532	0.16		ZS	[10]
Potassium titanyl phosphate (110)	532	0.14		ZS	[10]
Rubidium bromide	355	2.43		NLT	[4]
Rubidium bromide	266	2.18		NLT	[4]
Rubidium chloride	266	1.1		NLT	[4]
Rubidium iodide	355	5.1		NLT	[4]

Rubidium iodide	266	2.5	NLT	[4]
Silicon dioxide	266	< 0.045	NLT	[4]
Sodium bromide	266	2.5	NLT	[4]
Sodium chloride	266	3.5	NLT	[4]
Sodium niobate-doped-glass ($f = \text{vol. fraction}$)				[81]
($f = 0.4$)	532	7		
($f = 0.2$)	532	9		
($f = 0.08$)	1064	0.008		
($f = 0.025$)	532	6		
SrBi ₂ Ta ₂ O ₉	532	0.003		
Strontium fluoride	355	5	ZS	[90]
Strontium fluoride	266	7.3	NLT	[6]
Strontium fluoride	248	< 0.0057	NLT	[6]
Suprasil glass	266	> 0.0054	NLT	[7]
Suprasil glass	248	< 0.011	NLT	[6]
Suprasil glass (Heraeus)	264	0.017	NLT	[12]
Titanium dioxide ($E \parallel c$)	532	0.058	NLT	[84]
Titanium dioxide ($E \perp c$)	532	0.017 \pm 0.002	ZS	[14]
Titanium:sapphire	807	18.6 \pm 4.4	ZS	[14]
		14.8 \pm 2.9	TBC	[89]
		< 1 \times 10 ⁻⁴		

^a NLT, nonlinear transmission; ZS, Z-scan.

The primary measurement methods listed in Table 1 are nonlinear transmission and Z-scan. These methods were discussed in Chapters 7 and 10.

Two-photon absorption coefficients in wide bandgap materials are important since many of these are considered for use either as laser window materials in the visible and ultraviolet, or as frequency conversion materials in these wavelength regimes.

II. SEMICONDUCTORS

Nonlinear absorption data for semiconductor materials are found in Table 2. Some three-photon as well as two-photon absorption coefficients are included. Measurement methods include laser calorimetry, nonlinear transmission, Z-scan, and top-hat Z-scan, all of which were discussed in Chapters 7 and 10.

Two-photon and three-photon absorption are detrimental in semiconductors considered for use in all-optical switches. These coefficients generally place limits on the usefulness of available materials. It is important to find materials with low nonlinear absorption coefficients, especially in the optical communication wavebands near $1.3\text{ }\mu\text{m}$ and $1.5\text{ }\mu\text{m}$.

Large two-photon absorption coefficients are desirable for some applications such as optical limiting, discussed in Chapter 9. Some semiconductors show promise for this application. Nonlinear refractive effects are also considered for optical limiting. For example, ZnSe is a potential candidate for the visible and near infrared spectral regions. However, the far infrared spectral region is where semiconductors are likely to be especially attractive for optical limiting. A leading candidate in this regime is InSb.

III. ORGANIC MATERIALS

Table 3 gives some two-photon and three-photon absorption coefficients for selected organic materials. The primary measurement methods are nonlinear transmission and Z-scan.

Organic materials have been under consideration for all-optical switches, especially in the telecommunication bands near $1.3\text{ }\mu\text{m}$ and $1.5\text{ }\mu\text{m}$, because of the promise of large, fast nonlinear refractive effects. Again, two-photon and three-photon absorption place limits on the effectiveness of these materials for this application.

Table 2 Nonlinear Absorption Coefficients for Selected Semiconductor Materials

Material	λ (nm)	β (10^{-9} cm/W)	γ (10^{-18} cm 3 /W 2)	Method ^a	Ref.
Aluminum gallium arsenide (Al _{0.18} Ga _{0.82} As waveguide)	1660	<0.05	0.13	NLT	[24]
Aluminum gallium arsenide (Al _{0.18} Ga _{0.82} As waveguide)	1655		0.12	NLT	[24]
Aluminum gallium arsenide (Al _{0.18} Ga _{0.82} As waveguide)	1630	0.07		NLT	[24]
Aluminum gallium arsenide (Al _{0.18} Ga _{0.82} As waveguide)	1610		0.082	NLT	[24]
Aluminum gallium arsenide (Al _{0.18} Ga _{0.82} As waveguide)	1600	0.19		NLT	[24]
Aluminum gallium arsenide (Al _{0.18} Ga _{0.82} As waveguide)	1580		0.075	NLT	[24]
Aluminum gallium arsenide (Al _{0.18} Ga _{0.82} As waveguide)	1575	0.28		NLT	[24]
Aluminum gallium arsenide (Al _{0.18} Ga _{0.82} As waveguide)	1550	0.34	0.050 ± 0.020	NLT	[24]
Aluminum gallium arsenide (Al _{0.18} Ga _{0.82} As waveguide)	1530		0.040	NLT	[24]
Aluminum gallium arsenide (Al _{0.18} Ga _{0.82} As waveguide)	1525	0.50		NLT	[24]
Aluminum gallium arsenide (Al _{0.18} Ga _{0.82} As waveguide)	1500	0.34	0.035	NLT	[24]
Aluminum gallium arsenide (Al _{0.18} Ga _{0.82} As waveguide)	1490		0.7–1.3	NLT	[24]

(continued)

Table 2 Continued

Material	λ (nm)	β (10^{-9} cm/W)	γ (10^{-18} cm 3 /W 2)	Method ^a	Ref.
(Al _{0.18} Ga _{0.82} As waveguide)					
Cadmium selenide	1064	30		NLT	[26]
Cadmium sulfide	1270	<0.01		ZS	[16]
Cadmium sulfide	780	6.4		ZS	[16]
Cadmium sulfide	610	3.2		ZS	[16]
Cadmium sulfide	532	5.5		NLT	[25]
Cadmium sulfide selenide (Cd _{0.15} Se _{0.75})	1064	65 ± 20		LC	[17]
Cadmium sulfide selenide (Cd _{0.5} Se _{0.5})	1064	10		NLT	[25]
Cadmium sulfide selenide (Cd _{0.25} Se _{0.75})	1064	15		NLT	[25]
Cadmium telluride	1064	26		ZS	[18]
Copper bromide	694	200		NLT	[27]
Copper chloride	694	45		NLT	[27]
Copper iodide	694	89		NLT	[27]
Gallium arsenide	1064	26		ZS	[18]
Gallium arsenide (100)	1064	18		ZS	[10]
Gallium arsenide (110)	1064	24		ZS	[10]
Gallium arsenide (111)	1064	25		ZS	[10]
Gallium nitride	400	16		NLT, ZS	[92]
Gallium nitride	690	7			
Gallium nitride	720	3	17–20	ZS	[95]
Gallium nitride	527				

Gallium phosphide	1064	0.2	NLT	[26]
Gallium phosphide	532	19	THZS	[23]
Indium antimonide	10,600	2500	NLT	[20]
Indium antimonide	10,600	5600–11,000	ZS	[20]
Indium antimonide	9600	4300–8500	ZS	[22]
Indium phosphide (bulk)	1064	~90	ZS	[19]
Indium phosphide (7 nm crystals in porous Vycor glass)	1064	~9	ZS	[19]
Mercury cadmium telluride (Hg _{0.78} Cd _{0.22} Te)	10,600	14,000	NLT	[30]
Silicon	1318	21 ± 0.6	LC	[17]
Silicon (100 K)	1064	1.5	NLT	[28]
Silicon (20 K)	1064	1.9	NLT	[28]
Silicon (porous)	665	2700	ZS	[21]
Silicon (nanocluster film)	9000	7450	ZS	[96]
	9200	1.66 × 10 ⁴		
	9400	597		
	9600	3400		
Silver gallium selenide	1064	1.4	NLT	[29]
Sr ₂ CuO ₃ ^b ($E \parallel b$)	950 (ex), 590 (pr)	150	NLT	[94]
Zinc oxide	705	1.3 ± 0.4	NLT	[23]
Zinc oxide	532	5.0	NLT	[25]
Zinc selenide	1270	<0.005	ZS	[16]
Zinc selenide	780	3.5	ZS	[16]
Zinc selenide	705	5 ± 1	NLT	[23]

(continued)

Table 2 Continued

Material	λ (nm)	β (10^{-9} cm/W)	γ (10^{-18} cm 3 /W 2)	Method ^a	Ref.
Zinc selenide	610	2.4		ZS	[16]
Zinc selenide	532	5.8		ZS	[15, 31]
Zinc sulfide	1270	<0.003		ZS	[16]
Zinc sulfide	780	<0.02		ZS	[16]
Zinc sulfide	610	1.0		ZS	[16]
Zinc sulfide	532	3.4		ZS	[32]
Zinc sulfide ^b	480	5.9		NLT ^c	[93]
	500	4.7			
	532	2.5			
	570	1.0			
	580	0.2			
Zinc telluride	600	0.1		ZS	[18]
	1064	4.2			

^aTBC, two-beam coupling; LC, laser calorimetry; NLT, nonlinear transmission; ZS, Z-scan; THZS, top-hat Z-scan.^bNondegenerate.^cWhite light probe.

Table 3 Nonlinear Absorption Coefficients for Selected Organic Materials

Material	λ (nm)	β (10^{-9} cm/W)	γ (10^{-18} cm 3 /W 2)	Method ^a	Ref.
2,5-Benzothiazole 3,4-didecyloxy thiophene in tetrahydrofuran (0.18 M)	1064		2.7	NLT	[33]
Dialkyl-amino-nitrostilbene (DANS) side-chain polymer	1064	2.8		ZS	[34]
Dialkyl-amino-nitrostilbene (DANS) side-chain polymer	920	5.5		ZS	[34]
Poly(4,6-deadiyne-1, 10-diol bis{(<i>n</i> -urethane)} [poly(3BCMU waveguide)]	1525	<0.02		NLT	[35]
Poly(4,6-deadiyne-1, 10-diol bis{[(<i>n</i> -butoxycarbonyl)methyl]-urethane}) poly(3BCMU waveguide)	1064	1.1 ± 0.4	-0.24 ± 0.06	NLT	[35]
Poly(4,6-deadiyne-1, 10-diol bis{[(<i>n</i> -butoxycarbonyl)methyl]-urethane}) [poly(3BCMU waveguide)]	800	24 ± 5		NLT	[35]
Poly-[2,4 hexadiyne-1,6 diol-bis-(<i>p</i> -toluene sulfonate)]	720	200		NLT	[97]
	800	390			
	900	270			
	910	560			
	1064	80			
Poly(<i>p</i> -phenylenevinylene) ($\lambda_{\max} \sim 355$ –460 nm) ^b	800	~11–80		NLT	[36]
PSTF66 ^c	1630	1.2		NLT	[37]
PSTF66 ^c	1590	0.8		NLT	[37]
PSTF66 ^c	1550	0.8		NLT	[37]
PSTF66 ^c	1510	1.2		NLT	[37]
PSTF66 ^c	1480	2.4		NLT	[37]
<i>p</i> -toluene sulfonate	1320	20 ± 4	5.2 ± 0.3	ZS	[38]
<i>p</i> -toluene sulfonate	1064		-5 ± 1	ZS	[39]
Trans-4-[<i>p</i> -(<i>N</i> -ethyl- <i>N</i> -hydroxylethylamino)styrl]- <i>N</i> -methylpyridinium tetraphenylborate-doped epoxy (0.004 mole/liter)	1064	6		NLT	[79]

^a NLT, Nonlinear transmission; ZS, Z-scan.^b β varies with λ_{\max} .^c 66 wt-% symmetrically substituted tri-azo dye in partially fluorinated alkyl backbone main chain polymer. For details of chemical structure and waveguide fabrication, see Ref. [40].

Note that in some cases the three-photon absorption coefficient is negative. This implies that the two-photon transition in these materials is saturating at higher intensities.

Large nonlinear absorption coefficients can again be of benefit for some applications. Organic materials are being examined also for a potential role in optical limiting.

IV. FREQUENCY CONVERSION MATERIALS

Two-photon absorption can be detrimental in second order nonlinear frequency conversion processes. It not only serves as a loss mechanism but can also be a heat source producing beam distortion by thermal lensing. Two-photon absorption coefficients for some selected frequency conversion materials are given in Table 4. Apparently, not much data are available yet for newer organic materials.

Table 4 Nonlinear Absorption Coefficients for Selected Second Order Nonlinear Frequency Conversion Materials

Material	Abbreviation	λ (nm)	β (10^{-12} cm/W)	Ref.
Ammonium dihydrogen arsenate	ADA	355	35	[4]
Ammonium dihydrogen arsenate	ADP	355	6.8	[4]
Ammonium dihydrogen arsenate	ADP	308	230	[41]
Ammonium dihydrogen arsenate	ADP	266	240	[4]
Ammonium dihydrogen arsenate	ADP	266	60	[42]
Ammonium dihydrogen arsenate	ADP	266	110	[42]
Cesium dihydrogen arsenate	CDA	355	28	[4]
Lithium iodate		532	30	[44]
Lithium niobate		532	150	[4]
Potassium dideuterium phosphate	KD*P	355	5.4	[4]
Potassium dideuterium phosphate	KD*P	266	20	[42]
Potassium dideuterium phosphate	KD*P	266	27	[43]
Potassium dihydrogen arsenate	KDA	355	48	[4]
Potassium dihydrogen phosphate	KDP	355	5.9	[4]
Potassium dihydrogen phosphate	KDP	266	270	[4]
Potassium titanyl phosphate	KDP	532	100	[45]
Prousite (Ag_3AsS_3)		1064	20,000	[46]
Quartz($\alpha\text{-SiO}_2$)		266	45	[4]
Rubidium dihydrogen arsenate	RDA	355	50	[4]
Rubidium dihydrogen arsenate	RDP	355	5.9	[4]

Table 5 Two-Photon Absorption Cross-Sections for Selected Organic Materials

Material	Solvent	λ (nm)	σ_2 (10 ⁻⁵⁰ cm ⁴ ·s/ photon-molecule)	(10 ⁻³⁰ cm ⁴ /W)	σ_2	ZS	Method ^a	Ref.
α,β -unsaturated ketone derivative (R = NO ₂) (R = CN)	toluene	532		5880				[103]
Benzene	(neat)	370	2.5	1040			TWM	[47]
Benzene	(neat)	532	0.00025				TPF	[48]
Bis[4-(N-dipropylamino)phenyl]] squarylium	1,2-dichloroethane	770	108				NLT	[99]
Canthaxanthin	tetrahydrofuran	620	86,000 ^b				OKE	[52]
Carbon disulfide	(neat)	694	0.5				NLT	[49]
Carbon disulfide	(neat)	694	0.26				NLT	[50]
Carbon tetrachloride	(neat)	525	<0.014				TWM	[51]
1-Chloronaphthalene	(neat)	476	5.0				NLT	[53,54]
Cyclohexane	(neat)	633	1.9				TWM	[55]
Didecyloxy-substituted <i>p</i> -polyphenyl heptamer	tetrahydrofuran	602	45 ^c				DFWM	[56]
(7-5-(7-diphenylamino)- 9,9-didecyfluoren-2-yl)-3- (7-(diphenylamino)-9,9-didecyfluoren- 3-yl)(2,4,6)	tetrahydrofuran	790		8.5 × 10 ⁹			NLT	[104]
4,4'-bis(diphenylamino)stilbene (DPAS)	dichloromethane	690	325				TPF	[98]
DPAS dendrimer (5 stilbenes)	dichloromethane	705	2800				TPF	[98]
DPAS dendrimer (13 stilbenes)	dichloromethane	714	4500				TPF	[98]
DPAS dendrimer (29 stilbenes)	dichloromethane	713	1.1 × 10 ⁴				TPF	[98]

(continued)

Table 5 Continued

Material	Solvent	λ (nm)	σ_2 (10^{-50} cm 4 -s/ photon-molecule)	$(10^{-30})\sigma_2$ cm 4 /W)	Method ^a	Ref.
Diphenylbutadiene	chloroform	532	40 ± 8		DFWM	[57]
Diphenylbutadiene	chloroform (molten)	532	34 ± 12		NLT	[57]
Diphenylbutadiene	carbontetrachloride	600	38 ± 8		ZS	[58]
Diphenylbutadiene	benzene	608	30		PTL	[59]
Diphenylbutadiene	cyclohexane	708	14.4		TWM	[60]
Diphenylbutadiene	benzene	608	1.0		TPF	[61]
Diphenylhexatriene	benzene	608	43.3		TWM	[60]
Diphenyloctatetraene	benzene	608	61.0		TWM	[60]
Fluorescein	methanol (neat)	1064	0.014 ± 0.003		HRS	[100]
Hexatriene	cyclohexane	476	2.0		PTL	[62]
2-(2'-hydroxyphenyl)benzoxazole	cyclohexane	1064			ZS	[101]
Hypocrellin A	toluene (neat)	532			ZS	[102]
Mesitylene	toluene (neat)	532	0.096		TPF	[48]
Methylene iodide	toluene	800	2.1		NLT	[63]
N,N-Diphenyl-7-[2-(4-pyridinyl) ethenyl]-9,9-di- <i>n</i> -decyl-9H-fluorene-2-amine			2.6×10^8		NLT	[104]
	ethanol	750	5.2×10^8			
	hexane	790	3.1×10^9			
	tetrahydrofuran	790	1.5×10^9			
	carbontetrachloride (neat)	606	2.7×10^9			
Naphthalene			0.4		PTL	[59]
Nitrobenzene			3.1 × 10 ⁹		TWM	[51]
Phenyl compound I ^d			1.5 × 10 ⁹		NLT	[78]
Phenyl compound II ^e			2.7 × 10 ⁹		NLT	[78]

Rhodamine 6G	acidic methanol	694	180	NLT	[64]	
Rhodamine 6G	Methanol	1064	2.0 ± 0.4	HRS	[100]	
Rhodamine B	acidic methanol	694	120	NLT	[64]	
Rhodamine B	Methanol	1064	1.5 ± 0.3	HRS	[100]	
<i>trans</i> -Stilbene	Chloroform	694	80	NLT	[65]	
Stilbene	Cyclohexane	514	12.1	TWM	[60]	
Thiophene Compound I ^f	Tetrahydrofuran	602	850	NLT	[78]	
Thiophene Compound II ^g	Tetrahydrofuran	602	1100	NLT	[78]	
Toluene	(neat)	532	0.0036	TPF	[48]	
Trans-4-[<i>p</i> -(<i>N</i> -ethyl- <i>N</i> -hydroxylethylamino)styryl]- <i>N</i> -methylpyridinium tetraphenylborate	epoxy (EPO-TEX301)	1064	47,000	NLT	[79]	
Tris(3-(7-benzothiazol-2-yl)-9,9-diethylfluoren-2-yl)amine	tetrahydrofuran	790	3700	5.5 × 10 ⁹	NLT	[104]
<i>m</i> -Xylene	(neat)	532	0.028	TPF	[48]	
<i>o</i> -Xylene	(neat)	532	0.035	TPF	[48]	
<i>p</i> -Xylene	(neat)	532	0.096	TPF	[48]	

^aDFWM, degenerate four-wave mixing; HRS, hyper-Rayleigh scattering; NLT, nonlinear transmission. OKE, optical Kerr effect. PTL, Photothermal lensing; TPF, two-photon fluorescence; TWM, Three-wave mixing; ZS, Z-scan.

^b4.2 × 10⁻²⁵ cm⁴ s erg² [56].

^cComputed from imaginary part of second hyperpolarizability, Im(γ) = 2.1 × 10⁻³¹ esu [52].

^d2^{2''},5^{2''}-diidocyloxy-1,1';4^{1''};4^{2''},1^{3''},4^{4''},1^{5''}-pentaphenyl.

^e2^{2''},5^{2''}-diidocyloxy-1,1';4^{1''};4^{2''},1^{3''},4^{4''},1^{5''},4^{6''},1^{7''}-septiphenyl.

^f3,4 bis(idocyloxy)-2,5-bis(benzothiazol-2-yl)thiophene.

^g3-(thio-2,6-dimethylphenyl)-2,5-bis(benzothiazol-2-yl) thiophene.

Table 6 Photophysical Data for Some Selected Nonlinear Absorber Materials (Reverse Saturable Absorption)

Material	Solvent	$\lambda(\text{nm})$	σ_1^{a} (10^{-18} cm^2)	σ_1^{b} (10^{-18} cm^2)	ϕ_T^{c}	$\frac{\phi_T \sigma_2^{\text{d}}}{(10^{-18} \text{ cm}^2)}$	$\sigma_{\text{eff}}^{\text{e}}$ (10^{-18} cm^2)	$\phi_T \sigma_2 / \sigma_0^{\text{e}}$	$\sigma_{\text{eff}} / \sigma_0^{\text{e}}$	k_{ic}^{f} (10^{-9} s^{-1})	k_f^{g} (10^{-9} s^{-1})	Ref.
Aluminum phthalocyanine	toluene	532	~2.3		0.35	~18 ⁱ		~7.8	~ 10^{-16}^j	0.051	0.094	[66]
Asymmetric penta-azadentate porphyrin-like metal complexes (APPC)												[109]
(I) $(\text{OCH}_3)_6\text{C}_6\text{H}_3\text{-APPC})\text{Cd}^{\text{II}}\text{Cl}$	methanol											
(II) $(\text{CO}_2\text{NaC}_6\text{H}_3\text{-APPC})\text{Cd}^{\text{II}}\text{Cl}$	methanol											
(III) $(\text{C}_6\text{H}_4\text{-APPC})\text{Cd}^{\text{II}}\text{Cl}$	methanol											
(IV) $(\text{C}_6\text{H}_3\text{-APPC})\text{Cd}^{\text{II}}\text{Cl}$	methanol											
(V) $(\text{NO}_2\text{C}_6\text{H}_3\text{-APPC})\text{Cd}^{\text{II}}\text{Cl}$	methanol											
(VI) $(\text{NC})_2\text{C}_2\text{-APPC})\text{Cd}^{\text{II}}\text{Cl}$	chloroform											
(VII) $(\text{C}_10\text{H}_6\text{-APPC})\text{Cd}^{\text{II}}\text{Cl}$	methanol											
Bis[4-(N-ethyl-N-octadecylamino)-2-hydroxyphenyl] squarine	Dichloromethane	476	<29	210								[67]
Bis[(4-(phenylethynyl)phenyl)ethynyl] bis(triethylphosphine)platinum (II)	1,2-dichloroethane	600						220				[105]
Buckminsterfullerene, C ₆₀	toluene	532	3.1	16	~1	95				3.1	440 ^k	[68]
Buckminsterfullerene, C ₆₀	benzene	694	0.060								650 ^k	[69]
Buckminsterfullerene, C ₆₀	chlorobenzene	694	0.032								2100 ^k	[69]
Buckminsterfullerene, C ₆₀	1,2-dichlorobenzene	694	0.024									[69]
Buckminsterfullerene, C ₆₀	ethylbenzene	694	0.048								59.2 ^k	[69]
Buckminsterfullerene, C ₆₀	nitrobenzene	694	0.049								3.9 ^k	[69]
Buckminsterfullerene, C ₆₀	Pyridine	694	0.162								2.1 ^k	[69]
Buckminsterfullerene, C ₆₀	toluene	694	0.016								6.5 ^k	[69]
Buckminsterfullerene, C ₆₀	<i>o</i> -xylene	694	0.087								42.1 ^k	[69]

Buckminsterfullerene, C ₆₀	<i>m</i> -xylene	694	0.092	48.1 ^k	520 ^k
Buckminsterfullerene, C ₆₀	<i>p</i> -xylene	694	0.076	42.7 ^k	560 ^k
C ₆₀ chromium derivative	dichloro-methane	532	7.5	35	[69]
Cadmium texaphyrin	acetonitrile	532	13	~13–100	[69]
Chloroaluminum phthalocyanine	ethanol	532	2.2	23	[108]
Chloroaluminum phthalocyanine	methanol	532	1.5	23	[110]
Cubane cluster I (<i>n</i> -Bu ₄ N) ₃	acetonitrile or acetone	532	0.44	footnote ^l	[72]
[WCu ₃ Br ₄ S ₄] ⁺	acetonitrile or acetone	532	1.4	footnote ^l	[72]
Cubane cluster II (<i>n</i> -Bu ₄ N) ₃	acetonitrile or acetone	532	18	footnote ^l	[72]
[WAg ₃ Br ₄ S ₄] ⁺	acetonitrile or acetone	532	4.6	footnote ^l	[72]
Cubane cluster III (<i>n</i> -Bu ₄ N) ₃	acetonitrile or acetone	532	8	~8 ^m	[73,77]
[MoAg ₃ Br ₄ S ₄] ⁺	acetonitrile or acetone	532	4.1	~1.9 ^m	0.36
Cubane cluster IV (<i>n</i> -Bu ₄ N) ₃	methylene chloride	532	8	0.04	8.3
Cyclopentadienyliron carbonyl tetramer, King's complex					
[C ₅ H ₅]Fe(CO) ₄	toluene	532	~2.3	0.51	~10.9
Gallium phthalocyanine ^b	toluene	532	2.3	~25 ⁱ	~10–16 ^j
Germanium phthalocyanine ^a	methanol	523	12 ± 1	30 384 ± 40	8.3 ~380°
1,1',3,3',3'-Hexamethylindodicarbocyanine iodide		532	25	19 ≤1	~10–18 ^j ~30°
1,1',3,3',3'-hexamethylindodicarbocyanine iodide		532	~2.3	0.88	~19.1
Indium phthalocyanine ^b	toluene	532	1.4	~44 ^j	~10–16 ^j
Lead tetra (t-butyl) phthalocyanine		532	42	30	21
(Me ₄ N) ₂ [Cddmmt](Sph) ₂] ⁺	acetone	532	18	33	~10–18 ^j
Polymethine dyes	ethanol	532	40	1.8	2.9
PD1		30	150 ± 2	0.40	0.23
PD2		7	600 ± 50	5.0	1.25
PD3				107	3.3

(continued)

Table 6 Continued

Material	Solvent	$\lambda(\text{nm})$	σ_0^{a} (10^{-18} cm^2)	σ_1^{b} (10^{-18} cm^2)	ϕ_T^{c}	$\phi_T \sigma_2^{\text{d}}$ (10^{-18} cm^2) (10^{-18} cm^2)	$\sigma_{\text{eff}}^{\text{e}}$ (10^{-18} cm^2)	$\phi_T \sigma_2 / \sigma_0$	$\sigma_{\text{eff}} / \sigma_0^{\text{e}}$	$k_{\text{isc}}^{\text{f}}$ (10^9 s^{-1})	k_{f}^{g} (10^9 s^{-1})	Ref.
PD4		32	240 ± 3							3.3		
PD5		7	55 ± 6							33		
Silicon naphthalocyanine ^p	toluene	532	2.8	39	0.20	18	6.4			0.063	0.25	[71,74]
Silicon phthalocyanine ^a	toluene	532	2.4	30	0.35	32	13.3	$\sim 10\text{-}18^j$	0.078	0.14	[66,74]	
Tetrabenzporphyrine	tertahydrofuran	532	8.0				23.9 ^q	$\sim 10\text{-}18^j$	30^k		[76]	
Tin phthalocyanine ⁿ	toluene	532	2.1	22	0.62	42	20	$\sim 10\text{-}18^j$	0.31	0.19	[66,74]	

^a Ground state absorption cross-section.^b Excited singlet state absorption cross-section.^c Triplet state quantum yield.^d Effective excited triple state absorption cross-section.^e Effective excited state; absorption cross-section is some combination of ground and excited singlet and triplet cross-sections, depending on laser pulse width.^f Intersystem crossing rate.^g Fluorescence rate; total excited singlet relaxation rate is $k_{\text{isc}} + k_f$.^h [tri-(*n*-hexyl)siloxy] metal phthalocyanine.ⁱ Based on a typical value of $\sigma_2 \sim 50 \times 10^{-18} \text{ cm}^2$ [66].^j Lower bounds, increasing as the metal becomes heavier [66]; pulse width = 8 ns.^k Pulse width = 4.4 ns.^l I, $\alpha_T \sigma_1 \sigma_2 / k_f = 1.0 \times 10^{-35} \text{ cm}^4 - \text{ns}$; II, $\alpha_T \sigma_1 \sigma_2 / k_f = 8.5 \times 10^{-35} \text{ cm}^4 - \text{ns}$; III, $\alpha_T \sigma_1 \sigma_2 / k_f = 9.6 \times 10^{-35} \text{ cm}^4 - \text{ns}$; IV, $\alpha_T \sigma_1 \sigma_2 / k_f = 10.0 \times 10^{-35} \text{ cm}^4 - \text{ns}$; model values, assuming the lowest triplet state is populated primarily through an ionization-recombination process, where α_T = probability of recombination in triplet state and σ_1 = ionization cross-section; effective excited state absorption coefficient displays a cubic dependence on fluence and is proportional to $\alpha_T \sigma_1 \sigma_2 / k_f$.^m Pulse width = 25 ps.ⁿ bis[tri-(*n*-hexyl)siloxy] metal phthalocyanine.^o Pulse width = 1.5 ns.^p bis[tri-(*n*-hexyl)siloxy] metal phthalocyanine.^q Pulse width = 9 ns.

V. TWO-PHOTON ABSORPTION CROSS-SECTION DATA

The two-photon absorption coefficient of a material depends on the molecular concentration. Often, measurements are performed on dilute solutions of materials, and the solvent can also contribute to the two-photon induced loss. Under these conditions, it is more common to report the inherent two-photon absorption cross-section of the material, which is a molecular property.

Table 5 lists these cross-sections for several organic materials, including some common solvents. A variety of measurement methods are used, such as degenerate four-wave mixing, nonlinear transmission, optical Kerr effect, photothermal lensing, two-photon fluorescence (sometimes also called two-photon excitation), three-wave mixing, and Z-scan. All of these methods were discussed in Chapter 10.

VI. REVERSE SATURABLE ABSORPTION MATERIALS

Saturable absorption and reverse saturable absorption are topics treated in Chapter 9. Several materials that serve as saturable two-level absorbers are listed in Chapter 8, Tables 2–4, 10, and 13. Other dyes exhibiting saturable absorption are discussed in the references of Chapter 9, Section VII.2.

Reverse saturable absorption materials (RSA) are currently under consideration for optical limiting applications. Therefore it is of interest to include data for some selected materials. Often, the properties of these materials may be solvent dependent, as most of the measurements are done on solutions. Table 6 lists photophysical data for several RSA materials.

In the literature, the absorption data are often given in terms of the molar extinction coefficient ϵ rather than in terms of the cross section σ . The physical units for ϵ are $M^{-1}\text{-cm}^{-1}$, where M = mole/liter. The conversion between these two parameters is given by

$$\sigma(\text{cm}^2) = \frac{(2.3 \times 10^3)\epsilon(\text{M}^{-1}\text{cm}^{-1})}{N_A}$$

where $N_A = 6.022 \times 10^{23}$ is Avogadro's number.

REFERENCES

1. W. L. Smith, Two-photon absorption in condensed media, *Handbook of Laser Science and Technology*, Vol. III Optical materials: Part 1 (M. J. Weber, ed), CRC Press, Boca Raton, FL, 1986, pp. 229–258.

2. E. W. Van Stryland and L. Chase, Inorganic materials, *Handbook of Laser Science and Technology*, Supplement 2: Optical materials (M. J. Weber, ed), CRC Press, Boca Raton, FL, 1995, pp. 299–328.
3. A. F. Garito and M. Kuzyk, Organic materials, *Handbook of Laser Science and Technology*, Supplement 2: Optical materials (M. J. Weber, ed), CRC Press, Boca Raton, FL, 1995, pp. 329–333.
4. P. Liu, W. L. Smith, H. Lotem, J. H. Bechtel, N. Bloembergen, and R. S. Adhav, Absolute two-photon absorption coefficients at 355 and 266 nm, *Phys. Rev. B* 17:4620 (1978).
5. Y. P. Kim and H. M. R. Hutchinson, Intensity-induced nonlinear effects in UV window materials, *Appl. Phys. B* 49:469 (1989).
6. P. Liu, R. Yen, and N. Bloembergen, Two-photon absorption coefficients in UV window and coating materials, *Appl. Opt.* 18:1015 (1979).
7. A. J. Taylor, R. B. Gibson, and J. P. Roberts, Two-photon absorption at 248 nm in ultraviolet window materials, *Opt. Lett.* 13:814 (1988).
8. J. I. Dadap, G. B. Focht, D. H. Reitze, and M. C. Downer, Two-photon absorption in diamond and its application to ultraviolet femtosecond pulse-width measurement, *Opt. Lett.* 16:499 (1991).
9. W. Blau and A. Penzkofer, Intensity detection of picosecond ruby laser pulses by two-photon absorption, *Opt. Commun.* 36:419 (1981).
10. R. DeSalvo, M. Sheik-Bahae, A. A. Said, D. J. Hagan, and E. W. Van Stryland, Z-scan measurements of the anisotropy of nonlinear refractive and absorption in crystals, *Opt. Lett.* 18:194 (1993).
11. S. Preuss and M. Stuke, Subpicosecond ultraviolet laser ablation of diamond: nonlinear properties at 248 nm and time-resolved characterization of ablation dynamics, *Appl. Phys. Lett.* 67:338 (1995).
12. P. Simon, H. Gerhardt, and S. Szatmari, Intensity-dependent loss properties of window materials at 248 nm, *Opt. Lett.* 14:1207 (1989).
13. K. Hata, M. Watanabe, and S. Watanabe, Nonlinear processes in UV optical materials at 248 nm, *Appl. Phys. B* 50:55 (1990).
14. Y. Watanabe, M. Ohnishi, and T. Tsuchiya, Measurement of nonlinear absorption and refraction in titanium dioxide single crystal by using a phase distortion method, *Appl. Phys. Lett.* 66:3431 (1995).
15. A. A. Said, M. Sheik-Bahae, D. J. Hagan, T. H. Wei, J. Wang, J. Young, and E. W. Van Stryland, Determination of bound-electronic and free-carrier nonlinearities in ZnSe, GaAs, CdTe, and ZnTe, *J. Opt. Soc. Am. B* 9:405 (1992).
16. T. D. Krauss and F. W. Wise, Femtosecond measurement of nonlinear absorption and refraction in CdS, ZnSe, and ZnS, *Appl. Phys. Lett.* 65:1739 (1994).
17. A. E. Stewart and M. Bass, Intensity-dependent absorption in semiconductors, *Appl. Phys. Lett.* 37:1040 (1980).
18. A. A. Said, M. Sheik-Bahae, D. J. Hagan, T. H. Wei, J. Wang, J. Young, and E. W. Van Stryland, Determination of bound-electronic and free-carrier nonlinearities in ZnSe, GaAs, CdTe, and ZnTe, *J. Opt. Soc. Am. B* 9:405 (1992).

19. M. D. Dvorak, B. L. Justus, D. K. Gaskill, and D. G. Hendershot, Nonlinear absorption and refraction of quantum confined InP nanocrystals grown in porous glass, *Appl. Phys. Lett.* 66:804 (1995).
20. M. Sheik-bahae, P. Mukherjee, and H. S. Kwok, Two-photon and three-photon absorption coefficients of InSb, *J. Opt. Soc. Am. B* 3:379 (1986).
21. F. Z. Henari, K. Morgenstern, W. J. Blau, V. A. Karavanskii, and V. S. Dneprovskii, Third-order optical nonlinearity and all-optical switching in porous silicon, *Appl. Phys. Lett.* 67:323 (1995).
22. A. E. Smith, R. G. McDuff, and N. R. Heckenberg, Nonlinear optical parameters for InSb at 10.6 and 9.6 μm with microsecond pulses, *J. Opt. Soc. Am. B* 12:393 (1995).
23. S. Rychnovsky, G. R. Allan, C. H. Venzke, and T. F. Boggess, Picosecond measurements of absorptive and refractive optical nonlinearities in GaP at 532 nm, *Opt. Lett.* 19:527 (1994).
24. J. U. Kang, A. Villeneuve, M. Sheik-Bahae, C. I. Stegeman, K. Al-hemyari, J. S. Aitchison, and C. N. Ironside, Limitation due to three-photon absorption on the useful spectral range for nonlinear optics in AlGaAs below half band gap, *Appl. Phys. Lett.* 65:147 (1994).
25. E. W. Van Stryland, H. Vanherzele, M. A. Woodall, M. J. Soileau, A. L. Smirl, S. Guha, and T. F. Boggess, Two-photon absorption, nonlinear refraction, and optical limiting in semiconductors, *Opt. Eng.* 24:613 (1985).
26. J. H. Bechtel and W. L. Smith, Two-photon absorption in semiconductors with picosecond laser pulses, *Phys. Rev. B* 13:3515 (1976).
27. G. Kobbe and C. Klingshrin, Quantitative investigation of the two-photon absorption of ruby-laser-light in various semiconductors, *Z. Phys. B* 37:9 (1980).
28. J. F. Reintjes and J. C. McGroddy, Indirect two-photon transitions in Si at 1.06 μm , *Phys. Rev. Lett.* 30:901 (1973).
29. A. Miller and G. S. Ash, Two-photon absorption and short pulse stimulated recombination in AgGaSe₂, *Opt. Commun.* 33:297 (1980).
30. A. Miller, A. Johnston, J. Dempsey, J. Smith, C. R. Pidgeon, and G. D. Holah, Two-photon absorption in InSb and Hg_{1-x}Cd_xTe, *J. Phys. C* 12:4839 (1979).
31. M. Sheik-Bahae, A. A. Said, T.-H. Wei, D. J. Hagan, and E. W. Van Stryland, Sensitive measurement of optical nonlinearities using a single beam, *IEEE J. Quant. Electron.* 26:760 (1990).
32. J. Wang, M. Sheik-Bahae, A. A. Said, D. J. Hagan, and E. W. Van Stryland, Time-resolved Z-scan measurements of optical nonlinearities, *J. Opt. Soc. Am. B* 11:1009 (1994).
33. G. S. He, J. D. Bhawalkar, P. N. Prasad, and B. A. Reinhardt, Three-photon-absorption-induced fluorescence and optical limiting effects in an organic compound, *Opt. Lett.* 20:1524 (1995).
34. M. Cha, W. E. Torruellas, G. I. Stegeman, W. H. G. Horsthuis, G. R. Mohlmann, and J. Meth, Two photon absorption of di-alkyl-amino-nitro-stilbene side chain polymer, *Appl. Phys. Lett.* 65:2648 (1994).
35. W. A. Pender, A. J. Boyle, P. Lambkin, W. J. Blau, K. Mazaheri, D. J. Westland, V. Skarda, and M. Sparpaglione, Nonlinear absorption in polydiacetylene waveguides, *Appl. Phys. Lett.* 66:786 (1995).

36. A. Samoc, M. Samoc, M. Woodruff, and B. Luther-Davies, Tuning the properties of poly(*p*-phenylenevinylene) for use in all-optical switching, *Opt. Lett.* 20:1241 (1995).
37. M. Asobe, I. Yokohama, T. Kaino, S. Tomaru, and T. Kurihara, Nonlinear absorption and refraction in an organic dye functionalized main chain polymer waveguide in the 1.5 μm wavelength region, *Appl. Phys. Lett.* 67:891 (1995).
38. D. Y. Kim, B. L. Lawrence, W. E. Torruellas, G. I. Stegeman, G. Baker, and J. Meth, Assessment of single crystal *p*-toluene sulfonate as an all-optical switching material at 1.3 μm , *Appl. Phys. Lett.* 65:1742 (1994).
39. B. L. Lawrence, M. Cha, W. E. Torruellas, G. I. Stegeman, S. Etamad, G. Baker, and F. Kajzar, Measurement of the complex nonlinear refractive index of single crystal *p*-toluene sulfonate at 1064 nm, *Appl. Phys. Lett.* 64:2773 (1994).
40. T. Kaino, T. Kurihara, and S. Tomaru, Molecular design of nonlinear optical polymeric materials for switching device applications, *Mol. Cryst. Liq. Cryst.* 255:177 (1994).
41. Y. P. Kim and H. M. R. Hutchinson, Intensity-induced nonlinear effects in UV window materials, *Appl. Phys. B* 49:469 (1989).
42. J. Reintjes and R. C. Eckardt, Efficient harmonic generation from 532 to 266 nm in ADP and KD*P, *Appl. Phys. Lett.* 30:91 (1977).
43. J. Reintjes and R. C. Eckardt, Two-photon absorption in ADP and KD*P at 266.1 nm, *IEEE J. Quant. Electron. QE-13:791* (1977).
44. N. M. Bityurin, V. I. Bredikhin, and V. N. Genkin, Nonlinear optical absorption and energy structure of LiNbO₃ and α -LiIO₃ crystals, *Sov. J. Quant. Electron.* 8:1377 (1978).
45. R. DeSalvo, D. J. Hagan, M. Sheik-Bahae, G. Stegeman, and E. W. Van Stryland, Self-focusing and self-defocusing by cascaded second-order effects in KTP, *Opt. Lett.* 17:28 (1992).
46. D. C. Hanna and A. J. Turner, Nonlinear absorption measurements in proustite (Ag₃AsS₃) and CdSe, *Opt. Quant. Electron.* 8:213 (1976).
47. A. F. Stewart and M. Bass, Intensity-dependent absorption in semiconductors, *Appl. Phys. Lett.* 37:1040 (1980).
48. C. H. Chen and M. P. McCann, Measurements of two-photon absorption cross sections for liquid benzene and methyl benzenes, *J. Chem. Phys.* 88:4671 (1988).
49. J. A. Giordmaine and J. A. Howe, Intensity-induced optical absorption cross section CS₂, *Phys. Rev. Lett.* 11:207 (1963).
50. P. D. Maker and R. W. Terhune, Study of optical effects due to an induced polarization third order in the electric field strength, *Phys. Rev.* 137:A801 (1965).
51. M. D. Levenson and N. Bloembergen, Dispersion of the nonlinear optical susceptibilities of organic liquids and solutions, *J. Chem. Phys.* 60:1323 (1974).
52. M. E. Orczyk, M. Samoc, J. Swiatkiewicz, M. Tomoaia-Cotisel, and P. N. Prasad, Optical heterodyning of the phase-tuned femtosecond optical Kerr gate signal for the determination of complex third-order susceptibilities, *Appl. Phys. Lett.* 60:2837 (1992).
53. K. B. Eisenthal, M. W. Dowley, and W. L. Peticolas, Two-photon spectrum of a liquid, *Phys. Rev. Lett.* 20:93 (1968).

54. P. R. Monson and W. M. McClain, Polarization dependence of the two-photon absorption of tumbling molecules with application to liquid 1-chloronaphthalene and benzene, *J. Chem. Phys.* 53:29 (1970).
55. H. Lotem and C. B. de Araujo, Absolute determination of the two-photon absorption coefficient relative to the inverse Raman cross section, *Phys. Rev. B* 16:1711 (1977).
56. M. Zhao, Y. Cui, M. Samoc, P. N. Prasad, M. R. Unroe, and B. A. Reinhardt, Influence of two-photon absorption on third-order nonlinear optical processes as studied by degenerate four-wave mixing: the study of soluble didecyloxy substituted polyphenyls, *J. Chem. Phys.* 95:3991 (1991).
57. R. L. Sutherland, E. Rea, L. V. Natarajan, T. Pottenger, and P. A. Fleitz, Two-photon absorption and second hyperpolarizability measurements in diphenylbutadiene by degenerate four-wave mixing, *J. Chem. Phys.* 98:2593 (1993).
58. P. A. Fleitz, R. S. Sutherland, and T. J. Bunning, Z-scan measurements on molten diphenylbutadiene in the isotropic liquid state, *Proc. Mat. Res. Soc.* 374:211 (1995).
59. H. W. Fang, T. L. Gustafson, and R. L. Swofford, Two-photon absorption photothermal spectrometry using a synchronously pumped picosecond dye laser. Thermal lensing spectra of naphthalene and diphenylbutadiene, *J. Chem. Phys.* 78:1663 (1983).
60. R. J. M. Anderson, G. R. Holtom, and W. M. McClain, Two-photon absorptivities of the all *trans* $\alpha\omega$ -diphenylpolyenes from stilbene to diphenyloctatetraene via three wave mixing, *J. Chem. Phys.* 70:4310 (1979).
61. R. L. Swofford and W. M. McClain, Two-photon absorption studies of diphenylbutadiene: the location of a 1A_g excited state, *J. Chem. Phys.* 59:5740 (1973).
62. A. J. Twarowski and D. S. Klier, A search for a low-lying excited 1A state in 1,3,5-bexatriene, *Chem. Phys. Lett.* 50:36 (1977).
63. A. Penzkofer and W. Falkenstein, Direct determination of the intensity of picosecond light pulses by two-photon absorption, *Opt. Commun.* 17:1 (1976).
64. P. Serber and A. Penzkofer, S_0-S_n two-photon absorption dynamics of rhodamine dyes, *Opt. Quant. Electron.* 18:281 (1986).
65. J. Kleinschmidt, S. Rentsch, W. Tottleben, and B. Wilhelmi, Measurement of strong nonlinear absorption in stilbene-chloroform solutions, explained by the superposition of two-photon absorption and one-photon absorption from the excited state, *Chem. Phys. Lett.* 24:133 (1974).
66. J. W. Perry, K. Mansour, S. R. Marder, K. J. Perry, D. Alvarez, Jr., and I. Choong, Enhanced reverse saturable absorption and optical limiting in heavy-atom-substituted phthalocyanines, *Opt. Lett.* 19:625 (1994).
67. Y. Z. Yu, R. F. Shi, A. F. Garito, and C. H. Grossman, Origin of negative $\Xi^{(3)}$ in squaraines: experimental observation of two-photon states, *Opt. Lett.* 19:786 (1994).
68. D. G. McLean, R. L. Sutherland, M. C. Brant, D. M. Brandelik, P. A. Fleitz, and T. Pottenger, Nonlinear absorption study of a C_{60} -toluene solution, *Opt. Lett.* 18:858 (1993).

69. D. G. McLean, D. M. Brandelik, M. C. Brant, R. L. Sutherland, and L. Frock, Solvent effects on C_{60} excited state cross sections, *Proc. Mat. Res. Soc.* 374:293 (1995).
70. J. Si, M. Yang, Y. Wang, L. Zhang, C. Li, D. Wang, S. Dong, and W. Sun, Nonlinear excited state absorption in cadmium texaphyrin solution, *Appl. Phys. Lett.* 64:3083 (1994).
71. T. H. Wei, D. J. Hagan, M. J. Sence, E. W. Van Stryland, J. W. Perry, and D. R. Coulter, Direct measurements of nonlinear absorption and refraction in solutions of phthalocyanines, *Appl. Phys. B* 54:46 (1992).
72. W. Ji, H. J. Du, S. H. Tang, and S. Shi, Nanosecond reverse saturable absorption in cubanlike transition-metal clusters, *J. Opt. Soc. Am. B* 12:876 (1995).
73. T. F. Boggess, G. R. Allan, S. J. Rychnovsky, D. R. Labergerie, C. H. Venzke, A. L. Smirl, L. W. Tutt, A. R. Kost, S. W. McCahon, and M. B. Klein, Picosecond investigations of optical limiting mechanisms in King's complex, *Opt. Eng.* 32:1063 (1993).
74. K. Mansour, D. Alvarez, Jr., K. J. Perry, I. Choong, S. R. Marder, and J. W. Perry, Dynamics of optical limiting in heavy-atom substituted phthalocyanines, *Proc. SPIE* 1853:132 (1993).
75. S. N. R. Swatton, K. R. Welford, S. J. Till, and J. R. Sambles, Nonlinear absorption of a carbocyanine dye 1,1'3,3,3',3'-hexamethylindotricarbocyanine iodide using a Z-scan technique, *Appl. Phys. Lett.* 66:1868 (1995).
76. G. L. Wood, M. J. Miller, and A. G. Mott, Investigation of tetrabenzporphyrin by the Z-scan technique, *Opt. Lett.* 20:973 (1995).
77. L. W. Tutt and T. F. Boggess, A review of optical limiting mechanisms and devices using organics, fullerenes, semiconductors and other materials, *Prog. Quant. Electron.* 17:299 (1993).
78. G. S. He, G. C. Xu, P. N. Prasad, B. A. Reinhardt, J. C. Bhatt, and A. G. Dillard, Two-photon absorption and optical-limiting properties of novel organic compounds, *Opt. Lett.* 20:435 (1995).
79. G. S. He, J. D. Bhawalkar, C. F. Zhao, and P. N. Prasad, Optical limiting effect in a two-photon absorption dye doped solid matrix, *Appl. Phys. Lett.* 67:2433 (1995).
80. K. Tanaka, Two-photon absorption spectrometry of As_2S_3 glass, *Appl. Phys. Lett.* 80:177 (2002).
81. G. S. Maciel, N. Rakov, C. B. de Araújo, A. A. Lipovskii, and D. K. Tagantsev, Optical limiting behavior of a glass-ceramic containing sodium niobate crystallites, *Appl. Phys. Lett.* 79:584 (2001).
82. W. F. Zhang, Y. B. Huang, M. S. Zhang, and Z. G. Liu, Nonlinear optical absorption in undoped and cerium-doped $BaTiO_3$ thin films using Z-scan technique, *Appl. Phys. Lett.* 76:1003 (2000).
83. A. D. Ludlow, H. M. Nelson, and S. D. Bergeson, Two-photon absorption in potassium niobate, *J. Opt. Soc. Am. B* 18:1813 (2001).
84. A. Dragomir, J. G. McInerney, D. N. Nikogosyan, and P. G. Kazansky, Two-photon absorption properties of commercial fused silica and germanosilicate glass at 264 nm, *Appl. Phys. Lett.* 80:1114 (2002).

85. K. S. Bindra, H. T. Bookey, A. K. Kar, B. S. Wherrett, X. Liu, and A. Jha, Nonlinear optical properties of chalcogenide glasses: Observation of multiphoton absorption, *Appl. Phys. Lett.* 79:1939 (2001).
86. Y. X. Jie, Y. N. Xiong, A. T. S. Wee, C. H. A. Huan, and W. Ji, Dynamics of optical nonlinearity of Ge nanocrystals in a silica matrix, *Appl. Phys. Lett.* 77:3926 (2000).
87. J.-K. Wang, T.-L. Chiu, C.-H. Chi, and C.-K. Sun, Nonlinear refraction and absorption measurements with chirped femtosecond laser pulses: experiments and simulations, *J. Opt. Soc. Am. B* 16:651 (1999).
88. C. H. Kwak, Y. L. Lee, and S. G. Kim, Analysis of asymmetric Z-scan measurement for large optical nonlinearities in an amorphous AS_2S_3 thin film, *J. Opt. Soc. Am. B* 16:600 (1999).
89. S. Smolorz and F. Wise, Time-resolved nonlinear refraction in femtosecond laser gain media, *Opt. Lett.* 23:1381 (1998).
90. Y. Z. Gu, W. F. Zhang, D. H. Gu, and F. X. Gan, Nonlinear response and optical limiting in $\text{SrBi}_2\text{Ta}_2\text{O}_9$ thin films, *Opt. Lett.* 26:1788 (2001).
91. J. M. Harbold, F.Ö. Ilday, F. W. Wise, J. S. Sanghera, V. Q. Nguyen, L. B. Shaw, and I. D. Aggarwal, Highly nonlinear As-S-Se glasses for all-optical switching, *Opt. Lett.* 27:119 (2002).
92. C.-K. Sun, J.-C. Liang, J.-C. Wang, F.-J. Kao, S. Keller, M. P. Mack, U. Mishra, and S. P. DenBaars, Two-photon absorption study of GaN, *Appl. Phys. Lett.* 76:439 (2000).
93. R. A. Negres, J. M. Hales, A. Kobyakov, D. J. Hagan, and E. W. Van Stryland, Two-photon spectrometry and analysis with a white-light continuum probe, *Opt. Lett.* 27:270 (2002).
94. M. Ashida, T. Ogasawara, Y. Tokura, S. Uchida, S. Mazumdar, and M. KuwataGonokami, One-dimensional cuprate as a nonlinear optical material for ultrafast all-optical switching, *Appl. Phys. Lett.* 78:2831 (2001).
95. A. Pačebutas, A. Stainionis, A. Krotkus, T. Suski, P. Perlin, and M. Leszczynski, Picosecond Z-scan measurements on bulk GaN crystals, *Appl. Phys. Lett.* 78:4118 (2001).
96. S. Vijayalakshmi, J. Sturmann, and H. Grebel, Linear and nonlinear properties of laser-ablated Si films in the 9.0–9.6- μm wavelength region, *J. Opt. Soc. Am. B* 16:1286 (1999).
97. A. K. Bhowmik and M. Thakur, Self-phase modulation in polydiacetylene single /crystal measured at 720–1064 nm, *Opt. Lett.* 26:902 (2001).
98. M. Drobizhev, A. Karotki, A. Rebane, and C. W. Spangler, Dendrimer molecules with record large two-photon absorption cross section, *Opt. Lett.* 26:1081 (2001).
99. M. Furuki, M. Tian, Y. Sato, L. S. Pu, S. Tatsuura, and S. Abe, Absorption bleaching of squarylium dye *J* aggregates via a two-photon excitation process, *Appl. Phys. Lett.* 79:708 (2001).
100. P. Kaatz and D. P. Shelton, Two-photon fluorescence cross-section measurements calibrated with hyper-Rayleigh scattering, *J. Opt. Soc. Am. B* 16:998 (1999).
101. X. Shang, G. Tang, G. Zhang, Y. Liu, W. Chen, B. Yang, and X. Zhang, Optical nonlinearities and transient dynamics of 2-(2'-hydroxyphenyl)benzoxazole studied

- by single-beam and time-resolved two-color Z-scan techniques, *J. Opt. Soc. Am. B* 15:854 (1998).
- 102. X. Shang, Y. Liu, G. Tang, G. Zhang, and W. Chen, Optical nonlinearities of hypocrellin A with the excitation of nanosecond pulses, *J. Opt. Soc. Am. B* 15:1502 (1998).
 - 103. J. Zhou, E. Y. B. Pun, and X. H. Zhang, Nonlinear optical refractive indices and absorption coefficients of $\alpha\beta$ -unsaturated ketone derivatives, *J. Opt. Soc. Am. B* 18:1456 (2001).
 - 104. S. Kirkpatrick, Air Force Wright Laboratory, Wright Patterson Air Force Base, Ohio (private communication, May 2002).
 - 105. T. J. McKay, J. Staromlynska, J. R. Davy, and J. A. Bolger, Cross sections for excited-state absorption in a Pt:ethynyl complex, *J. Opt. Soc. Am. B* 18:358 (2001).
 - 106. Z. Sun, M. Tong, H. Zeng, L. Ding, Z. Wang, J. Dai, G. Bian, and Z. Xu, Nanosecond reverse saturable absorption and optical limiting in $(Me_4N)_2[Cd(dmit)(Sph)_2]$, *J. Opt. Soc. Am. B* 18:1464 (2001).
 - 107. O. V. Przhonska, J. H. Lim, D. J. Hagan, E. W. Van Stryland, M. V. Bondar, and Y. Slominsky, Nonlinear light absorption of polymethine dyes in liquid and solid media, *J. Opt. Soc. Am. B* 15:802 (1998).
 - 108. Y. Song, G. Fang, Y. Wang, S. Liu, C. Li, L. Song, Y. Zhu, and Q. Hu, Excited-state absorption and optical-limiting properties of organometallic fullerene-C₆₀ derivatives, *Appl. Phys. Lett.* 74:332 (1999).
 - 109. W. Sun, C. C. Byeon, M. M. McKerns, C. M. Lawson, G. M. Gray, and D. Wang, Optical limiting performances of asymmetric pentaazadentate porphyrin-like cadmium complexes, *Appl. Phys. Lett.* 73:1167 (1998).
 - 110. T.-H. Wei, T.-H. Huang, and M.-S. Lin, Signs of nonlinear refraction in chloroaluminum phthalocyanine solution, *Appl. Phys. Lett.* 72:2505 (1998).
 - 111. R. Lepkowicz, A. Kobyakov, D. J. Hagan, and E. W. Van Stryland, Picosecond optical limiting in reverse saturable absorbers: a theoretical and experimental study, *J. Opt. Soc. Am. B* 19:94 (2002).

14

Stimulated Raman Scattering

Raman scattering is a two-photon process [1]. As illustrated in Fig. 1a, an incident photon is annihilated and a new photon of a different frequency is created. This implies that the scattering is inelastic, and the medium is left in a different energy state. When the scattered photon is lower in energy, or frequency, it is said to be Stokes shifted. The shift in frequency of the Stokes photon is related to a characteristic frequency of the medium. This is illustrated in Fig. 2a. Calling this characteristic material excitation frequency ω_v , the Stokes frequency is then $\omega_S = \omega_L - \omega_v$, where ω_L is the incident laser frequency. Thus, Raman (Stokes) scattering results in an excitation from the ground state of the medium to an excited state mediated by a two-photon inelastic scattering. The internal material excitation can involve the creation of an excited electronic state, an excited vibrational–rotational state, a lattice vibration, a spin flip in semiconductors, or electron waves in plasmas [2]. The phenomenon occurs in gases, liquids, solids, and plasmas.

If the material is already in an excited state (e.g., by thermal excitation), as illustrated in Fig. 2b, then the scattered photon can be higher in energy, or frequency, and is called an anti-Stokes photon. The probability of anti-Stokes scattering is smaller than that of Stokes scattering by a Boltzmann factor $\exp(-\hbar\omega_v/k_B T)$, where k_B is Boltzmann's constant and T is the temperature. Since typically $\hbar\omega_v \gg k_B T$, spontaneous Raman scattering is dominated by Stokes emission.

Stimulated Raman scattering (SRS) involves the incidence of both Stokes and laser photons on a medium, as illustrated in Fig. 1b. The result is the stimulation of an additional Stokes photon coherent with the incident Stokes photons. Thus the Stokes photon field experiences gain. As in spontaneous Raman scattering, SRS leaves the medium in an excited state.

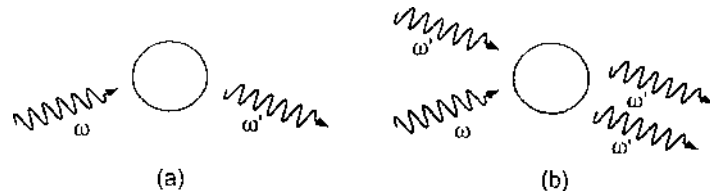


Figure 1 Schematic diagram of (a) spontaneous Raman scattering and (b) stimulated Raman scattering.

SRS is strictly a Stokes generation process. However, in practice, coherent anti-Stokes photons are also produced, sometimes in nearly equal amounts to the Stokes photons. This is in stark contrast to the spontaneous Raman scattering case. The anti-Stokes generation is not readily described in the photon picture, but it can be understood in terms of third order nonlinear optics as a four-wave mixing process.

SRS is of considerable scientific and technological significance. It is used in such diverse areas as spectroscopy and coherent frequency conversion. Other uses include signal amplification, beam combining, and beam cleanup (i.e., removal of phase as well as amplitude distortions in optical beams). In the sections that follow, some of the important formulas used in the description of SRS are given. The last section briefly describes some of the applications of SRS.

Several of the parameters that appear in formulas related to SRS are given in Table 1, including both SI and cgs units. Sometimes units are mixed, such as

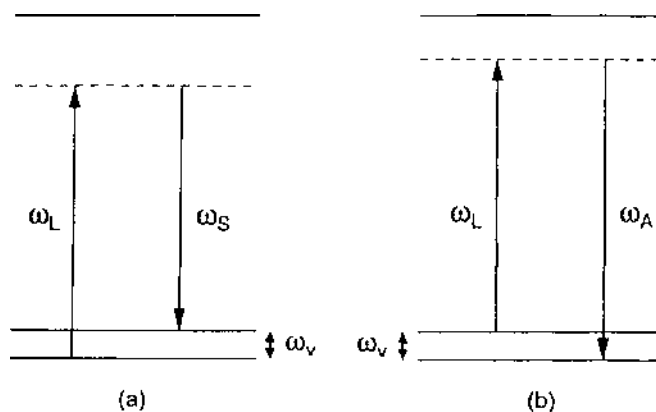


Figure 2 Energy level diagrams for (a) Stokes Raman scattering and (b) anti-Stokes Raman scattering.

Table 1 Physical Units of Important Physical Parameters Utilized in Formulas Related to Stimulated Raman Scattering

Physical parameter	SI	cgs
Differential Raman scattering cross-section	$[d\sigma/d\Omega] = \text{m}^2/\text{strad}$	$[d\sigma/d\Omega] = \text{cm}^2/\text{strad}$
Differential polarizability	$[\partial\alpha/\partial q] = \text{C}\cdot\text{m}/\text{V}$	$[\partial\alpha/\partial q] = \text{cm}^2$
Mass	$[m] = \text{kg}$	$[m] = \text{g}$
Boltzmann's constant	$[k_B] = \text{J/K}$	$[k_B] = \text{erg/K}$
Temperature	$[T] = \text{K}$	$[T] = \text{K}$
Molecular number density	$[N] = \text{m}^{-3}$	$[N] = \text{cm}^{-3}$
Third order polarization	$[P^{(3)}] = \text{C/m}^2$	$[P^{(3)}] = \text{sV/cm} = (\text{erg/cm}^3)^{1/2}$
Electric field amplitude	$[A] = \text{V/m}$	$[A] = \text{sV/cm} = (\text{erg/cm}^3)^{1/2}$
Third order Raman susceptibility	$[\chi_R^{(3)}] = \text{m}^2/\text{V}^2$	$[\chi_R^{(3)}] = \text{cm}^2/\text{sV}^2$ $= \text{cm}^3/\text{erg} = \text{esu}$
Raman gain coefficient	$[G(\omega_S)] = \text{m}^{-1}$	$[G(\omega_S)] = \text{cm}^{-1}$
Raman gain intensity factor	$[g_s] = \text{m/W}$	$[g_s] = \text{cm}\cdot\text{s/erg}$
Vacuum permittivity	$[\epsilon_0] = \text{F/m} = \text{C/V}\cdot\text{m}$	—
Distance, length	$[z] = [L] = \text{m}$	$[z] = [L] = \text{cm}$
Speed of light	$[c] = \text{m/s}$	$[c] = \text{cm/s}$
Wave vector	$[k] = \text{m}^{-1}$	$[k] = \text{cm}^{-1}$
Circular frequency	$[\omega] = \text{Hz} = \text{s}^{-1}$	$[\omega] = \text{Hz} = \text{s}^{-1}$
Raman line width	$[\Gamma] = \text{Hz} = \text{s}^{-1}$	$[\Gamma] = \text{Hz} = \text{s}^{-1}$
Planck's constant	$[\hbar] = [h/2\pi] = \text{J}\cdot\text{s}$	$[\hbar] = [h/2\pi] = \text{erg}\cdot\text{s}$
Intensity	$[I] = \text{W/m}^2$	$[I] = \text{erg/s}\cdot\text{cm}^2$
Power	$[\mathcal{P}] = \text{W}$	$[\mathcal{P}] = \text{erg/s}$

when the Raman gain intensity factor is quoted in cm/W (centimeters per watt). Table 2 gives conversion factors between parameters in SI and cgs or mixed units.

I. SPONTANEOUS RAMAN SCATTERING

The incoherent spontaneous Raman scattering from an incident laser beam is depicted schematically in Fig. 3. The transmitted laser radiation is attenuated by the conversion of laser photons to scattered photons. This attenuation is described in terms of the total Raman scattering cross-section defined by [3]

$$\frac{dI_L}{dz} = -\sigma_R N I_L \quad (1)$$

where I_L is the laser intensity, N is the number density of Raman scatterers

Table 2 Conversion Formulas Between the SI and cgs Systems of Units for Several Physical Parameters Utilized in Stimulated Raman Scattering

$\frac{d\sigma}{d\Omega}$	(SI) = $10^{-4} \frac{d\sigma}{d\Omega}$	(cgs)	
$\frac{\partial \alpha}{\partial q}$	(SI) = $(\frac{1}{3})^2 \times 10^{-13} \frac{\partial \alpha}{\partial q}$	(cgs)	
m	(SI) = $10^{-3} m$	(cgs)	
N	(SI) = $10^6 N$	(cgs)	
$P^{(3)}$	(SI) = $\frac{1}{3} \times 10^{-5} P^{(3)}$	(cgs)	
A	(SI) = $3 \times 10^4 A$	(cgs)	
$\chi_R^{(3)}$	(SI) = $\frac{4\pi}{3^2} \times 10^{-8} \chi_R^{(3)}$	(cgs)	
G	(SI) = $10^2 G$	(cgs)	
g_s	(SI) = $10^5 g_s$	(cgs)	
$g_s(\text{cm}/\text{W})$	= $10^2 g_s$	(SI) = $10^7 g_s$	(cgs)
L	(SI) = $10^{-2} L$	(cgs)	
c	(SI) = $10^{-2} c$	(cgs)	
k	(SI) = $10^2 k$	(cgs)	
I	(SI) = $10^{-3} I$	(cgs)	
$I(\text{W}/\text{cm}^2)$	= $10^{-4} I$	(SI) = $10^{-7} I$	(cgs)
\mathcal{P}	(SI) = $10^{-7} \mathcal{P}$	(cgs)	

(e.g., molecular density), and σ_R is the Raman scattering cross-section (m^2 or cm^2) for laser photons scattered into *all* Raman modes (ω, \mathbf{k}).

In the quantum mechanical picture, the laser and Stokes fields are described in the terms of the laser and Stokes photon numbers, m_L and m_S , respectively. The generation of Stokes photons is given by the relation [3]

$$\frac{dm_S}{dt} = \frac{c}{n} \frac{dm_S}{dz} \propto m_L(m_S + 1) \quad (2)$$

where c/n is the speed of light in the medium. The vacuum state is characterized by $m_S = 0$, and the unity term in Eq. (2) yields spontaneous Raman scattering. The spontaneous scattering regime is thus characterized by $m_S \ll 1$, and

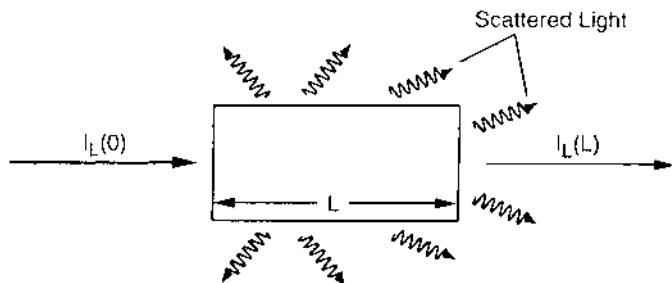


Figure 3 Incoherent Raman scattering and laser attenuation in a Raman active medium.

$m_L \approx$ constant over distances small compared to $(\sigma_R N)^{-1}$. Then, for scattering into a single Stokes mode, $m_S \propto m_L z$.

Experimentally, photon numbers can be related to optical power. The experimental geometry for measuring Stokes emission is illustrated in Fig. 4. The angles θ and ϕ represent the scattering direction from a volume element of the material of length δz . The measurement yields the Stokes power emitted in a small solid angle $\Delta\Omega$ and is given by [4]

$$\delta P_S = N \frac{d\sigma}{d\Omega}(\theta, \phi) \Delta\Omega \delta z P_L \quad (3)$$

The quantity $d\sigma/d\Omega$, which is a function of the angles θ and ϕ , is called the differential Raman scattering cross-section. It is measurable since the other quantities in Eq. (3) are either measurable or established by the experimental conditions. This quantity is then related to the total Raman cross-section by [4]

$$\sigma_R = \frac{\omega_L}{\omega_S} \int_{4\pi} \frac{d\sigma}{d\Omega}(\theta, \phi) d\Omega \quad (4)$$

For dipole scattering [4],

$$\frac{d\sigma}{d\Omega}(\theta, \phi) = \left(\frac{d\sigma}{d\Omega} \right)_{\theta=90^\circ} \sin^2 \theta \quad (5)$$

and the total cross-section is thus

$$\sigma_R = \frac{8\pi}{3} \frac{\omega_L}{\omega_S} \left(\frac{d\sigma}{d\Omega} \right)_{90^\circ} \quad (6)$$

The important physical quantity in SRS formulas is the differential scattering cross-section $d\sigma/d\Omega$

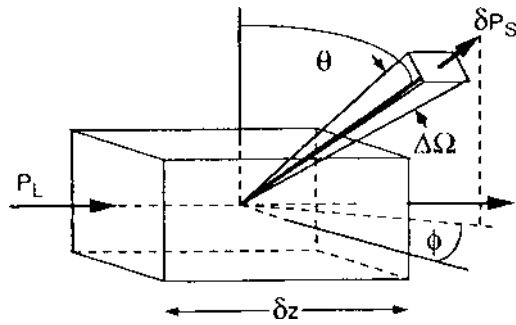


Figure 4 Raman scattering measurement geometry.

II. STOKES GAIN

When the Stokes photon number is large ($m_S \gg 1$), the unity term in Eq. (2) can be ignored. Thus if the laser photon number is approximately constant, m_S will experience exponential gain.

In the classical picture, the photon numbers relate to power (or intensity), and the Stokes intensity experiences gain as it propagates a distance z through the Raman gain medium:

$$I_S(z) = I_S(0)\exp[G(\omega_S)z] \quad (7)$$

The Raman gain coefficient $G(\omega_S)$ is given in Table 3, where it is related to the differential scattering cross-section. It is also seen to be proportional to the normalized Raman lineshape function $g(\omega_S)$, where $g(\omega_S) \sim T_2$ for $\omega_L - \omega_S \approx \omega_v$. T_2 is the relaxation time of the Raman mode of excitation [2]. The Raman gain coefficient can also be expressed in terms of the Raman gain intensity factor

Table 3 Formulas Related to Stimulated Raman Scattering

Quantum approach

$$\text{Raman gain coefficient} \quad G(\omega_S) = \frac{8\pi^3 c^2 N}{3n_S^2 \hbar \omega_S^3} \left(\frac{d\sigma}{d\Omega} \right)_{90^\circ} \{ 1 - \exp[\hbar(\omega_L - \omega_S)/k_B T] \} I_L g(\omega_S) \quad (\text{SI})$$

$$\text{Raman gain intensity factor} \quad g(\omega_S) = \frac{\Gamma}{[\omega_v - (\omega_L - \omega_S)]^2 + \Gamma^2}$$

$$g_S = \frac{G(\omega_S)}{I_L}$$

Nonlinear optics approach

$$\text{Raman susceptibility} \quad \chi_R^{(3)}(-\omega_S; \omega_L, -\omega_L, \omega_S) = \frac{N(\partial\alpha/\partial q)_0^2}{6\epsilon_0 m [\omega_v^2 - (\omega_L - \omega_S)^2 + i\Gamma(\omega_L - \omega_S)]} \quad (\text{SI})$$

$$\chi_R^{(3)}(-\omega_S; \omega_L, -\omega_L, \omega_S) = \frac{N(\partial\alpha/\partial q)_0^2}{6m [\omega_v^2 - (\omega_L - \omega_S)^2 + i\Gamma(\omega_L - \omega_S)]} \quad (\text{cgs})$$

$$\text{Raman gain coefficient} \quad G(\omega_S) = -6 \left(\frac{\omega_S}{n_S c} \right) \text{Im}[\chi_R^{(3)}(-\omega_S; \omega_L, -\omega_L, \omega_S)] |A_L|^2 \quad (\text{SI})$$

$$G(\omega_S) = -24\pi \left(\frac{\omega_S}{n_S c} \right) \text{Im}[\chi_R^{(3)}(-\omega_S; \omega_L, -\omega_L, \omega_S)] |A_L|^2 \quad (\text{cgs})$$

$$G(\omega_S) \simeq \frac{\omega_S N(\partial\alpha/\partial q)_0^2}{2\epsilon_0^2 mc^2 n_L n_S \omega_v} \frac{\Gamma/2}{[\omega_v - (\omega_L - \omega_S)]^2 + (\Gamma/2)^2} I_L \equiv g_S I_L \quad (\text{SI})$$

$$G(\omega_S) \simeq \frac{16\pi^2 \omega_S N(\partial\alpha/\partial q)_0^2}{mc^2 n_L n_S \omega_v} \frac{\Gamma/2}{[\omega_v - (\omega_L - \omega_S)]^2 + (\Gamma/2)^2} I_L \equiv g_S I_L \quad (\text{cgs})$$

$$\text{Stokes-pump coupling outputs} \quad I_S(L) = \frac{[I_S(0) + (\omega_S/\omega_L) I_L(0)] I_S(0) \exp(u)}{(\omega_S/\omega_L) I_L(0) + I_S(0) \exp(u)}$$

$$I_L(L) = \frac{[I_L(0) + (\omega_L/\omega_S) I_S(0)] I_L(0) \exp(-u)}{(\omega_L/\omega_S) I_S(0) + I_L(0) \exp(-u)}$$

$$u = [(\omega_L/\omega_S) I_S(0) + I_L(0)] g_S$$

g_S , where

$$g_S = \frac{G(\omega_S)}{I_L} \quad (8)$$

It is possible to relate SRS to third order nonlinear optics. As noted by Shen [1], the rate of Stokes photon generation, in the limit of large photon numbers, is related classically to the polarization through the energy theorem, i.e.,

$$\hbar\omega_S \frac{dm_S}{dt} \propto \text{Re}[(i\omega_S)\mathbf{E}_S \cdot \mathbf{P}_S^*] \propto m_L m_S \propto |\mathbf{E}_L|^2 |\mathbf{E}_S|^2 \quad (9)$$

The last relation implies that the Stokes polarization is third order in the field, i.e., $\mathbf{P}_S \propto |\mathbf{E}_L|^2 \mathbf{E}_S$. Thus a third order Raman susceptibility can be defined through

$$P_i^{(3)}(\omega_S) = 6\epsilon_0 \sum_{jkl} \chi_{ijkl}^{(3)}(-\omega_S; \omega_L, -\omega_L, \omega_S) E_j(\omega_L) E_k^*(\omega_L) E_l(\omega_S) \quad (10)$$

With the field amplitude written as $E = A \exp(i\mathbf{k} \cdot \mathbf{r})$, the form of Eq. (10) shows that the SRS process is automatically phase matched. The Raman gain coefficient is related to the imaginary part of the third order susceptibility, which can be seen through the relation given by Eq. (9).

The most common form of SRS is by molecular vibrational Raman scattering in a macroscopically isotropic medium. A simple one-dimensional molecular vibrator model has been developed to describe this phenomenon [5]. The central idea of the model is that the linear polarizability of the molecule changes as the molecule vibrates. To first order, the polarizability is related to a normal mode of vibration q by the relation

$$\alpha = \alpha_0 + \left(\frac{\partial \alpha}{\partial q} \right)_0 q \quad (11)$$

where α_0 is the ordinary polarizability, governing molecular absorption and index of refraction, typically in the infrared, and $(\partial \alpha / \partial q)_0$ represents the first term in a Taylor series expansion of the polarizability in terms of the displacement of the vibrator about its equilibrium position and is called the differential polarizability.

The physics of SRS can be understood in terms of the simple model. The normal mode q oscillates at the characteristic material excitation frequency ω_v (e.g., the vibrational frequency of the molecule). This modulation of the molecular polarizability, through Eq. (11), causes the molecule to radiate at the sideband frequency $\omega_S = \omega_L - \omega_v$ as well as at the incident laser frequency ω_L . The superposition of the waves at ω_L and ω_S produces a beat wave at $\omega_L - \omega_S$ that coherently drives the normal mode vibration. This reinforced molecular vibration then coherently amplifies the wave at ω_S . (Classically, there is also a sideband generated at $\omega_A = \omega_L + \omega_v$, which is the anti-Stokes frequency.)

However, the phase of this wave is π radians out of phase with the time derivative of the polarization driving it. By the energy theorem, it is thus attenuated, as discussed further below.)

The Raman susceptibility for Stokes emission is found by solving the equation of motion for the normal mode, assuming the presence of both Stokes and laser fields, and relating the polarization to the induced dipole moment [3,4]. The Raman susceptibility given by this model is shown in Table 3. A damping force term proportional to $-\Gamma(dq/dt)$, where Γ is the damping coefficient, has been assumed to be acting on the molecular vibrator. Γ is also known as the Raman line width, as it measures the full width at half maximum of the spectral response of the susceptibility.

As noted above, the Raman gain coefficient, as well as the Raman gain intensity factor, is proportional to the imaginary part of the Raman susceptibility. This is shown by the two relations for $G(\omega_S)$ given in Table 3. The last relation, which gives the Raman line shape explicitly, is approximately true and holds well in the typical case of a narrow Raman line such that $\Gamma \ll \omega_v$. (Note that the real part of the Raman susceptibility plays an important role in nonlinear refraction and leads to the Raman induced Kerr effect that was discussed in Chapter 6.)

The Raman susceptibility governs the interaction of the Stokes and laser waves and thus is strong for waves such that $\omega_L - \omega_S \approx \omega_v$. For this reason, it is called a resonant contribution to the third order susceptibility. It should be noted that for the third order interaction of waves in any medium there is always also a background nonresonant susceptibility, due to, for example, electron orbital distortion.

III. STOKES AMPLIFICATION

For efficient Stokes amplification, the depletion of the pump laser cannot be ignored. To describe the coupling between the Stokes and pump waves, the nonlinear polarizations for both waves, within the simple one-dimensional model, are introduced:

$$P_S^{(3)} = 6\epsilon_0\chi_R^{(3)}(-\omega_S; \omega_L, -\omega_L, \omega_S)|E_L|^2 E_S \quad (12)$$

$$P_L^{(3)} = 6\epsilon_0\chi_R^{(3)}(-\omega_L; \omega_S, -\omega_S, \omega_L)|E_S|^2 E_L \quad (13)$$

The Stokes and laser susceptibilities are related by [1]

$$\chi_R^{(3)}(-\omega_L; \omega_S, -\omega_S, \omega_L) = \chi_R^{(3)*}(-\omega_S; \omega_L, -\omega_L, \omega_S) \quad (14)$$

Note again by the form of the nonlinear polarizations that the Stokes–laser coupling is automatically phase matched.

In terms of the complex wave amplitudes $E = A \exp(i\mathbf{k} \cdot \mathbf{r})$, the coupling of the waves is described through the differential equations

$$\frac{dA_S}{dz} = i \frac{3\omega_S}{n_{SC}} \chi_R^{(3)}(\omega_S) |A_L|^2 A_S \quad (15)$$

$$\frac{dA_L}{dz} = i \frac{3\omega_L}{n_{LC}} \chi_R^{(3)}(\omega_L) |A_S|^2 A_L \quad (16)$$

Again, for $|A_L| \approx \text{constant}$, Eq. (15) predicts gain for $|A_S|$, with the gain factor proportional to $\text{Im}(\chi_R^{(3)})$. Note also that since the gain is a function of $|A_L|^2$, phase distortions in the laser beam are not directly transferred to the Stokes wave. This is the basis (partially) for amplifying a “clean” Stokes wave with a “dirty” pump wave. The phase of the Stokes wave will depend on the $\text{Re}(\chi_R^{(3)})$.

Differential equations describing the spatial evolution of the field modulus for both laser and Stokes beams follow directly from Eqs. (15) and (16):

$$\frac{n_S}{\omega_S} \frac{d|A_S|^2}{dz} = -\frac{6}{c} \text{Im}[\chi_R^{(3)}(\omega_S)] |A_L|^2 |A_S|^2 \quad (17)$$

$$\frac{n_L}{\omega_L} \frac{d|A_L|^2}{dz} = -\frac{6}{c} \text{Im}[\chi_R^{(3)}(\omega_L)] |A_S|^2 |A_L|^2 \quad (18)$$

Since $\text{Im}[\chi_R^{(3)}(\omega_S)] < 0$, it is obvious by Eqs. (14), (17), and (18) that the Stokes wave experiences gain at the expense of the pump, which experiences loss.

Equations (17) and (18) can be combined to show that the following invariant exists for Stokes–pump coupling:

$$\frac{I_S(z)}{\omega_S} + \frac{I_L(z)}{\omega_L} = \frac{I_S(0)}{\omega_S} + \frac{I_L(0)}{\omega_L} = \text{constant} \quad (19)$$

This equation states that the total number of photons in the two-photon scattering process remains a constant. It also allows the Stokes and laser outputs at the end of a medium of length L to be expressed in terms of the input intensities. These expressions are given in Table 3.

The behavior of the Stokes and pump intensities as functions of the Raman gain-length product is shown in Fig. 5 for three values of the input Stokes-to-pump photon flux ratio, $r = (\omega_L/\omega_S)I_S(0)/I_L(0)$. Note that the growth of the Stokes photon flux is initially exponential but begins to saturate as the pump is depleted. The saturation is more apparent when the input Stokes photon flux is larger.

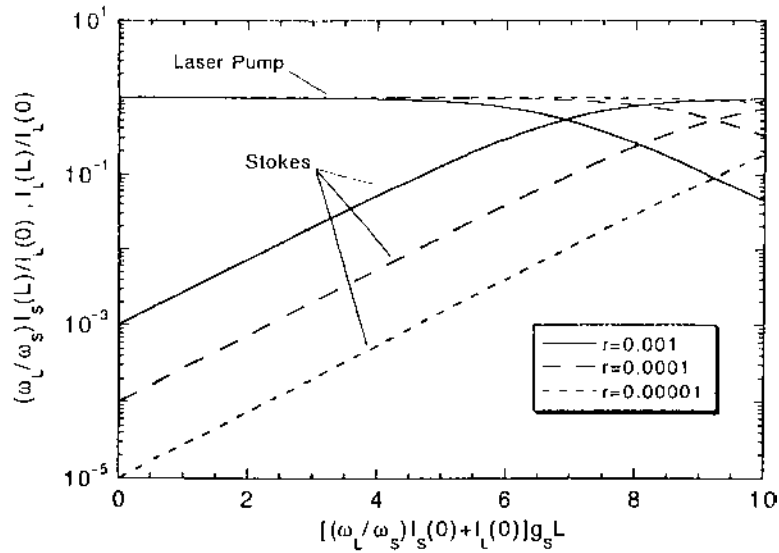


Figure 5 Laser and Stokes photon flux as functions of Raman gain at the output of a medium of thickness L .

In many cases, $I_L(0) \gg (\omega_L/\omega_S)I_S(0)$, particularly when the Stokes mode grows from quantum noise (i.e., spontaneous Raman scattering). Then, as $g_S I_L(0)L \rightarrow \infty$, $I_S(L) \rightarrow (\omega_S/\omega_L)I_L(0)$, i.e., pump photons are entirely converted to Stokes photons, with the energy difference showing up as material excitation. In reality, before this occurs, higher-order Stokes and anti-Stokes modes appear and drain off energy.

Since there is no phase matching condition imposed on Stokes amplification, Stokes generation from noise can occur in both the forward and backward directions along the pump beam. However, this symmetry is broken in some cases. For a broadband-pump source of line width Γ_L , where $\Gamma_L \sim \Gamma$, the Raman line width, the forward Stokes gain is proportional to Γ^{-1} , while the backward gain is proportional to $(\Gamma_L + \Gamma)^{-1}$ [1]. Thus the forward gain can be much stronger. Backward SRS is generally not observed when picosecond laser pump pulses are used, since this pulse duration limits the effective interaction length for backward Stokes amplification [2].

The Stokes photon can serve as an input to generate a new photon (by Raman scattering) at frequency $\omega_S - \omega_v = \omega_L - 2\omega_v$. This is called the second Stokes wave. As the incident pump power is increased, the first Stokes wave grows from noise and then saturates as the pump is depleted. The second Stokes

wave is then generated and eventually saturates as the first Stokes wave is depleted. This process continues to higher Stokes generation as the pump power is continually increased. This process has been demonstrated experimentally using picosecond pulses to avoid backward Stokes generation. The Gaussian nature of the beams causes a gradual depletion of the pump as well as a gradual growth of the higher-order Stokes beams as illustrated in Fig. 6[1, 6].

IV. ANTI-STOKES GENERATION

As mentioned in Section II, the vibration of the normal coordinate q produces a sideband at the anti-Stokes frequency $\omega_A = \omega_L + \omega_v$. The phase of this wave is such that it experiences loss instead of gain, in contrast to the Stokes wave. This can be shown by considering the normal mode excitation produced by the beating of the anti-Stokes and laser pump waves and calculating the resultant Raman susceptibility for the anti-Stokes wave [1, 3]. The result is an expression nearly identical to the Stokes susceptibility, shown in Table 3, with $\omega_L - \omega_S$ replaced by $\omega_A - \omega_L$ (which are both equal to ω_v); *the major exception is that the imaginary part of the resonant frequency denominator expression has the opposite sign.* Thus $\text{Im}[\chi_R^{(3)}(-\omega_A; \omega_L, -\omega_L, \omega_A)] > 0$, which implies loss instead of gain.

It turns out, however, that there is another way to generate the anti-Stokes wave. This is the four-wave mixing process governed by the Raman susceptibility, and also possibly by the background nonresonant susceptibility, which produces a nonlinear polarization oscillating at the frequency $\omega_A = \omega_L + \omega_L - \omega_S = \omega_L + \omega_L - (\omega_L - \omega_v) = \omega_L + \omega_v$. The quantum mechanical picture of this interaction is shown schematically in Fig. 7. Note that anti-Stokes

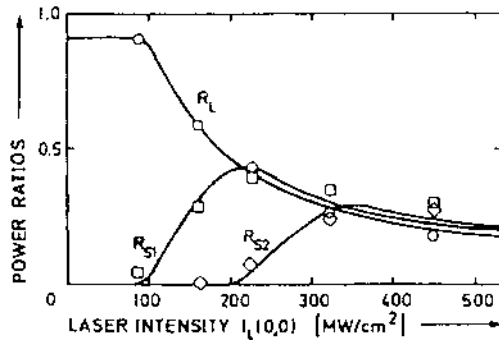


Figure 6 Normalized laser (circles), first Stokes (squares), and second Stokes (diamonds) power as functions of incident laser intensity. (From Ref. 6.)

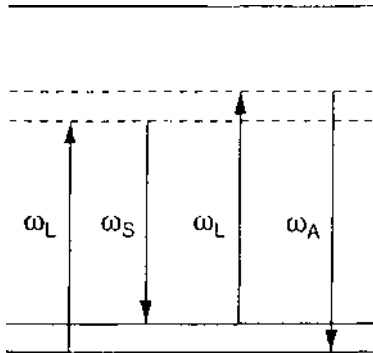


Figure 7 Anti-Stokes generation by four-wave mixing of laser and Stokes waves.

generation by four-wave mixing is a parametric process, leaving the material in its ground state, in contrast to SRS, which leaves the material in an excited state.

The nonlinear polarization produced by the third order interaction of the laser and Stokes waves is given by

$$P_A^{(3)}(\omega_A) = 3\epsilon_0 \chi^{(3)}(-\omega_A; \omega_L, \omega_L, -\omega_S) A_L A_L A_S^* \exp[i(2\mathbf{k}_L - \mathbf{k}_S) \cdot \mathbf{r}] \quad (20)$$

Two things should be noticed in this expression. First, the anti-Stokes polarization does not depend on the anti-Stokes field amplitude. Thus the anti-Stokes wave cannot directly achieve exponential gain. Second, the process is not automatically phase matched. Efficient anti-Stokes generation can only be achieved for $\mathbf{k}_A \simeq 2\mathbf{k}_L - \mathbf{k}_S$. In fact, in a normally dispersive isotropic medium, the anti-Stokes wave cannot be efficiently generated along the direction of the pump [4]. The usual phase matching condition is sketched in Fig. 8. It is noted that the anti-Stokes wave must couple to a Stokes wave generated off-axis. Thus the anti-Stokes wave is emitted in a conical shell about the pump direction.

In general, the anti-Stokes wave will be coupled to the Stokes wave through the four-wave mixing process and will affect the amplification of the Stokes wave. This problem has been treated within the nondepleted pump approximation [1,3]. The coupled mode equations are given by [3]

$$\frac{dA_S}{dz} = -G'_S A_S + \kappa_S A_A^* \exp(i\Delta kz) \quad (21)$$

and

$$\frac{dA_A}{dz} = -G'_A A_A + \kappa_A A_S^* \exp(i\Delta kz) \quad (22)$$

Complex Raman gain coefficients G'_j ($G'_j = \text{Re}[G'_j]$, with $j = S, A$) and coupling

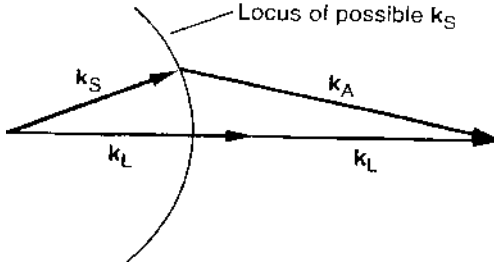


Figure 8 Phase matching diagram for anti-Stokes generation by four-wave mixing.

coefficients $\kappa_j \propto \chi^{(3)}(\omega_j)$ have been introduced, and

$$\Delta k = (2\mathbf{k}_L - \mathbf{k}_S - \mathbf{k}_A) \cdot \hat{z} \quad (23)$$

is the phase mismatch along the propagation direction (z -axis). The phase matching condition is illustrated in Fig. 8.

Equations (21) and (22) allow two modes each for the Stokes and anti-Stokes waves. These waves have the same eigenvalues for the wave propagation factors b (i.e., $A_j \sim e^{bz}$), which for the two modes ("+" and "-") are given by

$$b_{\pm} = -\frac{1}{2}(G'_S + G'^{*}_A) \pm \frac{1}{2}[(G'_S - G'^{*}_A + i\Delta k)^2 + 4\kappa_S \kappa_A^*]^{1/2} \quad (24)$$

The ratio of the normal mode amplitudes for the anti-Stokes and Stokes waves is given as

$$\frac{A_A^{\pm*}}{A_S^{\pm}} = \left[\frac{\kappa_A^*(b_{\pm} + G'_S + i\Delta k/2)}{\kappa_S(b_{\pm} + G'^{*}_A - i\Delta k/2)} \right]^{1/2} \quad (25)$$

The following relationships apply:

$$\begin{aligned} G'_A &= -\left(\frac{n_S \omega_A}{n_A \omega_S}\right) G'^{*}_S, \quad \kappa_S = -G'_S \exp(i2\varphi_L), \\ \kappa_A &= \left(\frac{n_S \omega_A}{n_A \omega_S}\right) G'^{*}_S \exp(i2\varphi_L), \end{aligned} \quad (26)$$

with φ_L the phase of the laser field, $A_L = |A_L| \exp(i\varphi_L)$. Normally $n_S \omega_A / n_A \omega_S \approx 1$, and Eq. (24) reduces to the approximate form [3]

$$b_{\pm} \approx \pm i \frac{\Delta k}{2} \left(1 - i \frac{4G'_S}{\Delta k} \right)^{1/2} \quad (27)$$

Three propagation regimes can be identified.

Strongly phase mismatched regime. In this regime $|\Delta k| \gg |G'_S|$, and the following approximations hold:

$$b_{\pm} \simeq \pm \left(G'_S + \frac{i\Delta k}{2} \right) \quad (28)$$

$$\frac{A_A^{+*}}{A_S^+} \simeq i \frac{\Delta k}{G'_S} \quad (29)$$

$$\frac{A_A^{-*}}{A_S^-} = 0 \quad (30)$$

These equations imply that the anti-Stokes and Stokes waves are effectively decoupled, with one mode (+) primarily anti-Stokes experiencing loss and the other mode (-) primarily Stokes experiencing gain, since $\text{Re}(G'_S) < 0$.

Strongly phase matched regime. Here $\Delta k = 0$, and

$$b_+ = 0 \quad (31)$$

$$b_- = -G'_S \left(1 - \frac{n_S \omega_A}{n_A \omega_S} \right) \simeq 0 \quad (32)$$

$$\frac{A_A^{\pm*}}{A_S^{\pm}} = -1 \quad (33)$$

In this regime, the Stokes and anti-Stokes waves are strongly coupled so that each eigenmode is an equal combination of both Stokes and anti-Stokes components, and neither experiences appreciable gain. The anti-Stokes wave, which normally experiences loss, is so strongly coupled to the Stokes wave in this regime that it effectively prevents the Stokes wave from experiencing gain, and both waves thus have equal strength.

Weakly phase matched regime. In this regime $|\Delta k| \sim |G'_S|$. Here, $\text{Re}(b_-)$ as well as $|A_A^{-*}/A_S^-|$ are sufficiently large such that the anti-Stokes generation is appreciable [1].

In the non-phase-matched cases, the material is left in an excited state due to the strong Stokes generation. However, when $\Delta k = 0$, the material excitation is strongly damped while the Stokes and anti-Stokes waves achieve constant intensities after propagating through a distance $\sim (b_-)^{-1}$ with no change as they propagate further into the medium [3].

V. APPLICATIONS

A. Raman Gain Spectroscopy

In ordinary Raman spectroscopy, a single fixed frequency laser is incident on the Raman active medium, and the scattered radiation is detected with a grating tuned

monochrometer to obtain the Raman spectrum. It is noted that in SRS, both the Stokes amplification and the pump attenuation are proportional to the Raman line shape. Thus a measurement of the Stokes gain or the pump loss, using two tunable lasers, as functions of $\omega_L - \omega_S$, will yield the Raman spectrum, without the need of a monochromometer. In this case, the resolution of the measurement is limited only by the laser line widths. The technique is known as stimulated Raman gain spectroscopy, and examples may be found in Ref. 1.

B. Coherent Anti-Stokes Raman Spectroscopy (CARS)

CARS is a Raman spectroscopy technique that uses four-wave mixing to generate a coherent anti-Stokes signal. This coherent output has a much higher signal-to-noise ratio than ordinary spontaneous anti-Stokes Raman scattering.

The method utilizes two laser inputs at frequencies ω_1 and ω_2 . These are mixed in a Raman-active medium to form the new frequency $\omega_A = 2\omega_1 - \omega_2$. A resonant enhancement of the signal is achieved when $\omega_1 - \omega_2 \approx \omega_v$, i.e., when $\omega_2 \approx \omega_S$. The quantum mechanical picture of this process is illustrated in Fig. 9. The phase matching condition is like that of anti-Stokes SRS as given in Fig. 8.

The CARS signal, due to four-wave mixing, has contributions from the resonant Raman susceptibility $\chi_R^{(3)}(-\omega_A; \omega_1, \omega_1, -\omega_2)$ as well as a nonresonant background susceptibility $\chi^{(3)}$. Thus the net anti-Stokes susceptibility is given

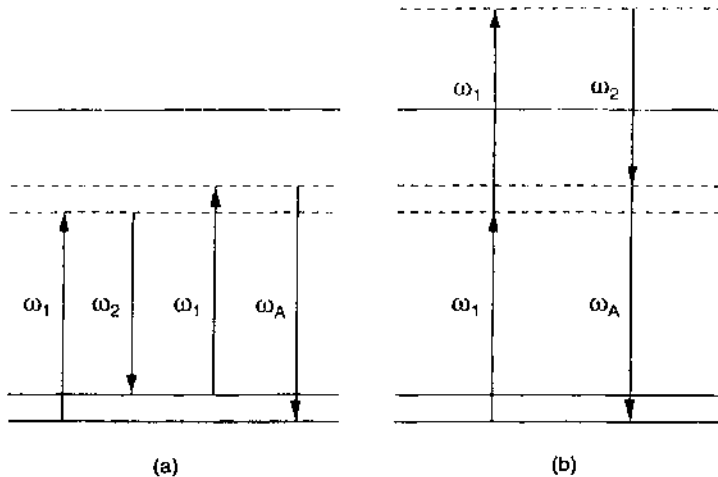


Figure 9 CARS by four-wave mixing. (a) Resonant Raman process and (b) nonresonant process.

as [1]

$$\chi_A^{(3)} = \chi^{(3)} + \frac{a}{\omega_v - (\omega_1 - \omega_2) + i\Gamma/2} \quad (34)$$

where Γ is the Raman line width, and a is a constant depending on the material (i.e., proportional to the differential Raman scattering cross-section). In the non-depleted pump approximation, the CARS signal is thus proportional to $|\chi_A^{(3)}|^2$ and is given by [1]

$$I_A = \frac{\omega_A^2 |\chi_A^{(3)}|^2}{16\epsilon_0^2 n_1^2 n_2 n_{AC} c^4} I_1^2 I_2 L^2 \frac{\sin^2(\Delta kL/2)}{(\Delta kL/2)^2} \quad (\text{SI})$$

$$I_A = \frac{16\pi^4 \omega_A^2 |\chi_A^{(3)}|^2}{n_1^2 n_2 n_{AC} c^4} I_1^2 I_2 L^2 \frac{\sin^2(\Delta kL/2)}{(\Delta kL/2)^2} \quad (\text{cgs})$$
(35)

where L is the sample thickness, and

$$\Delta k = (2\mathbf{k}_1 - \mathbf{k}_2 - \mathbf{k}_A) \cdot \hat{z} \quad (36)$$

is the phase mismatch. Thus the CARS spectrum relative to the nonresonant background will be proportional to

$$\left| \frac{\chi_A^{(3)}}{\chi^{(3)}} \right|^2 = \left[1 + \frac{2a}{\Gamma \chi^{(3)}} \frac{2\Delta/\Gamma}{1 + (2\Delta/\Gamma)^2} \right]^2 + \left[\frac{(2a/\Gamma \chi^{(3)})}{1 + (2\Delta/\Gamma)^2} \right]^2 \quad (37)$$

where $\Delta = \omega_v - (\omega_1 - \omega_2)$.

The input lasers are tuned to generate the anti-Stokes spectrum, and the signal is asymmetric about $\omega_1 - \omega_2 = \omega_v$. The behavior of the relative CARS spectral signal is shown in Fig. 10. Spectral measurements about the peak and dip in this curve yield information relating to Γ , $\chi^{(3)}$, ω_v , and $d\sigma/d\Omega$. In principle, all four of these parameters may be characterized.

CARS has found particularly good applications in combustion studies, where it can be used to monitor the temporal and spatial distributions of different species and their internal energies. The spatial and temporal coherence of the anti-Stokes output allows filtering of the signal to suppress the strong luminescent background. See Ref. 1 and references cited therein for additional information.

Another coherent spectroscopy technique that has been developed stemming from SRS is the coherent Stokes Raman spectroscopy (CSRS). This technique has some features analogous to CARS. Shen [1] gives a brief overview of this technique.

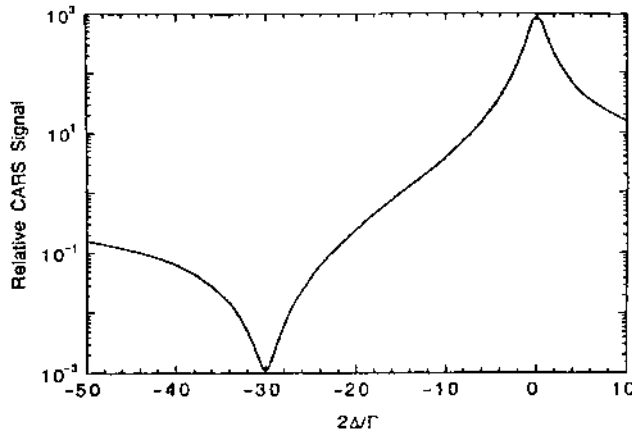


Figure 10 Relative CARS signal as a function of the laser detuning parameter $2\Delta/\Gamma$.

C. Raman Shifters (Stokes Generators)

The frequency shift and accompanying gain associated with Stokes generation makes SRS a convenient method for down-shifting laser radiation for practical purposes [7–9]. One example of this is the red-shifting of available laser outputs to a region that allows third harmonic generation studies in organic materials [10,11]. Red-shifting the pump frequency allows the third harmonic to be in a region away from the UV where many promising nonlinear organic materials have strong absorption bands.

The usual configuration utilizes a single pass of the pump laser through a Raman cell. The Stokes output grows from noise (i.e., spontaneous Raman scattering) originating at the cell input. The steady-state Stokes output can be expressed as [2,12]

$$I_S(L) \approx \frac{\hbar\omega_S}{2\pi w_0^2} \Gamma G(\omega_S) L \left[I_0\left(\frac{GL}{2}\right) - I_1\left(\frac{GL}{2}\right) \right] \exp\left(\frac{GL}{2}\right) \quad (38)$$

where w_0 is the $1/e^2$ radius of the pump beam, and I_0 and I_1 are modified Bessel functions of order 0 and 1.

The threshold for Stokes generation is often defined as the pump intensity for which the Stokes intensity is $\sim 1\%$ of the pump. This implies a gain $\sim e^{23} - e^{30}$ [2]. For example, a typical Raman shifter may consist of a 1 m H_2 cell at a pressure of several atmospheres (typically ~ 10 atm). The Q(1) Raman mode produces a frequency shift of $\nu_R = 4155 \text{ cm}^{-1}$, while the S(1) mode yields $\nu_R = 587 \text{ cm}^{-1}$ [2]. Taking the pump to be a Nd:YAG laser with a fundamental wavelength at $1.064 \mu\text{m}$, the Q(1) mode would thus provide a shift to $1.907 \mu\text{m}$,

while the S(1) mode would yield $1.13 \mu\text{m}$ output. Assuming a Raman gain intensity factor of $g_S \sim 10^{-3} \text{ cm/MW}$ [1–3], the threshold pump intensity would then be $\sim 600 \text{ MW/cm}^2$. For a Q-switched laser with a 10 ns output, this would imply an approximately 375 mJ pulse focused to a spot of radius $w_0 = 200 \mu\text{m}$.

The quality of the Stokes beam produced in a Raman shifter will often depend on the quality of the pump. If the Fresnel number of the pump $F \sim \pi w_0^2 / \lambda L \sim 1$, then the Stokes spatial profile will be approximately Gaussian [2]. The Stokes spectral line width generally varies from a value several times the gain-narrowed width to on the order of the pump laser line width [2,13].

As with any system exhibiting exponential gain, the possibility of producing a Raman oscillator exists. Only a small amount of feedback is actually necessary to set a Stokes generator into oscillation. For negligible linear scattering and absorption losses, the oscillation threshold condition is determined by $R \exp(GL) = 1$, where R is the reflectance of the cavity reflector. Fresnel reflection from a cell window can be sufficient in a high gain Stokes generator. Yariv [4] gives an example of a ruby laser pumping a 5 cm cell of CS_2 , converting 694 nm to 728 nm, and calculates a threshold pump intensity of $\sim 70 \text{ MW/cm}^2$ for the onset of oscillation.

D. Raman Amplifier/Beam Cleanup/Beam Combiner

SRS has been applied not only to the case of amplifying the Stokes wave but also to cleaning up a phase or amplitude distorted pump beam. Actually, this is a slight misnomer, since the pump beam does not get cleaned up in any way. Rather, a clean Stokes seed beam is amplified, draining energy away from the pump beam, but the pump distortions are not transferred to the Stokes wave. Thus a strong yet clean Stokes beam is generated.

The simple physics behind this concept can be seen in the expression for the Stokes amplitude in the nondepleted pump approximation:

$$A_S(z) = A_S(0) \exp \left[i3 \left(\frac{\omega_S}{n_S c} \right) (\chi_R^{(3)}) |A_L(z)|^2 z \right] \quad (39)$$

Thus since $\text{Im}[\chi_R^{(3)}] < 0$, the phase information of the pump wave is lost in the amplification process, because the Raman gain depends only on the modulus of the pump amplitude. Thus whatever phase information the Stokes seed carried is retained in the amplification process.

It should be obvious though from Eq. (39) that amplitude distortions on the pump wave can corrupt the Stokes wave amplitude. It turns out that pump phase distortions can also corrupt the Stokes wave when these phase aberrations yield amplitude distortions as the beam diffracts through the Raman cell. Reintjes et al. give a discussion of several cases under which the Stokes beam can be degraded in a Raman amplification/beam cleanup application [14].

Amplitude distortions, or phase distortions leading to amplitude distortions, are thus a serious impediment to Raman beam cleanup. However, pump intensity averaging techniques can be used to average out these amplitude distortions. Two types can be employed: collinear intensity averaging, and crossed beam intensity averaging [14].

In collinear intensity averaging, the pump is allowed to diffract over the cell length across the Stokes wave. The condition under which this will lead to good intensity averaging is given by

$$\theta_{\text{div}} \gg 2\bar{G}(\omega_S) \left(\frac{\lambda L}{2\pi} \right)^{1/2} \quad (40)$$

where θ_{div} is the divergence angle of the pump beam, and

$$\bar{G}(\omega_S) = g_S \bar{I}_L \quad (41)$$

is the average Raman gain coefficient, related to the average pump intensity [14]. This condition merely states that the diffraction length of the pump should be much smaller than the gain length of the Stokes wave.

In crossed beam averaging, the Stokes wave is injected along the axis bisecting the angle between two crossed pump beams. The averaging occurs as the pump beams propagate across the Stokes wave front. This requires that the averaging occur over a distance small compared to the gain length. This technique is made possible by the fact that phase matching is automatic in the SRS process; the direction at which growth of the Stokes wave takes place is dictated by the incident Stokes seed beam. The Stokes seed beam robs gain from other possible modes. In this geometry, though, it is possible that phase matched four-wave mixing may occur between the beams, which will tend to degrade the Stokes wave [14]. Several authors have discussed Raman beam cleanup and beam control processes [15–22].

Stokes amplification with crossed beams is also the basis of Raman beam combining [14]. In this case, the pump beams (there can be many, >2) are derived from different lasers. All of the beams serve as pumps to amplify and transfer their energies to a single Stokes beam.

REFERENCES

1. Y. R. Shen, *The Principles of Nonlinear Optics*, John Wiley, New York, 1984.
2. J. F. Reintjes, Stimulated Raman and Brillouin Scattering, *Handbook of Laser Science and Technology, Supplement 2: Optical Materials* (M. J. Weber, ed), CRC Press, Boca Raton, FL, 1995, pp. 334–364.
3. R. W. Boyd, *Nonlinear Optics*, Academic Press, New York, 1992, pp. 325–364.
4. A. Yariv, *Quantum Electronics*, 3rd ed., John Wiley, New York, 1989, pp. 453–494.

5. E. Garmire, F. Pandarese, and C. H. Townes, Coherently driven molecular vibrations and light modulation, *Phys. Rev. Lett.* 11:160 (1963).
6. D. von der Linde, M. Maier, and W. Kaiser, Quantitative investigations of the stimulated raman effect using subnanosecond light pulses, *Phys. Rev.* 178:11 (1969).
7. T. R. Loree, R. C. Sze, and D. L. Barker, Efficient shifting of ArF and KrF laser wavelengths, *Appl. Phys. Lett.* 31:37 (1977).
8. R. Burnham and N. Djeu, Efficient Raman conversion of XeCl-laser radiation in metal vapors, *Opt. Lett.* 3:215 (1978).
9. H. Komine and E. A. Stappaerts, Efficient higher-stokes-order Raman conversion in molecular gases, *Opt. Lett.* 4:398 (1979).
10. F. Kajzar and J. Messier, Third harmonic generation in liquids, *Phys. Rev. A* 32:2352 (1985).
11. L.-T. Chang, W. Tam, S. H. Stevenson, G. R. Meredith, G. Rikken, and S. R. Marder, Experimental investigations of organic molecular nonlinear optical polarizabilities. I. Methods and results on benzene and stilbene derivatives, *J. Phys. Chem.* 95:10631 (1991).
12. M. E. Raymer and J. Mostowski, Stimulated Raman scattering: unified treatment of spontaneous initiation and spatial propagation, *Phys. Rev. A* 24:1980 (1981).
13. D. C. MacPherson, R. C. Swanson, and J. L. Carlsten, Quantum fluctuations in the stimulated scattering linewidth, *Phys. Rev. Lett.* 61:66 (1988).
14. J. Reintjes, R. H. Lehmberg, R. S. F. Chang, M. T. Duignam, and G. Calame, Beam cleanup with stimulated Raman scattering in the intensity averaging regime, *J. Opt. Soc. Am. B* 3:1408 (1986).
15. D. Korff, E. Mazur, C. Duzy, and A. Flusberg, Raman conversion using crossed broadband beams and bisecting stokes, *J. Opt. Soc. Am. B* 3:1333 (1986).
16. A. Flusberg and D. Korff, Transient refractive-index changes in stimulated Raman scattering, *J. Opt. Soc. Am. B* 3:1338 (1986).
17. C. Warner and B. Bobbs, Effects of off-resonant Raman interactions on multimode stokes conversion efficiency and output wave front, *J. Opt. Soc. Am. B* 3:1345 (1986).
18. S. J. Pfeifer, Multiline Raman beam combination, *J. Opt. Soc. Am. B* 3:1368 (1986).
19. J. P. Partanen and M. J. Shaw, High-power forward raman amplifiers employing low-pressure gases in light guides. I. Theory and applications, *J. Opt. Soc. Am. B* 3:1374 (1986).
20. J. M. Eggleston, Solutions to Raman-scattering equations in the presence of multiple equivalent incoherent multiaxial-mode laser beams, *J. Opt. Soc. Am. B* 3:1390 (1986).
21. H. Komine, W. H. Long, Jr., E. A. Stappaerts, and S. J. Brosnan, Beam cleanup and low-distortion amplification in efficient high-gain hydrogen Raman amplifiers, *J. Opt. Soc. Am. B* 3:1428 (1986).
22. J. C. van den Heuvel, Numerical study of beam cleanup by stimulated Raman scattering, *J. Opt. Soc. Am. B* 12:650 (1995).

15

Stimulated Brillouin Scattering

Brillouin scattering is the scattering of light from acoustic disturbances in a medium. Classically, the source of the scattered wave can be linked to a fluctuation in the dielectric constant of the medium. The change in the dielectric constant is related to a change in the mass density of the medium [1] by

$$\Delta\epsilon = \frac{\partial\epsilon}{\partial\rho}\Delta\rho \quad (1)$$

where $\Delta\epsilon$ and $\Delta\rho$ are the small changes in dielectric constant and density, respectively. The density fluctuation is further related to the thermodynamic variables p (pressure) and S (entropy):

$$\Delta\rho = \left(\frac{\partial\rho}{\partial p}\right)_S \Delta p + \left(\frac{\partial\rho}{\partial S}\right)_p \Delta S \quad (2)$$

Entropy fluctuations ΔS lead to Rayleigh scattering (no frequency shift). Brillouin scattering can thus be described as scattering of light from acoustic density or pressure waves, or from acoustic phonons.

The scattered light in Brillouin scattering can be thought of as a Doppler-shifted reflection from an acoustic wave front, or as the scattering of a photon from an acoustic phonon. These ideas are illustrated schematically in Fig. 1, where an incident optical wave interacts with an incoming or outgoing acoustic wave. Conservation of momentum and energy requires that the wave vector and frequency of the scattered wave (ω', \mathbf{k}') be related to those of the incident wave (ω, \mathbf{k}) by the relations

$$\mathbf{k}' = \mathbf{k} \pm \mathbf{K} \quad \omega' = \omega \pm \Omega \quad (3)$$

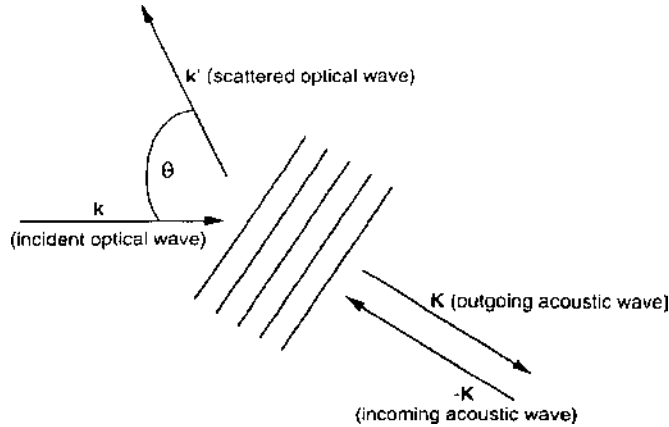


Figure 1 Brillouin scattering of an optical wave (k) from an outgoing (\mathbf{K}) or incoming ($-\mathbf{K}$) acoustic wave.

where $\pm \mathbf{K}$ and Ω are the wave vector and frequency of the acoustic wave, respectively. The lower sign in Eq. (3) corresponds to the Stokes-shifted wave scattered from an outgoing acoustic wave, and the upper sign corresponds to the anti-Stokes wave. Stokes and anti-Stokes waves are of equal strength in spontaneous Brillouin scattering.

The frequency shift of the Brillouin scattered wave is a maximum for $\theta = 180^\circ$ scattering (i.e., backscattering). At this angle the frequency shift is called the Brillouin frequency and is defined as

$$\Omega_B = 2 \frac{v_a}{c/n} \omega \quad (4)$$

where v_a is the velocity of the acoustic wave, and c/n is the velocity of the light of frequency ω in the medium. A typical acoustic velocity is $v_a \sim 10^3$ m/s, and a typical frequency shift in Brillouin scattering is $\Omega_B/2\pi \sim 1-10$ GHz. Spontaneous Brillouin scattering occurs due to scattering from thermally excited phonons.

In laser scattering from acoustic disturbances, the incident laser and Brillouin scattered waves superimpose to form a traveling beat wave with frequency Ω and wave vector \mathbf{K} . If the laser is sufficiently intense, this beat wave can coherently drive the acoustic wave through electrostrictive, and possibly thermal (for absorptive media), forces. The enhanced acoustic wave more strongly scatters the incident laser radiation, which in turn leads to a stronger beat wave. This mutual reinforcement results in an amplified Brillouin wave. The process is called stimulated Brillouin scattering (SBS).

SBS occurs in all gases, liquids, solids, and plasmas. It is reasonably strong for intense lasers, and in some cases the incident laser can be almost entirely converted into a Brillouin backscattered wave. (The forward scattered, anti-Stokes shifted Brillouin wave is attenuated [2–4].) In liquids the overpressure developing from this interaction using Q-switched lasers can be strong enough to produce an audible pop and shatter cell windows [3]. In addition, the backscattered SBS wave can enter the laser cavity, be amplified, and produce a Brillouin-shifted component in the laser output. Aside from these deleterious effects, SBS is important for certain applications, such as optical phase conjugation, optical pulse compression, and wave amplification [4].

Table 1 contains a list of many of the physical parameters appearing in formulas pertaining to SBS, along with their units in SI and cgs systems. In some cases, the units are mixed, such as when the Brillouin gain intensity factor is quoted in cm/W (centimeters per watt). A list of conversion formulas for converting values from cgs to SI units, as well as mixed units, is given in Table 2.

Table 1 Physical Units of Important Physical Parameters Utilized in Formulas Related to Stimulated Brillouin Scattering

Physical parameter	SI	cgs
Electrostriction coefficient	$[\gamma_e] = \text{C/V}\cdot\text{m}$	$[\gamma_e] = \text{unitless}$
Density	$[\rho] = \text{kg/m}^3$	$[\rho] = \text{g/cm}^3$
Specific heat	$[c_p] = \text{J/kg}\cdot\text{K}$	$[c_p] = \text{erg/g}\cdot\text{K}$
Volume expansion coefficient	$[\beta_p] = \text{K}^{-1}$	$[\beta_p] = \text{K}^{-1}$
Third order polarization	$[P^{(3)}] = \text{C/m}^2$	$[P^{(3)}] = \text{sV/cm}$ $= (\text{erg/cm}^3)^{1/2}$
Electric field amplitude	$[E] = [A] = \text{V/m}$	$[E] = [A] = \text{sV/cm}$ $= (\text{erg/cm}^3)^{1/2}$
Third order Brillouin susceptibility	$[\chi_B^{(3)}] = \text{m}^2/\text{V}^2$	$[\chi_B^{(3)}] = \text{cm}^2/\text{sV}^2$ $= \text{cm}^3/\text{erg} = \text{esu}$
Brillouin gain intensity factor	$[g_B] = \text{m/W}$	$[g_B] = \text{cm}\cdot\text{s}/\text{erg}$
Vacuum permittivity	$[\epsilon_0] = \text{F/m} = \text{C/V}\cdot\text{m}$	—
Distance, length	$[z] = [L] = \text{m}$	$[z] = [L] = \text{cm}$
Speed of light; acoustic speed (hypersonic)	$[c] = [v_a] = \text{m/s}$	$[c] = [v_a] = \text{cm/s}$
Wave vector	$[k] = [K] = \text{m}^{-1}$	$[k] = [K] = \text{cm}^{-1}$
Circular frequency	$[\omega] = [\Omega] = \text{Hz} = \text{s}^{-1}$	$[\omega] = [\Omega] = \text{Hz} = \text{s}^{-1}$
Brillouin line width	$[\Gamma_B] = \text{Hz} = \text{s}^{-1}$	$[\Gamma_B] = \text{Hz} = \text{s}^{-1}$
Absorption coefficient	$[\alpha] = \text{m}^{-1}$	$[\alpha] = \text{cm}^{-1}$
Intensity	$[I] = \text{W/m}^2$	$[I] = \text{erg/s}\cdot\text{cm}^2$
Power	$[\mathcal{P}] = \text{W}$	$[\mathcal{P}] = \text{erg/s}$
Energy	$[\mathcal{E}] = \text{J}$	$[\mathcal{E}] = \text{erg}$

Table 2 Conversion Formulas Between the SI and cgs Systems of Units for Several Physical Parameters Utilized in Stimulated Brillouin Scattering

γ_e	(SI) = 8.85×10^{-12}	γ_e	(cgs)
ρ	(SI) = $10^3 \rho$		(cgs)
c_p	(SI) = $10^{-4} c_p$		(cgs)
$P^{(3)}$	(SI) = $\frac{1}{3} \times 10^{-5} P^{(3)}$		(cgs)
E	(SI) = $3 \times 10^4 E$		(cgs)
$\chi_B^{(3)}$	(SI) = $\frac{4\pi}{3^2} \times 10^{-8} \chi_B^{(3)}$		(cgs)
g_B	(SI) = $10^5 g_B$		(cgs)
g_B	(cm/W) = $10^2 g_B$	(SI) = $10^7 g_B$	(cgs)
L	(SI) = $10^{-2} L$		(cgs)
c	(SI) = $10^{-2} c$		(cgs)
v_a	(SI) = $10^{-2} v_a$		(cgs)
k	(SI) = $10^2 k$		(cgs)
α	(SI) = $10^2 \alpha$		(cgs)
I	(SI) = $10^{-3} I$		(cgs)
I	(W/cm ²) = $10^{-4} I$	(SI) = $10^{-7} I$	(cgs)
\mathcal{P}	(SI) = $10^{-7} \mathcal{P}$		(cgs)
\mathcal{E}	(SI) = $10^{-7} \mathcal{E}$		(cgs)

This chapter gives a brief presentation of some of the physics and formulas associated with SBS. This includes important formulas for spontaneous Brillouin scattering, Brillouin gain due to electrostrictive and thermal forces, and laser–Brillouin wave coupling. The last section considers two of the applications of SBS.

I. SPONTANEOUS BRILLOUIN SCATTERING

An acoustic wave propagating in an isotropic medium can be described by

$$\rho^{(\sim)}(z, t) = \rho_0 + \Delta\rho(z, t)\exp[i(qz - \Omega t)] + \text{c.c.} \quad (5)$$

where ρ_0 is the average density of the medium, and q is a complex wave vector. The rapidly varying density fluctuation $\Delta\rho^{(\sim)}$ satisfies the acoustic wave equation

$$\left[\frac{\partial^2}{\partial t^2} - \Gamma \nabla^2 \frac{\partial}{\partial t} - v_a^2 \nabla^2 \right] \Delta\rho^{(\sim)} = 0 \quad (6)$$

where Γ is a damping constant defined by

$$\Gamma = \frac{1}{\rho_0} \left(\frac{4}{3} \eta_s + \eta_b \right) \quad (7)$$

In Eq. (7), η_s is the shear viscosity and η_b is the bulk viscosity. The acoustic velocity is given by $v_a = (B/\rho_0)^{1/2}$, where $B = \rho_0(\partial\rho/\partial p)^{-1}$ is the bulk modulus of the medium.

The middle term in Eq. (6), involving viscous forces, is a dissipative force which leads to a complex dispersion relation:

$$q(\Omega) = \left(\frac{\Omega^2}{v_a^2 - i\Omega\Gamma} \right)^{1/2} \simeq \frac{\Omega}{v_a} \left(1 + i \frac{\Omega\Gamma}{v_a^2} \right)^{1/2} \simeq K(\Omega) + i \frac{\Gamma_B}{2v_a} \quad (8)$$

where

$$K(\Omega) = \frac{\Omega}{v_a} \quad (9)$$

is the real acoustic wave vector, and

$$\Gamma_B = K^2\Gamma \quad (10)$$

is the Brillouin line width. The acoustic wave intensity is thus damped, with

$$|\Delta\rho(z)|^2 = |\Delta\rho(0)|^2 \exp(-\alpha_s z) \quad (11)$$

where $\alpha_s = \Gamma_B/v_a$ is the sound absorption coefficient. Typically, the acoustic wave is highly damped, with an absorption depth $(\alpha_s)^{-1}$ of the order of a few micrometers.

By Eq. (1), density fluctuations produce small changes in the dielectric constant. Thus the dipole moment per unit volume of the medium is doubly modulated, at the optical frequency and at the acoustic frequency:

$$\mathbf{P}^{(\sim)} = \epsilon_0 \chi^{(\sim)} \mathbf{E}^{(\sim)} = (\epsilon^{(\sim)} - \epsilon_0) \mathbf{E}^{(\sim)} \quad (12)$$

where $\epsilon^{(\sim)} = \epsilon(\omega) + \Delta\epsilon^{(\sim)}$ is the rapidly varying (at acoustic frequencies) dielectric constant with a small oscillation $\Delta\epsilon^{(\sim)}$ about its nominal value at frequency ω . Thus in addition to the usual polarization component that oscillates at the frequency of the incident optical wave, there is a small modulation of the polarization given by

$$\Delta\mathbf{P}^{(\sim)} = \frac{\partial\epsilon}{\partial\rho} \Delta\rho^{(\sim)} \mathbf{E}^{(\sim)} \quad (13)$$

This polarization modulation thus oscillates at the sideband frequencies $\omega \pm \Omega$. The fields radiated by these oscillations produce the anti-Stokes and Stokes-shifted Brillouin scattered waves.

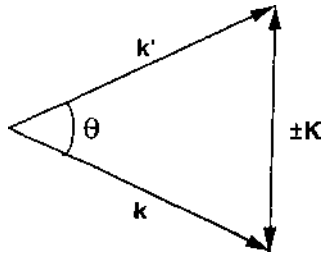


Figure 2 Illustration of the relation between optical and acoustic wave vectors in Brillouin scattering.

The modulated polarization has a wave vector \mathbf{k}' that is related to the optical field and acoustic wave vectors as shown in Fig. 2. Since the frequency shift in Brillouin scattering is small, $|\mathbf{k}'| \approx |\mathbf{k}|$ and the acoustic wave vector is thus given by

$$|K| = 2 \frac{n v_a}{c} \omega \sin\left(\frac{\theta}{2}\right) = \Omega_B \sin\left(\frac{\theta}{2}\right) \quad (14)$$

The maximum frequency shift is thus for backscattering at $\Omega_{\max}(\theta = 180^\circ) = \Omega_B$, which is the Brillouin frequency. Thus the spectrum of scattered light shows two peaks at the Stokes and anti-Stokes frequencies ($\omega \mp \Omega$) with line widths of Γ_B .

II. BRILLOUIN (STOKES) WAVE AMPLIFICATION

When oscillating body forces are present in a deformable medium, the density wave must satisfy a driven acoustic wave equation:

$$\left[\frac{\partial^2}{\partial t^2} - \Gamma \nabla^2 \frac{\partial}{\partial t} - v_a^2 \nabla^2 \right] \Delta \rho^{(\sim)} = -\nabla \cdot \mathbf{f}^{(\sim)} \quad (15)$$

where $\mathbf{f}^{(\sim)}$ is the rapidly varying body force (force per unit volume) acting on the medium. In absorptive media, acoustic waves can be driven thermally through thermalization of absorbed optical energy as well as by the electrostrictive force. Electrostriction is the only force active in transparent media.

A. Electrostriction

Electrostriction is the force that attracts material in a deformable medium to regions of high field strength. It requires the presence of a nonuniform field (i.e., a field gradient). Boyd [2] gives a good discussion of this force in terms of

dielectric energy density changes and thermodynamic relations. It can also be understood in terms of the microscopic forces acting on a dilute collection of electric dipoles situated in a nonuniform electromagnetic field.

The rapidly varying molecular induced dipole moment due to an applied field that is slowly varying (spatially) over a distance comparable to the size of the dipole is given by $\mu^{(\sim)} = \alpha E^{(\sim)}$, where α is the linear polarizability of the molecule. Corson and Lorrain [5] treat the force on a dipole in a nonuniform field. Basically, one end of the dipole feels a stronger electric force than the other end due to the field nonuniformity. This will cause a translatable motion of the dipole. (A dipole in a uniform field will only experience a torque.) The gradient force acting on the dipole is expressed as

$$\mathbf{F}_E^{(\sim)} = (\mu^{(\sim)} \cdot \nabla) \mathbf{E}^{(\sim)} \quad (16)$$

In addition to this force, an oscillating dipole in an electromagnetic field will experience a ponderomotive force (Lorentz-like force)

$$\mathbf{F}_B^{(\sim)} = \frac{d\mu^{(\sim)}}{dt} \times \mathbf{B}^{(\sim)} \quad (17)$$

where $\mathbf{B}^{(\sim)}$ is the rapidly varying magnetic induction of the optical wave. Relating the dipole moment to the electric field through the polarizability and employing Maxwell's equations and some vector identities, a time-averaged force per unit volume acting on the molecular dipoles can be derived, given by

$$\mathbf{f}_e^{(\sim)} = \frac{1}{2} \alpha N \nabla \langle \mathbf{E}^{(\sim)} \cdot \mathbf{E}^{(\sim)} \rangle \quad (18)$$

where N is the number of dipoles per unit volume, and the angular brackets indicate a time average over many optical cycles, but a time short compared to an acoustic period. Thus the rapidly varying body force can oscillate at an acoustic frequency. Through the relation $\alpha N = \rho (\partial \epsilon / \partial p)$, the electrostrictive force can be written as

$$\mathbf{f}_e^{(\sim)} = \frac{1}{2} \gamma_e \nabla \langle \mathbf{E}^{(\sim)} \cdot \mathbf{E}^{(\sim)} \rangle \quad (19)$$

where

$$\gamma_e = \rho \frac{\partial \epsilon}{\partial p} \quad (20)$$

is called the electrostrictive coefficient. This same relation holds in dense media [2–4]. Formulas for γ_e in centrosymmetric media are given in Table 3.

The term in angular brackets in Eq. (19) is proportional to the optical intensity. Thus the electrostrictive force is due to a gradient in the intensity. In SBS, this gradient is due to the beating of the laser wave with the Brillouin scattered wave.

Table 3 Formulas Related to Stimulated Brillouin Scattering

Electrostrictive coefficient	$\gamma_e = \frac{1}{3}\epsilon_0(n^2 - 1)(n^2 + 2)$ (SI) $\gamma_e = \frac{1}{3}(n^2 - 1)(n^2 + 2)$ (cgs)
Brillouin susceptibility	$\chi_B^{(3)}(-\omega_B; \omega_L, -\omega_L, \omega_B)$ $= \left(\frac{\gamma_e^2 n_L \omega_L}{6\epsilon_0 \rho_0 c v_a}\right) \frac{1}{\Omega_B - (\omega_L - \omega_B) - i\Gamma_B/2}$ (SI)
Brillouin gain intensity factor	$\chi_B^{(3)}(-\omega_B; \omega_L, -\omega_L, \omega_B)$ $= \left(\frac{\gamma_e^2 n_L \omega_L}{96\pi^2 \rho_0 c v_a}\right) \frac{1}{\Omega_B - (\omega_L - \omega_B) - i\Gamma_B/2}$ (cgs)
Electrostrictive component	$g_B^e = \frac{\gamma_e^2 \omega_L^2}{\epsilon_0^2 \rho_0 n_B v_a c^3 \Gamma_B} \frac{(\Gamma_B/2)^2}{[\Omega_B - (\omega_L - \omega_B)]^2 + (\Gamma_B/2)^2}$ (SI)
Absorptive component	$g_B^a = -\frac{\alpha \beta_p \gamma_e \omega_L}{2\epsilon_0 \rho_0 n_B c_p c \Gamma_B} \frac{4[\Omega_B - (\omega_L - \omega_B)]/\Gamma_B}{[\Omega_B - (\omega_L - \omega_B)]^2 + (\Gamma_B/2)^2}$ (SI)
Brillouin output intensity (no pump depletion)	$g_B^a = -\frac{\alpha \beta_p \gamma_e \omega_L}{2\rho_0 n_B c_p c \Gamma_B} \frac{4[\Omega_B - (\omega_L - \omega_B)]/\Gamma_B}{[\Omega_B - (\omega_L - \omega_B)]^2 + (\Gamma_B/2)^2}$ (cgs)
No absorption	$\Omega_B = 2n_L \frac{v_a}{c} \omega_L$ $I_B(z) = I_B(L) \exp[g_B^a I_L(L - z)]$
Absorption	$I_B(z) = I_B(L) \exp[(g_B I_L - \alpha)(L - z)]$
Brillouin pump coupled outputs	$I_B(L) = \frac{[I_B(0)/I_L(0)][1 - I_B(0)/I_L(0)]}{\exp\{[1 - I_B(0)/I_L(0)]g_B^a I_L(0)L\} - I_B(0)/I_L(0)}$
No absorption	

B. Optical Wave-Material Excitation Wave Coupling

Three waves are assumed to be present in the medium: the laser wave at (ω_L, \mathbf{k}_L) , the Brillouin scattered wave at (ω_B, \mathbf{k}_B) , and the acoustic wave at (Ω, \mathbf{K}) . The waves are related by $\omega_L - \omega_B = \Omega$ and $\mathbf{k}_L - \mathbf{k}_B \approx \mathbf{K}$. The electrostrictive force of Eq. (19) is due to the total field, i.e., the superposition of the two optical waves.

The component of the electrostrictive force that drives the acoustic excitation is proportional to $|\mathbf{k}_L - \mathbf{k}_B|^2 A_L A_B^*$, by Eq. (19), with field amplitudes

given by A_L and A_B . Hence, by the relation above for the wave vectors and by Eq. (14), this term will be largest for a backscattered ($\theta = 180^\circ$) Brillouin wave. The laser and acoustic waves are then taken to be propagating along the $+z$ direction, and the Brillouin wave along $-z$:

$$E_L^{(\sim)}(z, t) = A_L(z, t) \exp[i(k_L z - \omega_L t)] + \text{c.c.} \quad (21)$$

$$E_B^{(\sim)}(z, t) = A_B(z, t) \exp[i(-k_B z - \omega_B t)] + \text{c.c.} \quad (22)$$

$$\Delta\rho^{(\sim)}(z, t) = \Delta\rho(z, t) \exp[i(Kz - \Omega t)] + \text{c.c.} \quad (23)$$

The polarization directions of the laser and Brillouin waves have been assumed to be parallel, and the density wave is a nonpolarized longitudinal wave. The Brillouin wave could be generated by noise phonons or could be an injected wave counterpropagating to the laser wave.

Nonlinear polarizations oscillating at ω_L and ω_B are produced by the interactions of the laser and Brillouin fields through the fluctuations in the dielectric constant:

$$P_L^{(3)} = \frac{\partial\epsilon}{\partial\rho} \Delta\rho A_B \exp[i(k_B + K)z] \quad (24)$$

$$P_B^{(3)} = \frac{\partial\epsilon}{\partial\rho} \Delta\rho^* A_L \exp[i(k_L - K)z] \quad (25)$$

The density variation in turn depends on the product of the laser and Brillouin field amplitudes through the electrostrictive force, which makes the nonlinear polarization third order.

The density variation is found by solving the driven acoustic wave equation in the slowly varying amplitude approximation, with $|\Delta\rho| \ll \rho_0$. A key intermediate step is given by [2]

$$-i2\Omega \frac{\partial\Delta\rho}{\partial t} + (\Omega_B^2 - \Omega^2 - i\Omega\Gamma_B)\Delta\rho - i2Kv_a^2 \frac{\partial\Delta\rho}{\partial z} = \gamma_e K^2 A_L A_B^* \quad (26)$$

Since the density wave is highly damped (see Section I above), it is common to consider the interaction over a short distance where the source term on the right-hand side of Eq. (26) is approximately constant, and the $\partial(\Delta\rho)/\partial z$ term is thus ignored [2–4]. Steady state is also assumed, which allows the time derivative term to be set equal to zero. The result for the density variation is, remembering $\omega_L - \omega_B = \Omega$,

$$\Delta\rho(z) \simeq \gamma_e K^2 \frac{A_L(z) A_B^*(z)}{\Omega_B^2 - (\omega_L - \omega_B)^2 - i(\omega_L - \omega_B)\Gamma_B} \quad (27)$$

This expression for $\Delta\rho$ is used in the nonlinear polarizations of Eqs. (24) and (25). The coupled wave equations for the laser and Brillouin fields are then developed in the slowly varying amplitude approximation, with the results given in terms of a third order Brillouin susceptibility:

$$\frac{dA_L}{dz} = i \frac{3\omega_L}{n_L c} \chi_B^{(3)} |A_B|^2 A_L \quad (28)$$

$$\frac{dA_B^*}{dz} = i \frac{3\omega_B}{n_B c} \chi_B^{(3)} |A_L|^2 A_B^* \quad (29)$$

Expressions for the Brillouin susceptibility are given in Table 3. By Eq. (29), gain or loss of the Brillouin wave will be determined by the imaginary part of the Brillouin susceptibility. Note that in contrast to the Raman susceptibility, discussed in Chapter 14, $\text{Im}(\chi_B^{(3)}) > 0$. Hence gain can occur only for propagation in the backward direction.

Equations for the laser and Brillouin wave intensities can be developed from Eqs. (28) and (29):

$$\frac{dI_L}{dz} = -g_B^e I_L I_B \quad (30)$$

$$\frac{dI_B}{dz} = -g_B^e I_L I_B \quad (31)$$

where g_B^e is the electrostrictive component of the Brillouin gain intensity factor. This quantity is given in Table 3. In the development of these equations, the approximation $\omega_B \approx \omega_L$ has been used. An immediate consequence of Eqs. (30) and (31) is the invariant

$$I_L(z) - I_B(z) = \text{constant} \quad (32)$$

However, in the nondepleted pump approximation ($I_L = \text{constant}$), the backward propagating Brillouin wave experiences exponential gain, as shown by the formula in Table 3.

C. Thermal Contributions to Brillouin Gain

In an absorptive medium, linear absorption followed by thermalization of the energy leads to temperature and thus density waves that can also drive SBS. Both absorptive and electrostrictive contributions must then be considered. The analysis requires solutions of the coupled Navier–Stokes and heat transport equations, using also the equation of continuity for fluid flow [2]. The result is

that the Brillouin gain intensity factor has two terms:

$$g_B = g_B^e + g_B^a \quad (33)$$

where g_B^e is the electrostrictive part introduced in the last section, and the absorptive contribution is given by g_B^a . Expressions for this factor are also given in Table 3. Included in these formulas are factors corresponding to the specific heat at constant pressure, c_p , and the volume expansion coefficient at constant pressure, $\beta_p = \rho^{-1}(\partial\rho/\partial T)_p$.

Note that g_B^e has a maximum at $\omega_L - \omega_B = \Omega_B$, while g_B^a peaks at $\omega_L - \omega_B = -\Gamma_B/2$. In fact, the absorptive part leads to loss ($g_B^a < 0$) for $\omega_L - \omega_B < \Omega_B$. The absorptive component of g_B can be made strong by simply increasing the absorption coefficient α by, for example, doping a liquid with a small amount of absorbing dye. For an approximately constant pump intensity, the Brillouin wave will only experience gain for $g_B I_L > \alpha$, as shown by the formula in Table 3.

III. LASER-BRILLOUIN WAVE COUPLING

For high efficiency generation of the Brillouin wave by SBS, pump depletion cannot be ignored. Then the coupled wave equations must be solved simultaneously. Using the relation given by Eq. (32), the laser intensity at some point z in the medium can be expressed as

$$I_L(z) = I_L(0) + I_B(z) - I_B(0) \quad (34)$$

It should be noted that $I_B(0)$ is the output Brillouin wave intensity.

The solutions to the coupled wave equations in the pump depletion region are given in Table 3. Notice that the solution is a transcendental equation. This can be solved numerically to yield the relative Brillouin output $I_B(0)/I_L(0)$ as a function of the input gain-length product $g_B^e I_L(0)L$, parameterized by the relative Brillouin input $I_B(L)/I_L(0)$. The behavior of these solutions is shown in Fig. 3 for various values of input. It should be emphasized that these are solutions for the case of no absorption, and hence the gain-length product involves only the electrostrictive component of the Brillouin gain intensity factor.

Note that the Brillouin wave experiences exponential gain initially but then saturates as the pump becomes depleted, and $I_B(0) \rightarrow I_L(0)$. The limit of the output is actually $I_B(0) = (\omega_B/\omega_L)I_L(0)$, with the small fraction of the input intensity ($\Omega/\omega_L \sim 10^{-6}$) dissipated as heat in the medium by viscous forces.

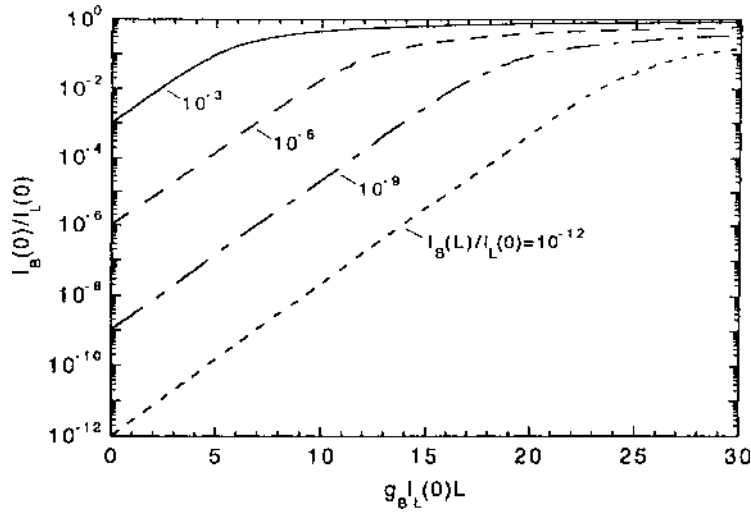


Figure 3 Relative Brillouin wave intensity output for backward SBS as a function of the Brillouin gain-length product for various values of relative input Brillouin wave intensity.

In the general case, absorption is included along with the full Brillouin gain intensity factor. The coupled intensity equations then become

$$\frac{dI_L}{dz} = -g_B I_L I_B - \alpha I_L \quad (35)$$

$$\frac{dI_B}{dz} = -g_B I_L I_B + \alpha I_B \quad (36)$$

These equations must be solved numerically.

SBS generator. Boyd [2] discusses the case where the input $I_B(L)$ is due to noise photons (i.e., spontaneous Brillouin scattering near $z = L$). He estimates that the input noise is $I_B(L)/I_L(0) \sim 10^{-12}-10^{-11}$. A gain-length product of $g_B I_L(0)L \sim 25-30$ would be required to amplify this noise to a level comparable to the incident laser intensity.

Figure 4 shows the curves of Fig. 3 plotted on a linear scale. These plots illustrate the threshold behavior of SBS, even in the absence of absorption. Note that for $I_B(L)/I_L(0) = 10^{-12}$, the Brillouin output is nearly zero until the gain-length product is of the order of 25–30 where $I_B(0)$ grows appreciably. For example, in a 5 cm cell of CS₂, for which $g_B^e = 0.13 \text{ cm/MW}$ [3,4], the input intensity required to achieve an SBS generator would be $I_L(0) \sim 40 \text{ MW/cm}^2$.

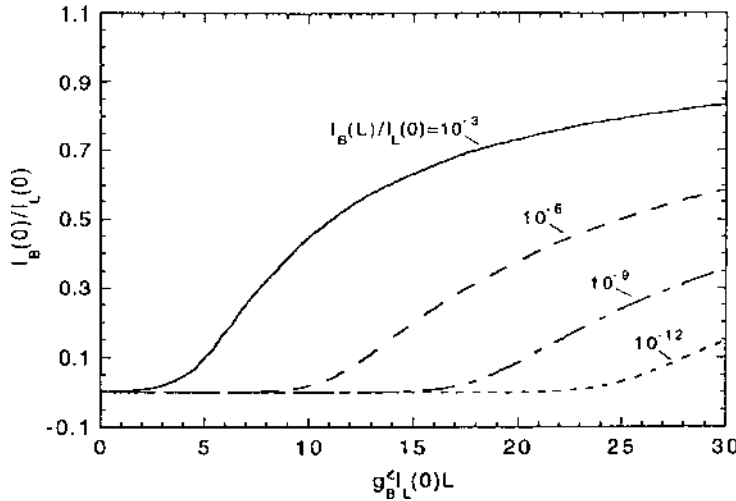


Figure 4 The plot of Fig.3 shown on a linear output scale.

With nanosecond and picosecond lasers, SBS often occurs in the transient regime rather than a quasi-steady state as treated here. Several authors have examined transient SBS. See, for example, Refs. 6–9.

IV. APPLICATIONS

A. Optical Phase Conjugation

Optical phase conjugation was introduced in Chapter 6, Section III.B. Properties of the phase conjugate wave are discussed in that chapter. The technique employed in Chapter 6 was degenerate four-wave mixing (DFWM).

Optical phase conjugation by SBS was discovered in 1972 by Zel'dovich et al. [10]. In their experiment, they focused an aberrated ruby laser beam into a 1 m long multimode waveguide (4×4 mm) filled with 125 atm of methane gas. When the generated backward Brillouin wave was passed back through the aberrator, the resultant beam replicated the incident unaberrated laser beam in the far field. In other words, the backward Brillouin wave behaved as the phase conjugate to the aberrated pump wave.

In DFWM, the phase conjugate of the probe wave appears naturally in the theory as the generated wave counterpropagating to the incident probe wave. The physical interpretation of this in terms of real-time holography was given in Chapter 6. This is not the case for phase conjugation by SBS. As seen by Eq. (29),

the phase conjugate of the incident pump wave does not appear in the equation describing the growth of Brillouin wave. In fact, it would appear from the form of Eq. (29) that pump phase information has been lost. Note also that phase conjugation by SBS apparently does not require the overlap of several incident beams. It merely requires the input of a pump beam, and the Brillouin phase conjugate beam arises naturally counterpropagating to the pump.

Phase conjugation by SBS actually works better the more aberrated the pump. The reasons for this phase conjugation are subtle. Zel'dovich et al. [10] were the first to offer an explanation of the phenomenon, and the theory was further advanced by Sidorovich [11].

Two basic properties of SBS underlie the phase conjugation phenomenon. First is the high gain inherent in the SBS process. Second is the sensitivity of the gain to the local pump intensity [12]. This can be illustrated by examining the growth equation for the total power in the Brillouin wave. It is assumed that the intensities of the pump and Brillouin waves are nonuniform. Let $f(\mathbf{r}_\perp, z)$ be a normalized function describing the intensity distribution of a wave, where \mathbf{r}_\perp is a vector coordinate transverse to the direction of propagation (i.e., the z -direction). Eq. (31) is integrated over the beam area to obtain

$$\frac{d\mathcal{P}_B(z)}{dz} = -g_B^{\text{eff}} \mathcal{P}_L(z) \mathcal{P}_B(z) \quad (37)$$

where

$$g_B^{\text{eff}} = g_B \frac{\iint f_L(\mathbf{r}_\perp, z) f_B(\mathbf{r}_\perp, z) d^2\mathbf{r}}{\iint f_L(\mathbf{r}_\perp, z) d^2\mathbf{r} \iint f_B(\mathbf{r}_\perp, z) d^2\mathbf{r}} \quad (38)$$

The factor containing integrals in Eq. (38) is basically a correlation function for the two intensity distributions. If the two intensity distributions are totally uncorrelated, the effective Brillouin gain intensity factor is zero, and there would be no net power growth in the Brillouin wave. The gain will be a maximum if the two intensity distributions are perfectly correlated, i.e., if $f_B(\mathbf{r}_\perp, z) = f_L(\mathbf{r}_\perp, z)$. The selectivity of the Brillouin gain intensity factor driven by a highly aberrated pump wave favors the growth of this type of Brillouin wave.

This fact may be visualized further by the illustration in Fig. 5. When a beam with an aberrated wave is focused into the far field, a speckle pattern is developed in the focal region [2,12]. The aberrated phase front produces inhomogeneities $\Delta\theta(\mathbf{r}_\perp)$ in the beam divergence angle. The speckles have a typical transverse dimension of $\sim \lambda/(\Delta\theta)^2$ and a longitudinal dimension of $\lambda/\Delta\theta$. These dimensions are assumed to be small compared to the interaction region in a Brillouin medium. By the discussion above, the gain will be a maximum if the Brillouin wave amplitude is related to the pump wave amplitude in this region by $|A_B(\mathbf{r}_\perp, z)| = \text{const} \times |A_L(\mathbf{r}_\perp, z)|$. Since the pump and Brillouin

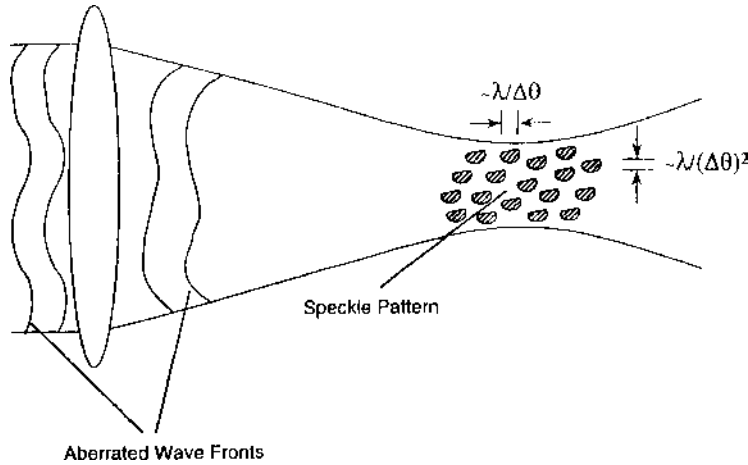


Figure 5 Speckle pattern formed at the focus of a beam for a wave with an irregular, inhomogeneous wave front.

waves both diffract over the interaction region, with the Brillouin wave counterpropagating to the pump, it follows that the condition for maximum spatial overlap of the two waves over the entire interaction region is $A_B(\mathbf{r}_\perp, z) = \text{const} \times A_L^*(\mathbf{r}_\perp, z)$.

At the end of the SBS cell, several different Brillouin waves are created by spontaneous Brillouin scattering. By the discussion of the SBS generator in Section III, the growth of the Brillouin power from noise to a value of the order of the incident pump power requires a net amplification $\sim e^{30}$. It turns out that the effective gain power factor for the wave of maximum spatial overlap (i.e., the conjugate wave) is about a factor of 2 larger than that for any other type of wave [12]. Hence the amplification of the phase conjugate is $\sim e^{15} \simeq 3 \times 10^6$ times larger than any other wave created from noise. Thus a highly aberrated pump wave favors the amplification of a unique wave that is the phase conjugate Brillouin wave.

A typical SBS phase conjugate mirror (Brillouin mirror) is shown in Fig. 6. Often, the cell is in the form of a multimode waveguide to concentrate the pump intensity over a long interaction region in the gain medium. The Brillouin medium is often a gas (e.g., methane, nitrogen, etc.) at high pressure (several atmospheres). Because of the simplicity of this form of phase conjugate mirror and its ability to correct phase aberrations in laser systems (especially high-energy systems), a significant amount of research has been devoted to its development and application. Recently, a commercial product has appeared. The Coherent Infinity™ Nd:YAG laser has a high pressure gas SBS phase conjugate

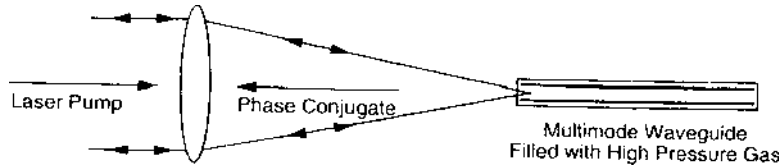


Figure 6 Schematic illustration of a typical Brillouin mirror.

mirror as part of the optical train. This high energy (500 mJ) Q-switched laser has a nearly diffraction-limited output beam.

Two important parameters characterize the output from a Brillouin phase conjugate mirror: the mirror reflectance R and the phase conjugate fidelity F . The reflectance is given by

$$R = \frac{\mathcal{E}_B}{\mathcal{E}_L} \quad (39)$$

where \mathcal{E}_B (\mathcal{E}_L) is the total energy in the Brillouin (laser) beam. The reflectance of a Brillouin mirror can be quite high, approaching unity.

The fidelity (or phase conjugate fraction) measures the quality of the phase conjugate beam, or the amount by which it faithfully replicates the incident pump wave in the far field. Zel'dovich et al. [13] have given the definition

$$F = \left(\frac{\mathcal{E}_L}{\mathcal{E}_B} \right) \left(\frac{B_B}{B_L} \right) = R^{-1} \left(\frac{B_B}{B_L} \right) \quad (40)$$

where B is the beam brightness or radiance, measured in $\text{W/m}^2\text{-strad}$ (or $\text{W/cm}^2\text{-strad}$ in mixed units). Eq. (40) basically states that the fidelity is the ratio of the brightness to the total beam energy for the conjugate wave normalized to the same ratio for the laser as measured in the far field. Mangir and Rockwell [14] have defined the fidelity in terms of the energy contained in the central lobe of the far field beam:

$$F = \left(\frac{\mathcal{E}_L}{\mathcal{E}_B} \right) \left(\frac{\mathcal{E}_B^c}{\mathcal{E}_L^c} \right) = R^{-1} \left(\frac{\mathcal{E}_B^c}{\mathcal{E}_L^c} \right) \quad (41)$$

where \mathcal{E}^c is the energy contained in the center lobe.

A typical experimental arrangement for measuring these quantities is shown in Fig. 7. A phase aberration plate is employed as shown (e.g., a HF-etched piece of glass to produce phase aberrations $\delta\phi(\mathbf{r}_\perp) = 2\pi(n - 1)\delta L(\mathbf{r}_\perp)/\lambda \sim 2\pi$, where $\delta L(\mathbf{r}_\perp)$ is the inhomogeneous thickness variation of the plate). The phase conjugate reflectance R is determined by calorimetric measurements of the total beam energies. The phase conjugate fidelity F is determined by recording the beam spatial profiles in the far field on film or a CCD camera. Another approach

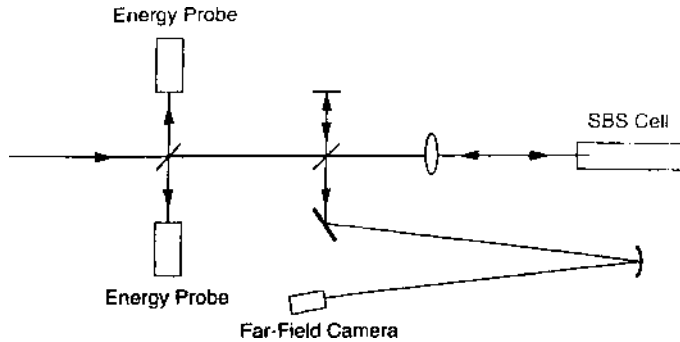


Figure 7 Schematic illustration of the measurement of the phase conjugate reflectance (R) and beam fidelity (F) in a phase conjugation experiment.

is to measure the total beam energies passing through an appropriately sized aperture in the far field. This technique is sensitive to errors produced by beam angular jitter. The limited dynamic range of the camera or film can be overcome by appropriately attenuating the beams. The measurements can also be calibrated by replacing the Brillouin mirror with an ordinary 100% reflector [14].

B. Brillouin-Enhanced Four-Wave Mixing

Brillouin-enhanced four-wave mixing (BEFWM) is a form of nearly degenerate four-wave mixing (DFWM). A general four-wave mixing interaction is shown in Fig. 8. Similar geometries were considered in Chapter 6, Section III.B. Note the similarity to DFWM with the forward and backward pump waves (E_f and E_b , respectively), the probe wave E_p , and the signal wave E_s . In the general case, all waves may have different frequencies ($\omega_f, \omega_b, \omega_p, \omega_s$).

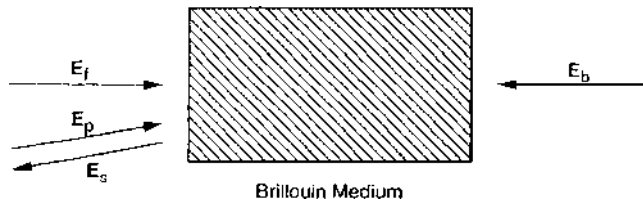


Figure 8 A four-wave mixing interaction of the type used in Brillouin-enhanced four-wave mixing.

Of all the possible mixing terms, consider the nonlinear polarization that oscillates at $\omega_s = \omega_f + \omega_b - \omega_p$. Then $E_s \propto E_p^*$ since the polarization must be proportional to $E_f E_b E_p^*$ to be oscillating at ω_s . If the probe wave is anti-Stokes shifted from the pump waves, such that $\omega_f = \omega_b \equiv \omega$, and $\omega_p \equiv \omega + \Delta\omega$, then the signal frequency is $\omega_s = \omega - \Delta\omega$, i.e., it is Stokes shifted from the pump beams. Another possibility, considered by Skeldon et al. [15], is the case where $\omega_f \equiv \omega$, $\omega_b \equiv \omega - 2\Delta\omega$, and $\omega_p \equiv \omega - \Delta\omega$. Then the signal wave is again Stokes shifted from the forward pump wave, $\omega_s = \omega - \Delta\omega$.

When $\Delta\omega \sim \Omega \sim \Omega_B$, i.e., an acoustic frequency of the order of the Brillouin frequency, then the four-wave mixing process is called BEFWM. There will then be a phase mismatch between the driving nonlinear polarization and the signal wave of $|\Delta\mathbf{k}| = |(\mathbf{k}_f + \mathbf{k}_b - \mathbf{k}_p - \mathbf{k}_s)\hat{z}| = 2n\Omega/c$. Physically, the probe wave beats with the backward pump to form an interference grating propagating in the backward direction (counter to the backward pump) at an acoustic velocity. This drives an acoustic wave, through the electrostrictive force, at a frequency Ω . This acoustic wave is much larger than thermal phonons and thus is the dominant source in the nonlinear polarization that drives an SBS process. The forward pump and signal waves are thus the appropriate pump and Brillouin waves, respectively, and the signal wave is amplified by SBS. The signal wave is also the phase conjugate of the probe wave, and the phase conjugate reflectance $R = |E_s|^2/|E_p|^2$ can be very large due to the amplification of E_s . This is the technological significance of BEFWM.

In principle, DFWM can also yield a large phase conjugate reflectance, but in practice the values are limited to ~ 100 . The reason is that the conditions for very high reflectance in DFWM are very precise and not feasible to achieve with real optical beams. By contrast, BEFWM can yield $R \sim 10^6$, can conjugate extremely weak probe beams (energy $\sim 10^{-14}$ J), and can efficiently transfer energy from the pump to the conjugate wave ($> 70\%$). Scott and Ridely [16] cite other advantages of BEFWM over DFWM, including its independence of the Kerr-type nonlinearity that can produce self-focusing and thereby degrade both the pump and conjugate waves.

A steady-state analysis of BEFWM in the nondepleted pump regime has shown that under conditions of high pump intensities, i.e., $|g_B^e(I_f - I_b)| \gg |\Delta k|$ and $\exp[g_B^e(I_f + I_b)L] \gg 1$ and I_f/I_b , the phase conjugate reflectance is $R \approx I_f/I_b$ [15,17]. Thus the phase conjugate reflectance can be larger than 1 if $I_f > I_b$, according to the steady-state analysis.

Reflectances larger than this ratio have been observed, however. Scott and Ridely [16] have given an extensive review of BEFWM research and maintain that the steady-state analysis cannot account for very high reflectances. They describe a transient analysis of the acoustic wave that shows that above a critical pump intensity an acoustic instability causes a nearly exponential growth, in time, of the signal wave until “saturation,” when the pump experiences

significant depletion. The exponential growth rate coefficient is given by [16]

$$\gamma_0 = \frac{1}{2} \Gamma_B \left(\frac{M}{M_{cr}} - 1 \right) \quad (42)$$

where Γ_B is the Brillouin line width, $M = g_B^e (I_f + I_b)L$, and M_{cr} is the value corresponding to the critical intensity. M_{cr} depends on the ratio I_f/I_b and the phase mismatch, and it shows a minimum value for $\Delta kL \approx 5$ [16].

The acoustic instability arises because of the way the acoustic wave interacts with the pump waves. The acoustic wave is attenuated by viscous damping forces as well as when the backward pump wave scatters from it to add to the anti-Stokes-shifted probe wave. On the other hand, the acoustic wave is amplified by the beating of the forward pump wave with the signal wave, through the electrostrictive force. Above a critical pump intensity, the acoustic amplification exceeds the attenuation, and the acoustic wave grows explosively until pump depletion. Hence there is a corresponding rapid growth of the signal wave.

The exponential growth rate is larger when the probe wave is counterpropagating to the weaker pump wave. Thus $I_f > I_b$ is chosen for the experimental condition. The reason this is so is as follows. An anti-Stokes-shifted probe wave will drive an acoustic wave in the same direction in which it propagates. The beating of E_f with E_p amplifies this acoustic wave, whereas the anti-Stokes scattering of E_b from this wave attenuates it. Hence the acoustic wave will grow more rapidly if $I_f > I_b$ rather than if $I_f < I_b$.

In a typical BEFWM experiment, the probe beam will be a small part of the incident laser beam picked off with a beam splitter. The forward pump beam, Stokes shifted from the probe (laser), is created by “reflection” from a separate Brillouin mirror (SBS generator). A portion of the forward pump beam that has passed through the BEFWM cell is retroreflected and attenuated to form the backward pump. More details on this subject can be found in the literature [15–38].

REFERENCES

1. I. L. Fabelinski, *Molecular Scattering of Light*, Plenum Press, New York, 1968.
2. R. W. Boyd, *Nonlinear Optics*, Academic Press, New York, 1992, pp. 325–364.
3. Y. R. Shen, *The Principles of Nonlinear Optics*, John Wiley, New York, 1984, pp. 187–192.
4. J. F. Reintjes, Stimulated Raman and Brillouin Scattering, *Handbook of Laser Science and Technology, Supplement 2: Optical Materials* (M. J. Weber, eds), CRC Press, Boca Raton, FL, 1995, pp. 346–364.

5. D. Corson and P. Lorrain, *Introduction to Electromagnetic Fields and Waves*, W. H. Freeman, San Francisco, 1962, p. 116.
6. M. M. Kroll, Excitation of hypersonic vibrations by means of photoelastic coupling of high intensity light waves to elastic waves, *J. Appl. Phys.* 36:34 (1965).
7. G. W. Faris, M. J. Dyer, and A. P. Hickman, Transient effects on stimulated Brillouin scattering, *Opt. Lett.* 17:1049 (1992).
8. D. Pohl, M. Maier, and W. Kaiser, Transient and steady-state gain in stimulated Brillouin amplifiers, *IEEE J. Quant. Electron.* QE-14:320 (1968).
9. D. Pohl and W. Kaiser, Time-resolved investigations of stimulated Brillouin scattering in transparent and absorbing media: determination of phonon lifetimes, *Phys. Rev. B* 1:31 (1970).
10. B. Ya. Zel'dovich, V. I. Popovichev, V. V. Ragal'skii, and F. S. Faizullov Connection between the wave fronts of the reflected and exciting light in stimulated Mandelshtam–Brillouin scattering, *Sov. Phys. JETP* 15:109 (1972).
11. V. G. Sidorovich, Theory of the Brillouin mirror, *Sov. Phys. Tech. Phys.* 21:1270 (1976).
12. B. Ya. Zel'dovich, N. F. Pilipetski, and V. V. Shkunov, Experimental investigation of wave-front reversal under stimulated scattering, *Optical Phase Conjugation* (R. A. Fisher, eds), Academic Press, New York, 1983, pp. 135–168.
13. B. Ya. Zel'dovich, N. F. Pilipetski, and V. V. Shkunov, *Principles of Optical Phase Conjugation*, Springer-Verlag, New York, 1985, p. 106.
14. M. S. Mangir and D. A. Rockwell, 4.5-J Brillouin phase-conjugate mirror producing excellent near- and far-field fidelity, *J. Opt. Soc. Am. B* 10:1396 (1993).
15. M. D. Skeldon, P. Narum, and R. W. Boyd, Non-frequency-shifted, high-fidelity phase conjugation with aberrated pump waves by Brillouin-enhanced four-wave mixing, *Opt. Lett.* 12:343 (1987).
16. A. M. Scott and K. D. Ridely, A review of Brillouin-enhanced four-wave mixing, *IEEE J. Quant. Electron.* 25:438 (1989).
17. A. M. Scott, Efficient phase conjugation by Brillouin enhanced four-wave mixing, *Opt. Commun.* 45:127 (1983).
18. N. F. Andreev, V. I. Bespalov, A. M. Kiselev, A. Z. Matveev, G. A. Pasmanik, and A. A. Shilov, Wavefront inversion of weak optical signals with a large reflection coefficient, *Sov. Phys. JEPT Lett.* 32:625 (1981).
19. V. I. Bespalov, A. Z. Matveev, and G. A. Pasmanik, Limiting sensitivity of a stimulated-Brillouin-scattering amplifier and a four-wave hypersonic phase-conjugating mirror, *Radiophys. Quant. Electron.* 29:818 (1987).
20. N. F. Andreev, V. I. Bespalov, M. A. Dvoretskii, and G. A. Pasmanik, Four-wave hypersonic reversing mirrors in the saturation regime, *Sov. J. Quant. Electron.* 14:999 (1984).
21. V. I. Bespalov and G. A. Pasmanik, Wavefront inversion and the problem of shaping the structure of laser radiation, *Bull. Acad. Sci. USSR Phys. Ser. A.* 17 (1980).
22. B. Ya. Zel'dovich, M. A. Oriova, and V. V. Shkunov, Nonstationary theory and calculation of the time of establishment of four-wave wavefront reversal, *Sov. Phys. Dokl.* 25:390 (1980).

23. B. Ya. Zel'dovich and A. A. Shkunov, Characteristics of stimulated scattering in opposite pump beams, *Sov. J. Quant. Electron.* 12:223 (1982).
24. V. I. Bespalov, E. L. Bubis, S. N. Kalugina, V. G. Manishin, A. Z. Mateev, G. A. Pasmanik, P. S. Razenshtain, and A. A. Shilov, Stimulated Brillouin scattering in a field of opposite light waves, *Sov. J. Quant. Electron.* 12:1544 (1982).
25. J. R. Ackerman, Optimization of the field of view of a Brillouin-enhanced four-wave-mixing phase conjugator, *Opt. Lett.* 19:2015 (1994).
26. J. R. Ackerman, Demonstration of the spectral and the geometrical criteria that control high-reflectivity Brillouin-enhanced four-wave mixing, *J. Opt. Soc. Am. B* 11:1000 (1994).
27. S. Sternklar, Double phase conjugation and double color-pumped oscillation in Brillouin four-wave mixing: theory and demonstration, *Opt. Lett.* 17:1403 (1992).
28. R. D. Rikley, A. M. Scott, and D. C. Jones, Frequency detuning in Brillouin induced four-wave mixing, *Int. J. Nonlinear Opt. Phys.* 1:563 (1992).
29. M. Winter, Nearly degenerate four-wave mixing using phase-conjugate pump beams, *Opt. Lett.* 17:320 (1992).
30. I. Yu. Anikeev, D. A. Glazkov, I. G. Zubarev, and S. I. Mikhailov, Kinetics of the evolution of an absolute instability due to the Brillouin nonlinearity under four-wave mixing, *Sov. J. Quant. Electron.* 21:651 (1991).
31. J. P. Dansereau, L. S. Hills, and S. A. Mani, Analysis of Brillouin-enhanced four-wave mixing phase conjugate systems, *Proc. SPIE* 1409:67 (1991).
32. P. S. Lebow and J. R. Ackerman, Spectral characteristics of Brillouin-enhanced four wave mixing for pulsed and CW inputs, *Proc. SPIE* 1409:60 (1991).
33. D. C. Jones, G. Cook, K. D. Ridley, and A. M. Scott, High-power beam steering using phase conjugation through Brillouin-induced four-wave mixing, *Opt. Lett.* 16:1551 (1991).
34. J. R. Ackerman, Observation and compensation of frequency detuning in high-reflectivity Brillouin enhanced four-wave mixing, *J. Opt. Soc. Am. B* 8:1028 (1991).
35. R. W. F. Gross, S. T. Amimoto, and L. Garman-DuVall, Gain and phase-conjugation fidelity of a four-wave Brillouin mirror based on methane, *Opt. Lett.* 16:94 (1991).
36. R. B. Holmes, A perturbation analysis of polarization-decoupled Brillouin-enhanced four wave mixing, *IEEE J. Quant. Electron.* 26:1980 (1990).
37. D. E. Watkins, Effect of signal frequency on four-wave mixing through stimulated Brillouin scattering, *Opt. Lett.* 15:1267 (1990).
38. W. A. Schroeder, M. J. Damzen, and M. H. R. Hutchinson, Polarization-decoupled Brillouin-enhanced four-wave mixing, *IEEE J. Quant. Electron.* 25:460 (1989).

16

Properties of Selected Stimulated Light-Scattering Materials

This chapter presents gain intensity factors and related parameters for stimulated Raman and Brillouin scattering in selected materials. Data have been extracted from several sources. Raman and Brillouin gain factors for several liquids, gases, and solids can be found in Refs. 1 and 2 (Ref. 2 contains Raman data only). Specific formulas and data for differential Raman scattering cross-sections, Raman line widths, and Raman frequency shifts, including temperature and density dependence, for H₂ and N₂ can be found in Ref. 1. Raman shifts for several liquids, solids, and gases are listed in Ref. 2.

I. STIMULATED RAMAN SCATTERING

Raman gain measurements typically include the Raman frequency shift ω_v , the Raman linewidth Γ_R , and either the Stokes gain intensity factor g_s or the differential scattering cross-section $d\sigma/d\Omega$. Some gain factors are computed from $d\sigma/d\Omega$ (see Chapter 14).

Selected data for several materials, including gases, liquids, and solids, are given in Table 1. The material most studied and often used in experiments is H₂.

The line widths and frequency shifts are typically given at the stated density or pressure, for gases, and room temperature. The frequency shift in gases typically has the form [6]

$$\omega_v \sim \omega_v(0) + D\rho + E\rho^2$$

Table 1 Raman Gain Intensity Factor for Some Selected Materials

Material ^a	λ_L (nm) ^b	λ_S (nm) ^c	$\alpha\sqrt{2\pi c}$ (cm ⁻¹) ^d	$\Gamma_R/2\pi$ (GHz) ^e	g_s (10 ⁻⁹ cm W ⁻¹) ^f	Ref.
Arsenic sulfide (As ₂ S ₃) glass fiber	1545	1632	344	1580	0.44	[3]
Carbon tetrafluoride gas, CF ₄	248	254	908	0.020	0.008 amagat ⁻¹ _g	[4]
Deuterium gas, D ₂ ($\rho = 60$ amagat)	532	633	2987	7.2	0.45 ± 0.05	[10]
Germane gas, GeH ₄	248	262	2111	0.015	0.27 amagat ⁻¹ _g	[4]
Hydrogen gas, <i>para</i> -H ₂ (≥ 500 Torr)	10,812 [10R(30) CO ₂ line]	[S(0) mode]			0.042 ± 0.005	[13]
Hydrogen gas, H ₂ ($\rho \geq 20$ amagat)	694	975	4155	6.0	1.5	[5]
Hydrogen gas, H ₂ ($\rho = 20$ amagat)	532	683	4155	1.1	2.5 ± 0.4	[6]
Hydrogen gas, H ₂ ($\rho = 60$ amagat)	532	683	4155	3.1	2.64 ± 0.20	[10]
Hydrogen gas, H ₂	530	680	4155		1.8 ± 0.4	[7]
Hydrogen gas, H ₂ ($\rho = 20$ amagat)	477	595	4155	1.1	3.5 ± 0.3	[6]
Hydrogen gas, H ₂	353	414	4155		5.0 ± 0.5	[6]
Hydrogen gas, H ₂ ($\rho = 20$ amagat)	308	353	4155	1.1	6.6 ± 0.8	[6]
Hydrogen gas, H ₂	265	298	4155		5.5 ± 1.6	[6]
Liquid benzene, C ₆ H ₆	694	746	992		2.8 ^g	[8]
Liquid carbon disulfide, CS ₂	694	727	655.6	15.0	24 ^g	[8]
Liquid nitrogen, N ₂	694	828	2326.5	2.0	16 ± 5	[8]

Liquid nitrogen, N ₂	694	828	2326.5	2.0	17 ± 5 ^g	[8]
Liquid oxygen, O ₂	694	776	1522	5.3	16 ± 5	[8]
Liquid oxygen, O ₂	694	776	1522	5.3	14.5 ± 4 ^g	[8]
Methane gas, C ₄ H ₄ (20–40 atm)	532	630	2916.4–2917.9	36	0.20–0.34	[9]
Methane gas, C ₄ H ₄ ($\rho = 115$ amagat)	532	630	2917	52	1.26 ± 0.10	[10]
Methane gas, C ₄ H ₄	248	267	2917	9.0	0.12 amagat ^{-1g}	[11]
Nitrogen gas, N ₂	248	263	2327	0.0225	0.003 amagat ^{-1g}	[11]
Oxygen gas, O ₂	248	258	1552	0.054	0.012 amagat ^{-1g}	[11]
Silane gas, SiH ₄	248	262	2186	0.015	0.19 amagat ^{-1g}	[11]
Silica fiber	795.5	824.6	440	7080	0.0012 ± 0.0001	[12]
Sulfur hexafluoride, SF ₆	248	253	775	0.030	0.014 amagat ^{-1g}	[11]
Titanium dioxide, TiO ₂ (rutile, $E \perp c$)	1054	1127	612	0.83	0.83	[14]

^a Density in amagats (1 amagat = 0.044617 g mol/L = 2.7037×10^{19} molecules/cm³).

^b Laser pump wavelength.

^c Raman Stokes wavelength.

^d Raman frequency shift.

^e Raman line width.

^f Raman (Stokes) gain intensity factor.

^g Calculated from measured differential scattering cross-section, $d\sigma/d\Omega$, at laser wavelength, or scaled from measurement of $d\sigma/d\Omega$ at different wavelength.

Table 2 Brillouin Gain Intensity Factor for Some Selected Materials

Material ^a	λ_L (nm) ^b	$\Omega_B/2\pi$ ^c (GHz)	$\Gamma_B/2\pi$ ^d (MHz)	g_B (10^{-9} cm W $^{-1}$) ^e	Ref.
Acetone	1060	2.987	119 ± 5	15.8	[15]
Acetone	694	4.60	180	20	[16]
Acetone	694	1.60		10.8	[17]
Acetone	532	6.0	320	20	[18]
Benzene	1060	4.124	228	9.6	[15]
Benzene	694	6.47	289	18	[17]
Borate glass, 4.97Li ₂ O-94.27B ₂ O ₃ -0.13Al ₂ O ₃	488	19.04	100	12.88 ^f	[19]
Borate glass, 7.46Li ₂ O-91.79B ₂ O ₃ -0.13Al ₂ O ₃	488	18.98	116	14.29 ^f	[19]
Borate glass, 7.48Li ₂ O-91.17B ₂ O ₃ -0.13Al ₂ O ₃	488	17.54	113	11.74 ^f	[19]
Borate glass, 7.48Li ₂ O-81.80B ₂ O ₃ -10.09Al ₂ O ₃	488	22.69	124	10.93 ^f	[19]
Borate glass, 9.98Li ₂ O-89.28B ₂ O ₃ -0.12Al ₂ O ₃	488	20.52	138	12.66 ^f	[19]
Borate glass, 14.97Li ₂ O-84.31B ₂ O ₃ -0.12Al ₂ O ₃	488	23.31	104	3.441 ^f	[19]
Borate glass, 10K ₂ O-90B ₂ O ₃	488	18.26	104	8.169 ^f	[19]
Borate glass, 30K ₂ O-70B ₂ O ₃	488	21.36	134	4.675 ^f	[19]
Calcium fluoride	532	37.2	46	4.11 ± 0.65	[20]
Carbon disulfide	1060	3.761	50	68	[15]
Carbon disulfide	694	5.85	75	130	[16]
Carbon disulfide	694	5.85	66.4	45	[17]
Carbon disulfide	532	7.7	120	130	[18]
Carbon tetrachloride	1060	2.772	528	3.8	[15]
Carbon tetrachloride	694	4.39	650	6	[16]
Carbon tetrachloride	694	4.39	556	8	[17]
Cyclohexane	694	5.55	774	6.8	[17]
Fused silica	532	32.6	168	2.69 ± 0.22	[20]
Halide glass, 62ZrF ₄ -33BaF ₂ -5LaF ₃	488	17.64	213.6	2.832 ^f	[19]

Halide glass, 57ZrF ₄ –36BaF ₂ –3LaF ₃ –4AlF ₃	488	17.80	98.7	1.713 ^f	[19]
Halide glass,	488	18.82	96.0	3.608 ^f	[19]
55.8ZrF ₄ –14.4BaF ₂ –5.8LaF ₃ –3.8AlF ₃ –20.2NaF					
Halide glass, 62HF ₄ –33BaF ₂ –5LaF ₃	488	15.83	[151].4	1.127 ^f	19
Halide glass, 57HF ₄ –36BaF ₂ –3LaF ₃ –4AlF ₃	488	15.63	162.3	0.96 ^f	[19]
Halide glass,	488	17.82	179.5	1.023 ^f	[19]
68.8HfF ₄ –11.5BaF ₂ –3LaF ₃ –3.8AlF ₃ –10.4PbF ₂ –4CsF	488	17.19	52.5	16.02 ^f	[19]
Halide glass, BeF ₂	488	17.61	74.8	11.54 ^f	[19]
Halide glass, 95BeF ₂ –5ThF ₄	488	19.33	42.8	12.44 ^f	[19]
Halide glass, 91BeF ₂ –9ThF ₄	488	18.40	21.3	24.69 ^f	[19]
Halide glass, 88BeF ₂ –12ThF ₄	694		106	17,000	[16]
Lucite				8	[21]
Methane gas (11.0 × 10 ⁶ Pascal = 1600 psi)	1064	0.864	106		
Methanol	694	4.25	250	13	[17]
Methanol	530	5.6	210	13	[18]
<i>n</i> -Hexane	694		220	26	[16]
<i>n</i> -Hexane	694		212	19	[16]
Nitrobenzene	1060	4.255	396	7.2	[15]
Quartz (<i>x</i> -cut)	694		<40	1.5	[16]
Schott glass, BK7	694		80	350	[16]
Schott glass, BK7	532	35.7	165	2.15 ± 0.21	[20]
Schott glass, F2	694		45	2100	[16]
Schott glass, FK3	694		<40	1800	[16]
Schott glass, SF6	694		45	2000	16
Silicate glass ^g , 6K ₂ O–94SiO ₂ (637.8°C@78.56 hr)	488	23.38	184	3.905 ^f	19
Silicate glass ^g , 6K ₂ O–94SiO ₂ (604.8°C@231.8 hr)	488	23.41	186	2.783 ^f	19
Silicate glass ^g , 8K ₂ O–92SiO ₂ (547°C)	488	22.93	175	3.354 ^f	19

(continued)

Table 2 Continued

Material ^a	λ_L (nm) ^b	$\Omega_B/2\pi^c$ (GHz)	$\Gamma_B/2\pi^d$ (MHz)	$(10^{-9} g_B$ $cm W^{-1})^e$	Ref.
Silicate glass ^g , 8K ₂ O–92SiO ₂ (627°C@59.96 hr)	488	22.95	190	3.587 ^f	[19]
Silicate glass ^g , 8K ₂ O–92SiO ₂ (603.5°C@103.42 hr)	488	22.94	177	5.181 ^f	[19]
Silicate glass ^g , 8K ₂ O–92SiO ₂ (589.5°C@141.793 hr)	488	22.89	170	3.704 ^f	[19]
Silicate glass ^g , 8K ₂ O–92SiO ₂ (574.3°C@345.68 hr)	488	22.97	187	4.038 ^f	[19]
Silicate glass ^g , 10K ₂ O–90SiO ₂ (573.4°C@84.66 hr)	488	21.79	208	3.122 ^f	[19]
Silicate glass, SiO ₂	488	25.18	156	4.482 ^f	[19]
Water	1060	3.703	170	3.8	[15]
Water	694	5.69	317	4.8	[17]
Xenon gas (7599 Torr)	532	0.654	98.1	1.38 ± 0.19	[20]

^a Glass compositions given in mole%.^b Laser pump wavelength.^c Brillouin frequency shift.^d Brillouin line width.^e Brillouin gain intensity factor.^f Calculated from Brillouin line width, Brillouin intensity, and Brillouin frequency shift measured in Rayleigh–Brillouin scattering experiments [19].^g Annealing temperature and time given in parentheses.

while the line width can be fitted to a form [10]

$$\Gamma_R \sim A + B\rho + \frac{C}{\rho}$$

where ρ is the density in amagat units and A , B , C , D , and E are constants depending on the material. Also, these parameters can be temperature dependent. See Ref. 1 for the form of these for H₂ and N₂.

II. STIMULATED BRILLOUIN SCATTERING

Stimulated Brillouin scattering measurements typically include the Brillouin frequency shift Ω_B , the Brillouin line width Γ_B , and the Brillouin gain intensity factor g_B . In some cases, the gain factor is calculated. Γ_B , Ω_B , and the Brillouin intensity are measured in a Brillouin scattering experiment. These permit calculations of the phonon attenuation factor, the elastooptic coefficient, and the elastic constants. From these, the gain intensity factor may also be computed [19]. Brillouin frequency shifts are typically on the order of a few GHz, so the Stokes-shifted wavelength is approximately equal to the laser pump wavelength.

Selected data are listed in Table 2. The materials include some typical liquid solvents, some gases, and a few selected glasses.

REFERENCES

1. J. F. Reintjes, Stimulated Raman and Brillouin Scattering, *Handbook of Laser Science and Technology*, Supplement 2: Optical Materials (M. J. Weber, ed), CRC Press, Boca Raton, FL, 1995, pp. 334–364.
2. F. P. Milanovich, Stimulated Raman Scattering, *Handbook of Laser Science and Technology*, Vol. III, Optical materials: Part 1 (M. J. Weber, ed), CRC Press, Boca Raton, FL, 1986, pp. 283–296.
3. M. Asobe, T. Kanamori, K. Naganuma, H. Itoh, and T. Kaino, Third-order nonlinear spectroscopy in As₂S₃ chalcogenide glass fibers, *J. Appl. Phys.* 77:5518 (1995).
4. J. R. Murray, J. Goldhar, D. Eimerl, and A. Szoke, Raman pulse compression of excimer lasers for application to Laser Fusion, *IEEE J. Quant. Electron.* QE-15:342 (1979).
5. N. Bloembergen, G. Bret, P. Lallement, A. Pine, and P. Simova, Controlled stimulated Raman amplification and oscillation in hydrogen gas, *IEEE J. Quant. Electron.* QE-3; 197 (1967); E. E. Hagenlocker, R. W. Minck, and W. G. Rado, Effects of phonon lifetime on stimulated optical scattering in gases, *Phys. Rev.* 154: 226. (1967);
6. W. K. Bischel and M. J. Dyer, Wavelength dependence of the absolute Raman gain coefficient for the Q(1) Transition in H₂, *J. Opt. Soc. Am. B* 3:677 (1986).

7. G. V. Venkin, L. L. Kulyuk, and D. I. Maleev, Investigation of stimulated Raman scattering in gases excited by fourth harmonic of neodymium laser radiation, *Sov. J. Quantum Electron.* 5:1348 (1976).
8. J. B. Grun, A. K. McQuillan, and B. P. Stoicheff, Intensity and gain measurements on stimulated Raman emission in liquid O₂, and N₂, *Phys. Rev.* 180:61 (1969).
9. C.-S. Go, J.-H. Lee, and J.-S. Chang, Raman-amplification and polarization dependence measurement in a methane Raman shifter seeded by a liquid Raman oscillator, *Appl. Opt.* 34:2671 (1995).
10. J. J. Ottusch and D. A. Rockwell, Measurement of Raman gain coefficients of hydrogen, deuterium, and methane, *IEEE J. Quantum Electron.* 24:2076 (1988).
11. J. R. Murray, J. Goldhar, D. Eimerl, and A. Szoke, Raman pulse compression of excimer lasers for application to laser fusion, *IEEE J. Quantum Electron.* QE-15:342 (1979).
12. D. J. Dougherty, F. X. Kartner, H. A. Haus, and E. P. Ippen, Measurement of the Raman gain spectrum of optical fibers, *Opt. Lett.* 20:31 (1995).
13. A. Tsunemi, K. Nagasaka, and H. Tashiro, Precise measurement of the rotational Raman gain coefficient in para-hydrogen by the large-signal method, *Appl. Opt.* 31:4165 (1992).
14. P. Sathy and A. Penzkofer, Three-photon absorption and Its limitation of third-order nonlinear optical effects in rutile, *Appl. Phys. B* 61:127 (1995).
15. A. I. Erohkin, V. I. Kovalev, and F. S. Faizullov, Determination of the parameters of a nonlinear response of liquids in an acoustic resonance region by the method of nondegenerate four wave interaction, *Sov. J. Quantum Electron.* 16:872 (1986).
16. D. Pohl and W. Kaiser, Time-resolved investigations of stimulated brillouin scattering in transparent and absorbing media: determination of phonon lifetimes, *Phys. Rev. B* 1:31 (1970).
17. M. Denariez and G. Bret, Investigation of rayleigh wings and brillouin-stimulated Scattering in Liquids, *Phys. Rev.* 171:160 (1968).
18. P. Narum, M. D. Skeldon, and R. W. Boyd, Effect of laser mode structure on stimulated brillouin scattering, *IEEE J. Quantum Electron.* QE-22:2161 (1986).
19. L.-G. Hwa, J. Schroeder, and X.-S. Zhao, Intrinsic brillouin linewidths and stimulated brillouin gain coefficients in glasses studied by inelastic light scattering, *J. Opt. Soc. Am. B* 6:833 (1989).
20. G. W. Faris, L. E. Jusinski, and A. P. Hickman, High resolution stimulated brillouin gain spectroscopy in glasses and crystals, *J. Opt. Soc. Am. B* 10:587 (1990).
21. R. W. F. Gross, S. T. Amimoto, and L. Garman-DuVall, Gain and phase-conjunction fidelity of a four-wave brillouin mirror based on methane, *Opt. Lett.* 16:94 (1991).

17

Electro-Optic Effects

The previous chapters of this book dealt with phenomena associated with the effects of optical electric fields on the properties of matter. Optical parameters can also be modified by the application of other external stimuli, such as mechanical stress, acoustic waves, low frequency electric fields, and magnetic fields. The study of the effects produced by such stimuli has led to the development of disciplines called acousto-optics, electro-optics, and magneto-optics. Although all of these are of technological significance, the subject of electro-optics has spawned a larger industry and is also more closely related to the subject of nonlinear optics presented in this book. Because electro-optics plays such an important role in the applications of optics today, including many that also employ other aspects of nonlinear optics, it deserves a separate treatment that is given in this chapter.

Electro-optic effects refer to changes in the optical dielectric tensor of a medium when a low frequency (low compared to optical frequencies) or dc electric field is applied to the medium. This is usually achieved by placing the medium between two electrodes and applying a potential difference (a voltage) to the electrodes. In general, the change can refer to changes in both the absorptive and refractive properties of the medium. When the former is important, the effect is called electro-absorption. Although this phenomenon is used in some devices, it will not be considered here. A change of refractive properties of a medium with an applied electric field is an electro-optic effect called electro-refraction. It is this phenomenon that will be implied by the term “electro-optic effect” in this chapter.

A change in refractive index can lead to modifications of the phase or polarization of an optical beam. This can be applied to several devices, such as

frequency modulators, amplitude modulators, tunable filters, and beam scanners. These perform important tasks in several optical applications, including switching, information displays, optical computing, signal processing, telecommunications, and beam steering.

This chapter describes electro-optic effects in a variety of materials. Specifically, changes in refractive index that are linear (Pockels effect) and quadratic (Kerr effect) in the applied field are detailed. Electro-optic effects in liquid crystals are also described in a separate section since they differ quite significantly from Pockels and Kerr effects. Since the induced effect usually creates an anisotropic medium, or the medium is quite often anisotropic to begin with, the subject of birefringent optics is considered first. This is followed by a discussion of the formalisms describing the changes in the anisotropic refractive properties of crystals and liquids in the presence of an electric field, both to first and second order in the applied field. Electro-optic effects in liquid crystals are then described in a separate section. This is followed by a section giving examples of several applications of electro-optic effects in crystals, liquids, and liquid crystals.

The physical units, in both SI and cgs systems, of several parameters used in describing electro-optic effects are given in Table 1. Formulas for converting parameters from cgs units to SI units are presented in Table 2. In the discussion that follows, SI units will be used exclusively.

Table 1 Units of Important Physical Parameters Used in Electro-Optic Effect Formulas

Parameter	SI units	cgs units
Linear electro-optic (Pockels) coefficient	$[r] = \text{m/V}$	$[r] = \text{cm/sV}$
Quadratic electro-optic coefficient	$[s] = \text{m}^2/\text{V}^2$	$[s] = \text{cm}^2/\text{sV}^2$
Kerr coefficient	$[B] = \text{m/V}^2$	$[B] = \text{cm/sV}^2$
Electric field	$[E] = \text{V/m}$	$[E] = \text{sV/cm}$
Electric potential	$[V] = \text{V}$	$[V] = \text{sV}$
Displacement	$[D] = \text{C/m}^2$	$[D] = \text{sC/cm}^2$
Dielectric tensor	$[\epsilon] = \text{F/m} = \text{C/V-m}$	$[\epsilon] = \text{unitless}$
Vacuum permittivity	$[\epsilon_0] = \text{F/m} = \text{C/V-m}$	—
Elastic force constant	$[K] = \text{N}$	$[K] = \text{dyne}$
Viscosity	$[\gamma_1] = \text{Pa-s} = \text{N-s/m}^2$	$[\gamma_1] = \text{poise} = \text{dyn-s/cm}^2$
Response time	$[\tau] = \text{s}$	$[\tau] = \text{s}$
Length, distance	$[L] = \text{m}$	$[L] = \text{cm}$
Speed of light	$[c] = \text{m/s}$	$[c] = \text{cm/s}$
Wavelength	$[\lambda] = \text{m}$	$[\lambda] = \text{cm}$
Wave vector	$[k] = \text{m}^{-1}$	$[k] = \text{cm}^{-1}$

Table 2 Conversion Formulas

E	(SI) = $3 \times 10^4 E$	(cgs)
V	(SI) = $3 \times 10^2 V$	(cgs)
D	(SI) = $3.34 \times 10^{-14} D$	(cgs)
r	(SI) = $\frac{1}{3} \times 10^{-4} r$	(cgs)
s	(SI) = $\frac{1}{9} \times 10^{-8} s$	(cgs)
B	(SI) = $\frac{1}{9} \times 10^{-6} B$	(cgs)
K	(SI) = $10^{-5} K$	(cgs)
γ_1	(SI) = $10^{-1} \gamma_1$	(cgs)
λ	(SI) = $10^{-2} \lambda$	(cgs)
L	(SI) = $10^{-2} L$	(cgs)
c	(SI) = $10^{-2} c$	(cgs)
k	(SI) = $10^2 k$	(cgs)

I. BIREFRINGENT OPTICS

A. Normal Modes of Propagation

One of the key problems in the optics of birefringent media is to find the normal modes of propagation, i.e., the two orthogonally polarized waves that propagate with unique phase velocities. Optical wave propagation in anisotropic media was introduced in Chapter 1. By the definition of the displacement vector in Eq. (45) of Chapter 1, the general relationship between the complex Fourier components of $\mathbf{D}^{(\sim)}$ and $\mathbf{E}^{(\sim)}$ is

$$D_i = (\boldsymbol{\epsilon} \cdot \mathbf{E})_i = \sum_{j=x,y,z} \epsilon_{ij} E_j \quad (1)$$

where $i = x, y, z$, and $\boldsymbol{\epsilon} = \epsilon_0(\mathbf{1} + \boldsymbol{\chi}^{(1)})$ is the dielectric tensor of the medium; ($\mathbf{1}$ is the unit tensor and $\boldsymbol{\chi}^{(1)}$ is the linear susceptibility tensor—see Chapter 1). The dielectric tensor has nine components, but not all of them are independent. It can be shown that $\boldsymbol{\epsilon}$ is symmetric ($\epsilon_{ij} = \epsilon_{ji}$) [1]. Also, by the assumptions made for this chapter, $\epsilon_{ij} = \epsilon_{ij}^*$. In other words, the components of $\boldsymbol{\epsilon}$ are real (no absorption).

Given these properties of the dielectric tensor, the average electromagnetic energy density in an anisotropic medium is given by

$$\begin{aligned} \langle u_e \rangle &= \frac{1}{2} \mathbf{E} \cdot \mathbf{D}^* + \text{c.c.} \\ &= \epsilon_{xx} |E_x|^2 + \epsilon_{yy} |E_y|^2 + \epsilon_{zz} |E_z|^2 + 2\epsilon_{xy} \operatorname{Re}(E_x E_y^*) \\ &\quad + 2\epsilon_{yz} \operatorname{Re}(E_y E_z^*) + 2\epsilon_{xz} \operatorname{Re}(E_x E_z^*) \end{aligned} \quad (2)$$

A linear, orthogonal transformation of coordinate axes can be found that reduces the quadratic form of Eq. (2) to diagonal form [2]. In the new coordinate system, called the principal axes system, Eq. (2) reduces to

$$\langle u_e \rangle = \epsilon_{XX}|E_X|^2 + \epsilon_{YY}|E_Y|^2 + \epsilon_{ZZ}|E_Z|^2 \quad (3)$$

where XYZ denotes the principal axes. In the principal axes system, relation (1) can be written in the form

$$\begin{pmatrix} D_X \\ D_Y \\ D_Z \end{pmatrix} = \begin{pmatrix} \epsilon_{XX} & 0 & 0 \\ 0 & \epsilon_{YY} & 0 \\ 0 & 0 & \epsilon_{ZZ} \end{pmatrix} \begin{pmatrix} E_X \\ E_Y \\ E_Z \end{pmatrix} \quad (4)$$

and ϵ_{XX} , ϵ_{YY} , ϵ_{ZZ} are called the principal dielectric constants of the medium.

Combining Eqs. (3) and (4) leads to an equivalent expression for the energy density in the principal axes system:

$$\langle u_e \rangle = \frac{|D_X|^2}{\epsilon_{XX}} + \frac{|D_Y|^2}{\epsilon_{YY}} + \frac{|D_Z|^2}{\epsilon_{ZZ}} \quad (5)$$

Thus, constant energy density surfaces are ellipsoids in \mathbf{D} -space. Defining principal refractive indices $n_i = (\epsilon_{ii}/\epsilon_0)^{1/2}$, using SI units, and a vector $\mathbf{r} = (X, Y, Z) = \mathbf{D}/\sqrt{\epsilon_0\langle u_e \rangle}$, Eq. (5) yields the form of the index ellipsoid

$$\frac{X^2}{n_X^2} + \frac{Y^2}{n_Y^2} + \frac{Z^2}{n_Z^2} = 1 \quad (6)$$

See the discussion in Chapter 1 relating to this mathematical construct.

The form of Eqs. (3) and (5) suggests that it would be useful to invert relation (1) to yield

$$E_i = (\boldsymbol{\eta} \cdot \mathbf{D})_i = \sum_{j=x,y,z} \eta_{ij} D_j \quad (7)$$

where $\boldsymbol{\eta} = \boldsymbol{\epsilon}^{-1}$ is the inverse tensor of $\boldsymbol{\epsilon}$ and is called the impermeability tensor. In the principal axes system, $\boldsymbol{\eta}$ has a particularly simple form given by

$$\boldsymbol{\eta} = \begin{pmatrix} 1/\epsilon_{XX} & 0 & 0 \\ 0 & 1/\epsilon_{YY} & 0 \\ 0 & 0 & 1/\epsilon_{ZZ} \end{pmatrix} = \epsilon_0^{-1} \begin{pmatrix} 1/n_X^2 & 0 & 0 \\ 0 & 1/n_Y^2 & 0 \\ 0 & 0 & 1/n_Z^2 \end{pmatrix} \quad (8)$$

For this reason, $\epsilon_0\boldsymbol{\eta}$ is called the index tensor and is often represented as $(1/n^2)_{ij}$. This tensor is also symmetric in any coordinate system.

Consider now the propagation of an electromagnetic plane wave in an arbitrary direction with respect to the principal axes of an anisotropic medium. The electric field of such a wave is written as $\mathbf{E}^{(\sim)} = \mathbf{E}\exp(-i\omega t) + \text{c.c.}$ with

$$\mathbf{E} = \hat{e}A\exp(i\mathbf{k}\cdot\mathbf{r}) = \hat{e}A\exp(in\omega\hat{s}\cdot\mathbf{r}/c) \quad (9)$$

where the wavevector $\mathbf{k} = (n\omega/c)\hat{s}$, and \hat{s} is a unit vector in a direction normal to the wavefront (plane of constant phase). The wave thus travels with a phase velocity given by

$$\mathbf{v}_p = \frac{c}{n}\hat{s} \quad (10)$$

If the wave propagates along a principal axis and the polarization \hat{e} of the wave coincides with one of the other principal axes, then $n = n_i$ where $i = X, Y$, or Z . For any other situation, the problem is to find the relationship of n to the principal refractive indices.

The magnetic component \mathbf{H} of the wave has the same form as Eq. (9) with the same phase. Substituting these plane waves into Maxwell's equations leads to the following relationships between the fields and the direction of wavefront propagation:

$$\begin{aligned} \mathbf{D} &= -(n/c)\hat{s} \times \mathbf{H} \\ \mathbf{H} &= \epsilon_0 n c \hat{s} \times \mathbf{E} \end{aligned} \quad (11)$$

Consequently, \mathbf{D} and \mathbf{H} are perpendicular to each other and to \hat{s} . \mathbf{E} and \mathbf{H} are also perpendicular, and the Poynting vector $\mathbf{S} = \mathbf{E} \times \mathbf{H}^* + \text{c.c.}$ is also perpendicular to \mathbf{E} . These relationships are shown graphically in Fig. 1. The consequence of \mathbf{D} not being parallel to \mathbf{E} is that the direction of energy flow in the medium is not parallel to the phase velocity of the wave. When one observes a beam of light propagating in an anisotropic medium, the beam is along the direction of energy flow \mathbf{S} , while its phase velocity is directed at an angle α with respect to \mathbf{S} . \mathbf{D} and \mathbf{E} also make an angle α , which is given by Eq. (51) in Chapter 1.

Equations (11) can be combined to form a relation between \mathbf{D} and \mathbf{E} , which when combined with Eq. (4) leads to the following equation for n :

$$\frac{s_X^2}{n^2 - n_X^2} + \frac{s_Y^2}{n^2 - n_Y^2} + \frac{s_Z^2}{n^2 - n_Z^2} = \frac{1}{n^2} \quad (12)$$

where s_i are the components of the unit vector \hat{s} . When these are expressed in terms of conventional spherical angles θ and ϕ , Eq. (12) is equivalent to the Fresnel equation given by Eq. (50) in Chapter 1. Since Eq. (12) is quadratic in n^2 , it follows that there exist two separate values, n' and n'' , of the refractive index for any direction of propagation in the medium. (Actually, there are four solutions to Eq. (12), given by $\pm n'$ and $\pm n''$, but the \pm sign just indicates phase velocities in opposite directions.) Therefore, for any direction of propagation of a plane wave

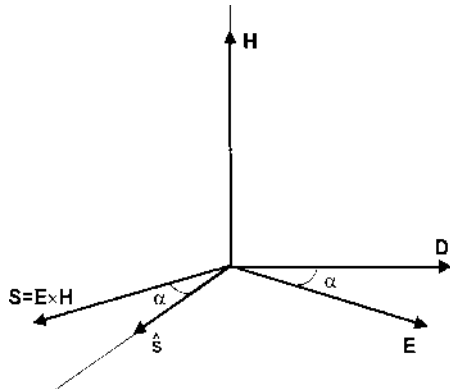


Figure 1 Directions of field vectors, wave normal, and Poynting vector in an optically anisotropic medium.

in an anisotropic medium, there are two independent modes that propagate at different phase velocities. These independent modes correspond to two orthogonal \mathbf{D} vectors, and the polarization of these two modes does not change as they propagate [1]. If $n' < n''$, then the component of \mathbf{D} associated with n' is called the fast wave (i.e., $c/n' > c/n''$), and the corresponding direction of the \mathbf{D} -component is called the fast axis. The other axis is called the slow axis. The two component waves traveling at different phase velocities experience a different phase shift and hence a change in relative phase when propagating through the medium. This implies a modification of the polarization of the resultant field [1]. It is this principle that forms the basis of most electro-optic (electro-refractive) applications of optically anisotropic media.

The index ellipsoid, or optical indicatrix, is a tool often used to determine the fast and slow axes and their corresponding refractive indices. The prescription for this method is illustrated in Fig. 2, which shows the index ellipsoid and the wavevector of propagation with respect to the principal axes of the system. A plane normal to \mathbf{k} and passing through the origin will intersect the index ellipsoid at points describing an ellipse. The semi-minor and semi-major axes of this ellipse are parallel to the fast and slow axes, respectively, for the given direction of propagation, and their lengths are equal to the corresponding refractive indices. The rationale for focusing on the intersection ellipse is that \mathbf{D} must lie in this plane since $\mathbf{D} \perp \mathbf{k}$, and the indices must lie on this ellipse since they satisfy the index ellipsoid equation. It can be shown that the extrema of the ellipse satisfy the Fresnel equation [1].

To use this prescription, refer to Fig. 3, which shows the unit vector of wave propagation with respect to the principal axes. The orientation of this vector is described by spherical angles θ and ϕ as shown in the figure. First, introduce

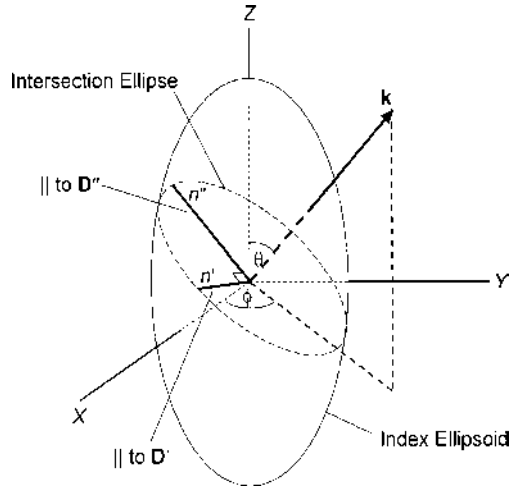


Figure 2 Illustration of the index ellipsoid in an optically anisotropic medium.

a coordinate system xyz by rotating through an angle ϕ about Z , followed by a rotation θ about the new y axis to align the z axis with \hat{s} , as shown in Fig. 3. The ensuing coordinate transform is given by

$$X = x \cos \theta \cos \phi - y \sin \phi + z \sin \theta \cos \phi \quad (13)$$

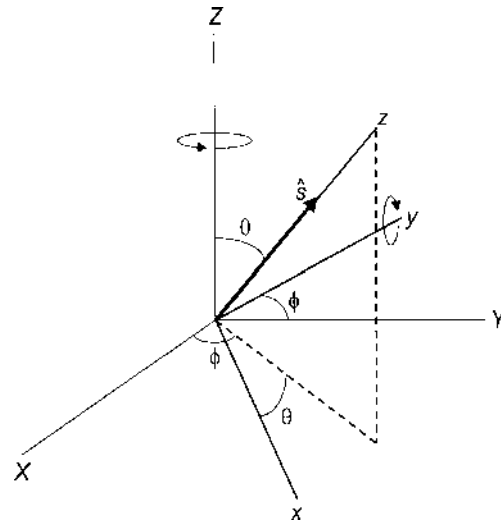


Figure 3 Orientation of the wave normal to the principal axes system.

$$Y = x \cos \theta \sin \phi + y \cos \phi + z \sin \theta \sin \phi$$

$$Z = -x \sin \theta + z \cos \theta$$

Substituting Eqs. (13) into Eq. (6) and setting $z = 0$ yields the index ellipse in a plane normal to \hat{s} passing through the origin. The form of the resulting expression is that of an ellipse with major and minor axes rotated by an angle ρ about z . Therefore, create a new set of coordinates $x'y'z'$ by rotating x and y through ρ about z . The new coordinate system is given by

$$\begin{aligned} x' &= x \cos \rho + y \sin \rho \\ y' &= -x \sin \rho + y \cos \rho \end{aligned} \tag{14}$$

$$z' = z$$

where

$$\rho = \frac{1}{2} \tan^{-1} \left(\frac{2C}{A - B} \right) \tag{15}$$

$$A = \frac{\cos^2 \theta \cos^2 \phi}{n_X^2} + \frac{\cos^2 \theta \sin^2 \phi}{n_Y^2} + \frac{\sin^2 \theta}{n_Z^2} \tag{16}$$

$$B = \frac{\sin^2 \phi}{n_X^2} + \frac{\cos^2 \phi}{n_Y^2} \tag{17}$$

$$C = \left(\frac{1}{n_Y^2} - \frac{1}{n_X^2} \right) \cos \theta \sin \phi \cos \phi \tag{18}$$

In this coordinate system, the two orthogonal normal modes \mathbf{D}' and \mathbf{D}'' are parallel to the x' and y' axes, respectively. The respective refractive indices are given by

$$n' = (A \cos^2 \rho + B \sin^2 \rho + 2C \sin \rho \cos \rho)^{-1/2} \tag{19}$$

$$n'' = (A \sin^2 \rho + B \cos^2 \rho - 2C \sin \rho \cos \rho)^{-1/2} \tag{20}$$

The smaller of Eqs. (19) and (20) corresponds to the fast axis while the other corresponds to the slow axis. The coordinate system $x'y'z'$ is useful for describing wave propagation since in this system the orthogonal components of \mathbf{D} along x' and y' are the unique modes that propagate without a change in polarization state. They do, however, experience a different phase accumulation and hence the polarization state of the resultant vector \mathbf{D} changes.

In a uniaxial crystal, $n_X = n_Y = n^\circ$ and $n_Z = n^e$. (See Chapter 1 for a discussion of uniaxial and biaxial crystals.) In this case $\rho = 0$, and Eqs. (19) and (20) reduce to

$$n' = n^e(\theta) = \left(\frac{\cos^2 \theta}{(n^\circ)^2} + \frac{\sin^2 \theta}{(n^e)^2} \right)^{-1/2} \quad (21)$$

$$n'' = n^\circ \quad (22)$$

These are the extraordinary and ordinary indices, respectively, of a uniaxial medium.

Figure 4 illustrates these coordinate systems in relation to a crystal, where propagation is typically perpendicular to the face of the crystal, and the fast and slow axes are in the crystal face. Note that if $\theta = 90^\circ$, then $\rho = 0$, Z is in the face of the crystal, and the indices n' and n'' become

$$\begin{aligned} n' &= n_Z \\ n'' &= \left(\frac{\sin^2 \phi}{n_X^2} + \frac{\cos^2 \phi}{n_Y^2} \right)^{-1/2} \end{aligned} \quad (23)$$

For a uniaxial crystal these reduce to $n' = n^e$ and $n'' = n^\circ$. In a positive uniaxial crystal ($n^e - n^\circ > 0$), $x' = x = -Z$ is the slow axis and $y' = y$ is the fast axis. These are reversed for a negative uniaxial crystal.

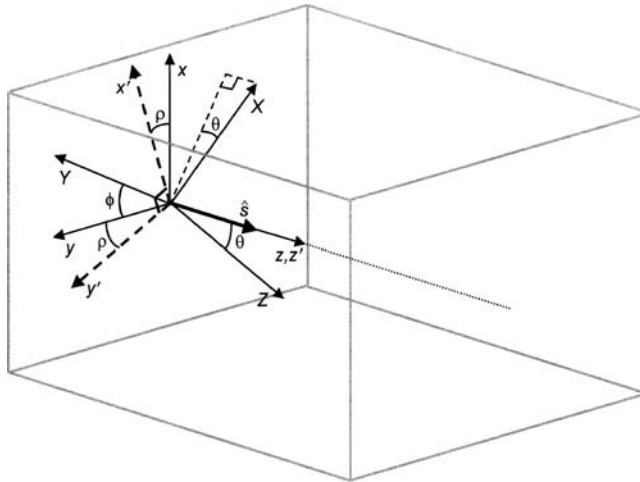


Figure 4 Schematic illustration of the principal axes frame and laboratory reference frame in an anisotropic crystal.

B. Jones Calculus

The orientation of the fast and slow axes depends on the azimuth angle ϕ measured with respect to the principal axes of the crystal. For purposes of analysis, it is common to orient the face of the crystal parallel to the xy plane of a fixed lab coordinate system, and describe the orientation of the slow (s) axis by an acute angle ψ with respect to the x axis, as illustrated in Fig. 5. The fast and slow indices are indicated by n_f and n_s , respectively. This notation is applicable to both positive and negative uniaxial media and to biaxial media.

The analysis of propagation in an anisotropic medium is commonly facilitated by the Jones matrix method or Jones calculus [3]. The polarization state of a beam of light propagating along z in the xyz lab coordinate system is described by the so-called Jones vector,

$$\mathbf{V} = \begin{pmatrix} V_x \\ V_y \end{pmatrix} \quad (24)$$

where V_x and V_y are complex numbers giving the magnitude and relative phase of the polarization vector components along the fixed x and y axes. Special polarization states are linear polarization parallel to x and y , respectively,

$$\mathbf{X} = \begin{pmatrix} 1 \\ 0 \end{pmatrix} \quad \mathbf{Y} = \begin{pmatrix} 0 \\ 1 \end{pmatrix} \quad (25)$$

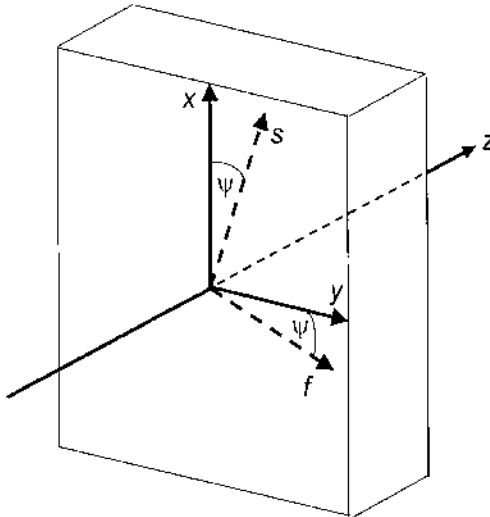


Figure 5 Schematic illustration of the laboratory reference frame and the slow and fast axes in an anisotropic crystal.

polarization oriented at some angle Φ with respect to the x axis,

$$\mathbf{V}(\Phi) = \begin{pmatrix} \cos \Phi \\ \sin \Phi \end{pmatrix} \quad (26)$$

and right or left circular polarization, respectively,

$$\mathbf{R} = \frac{1}{\sqrt{2}} \begin{pmatrix} 1 \\ -i \end{pmatrix} \quad \mathbf{L} = \frac{1}{\sqrt{2}} \begin{pmatrix} 1 \\ +i \end{pmatrix} \quad (27)$$

It is useful to decompose the incident polarization vector along the slow and fast axes. This is done by applying a rotation matrix to the incident polarization vector:

$$\begin{pmatrix} V_s \\ V_f \end{pmatrix} = \mathbf{R}(\psi) \begin{pmatrix} V_x \\ V_y \end{pmatrix} = \begin{pmatrix} \cos \psi & \sin \psi \\ -\sin \psi & \cos \psi \end{pmatrix} \begin{pmatrix} V_x \\ V_y \end{pmatrix} \quad (28)$$

Since the components of this vector travel at unique phase velocities with constant polarization, the output polarization state, after propagation through a crystal of thickness L , is related to the input state by a diagonal matrix:

$$\begin{pmatrix} V'_s \\ V'_f \end{pmatrix} = \mathbf{W}_0 \begin{pmatrix} V_s \\ V_f \end{pmatrix} = e^{i\varphi} \begin{pmatrix} e^{i\Gamma/2} & 0 \\ 0 & e^{-i\Gamma/2} \end{pmatrix} \begin{pmatrix} V_s \\ V_f \end{pmatrix} \quad (29)$$

where

$$\varphi = \frac{n_s + n_f}{2} \frac{2\pi}{\lambda} L \quad (30)$$

and

$$\Gamma = (n_s - n_f) \frac{2\pi}{\lambda} L \quad (31)$$

with λ the free-space wavelength of the incident light. To transform the output back to lab coordinates requires another rotation matrix $\mathbf{R}(-\psi)$. Thus, the net matrix transforming input polarization state to output polarization state in the laboratory coordinate system is given by

$$\mathbf{W} = \mathbf{R}(-\psi) \mathbf{W}_0 \mathbf{R}(\psi) \quad (32)$$

The output state for any input state to an arbitrary number of birefringent optical elements can be obtained by successive matrix operations of the form given by Eq. (32), with the understanding that the order of matrix multiplication for successive optical elements goes from left to right. Hence, for N optical

elements,

$$\mathbf{V}' = \mathbf{W}_N \mathbf{W}_{N-1} \cdots \mathbf{W}_2 \mathbf{W}_1 \mathbf{V} \quad (33)$$

where \mathbf{W}_i ($i = 1 \dots N$) is the transformation matrix (32) for the i th optical element in the optical train.

In a typical application, the final output field is passed through a polarizer before it is detected. Hence the last operation is to apply a polarization matrix \mathbf{P} to Eq. (33), and then calculate the transmittance T . An ideal thin polarizer will be represented by the following types of matrices: for orientation of the polarizer axis at an angle Φ' with respect to the x axis,

$$\mathbf{P}(\Phi') = \begin{pmatrix} \cos^2\Phi' & \cos\Phi'\sin\Phi' \\ \cos\Phi'\sin\Phi' & \sin^2\Phi' \end{pmatrix} \quad (34)$$

while for polarization parallel to the x and y axes, respectively,

$$\mathbf{P}_x = \begin{pmatrix} 1 & 0 \\ 0 & 0 \end{pmatrix} \quad \mathbf{P}_y = \begin{pmatrix} 0 & 0 \\ 0 & 1 \end{pmatrix} \quad (35)$$

In general, the input wave is conditioned by an input polarizer as well, so that

$$\begin{aligned} \mathbf{V} &= \mathbf{P}(\Phi)\mathbf{V}_{\text{in}} \\ \mathbf{V}_{\text{out}} &= \mathbf{P}(\Phi')\mathbf{V}' \end{aligned} \quad (36)$$

The net transmittance of the system is given by

$$T = \frac{(|V_x|^2 + |V_y|^2)_{\text{out}}}{(|V_x|^2 + |V_y|^2)_{\text{in}}} \quad (37)$$

The above results using the Jones calculus are for ideal conditions where the light is incident along the normal to the surfaces of polarizers and birefringent media, Fresnel reflections are ignored, and ideal polarizers have no absorption. The absorption of nonideal polarizers and Fresnel losses at interfaces can be easily factored in for small angles of incidence, as long as multiple reflections can be safely ignored. However, the phase retardation may change for off-normal incidence, because the physical path length is increased and the refractive index can also be a function of the direction of propagation. For example, when the medium is uniaxial and the optic axis is in the face of the crystal, the phase retardation becomes

$$\Gamma = [n^e(\theta_e)\cos\theta_e - n^o\cos\theta_o]\frac{2\pi}{\lambda}L \quad (38)$$

where θ_e and θ_o are the angles of refraction in the uniaxial medium for

the extraordinary and ordinary waves, respectively, and are related to the angle of incidence θ by Snell's law:

$$n \sin \theta = n^e(\theta_e) \sin \theta_e = n^o \sin \theta_o \quad (39)$$

In Eq. (39), n is the refractive index of the incident medium, which is assumed to be isotropic (e.g., air). The extraordinary index is angle dependent and given by Eq. (21). However, it is important to note that the angles of incidence and refraction are defined with respect to the laboratory z axis in this case. Thus θ_e is complementary to the angle in Eq. (21), which is measured with respect to the optic Z axis.

The propagation of light through birefringent media under more general conditions can be treated exactly using the so called 4×4 matrix method [4]. If the effects of multiple reflections can be neglected, an extended Jones matrix method employing 2×2 matrices can be used [5,6]. See the literature for a discussion of these methods and examples.

II. LINEAR AND QUADRATIC ELECTRO-OPTIC EFFECTS

A. Electro-Optic Coefficients

Consider the presence of two electric fields in a nonlinear optical medium: an optical field oscillating at the optical frequency ω , $\mathbf{E}_{\text{opt}}^{(\sim)} = \mathbf{E}_\omega \exp(-i\omega t) + \text{c.c.}$, and an applied electrical field oscillating at low frequency Ω , $\mathbf{E}_{\text{elec}}^{(\sim)} = \mathbf{E}_\Omega \exp(-i\Omega t) + \text{c.c.}$, where $\Omega \ll \omega$. Assume that both frequencies are far from any resonance in the medium (i.e., no absorption) and that dispersion is small. The expressions given by Eqs. (7), (53), and (54) in Chapter 1 (in SI units) can be used to express the linear and nonlinear polarization to third order. The first, second, and third dielectric response tensors have delta-function time response, and the integrals reduce to relatively simple tensor expressions. Because of the intrinsic permutation symmetry of the susceptibilities (see Chapter 1), the i th component of the polarization (to third order) oscillating at frequency ω can be written as

$$\begin{aligned} P_i(\omega) = & \epsilon_0 \left[\sum_j \chi_{ij}^{(1)}(E_\omega)_j + 2 \sum_{jk} \chi_{ijk}^{(2)}(E_\omega)_j (E_{\text{elec}}^{(\sim)})_k \right. \\ & \left. + 3 \sum_{jkl} \chi_{ijkl}^{(3)}(E_\omega)_j (E_{\text{elec}}^{(\sim)})_k (E_{\text{elec}}^{(\sim)})_l \right] \end{aligned} \quad (40)$$

Note that Eq. (40) contains only those parts of the nonlinear polarization that are

proportional to $\exp(-i\omega t)$. It follows that the nonlinear optical dielectric tensor of the medium under these conditions is

$$\epsilon_{ij} = \epsilon_0 \left[\delta_{ij} + \chi_{ij}^{(1)} + 2 \sum_k \chi_{ijk}^{(2)} (E_{\text{elec}}^{(\sim)})_k + 3 \sum_{kl} \chi_{ijkl}^{(3)} (E_{\text{elec}}^{(\sim)})_k (E_{\text{elec}}^{(\sim)})_l \right] \quad (41)$$

The field dependent terms are assumed to be small ($\ll 1$). Since the medium is lossless, the susceptibilities are real, and full permutation symmetry requires that $\chi_{ijk}^{(2)} = \chi_{jik}^{(2)}$ and $\chi_{ijkl}^{(3)} = \chi_{jikl}^{(3)}$ (see Chapter 1). The electric field components appearing in Eq. (41) are also real (and potentially time and space dependent, in general). Thus, ϵ_{ij} is both real and symmetric. In what follows, the subscript “elec” and superscript “(\sim)” will be dropped with the understanding that the dielectric tensor depends only on the applied electrical field, which may be time and space dependent. In fact, the applied field may be non-sinusoidal. For example, it could be a rectangular or triangular waveform, a string of pulses, or a traveling wave, as long as the frequencies of its dominant Fourier components are small compared to the optical frequency and are far from any material resonance.

Assume that the dielectric tensor is expressed in the principal axes system of the medium, where these axes are established under the condition of no applied electric field. Then $\chi_{ij}^{(1)}$ is diagonal. The general result of the applied field is to produce small changes in the diagonal components of ϵ and create non-zero off-diagonal elements. The off-diagonal elements will be small compared to the new diagonal elements. Thus, the diagonal components of the impermeability tensor can be approximated as

$$\eta_{ii} \approx \frac{1}{\epsilon_{ii}} \quad (42)$$

and the off-diagonal elements as

$$\eta_{ij} \approx -\frac{\epsilon_{ij}}{\epsilon_{ii}\epsilon_{jj}} \quad (i \neq j) \quad (43)$$

Equation (41) is substituted into Eqs. (42) and (43). Due to the smallness of the nonlinear terms, only the linear terms are included in the denominator of Eq. (43), while the denominator of Eq. (42) includes nonlinear terms. The latter is expanded in a Taylor series. Using the index tensor defined above,

the components of this tensor can be approximated as

$$\left(\frac{1}{n^2}\right)_{ii} = \frac{1}{n_i^2} - \frac{2\sum_k \chi_{iik}^{(2)} E_k}{n_i^2 n_i^2} - \frac{3\sum_{kl} \chi_{iikl}^{(3)} E_k E_l}{n_i^2 n_i^2} \quad (44)$$

$$\left(\frac{1}{n^2}\right)_{ij} = -\frac{2\sum_k \chi_{ijk}^{(2)} E_k}{n_i^2 n_j^2} - \frac{3\sum_{kl} \chi_{ijkl}^{(3)} E_k E_l}{n_i^2 n_j^2} \quad (i \neq j) \quad (45)$$

where the subscripts $ijkl$ are indices running over the principal coordinates XYZ . The change in all of the components (diagonal and off-diagonal) of the index tensor can be written compactly as

$$\Delta \left(\frac{1}{n^2}\right)_{ij} = \sum_k r_{ijk} E_k + \sum_{kl} s_{ijkl} E_k E_l \quad (46)$$

where

$$r_{ijk} = -\frac{2\chi_{ijk}^{(2)}}{n_i^2 n_j^2} \quad (47)$$

is the linear electro-optic tensor (or Pockels tensor), and

$$s_{ijkl} = -\frac{3\chi_{ijkl}^{(3)}}{n_i^2 n_j^2} \quad (48)$$

is the quadratic electro-optic tensor. Notice that these tensors have the same symmetry properties as the nonlinear susceptibility tensors.

The full permutation symmetry of the Pockels tensor is used to contract the first two subscripts and write $r_{ijk} = r_{jik} \rightarrow r_{lk}$. The subscripts are then written as numbers instead of letters using the following scheme:

XY	1					
YY	2					
ZZ	3					
$ij = l :$						
$YZ = ZY$	4	$k :$	1			
$XZ = ZX$	5		2			
$XY = YX$	6		3			

(49)

Using this notation, the change in the components of the index tensor due to

the Pockels effect alone can be written as

$$\begin{pmatrix} \Delta(1/n^2)_1 \\ \Delta(1/n^2)_2 \\ \Delta(1/n^2)_3 \\ \Delta(1/n^2)_4 \\ \Delta(1/n^2)_5 \\ \Delta(1/n^2)_6 \end{pmatrix} = \begin{pmatrix} r_{11} & r_{12} & r_{13} \\ r_{21} & r_{22} & r_{23} \\ r_{31} & r_{32} & r_{33} \\ r_{41} & r_{42} & r_{43} \\ r_{51} & r_{52} & r_{53} \\ r_{61} & r_{62} & r_{63} \end{pmatrix} \begin{pmatrix} E_1 \\ E_2 \\ E_3 \end{pmatrix} \quad (50)$$

For example,

$$\Delta\left(\frac{1}{n^2}\right)_6 = r_{61}E_1 + r_{62}E_2 + r_{63}E_3 \quad (51)$$

Note that r_{ijk} carries all the same symmetry properties of $\chi_{ijk}^{(2)}$ due to crystal structure. Thus, not all components of r_{lk} are necessarily independent, and some may be zero. The forms of the r -matrix for crystals of several different symmetry classes are given in Table 3. Values of Pockels coefficients for several different materials are given in Table 4.

The above discussion has assumed that any frequency of the applied electrical field is far from any material resonance. Acoustic resonances in materials are in the range of 10^4 – 10^6 Hz. Optical phonon resonances are in the 10^{12} – 10^{13} Hz range. Typical operation of devices using electro-optic materials is in the regions below the acoustic resonance or between the acoustic and optical phonon resonance. In the low frequency range, the crystal is free to deform by the piezoelectric effect. The variation of the strain in the material follows the modulation field. The Pockels coefficient measured in this regime is designated r_{ijk}^T and is called the “unclamped” value. At frequencies above the acoustic resonance, the crystal does not deform and is under a constant strain. The measured Pockels coefficient in this regime, the so-called “clamped” value, is designated r_{ijk}^S . The two coefficients are related by

$$r_{ijk}^T = r_{ijk}^S + \sum_{lm} p_{ijlm} d_{lmk} \quad (52)$$

where p_{ijlm} and d_{lmk} are the elasto-optic and piezoelectric tensors, respectively [3,7,8].

Pockels coefficients will also display some dispersion over the visible and near infrared regions, although the variation is relatively small if there is no optical absorption band. Ferroelectrics and other materials that exhibit a phase transition will have strong temperature dependence near a critical temperature T_c , and the Pockels coefficient will diverge as $(T - T_c)^{-1}$. Although T_c may be well

Table 3 Form of the r -matrix for Different Symmetry Classes

Symmetry class	Biaxial crystals
1	$\begin{pmatrix} r_{11} & r_{12} & r_{13} \\ r_{21} & r_{22} & r_{23} \\ r_{31} & r_{32} & r_{33} \\ r_{41} & r_{42} & r_{43} \\ r_{51} & r_{52} & r_{53} \\ r_{61} & r_{62} & r_{63} \end{pmatrix}$
2	$\begin{pmatrix} 0 & r_{12} & 0 \\ 0 & r_{22} & 0 \\ 0 & r_{32} & 0 \\ r_{41} & 0 & r_{43} \\ 0 & r_{52} & 0 \\ r_{61} & 0 & r_{63} \end{pmatrix}$
m	$\begin{pmatrix} r_{11} & 0 & r_{13} \\ r_{21} & 0 & r_{23} \\ r_{31} & 0 & r_{33} \\ 0 & r_{42} & 0 \\ r_{51} & 0 & r_{53} \\ 0 & r_{62} & 0 \end{pmatrix}$
222	$\begin{pmatrix} 0 & 0 & 0 \\ 0 & 0 & 0 \\ 0 & 0 & 0 \\ r_{41} & 0 & 0 \\ 0 & r_{52} & 0 \\ 0 & 0 & r_{63} \end{pmatrix}$
$mm2$	$\begin{pmatrix} 0 & 0 & r_{13} \\ 0 & 0 & r_{23} \\ 0 & 0 & r_{33} \\ 0 & r_{42} & 0 \\ r_{51} & 0 & 0 \\ 0 & 0 & 0 \end{pmatrix}$

Uniaxial Crystals

3	$\begin{pmatrix} r_{11} & r_{12} & r_{13} \\ -r_{11} & -r_{12} & r_{13} \\ 0 & 0 & r_{33} \\ r_{41} & r_{42} & 0 \\ r_{42} & -r_{41} & 0 \\ r_{12} & -r_{11} & 0 \end{pmatrix}$
---	---

(continued)

Table 3 Continued

Symmetry class	<i>Uniaxial crystals</i>
$3m$	$\begin{pmatrix} 0 & r_{12} & r_{13} \\ 0 & -r_{12} & r_{13} \\ 0 & 0 & r_{33} \\ 0 & r_{42} & 0 \\ r_{42} & 0 & 0 \\ r_{12} & 0 & 0 \end{pmatrix}$
$\bar{6}$	$\begin{pmatrix} r_{11} & r_{12} & 0 \\ -r_{11} & -r_{12} & 0 \\ 0 & 0 & 0 \\ 0 & 0 & 0 \\ 0 & 0 & 0 \\ r_{12} & -r_{11} & 0 \end{pmatrix}$
$\bar{6}m2$	$\begin{pmatrix} 0 & r_{12} & 0 \\ 0 & -r_{12} & 0 \\ 0 & 0 & 0 \\ 0 & 0 & 0 \\ 0 & 0 & 0 \\ r_{12} & 0 & 0 \end{pmatrix}$
$6,4$	$\begin{pmatrix} 0 & 0 & r_{13} \\ 0 & 0 & r_{13} \\ 0 & 0 & r_{33} \\ r_{41} & r_{42} & 0 \\ r_{42} & -r_{41} & 0 \\ 0 & 0 & 0 \end{pmatrix}$
$6mm,4mm$	$\begin{pmatrix} 0 & 0 & r_{13} \\ 0 & 0 & r_{13} \\ 0 & 0 & r_{33} \\ 0 & r_{42} & 0 \\ r_{42} & 0 & 0 \\ 0 & 0 & 0 \end{pmatrix}$
$622,422$	$\begin{pmatrix} 0 & 0 & 0 \\ 0 & 0 & 0 \\ 0 & 0 & 0 \\ r_{41} & 0 & 0 \\ 0 & -r_{41} & 0 \\ 0 & 0 & 0 \end{pmatrix}$

(continued)

Table 3 Continued

Symmetry class	<i>Uniaxial crystals</i>
4	$\begin{pmatrix} 0 & 0 & r_{13} \\ 0 & 0 & -r_{13} \\ 0 & 0 & 0 \\ r_{41} & r_{42} & 0 \\ -r_{42} & r_{41} & 0 \\ 0 & 0 & r_{63} \end{pmatrix}$
32	$\begin{pmatrix} r_{11} & 0 & 0 \\ -r_{11} & 0 & 0 \\ 0 & 0 & 0 \\ r_{41} & 0 & 0 \\ 0 & -r_{41} & 0 \\ 0 & -r_{11} & 0 \end{pmatrix}$
$\bar{4}2m$	$\begin{pmatrix} 0 & 0 & 0 \\ 0 & 0 & 0 \\ 0 & 0 & 0 \\ r_{41} & 0 & 0 \\ 0 & r_{41} & 0 \\ 0 & 0 & r_{63} \end{pmatrix}$
<i>Isotropic Crystals</i>	
$\bar{4}3m, 23$	$\begin{pmatrix} 0 & 0 & 0 \\ 0 & 0 & 0 \\ 0 & 0 & 0 \\ r_{41} & 0 & 0 \\ 0 & r_{41} & 0 \\ 0 & 0 & r_{41} \end{pmatrix}$
432	$\begin{pmatrix} 0 & 0 & 0 \\ 0 & 0 & 0 \\ 0 & 0 & 0 \\ 0 & 0 & 0 \\ 0 & 0 & 0 \\ 0 & 0 & 0 \end{pmatrix}$

Table 4 Pockels Coefficients for Selected Materials

Material	Symmetry class	Dielectric constants ^a		Wavelength (nm)	Refractive index	Pockels coefficients ^a (pm/V)	
		(T)	(S)			(T)	(S)
BaTiO ₃	4mm	$\epsilon_1 = 3600\epsilon_0$ $\epsilon_3 = 135\epsilon_0$		546	$n^o = 2.437$ $n^e = 2.365$	$r_{42} = 1640$ [3]	$r_{42} = 820$ [7]
GaAs	43m	$\epsilon = 12.3\epsilon_0$	$\epsilon = 13.2\epsilon_0$	900 1150 3390 10,600	$n = 3.60$ $n = 3.43$ $n = 3.3$ $n = 3.5$	$r_{41} = 1.43$ [3] $r_{41} = 1.24$ [3] $r_{41} = -1.17$ [3] $r_{41} = 3.4$ [8]	$r_{41} = 1.2$ [7] $r_{41} = -1.5$ [7] $r_{41} = x - 1.33$ [3]
Bi ₁₂ GeO ₂₀ (BGO)	23	$\epsilon = 40\epsilon_0$		633	$n = 2.54$		
Bi ₁₂ SiO ₂₀ (BSO)	23	$\epsilon = 56\epsilon_0$		633	$n = 2.54$	$r_{41} = 5$ [8]	
LiNbO ₃	3m	$\epsilon_1 = 78\epsilon_0$ $\epsilon_3 = 32\epsilon_0$	$\epsilon_1 = 43\epsilon_0$ $\epsilon_3 = 28\epsilon_0$	633 1150 3390	$n^o = 2.286$ $n^e = 2.200$ $n^o = 2.150$ $n^e = 2.136$ $n^e = 2.073$	$r_{13} = 9.6$ [3] $r_{22} = 6.8$ [3] $r_{33} = 30.9$ [3] $r_{42} = 32.6$ [3] $r_{22} = 5.4$ [3]	$r_{13} = 8.6$ [3] $r_{22} = 3.4$ [3] $r_{33} = 30.8$ [3] $r_{42} = 28$ [3] $r_{13} = 6.5$ [3] $r_{22} = 3.1$ [3] $r_{33} = 28$ [3] $r_{42} = 23$ [3]

KH ₂ PO ₄ (KDP)	$\bar{4}2m$	$\varepsilon_1 = 42\varepsilon_0$ $\varepsilon_3 = 21\varepsilon_0$	546	$n^o = 1.5115$ $n^e = 1.4698$	$r_{41} = 8.77 [3]$ $r_{63} = 10.3 [3]$
			633	$n^o = 1.5074$ $n^e = 1.4669$	$r_{41} = 8.77 [7]$ $r_{63} = -10.3 [7]$
KNbO ₃	$mm2$	$\varepsilon_1 = 160\varepsilon_0$ $\varepsilon_2 = 1000\varepsilon_0$ $\varepsilon_3 = 55\varepsilon_0$	633	$n_1 = 2.279$ $n_2 = 2.329$ $n_3 = 2.167$	$r_{13} = 28 [7]$ $r_{23} = 1.3 [7]$ $r_{33} = 64 [7]$ $r_{33} = 25 [7]$
Urea (NH ₂) ₂ CO	$\bar{4}2m$		633	$n^o = 1.477$ $n^e = 1.583$	$r_{51} = 105 [7]$ $r_{41} = 0.83 [7]$ $r_{63} = 1.9 [7]$
ZnSe	$\bar{4}3m$	$\varepsilon = 9.1\varepsilon_0$	550 633 10,600	$n = 2.66$ $n = 2.60$ $n = 2.39$	$r_{41} = 2.0 [7]$ $r_{41} = 2.2 [3]$ $r_{41} = 2.2 [3]$

^a (T) unclamped value; (S) clamped value.

below 0°C, the thermal effect at room temperature can still be significant in some cases.

The quadratic electro-optic tensor also displays symmetry in the last two indices since it makes no difference physically the order in which the components of the field are written. Hence, both pairs of subscripts may be contracted, with $s_{ijkl} = s_{jilk} \rightarrow s_{mn}$, and the following scheme is used:

$$\begin{array}{ll}
 \begin{array}{ll}
 XX & 1 \\
 YY & 2 \\
 ZZ & 3 \\
 ij = m : & \\
 YZ = ZY & 4 \\
 XZ = ZX & 5 \\
 XY = YX & 6
 \end{array}
 &
 \begin{array}{ll}
 XX & 1 \\
 YY & 2 \\
 ZZ & 3 \\
 kl = n : & \\
 YZ = ZY & 4 \\
 XZ = ZX & 5 \\
 XY = YX & 6
 \end{array}
 &
 \begin{array}{ll}
 X & 1 \\
 Y & 2 \\
 Z & 3
 \end{array}
 \quad (53)
 \end{array}$$

The change in the components of the index tensor for situations in which only the quadratic electro-optic effect is important (e.g., in centrosymmetric media) can thus be written as

$$\begin{pmatrix}
 \Delta(1/n^2)_1 \\
 \Delta(1/n^2)_2 \\
 \Delta(1/n^2)_3 \\
 \Delta(1/n^2)_4 \\
 \Delta(1/n^2)_5 \\
 \Delta(1/n^2)_6
 \end{pmatrix} = \begin{pmatrix}
 s_{11} & s_{12} & s_{13} & s_{14} & s_{15} & s_{16} \\
 s_{21} & s_{22} & s_{23} & s_{24} & s_{25} & s_{26} \\
 s_{31} & s_{32} & s_{33} & s_{34} & s_{35} & s_{36} \\
 s_{41} & s_{42} & s_{43} & s_{44} & s_{45} & s_{46} \\
 s_{51} & s_{52} & s_{53} & s_{54} & s_{55} & s_{56} \\
 s_{61} & s_{62} & s_{63} & s_{64} & s_{65} & s_{66}
 \end{pmatrix} \begin{pmatrix}
 E_1^2 \\
 E_2^2 \\
 E_3^2 \\
 2E_2E_3 \\
 2E_1E_3 \\
 2E_1E_2
 \end{pmatrix} \quad (54)$$

The forms of the s -matrix for crystals of different symmetry classes are given in Table 5. Values of quadratic electro-optic coefficients for several different materials are given in Table 6.

A common application of the second order electro-optic effect is in centrosymmetric media where the applied field creates a uniaxial symmetry in a normally isotropic medium, and the optic axis is along the direction of the applied field. The induced birefringence is given by

$$n^e - n^\circ = \frac{1}{2}n^3(s_{12} - s_{11})E^2 = -n^3s_{44}E^2 \quad (55)$$

This is often written as

$$n^e - n^\circ = B\lambda E^2 \quad (56)$$

Table 5 Form of the s -matrix for Different Symmetry Classes

Symmetry class	$s_{11} \quad s_{12} \quad s_{13} \quad s_{14} \quad s_{15} \quad s_{16}$	$s_{21} \quad s_{22} \quad s_{23} \quad s_{24} \quad s_{25} \quad s_{26}$	$s_{31} \quad s_{32} \quad s_{33} \quad s_{34} \quad s_{35} \quad s_{36}$	$s_{41} \quad s_{42} \quad s_{43} \quad s_{44} \quad s_{45} \quad s_{46}$	$s_{51} \quad s_{52} \quad s_{53} \quad s_{54} \quad s_{55} \quad s_{56}$	$s_{61} \quad s_{62} \quad s_{63} \quad s_{64} \quad s_{65} \quad s_{66}$	
Triclinic $1, \bar{1}$	$\begin{pmatrix} s_{11} & s_{12} & s_{13} & s_{14} & s_{15} & s_{16} \\ s_{21} & s_{22} & s_{23} & s_{24} & s_{25} & s_{26} \\ s_{31} & s_{32} & s_{33} & s_{34} & s_{35} & s_{36} \\ s_{41} & s_{42} & s_{43} & s_{44} & s_{45} & s_{46} \\ s_{51} & s_{52} & s_{53} & s_{54} & s_{55} & s_{56} \\ s_{61} & s_{62} & s_{63} & s_{64} & s_{65} & s_{66} \end{pmatrix}$						
Monoclinic $2,m,2/m$	$\begin{pmatrix} s_{11} & s_{12} & s_{13} & 0 & s_{15} & s_{16} \\ s_{21} & s_{22} & s_{23} & 0 & s_{25} & 0 \\ s_{31} & s_{32} & s_{33} & 0 & s_{35} & 0 \\ 0 & 0 & 0 & s_{44} & 0 & s_{46} \\ s_{51} & s_{52} & s_{53} & 0 & s_{55} & 0 \\ 0 & 0 & 0 & s_{64} & 0 & s_{66} \end{pmatrix}$						
Orthorhombic $2mm, 222, mmm$	$\begin{pmatrix} s_{11} & s_{12} & s_{13} & 0 & 0 & 0 \\ s_{21} & s_{22} & s_{23} & 0 & 0 & 0 \\ s_{31} & s_{32} & s_{33} & 0 & 0 & 0 \\ 0 & 0 & 0 & s_{44} & 0 & 0 \\ 0 & 0 & 0 & 0 & s_{55} & 0 \\ 0 & 0 & 0 & 0 & 0 & s_{66} \end{pmatrix}$						
Tetragonal $4,\bar{4},4/m$	$\begin{pmatrix} s_{11} & s_{12} & s_{13} & 0 & 0 & s_{16} \\ s_{12} & s_{11} & s_{13} & 0 & 0 & -s_{16} \\ s_{31} & s_{31} & s_{33} & 0 & 0 & 0 \\ 0 & 0 & 0 & s_{44} & s_{45} & 0 \\ 0 & 0 & 0 & -s_{45} & s_{44} & 0 \\ s_{61} & -s_{61} & 0 & 0 & 0 & s_{66} \end{pmatrix}$						

(continued)

Table 5 Continued

Symmetry class	
Tetragonal $422, 4mm, \bar{4}2m, 4/mmm$	$\begin{pmatrix} s_{11} & s_{12} & s_{13} & 0 & 0 & 0 \\ s_{12} & s_{11} & s_{13} & 0 & 0 & 0 \\ s_{31} & s_{31} & s_{33} & 0 & 0 & 0 \\ 0 & 0 & 0 & s_{44} & 0 & 0 \\ 0 & 0 & 0 & 0 & s_{44} & 0 \\ 0 & 0 & 0 & 0 & 0 & s_{66} \end{pmatrix}$
Trigonal $3, \bar{3}$	$\begin{pmatrix} s_{11} & s_{12} & s_{13} & s_{14} & s_{15} & -2s_{61} \\ s_{12} & s_{11} & s_{13} & -s_{14} & -s_{15} & 2s_{61} \\ s_{31} & s_{31} & s_{33} & 0 & 0 & 0 \\ s_{41} & -s_{41} & 0 & s_{44} & s_{45} & -2s_{51} \\ s_{51} & -s_{51} & 0 & -s_{45} & s_{44} & 2s_{41} \\ s_{61} & -s_{61} & 0 & -s_{15} & s_{14} & s_{11} - s_{12} \end{pmatrix}$
Trigonal $32, 3m, \bar{3}m$	$\begin{pmatrix} s_{11} & s_{12} & s_{13} & s_{14} & 0 & 0 \\ s_{12} & s_{11} & s_{13} & -s_{14} & 0 & 0 \\ s_{31} & s_{31} & s_{33} & 0 & 0 & 0 \\ s_{41} & -s_{41} & 0 & s_{44} & 0 & 0 \\ 0 & 0 & 0 & 0 & s_{44} & 2s_{41} \\ 0 & 0 & 0 & 0 & s_{41} & s_{11} - s_{12} \end{pmatrix}$
Hexagonal $6, \bar{6}, 6/m$	$\begin{pmatrix} s_{11} & s_{12} & s_{13} & 0 & 0 & 2s_{61} \\ s_{12} & s_{11} & s_{13} & 0 & 0 & -2s_{61} \\ s_{31} & s_{31} & s_{33} & 0 & 0 & 0 \\ 0 & 0 & 0 & s_{44} & s_{45} & 0 \\ 0 & 0 & 0 & -s_{45} & s_{44} & 0 \\ s_{61} & -s_{61} & 0 & 0 & 0 & s_{11} - s_{12} \end{pmatrix}$

(continued)

Table 5 Continued

Symmetry class	
Hexagonal $622,6mm$, $\bar{6}m2,6/mmm$	$\begin{pmatrix} s_{11} & s_{12} & s_{13} & 0 & 0 & 0 \\ s_{12} & s_{11} & s_{13} & 0 & 0 & 0 \\ s_{31} & s_{31} & s_{33} & 0 & 0 & 0 \\ 0 & 0 & 0 & s_{44} & 0 & 0 \\ 0 & 0 & 0 & 0 & s_{44} & 0 \\ 0 & 0 & 0 & 0 & 0 & s_{11} - s_{12} \end{pmatrix}$
Cubic $23,m\bar{3}$	$\begin{pmatrix} s_{11} & s_{12} & s_{13} & 0 & 0 & 0 \\ s_{13} & s_{11} & s_{12} & 0 & 0 & 0 \\ s_{12} & s_{13} & s_{11} & 0 & 0 & 0 \\ 0 & 0 & 0 & s_{44} & 0 & 0 \\ 0 & 0 & 0 & 0 & s_{44} & 0 \\ 0 & 0 & 0 & 0 & 0 & s_{44} \end{pmatrix}$
Cubic $432,m\bar{3}m,\bar{4}3m$	$\begin{pmatrix} s_{11} & s_{12} & s_{12} & 0 & 0 & 0 \\ s_{12} & s_{11} & s_{12} & 0 & 0 & 0 \\ s_{12} & s_{12} & s_{11} & 0 & 0 & 0 \\ 0 & 0 & 0 & s_{44} & 0 & 0 \\ 0 & 0 & 0 & 0 & s_{44} & 0 \\ 0 & 0 & 0 & 0 & 0 & s_{44} \end{pmatrix}$
Isotropic	$\begin{pmatrix} s_{11} & s_{12} & s_{12} & 0 & 0 & 0 \\ s_{12} & s_{11} & s_{12} & 0 & 0 & 0 \\ s_{12} & s_{12} & s_{11} & 0 & 0 & 0 \\ 0 & 0 & 0 & s_{11} - s_{12} & 0 & 0 \\ 0 & 0 & 0 & 0 & s_{11} - s_{12} & 0 \\ 0 & 0 & 0 & 0 & 0 & s_{11} - s_{12} \end{pmatrix}$

Table 6 Quadratic Electro-Optic Coefficients for Selected Materials

Material	Symmetry class	Wavelength (nm)	Refractive index	Electro-optic coefficients ($10^{-18} \text{ m}^2/\text{V}^2$)
BaTiO ₃	<i>m3m</i>	633	$n = 2.42$	$s_{11} - s_{12} = 2300$ [3]
CCl ₄	Isotropic	633	$n = 1.456$	$s_{44} = 1.5 \times 10^{-4}$ [7]
CS ₂	Isotropic	546	$n = 1.633$	$s_{44} = 0.5$ [7]
KH ₂ PO ₄ (KDP)	$\bar{4}2m$	546	$n^\circ = 1.5115$ $n^e = 1.4698$	$s_{12} - s_{11} = 2.6$ [7] $s_{31} - s_{11} = 3.9$ [7] $s_{33} - s_{13} = 9.7$ [7] $s_{66} = 0.9$ [7]
K(Nb _{0.37} Ta _{0.63})O ₃	<i>m3m</i>	633	$n = 2.29$	$s_{11} - s_{12} = 2890$ [3]
KTaO ₃	<i>m3m</i>	633	$n = 2.24$	$s_{11} - s_{12} = 10$ [3]

where

$$B = -\frac{n^3 s_{44}}{\lambda} \quad (57)$$

is called the Kerr constant, n is the isotropic index, and λ is the optical wavelength. Table 7 gives the Kerr constant for several common materials.

B. New Fast and Slow Axes and Refractive Indices

The field-modified index tensor in the principal axes system is now

$$\left(\frac{1}{n^2} \right) = \begin{pmatrix} 1/n_X^2 + \Delta(1/n^2)_1 & \Delta(1/n^2)_6 & \Delta(1/n^2)_5 \\ \Delta(1/n^2)_6 & 1/n_Y^2 + \Delta(1/n^2)_2 & \Delta(1/n^2)_4 \\ \Delta(1/n^2)_5 & \Delta(1/n^2)_4 & 1/n_Z^2 + \Delta(1/n^2)_3 \end{pmatrix} \quad (58)$$

and the new index ellipsoid is given by

$$\begin{aligned} &[1/n_X^2 + \Delta(1/n^2)_1]X^2 + [1/n_Y^2 + \Delta(1/n^2)_2]Y^2 + [1/n_Z^2 + \Delta(1/n^2)_3]Z^2 \\ &+ 2\Delta(1/n^2)_4YZ + 2\Delta(1/n^2)_5XZ + 2\Delta(1/n^2)_6XY = 1 \end{aligned} \quad (59)$$

Hence, the result of the applied field is to create a new set of principal axes and principal refractive indices. The problem is to find these by diagonalizing Eq. (59). Once these are determined, the new fast and slow axes and corresponding indices can be found by the methods outlined in Section I.A.

Table 7 Kerr Coefficients for Selected Materials

Material	Wavelength (nm)	Refractive index	B (m/V ²)
Benzene	546	1.503	4.9×10^{-15} [3]
CS ₂	546	1.633	3.88×10^{-14} [3]
	633	1.619	3.18×10^{-14} [3]
	694	1.612	2.83×10^{-14} [3]
	1060	1.596	1.84×10^{-14} [3]
CCl ₄	546	1.460	8.6×10^{-16} [3]
	633	1.456	7.4×10^{-16} [3]
Nitrobenzene	589	1.54	2.44×10^{-12} [3]
Nitrotoluene	589	1.54	1.37×10^{-12} [3]
Water	589	1.33	5.1×10^{-14} [3]

Propagation through the medium can then be analyzed by means of the Jones calculus.

Diagonalizing a quadratic form is a classical eigenvalue problem in linear algebra [2]. The eigenvalues, which determine the new principal refractive indices, are found by solving the secular equation

$$|(1/n^2) - \nu\mathbf{I}| = 0 \quad (60)$$

where the vertical lines denote the determinant, $(1/n^2)$ is the index matrix, \mathbf{I} is the identity matrix, and ν_i ($i = 1, 2, 3$) are the solutions (eigenvalues) of the resultant cubic equation in ν . Substituting these solutions one at a time into the eigenvalue equation,

$$(1/n^2)\mathbf{N}_i = \nu_i\mathbf{N}_i \quad (i = 1, 2, 3) \quad (61)$$

yields the three eigenvectors \mathbf{N}_i . The three components of \mathbf{N}_i corresponding to the eigenvalue ν_i , when normalized so that the length of \mathbf{N}_i is 1 (i.e., $\|\mathbf{N}_i\| = 1$), give the projections (direction cosines) of the eigenvector along the X , Y , and Z axes. The vectors \mathbf{N}_1 , \mathbf{N}_2 , and \mathbf{N}_3 are the new principal axes of the system. One should note that the eigenvalues ν_i are the diagonal values of the index tensor in the new principal axes system, not the principal indices themselves. The principal indices are given by $n_i = (1/\nu_i)^{1/2}$.

In some simple cases [e.g., the field applied along the optic axis of the uniaxial medium KH₂PO₄ (KDP)], the new principal axes can be determined by an inspection of the symmetry of the index ellipsoid. In other instances (e.g., field applied along the $\langle 111 \rangle$ direction in a crystal of $\bar{4}3m$ symmetry), an algebraic solution of the eigenvalue problem is straightforward. However, the ordering (labeling) of the new principal axes $X'Y'Z'$ is somewhat arbitrary. In general, the eigenvalue problem must be solved numerically and has the disadvantage of

being numerically unstable. Several alternative methods have been developed for determining the new principal axes and refractive indices. Maldonado and Gaylord [9] discuss the advantages and problems associated with these. They also present a similarity transformation approach for diagonalizing the index ellipsoid that yields stable, accurate eigenvalues and eigenvectors for any symmetry class and field orientation. The method is applicable to both linear and quadratic electro-optic effects.

The similarity transformation approach is based on the fact from linear algebra that, for any symmetric matrix \mathbf{A} , a similarity matrix \mathbf{S} may be found such that the similarity transform $\mathbf{S}\mathbf{A}\mathbf{S}^T = \nu$ diagonalizes \mathbf{A} [2], where \mathbf{S}^T is the transpose of \mathbf{S} , and ν is a diagonal matrix whose components are the eigenvalues. The corresponding columns of \mathbf{S}^T are the eigenvectors.

The eigenvalue problem is reduced to finding the similarity matrix \mathbf{S} . This can be found to any desired accuracy by a finite sequence of consecutive similarity transformations with similarity matrices $\mathbf{S}_1, \mathbf{S}_2, \dots, \mathbf{S}_m$, where $\mathbf{S} = \mathbf{S}_m \mathbf{S}_{m-1} \cdots \mathbf{S}_1$. There are a number of numerical techniques available that perform the similarity transformation. However, the Jacobi method achieves accurate eigenvalues and orthogonal eigenvectors, is reliable for even very small off-diagonal elements of the index tensor as well as degenerate eigenvalues, and is relatively simple to implement [9]. The Jacobi method is an iterative procedure, employing elementary plane rotations at each step to zero an off-diagonal matrix element. It diagonalizes the matrix by minimizing the norm of off-diagonal elements to a desired level of accuracy. For m steps, the updated index matrix is given by

$$\left(\frac{1}{n^2}\right)_m = \mathbf{S}_m \mathbf{S}_{m-1} \cdots \mathbf{S}_2 \mathbf{S}_1 \left(\frac{1}{n^2}\right)_0 \mathbf{S}_1^T \mathbf{S}_2^T \cdots \mathbf{S}_{m-1}^T \mathbf{S}_m^T \quad (62)$$

where $(1/n^2)_0$ is the index matrix in the XYZ coordinate system.

Figure 6 shows the elementary plane rotations in the ij planes ($i < j$), where $i, j = X, Y, Z = 1, 2, 3$. To avoid confusion with the spherical angles θ and ϕ , the rotation angles are designated α, β, γ . The elementary rotation is represented by the rotation matrix

$$\mathbf{R}(\xi) = \begin{pmatrix} \cos \xi & \sin \xi \\ -\sin \xi & \cos \xi \end{pmatrix} \quad (63)$$

where $\xi = \alpha, \beta, \gamma$, and the rotation is restricted to $|\xi| \leq 45^\circ$. For the off-diagonal element $(1/n^2)_{ij}$, the rotation angle required to zero that element is given by

$$\xi = \frac{1}{2} \tan^{-1} \left[\frac{2(1/n^2)_{ij}}{(1/n^2)_{ii} - (1/n^2)_{jj}} \right] \quad (64)$$

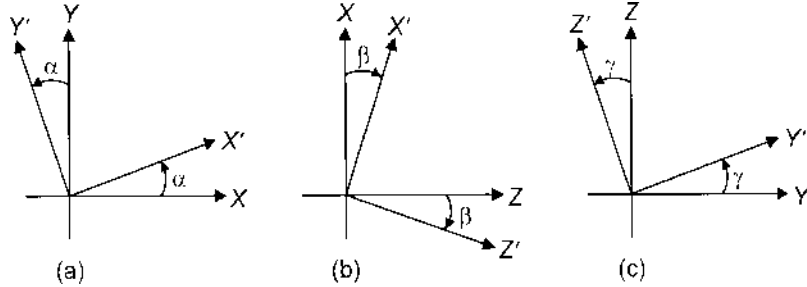


Figure 6 Elementary plane rotations for implementing a similarity transformation by the Jacobi method for diagonalizing the index matrix.

If $(1/n^2)_{ii} = (1/n^2)_{jj}$, then $|\xi|$ is set equal to 45° . The sense of the rotation is such that a positive (negative) angle corresponds to a counterclockwise (clockwise) rotation in the XY and YZ planes, and to a clockwise (counterclockwise) rotation in the XZ plane.

The steps of the diagonalization algorithm are illustrated in Fig. 7. First, the largest off-diagonal element $(1/n^2)_{ij}$ is selected, and the rotation specified by Eqs. (63) and (64) is executed in the ij plane. Then the elements of the new index matrix are updated. The form of the similarity matrix for each plane rotation is given in Table 8 along with formulas for the updated index matrix elements. This procedure is then repeated by selecting the largest off-diagonal element of the updated matrix. The process is terminated after N steps when the magnitude of the largest off-diagonal element is smaller than some pre-selected value (e.g., 10^{-10}). The diagonal of the last updated index matrix contains the eigenvalues ν_i ($i = 1, 2, 3$) corresponding to the new principal axes X', Y', Z' , respectively. The corresponding eigenvectors are computed by the following operations:

$$\begin{aligned}\hat{X}' &= \begin{pmatrix} X_1 \\ X_2 \\ X_3 \end{pmatrix} = \mathbf{S}_1^T \mathbf{S}_2^T \cdots \mathbf{S}_N^T \begin{pmatrix} 1 \\ 0 \\ 0 \end{pmatrix} \\ \hat{Y}' &= \begin{pmatrix} Y_1 \\ Y_2 \\ Y_3 \end{pmatrix} = \mathbf{S}_1^T \mathbf{S}_2^T \cdots \mathbf{S}_N^T \begin{pmatrix} 0 \\ 1 \\ 0 \end{pmatrix}\end{aligned}\quad (65)$$

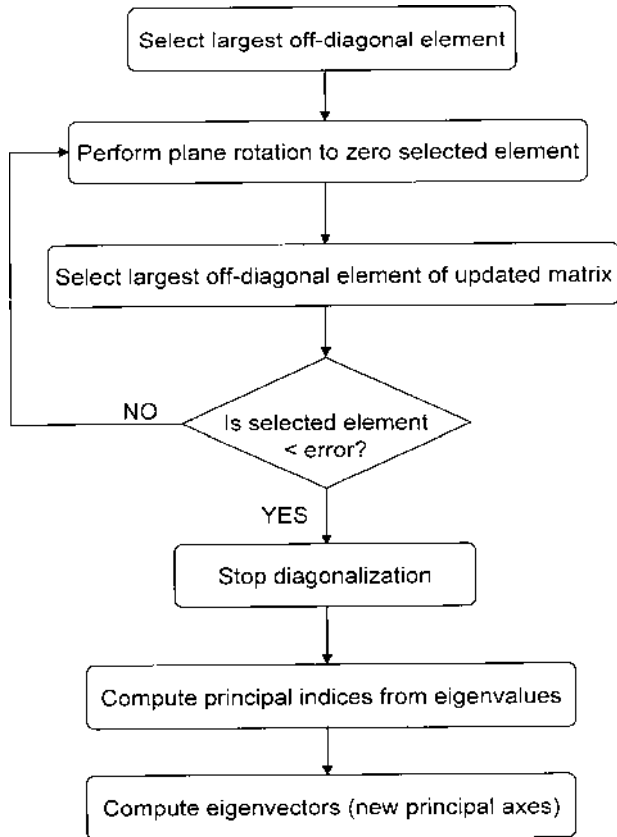


Figure 7 Algorithm for implementing the similarity transformation by the Jacobi method to diagonalize the index matrix.

$$\hat{\mathbf{Z}}' = \begin{pmatrix} Z_1 \\ Z_2 \\ Z_3 \end{pmatrix} = \mathbf{S}_1^T \mathbf{S}_2^T \cdots \mathbf{S}_N^T \begin{pmatrix} 0 \\ 0 \\ 1 \end{pmatrix}$$

These are orthonormal vectors whose elements X_i , Y_i , and Z_i ($i = 1, 2, 3$) are the direction cosines of the vectors relative to the XYZ system. The new principal indices are given by $n_X = (1/\nu_1)^{1/2}$, $n_Y = (1/\nu_2)^{1/2}$, and $n_Z = (1/\nu_3)^{1/2}$.

The final step is to find the new fast and slow axes and their corresponding indices. This is done by extending the procedure given in Section I.A. The index

Table 8 Form of the Similarity Transformation Matrix for Elementary Plane Rotations and Updated Index Matrix Elements

Rotation in the XY plane	$\alpha = \frac{1}{2} \tan^{-1} \left[\frac{2(1/n^2)_{12}}{(1/n^2)_{11} - (1/n^2)_{22}} \right]$	$S(\alpha) = \begin{pmatrix} \cos \alpha & \sin \alpha & 0 \\ -\sin \alpha & \cos \alpha & 0 \\ 0 & 0 & 1 \end{pmatrix}$
Rotation angle to zero $(1/n^2)_{12}$ element		
Transformation matrix		
Elements of updated index matrix		
	$(1/n^2)'_{11} = (1/n^2)_{11} \cos^2 \alpha + (1/n^2)_{22} \sin^2 \alpha + 2(1/n^2)_{12} \sin \alpha \cos \alpha$	
	$(1/n^2)'_{22} = (1/n^2)_{11} \sin^2 \alpha + (1/n^2)_{22} \cos^2 \alpha - 2(1/n^2)_{12} \sin \alpha \cos \alpha$	
	$(1/n^2)'_{33} = (1/n^2)_{33}$	
	$(1/n^2)'_{12} = (1/n^2)'_{21} = 0$	
	$(1/n^2)'_{13} = (1/n^2)'_{31} = (1/n^2)_{13} \cos \alpha + (1/n^2)_{23} \sin \alpha$	
	$(1/n^2)'_{23} = (1/n^2)'_{32} = -(1/n^2)_{13} \sin \alpha + (1/n^2)_{23} \cos \alpha$	
Rotation in the XZ plane		
Rotation angle to zero $(1/n^2)_{13}$ element	$\beta = \frac{1}{2} \tan^{-1} \left[\frac{2(1/n^2)_{13}}{(1/n^2)_{11} - (1/n^2)_{33}} \right]$	$S(\beta) = \begin{pmatrix} \cos \beta & 0 & \sin \beta \\ 0 & 1 & 0 \\ -\sin \beta & 0 & \cos \beta \end{pmatrix}$
Transformation matrix		
Elements of updated index matrix		
	$(1/n^2)'_{11} = (1/n^2)_{11} \cos^2 \beta + (1/n^2)_{33} \sin^2 \beta + 2(1/n^2)_{13} \sin \beta \cos \beta$	
	$(1/n^2)'_{22} = (1/n^2)_{22}$	

(continued)

Table 8 Continued

$(1/n^2)_{33} = (1/n^2)_{11}\sin^2\beta + (1/n^2)_{33}\cos^2\beta - 2(1/n^2)_{13}\sin\beta\cos\beta$	
$(1/n^2)_{12} = (1/n^2)_{21} = (1/n^2)_{12}\cos\beta + (1/n^2)_{23}\sin\beta$	
$(1/n^2)_{13} = (1/n^2)_{31} = 0$	
$(1/n^2)_{23} = (1/n^2)_{32} = -(1/n^2)_{12}\sin\beta + (1/n^2)_{23}\cos\beta$	
Rotation in the YZ plane	
Rotation angle to zero $(1/n^2)_{23}$ element	
	$\gamma = \frac{1}{2} \tan^{-1} \left[\frac{2(1/n^2)_{23}}{(1/n^2)_{22} - (1/n^2)_{33}} \right]$
Transformation matrix	$\mathbf{S}(\gamma) = \begin{pmatrix} 1 & 0 & 0 \\ 0 & \cos\gamma & \sin\gamma \\ 0 & -\sin\gamma & \cos\gamma \end{pmatrix}$
Elements of updated index matrix	
$(1/n^2)'_{11} = (1/n^2)_{11}$	
$(1/n^2)'_{22} = (1/n^2)_{22}\cos^2\gamma + (1/n^2)_{33}\sin^2\gamma + 2(1/n^2)_{23}\sin\gamma\cos\gamma$	
$(1/n^2)'_{33} = (1/n^2)_{22}\sin^2\gamma + (1/n^2)_{33}\cos^2\gamma - 2(1/n^2)_{23}\sin\gamma\cos\gamma$	
$(1/n^2)'_{12} = (1/n^2)_{21} = (1/n^2)_{12}\cos\gamma + (1/n^2)_{13}\sin\gamma$	
$(1/n^2)'_{13} = (1/n^2)_{31} = -(1/n^2)_{12}\sin\gamma + (1/n^2)_{13}\cos\gamma$	
$(1/n^2)'_{23} = (1/n^2)_{32} = 0$	

ellipsoid in the new principal axes system is given in diagonal form by

$$\frac{X'^2}{n_{X'}^2} + \frac{Y'^2}{n_{Y'}^2} + \frac{Z'^2}{n_{Z'}^2} = 1 \quad (66)$$

where

$$X' = X_1X + X_2Y + X_3Z$$

$$Y' = Y_1X + Y_2Y + Y_3Z \quad (67)$$

$$Z' = Z_1X + Z_2Y + Z_3Z$$

Substituting Eqs. (67) into Eq. (66) gives

$$A''X^2 + B''Y^2 + C''Z^2 + 2D''YZ + 2E''XZ + 2F''XY = 1 \quad (68)$$

where

$$A'' = \frac{X_1^2}{n_{X'}^2} + \frac{Y_1^2}{n_{Y'}^2} + \frac{Z_1^2}{n_{Z'}^2} \quad (69)$$

$$B'' = \frac{X_2^2}{n_{X'}^2} + \frac{Y_2^2}{n_{Y'}^2} + \frac{Z_2^2}{n_{Z'}^2} \quad (70)$$

$$C'' = \frac{X_3^2}{n_{X'}^2} + \frac{Y_3^2}{n_{Y'}^2} + \frac{Z_3^2}{n_{Z'}^2} \quad (71)$$

$$D'' = \frac{X_2X_3}{n_{X'}^2} + \frac{Y_2Y_3}{n_{Y'}^2} + \frac{Z_2Z_3}{n_{Z'}^2} \quad (72)$$

$$E'' = \frac{X_1X_3}{n_{X'}^2} + \frac{Y_1Y_3}{n_{Y'}^2} + \frac{Z_1Z_3}{n_{Z'}^2} \quad (73)$$

$$F'' = \frac{X_1X_2}{n_{X'}^2} + \frac{Y_1Y_2}{n_{Y'}^2} + \frac{Z_1Z_2}{n_{Z'}^2} \quad (74)$$

In a manner identical to that in Section I.A, the transformation to lab coordinates given by Eq. (13) is used in Eq. (68), setting $z = 0$, to find the new index ellipse in the lab reference frame:

$$A'x^2 + B'y^2 + 2C'xy = 1 \quad (75)$$

where

$$\begin{aligned} A' &= (A'' \cos^2 \phi + B'' \sin^2 \phi + F'' \sin 2\phi) \cos^2 \theta + C'' \sin^2 \theta \\ &\quad - (D'' \sin \phi + E'' \cos \phi) \sin 2\theta \end{aligned} \quad (76)$$

$$B' = A'' \sin^2 \phi + B'' \cos^2 \phi - F'' \sin 2\phi \quad (77)$$

$$\begin{aligned} C' &= \frac{1}{2} [(B'' - A'') \cos \theta \sin 2\phi + 2(E'' \sin \phi - D'' \cos \phi) \sin \theta \\ &\quad + 2F'' \cos \theta \cos 2\phi] \end{aligned} \quad (78)$$

The new fast and slow axes are at angles ρ' and $\rho' + 90^\circ$, with respect to the x axis, where

$$\rho' = \frac{1}{2} \tan^{-1} \left(\frac{2C'}{A' - B'} \right) \quad (79)$$

The new fast axis corresponds to the lesser of the two new indices, where

$$\begin{aligned} n'_{\text{new}} &= (A' \cos^2 \rho' + B' \sin^2 \rho' + 2C' \sin \rho' \cos \rho')^{-1/2} \\ n''_{\text{new}} &= (A' \sin^2 \rho' + B' \cos^2 \rho' - 2C' \sin \rho' \cos \rho')^{-1/2} \end{aligned} \quad (80)$$

The change in phase retardation for the optical modes propagating through a medium in the presence of an applied field has the general form

$$|\Delta\Gamma| \propto n^3 r_{\text{eff}} E \quad (81)$$

for the linear electro-optic effect, and

$$|\Delta\Gamma| \propto n^3 s_{\text{eff}} E^2 \quad (82)$$

for the quadratic electro-optic effect, where n is an average index of the medium, E is the magnitude of the applied field, and r_{eff} and s_{eff} are some linear combination of linear and quadratic electro-optic coefficients, respectively. Thus, the phase and polarization properties of transmitted light have a simple dependence on the applied voltage. The quantities $n^3 r_{\text{eff}}$ and $n^3 s_{\text{eff}}$ are figures of merit, providing a measure of the strength of the electro-optic effect.

III. ELECTRO-OPTIC EFFECTS IN LIQUID CRYSTALS

Physical mechanisms producing a change in refractive index to second order in the applied field were discussed in Chapter 6. Two of these are also of importance

in producing electro-optic effects in materials. One is distortion of the electron cloud, creating changes in the polarizability. This mechanism is at work in crystals, leading to both linear and quadratic electro-optic effects. The second one is reorientation of anisotropic molecules in an isotropic liquid by an electrically induced torque. Since the medium is centrosymmetric, only second order effects in the applied field are observable. This leads to the Kerr effect in isotropic liquids, which was discussed above. Molecular reorientation is also the most common mechanism employed in applications of liquid crystals (LCs). The phenomenon, however, is not simply described as the Kerr effect due to the fact that liquid crystals are in a state somewhere between that of solid crystals and isotropic liquids. In this state the molecules will reorient in the presence of an applied field, but will also be constrained by elastic forces that are not present in an isotropic liquid. The result is a more complicated relation between the birefringence change and the applied field. Also, the small elastic forces and large polarizability lead to relatively large changes in the optical properties that cannot be analyzed by a simple power series expansion of the dielectric polarization. Therefore, electro-optic effects in LCs deserve a separate discussion, although device applications may be similar in objective to those employing the Pockels and Kerr effects.

It should be noted that other electro-optic effects in LCs have been explored for devices, such as dynamic light scattering (electro-hydrodynamic instabilities) and flexoelectricity (similar to piezoelectricity in solid crystals) [10]. These are not very common, however, and the majority of applications today utilize the field controlled birefringence change that accompanies molecular reorientation in LCs.

Liquid crystals flow like liquids yet exhibit anisotropy in their mechanical, electrical, magnetic, and optical properties. Hence they form a phase which is intermediate between solid crystal and isotropic liquid. Certain rodlike or disklike molecules will exhibit a liquid crystalline phase. For the effects and applications described here, only rodlike ("calamitic") molecules [10] will be considered. These linear, organic calamitic molecules have a large length-to-breadth ratio, and typically consist of at least two carbon rings (either benzene or cyclohexane rings) linked together by some chemical group and having two different terminal groups on each end [11]. The rings provide the source of short-range intermolecular forces that lead to alignment of molecules in the liquid crystalline phase. Thus, LC molecules tend to orient with their long axes more or less parallel, exhibiting a degree of order that depends on temperature.

Figure 8 shows schematically the change in structure with temperature of a substance formed from organic calamitic molecules. The solid crystalline structure is characterized by both positional and orientational order in three dimensions. As the temperature is increased, the solid becomes relatively disordered, but retains orientational order and positional order in one dimension

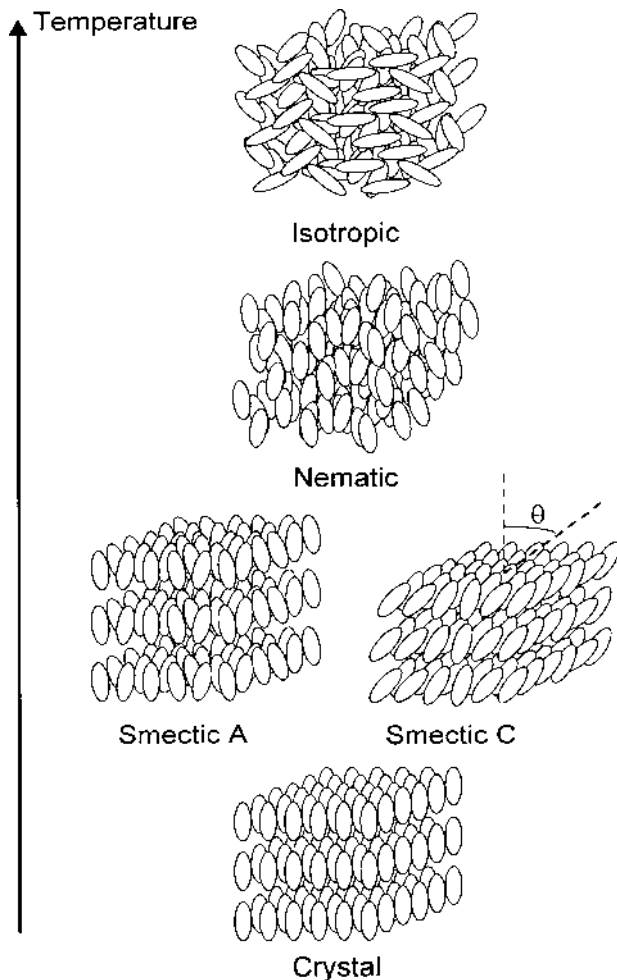


Figure 8 Schematic illustration of liquid crystal molecules in the solid crystalline, smectic, nematic, and isotropic phases as functions of temperature.

(i.e., in layers). This is called the smectic phase. Two smectic phases, smectic A and smectic C, are important. In the smectic A phase the long axes of the molecules orient on average along an axis normal to the layers. The long molecular axes in the smectic C phase have an average orientation along a finite angle with respect to the layer normal. At a higher temperature the material melts and another transition is reached at which all positional order disappears, but

orientational order remains. This is the nematic phase. Most LCs employed in electro-optic devices are in the nematic phase.

One additional type of LC phase is of technological significance. This is called the cholesteric phase and is illustrated in Fig. 9. The cholesteric LC is actually a nematic LC doped with a chiral agent. In any given plane, the molecules exhibit nematic orientational order. However, steric hindrances prohibit molecules in contiguous planes from achieving the same average orientation. Hence, the average orientation direction is slightly rotated from layer to layer. The sense of rotation is the same in each layer, resulting in a periodic twist of the average nematic orientation through the bulk of the liquid. The sense of the rotation depends on the chiral agent, and both right-handed and left-handed twists are possible.

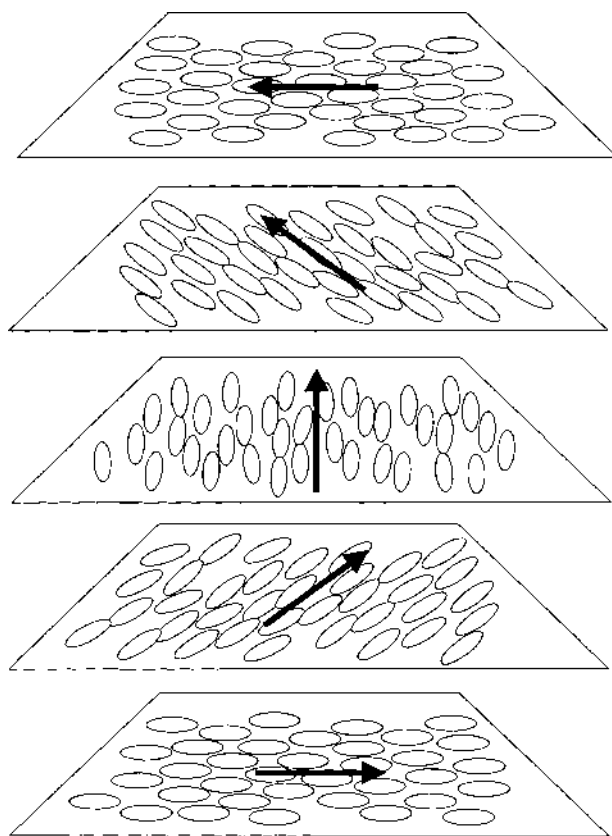


Figure 9 Schematic illustration of liquid crystal molecules in the cholesteric phase.

The orientation of LC molecules is characterized by a unit vector \mathbf{n} called the director. The director defines the average direction at a point in space of the long axis of the molecules, where the average is over a volume large compared to the size of the molecules but small compared to an optical wavelength. Thus, the director is a field quantity and may vary from point to point in space. The orientation of individual LC molecules fluctuates about \mathbf{n} . The degree of orientational order is characterized by the order parameter S defined as

$$S = \frac{1}{2} \langle 3 \cos^2 \theta - 1 \rangle \quad (83)$$

where θ is an angle between the long axis of an individual molecule and \mathbf{n} , and the angular brackets denote a statistical average. Perfect orientational order, approximated in the solid crystalline phase, corresponds to $S = 1$. In the isotropic liquid phase the orientation is totally random and $S = 0$ ($\langle \cos^2 \theta \rangle = 1/3$). Typical values of S at temperatures well below the nematic-isotropic transition are in the range of 0.4–0.7 [10,11]. Macroscopic physical parameters (mechanical, electrical, and optical) depend on the order parameter and hence may be strongly temperature dependent. For example, elastic force constants (defined below) are proportional to S^2 [12].

As discussed in Chapter 6, long rodlike molecules have an anisotropic polarizability. Axial symmetry dictates that the polarizability is identical in any direction perpendicular to the long axis. Thus, only two components are required to characterize the molecular polarizability α : the component α_{\parallel} parallel to the long axis, and the component α_{\perp} perpendicular to this axis. Since in the liquid crystalline state the molecules order parallel to their long axes, they form a macroscopically uniaxial medium with symmetry axis along the director \mathbf{n} . Thus, dielectric (ϵ) and refractive index properties are anisotropic and described by two components. The low frequency dielectric tensor is characterized by components parallel (ϵ_{\parallel}) and perpendicular (ϵ_{\perp}) to \mathbf{n} . The dielectric anisotropy $\Delta\epsilon = \epsilon_{\parallel} - \epsilon_{\perp}$ can be either positive or negative. Most commercially available LCs have positive $\Delta\epsilon$ at low frequencies (generally below a few kilohertz). Because ϵ_{\parallel} exhibits larger dispersion than ϵ_{\perp} , at high frequencies (generally > 10 kHz) it can become smaller than ϵ_{\perp} , making $\Delta\epsilon < 0$. The frequency at which $\Delta\epsilon$ changes sign is called the crossover frequency. There are, however, some LCs that have negative $\Delta\epsilon$ at low frequencies due to their structure. These generally have a polar group attached at some lateral position of the molecule, making $\epsilon_{\perp} > \epsilon_{\parallel}$. However, most commercially available LCs have a strong polar group, such as CN, F, or Cl, as one of the terminal groups and thus exhibit positive dielectric anisotropy.

The refractive index of an LC is determined to a great extent by UV electronic transition bands of σ or π electrons in the ring structures of the molecule, as well as being influenced by the polar terminating group. Since an

aligned nematic LC is uniaxial, it is characterized by an extraordinary index n^e for light polarized along the director \mathbf{n} and by an ordinary index n^o for light polarized perpendicular to this direction. The birefringence $\Delta n = n^e - n^o$ is positive for virtually all commercially important LCs.

Since the director \mathbf{n} defines the symmetry axis, it is imperative to find this direction for a given LC and its environmental conditions. For a given director field $\mathbf{n}(\mathbf{r})$ at equilibrium, elastic forces and torques arise when the system is perturbed by any distortion and will attempt to restore \mathbf{n} to its equilibrium configuration. Basic distortions are described by the divergence and the curl of \mathbf{n} . According to Oseen–Frank theory [11,12], the elastic contribution to the free energy density of a deformed LC can be written by

$$F_{\text{elastic}} = \frac{1}{2} K_1 |\nabla \cdot \mathbf{n}|^2 + \frac{1}{2} K_2 |\mathbf{n} \cdot \nabla \times \mathbf{n}|^2 + \frac{1}{2} K_3 |\mathbf{n} \times \nabla \times \mathbf{n}|^2 \quad (84)$$

where K_i ($i = 1, 2, 3$) are positive definite constants of the medium with units of force. With no other external conditions supplied, the equilibrium configuration of \mathbf{n} is the one that minimizes F_{elastic} . Since $F_{\text{elastic}} \geq 0$ and all of the terms in Eq. (84) are either positive or zero, the obvious equilibrium condition is $\mathbf{n} = \text{constant}$ (uniform parallel configuration). With this in mind, the three terms in Eq. (84) have the following geometric interpretation.

It is helpful to visualize the directors as a bundle of flexible soda straws. In the force-free equilibrium state they are all parallel, and we assume that they are parallel to the xy plane of a fixed laboratory coordinate system. If this bundle is clamped at one end, but forced to spread out radially at the other end, the director field will have a non-zero divergence. Hence the first term of Eq. (84) contributes a positive change to the free energy. This type of deformation is called splay, and K_1 is the splay force constant. The curl operation is associated with a rotation. The second term of Eq. (84) is related to a component of the curl along the local director, while the third term is related to a component of the curl perpendicular to the director. One type of rotation of directors keeps them parallel in any plane parallel to the xy plane, but rotates by a small amount each contiguous plane separated by an infinitesimal distance in the z direction. This is called a twist deformation. In this situation, there is no z component of \mathbf{n} , and the x and y components are functions of z only. This places the curl of \mathbf{n} in the xy plane where it may have a component along the local direction of \mathbf{n} . Hence, the second term in Eq. (84) is associated with a twist deformation, and K_2 is the twist force constant. Finally, a second type of director rotation is one about z that bends the soda straws in all planes parallel to the xy plane by the same amount. Again there is no z component of \mathbf{n} , and the x and y components both depend on x and y but are independent of z . The curl of \mathbf{n} is then in the z direction and hence perpendicular to the local \mathbf{n} . This produces a non-zero value of the third component of Eq. (84), with K_3 the bend force constant.

It should be noted that the force constants often appear in the literature with two subscripts, such that the splay, twist, and bend constants are written as K_{11} , K_{22} , and K_{33} , respectively. This is helpful when additional surface interaction terms, such as the saddle-splay K_{13} term [12], appear in the expression for the free energy. This is not important in the present discussion, however, and a single subscript convention will be employed.

Finally, one additional term in the elastic free energy expression should be considered. This one is associated with a naturally occurring twist of the director such as that seen in the cholesteric phase. The twist is assumed to be along the z direction, with the azimuth angle of the twist linearly proportional to z . Thus the natural twist angle is given by $q_0 z$, where q_0 is a positive number for a right-handed twist and negative for a left-handed twist. The sense of rotation of a right-handed twist is the same as that of a right-handed screw along the positive z direction. In other words, if the thumb of a right hand points along $+z$ and the fingers curl around the axis, the twist follows the direction of the curled fingers. The director field traces out a helix along z . The naturally occurring twist affects only the twist term of the elastic free energy, modifying it to become $(1/2)K_2|\mathbf{n} \cdot \nabla \times \mathbf{n} + q_0|^2$ [11,12].

Although the equilibrium condition of an LC in a force-free environment is given by $\mathbf{n} = \text{constant}$, the elastic forces are typically not strong enough to compete with thermal energy or mechanical vibrations and induce long-range order over distances large compared to an optical wavelength. Thus, a vial of LC will exhibit turbidity because small domains of LC (regions over which ordered orientation exists) scatter light profusely. The random thermal fluctuation of domain orientation produces random differences in refractive index over regions comparable to a wavelength. The liquid will become clear when the temperature is raised above the N-I transition where the order in all domains is reduced to zero (see Fig. 8). Then fluctuations in index occur only over regions small compared to a wavelength. Hence, this temperature is often called the clearing point. In order to make the nematic state optically clear, some external condition must be supplied that orders or aligns molecules over large regions. Typically, this is done by applying appropriate boundary conditions at the interface of the LC with a confining substrate.

Two typical interface alignments of LC molecules are illustrated in Fig. 10. Homeotropic or vertical alignment can be induced by, for example, depositing silane coupling agents on a glassy surface. These molecules promote bonding of terminal groups on the surface such that the long axes of the molecules are perpendicular to the surface. However, the orientation is not always exactly perpendicular, and other angles can be achieved. A typical technique for achieving a homogenous parallel alignment (long axes parallel to the substrate) is by unidirectional rubbing of the substrate with a linen cloth or lens tissue. Molecules tend to align with the rubbing direction. It is generally believed that



Figure 10 Schematic illustration of liquid crystal anchoring on a substrate. (a) Homeotropic anchoring; (b) homogeneous parallel alignment; and (c) homogeneous parallel alignment with pretilt.

physical rubbing produces a uniform and unidirectional tilt of dangling bonds or side chains on the surface of the substrate. Thus the LC director does not lie exactly parallel to the substrate, but tilts up in the direction of the rubbing. This small pretilt angle is important in ensuring a single LC domain and also providing different types of equilibrium elastic distortions for various applications (e.g., twisted nematic configuration, see below).

In general, interface energy terms should be added to the free energy to determine the equilibrium director configuration. However, under the approximation of strong surface anchoring, these surface terms approach ∞ and can be ignored in the variational problem. Instead, the director at the interface is assumed to be locked into position, and its orientation is given as a boundary condition. Intermolecular forces cause molecules near the interface to align with the surface director. This orientation can propagate into the bulk of the LC and be maintained, at least for relatively thin LC layers (e.g., $\sim 1\text{--}100\ \mu\text{m}$). However, an LC is normally bounded by at least two substrates, and their surface orientations may be dissimilar. To minimize elastic free energy, the director field must then assume a configuration that smoothly and continuously varies through the bulk to match the surface configurations on both substrates. It will be assumed, though, that the directors at the interfaces are locked so strongly that they never change when a distortion is applied. A distortion of the medium (i.e., a nonuniform director field) implies that the principal dielectric coordinate system (principal axes) or, equivalently in a uniaxial medium, the optic axis has a nonuniform orientation throughout the medium. Thus, the medium is optically inhomogeneous. The analysis of light propagation in such a medium can be facilitated by the Jones calculus.

Once an equilibrium director configuration is established, it can be distorted by an applied field that induces an electrical torque on the LC molecules. An electrical interaction energy term must be added to the free energy to account for this. This term is given by [11,12]

$$F_{\text{electrical}} = \frac{1}{2} \mathbf{E}_{\text{elec}}^{(\sim)} \cdot \mathbf{D}_{\text{elec}}^{(\sim)} \quad (85)$$

where the product of field with displacement vector includes the energy of

interaction of the field with the medium through the dielectric tensor. The field quantities in Eq. (85) are written in a way to emphasize that these are related to the applied electrical field at low frequency, not the optical field, and that these quantities are real. Again, the actual time dependence of the applied field can be nonsinusoidal, but the frequencies of Fourier components are assumed to be far from any material resonance. In what follows, the superscript “(\sim)” and subscript “elec” will be dropped when it is clear from the context that applied electrical fields are being addressed. Director orientation can be changed dramatically with modest applied voltages. This is the source of the large electro-optic effects in LCs.

In the majority of LC devices, a uniform layer of LC is sandwiched between two parallel substrates, and the director field is approximately uniform in planes parallel to the substrates. Thus, the director is a function of only the coordinate perpendicular to the substrates, usually taken to be the z axis, i.e., $\mathbf{n} = \mathbf{n}(z)$. Two conditions are assumed to apply: 1) no free charges exist in the bulk of the LC (this is only an approximation, but holds well in most cases); 2) no time-varying magnetic fields are present in the LC (this would apply even with ac electric fields as long as there are no free charges to form currents, again a fairly good approximation). These conditions imply that $\nabla \cdot \mathbf{D} = 0$ and $\nabla \times \mathbf{E} = 0$.

The applied electrical field is assumed to be uniform and either perpendicular to or parallel to the substrates. In the former case, $\nabla \cdot \mathbf{D} = 0$ implies that the component of \mathbf{D} normal to the substrates (e.g., D_z) is constant. [\mathbf{D} is independent of x and y because of the assumption that $\mathbf{n} = \mathbf{n}(z)$.] Boundary conditions dictate that $D_z = \sigma$, where σ is the surface charge density on the electrodes. Thus, even though the dielectric tensor components may change due to the applied field, the charge on the electrodes will remain constant. The magnitude of the electric field E is directly proportional to D_z through the impermeability, which may not be constant since it depends on the director orientation. Thus, the electric field in this case is not a constant [i.e., $E = E(z)$]. However, Eq. (85) can be expressed in terms of D_z^2 , which is a constant, and the impermeability, which is a function of z and subject to change. If the impermeability changes, this changes the electrical interaction energy through Eq. (85).

When the applied field is parallel to the substrates, then $\nabla \times \mathbf{E} = 0$ implies that $\mathbf{E} = \text{constant}$ independent of z since \mathbf{E} is uniform and parallel to the substrates. Thus, components of \mathbf{D} parallel to the substrates will not in general be constant. This implies that the charge on the electrodes will not remain constant, and the power supply must do work by supplying charge to keep the applied field (voltage) constant. Hence, in this case the additional energy supplied by the power supply must also be included in the free energy of the system. It turns out that the net electrical energy can be expressed in terms of E^2 [11,12], which is a constant, and components of the dielectric tensor, which are functions of z .

If these change due to the applied field, then the electrical interaction energy will change. Thus, the final equilibrium state is given by the director configuration that minimizes the total free energy, which includes the elastic energy, the electrical interaction energy, and possibly energy provided by an external power supply.

Although equilibrium states are important for determining the optical properties of LCs in devices, often the time response to a change in equilibrium states is of interest. The dynamic response of an LC will be determined not only by its elastic properties, but also by its viscosity since the medium is fluid. The bulk viscosity of an LC is related to its flow properties and is generally anisotropic. However, devices discussed here do not involve fluid flow. Torques on LC molecules will be resisted by rotational viscosity. The rotational viscosity coefficient is designated by γ_1 . Most nematic LCs have a rotational viscosity comparable to that of light machine oils, with $\gamma_1 \sim 0.02\text{--}0.50 \text{ Pa}\cdot\text{s}$ (pascal-seconds) [11]. The unit of Pa-s is equivalent to $1 \text{ N}\cdot\text{s}/\text{m}^2$ in SI units. Water at 20°C has a viscosity coefficient of $0.001 \text{ Pa}\cdot\text{s}$. Viscosity coefficients are also often stated in the cgs unit of poise, where $1 \text{ poise} = 1 \text{ dyn}\cdot\text{s}/\text{cm}^2$. For reference, $1 \text{ Pa}\cdot\text{s} = 10 \text{ poise}$.

A single pure LC compound usually has a rather limited temperature range between its melting and clearing points. To extend this range, mixtures of LC compounds are used in commercial products. The melting point of a mixture is less than any of its constituents and depends on the mixture ratio. The melting point reaches a minimum at the eutectic point, and such a mixture is called a eutectic mixture. Most commercially available LCs for applications are eutectic mixtures. The clearing point for the mixture is usually a linear average of the components. Many other physical parameters depend on the mixture ratio as well. Table 9 lists the physical properties of several commercially available LC mixtures. (See Ref. 10 for a discussion of several different liquid crystals.)

A. Electro-Optic Effects in Nematic Liquid Crystals

Common configurations of nematic LCs are the planar aligned, homeotropic (vertically aligned), and twisted nematic LC cells. Planar aligned cells can employ either longitudinal or transverse (in-plane) electric field control (relative to the direction of optical beam propagation).

Planar aligned nematic liquid crystal cell. A schematic diagram of a planar aligned nematic cell is shown in Fig. 11. The directors at either substrate are locked in positions parallel to those at the opposite substrate, and the equilibrium configuration consists of directors that are everywhere parallel to the substrate directions through the bulk of the cell. The directors are originally parallel to the y axis of a laboratory coordinate system. An electric field is applied perpendicular to the substrates along the z axis. This results in a reorientation (tilt)

Table 9 Physical Properties of Selected Commercial Liquid Crystal Mixtures

Liquid crystal mixture designation	T _{melt} (°C)	T _{SN} (°C)	T _{Ni} (°C)	$\epsilon_{ }/\epsilon_0$	$\Delta\epsilon/\epsilon_0$	n° (589 nm, 20°C)	Δn (589 nm, 20°C)	K ₁ (10 ⁻¹² N)	K ₂ (10 ⁻¹² N)	K ₃ (10 ⁻¹² N)	γ_1 (10 ⁻³ Pa·s)
BL006 [13]	-15	<-20	113	22.8	+17.3	1.5300	0.2860	17.9	—	33.5	—
BL037 [13]	—	<-20	109	21.1	+15.9	1.5260	0.2820	15.9	—	30.8	—
BL045 [13]	—	<-20	74	20.7	+15.3	1.5231	0.2303	12.7	—	20.8	—
BL046 [13]	—	<-20	83	18.2	+13.2	1.5201	0.2155	14.2	—	18.4	—
E7 [14,15,16]	-10	<-20	60.5	19.6	+14.5	1.5210	0.2250	12.0	9.0	19.5	270
E44 [15]	-6	—	100	22.0	+16.8	1.5277	0.2627	—	—	—	—
MLC-6609 [13]	—	<-30	91.5	3.4	-3.7	1.4737	0.0777	17.2	—	17.9	162
MLC-6610 [13]	—	<-40	79.5	3.5	-3.1	1.4828	0.0996	14.6	—	16.5	148
MLC-6692 [13]	—	<-40	77.5	14.7	+10.3	1.4771	0.0850	9.2	—	14.6	104
MLC-6694-000 [13]	—	<-40	112.5	10.1	+6.8	1.4865	0.1060	—	—	—	194
TL202 [13]	+29	+1	83	9.6	+6.1	1.5230	0.1851	19.1	—	20.1	—
TL205 [13]	—	<-20	87	9.1	+4.8	1.5270	0.2170	17.3	—	20.4	—
TL213 [13]	+5	<-20	87	10.0	+5.7	1.5270	0.2390	16.8	—	22.0	—
ZLI-1646 [J]	-7	—	60	10.6	+6	1.4780	0.0800	7.7	4.0	12.2	—
ZLI-1840 [13]	—	<-20	90	16.2	+11.9	1.4653	0.1727	—	—	—	238
ZLI-3201-100 [13]	—	<-40	88	11.8	+7.9	1.5008	0.1311	—	—	—	133

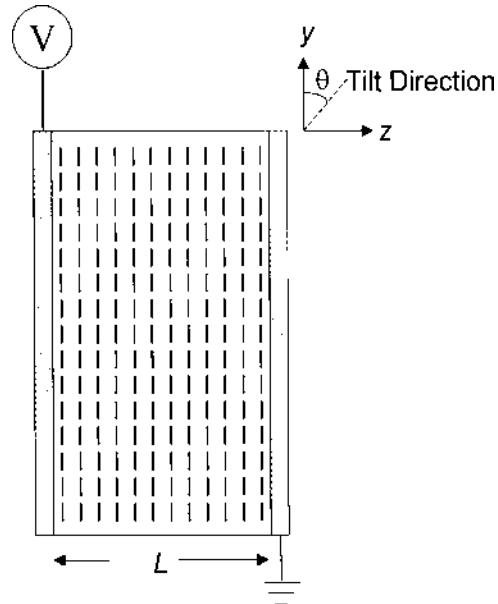


Figure 11 Planar aligned nematic liquid crystal cell.

of the directors toward the direction of the field. The orientation of the director field is given by the angle θ between the director and the y axis. Notice that this angle is complementary to the ordinary polar angle, which is measured with respect to the z axis. Therefore, the director is given by $\mathbf{n} = (0, \cos\theta, \sin\theta)$, where $\theta = \theta(z)$ is a function of z only. The boundary conditions are such that $\theta(0) = \theta(L) = 0$.

The director configuration for any field strength is obtained by minimizing the free energy of the system [11,12]. The total free energy is given by the integral of the sum of Eqs. (84) and (85) over the volume of the cell. The director field that minimizes this integral is found by the calculus of variations [1,11,12]. Elastic forces constrain molecular reorientation so that there is no tilt of the directors until a critical voltage V_{c1} is exceeded, where

$$V_{c1} = \pi \sqrt{\frac{K_1}{\Delta\epsilon}} \quad (86)$$

Above this applied voltage the directors begin to tilt toward the z axis, but the director field becomes inhomogeneous since directors at the substrates are locked into a parallel orientation. The magnitude of the tilt angle is symmetric about the center of the cell. Surface correlation forces become relatively weak a distance ξ

away from the substrate, where

$$\xi = \frac{1}{E} \sqrt{\frac{K_1}{\Delta\epsilon}} \quad (87)$$

and E is the strength of the local electric field. Therefore, this correlation distance becomes smaller at higher voltages, and the tilt is largest at the center of the cell. Calling the midlayer tilt angle θ_m , the value of θ_m for any applied voltage V is found by numerically solving the following equation [11]:

$$\frac{V}{V_{c1}} = \frac{2}{\pi} \int_0^{\pi/2} \left[\frac{(1 + \kappa \sin^2 \theta_m \sin^2 u)(1 + v \sin^2 \theta_m)}{(1 - \sin^2 \theta_m \sin^2 u)(1 + v \sin^2 \theta_m \sin^2 u)} \right]^{1/2} du \quad (88)$$

where

$$\kappa = \frac{K_3 - K_1}{K_1} \quad (89)$$

is a measure of the bend-splay elastic anisotropy, and

$$v = \frac{\Delta\epsilon}{\epsilon_\perp} \quad (90)$$

is a measure of the dielectric anisotropy. Once $\theta_m(V)$ is determined [actually, $\sin^2 \theta_m(V)$], it can be used to numerically solve the differential equation for the tilt angle $\theta(z)$:

$$(1 + \kappa \sin^2 \theta) \left(\frac{d\theta}{dz} \right)^2 = \left(\frac{2}{L} f(\theta_m) \right)^2 \left(\frac{1}{1 + v \sin^2 \theta} - \frac{1}{1 + v \sin^2 \theta_m} \right) \quad (91)$$

where

$$\begin{aligned} f(\theta_m) \\ = \int_0^{\pi/2} & \left[\frac{(1 + \kappa \sin^2 \theta_m \sin^2 u)(1 + v \sin^2 \theta_m)(1 + v \sin^2 \theta_m \sin^2 u)}{1 - \sin^2 \theta_m \sin^2 u} \right]^{1/2} du \end{aligned} \quad (92)$$

The result is the tilt angle as a function of z for any applied voltage V , i.e., $\theta(z, V)$.

The normal modes of propagation along z are the extraordinary wave polarized along y with index $n^e(\theta)$ and the ordinary wave polarized along x with index n^o . When a voltage is applied, the extraordinary index is nonuniform. Thus, the relative phase retardation is given by

$$\Gamma = \frac{2\pi}{\lambda} \int_0^L [n^e(\theta) - n^o] dz \quad (93)$$

where

$$\frac{1}{[n^e(\theta)]^2} = \frac{\cos^2 \theta}{(n^e)^2} + \frac{\sin^2 \theta}{(n^o)^2} \quad (94)$$

is z -dependent through $\theta(z, V)$.

The result of an applied voltage on the planar nematic cell is a negative change in the effective birefringence of the cell determined by Eq. (93), i.e., $\Delta n_{\text{eff}} = \lambda \Gamma / 2\pi L$. There is no analytical expression for $\Delta n_{\text{eff}}(V)$, but it can be found numerically by the solution of Eqs. (88)–(94). Alternatively, it can be measured for a specific LC and cell geometry. Generally, for $V < V_{\text{cl}}$ there is no change in Δn_{eff} . V_{cl} is thus often called a threshold voltage. For the liquid crystal E7, with $K_1 = 12 \times 10^{-12}$ N and $\Delta \epsilon = 14.5 \epsilon_0$ [14], $V_{\text{cl}} \sim 1$ volt. Above V_{cl} , Δn_{eff} decreases nonlinearly and eventually approaches zero asymptotically at $V \gg V_{\text{cl}}$ (e.g., $V \sim 5V_{\text{cl}}$).

For a step increase in voltage from 0 to V , the response time τ_{ON} for the change in Δn_{eff} to occur (e.g., the time it takes for Δn_{eff} to change from 10% to 90% of its maximum change at that voltage) is a function of V , i.e.,

$$\tau_{\text{ON}} \propto \frac{\gamma_1 L^2}{K_1} \left[\left(\frac{V}{V_{\text{cl}}} \right)^2 - 1 \right]^{-1} \quad (95)$$

while the relaxation time τ_{OFF} with the voltage turned off is given by the relation

$$\tau_{\text{OFF}} \propto \frac{\gamma_1 L^2}{K_1} \quad (96)$$

A typical OFF time is ~ 10 ms.

These results reveal some interesting physical properties of the aligned nematic LC cell. First, the initial alignment of the directors would seem to preclude any switching. There is no initial component of the electric field in the average long direction of the molecule. Hence, the induced dipole moment μ will be along the direction of the applied field, and the resultant torque ($\mu \times E$) is zero. However, the director actually fluctuates about its equilibrium orientation. Thus at some moment in time a component of the applied field will be along the long molecular axis, and the molecule will experience a nonzero torque. The analysis of minimizing the free energy examines potential equilibrium states, of which those where an electrical torque exists are included, and yields the resultant equilibrium state for given conditions. Of course, the interesting state is where the molecules tilt in the direction of the field. Equilibrium is established when an elastic restoring torque exactly balances the nonzero electrical torque. This is the origin of the dependence of the threshold voltage on elastic and dielectric constants in Eq. (86). Hence for a sufficiently strong field, the configuration of

parallel alignment becomes one of unstable equilibrium, and a small fluctuation will allow a transition to the state of lower energy where the directors tilt toward the direction of the applied field. When the elastic force constant goes to zero at the nematic–isotropic transition ($K_1 \propto S^2 \rightarrow 0$ at T_{N-I}), V_{c1} goes to zero (i.e., there is no threshold for molecular reorientation). This is thus the regime of the ordinary Kerr effect. The threshold voltage is smaller for LCs with large dielectric anisotropy since a smaller voltage is required to balance the elastic torque.

If the LC molecules have no permanent dipole moment, the electrical torque is due to induced dipole moments. Since the interaction depends on the strength of this induced dipole, the turn-on time is field (voltage) dependent and can be decreased by applying voltages large compared to the threshold voltage. On the other hand, the response time diverges as the applied voltage approaches V_{c1} . When the applied voltage is turned off, the molecules relax by elastic restoration forces. Hence, τ_{OFF} is inversely proportional to the elastic force constant. Since the reorientation is resisted by rotational viscous forces, the relaxation time is directly proportional to γ_1 .

In-plane switching (transverse field). In the discussion above, the field was applied longitudinally with respect to the direction of beam propagation. A schematic illustrating a transverse field applied to a planar aligned nematic cell is shown in Fig. 12. This is often referred to as in-plane switching since the applied field is in the plane of the nematic LC film. These are called fringe fields and, although strictly speaking nonuniform, for practical purposes they are approximately uniform within the bulk of the LC. The directors have the same initial distribution as the planar aligned nematic cell defined above. The electrodes, however, are small stripes of width w and separation d (such that $d \sim w \sim L$) deposited on the substrates of the cell. The same voltage V is applied to every other electrode with the electrodes in between held at ground potential. This creates a local in-plane field $E = V/d$. The directors are originally taken to be parallel to the x axis of the laboratory coordinate system, and the applied field is along the y axis. This results in a reorientation (twist) of the directors toward the direction of the field. The orientation of the director field is given by the angle ϕ between the director and the x axis. Therefore, the director is given by $\mathbf{n} = (\cos \phi, \sin \phi, 0)$, where $\phi = \phi(z)$ is a function of z only. The boundary conditions are such that $\phi(0) = \phi(L) = 0$.

The director configuration for any field strength is again obtained by minimizing the free energy of the system [11]. There is no twist of the directors until a critical voltage V_{c2} is exceeded, where

$$V_{c2} = \pi \frac{d}{L} \sqrt{\frac{K_2}{\Delta \epsilon}} \quad (97)$$

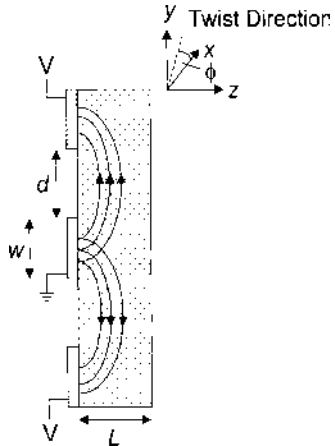


Figure 12 Planar aligned nematic liquid crystal cell with in-plane switching.

For example, in E7 $V_{c2} \sim (d/L)$ volts. Above this applied voltage the directors begin to twist toward the y axis, but the director field becomes inhomogeneous since directors at the substrates are locked into a parallel orientation. The magnitude of the twist angle is symmetric about the center of the cell. Calling the midlayer twist angle ϕ_m , the value of ϕ_m for any applied voltage V is found by numerically solving the following equation:

$$\frac{V}{V_{c2}} = \frac{2}{\pi} \int_0^{\pi/2} \left[\frac{1}{1 - \sin^2 \phi_m \sin^2 u} \right]^{1/2} du \quad (98)$$

Once $\phi_m(V)$ is determined [actually, $\sin^2 \phi_m(V)$], it can be used to numerically solve the differential equation for the twist angle $\phi(z)$:

$$\left(\frac{d\phi}{dz} \right)^2 = \left(\frac{\pi}{L} \frac{V}{V_{c2}} \right)^2 (\sin^2 \phi - \sin^2 \phi_m) \quad (99)$$

The result is the twist angle as a function of z for any applied voltage V , i.e., $\phi(z, V)$.

The propagation of polarized light through a nematic cell with a nonuniform twist angle must be analyzed by the Jones calculus. The method employs dividing the cell into a relatively large number of layers, where in each layer the twist angle ϕ is assumed to be approximately constant, but varies from layer to layer according to the computed angle $\phi(z, V)$. The number of layers is chosen to make the change in ϕ from layer to layer suitably small. Generally, for $V < V_{c2}$ there is no change in the propagation properties of the cell. Above V_{c2} ,

the retardation of the cell increases nonlinearly and eventually approaches some asymptote for $V \gg V_{c2}$ (e.g., $V \sim 5V_{c2}$). The response time τ_{ON} is given by

$$\tau_{ON} \propto \frac{\gamma_1 L^2}{K_2} \left[\left(\frac{V}{V_{c2}} \right)^2 - 1 \right]^{-1} \quad (100)$$

while the relaxation time τ_{OFF} with the voltage turned off is given by the relation

$$\tau_{OFF} \propto \frac{\gamma_1 L^2}{K_2} \quad (101)$$

Homeotropic nematic liquid crystal cell. A schematic diagram of this cell is shown in Fig. 13. The directors at either substrate are locked in positions perpendicular to both substrates, and the equilibrium configuration consists of directors that are everywhere parallel through the bulk of the cell and perpendicular to the substrates. The directors are originally parallel to the z axis of a laboratory coordinate system. An electric field is applied parallel to the y axis, perpendicular to the direction of beam propagation. The electrodes have a separation d , which yields a uniform field $E = V/d$ for an applied voltage V . This results in a reorientation (tilt) of the directors toward the direction of the field. The orientation of the director field is given by the angle θ between the director and the z axis, which in this case is the ordinary polar angle. Therefore, the director is given by $\mathbf{n} = (0, \sin \theta, \cos \theta)$, where $\theta = \theta(z)$ is a function of z only. The boundary conditions are such that $\theta(0) = \theta(L) = 0$.

The director configuration for any field strength is once again obtained by minimizing the free energy of the system [11]. The total free energy is given by the integral of the sum of Eqs. (84) and (85) over the volume of the cell. There is

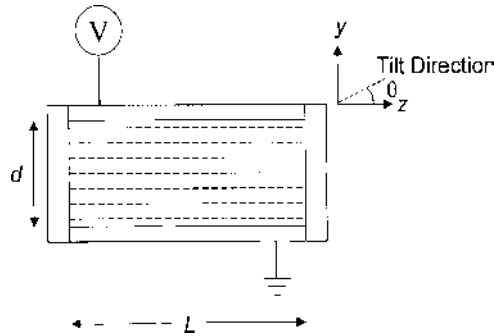


Figure 13 Homeotropic aligned nematic liquid crystal cell.

no tilt of the directors until a critical voltage V_{c3} is exceeded, where

$$V_{c3} = \pi \frac{d}{L} \sqrt{\frac{K_3}{\Delta \epsilon}} \quad (102)$$

For example, in E7 $V_{c3} \sim (d/L)$ volts. Above this applied voltage the directors begin to tilt toward the y axis (i.e., parallel to the substrates), but the director field becomes inhomogeneous since directors at the substrates are locked into a perpendicular orientation. The magnitude of the tilt angle is symmetric about the center of the cell. The midlayer tilt angle θ_m for any applied voltage V is found by numerically solving the following equation:

$$\frac{V}{V_{c3}} = \frac{2}{\pi} \int_0^{\pi/2} \left[\frac{1 + \kappa' \sin^2 \theta_m \sin^2 u}{1 - \sin^2 \theta_m \sin^2 u} \right]^{1/2} du \quad (103)$$

where

$$\kappa' = \frac{K_1 - K_3}{K_3} \quad (104)$$

Once $\theta_m(V)$ is determined [actually, $\sin^2 \theta_m(V)$], it can be used to numerically solve the differential equation for the tilt angle $\theta(z)$:

$$(1 + \kappa' \sin^2 \theta) \left(\frac{d\theta}{dz} \right)^2 = \left(\frac{\pi}{L V_{c3}} \right)^2 (\sin^2 \theta_m - \sin^2 \theta) \quad (105)$$

The result is the tilt angle as a function of z for any applied voltage V , i.e., $\theta(z, V)$.

The normal modes of propagation along z are the extraordinary wave polarized along y with index $n^e(\theta)$ and the ordinary wave polarized along x with index n^o . When a voltage is applied, the extraordinary index is nonuniform. Thus, the relative phase retardation is given by

$$\Gamma = \frac{2\pi}{\lambda} \int_0^L [n^e(\theta) - n^o] dz \quad (106)$$

where

$$\frac{1}{[n^e(\theta)]^2} = \frac{\cos^2 \theta}{(n^o)^2} + \frac{\sin^2 \theta}{(n^e)^2} \quad (107)$$

is z -dependent through $\theta(z, V)$.

The result of an applied voltage on the homeotropic nematic cell is a positive change in the effective birefringence of the cell determined by Eq. (106), i.e., $\Delta n_{\text{eff}} = \lambda \Gamma / 2\pi L$. There is no analytical expression for $\Delta n_{\text{eff}}(V)$, but it can be found numerically by the solution of Eqs. (103–107). Alternatively, it can be measured for a specific LC and cell geometry. Generally, for $V < V_{c3}$ there is no

change in Δn_{eff} . Above V_{c3} , Δn_{eff} increases nonlinearly and eventually approaches an asymptote at $V \gg V_{c3}$ (e.g., $V \sim 5V_{c3}$). The response time τ_{ON} for the change in Δn_{eff} to occur is a function of V , i.e.,

$$\tau_{\text{ON}} \propto \frac{\gamma_1 L^2}{K_3} \left[\left(\frac{V}{V_{c3}} \right)^2 - 1 \right]^{-1} \quad (108)$$

while the relaxation time τ_{OFF} with the voltage turned off is given by the relation

$$\tau_{\text{OFF}} \propto \frac{\gamma_1 L^2}{K_3} \quad (109)$$

Twisted nematic liquid crystal cell. A twisted nematic (TN) cell is illustrated schematically in Fig. 14. The substrates are treated for parallel alignment by, e.g., unidirectional rubbing, but the alignment directions of the two substrates are rotated by an angle $\Phi \leq 90^\circ$ with respect to one another. The director at each substrate is forced to align with the rubbed direction. Near each substrate, intermolecular forces induce alignment nearly parallel with the substrate alignment. However, to minimize elastic free energy, the directors rotate slowly through the bulk of the LC in such a way that at the substrates they align parallel to the rubbed direction. This creates a uniform twist of the director

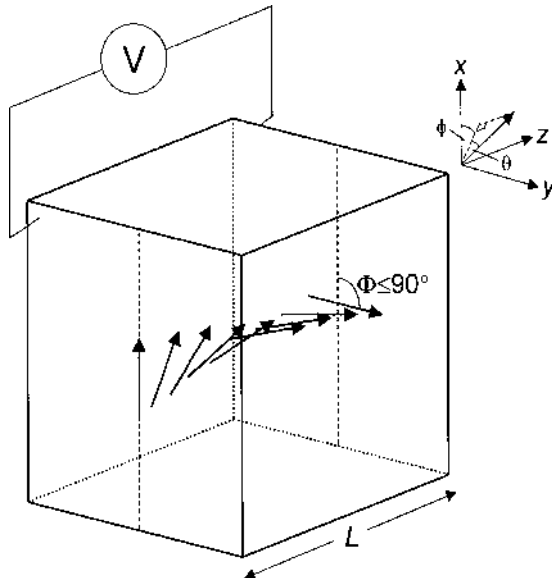


Figure 14 Twisted nematic liquid crystal cell.

field in the cell. (Note that this twist is induced by the boundary conditions and is not a natural twist such as occurs in cholesteric LCs.) This is an inhomogeneous optical system, and the propagation of light through it can be analyzed using the Jones calculus. In the absence of an applied field, the twist angle ϕ is uniform and proportional to z while the tilt angle θ , measured with respect to the projection of the director in the xy plane, is zero. The initial director is given by $\mathbf{n} = (\cos \phi, \sin \phi, 0)$, where $\phi = \phi(z) = (\Phi/L)z$, and the boundary conditions are $\theta(0) = \theta(L) = 0$, $\phi(0) = 0$ and $\phi(L) = \Phi$. When a field is applied, both the tilt and twist angles will change and be functions of z . Thus, in the presence of the field the director becomes $\mathbf{n} = (\cos \theta \cos \phi, \cos \theta \sin \phi, \sin \theta)$. The problem then is to determine $\theta(z)$ and $\phi(z)$.

There is no induced tilt or untwisting of the directors until a threshold voltage V_{th} is exceeded [11], where

$$V_{th} = V_{c1} \sqrt{1 + \frac{K_3 - 2K_2}{K_1} \left(\frac{\Phi}{\pi}\right)^2} \quad (110)$$

with V_{c1} given by Eq. (86). For E7, $V_{th} \sim 1$ volt. Notice that the threshold voltage of a TN cell is larger than that of a parallel aligned cell (i.e., zero twist), and is largest for a total twist of 90° (π radians). For any voltage larger than V_{th} , the value of the midlayer tilt angle θ_m is found by solving

$$\frac{V}{V_{c1}} = \frac{2}{\pi} \int_0^{\pi/2} \frac{1}{1 + v \sin^2 \theta} \left[\frac{1 + \kappa \sin^2 \theta}{h(\theta_m) - h(\theta)} \right]^{1/2} d\theta \quad (111)$$

where θ_m is associated with a constant C that can be found by solving

$$\frac{\Phi}{2} = C \sqrt{\frac{K_1}{K_2}} \int_0^{\theta_m} \frac{1}{\cos^2 \theta (1 + \kappa'' \sin^2 \theta)} \left[\frac{1 + \kappa \sin^2 \theta}{h(\theta_m) - h(\theta)} \right]^{1/2} d\theta \quad (112)$$

In these equations, κ and v are given by Eqs. (89) and (90), respectively, and

$$h(\theta) = \frac{C^2}{\cos^2 \theta (1 + \kappa'' \sin^2 \theta)} - \frac{1}{v(1 + v \sin^2 \theta)} \quad (113)$$

where

$$\kappa'' = \frac{K_3 - K_2}{K_2} \quad (114)$$

is a measure of the bend-twist elastic anisotropy. Once $\theta_m(V)$ and the associated parameter C are determined, they can be used to numerically solve the differential

equation for tilt angle $\theta(z)$:

$$(1 + \kappa \sin^2 \theta) \left(\frac{d\theta}{dz} \right)^2 = \left(\frac{2}{L} g(\theta_m) \right)^2 [h(\theta_m) - h(\theta)] \quad (115)$$

where

$$g(\theta_m) = \int_0^{\theta_m} \left[\frac{1 + \kappa \sin^2 \theta}{h(\theta_m) - h(\theta)} \right]^{1/2} d\theta \quad (116)$$

With $\theta(z)$ determined by Eqs. (115) and (116), the twist angle $\phi(z)$ is given by numerically integrating

$$\phi(z) = C \sqrt{\frac{K_1}{K_2}} \int_0^{\theta(z)} \frac{1}{\cos^2 \theta (1 + \kappa'' \sin^2 \theta)} \left[\frac{1 + \kappa \sin^2 \theta}{h(\theta_m) - h(\theta)} \right]^{1/2} d\theta \quad (117)$$

The results of these calculations are the tilt and twist angles as functions of z for any applied voltage V , i.e., $\theta(z, V)$ and $\phi(z, V)$.

The tilt and twist angles exhibit symmetries given by $\theta(z) = \theta(L - z)$ and $\phi(z) + \phi(L - z) = \pi/2$. The tilt angle exhibits a behavior similar to that of the parallel aligned nematic cell. Below V_{th} , the twist angle is linearly proportional to z . Significantly above threshold, the twist is nearly zero on one side of the midlayer and nearly 90° on the other side to match up with the boundary conditions. There is a sharp transition in ϕ from 0° to 90° in a thin region across the midlayer, while at the midlayer $\phi = 45^\circ$ for all voltages. The tilt angle for high voltages is approximately 90° over most of the cell. The response and relaxation times (for a 90° -twist cell) are given by

$$\tau_{ON} \propto \frac{\gamma_1 L^2}{K_{eff}} \left[\left(\frac{V}{V_{th}} \right)^2 - 1 \right]^{-1} \quad (118)$$

$$\tau_{OFF} \propto \frac{\gamma_1 L^2}{K_{eff}} \quad (119)$$

where

$$K_{eff} = K_1 + \frac{1}{4}(K_3 - 2K_2) \quad (120)$$

B. Supertwisted Nematic and Cholesteric Liquid Crystals

Nematic LCs doped with chiral agents achieve a natural twist of the director field as discussed above in the introduction to Section III. The twist is linearly proportional to z , and the natural twist rate is q_0 . This rate is determined by

the concentration of the chiral dopent. A wide range of q_0 is possible. The distance along z over which the twist angle goes through a 360° rotation is called the pitch p_0 , where $p_0 = 2\pi/q_0$. The total twist angle Φ in a cell with these chiral-doped LCs depends on the natural twist rate, the cell thickness, and boundary conditions at the confining substrates. The actual twist rate q and pitch p may differ slightly from the natural values.

Supertwisted nematic liquid crystal cell. A supertwisted nematic (STN) cell is illustrated in Fig. 15. The cell substrates are treated for parallel alignment (e.g., by rubbing), often with a small pretilt angle θ_0 . The substrate alignment directions are rotated with respect to one another, and the total twist angle for an STN cell is $\Phi > 90^\circ$. In standard nematic LCs a total twist of $\Phi > 90^\circ$ would be unstable, and the director configuration would revert to a lower energy state for which $\Phi < 90^\circ$. The actual twist would also be in the opposite sense of that expected for the higher energy state of $\Phi > 90^\circ$. Therefore, a stable STN cell must be composed of LCs with a chiral dopant that induces a natural twist with a specific sense to the twist angle. A positive twist rate is associated with a right-handed twist. The actual pitch for a cell of thickness L is determined by the condition

$$p = 2\pi \frac{L}{\Phi} \quad (121)$$

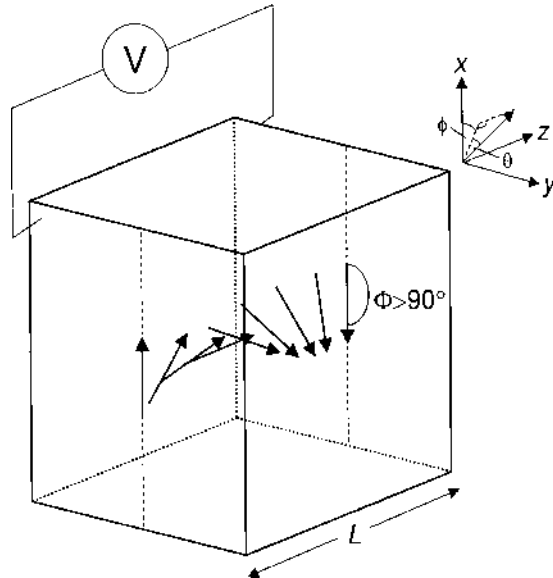


Figure 15 Supertwisted nematic liquid crystal cell.

Many STN cells used in LC displays are within the Grandjean zone given by $\Phi - \pi/2 < q_0 L < \Phi + \pi/2$, or the cell gap is within a quarter of the natural pitch [11]. Thus, STN cells are characterized by $p_0 \sim L$. This does not preclude, however, the possibility that the total twist can be $< 360^\circ$ or $> 360^\circ$.

With no field applied to the STN cell, the director is given by $\mathbf{n} = (\cos qz, \sin qz, 0)$, with $\phi(0) = 0$ and $\theta(0) = \theta_0$, where θ_0 is generally small and can be zero. However, a small pretilt angle helps to promote a single LC domain with a uniform twist. A field applied perpendicular to the substrates leads to a director redistribution in the bulk of the cell with tilt angle $\theta(z)$ and twist angle $\phi(z)$. The director now becomes $\mathbf{n} = (\cos \theta \cos \phi, \cos \theta \sin \phi, \sin \theta)$. The director distribution is found by minimizing the total free energy subject to the boundary conditions $\phi(0) = 0$, $\phi(L) = \Phi$, $\theta(0) = \theta_0$, $\theta(L) = -\theta_0$ [11].

With the field perpendicular to the substrates, the z component of the displacement vector is a constant. The tilt angle is symmetric about the midlayer. Tilt and twist angles satisfy the following differential equations:

$$\begin{aligned} K_1(1 + \kappa \sin^2 \theta) \left(\frac{d\theta}{dz} \right)^2 &= C_1 + \frac{D_z^2}{\varepsilon_{\perp}(1 + \nu \sin^2 \theta)} \\ &\quad - \frac{(C_2 + K_2 q_0 \cos^2 \theta)^2}{K_2 \cos^2 \theta (1 + \kappa'' \sin^2 \theta)} \end{aligned} \quad (122)$$

$$K_2 \cos^2 \theta (1 + \kappa'' \sin^2 \theta) \left(\frac{d\phi}{dz} \right)^2 = C_2 + K_2 q_0 \cos^2 \theta \quad (123)$$

where C_1 and C_2 are constants of integration determined by

$$C_1 = K_2 \cos^2 \theta_m (1 + \kappa'' \sin^2 \theta_m) \left(\frac{d\phi}{dz} \right)_m^2 - \frac{D_z^2}{\varepsilon_{\perp}(1 + \nu \sin^2 \theta_m)} \quad (124)$$

$$C_2 = K_2 \cos^2 \theta_m (1 + \kappa'' \sin^2 \theta_m) \left(\frac{d\phi}{dz} \right)_m - K_2 q_0 \cos^2 \theta_m \quad (125)$$

In these equations, θ_m is the midlayer tilt angle, $(d\phi/dz)_m$ is the midlayer twist angle gradient, and the parameters κ , ν and κ'' , are defined in Eqs. (89), (90), and (114), respectively. D_z is related to applied voltage V by

$$V = D_z \int_0^L \frac{dz}{\varepsilon_{\perp}(1 + \nu \sin^2 \theta)} \quad (126)$$

Thus, D_z is the independent variable, and Eqs. (122) and (123) are solved numerically. To do this requires that the constants C_1 and C_2 be known, which further requires knowledge of θ_m and $(d\phi/dz)_m$. Unfortunately, these are not

known *a priori* and must be guessed. An initial guess of these parameters allows Eqs. (122) and (123) to be solved. The solutions must satisfy the following conditions:

$$\theta(L/2) - \theta(0) = \theta_m - \theta_0 \quad (127)$$

$$\phi(L) - \phi(0) = \Phi$$

If these conditions are not satisfied, then new guesses of θ_m and $(d\phi/dz)_m$ are tried and the process iterated until Eqs. (127) are satisfied to some degree of precision.

Since D_z is not a commonly used field parameter its values may seem foreign to many scientists and engineers. Note that for some nominal voltage V' , $D_z \sim (1/2)(\epsilon_{\perp} + \epsilon_{\parallel})V'/L$. For example, in the well known LC E7, $\epsilon_{\perp} = 5.1\epsilon_0$ and $\epsilon_{\parallel} = 19.6\epsilon_0$ [14]. At 1 volt across a 5-μm cell, $D_z \sim 2 \times 10^{-5}$ C/m². In practice, for a given LC and cell thickness, nominal voltages can be used to generate values of the independent variable D_z . Once the angles $\theta(z)$ and $\phi(z)$ are determined, Eq. (126) can be used to calculate the actual voltages.

In a cell with a non-zero pretilt angle, the midlayer angle at equilibrium (no field) may actually be smaller than θ_0 . Thus, a threshold voltage is defined for which a uniform tilt $\theta(z) = \theta_0$ and a uniform twist $d\phi/dz = \Phi/L$ are achieved. This voltage is given by

$$V_{th} = \sqrt{\frac{2(K_3 - K_2)\cos^2\theta_0\Phi^2 + 4\pi K_2(L/p_0)\Phi}{\Delta\epsilon}} \quad (128)$$

This equation does not apply for $\theta_0 \rightarrow 0$ since the pretilt angle is already uniform at zero voltage. Therefore, at $\theta_0 = 0$ it is more meaningful to define the threshold voltage as the voltage required to produce a small distortion in the cell. This threshold is given by

$$V_{th} = V_{cl} \sqrt{1 + \frac{K_3 - 2K_2}{K_1} \left(\frac{\Phi}{\pi}\right)^2 + 4 \frac{K_2}{K_1} \frac{L}{p_0} \frac{\Phi}{\pi}} \quad (129)$$

Note that Eq. (128) does not, and should not, reduce to Eq. (129) as $\theta_0 \rightarrow 0$ since the two voltages are defined differently. For an infinite pitch, Eq. (129) reduces to Eq. (110) for a normal TN cell.

STN cells are advantageous for producing sharp switching of the midlayer angle, i.e., sharper than obtained in an ordinary TN cell. For $\Phi \sim 270^\circ$, depending on cell and material parameters, the slope at switching can become infinite. When the twist angle is large (e.g., $> 270^\circ$), $\theta_m(V)$ can develop a region of negative slope, which is unstable. Thus the midlayer angle will switch discontinuously between low and high values and exhibit bistability. In other

words, the switch-off voltage will be lower than the switch-on voltage. This region of bistability generally increases as the total twist angle increases.

Cholesteric liquid crystal cells. Cholesteric LC (CLC) cells differ from STN cells only in degree. The pitch is much smaller for a CLC, with $p \sim \lambda$ where λ is an optical wavelength. A single domain CLC will exhibit selective Bragg reflection over the wavelength range $n^{\circ}p < \lambda < n^{\circ}p$. This is discussed further below in Section IV. Noting that the total twist angle in a CLC is $\Phi \sim 2\pi L/p_0$, where again p_0 is the natural pitch of the CLC, the threshold voltage for switching a CLC (in the limit $L \gg p_0$) is found from Eq. (129) to be

$$V_{th} \approx \pi \frac{2L}{p_0} \sqrt{\frac{K_3}{\Delta\epsilon}} \quad (130)$$

At some voltage the CLC will be completely untwisted and be in a homeotropic nematic state. This is sometimes referred to as a cholesteric-nematic transition. In the homeotropic state the selective Bragg reflection is destroyed. When the voltage is turned off, the cell returns to the twisted CLC condition.

A CLC cell can also exist in what is known as the focal conic state. In this state there are multiple domains of CLC with helical axes approximately parallel to the substrates. At domain boundaries the azimuth angle of the helix changes abruptly. This produces strong light scattering. If a field is applied parallel to the substrates, a single domain CLC can be induced. A perpendicularly applied field will induce the homeotropic state.

C. Ferroelectric Liquid Crystals

Ferroelectric liquid crystals (FLCs) can achieve a macroscopic electrical polarization in the absence of an applied field, similar to the phenomenon of spontaneous polarization in ferroelectric crystals. This is due to their molecular structure and their confinement to a very thin cell.

FLCs exist in the smectic C phase illustrated in Fig. 8. Because the thickness of each layer in the smectic C phase is smaller than the molecular length, molecular packing in the layered structure forces the long axes of the molecules to incline at an angle θ with respect to the layer normal s . The molecules possess a permanent dipole moment that is not parallel with the molecular axis. If, however, the azimuth angle is fixed and equal in each layer, then there is inversion symmetry through the mirror plane formed by \mathbf{n} and \mathbf{s} and two-fold rotation symmetry about the direction $\mathbf{n} \times \mathbf{s}$. These symmetries result from an equal distribution of molecules aligned along \mathbf{n} and $-\mathbf{n}$. Hence the dipole fields cancel out on average, and there is no net polarization.

If the LC is doped with a chiral agent, it can form a smectic C* phase. In this phase the angle θ in each layer is constant, but the director precesses about

the \mathbf{s} axis in a helical fashion. This breaks the inversion symmetry and leads to a net dipole moment that is parallel to the direction of $\mathbf{n} \times \mathbf{s}$ and thus perpendicular to \mathbf{n} .

The smectic C* LC is placed in a very thin cell with alignment layers on each substrate that are parallel to one another. The boundary conditions imposed by the substrates are strong enough to suppress the helix when the cell gap is sufficiently small (generally $\sim 1\text{--}2\ \mu\text{m}$). This is called the surface stabilized mode. It results in a director geometry called the bookshelf alignment as illustrated in Fig. 16. Each molecule possesses a permanent dipole moment with a component transverse to the molecular axis, which in this case is also perpendicular to the substrates. This leads to a net polarization along this axis. The direction of the polarization may be up or down this axis.

If an electric field is applied perpendicular to the substrates, the polarization will attempt to align with the direction of the field to achieve a minimum energy state. Above a critical field E_c defined by

$$E_c = \frac{\pi^4 K_2}{4 P p^2} \quad (131)$$

where P is the magnitude of the spontaneous polarization and p is the pitch of the undistorted helix, the polarization direction will reverse (i.e., align parallel to the field). This causes the director to precess about the axis \mathbf{s} by 180° . As illustrated in Fig. 16, this is equivalent to rotating the director by an angle 2θ about the direction $\mathbf{n} \times \mathbf{s}$, i.e., a direction perpendicular to the substrates or along the field \mathbf{E} . Since the field couples to a permanent dipole, the reorientation speed can be fast with switching time generally in the microsecond regime. The switch-on and

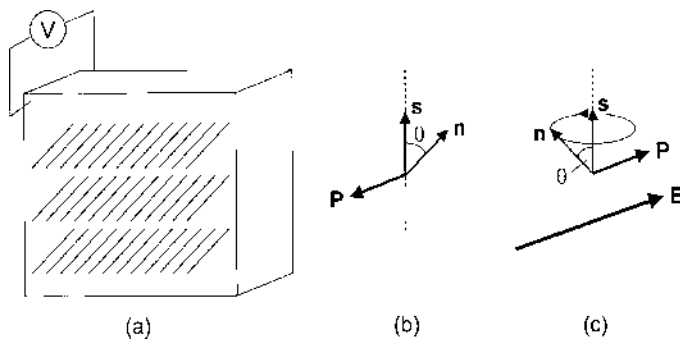


Figure 16 Ferroelectric liquid crystal cell. (a) Bookshelf alignment of smectic C* ferroelectric liquid crystals; (b) directions of director, layer normal, and spontaneous polarization vectors; and (c) realignment of \mathbf{P} and precession of \mathbf{n} with an applied field \mathbf{E} .

switch-off times are equal and are achieved by opposite polarity fields. Moreover, the reorientation is bistable so that once the cell is switched, it will remain in that orientation even when the field is turned off. The orientation will not change until a field of sufficient strength and opposite polarity is applied.

The reorientation of the optic axis in an FLC cell results in a change of its birefringence. For light polarized along the original direction of the optic axis, the change in retardation upon switching is

$$\Delta\Gamma = \frac{2\pi}{\lambda} [n^e - n^e(2\theta)]L \quad (132)$$

where

$$\frac{1}{[n^e(2\theta)]^2} = \frac{\cos^2 2\theta}{(n^e)^2} + \frac{\sin^2 2\theta}{(n^o)^2} \quad (133)$$

D. Polymer-Dispersed Liquid Crystals

Polymer-dispersed liquid crystals (PDLCs) are composite media comprised of two phases: solid polymer and nematic LC. As the name implies, the polymer is the host phase and the LC is the dispersed phase. Several different types of PDLC have been studied [17]. In general, all of these systems are formed from an initial homogenous mixture of polymerizable monomer and LC. As the system undergoes a polymerization chemical reaction, a point is reached at which the LC and the forming polymer are not miscible. The LC then separates as a distinct phase. A very common morphology is that of small LC droplets or domains (linear scale $\leq 10 \mu\text{m}$) suspended in a solid polymer host. These droplets have an effective refractive index that differs from that of the polymer and hence will scatter light. The strength of the optical scattering, i.e., the scattering cross section, depends both on this refractive index mismatch and on the size of the droplet. In some systems the shape of the droplets is roughly spherical or ellipsoidal. Thus, the scattering cross section can be approximated by the analytical expressions for such geometric shapes. The effective refractive index is some admixture of the ordinary and extraordinary indices of the LC.

It is interesting that these LC droplets retain liquid crystalline behavior even when the LC is confined to a small space in all three dimensions. For large enough droplets this is evident in polarized optical microscopy where the birefringence of the droplets causes them to appear bright on a dark background for PDLC samples between crossed polarizers. Even for smaller droplets the liquid crystalline behavior is evident in the electro-optical properties of PDLCs. An applied field reorients LC molecules and changes the effective refractive index of the droplets. This is most striking when the field-induced effective index

matches that of the surrounding polymer, and the PDLC sample changes from a white opaque film to a transparent one under a suitably applied field. The threshold-like behavior of the transmittance with applied voltage and the reversal to the opaque state when the voltage is turned off are both evidence of anisotropic elastic and dielectric properties of the LC droplets.

It is obvious that the confining geometry of PDLCs will not allow nematic configurations that are as simple as the planar homogeneous alignments discussed above; the curved LC-polymer interface will induce distortions in the director field. Still, it is possible to observe parallel (tangential) and homeotropic (normal) anchoring of LC molecules at the polymer surface, and strong anchoring conditions can still apply. The application of the Oseen-Frank theory [see Eq. (84)] is nontrivial, but computer simulations of nematic director configurations in large ($> 1\text{-}\mu\text{m}$ diameter) spherical droplets have been performed [18]. The most common configuration seen in these types of droplets with tangential anchoring is the bipolar configuration. This is shown schematically in Fig. 17. The director field follows the curvature of the surface, but becomes more parallel near the center of the droplet. An axis of symmetry exists along a diameter of the sphere and terminates in two point defects at the poles where conflicting nematic directors (normal and parallel) converge. The bipolar configuration yields a distinctive white-cross interference pattern on a dark background under polarized microscopy.

Computer simulations of spherical bipolar droplets under the influence of an applied field indicate an alignment of the symmetry axis with the electric field with minimal effect on the bipolar nematic configuration [19]. Thus, the alignment of a perfectly spherical droplet requires little elastic distortion, and there appears to be no energetically favorable position to which the droplet will relax once the field is turned off. A possible reason that such orientational relaxation is actually observed is that droplets are almost never perfectly spherical; a slightly elongated shape would favor a minimum elastic energy where the symmetry axis of the director field aligns with the long axis of the droplet, as computer simulations have verified [19]. An applied field still distorts

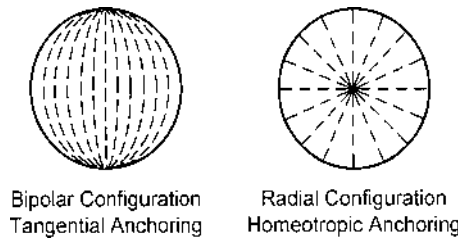


Figure 17 Nematic director configurations in spherical liquid crystal droplets.

the director field, with molecules attempting to align with the field, but elastic forces return the directors to their original orientation when the field is removed. In essence, the symmetry axis appears to reorient with an applied field, and then relaxes to its original orientation when the field is turned off.

Other nematic configurations are possible depending on the surface anchoring conditions and droplet size. Another common configuration resulting from normal surface anchoring, called the radial or star configuration, is also illustrated schematically in Fig. 17. In this case a perfectly spherical droplet exhibits a point defect at its center, and there is no apparent preferred symmetry axis. However, a slightly elongated droplet will have a symmetry axis coincident with the long droplet axis. Other more complicated configurations may occur, especially in very small droplets, particularly for irregularly shaped droplets, but experimental evidence still seems to indicate that elongated droplets act as if they possess an axis of symmetry [20]. Thus the droplets behave effectively as optically uniaxial domains. Since the droplet is obviously inhomogenous, it cannot be simply characterized by the ordinary and extraordinary refractive indices of the bulk LC. The refractive index is some admixture of n^o and n^e , with an effective value given by $n_{||}$ for light polarized parallel to the symmetry axis and by n_{\perp} for light polarized perpendicular to the symmetry axis. The droplet also exhibits an effective dielectric anisotropy $\Delta\epsilon$ that is close to that of the bulk LC.

Wu et al. [19] developed an electro-elastic model of LC droplets for reorientation of the droplet symmetry axis in an applied electric field. The droplet consists of a LC residing in an elongated cavity with axial symmetry (e.g., an ellipsoid of revolution) in the polymer host. The elastic free energy of the nematic directors is governed by the radius of curvature of the cavity. For a bipolar droplet, the elastic deformation at the droplet equator near the cavity wall is pure bend with a free energy density of $K_3/2R^2$, where R is the radius of curvature at the equator [19]. This concept is generalized for the entire droplet by assuming that the elastic free energy density of the droplet can be written as $F_d = K/2R^2$, where R is now the local radius of curvature at some position on the cavity wall, and K is an effective elastic force constant (i.e., in general some average of K_1 , K_2 , and K_3). Note that an infinite radius of curvature (i.e., a plane parallel interface) would provide an absolute minimum of this energy. The details of the nematic configuration are ignored, and it is assumed that an applied field reorients the symmetry axis, called the droplet director N . The geometry of the interaction is shown in Fig. 18.

N is initially coincident with the long axis of the droplet, which makes an angle γ_0 with respect to the direction of the applied field. With the application of the field the droplet director attempts to reorient with the field at the cost of increasing elastic energy. The resultant elastic torque exerted on the droplet director is given by $dF_d/d\gamma$, where γ is the new orientation angle with respect to the field. The electric torque $dF_e/d\gamma$ is related to the electrostatic free energy

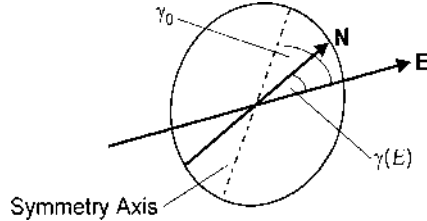


Figure 18 Liquid crystal droplet director reorientation with an applied field.

density of the droplet given by $F_e = -(1/2)[\epsilon_{\perp} E_{loc}^2 + \Delta\epsilon(\mathbf{N}\cdot\mathbf{E}_{loc})^2]$. The new equilibrium orientation $\gamma(E_{loc})$ is determined by the condition that the net torque acting on the droplet is zero, i.e., $d(F_d + F_e)/d\gamma = 0$.

An important point is that the field strength determining the electrical torque is the local field at the LC droplet. This is not the same as the applied field $E = V/L$, where L is the thickness of the PDLC film, due to the electrostatic screening effect of the polymer (and possibly neighboring LC droplets). A simple and crude approximation is made by assuming that the electrostatic screening is effectively the same as that due to an isolated, homogeneous, isotropic dielectric sphere embedded in a second infinite, homogenous, isotropic dielectric medium. This is a problem of classical electrostatics that yields the local field E_{loc} in the sphere [21]:

$$E_{loc} = \frac{3}{2 + \epsilon_{LC}/\epsilon_p} E \quad (134)$$

where ϵ_{LC} and ϵ_p are the effective dielectric constants of the droplet and polymer, respectively. In general, the dielectric constants will be complex with $\epsilon = \epsilon' + i\sigma/\omega$, where ϵ' is the real part, σ is the conductivity, and ω is the frequency of the applied field. All real LCs and polymers will have finite electrical conductivity due to the presence of ionic impurities. In the low frequency (dc) limit, $\epsilon_{LC}/\epsilon_p \approx \sigma_{LC}/\sigma_p$.

The elongated droplet model requires an expression for the droplet radius of curvature. The cavity is assumed to be approximately ellipsoidal in shape with semi-major axis a and semi-minor axis b . If the droplet aspect ratio $\ell = a/b$ is not too large ($\ell - 1 \ll 1$), a simple approximate expression for the radius of curvature can be given by [19]

$$R(\gamma) = a[\cos^2(\gamma - \gamma_0) + \ell^2 \sin^2(\gamma - \gamma_0)]^{-1/2} \quad (135)$$

Note that this leads to a minimum of $F_d = K/2a^2$ when $\gamma = \gamma_0$. Using Eq. (135) and setting the total torque equal to zero yields the equilibrium orientation angle

for applied field strength E ,

$$\gamma(E) = \frac{1}{2} \tan^{-1} \left[\frac{\sin 2\gamma_0}{\cos 2\gamma_0 + (E/E_c)^2} \right] \quad (136)$$

where E_c is a critical field defined by

$$E_c = \frac{1}{3a} \left(\frac{\varepsilon_{LC}}{\varepsilon_p} + 2 \right) \sqrt{\frac{K(\ell^2 - 1)}{\Delta\varepsilon}} \quad (137)$$

Note that $\gamma \rightarrow \gamma_0$ as $E \rightarrow 0$, and $\gamma \rightarrow 0$ asymptotically for $E > E_c$.

The orientation of the droplet director with respect to a fixed laboratory coordinate system is illustrated in Fig. 19. In an ordinary PDLC the droplets form in random positions with completely random orientations, unless some external process is used to orient forming droplets. The effective refractive indices of the droplets are thus found by averaging over the angles γ and ϕ . It is assumed that the azimuth angle is distributed isotropically among the droplets. Only the angle γ changes with an applied field by Eq. (136). The off-diagonal elements of the dielectric tensor in the lab frame then average to zero. Hence, the lab frame serves as an effective principal axes system. When the applied field is zero, the effective droplet index is isotropic with a value given by

$$n_d = \sqrt{\frac{2n_\perp^2 + n_\parallel^2}{3}} \quad (138)$$

When the sample is fully switched ($E > E_c$) so that $\gamma \rightarrow 0$, the effective index seen by light propagating along the z axis is $n_d \approx n_\perp$.

For intermediate values of the applied field the droplets will behave as anisotropic domains. The effective refractive indices can be obtained by averaging the diagonal components of the dielectric tensor. Note that these depend on the angle $\gamma(E)$, which for any given droplet is parameterized by the droplet's initial orientation γ_0 . Hence the angle $\gamma(E)$ will have a distribution determined by the distribution of γ_0 . Assuming that the droplets have a distribution of initial orientation angles with a normalized probability density $p(\gamma_0)$, the average principal droplet indices are given by

$$\begin{aligned} \bar{n}_{dx}(E) &= \left[\int_0^\pi \left[n_\perp^2 + \frac{1}{2}(n_\parallel^2 - n_\perp^2) \sin^2 \gamma(E, \gamma_0) \right] p(\gamma_0) \sin \gamma_0 d\gamma_0 \right]^{1/2} \\ &= \bar{n}_{dy}(E) \end{aligned} \quad (139)$$

$$\bar{n}_{dz}(E) = \left[\int_0^\pi [n_\perp^2 + (n_\parallel^2 - n_\perp^2) \cos^2 \gamma(E, \gamma_0)] p(\gamma_0) \sin \gamma_0 d\gamma_0 \right]^{1/2}$$

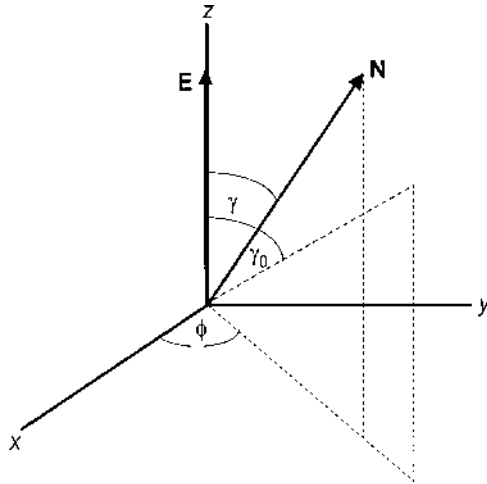


Figure 19 Droplet director orientation and electric field direction with respect to a laboratory reference frame.

If γ_0 is isotropically distributed, then $p(\gamma_0) = 1/2$. Note, however, that for an arbitrary field the droplet is effectively uniaxial.

Scattering of light by LC droplets in a PDLC can be formally treated as scattering from birefringent spheres [22]. However, useful approximations for scattering efficiency can be obtained by treating the droplet as a uniform, isotropic sphere with an effective index given by the average of the principal indices. Single particle scattering in the Rayleigh-Gans approximation [23] is often employed, for which the scattering cross section σ_{sc} for a sphere of radius a is given by

$$\sigma_{sc} = \pi a^2 \left(\frac{n_d}{n_p} - 1 \right)^2 \Phi \left(\frac{2\pi a}{\lambda} \right) \quad (140)$$

where for unpolarized light with scattering angle θ_s ,

$$\Phi(ka) = \frac{4}{9} (ka)^4 \int_0^\pi (1 + \cos^2 \theta_s) G^2(2ka \sin \frac{1}{2} \theta_s) \sin \theta_s d\theta_s \quad (141)$$

$$G(u) = \frac{3}{u^3} (\sin u - u \cos u) \quad (142)$$

The time response of the system is found by including a viscous torque $\gamma_1 d\gamma/dt$. For elastic relaxation of the droplet director in the absence of an applied

field, the orientation angle is found to follow an exponential time decay with time constant given by [19]

$$\tau_{\text{OFF}} = \frac{\gamma_1 a^2}{K(\ell^2 - 1)} \quad (143)$$

The response time to an applied field is also approximately exponential with a time constant given by (for $\gamma(0) \approx \pi/2$ and $\gamma(E) \sim 0$)

$$\tau_{\text{ON}} \approx \frac{\gamma_1}{\Delta\epsilon E^2 + K(\ell^2 - 1)/a^2} \quad (144)$$

E. Holographic Polymer-Dispersed Liquid Crystals

When LC droplets condense in a developing polymer, the process is called polymerization-induced phase separation (PIPS). An important class of PIPS processes proceeds through photopolymerization, a polymer chemical reaction controlled by ultraviolet or visible light. If a monomer-liquid crystal system with a photoinitiator is irradiated by an inhomogenous pattern of light, that pattern can be impressed on the resulting PDLC. When this is done using coherent beams of light in a typical holography exposure, the result is called a holographic PDLC (HPDLC).

A simple HPDLC grating consists of periodic channels of PDLC separated by solid polymer channels [24]. The droplets can be small compared to an optical wavelength. This leads effectively to a medium with a spatially periodic dielectric tensor. For a mixture of two homogeneous, isotropic dielectric materials, the effective dielectric constant of the medium can be expressed in terms of the dielectric constants of the two pure components approximately by $\epsilon = \epsilon_a + f(\epsilon_b - \epsilon_a)$, where ϵ_a and ϵ_b are the dielectric constants of the host and dispersed materials, respectively, and f is the volume fraction of the dispersed material in the host. The approximation holds well as long as $\epsilon_a \approx \epsilon_b$. This relation can be extended to anisotropic media as long as the two tensors are nearly equal, component by component.

The periodic rectangular PDLC distribution can be Fourier analyzed. Including only terms up to first order in the Fourier expansion, the spatially periodic dielectric tensor can be written as

$$\boldsymbol{\epsilon}(\mathbf{r}) = \boldsymbol{\epsilon}^{(0)} + \boldsymbol{\epsilon}^{(1)} \cos(\mathbf{K}_g \cdot \mathbf{r}) \quad (145)$$

where

$$\boldsymbol{\epsilon}^{(0)} = (1 - \alpha f_c) \boldsymbol{\epsilon}_p + \alpha f_c \boldsymbol{\epsilon}_d \quad (146)$$

$$\boldsymbol{\epsilon}^{(1)} = \frac{2f_c}{\pi} \sin(\alpha\pi)(\boldsymbol{\epsilon}_d - \boldsymbol{\epsilon}_p) \quad (147)$$

In these equations, α is the ratio of the PDLC channel width to the grating period Λ , \mathbf{K}_g is the grating vector ($|\mathbf{K}_g| = 2\pi/\Lambda$), f_c is the volume fraction of LC in the PDLC channel, and $\boldsymbol{\epsilon}_d$ and $\boldsymbol{\epsilon}_p$ are the dielectric tensors for the LC droplet and polymer, respectively. The polymer is assumed to be isotropic, so $\boldsymbol{\epsilon}_p$ is a scalar quantity. The droplet dielectric tensor is symmetric and thus will have nine components in general, but only six of which are independent. For an unslanted reflection grating (see Section IV), the applied field is parallel to the z axis and there is assumed to be orientational symmetry of the droplet director distribution in the grating planes. Under these conditions the probability distribution function is independent of the azimuth angle, and the off-diagonal tensor elements average to zero. With the geometry shown in Fig. 19, the diagonal components are given by

$$\begin{aligned} \epsilon_{dx}(E) &= \int_0^\pi \left[\epsilon_\perp + \frac{1}{2}(\epsilon_\parallel - \epsilon_\perp) \sin^2 \gamma(E, \gamma_0) \right] p(\gamma_0) \sin \gamma_0 d\gamma_0 = \epsilon_{dy}(E) \\ \epsilon_{dz}(E) &= \int_0^\pi \left[\epsilon_\perp + \frac{1}{2}(\epsilon_\parallel - \epsilon_\perp) \cos^2 \gamma(E, \gamma_0) \right] p(\gamma_0) \sin \gamma_0 d\gamma_0 \end{aligned} \quad (148)$$

Note the relations $\epsilon_\perp/\epsilon_0 = n_\perp^2$ and $\epsilon_\parallel/\epsilon_0 = n_\parallel^2$.

For an unslanted transmission grating (see Section IV), the situation is somewhat different. It is often found that the droplet directors have a probability distribution sharply peaked about the grating vector (e.g., the x axis in the lab frame). This would correspond to a peak near the angles $\theta = 90^\circ$ and $\phi = 0$. Those off-diagonal elements of the droplet dielectric tensor that are proportional to $\sin \phi$ are thus very small when averaged over ϕ . However, those that are proportional to $\cos \phi$ only can be significant. The coupling of reference and signal (diffracted) waves (see Section IV) can be considered for three different cases: 1) both reference and signal waves are s-polarized, 2) both reference and signal waves are p-polarized, and 3) the reference wave is s-polarized and the signal wave is p-polarized, or vice versa. It turns out that for cases 1 and 2, the coupling coefficients depend only on the diagonal components of the droplet tensor. For case 3, the coupling coefficients depend only on the off-diagonal elements that are proportional to $\sin \phi$, and are hence very small. If the probability distribution is an even function of γ_0 and ϕ , then all off-diagonal elements will be strictly zero on average. As a practical matter, the coupling between s- and p-polarized waves can be ignored. Thus, only the diagonal elements of the droplet tensor are important. The droplet directors must be assumed to have a normalized probability distribution $p(\gamma_0, \phi)$. Since

the applied field does not affect the azimuth angle, the diagonal components can be written as

$$\begin{aligned}\varepsilon_{dx} &= \int_0^{2\pi} \int_0^{\pi} [\varepsilon_{\perp} + (\varepsilon_{\parallel} - \varepsilon_{\perp}) \sin^2 \gamma(E, \gamma_0) \cos^2 \phi] p(\gamma_0, \phi) \sin \gamma_0 d\gamma_0 d\phi \\ \varepsilon_{dy} &= \int_0^{2\pi} \int_0^{\pi} [\varepsilon_{\perp} + (\varepsilon_{\parallel} - \varepsilon_{\perp}) \sin^2 \gamma(E, \gamma_0) \sin^2 \phi] p(\gamma_0, \phi) \sin \gamma_0 d\gamma_0 d\phi \\ \varepsilon_{dz} &= \int_0^{2\pi} \int_0^{\pi} [\varepsilon_{\perp} + (\varepsilon_{\parallel} - \varepsilon_{\perp}) \cos^2 \gamma(E, \gamma_0)] p(\gamma_0, \phi) \sin \gamma_0 d\gamma_0 d\phi\end{aligned}\quad (149)$$

With $p(\gamma_0, \phi)$ sharply peaked about $\theta = 90^\circ$ and $\phi = 0$, ε_{dy} will always be approximately equal to ε_{\perp} for a transmission grating.

A periodic array of dissimilar dielectrics will produce coherent scattering of light. Hence the HPDLC is a diffraction grating with a diffraction efficiency that depends on the difference between the dielectric tensor elements of the LC droplet and the polymer. Since the droplet tensor elements are field dependent, the diffraction efficiency of the grating can be tuned. In certain cases the grating can be switched off completely. The relevant physical parameter characterizing this is the grating coupling coefficient, which is described further in the following section.

IV. APPLICATIONS

The main utility of electro-optic effects is that they allow one to electronically control or impress information on an optical beam. The effects discussed in Sections II and III can be used to induce changes in the phase, frequency, polarization, and amplitude (intensity) of a beam of light. This section examines several applications of electro-optic effects. It is not meant to be exhaustive or provide in-depth analyses of device designs. Rather, it presents the principles of operation for several devices and illustrates the variety of applications possible.

A. Phase Modulators

These devices serve to modulate only the phase of a light beam without changing its amplitude. In general, polarized light is incident on the device, and the device is configured so that the light experiences no change in its polarization state. When an electric field is applied, one of the principal axes of the system is along

the direction of the polarization. In this way, the light sees only a change in the refractive index and hence a change in the optical path length of the device. A step change of index can be used, for example, to tune an interferometer. A time dependent change of index can be used to modify the frequency of the light. In general, linear and quadratic electro-optic effects can be employed. Although liquid crystals can also be used, their slower time response limits their range of applicability for phase modulation. Below, three different applications of phase modulation are examined.

Frequency shifters. This type of device produces a constant frequency shift in a monochromatic beam of light by the application of a linear voltage ramp $V(t) = V_0(t/T)$ to a Pockels cell. V_0 is the maximum voltage applied, and T is the duration of the ramp. As an example, consider a longitudinal field applied to a crystal of $\bar{4}2m$ symmetry (e.g., KDP). This is a uniaxial optical medium. The optic axis Z is taken to be along the direction of beam propagation. When a field $E(t)$ is applied along this direction, the new principal axes generated in the crystal are X' and Y' in the XY plane at angles of 45° with respect to the old X and Y axes, and $Z' = Z$ [3]. The new principal refractive indices are

$$\begin{aligned} n_{X'} &\approx n^\circ - \frac{1}{2}(n^\circ)^3 r_{63} E \\ n_{Y'} &\approx n^\circ + \frac{1}{2}(n^\circ)^3 r_{63} E \\ n_{Z'} &= n^e \end{aligned} \tag{150}$$

If the incident beam is polarized along the X' axis, it will experience an additional phase delay upon propagation through a crystal of length L given by

$$\Delta\varphi(t) = -\pi(n^\circ)^3 r_{63} E(t)L/\lambda = -\pi(n^\circ)^3 r_{63} V_0 t / T \lambda \tag{151}$$

The outgoing wave is then of the form

$$E(z, t) = A \exp[i(kz - \omega t + \Delta\varphi(t))] \tag{152}$$

The time dependent phase shift is thus manifested as a frequency shift $\Delta\omega$ given by

$$\Delta\omega = -\frac{d(\Delta\varphi)}{dt} = \pi(n^\circ)^3 r_{63} \frac{V_0}{\lambda T} \tag{153}$$

The frequency shift is generally such that $\Delta\omega \ll \omega$ (e.g., $\Delta\omega \sim 10^5 - 10^6$ Hz).

Frequency chirp. Consider now the same phase modulator as above but where a quadratic voltage ramp, $V_0(t/T)^2$, is applied. The frequency shift will

then be

$$\Delta\omega(t) = -\frac{d(\Delta\varphi)}{dt} = 2\pi(n^\circ)^3 r_{63} \frac{V_0}{\lambda T} \frac{t}{T} \quad (154)$$

which is linearly proportional to t . The result is a linear frequency chirp that is impressed upon the wave.

A linear frequency chirp can also be achieved by applying a linear voltage ramp to a Kerr cell. The field is applied transverse to the direction of propagation by electrodes with separation d , and the incident field is polarized parallel to the applied field. The medium is centrosymmetric. The extraordinary index induced by the field is

$$n^e \approx n - \frac{1}{2} n^3 s_{11} E^2 \quad (155)$$

where n is the isotropic index. The linear frequency chirp in this case is given by

$$\Delta\omega(t) = 2\pi n^3 s_{11} \frac{L}{\lambda d^2} \left(\frac{V_0}{T} \right)^2 t \quad (156)$$

Frequency modulators. A modulated voltage $V(t) = V_0 \sin \Omega t$ is applied to the longitudinal Pockels cell phase modulator described above. The induced phase delay is

$$\Delta\varphi(t) = -\pi(n^\circ)^3 r_{63} V_0 \sin \Omega t / \lambda \equiv \Delta\varphi_0 \sin \Omega t \quad (157)$$

The output field has an induced phase modulation, with

$$E_{\text{out}}^{(\sim)}(L, t) = E_0 \exp(i2\pi n^\circ L / \lambda) \exp[-i(\omega t + \Delta\varphi_0 \sin \Omega t)] + \text{c.c.} \quad (158)$$

This can be written as

$$\begin{aligned} E_{\text{out}}^{(\sim)} = & E_0 \{ J_0(\Delta\varphi_0) \cos[\varphi_0 - \omega t] + J_1(\Delta\varphi_0) \cos[\varphi_0 - (\omega + \Omega)t] \\ & - J_1(\Delta\varphi_0) \cos[\varphi_0 - (\omega - \Omega)t] + J_2(\Delta\varphi_0) \cos[\varphi_0 - (\omega + 2\Omega)t] \\ & - J_2(\Delta\varphi_0) \cos[\varphi_0 - (\omega - 2\Omega)t] + J_3(\Delta\varphi_0) \cos[\varphi_0 - (\omega + 3\Omega)t] \quad (159) \\ & - J_3(\Delta\varphi_0) \cos[\varphi_0 - (\omega - 3\Omega)t] + J_4(\Delta\varphi_0) \cos[\varphi_0 - (\omega + 4\Omega)t] \\ & - J_4(\Delta\varphi_0) \cos[\varphi_0 - (\omega - 4\Omega)t] + \dots \} \end{aligned}$$

where $\varphi_0 = 2\pi n^\circ L / \lambda$ and J_n is the n th order Bessel function of the first kind. The output field thus contains the fundamental wave and sidebands at all harmonics of the modulation frequency.

B. Polarization Converters

These devices convert an input polarization state to an output polarization state. They are often called voltage-controlled waveplates or retarders. An example of such a device is illustrated in Fig. 20. Here the input light is polarized along the principal axis X (i.e., at a direction at 45° with respect to the principal axis X') of the longitudinal KDP Pockels cell described in Section IV.A above. The output polarization will be parallel to the input polarization when no field is applied. When a voltage V is applied, the induced phase retardation is given by

$$\Gamma = \pi \frac{V}{V_\pi} \quad (160)$$

where

$$V_\pi = \frac{\lambda}{2(n^\circ)^3 r_{63}} \quad (161)$$

is called the half-wave voltage (i.e., the voltage that induces a retardation of π radians). Using the Jones calculus described in Section I.B, it can easily be shown that the output wave is polarized along Y when a voltage of V_π is applied to the Pockels cell. Thus, the polarization converter with a half-wave voltage converts a linearly polarized wave to an orthogonal linearly polarized wave.

When a voltage of $(1/2)V_\pi$ is applied to the Pockels cell, the retardation is $\pi/2$. This is a quarter-wave retardation, and the output is circularly polarized. Specifically, the Jones calculus can be used to show that, in the example given, the output is a left circularly polarized wave. If a mirror is placed at the output of the cell to provide a retroreflection back through the cell, the wave will experience an additional quarter-wave retardation and be converted to a linearly polarized state that is orthogonal to the input polarization. Hence the input

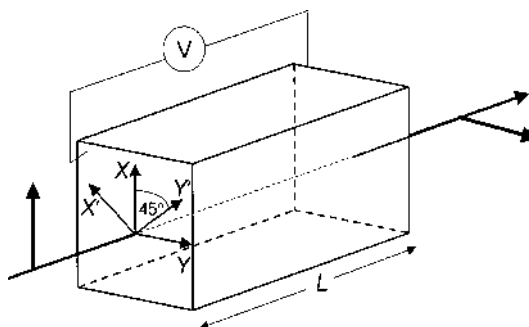


Figure 20 Electro-optic polarization converter using a crystal with $\bar{4}2m$ symmetry (longitudinal field).

polarizer will block the wave from propagating back through the optical system. This device is called an optical isolator, and it is used as a fast electro-optic Q-switch in lasers [7].

Several different types of crystals can be used as polarization converters. Each type will have its own half-wave voltage, which will differ some from the formula given in Eq. (161). An example of a transverse polarization converter is given in Fig. 21. The crystal has $\bar{4}3m$ symmetry and is optically isotropic. The field direction is along the diagonal of the cubic lattice (the $\langle 111 \rangle$ direction), i.e., along a direction $(\hat{X} + \hat{Y} + \hat{Z})/\sqrt{3}$ in the crystal principal axes frame, and the electrode separation is d . The new principal axes are given by [3]

$$\begin{aligned}\hat{X}' &= \frac{1}{\sqrt{2}}\hat{Y} - \frac{1}{\sqrt{2}}\hat{Z} \\ \hat{Y}' &= -\frac{2}{\sqrt{6}}\hat{X} + \frac{1}{\sqrt{6}}\hat{Y} + \frac{1}{\sqrt{6}}\hat{Z} \\ \hat{Z}' &= \frac{1}{\sqrt{3}}\hat{X} + \frac{1}{\sqrt{3}}\hat{Y} + \frac{1}{\sqrt{3}}\hat{Z}\end{aligned}\quad (162)$$

and the new principal refractive indices are

$$\begin{aligned}n_{X'} &\approx n + \frac{1}{2\sqrt{3}}n^3r_{41}E \\ n_{Y'} &\approx n + \frac{1}{2\sqrt{3}}n^3r_{41}E \\ n_{Z'} &\approx n - \frac{1}{\sqrt{3}}n^3r_{41}E\end{aligned}\quad (163)$$

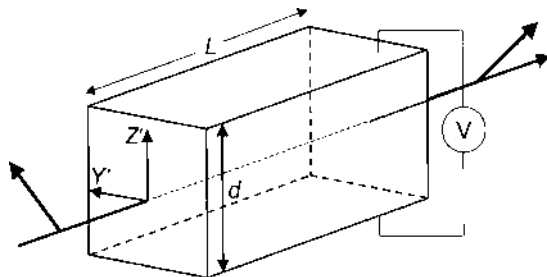


Figure 21 Electro-optic polarization converter using a crystal with $\bar{4}3m$ symmetry (transverse field).

where n is the isotropic refractive index, and $E = V/d$ is the applied field. The input wave is polarized at 45° with respect to the applied field (i.e., 45° with respect to the Z or Z' axis). The half-wave voltage in this case works out to be

$$V_\pi = \frac{\lambda d}{\sqrt{3}n^3 r_{41} L} \quad (164)$$

Note that in this case the half-wave voltage scales with the ratio d/L . Typical half-wave voltages for bulk crystals range from $\sim 1 - 10$ kV, for both longitudinal and transverse geometries [7].

A polarization converter can also be made using an isotropic Kerr medium in a transverse electrode cell. A uniaxial medium is induced by the applied field, with the optic axis parallel to the field. The induced ordinary and extraordinary refractive indices are given by

$$n^o \approx n - \frac{1}{2}n^3 s_{12} E^2 \quad (165)$$

$$n^e \approx n - \frac{1}{2}n^3 s_{11} E^2$$

where n is the isotropic index and $E = V/d$ is the electric field. The input wave is polarized at 45° with respect to the applied field, and the induced birefringence of the medium is given by Eq. (56). The resulting retardation is

$$\Gamma = 2\pi LB(V/d)^2 = \pi(V/V_\pi)^2 \quad (166)$$

and the half-wave voltage is thus given by

$$V_\pi = \frac{d}{\sqrt{2LB}} \quad (167)$$

The half-wave voltage for nitrobenzene in a cell of dimensions $d = 1$ cm, $L = 5$ cm is 20 kV.

It is noted that a polarization converter can also be made with a parallel aligned nematic liquid crystal cell with a field applied longitudinally to the cell. The input wave is polarized at 45° with respect to the director, and the cell thickness is such that $\Delta n L/\lambda = (2m + 1)/2$, where m is an integer and Δn is the birefringence of the LC. This produces an equivalent retardation of $\pi \pmod{2\pi}$, and the output wave has a polarization orthogonal to the input. When a voltage large compared to V_{c1} is applied, the relative retardation is essentially zero (propagation parallel to the new optic axis), and the output polarization is switched to a state parallel to that of the input.

C. Amplitude Modulators

In these devices, a voltage modulation is converted into an amplitude (intensity) modulation of a beam of light. In many cases these consist of a polarization converter followed by an analyzer (polarizer). Two additional types of amplitude modulators will also be discussed, however. One of these is the twisted nematic liquid crystal cell. The second involves electro-optic scattering of unpolarized light in a PDLC.

There are two types of amplitude modulator based on polarization conversion: a normally black mode and a normally white mode. This depends on the orientation of the analyzer with respect to the input polarization, either parallel or orthogonal. In what follows, only the normally black mode will be discussed. If the voltage dependent phase retardation is $\Gamma(V)$, then the transmittance after the output polarizer relative to the input polarized light can be found by the Jones calculus and is given by

$$T(V) = \sin^2 \Gamma(V)/2 \quad (168)$$

For a normally white mode, sin is replaced by cos. Note that if the transmittance were defined with respect to unpolarized light incident on the first polarizer, the right hand side of Eq. (168) would be multiplied by the transmittance of the first polarizer, which is generally less than 0.5. The transmittance for devices not based on polarization converters will not be as simple as Eq. (168).

Pockels cell amplitude modulators. These modulators may employ either longitudinal or transverse electrode geometries. The transmittance is written as

$$T(V) = \sin^2 \left[\frac{1}{2} \pi (V/V_\pi) \right] \quad (169)$$

The modulator has a minimum transmittance of zero and a maximum transmittance of 1.

To obtain an approximate linear modulation, the cell is biased as a quarter-wave cell. This can be done by applying a bias voltage of $(1/2)V_\pi$ and modulating with a small voltage V_m about this, or by inserting a quarter-wave plate to yield a static bias and modulating with a small voltage about zero. In either case, the resultant transmittance is given by

$$T = \frac{1}{2} [1 + \sin(\Gamma_m \sin \Omega t)] \quad (170)$$

where $\Gamma_m = \pi(V_m/V_\pi)$ and the modulating part of the voltage is $\Delta V(t) = V_m \sin \Omega t$, with Ω the modulation frequency. Equation (170) can also be written as

$$T = \frac{1}{2} [1 + 2J_1(\Gamma_m) \sin \Omega t + 2J_3(\Gamma_m) \sin 3\Omega t + \dots] \quad (171)$$

If $\Gamma_m \ll 1$, then

$$T \approx \frac{1}{2}[1 + \Gamma_m \sin \Omega t] \quad (172)$$

and the modulated voltage produces a linear modulation of the transmittance about 0.5. If the modulation becomes too large, the output will be distorted with an appreciable contribution from higher harmonics.

High frequency amplitude modulators. The Pockels cell is essentially a capacitor (dielectric sandwiched between two electrodes). It therefore presents a capacitive load to the power supply driving it, acting as a lumped circuit element in series with the source impedance. At high modulation frequencies the capacitive impedance ($X_C = 1/i\omega C$) is low, and the voltage drop is mainly across the source impedance. Thus the field across the Pockels cell is low, and high source voltages are required to reach a half-wave voltage drop across the capacitor. This draws more power from the source and may be prohibitive. To alleviate this, the amplitude modulator is often integrated into a resonant circuit [3] as illustrated in Fig. 22. The resonant frequency $\omega_0 = (LC)^{-1/2}$ of the circuit is approximately matched to the modulation frequency Ω , where L is the circuit inductance and C is the capacitance of the modulator. Near this frequency the circuit impedance Z is approximately R , the resistance of the parallel resistor in Fig. 22. Note that for $R \gg R_s$, most of the voltage from the power supply drops across the Pockels cell. However, Z is large only over a finite bandwidth $\Delta\Omega \approx (RC)^{-1}$. The bandwidth for high frequency modulation is thus limited by the power available from the source.

Another problem with high frequency modulators is the transit time effect, where the field applied to the Pockels cell may vary appreciably during the transit time $\tau = nL/c$ of an optical wave across a cell of length L . If the modulating voltage is given by $V(t) = V_m \cos \Omega t = V_m \exp(-i\Omega t) + \text{c.c.}$, then the time dependent retardation will be given by

$$\Gamma(t) = \eta \Gamma_m \exp(-i\Omega t) + \text{c.c.} \quad (173)$$

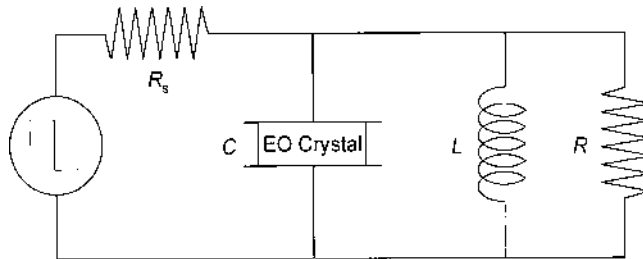


Figure 22 Resonantly-coupled high-frequency electro-optic amplitude modulator.

where Γ_m is the peak retardation achievable, and η is an efficiency factor, with

$$\eta = \frac{1 - \exp(-i\Omega\tau)}{i\Omega\tau} \quad (174)$$

If $\Omega\tau \ll 1$, then $\eta \approx 1$. However, if the modulation frequency becomes comparable to τ^{-1} , then η can become significantly less than 1. Note for $n = 1.5$ and $L = 1$ cm, this condition becomes $\Omega \sim 20$ GHz.

A solution to the transit time effect is a traveling wave modulator [3]. In this device, illustrated in Fig. 23, the Pockels cell becomes part of a transmission line where a traveling electrical wave and the optical wave co-propagate. The traveling electrical wave has a phase velocity v determined by the modulation frequency and the properties of the transmission line. The time dependent retardation is again given by Eq. (173), but the efficiency factor now becomes

$$\eta = \frac{1 - \exp[-i\Omega\tau(1 - c/nv)]}{i\Omega\tau(1 - c/nv)} \quad (175)$$

Note that $\eta \rightarrow 1$ as $v \rightarrow c/n$. In other words, if the phase velocities of the two waves are matched, the traveling optical wavefront will see a constant voltage equal to the maximum modulation voltage.

Kerr cell amplitude modulators. In this case the modulator utilizes a Kerr cell with a transverse electrode geometry. The transmittance is given by

$$T(V) = \sin^2 \left[\frac{1}{2} \pi (V/V_\pi)^2 \right] \quad (176)$$

where the half-wave voltage is defined by Eq. (167). With the phase retardation $\Gamma_m = \pi(V/V_\pi)^2$ for a modulation voltage $V(t) = V_m \sin \Omega t$, the small signal

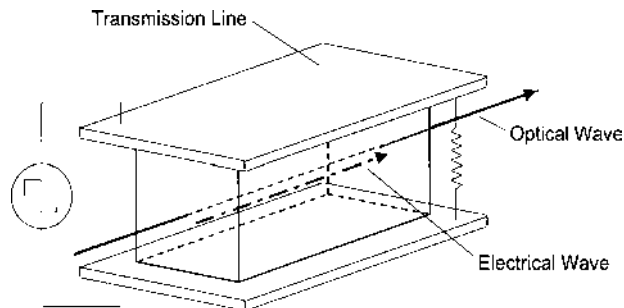


Figure 23 Traveling-wave high-frequency electro-optic amplitude modulator.

transmittance ($\Gamma_m \ll 1$) is

$$T \approx \frac{1}{2} \left[1 + \frac{1}{2} \Gamma_m (1 - \cos 2\Omega t) \right] \quad (177)$$

which oscillates at the second harmonic of the modulation frequency.

Nematic liquid crystal amplitude modulator. This device utilizes the parallel-aligned nematic LC cell discussed in Section III.A. The input wave is polarized at 45° with respect to the director, and the cell thickness is such that $\Delta n L / \lambda = (2m + 1)/2$, where m is an integer and Δn is the birefringence of the LC. This produces an equivalent retardation of $\pi \pmod{2\pi}$, and the output wave has a polarization orthogonal to the input. Thus, the output polarizer in this case is parallel to the input polarization for the normally black mode. The transmittance is given by

$$T = \sin^2 \frac{1}{2} \Gamma(V) \quad (178)$$

where

$$\Gamma(V) = \frac{2\pi}{\lambda} \int_0^L \{n^e[\theta(z, V)] - n^o\} dz \quad (179)$$

and the tilt angle $\theta(z, V)$ is found by the methods outlined in Section III.A. The extraordinary index $n^e(\theta)$ is given by Eq. (94). A closed form solution of $\Gamma(V)$ cannot be found. Due to the slow response time of nematic liquid crystal cells ($\tau_{OFF} \sim 10$ ms), these modulators cannot be driven at high frequencies. They are also limited on the low end to ~ 100 Hz due to ionic current that can screen the charge on the capacitor and lower the effective voltage across the cell.

Twisted nematic liquid crystal amplitude modulator. The TN cell was discussed in Section III.A. Here, only a cell with total twist $\Phi = 90^\circ$ will be considered. The director undergoes a continuous twist through the cell, where the local twist angle is proportional to the position z in the cell. At the input, the director is parallel to the input polarization. At the output, the director is at 90° with respect to the input, and the output polarizer is oriented parallel to the input polarization. This yields a normally black mode amplitude modulator. The TN amplitude modulator is shown schematically in Fig. 24.

The operation of the TN modulator can be analyzed by the Jones calculus [11] as described in Section I.B. The cell is divided into N layers of thickness L/N , where the azimuth angle in each cell is rotated by Φ/N with respect to the previous layer. Each layer is assumed to have constant retardation Γ/N , where

$$\Gamma = (n^e - n^o) \frac{2\pi}{\lambda} L = \Delta n L \frac{2\pi}{\lambda} \quad (180)$$

and Δn is the birefringence of the LC. The analysis follows Eqs. (32–37), where

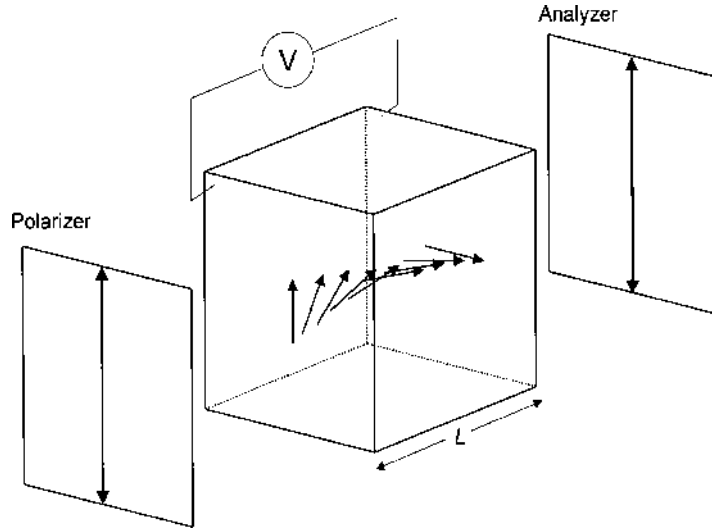


Figure 24 Twisted nematic liquid crystal amplitude modulator.

the retardance per layer is Γ/N , the orientation of each layer's optic axis is Φ/N with respect to the previous layer, and the output polarizer is oriented parallel to the input polarization and to the input director. This yields the transmittance of the modulator:

$$T = \frac{\sin^2 \left[\frac{1}{2} \pi \sqrt{1 + (2\Delta n L / \lambda)^2} \right]}{1 + (2\Delta n L / \lambda)^2} \quad (181)$$

The transmittance function is plotted in Fig. 25. Note that $T = 0$ when the argument of sin is an integer multiple of π . This corresponds to $(2\Delta n L / \lambda)^2 = 3, 15, 35$, etc., which depends on the wavelength. Under the Mauguin condition, defined by $\Delta n L \gg \lambda$, $T \approx 0$ independent of λ (i.e., for white light). This is known as the waveguiding regime, in which the wave polarization appears to follow the director twist and rotates by 90° . Actually, the wave is highly elliptically polarized, and a small amount of light will leak through the output polarizer [11].

Note that the expression in Eq. (181) is exact for the 90° -TN cell. For applied voltages larger than V_{th} , defined by Eq. (110), the directors begin to tilt toward the field and start to untwist. Equation (180) then no longer applies. For voltages $V \gg V_{th}$, the directors are nearly normal to the substrates. Under this condition, there is no polarization rotation (light propagates along the optic axis), and the transmittance goes to 1. For intermediate voltages, the angles $\theta(z, V)$ and

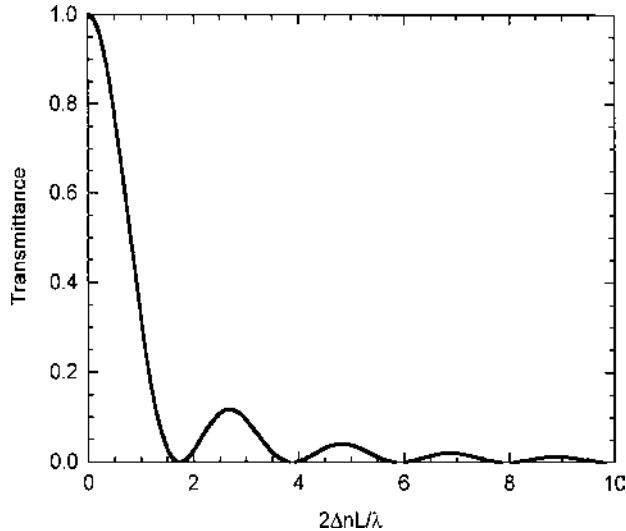


Figure 25 Transmittance of a twisted nematic liquid crystal amplitude modulator as a function of $2\Delta n L/\lambda$.

$\phi(z, V)$ can be found numerically by the methods outlined in Section III.A. for the TN cell. The propagation of light is then analyzed by the Jones calculus, dividing up the cell into a large number of layers (e.g., 20–100). Each layer has constant retardation determined by the local tilt angle θ and constant orientation determined by the local twist angle ϕ . In general, the transmittance is approximately zero for $V < V_{\text{th}}$, increases nonlinearly for $V > V_{\text{th}}$, then approaches 1 asymptotically for $V \gg V_{\text{th}}$, (e.g., $V \sim 5V_{\text{th}}$).

Polymer-dispersed liquid crystal amplitude modulator. PDLCs were discussed in Section III.D. A PDLC amplitude modulator is based on scattered light and is illustrated in Fig. 26. For LC droplet size on the order of a wavelength the scattering is strong, and the scattered light is distributed in a 4π -steradian solid angle about the PDLC. The transmittance of light through a small, on-axis aperture of radius r a distance D from the PDLC, such that $\theta \sim r/D \ll 1$, is given by

$$T = \exp(-\alpha_{\text{sc}}L) \quad (182)$$

where $\alpha_{\text{sc}} = f\nu^{-1}\sigma_{\text{sc}}$ is the scattering extinction coefficient, f is the volume fraction of LC droplets in the PDLC, ν is the average droplet volume, and σ_{sc} is the scattering cross section given by Eqs. (140–142) in the Rayleigh–Gans approximation. For light incident along the normal to the PDLC film, the droplets appear effectively as uniaxial domains with optic axis along the direction of

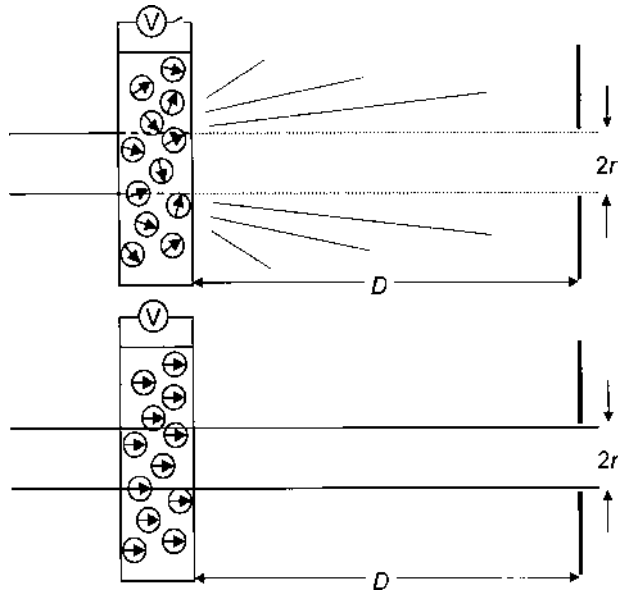


Figure 26 Polymer-dispersed liquid crystal amplitude modulator based on electro-optical light scattering.

propagation. Thus the apparent droplet index is isotropic, with $\bar{n}_{dx} = \bar{n}_{dy} \equiv \bar{n}_d$, where expressions for these indices are given in Eq. (139). If the droplets are nearly spherical with radius a , then the scattering coefficient can be written as

$$\alpha_{sc} = \frac{3f}{4a} \left(\frac{\bar{n}_d}{n_p} - 1 \right)^2 \Phi \left(\frac{2\pi a}{\lambda} \right) \quad (183)$$

with Φ given by Eqs. (141) and (142). In general, for an applied field $E = V/L < E_c$ (see Eqs. (136) and (137)) the transmittance is much less than one, rises nonlinearly for $E \sim E_c$, and then approaches 1 asymptotically for $E \gg E_c$.

D. Optical Shutters and Switches

Polarization shutters. The polarization converters and amplitude modulators discussed above that are based on field induced birefringence changes can also be used as optical shutters. An optical shutter changes transmittance from a maximum to a minimum (ideally from 1 to 0) or vice versa when an appropriate voltage is applied. For Pockels and Kerr cells, this would be the half-wave voltage, while for nematic liquid crystal cells, it would be a voltage large compared to

the threshold voltage. In the normally black mode the transmittance is switched on, while in the normally white mode the transmittance is switched off.

One additional type of optical shutter is described here. The surface stabilized ferroelectric liquid crystal shutter is illustrated in Fig. 27. The directors of the smectic C* liquid crystal are aligned by surface treatment in the "bookshelf" geometry, where the directors resemble a bookshelf with all books tilting in the same direction. Hence the optic axis is tilted by an angle θ with respect to the vertical axis, which is along the layer normal of the smectic C* LC. The spontaneous polarization of the FLC is along the direction of light propagation, which is also the direction of the applied field. When a field larger than that given in Eq. (131) is applied, the polarization flips by 180°, which causes the directors to precess about the layer normal by 180°. This is equivalent to rotating the director tilt by 2 θ about the direction of propagation. With the output polarizer oriented orthogonal to the input polarization, the transmittance of the FLC shutter is [11]

$$T = \sin^2 4\theta \sin^2 \frac{1}{2} \Gamma(E) \quad (184)$$

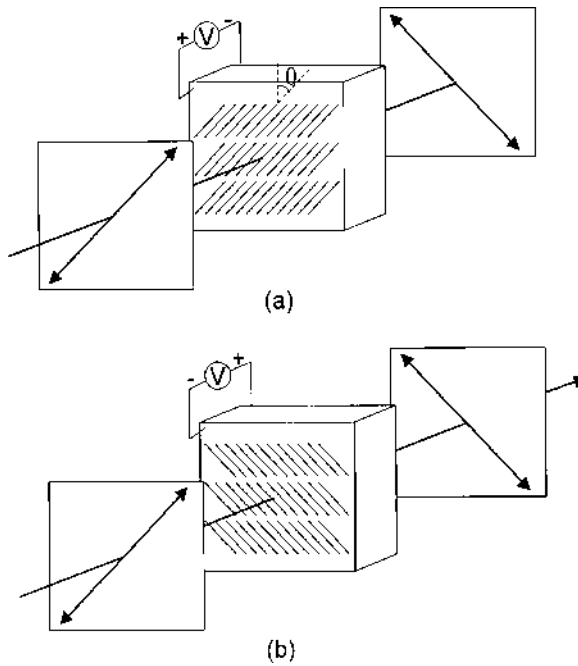


Figure 27 Ferroelectric liquid crystal optical shutter. (a) Dark state and (b) bright state.

If Γ is selected to be π at the switching voltage of the cell, then the transmittance will be a maximum for $\theta = 22.5^\circ$.

Integrated optical switches. Two types of waveguide switch are described, both based on optical interference rather than polarization. The first is called a 1×1 switch or an ON-OFF modulator. It is based on a two-dimensional channel-waveguide Mach-Zehnder interferometer that is illustrated in Fig. 28. An incident guided wave is split into two equal parts at the Y-junction of the waveguide. The two parts travel an equal distance and recombine at the output Y-junction. If the phase delay of each leg of the interferometer is identical, the waves will constructively interfere at the output, and the transmittance will be a maximum. When a half-wave voltage is applied at the electrodes on one leg, a relative phase difference of π radians will be induced between the two waves. Destructive interference at the output results in a minimum transmittance. The transmittance function is given by [25]

$$T(V) = \cos^2\left(\frac{\pi}{2} \frac{V}{V_\pi}\right) \quad (185)$$

A typical material is LiNbO_3 with a Ti-diffused waveguide. As illustrated in Fig. 28, the surface electrodes produce a transverse field in the waveguide. V_π in a waveguide may be $\sim 10^3$ smaller than typical values for bulk crystals.

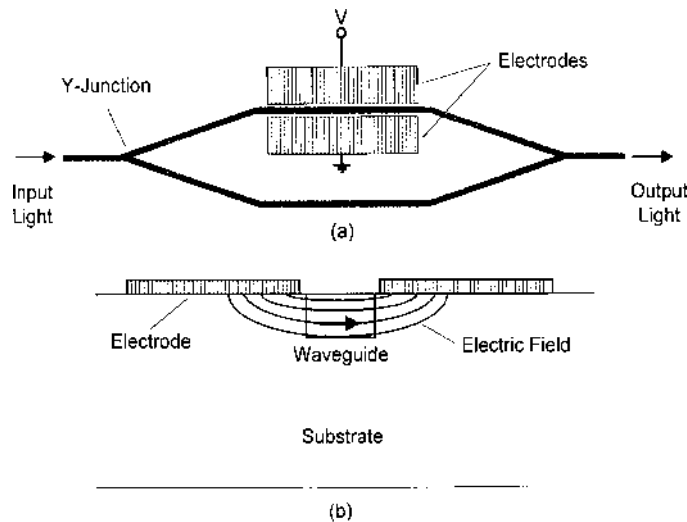


Figure 28 Waveguide electro-optical switch based on a Mach-Zehnder interferometer.
(a) Waveguide switch geometry and (b) electrode geometry illustrating electric field lines.

The second type of switch is called a 2×2 crossbar switch and is based on the coupling between two adjacent waveguides. It is illustrated in Fig. 29. Two symmetric waveguides are separated by a distance d that is small compared to the decay length of the guided modes in the cladding. The evanescent fields of the modes overlap the guided wave region of the adjacent waveguide. This produces a dielectric polarization that couples the two modes so that they interfere and exchange energy. Light is input to channel 1 and can exit at both channels 1 and 2. The optical power at some position z along the waveguide coupler in channel 2 is given by [25]

$$\mathcal{P}_2(z) = \mathcal{P}_1(0) \frac{|\kappa|^2}{\gamma^2} \sin^2 \gamma z \quad (186)$$

where κ is the coupling coefficient, which depends on the refractive index difference of the waveguide and cladding and the overlap of the two modes, and

$$\gamma^2 = \left(\frac{\Delta\beta}{2} \right)^2 + |\kappa|^2 \quad (187)$$

with $\Delta\beta$ the difference between the propagation constants of the two modes. For symmetric waveguides $\Delta\beta = 0$. If the length of the coupling region L is adjusted to be the beat length $L_0 = \pi/2|\kappa|$, then all of the power input to channel 1 is transferred to channel 2 at the output. This is called the cross state. A phase

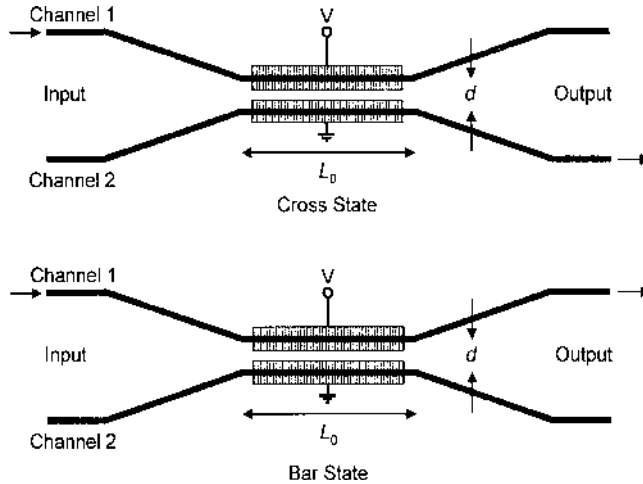


Figure 29 Waveguide electro-optic crossbar switch based on beam coupling between adjacent waveguides. The arrows indicate the input and output signals.

mismatch $\Delta\beta \neq 0$ can be induced between the waveguides by the application of a voltage to the electrodes shown in Fig. 29. In this configuration an applied voltage V creates a field $E \approx V/d$ at one waveguide and $E \approx -V/d$ at the other waveguide [7]. The power transfer ratio $T = \mathcal{P}_2/\mathcal{P}_1$ can now be written as

$$T(V) = \frac{\sin^2\left\{\frac{\pi}{2}[1 + (\Delta\beta(V)L_0/\pi)^2]^{1/2}\right\}}{1 + (\Delta\beta(V)L_0/\pi)^2} \quad (188)$$

Note that if the phase mismatch is such that $\Delta\beta L_0 = \sqrt{3}\pi$, then T will be zero and all of the optical power will exit channel 1. This is known as the bar state. With $\Delta\beta = 2\pi\Delta n/\lambda$ and writing $\Delta n = -(1/2)n^3 r_{\text{eff}} E$, where n is the average waveguide index and r_{eff} is the effective Pockels coefficient, a switching voltage V_s can be derived which is the voltage necessary to achieve $\Delta\beta L_0 = \sqrt{3}\pi$,

$$V_s = \sqrt{3} \frac{\lambda}{2n^3 r_{\text{eff}}} \frac{d}{L_0} = \frac{\sqrt{3} |\kappa| \lambda d}{\pi n^3 r_{\text{eff}}} \quad (189)$$

Equation (187) can now be written as

$$T(V) = \frac{\sin^2\left\{\frac{\pi}{2}[1 + 3(V/V_s)^2]^{1/2}\right\}}{1 + 3(V/V_s)^2} \quad (190)$$

E. Tunable Filters

The devices discussed up to this point have been applied to monochromatic light. When white light, or light containing more than one frequency, is incident on a device, an often desired property is to filter out certain frequencies (wavelengths). This, of course, can be done with static filters. However, there are many applications where the filter needs to be tuned so that the wavelength that is being passed or blocked can change. Examples are color multiplexing in color video projectors and wavelength division multiplexing in telecommunications. Some of the devices described above can be employed as tunable filters. Tunable birefringent and Fabry–Perot filters will be discussed in this section. Operation with a Pockels material and a nematic liquid crystal will be contrasted.

Tunable birefringent filters. A simple filter can be made using the birefringent amplitude modulators described above. An example using a uniaxial crystal is shown in Fig. 30. It employs a birefringent material between crossed polarizers. A second example would be the same as Fig. 30, but with the crystal between parallel polarizers. The optic axis is in the face of the crystal and makes an angle of 45° with respect to the orientation of the polarizers. For the discussion that follows, it is assumed that unpolarized light is incident on the first polarizer.

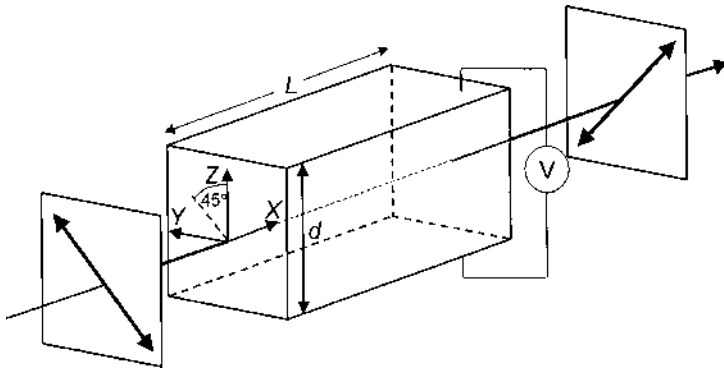


Figure 30 Electro-optic tunable birefringent filter using a crystal with $3m$ symmetry.

From the discussion in Section IV.C, the transmittance for the crossed polarizer case is given by

$$T = T_0 \sin^2(\pi \Delta n L / \lambda) \quad (191)$$

where T_0 is the transmittance through two parallel polarizers, which may be less than 50%, and $\Delta n = n^e - n^o$ is the birefringence of the material. Ignoring the dispersion of the birefringence, it is obvious from Eq. (191) that the transmittance will be a maximum for certain wavelengths. The peaks of the transmittance are located at wavelengths

$$\lambda_m = \frac{2\Delta n L}{2m + 1} \quad m = 0, 1, 2, \dots \quad (192)$$

while the valleys are located at

$$\lambda_m = \frac{\Delta n L}{m} \quad m = 1, 2, 3, \dots \quad (193)$$

For the case of parallel polarizers,

$$T = T_0 \cos^2(\pi \Delta n L / \lambda) \quad (194)$$

The peaks in this case are located at wavelengths given by Eq. (193) and valleys at wavelengths given by Eq. (192). Thus these two cases are very similar, with the roles of peaks and valleys interchanged.

Three quantities of interest in tunable filters are the free spectral range, the bandwidth, and the tuning range. The free spectral range (FSR) is the distance in wavelength (or frequency) between two adjacent modes or transmittance peaks.

For the m th mode of a birefringent filter, this is

$$\begin{aligned}\Delta\lambda_{\text{FSR}} &= \frac{2}{2m+3}\lambda_m \quad m = 0, 1, 2, \dots \quad (\text{crossed polarizers}) \\ \Delta\lambda_{\text{FSR}} &= \frac{1}{m+1}\lambda_m \quad m = 1, 2, 3, \dots \quad (\text{parallel polarizers})\end{aligned}\tag{195}$$

When m is large, the FSR is simply λ_m/m for both cases.

The bandwidth of the filter is the full width of the transmission notch between points where the transmittance is half the maximum value (FWHM). This quantity for the m th mode is

$$\Delta\lambda_{\text{BW}} = \frac{8m+4}{(4m+1)(4m+3)}\lambda_m \quad m = 0, 1, 2, \dots \quad (\text{crossed polarizers})\tag{196}$$

$$\Delta\lambda_{\text{BW}} = \frac{8m}{(4m-1)(4m+1)}\lambda_m \quad m = 1, 2, 3, \dots \quad (\text{parallel polarizers})$$

For large m the FWHM bandwidth reduces to $\lambda_m/2m = \lambda_m^2/2\Delta nL$ for both cases.

The peak wavelengths are directly proportional to the birefringence. Hence, the tuning range is given by

$$\delta\lambda = \frac{\delta(\Delta n)}{\Delta n} \lambda_m\tag{197}$$

where $\delta(\Delta n)$ is the variation of the birefringence induced by an applied field.

Consider, as an example, the case of a Pockels cell made with LiNbO₃. Lithium niobate has point group symmetry $3m$. When an electric field is applied along the optic (Z) axis, the principal axes remain unchanged, but the principal refractive indices are modified so that [3]

$$\begin{aligned}n_X &= n^\circ - \frac{1}{2}(n^\circ)^3 r_{13} E \\ n_Y &= n^\circ - \frac{1}{2}(n^\circ)^3 r_{13} E \\ n_Z &= n^e - \frac{1}{2}(n^e)^3 r_{33} E\end{aligned}\tag{198}$$

The filter is shown schematically in Fig. 30. A LiNbO₃ crystal of length L and thickness d is situated between crossed polarizers. The optic axis lies in the face of the crystal, and the X axis coincides with the direction of light propagation. The incident light is polarized at an angle of 45° with respect to the Y and Z axes, and a field is applied transverse to the propagation, along the Z axis. The

birefringence seen by the light is $\Delta n = n_Z - n_Y$, so the variation in birefringence due to the applied voltage is

$$\delta(\Delta n) = -\frac{1}{2} [(n^e)^3 r_{33} - (n^o)^3 r_{13}] V/d \quad (199)$$

If $L = 1$ mm and $m = 50$, the peak transmittance is at 1564 nm. The FSR with respect to this mode is 30 nm, and the FWHM bandwidth of the mode is 15 nm. The optical and electro-optical parameters for LiNbO₃ are approximately $n^e = 2.229$, $n^o = 2.150$, $r_{13} = 9.6$ pm/V, and $r_{33} = 30.9$ pm/V (see Table 4). Assuming $d = 1$ mm, the tuning range is thus $\delta\lambda = 2.0$ nm/kV.

As a second example, consider a parallel aligned liquid crystal using E7. The filter is shown in Fig. 31. Input and output polarizers are parallel and aligned at 45° with respect to the optic axis (director). A field is applied longitudinally to a cell of length L . The birefringence of E7 is $\Delta n = 0.22$ [14]. For a cell of length $L = 10$ μm, the third mode ($m = 3$) is at $\lambda = 630$ nm. The FSR with respect to this mode is 140 nm, and its bandwidth (FWHM) is 90 nm. Note that a thin birefringent filter has less densely packed modes, but they are broader. The splay force constant for E7 is $K_1 = 12$ pN (piconewtons) while its dielectric anisotropy is $\Delta\epsilon = 14.6\epsilon_0$ [14]. The threshold voltage V_{c1} is thus ~ 1 V. Since the directors can be tilted almost entirely along the normal to the substrates for a voltage large compared to V_{c1} (e.g., 4–5 V), the tuning range is essentially $\delta\lambda \sim 300$ nm (i.e., the entire visible spectrum) for just a few volts. A plot of the spectral transmittance for an E7 birefringent filter is shown in Fig. 32, illustrating λ_m , $\Delta\lambda_{FSR}$, and $\Delta\lambda_{BW}$.

Multistage birefringent filters. Many applications require filters with a much narrower bandwidth than can be obtained with a single-stage birefringent filter. This can be achieved by building a filter consisting of many birefringent stages. One such filter is the Šolc filter, of which there are two types: fan and fold.

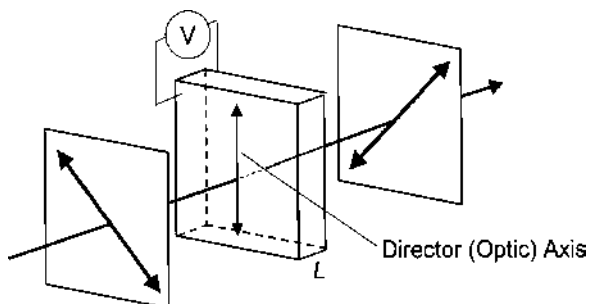


Figure 31 Electro-optic tunable birefringent filter using a nematic liquid crystal.

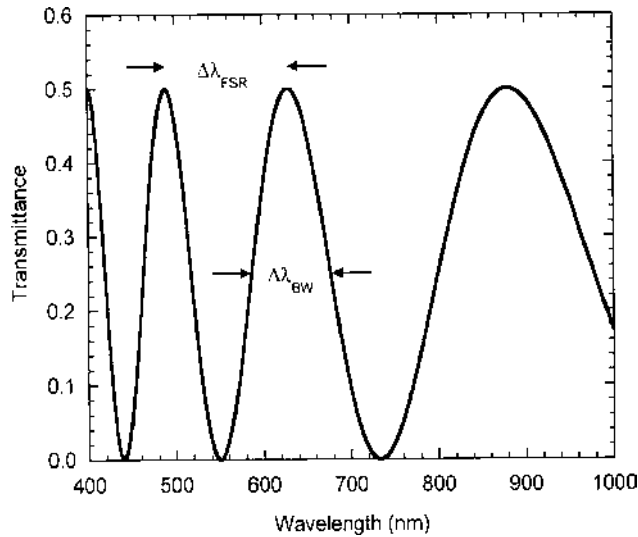


Figure 32 Spectral transmittance of a liquid-crystal birefringent filter illustrating transmittance peaks λ_m , free spectral range $\Delta\lambda_{FSR}$, and FWHM bandwidth $\Delta\lambda_{BW}$.

The Šolc filter consists of a stack of N birefringent plates, which have identical retardance at any wavelength, and are placed between two polarizers. In the fan filter, the polarizers are parallel, and the slow axis of the first plate is rotated by a small angle $\rho = \pi/4N$ with respect to the polarizer orientation. Each successive birefringent plate is rotated by an additional angle 2ρ so that the azimuth angles of successive plates, with respect to the polarizer orientation, are $\rho, 3\rho, 5\rho, \dots$. The azimuth angle of the final plate is $(1/2)\pi - \rho$. This chain of birefringent elements can be analyzed by the Jones calculus. The transmittance is given by [3]

$$T = T_0 \left| \tan 2\rho \cos \chi \frac{\sin N\chi}{\sin \chi} \right|^2 \quad (200)$$

where

$$\cos \chi = \cos 2\rho \cos \frac{1}{2}\Gamma \quad (201)$$

and $\Gamma = 2\pi\Delta n L/\lambda$ is the retardance of each plate. T will have a maximum of T_0 for wavelengths

$$\lambda_m = \frac{\Delta n L}{m} \quad m = 1, 2, 3, \dots \quad (202)$$

with a FSR with respect to the m th mode

$$\Delta\lambda_{\text{FSR}} = \frac{\lambda_m}{m+1} \quad (203)$$

and bandwidth

$$\Delta\lambda_{\text{BW}} \approx 0.8 \frac{\lambda_m}{mN} \quad (204)$$

for $N \gg 1$. The tuning range is identical to that for the simple birefringent filter,

$$\delta\lambda = \frac{\delta(\Delta n)}{\Delta n} \lambda_m \quad (205)$$

Hence the examples given above for LiNbO₃ and E7 can be directly applied here. For the case of LiNbO₃ with $m = 50$, $\lambda_{50} = 1580$ nm, $\Delta\lambda_{\text{FSR}} = 31$ nm, and $\Delta\lambda_{\text{BW}} = 2.6$ nm for $N = 10$. For the E7 example, the FWHM bandwidth for $N = 10$ is reduced to 19.4 nm, while $\lambda_3 = 730$ nm and $\Delta\lambda_{\text{FSR}} = 180$ nm. Figure 33 illustrates the spectral transmittance for the E7 Šolc filter ($N = 10$). This should be compared to Fig. 32 for the single-stage birefringent filter.

The fold filter consists of N birefringent plates of identical retardance sandwiched between crossed polarizers. The slow axis of the first plate is rotated by an angle $\rho = \pi/4N$ with respect to the orientation of the first polarizer. The second plate has its slow axis rotated by ρ in the opposite sense with respect to the orientation of the first polarizer. Thus the angle between the slow axes of the first and second plates is 2ρ . Each successive plate is oriented by $\pm\rho$ in an identical manner. Applying the Jones calculus to this filter leads to a transmittance [11]

$$T = T_0 \left| \tan 2\rho \cos \chi \frac{\sin N\chi}{\sin \chi} \right|^2 \quad (206)$$

which looks identical to that for the fan filter, except in this case

$$\cos \chi = \cos 2\rho \sin \frac{1}{2} \Gamma \quad (207)$$

The peak transmittance wavelengths for the fold filter are located at

$$\lambda_m = \frac{2\Delta n L}{2m+1} \quad m = 0, 1, 2, \dots \quad (208)$$

and the FSR with respect to this mode is

$$\Delta\lambda_{\text{FSR}} = \frac{2}{2m+3} \lambda_m \quad (209)$$

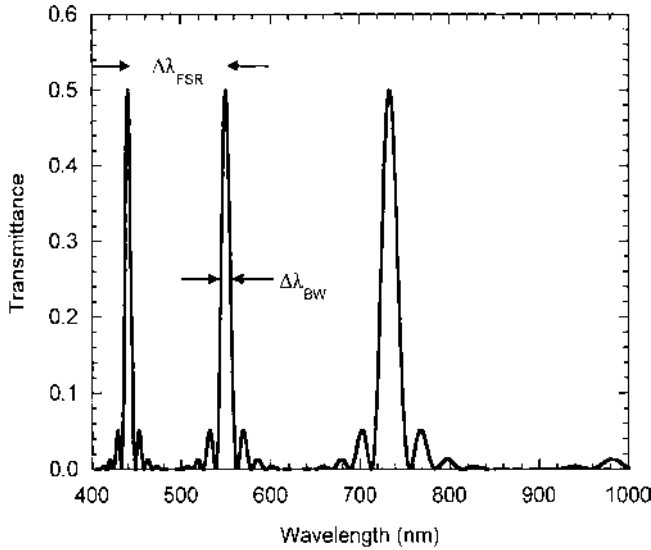


Figure 33 Spectral transmittance of a liquid-crystal Šolc fan filter illustrating transmittance peaks λ_m , free spectral range $\Delta\lambda_{FSR}$, and FWHM bandwidth $\Delta\lambda_{BW}$.

with bandwidth

$$\Delta\lambda_{BW} \approx 1.6 \frac{\lambda_m}{(2m+1)N} \quad (210)$$

The tuning range is

$$\delta\lambda = \frac{\delta(\Delta n)}{\Delta n} \lambda_m \quad (211)$$

The operation of the fold filter can be understood by the following argument. For a peak wavelength λ_m , each plate is a perfect half-wave plate. Light that travels through a half-wave plate, with its polarization at an angle ρ with respect to the slow axis, has its polarization rotated through an angle 2ρ . This is what occurs at the first plate in the fold filter. The light incident on the second stage is thus polarized at an angle 2ρ with respect to the slow axis of that plate. Transmitted light is now rotated through an angle 4ρ , but in the opposite sense. This process progresses at each stage so that the next successive rotations are 6ρ , -8ρ , 10ρ , -12ρ , etc. At the last stage the polarization is rotated parallel to the exit polarizer axis. Polarized light at other nearby wavelengths is not so perfectly rotated and is thus attenuated.

Tunable Fabry–Perot filters. A Fabry–Perot filter is an example of a tunable filter that is not based on birefringence. It consists of a dielectric medium sandwiched between two high-reflectance, parallel mirrors as illustrated in Fig. 34. Incident light leaks through the first mirror and undergoes multiple reflections in the mirror cavity. If the round-trip optical path length of the cavity is an integer multiple of a wavelength λ , light at that wavelength will experience a maximum transmittance (theoretically 100%) through the filter. The transmittance of the Fabry–Perot filter is given by

$$T = \frac{1}{1 + F \sin^2(2\pi nL/\lambda)} \quad (212)$$

where

$$F = \frac{4R}{(1 - R)^2} \quad (213)$$

is called the fringe contrast, with R the reflectance of each mirror. The transmittance depends on the refractive index of the medium, and the peak transmittance wavelengths are

$$\lambda_m = \frac{2nL}{m} \quad m = 1, 2, 3, \dots \quad (214)$$

The mode number m for the Fabry–Perot can be quite large. The peak transmittance is 1, and the minimum is $(1 + F)^{-1}$. The fringe contrast can be large for high reflectivity mirrors. For example, if $R = 0.9$, $F = 360$. The FSR is

$$\Delta\lambda_{\text{FSR}} \approx \frac{\lambda_m}{m} = \frac{\lambda_m^2}{2nL} \quad (215)$$

for $m \gg 1$, while the bandwidth is

$$\Delta\lambda_{\text{BW}} \approx \frac{\lambda_m^2}{\pi nL\sqrt{F}} \quad (216)$$

for $F \gg 1$.

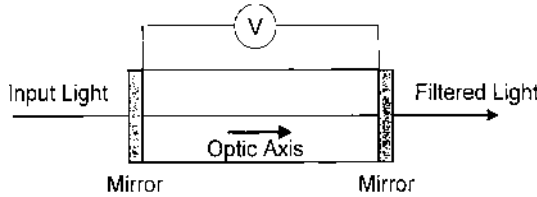


Figure 34 Electro-optic tunable Fabry–Perot filter using a crystal with $3m$ symmetry.

As an example of a tunable Fabry–Perot filter, consider LiNbO₃ with its optic axis normal to the mirrors and a field applied in this direction, as illustrated in Fig. 34. Unpolarized light incident normally on the filter will see an index given by

$$n = n^o - \frac{1}{2}(n^o)^3 r_{13} E \quad (217)$$

where $E = V/L$. For $L = 1$ mm and $m = 2800$, $\lambda_m = 1536$ nm. For this mode the tuning range is 3.4×10^{-5} nm/V, or 34 nm for 1 MV. The FSR would be 0.5 nm, while the bandwidth for $R = 0.8$ mirrors would be 0.04 nm.

Now consider the parallel aligned nematic LC cell with E7 in the same Fabry–Perot arrangement, but with a mirror spacing of 10 μm . Polarized light is incident on the filter, as shown in Fig. 35, with the polarization along the optic (director) axis. Thus, with no voltage applied, incident light will see an index $n^e = 1.75$ for E7. For $m = 50$, the transmitted wavelength is 700 nm. The FSR with respect to this mode is 14 nm, while the bandwidth is 1.0 nm. Note again that modes are more densely packed for thicker filters. Since the net index change, for an applied voltage of 4–5 V, is in this case approximately the birefringence of the LC, the tuning range is $\delta\lambda = (\Delta n/n^e)\lambda_m = 88$ nm. The spectral transmittance for an E7 Fabry–Perot filter is shown in Fig. 36.

F. Switchable Filters

Whereas tunable filters are adjusted to filter a specific wavelength, or set of wavelengths, sometimes it is desirable to adjust the efficiency of a filter at

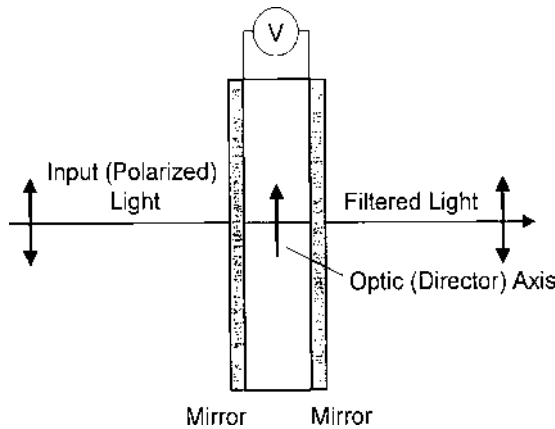


Figure 35 Electro-optic tunable Fabry–Perot filter using a nematic liquid crystal.

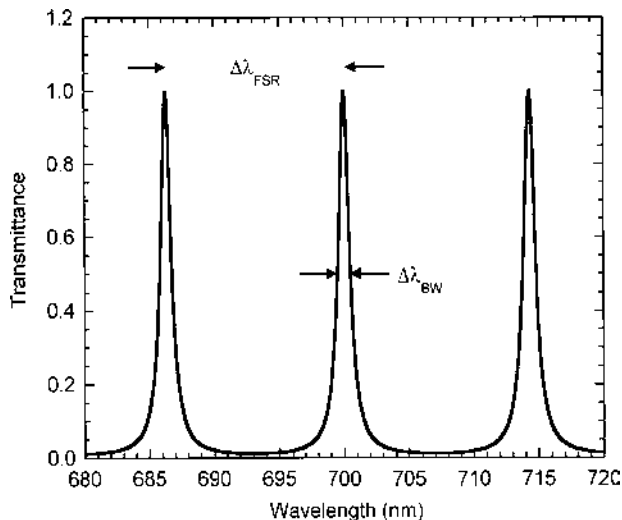


Figure 36 Spectral transmittance of a liquid-crystal Fabry–Perot filter illustrating transmittance peaks λ_m , free spectral range $\Delta\lambda_{FSR}$, and FWHM bandwidth $\Delta\lambda_{BW}$.

a specific wavelength. In particular, one may want to turn the filter efficiency on (a maximum) or off (a minimum). This type of device is called a switchable filter. Two types of electrically switchable filters will be examined here. Both are based on the theory of Bragg diffraction. The first is a holographic polymer-dispersed liquid crystal (HPDLC) reflection filter, and the second is a cholesteric liquid crystal (CLC) filter.

HPDLC switchable reflection filter. HPDLCs were discussed in Section III.E. They are based on a periodic perturbation of the dielectric tensor, which is a tensor hologram. An unslanted reflection hologram is illustrated in Fig. 37. Unslanted implies that the grating vector \mathbf{K}_g is normal to the surfaces of the hologram. Incident light scatters from the grating planes. If certain conditions are met (see below), the scattered light from all grating planes interferes constructively to produce a coherent diffracted beam in a specific direction. In all other directions the scattered light interferes destructively. Since the diffracted beam appears on the same side of the hologram on which the incident light impinges, this hologram is called a reflection grating or reflection hologram. The ratio of reflected optical power to incident optical power is called the diffraction efficiency η .

The type of diffraction described above is called Bragg diffraction. To achieve this type of diffraction (single coherent diffracted beam), the grating must be optically thick. The criteria for this are established with reference to two

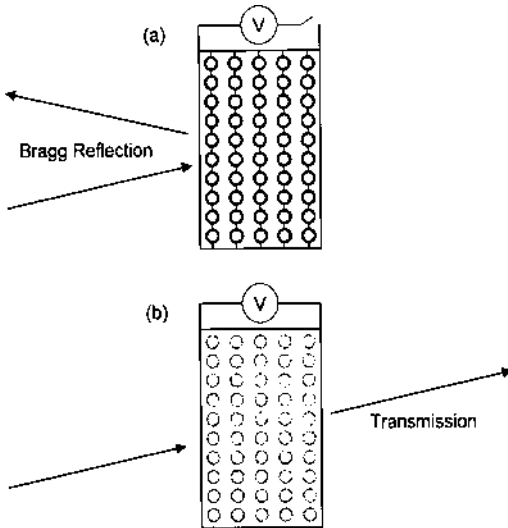


Figure 37 Electro-optic switchable Bragg filter using holographic polymer-dispersed liquid crystals. (a) Reflecting state and (b) transmitting state.

parameters, namely

$$Q = 2\pi \frac{\lambda L}{n\Lambda^2} \quad (218)$$

and

$$\Omega = \frac{\lambda^2}{nn_1\Lambda^2} \quad (219)$$

where λ is the wavelength of incident light, L is the grating thickness, $\Lambda = 2\pi/|\mathbf{K}_g|$ is the grating period (also called the pitch, grating spacing, or grating constant), n is the average refractive index, and n_1 is the average index modulation amplitude (see below for a further discussion of refractive index parameters for a tensor grating). The optically thick grating regime is determined by the conditions $Q \gg 1$ and $\Omega \gg 1$ [26]. Generally, this implies that $L \gg \lambda$ and $n_1 \ll 1$. If these conditions are met, then light at a specific wavelength, called the Bragg wavelength λ_B , will be diffracted with high efficiency. For an unslanted grating, the angle of diffraction will equal the angle of incidence θ , and the Bragg wavelength λ_B is determined by the Bragg condition,

$$\lambda_B = 2n\Lambda \cos \theta \quad (220)$$

A grating in the optically thick regime (i.e., a Bragg hologram) can be analyzed using coupled-wave theory [27]. Under the conditions described in Section III.E, the average dielectric tensor of the medium is given by

$$\boldsymbol{\epsilon}^{(0)} = \begin{pmatrix} \epsilon_x^{(0)} & 0 & 0 \\ 0 & \epsilon_y^{(0)} & 0 \\ 0 & 0 & \epsilon_z^{(0)} \end{pmatrix} \quad (221)$$

while the modulation tensor of the medium is

$$\boldsymbol{\epsilon}^{(1)} = \begin{pmatrix} \epsilon_x^{(1)} & 0 & 0 \\ 0 & \epsilon_y^{(1)} & 0 \\ 0 & 0 & \epsilon_z^{(1)} \end{pmatrix} \quad (222)$$

and the tensor components are given by the combination of Eqs. (146–148). Note that by Eq. (148), the HPDLC medium is essentially uniaxial with $\epsilon_x^{(0)} = \epsilon_y^{(0)} = \epsilon_0(n^o)^2$, but $\epsilon_z^{(0)} = \epsilon_0(n^e)^2$ and $\epsilon_x^{(1)} = \epsilon_y^{(1)}$. Thus, the effective average index of the medium, as used in the discussion above, depends on the polarization of the light and its direction of propagation. Note also that both ordinary and extraordinary refractive indices will change with the applied voltage. For many applications these indices, however, are approximately equal. The average index modulation is related to the components of $\boldsymbol{\epsilon}^{(1)}$ and will also depend on polarization and direction of propagation.

The incident and diffracted waves are often called the reference (R) and signal (S) waves, respectively. The diffraction efficiency for a beam of wavelength λ incident at θ_R and diffracted at an angle θ_s with respect to the film normal is given by [3,27]

$$\eta = \frac{\kappa^2 \sinh^2 [\sqrt{(\kappa L)^2 - (\Delta k L/2)^2}]}{[\kappa^2 - (\Delta k/2)^2] \cosh^2 [\sqrt{(\kappa L)^2 - (\Delta k L/2)^2}] + (\Delta k/2)^2 \sinh^2 [\sqrt{(\kappa L)^2 - (\Delta k L/2)^2}]} \quad (223)$$

where

$$\kappa = \frac{\pi \hat{e}_S \cdot \boldsymbol{\epsilon}^{(1)} \cdot \hat{e}_R}{2\epsilon_0 n g \lambda \sqrt{|\cos \theta_S| \cos \theta_R}} \quad (224)$$

is the grating coupling coefficient, with

$$n = \sqrt{n_S n_R} \quad (225)$$

$$g = \sqrt{\cos \alpha_S \cos \alpha_R} \quad (226)$$

In these equations, \hat{e}_S and \hat{e}_R are the polarization vectors, n_S and n_R the refractive indices, α_S and α_R the angles between the wavevectors and Poynting vectors of the respective waves. Note that $\theta_S = \pi - \theta_R$, so $\cos \theta_S < 0$. The quantity Δk is the phase mismatch or detuning factor from the Bragg wavelength and is given by

$$\Delta k = 2\pi \left(\frac{2n}{\lambda} - \frac{1}{\Lambda} \right) \quad (227)$$

where n is a function of the applied voltage.

An example of the filter function for $\lambda_B = 540$ nm and normal incidence, illustrating switching for various values of the applied field, is plotted in Fig. 38. The peak efficiency is given by

$$\eta^{(\text{peak})} = \tanh^2 \kappa L \quad (228)$$

and the bandwidth is

$$\Delta\lambda_{\text{BW}} \approx \frac{\kappa\lambda_B^2}{\pi n} \quad (229)$$

The expression for the bandwidth in Eq. (228) is not exactly the FWHM value; it is given by the detuning condition for which the argument of the hyperbolic sine becomes imaginary. It gives an approximate measure of the FWHM bandwidth,

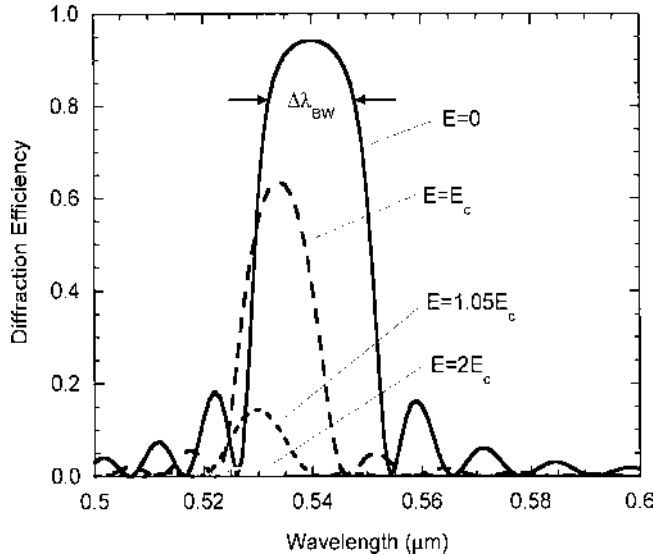


Figure 38 Spectral transmittance of an HPDLC Bragg filter illustrating reflectance peak λ_B , bandwidth $\Delta\lambda_{\text{BW}}$, and switching. Field values are given in terms of the critical field E_c .

as illustrated in Fig. 38. Another expression for the bandwidth is given by the wavelengths of the first zeros in the diffraction efficiency. This yields

$$\Delta\lambda'_{\text{BW}} = \frac{\lambda_b^2}{\pi n} \sqrt{\kappa^2 + (\pi/L)^2} \quad (230)$$

and is seen to decrease with increasing thickness L . The bandwidth limit for large L reduces to Eq. (229). Fig. 38 illustrates the bandwidth and switching for an HPDLC Bragg filter.

The coupling coefficient and hence the diffraction efficiency are polarization dependent. Note that the reference and signal waves will have the same polarization. In an unslanted grating, $\pi - \theta_S \equiv \theta_R \equiv \theta$. Since the film is overall weakly birefringent, $\cos \alpha_R = \cos \alpha_S \approx 1$. For s-polarized waves,

$$\kappa_s = \frac{\pi}{2\epsilon_0 n^\circ \lambda \cos \theta} \epsilon_y^{(1)} \quad (231)$$

while for p-polarized waves,

$$\kappa_p = \frac{\pi}{2\epsilon_0 n^e(\theta) \lambda \cos \theta} (\epsilon_x^{(1)} \cos^2 \theta - \epsilon_z^{(1)} \sin^2 \theta) \quad (232)$$

Hence, the index modulation n_1 , referred to above, depends on polarization and angle of incidence. It is of magnitude $\epsilon^{(1)}/2\epsilon_0 n$, given in terms of the appropriate components.

The switching of the filter for off-normal incidence will depend on polarization. For an s-polarized wave, the filter will be switched off at an applied field $E > E_c$, where E_c is given by Eq. (137), for which $\epsilon_{dy} \rightarrow \epsilon_p$, with ϵ_{dy} given by Eq. (148). For p-polarization, the switching will be determined by a zero-crossing of κ_p , i.e., when $\epsilon_x^{(1)} = \epsilon_z^{(1)} \tan^2 \theta$. Note that this will occur at some nonzero value of the applied field since $\epsilon_x^{(1)}$ decreases while $\epsilon_z^{(1)}$ increases with increasing field, cf. Eqs. (147) and (148). For normal incidence, the switching will be independent of polarization.

CLC switchable reflection filter. CLC cells were discussed in Section III.B. The azimuth angle of the CLC directors precesses about the z axis, which is normal to the substrates, at a rate q , viz.

$$\phi(z) = qz = 2\pi \frac{z}{p} \quad (233)$$

where p is the pitch of the CLC and $q > 0$ ($q < 0$) corresponds to a right-hand (left-hand) twist. Light polarized along the local director sees a refractive index n^e , while light polarized perpendicular to this direction sees n° , where $\Delta n = n^e - n^\circ$ is the birefringence. For light propagating along the z axis, the normal modes of propagation in this inhomogeneous medium can be computed exactly in terms of Bloch waves [11]. The normal modes are elliptically polarized, in

general. Four distinct regimes appear in the dispersion relations, depending on wavelength.

1. Mauguin regime ($\lambda \ll (1/2)p\Delta n$). In this short wavelength regime, the normal modes are almost linearly polarized parallel and perpendicular to the local director.
2. Short wavelength circular regime ($((1/2)np\Delta n \ll \lambda \ll p)$). In this regime, the normal modes are almost circularly polarized with opposite handedness (i.e., right and left circularly polarized modes).
3. Bragg regime ($n^e p < \lambda < n^o p$). Here the wavevector of one mode is purely imaginary, which corresponds to an evanescent wave. This mode cannot propagate in the medium. The other normal mode is almost circularly polarized with the same handedness as the CLC helix.
4. Long wavelength circular regime ($\lambda \gg n^e p$). In this long wavelength regime, the normal modes are both almost circularly polarized with opposite handedness.

The interesting regime for filters is the Bragg regime, where the CLC acts as a reflection filter. The incident light is not necessarily one of the normal modes. If the birefringence is not too large, so that $(n^e)^2 - (n^o)^2 \ll (n^e)^2 + (n^o)^2$, then the wave propagation can be analyzed using coupled-wave theory [11]. The field inside the CLC is taken to be a superposition of incident and reflected waves with wavevectors $\pm k$ given by

$$k = \frac{2\pi}{\lambda} \sqrt{\frac{(n^e)^2 + (n^o)^2}{2}} \quad (234)$$

If a left-hand circularly polarized wave is incident on a CLC with a right-hand twist (or, a right-hand circularly polarized wave incident on a left-handed CLC), then the wave is reflected with an efficiency R given by

$$R = \frac{\kappa^2 \sinh^2 sL}{s^2 \cosh^2 sL + (\Delta k/2)^2 \sinh^2 sL} \quad (235)$$

where

$$s^2 = \kappa^2 - (k - q)^2 \quad (236)$$

$$\Delta k = 2(k - q) \quad (237)$$

$$\kappa = \frac{\frac{1}{\sqrt{2}}\pi[(n^e)^2 - (n^o)^2]}{\lambda \sqrt{(n^e)^2 + (n^o)^2}} \quad (238)$$

Note the similarity of Eq. (235) to Eq. (223). The filter efficiency has the same

form as shown in Fig. 38 for the HPDLC Bragg reflection filter. However, for unpolarized incident light, the CLC filter has a peak reflection efficiency of

$$R_{\text{unpolarized}}^{\text{peak}} = \frac{1}{2} \tanh^2 \kappa L \quad (239)$$

Thus, to obtain high rejection efficiency for unpolarized light (or for linearly polarized light) two CLC filters of opposite handedness in tandem are required. When a voltage $V \gg V_{\text{th}}$ is applied, where V_{th} is given by Eq. (130), R is switched to a value near zero.

G. Beam Deflectors and Scanners

Two types of beam deflector or scanner are described. One is called an analog deflector (or continuous scanner), and the second is a digital deflector.

Analog deflectors. Analog deflectors or scanners can be based on prismatic refraction. One example is shown in Fig. 39. An electric field is applied as shown. At zero field, the prism is adjusted so that $\theta_e = \theta_i$. When a field is applied, the index of the prism changes from n to $n + \Delta n$. The exit beam is then deflected by an angle $\theta_i + \delta\theta$, where

$$\delta\theta = 2 \frac{\Delta n}{n} \tan \theta_i \quad (240)$$

With $\tan \theta_i \sim 1$ and $\Delta n \sim (1/2)n^3 r_{\text{eff}} E$, $\delta\theta \sim n^2 r_{\text{eff}} E$. Thus, for an applied field of order 1 kV/cm, the angle scanned is of the order of a few microradians.

A second example of an analog deflector is shown in Fig. 40. In this case, two prisms of KDP are combined, with the optic axes of the two prisms oriented in opposite directions [28]. The field is applied along the optic axis. Incident light is polarized along either the X' or Y' axis (i.e., along one of the principal axes that is induced by the applied field). With zero field, the beam is not deflected. When

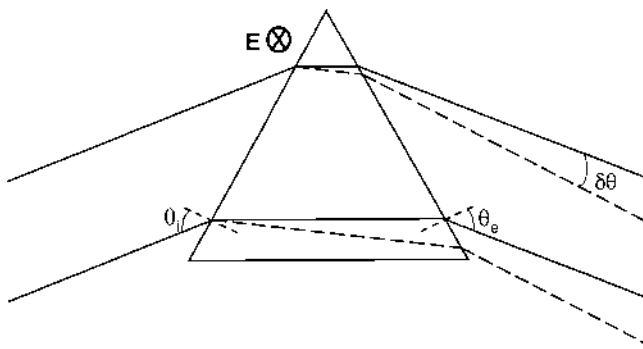


Figure 39 Electro-optic analog beam scanner based on a triangular Pockels prism.

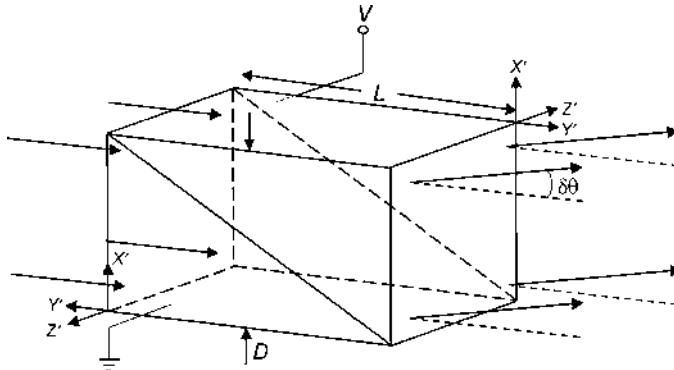


Figure 40 Electro-optic analog beam scanner based on a pair of Pockels prisms with $\bar{4}2m$ symmetry.

a field is applied, the index of the upper prism decreases while the index of the lower prism increases. This produces an effective index gradient that deflects the beam by

$$\delta\theta = (n^\circ)^3 r_{63} E \frac{L}{D} \quad (241)$$

where L is the length of the deflector prisms and D is the aperture. Note that the deflection for this device is $\sim n(L/D)$ larger than that of the first example. However, the deflection is still of the order of a few tens of microradians for a field of order 1 kV/cm. Thus, analog deflectors/scanners can fine tune the beam deflection, but digital deflectors are required to obtain larger deflections.

Digital deflectors. One example of a digital beam deflector is illustrated in Fig. 41. Polarized light is incident on an electro-optic polarization converter (e.g., one of the types discussed earlier in this section), which is followed by a static birefringent beam deflector. There may be a variety of these, but the one illustrated in this example consists of two prisms composed of a uniaxial medium with optic axes oriented orthogonally. With no voltage applied to the polarization converter, the light incident on the deflector is vertically polarized. Thus, the first prism has an index n° while the second prism has a larger index ($\sim n^\circ$ if the beam deflection is only a few degrees). In this case the beam is deflected upward (toward the normal to the interface). When a half-wave voltage is applied to the polarization converter, light incident on the beam deflector is now horizontally polarized. In this case the first prism has a high index (n°) while the second prism has a low index (n°), so the beam is deflected downward (away from the normal to the interface). For a prism angle α (as illustrated in Fig. 41), the exit angles θ_1 and

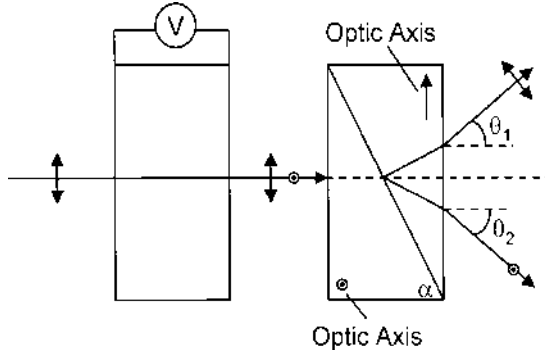


Figure 41 Digital beam scanner using an electro-optic polarization converter followed by a static birefringent beam deflector.

θ_2 are found by solving the following equations:

$$\begin{aligned} \sin \theta_1 &= n^e(\alpha - \theta'_1) \sin(\alpha - \theta'_1) \\ n^e(\alpha - \theta'_1) \sin \theta'_1 &= n^o \sin \alpha \\ \frac{1}{[n^e(\alpha - \theta'_1)]^2} &= \frac{\sin^2(\alpha - \theta'_1)}{(n^o)^2} + \frac{\cos^2(\alpha - \theta'_1)}{(n^e)^2} \end{aligned} \quad (242)$$

and

$$\begin{aligned} \sin \theta_2 &= n^o \sin(\theta'_2 - \alpha) \\ n^o \sin \theta'_2 &= n^e \sin \alpha \end{aligned} \quad (243)$$

A second example of a digital deflector is an unslanted HPDLC transmission grating illustrated in Fig. 42. For a transmission hologram, the diffracted signal wave is on the opposite side of the hologram from which the incident reference wave impinges, and “unslanted” implies that the grating vector is parallel to the hologram substrates. A transmission hologram can theoretically have a diffraction efficiency of 100%. Thus, when no voltage is applied to the HPDLC, the exit beam is deflected (diffracted 100%) by an angle equal to twice the Bragg angle. With a voltage applied such that the index modulation reduces to zero (zero diffraction efficiency), the exit beam will not be deflected [29]. Relatively large deflection angles (ten’s of degrees) can be readily achieved. For s-polarized light, the coupling coefficient is proportional to $\epsilon_{dy} - \epsilon_p$. Since $\epsilon_{dy} \approx \epsilon_p$ for any voltage, the diffraction efficiency of s-polarized light will always be weak. Hence, this beam deflector will only work well for p polarization. For this

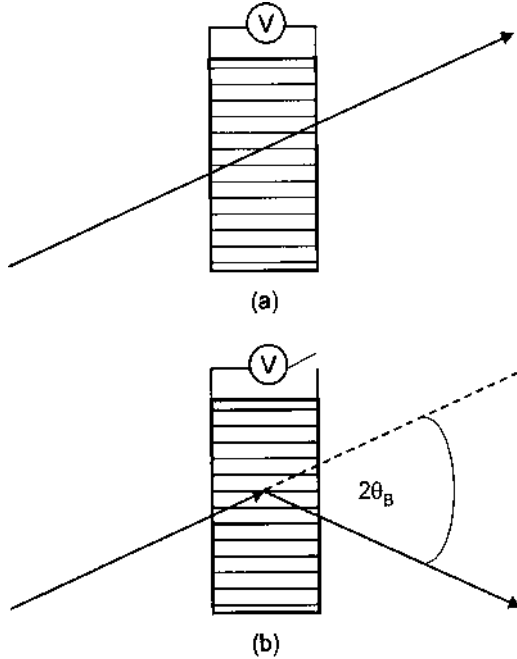


Figure 42 Digital beam scanner using an HPDLC switchable Bragg transmission grating. (a) Transparent state and (b) diffracting state.

case, the coupling coefficient is proportional to $(\epsilon_{dx} - \epsilon_p)\cos^2\theta_B - (\epsilon_{dz} - \epsilon_p)\sin^2\theta_B$, where θ_B is the Bragg angle. The droplet tensor elements are given in Eqs. (149). The diffraction efficiency is given by

$$\eta = \sin^2 \left(\frac{\hat{e}_S \cdot \hat{e}^{(1)} \cdot \hat{e}_R}{2\epsilon_0 n \lambda \cos \theta_B} L \right) \quad (244)$$

where \hat{e}_S (\hat{e}_R) is the polarization unit vector of the signal (reference) wave, and $n = n^\circ$ for s polarization and $n = n^\circ(\theta_B)$ for p polarization.

REFERENCES

1. M. Born and E. Wolfe, *Principles of Optics*, 5th ed., Pergamon Press, New York, 1975.
2. V. I. Smirnov, *Linear Algebra and Group Theory*, Dover Publications, Inc., New York, 1961.

3. A. Yariv and P. Yeh, *Optical Waves in Crystals*, John Wiley, New York, 1984.
4. D. W. Berreman, Optics in stratified and anisotropic media: 4×4 matrix formulation, *J. Opt. Soc. Am.* 62:502 (1972).
5. P. Yeh, Extended Jones matrix method, *J. Opt. Soc. Am.* 72:507 (1982).
6. C. Gu and P. Yeh, Extended Jones matrix method II, *J. Opt. Soc. Am. A* 10:966 (1993).
7. F. Agulló-López, J. M. Cabrera, and F. Agulló-Rueda, *Electrooptics: Phenomena, Materials and Applications*, Academic Press, New York, 1994.
8. I. P. Kaminov, Linear electrooptic materials: tables of linear electrooptic coefficients, *Handbook of Laser Science and Technology*, Volume IV, Optical Materials: Part 2 (M. J. Weber, eds), CRC Press, Boca Raton, 1986, pp. 253–278.
9. T. A. Maldonado and T. K. Gaylord, Electrooptic effect calculations: simplified procedure for arbitrary cases, *Appl. Opt.* 27:5051 (1988).
10. S. M. Kelly and M. O'Neill, Liquid crystals for electro-optic applications, *Handbook of Advanced Electronic and Photonic Materials and Devices*, Volume 7, Liquid Crystals, Display and Laser Materials (H. S. Nalwa, eds), Academic Press, New York, 2001, pp. 2–66.
11. P. Yeh and C. Gu, *Optics of Liquid Crystal Displays*, John Wiley & Sons, Inc., New York, 1999.
12. G. Barbero, and R. Barberi, Elastic properties of nematic liquid crystals, *Physics of Liquid Crystalline Materials* (I. C. Khoo, and F. Simoni, eds), Gordon and Breach, Philadelphia, 1991, pp. 183–213.
13. Merck product literature.
14. S. D. Jacobs, Liquid crystals for laser applications, *Handbook of Laser Science and Technology*, Volume IV, Optical Materials: Part 2 (M. J. Weber, eds), CRC Press, Boca Raton, 1986, pp. 409–465.
15. BDH, Limited product literature.
16. I.-C. Khoo and S.-T. Wu, *Optics and Nonlinear Optics of Liquid Crystals*, World Scientific, Singapore, 1993.
17. P. Drzaic, *Liquid Crystal Dispersions*, World Scientific, Singapore, 1995.
18. A. Golemme, S. Žumer, J. W. Doane, and M. E. Neubert, Deuterium NMR of polymer dispersed liquid crystals, *Phys. Rev. A* 37:559 (1988).
19. B.-G. Wu, J. H. Erdmann, and J. W. Doane, Response times and voltages for PDLC light shutters, *Liq. Cryst.* 5:1453 (1989).
20. G. S. Iannacchione, D. Finotello, L. V. Natarajan, R. L. Sutherland, V. P. Tondiglia, T. J. Bunning, and W. W. Adams, Deuterium NMR and morphology study of polymer dispersed liquid crystal Bragg gratings, *Europhys. Lett.* 36:425 (1996).
21. J. D. Jackson, *Classical Electrodynamics*, 2nd ed., John Wiley & Sons, Inc., New York, 1962.
22. S. Žumer and J. W. Doane, Light scattering from a small nematic droplet, *Phys. Rev. A* 34:3373 (1986).
23. C. F. Bohren and D. R. Huffman, *Absorption and Scattering of Light by Small Particles*, John Wiley & Sons, Inc., New York, 1983.

24. R. L. Sutherland, L. V. Natarajan, V. P. Tondiglia, and T. J. Bunning, Bragg gratings in an acrylate polymer consisting of periodic polymer-dispersed liquid-crystal planes, *Chem. Mater.* 5:1533 (1993).
25. B. E. A. Saleh and M. C. Teich, *Fundamentals of Photonics*, John Wiley & Sons, Inc., New York, 1991.
26. L. Solymer and D. J. Cooke, *Volume Holography and Volume Gratings*, Academic Press, New York, 1981.
27. G. Montemezzan and M. Zgonik, Light diffraction at mixed phase and absorption gratings in anisotropic media for arbitrary geometries, *Phys. Rev. E* 55:1035 (1997).
28. A. Yariv, *Quantum Electronics*, 3rd ed., John Wiley & Sons, Inc., New York, 1989.
29. R. L. Sutherland, V. P. Tondiglia, L. V. Natarajan, T. J. Bunning, and W. W. Adams, Electrically switchable volume gratings in polymer-dispersed liquid crystals, *Appl. Phys. Lett.* 64:1074 (1994).